

Pradeep L. Menezes · Sudeep P. Ingole
Michael Nosonovsky · Satish V. Kailas
Michael R. Lovell *Editors*

Tribology for Scientists and Engineers

 Springer

Tribology for Scientists and Engineers

Pradeep L. Menezes • Sudeep P. Ingole
Michael Nosonovsky • Satish V. Kailas
Michael R. Lovell
Editors

Tribology for Scientists and Engineers

From Basics to Advanced Concepts

 Springer

Editors

Pradeep L. Menezes
Department of Industrial Engineering
University of Wisconsin-Milwaukee
Milwaukee, WI, USA

Sudeep P. Ingole
Department of Mechanical Engineering
Texas A&M University
Galveston, TX, USA

Michael Nosonovsky
Department of Marine Engineering
University of Wisconsin-Milwaukee
Milwaukee, WI, USA

Satish V. Kailas
Department of Mechanical Engineering
Indian Institute of Science
Bangalore, India

Michael R. Lovell
Department of Industrial Engineering
University of Wisconsin-Milwaukee
Milwaukee, WI, USA

ISBN 978-1-4614-1944-0

ISBN 978-1-4614-1945-7 (eBook)

DOI 10.1007/978-1-4614-1945-7

Springer New York Heidelberg Dordrecht London

Library of Congress Control Number: 2013954410

© Springer Science+Business Media New York 2013

This work is subject to copyright. All rights are reserved by the Publisher, whether the whole or part of the material is concerned, specifically the rights of translation, reprinting, reuse of illustrations, recitation, broadcasting, reproduction on microfilms or in any other physical way, and transmission or information storage and retrieval, electronic adaptation, computer software, or by similar or dissimilar methodology now known or hereafter developed. Exempted from this legal reservation are brief excerpts in connection with reviews or scholarly analysis or material supplied specifically for the purpose of being entered and executed on a computer system, for exclusive use by the purchaser of the work. Duplication of this publication or parts thereof is permitted only under the provisions of the Copyright Law of the Publisher's location, in its current version, and permission for use must always be obtained from Springer. Permissions for use may be obtained through RightsLink at the Copyright Clearance Center. Violations are liable to prosecution under the respective Copyright Law.

The use of general descriptive names, registered names, trademarks, service marks, etc. in this publication does not imply, even in the absence of a specific statement, that such names are exempt from the relevant protective laws and regulations and therefore free for general use.

While the advice and information in this book are believed to be true and accurate at the date of publication, neither the authors nor the editors nor the publisher can accept any legal responsibility for any errors or omissions that may be made. The publisher makes no warranty, express or implied, with respect to the material contained herein.

Printed on acid-free paper

Springer is part of Springer Science+Business Media (www.springer.com)

Preface

Tribology is an interdisciplinary field enjoying increased attention in research fields from engineering to life sciences. Despite growing attention towards this field and its demonstrated applications and usefulness, there are not many devoted degree programs focusing on it. In several university education programs specialized courses on topics are offered. As it is not a traditional area of teaching, there are not many textbooks developed for this subject matter. Additionally, the advancement in nanoscience and technologies opened new avenues for higher educational initiatives (graduate programs in nanoscience, nanotechnology, nanomanufacturing, etc.). Many books are focused on advanced topics and easily adopted by the readers who are already exposed to the field. There is growing need for a textbook that can be adopted for undergraduate or graduate classroom and for the professionals newly entered in the field of tribology. The goal of this book is to bridge this gap and serve as tabletop quick reference guide as well as the problem-solving resource.

Early career track professionals and university students need the concise information of various disciplines under the broader area of surface science, tribology, and lubrication science which this book will precisely provide. This book showcases latest knowledge and technologies available in the field that will benefit targeted reader from education, engineering industry, and scientific disciplines including but not limited to mechanical, materials, manufacturing, automotive, aerospace, chemical, and biomedical.

The editors of this book are from the education industry and are closely working on industry problems. Contributors chosen for this book are authoritative expertise in the field and across the world. This book will find a place in middle way between the reference resources such as encyclopedia or handbooks and the regular research books. Twenty-seven chapters are divided into seven distinct sections for the purpose of strategically individuating the major focus of the aspect in a detailed and vivid manner. The unique feature of this book is that each chapter consists of exercise problems and/or case studies that will relate the knowledge gained to the current real-life applications. Due to the unique design of each chapter, this book

serves as a good resource until there is a major breakthrough in the field of surface science and tribology. It consists of 948 total pages with 200 illustrations.

Key Features

- This will be the *book* that serves as textbook and concise reference.
- The case studies and/or solved problems for each chapter are the key factor for the readers.
- The current fundamental understanding, applications, and advancement in the field of surface science, materials and manufacturing, tribology, and lubrication science are elucidated with sufficient schematics and diagrams and serve as a perfect handbook for targeted readers.
- All editors of this book are from the education industry with expertise in the field and are well experienced in publishing and knowledge creation through scientific enquires.

Part I, “*Fundamental Science in Tribology*,” encompasses five chapters which provide basic knowledge on the subject matter that is required to follow the rest of the textbook and quick start in the field of tribology. Chapter 1 (*Fundamentals of Engineering Surfaces*) deals with the basic information about the surfaces and surface textures and presents the quantitative measurements of surfaces. Information on friction and wear, various theories, mechanisms, and factors affecting friction and wear are discussed in Chap. 2 (*Friction and Wear*). When two surfaces interact during relative motion or when at stationary, the forces acting and stresses developed at the interface play a vital role. Chapter 3 covers these aspects of *contact mechanics* in a very vivid manner. Quantitative expression of parameters that define the performance of sliding interfaces is equally important; therefore, we have included this information in Chap. 4 (*Experimental Methods in Tribology*). This chapter describes various test configurations for measurement of tribological parameters. It is well known that heat energy is generated during rubbing of two surfaces; therefore, temperature at these sliding interfaces is one of the important parameters. We have included one devoted chapter for it which is Chap. 5 (*Interface Temperature of Sliding Surfaces*).

Part II, “*Tribology of Engineering Materials*,” is divided into four chapters. These chapters discuss tribological phenomenon for different material systems such as *tribology of metals and alloys* in Chap. 6, *tribology of ceramics and ceramic matrix composites* in Chap. 7, *tribology of metal matrix composites* in Chap. 8, and *coating tribology* in Chap. 9. The metals and alloys differ from the ceramics and thus their tribological performances. When composites are made involving these materials interesting phenomena are observed at their interfaces. Further this knowledge applies to a wider variety of engineering application.

Dry sliding of the materials system discussed in Part II limits their applications. These limitations are often overcome by using external agent as lubrication. Part III, “*Lubrication Science*,” consists of five chapters covering basic information in Chap. 10 (*Fundamentals of Lubrication*). Advanced mechanisms to mitigate higher friction using *self-lubricating graphite-reinforced composites* are discussed

in Chap. 11. Several industrial applications utilize functional particles as lubricating agents. The latest information on this subject is presented in Chap. 12 on *Particle Tribology*. Sometimes usage of liquid lubrication is not permitted at the sliding interfaces; therefore, solid lubrication is used to provide required lubrication which is discussed in Chap. 13 (*Tribology of Solid Lubricants*). Commercial lubrication available poses some serious threat to the environment; therefore, there is worldwide initiative to develop and study sustainable and environmentally friendly lubrication. Readers are provided with the current status on this topic in Chap. 14 (*Tribology of Green Lubricants*).

Focus of Part IV, “*Tribology at Nanometer Length Scale*,” is on the latest field of tribology, i.e., nanotribology and tools required for its study. Chapter 15 (*Nanotribology*) consists of recent development of nanotribology which is different from the conventional tribology with the fact that the surface forces interact differently at nanometer length scale. Special tool requires conducting the study at nanometer length. Techniques to study these issues are included in Chap. 16 (*Surface Probe Techniques*).

As we know the nature has engineering wonders that are yet to understand completely. Understanding the nature’s engineering and applying the knowledge gained to solve real-life problems have gained attentions in recent times and benefited mankind to improve the life. Also, understanding of tribology in biological system has prime importance for example in human joint application. Part V, “*Tribology in Nature*,” deals with information on such topics. Chapter 17, *Biotribology and Human Tribology*, focuses on the human tribology fields, slip-and-fall accidents, hand–object interaction, and biotribology fields, ocular and oral tribology. Chapter 18, *Green and Biomimetic Tribology*, discusses areas and principles of green tribology and current developments in biomimetic materials and surfaces. Chapter 19, *Fundamentals of Linking Tribology and Corrosion for Medical Applications*, describes some fundamental aspects about this new research area and focuses on its significances in biomedical application, namely, orthopedics and dentistry. Chapter 20, *Wear of Biomedical Implants*, is focused on the wear of biomedical implants, its causes and concerns, and critical issues related to these problems, enabling a neophyte to understand the current scenario.

The information on the engineering application of tribology, especially in manufacturing, is covered in Part VI, “*Tribology in Manufacturing*.” This section has four chapter contributions. Chapter 21, *Tribology in Metal Cutting*, reviews the information in terms of process parameters that can affect the performance and have tribological importance, primarily coefficient of friction. When two surfaces interact the thermodynamically favorable condition occurs. Chapter 22, *Tribo-chemistry and Tribo-corrosion*, discusses such parameters that can affect the sliding condition and performance of the sliding surfaces. One of the successful commercial applications of tribological process is discussed in Chap. 23, *Tribology in Chemical–Mechanical Planarization*, and it discusses evolution, roles, and effects of tribology in this important industrial process. Further, Chap. 24, *Tribology in Metal Forming*, introduces the fundamental concept of forming processes and the influence of coefficient friction in metal-forming process.

In the end one of the important applications of tribology in engineering components is described in Part VII, “*Applications and Components.*” Chapter 25, *Tribology in Machine Components*, include concise information on the design and performance of some machine components where tribology is crucial. Chapters 26 and 27 discuss *macroscale and microscale applications in tribology*, respectively.

We thank all the authors for their valuable contributions. We are confident that you will find this book enough of interest to refer for your learning needs and hopefully guide you through your adventures in tribology in years to come.

Milwaukee, WI, USA
Galveston, TX, USA
Milwaukee, WI, USA
Bangalore, India
Milwaukee, WI, USA

Pradeep L. Menezes
Sudeep P. Ingole
Michael Nosonovsky
Satish V. Kailas
Michael R. Lovell

Contents

Part I Fundamental Science in Tribology

1	Fundamentals of Engineering Surfaces	3
	Pradeep L. Menezes, Satish V. Kailas, and Michael R. Lovell	
2	Friction and Wear	43
	Pradeep L. Menezes, Michael Nosonovsky, Satish V. Kailas, and Michael R. Lovell	
3	Contact Mechanics	93
	Robert L. Jackson, Hamed Ghaednia, Hyeon Lee, Amir Rostami, and Xianzhang Wang	
4	Experimental Methods in Tribology	141
	Nicholas X. Randall	
5	Interface Temperature of Sliding Surfaces	177
	R. Arvind Singh	

Part II Tribology of Engineering Materials

6	Tribology of Metals and Alloys	197
	Sudeep P. Ingole	
7	Tribology of Ceramics and Ceramic Matrix Composites	211
	Prasanta Sahoo and J. Paulo Davim	
8	Tribology of Metal Matrix Composites	233
	Pradeep K. Rohatgi, Meysam Tabandeh-Khorshid, Emad Omrani, Michael R. Lovell, and Pradeep L. Menezes	
9	Coatings Tribology	269
	Sudeep P. Ingole	

Part III Lubrication Science

- 10 Fundamentals of Lubrication** 295
Pradeep L. Menezes, Carlton J. Reeves, and Michael R. Lovell
- 11 Self-Lubricating Behavior of Graphite-Reinforced Composites** 341
Pradeep L. Menezes, Carlton J. Reeves, Pradeep K. Rohatgi,
and Michael R. Lovell
- 12 Particle Tribology: Granular, Slurry,
and Powder Tribosystems** 391
C. Fred Higgs III, Martin Marinack Jr., Jeremiah Mpagazehe,
and Randyka Pudjoprawoto
- 13 Tribology of Solid Lubricants** 447
Carlton J. Reeves, Pradeep L. Menezes, Michael R. Lovell,
and Tien-Chien Jen
- 14 Tribology of Green Lubricants** 495
Jagadeesh K. Mannekote, Pradeep L. Menezes, Satish V. Kailas,
and Sathwik Chatra K.R.

Part IV Tribology at Nanometer Length Scale

- 15 Nanotribology** 525
Seung Ho Yang and Eui-Sung Yoon
- 16 Surface Probe Techniques** 555
K. Anantheshwara and M.S. Bobji

Part V Tribology in Nature

- 17 Biotribology and Human Tribology** 583
Kurt E. Beschorner
- 18 Green and Biomimetic Tribology** 605
Michael Nosonovsky, Vahid Hejazi, and Vahid Mortazavi
- 19 Fundamentals of Linking Tribology
and Corrosion (Tribocorrosion) for Medical Applications:
Bio-tribocorrosion** 637
V.A. Barão, C. Sukotjo, and M.T. Mathew
- 20 Wear of Biomedical Implants** 657
P.S. Rama Sreekanth and S. Kanagaraj

Part VI Tribology in Manufacturing

21 Tribology in Metal Cutting 677
 Valentino Anok Melo Cristino, Pedro Alexandre
 Rodrigues Carvalho Rosa, and Paulo António Firme Martins

22 Tribo-chemistry and Tribo-corrosion 729
 Sudeep P. Ingole and John Valdes

23 Tribology in Chemical–Mechanical Planarization 747
 Sukbae Joo and Hong Liang

24 Tribology in Metal Forming 783
 Pradeep L. Menezes, Carlton J. Reeves, Satish V. Kailas,
 and Michael R. Lovell

Part VII Applications and Components

25 Tribology in Machine Components 821
 Satish C. Sharma

26 Macroscale Applications in Tribology 881
 Carlton J. Reeves, Pradeep L. Menezes, Michael R. Lovell,
 and Tien-Chien Jen

27 Microscale Applications in Tribology 921
 Carlton J. Reeves, Pradeep L. Menezes, Michael R. Lovell,
 and Tien-Chien Jen

Erratum E1

Part I
Fundamental Science in Tribology

Chapter 1

Fundamentals of Engineering Surfaces

Pradeep L. Menezes, Satish V. Kailas, and Michael R. Lovell

Abstract Understanding engineered surfaces is very important for solving many scientific problems that involve friction, contact mechanics, heat conduction, electric current conduction, and component design. In this chapter, the fundamentals of engineering surfaces and surface texturing are discussed. Various surface layer types are defined, and techniques for generating and characterizing them are presented. Surface roughness measurement techniques to obtain and define roughness parameters using surface profilometry and optical methods are discussed in detail. Surface textures and structures are then classified in terms of various roughness parameters. Finally, experimental results that demonstrate the influence of surface texture on friction are discussed.

1 Introduction

The word tribology is derived from the Greek word *tribos*, meaning rubbing. Tribology is defined as the science and technology of interacting surfaces in relative motion. It comprises the study of friction, wear, and lubrication. Whenever two solids touch each other—forces of action and reaction are brought into play—a surface interaction occurs. In addition, surface structure changes during interaction. Bits of matter may transfer from one surface to another surface or break away and fall out of the contact region.

P.L. Menezes (✉) • M.R. Lovell
Department of Industrial Engineering, University of Wisconsin-Milwaukee,
Milwaukee, WI 53201, USA
e-mail: menezesp@uwm.edu

S.V. Kailas
Department of Mechanical Engineering, Indian Institute of Science,
Bangalore 560 012, India

2 Surface Layers

The surface of a solid body is the geometrical boundary between the solid and the environment. In addition to surface deviations, the solid surface itself consists of several zones. These zones are extremely important because their properties can be entirely different from the bulk material properties [1]. Tribology is associated with surface and near surface regions. The various surface layers are physisorbed layer, chemisorbed layer, chemically reacted layer, Beilby layer, heavily deformed layer, lightly deformed layer, and the base material. Figure 1.1 shows the schematic diagram of various surface layers.

Physisorbed layer: Physisorbed layer may be formed from the environment on both metallic and nonmetallic surfaces. The most common constituents of adsorbate layers are molecules of water vapor, oxygen, or hydrocarbons from the environment that may be condensed and become physically adsorbed to the solid surfaces. This layer can be either monomolecular (about 0.3 nm thick) or polymolecular. In physisorption, no exchange of electrons takes place between the molecules of the adsorbate and those of the adsorbent. The physisorption process typically involves weak van der Waals forces. It takes very little energy (1–2 kcal/mol) to remove physisorbed species from a solid surface. All surfaces in high vacuum (10^{-8} Pa) are free from physisorbed layers.

Chemisorbed layer: In chemisorption, there is an actual sharing of electrons or electron exchange between the chemisorbed species and the solid surface. The solid surface very strongly bonds to the adsorbed species through covalent bonds. Therefore, it requires a high energy (10–100 kcal/mol) to remove the adsorbed species. The chemisorbed layer is limited to a monolayer.

Chemically reacted layer: All (other than noble) metals and alloys react with oxygen and form oxide layers in air. In other environments, they are likely to form other layers, e.g., nitride, sulfide, and chloride layers are formed when the

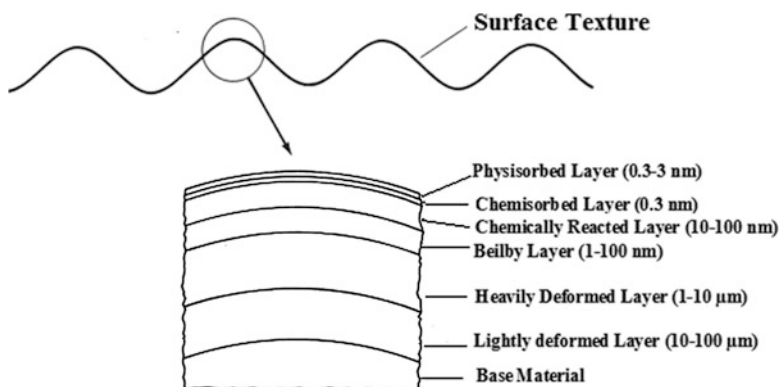


Fig. 1.1 Schematic diagram of various surface layers

surface is exposed to nitrogen, sulfur, and chlorine, respectively. The thickness of the oxide and other chemically reacted layer depends on the reactivity of the materials to the environment, reaction temperature, and reaction time. Typical thickness of these layers ranges from 10 to 100 nm. Oxide layers can also be produced during the machining process. During the machining process, due to rise in temperature, the chemical reaction with the environment is accelerated. The presence of lubricant and additives causes the formation of reaction layers that are important in surface protection of the materials.

Beilby layer: Beilby layer in metals and alloys is produced by melting and surface flow during machining of molecular layers that are subsequently hardened by quenching as they are deposited on the cool underlying material. The layer has an amorphous or microcrystalline structure. The thickness typically ranges from 1 to 100 nm. This layer is present even in super finished components. Careful finishing procedures (lapping or wet polishing) can reduce the thickness of the Beilby layer.

Deformed layer: The metallurgical properties of the surface layer of a metal or alloy can vary markedly from the bulk of the material during surface preparation such as grinding, polishing, or machining operations. The surface layers are plastically deformed with or without a temperature gradient and become highly strained. Sometimes residual stresses are also present. The strained layer is called the deformed (work-hardened) layer and is an integral part of the material itself in the surface region. The deformed layer can also be produced during the machining process. The deformed layer would be more severely strained near the surface. The thickness of the lightly deformed layer ranges from 10 to 100 μm . The thickness of the heavily deformed layer ranges from 1 to 10 μm .

3 Characterization of Surface Layers

Numerous surface analytical techniques are commercially available for the characterization of surface layers:

- The metallurgical properties like grained structure of the deformed layer can be obtained by sectioning the surface, then polishing and etching the sectioned surfaces using conventional metallographic techniques, and finally examining the grained structure of the cross section with the help of a high-magnification optical microscopes (OM) and scanning electron microscopes (SEMs).
- The microcrystalline structure and dislocation density can be studied by preparing thin samples (a few hundred nanometers thick) of cross section and examining them under transmission electron microscopes (TEM).
- The crystal structure of a surface layer can be studied by using X-ray and electron diffraction techniques.

- An elemental analysis of a surface layer can be performed by using an energy-dispersive X-ray spectroscopy (EDS), Auger electron spectroscopy (AES), and electron probe microanalyzer (EPMA) available with most SEMs.
- The chemical analysis can be performed by X-ray photoelectron spectroscopy (XPS), secondary ion mass spectrometry (SIMS), Fourier transform infrared spectroscopy (FTIR), Raman scattering (RS), and nuclear magnetic resonance (NMR).
- The thickness of various layers can be measured by focused ion beam (FIB).

4 Surface Structure

All solid surfaces are rough when studied carefully on at different length scales. Roughness is typically characterized by asperities of varying amplitude and spacing. The distribution of asperities is directional when a finishing process is directional dependent (e.g., turning, milling) and homogeneous for nondirectional finishing process (e.g., lapping, electropolishing, sand blasting). Most engineering surfaces are either isotropic or anisotropic. The surface structure may include roughness, waviness, lay, and flaw. Figure 1.2 shows the schematic diagram of surface structure [2].

Roughness: Roughness is produced by fluctuations of short wavelength characterized by asperities (local maxima) and valleys (local minima) of varying amplitude and spacing.

Waviness: Waviness is the surface irregularities of longer wavelengths. It may result from such factors as machine or workpiece deflections, vibration, chatter, heat treatment, or warping strains.

Lay: Lay is the principal direction of the predominant surface pattern.

Flaws: Flaws are unexpected and unintentional interruptions in the surface structure caused by dislocations and other material defects.

5 Surface Texturing

Surface texture is the local deviations of a surface from a perfectly flat plane. The measure of the surface texture is generally determined in terms of its roughness, waviness, and form.

There are many ways to produce surface textures. They include grinding, polishing, cutting, lapping, blasting, honing, electric discharge machining (EDM), milling, lithography, and laser texturing. Surface textures are usually characterized in terms of roughness parameters using a profilometer. Figure 1.3 shows the three-dimensional optical profilometer images of various surfaces. Figure 1.3a shows an

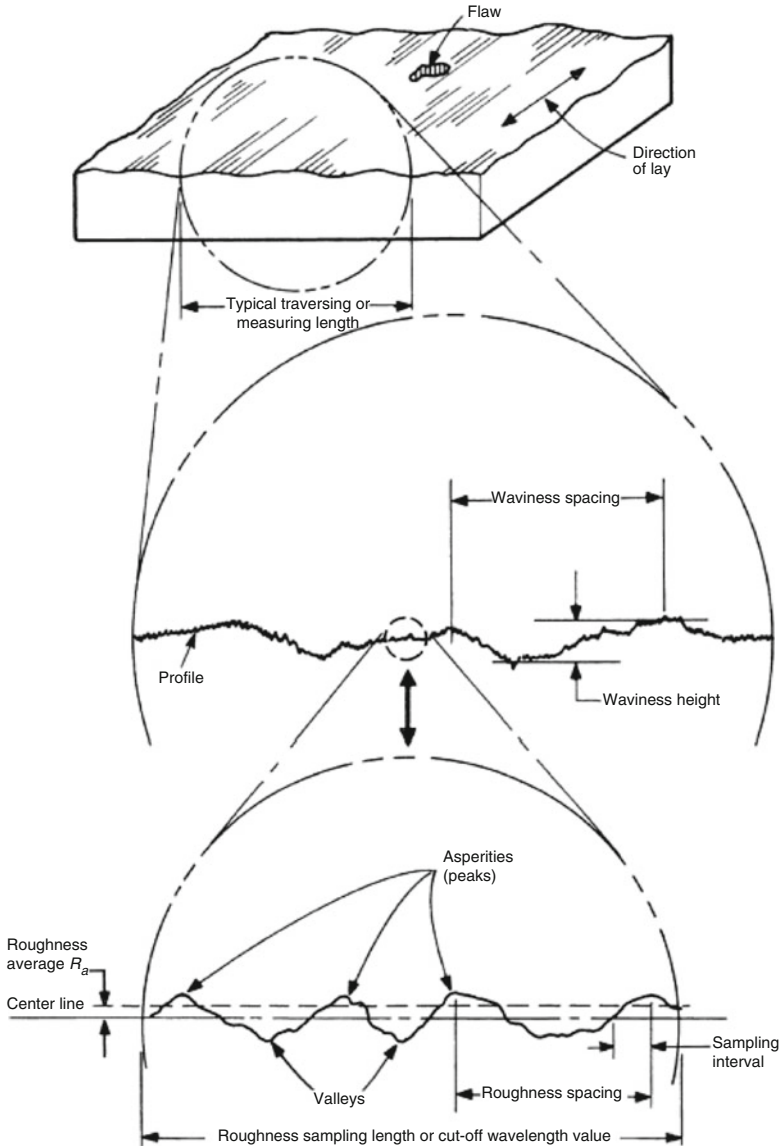
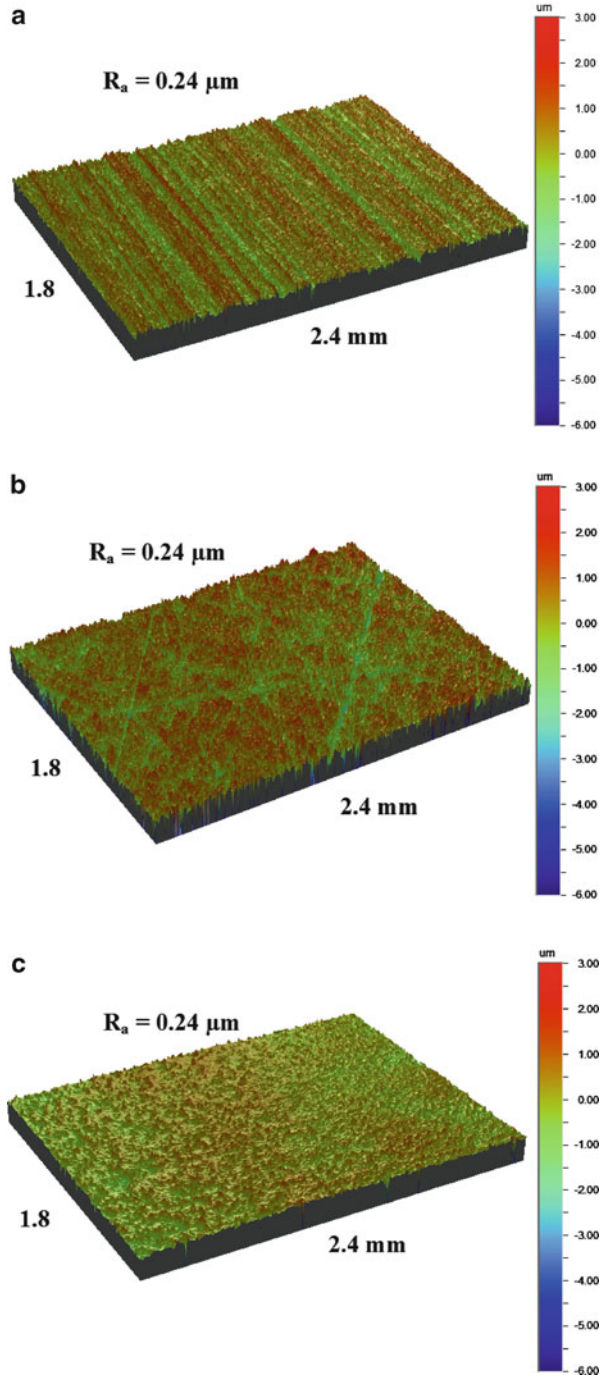


Fig. 1.2 Schematic diagram of surface structure [2]

anisotropic surface that was ground in a unidirectional fashion using dry emery papers, Fig. 1.3b shows a surface which is essentially isotropic and was ground in random fashion using dry emery papers, and Fig. 1.3c shows a surface which is isotropic and was polished in random fashion using different abrasive powders in the wet grinding conditions.

Fig. 1.3 Three-dimensional optical profilometer images of various kinds of surfaces



6 Classification of Surface Roughness Parameters

Surface roughness has been the subject of experimental and theoretical investigation for many decades. Surface roughness basically refers to the variations in the height of the surface relative to a reference plane. It is measured either along a single line (2D) profile or along a set of parallel line profiles (3D) as in the case of a surface map.

A real surface geometry is so complicated that a finite number of parameters cannot provide a full description. If the number of parameters used is increased, a more accurate description can be obtained. This is one of the reasons that new parameters are introduced for surface evaluation. Surface roughness parameters are normally categorized into three groups according to their functionality [3]. These groups are defined as:

- Amplitude parameters
- Spacing parameters
- Hybrid parameters

Amplitude parameters: Amplitude parameters are used to measure the vertical characteristics of the surface deviations. They are the most important parameters to characterize surface textures. Table 1.1 presents some examples of amplitude roughness parameters.

Spacing parameters: The spacing parameters are those which measure the horizontal characteristics of the surface deviations. Like roughness amplitude, the spacing of the roughness peaks is equally important. Table 1.2 presents some examples of spacing roughness parameters.

Hybrid parameters: Hybrid parameters are a combination of the vertical and horizontal characteristics of the surface deviations (i.e., combinations of amplitude and spacing roughness parameters). Any changes, which occur in either amplitude or

Table 1.1 Amplitude roughness parameters

Amplitude parameters	Description
R_a	Average roughness
R_q	Root-mean-square roughness
R_p	Maximum height of peaks
R_v	Maximum depth of valleys
R_t	Maximum height of the profile
R_{sk}	Skewness
R_{ku}	Kurtosis
R_{pm}	Mean height of peaks
R_{vm}	Mean depth of valleys
R_z	Ten-point height

Table 1.2 Spacing roughness parameters

Spacing parameters	Description
P_c	Peak count
S	Mean spacing of adjacent local peaks
S_m	Mean spacing at mean line

Table 1.3 Hybrid roughness parameters

Hybrid parameters	Description
Δ_a	Mean slope of the profile
Δ_q	RMS slope of the profile
λ_a	Average wavelength
λ_q	RMS wavelength
R_k	Core roughness depth
R_{pk}	Reduced peak height
R_{vk}	Reduced valley depth
Mr1	Peak material component
Mr2	Valley material component

spacing, may have effects on the hybrid property. Hybrid parameters are considered to be more powerful than a parameter solely based on amplitude or spacing to characterize the surface texture. Table 1.3 presents some examples of hybrid roughness parameters.

Different manufacturing processes produce different surface textures. Specific applications of engineered materials require different surface textures. Surface roughness parameters are therefore different and wide ranging. Each of these parameters indicates a particular property of the surface, and it could be the most important for a particular application. Figure 1.4 shows the surface roughness profile and surface roughness values recorded for a unidirectional surface. Figure 1.5 shows the surface profiles of anisotropic and isotropic surfaces in the x and y directions. It can be seen that the roughness values (e.g., R_a and R_q) and profile shapes are the same in x and y directions for the isotropic surfaces (Fig. 1.5b), whereas it is different for the anisotropic surfaces (Fig. 1.5a).

7 Various Roughness Parameters

7.1 Amplitude Parameters

Average roughness (R_a): This roughness parameter is also known by center line average (CLA) and arithmetic average (AA). It is defined as the arithmetic mean of the absolute values of vertical deviation from the mean line through the profile [4]. This parameter is defined as follows in (1.1):

$$R_a = \frac{1}{n} \sum_{i=1}^n |z_i - \bar{z}| \quad (1.1)$$

Here, n is the number of data points on the profile, and z and \bar{z} are the data points on the profile and the average, respectively. The mean line is the line such that the area between the profile and the mean line above the line is equal to that below the mean line. This is shown in Fig. 1.6.

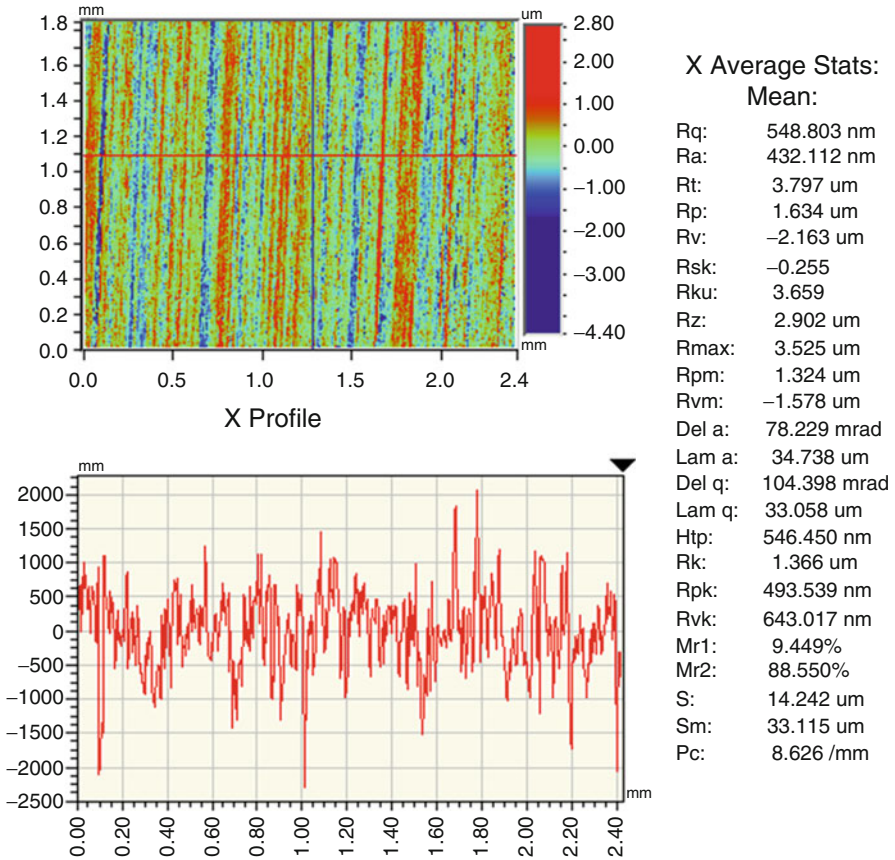


Fig. 1.4 Surface roughness profile and roughness values recorded for a unidirectional surface using an optical profilometer

R_a is the most universally used roughness parameter for general quality control. Historically, R_a was one of the first parameters used to quantify surface texture. This parameter is easy to define, easy to measure, and useful for detecting general variations in overall surface height characteristics. Unfortunately, R_a may be misleading in that many surfaces with grossly different features (e.g., ground vs. polished) may have the same R_a , but function quite differently. R_a only quantifies the “absolute” magnitude of the surface heights (see Fig. 1.7) and is insensitive to the spatial distribution of the surface heights. R_a is also insensitive to the “polarity” of the surface texture in that a deep valley or a high peak will result in the same R_a value.

Various surface profiles with same R_a : It is possible for surfaces of widely varying profiles with different frequencies and shapes to have the same R_a values (see Fig. 1.3). R_a fails to distinguish between a sharp spiky profile and a gently wavy profile. Figure 1.8 shows the various 2D profiles that can have the same R_a values.

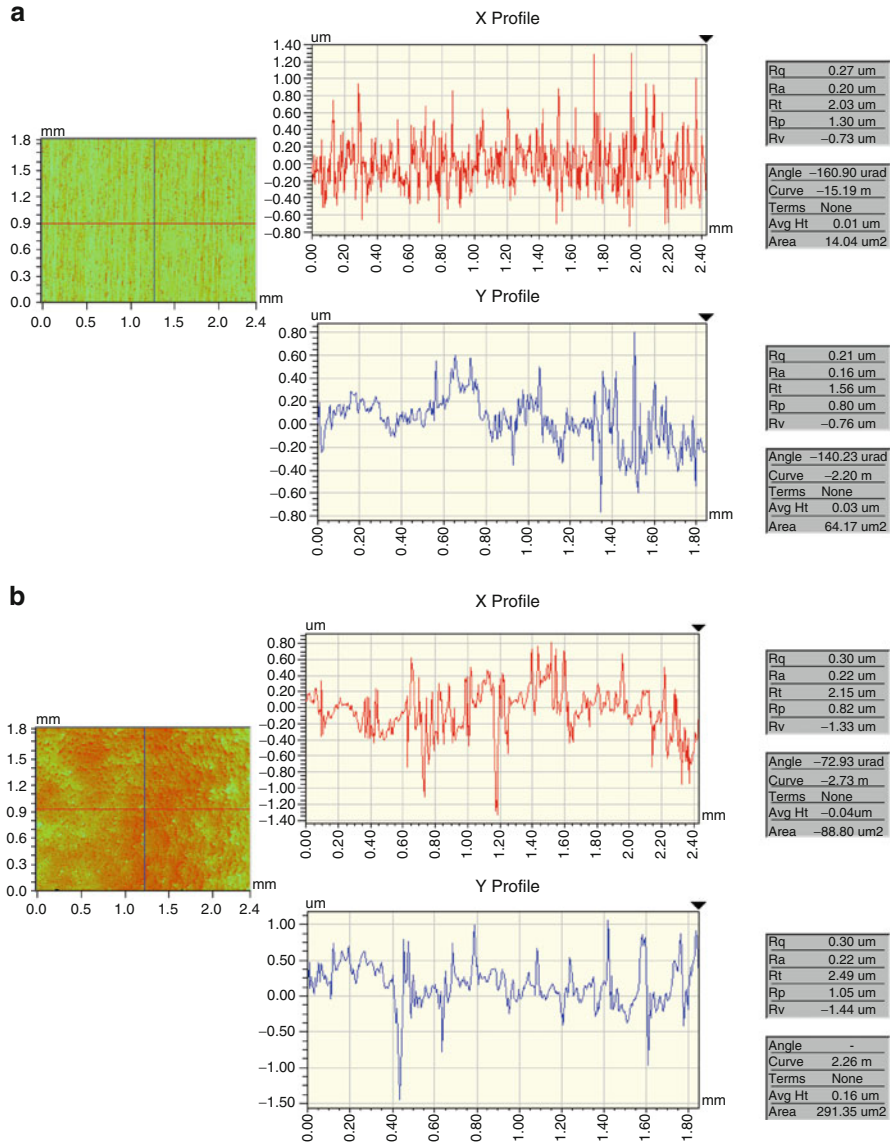


Fig. 1.5 Surface profiles of (a) anisotropic and (b) isotropic surfaces

R_a values for various surfaces: *R_a* value of a surface profile depends on its manufacturing method. *R_a* values for various surfaces are as follows:

- Rough casting: >10 μm
- Coarse machining: 3–10 μm
- Fine machining: 1–3 μm

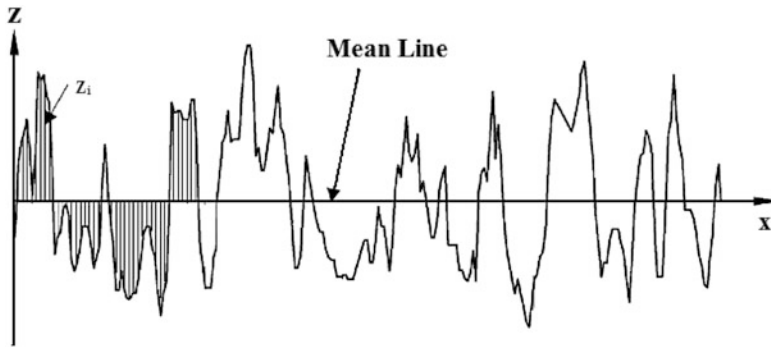


Fig. 1.6 Surface profile used to calculate the roughness R_a value

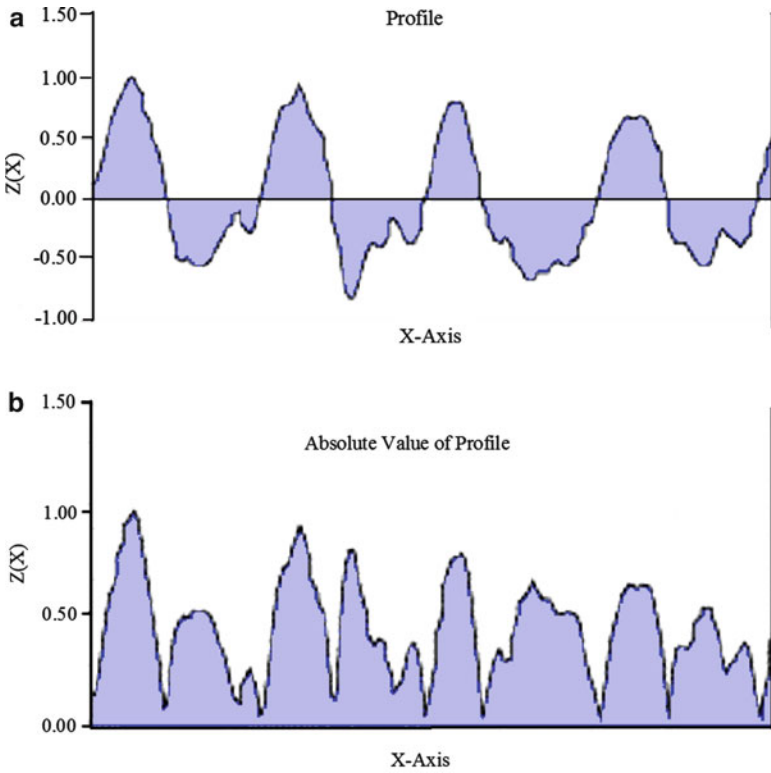
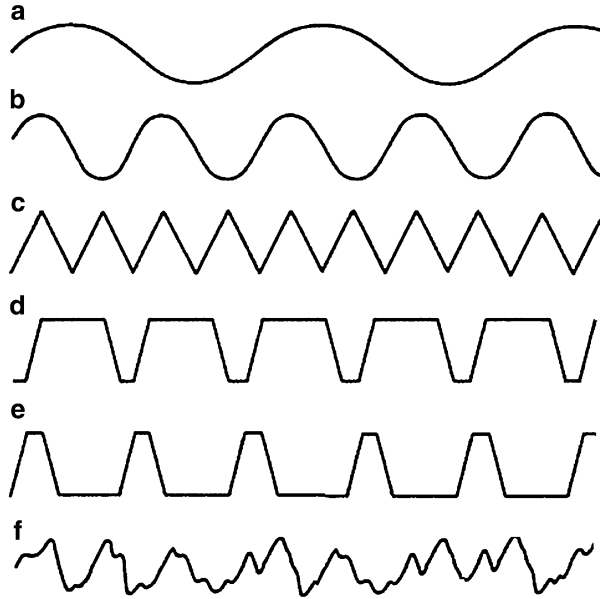


Fig. 1.7 Measurement of R_a value

Fig. 1.8 Various surface profiles having the same R_a values



- Grinding and polishing: 0.2–1 μm
- Lapping: 0.02–0.4 μm

Root-mean-square roughness (R_q): R_q is the standard deviation of the distribution of surface heights. This parameter is also known as variance (σ) or RMS. R_q is defined as the square root of the arithmetic mean of the square of the vertical deviation from the mean line. It is defined as follows in (1.2):

$$R_q = \sqrt{\frac{1}{n} \sum_{i=1}^n (z_i - \bar{z})^2} \quad (1.2)$$

Here, n is the number of data points on the profile, and z and \bar{z} are the data points on the profile and the average, respectively.

R_q is very similar to R_a and will usually correlate with R_a . Like R_a , a series of high peaks or a series of deep valleys of equal magnitude will produce the same R_q value. The R_q value is also insensitive to the spatial distribution of the surface heights. Because height values are squared in the calculation, the RMS roughness statistics are more sensitive to peaks and valleys than average roughness statistics (see Fig. 1.9).

Skewness (R_{sk}): R_{sk} is used to measure the symmetry of the profile about the mean line. The skewness parameter can be used to differentiate between surfaces which have different shapes and have the same value of R_a . It can be defined as follows in (1.3):

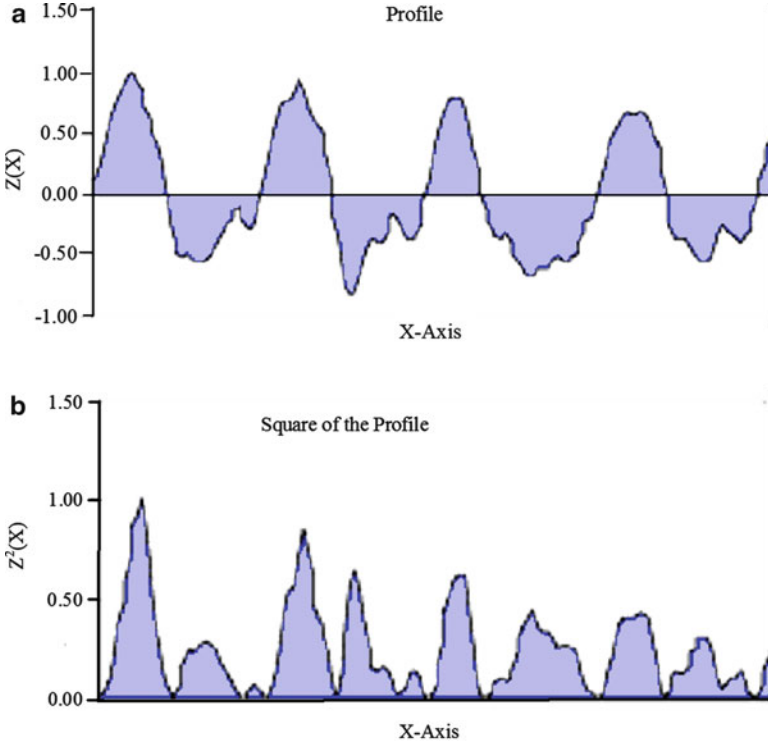


Fig. 1.9 Measurement of R_q value

$$R_{sk} = \frac{1}{nR_q^3} \sum_{i=1}^n (z_i - \bar{z})^3 \tag{1.3}$$

Profiles with high peaks have positive skewness. Profiles with deep scratches have negative skewness. Turning, EDM produces positive skewed surfaces. Milling, honing, and grinding produce negative skewed surfaces. Figure 1.10 shows two profiles that have the same R_a values but they have different shapes.

Skewness is similar to a mean-cubed roughness. Points farther from the mean surface level when raised to powers of 3 have proportionately more weight than those closer to the mean surface level. Since the height values are “cubed” prior to the integration/averaging, the polarity of the surface is maintained (see Fig. 1.11). Thus, a surface with predominantly deep valleys will tend to have a negative skew, whereas a surface comprised predominantly of peaks will have a positive skew. The R_{sk} parameter does not provide information about the spatial distribution of the texture and thus suffers the same limitations as R_a and R_q . R_{sk} may be used to quantify the symmetry of the surface as it may relate to various applications such as conductivity and lubricant retention.

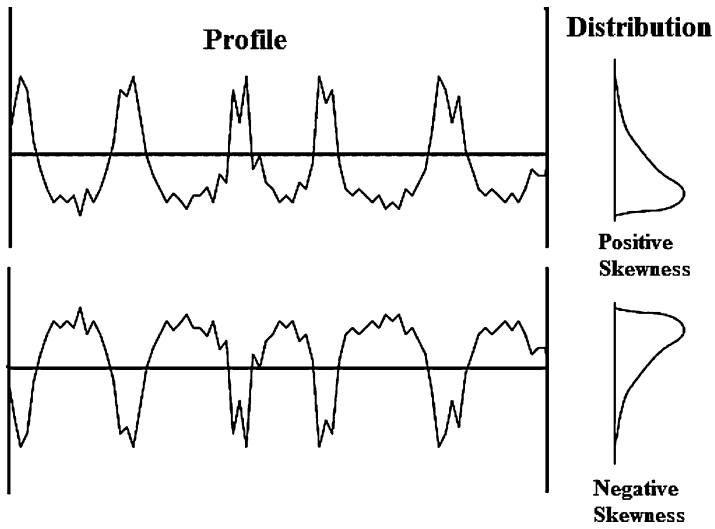


Fig. 1.10 Two profiles with the same R_a value but have different shapes

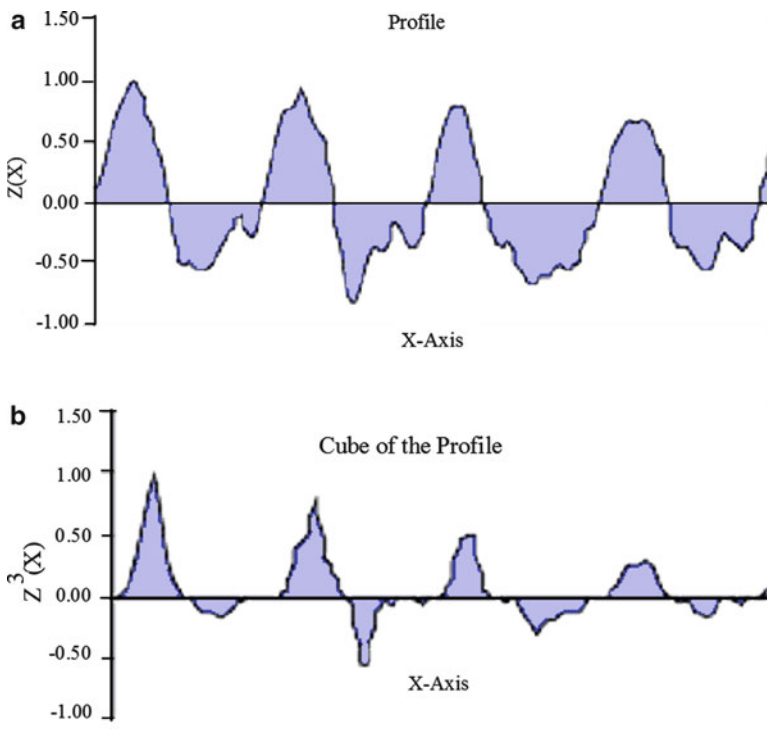
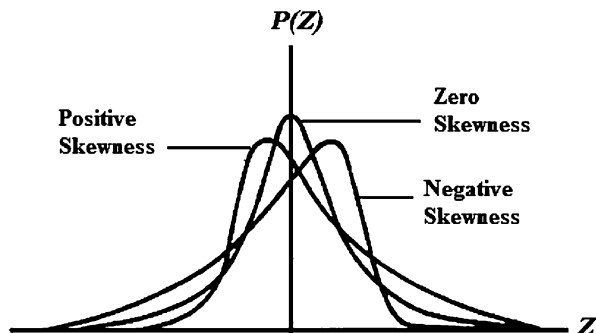


Fig. 1.11 Measurement of R_{sk} parameter

Fig. 1.12 Probability density function with different skewness values



Another way of statistical treatment of a surface profile is to consider the probability distribution function of the height Z . It is denoted by $P(z)$ and is obtained by plotting the number of occurrences of a particular value of Z in the data against the value of Z and normalizing the best fit curve to the data so that the total area enclosed by the distribution curve is unity. The distribution function for most real surfaces is in the form of a bell-shaped curve and can be described approximately by a Gaussian distribution. Figure 1.12 shows a Gaussian distribution function as well as distribution function with various skewness values. A surface with a Gaussian distribution has peaks and valleys distributed evenly about the mean. A surface with positive value of skewness has a wider range of peak heights that are higher than the mean. A surface with negative value of skewness has more peaks with heights close to the mean as compared to a Gaussian distribution. In practice, many engineering surfaces follow symmetrical Gaussian height distribution [5].

Kurtosis (R_{ku}): R_{ku} is used to measure the sharpness of the profile about the mean line. It provides information about the distribution of spikes above and below the mean line [4]. This parameter can be defined as follows in (1.4):

$$R_{ku} = \frac{1}{nR_q^4} \sum_{i=1}^n (z_i - \bar{z})^4 \quad (1.4)$$

The profile generating for the kurtosis is shown in Fig. 1.13. Spiky surfaces have a high kurtosis value ($R_{ku} > 3$), bumpy surfaces have a low kurtosis ($R_{ku} < 3$), and perfectly random surfaces have a kurtosis of 3 (see Fig. 1.14). The kurtosis parameter can be used to differentiate between surfaces, which have different shapes and have the same value of R_a (see Fig. 1.15). R_{ku} characterizes the anomalies in the surface height distributions in that a normally distributed surface texture would tend to have an R_{ku} of 3. When the surface texture is composed of non-normally distributed high peaks or deep valleys, the R_{ku} becomes very large (e.g., 23). When the surface is composed of a slowly varying, “rolling” hill-type texture, the R_{ku} will be less than 3. R_{ku} might be used to identify the presence of surface defects and inordinate peaks or valleys.

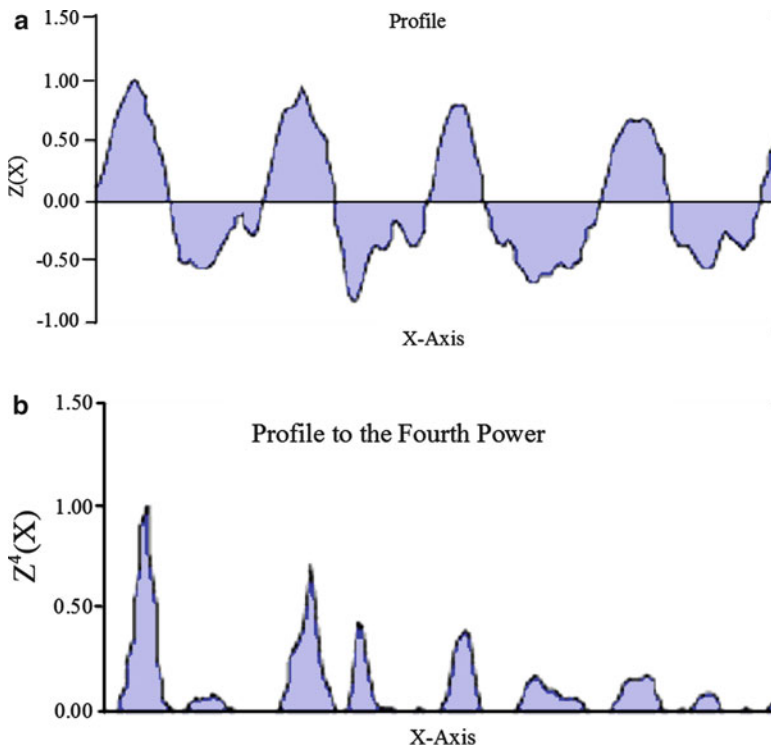
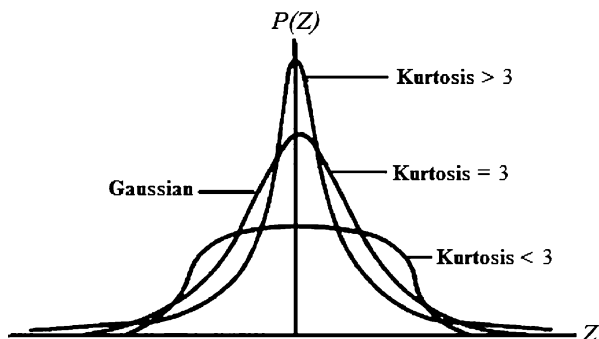


Fig. 1.13 Measurement of R_{ku} parameter

Fig. 1.14 Probability density function with different kurtosis values



Moments of distribution: The shape of the distribution function may be quantified by means of the moments of the distribution. The first moment m_1 represents the R_a . The second moment m_2 is equal to the variance of the distribution (σ^2). It was shown that R_q/R_a for a Gaussian distribution comes out to be nearly 1.25. The third

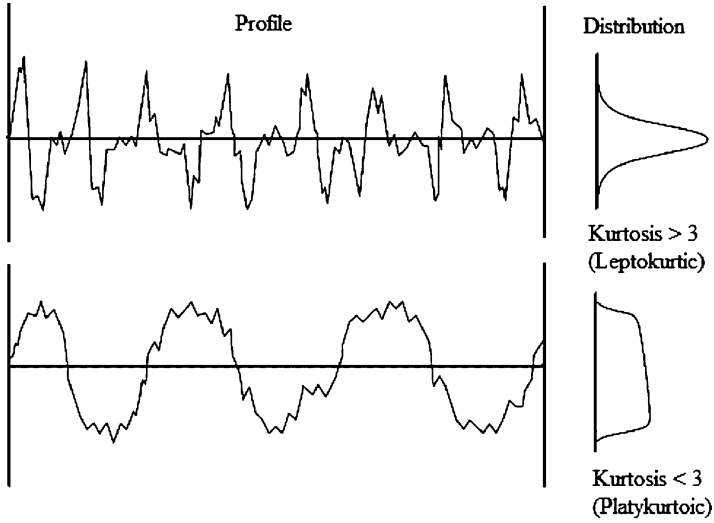


Fig. 1.15 Two profiles with the same R_a value but have different shapes

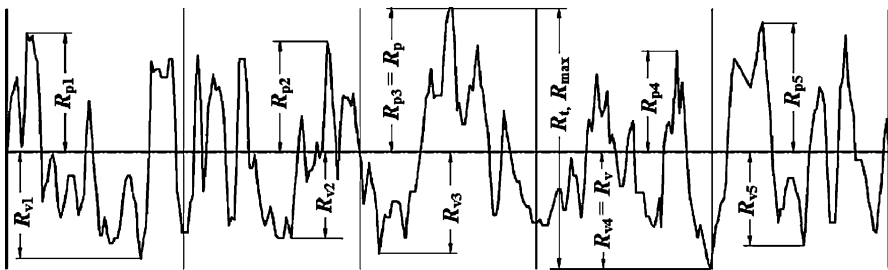


Fig. 1.16 Profile showing the method of calculating various roughness parameters such as R_p , R_v , and R_t [3]

moment m_3 in normalized form gives the skewness. The fourth moment m_4 in normalized form gives the kurtosis. It is expressed as follows:

- First moment (m_1) = R_a
- Second moment (m_2) = R_q
- Third moment (m_3) = R_{sk}
- Fourth moment (m_4) = R_{ku}

Maximum height of peaks (R_p): R_p is used to measure the maximum height of the profile above the mean line. It is the height difference between the mean line and the highest point over the evaluation length (see Fig. 1.16). Because R_p is a single extreme height value, it is not a very repeatable parameter. It may be a true peak or it may be a particle of dust.

Maximum depth of valleys (R_v): R_v is used to measure the maximum depth of the profile below the mean line. It is the height difference between the mean line and the lowest point over the evaluation length (see Fig. 1.16). The valleys in a surface provide information about how a part might retain a lubricant. Because R_v is a single extreme depth value, it is not a very repeatable parameter. It may be a true valley or it may be a scratch.

Maximum height of the profile (R_t): R_t is used to measure the peak-to-valley difference calculated over the entire measured array. It is defined as the vertical distance between the highest peak and the lowest valley along the assessment length of the profile, i.e., $R_t = R_p + R_v$. R_t is sensitive to high peaks and deep valleys, some of which may be stray particles, flaws, dents, or scratches.

Mean height of peaks (R_{pm}): R_{pm} is defined as the mean of the maximum height of peaks (R_p) obtained for each sampling length of the assessment length. This parameter can be calculated from the following equation in (1.5):

$$R_{pm} = \frac{1}{n} \sum_{i=1}^n R_{pi} \quad (1.5)$$

In Fig. 1.16, $R_{pm} = (R_{p1} + R_{p2} + R_{p3} + R_{p4} + R_{p5})/5$. Here, several peak heights are averaged. This makes the value more repeatable than R_p .

In many tribological applications, height of the highest asperities above the mean line is an important parameter because damage of the interface may be done by the few high asperities present on one of the two surfaces.

Mean depth of valleys (R_{vm}): R_{vm} is defined as the mean of the maximum depth of valleys (R_v) obtained for each sampling length of the assessment length. This parameter can be calculated from the following equation (1.6):

$$R_{vm} = \frac{1}{n} \sum_{i=1}^n R_{vi} \quad (1.6)$$

In Fig. 1.16, $R_{vm} = (R_{v1} + R_{v2} + R_{v3} + R_{v4} + R_{v5})/5$. Here, several valley depths are averaged. This makes the value more repeatable than R_v .

Ten-point height (R_z): R_z is defined as the difference in height between the average of the five highest peaks and the five lowest valleys in the assessment length of the profile. The following equation (1.7) is used for calculating R_z parameter:

$$R_z = \frac{1}{n} \left(\sum_{i=1}^n R_{pi} - \sum_{i=1}^n R_{vi} \right) \quad (1.7)$$

R_z has the advantage over a peak-to-valley height (R_t) in that more than two points on the profile contribute to the value. The R_z calculation reduces the effects of odd scratches or nontypical irregularities.

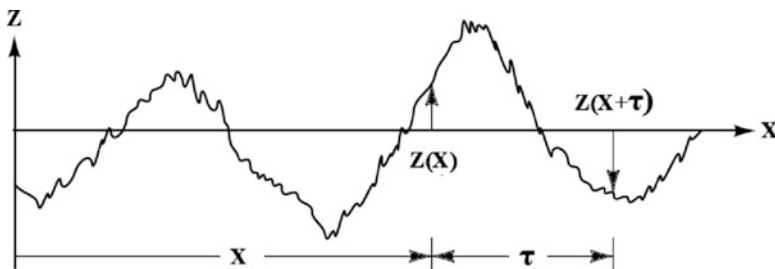


Fig. 1.17 Profile to calculate autocovariance function

Autocovariance function: Autocovariance function (ACVF) is one of the statistical measures to describe the spatial arrangement of a surface. It is generated from a profile that is multiplied by itself for successively larger offset (lag length) in the profile direction.

As shown in Fig. 1.17, ACVF or $R(\tau)$ is defined as in (1.8):

$$R(\tau) = \lim_{L \rightarrow \infty} \frac{1}{L} \int_0^L Z(x)Z(x+\tau)dx \tag{1.8}$$

where τ is the spatial distance (m), L is the sampling length (m), and Z is the height of the profile along “x” direction (m).

Autocorrelation function: Autocorrelation function (ACF) is a mathematical representation of the degree of similarity between a given time series and a lagged version of itself over successive time intervals. It is the same as calculating the correlation between two different time series, except that the same time series is used twice—once in its original form and once lagged one or more time periods.

ACF or $\rho(\tau)$ is defined as

$$\rho(\tau) = \frac{R(\tau)}{R_q^2} \tag{1.9}$$

Sometimes $\rho(\tau)$ is defined as $\rho(\tau) = e^{-\tau/\beta^*}$.

β^* can be calculated from Fig. 1.18 where the 10 % of $\rho(\tau)$ intersects the curve to a value of $2.3\beta^*$.

7.2 Spacing Parameters

Peak count (P_c): P_c is defined as the number of local peaks, which is projected through a selected band located above and below the mean line by the same distance. The boundary lines are located parallel to and equidistant from the profile mean line and are set by the operator for each application. The number of peak count is determined along the assessment length, and the result is given in peaks

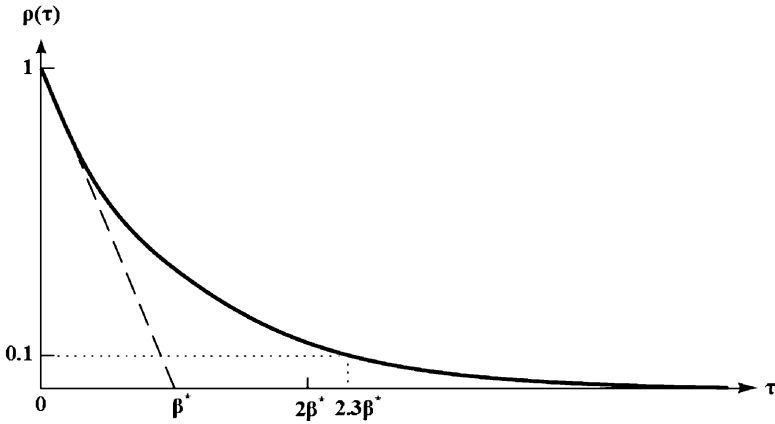


Fig. 1.18 Method of calculating the correlation length β^*

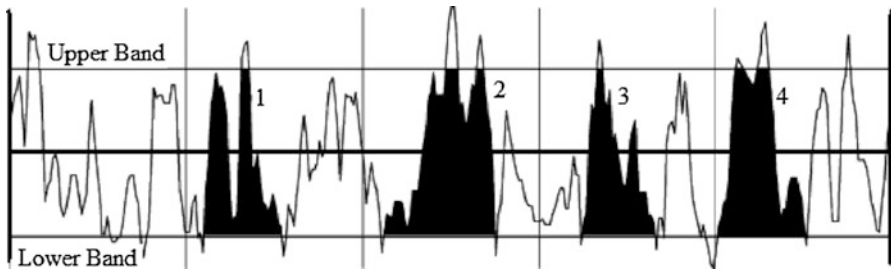


Fig. 1.19 Calculating peak count parameter within a selected band [3]

per millimeter. If the assessment length is less than 1 mm, the result should be multiplied by a factor to get the peak count per millimeter. As shown in Fig. 1.19, peak count is determined only for the closed areas of the profile in which the profile intersects each the lower and upper bands in at least two points. By controlling the roughness peak spacing, it is possible to obtain better bonding of finishes, more uniform plating finishes, and reduced risks of crack formation during drawing or forming operations. Peak spacing is also an important factor in the performance of friction surfaces such as a brake drum.

Mean spacing of adjacent local peaks (S): S is defined as the average spacing of adjacent local peaks of the profile measured along the assessment length (see Fig. 1.20). The local peak is defined as the highest part of the profile measured between two adjacent minima and is only measured if the vertical distance between the adjacent peaks is greater than or equal to 10 % of the R_t of the profile. This parameter can be calculated from the following equation:

$$S = \frac{1}{n} \sum_{i=1}^n S_i \tag{1.10}$$

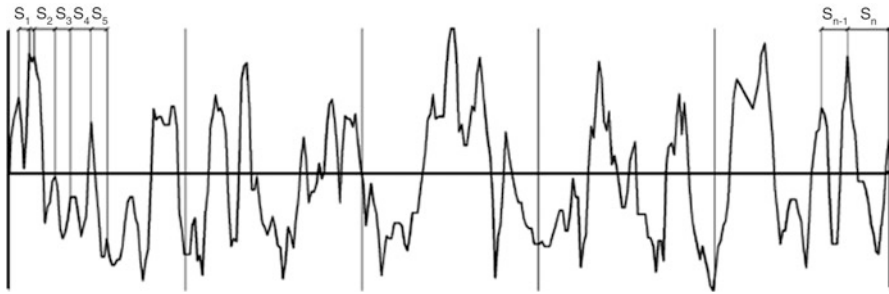


Fig. 1.20 Calculating the mean spacing of adjacent local peaks [3]

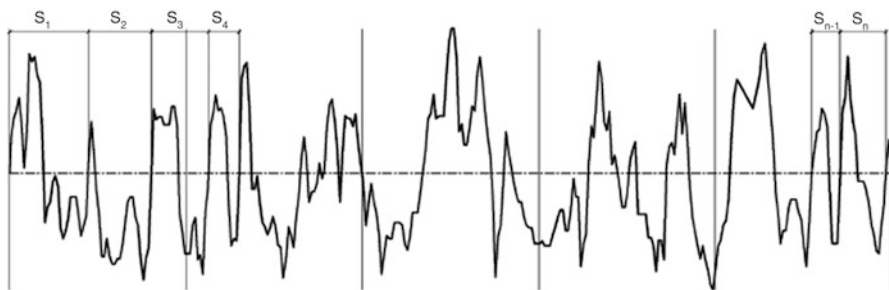


Fig. 1.21 Calculating the mean spacing at mean line [3]

where n is the number of local peaks along the profile.

Mean spacing at mean line (S_m): S_m is defined as the mean spacing between profile peaks at the mean line measured along the assessment length. The profile peak is the highest point of the profile between upwards and downwards crossing the mean line. Figure 1.21 shows the method to measure the mean spacing at mean line parameter. This parameter can be calculated from the following equation:

$$S_m = \frac{1}{n} \sum_{i=1}^n S_i \tag{1.11}$$

where n is the number of profile peaks at the mean line.

Difference between S and S_m : The difference between the two types of mean spacing parameters, S and S_m , is that the first parameter is measured at the height peaks of the profile, while the second parameter is measured at the intersection of the profile with the mean line. S provides information about the distance between peaks spaced closely together, while S_m provides information about the distance between peaks spaced farther apart. Useful applications include characterizing the spacing of texture on a hard disk and the effect of abrasive during polishing.

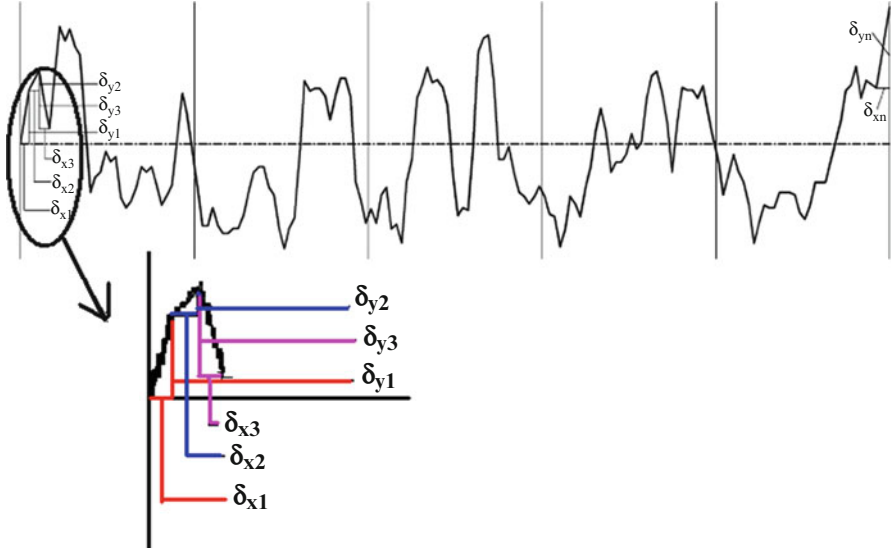


Fig. 1.22 Calculating the mean slope of the profile at the mean line

7.3 Hybrid Parameters

Mean slope of the profile (Δ_a): Δ_a is defined as the mean absolute profile slope over the assessment length. This parameter can be calculated by calculating all slopes between each two successive points of the profile and then calculating the average of these slopes (see Fig. 1.22). The mathematical and numerical formulas for calculating the mean slope parameter are as follows:

$$\Delta_a = \frac{1}{L} \int_0^L \left| \frac{dy}{dx} \right| \cdot dx \tag{1.12}$$

$$\Delta_a = \frac{1}{n-1} \sum_{i=1}^{n-1} \frac{\delta_{yi}}{\delta_{xi}} \tag{1.13}$$

RMS slope of the profile (Δ_q): This parameter is the root-mean-square of the mean slope of the profile. The mathematical and numerical formulas for calculating this parameter are as follows:

$$\Delta_q = \sqrt{\frac{1}{L} \int_0^L (\theta(x) - \theta)^2 dx} \quad \text{where} \quad \theta = \frac{1}{L} \int_0^L \theta(x) dx \tag{1.14}$$

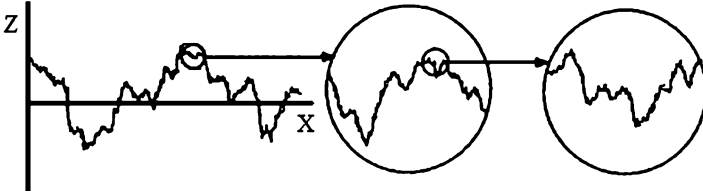


Fig. 1.23 Self-similarity of the profile at various magnifications

$$\Delta_q = \sqrt{\frac{1}{n-1} \sum_{i=1}^{n-1} \left(\frac{\delta_{yi}}{\delta_{xi}} - \theta_m \right)^2} \quad \text{where} \quad \theta_m = \frac{1}{n-1} \sum_{i=1}^{n-1} \left(\frac{y_i - y_{i-1}}{x_i - x_{i-1}} \right) \quad (1.15)$$

Average wavelength (λ_a): The average wavelength parameter is a measure of the spacing between local peaks and valleys, taking into consideration their relative amplitude and individual spatial frequencies. This parameter can be calculated from the following equation:

$$\lambda_a = \frac{2\pi R_a}{\Delta_a} \quad (1.16)$$

where R_a is the arithmetic average and Δ_a is the mean slope of the profile.

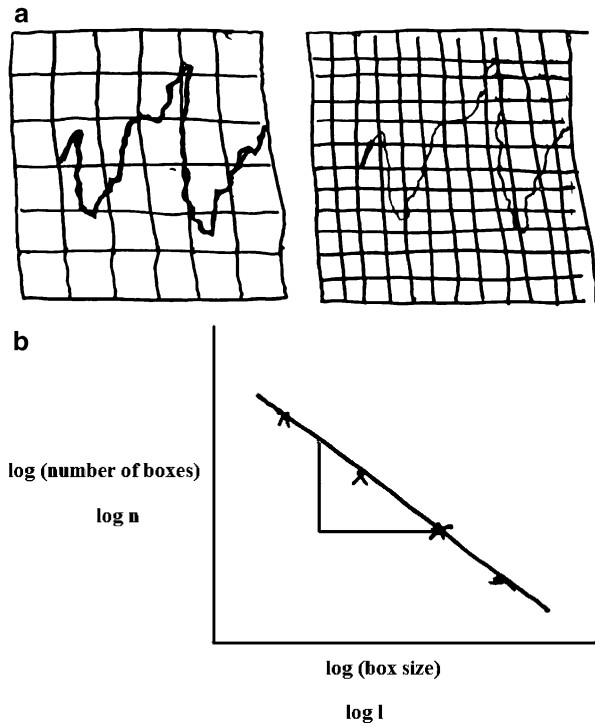
RMS wavelength (λ_q): This parameter is similar to the average wavelength parameter. It is defined as the root mean of the measure of the spacing between local peaks and valleys, taking into consideration their relative amplitudes and individual spatial frequencies. This parameter can be calculated from the following equation:

$$\lambda_q = \frac{2\pi R_q}{\Delta_q} \quad (1.17)$$

7.4 Fractal Dimension (FD)

The deviation of a surface from its mean plane is assumed to be a random process, which is characterized by the statistical parameters such as the variance of the height, the slope, and the curvature. Surface topography is a nonstationary random process; variance of the height distribution is related to the sampling length and hence is not unique for a particular surface. Most of surface structure has complicated shapes that cannot be explained by the Euclidean geometry. These shapes occur repetitively even when they are observed under different magnifications (Fig. 1.23)—this is called self-similarity. The degree of complexity of a surface shape can be represented by a value called fractal dimension [4, 6]; a higher degree of complexity shows a bigger value. Fractal refers to a structure having self-similarity. Thus, a new geometry that can describe the structural irregularities and complexities of the natural system, fractal is widely used to explain the natural substance. The variance of slope and curvature depend strongly on the resolution of the roughness-measuring instrument and are

Fig. 1.24 Calculation of fractal dimension using box counting method



therefore not unique. It is therefore necessary to characterize rough surfaces by intrinsic parameters, which are independent of all scales of roughness. So, multiscale characterization methods need to be developed. There are many ways of calculating fractal dimensions [4]. These methods are:

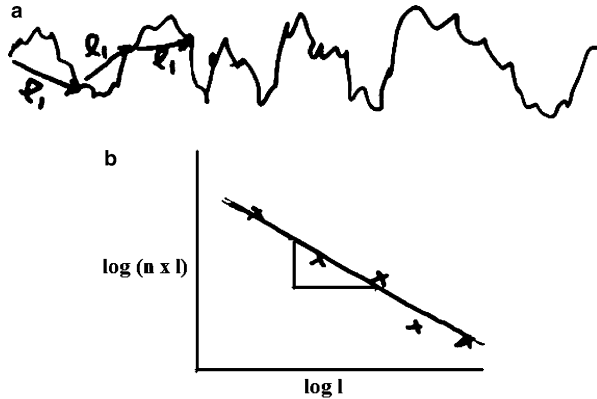
- The rectangular box/cell counting
- The compass/cover
- The variation
- The power spectrum

The two methods, namely, rectangular cell counting and the cover method, are described briefly in the following section.

Rectangular box/cell counting method: The procedure for calculating fractal dimension using box counting method is as follows:

- Draw the profile in the graph sheet (see Fig. 1.24a).
- Count the number of squares that contain the curve.
- Vary the box size and again count the number of squares that contain the curve.
- Draw a graph between box size and the number of boxes (see Fig. 1.24b).
- Fit a straight line.
- Find the slope.
- Absolute value of the slope is the fractal dimension.

Fig. 1.25 Calculation of fractal dimension using compass method



Compass/cover method: The procedure for calculating fractal dimension using compass method is as follows:

- Consider compass length l_1 as shown in Fig. 1.25a.
- Find the number of steps to scan the profile. Let it be n_1 .
- Then, length of the profile = $n_1 \times l_1 = L_1$.
- Now consider compass length $l_2 < l_1$.
- Let n_2 be the number of steps to scan the profile ($n_2 > n_1$).
- Therefore, length of the profile = $n_2 \times l_2 = L_2$.
- It can be seen that the $L_2 > L_1$, i.e., the length of an irregular curve is not finite. It depends on the method of measurement.
- Plot graphs between l and $(n \times l)$.
- Fit a straight line; find the modulus of the slope.
- The absolute value of the slope should be added to 1 to get the fractal dimension value.

7.5 Bearing Length (Htp) Parameters and Bearing Ratio Curve

The bearing length parameter is defined as the percentage of solid material of the profile lying at a certain height. The bearing ratio curve (also called material ratio curve) is a graphical representation of the Htp parameter relative to the profile level. This curve contains all of the amplitude information of the profile. The bearing ratio curve is the curve generated by running a plane, extending parallel to the mean surface plane, down through the surface and is defined as the percentage of the plane that intercepts material versus the depth of the plane into the surface. It gives the ratio of air to material at any level, starting from highest peak, as shown in Fig. 1.26. The various bearing ratio parameters obtained from the bearing ratio curve are shown in Fig. 1.27, and the details are presented as follows:

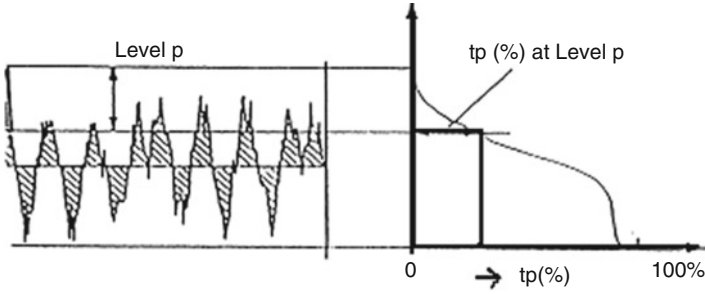
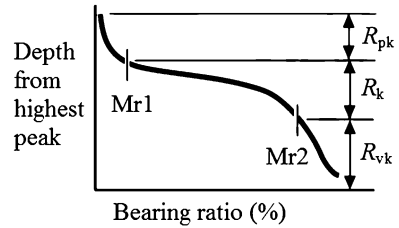


Fig. 1.26 Calculation of Htp parameter

Fig. 1.27 Bearing ratio plot and parameters



Reduced peak height (R_{pk}): The top portion of the surface which will be worn away in the running-in period.

Core roughness depth (R_k): This is working part of the surface. After the initial running-in period, it will carry the load and influence life and performance.

Reduced valley depth (R_{vk}): The lowest part of the surface which has the function of retaining the lubricant.

Peak material component ($Mr1$): The bearing ratio at which R_{pk} and R_k meet. This is the upper limit of the core roughness profile. This parameter is derived from the bearing ratio plot.

Valley material component ($Mr2$): The bearing ratio at which R_{vk} and R_k meet. This is the lower limit of the core roughness profile. This parameter is derived from the bearing ratio plot.

8 Surface Roughness Measurements

In general, roughness of the surface is measured using profilometers. There are two types of profilometers: (a) contact and (b) noncontact type (optical).

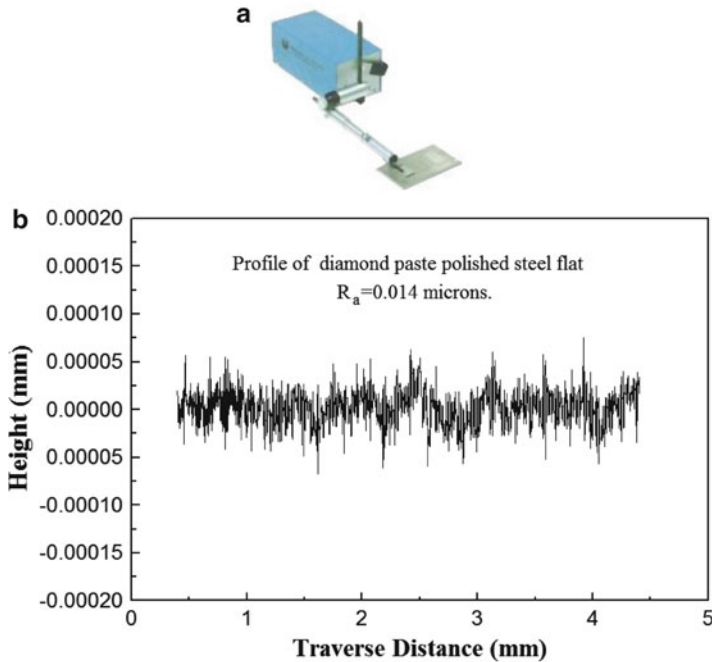


Fig. 1.28 (a) Photograph of 2D contact-type stylus profilometer and (b) surface profile

Contact-type profilometer: The most common method of studying surface texture features is the contact-type stylus profilometer. A fine, very lightly loaded stylus is dragged smoothly at a constant speed across the surface under examination. The height position of the stylus generates an analog signal which is converted into a digital signal that is stored, analyzed, and displayed, and the output provides a magnified view of the original profile. A photograph of 2D contact-type profilometer and the profile generated are shown in Fig. 1.28a, b, respectively.

The graphical representation differs from the actual surface profile because of differences in magnifications employed in vertical and horizontal directions. The tip radius of the stylus varies from 20 nm to 25 μm for a diamond stylus. A typical profilometer can measure small vertical features ranging in height from 10 nm to 1 mm. Sometimes some errors are also introduced by the stylus in terms of distortion or damage of a very delicate surface because of the load applied on it. In such cases, non-contacting optical profilometer is used.

Most of the world's surface finish standards are written using contact-type profilometers. Contacting the surface is often an advantage in dirty environments where noncontact methods can end up measuring surface contaminants instead of the surface itself. As the stylus is in contact with the surface, this method is not sensitive to surface reflectance or color.

Fig. 1.29 Schematic diagram of optical profilometer

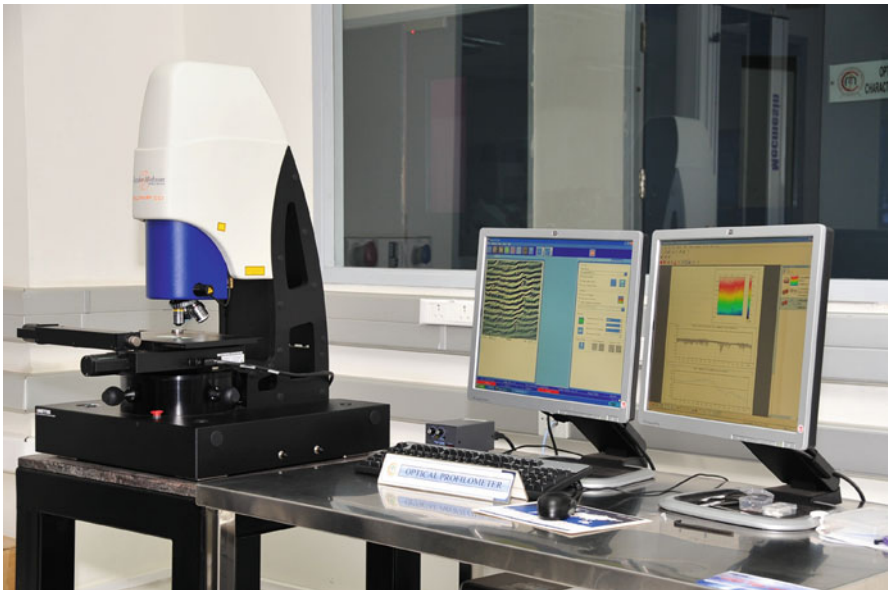
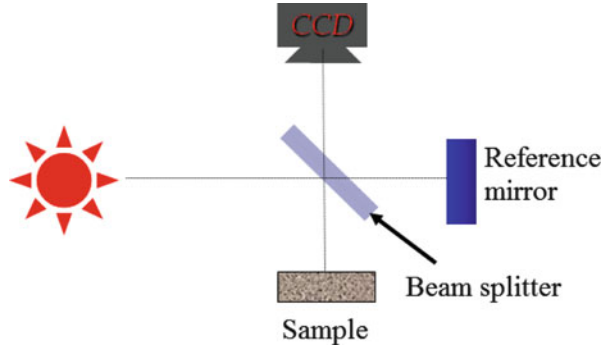


Fig. 1.30 Photograph of 3D optical profilometer

Noncontact-type profilometer (optical profilometer): Figure 1.29 shows the schematic diagram of the optical profilometer. In this case, the expanded beam exiting from a light source is divided by a beam separator into two beams, one for the reference mirror and the other for the sample. The two beams (reflected from the reference mirror and from the sample) are recombined by the beam separator to interfere. The interference fringes are then recorded using a CCD camera. Hence, an image of the surface is produced and is analyzed. In optical profilometers, the depth of field achievable is up to $5\ \mu\text{m}$. Success of the methods depends on the reflective property of the material, which can limit its range of applications. Optical profilometers do not touch the surface and therefore cannot be damaged by surface wear or careless operation. A photograph of the optical profilometer is shown in Fig. 1.30. Optical profilometer images for various kinds of surfaces are shown in Fig. 1.3.

9 Experimental Case Study

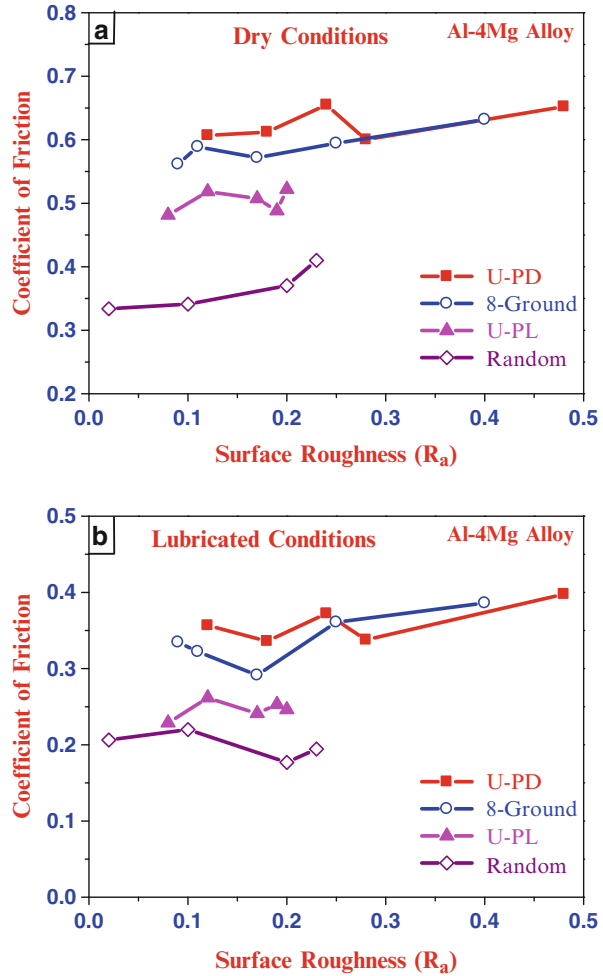
Efforts have been made to study the influence of surface texture on friction and wear during sliding conditions. In the experiments, various kinds of surface textures were generated on steel plate surfaces. These textures are categorized as unidirectional, 8-ground, and random. The unidirectional and 8-ground surfaces with varying roughness were created by dry grinding the plates with silicon carbide (SiC) emery papers of 220, 400, 600, 800, or 1,000 grit sizes. For the unidirectional case, care was taken so that the grinding marks were unidirectional in nature. The 8-ground surface was generated by moving the steel plate against dry emery papers along a path with the shape of an “8” for 500 cycles. The random surface with varying roughness was generated under wet grinding conditions using a polishing wheel and one of the three abrasive media—SiC powder (220, 600, and 1,000 grit), Al_2O_3 powder (0.017 μm), and diamond paste (1–3 μm). The 3D profiles of unidirectional, 8-ground, and random surfaces are shown in Fig. 1.3a–c, respectively. For the unidirectional case, the sliding tests were conducted in both perpendicular (UPD) and parallel (UPL) to the unidirectional grinding marks. Hence, four sets of textured conditions were utilized. Experiments were conducted using pin-on-plate sliding tester [7] for a sliding velocity of 2 mm/s under both dry and lubricated conditions.

Figure 1.31a, b shows the variation of average coefficient of friction with R_a when Al-4Mg alloy slid on steel plate of different surface textures under dry and lubricated conditions, respectively [8]. It can be seen that surface roughness (R_a) values for different textured surfaces are comparable with each other although they were ground against different grinding media. It can be seen from Fig. 1.31a, b that no particular relation exists between surface roughness (in the present test range) and coefficient of friction. In addition, it can be seen that for a given kind of texture, the coefficient of friction did not vary much with surface roughness.

Figure 1.32 illustrates the variation of coefficient of friction with surface textures when Al-4Mg alloy slid on steel plate of various surface textures under dry and lubricated conditions [9]. The error bar in the figure indicates the maximum and minimum friction values obtained for different surface roughness, whereas the connecting line indicates the average friction values obtained for different surface textures. It can be seen that the coefficient of friction considerably depends on the surface texture of the harder counter surface. More specifically, the friction values were more for the sliding tests conducted perpendicular to the unidirectional grinding marks (UPD) than parallel to the unidirectional grinding marks (UPL). The friction values of 8-ground surfaces lie in between UPD and UPL tests. The randomly polished surfaces showed the least frictional values. Similar observations can be made for pure metals [7, 10–15], alloys [9, 16–18], and polymers [19, 20]. Figure 1.33 depicts the variation of average coefficient of friction with surface texture for various materials [20].

It is important to note that the surface texture of both sliding materials (harder and softer) plays an important role in controlling the frictional behavior. However,

Fig. 1.31 Variation of average coefficient of friction with surface roughness (R_a) for various surface textures under (a) dry and (b) lubricated conditions



it was found that the harder surface texture plays a crucial role in controlling the frictional phenomenon when compared to the softer surface texture during sliding [21].

In another investigation [4, 22–26], experiments were conducted to study the influence of grinding marks direction on friction during sliding. The results showed that the friction is lowest for 0° grinding angle (UPL) and highest for 90° grinding angle (UPD). The friction values increase sharply from 0° up to about 25° grinding angle and then the rate of change decreases [4, 22]. The variation of coefficient of friction with grinding angle for the case of Al-4Mg alloy is shown in Fig. 1.34 [22].

The stick-slip friction phenomena also depend on surface textures [4, 7, 14, 23, 27]. In general, it was observed that the stick-slip friction phenomena were observed when hexagonal close-packed (HCP) metals slid against specific surface textures

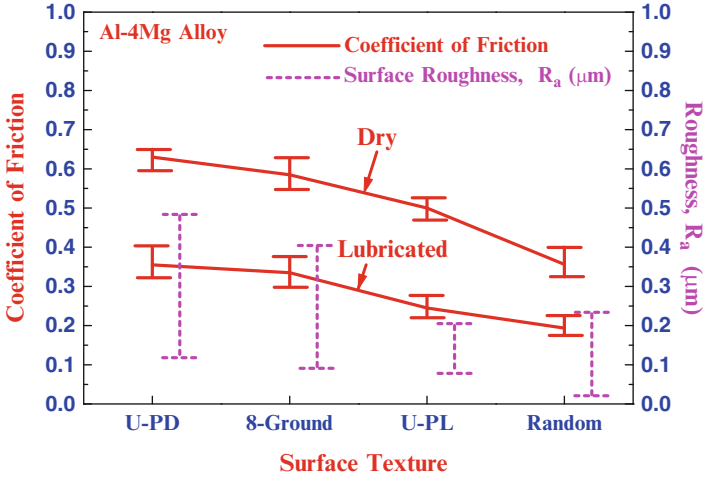


Fig. 1.32 Variation of average coefficient of friction and surface roughness (R_a) with surface texture for Al-4Mg alloy

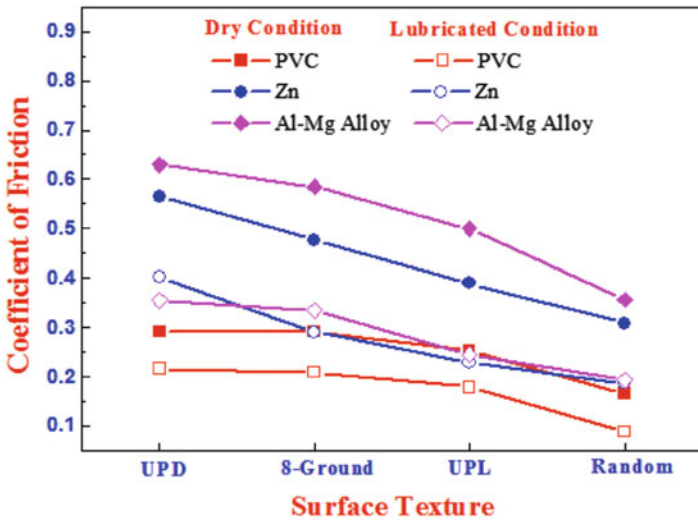


Fig. 1.33 Variation of average coefficient of friction with surface texture for various materials

[28–30]. However, face-centered cubic (FCC) metals did not show such response against any surface textures [31].

Figure 1.35 shows the variation of stick-slip friction when pure Mg slid on various surface textures [32]. As shown in the figure, the stick-slip phenomenon was observed for the UPD, 8-ground, and UPL case under dry conditions, the amplitude of which was highest for the UPD, followed by the 8-ground, and least for the UPL case. However, under lubricated conditions stick-slip was observed

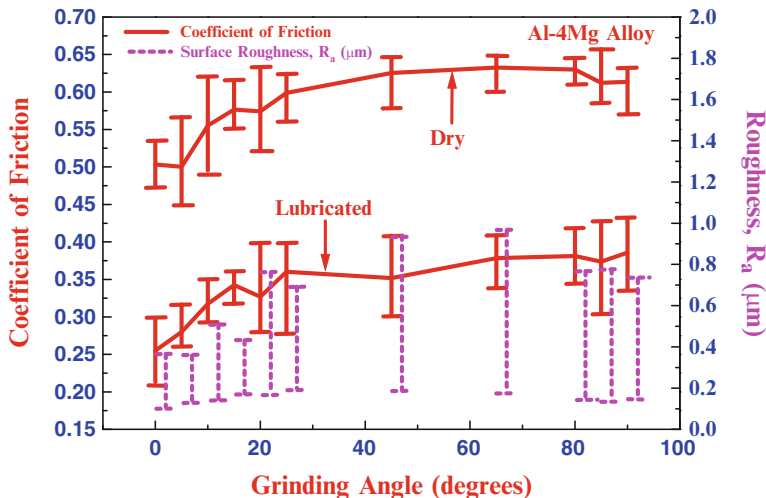


Fig. 1.34 Variation of coefficient of friction with grinding angle for the case of Al-4Mg alloy

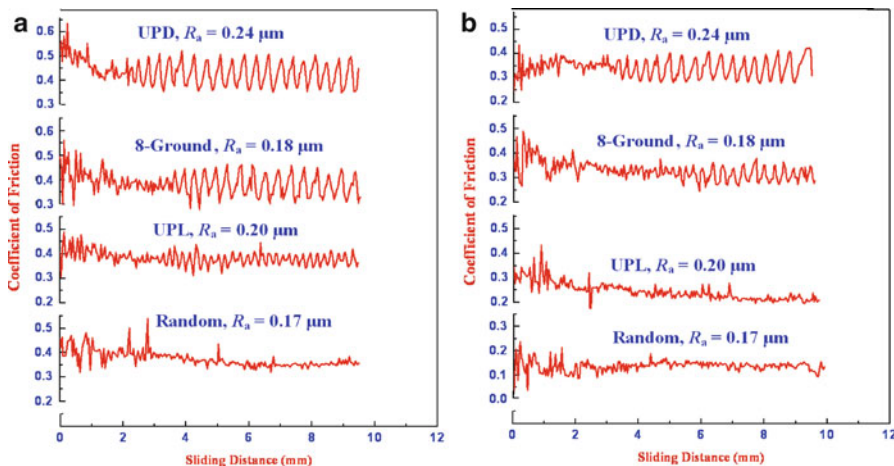


Fig. 1.35 Variation of friction with sliding distance for various surface textures under (a) dry and (b) lubricated conditions

only for the case of UPD and 8-ground, where the amplitude of oscillation was greater for the UPD case.

Based on the above results, it is clear that the surface texture indeed has an important role on coefficient of friction values during sliding. Thus, surface textures were characterized by means of surface roughness parameters. It was reported that the roughness as given by R_a within the test range does not significantly affect the friction values. Hence, it is important to study other roughness parameters

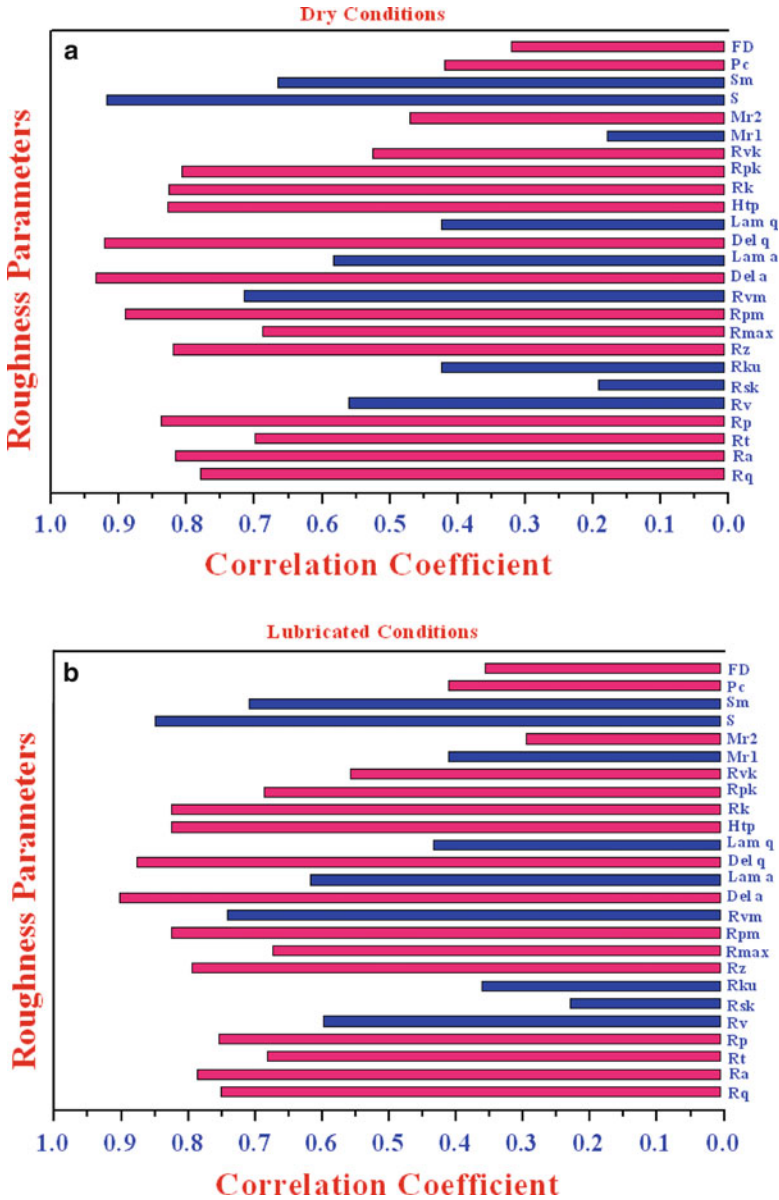


Fig. 1.36 Correlation coefficient between coefficient of friction and roughness parameters under (a) dry and (b) lubricated conditions. Red and blue bars represent positive and negative correlations, respectively

of surface texture and to correlate them with coefficient of friction. Hence, efforts were made to correlate various roughness parameters with coefficient of friction. Twenty-five surface roughness parameters were taken into consideration. Figure 1.36a, b shows the results of the correlation analysis between surface

roughness parameters and coefficient of friction under both dry and lubricated conditions, respectively. The maximum correlation coefficient (Pearson product moment correlation coefficient) was found between coefficient of friction and surface roughness parameters Δ_a (Del a) for the case of Al-4Mg alloy [8]. Similar observations can be made for other materials. Further, new nondimensional roughness parameters were formulated, and these newly formulated roughness parameters correlated with coefficient of friction better than the hybrid roughness parameters [12, 13, 33].

Like friction, the transfer layer formation (or wear) is also dependent on the surface texture. Figure 1.37 shows the backscattered scanning electron micrographs of steel plates when Al-4Mg alloy pins slid on various surface textures under dry and lubricated conditions [9]. It can be noticed that the amount of transfer layer formed on a steel plate surface is highest for the UPD case, followed by 8-ground plates, UPL case, and then the randomly polished steel plates. The amount of transfer layer formation is less under lubricated conditions when compared to that under dry conditions.

Surface texturing technology can be utilized in metal-forming processes to design a particular texture at different locations of the die so that the coefficient of friction can be varied according to the requirements. In locations where the coefficient of friction needs to be high, a unidirectionally ground surface with the flow perpendicular to the grinding marks direction can be machined, and in locations where the coefficient of friction needs to be low, a randomly polished surface can be machined. Designing textures on the die may also enable a reduction in the amount of conventional lubricants needed to achieve the required friction. The die-workpiece friction affects material flow [34, 35], stresses, and strain rate distribution in the deformed material [36, 37], which in turn influences the microstructural evolution in the material [38]. The microstructural evolution will affect the mechanical properties of the formed product. The mechanical properties of the formed product at different locations can also be tailored by designing a proper surface texture.

It was seen that the coefficient of friction could be altered by more than 200 % by changing surface textures. This research, however, was confined to a single sliding event. In forming operations, however, the dies can be reused for multiple operations. Thus, it is important to analyze the effect of surface texture of the die on friction during sliding at various numbers of cycles against soft materials. Hence, efforts have been made to study the influence of surface texture on coefficient of friction during sliding at various numbers of cycles [39–41]. Figure 1.38a, b presents the range in which the coefficient of friction values falls for different roughness when Al-4Mg alloy pin slid on different surface textures at different numbers of cycles under dry and lubricated conditions, respectively [40]. It was noticed under both dry and lubricated conditions that the coefficient of friction decreases for UPD, 8-ground, and UPL surfaces as a function of cycles. The randomly ground surfaces, in contrast, show an increase in friction with the number

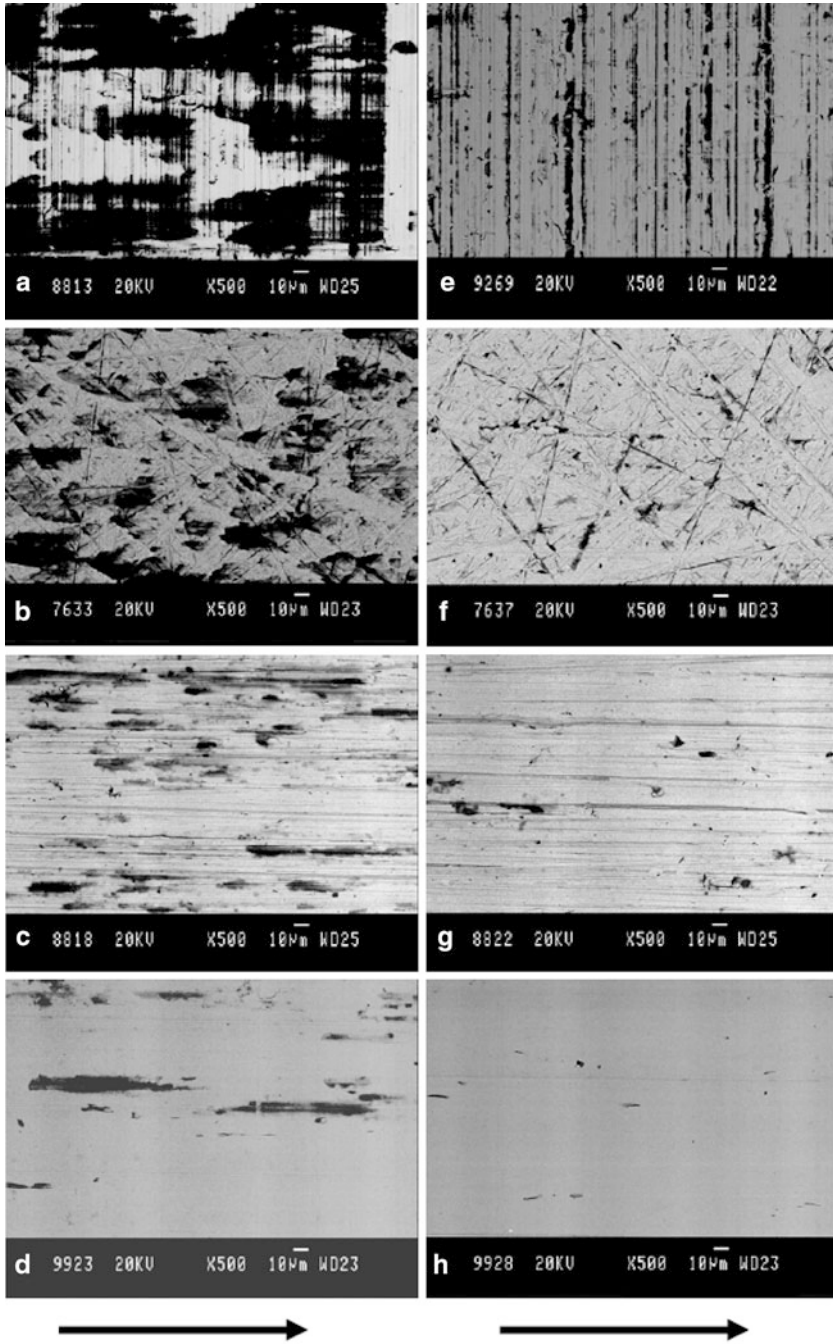


Fig. 1.37 Backscattered scanning electron micrographs of steel plates with different textures after sliding tests under dry (a–d) and lubricated (e–h) conditions with (a, e) UPD, (b, f) 8-ground, (c, g) UPL, and (d, h) random. The *arrows* indicate the sliding direction of the pin relative to the plate

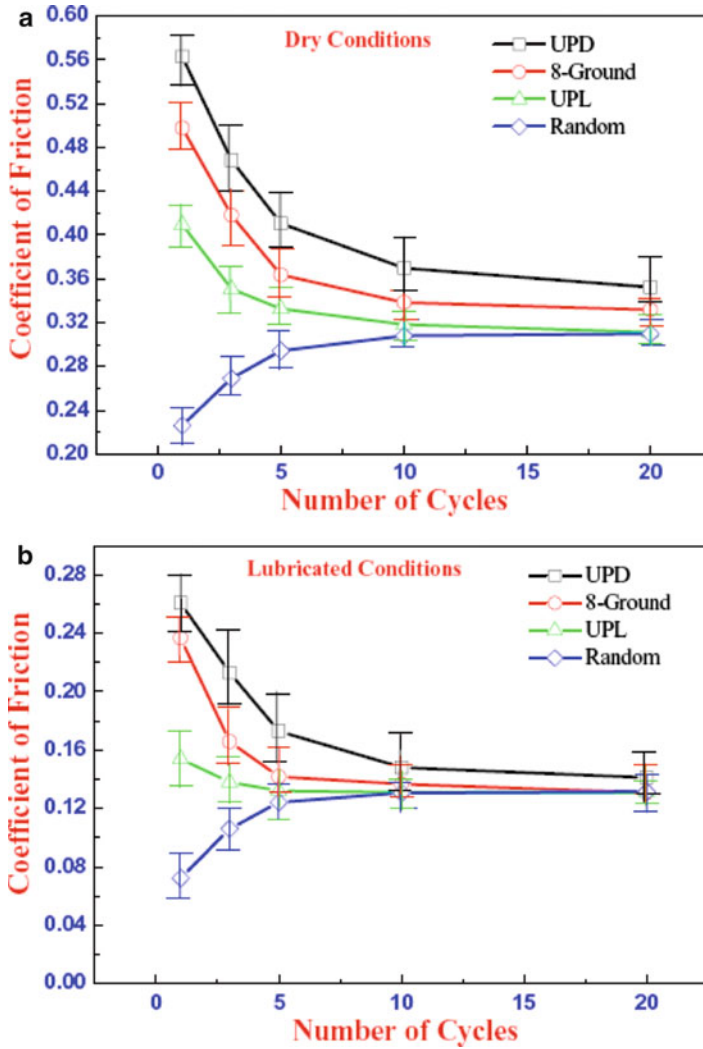


Fig. 1.38 Variation of average coefficient of friction with number of cycles for different surface textures under (a) dry and (b) lubricated conditions

of cycles. It can also be observed that the coefficient of friction depends significantly on the surface textures during the first few cycles. The difference in friction values among these surfaces decreases with increasing number of cycles. The variation in the coefficient of friction with number of cycles under both dry and lubrication conditions is attributed to the self-organization of texture of the surfaces at the interface during sliding.

10 Conclusions

In this chapter, attempts have been made to study various surface layers, surface texturing, and designing and characterization process of surface texturing. The properties of surface layers are very important to understand the tribological performance. Surface texture is one of the most important parameters that controls the tribological behavior. Various methods have been employed to design and characterize the surface textures. The profilometry technique is more common characterization method. Various types of roughness parameters, such as amplitude, spacing, and hybrid, have been employed to define the surfaces. More recently, nondimensional roughness parameters have also been developed to better understand the friction and wear phenomena as a function of surface textures.

Questions

1. Explain various surface layers in detail using suitable schematic diagrams.
2. Explain various methods of characterizing surface layers.
3. Classify surface roughness parameters. Define any one surface roughness parameter under each classification using necessary diagrams and equations.
4. What is fractal dimension? List various methods to calculate fractal dimension.
5. Explain the terms skewness and kurtosis.
6. Explain autocorrelation and autocovariance functions.
7. Write a note on amplitude parameters.
8. Define the terms roughness and mean line.
9. Explain the differences between roughness and surface texture.
10. List various methods of preparation of surface textures.
11. Write a note on bearing length parameters and bearing ratio curve.
12. Explain various surface texture characterization techniques.
13. Explain contact and noncontact profilometers. List the advantages and disadvantages.

References

1. Buckley DH (1981) Surface effects in adhesion, friction, wear and lubrication. Elsevier, New York
2. Bhushan B (2002) Introduction to tribology. Wiley, New York
3. Gadelmawla ES, Koura MM, Maksoud TMA, Elewa IM, Soliman HH (2002) Roughness parameters. *J Mater Process Technol* 123(1):133–145
4. Menezes PL, Kishore, Kailas SV (2006) Effect of directionality of unidirectional grinding marks on friction and transfer layer formation of Mg on steel using inclined scratch test. *Mater Sci Eng, A* 429(1–2):149–160
5. Whitehouse DJ (1994) Handbook of surface metrology. IOP Publishing Ltd., London

6. Feder J (1988) *Fractals*. Plenum, New York
7. Menezes PL, Kishore, Kailas SV (2006) Influence of surface texture on coefficient of friction and transfer layer formation during sliding of pure magnesium pin on 080 M40 (EN8) steel plate. *Wear* 261(5–6):578–591
8. Menezes PL, Kishore, Kailas SV (2008) Influence of roughness parameters of harder surface on coefficient of friction and transfer layer formation. *Int J Surf Sci Eng* 2(1–2):98–119
9. Menezes L, Kishore P, Kailas SV (2006) Studies on friction and transfer layer using inclined scratch. *Tribol Int* 39(2):175–183
10. Menezes PL, Kishore K, Kailas SV (2006) Studies on friction and transfer layer: role of surface texture. *Tribol Lett* 24(3):265–273
11. Menezes PL, Kishore, Kailas SV (2008) Effect of surface roughness parameters and surface texture on friction and transfer layer formation in tin-steel tribo-system. *J Mater Process Technol* 208(1–3):372–382
12. Menezes P, Kishore K, Kailas S (2009) Influence of roughness parameters and surface texture on friction during sliding of pure lead over 080 M40 steel. *Int J Adv Manuf Technol* 43(7):731–743
13. Menezes PL, Kishore, Kailas SV (2009) Study of friction and transfer layer formation in copper-steel tribo-system: role of surface texture and roughness parameters. *Tribol Trans* 52(5):611–622
14. Menezes PL, Kishore, Kailas SV (2008) Role of surface texture and roughness parameters in friction and transfer layer formation under dry and lubricated sliding conditions. *Int J Mater Res* 99:795–807
15. Menezes PL, Kishore, Kailas SV (2008) Studies on friction in an iron-steel tribo-system under dry and lubricated conditions. *Mater Manuf Process* 23:698–707
16. Menezes PL, Kishore S, Kishore, Kailas SV (2007) Influence of surface texture on friction and transfer layer formation in Mg-8Al alloy/steel tribo-system. *Indian J Tribol* 2(1):46–54
17. Kumar C, Kishore, Kailas SV (2008) Role of surface texture on friction under boundary lubricated conditions. *Tribol Online* 3(1):12–18
18. Menezes PL, Kishore, Kailas SV (2008) Effect of surface topography on friction and transfer layer during sliding. *Tribol Online* 3(1):25–30
19. Menezes PL, Kishore, Kailas SV, Lovell MR (2011) Friction and transfer layer formation in polymer-steel tribo-system: role of surface texture and roughness parameters. *Wear* 271(9–10):2213–2221
20. Menezes PL, Kishore, Kailas SV, Lovell MR (2010) Response of metals and polymers during sliding: role of surface texture. *ASME Conf Proc* 2010(44199):267–269
21. Menezes PL, Kishore, Kailas SV, Lovell MR (2011) Studies on friction in steel-aluminum alloy tribo-system: role of surface texture of the softer material. *STLE 2011 annual meeting & exhibition, STLE, Atlanta, Georgia, USA*
22. Menezes PL, Kishore, Kailas SV (2006) Effect of roughness parameter and grinding angle on coefficient of friction when sliding of Al-Mg alloy over EN8 steel. *J Tribol* 128:697–704
23. Menezes PL, Kishore, Kailas SV (2008) On the effect of surface texture on friction and transfer layer formation—a study using Al and steel pair. *Wear* 265(11–12):1655–1669
24. Menezes PL, Kishore, Kailas SV (2009) Influence of inclination angle of plate on friction, stick-slip and transfer layer-A study of magnesium pin sliding against steel plate. *Wear* 267(1–4):476–484
25. Menezes PL, Kishore, Kailas SV, Bobji MS (2010) Influence of tilt angle of plate on friction and transfer layer-A study of aluminium pin sliding against steel plate. *Tribol Int* 43(5–6):897–905
26. Menezes PL, Kishore, Kailas SV, Lovell MR (2011) Influence of inclination angle and machining direction on friction and transfer layer formation. *J Tribol Trans Asme* 133(1)
27. Menezes PL, Kishore, Kailas SV (2009) Influence of surface texture and roughness parameters on friction and transfer layer formation during sliding of aluminium pin on steel plate. *Wear* 267(9–10):1534–1549

28. Menezes PL, Kishore, Kailas SV, Lovell MR (2009) Studies on friction and formation of transfer layer in HCP metals. *J Tribol Trans Asme* 131(3)
29. Menezes PL, Kishore, Kailas SV, Lovell MR (2010) Response of materials as a function of grinding angle on friction and transfer layer formation. *Int J Adv Manuf Technol* 49(5–8):485–495
30. Menezes PL, Kishore, Kailas SV, Lovell MR (2011) Response of materials during sliding on various surface textures. *J Mater Eng Perform* 20(8):1438–1446
31. Menezes P, Kishore K, Kailas S, Lovell M (2011) Role of surface texture, roughness, and hardness on friction during unidirectional sliding. *Tribol Lett* 41(1):1–15
32. Menezes PL, Kishore, Kailas SV, Kishore K, Lovell MR (2011) Factors influencing stick-slip motion: effect of hardness, crystal structure and surface texture. *ASME Conf Proc* 2011 (54747):71–73
33. Pottirayil A, Menezes PL, Kailas SV (2010) A parameter characterizing plowing nature of surfaces close to Gaussian. *Tribol Int* 43(1–2):370–380
34. Menezes PL, Kishore, Kailas SV (2009) Role of surface texture of harder surface on subsurface deformation. *Wear* 266(1–2):103–109
35. Menezes PL, Kishore, Kailas SV (2008) Subsurface deformation and the role of surface texture—a study with Cu pins and steel plates. *Sadhana Acad Proceed Eng Sci Compendex* (3):191–201
36. Menezes PL, Kumar K, Kishore, Kailas SV (2009) Influence of friction during forming processes—a study using a numerical simulation technique. *Int J Adv Manuf Technol* 40(Compendex):1067–1076
37. Menezes PL, Kishore, Kailas SV (2010) Influence of die surface textures during metal forming—a study using experiments and simulation. *Mater Manuf Process* 25(9):1030–1039
38. Menezes PL, Kishore, Kailas SV, Lovell MR (2012) Analysis of strain rates and microstructural evaluation during metal forming: role of surface texture and friction. *Tribol Trans* 55(5):582–589
39. Menezes PL, Kishore, Kailas SV (2009) Studies on friction and formation of transfer layer when Al-4Mg alloy pins slid at various numbers of cycles on steel plates of different surface texture. *Wear* 267(1–4):525–534
40. Menezes PL, Kishore, Kailas SV, Lovell MR (2011) The role of surface texture on friction and transfer layer formation during repeated sliding of Al-4Mg against steel. *Wear* 271(9–10):1785–1793
41. Menezes PL, Kishore, Kailas SV, Lovell MR (2013) Tribological response of soft materials sliding against hard surface textures at various numbers of cycles. *Lubricat Sci* 25(2):79–99

Chapter 2

Friction and Wear

**Pradeep L. Menezes, Michael Nosonovsky, Satish V. Kailas,
and Michael R. Lovell**

Abstract Friction is a universal phenomenon which is observed in a great variety of sliding and rolling situations. The study of friction and wear has long been of enormous practical importance, since the functioning of many mechanical, electro-mechanical, and biological systems depends on the appropriate friction and wear values. In recent decades, this field has received increasing attention as it has become evident that the consumption of resources resulting from high friction and wear is greater than 6 % of the Gross National Product of the USA. In this chapter, various theories, mechanisms, and factors affecting of friction and wear were discussed.

1 Introduction

Friction plays a great role in the everyday life. Without friction it would be impossible to walk, use automobiles on a roadway, or pick up objects. In various situations, either low or high friction may be desirable. For example, in some machine applications such as vehicle brakes and clutches and frictional transmission of power, high friction is needed. However, in most other sliding and rolling components such as bearing and seals, friction is undesirable. Friction causes energy loss and the wear of materials that are in contact. In these cases, friction should be minimized.

P.L. Menezes (✉) • M. Nosonovsky • M.R. Lovell
College of Engineering & Applied Science, University of Wisconsin-Milwaukee,
Milwaukee, WI 53201, USA
e-mail: menezesp@uwm.edu

S.V. Kailas
Department of Mechanical Engineering, Indian Institute of Science,
Bangalore, Karnataka 560012, India

2 Friction

Friction is the resistance to relative motion of two bodies that are in contact. Friction is not a material property; it is a property of tribological system that consists of at least two bodies in contact, along with the surrounding environment and the interface. There are two types of friction that are commonly encountered: dry friction and fluid friction. Dry friction is also called “Coulomb” friction. Dry friction occurs during the contact under dry conditions, while the fluid friction occurs during the contact under lubricated conditions. If two solid surfaces are smooth and clean without chemical films and adsorbates, friction is usually high. Surface contaminants or thin films affect friction. With well-lubricated surfaces, low friction is generally observed.

2.1 Basic Concepts

2.1.1 Coefficient of Friction

Friction can often be described by a quantitative parameter called the coefficient of friction, μ . It is known from experiments that the friction force is often linearly proportional to the normal load force applied to the body. This is the so-called Coulomb friction. The coefficient of friction, also known as friction coefficient, is a dimensionless scalar value defined as the ratio of tangential friction force (F) to the normal load force (W).

$$\mu = \frac{F}{W} \quad (2.1)$$

As illustrated in Fig. 2.1, a tangential force (F) is needed to move the upper body over the stationary counterface. As explained above, the ratio between these two forces is known as the coefficient of friction.

In technical terms, friction force or tangential force is the resisting force which acts in a direction directly opposite to the direction of motion. The normal force is defined as the net force compressing two parallel surfaces together, and its direction is perpendicular to the surfaces. In the simple case of a mass resting on a horizontal

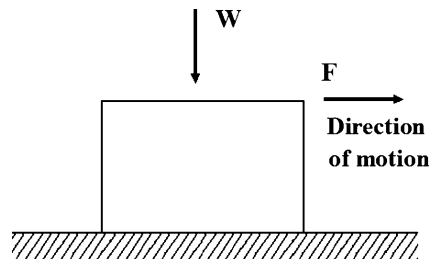


Fig. 2.1 Schematic diagram of a body sliding on a surface

surface, the only component of the normal force is the weight force due to gravity. In this case, the maximum magnitude of the friction force is the product of the mass of the object, the acceleration due to gravity, and the coefficient of friction. However, the coefficient of friction is not a function of mass or volume; it depends only on the mating materials and testing conditions. For instance, a large aluminum block in contact with steel has the same coefficient of friction as a small aluminum block contacting steel. However, the magnitude of the friction force itself depends on the normal force and hence the mass of the block.

The coefficient of friction is an empirical parameter—it has to be measured experimentally and cannot be found through calculations. The coefficient of friction can vary over a wide range: from 0.001 in a lightly loaded rolling bearing to greater than 10 for clean metals sliding against themselves in vacuum. For most common materials, sliding in air, the value of the coefficient of friction lies in the narrower range from about 0.1 to 1.

2.1.2 Static Friction

Static friction is the friction between two solid objects that are not moving relative to each other. For example, static friction can prevent an object from sliding down a sloped surface. The coefficient of static friction, typically denoted as μ_s , is usually higher than the coefficient of kinetic friction, μ_k . This happens because when no sliding occurs, the surfaces tend to “stick” to each other due to adhesive bonds between them. This phenomenon is sometimes referred to as “stiction.” The static friction force must be overcome by an applied force before an object can move. The instant of sliding occurs, static friction is no longer applicable, and kinetic friction becomes applicable.

2.1.3 Kinetic Friction

Kinetic (or dynamic) friction occurs when two bodies are moving relative to each other and rub each other. The coefficient of kinetic friction is typically denoted as μ_k and is usually less than the coefficient of static friction for the same material combination. Figure 2.2 demonstrates the static and kinetic friction with time.

2.1.4 Angle of Friction

For certain applications, it is more useful to define static friction in terms of the maximum angle before which one of the items will begin sliding. This is called the *angle of friction* or *friction angle*. It is defined as

$$\tan \theta = \mu \quad (2.2)$$

where θ is the angle from horizontal and μ is the static coefficient of friction between the objects.

Fig. 2.2 Variation of tangential force with time. F_{static} is the force required to initiate sliding and F_{kinetic} is the force required to maintain sliding

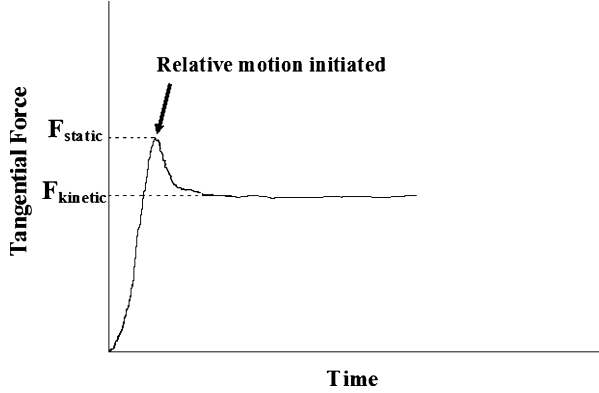
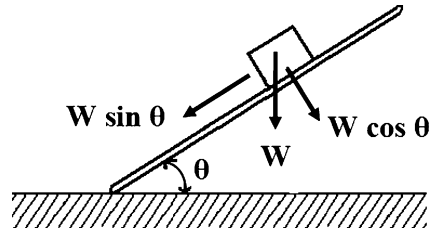


Fig. 2.3 Measurement of friction using the inclined plane test



Consider a block of weight W is placed upon an inclined plane of angle θ to the horizontal as shown in Fig. 2.3, the coefficient of friction can be defined as

$$\mu = \frac{F}{W} = \frac{W \sin \theta}{W \cos \theta} = \tan \theta \tag{2.3}$$

In (2.2), θ is the angle such that a body of any weight, placed on a plane inclined at an angle less than θ from the horizontal, will remain stationary. However, if the inclination angle is increased to θ , the body will start to slide down. This formula can also be used to calculate μ from empirical measurements of the friction angle.

2.1.5 Stick–Slip Phenomenon

An important phenomenon during sliding is the stick–slip motion. During the stick–slip motion, the frictional force does not remain constant, but rather oscillates significantly as a function of sliding distance or time. During the stick phase, the friction force builds to a critical value. Once the critical force has been attained (to overcome the static friction), slip occurs at the interface and energy is released so that the frictional force decreases. This stick–slip phenomenon can occur if the coefficient of static friction is greater than the coefficient of kinetic friction [1].

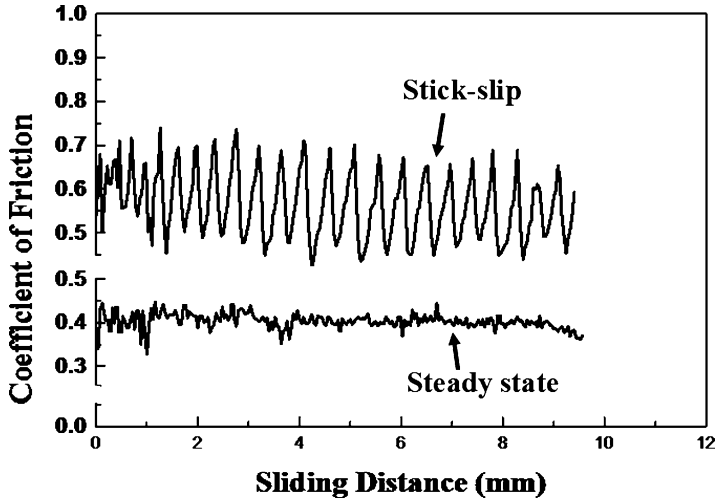


Fig. 2.4 Variation of steady-state and stick–slip friction with sliding distance

Fig. 2.5 Schematic view of real area of contact between two bodies

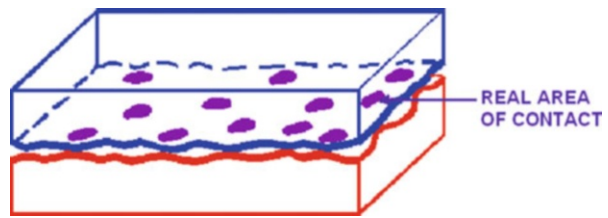


Figure 2.4 shows the variation of steady-state motion and stick–slip motion with sliding distance [2].

The stick–slip phenomenon is found in many situations, such as car brake vibration and squeal. However, it is particularly common at the atomic scale. For example, during the contact of an atomic force microscope tip with an atomically smooth surface, the energy dissipation takes place through stick–slip movement of individual atoms at the contact interface [3].

2.1.6 Real Area of Contact

Even nominally flat surfaces are not perfectly smooth and have asperities at some length scale. When two surfaces are brought into contact, the contact occurs only at the tops of the asperities, so the load is supported by the deformation of contacting asperities. Therefore, the real (or actual) area of contact constitutes only a small fraction of the nominal (or apparent) area of contact. Figure 2.5 shows the real area of contact, schematically. In general, the real area of contact varies with the pressure and is very small compared to the nominal area of contact. For flat steel

surfaces under typical loads, the real area of contact may be less than 0.01 % of the apparent area. The real area of contact is not greatly affected by the size, shape, and degree of roughness of the surface; it depends mainly on the pressure. However, during sliding locations of the contact spots do not remain permanent, but are changing rapidly during sliding, as new asperities come into contact while other contacts break.

2.1.7 Friction Paradoxes and Dynamic Instabilities

Despite the linear dependence of the Coulomb friction force upon the normal load given by (2.1), friction is an inherently nonlinear phenomenon. Direction of the friction force depends upon the direction of motion, so that in the vector form, the friction force is given by

$$\vec{F} = \frac{\vec{V}}{|\vec{V}|} \mu |\vec{W}| \quad (2.4)$$

where \vec{V} is the sliding velocity. The ratio $\vec{V}/|\vec{V}|$ is nonlinear. This nonlinearity results in some static frictional problems having no solution or a nonunique solution, e.g., the so-called Painlevé paradoxes. These paradoxes show that the rigid-body dynamics with contact and Coulomb friction is inconsistent. To resolve these problems, the dynamic friction and elastic deformation should be considered [3].

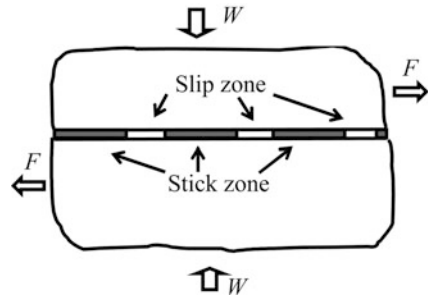
Despite the simplicity of (2.1) to describe friction, there are a number of difficulties in integrating friction with the mechanics of a deformable body. In continuum mechanics, stress is the measure of force exerted per unit area at a given point. The maximum shear stress τ_{xy} at the interface between two bodies during friction is proportional to the normal stress σ_{yy} at the same point

$$\tau_{xy} = \mu \sigma_{yy} \quad (2.5)$$

However, the sign of the shear stress depends upon the sign of the local sliding velocity. This leads to friction paradoxes when formal mathematical solutions of the continuum mechanics problems with the boundary condition given by (2.3) yield nonunique solution or to the sign of the shear stress not necessarily opposite to the sign of the local velocity of sliding. Adams et al. [4] demonstrated that dynamic effects lead to new types of frictional paradoxes, in the sense that the assumed direction of sliding used for Coulomb friction is opposite that of the resulting slip velocity. In a strict mathematical sense, the Coulomb friction is inconsistent not only with the rigid-body dynamics (the Painlevé paradoxes) but also with the dynamics of elastically deformable bodies.

The mathematical formulation of quasi-static sliding of two elastic bodies (half-spaces) with a frictional interface, governed by (2.4), is a classical contact mechanics problem. Interestingly, the stability of such sliding has not been

Fig. 2.6 Friction reduction due to propagating stick–slip zones



investigated until the 1990s, when Adams [5] showed that the steady sliding of two elastic half-spaces is dynamically unstable, even at low sliding speeds. The instability mechanism is essentially one of slip-wave destabilization. Steady-state sliding was shown to give rise to a dynamic instability in the form of self-excited motion. These self-excited oscillations are confined to a region near the sliding interface and can eventually lead to either partial loss of contact or to propagating regions of stick–slip motion (slip waves). The existence of these instabilities depends upon the elastic properties of the surfaces; however, it does not depend upon the friction coefficient, nor does it require a nonlinear contact model. The same effect was predicted theoretically by Nosonovsky and Adams [6] for the contact of rough periodic elastic surfaces.

The abovementioned instabilities are a consequence of energy being pumped into the interface as a result of the positive work of the driving force (that balances the friction force). As a result, the amplitude of the interface waves grows with time. In a real system, of course, the growth is limited by the limits of applicability of the linear elasticity and linear vibration theory. This type of friction-induced vibration may be, at least partially, responsible for noise and other undesirable effects during friction [6]. These instabilities are a consequence of the inherent nonlinearity of the boundary conditions with the Coulomb friction. The stick–slip phenomenon is another important nonlinear effect similar to the dynamic instability due to decrease of friction force with increasing velocity.

Another important dynamic effect is the slip waves that can propagate along a frictional interface between two bodies. The slip wave is a propagating stick–slip motion. In a slip wave, a region of slip propagates along the interface, which is otherwise at the stick state (Fig. 2.6). As a result, two bodies shift relative to each other in a “caterpillar” or “carpet” motion at a shear force F smaller than μW , effectively resulting in the decrease of the apparent coefficient of friction. The concept of the slip waves has been applied in seismology for the study of the motion of earth plates as well as in the solid state physics for the gliding of the dislocation at an interface between two bodies [7].

When the interface waves occur for slightly dissimilar (in the sense of their elastic properties) materials, waves for very dissimilar materials would be radiated along the interfaces to provide a different mechanism of pumping the energy away from the interface [8].

2.1.8 Time-Dependent Friction

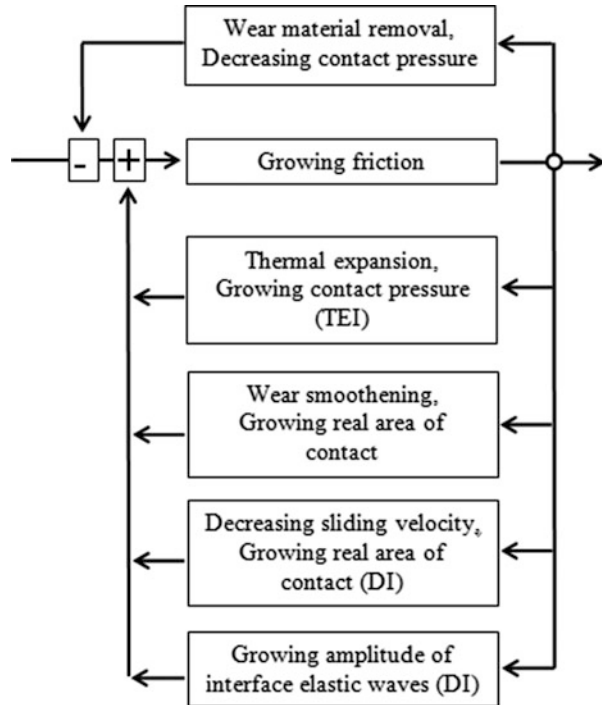
It is known from experiments that the absolute value of the friction force is not completely independent of the sliding velocity. In fact, it has been known already to Coulomb, who claimed that for very small velocities friction force grows with increasing velocity, for moderate velocities friction force remains constant, and for high velocities it decreases. It is known from experiments also the normal degree of freedom plays an important role in many dynamic effects [9]. The separation distance between the sliding bodies grows with increasing velocity. At high sliding velocities there is less time for the individual asperity contacts and, therefore, less time for asperities to deform (e.g., viscoplastically). This usually results in a decrease of the real area of contact and decrease of the friction force with increasing velocity. Various dynamic models have been suggested, based on various physical effects, such as time-dependent creep-like relaxation and viscosity [10].

It is usually believed that increasing velocity in dry friction results in decreasing friction (the so-called negative viscosity), although for some material combinations and friction regimes, the opposite trend is observed. Note that the decrease of friction with increasing velocity may lead to a dynamic instability since decreased frictional resistance will lead to acceleration and further increase of velocity and decrease in friction.

To analyze frictional dynamic instabilities (DI), the so-called state-and-rate models of friction have been introduced [10–12]. These models, used at first to study sliding friction for seismic and geophysical applications, showed reasonable agreement with the experimental data. Based on the state-and-rate models, when sliding velocity changes, the friction force first increases and then decreases (due to creep relaxation) to a velocity-dependent steady-state value (which, itself, is dependent upon the sliding velocity).

Another type of instability is a result of interaction between frictional heating, thermoelastic distortion, and contact pressure and known as the “thermoelastic instability” (TEI). As the interface temperature grows, the near-surface volumes of the contacting bodies expand and the contact pressure grows. As a result, the friction force increases as well resulting in excess heat generation and the further growth of the temperature. The TEI leads to the formation of “hot spots” or localized high-temperature regions at the interface [13]. The TEI occurs for sliding velocities greater than a certain critical value. The coupling between the two types of instabilities constitutes thermoelastodynamic instability (TEDI). Another mechanism that may provide instability is the coupling between friction and wear. As friction increases, so does the wear, which may result in an increase of the real area of contact between the bodies and in further increase of friction. The sliding bodies adjust to each other, and the process is known as the frictional self-organization [14, 15]. On the other hand, wear produces smoothening of the surface distorted by the TEI mechanism, and thus the wear and thermal expansion are competing factors, with the wear leading to stabilization of sliding and the thermal expansion leading to destabilization (Fig. 2.7).

Fig. 2.7 Various mechanisms can create positive or negative feedbacks that lead to instabilities during friction



2.1.9 Self-Organization During Friction

Sliding friction does not always lead to wear and deterioration but has potential for self-organization. This is because friction is a nonequilibrium process that results in the dissipation of large amounts of energy and in the flow of heat, entropy, and material away from the frictional interface. It is well known that when the sliding starts friction and wear are usually high during the initial “run-in” regime. However, with time the surfaces “adjust” to each other due to wear, relaxation, and other process, so the friction and wear decrease. This is perhaps the simplest model example of frictional self-organization, which also shows why the system that underwent the transition to a self-organized state has lower friction and wear rate. In this case the self-organization occurs due to the coupling of friction and wear [15].

The coupling of friction and elasticity can lead to the formation of a set of slip pulses, as shown in Fig. 2.6, which results in the effective decrease of the apparent coefficient of friction discussed above.

A different type of self-organization arises from coupling friction with a tribochemical reaction at the interface and formation of in situ protective tribofilms. For example, in a bronze–steel lubricated frictional system, a protective copper or lead film can form, which reduces the wear to very small values. The copper film is formed due to the anodic dissolution of bronze (an alloy of copper and tin with

additive elements). The additives, such as iron, zinc, lead, and aluminum, as well as tin, dissolved in the lubricant, while copper forms a film on the surfaces of the contacting materials. The film is in a dynamic equilibrium, while contacting layers are worn and destroyed, new layers of copper or lead are formed, resulting in virtual absence of wear and the friction force reduction by an order of magnitude. A similar effect can be achieved by the diffusion of copper ion dissolved in a lubricant. A protective layer can be formed also due to a chemical reaction of oxidation or a reaction with water vapor. For example, a self-lubricating layer of the boric acid (H_3BO_3) is formed as a result of a reaction of water molecules with B_2O_3 coating.

In general, the self-organization during friction leads in the formation of self-organized structures that result in the decrease of friction and wear and thus can be beneficial to applications. Various criteria of whether self-organization can occur in a particular tribo-system have been suggested in the literature [16–23].

2.2 Empirical Laws of Friction

In literature, a study of friction by Themistius (317–390 CE) has been regarded as the oldest ever attempt to understand friction. He found that the friction for sliding is greater than that for rolling. A more systematic experimental investigation of friction was conducted by Leonardo da Vinci in the 1500s and later by Amontons in 1699, verified by Euler in 1750 and Coulomb in 1781; are the other empirical laws of friction. They are presented as follows.

1. The friction force is directly proportional to the normal load.
2. The friction force is independent of the apparent area of contact.
3. The friction force is almost independent of the sliding velocity. Once sliding is established, the coefficient of dynamic friction is found for many systems to be nearly independent of sliding velocity over quite a wide range, although at high sliding speeds, of the order of tens or hundreds of meters per second for metals.

To explain these empirical laws, it is usually assumed that (1) the friction force is proportional to the real area of contact, A , and (2) the real area of contact is proportional to the normal load, W . Thus, the friction force depends upon the real area of contact, and thus it is independent of the apparent area of contact (A_a), and the friction force is proportional to the normal load. In other words, these three rules state that the ratio of the friction force to the normal load, also called the coefficient of kinetic friction, $\mu = F/W$, is a constant, which does not change with changing W , A_a , and V , i.e., independent of W , A_a , and V [12].

The first and second Amontons–Coulomb’s rules are related to each other. To illustrate, let us consider an apparent area of contact A_a which supports a normal load W , resulting in the friction force $F = \mu W$. A part of the apparent area of contact A_a/c supports the normal load W/c resulting in the friction force $F/c = \mu W/c$, where c is a constant. Let us now increase the normal load from W to cW . According to the first Amontons–Coulomb’s rule, which states that F is proportional to W , such an

increase results in the friction force F and normal load W acting upon the part of apparent area of contact A_a/c . In other words, both for the whole apparent area of contact A_a and for its fraction A_a/c , the same friction force F corresponds to the load W . Thus, using only the first Amontons–Coulomb’s law, it was shown that the ratio F/W is independent of the apparent area of contact, which constitutes the second Amontons–Coulomb’s rule. Therefore, the load dependence of friction is coupled with its dependence on the apparent area or size of contact. In the case the load independence is violated (i.e., the μ is dependent on load), the size independence will be violated too (i.e., the μ will depend on the apparent area of contact) [12].

It is emphasized that the Amontons–Coulomb’s empirical laws of friction are not fundamental laws of nature and they are not satisfied in many cases, especially at micro-/nanoscale. It is known from experiments that friction is size dependent and the coefficient of friction at micro-/nanoscale is different from that at the macroscale; load and velocity dependence of the coefficient of friction is also well established [24, 25]. Several approaches have been suggested to deal with the laws of friction at micro-/nanoscale, which include formulation of “scaling laws of friction” [24, 26–28] as well as specific nanofriction laws, which should substitute for the Amontons–Coulomb’s laws at the nanoscale [25, 28].

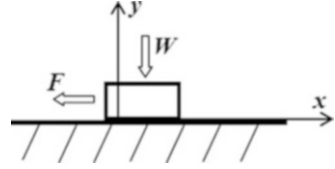
Despite the fact that Amontons–Coulomb’s laws are only approximations, they have striking universality. Equation (2.1) is valid for a very diverse range of material combinations including such classes of materials as metals, polymers, ceramics, composites, and virtually any other materials. It is also valid for normal loads ranging from nano-Newtons (in many nano-tribological applications) to thousands of tons (in geophysical applications). Furthermore, friction is a complex phenomenon that involves various apparently unrelated physical mechanisms, such as the van der Waals, covalent, and capillary adhesion, elastic and plastic deformation, brittle fracture, the so-called ratchet, cobblestone, and “third-body” mechanisms.

One way to formally explain the universality of the linear friction law is to view it as a limiting case of the viscous friction law. The viscous friction law states that the friction force is linearly proportional to the sliding velocity, and it is similar to other linear empirical laws of physics, such as the Ohm’s law of electrical conductivity, the Fourier law of heat conduction, or Fick’s law of diffusion. These laws describe nonequilibrium thermodynamic processes and are viewed as a consequence of nonequilibrium thermodynamic linear Onsager relationships between the so-called generalized thermodynamic forces and flows [29]. Taking into consideration the normal degree of freedom, the Onsager relationships state the linear proportionality of the velocity and forces

$$\begin{aligned}\dot{x} &= L_{11}F + L_{12}W \\ \dot{y} &= L_{21}F + L_{22}W\end{aligned}\tag{2.6}$$

where L_{ij} are the Onsager coefficients. The interface between sliding bodies has highly anisotropic properties, because a small force in the direction of the interface causes

Fig. 2.8 The normal degree of freedom, y , in dynamic friction



large displacements, whereas a small force in the normal direction causes only small displacements (Fig. 2.8). To compensate for this anisotropy, we substitute coordinates using a small parameter ε as $(x,y) \rightarrow (\varepsilon x,y)$. This yields $\dot{x} = (L_{11}F + L_{12}W)/\varepsilon$, and, in the limit of $\varepsilon \rightarrow 0$, any velocity \dot{x} satisfies (2.6), provided $L_{11}F + L_{12}W = 0$, which is exactly the case of Coulomb friction if $\mu = -L_{12}/L_{11}$ [29].

2.3 Friction Mechanisms

Bowden and Tabor [30] established the friction theory to explain causes of friction. According to this theory, friction has two components, namely, (a) adhesive component (μ_a) and (b) plowing component (μ_p). These components are independent to each other, such that

$$\mu = \mu_a + \mu_p \quad (2.7)$$

μ_a depends on the material pair, lubrication, and also on the real area of contact, while μ_p depends on the degree of plastic deformation taking place at the asperity level.

2.3.1 Adhesive Component

In this case contacts between two clean metal surfaces were considered. When metal surfaces are loaded against each other, they make contact only at the tips of the asperities. As the real area of contact is small, the pressure over the contacting asperities is assumed high enough to cause them to deform plastically. This plastic flow of the contacts causes an increase in the real area of contact until the real area of contact is just sufficient to support the load.

The normal force which is balanced by real area of contact is given by

$$W = AH \quad (2.8)$$

where A is the real area of contact, H is the hardness of the softer materials, and W is the normal load.

Depending on the degree of interpenetration of asperities and the surface energy, adhesive bonding occurs at the real area of contact of asperities. When these two surfaces move relative to each other, a lateral force is required to shear the adhesive

bonds formed at the interface in the regions of real area of contact. The friction force depends on the surface shear strength of the materials. The mean shear strength of the weakest junctions at real area of contact is denoted as S . Neglecting the effect of junction growth, the frictional force is given by

$$F = AS \quad (2.9)$$

$$F = \frac{W}{H}S \quad (2.10)$$

$$\frac{F}{W} = \frac{S}{H} \quad (2.11)$$

Therefore,

$$\mu = \frac{F}{W} = \frac{S}{H} \quad (2.12)$$

Thus, if adhesive component dominates frictional behavior, the friction coefficient is calculated from the ratio of shear strength of interface and hardness of soft material.

For most metals

$$S \approx \frac{H}{5} \quad (2.13)$$

Thus, in general, the adhesion theory predicts that $\mu = 0.2$, when the material pairs are similar. It should be true for any combination of the same material. But it is not true usually because of junction growth and work hardening.

2.3.2 Plowing Component

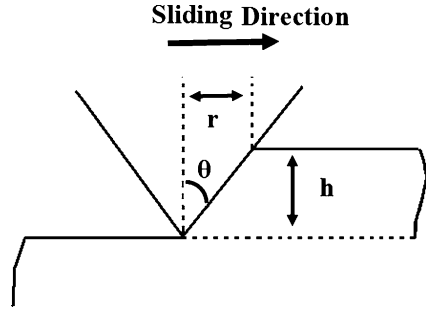
Plowing action occurs when asperities of a hard metal penetrate into a softer metal and plow out a groove by plastic deformation in the softer material. This is a major component of friction during abrasion processes, and this is probably an important factor when adhesion component is small.

Consider a harder material slides over a softer material. The harder surface was assumed to consist of large number of similar conical asperities of semi-angle θ in contact with a softer material whose surface is comparatively flat. During sliding the front surface of each conical asperity is in contact with the opposing material as shown in Fig. 2.9. Thus, the vertically projected area of contact is given by

$$A = \frac{1}{2}n\pi r^2 \quad (2.14)$$

where n is the total number of asperities.

Fig. 2.9 Schematic diagram shows the plowing of a soft surface by a hard conical asperity



We know that $W = AH$; therefore,

$$W = \frac{1}{2}n\pi r^2 H \quad (2.15)$$

The friction force F is obtained in a similar manner by considering the total projected area of material, which is being displaced by plastic deformation, that is,

$$F = nrhH \quad (2.16)$$

Therefore,

$$\mu = \frac{F}{W} = \frac{2h}{\pi r} \quad (2.17)$$

However,

$$\frac{h}{r} = \cot \theta \quad (2.18)$$

Therefore,

$$\mu = \frac{2}{\pi} \cot \theta \quad (2.19)$$

2.3.3 Rolling Friction

Rolling friction is the resistance to motion that takes place when a surface is rolled over another surface. The coefficient of rolling friction between a cylindrical or spherical body against itself and a flat body generally is in the range of 5×10^{-3} to 10^{-5} . In comparison, the coefficient of sliding friction ranges typically from 0.1 to 1.

Rolling friction is not as straightforward as sliding friction. But still, there is a relationship between the rolling friction and the normal force, similar to that in sliding friction. It can be stated as

$$F_R = \mu_R W \quad (2.20)$$

where F_R is the resistive force of rolling friction, μ_R is the coefficient of rolling friction for the two surfaces, W is the normal force.

The force of rolling resistance can also be calculated by

$$F_R = \frac{(\mu_R W)}{r} \quad (2.21)$$

where F_R is the resistive force of rolling friction, r is the wheel radius, μ_R is the coefficient of rolling friction, and W is the normal force.

2.3.4 Ratchet Mechanisms

Interlocking of asperities may result in one asperity climbing upon the other, leading to the so-called ratchet mechanism. In this case, in order to maintain sliding, a driving force should be applied which is proportional to the slope of the asperity. At the atomic scale, a similar situation exists when an asperity slides upon a molecularly smooth surface and passes through the tops of molecules and valleys between them. This sliding mechanism is called “cobblestone mechanism.” This mechanism implies that the strong bonds are acting in the bulk of the body, whereas interface bonds are weak.

2.3.5 Brittle Fracture and Plastic Inception Mechanisms

For a brittle material, asperities can break forming wear debris. Therefore, fracture also can contribute to friction. There is also an analogy between mode II crack propagation and sliding of an asperity [31–33]. When an asperity slides, the bonds are breaking at the rear, while new bonds are being created at the front end. Thus, the rear edge of an asperity can be viewed as a tip of a propagating mode II crack, while the front edge can be viewed as a closing crack. Gliding dislocations, emitted from the crack tip, can also lead to the microslip or local relative motion of the two bodies [24]. Calculations have been conducted to relate the stress intensity factors with friction parameters [31–33]. Crack and dislocation propagation along the interface implies that the interface is weak compared to the bulk of the body.

Chang et al. [34] proposed a model of friction based upon plastic yield, which was later modified by Kogut and Etzion [35]. They considered a single-asperity contact of a rigid asperity with an elastic–plastic material. With an increasing normal load, the maximum shear strength grows and the onset of yielding is possible. The maximum shear strength occurs at a certain depth in the bulk of the body. When the load is further increased and the tangential load is applied, the plastic zone grows and reaches the interface. This corresponds to the onset of sliding. Kogut and Etzion [35] calculated the tangential load at the onset of sliding as a function of the normal load using the finite elements analysis and found a nonlinear dependence between the shear and tangential forces. This mechanism involves plasticity and implies structural vulnerability of the interface compared to the bulk of the contacting bodies.

2.3.6 The “Third-Body” Mechanism

During the contact of two solid bodies, wear and contamination particles can be trapped at the interface between the bodies. Along with liquid which condensates at the interface, they form the so-called third body which plays a significant role in friction. The trapped particles can significantly increase the coefficient of friction due to plowing. Some particles can also roll and thus serve as rolling bearings, leading to reduced coefficient of friction. However, in most engineering situations, only 10 % of the particles roll and thus the third-body mechanism leads to an increase of the coefficient of friction. At the atomic scale, adsorbed mobile molecules can constitute the “third body” and lead to significant friction increase [36]. The third body has much weaker bonds to the surface, than those in the bulk of the body.

2.3.7 Effect of Surface Roughness

Various statistical models of contacting rough surfaces have been proposed following the pioneering work by Greenwood and Williamson [37] that considered a random distribution of asperity heights. These models conclude, using the numerical computations, that for typical roughness height distributions (such as the Gaussian roughness) for both elastic and plastic materials, the real area of contact is almost linearly proportional to the load [7]. For the elastic contact of a smooth surface and a rough surface with the correlation length β^* and standard deviation of profile height σ , the real area of contact is given by

$$A_r \propto \frac{\beta^*}{E^* \sigma} W \quad (2.22)$$

where E^* is the composite elastic modulus of the two bodies [3]. Note that σ is the vertical and β^* is the horizontal roughness parameters with the dimension of length. The smoother the surface (the higher the ratio β^*/σ), the larger the A_r is. Physically, the almost linear dependence of the real area of contact upon the normal load in this case is a result of the small extent of contact; in other words, it is the consequence of the fact that the real area of contact is a small fraction of the nominal area of contact. With increasing load, as the fraction of the real area of contact grows, or for very elastic materials, such as the rubber, the dependence is significantly nonlinear. However, for small real area of contact, with increasing load the area of contact for every individual asperity grows, but the number of asperity contacts also grows, so the average contact area per asperity remains almost constant.

For plastic contact, the real area of contact is independent of roughness parameters and given by the ratio of the normal load to the hardness of a softer material H [3]

$$A_r = \frac{W}{H} \quad (2.23)$$

Hardness is usually defined in indentation experiments as force divided by the indentation area, so (2.23) naturally follows from this definition. In many cases it may be assumed that the hardness is proportional to the yield strength. Whether the contact is elastic or plastic may depend upon the roughness parameters, elastic modulus, and hardness. Interestingly, Greenwood and Williamson [37] showed whether the contact is elastic or plastic does not depend upon the load, but solely upon the so-called plasticity index $\psi = (\sqrt{\sigma/R_p})E^*/H$, where σ is the standard deviation of peak heights and R_p is the mean asperity peak radius.

Fractal models provide an alternative description of a rough surface. Long before the discovery of fractals by mathematicians, Archard [38] studied multi-scale roughness with small asperities on top of bigger asperities, with even smaller asperities on top of those, and so on. According to the Hertzian model, for the contact of an elastic sphere of radius R loaded against an elastic flat with the contact radius a , the contact area $A = \pi a^2$ are related the normal load as

$$A_r = \pi \left(\frac{3RW}{4E^*} \right)^{2/3} \quad (2.24)$$

The pressure distribution as the function of the distance from the center of the contact spot, r , is given by

$$p = \left(\frac{6WE^{*2}}{\pi^3 R^2} \right)^{1/3} \sqrt{1 - (r/a)^2} \quad (2.25)$$

Let us now assume that the big spherical asperity is covered uniformly by many asperities with a much smaller radius, and these asperities form the contact. For an asperity located at the distance r from the center, the load is proportional to the stress given by (2.25). The area of contact of this small asperity is still given by (2.24) with using the corresponding load. The dependence of total contact area upon W is then given by the integration of the individual contact areas by r as [38]

$$\begin{aligned} A_r &\propto \int_0^a \left[W^{(1/3)} \sqrt{1 - r^2/a^2} \right]^{2/3} 2\pi r dr \\ &\propto \int_0^\pi \left[W^{(1/3)} \cos \phi \right]^{2/3} 2\pi (a \sin \phi) a \cos \phi d\phi \\ &\propto W^{(2/9)} a^2 \propto W^{(2/9)} W^{(2/3)} \propto W^{(8/9)} \end{aligned} \quad (2.26)$$

In the above derivation, the variable change $r = a \sin \phi$. The integral of the trigonometric functions can be easily calculated; however, its value is not important for us, because it is independent of a and W .

If the small asperities are covered by the “third-order” asperities of even smaller radius, the total area of contact can be calculated in a similar way as

$$A_r \propto \int_0^a \left[W^{(1/3)} \sqrt{1 - r^2/a^2} \right]^{8/9} 2\pi r dr \propto W^{(8/27)} a^2 \propto W^{(26/27)} \quad (2.27)$$

For elastic contact, it is found

$$A_r \propto W^{\frac{3n-1}{3n}} \quad (2.28)$$

where n is the number of orders of asperities, leading to an almost linear dependence of A_r upon W with increasing n . Later more sophisticated fractal surface models were introduced, which lead to similar results.

Thus both statistical and fractal roughness, for elastic and plastic contact, combined with the adhesive friction law results in an almost linear dependence of the friction force upon the normal load.

2.4 Factors Affecting Friction

Surface roughness: One of the early attempts to explain friction was to relate it to surface roughness because surface is not generally smooth; instead it consists of asperities (i.e., short-range perturbations from the mean) and waviness (i.e., long-range perturbations from the mean). The roughness theory assumed that the frictional force is equal to the force required to climb up the asperity of slope θ and the coefficient of friction was described as a function of $\tan \theta$ [39]. However, it is clear that asperities undergo deformation due to the sliding action rather than simply sliding over each other. In very smooth surfaces, the real area of contact grows rapidly, and so is the friction, whereas with very rough surfaces the friction is high again because of the need to lift one surface over the asperities on the other. In the intermediate range of roughness that normally used in engineering practice, the friction is at minimum and almost independent of the roughness [40].

Surface topography: The influence of the surface topography on friction reduction is not well established. Early research in this direction focused on aspects such as the real area of contact and the lubricant trapping and tried to highlight the significance of surface topography [41]. Later on the effect of surface topography on friction was studied in detail [42–52]. Several well-known roughness parameters were used to quantify surface topography [53–62]. Surface roughness parameter such as the average roughness, R_a , is used to describe a surface topography. However, such a single roughness parameter cannot describe a functional characteristic like friction, and it is possible that two surface topographies can have the same R_a , but their frictional characteristics could be significantly different [63–65]. Attempts were made to correlate surface roughness parameters with friction [66–68]. In addition, new roughness parameters were formulated to correlate with friction [61, 69–71]. In general, the correlation coefficient between the coefficient of friction and the roughness parameters was system dependent.

Crystal structure: Effect of material crystal structure on friction depends on how easily material can undergo plastic deformation. Ease of plastic deformation of a material depends on the number of slip systems available. It is well known that a

minimum of five independent slip systems are required for plastic deformation to take place by slip. Hexagonal metals have a limited number of slip systems, and thus the chance for forming higher real area of contact is less due to lack of plastic deformation when compared with FCC metals. Hence, HCP metals experience lower friction coefficients than FCC and BCC metals in which a larger number of slip systems are available for plastic deformation [72–76]. Since crystal structures affect friction, it could be expected that allotropic metals exhibit a similar influence on either side of a transition temperature due to phase transformation. Further, the lattice parameters in HCP metals influence the number of operating slip systems and thus more easily undergo plastic deformation which in turn influences the friction. HCP metals with close to ideal atomic stacking ratio ($c/a = 1.633$), e.g., Co, Rh, and Mg, primarily slip along basal planes and have low friction coefficients. Metals which deviate considerably from ideal stacking such as titanium ($c/a = 1.587$) will exhibit primarily non-basal slip mechanisms and higher friction coefficients.

Strain hardening and hardness: It is well established that severe plastic deformation occurs in the surface regions (e.g., asperity contacts) of a metal sliding over a harder surface. This results in the surface of the metal being progressively work hardened, and the surface will reach a maximum hardness that depends on the method by which it has been deformed [77, 78]. In general, coefficient of friction is an inverse function of hardness of a metal. The effect of hardness on friction is attributed to the fact that lack of plastic deformability of hard metals, with subsequent decrease in the ability of metals to adhere, results in low friction [71, 79, 80]. The atomic bonds in harder metals are strong and hence the resistance to adhesion is increased, providing low frictional characteristics. However, coefficient of friction is not necessarily lower for harder materials; hardness alone cannot be used as a criterion for predicting the coefficient of friction [81].

Elastic and shear modulus: Any increase in elastic modulus results in a decrease in real area of contact and thus reduces the adhesion and friction. The shear modulus, behaves like the elastic modulus because it relates by $E = 2.6 G$, affects the frictional behavior of metals. Thus, the friction coefficient decreases with an increase in shear modulus [82].

Grain size: Effects of grain size on frictional characteristics of many materials have been studied in combination with their wear behavior. It was stated that friction coefficient decreases with a decrease in grain size [83–86]. One of the important consequences of this is the improved mechanical and chemical properties of nanocrystalline materials. Thus, nanocrystalline materials are of great industrial importance, and their wide spread use in modern technology is quite evident in areas such as MEMS. These materials are used as bulk as well as coatings to engineering substrates.

Surface energy: In dry clean conditions, adhesion and friction strongly depend upon the surface energy of the materials [40]. Metals which have high surface energies form adsorbed layers by reacting with gaseous and liquid molecules in air.

The existence of adsorbed layer reduces surface energy of metals and also decreases the friction coefficient. When there is no gaseous environment, higher values of the ratio of surface energy to hardness of metals correspond to large adhesion and a high friction coefficient.

Normal load: Some metals (e.g., Cu, Al) which oxidize in air show lower friction at low loads as a result of oxide film formation that effectively separates the two metal surfaces and exhibits high friction at high loads due to breakdown of the oxide film [87].

Sliding velocity: High sliding velocities result in surface frictional heating and thus formation of a thin molten layer at the asperity contacts which reduces the shear strength at the contact resulting in very low friction coefficient. This thin molten film acts as lubricant between sliding surfaces [88]. Generally, the friction coefficient decreases with an increase in sliding velocity. Formation of oxide layers on metal surfaces at high temperature, which is induced by sliding speed, results in low friction. On the other hand, softening of the metal surface may result in high friction due to increased plowing in the softer material. Both of these two factors make it difficult to predict the effect of sliding velocity on friction.

Environment: In ambient conditions, most metals oxidize and form oxide films, typically between 1 and 10 nm thick within a few minutes of exposure of clean surfaces. This oxide films act as low shear strength film and minimize the metal–metal contact at asperity level and thus lead to low friction. On the other hand, in vacuum condition, there is less chance of oxidation and direct contact existing between metal–metal surfaces. In this case, depending on metallurgical compatibility, the level of adhesion governs the frictional behavior of the metals. The values of the friction coefficient in vacuum were about 10 times higher than values measured in air [89].

Temperature: An increase in the temperature generally results in metal softening. When the temperature of a sliding metal is increased, several effects occur. The mechanical properties of the contacting metals will change, the rate of oxidation will increase, and a phase transformation may take place. All these factors will influence the frictional behavior.

2.5 Friction of Materials

The coefficient of friction depends on the experimental conditions under which it is measured [90]. In general, clean metal surfaces under vacuum show strong adhesion and high coefficient of friction, typically 2–10. Strong metallic bonds are formed across the interface in high vacuum. However, in most practical application, metals slide against one another in air, and the coefficient of friction values are much lower than in vacuum and lie typically for dry sliding, in the range from 0.2 to 1.0. Some metals oxidize in air to form oxide films that are typically between 1 and

10 nm thick within a few minutes of exposure. The oxide film acts as a low shear strength film and also due to low ductility of the film leads to low friction. The oxide film may effectively separate the two metallic surfaces. The friction between oxide surfaces or between oxide and bare metal surfaces is almost always less than between surfaces of bare metals. At low normal loads, the oxide films effectively separate the two metal surfaces, and there is little or no true metallic contact. Thus, the coefficient of friction is low. As the normal load is increased, a transition occurs to a higher value of the coefficient of friction. This could be due to the breakdown of oxide films due to higher loads imposed during sliding. Hexagonal metals such as Mg, Zn, and Co exhibit low friction. In general, the coefficient of friction for an alloy tends to be rather less than that for its pure components [91].

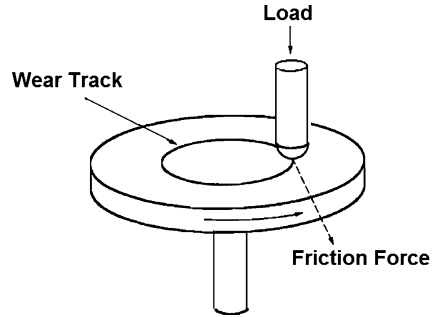
Ceramics exhibit high mechanical strength, do not lose their strength or oxidize readily at elevated temperatures, and are resistant to corrosive environments. Ceramic materials are much less ductile than metals. The mechanical behavior of ceramics differs from that of metals or alloys due to the different nature of the interatomic forces with covalent or ionic bonding in ceramics compared to that of metallic bonding in metals or alloys. The nature of contact between ceramics is more likely to be elastic than in metals. Although adhesive forces (due to covalent, ionic, or van der Waals bonds) are present between ceramic materials in contact, low real area of contact results in relatively low values of coefficient of friction comparable to metallic couples. The coefficient of friction of ceramic pairs does not reach as high values as that of metals under similar testing conditions. The coefficient of friction value for ceramic–ceramic contacts lies typically in the range from 0.2 to 0.8. These are similar to the values seen for metallic couples sliding in air in the presence of intact oxide films, and indeed, there is much similarity between the contact of oxidized metal surfaces and that of bulk oxide ceramics.

Polymers are more compliant than metals or ceramics with elastic modulus values typically one-tenth or even less. Their strength is also much lower. They are often used in sliding applications against hard mating surfaces. In polymers, the contact between polymers or between a polymer and a metal is often predominantly elastic and creates transfer layers. In this respect, the friction of polymers differs fundamentally from that of metals. Coefficient of friction between polymers sliding against themselves or against metals or ceramics commonly lies in the range from 0.1 to 0.5. The friction of polymers, like that of metals, can be attributed to two sources, namely, adhesion and plowing. Many polymers sliding against hard counterfaces (e.g., metals) transfer detectable films of polymers onto the counterface [60, 92, 93]. The formation and behavior of the transfer films are important factors in the friction and wear of these polymers.

2.6 Friction Measurement Devices

Any apparatus for measuring friction must be capable of supplying relative motion between two specimens, of applying a measurable normal load, and of measuring the tangential resistance to motion. Many accelerated test apparatuses are commercially

Fig. 2.10 Schematic of pin-on-disk test system



available that allow control of such variables like sample geometry, load, velocity, temperature, and environment. The most commonly used device is a pin-on-disk apparatus. As shown in Fig. 2.10, the disk is driven continuously while the pin is normally stationary with a load applied to it. In the pin-on-disk apparatus, the pin is held stationary and the disk rotates. The pin can be a nonrotating ball (ball-on-disk configuration), a hemispherically tipped rider, or a flat-ended cylinder.

2.6.1 Other Important Apparatus

Pin-on-flat: In the pin-on-flat apparatus, a flat moves relative to a stationary pin in reciprocating motion. In some cases, the flat is stationary and the pin reciprocates. The pin can be a ball, a hemispherically tipped pin, or a flat-ended cylinder.

Pin-on-cylinder: The pin-on-cylinder apparatus is similar to the pin-on-disk apparatus, except that loading of the pin is perpendicular to the axis of rotation. The pin can be flat or hemispherically tipped.

Flats-on-rotating-cylinder: In the flats-on-rotating-cylinder apparatus, two rectangular flats are loaded perpendicular to the axis of rotation of the disk.

Crossed-cylinder: The crossed-cylinder apparatus consists of a stationary solid cylinder and a rotating solid cylinder that operates perpendicular to the stationary cylinder.

Four-ball: The four-ball apparatus consists of four balls in the configuration of an equilateral tetrahedron. The upper ball rotates and rubs against the lower three balls which are held in a fixed position.

3 Wear

Wear is the progressive loss of substance from the surface of a body brought about by mechanical action. In most cases, wear occurs due to surface interactions at the asperities. During relative motion, material on the contact surface may be displaced

Table 2.1 Different types of wear mechanisms, definitions, and characteristics

Mechanisms	Definitions	Characteristics
Adhesion	Wear due to transfer of material from one surface to another surface by shearing of solid welded junctions of asperities	Adhesive bonding, shearing, and material transfer
Abrasion	Wear due to hard particles or protuberances sliding along a soft solid surface	Plowing, wedging, and cutting
Delamination	Wear caused by delamination of thin material sheets beneath the interface in the subsurface	Plastic deformation, crack nucleation, and propagation
Erosion	Wear due to mechanical interaction between solid surface and a fluid, or impinging liquid or solid particles	Angle of incidence, large-scale subsurface deformation, crack initiation, and propagation
Fretting	Wear due to small amplitude oscillatory tangential movement between two surfaces	Relative displacement amplitude and entrapment of wear particles
Fatigue	Wear caused by fracture arising from surface fatigue	Cyclic loading and fatigue crack propagation
Corrosive/oxidative wear	Wear occurs when sliding takes place in corrosive/oxidative environment	Formation of weak, mechanically incompatible corrosive/oxide layer

so that properties of the solid body near the surface are altered; then material may be removed from a surface and may result in the transfer to the mating surface or may break lose as a wear particle. Wear, as friction, is not a material property; it is a system response. Operating conditions affect the wear process. Sometimes it is assumed that high friction correlates to a high wear rate. This is necessarily not true. Wear is quantified by the term “wear rate” which is defined as the mass or volume or height loss of material removed per unit time or sliding distance.

3.1 Wear Mechanisms

The important wear mechanisms are adhesive wear, abrasive wear, delamination wear, erosive wear, fretting wear, fatigue wear, and corrosive/oxidative wear. The characteristic features and definitions of different wear mechanisms are given in Table 2.1. In general, two-thirds of all wear processes encountered in industrial situations occurs due to adhesive and abrasive wear mechanisms. In many cases, wear is initiated by one mechanism, and it may proceed by other wear mechanisms. Wear components are generally examined to determine the type of wear mechanism by using microscopy or surface analytical techniques.

Wear is also expressed based on scale size of wear debris such as mild wear and severe wear. In mild wear, wear occurs at the outer surface layers and worn

debris contains fine oxide particles of size that varies from 0.01 to 100 nm. In severe wear, wear occurs at deep surfaces and size of wear debris ranges from 100 nm to 100 μm .

3.1.1 Adhesive Wear

When two atomically clean solid surfaces are brought together, the atoms must be in contact at some points. Thus, two surfaces will experience short-range van der Waals forces. At distance of about 1 nm, strong short-range forces come into action, and strong adhesive junctions may be formed at the real area of contact. When there is relative motion, the adhered junctions are sheared. The net result is that softer material is transferred to harder surface. Soft material may adhere to hard surface, or on the other hand, subsequent sliding produces a loose wear debris. The amount of wear depends on the location at the junctions that is sheared. More specifically, if shear takes place at the original interface, then the wear is zero. However, if shear takes place away from the interface, a fragment of material is transferred from one surface to the other. In practice, the transfer of material is observed from the softer material to the harder material, but occasionally from the harder material to the softer material. Adhesive wear is often called galling, scuffing, cold welding, or smearing.

Archard [94] derived a theoretical expression for the rate of adhesive wear. In this theory, it was assumed that the area of contact comprises a number of circular contact spots, each of radius a . Then the area of each contact spot is πa^2 .

Each contact supports a normal load

$$W = \pi a^2 H \quad (2.29)$$

where H is the hardness of the soft material.

If there are n number of contacts, then the total normal load $W = n\pi a^2 H$ or

$$n\pi a^2 = \frac{W}{H} \quad (2.30)$$

During sliding, the opposing surface will pass over the asperity for a sliding distance $2a$.

It is assumed that the wear fragment produced from each asperity is hemispherical in shape and of volume

$$v = \frac{2}{3} \pi a^3 \quad (2.31)$$

Then the wear volume δQ produced by one asperity contact in unit sliding distance is given by

$$\delta Q = \frac{\frac{2}{3} \pi a^3}{2a} = \frac{\pi a^2}{3} \quad (2.32)$$

The total wear volume Q per unit sliding distance is

$$Q = \frac{n\pi a^2}{3} \quad (2.33)$$

where n is the total number of contacts.

Substituting (2.30) in (2.33), we get

$$Q = \frac{W}{3H} \quad (2.34)$$

This equation suggests that:

- (a) Wear volume is proportional to the load.
- (b) Wear volume is inversely proportional to the hardness of the softer material.
- (c) Wear volume is proportional to the sliding distance.

In general, the experimental results proved that the wear volume is much less than the theoretical predictions by several orders of magnitude. Equation (2.34) was derived by assuming that a wear particle was produced at each asperity encounter. Thus, this theory is modified by considering the experimental results and postulating that wear particles produced only a fraction k of such encounter, so that

$$Q = k \frac{W}{3H} \quad (2.35)$$

Or $Q = K \frac{W}{H}$ or for “ x ” sliding distance

$$Q = K \frac{Wx}{H} \quad (2.36)$$

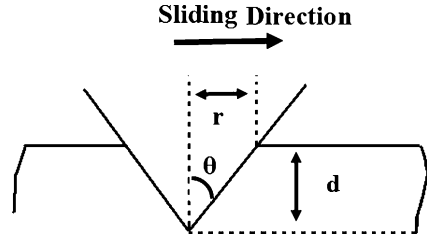
where $K = \frac{k}{3}$ and is called wear coefficient.

Thus, the uncertainty in predicting a wear rate is due to the uncertainty in the value of K , and this must be found experimentally for different combination of sliding materials and different conditions of rubbing. The value of K ranges typically from 10^{-8} to 10^{-4} for mild wear and from 10^{-4} to 10^{-2} for severe wear for most material combinations, depending on the operating conditions.

3.1.2 Abrasive Wear

Consider a situation in which a hard material is kept in contact with the soft solid surface. The asperities of hard materials are pressed into the soft surface with plastic flow of the soft surface. When tangential movement is imposed, the hard material will slide and remove the soft material by plowing. Thus, the abrasion process includes several deformation modes such as plowing, wedge formation, and cutting. Plowing causes a series of grooves as a result of plastic flow of the softer material.

Fig. 2.11 Abrasive wear by conical asperity



In wedge formation, an abrasive tip plows a groove and develops a wedge on its front. In cutting form, an abrasive tip cuts a groove and removes the material. Abrasion is typically categorized according to type of contact as two-body and three-body abrasion. In two-body abrasion, a hard material slides along a soft surface. In three-body abrasion, wear debris are caught between two surfaces and cause one or both of them to be abraded. Wear loss in a two-body abrasion is typically 10–1,000 times greater than three-body abrasion for given load and sliding distance.

The well-known model of abrasive wear assumes that the abrasive asperity is like a sharp tool which has a conical shape, defined by the angle θ , plowing a track through the softer flat surface and removes a material as shown in Fig. 2.11. In traversing unit distance, it displaces a volume of material

$$v = rd \quad (2.37)$$

It can be seen from Fig. 2.11 that

$$d = r \tan \theta \quad (2.38)$$

Therefore,

$$v = r^2 \tan \theta \quad (2.39)$$

The total volume of material displaced in unit sliding distance

$$Q = nr^2 \tan \theta \quad (2.40)$$

where n is the number of asperity contacts.

For simplicity, we assume that the softer material has yielded due to normal load alone. Therefore, the abrasive wear particle transmits a normal load of

$$W = \pi r^2 \frac{H}{2} \quad (2.41)$$

where H is the hardness of the softer material.

Thus, if there are n asperity contacts, the normal load

$$W = n\pi r^2 \frac{H}{2} \quad (2.42)$$

or

$$nr^2 = \frac{2}{\pi} \frac{W}{H} \quad (2.43)$$

Substituting (2.43) in (2.40), we get

$$Q = \frac{2}{\pi} \frac{W}{H} \tan \theta \quad (2.44)$$

Similar to adhesive wear, it is found that not all abrasive particles produce loose wear debris.

Thus,

$$Q = k \frac{W}{H} \frac{\tan \theta}{\pi} \quad (2.45)$$

where k is the proportion of events that actually produces wear particles.

Or

$Q = K \frac{W}{H}$ or for “ x ” sliding distance

$$Q = K \frac{Wx}{H} \quad (2.46)$$

where $K = k \frac{\tan \theta}{\pi}$

Equation (2.46) is of the same form of as the adhesive wear (2.36), and according to this simple derivation, the laws of wear which are derived from (2.36) should apply equally well to abrasive wear.

In the above derivation we assumed that all the material displaced by the abrasive particles becomes loose wear debris. However, this is not true. Examination of abraded surfaces showed that much of the displaced material can be simply piled up at the sides of the grooves and not lost to the surface. The value of K typically ranges from 10^{-6} to 10^{-1} .

3.1.3 Delamination Wear

The delamination theory of wear was first put forward by Suh [95] to describe the wear of surfaces in sliding contact. This theory describes the production of laminate wear debris in the following way:

1. When two surfaces come in to contact, normal and tangential loads are transmitted through the contact points. The material at the surface and very near the surface does not have a high dislocation density during sliding. This is due to the

elimination of dislocations by the image force acting on those dislocations which are parallel to the surface. Therefore, cold-working of the material very near the surface is less than that at the subsurface.

2. The surface traction exerted by the harder asperities at the contact points induces incremental plastic shear deformation which accumulates with repeated loading in the subsurface. As subsurface deformation continues, there will be pileups of dislocations at finite distance from the surface. As time progresses, the piled up dislocations will lead to the formation of microvoids or cracks. Thus, cracks are nucleated below the surface.
3. As time progresses further, these cracks will coalesce, either by growth or shearing of the metal, and propagate parallel to the wear surface. The depth of crack nucleation and distance of propagation depend on material properties, normal load, and friction characteristics of the surface. When this crack reaches a critical length, the material between the crack and the surface will shear, yielding long and thin laminated wear debris.

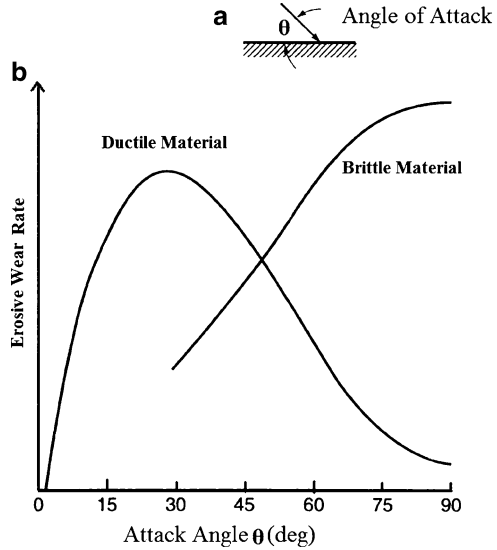
3.1.4 Erosion Wear

Erosion is the form of damage experienced by a solid body when liquid or solid particles impinge on a solid surface. There are basically two types, namely, solid erosion and fluid erosion.

Solid erosion is a form of abrasive wear and is treated differently because the contact stress arises from the kinetic energy of particles flowing in air as it encounters the surface. The particle velocity, impact angle, and the size of the abrasive particle give a measure of the kinetic energy of the impinging particle. Wear debris are formed in erosion as a result of repeated impacts. As in the case of abrasive wear, erosive wear occurs by plastic deformation and/or brittle fracture, depending on material being eroded away and on operating conditions. Wear rate dependence on the impact angle for ductile and brittle materials is different (see Fig. 2.12). For ductile materials the maximum erosion occurs at an angle of approximately 20° . Ductile material will undergo wear by a process of plastic deformation in which the material is removed by the displacing or cutting action of the eroded particle. In brittle materials, the material is removed by the formation and intersection of cracks that radiate out from the point of impact of the eroded particle. The shape of the abrasive particles also affects the wear rate. Sharper particles would lead to more localized deformation and hence higher wear rates as compared to the rounded particles.

In fluid erosion, there are basically two types—liquid impact erosion and cavitation erosion. When tiny liquid drops strike the solid surface at high speeds, due to high pressure, materials can undergo plastic deformation or fracture, and repeated impacts lead to pitting and erosive wear. In many cases, pure liquid impingement erosion is an unlikely mechanism, and erosion–corrosion mechanism usually does more damage. In ductile materials, a single intense impact may produce a central depression with a ring of plastic deformation around it where

Fig. 2.12 Rate of erosive wear as a function of attached angle of impinging particles for ductile and brittle materials

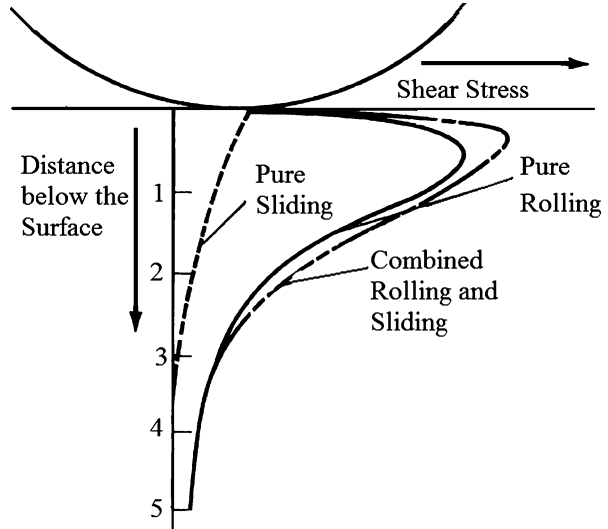


the jetting outflow may remove the material by a tearing action. In brittle materials, circumferential cracks may form around the impact site, caused by tensile stress waves propagating outward along the surface. With continued impacts, material can spall off the inside surface due to the compressive stress wave from the impact reflecting there as a tensile wave. Cavitation damage occurs when bubbles entrained in a liquid become unstable and implode against the surface of a solid. When bubbles collapse that are in contact with or very close to a solid surface, it will collapse asymmetrically, forming a micro-jet of liquid directed towards the solid. The solid material will absorb the impact energy as elastic deformation, plastic deformation, or fracture. The latter two processes may cause localized deformation and/or erosion of the solid surface.

3.1.5 Fatigue Wear

Fatigue wear can be an important phenomenon on two scales: macroscopic and microscopic. Macroscopic fatigue occurs at nonconforming loaded surfaces, such as those found in rolling contacts, whereas microscopic fatigue occurs at the contacts between sliding asperities. In other words, subsurface fatigue and surface fatigue are observed during repeated rolling and sliding, respectively. The repeated loading and unloading cycles may induce the formation of subsurface or surface cracks. Eventually, after a critical number of cycles, these cracks will result in the breakup of the surface with the formation of large fragments, leaving large pits in the surface, also known as pitting. Prior to the critical number of cycles, negligible wear takes place, which is in contrast to the wear caused by an adhesive or abrasive mechanism, where wear causes a gradual deterioration from the start of running.

Fig. 2.13 Variation of principal shear stress at various depths directly below the point of contact of two hard surfaces in pure rolling, pure sliding, and a combination contact. The “ z ” is the distance below the surface in the vertical direction and “ a ” is half of the Hertzian diameter



Rolling contact fatigue: In rolling fatigue, under dry conditions, adhesive and abrasive wear mechanisms are operative during direct physical contact between two moving surfaces relative to each other. In well-lubricated rolling conditions, these wear mechanisms do not operate and there is no progressive visible wear. However, the life of rolling components is limited by the fatigue. At the rolling interface, the contact stresses are very high and fatigue mechanism can be operative. In these cases, although direct solid–solid contact does not occur, the mating surfaces experience large stresses which are transmitted through the lubricating film during the rolling motion. In the presence of such stresses, the maximum compressive stress occurs at the surface, but the maximum shear stress occurs at some distance below the surface (Fig. 2.13). As rolling proceeds, any subsurface element is subject to a stress cycle for each passage of a roller. Time to fatigue failure is dependent on the amplitude of the reversed shear stresses. If the stress amplitude is above the fatigue limit, fatigue failure will eventually occur. The position of failure in a perfect material subjected to pure rolling contact would be defined by the position of maximum shear stress given by the Hertz equations. In practice, materials are never perfect and the position of failure would normally depend on microstructural factors such as the presence of inclusions or microcracks. When a fatigue crack does develop, it occurs below the surface until a region of metal is separated to some extent from the base metal by the crack and ultimately becomes detached and spalls out. By the time cracks grow large enough to emerge at the surface and produce wear particles, these particles may become large flakes.

Sliding contact fatigue: When sliding surfaces make contact at the asperities, wear takes place by adhesion and abrasion. However, in sliding fatigue, asperities can make contact without adhering or abrading and can pass each other, leaving one or

both asperities plastically deformed due to contact stresses. As the surface and subsurface deformation continues, cracks nucleate at and below the surface. Once the cracks are formed, further loading and deformation causes cracks to extend and propagate. After a critical number of cyclic contacts, an asperity fails due to fatigue, producing a wear fragment. In sliding contact, friction is generally high compared to a rolling contact; the maximum shear stress occurs at the surface which leads to surface fatigue.

3.1.6 Fretting Wear

Fretting can occur whenever low-amplitude oscillatory motion in the tangential direction takes place between the contacting surfaces. This is a common occurrence in machinery which is subjected to vibration. Fretting can combine many of the wear process. Basically, fretting is a form of adhesive or abrasive wear, where the normal load causes adhesion between asperities and oscillatory movement causes rupture, resulting in wear debris. Most commonly, fretting is combined with corrosion, in which case the wear mode is known as fretting corrosion. Fretting in corrosive environment produces wear particles which are harder than their parent metals and this can lead to abrasion. The fact that there is no macroscopic sliding at fretting contacts so the fretting wear debris cannot escape easily but is trapped between the surfaces. Therefore, the amount of wear per unit sliding distance due to fretting may be larger than that of adhesive and abrasive wear. The oscillatory sliding can also cause vibration and thus chances of forming fatigue failure. This kind of failure is known as fretting fatigue.

3.1.7 Corrosive/Oxidative Wear

Corrosive wear occurs when sliding takes place in a corrosive environment. In air, the most dominant corrosive medium is oxygen. Therefore, corrosive wear in air is generally called oxidative wear. However, the same principles would apply to wear in any other type of corrosive medium. In the absence of sliding, oxide films typically less than a micrometer thick form on the surfaces. Sliding action wears the oxide film away so that corrosive attack can continue. Thus, corrosive wear requires corrosion and rubbing. Machinery operating near the coast generally produces corrosive wear more rapidly than that operating in a clean environment.

It is important to note that oxidation on the sliding surfaces is usually beneficial. Formations of oxide films act as solid lubricant and prevent metal-metal contact and thus mitigate against the severe adhesion-enhanced wear which would otherwise occur. Oxidation can reduce the wear rate of metallic pairs by two orders of magnitude, as compared with that of the same pair in an inert atmosphere. Very often, when surfaces are oxidized, the wear debris is finely divided oxide, the rubbing surfaces remain smooth, and the rate of loss of material is low. The effects of oxidation depend not only on the oxidation rate but also on the mechanical properties of both the oxide and the base metal and the adhesion of the oxide to the

base metal. Oxidation is a thermally activated process; the rate of oxidation can increase exponentially with temperature. A change of only few degrees in surface temperature can change the rate of oxidation by an order of magnitude.

3.2 Thermodynamic Models of Wear

Friction and wear are dissipative irreversible processes. Entropy is the measure of irreversibility and dissipation. Therefore, entropy can be used to characterize wear and related degradation processes. Manufacturing, which transforms nature's raw materials into highly organized finished components, reduces entropy. Aging or degradation from friction and wear tends to return these components back to natural states. Accordingly, entropy must monotonically increase to be consistent with laws of thermodynamics.

The attempts to use thermodynamic methods for a general theory of wear have been taken by many researchers; however, most of these attempts had limited success due to the complexity of the equations involved and the difficulty of their solution [96–98]. Doelling et al. [99] experimentally correlated wear with entropy flow, dS/dt , at a wearing surface and found that wear was roughly proportional to the entropy produced for the steady sliding of copper on steel under boundary lubricated conditions. Bryant et al. [100] conducted an interesting entropic study of wear. They started from the assumption that friction and wear are manifestations of the same dissipative physical processes occurring at sliding interfaces. The production of irreversible entropy by interfacial dissipative processes is associated with both friction and wear. Friction force dissipates power and generates entropy, whereas wear irreversibly changes material's structure, often with loss of material. Bryant [98] identified entropy production mechanisms during various dissipative processes relevant to friction and wear, which are summarized in Table 2.2. It is observed that the change of entropy has the general form of $dS = Yd\xi$, that is, a thermodynamic force Y times the change of the generalized coordinate $d\xi$.

The concept of entropy can be applied to friction, surface degradation, and self-organization. Manufacturing transforms raw materials into highly organized components, while aging and degradation tend to return them into their natural disordered state [100]. The entropy production rate is given by

$$\frac{dS}{dt} = XJ \quad (2.47)$$

where J is the thermodynamic flow rate and X is a generalized thermodynamic force [15].

Consider now frictional sliding with the velocity $V = dx/dt$, applied normal load W , and friction force $F = \mu W$. The work of the friction force is equal to the dissipated energy, and we will assume now that all dissipation energy is converted into the heat

Table 2.2 Entropy change during various dissipative processes (based on Bryant 98)

Process	Entropy change
Adhesion	$dS = \frac{\gamma dA}{T}$, where γ is the surface energy, A area
Plastic deformation	$dS = \frac{U_p dV}{T}$, where U_p is the work per volume, V volume
Fracture	$dS = \frac{(\frac{\partial U}{\partial a} - 2\gamma) da}{T}$, where $\frac{\partial U}{\partial a}$ is the energy release rate, a is crack length
Phase transition	$dS = \frac{dH}{T}$, where H is the enthalpy
Chemical reaction	$dS = \frac{\sum_{react} \mu_i dN_i - \sum_{products} \mu_i dN_i}{T}$, where N_i are the numbers of molecules and μ_i are the chemical potentials for reactants and products
Mixing	$\Delta S = -R \sum_i^n \frac{N_i}{N} \ln \frac{N_i}{N}$, where N_i are the numbers of molecules
Heat transfer	$dS = \left(\frac{1}{T_1} - \frac{1}{T_2} \right) dQ$, where T_1 and T_2 are the temperatures of the two bodies

$$dQ = \mu W dx \quad (2.48)$$

The rate of entropy generation during friction is now given by

$$\frac{dS}{dt} = \frac{\mu W V}{T} \quad (2.49)$$

with the flow rate $J = V$ and the thermodynamic force $X = \mu W/T$ [15].

Bryant et al. [100] suggested a degradation measure w that is a parameter associated with a particular degradation mechanism, so that the rate of degradation is given by

$$\frac{dw}{dt} = B \frac{dS_f}{dt} = YJ \quad (2.50)$$

where $Y = BX$ is the generalized degradation force and B is a constant degradation coefficient (a material property).

For the wear process, it is natural to take wear volume as the degradation measure w [15]. Using the relation between the degradation rate $\dot{w} = B\dot{S}$ and entropy rate, we obtain the wear rate

$$\frac{dw}{dt} = B \frac{\mu W V}{T} \quad (2.51)$$

For plastic contact, (2.47) can be rewritten by setting the wear coefficient $k = \mu HB/T$ as

$$\frac{dw}{dt} = k \frac{WV}{H} \quad (2.52)$$

where H is the hardness of a softer material in contact. This is the Archard equation for adhesive wear. For elastic contact, $k = \mu E^* (\sigma/\beta^*) B/T$ yields

$$\frac{dw}{dt} = k \frac{WV}{E^* (\sigma/\beta^*)} \quad (2.53)$$

where E^* is the effective elastic modulus, σ is the standard deviation of rough profile height, and β^* is the correlation length of profile roughness (in a sense, σ is the height, and β^* is the length of a typical asperity) [15].

The nontrivial part of this derivation is that the wear volume per unit time is linearly proportional to the friction force. This implies that (a) a constant value of energy dissipated by friction is consumed for wear debris generation and (b) a constant amount of energy is consumed, in average per wear particle volume. Wear and friction are essentially the same dissipative process, as the energy consumed for creating wear particles is related to the work of friction. The model, however, cannot predict actual values of the wear coefficients, and its advantage is in providing theoretical foundation of the empirical laws of wear.

A different approach was taken by Fedorov [101], who pointed out that thermodynamically wear is an irreversible mass transfer process dependent upon the local gradients of chemical potentials. The balance of energy in a tribo-system is given by

$$\rho T dS = \rho dU - \sigma_{ik} \cdot d\bar{\epsilon}_{ik} - N_j d\mu_i \quad (2.54)$$

where ρ is the density and σ_{ik} and $\bar{\epsilon}_{ik}$ are the stress and strain tensors. The mass transfer in a frictional system depends upon the heat flow, dissipation, and chemical potentials of components in the system.

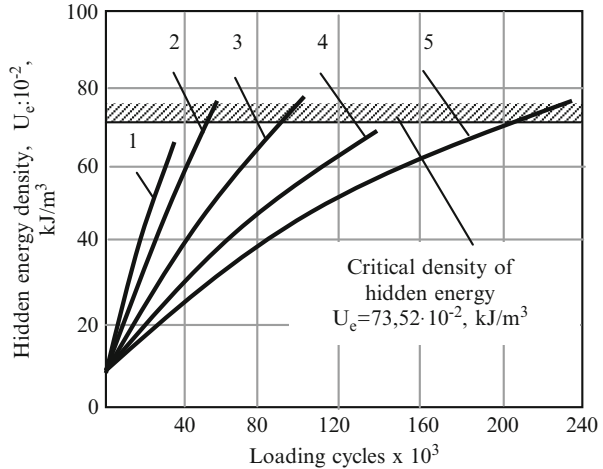
According to Fedorov, the probability of deterioration is proportional to the exponent of the entropy flow and relaxation time τ , which characterizes the process of restoring the thermodynamic equilibrium

$$\omega \propto \exp\left(\frac{\dot{S}\tau}{k}\right) \quad (2.55)$$

The hidden energy of degradation is created by the fluctuation of thermal energy in the mechanical stress field. When the hidden energy reaches its critical density, the destruction occurs. The hidden area density as a function of time for steel is shown in Fig. 2.14 for the values of stress $s = (25.3, 24.8, 23.9, 23.1, 22.5)$ kg/mm².

It is of interest also to consider the model, suggested by Bershadsky [102], who also believed that friction and wear are related processes that represent the trend to deteriorate for energy and matter, respectively. Bershadsky [102] introduced the concept of structural adjustment. During the structural adjustment, all types of interactions (adhesion, deformation, and material transfer are localized at the

Fig. 2.14 Variation of hidden energy density with loading cycles (Berkovich and Gromakovsky, 2000)



surface), which decreases the absorbed energy ΔE in the work of friction $A = \Delta E + Q$. Bershadsky [102] formulated the variational principle

$$\delta \int_V \frac{\Delta E(V)}{A} dV = 0 \tag{2.56}$$

According to this principle, most work is converted into heat. Dissipative ability of the material, along with its hardness, defines the wear resistance.

To summarize, the thermodynamic theories of wear provide foundation for the empirical wear laws (such as the Archard law) and suggest the principles to calculate the parameters of these laws (such as the wear coefficient).

3.3 Factors Affecting Wear

It is well known that no single wear mechanism operates over a wide range of operating conditions. The transitions in dominant wear mechanisms occur as operating conditions are changed. In this regard, efforts were made to develop wear mechanism maps [103]. The wear mechanism map shows various regimes of wear at wide operating conditions.

Normal load: Increasing the normal load results in an increase in the real area of contact and hence the number of adhesive junctions. In general, it is stated that the wear loss is proportional to applied normal load during sliding [40]. Archard [94] observed the transition from mild to severe wear, when the contact pressure is about one-third of hardness of metals. This is due to interaction of plastic zones beneath the contacting asperities. In high load regime, mechanical damage of material occurs due to high surface stresses. Also increase in load results in monotonic increase in

interface temperature, which reduces the yield stress of a material. Hence, it is clear that wear rate of material is linear function of normal load. However, rate of increase in wear rate does not remain constant over range of normal load.

Sliding velocity: In dry sliding condition, with increasing sliding speed, the frictional heat generated becomes greater causing oxidation and forms an oxide film at the interface. This oxide film serves as lubricant which reduces the wear rate of metals. In the case of lubricated condition, at higher sliding speed, the formation of hydrodynamic lubricant film at the interface minimizes the wear rate. Normally, wear rate of metals decreases with sliding speed both in dry and lubricated sliding conditions [104]. However, if interfacial temperature reaches the melting point of a metal, it lowers the hardness of the metals drastically and causes severe wear.

Temperature: The temperature is an important parameter which influences the wear response of metals by accelerating the chemical reactivity of a metal surface, altering the physical and mechanical properties of the metals and changing the microstructural response of the metals. To study the effect of temperature, sliding tests were performed on cobalt–steel pair at different temperatures. It was noted that wear rate at 653 K is about 100 times than that observed at 553 K. The reason is due to phase transformation from HCP to FCC structure [40].

Environment: In ambient conditions, an oxide film is easily formed on metal surface, and if oxide film is strong enough to prevent the direct contact between metal–metal surfaces, wear rate of metals will be low as compared to inert atmosphere. One could expect that wear rate of metals is higher in vacuum than in air owing to the less chance of formation of oxide films. This leads to direct metal–metal contact and results in high wear.

Hardness: Archard's model considers wear rate of metals as an inverse function of their hardness. Harder materials resist cutting and penetration. In the case of abrasive wear, it is easy to correlate hardness with wear rate as it involves penetration process.

Elastic modulus: The wear resistance of a material is directly related to elastic modulus in accordance with adhesive theory of wear [105]. For metals that have high elastic modulus decrease the real area of contact leading to low adhesion and wear. The abrasive wear resistance of a material can also be varied by varying hardness/modulus ratio (i.e., H/E ratio). The ratio shows that abrasive wear resistance of a material can be increased either by increasing the hardness or by decreasing the elastic modulus.

Fracture toughness: The high fracture toughness increases the wear resistance of brittle materials such as ceramics. During interaction of asperities, crack growth occurs with critical amount of strain. If the applied strain is smaller than critical strain, the wear rate of a metal is independent of fracture toughness. Once the critical strain is reached, there is an increased probability of crack growth and wear rate of metals depends upon the fracture toughness. Hornbogen [106] proposed a model that there are three regions of wear behavior as a function of fracture toughness. In the first region, wear is not affected by toughness in which Archard's

law is obeyed. Second region involves transition from mild to severe wear. Factors which induce the transition are an increased pressure, strain rate, and decreased fracture toughness. Third region is highly brittleness condition which shows high wear rate because of low fracture toughness.

Crystal structure: Sliding of metals produces large plastic deformation, which in turn forms dislocation cell wall structures near the surface region. Since cell walls serve as pathway for subsurface cracks, metals with limited number of slip systems (HCP) exhibit lower wear rate than metals with large number of slip systems (FCC). Buckley [107] showed experimentally that cubic crystals wear at about twice the rate of hexagonal crystals.

Thermal diffusivity: If a metal has low thermal diffusivity, it cannot dissipate the frictional heat away from the interface. This thermal accumulation degrades the mechanical strength of a metal and causes high wear. Wear is an inverse function of thermal diffusivity. Abdel-Aal [108] related the heat dissipation capacity of metals with wear transition. He postulated that transition from mild to severe wear occurs once the quantity of heat generated is higher than the quantity of heat dissipated. He also noted that if the amount of thermal accumulation reaches a critical value, delamination of oxide flake results in higher wear rate.

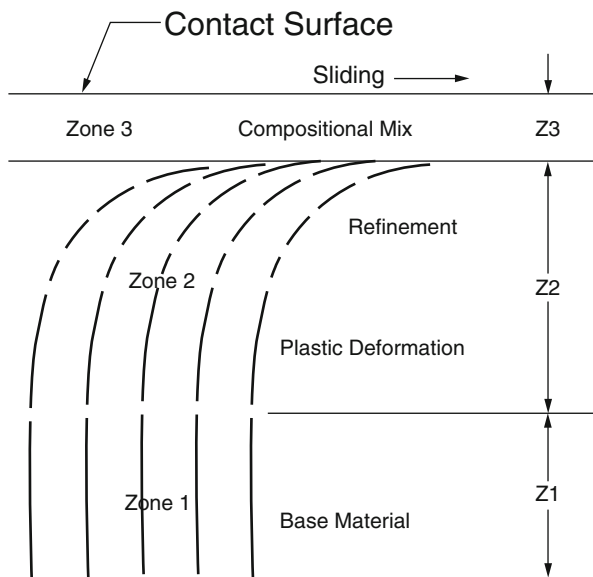
3.4 Role of Subsurface Zone on Wear

Sliding of metals produces large plastic deformation at the interface and there exist large strain gradients in the near-surface zone. The structure and properties of such zones are central to the formation of wear debris, since they come out directly from the near-surface zone.

Prior to the introduction of the delamination theory, a unifying thread to gain insight into the basis of wear was less apparent. However, Suh's theory [39] requires an examination of subsurface region of wear specimens, and hence, investigators began to study the mechanics of deformation and crack nucleation beneath the wear interface.

To study the subsurface features following a sliding test, specimens were sectioned perpendicular to a worn surface and along the sliding direction and then polished and examined. Figure 2.15 shows, schematically, the major features observed in a section of the specimen after a wear test. These are characteristic subsurface zones, which depend (morphologically and compositionally) upon specimen/counterface materials and geometry, the environment, and the mechanical conditions of contact. In Fig. 2.15, zone 1 represents original specimen material in an undisturbed state. That is, this zone experiences elastic deformation and thermal cycling when loaded during tribo-contact. However, the structure and properties of zone 1 following a sliding test are similar to those prior to the test. But unlike zone 1, the zone 2 material has acquired new structure and properties due to repetitive tribo-contact, and considerable plastic deformation occurs in ductile

Fig. 2.15 A schematic diagram of subsurface zones observed beneath wear surfaces



materials. Depending upon the materials, environment, and contact conditions, zone 2 may become harder or softer than the original material. Voids may develop within zone 2, and cracks may nucleate within this region. In many cases the reorientation and disintegration of crystallites are observed in zone 2, with attendant refinement in microstructure that increases as the contact interface is approached. However, in zone 2, no constituents from the counterface or stemming from interaction with the environment are present. The extent of deformation in zone 2 ranges from zero at the zone 1 to zone 2 interface to a maximum at the zone 2 to zone 3 interface. Zone 3 is a tribo-layer which forms in situ. Zone 3 is the region containing the surface of contact, and it commonly differs compositionally as well as morphologically from the base material (zones 1 and 2). Often, zone 3 appears to be homogeneous and very finely structured consisting of both the specimen and counterface material, as well as constituents from the operating environment. In single-phase materials it is difficult to quantify the extent of deformation while the use of suitable two phase alloys enabled measurement of the depth of damage from the structural changes that result [109].

Origin of subsurface zone: The development of a subsurface zone involves several stages. During initial stage of sliding, the forces acting on the sliding surface are transmitted to the subsurface zone. The tangential shear forces induced by the frictional contact between contacting asperities tend to deform the near-surface material plastically. The frictional force increases with sliding distance until it reaches a steady value. At this steady-state sliding, the subsurface material is subjected to plastic deformation of considerable stable depth. In addition, crack-like elongated voids appear within the plastic zone due to the presence of secondary phase particles in the metal matrix. These cracks tend to propagate and link up with

adjacent cracks to produce loose wear debris in the near-surface material. When the surface layers are removed, material in the lower region of zone 2 comes into high strain region and finally becomes zone 3. In the same manner, the material in the zone 3 enters into zone 2. The depth of plastic deformed zone remains constant during subsequent removal of surface material in sliding wear.

3.5 Strain Rate Response Approach

Wear is a dynamic process and its behavior can be related to the strain rate response of a material. A strain rate response approach is associated with microstructural responses of metals to imposed conditions of strain, strain rate, and temperature. Depending on the combination of strain rate and temperature, various kinds of microstructural mechanisms will operate leading to different microstructure. The microstructural response is mainly based on dynamics material modeling (DMM) [110]. DMM is based upon the principle that the efficiency by which material dissipates power decides its microstructural response. The power involved during plastic deformation is given by $P = \sigma \dot{\epsilon}$, where σ is the flow stress and $\dot{\epsilon}$ is the applied strain rate. According to DMM, this power is consumed in heat dissipation and microstructural changes. This power partitioning is decided by strain rate sensitivity of flow stress (m) of the material. The efficiency in utilizing the power in undergoing microstructural change decides the microstructural response of material. The material when subjected to various conditions of strain, strain rate, and temperature exhibits a large spectrum of microstructural responses. The various microstructural responses of materials include dynamic recrystallization (DRX), dynamic recovery (DRY), adiabatic shear banding (ASB), flow banding (FB), wedge cracking (WC), void formation (VF), superplastic deformation (SPD), intercrystalline cracking (ICC), and prior particle boundary (PPB) cracking. Some of these like DRX, DRY, and SPD microstructure evolution lead to desirable microstructure, and the others like ASB, FB, WC, VF, PPB, and ICC can lead to undesirable microstructure that destroys the integrity of the material. For a given metal or alloy, the specific microstructural evolution was found to be related to the imposed strain rate and temperature and therefore designated as strain rate response. This frame of work may be extended to a wear situation, as in the subsurface regions a large gradient of strain exists [78, 111]. This, during sliding, means that a particular combination of strain rate and temperature exists at the surface and the near-surface regions where plastic deformation is occurring. In such a situation, the regions where the strain rate and temperature combination is such that a deleterious strain rate response may occur, it will be easier for cracks to be nucleated and propagated, thus generating wear debris. Figure 2.16 shows the strain rate microstructural response map for titanium obtained from the uniaxial compression tests done at various constant true strain rates and temperatures. The curves represent the strain rates and temperatures estimated in the subsurface of the titanium pin at various sliding speeds and depths. In case of titanium, Kailas and

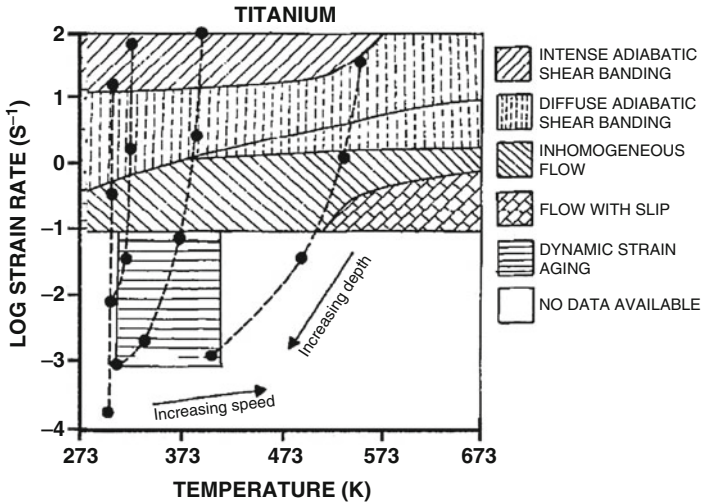


Fig. 2.16 Strain rate microstructural response map for titanium [113]

Biswas [112] observed experimentally that wear rate reduces with an increase in sliding speed. This was postulated to be due to the reduction in the intensity of ASB (microstructural instability) in near-surface regions of the titanium pin. Strain rate response approach made a good correlation between the wear rate and microstructural evolution in the near-surface region [113].

3.6 Wear of Materials

Wear is a complex phenomenon. Wear rate may vary with time or sliding distance. Also, wear rate may vary if transition from one mechanism to another occurs during the wear process. The initial period during which wear rate changes is known as the run-in period. Wear during run-in depends on the initial material properties and surface conditions. During the transition period, the surface is modified to a steady-state condition by plastic deformation. The wear rate, like friction of a material, is dependent on the mating materials, surface finish, and operating conditions.

Metals and alloys: Under dry condition, clean metals and alloys exhibit high adhesion and thus high friction and wear. In vacuum, wear rate of metallic materials is very high. Under lubricated conditions or in the presence of chemical films, metals and alloys exhibit low adhesion and thus the friction and wear. In soft metals, such as Pb and Sn, the real area of contact is high, even at light loads, which results in high wear rates. Hexagonal (HCP) metals such as Mg and Zn exhibit low friction and wear when compared to FCC metals. In general, wear for alloys tends to be lower than that of pure components.

Ceramics: Ceramic–ceramic or ceramic–metal exhibits moderate friction but extremely low wear. This is due to high mechanical properties of ceramics which result in very low real area of contact responsible for low friction and wear. Under clean environment, coefficient of friction and wear rates of ceramic pair do not reach the very high values as observed in clean metals, especially in ultra-high vacuum. Ceramic materials respond to conventional lubricants similar to metals.

Polymers: Polymers generally exhibit low friction and moderates wear as compared to metals and ceramics. Dominant wear mechanisms are adhesive, abrasive, and fatigue. If the mating surfaces are smooth, then the wear primarily occurs from adhesion. If the mating surfaces are rough, then the wear is due to abrasion. The fatigue mechanism is important in harder polymers sliding against smooth surfaces. In this case, asperity deformations are primarily elastic and wear due to fatigue results from the formation of cracks associated with predominantly elastic deformation. Wear particles are produced by propagation and intersection of cracks. Polymers flow readily at modest pressure and temperature. Therefore, polymers are used at relatively low loads, speed, and temperatures, lower than that in the case of metals and ceramics. Polymers generally have low thermal conductivities and thus high interface temperature during sliding. Sometimes, polymers start to melt at the interface even at ambient temperature and hence the wear rate increases rapidly.

3.7 Correlation Between Friction and Wear

As explained earlier, friction and wear are not intrinsic material properties, but they are a responsive of tribo-system. These processes are not always linearly related to each other and assuming so would be erroneous. One could expect that high friction coefficients are correlated with high wear rates. Friction and wear, as two kinds of responses from one tribo-system, could be exactly related with each other in each state of contact in the system, although a comprehensive simple relationship should not be obtained. Kato [114] suggested that it would be helpful for the understanding of the relationship between friction and wear by describing the tribo-system with respective terms of hardness, ductility, oxide film layer, and adhesive transfer. The mathematical relation between friction coefficient and wear rate for the case of sliding wear was formulated based on delamination theory of wear and energy criteria [115]. According to this model, friction and wear coefficients are related to each other by material properties and are proportional to each other in normal range of sliding condition.

4 Conclusions

Friction is very important in our day-to-day lives. Many techniques have been used to control, decrease, or increase friction based on applications. In this chapter, the fundamentals of friction and wear are presented. More specifically, the empirical

laws, mechanisms, and factor affecting friction and wear were discussed. Friction measuring devices, friction and wear studies of various materials, and the correlation between friction and wear were also discussed.

References

1. Menezes PL, Kishore, Kailas SV, Lovell MR (2011) Response of materials during sliding on various surface textures. *J Mater Eng Perform* 20(8):1438–1446
2. Menezes PL, Kishore, Kailas SV (2008) Role of surface texture and roughness parameters in friction and transfer layer formation under dry and lubricated sliding conditions. *Int J Mater Res* 99(7):795–807
3. Nosonovsky M, Bhushan B (2008) Multiscale dissipative mechanisms and hierarchical surfaces: friction, superhydrophobicity, and biomimetics. Springer, Heidelberg
4. Adams GG, Barber JR, Ciavarella M, Rice JR (2005) A paradox in sliding contact with friction. *ASME J Appl Mech* 72:450–452
5. Adams GG (1995) Self-excited oscillations of two elastic half-spaces sliding with a constant coefficient of friction. *ASME J Appl Mech* 62:867–872
6. Nosonovsky M, Adams GG (2004) Vibration and stability of frictional sliding of two elastic bodies with a wavy contact interface. *ASME J Appl Mech* 71:154–161
7. Adams GG, Nosonovsky M (2000) Contact modeling—forces. *Tribol Int* 33:441–442
8. Nosonovsky M, Adams GG (2001) Dilatational and shear waves induced by the frictional sliding of two elastic half-spaces. *Int J Eng Sci* 39:1257–1269
9. Tolstoi DM (1967) Significance of the normal degree of freedom and natural normal vibrations in contact friction. *Wear* 10:199–213
10. Persson BNJ (2000) Sliding friction: physical principles and applications. Springer, Berlin
11. Rice JR, Lapusta N, Ranjith K (2001) Rate and state dependent friction and the stability of sliding between elastically deformable solids. *J Mech Phys Solids* 49:1865–1898
12. Nosonovsky M (2007) Modeling size, load, and velocity effect on friction at micro/nanoscale. *Int J Surf Sci Eng* 1:22–37
13. Barber JR (1969) Thermoelastic instabilities in the sliding of conforming solids. *Proc R Soc Lond A* 312:381–394
14. Fox-Rabinovich GS, Totten GE (eds) (2006) Self-organization during friction. CRC, Boca Raton, FL
15. Nosonovsky M, Bhushan B (2009) Thermodynamics of surface degradation, self-organization, and self-healing for biomimetic surfaces. *Philos Trans R Soc A* 367:1607–1627
16. Menezes PL, Kishore, Kailas SV (2009) Studies on friction and formation of transfer layer when Al-4Mg alloy pins slid at various numbers of cycles on steel plates of different surface texture. *Wear* 267(1–4):525–534
17. Menezes PL, Kishore, Kailas SV, Lovell MR (2010) “Studies on friction and transfer layer formation when pure Mg pins slid at various numbers of cycles on steel plates of different surface texture.” ASME/STLE international joint tribology conference (IJTC2010) San Francisco, USA, pp 263–265
18. Menezes PL, Kishore, Kailas SV, Lovell MR (2011) The role of surface texture on friction and transfer layer formation during repeated sliding of Al-4Mg against steel. *Wear* 271(9–10):1785–1793
19. Menezes PL, Kishore, Kailas SV, Lovell MR (2012) “Self-organization and friction during sliding.” ASME/STLE international joint tribology conference (IJTC2012), Denver, USA
20. Menezes PL, Kishore, Kailas SV, Lovell MR (2013) Tribological response of soft materials sliding against hard surface textures at various numbers of cycles. *Lubrication Sci* 25(2):79–99

21. Mortazavi V, Menezes PL, Nosonovsky M (2011) Studies of Shannon entropy evolution due to self-organization during the running-in. ASME/STLE international joint tribology conference (IJTC2011), Los Angeles, USA, pp 303–305
22. Menezes PL, Kishore, Kailas SV, Lovell MR (2010) Studies on friction and transfer layer formation when high purity Al pins slid at various numbers of cycles on steel plates of different surface texture. Proceedings of the 2010 STLE annual meeting & exhibition, Las Vegas, USA
23. Menezes PL, Kishore, Kailas SV, Lovell MR (2010) Role of surface texture on friction and transfer layer formation when pure Al pins slid at various numbers of cycles on steel plates. 2011 STLE annual meeting & exhibition, Atlanta, USA
24. Bhushan B, Nosonovsky M (2003) Scale effects in friction using strain gradient plasticity and dislocation-assisted sliding (microslip). *Acta Mater* 51:4331–4345
25. Carpinteri A, Paggi M (2005) Size-scale effect on the friction coefficient. *Int J Solid Struct* 42:2901–2910
26. Niederberger S, Gracias DH, Komvopoulos K, Somorjai GA (2000) Transition from nano-scale to microscale dynamic friction mechanisms on polyethylene and silicon surfaces. *J Appl Phys* 87:3143–3150
27. Zhang LC, Johnson KL, Cheong WCD (2001) A molecular dynamics study of scale effects on the friction of single-asperity contacts. *Tribol Lett* 10:23–28
28. Wenning L, Müser MH (2001) Friction laws for elastic nanoscale contacts. *Europhys Lett* 54:693–699
29. Nosonovsky M (2009) From wear to self-healing in nanostructured biological and technical surfaces. Proceedings of ASME/STLE international joint tribology conference IJTC2009, Memphis, USA, ASME
30. Bowden FP, Tabor D (1950) *The friction and lubrication of solids*, Part-I. Clarendon, UK
31. Rice J (1991) Dislocation nucleation from a crack tip: an analysis based on the peierls concept. *J Mech Phys Solids* 40:239–271
32. Gerde E, Marder M (2001) Friction and fracture. *Nature* 413:285–288
33. Kessler DA (2001) Surface physics: a new crack on friction. *Nature* 413:260–261
34. Chang WR, Etsion I, Bogy DB (1987) An elastic-plastic model for the contact of rough surfaces. *ASME J Tribol* 109:257–263
35. Kogut L, Etsion I (2004) A static friction model for elastic-plastic contacting rough surfaces. *ASME J Tribol* 126:34–40
36. He G, Müser MH, Robbins MO (1999) Adsorbed layers and the origin of static friction. *Science* 284:1650–1652
37. Greenwood JA, Williamson JBP (1966) Contact of nominally flat surfaces. *Proc R Soc Lond A* 295:300–319
38. Archard JF (1957) Elastic deformation and the laws of friction. *Proc R Soc Lond A* 243:190–205
39. Suh NP (1986) *Tribophysics*. Prentice-Hall, Inc, Englewood Cliffs, NJ
40. Rabinowicz E (1995) *Friction and wear of materials*. Wiley, USA
41. Kudo H (1965) A note on the role of microscopically trapped lubricant at the tool-work interface. *Int J Mech Sci* 7(5):383–388
42. Staph HE, Ku PM, Carper HJ (1973) Effect of surface roughness and surface texture on scuffing. *Mech Mach Theor* 8:197–208
43. Koura MM (1980) The effect of surface texture on friction mechanisms. *Wear* 63(1):1–12
44. Lakshmipathy R, Sagar R (1992) Effect of die surface topography on die-work interfacial friction in open die forging. *Int J Mach Tool Manuf* 32(5):685–693
45. Saha PK, Wilson WRD, Timsit RS (1996) Influence of surface topography on the frictional characteristics of 3104 aluminum alloy sheet. *Wear* 197(1–2):123–129
46. Hu ZM, Dean TA (2000) A study of surface topography, friction and lubricants in metal forming. *Int J Mach Tool Manuf* 40(11):1637–1649

47. Rasp W, Wichern CM (2002) Effects of surface-topography directionality and lubrication condition on frictional behaviour during plastic deformation. *J Mater Process Technol* 125–126:379–386
48. Menezes PL, Kishore, Kailas SV (2006) Studies on friction and transfer layer: role of surface texture. *Tribol Lett* 24(3):265–273
49. Menezes PL, Kishore, Kailas SV, Lovell MR (2009) Studies on friction and formation of transfer layer in HCP metals. *ASME J Tribol* 131(3):031604.1–031614.9
50. Menezes PL, Kishore, Kailas SV, Bobji MS (2010) Influence of tilt angle of plate on friction and transfer layer - A study of aluminium pin sliding against steel plate. *Tribol Int* 43(5–6):897–905
51. Menezes PL, Kishore, Kailas SV, Lovell MR (2012) Analysis of strain rates and microstructural evaluation during metal forming: role of surface texture and friction. *Tribol Trans* 55(5):582–589
52. Kumar PC, Menezes PL, Kailas SV (2008) Role of surface texture on friction under boundary lubricated conditions. *Tribol Online* 3(1):12–18
53. Gadelmawla ES, Koura MM, Maksoud TMA, Elewa IM, Soliman HH (2002) Roughness parameters. *J Mater Process Technol* 123(1):133–145
54. Menezes PL, Kishore, Kailas SV (2006) Influence of surface texture on coefficient of friction and transfer layer formation during sliding of pure magnesium pin on 080 M40 (EN8) steel plate. *Wear* 261(5–6):578–591
55. Menezes PL, Kishore, Kailas SV (2008) Effect of surface roughness parameters and surface texture on friction and transfer layer formation in tin-steel tribo-system. *J Mater Process Technol* 208(1–3):372–382
56. Menezes PL, Kishore, Kailas SV (2006) Effect of roughness parameter and grinding angle on coefficient of friction when sliding of Al-Mg alloy over EN8 steel. *ASME J Tribol* 128(4):697–704
57. Menezes PL, Kishore, Kailas SV (2008) Influence of roughness parameters on coefficient of friction under lubricated conditions. *Sadhana* 33(3):181–190
58. Menezes PL, Kishore, Kailas SV (2009) Influence of surface texture and roughness parameters on friction and transfer layer formation during sliding of aluminium pin on steel plate. *Wear* 267(9–10):1534–1549
59. Menezes PL, Kishore, Kailas SV, Lovell MR (2011) Influence of inclination angle and machining direction on friction and transfer layer formation. *ASME J Tribol* 133(1):014501.1–014501.8
60. Menezes PL, Kishore, Kailas SV, Lovell MR (2011) Friction and transfer layer formation in polymer-steel tribo-system: Role of surface texture and roughness parameters. *Wear* 271(9–10):2213–2221
61. Pottirayil A, Menezes PL, Kailas SV (2010) A parameter characterizing plowing nature of surfaces close to Gaussian. *Tribol Int* 43(1–2):370–380
62. Pottirayil A, Menezes PL, Kailas SV (2008) Correlating the features of topography to friction by sliding experiments. *Proceedings of the 9th biennial ASME conference on engineering systems design and analysis (ESDA 2008)*, Israel, pp 361–364
63. Menezes PL, Kishore, Kailas SV (2006) Studies on friction and transfer layer using inclined scratch. *Tribol Int* 39(2):175–183
64. Menezes PL, Kishore, Kailas SV (2008) On the effect of surface texture on friction and transfer layer formation—a study using Al and steel pair. *Wear* 265(11–12):1655–1669
65. Menezes PL, Kishore, Kailas SV (2009) Influence of inclination angle of plate on friction, stick-slip and transfer layer—a study of magnesium pin sliding against steel plate. *Wear* 267(1–4):476–484
66. Menezes PL, Kishore, Kailas SV (2006) Effect of directionality of unidirectional grinding marks on friction and transfer layer formation of Mg on steel using inclined scratch test. *Mater Sci Eng A* 429(1–2):149–160

67. Menezes PL, Kishore, Shimjith M, Kailas SV (2007) Influence of surface texture on friction and transfer layer formation in Mg-8Al alloy/steel tribo-system. *Indian J Tribol* 2(1):46–54
68. Menezes PL, Kishore, Kailas SV (2008) Influence of roughness parameters of harder surface on coefficient of friction and transfer layer formation. *Int J Surf Sci Eng* 2(1–2):98–119
69. Menezes PL, Kishore, Kailas SV (2009) Influence of roughness parameters and surface texture on friction during sliding of pure lead over 080 M40 steel. *Int J Adv Manuf Technol* 43(7):731–743
70. Menezes PL, Kishore, Kailas SV (2009) Study of friction and transfer layer formation in copper-steel tribo-system. *Tribol Trans* 52(5):611–622
71. Menezes PL, Kishore, Kailas SV, Lovell MR (2011) Role of surface texture, roughness and hardness on friction during unidirectional sliding. *Tribol Lett* 41(1):1–15
72. Buckley DH, Johnson RL (1968) The influence of crystal structure and some properties on hexagonal metals on friction and adhesion. *Wear* 11(6):405–419
73. Menezes PL, Kishore, Kailas SV, Lovell MR (2012) ‘Tribological response of materials with varying hardness and crystal structure during sliding on various surface textures. *Materials and Surface Engineering: Research and Development*, Woodhead, pp 207–242
74. Menezes PL, Kishore, Kailas SV, Lovell MR (2010) Response of materials as a function of grinding angle on friction and transfer layer formation. *Int J Adv Manuf Technol* 49(5):485–495
75. Menezes PL, Kishore, Kailas SV, Lovell M R (2011) Factors influencing stick-slip motion: Effect of hardness, crystal structure and surface texture. ASME/STLE international joint tribology conference (IJTC2011), Los Angeles, USA, 2011, pp 71–73
76. Menezes PL, Kishore, Kailas SV, Lovell MR (2012) Tribological response of materials with varying hardness and crystal structure during sliding on various surface textures. *Materials and Surface Engineering: Research and Development*, Woodhead, pp 207–242
77. Menezes PL, Kishore, Kailas SV (2008) Subsurface deformation and the role of surface texture—a study with Cu pins and steel plates. *Sadhana* 33(3):191–201
78. Menezes PL, Kishore, Kailas SV (2009) Role of surface texture of harder surface on subsurface deformation. *Wear* 266(1–2):103–109
79. Moore MA, King FS (1980) Abrasive wear of brittle solids. *Wear* 60(1):123–140
80. Menezes PL, Kishore, Kailas SV (2008) Effect of surface topography on friction and transfer layer during sliding. *Tribol Online* 3(1):25–30
81. Menezes PL, Kishore, Kailas SV, Lovell MR (2013) The role of strain rate response on tribological behavior of metals. *ASME J Tribol* 135(1):011601.1–011601.7
82. Miyoshi K (1990) Fundamental considerations in adhesion, friction and wear for ceramic-metal contacts. *Wear* 141(1):35–44
83. Farhat ZN, Ding Y, Northwood DO, Alpas AT (1996) Effect of grain size on friction and wear of nanocrystalline aluminum. *Mater Sci Eng A* 206(2):302–313
84. Bregliozzi G, Schino AD, Kenny JM, Haefke H (2003) The influence of atmospheric humidity and grain size on the friction and wear of AISI 304 austenitic stainless steel. *Mater Lett* 57(29):4505–4508
85. Wang ZB, Taa NR, Li S, Wang W, Liu G, Lu J, Lu K (2003) Effect of surface nanocrystallization on friction and wear properties in low carbon steel. *Mater Sci Eng A* 352(1–2):144–149
86. Mishra R, Basu B, Balasubramaniam R (2004) Effect of grain size on the tribological behavior of nanocrystalline nickel. *Mater Sci Eng A* 373(1–2):370–373
87. Whitehead JR (1950) Surface deformation and friction of metals at light loads. *Proc R Soc Lond A* 201:109–124
88. Bowden FP, Young JE (1951) Friction of clean metals and the influence of adsorbed films. *Proc R Soc Lond A* 208:311–325
89. Tsuya Y (1975) Microstructure of wear, friction and solid lubrication. *Tech. Rep. of Mech. Eng. Lab.* 3(81), Japan

90. Menezes PL, Kishore, Kailas SV, Lovell MR (2011) Studies on friction in steel-aluminum alloy tribo-system: role of surface texture of the softer material. 2011 STLE annual meeting & exhibition, Atlanta, USA
91. Menezes PL, Kishore, Kailas SV, Lovell MR (2009) Influence of alloying element addition on friction and transfer layer formation in Al-Mg system: role of surface texture. Proceedings of ASME/STLE international joint tribology conference IJTC2009, Memphis, USA, ASME, 2009, pp 459-461
92. Menezes PL, Kishore, Kailas SV, Lovell MR (2010) Response of metals and polymers during sliding: Role of surface texture. ASME/STLE international joint tribology conference (IJTC2010), San Francisco, USA, 2010, pp 267-269
93. Menezes PL, Kishore, Kailas SV, Lovell MR (2010) Role of surface texture on friction and transfer layer formation during sliding of PVC pin on steel plate. Proceedings of the 2010 STLE annual meeting & exhibition, Las Vegas, USA, 2010
94. Archard JF (1953) Contact and rubbing of flat surfaces. *J Appl Phys* 24(8):981-988
95. Suh NP (1973) The delamination theory of wear. *Wear* 25(1):111-124
96. Klamecki BE (1980) Wear—an entropy production model. *Wear* 58(2):325-330
97. Zmitrowicz A (1987) A thermodynamical model of contact, friction, and wear. *Wear* 114(2):135-221
98. Bryant MD (2009) Entropy and dissipative processes of friction and wear. *FME Trans* 37:55-60
99. Doelling KL, Ling FF, Bryant MD, Heilman BP (2000) An experimental study of the correlation between wear and entropy flow in machinery components. *J Appl Phys* 88 (5):2999-3003
100. Bryant MD, Khonsari MM, Ling FF (2008) On the thermodynamics of degradation. *Proc R Soc Lond A* 464(2096):2001-2014
101. Berkovich II, Gromakovskiy DG (2000) Tribology: physical fundamentals, mechanical and technical applications. Samara, Russia
102. Bershadski LI (1993) B I Kostetski and the general concept in tribology. *Trenie I Iznos* 14:6-18
103. Lim SC, Ashby MF (1987) Overview no. 55 wear-mechanism maps. *Acta Metal* 35(1):1-24
104. Saka N, Eleiche AM, Suh NP (1977) Wear of metals at high sliding speeds. *Wear* 44(1):109-125
105. Khrushchov MM (1974) Principles of abrasive wear. *Wear* 28(1):69-88
106. Hornbogen E (1975) The role of fracture toughness in the wear of metals. *Wear* 33(2):251-259
107. Buckley DH (1978) The use of analytical surface tools in the fundamental study of wear. *Wear* 46(1):19-53
108. Abdel-Aal HA (2000) On the influence of thermal properties on wear resistance of rubbing metals at elevated temperatures. *ASME J Tribol* 122(3):657-660
109. Rice SL, Nowotny H, Wayne SF (1989) A survey of the development of subsurface zones in the wear of materials. *Key Eng Mater* 33:77-100
110. Prasad YVRK, Sasidhara S (1997) Hot working guide: a compendium of processing maps. ASM International, Materials Park, OH
111. Kailas SV, Biswas SK (1997) Strain rate response and wear of metals. *Tribol Int* 30:369-375
112. Kailas SV, Biswas SK (1995) The role of strain rate response in plane strain abrasion of metals. *Wear* 181-183:648-657
113. Kailas SV (2003) A study of the strain rate microstructural response and wear of metals. *J Mater Eng Perform* 12(6):629-637
114. Kato K (2000) Wear in relation to friction—a review. *Wear* 241(2):151-157
115. Suh NP, Sridharan P (1975) Relationship between the coefficient of friction and the wear rate of metals. *Wear* 34(3):291-299

Questions

1. Explain friction mechanisms. Calculate the friction coefficient when conical asperities slid against softer materials.
2. State empirical laws of friction. State and explain the adhesion theory of friction with suitable diagrams.
3. What are the factors affecting friction? Explain.
4. How does the crystal structure influence friction? Why do FCC metals have more friction than HCP metals?
5. Define wear. How do you measure wear?
6. Describe various wear mechanisms in detail.
7. What is adhesive wear? Derive Archard theory of adhesive wear.
8. What is abrasive wear? Derive the quantitative expression for abrasive wear.
9. Explain various subsurface zones that are formed during sliding.
10. What are the factors affecting wear process?
11. Explain the following:
 - (a) Static and kinetic friction
 - (b) Steady-state and stick–slip friction
 - (c) Coefficient of friction and angle of friction
 - (d) Real area and apparent area
 - (e) Adhesion friction and plowing friction
 - (f) Erosive wear and corrosive wear
 - (g) Two-body wear and three-body wear
 - (h) Fretting wear and fatigue wear

Problems

1. A steel ball is slid against an aluminum flat surface at two different normal loads. At low normal load, the coefficient of friction is 0.40 and the groove width is 0.4 mm. At high load, the coefficient of friction is 0.6 and the groove width is 0.8 mm. Calculate the adhesive component of friction. Given: $\mu_{\text{total}} = \mu_{\text{adhesion}} + \mu_{\text{plowing}}$.
2. A hard steel ball of 3 mm diameter slid against a soft aluminum surface, produces a groove of 1.5 mm width. Calculate the adhesive component of friction when coefficient of friction is recorded 0.4. Given: $\mu_{\text{total}} = \mu_{\text{adhesion}} + \mu_{\text{plowing}}$.
3. A steel surface with conical asperities of an average semi-angle of 60° slides against a soft aluminum surface of hardness, $H = 100$ MPa under a constant normal load of 20 N. Calculate the volume of aluminum displaced in unit slid distance.

4. A rigid cutter was used to cut a medium carbon steel bar of 5 mm diameter. The hardness of the carbon steel is 2 GPa. The width of cut is 0.5 mm. It took 5 min to cut and the energy expended was 50 W (Nm/s). The coefficient of friction between the cutter and the steel bar is 0.3. Calculate the wear coefficient of the steel bar during the cutting process.

Solutions

1. Given: $\mu_{total} = \mu_{adhesion} + \mu_{plowing}$

For a ball on flat surface, the above equation can be rewritten as

$$\mu_{total} = \mu_{adhesion} + \frac{4r}{3\pi R} \quad (1)$$

where $2r$ is the groove width and R is the radius of the steel ball.

At low load, (1) can be written as

$$0.4 = \mu_{adhesion} + \frac{4 \times 0.2}{3\pi R} \quad (2)$$

At high load, (1) becomes

$$0.6 = \mu_{adhesion} + \frac{4 \times 0.4}{3\pi R} \quad (3)$$

Solving (2) and (3), we get $\mu_{adhesion} = 0.2$.

2. Given: $\mu_{total} = \mu_{adhesion} + \mu_{plowing}$

For a ball on flat surface, the above equation can be rewritten as

$$\mu_{total} = \mu_{adhesion} + \frac{4r}{3\pi R} \quad (1)$$

Here $r = 0.75$ mm and $R = 1.5$ mm.

Solving (1), $0.4 = \mu_{adhesion} + \frac{4 \times 0.75}{3\pi \times 1.5}$,

we get $\mu_{adhesion} = 0.18$.

3. Total volume of material displaced in unit sliding distance is given by

$$Q = \frac{2}{\pi} \frac{W}{H} \tan \theta.$$

Substituting values, we get

$$Q = \frac{2}{\pi} \times \frac{20}{100 \times 10^6} \tan 30 = 7.35 \times 10^{-8}.$$

4. We know that the total wear volume is given by

$$Q = K \frac{W}{H} \quad \text{or} \quad K = \frac{QH}{W}.$$

Wear volume of steel bar

$$Q = \frac{\pi d^2}{4} \times w$$

where w is the width of cut. Solving the parameters, we get

$$Q = \frac{\pi \times 0.005^2}{4} \times 0.5 \times 10^{-3} = 9.8 \times 10^{-9}$$

Work done is given by

$$F = \text{Energy} \times \text{time}$$

$$F = 50 \times 5 \times 60 = 15000$$

$$W = \frac{F}{\mu} = \frac{15000}{0.3} = 50000$$

$$K = \frac{QH}{W} = \frac{9.8 \times 10^{-9} \times 2 \times 10^9}{50000} = 3.9 \times 10^{-4}$$

Chapter 3

Contact Mechanics

Robert L. Jackson, Hamed Ghaednia, Hyeon Lee, Amir Rostami,
and Xianzhang Wang

Abstract Contact mechanics is a fundamental field of tribology and generally refers to the interaction of solid surfaces. This interaction or contact can occur on many different scales, ranging from nanoscale asperities up to tires on roads and even contact between tectonic plates. This chapter reviews the basic technical information available in predicting the contact area, pressure, stresses, and forces that occur when surfaces interact. The chapter considers different geometries such as spheres and wavy surfaces and also outlines how to consider elastic and plastic deformation. The phenomena of creep and adhesion that are important for many tribological applications, and especially biological contacts, are also discussed. Finally, the chapter concludes by covering methods used to model the complicated situation of contact between rough surfaces that contain many different geometrical features.

Nomenclature

a	Radius of circular contact area
A	Area of contact
An	Nominal or apparent area of contact
b	Cylindrical contact half width
B	Aspect ratio
C	Critical yield stress coefficient
Cn	Creep material constant
d	Distance between the mean of the surface peaks and a material and geometry dependent exponent
e	Coefficient of restitution during impact

R.L. Jackson (✉) • H. Ghaednia • H. Lee • A. Rostami • X. Wang
Department of Mechanical Engineering, Auburn University, Auburn, AL, USA
e-mail: jacksr7@auburn.edu

e_y	Plastic strain (ratio of yield strength to effective elastic modulus)
E	Elastic modulus
E'	Reduced or effective elastic modulus
f	Spatial frequency (reciprocal of wavelength)
F	Contact force
h	Height of sinusoidal surface from base and distance between the mean of the surface heights
i	Scale or frequency number
I	Statistical contact integral
H	Hardness or normalized layer thickness
L	Length of cylindrical contact
m	Mass of impact sphere
m_n	n th spectral moment of the surface
N	Number of asperities or data points on surfaces
p	Average pressure over entire sinusoidal surface in contact
p^*	Average pressure for complete contact (elastic)
p_{ep}^*	Average pressure for complete contact (elastoplastic)
p_{ave}	Average pressure over entire asperity
P	Spherical contact force
Q_{max}	Tangential load required cause sliding
R	Radius of cylinder or sphere or asperity tip
S_y	Yield strength
t	Time or layer thickness
T	Temperature
V	Velocity
W_{nm}	Work of adhesion between surfaces n and m
x	Lateral surface coordinate
y_s	Distance between the mean of the surface peaks and mean of the surface heights
z	Surface height at location x
α	Layer model parameter and statistical contact parameter
β	Exponential creep material constant and surface roughness parameter
γ_n	Surface energy of surface n
γ_{nm}	Interfacial energy between surfaces n and m
Δ	Amplitude of the sinusoidal surface
δ	Deflection of cylindrical or sinusoidal asperity surface
ϵ	Strain
θ_a	Adhesion parameter
κ	Layer model parameter
λ	Asperity wavelength or layer model parameter
μ	Effective static friction coefficient
η	Areal asperity density
φ	Asperity height distribution
σ	Normal stress and RMS surface roughness

σ_s	The RMS roughness of the asperity peak heights
ν	Poisson's ratio
ω	Deflection or interference of spherical contact
ψ	Plasticity index

Subscripts

o	Initial or at $t = 0$
$1, 2$	Property for material 1, 2, etc.
c	Critical value at onset of plastic deformation
cr	Creep dependent parameter
a	Elastic area
ep	Elastic-plastic
max	Maximum
n	Normal direction and nominal or apparent area of contact
p	Elastic-plastic or elastic pressure integral
r	Real area of contact
t	Tangential

1 Introduction

Although friction and wear have been the subject of man's thoughts and creations since ancient times, the application of mechanics to contact problems probably first began with Heinrich Hertz (see Fig. 3.1) in solving the problem of elastic deformation between contacting parabolic surfaces. Many have since applied this to the contact of spherical surfaces. Many other well-known researchers have followed in Hertz's footsteps, including, but not limited to, Archard [1], Tabor [2], and Greenwood, and Williamson [3]. However, K. L. Johnson [4] may be the most well-known contemporary in the field and is the author of the seminal book on the subject, "Contact Mechanics."

Contact between solids is undeniably important because it is such a common and critical occurrence in our daily lives, health, in industry, and even on the scale of heavenly bodies and the universe. When two objects are brought together, their matter may initially attract, but as they get closer and closer, the attraction will eventually decrease and turn to repulsion which coincides with our intuitive description of contact. Contacts can and do cause very high stresses between objects that can cause failure in the form of fracture, yielding, surface fatigue, and wear. Predicting these stresses with a great deal of resolution can also be very difficult since surfaces are almost always significantly rough and possess a complicated and perhaps unpredictable geometry. Within these complex interactions, many phenomena such as friction, wear, and contact resistance are governed. Nevertheless, significant progress has been made in solving these problems in a practical manner, but still, many obstacles remain.

Fig. 3.1 Heinrich Hertz

There are analytical methods which in some cases render closed form solutions to contact mechanics problems. Numerical methods are also available which will provide an approximate solution when a closed form solution is not possible. We will concentrate mostly on existing analytical solutions to contact problems. However, methods such as finite elements and elastic superposition can be very powerful tools for contact problems that cannot be solved analytically.

In this chapter, we will begin our summary of some of these useful contact mechanics tools by first discussing the contact of elastic smooth curved surfaces as Hertz first described.

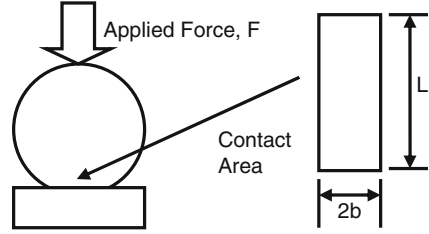
2 Single Peak Contact

2.1 *Elastic Cylindrical Contact (Line)*

Perhaps the most popular and widely used solution in contact mechanics is the contact of two elastic axisymmetric and parabolic structures, first solved by Heinrich Hertz (see Fig. 3.1), apparently while on his Christmas break over a 125 years ago [5]. Although the solution assumes a parabolic geometry, it can provide a precise approximation of elastic contact between cylinders and spheres. The Hertz solution assumes that the interference is small enough such that the geometry does not change significantly and that the surface interactions are frictionless and only repulsive.

When a cylinder contacts a flat surface, the contact area is initially a line until it grows and becomes a rectangle. The same is also true when two cylinders come into contact and their axes of symmetries are parallel. Therefore, cylindrical contacts are

Fig. 3.2 Schematic of the contact area between a cylinder and a flat surface



often referred to as line contacts. A cross section of a cylindrical contact is shown in Fig. 3.2.

Hamrock [6] provides the solution to the deflection of an elastic cylindrical contact:

$$\delta = \frac{F}{\pi E' L} \left[\ln \left(\frac{4\pi E' R L}{F} \right) - 1 \right] \quad (3.1)$$

and according to Johnson [4], the half contact width is (the contact area is the cylinder length multiplied by twice the half width)

$$b = \left(\frac{4FR}{\pi L E'} \right)^{1/2} \quad (3.2)$$

Note that E' is often referred to as the equivalent elastic modulus and can be used for the contact of many different surface geometries. E' is given by (each surface is denoted by subscript 1 and 2)

$$\frac{1}{E'} = \frac{1 - \nu_1^2}{E_1} + \frac{1 - \nu_2^2}{E_2} \quad (3.3)$$

Similarly, R is often referred to as the equivalent radius of curvature and can be used to consider the contact of two spheres with different radii of curvature, denoted R_1 and R_2 here, and calculated by

$$\frac{1}{R} = \frac{1}{R_1} + \frac{1}{R_2} \quad (3.4)$$

Note that contact between a convex and concave surface can also be considered, such as for the contact between a rolling element and a raceway in a bearing by simply making the curvature of the concave surface negative in (3.4).

When the cylinders come into contact, the pressure follows a nearly parabolic profile and is zero at the edge of contact and maximum at the initial or center point of contact. The maximum normal stress of the cylindrical contact is of course on the surface at the center of contact and is also the maximum contact pressure given by

$$p_{\max} = \frac{2F}{\pi bL} \quad (3.5)$$

However, the stresses that are recognized to cause yielding, the shear stress and von Mises stresses, are often maximum below the surface, as will be discussed next.

2.2 Elastic–Plastic Cylindrical Contact

If the force applied to a cylindrical contact increases enough, eventually the material will fail or yield. This usually occurs below the surface, because as mentioned previously, the maximum shear and von Mises stress are sometimes located not on the contacting surfaces but at a depth below them. Green [7] provides the following curve-fitted equations for the prediction of the initial yield or critical point for cylindrical contact according to the von Mises yield criteria. For the case of plane strain, the critical contact force to cause yielding is

$$\frac{F_c}{L} = \frac{\pi R (CS_y)^2}{E'} \quad (3.6)$$

where C is a piecewise equation given by

$$C = \frac{1}{\sqrt{1 + 4(v-1)v}} \quad \text{when } v \leq 0.1938 \quad (3.7)$$

$$C = 1.164 + 2.975v - 2.906v^2 \quad \text{when } v > 0.1938$$

In addition, the critical deflection and contact width are given by

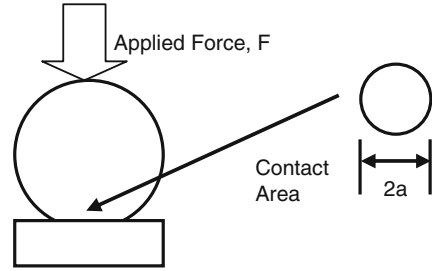
$$\delta_c = R \left(\frac{CS_y}{E'} \right)^2 \left[2 \ln \left(\frac{2E'}{CS_y} \right) - 1 \right] \quad (3.8)$$

$$b_c = \frac{2RCS_y}{E'}$$

Note that $v = 0.1938$ also indicates a threshold where when v is greater than this, the point of initial yielding occurs below the surface, and when it is less, the initial yielding occurs on the surface. In addition, the case of plane stress can also be predicted by simply setting $v = 0$.

Unfortunately, very little work has been performed on cylindrical contact once the critical force has been surpassed and significant plastic deformation occurs. Actually, the case of sliding cylindrical contact has been investigated using the finite element method, but not the case of pure normal loading in a thorough manner that can be easily applied [8].

Fig. 3.3 Schematic of the contact area between a sphere and a flat surface



2.3 Elastic Spherical and Parabolic Contact

Similar to cylindrical or line contact, Hertz also solved the case of an axisymmetric parabolic contact, which is often used to model spherical elastic contact (see Fig. 3.3). Since a sphere initially contacts a surface only at a single point, this case is sometimes also referred to as point contact. This is also probably the most widely used contact model employed to describe single asperity contact occurring between two rough surfaces, as will be discussed later. This widely used model provides the contact force as a function of interference or deflection as

$$F = \frac{4}{3} E' \sqrt{R} (\omega)^{3/2} \quad (3.9)$$

And the contact area, which is circular, is given as

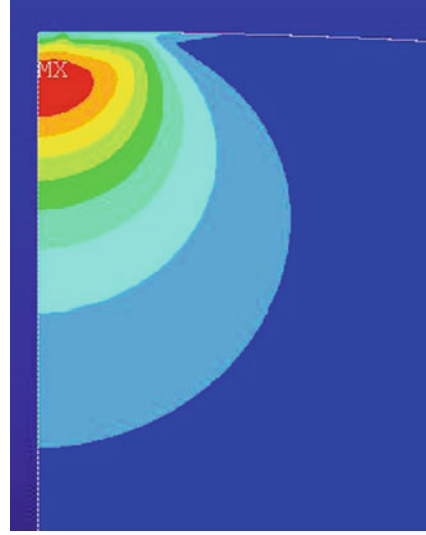
$$A = \pi R \omega = \pi a^2 \quad (3.10)$$

Note that E' and R are calculated using the same methodology outlined for cylindrical contact. It should also be noted that the maximum shear stress and von Mises stress occurs below the center of the contact area. Figure 3.4 shows the von Mises stress in a spherical contact as predicted by ANSYSTM finite element software. As will be characterized next, this causes initial yielding to occur below the surface. Similarly, surface fatigue can also initiate below the surface and allow cracks to propagate to the surface and cause large wear particles to detach and leave deep pits on the surface (i.e., pitting).

2.4 Elastic–Plastic Spherical Contact

Just as with cylindrical contact, when the contact force reaches a critical value, the stress state will start to cause yielding within the sphere. There are many models that have been devised to account for the plastic deformation in the sphere. Most models also assume that the deformation is elastic-perfectly plastic, meaning there

Fig. 3.4 The finite element predicted von Mises stress distribution in a spherical contact in the elastic regime ($\omega^* = 0.571$)



is no hardening in the material. However, there is no known analytical solution to this problem, and therefore, many previous models did not give the correct quantitative predictions, such as the groundbreaking model by Chang, Etsion, and Bogy (CEB) [9] and the work by Zhao, Maletta, and Chang [10] which attempted to improve on the CEB model by using a continuous template to bridge between the elastic and plastic regimes of deformation. Later, Kogut and Etsion [11] and Jackson and Green [12] improved upon these models by using the finite element method. Jackson and Green found the following equations for the prediction of initial yielding in the sphere according to the von Mises yield criteria [12]:

$$\omega_c = \left(\frac{\pi \cdot C \cdot S_y}{2E'} \right)^2 R \quad (3.11)$$

$$C = 1.295 \exp(0.736\nu) \quad (3.12)$$

$$A_c = \pi^3 \left(\frac{CS_y R}{2E'} \right)^2 \quad (3.13)$$

$$P_c = \frac{4}{3} \left(\frac{R}{E'} \right)^2 \left(\frac{C}{2} \pi \cdot S_y \right)^3 \quad (3.14)$$

We can then normalize the area, contact force, and displacement by these critical values as

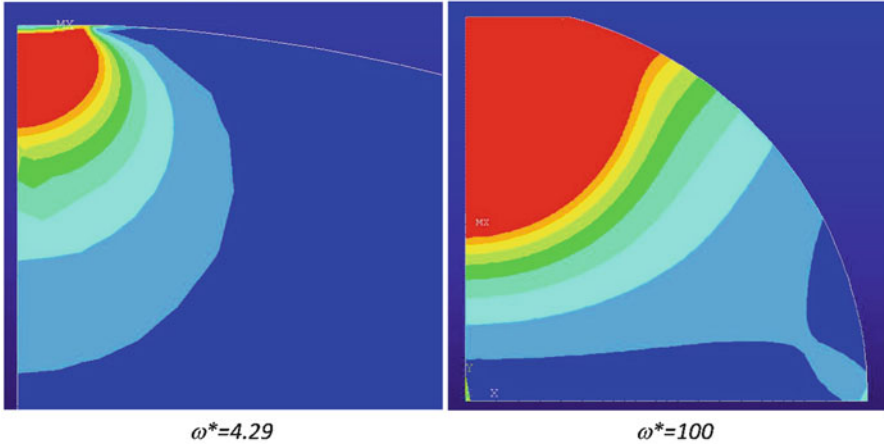


Fig. 3.5 The finite element predicted von Mises stress distributions for two interferences

$$A^* = A/A_c, \quad F^* = F/F_c, \quad \omega^* = \omega/\omega_c$$

Once yielding occurs, the volume of plastically deforming material spreads and surrounds an “island” of material near the center of contact that is under hydrostatic stress and therefore not yet yielded according to von Mises stress criteria (see Fig. 3.5). However, as the contact force is increased, eventually the entire surface in contact yields. When this occurs, it is usually referred to as fully plastic contact. Jackson and Green [12] found that the plastic deformation had a negligible effect on the contact until approximately $\omega^* = 1.9\omega_c$, which is now labeled as ω_t^* . According to the finite element-based empirical model by Jackson and Green, when the contact is effectively elastic ($0 \leq \omega^* \leq \omega_t^*$) the normalized contact force and area from Hertz contact simplify to

$$F^* = (\omega^*)^{3/2} \tag{3.15}$$

$$A^* = \omega^* \tag{3.16}$$

and once plastic deformation becomes more influential at $\omega_t^* \leq \omega^*$

$$F^* = \left[\exp\left(-\frac{1}{4}(\omega^*)^{\frac{5}{12}}\right) \right] (\omega^*)^{3/2} + \frac{4H}{CS_y} \left[1 - \exp\left(-\frac{1}{25}(\omega^*)^{\frac{5}{9}}\right) \right] \omega^* \tag{3.17}$$

and the contact area is then

$$A_F^* = \omega^* \left(\frac{\omega^*}{\omega_t^*} \right)^B \tag{3.18}$$

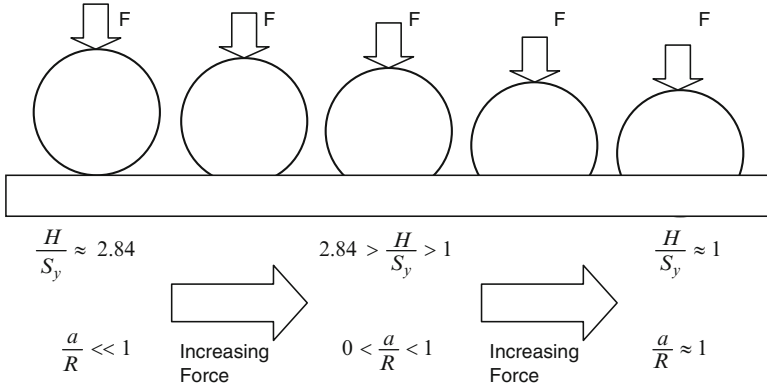


Fig. 3.6 Schematic showing how the pressure changes with the deformation of the sphere during fully plastic contact

$$B = 0.14 \exp\left(23 \cdot \frac{S_y}{E'}\right) \quad (3.19)$$

where H is the effective fully plastic contact pressure, sometimes referred to as the hardness, which is given in updated form as

$$\frac{H}{S_y} = 2.84 - 0.92 \left(1 - \cos\left(\pi \frac{a}{R}\right)\right) \quad (3.20)$$

Equation (3.20) captures the effect that large deformations of the sphere have on the contact pressure. As the sphere deforms, it changes from the shape of a curved contact toward a cylinder in contact with a flat (see Fig. 3.6). As this transition occurs, the average pressure for fully plastic contact changes from a value of approximately $2.8 \cdot S_y$, as found by Tabor [2], to S_y .

Note that the Jackson and Green [12] equations are only valid up to $a/R = 0.41$. However, recently, Wadwalkar et al. [13] used finite elements to find a model that is valid for much larger loads and deformations until the contact radius nearly equals the radius of the sphere. Note that in these cases of severe deformation, the sphere actually begins to behave similarly to a barreling cylinder in compression. Additional studies have also considered how the sphere rebounds and what the residual stresses are once the sphere is unloaded [14, 15].

As mentioned previously, Kogut and Etsion [11] also developed their own empirical finite element model prior to Jackson and Green [12]. The model by Kogut and Etsion is much more simple than the Jackson and Green model and might be useful for a complex systems of equations. Even though the models do agree in some ranges [16, 17], it must be emphasized that the model is limited to small values of a/R and low interferences. In addition, the solution is piecewise and noncontinuous at the boundaries. Using the same normalization scheme, the Kogut and Etsion [11] model is given as follows:

When

$$\begin{aligned} 1 &\leq \omega^* \leq 6 & (3.21a) \\ A_{KE}^* &= 0.93(\omega^*)^{1.136} \\ P_{KE}^* &= 1.03(\omega^*)^{1.425} \end{aligned}$$

When

$$\begin{aligned} 6 &\leq \omega^* \leq 110 \\ A_{KE}^* &= 0.94(\omega^*)^{1.146} \\ P_{KE}^* &= 1.40(\omega^*)^{1.263} & (3.21b) \end{aligned}$$

2.5 Spherical Indentation

In the elastic regime and at relatively small displacements, the contact of an elastic–plastic sphere against a rigid flat (i.e., flattening) and the contact of a rigid sphere against an elastic–plastic surface (i.e., indentation) are practically equivalent. However, as the displacements increase, the two cases begin to diverge [17]. Kogut and Komvopoulos [18] investigated elastic–plastic indentation and found a similar behavior of the fully plastic pressure to that of Jackson and Green [12]. This case is important for using indentation tests for the measurement of material properties. Kogut and Komvopoulos [18] found that the pressure during elastic–plastic indentation reached a maximum value that is less than the popular value of $2.84 \cdot S_y$ as a function of E'/S_y :

$$\frac{H}{S_y} = 0.201 \ln \left(\frac{E'}{S_y} \right) + 1.685 \quad (3.22)$$

which is analogous to (3.20) for spherical flattening, rather than indentation, although in terms of the material properties rather than the deformed geometry. Additional equations are provided in [18] relating contact area and pressure to the penetration depth, and readers are advised to obtain the paper for additional information.

2.6 Elastic 2-D Sinusoidal or Harmonic Wavy Surface

Westergaard [19] first solved the case of perfectly elastic two-dimensional sinusoidal contact. From Westergaard's work, p^* is defined as the average pressure that when applied to the surfaces yields complete contact (i.e., no gaps between the surfaces). The average pressure required to obtain complete contact between the surfaces can be calculated as

$$p_{2D,elastic}^* = \pi E' \Delta / \lambda \quad (3.23)$$

Then, the contact area is related to the nominal pressure, \bar{p} (including the regions out of contact), by

$$A = \lambda L (2/\pi) \sin^{-1} (\bar{p}/p^*)^{1/2} \quad (3.24)$$

Note that the contact area of the 2-D wavy surface is rectangular, similar to cylindrical contact, and might also be referred to as a “line” contact.

2.7 Elastic 3-D Sinusoidal or Harmonic Wavy Surface

Johnson et al. [20] characterized the contact of 3-D sinusoidal or harmonic surfaces. They found that no closed form analytical solution appears to exist over all ranges of deformation. First, they found that the average pressure to achieve complete contact for 3-D sinusoidal surfaces differs from the 2-D case and is

$$p_{3D,elastic}^* = \sqrt{2} \pi E' \Delta / \lambda \quad (3.25)$$

Then, using Hertz contact, they find the asymptotic solution to 3-D sinusoidal contact at low loads is

$$(A_{JGH})_1 = \frac{\pi}{f^2} \left[\frac{3}{8\pi} \frac{\bar{p}}{p^*} \right]^{2/3} \quad (3.26)$$

At high loads and when nearly all of the surfaces are in contact, Johnson et al. [20] found that the contact area is

$$(A_{JGH})_2 = \frac{1}{f^2} \left(1 - \frac{3}{2\pi} \left[1 - \frac{\bar{p}}{p^*} \right] \right) \quad (3.27)$$

Later, Jackson and Streator [21] fit an equation to these two asymptotic solutions that also appeared to agree with the numerical data in Johnson et al. [20]. This fit is given by

$$\begin{aligned} \text{For } \frac{\bar{p}}{p^*} < 0.8 \quad A &= (A_{JGH})_1 \left(1 - \left[\frac{\bar{p}}{p^*} \right]^{1.51} \right) + (A_{JGH})_2 \left(\frac{\bar{p}}{p^*} \right)^{1.04} \\ \text{For } \frac{\bar{p}}{p^*} > 0.8 \quad A &= (A_{JGH})_2 \end{aligned} \quad (3.28)$$

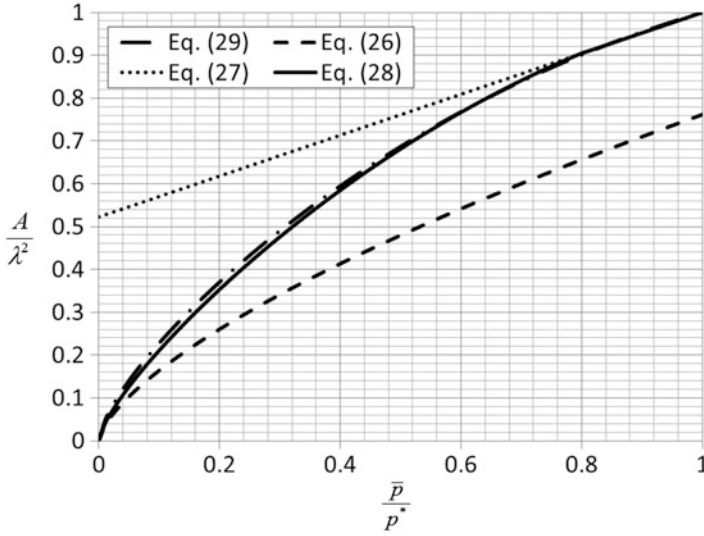


Fig. 3.7 The predicted contact area during sinusoidal contact as a function of average pressure

However, it was also later suggested that this equation could be approximated by the much more simple version here [22]:

$$\frac{A}{\lambda^2} = \left(\frac{\bar{p}}{p^*}\right) \wedge \left(\frac{2}{3} - \frac{\bar{p}}{4p^*}\right) \tag{3.29}$$

As shown in Fig. 3.7, (3.28) and (3.29) appear to agree well within most ranges of pressure and differ by an average error of approximately 2.7 %. However, at low pressures, (3.29) differs significantly from (3.28) by 30 % or more. Note that at very low pressures, Hertz contact can be assumed and that (3.29) does not asymptotically approach Hertz contact given by (3.26). Therefore, (3.29) does not appear to be a good approximation at low pressures and has errors above 5 % at approximately $\frac{\bar{p}}{p^*} < 0.2$.

2.8 *Elasto-Plastic 3-D Sinusoidal Contact*

Just as with spherical and cylindrical contact, as the contact force and pressure continues to increase, eventually it will cause yielding. If yielding initially occurs when only the tips of the sinusoidal surface are in contact, then it can still be modeled by spherical contact. Adapting the same critical equations derived for spherical contact for sinusoidal contact, the critical load and area are given by

$$F_c = \frac{1}{6\pi} \left(\frac{1}{\Delta f^2 E'} \right)^2 \left(\frac{C}{2} \cdot S_y \right)^3 \quad (3.30)$$

$$A_c = \frac{2}{\pi} \left(\frac{CS_y}{8\Delta f^2 E'} \right)^2 \quad (3.31)$$

where C is given as by (3.12). At low loads, $F < F_c$, and consequently small areas of contact, it is acceptable to assume that any deformation of the asperities in contact will behave perfectly elastically. However, as load increases to the critical value, plastic deformation will initiate within the asperities. Using the finite element method, Krithivasan and Jackson [23] developed empirical equations describing contacting sinusoidal surfaces by adapting existing spherical and elastic sinusoidal models:

$$A = (A_p) \left(1 - \left[\frac{\bar{P}}{p_p^*} \right]^{1.51} \right) + (A_{JGH})_2 \left(\frac{\bar{P}}{p_p^*} \right)^{1.04} \quad (3.32)$$

where

$$A_p = 2 \left(\frac{A_c}{2} \right)^{\frac{1}{1+d}} \left(\frac{3 \cdot \bar{P}}{4CS_y} \lambda^2 \right)^{\frac{d}{1+d}} \quad (3.33)$$

$$d = 3.8 \cdot \left(\frac{E'}{S_y} \cdot \frac{\Delta}{\lambda} \right)^{0.11} \quad (3.34)$$

and p_p^* is the average pressure required to obtain complete contact between 3-D sinusoidal surface and a rigid flat according to the analysis by Jackson et al. [24], giving

$$\frac{p_p^*}{p^*} = \left(\frac{11}{4 \cdot \Delta/\Delta_c + 7} \right)^{\frac{3}{5}} \quad (3.35)$$

Jackson et al. [24] also analytically derive from the stresses for complete contact between sinusoidal surfaces, and according to the von Mises yield criteria, that the surface will deform elastically if its amplitude, Δ , is less than

$$\Delta_c = \frac{\sqrt{2} \cdot S_y \exp\left(\frac{2\nu}{3}\right)}{3\pi E' f} \quad (3.36)$$

Likewise, when $\Delta > \Delta_c$, the surfaces deform elastic-plastically. It is very interesting to observe that the exact analytically derived (3.36) is very similar in form to (3.11) and (3.12) which were fit to a numerical solution. This gives greater confidence in those fits. Equation (3.35) predicts that the average pressure during heavily loaded contact can be much larger than the hardness, or three times S_y . This is due to the stress in sinusoidal contact becoming hydrostatic as complete contact

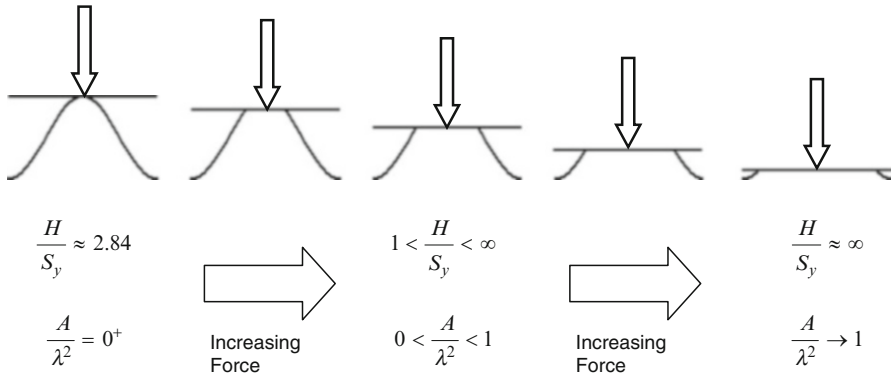


Fig. 3.8 The pressure change in the plastically deformed contact of sinusoidal surfaces

is approached. As shown in Fig. 3.8, this is in contrast to that predicted during spherical contact. In fact, the behavior is reversed. In elastic–plastic sinusoidal contact, the pressure can become much larger than yield strength as the contact area increases, while in spherical contact the contact pressure actually decreases toward a value of yield strength multiplied by unity.

2.9 Impact of Spheres

The impact of surfaces is very important for a wide variety of circumstances. For instance, it can be used to consider interactions in particulate flow, the performance of a particle damper, or perhaps even the impact of a bearing element against a raceway. Using (3.9), (3.10), (3.11), (3.12), (3.13), (3.14), (3.15), (3.16), (3.17), (3.18), (3.19), and (3.20), one can predict the energy lost in the impact of spheres due to elastic–plastic deformations. Here, we define V_I^* as the normalized velocity at the instant just before impact: $\left((V_I)^* = \frac{V_1}{V_c} \text{ and } V_c = \sqrt{\frac{4\omega_c P_c}{5m}} \right)$. Using two different methodologies to describe the rebound of the spheres [14, 15] results in two sets of equations that both appeared to compare well with experimental data. First, when the elastic recovery predictions in Jackson et al. [14] are used, the following is obtained:

For $0 < V_I^* < 1$

$$e = 1 \tag{3.37}$$

For $1 < V_I^* \leq 60$

$$e = 1 - 0.11 \ln(V_I^*) \left(\frac{V_I^* - 1}{59} \right)^{0.156}$$

For $60 \leq (V_I)^* \leq 1,000$

$$e = 1 - 0.11\ln(60) - 0.11\ln\left(\frac{V_1^*}{60}\right) (V_1^* - 60)^{2.36S_y/E'}$$

These equations combine to create a continuous prediction of e in the range of $0 < V_I^* < 1,000$. When the results of Etsion et al. [15] are used to predict the residual interference in the sequence to predict e , a good fit results from the following equation:

For $1 < (V_I)^*$

$$e = 1 - 0.0361 \left(S_y/E'\right)^{-0.114} \ln(V_1^*) (V_1^* - 1)^{9.5\epsilon_y} \quad (3.38)$$

These equations may not be valid outside the ranges considered in deriving them ($0.0005 < S_y/E' < 0.01$ and $0.2 < \nu < 0.45$). The effect of strain hardening was also recently considered by Chaise et al. [25], who also confirmed the equations above for the impact of elastic-perfectly plastic materials

2.10 Adhesion Between Single Peaks

Under some conditions, such as when surfaces are contaminated, very rough, or relatively rigid, the effect of adhesion is negligible. However, for many other cases when the surfaces are very clean, smooth, and relatively soft, adhesion can play a very important role. Adhesion is simply the ability of surfaces in contact to maintain a tensile pressure before being pulled apart. Small quantities of water or fluid can also cause adhesion by forming a meniscus between the surfaces.

Surfaces in close vicinity tend to attract one another resulting in an adhesive force. Various sources can originate adhesion such as chemical bonds and physical forces. Examples of such sources for chemical bonds are ionic and covalent bonds and for physical forces are van der Waals and meniscus forces. Adhesion should be differentiated from cohesion when two identical materials bond together to form a new single material. Cohesion is measured when a material is broken into two different parts whereas if two surfaces (even made of the same material) are brought together, the force acting in between is called adhesion. The adhesion force, like the friction force, depends on the externally applied normal force. However, unlike the friction force, the adhesion exists even when there is no applied normal force on the surface. The force required to separate two adhered surfaces by the force of adhesion is called the “pull off force.”

Adhesion happens in the interface of almost all materials and states of matter. A common example of the effect of adhesive forces between liquids and solids is the shape of a droplet on a surface. When the liquid/solid adhesive force is greater than the cohesive force of the liquid, the droplet tends to spread on the surface, such

as with water on glass. Whereas in the case of high liquid cohesion, droplet keeps a spherical form on the surface and minimizes the solid/liquid interfacial area, such as with oil on glass.

Molecules and atoms on the surface are the source of the adhesion. Therefore, contaminants, adsorbents, and thin films on the surface impose a great impact on the adhesive properties of a surface. Contaminants and adsorbents can dramatically reduce the adhesion of a surface. The existence of a liquid film can also result in the formation of a meniscus and affect the adhesion. Surface roughness decreases the real area of contact, and therefore, rougher surfaces tend to have less adhesion. Low stiffness, high normal load, creep, and other parameters that increase the real area of contact will also promote adhesion. Temperature changes the energy level of interfacial bonds and also the elasticity of the material which in turn can change the adhesion characteristics of the surface.

Generally, adhesion of a surface depends on many chemical and physical aspects of the surface and material which makes it difficult to calculate and characterize. Parameters such as work of adhesion, surface free energy, and interfacial energy are often used to avoid the complications of adhesion models [26]. The work of adhesion (W_{12}) is the energy change per unit area required to separate two surfaces (surface 1 and surface 2) from contact to separation by an infinite distance in a vacuum. The work of adhesion for two identical surfaces (W_{11}) is called the work of cohesion. The work of adhesion always has a positive value as the surfaces are attracted to one another in the vacuum. Surface energy (γ_l) is the energy required to increase the interfacial area of a media by a unit area. For liquids, γ_L is usually given in force per unit length (which is of the same dimension as energy per area) and referred to as surface tension. The surface energy of two immiscible liquids is called the interfacial energy (γ_{12}). Relations between these parameters are given in (3.39):

$$\begin{aligned} W_{12} &= \gamma_1 + \gamma_2 - \gamma_{12} \\ \gamma_{11} &= w_{11}/2 \end{aligned} \quad (3.39)$$

In small-scale geometries where the surface to volume ratio increases, adhesion is an important and may be a dominant force. The domination of adhesion at the small scale was cited as one source of the contradictions observed between the Hertz contact model and experiments in the early of 1970s [27]. The first attempt to model adhesion between rigid spheres was carried out by Bradley [28], and the pull off force was calculated. Since Bradley, many models have been developed for spherical single asperity contact under certain assumptions. Johnson, Kendall, and Roberts (JKR) [27] developed a contact model assuming the adhesive force inside the contact area. Based on JKR, the radius of contact (a) when two spheres (R_1, R_2) with the elastic modulus, E , are compressed together under the applied load, F , is given by

$$a^3 = \frac{R}{E} \left[F + 3\pi RW_{12} + \sqrt{6\pi RW_{12}F + (3\pi RW_{12})^2} \right] \quad (3.40)$$

where $R = R_1 R_2 / (R_1 + R_2)$. Note that this equation predicts an area of contact for the case even when no load is applied. The JKR model also predicts a pull off force of $F_s = -3\pi R W_{12} / 2$, meaning that when the applied force equals to F_s , the two surfaces suddenly jump out of contact.

Assuming the Hertz contact solution inside the contact region and the adhesive force outside the contact area, Derjaguin, Muller, and Toporov [29, 30] developed an adhesion model also known as the DMT model. Equation (3.41) presents the radius of contact and pull off force according to this model:

$$\begin{aligned} a^3 &= \frac{3R}{4E} (F + 2\pi R W_{12}) \\ F_s &= -2\pi R W_{12} \end{aligned} \quad (3.41)$$

For a while it was thought that the DMT and JKR model are contradicting one another until Tabor [31] shed light on the matter by proving the fact that the two models are the limiting cases characterized by the Tabor parameter. Maugis [32] and Carpick-Ogletree-Salmeron [33] bridge the gap between the two models by introducing new assumptions and fitting equations.

Adhesion between rough surfaces can also be characterized using single asperity models and approaches such as statistical or multiscale methods. Fuller and Tabor [34] provided an adhesion parameter, θ_a , that qualitatively predicts the importance of adhesion in rough surface contact and is given by

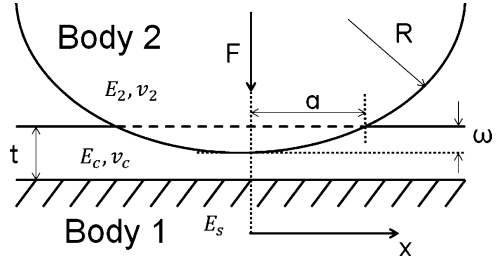
$$\theta_a = \frac{E' \sigma_s}{W_{12}} \left(\frac{\sigma_s}{R} \right)^{1/2} \quad (3.42)$$

where σ_s is the RMS roughness of the asperity heights which will be defined later in Sect. 3.2 when discussing statistical rough surface contact models. When θ_a is greater than 10, adhesion is usually considered to be negligible in the contact of rough surfaces. In conclusion, adhesion can act as a helpful (a gecko walking on the wall) or a destructive mechanism (micron-sized devices stuck together). Therefore, careful study and understanding of it is of great importance in the area of contact mechanics.

2.11 Layered or Coated Single Peak Contacts

The ability to estimate the contact between a sphere and a thin-layered or thin-coated foundation is practically of great interest since thin coatings are widely used in industry. We will introduce the extended Hertz theory for circular point contact of coated bodies developed by Liu et al. [35] in this section, but many other cases of contact between layered surfaces are available in the literature. Liu et al. [35] provide a model of this contact problem by modifying the Hertz contact theory using a numerical analysis. As shown in Fig. 3.9, there is a coated layer on

Fig. 3.9 Contact between a sphere and coated surface



body 1, which is considered the substrate, and body 2 is the elastic sphere. In this work the substrate (body 1) will be considered rigid ($E_s = \infty$).

The original Hertz solution is modified by using an equivalent elastic modulus (E^*) resulting in

$$F = \sqrt{\frac{16\omega^3 E^{*2}}{9}} \quad (3.43)$$

$$a = \sqrt[3]{\frac{3FR}{4E^*}} \quad (3.44)$$

$$\frac{1}{E^*} = \frac{1}{E_1} + \frac{(1 - \nu_2^2)}{E_2} \quad (3.45)$$

where ω is the contact approach or interference, a is the contact radius, t is the thickness of the coating, F is the externally applied force, and R is the radius of the sphere. An externally applied force can be obtained using (3.43), and the contact radius and area is predicted by (3.44). The following procedure should then be followed. First, calculate the value of each necessary parameter (λ , κ , E_c^* , and H) using (3.47), (3.48), (3.49), and (3.50). The subscripts “c,” “1,” and “2” stand for material properties of the coating, body 1, and body 2, respectively. Then, the equivalent elastic modulus of the layered surface is predicted by the fit equations from Liu et al. [35]:

$$E_1^* = E_c^* \frac{1 - (\lambda + \kappa + 4\kappa\alpha^2 H^2) \exp(-2\alpha H) + \lambda\kappa \exp(-4\alpha H)}{1 + 4\alpha H \kappa \exp(-2\alpha H) - \lambda\kappa \exp(-4\alpha H)} \quad (3.46)$$

$$\lambda = 4\nu_c - 3 \quad (3.47)$$

$$\kappa = 1/\lambda \quad (3.48)$$

$$E_c^* = \frac{E_c}{1 - \nu_c^2} \quad (3.49)$$

$$H = t/a \quad (3.50)$$

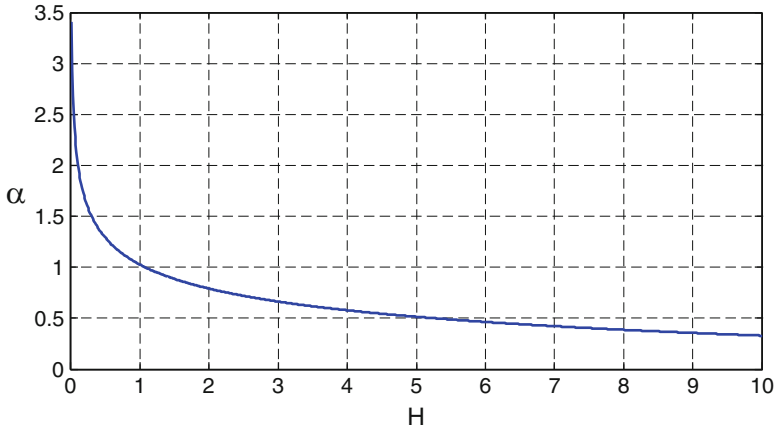


Fig. 3.10 Curve of α as a function of H

In order to find ω from a , use the Hertz contact theory (3.10). Next, obtain “ α ” from Fig. 3.10 with the H calculated above. Now, we can obtain E_1^* containing the overall characteristics of body 1 from (3.45) with the parameters we have calculated, and then, find E^* using (3.44). Finally, the applied force will be calculated using (3.43) with E^* . In this way, the applied force and resulting contact area on a circular point contact between a sphere and coated rigid substrate is obtained.

Liu et al. [35] also developed the ways to obtain applied force for the case of a circular point contact between a sphere and coated elastic substrate and an elliptical point contact. These other cases are omitted due to limited space but can easily be implemented from the original work.

An example of analysis for the contact between “aluminum” sphere and “glass” substrate coated with polydimethylsiloxane (PDMS) using the Liu et al. [35] model is presented next. The employed elastic modulus and Poisson’s ratio of PDMS are approximately 615 kPa and 0.5, respectively. Also, the values of R and t are 5 and 1 mm, respectively. The relation between ω and a is determined by Hertz contact (3.10). To compare this model with the classical Hertz contact theory, the forces obtained by the Liu et al. [35] model and the Hertz contact theory are plotted in Fig. 3.11. The lines of “Hertz 1” and “Hertz 2” represent the contact forces in elastic spherical contact situations obtained by (3.9). “Hertz 1” is the prediction of the contact between an aluminum sphere ($E = 73.1$ GPa, $\nu = 0.35$) and a glass substrate ($E = 77.5$ GPa, $\nu = 0.2$) without a layer. “Hertz 2” is the prediction of the contact between an aluminum sphere and an infinitely thick PDMS layer. As expected, the layered model predicts forces between the two limiting cases.

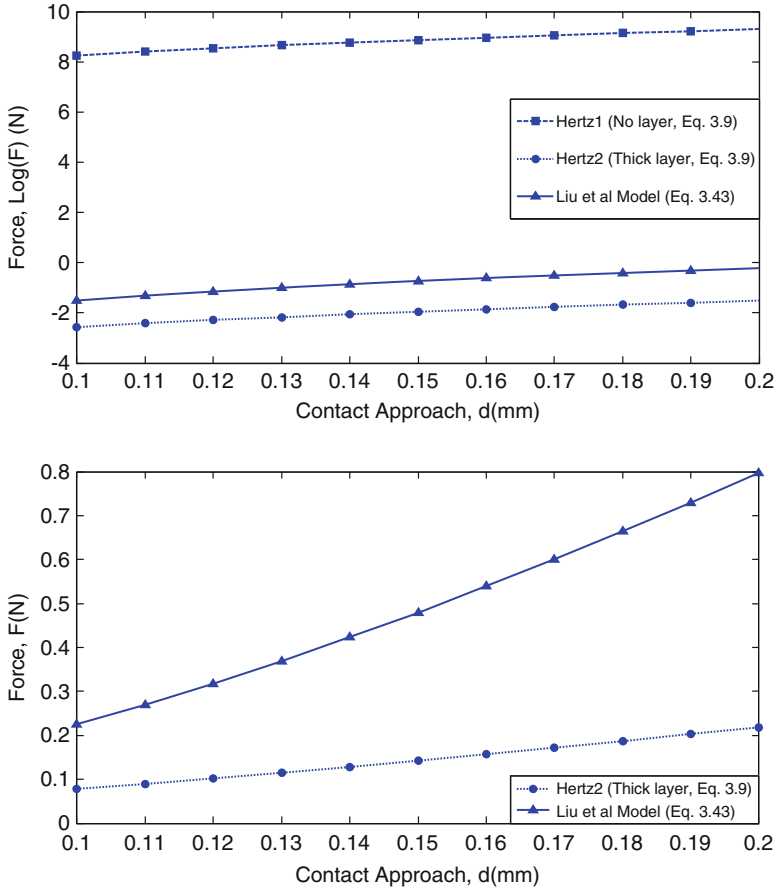


Fig. 3.11 Comparison of the layered contact model to the limiting Hertz contact cases

2.12 Creep in the Contact of Single Peaks

Creep is a time-dependent phenomenon which causes a change in the stress and strain in a material over time. In the contact between surfaces, creep causes a change in the contact area and contact pressure over time. Creep isn't an elastic behavior, and there is no recovered creep strain or reversible behavior under normal operating conditions, although elastic deformations are still recovered. Temperature and the presence of certain chemical solutions are environmental factors that may help some creeping materials to retrieve their initial shapes after a period of time. Any material may suffer from creep if certain conditions are met. It could be metals at high temperatures, polymers at room temperatures, and any material under the effect of nuclear radiation. There exists a variety of tribological applications that contact creep is of importance such as rail and wheel, MEMS RF switches, magnetic tapes, and also natural and artificial joints in the human body.

Different effects in contact between rough surfaces such as the rise in static friction due to dwell time and the rise in dynamic friction due to velocity and the friction lag and hysteresis can be described by the creep theory. The creep behavior depends on properties such as temperature and the stress level to which the material is exposed. Creep increases with temperature and is more dominant in materials that are exposed to heat for a long period of time.

For analyzing the creep behavior of materials, usually two approaches have been used in the literature. The first one is a classical approach [36] which is based on a combination of springs and dashpots, and the second approach uses empirical formulas which are based on experimental results to consider the effect of different creep parameters [37, 38]. In this text, the second approach is considered. Some of the empirical equations that have been used in creep modeling are listed as follows:

Power Law [39]

$$\dot{\epsilon}_{cr} = C\sigma^n \quad (3.51)$$

Exponential Creep Law [39]

$$\dot{\epsilon}_{cr} = C' \exp(\beta\sigma) \quad (3.52)$$

Garofalo Law [40]

$$\dot{\epsilon}_{cr} = C_1 \sinh^n(C_2\sigma) \quad (3.53)$$

Strain Hardening [39]

$$\dot{\epsilon}_{cr} = C_1 \sigma^{C_2} T^{C_3} \epsilon_{cr}^{C_4} e^{-C_4/T} \quad (3.54)$$

Modified Time Hardening [39]

$$\epsilon_{cr} = \frac{C_1 \sigma^{C_2} T^{C_3} e^{-C_4/T}}{(C_3 + 1)} \quad (3.55)$$

In the above equations, ϵ_{cr} is the creep component of the strain, σ is the nominal stress in the material, T is the temperature, and all the constants C , C' , β , n , and C_i ($i = 1 - 4$) are creep parameters which are obtained by curve fitting to the results of an accurate creep experiment.

It is suggested in [40] that the power creep law is only applicable to low stresses, but for high stresses, the exponential creep law gives better predictions. In addition, it is sometimes difficult to distinguish experimentally between the power and exponential creep laws. Therefore, the Garofalo creep law (3.53) was introduced which reduces to the power law for low stresses and to the exponential law for high stresses [40].

Only one case from two possible boundary conditions for analyzing creep will be considered in this chapter. Constant interference (i.e., relaxation) and constant load (i.e., creep) are the two possible cases, and only the first will be considered. Some models (i.e., [42] and [37]) assume constant normal force instead of constant displacement (i.e., [41]) for the contacting flat surface. The creep behavior of an elastic-perfectly plastic hemispherical asperity in fully plastic contact with a rigid flat surface, as analyzed by Goedecke and Mock [41], is discussed here. Fully plastic contact means that material has reached the yield stress everywhere in contact area.

We can write the following equation for the total strain tensor ε_{tot} , which can be separated into the creep, plastic, and elastic strain tensors:

$$\dot{\varepsilon}_{tot} = \dot{\varepsilon}_{cr} + \dot{\varepsilon}_{pl} + \dot{\varepsilon}_{el} \quad (3.56)$$

As the creep strain increases, the elastic strain, ε_{el} , decreases, and the total stress reduces to $\sigma = C : \varepsilon_{el}$ with C being the elasticity tensor.¹ It is sufficient to formulate the uniaxial creep law, $\dot{\varepsilon}_{cr}(\sigma)$, where ε_{cr} and σ denote the equivalent strain and stress (von Mises stress), respectively. Using the Garofalo creep law with this model, as used in numerical simulations by Goedecke and Mock [41], two distinct phases of creep relaxation can be distinguished [37]. The asperity creeps with an accelerated creep rate in the first phase, but in the second phase, the asperity creeps with a much slower rate and no contact area change can be seen. It should be noted that the inclusion of a time- or temperature-dependent material creep law is straightforward as long as the hyperbolic sine dependence on stress is retained. In this case, the constant C_1 becomes a time- and temperature-dependent function $C_1(t, T)$ and can be included trivially in the equations describing the asperity behavior.

As mentioned before, in this model (Goedecke and Mock [41]) the contact between a hemispherical asperity and a rigid flat is under a fixed interference boundary condition δ (Fig. 3.12). It is assumed that $n = 1$ in the Garofalo formula (3.53) which corresponds to Persson's creep theory [43]:

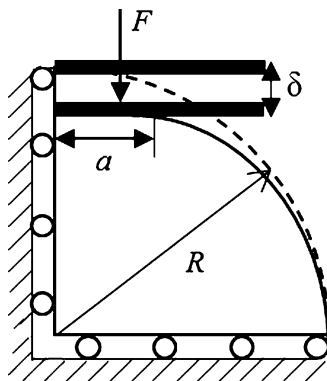
$$\dot{\varepsilon}_{cr} = C_1 \sinh(C_2 \sigma) \quad (3.57)$$

The creep constant C_1 in the Garofalo formula shows the characteristic time scale in the creep process, and the results are presented with respect to this scaled time:

$$\tau = t/t_1 = t \frac{EC_1}{H} \quad (3.58)$$

¹ In this notation, the colon ($:$) marks a reduction of the full tensor grade by 2; i.e., a multiplication of a tensor of the fourth grade with a tensor of the second grade yields a tensor of second grade.

Fig. 3.12 A hemispherical asperity with radius R before and after loading, showing the contact radius a , the displacement δ , and the load F



In Fig. 3.13, the force F and the contact area A dependence on τ for reference parameters (set number 1 in Table 3.1) are shown. It can be seen that the contact area change flattens and it remains constant after an initial rise of about 7%. The contact force, on the other hand, shows a steep initial reduction and a slowing creep rate as time increases.

The finite element simulations include two steps: (a) displacing the rigid flat to reach to a predefined interference δ as shown in Fig. 3.12 and (b) creep relaxation at this fixed interference. Jackson and Green [12] formulas can be used (see (3.11), (3.12), (3.13), (3.14), (3.15), (3.16), (3.17), (3.18), (3.19), and (3.20)) to obtain the state of the sphere before creep initiates (Step (a)). Using the Garofalo creep law (3.53) and considering the fact that the total strain is constant at ϵ_0 because of fixed interference boundary condition, the following equation can be obtained for the contact area as it changes in time due to creep:

$$A(t) \approx A_0 \left[1 - (1 - 2\nu) \left(\epsilon_0 - \frac{2}{EC_2} \operatorname{arctanh}(-C_1 C_2 t + \xi) \right) \right] \quad (3.59)$$

where A_0 is the initial contact area before creep starts and ξ is an integration constant. So a time evolution law for the change in contact area (ΔA) is

$$\frac{\Delta A(t, C_2, \delta)}{A_0} = \frac{\Delta A(C_2, \delta)}{A_0} [1 - 2c(p_1, p_2) \operatorname{arctanh}\{\exp(-p_1 \tau(t) + p_2)\}] \quad (3.60)$$

where

$$c(p_1, p_2) = [2 \operatorname{arctanh}(\exp(p_2))]^{-1} \quad (3.61)$$

to set $\Delta A(t = 0) = 0$. p_1 and p_2 are the fit parameters, and their values for the example material properties listed in Table 3.1 are given as

Fig. 3.13 Creep relaxation of force (*solid line*) and evolution of contact area (*dashed line*) with respect to normalized creep time in a logarithmic (a) and conventional (b) scale

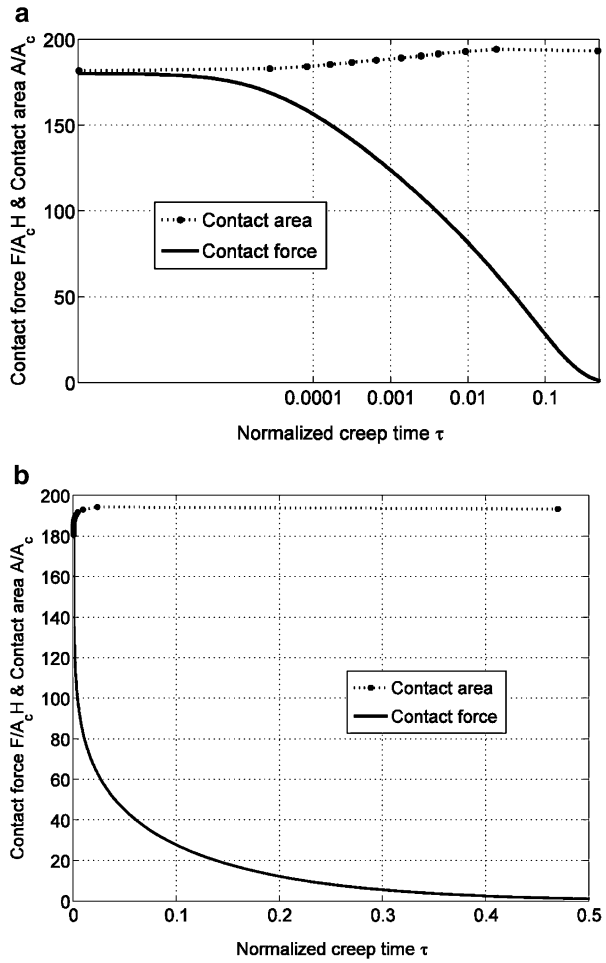


Table 3.1 Overview of parameter ranges used for simulation [36]

Run no.	Varied parameter	Range
1	None (reference)	$R = 1mm, E = 200GPa, \nu = 0.33$ $\sigma_Y = 400MPa, (C_1 = 10^{-4}s^{-1})$ $C_2 = 10/\sigma_Y, \delta = 100\delta_c$
2	Radius R	0.1 – 10mm
3	Interference δ	$25\delta_c - 600\delta_c$
4	Poisson's ratio ν	0.28 – 0.38
5	Yield stress σ_Y	200 – 2000MPa
6	Young's modulus E	70 – 300GPa
7	MCL parameters C_1, C_2	$C_1 = 10^{-3} - 10^{-5}s^{-1}, C_2 = 5 - 15/\sigma_Y$

$$p_1 = 27 \pm 5$$

and

$$p_2 = -(1 \pm 0.4) \times 10^{-3} \quad (3.62)$$

The pressure rate or relaxation rate for the second step (b) is obtained from the following equation:

$$\dot{p}(p) = -\sum_{i=1}^2 A_i \sinh(\alpha_i p) \quad (3.63)$$

The A_i and α_i are dependent on input parameters such as the fixed interference δ and the asperity radius R and are obtained by curve fitting to accurate numerical or experimental results. Extending (3.63),

$$-\dot{p} = A_1 \sinh(\alpha_1 p) + A_2 \sinh(\alpha_2 p) \quad (3.64)$$

where the constants A_i and α_i are obtained using the following empirical equations:

$$\begin{pmatrix} A_1 \\ A_2 \end{pmatrix} = EC_1 \left\{ \begin{pmatrix} 2.933 \pm 0.076 \\ -0.035 \pm 0.019 \end{pmatrix} + C_2 \sigma_Y \begin{pmatrix} 0.001 \pm 0.010 \\ 0.089 \pm 0.002 \end{pmatrix} \right\} \quad (3.65)$$

$$\begin{pmatrix} \alpha_1 \\ \alpha_2 \end{pmatrix} = \frac{1}{H} \left\{ \begin{pmatrix} 0.43 \pm 0.14 \\ 3.43 \pm 0.23 \end{pmatrix} + C_2 \sigma_Y \begin{pmatrix} 0.57 \pm 0.02 \\ 0.85 \pm 0.03 \end{pmatrix} \right\} \quad (3.66)$$

The second case that is considered here is creep under the constant force boundary condition as described by Brot et al. [38]. In reference [38], a polymeric biomaterial is used to model the single hemispherical asperity, and they also used a simplified form of the modified time hardening law (3.55) for their model because it better predicts the experimental results for polymers. Since biomaterials are used over a narrow range of temperatures, the temperature dependency can be ignored. Therefore, by substituting the simplified form of (3.55) into a sum of the different components of the strains, (3.56) gives

$$\varepsilon = \varepsilon_{elastic} + \varepsilon_{cr} = \frac{\sigma}{E} + \bar{C}_1 \sigma^{C_2} t^{C_3} \quad (3.67)$$

The above equation is called the simplified modified time hardening law (MTH) where E is the linear elastic modulus of the polymer and the parameter \bar{C}_1 is defined as

$$\bar{C}_1 = \frac{C_1}{(C_3 + 1)} \quad (3.68)$$

Brot et al. [38] found the following equations for the creep displacement and creep contact area using (3.67), and by performing a parametric analysis to study the effect of the various variables obtained the following

$$\omega_{cr}(t) = \omega_{cr}(t_r) \left(\frac{t}{t_r} \right)^{(0.71C_3+0.03)} \quad (3.69)$$

$$A_{cr}(t) = C_2 \pi R \omega_{cr}(t_r) \left(\frac{t}{t_r} \right)^{(0.71C_3+0.03)} \quad (3.70)$$

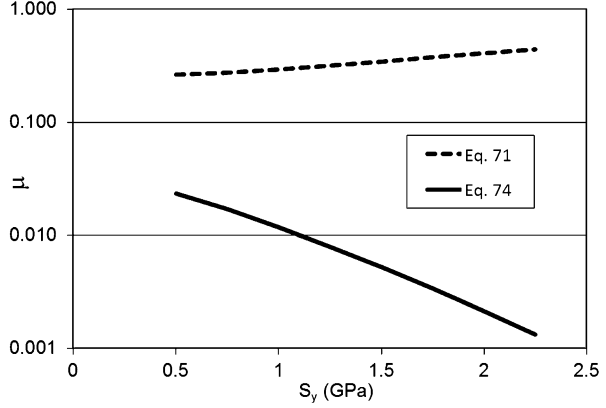
In the above equations, $\omega_{cr}(t)$ and $A_{cr}(t)$ are the time-dependent creep displacement and creep contact area, respectively. It should be noted that $\omega_{cr}(t_r)$ is the creep displacement at a convenient reference time t_r , R is the radius of the hemispherical asperity, and C_2 and C_3 are constants that are calculated by curve fitting the equation to the experimental results. As shown by the equations, Brot et al. [38] found a linear relation between the area evolution $A_{cr}(t)$ and interference $\omega_{cr}(t)$.

2.13 Sliding and Tangentially Loaded Contacts

Ultimately, the goal of many of the contact models is to be able to predict friction and wear between sliding surfaces. Unfortunately, no theoretical model of friction or wear has been universally successful in making predictions based on the material properties, surface geometries, operating conditions, etc. Nonetheless, we will briefly introduce some of the concepts of sliding in contact mechanics here. Sliding is essentially the application of a tangential load to a contacting asperity. Many previous works have considered the effect of tangential load on the elastic contact between a contacting sphere and a flat, and we suggest you look to these prior works for more information [44–46]. The elastic–plastic contact of a sphere against a flat surface has also been studied since Chang et al. [47] were first interested in predicting the static friction between metallic surfaces. The concept is that two asperities will bond together on the surface, and that the bond must be yielded by the combined stresses induced by normal and tangential loading for sliding to occur. An anomaly of this theory is that for very highly loaded surfaces on which the contacts are yielded, no additional force is needed to induce sliding, and the friction is theoretically nil. More recently, Brizmer et al. [48] used a finite element analysis to predict the tangential load, Q_{max} , required to break the contact or cause sliding between a sphere and a flat with a full stick condition initiated between the surfaces and provide an empirical fit as

$$\mu = \frac{Q_{max}}{F_n} = 0.26 \coth \left(0.27 \left(\frac{\omega}{\omega_c} \right)^{0.46} \right) \quad (3.71)$$

Fig. 3.14 Comparison of two elastic-plastic models of the tangential loading of spheres against a rigid flat (3.71) and against another identical sphere (3.74)



where F_n and ω are the normal preload and deflection before the tangential load is applied, respectively. Be careful to note that this is not the conventional friction coefficient, but the ratio of tangential to normal force for a single contact. Since (3.71) is intended to consider single asperity contact in order to predict friction between the surfaces, the full stick condition is intended to model the adhesive bonding or cold welding that can take place between asperities on surfaces and is believed to be one of the main sources of friction.

Alternatively, another finite element-based work characterized the lateral interaction of two spheres deforming in the elastic–plastic range [49]. This interaction might be considered the plowing or abrasive mechanism in friction and wear, as opposed to the adhesive mechanism. To isolate the plowing effect, the friction between the interacting spheres was set to zero. From an extensive finite element simulation, the following fit equations were found for average normal force, average tangential force, and single contact friction averaged over the entire interaction of the two spheres, respectively:

$$\frac{F_n}{P} = 0.59 \left[\left(\frac{\delta}{\omega_c} \right)^{1/5} \left(1 - 0.656 \left(\frac{1}{e_y} \right)^{1/20} \right) \left(\frac{\nu}{0.33} \right)^{1/10} \right] \quad (3.72)$$

$$\frac{F_t}{P} = 4.5 \cdot 10^{-7} \left[\ln \left(\frac{\delta}{\omega_c} \right)^{20/3} (113e_y)^2 \left(\frac{\nu}{0.33} \right)^{2/3} \right] \quad (3.73)$$

$$\mu = \frac{F_t}{F_n} = 7.63 \cdot 10^{-7} \left[\ln \left(\frac{\delta}{\omega_c} \right)^{20/3} \left(\frac{\omega_c}{\delta} \right)^{1/5} \frac{(113e_y)^2}{1 - 0.656(e_y)^{-0.05}} \left(\frac{\nu}{0.33} \right)^{0.56} \right] \quad (3.74)$$

where e_y is S_y/E' and δ is the interference between the interacting spheres. Note that the fits are limited in applicability to $0.01 < \delta/R < 0.025$ and $1.66 \times 10^{-3} < e_y < 22.5 \times 10^{-3}$. Since the fits presented by (3.71), (3.72), (3.73), and (3.74) represent the source of friction from two different mechanisms, it is possible to qualitatively compare the proportion of friction from the two mechanisms as shown in Fig. 3.14. The results shown are for $E = 200$ GPa, $\nu = 0.33$, $\delta = \omega = 0.1 \mu\text{m}$, and

$R = 10 \mu\text{m}$, and the yield strength is varied as shown. These values could represent an asperity on a steel surface. The results of this comparison suggest that the adhesive source of friction is much larger than the plowing portion. However, it is possible that under certain conditions this might not be the case, for instance if the surfaces are lubricated. In addition, it appears that for very soft materials that the two curves would cross and reverse order. Then, it is also interesting to note that the two mechanisms appear to be affected by the yield strength in opposite ways. They may result in the effect of yield strength cancelling out. Another recent paper uses a semianalytical method to also consider rolling motion [50]. Even more recently, Mulvihill et al. [51] examined a similar case but included the effect of a shear strength at the contact bond between the surfaces.

3 Rough Surface Contact

3.1 Background

All surfaces, if looked at the proper magnification, show some roughness or deviation from being perfectly smooth. In some cases, this may mean considering the atomic scale of the surface where roughness is inherent due to the particle-based structure of matter. In contrast, some surfaces appear rough with no magnification at all. Regardless of what scale the roughness appears, it will cause contact between surfaces to begin at the peaks and difficult to accurately model. This roughness also usually does not only appear at one scale but over many scales (see Fig. 3.15). This results in the geometry of surfaces being very difficult to describe in detail.

Even though the roughness of surfaces is very difficult to describe, the contact between rough surfaces governs many phenomena in our world, such as friction, wear, thermal contact resistance, and electrical contact resistance. Therefore, it is extremely important to be able to at least make reasonable predictions of the pressure and real area of contact between two contacting rough surfaces. The real area of contact between surfaces defines what solid material actually comes into contact when two surfaces are pressed together. For example, if you asked most people what the area of contact was between this textbook and a table is, they would identify the rectangular profile of the book, which is commonly referred to as the nominal or apparent area of contact. However, what's actually in contact are only the peaks or asperities on the surfaces of the book and the table. This results in the pressures on these asperities being much higher than what is nominally applied to the book.

Archard [1] was probably the first to model contact between rough surfaces by the stacking of spheres of different sizes. He was the first to show that the real contact area is often nearly linearly proportional to the contact force. This was later confirmed by others such as Bush et al. [52] and Greenwood and Williamson [3] and has important implications in explaining Amonton's friction equation

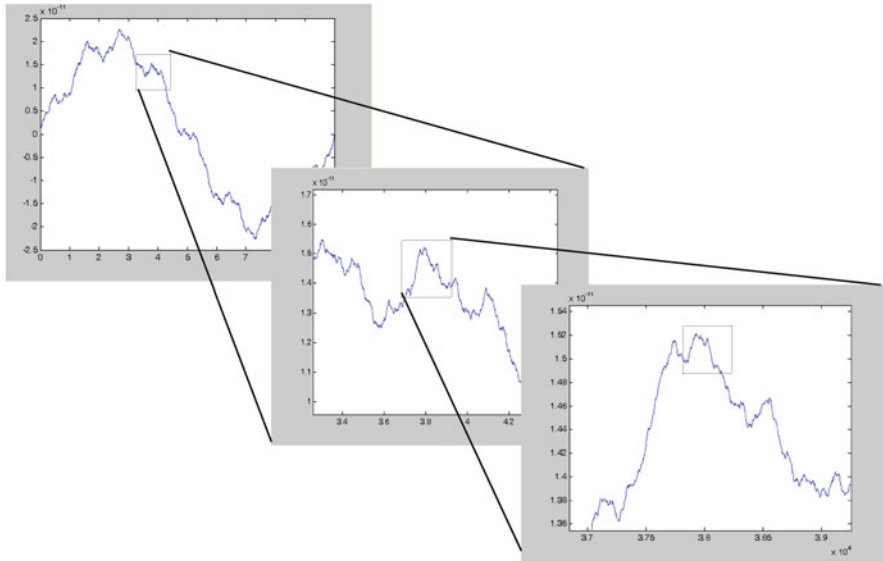


Fig. 3.15 Illustration of how surface roughness can appear at different magnifications and therefore at different scales

(i.e., friction is independent of nominal area and dependent on normal load). If the friction force is proportional to the real area of contact, then according to these models, Amonton's friction equation is explained.

In addition, it is extremely difficult, and perhaps even impossible, to measure the actual or real area of contact between many surfaces under practical conditions. This is because the individual asperity contact areas are not only often very small but hidden between the surfaces. Some researchers have had some success with acoustic [53], optical [54], electrical [55], and thermal measurements [56]. Nonetheless, it is difficult to verify the various rough surface contact models in the literature, and for these reasons, there are many of them. It would require another book to describe all rough surface contact models and is impractical to review them all here, but we will cover a few that we believe are the most practical and accurate.

If one attempts to consider the entire surface geometry, such as by meshing the entire surface and solving the contact and deformation using finite elements, then the method is considered to be deterministic. However, these models are not truly deterministic because it is currently practically impossible to adequately include all the detail of a rough surface. However, there are a few methods that have shown promise in this area. There are many methods that also seek to improve the computational efficiency via semianalytical approaches [57], multigrid methods, or by solving the problem in the frequency domain [58, 59]. Samples of a rough surface contact problem solved in the frequency domain using the method outlined by Stanley and Kato [59] are shown in Figs. 3.16, 3.17, and 3.18. For generality,

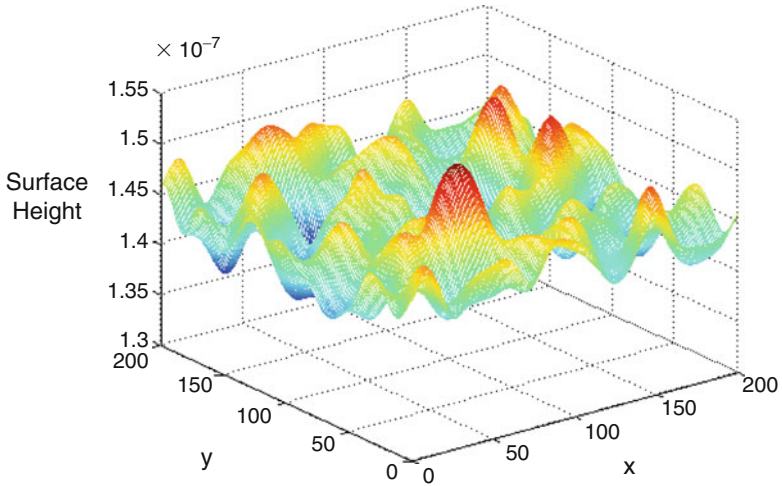


Fig. 3.16 A rough surface modeled using the FFT deterministic method for elastic contact (using Stanley and Kato [59])

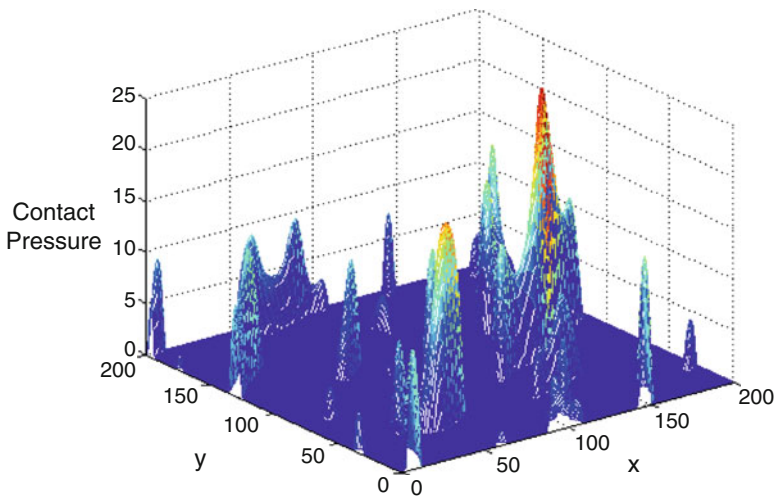


Fig. 3.17 The pressure distribution of the rough surface shown in Fig. 3.16 solved by using the FFT deterministic method for elastic contact

these figures are left without units. In Fig. 3.16, the initial geometry is shown. In Fig. 3.17, the contact pressure is shown, and finally, in Fig. 3.18, the deformed geometry of the surface is shown. It is easy to see in these figures how the peaks or asperities are only in contact and incur high pressures.

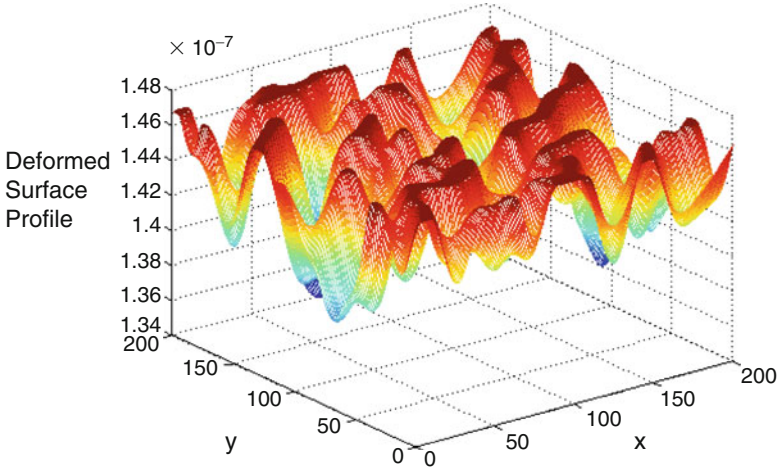


Fig. 3.18 The deformed profile of the rough surface shown in Fig. 3.16 solved by using the FFT deterministic method for elastic contact

Since deterministic methods are very computationally expensive, many methods have been developed by modeling the rough surface using different mathematical models. The main methods are here categorized by the implemented mathematical methodology as (1) statistical, (2) fractal, and (3) multiscale. Here, we will discuss only the statistical and multiscale models in detail. This is partly due to the fact that fractal-based models have been found to predict a nonphysical result: zero contact area. It should be emphasized that all rough surface contact models should be used with great care because they all make underlying assumptions about the surfaces that are in contact.

Since rough surfaces possess very complicated geometries and appear “random” in nature, it is logical to employ statistics to describe them. Greenwood and Williamson’s [3] seminal work first set the foundation for the statistical-based modeling of rough surface contact. In their work the height of a surface, z , is described by a Gaussian distribution as

$$\phi = (2\pi)^{-1/2} \left(\frac{\sigma}{\sigma_s} \right) \exp \left[-0.5 \left(\frac{z}{\sigma_s} \right)^2 \right] \quad (3.75)$$

where σ is the root mean squared (RMS) roughness of the surface, also commonly referred to as the standard deviation, and σ_s is the RMS roughness of just the peaks or asperities on the surface, since the asperities are what will come into contact when a rough surface is pressed against another surface. Now, consider that if one wishes to calculate the number of asperities that are taller than a height, d , one would solve the integral:

$$N(d) = \eta A_n \int_d^{\infty} \phi(z) dz \quad (3.76)$$

Now, consider if an opposing surface was a distance, d , away from the rough surface. Then, the peaks that are above this height would actually be in contact with the opposing surface. Therefore, to predict the area of contact between the surfaces, one would sum the individual areas of each asperity. This can be accomplished with the statistical model using the equation below provided by Greenwood and Williamson [3]:

$$A(d) = \eta A_n \int_d^{\infty} \bar{A}(z-d)\phi(z)dz \quad (3.77)$$

Similarly, the total contact force can be calculated by

$$P(d) = \eta A_n \int_d^{\infty} \bar{P}(z-d)\phi(z)dz \quad (3.78)$$

but note that this model neglects the lateral interactions between asperities. In the original Greenwood and Williamson model, the radius of curvature for all of the asperities was assumed to be constant, but later, Bush et al. [52] and Whitehouse and Archard [60] alleviated that assumption. Nonetheless, for simplicity this assumption was still adopted by many subsequent works. The individual asperity contact areas, \bar{A} , and asperity force, \bar{P} , can be predicted by many of the models discussed earlier in this chapter (see (3.9), (3.10), (3.17), and (3.18)), and many works have examined the effects of various asperity models, height distributions, the effect of lateral asperity surface interaction, a deformable substrate, etc. [9, 61–70]. However, in the original work by Greenwood and Williamson [3], the asperities were assumed to always remain elastic so that Hertz contact could be used. For many years, the model was only used by numerically integrating the equations or simplifying the distribution. However, very recently an analytical solution was found and is given as [71]

$$\frac{P}{A_n E'} = \beta \left(\frac{\sigma}{R}\right)^{1/2} J_p \quad (3.79)$$

$$\frac{A_r}{A_n} = \pi \beta \cdot J_a \quad (3.80)$$

$$J_a = \sqrt{\frac{1}{2\pi}} \sigma_s^* e^{-\alpha^2/2} - \frac{d^*}{2} \operatorname{erfc}\left(\frac{\alpha}{\sqrt{2}}\right) \quad (3.81)$$

for $d^* > 0$

$$J_p = \frac{\sigma_s^*}{4} \sqrt{\frac{d^*}{\pi}} e^{-\alpha^2/4} [(1 + \alpha^2)K_{1/4}(-\alpha^2/4) - \alpha^2 K_{3/4}(-\alpha^2/4)]$$

for $d^* = 0$

$$J_p = \frac{\Gamma(5/4)}{\sqrt{\pi}2^{1/4}} (\sigma_s^*)^{3/2}$$

for $d^* < 0$

$$J_p = \frac{s^*}{4} \times \sqrt{\frac{d^*}{2}} e^{2/4} [(1 + ^2)I_{1/4}(2/4) + (3 + ^2)I_{1/4}(2/4) + ^2(I_{3/4}(2/4) + I_{5/4}(2/4))] \tag{3.82}$$

where $\Gamma(\cdot)$ is the Gamma function, $I(\cdot)$ and $K(\cdot)$ are the modified Bessel functions of the first and second kinds, respectively, and $erfc(\cdot)$ is the complementary error function. Also note that “*” denotes a length normalized by σ_s , and the equations use the definitions $\beta = \eta\sigma R$, $d^* = h^* - y_s^*$, and $\alpha = d^*/\sigma_s^*$. In order to practically implement the Greenwood and Williamson model and other statistically based rough surface contact models, one must obtain the statistical parameters for the contacting surfaces. McCool [72] provides a widely used spectral moment-based approach. First, the spectral moments are calculated by

$$m_2 = \frac{1}{N} \sum_{n=1}^N \left(\frac{dz}{dx}\right)_n^2 \tag{3.83}$$

$$m_4 = \frac{1}{N} \sum_{n=1}^N \left(\frac{d^2z}{dx^2}\right)_n^2 \tag{3.84}$$

and m_0 is merely the mean squared roughness (σ^2). For discrete rough surface data, (3.83) and (3.84) can be calculated using the finite difference method. For two rough surfaces in contact, the spectral moment of each surface is added together to give the equivalent spectral moment used to calculate the statistical parameters. As an example, for two identical surfaces the spectral moments would merely be doubled. Then, the other required statistical quantities can be easily calculated as

$$\eta = \frac{m_4}{6\sqrt{3}\pi \cdot m_2} \tag{3.85}$$

$$R = 0.375 \cdot \left(\frac{\pi}{m_4}\right)^{0.5} \tag{3.86}$$

$$\sigma_s^2 = \sigma^2 - \frac{3.717 \cdot 10^{-4}}{\eta^2 R^2} \tag{3.87}$$

and from Front [73]

$$y_s = \frac{0.045944}{\eta R} \quad (3.88)$$

Greenwood and Williamson [3] also knew that the stresses in the asperities could be very high and therefore they are very likely deforming in the elastic–plastic range. To quantify the relative amount of the plastic deformation between contacting surfaces, they derived the dimensionless plasticity index given by

$$\psi = \sqrt{\frac{\sigma_s}{\omega_c}} \quad (3.89)$$

Recall that ω_c is the critical interference in spherical contact given by (3.11). One then uses the average radius of the asperities on the surface (3.86). The plasticity index can vary over several orders of magnitude. The meaning of ψ is qualitative, and higher values signify relatively more plastic deformation of the contacting asperities. Generally, it shows that plastic deformation increases with roughness and decreases with yield strength. Note that the amount of plastic deformation also depends on the force pressing the surfaces together. The transition from the elastic to elastic–plastic regime of rough surface contact is said to occur at approximately $\psi=1$. A similar prediction of the plasticity index was derived using the multiscale stacked asperity contact model that is discussed next. If a high plasticity index is calculated, it is recommended that a rough surface contact model that considers plastic deformation is used, such as by including the elastic–plastic asperity models in (3.17), (3.18), (3.19), (3.20), and (3.21) or by using the elastic–plastic multiscale models described next.

3.2 Multiscale-Based Models

Initiated from Archard’s theory [1] many years ago, recently, the multiscale modeling technique has become more popular [21, 56, 74–79]. Archard suggested that the asperities of rough surfaces must be modeled as “protuberance upon protuberance.” However, Archard first used spheres to model the scales of asperities or protuberances, which is difficult to relate to actual surfaces. To some extent, sinusoidal contact may be a more realistic depiction of surface asperity contact, especially at high loads, than spherical contact. A fairly recent multiscale rough surface contact model considering sinusoidal-shaped asperities is described here [21, 78, 79]. In this model, the different scales of asperities on a surface are characterized using a fast Fourier transform (FFT). Since the model needs an iterative numerical algorithm to solve, a simplified version of the model is then proposed which assumes that the real contact pressure is proportional to the maximum ratio of the amplitude to the wavelength for the surface acquired from FFT.

The full iterative version of the model also has the assumptions:

1. Asperities are arranged so that asperities of smaller cross-sectional surface area are located on top of larger asperities.
2. Each scale of asperities carries the same total load (i.e., the scales are in a mechanical series).
3. The load is divided equally among all the asperities at each scale (i.e., in mechanical parallel).
4. At each scale, the asperities deform according to a chosen contact model irrespectively of any smaller scales.

Using these assumptions and Archard's stacked asperity concept, the following equations are derived that predict the real area of contact:

$$A_r = \left(\prod_{i=1}^{i_{\max}} \bar{A}_i \eta_i \right) A_n \quad (3.90)$$

$$F = \bar{F}_i \eta_i A_{i-1} \quad (3.91)$$

where A_r is the real area of contact, F is the contact load, and A_n is the nominal contact area. Parameters \bar{A}_i and \bar{F}_i are the single asperity contact area and single asperity contact force at a given scale level, respectively. The subscript i denotes a scale or frequency level and i_{\max} denotes the highest frequency level considered. The area of contact at a given frequency level is denoted by A_i , and η_i is the corresponding areal asperity density. The parameters describing the surface topography (such as Δ and f) are calculated from an FFT performed of the surface profile. Then, the value of η is given by

$$\eta_i = 2f_i^2 \quad (3.92)$$

where f_i denotes the frequency (i.e., the reciprocal of wavelength).

The number of asperities at level i , N_i , is given by

$$N_i = \eta_i A_{i-1} \quad (3.93)$$

Hence, the load on each individual asperity at level i , \bar{F}_i , is given by (note that this is equivalent to (3.91))

$$\bar{F}_i = \frac{F}{N_i} \quad (3.94)$$

Using (3.94), one finds the contact area on each asperity at a given scale. Then, any of the asperity contact models described earlier in this work can be used to find the contact area of each asperity as a function of the force. In this way one could include the effects of elasticity, plasticity, adhesion, sliding, and layered contact. However, since (3.90) and (3.91) must be solved iteratively and can be complicated to code, a closed form version of the multiscale is also provided and described in the following paragraphs.

3.2.1 Elastic Contact

Provided here is a simplified solution of the full multiscale model, which predicts nearly the same trends as the full multiscale model. It first assumes that the surface is constructed from a series of sinusoidal waves, with the small scales of roughness being stacked onto the tips of larger scale asperities. Now, imagine that the average pressure required to flatten the surface within the real area of contact must overcome all the scales of roughness within the real area of contact. This average pressure can easily be calculated from the average pressure needed to flatten a sinusoidal surface as described earlier by (3.25). Since the real area of contact is calculated by the contact force divided by this pressure, we have

$$A_r = \frac{F}{p^*} \quad (3.95)$$

Then, the real contact pressure, P_r , is equal to p^* . p^* is the pressure required to flatten the sine wave on the surface with the maximum asperity aspect ratio (Δ/λ) or B_{max} . Recall that Δ and λ are the amplitude and wavelength of the sinusoidal surfaces, respectively. B_{max} is found from the Fourier transform of a surface and comparing all the amplitude to wavelength ratios over all known scales of the surface. The real area of contact can be obtained then by substituting (3.8) into (3.18) or

$$(A_r)_{elastic} = \frac{F}{\sqrt{2\pi E'} B_{max}} \quad (3.96)$$

which is a very simple and yet effective way to predict the real area of contact. However, this equation does not include the effect of plasticity which is likely to occur in the contact of rough surfaces.

3.2.2 Elastic–Plastic Contact

Consider that for sinusoidal surfaces the critical ratio between the amplitude and wavelength is analytically derived as [79]

$$B_c = \frac{\Delta_c}{\lambda} = \frac{\sqrt{2} S_y}{3\pi E'} e^{3\nu} \quad (3.97)$$

where the smaller yield strength S_y from the surfaces in contact is used. Then, for multiscale rough surface contact, if $B_{max} < B_c$, the contact is elastic contact even for very high loads, and (3.96) should be used. Alternatively, if $B_{max} > B_c$, then a version of the model which considers elastic–plastic deformation should be used. Since this ratio defines the existence of plastic deformation in a rough surface

contact within the multiscale contact framework, an analytically derived multiscale plasticity index is

$$\psi_c = \frac{B_{\max}}{B_c} = \frac{3\pi E'}{\sqrt{2}e^{2/3\nu} \cdot S_y} \left(\frac{\Delta}{\lambda} \right)_{\max} \quad (3.98)$$

Note that when this plasticity index is below unity, no plastic deformation should occur, even when loaded to complete contact (i.e., no gaps between the surfaces).

However, in many cases the plasticity index will be well above unity, and so plasticity must be considered. For multiscale elastic–plastic contact, (3.95) is adjusted to

$$A_r = \frac{F}{P_{ep}^*} \quad (3.99)$$

Therefore, to calculate the real area for elastic–plastic multiscale contact, the relatively simple equation next can be used:

$$(A_r)_{\text{elastic-plastic}} = \frac{F}{\sqrt{2}\pi E' B_{\max}} \left(\frac{\frac{12\pi E'}{\sqrt{2}S_y e^{3\nu}} B_{\max} + 7}{11} \right) \quad (3.100)$$

Just as (3.96) can easily be used for elastic contact, (3.100) can easily be implemented to make a prediction of the real area of contact for rough surfaces in contact and deforming in the elastic–plastic regime. These closed form versions of the multiscale contact model are plotted in Fig. 3.19 as a function of B_{\max} and the real contact pressure normalized by the yield strength. The initiation of plastic deformation as predicted by (3.97) is shown by a red line at $P_r/S_y = 0.83$ for a Poisson's ratio of $\nu = 0.33$. This threshold is found by simply substituting the critical amplitude, B_c , into p^* . Once this threshold is crossed, the pressure continues to increase with B_{\max} , but at a more gradual slope. Nonetheless, the P_r/S_y continues to rise well past the ratio of 3, which for many years was considered the maximum obtainable pressure in the contact of rough surfaces. It is clear that the pressure can rise far past that, even in the typical range of engineering surfaces (also shown in Fig. 3.19).

Actually, this increase in the real contact pressure well past the traditional limit of $3 \cdot S_y$ is also observed in a few papers which observe what is coined as “asperity persistence.” The asperity persistence is the measured ability of asperities to resist flattening even at very high pressures. As shown in the works by Childs [80], Uppal and Probert [81], Demkin and Izmailov [82], and Pullen and Williamson [83], the real contact pressure was sometimes measured to be as high as $6\text{--}10 \cdot S_y$ for aluminum surfaces of $2.25 \mu\text{m}$ to $6 \mu\text{m}$ in average roughness. Since the original surface data from these works was not readily available, this analysis is based solely on the limited data in Table 3.2. From the typical proportions shown in Table 3.2, the

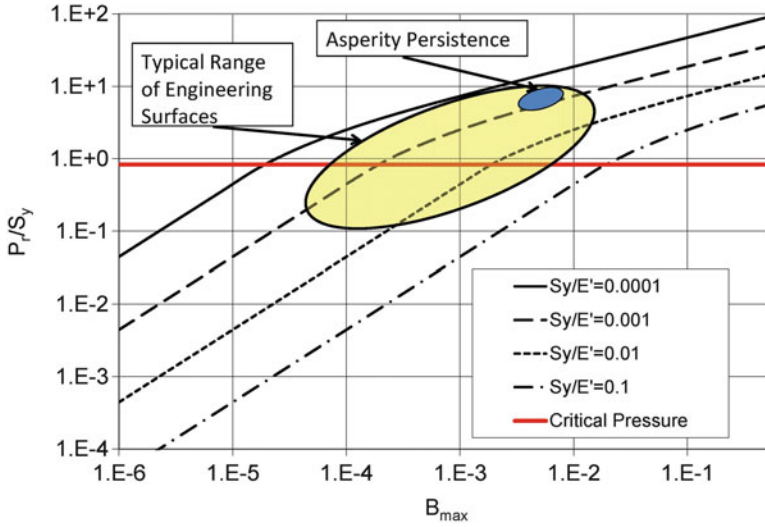


Fig. 3.19 The real contact pressure as predicted by the multiscale rough surface contact model

Table 3.2 Example roughness values and B_{max} values for four surfaces

Surface	R_q (μm)	B_{ave}	B_{max}
1	0.24	0.000257	0.000818
2	0.34	0.000181	0.00215
3	1.05	0.000525	0.00574
4	5.82	0.00182	0.00951

B_{max} values of these surfaces might be approximated as 0.006 (2.25 μm) and 0.01 (6 μm). Assuming aluminum to have approximate material properties of $S_y/E'=0.001$, it appears that the current model predicts the value of P_r/S_y for these two surfaces to be at $6\text{--}10 \cdot S_y$, as shown in Fig. 3.19.

It is more difficult to predict the surface separation between rough surfaces using the multiscale model approach. However, Wilson et al. [78] did show that reasonable predictions could be made by simply summing the deformed height of each scale in contact or

$$d = \sum_{i=1}^{i_{max}} (\bar{\delta})_i \tag{3.101}$$

where $\bar{\delta}$ is the deformed height of each asperity scale. Wilson et al. [78] and Johnson et al. [84] provide models to predict the surface separation for the contact of elastically deforming sinusoids. If one wishes to consider the contact of two identical surfaces, then the contact between them would be an axis of symmetry, and therefore, the surface separation will be the double of that predicted by (3.101). The multiscale model predicts that the surfaces will not come into significant contact

until they are in much closer proximity than the statistical models. Likewise, once the surfaces are in contact, the multiscale model predicts that the pressure will increase much more quickly as the surface separation decreases (i.e., the contact stiffness is much higher). This finding agrees with findings by Drinkwater et al. [85] who made measurements of the contact stiffness using acoustic methods.

3.3 *Scale-Dependent Properties*

When rough surfaces come into contact, the asperity contacts can be very small, even on the atomic scale. It is now well known that material properties can change significantly with scale so that the bulk properties of a material are different than the properties at the scale of contacting asperities. For instance, the yield strength of bulk materials is usually much smaller than the yield strength of nanoscale pillars [86] or nanowires [87]. One mechanism for this effect in metals is that as you reduce the scale, you may go below the scale of features such as grains and reach a state where the material is a stronger single lattice of atoms. Other material properties such as electrical and thermal conductivity can also change with scale. The scale-dependent properties can be included in the models of rough surface contact above as shown in these published works [88–90]. Recent works have also shown that even continuum-based models, if used in conjunction with an accurate material property model can on average accurately capture nanoscale contact mechanisms [91].

4 Conclusions

Contact mechanics is clearly an important and useful part of tribology and general science and engineering. It can help to predict the life and eventual failure on such components as bearings, gears, and wheels. It can also be used to model the contact between rough surfaces and then illuminate the mechanisms governing friction, wear, surface fatigue, and contact resistance. It can be a powerful tool but should still be used with caution, because predictions can often provide qualitatively accurate predictions but have significant quantitative error, especially when considering the contact of rough surfaces. Models exist not only to consider the normal contact of spheres and other geometries but also can include tangential loading, adhesion, and surface layers.

References

1. Archard JF (1957) Elastic deformation and the laws of friction. Proc R Soc Lond A 243:190–205
2. Tabor D (1951) The hardness of materials. Clarendon, Oxford

3. Greenwood JA, Williamson JBP (1966) Contact of nominally flat surfaces. *Proc R Soc Lond A* 295(1442):300–319
4. Johnson KL (1985) *Contact mechanics*. Cambridge University Press, New York
5. Johnson KL (1982) One hundred years of hertz contact. *Proc Inst Mech Eng* 196(1):363–378
6. Hamrock BJ (1994) *Fundamentals of fluid film lubrication*. McGraw-Hill, Inc., New York
7. Green I (2005) Poisson ratio effects and critical values in spherical and cylindrical Hertzian contacts. *Int J Appl Mech Eng* 10(3):451–462
8. Vijaywargiya R, Green I (2007) A finite element study of the deformation, forces, stress formation, and energy loss in sliding cylindrical contacts. *Int J Non-Linear Mech* 42:914–927
9. Chang WR, Etsion I, Bogy DB (1987) An elastic–plastic model for the contact of rough surfaces. *ASME J Tribol* 109(2):257–263
10. Zhao Y, Maletta DM, Chang L (2000) An asperity microcontact model incorporating the transition from elastic deformation to fully plastic flow. *ASME J Tribol* 122(1):86–93
11. Kogut L, Etsion I (2002) Elastic–plastic contact analysis of a sphere and a rigid flat. *ASME J Appl Mech* 69(5):657–662
12. Jackson RL, Green I (2005) A finite element study of elasto-plastic hemispherical contact. *ASME J Tribol* 127(2):343–354
13. Wadwalkar SS, Jackson RL, Kogut L (2010) A study of the elastic–plastic deformation of heavily deformed spherical contacts. *IMEchE Part J, J Eng Tribol* 224(10):1091–1102
14. Jackson RL, Chusoipin I, Green I (2005) A finite element study of the residual stress and strain formation in spherical contacts. *ASME J Tribol* 127(3):484–493
15. Etsion I, Kligerman Y, Kadin Y (2005) Unloading of an elastic–plastic loaded spherical contact. *Int J Solids Struct* 42(13):3716–3729
16. Quicksall JJ, Jackson RL, Green I (2004) Elasto-plastic hemispherical contact models for various mechanical properties. *IMEchE J Eng Trib Part J* 218(4):313–322
17. Jackson RL, Kogut L (2006) A comparison of flattening and indentation approaches for contact mechanics modeling of single asperity contacts. *ASME J Tribol* 128(1):209–212
18. Kogut L, Komvopoulos K (2004) Analysis of spherical indentation cycle of elastic-perfectly plastic solids. *J Mater Res* 19:3641–3653
19. Westergaard HM (1939) Bearing pressures and cracks. *ASME J Appl Mech* 6:49–53
20. Johnson KL, Greenwood JA, Higginson JG (1985) The contact of elastic regular wavy surfaces. *Int J Mech Sci* 27(6):383–396
21. Jackson RL, Streater JL (2006) A multiscale model for contact between rough surfaces. *Wear* 261(11–12):1337–1347
22. Shah S, Krithivasan V, Jackson RL (2011) An electro-mechanical contact analysis of a three-dimensional sinusoidal surface against a rigid flat. *Wear* 270:914–921
23. Krithivasan V, Jackson RL (2007) An analysis of three-dimensional elasto-plastic sinusoidal contact. *Trib Lett* 27(1):31–43
24. Jackson RL, Krithivasan V, Wilson WE (2008) The pressure to cause complete contact between elastic plastic sinusoidal surfaces. *IMEchE J Eng Trib Part J* 222(7):857–864
25. Chaise T, Nélias D, Sadeghi F (2011) On the effect of isotropic hardening on the coefficient of restitution for single or repeated impacts using a semi-analytical method. *Tribol Trans* 54(5):714–722
26. Israelachvili JN (1991) *Intermolecular and surface forces*, 2nd edn. Academic, San Diego, CA
27. Johnson KL, Kendall K, Roberts AD (1971) Surface energy and the contact of elastic solids. *Proc Roy Soc Lond Ser A (Math Phys Sci)* 324(1558):301–313
28. Bradley R (1932) The cohesive force between solid surfaces and the surface energy of solids. *Phil Mag Ser 7* 13(86):853–862
29. Derjaguin BV, Muller VM, Toporov YP (1975) Effect of contact deformations on adhesion of particles. *J Colloid Interface Sci* 53(2):314–326
30. Muller VM, Derjaguin BV, Toporov YP (1983) On two methods of calculation of the force of sticking of an elastic sphere to a rigid plane. *Colloids Surf* 7(3):251–259
31. Tabor D (1977) Surface forces and surface interactions. *J Colloid Interface Sci* 58(1):2–13

32. Maugis D (1992) Adhesion of spheres: the JKR-DMT transition using a dugdale model. *J Colloid Interface Sci* 150(1):243
33. Carpick RW, Ogletree DF, Salmeron M (1999) A general equation for fitting contact area and friction vs load measurements. *J Colloid Interface Sci* 211:395–400
34. Fuller KNG, Tabor D (1975) The effect of surface roughness on the adhesion of elastic solids. *Proc R Soc Lond A Math Phys Sci* 345:327–342
35. Liu SB et al (2005) An extension of the Hertz theory for three-dimensional coated bodies. *Tribol Lett* 18(3):303–314
36. Gittus J (1975) *Creep Viscoelasticity and creep fracture in solids*, Applied Science Publishers, London
37. Goedecke A, Jackson RL, Mock R (2010) Asperity creep under constant force boundary conditions. *Wear* 268(11):1285–1294
38. Brot C, Etsion I, Kligerman Y (2008) A contact model for a creeping sphere and a rigid flat. *Wear* 265(5):598–605
39. Tomlins P (1996) Comparison of different functions for modelling the creep and physical ageing effects in plastics. *Polymer* 37(17):3907–3913
40. Garofalo F (1965) *Fundamentals of creep and creep-rupture in metals*. Macmillan, New York
41. Goedecke A, Mock R (2009) Creep relaxation of an elastic-perfectly plastic hemisphere in fully plastic contact. *ASME J Tribol* 131:021407
42. Brot CC, Etsion I, Kligerman Y (2008) A contact model for a creeping sphere and a rigid flat. *Wear* 265(5–6):598–605
43. Persson B (2000) Theory of time-dependent plastic deformation in disordered solids. *Phys Rev B* 61(9):5949
44. Cattaneo C (1938) Sul contatto di due corpo elastici. *Atti Accad Naz Lincei Cl Sci Fis Mat Nat Rend* 27:342–348, 434–436, 474–478
45. Etsion I (2010) Revisiting the Cattaneo–Mindlin concept of interfacial slip in tangentially loaded compliant bodies. *ASME J Tribol* 132(2):020801, 9 pages
46. Mindlin RD, Deresiewicz H (1953) Elastic spheres in contact under varying oblique forces. *ASME Trans J Appl Mech* 20:327–344
47. Chang WR, Etsion I, Bogy DB (1988) Static friction coefficient model for metallic rough surfaces. *ASME J Tribol* 110(1):57–63
48. Brizmer V, Kligerman Y, Etsion I (2007) Elastic–plastic spherical contact under combined normal and tangential loading in full stick. *Tribol Lett* 25(1):61–70
49. Jackson RL et al (2007) An analysis of elasto-plastic sliding spherical asperity interaction. *Wear* 262(1–2):210–219
50. Boucly V, Nelias D, Green I (2007) Modeling of the rolling and sliding contact between two asperities. *J Tribol-Trans ASME* 129(2):235–245
51. Mulvihill DM et al (2011) An elastic–plastic asperity interaction model for sliding friction. *Tribol Int* 44(12):1679–1694
52. Bush AW, Gibson RD, Thomas TR (1975) The elastic contact of rough surfaces. *Wear* 35:87–111
53. Dwyer-Joyce RS, Reddyhoff T, Zhu J (2011) Ultrasonic measurement for film thickness and solid contact in elasto-hydrodynamic lubrication. *ASME J Tribol* 133(3):031501
54. McBride JW, Cross KC (2008) An experimental investigation of the contact area between a glass plane and both metallic and carbon-nano-tube electrical contacts in proceedings of the 54th IEEE Holm conference on electrical contacts. Orlando, FL
55. Kotake S et al (2008) Evaluation of electrical contact area between metal and semiconductor using photo-induced current. *Tribol Int* 41(1):44–48
56. Jackson RL, Ghaednia H, Yasser AE, Bhavnani S, Knight R (2012) A closed-form multiscale thermal contact resistance model, components, packaging and manufacturing technology. *IEEE Trans* 2(7):1158–1171
57. Sainsot P, Jacq C, Nelias D (2002) A numerical model for elastoplastic rough contact. *Comput Model Eng Sci* 3(4):497–506

58. Wang F et al. (2009) A multi-Scale model for the simulation and analysis of elasto-plastic contact of real machined surfaces. *ASME J Tribol* 131:021409-1-6
59. Stanley HM, Kato T (1997) FFT-based method for rough surface contact. *J Tribol Trans ASME* 119(3):481-485
60. Whitehouse DJ, Archard JF (1970) The properties of random surfaces of significance in their contact. *Proc R Soc Lond A* 316:97-121
61. Jackson RL, Green I (2003) A statistical model of elasto-plastic asperity contact between rough surfaces in proceedings of the ASME/STLE international tribology conference. Preprint 2003-TRIB102
62. Polycarpou A, Etsion I (1999) Analytical approximations in modeling contacting rough surfaces. *ASME J Tribol* 121(2):234-239
63. Yu N, Polycarpou AA (2004) Combining and contacting of two rough surfaces with asymmetric distribution of asperity heights. *J Tribol Trans ASME* 126(2):225
64. Kogut L, Etsion I (2003) A finite element based elastic-plastic model for the contact of rough surfaces. *Tribol Trans* 46(3):383-390
65. Greenwood JA, Tripp JH (1971) The contact of two nominally flat rough surfaces. *Proc Instn Mech Engrs Part J* 185:625-633
66. Ciavarella M, Delfino G, Demelio G (2006) A "re-vitalized" greenwood and williamson model of elastic contact between fractal surfaces. *J Mech Phys Solids* 54(12):2569-2591
67. Greenwood JA (2006) A simplified elliptical model of rough surface contact. *Wear* 261(2):191-200
68. McCool JI (1986) Comparison of models for the contact of rough surfaces. *Wear* 107(1):37-60
69. Mikic B (1971) Analytical studies of contact of nominally flat surfaces; effect of previous loading. *J Lubr Technol Trans ASME* 93(4):451-456
70. Sepehri A, Farhang K (2009) Closed-form equations for three dimensional elastic-plastic contact of nominally flat rough surfaces. *J Tribol Trans ASME* 131(4):041402-1-8
71. Jackson RL, Green I (2011) On the modeling of elastic contact between rough surfaces. *Tribol Trans* 54(2):300-314
72. McCool JI (1987) Relating profile instrument measurements to the functional performance of rough surfaces. *ASME J Tribol* 109(2):264-270
73. Front I (1990) The effects of closing force and surface. Roughness on leakage in radial face seals, MS Thesis, Technion, Israel Institute of Technology
74. Ciavarella M, Demelio G (2001) Elastic multiscale contact of rough surfaces: Archard's model revisited and comparisons with modern fractal models. *J Appl Mech* 68(3):496-498
75. Ciavarella M et al (2000) Linear elastic contact of the Weierstrass profile. *Proc R Soc Lond A* 456:387-405
76. Ciavarella M, Murolo G, Demelio G (2006) On the elastic contact of rough surfaces: numerical experiments and comparisons with recent theories. *Wear* 261(10):1102-1113
77. Almeida L et al (2007) Laterally actuated multicontact MEMS relay fabricated using MetalMUMPS process: experimental characterization and multiscale contact modeling. *J Micro/Nanolith MEMS MOEMS* 6(2):023009
78. Wilson WE, Angadi SV, Jackson RL (2010) Surface separation and contact resistance considering sinusoidal elastic-plastic multi-scale rough surface contact. *Wear* 268(1-2):190-201
79. Jackson RL (2010) An analytical solution to an Archard-type fractal rough surface contact model. *Tribol Trans* 53(4):543-553
80. Childs THC (1977) The persistence of roughness between surfaces in static contact. *Proc R Soc Lond A* 353(1672):35-53
81. Uppal AH, Probert SD (1973) Plastic contact between a rough and a flat surface. *Wear* 23(2):173-184
82. Demkin NB, Izmailov VV (1975) Plastic contact under high normal pressure. *Wear* 31(2):391-402
83. Pullen J, Williamson JBP (1972) On the plastic contact of rough surfaces. *Proc R Soc Lond A* 327(1569):159-173

84. Johnson KL, Greenwood JA, Higginson JG (1985) The contact of elastic regular wavy surfaces. *Int J Mech Sci* 27(6):383–396
85. Drinkwater BW, Dwyer-Joyce RS, Cawley P (1996) A study of the interaction between ultrasound and a partially contacting solid—solid interface. in mathematical, physical and engineering sciences. The Royal Society
86. Greer JR, Nix WD (2005) Size dependence of mechanical properties of gold at the sub-micron scale. *Appl Phys A: Mater Sci Process* 80(8):1625–1629
87. Hyde B, Espinosa HD, Farkas D (2005) An atomistic investigation of elastic and plastic properties of Au nanowires. *J Minerals Metals Mater* 57(9):62–66
88. Almeida L et al (2006) Study of the electrical contact resistance of multi-contact MEMS relays fabricated using the MetalMUMPs process. *J Micromech Microeng* 16(7):1189–1194
89. Jackson RL (2006) The effect of scale dependant hardness on elasto-plastic asperity contact between rough surfaces. *STLE Tribol Trans* 49(2):135–150
90. Jackson RL, Bhavnani SH, Ferguson TP (2006) A multi-scale model of thermal contact resistance between rough surfaces (IMECE2006-15277). In ASME international mechanical engineering congress and exposition. Chicago, IL
91. Wang H et al (2010) Nanoindentation modeling of a nanodot-patterned surface on a deformable substrate. *Int J Solids Struct* 47(22–23):3203–3213

Exercises

1. If a spherical shaped surface and a sinusoidal or wavy shaped surface with identical material properties are both brought into contact with a flat surface, and the contact force is continually increased, which shape will ultimately have the highest contact pressure.

For a sphere with the following properties, determine if the sphere will yield. Also determine the critical interference which will initiate yielding.

2. A person throws a bowling ball in the air and it lands with a force of 1 kN on the wooden lane. Assume that the bowling ball (diameter = 21.6 cm) properties are $E = 300$ GPa, $\nu = 0.4$ and the wood lane $E = 1$ GPa, and $\nu = 0.25$. Find the maximum real area of contact and estimate the combined maximum deflection (interference) of the ball and wood during contact.
3. Determine the maximum von Mises stress for a loaded sphere at $z = 0.48a$. Solve these equations and then estimate if the sphere will yield if it has the following properties:

$$R = 100 \mu\text{m}, E = 100 \text{ GPa}, \nu = 0.33, S_y = 0.5 \text{ GPa}, \text{ and the load is } 1 \text{ N}.$$

4. Solve the Greenwood and Williamson model using the assumption in class that

$$\varphi(z) = \frac{2}{\sigma_s} \exp\left(-\frac{2}{\sigma_s} z\right)$$

If the surface parameters are given as ($\eta = 10^{11}/\text{m}^2$, $R = 20 \mu\text{m}$, $\sigma = 0.2 \mu\text{m}$, $E = 200 \text{ GPa}$, $\nu = 0.33$, $S_y = 0.5 \text{ GPa}$), plot the curves of A_r/A_n versus d , $W/E/A_n$

Table 3.3 The MTH model parameters for different polymers

Material	C_2	C_3	E [Mpa]
PTFE	2	0.211	420
Delrin	1.101	0.278	3,100
Bakelite	1.695	0.232	2,500
Nylon-6	1.266	0.338	3,600
Polypropylene	1.607	0.173	1,520

versus d , and A_r/A_n versus $F/E/A_n$. Compare these results to results obtained from the model by Green (2002) for the same surface parameters.

- Assuming the material properties of a typical steel ($E = 200$ GPa, $\nu = 0.33$, $S_y = 0.5$ GPa, $\rho = 7,850$ kg/m³), find the smallest size sphere that will not deform *plastically* under its own weight when set on a rigid flat surface.
- Calculate the radius of contact under no applied load (a_0), based on the JKR model.
- Calculate the radius of contact right before separation (a_s) and write a_s as a function of a_0 (see problem 6).
- Considering the creep process of the polymer Delrin in contact with a rigid flat surface, calculate the creep displacement and contact area of the single asperity of this polymer after 350 min under a constant force.

We know that after 600 min the creep displacement of the single asperity is 8 μ m. You can use the parameters in Table 3.3 for required information.

- In a compression testing, a soft metal sample would be flattening against rigid flat surface (sapphire). The mechanical properties of the sample are as below: $E_1 = 12.74$ GPa, $E_2 = 345$ GPa, $\nu_1 = 0.4498$, $\nu_2 = 0.29$, $S_y = 1.4$ Mpa, E_1 , E_2 , ν_1 , ν_2 are the elastic moduli and Poisson's ratios of the sample and sapphire, respectively. S_y is the yield strength of the sample. The max value of ratio amplitude/wavelength is $B_{max} = 0.0011$. Please calculate the real area when load $F = 300$ N is applied.

Solutions

- The pressure in a sinusoidal contact should increase past that of a spherical contact under heavy loads. Since the boundary conditions at the base of these geometries are different, the sphere will become a pillar and the sinusoidal surface will become two flat surfaces in contact.
- The effective radius and elastic modulus for the contact is calculated as

$$E' = \left(\frac{1 - \nu_1^2}{E_1} + \frac{1 - \nu_2^2}{E_2} \right)^{-1} = 1.06 \text{ GPa}$$

$$\frac{1}{R} = \frac{1}{R_1} + \frac{1}{R_2} = 0.108 \text{ m}$$

From $F = \frac{4}{3} E' \sqrt{R}(\omega)^{3/2}$, the interference is 0.000167 m.

From $A = \pi R \omega = \pi a^2$, the contact radius is 0.00424 m.

3. Use the following equations provided earlier in the book to predict the critical contact force and interference:

$$C = 1.295 \exp(0.736v)$$

$$C = 1.651$$

$$\begin{aligned} P_c &= \frac{4}{3} \left(\frac{R}{E} \right)^2 \left(\frac{C}{2} \pi \cdot S_y \right)^3 \\ &= \frac{4}{3} \left(\frac{100 \cdot 10^{-6} m}{112 \cdot 10^9 N/m^2} \right)^2 \left(\frac{1.651}{2} \pi \cdot 500 \cdot 10^6 N/m^2 \right)^3 = 0.0023 N \end{aligned}$$

Clearly, the applied for 1 N is much larger than the critical force, and therefore, the sphere will yield. In addition,

$$\omega_c = \left(\frac{\pi \cdot C \cdot S_y}{2E'} \right)^2 R = 0.013 \mu m$$

4. Find the paper by Polycarpou and Etsion for the full derivation. This in itself is good practice.
5. Using the critical force equation given in the text and finding the force by multiplying the volume of the sphere x density x gravitational constant to obtain

$$P_c = \frac{4}{3} \left(\frac{R}{E} \right)^2 \left(\frac{C}{2} \pi \cdot S_y \right)^3 = \frac{4\pi}{3} R^3 \rho g$$

Solving for R,

$$R = \frac{1}{\rho g} \left(\frac{\pi}{E} \right)^2 \left(\frac{C}{2} S_y \right)^3 = 0.186 m$$

6. From the JKR model,

$$a^3 = \frac{R}{E} \left[F + 3\pi R W_{12} + \sqrt{6\pi R W_{12} F + (3\pi R W_{12})^2} \right]$$

Setting $F = 0$ results in

$$a^3 = \frac{R}{E} \left[F + 3\pi R W_{12} + \sqrt{6\pi R W_{12} F + (3\pi R W_{12})^2} \right]$$

$$a = \sqrt[3]{\frac{R}{E} (6\pi RW_{12})}$$

7. Recall that the pull off force is

$$F_s = -3\pi RW_{12}/2$$

Substituting this into the JKR model,

$$a = \sqrt[3]{\frac{R}{E} \left(\frac{3}{2}\pi RW_{12}\right)}$$

8. According to the information given in the problem,

$$\begin{aligned} R &= 1\text{mm} \\ \omega_{cr}(600) &= 8\mu\text{m} \end{aligned}$$

From Table 3.3, for polymer Derlin,

$$\begin{aligned} C_2 &= 1.101, C_3 = 0.278 \\ \omega_{cr}(t) &= 8 \times \left(\frac{350}{600}\right)^{(0.71 \times 0.278 + 0.03)} = 7.077\mu\text{m} \\ A_{cr}(350) &= 1.101 \times \pi \times 1000 \times 8 \times \left(\frac{350}{500}\right)^{0.71 \times 0.278 + 0.03} = 0.02448\text{mm}^2 \end{aligned}$$

9. First, we can calculate effective elastic modulus:

$$E' = \left(\frac{1 - \nu_1^2}{E_1} + \frac{1 - \nu_2^2}{E_2}\right)^{-1} = \left(\frac{1 - 0.4498^2}{12.74 \times 10^9} + \frac{1 - 0.29^2}{345 \times 10^9}\right)^{-1} = 1.5322 \times 10^{10}\text{Pa}$$

Then, critical ratio

$$B_c = \frac{\sqrt{2} S_y}{3\pi E'} e^{\frac{2}{3}\nu} = \frac{\sqrt{2}}{3 \times \pi} \frac{1.4 \times 10^6}{1.5322 \times 10^{10}} \times e^{\frac{2}{3} \times (0.4489)} = 1.8505 \times 10^{-5}$$

Compare to the value of B_{max}

$B_{max} > B_c$, it means elastic-plastic contact.

When $F = 300\text{N}$, the real contact area can be calculated by

$$\begin{aligned}
 (A_r)_{elastic-pastic} &= \frac{F}{\sqrt{2}\pi E' B_{max}} \left(\frac{\frac{12\pi E'}{2} B_{max} + 7}{\frac{2}{3} v_2 \sqrt{2} S_y e}}{11} \right)^{\frac{3}{5}} \\
 &= \frac{300}{\sqrt{2} \times \pi \times 1.5322 \times 10^{10} \times 0.0011} \left(\frac{\frac{12 \times \pi \times 1.5322 \times 10^{10}}{2} \times 0.0011 + 7}{\frac{2}{3} \times 0.4498 \sqrt{2} \times 1.4 \times 10^6 \times e}}{11} \right)^{\frac{3}{5}} \\
 &= 2.5773 \times 10^{-5} m^2
 \end{aligned}$$

Chapter 4

Experimental Methods in Tribology

Nicholas X. Randall

Abstract In order to conduct an accurate tribological investigation of two materials in sliding contact, a dedicated machine or *tribometer* is required which can measure both the friction and wear between the materials. A carefully selected tribometer configuration can be used to simulate all the critical characteristics of a certain specific situation or can be used as a quick way to screen various candidate materials before subjecting them to that situation. This chapter focuses on basic experimental methods as well as the most common test configurations. A good knowledge of tribometers will allow the engineer to choose the most appropriate system to fulfil requirements. Additional knowledge of the environment in which the test should be performed will aid the engineer in simulating true *in-service* conditions which will make the data produced more meaningful. Such conditions (e.g. temperature, humidity, gaseous environment) can then be combined with actual experimental conditions (applied load, sliding speed, contact pressure, etc.) to provide a focused and useful experiment.

1 Fundamentals of Experimental Tribology

Although the fundamentals of tribological testing are beyond the scope of this chapter and more fully covered in other sources [1–3], some basic explanation of the concepts will aid in the understanding of subsequent sections.

Tribology encompasses the study of friction and wear when two materials slide over each other. For two materials in dynamic contact, the coefficient of friction, μ , is defined as the ratio of the tangential force, F_t , and the normal force, F_n , as follows:

N.X. Randall (✉)
CSM Instruments SA, Peseux, Switzerland
e-mail: nra@csm-instruments.com

$$\mu = \frac{F_t}{F_n}$$

The basic laws of friction can be summarized as follows:

1. The tangential force is proportional to the normal load.
2. The tangential force is independent of the apparent area of contact.
3. The tangential force is independent of sliding velocity.

However, it should be noted that such laws are only a guide and have notable exceptions. For example, the first law is well obeyed by most metals and ceramics, but not by polymers which are often in elastic contact and exhibit high viscoelasticity. The third law is applicable once the velocity is high enough to initiate sliding, but the tangential force required to initiate sliding is usually greater than that necessary to maintain sliding. It is therefore common practice to distinguish between the coefficient of static friction, μ_s , and the coefficient of dynamic friction, μ_d . When quoting a friction coefficient value between two materials, one usually refers to the dynamic value.

2 Test Configurations and Equipment

Instrumentation and equipment for tribology testing of materials can be either commercially acquired or built to suit a specific application or a particular in-service condition which is to be simulated. In many cases, a commercially available machine may be adapted relatively easily to various environmental conditions (i.e. liquid sample submersion, heating to body temperature). Some of the most common tribometer test configurations are shown in Fig. 4.1 and have evolved from the need to be able to simulate specific *in-service* conditions which are to be simulated. Tribometers are usually designed for specific wear conditions (e.g. reciprocating sliding) or wear mechanisms (e.g. abrasive wear) and are often ill-suited for experimental conditions which are outside of their intended operating range. Invariably, a tribometer will consist of two or more *wear partners*, where one is usually static and the other(s) is sliding. The applied load between the *static* partner and the *dynamic* partner will usually be applied either by dead weights or by some form of load actuation, and both these systems have advantages and disadvantages. For example, a dead weight system will accurately provide a specific load without any drift or variation, whilst a load actuator can utilize a force-feedback loop which enables a constant load application even when the counterface is rough or has poor flatness. A load actuator is often advantageous when using high speeds and small amplitudes (commonly known as a fretting wear apparatus) as it can better control the load over such short and reversible cycles.

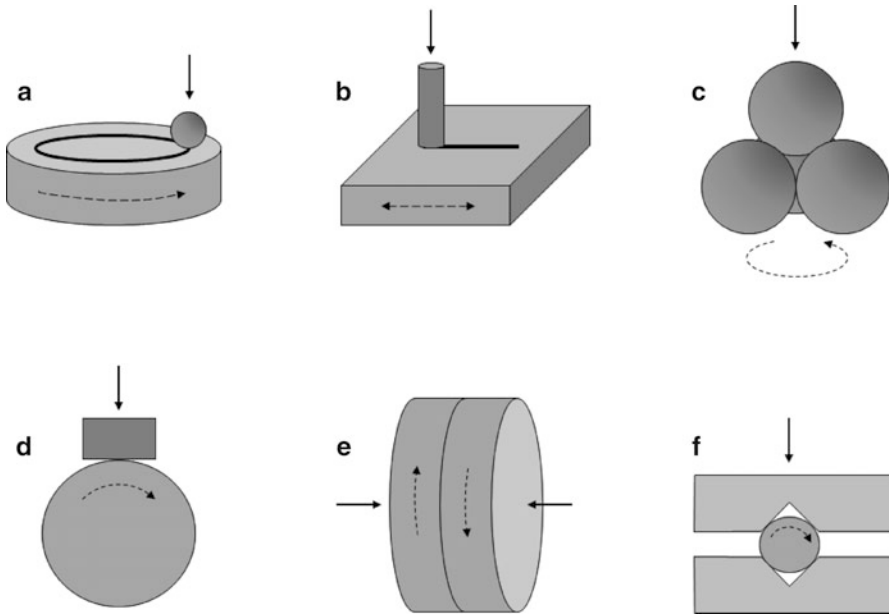


Fig. 4.1 A selection of common tribometer configurations where applied load is denoted by *solid arrows* and motion is denoted by *dotted arrows*; (a) ball-on-disk, (b) reciprocating pin-on-flat, (c) four-ball, (d) block-on-wheel, (e) flat-on-flat, (f) pin and vee-block

2.1 Pin-on-Disk Tribometer

The most commonly used configuration for testing materials is the pin-on-disk method in either rotating or linear-reciprocating modes. The corresponding ASTM standards, G99 [4] and G133 [5], include the measurement of friction coefficient as well as wear rate of the sample and the static partner. The pin-on-disk setup has been used for nearly 50 years for the reproducible measurement of friction and wear [6–12]. The basic principle is shown schematically in Fig. 4.2 and comprises a sample mounted in a chuck which is rotated by a motor. This is the *dynamic partner* of the material pair to be tested. The *static partner* is placed in contact with the sample via an elastic arm, and a dead weight or load cell is used to apply a known load to the contact. A tangential force (sometimes referred to as *friction force*) sensor records the friction between the static and dynamic partners. The static partner can be of any appropriate shape but is usually a flat-ended pin or a ball (the ASTM standards specify a 6 mm diameter ball) depending on the contact configuration desired. The vertically mounted pin has the advantage of a constant contact area throughout the test but has the disadvantage of tending to deviate from perfect alignment to the normal axis under the tangential force produced during the test. The ball has the advantage of a perfectly spherical shape which can be rotated

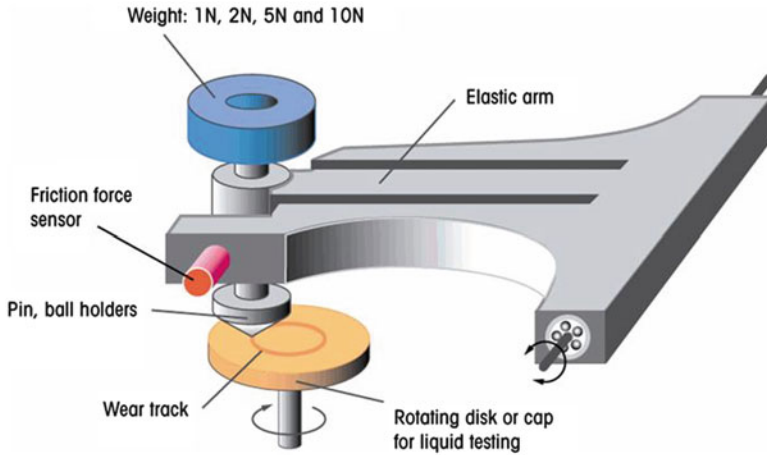


Fig. 4.2 Schematic of the pin-on-disk tribometer

many times so that a fresh area is always used for subsequent tests but has the disadvantage that the contact area will increase as the test progresses.

For some custom applications, both the static and dynamic partners may have specific geometries that simulate a desired condition. For example, when testing prosthetic joint materials, the experimental setup may include a ball (static partner) placed into a conformal cup (dynamic partner) in order to simulate a ball-and-socket configuration.

A typical test might consist of the following steps:

1. Dynamic and static partners mounted and alignment verified.
2. Arm balanced so that dead weight corresponds exactly to desired applied load. Most arms use counterweights to achieve perfect balance.
3. Static partner is brought into contact with sample.
4. Test is commenced and sample begins to rotate at preset speed.
5. Friction signal is recorded as a function of distance, time, or number of laps.

2.1.1 Measurement of Friction Coefficient

An example of a typical friction versus time plot is shown in Fig. 4.3. Most modern instruments will record the raw output of the friction force sensor and will then recalculate the friction coefficient based upon the actual normal load used. Both signals may be recorded. Note in Fig. 4.3 the common *running-in* behaviour as the two surfaces bed into each other, followed by a period of relatively smooth sliding (known as the *steady state*). Such datasets provide two important results:

Steady-state friction coefficient (μ): calculated as the average of the steady-state portion of the trace

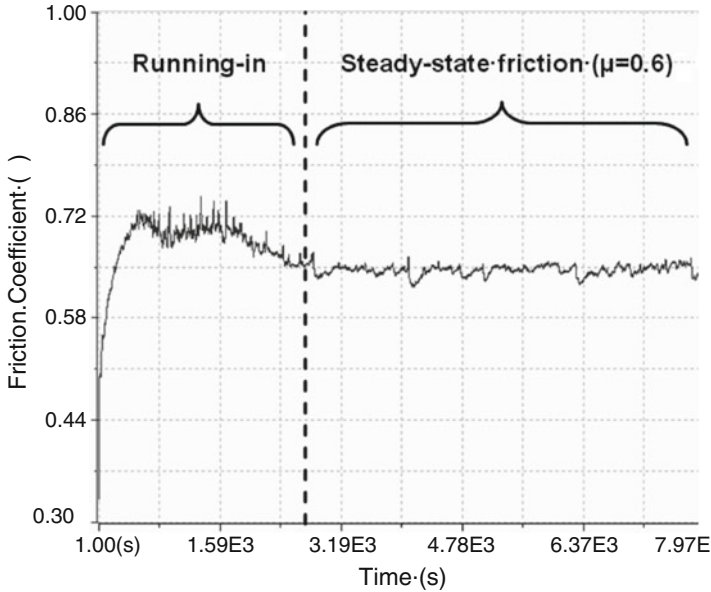


Fig. 4.3 Example of a friction coefficient versus time plot for a steel-on-steel contact

Static friction coefficient: calculated as the maximum value of friction reached during the initial running-in period

It should be noted that the friction coefficient is not a material property but a measured parameter which is highly dependent on the environmental conditions. For example, the coefficient of friction measured during a dry winter day (15 % RH) may be very different to that measured on the same material pair during a humid summer day (85 % RH). For this reason, it is very important to record the exact environmental conditions (temperature and humidity) during which the test was performed.

The duration of the tribology test will depend on whether the user only wants to measure a value of friction coefficient (in which case the test duration will be only up until steady-state conditions are reached) or whether the evolution of wear is of interest. In the latter case, the test duration may be for extended time periods, typically from several hours to several days, depending on the severity of the test conditions. In some cases, the test may be continued until one or both of the material pair are completely destroyed, such a condition being characterized by a very high friction value or even seizure of the contact. The time from test initiation to catastrophic failure may give an idea of the lifetime of the tested material pair and may be used to screen new materials using conditions which accelerate breakdown of the contact.

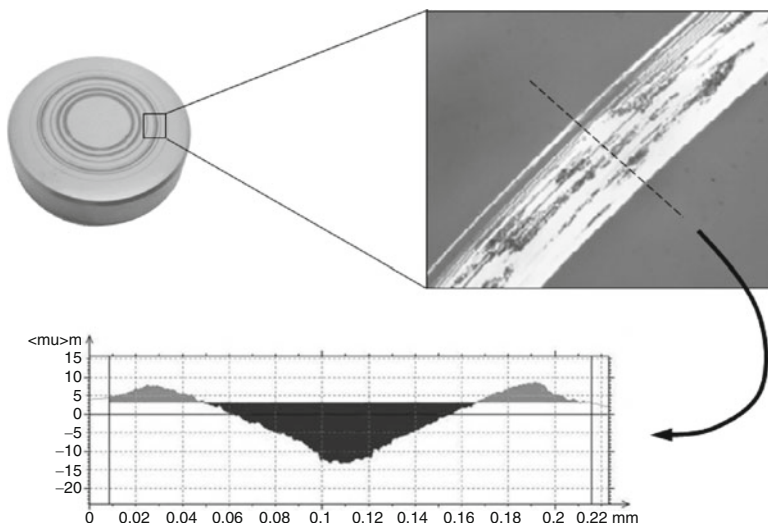


Fig. 4.4 Typical wear track section measured using a stylus profilometer

2.1.2 Measurement of Wear Rate

If sufficient material is removed during the test which is measurable, then the wear rates of both the dynamic and static partners can be calculated. The simplest method is to weigh both partners before and after the test and thus calculate the mass of material removed. However, if the material lost is so small as to be immeasurable using conventional techniques (e.g. high-resolution mass balance), then the amount of material lost must be directly calculated. In the case of the dynamic partner (usually a flat disk), it is relatively easy to measure a profile across the wear track using a profilometer (either stylus or optical), from which the area of the wear track section can be calculated. The volume of material lost is then calculated by multiplying the area by the circumference of the wear track. Figure 4.4 shows a typical example of such a measurement, and it should be noted that at least three profiles are usually measured per wear track and an average value used to calculate volume.

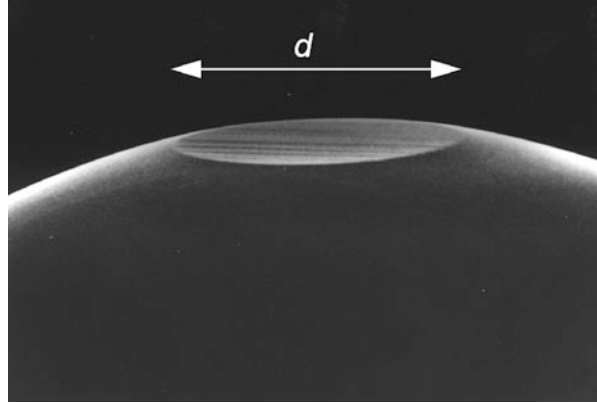
Some tribometer software packages automatically convert the worn track section (μm^2) into a volume loss (μm^3) and a wear rate (in $\text{mm}^3\text{N}^{-1}\text{m}^{-1}$).

The wear rate of the static partner is calculated in the same way but depending on the actual geometry. For a ball, the worn cap diameter can be measured using a calibrated microscope as shown in Fig. 4.5. The height, h , of the worn cap is given by

$$h = R - \sqrt{R^2 - \frac{d^2}{4}}$$

where R is the radius of the ball and d is the diameter of the worn cap.

Fig. 4.5 Worn cap diameter as viewed in a scanning electron microscope (SEM)



The volume, V , of the worn cap is then

$$V = \frac{1}{3} \pi h^2 (3R - h)$$

And the wear rate of the static partner is thus

$$\text{WearRate}_{\text{StaticPartner}} = \frac{V}{L.F_n}$$

where L is the distance travelled during the test and F_n the applied normal load.

When measuring the tribological properties of thin films and coatings, the minimum measurable mass loss is approximately 3 mg, if measured by conventional techniques such as a high-precision mass balance. For most engineering situations where coatings are employed, the actual mass loss may be significantly less than this threshold value. The data in Fig. 4.6 shows mass loss as a function of coating thickness for a range of common coatings where any mass loss below 3 mg must be calculated by the aforementioned indirect methods.

If investigating the evolution of friction and wear over the lifetime of the material pair, it may be interesting to pause the test at various intervals and look at the wear track through a microscope, as shown in Fig. 4.7. Such online analysis permits changes in wear mode to be detected, e.g. transition from abrasive to adhesive wear, and can help in understanding variations in the friction coefficient over the lifetime of the contact.

A summary of a complete dataset is shown in Fig. 4.8 for a ball-on-disk experiment performed in dry conditions. The friction signal has steadily increased over the lifetime of the contact as the debris produced from adhesive wear has created a third-body transfer film which has then, in turn, caused increased wear of both partners. The wear rates of the sample (disk) and the static partner (ball) have been calculated after having entered the worn track section and the worn cap

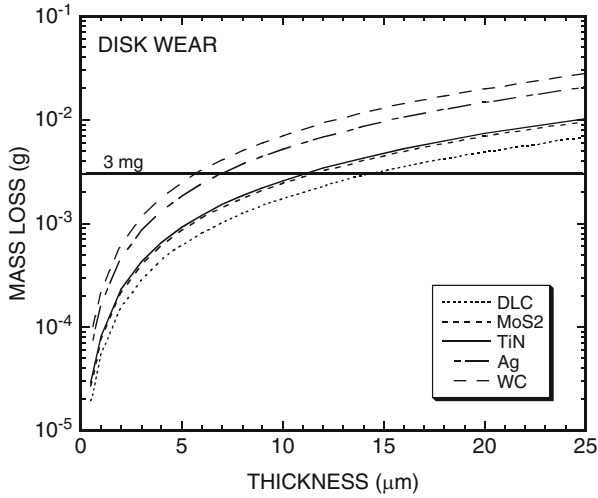


Fig. 4.6 Mass loss versus thickness for a range of coating materials

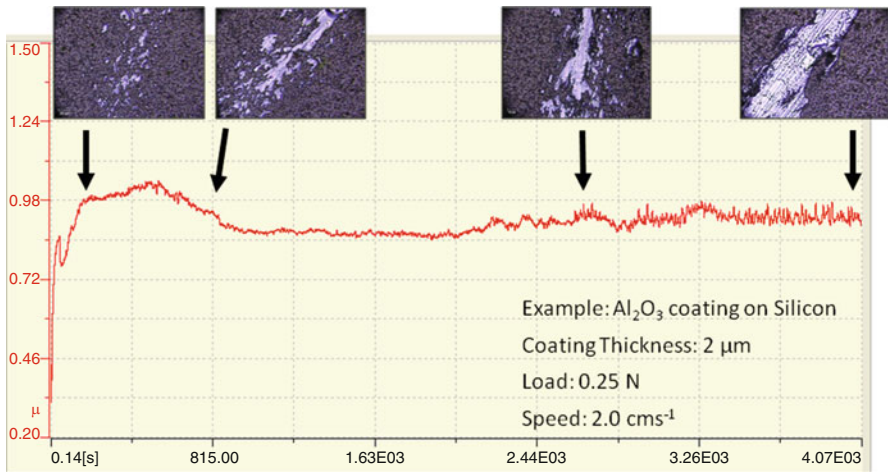


Fig. 4.7 Evolution of wear for an alumina coating in contact with a 100Cr6 steel ball

diameter, respectively. In addition, the maximum stress at the contact has also been calculated and displayed. In many applications, it may be necessary to use a suitable size ball which gives the approximate stress which the components may see in service. This is another advantage of using the ball-on-disk configuration instead of the pin-on-disk where it is much harder to fabricate suitable pins.

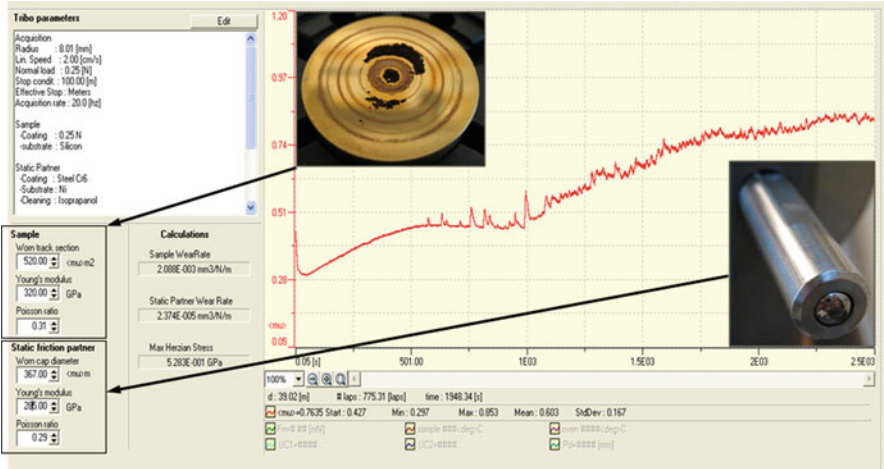


Fig. 4.8 Typical ball-on-disk results window from a commercial tribometer with (inset) images of wear debris produced on the disk and the ball

2.1.3 Tribocorrosion

The term “tribocorrosion” is defined as a material degradation process which is due to the combined effect of corrosion and wear, and it is common to describe the combined process as *corrosion-accelerated wear* or *wear-accelerated corrosion*, depending on how one views the process [13].

Whilst tribocorrosion phenomena may affect many materials, they are most critical for metals, especially the normally corrosion-resistant so-called passive metals. The vast majority of corrosion-resistant metals and alloys used in engineering (stainless steels, titanium, aluminium, etc.) fall into this category. These metals are thermodynamically unstable in the presence of oxygen or water, and they derive their corrosion resistance from the presence at the surface of a thin oxide film, called the *passive film*, which acts as a protective barrier between the metal and its environment [15]. Passive films are usually just a few atomic layers thick. Nevertheless, they can provide excellent corrosion protection because if damaged accidentally they spontaneously self-heal by metal oxidation. However, when a metal surface is subjected to severe rubbing or to a stream of impacting particles, the passive film damage becomes continuous and extensive. The self-healing process may no longer be effective and in addition it requires a high rate of metal oxidation. In other words, the underlying metal will strongly corrode before the protective passive film is reformed, if at all. In such a case, the total material loss due to tribocorrosion will be much higher than the sum of wear and corrosion one would measure in experiments with the same metal where only wear or only corrosion takes place. The example illustrates the fact that the rate of tribocorrosion is not simply the addition of the rate of wear and the rate of corrosion, but it is strongly

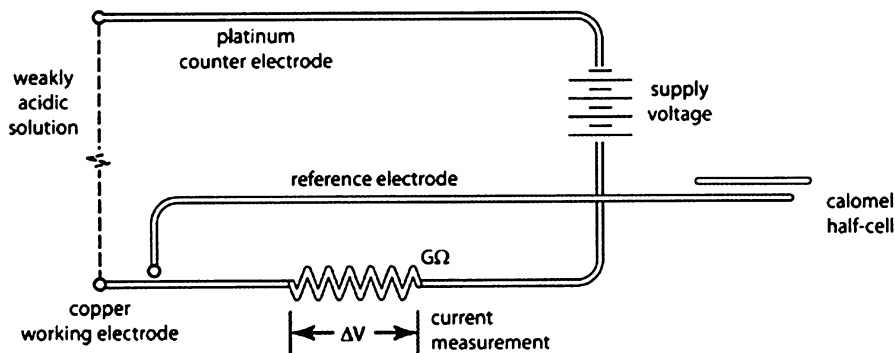


Fig. 4.9 Circuit diagram for a simple tribocorrosion setup

affected by synergistic and antagonistic effects between mechanical and chemical mechanisms. To study such effects in the laboratory, one most often uses mechanical wear testing rigs which are equipped with an electrochemical cell [16]. This permits one to control independently the mechanical and chemical parameters. For example, by imposing a given potential to the rubbing metal, one can simulate the oxidation potential of the environment, and in addition, under certain conditions, the current flow is a measure of the instantaneous corrosion rate. For a deeper understanding, tribocorrosion experiments are often supplemented by detailed microscopic and analytical studies of the contacting surfaces.

In the field of bioengineering, the term “biotribocorrosion” is often used to describe tribological systems exposed to biological environments and has been studied for artificial joint prostheses where an understanding of material degradation processes is key to achieving longer service life for such devices [14].

A practical tribocorrosion setup is shown as a circuit diagram in Fig. 4.9 and includes the following components:

- Sample (disk): this can be the working electrode, or a separate electrode can be placed in the liquid bath.
- Static partner (ball): typically of ceramic (Al_2O_3 or Si_3N_4) in order to be unreactive in a corrosive electrochemical environment.
- Ag/AgCl reference electrode.
- Pt counter electrode (provides stable potential and is corrosion resistant).
- Electrolyte solution (NaCl or body-mimicking fluid).
- Heating coil and thermostat if a stable temperature is required (e.g. body temperature).

Such a setup allows the user to perform wear tests in corrosive environments under well-defined electrochemical conditions and at controlled temperature. The following modes of operation can be used:

Open Circuit Potential (OCP): The free potential is monitored throughout the wear test and indicates changes occurring, e.g. corrosion/passivation of a metal or deterioration of a surface coating characterized by a decrease in the measured OCP.

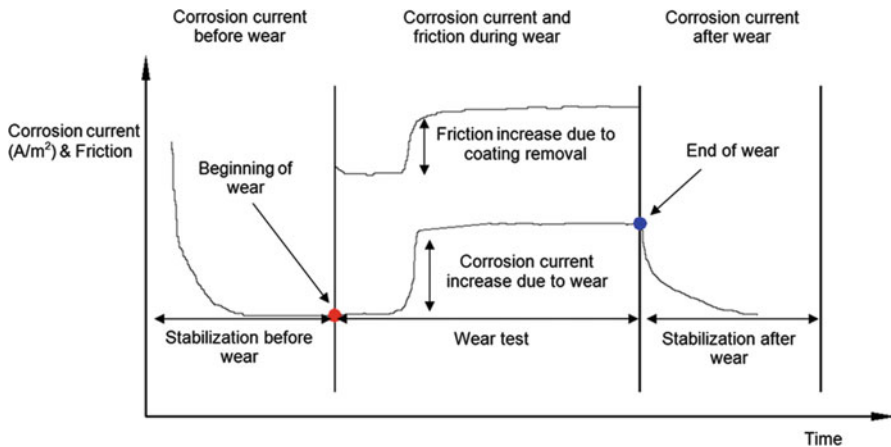


Fig. 4.10 Example of a fixed potential test where the corrosion current is monitored throughout the wear process

Fixed Potential: Also known as potentiostatic wear mode, this involves monitoring the evolution of the corrosion current at different phases in the test whilst maintaining a fixed potential which is chosen to accelerate the corrosion process. An example is shown in Fig. 4.10. This allows investigation of the wear-enhanced corrosion (increased corrosion as a direct result of rubbing) and the repassivation kinetics of the surface. An anodic potential is chosen to accelerate corrosion, whereas a cathodic potential is chosen to protect the surface and therefore isolate only mechanical wear at the interface.

Potential Scan: Also known as potentiodynamic wear mode, this allows the friction coefficient to be monitored as a function of the applied potential.

The synergy between corrosion and wear can be evaluated over wide ranges of both electrochemical and mechanical conditions [17–19]. Experimental setups will depend on the complexity of the system which is to be modelled and the aggressiveness of the electrolyte used [20–22]. An example of a tribocorrosion tribometer is shown in Fig. 4.11.

2.1.4 Electrical Contact Resistance (ECR)

In certain tribological situations, it may be of interest to monitor changes in electrical contact resistance (ECR) over the duration of a friction test. Changes in ECR can be used to detect the onset of failure in thin biomaterials which have been coated onto a conducting substrate (e.g. polymer coatings on heart valves, drug-eluting coatings, and pacemaker device packaging).

A typical ECR experimental arrangement is shown in Fig. 4.12 which enables an open circuit to be created between the static partner and the coated disk, with the coating acting as an insulating electrical barrier. As the static partner wears through

Fig. 4.11 Schematic of a commercial pin-on-disk tribometer modified for tribocorrosion testing with liquid cell and contacts for electrodes

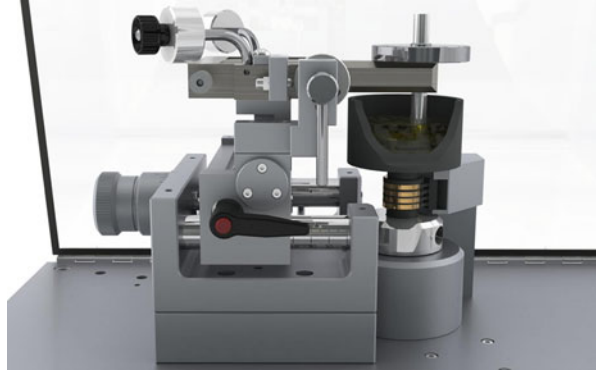
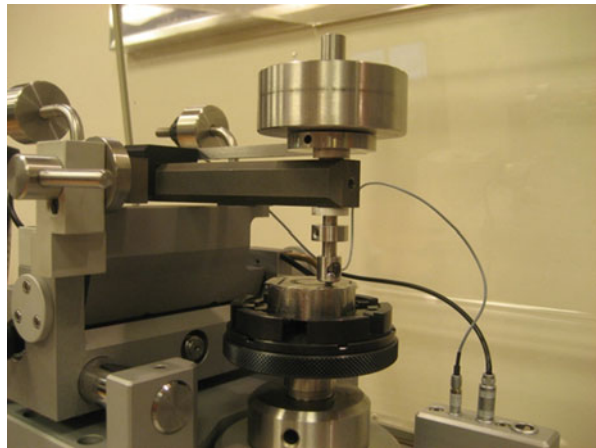


Fig. 4.12 Pin-on-disk tribometer setup for ECR measurement showing the ball holder which is electrically isolated from the system



the coating, changes in the measured resistance can be recorded simultaneously with the friction signal.

In some cases, a measured change in the ECR signal may correspond to a change in the tribological mode, for example, when a transfer film is built up from particles of the static partner mixing sufficiently with material from the insulating coating to cause current to pass. An example of a typical ECR test is shown in Fig. 4.13 for a polypropylene coating deposited on a polished steel substrate. Note that in this example the measured drop in contact resistance does not correspond to a marked transition in the friction signal.

2.1.5 Linear-Reciprocating Motion

In some cases, the friction/wear condition which is to be simulated may not correspond to a rotating pin-on-disk configuration and may be closer to a linear-reciprocating motion. Examples of the latter might be the deployment of a stent into

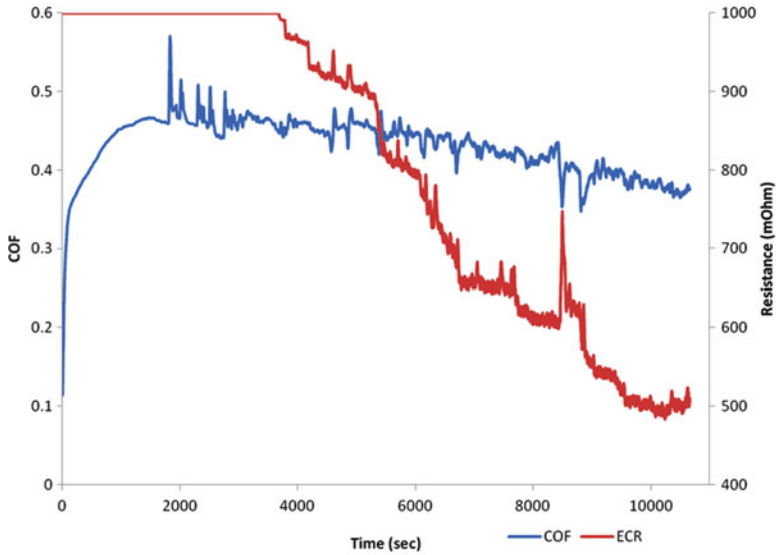
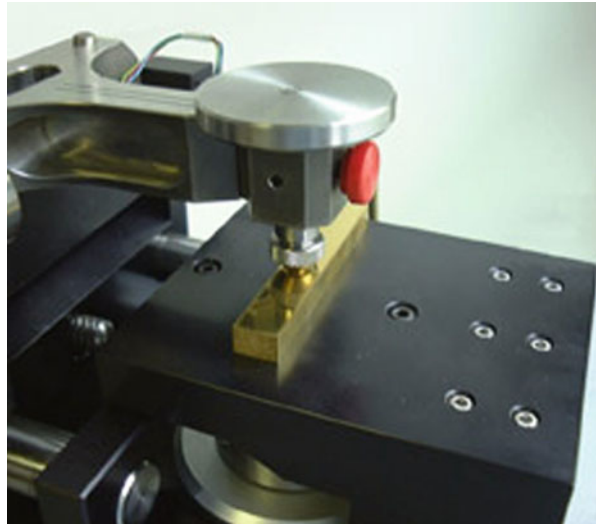


Fig. 4.13 Coefficient of friction (COF) and electrical contact resistance (ECR) plotted as a function of time for a 100Cr6 steel ball in contact with a polypropylene coating

Fig. 4.14 Experimental configuration for linear-reciprocating motion



an artery, a contact lens moving over the cornea, or the movement of a catheter. The basic pin-on-disk setup remains the same but the dynamic partner is reciprocated rather than rotated, as shown in Fig. 4.14.

The amplitude of the linear stroke (or stroke length) can usually be varied as well as the frequency of reciprocation in order to simulate in-service conditions in a

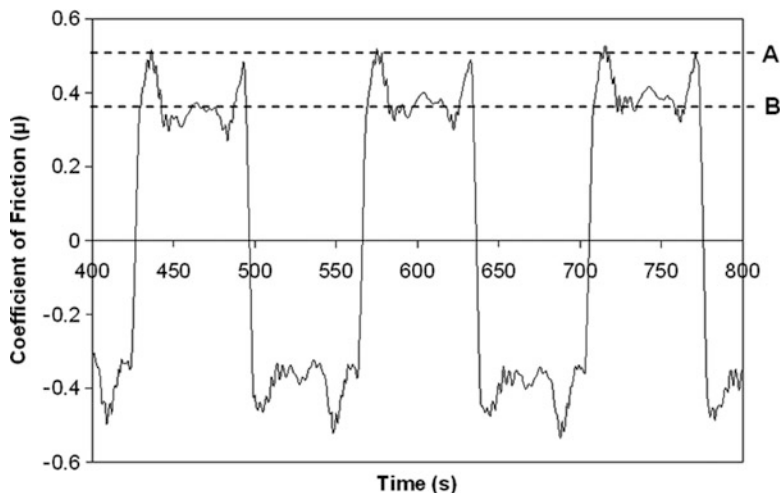


Fig. 4.15 Typical friction coefficient trace for a steel-on-steel contact showing the coefficient of static friction (a) and the coefficient of dynamic friction (b) measured from each cycle

controlled manner. Another main difference with a rotating test is that the linear reciprocation means that the tangential force can be measured in both directions and the speed is not constant: the movement accelerates from a standstill on every cycle. This means that the modes of wear may be quite different between a reciprocating test (where the wear debris may be pushed back into the contact zone) and a rotating test (where the sliding direction is always the same and debris tends to be pushed outside of the contact).

Because of the continuous acceleration/deceleration during linear reciprocating, it is possible to extract both the coefficient of static friction and the coefficient of dynamic friction from each cycle and in both directions, as shown in Fig. 4.15.

Modern software packages allow the measured values to be averaged as shown in Fig. 4.16. The user can select a specific point on each successive cycle in one direction (1st way extraction) and the opposite direction (2nd way extraction) and then can calculate an average of the 2 values (2-way extraction). This is a fast way to analyse friction and wear effects at different points in a reciprocating cycle. For example, the friction coefficient at maximum linear speed (in the middle of the cycle) could be compared to the friction coefficient during initial acceleration.

2.1.6 Heated Liquid Testing

Tribological testing in the laboratory allows many complex variables to be investigated individually and in combination with each other. A typical experimental arrangement for evaluating a biomaterial pair in a controlled physiological

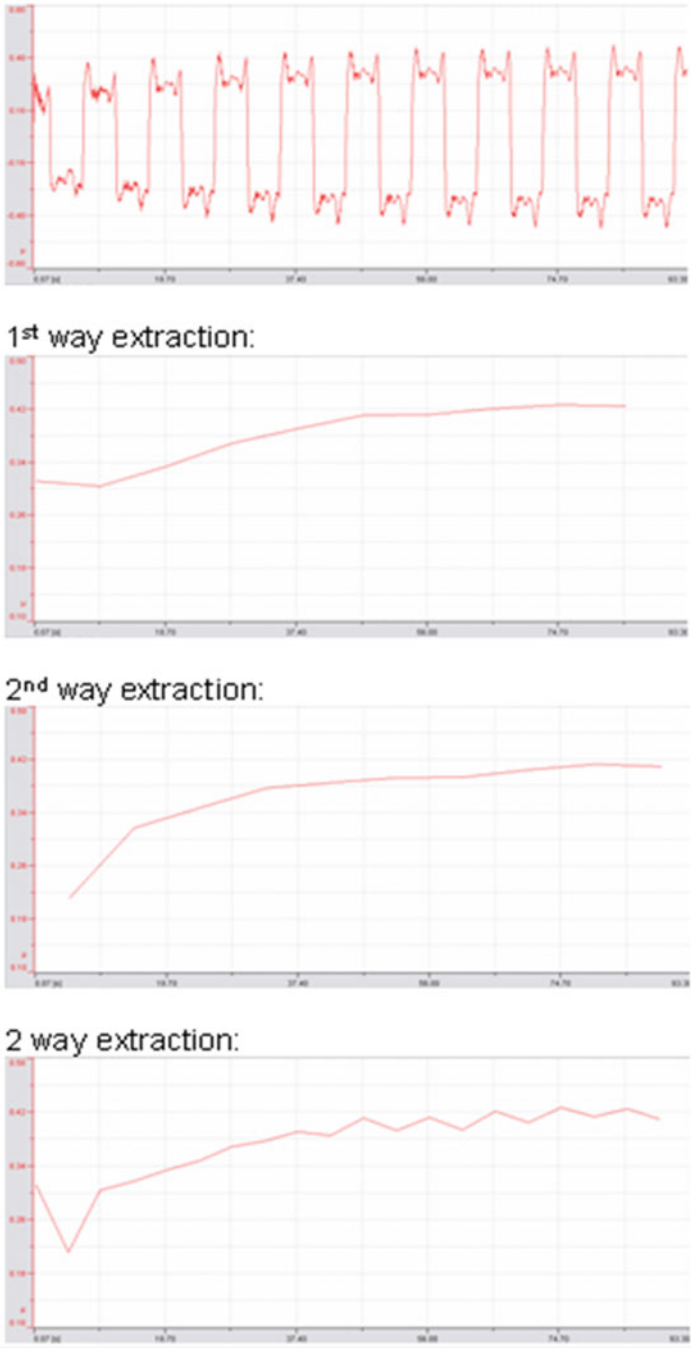


Fig. 4.16 Analysis of a linear-reciprocating dataset (*top*) consists of extracting the same point on each successive cycle in one direction (1st way extraction) and the opposite direction (2nd way extraction) and then averaging the 2 values (2-way extraction)

Fig. 4.17 Experimental arrangement for pin-on-disk testing of a biomaterial pair in simulated physiological saline solution. Tribological pair is submerged in a liquid cup whose contents are maintained at 37 °C by a heating coil



environment is shown in Fig. 4.17, where the static and dynamic partner materials are submerged in a cup containing the body-mimicking fluid (BMF) of choice and whose liquid temperature is maintained at a constant 37 °C by a submerged heating coil. This arrangement allows standardized testing to ASTM F-732 [23] with either rotating or angular reciprocating motion.

A common example of this configuration is the investigation of fatigue wear of ultra-high-molecular-weight polyethylene (UHMWPE) for hip implants, where the UHMWPE ball reciprocates against a flat metallic CoCr counterface. The counterface is usually in the form of a disk which must be held down by a retaining ring as shown schematically in Fig. 4.18. This reciprocating tribological test is very relevant to orthopaedic implants as most bearing surfaces have a reciprocating motion as opposed to a unidirectional motion. One important consideration is that the polymeric ball must be presoaked in the BMF to minimize fluid sorption during the wear test: without presoaking, UHMWPE materials can show a net increase in weight or volume during the initial wear intervals due to fluid sorption.

2.2 *Four-Ball Wear Tester*

The four-ball test configuration was originally designed to investigate the antiwear properties of a lubricant under boundary lubrication (metal-to-metal contact). The specific configuration ensures that the *extreme pressure* (EP) properties of the lubricant can be measured under high Hertzian contact and the results can help to determine the load-bearing properties of the lubricant at high applied pressures. The test configuration is shown in Fig. 4.19 where three steel balls (of half-inch diameter) are clamped together to form a cradle upon which a fourth ball rotates

Fig. 4.18 Schematic of the liquid cup used in the arrangement shown in Fig. 4.16, where the flat counterface (disk) must be retained by a sample holder (retaining ring)

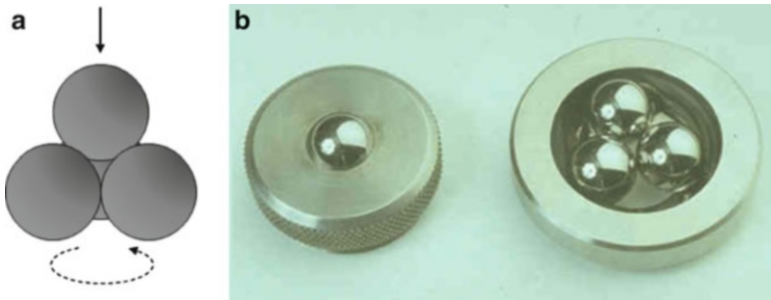
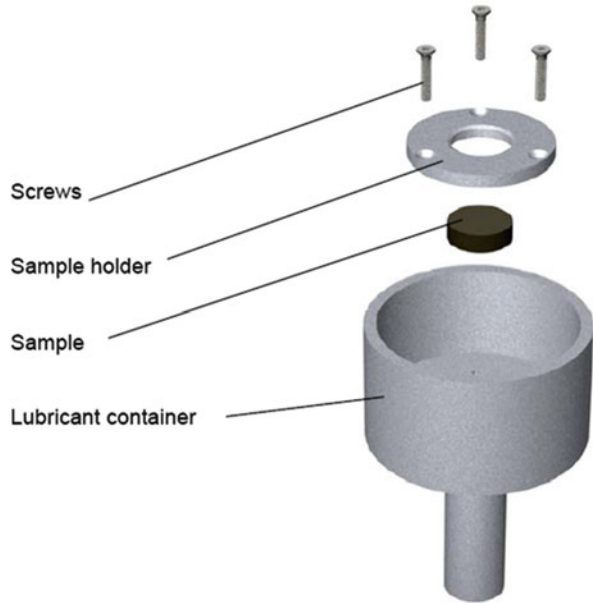
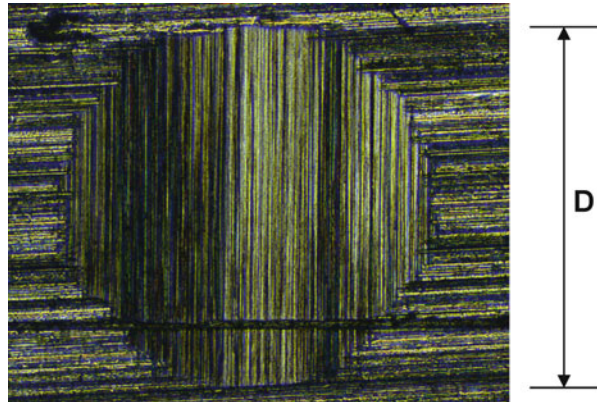


Fig. 4.19 The four-ball test configuration shown schematically (a) and the actual test pieces used (b)

on a vertical axis. The four balls are immersed in the oil sample at a specified speed, temperature, and load. At the end of a specified test time, the average diameter of the wear scars on the three lower balls is measured, an example of which is shown in Fig. 4.20. During the test, the load is increased every 10 min up to the point where the frictional trace indicates incipient seizure. The coefficient of friction may be measured at the end of each 10 min interval, provided the instrument has the necessary force sensors (see ASTM D5183 test method, [27]). The test is generally terminated at the load at which the rotating ball “welds” to the three stationary balls causing seizure.

Fig. 4.20 Typical example of a wear scar and the diameter measurement used in the wear rate calculation



The three most common parameters measured with the four-ball configuration are as follows:

1. Load-Wear Index (LWI): simple ratio which quantifies the degree of wear protection at each test load (often plotted as a function of applied load)
2. Last Non-Seizure Load (LNSL): provides an indication of the point of transition from elastohydrodynamic to boundary lubrication and metal-to-metal contact
3. Weld Point (WP): point at which seizure occurs

The most common standards used with the four-ball test configuration are ASTM D4172 [28] and ASTM D2266 [29].

2.3 Block-on-Ring Tester

The block-on-ring test is commonly used to determine the resistance of materials to sliding wear by ranking the particular material pair according to its wear characteristics under various conditions. One important attribute of this test is that it is very flexible as any material can be tested, as long as it can be fabricated into blocks or rings with relative ease. The test can be run either dry or with various lubricants, liquids, or gaseous atmospheres to simulate in-service conditions with the greatest accuracy.

The actual configuration is shown in Fig. 4.21 and the dimensions of the test pieces (both block and ring) will depend on the specific standard test procedure used.

Various machines are commercially available for this test, although they may differ slightly in lever arm ratio, load range, speed control (variable or fixed), speed range, and method of measuring friction (if any). In addition to measurement of the ranking resistance of materials to sliding wear, the block-on-ring method is also commonly used for measuring wear properties and extreme pressure properties of

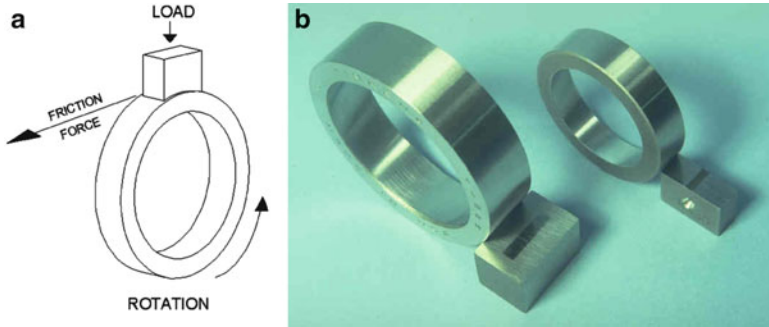


Fig. 4.21 The block-on-ring test configuration shown schematically (a) and the actual test pieces used (b)

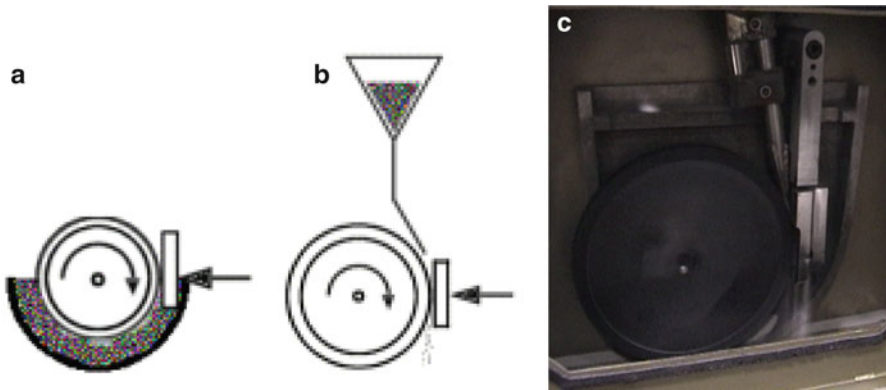


Fig. 4.22 The dry sand abrader test configuration shown schematically (a), (b), and actual test in progress (c)

lubricants and greases. The configuration can also be varied to provide different contact geometries between the test pieces, typically line, area, and point contacts. For a point contact, a ball-on-ring configuration is used.

2.4 Dry Sand Abrader

The dry sand abrader is used to test the abrasive resistance of solid materials to abrasive dry sand compositions. Materials such as metals, minerals, polymers, composites, ceramics, abrasives, and thick coatings can be tested with this instrument. The test is performed by loading a rectangular test sample against a rotating rubber wheel and depositing sand of controlled grit size, composition, and flow rate between them.

Typical test system setups are shown in Fig. 4.22, and the abrasive can be either static (as shown in (a)) or dynamically fed to the interface at a fixed flow rate. In the

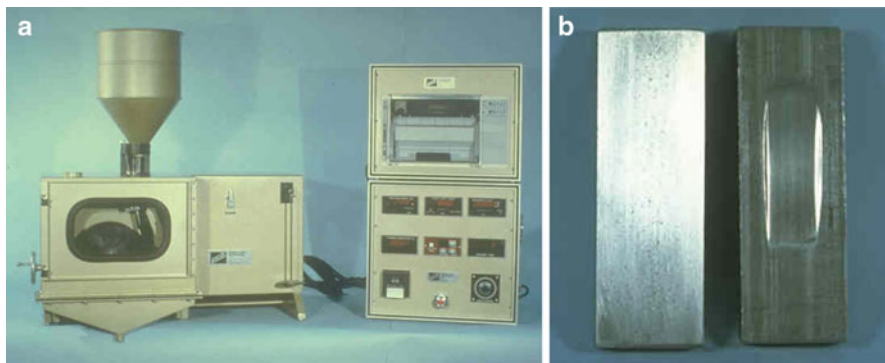


Fig. 4.23 Commercially available dry sand abrader (a) together with some typical steel test specimens before and after testing (b)

more common ASTM G65 method [30], the wheel, comprised of synthetic rubber of 60 Shore A hardness, is rotated in the direction of the flow of sand. The mass of the test sample is recorded before and after conducting a test, and the difference between the two values is the resultant mass loss due to dry sand abrasion. To develop a comparison table for ranking different materials with respect to each other, it is necessary to convert this mass loss to volume loss to account for the differences in material densities.

The test load and sand composition can be varied. The test parameters can be configured to perform tests as per ASTM G65 specifications. The test simulates what is commonly referred to as Low Stress Abrasion or Scratching Abrasion, both being characterized by the lack of any fracturing of the abrading material. This means that the abrasive sand particles retain their shape and size throughout the test procedure. This is in contrast to High Stress Abrasion or Grinding Abrasion where the sand particles are actually fractured into smaller pieces. Such newly created particles are very sharp and angular and will produce a very different wear mechanism due to the high degree of stress applied.

A typical commercial system for running such tests is shown in Fig. 4.23 as well as some typical test specimens. Weight loss is usually quoted in grams for such sample sizes. This test is an invaluable tool in the ranking of materials and prediction of component wear lifetime.

2.5 *Ball Crater Abrader*

The ball crater abrader (also commonly referred to as Calotest or Calowear Tester) provides a fast and simple method for measuring the wear coefficient of both bulk and coated materials. The basic principle is shown in Fig. 4.24a where a rotating

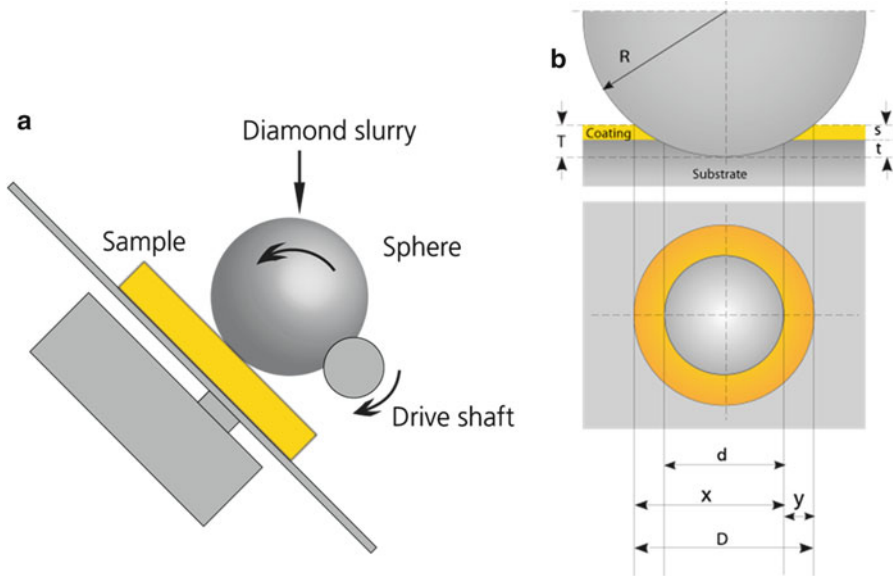


Fig. 4.24 Basic principle of the ball crater abrader (a) and summary of calculation parameters when abrading through a coating into the substrate (b)

sphere of known diameter is rotated on the sample surface with a preselected load. An abrasive slurry is applied to the contact causing a spherical depression to be produced in the sample. This depression, or ball crater, is also often referred to as a “calotte” and is subsequently viewed under an optical microscope in order to measure its diameter [31]. If the sample is coated, then it is possible to measure the thickness of the coating, s , using the parameters shown in Fig. 4.24b and the following equation:

$$S = \frac{1}{2} \left(\sqrt{4R^2 - d^2} - \sqrt{4R^2 - D^2} \right)$$

In addition, the ball crater technique can be used to calculate the abrasive wear coefficients of either a bulk material or a coating and substrate independently. This approach [32, 33] starts with a simple model for abrasive wear based on the Archard equation [34] which assumes independent wear coefficients for the coating and substrate. Taking into account the experimental geometry, the wear volumes are expressed assuming that the calotte diameter is much smaller than the ball diameter, leading to the following equation for the wear coefficient, K , of a bulk material:

$$K = \frac{\pi b^4}{32LF_N d}$$

where F_N is the normal force on the sample, b is the diameter of the wear crater, L is the sliding distance, and d is the diameter of the ball.

For coated materials, we consider the combined wear of a coating and substrate, each with an independent wear coefficient. Following the methodology of Rutherford and Hutchings [33], the following equation is used to derive the wear coefficients of the coating, K_C , and of the substrate, K_S :

$$\frac{LF_N}{b^4} = \left(\frac{K_S - K_C}{K_S K_C} \right) \left(\frac{\pi h}{4b^2} - \frac{\pi d h^2}{2b^4} \right) + \left(\frac{1}{K_S} \right) \left(\frac{\pi}{32d} \right)$$

Thus, a plot of $Y = \frac{L \cdot F_N}{b^4}$ versus $X = \frac{\pi \cdot h}{4b^2} - \frac{\pi \cdot d \cdot h^2}{2b^4}$ should be linear.

So we can consider this equation as a linear function: $Y = A \cdot X + B$ where

$$A = \frac{K_S - K_C}{K_S \cdot K_C}$$

and

$$B = \frac{1}{K_S} \cdot \frac{\pi}{32d}$$

Experimentally, several values are plotted and then fitted with a straight line which yields A and B, as shown in Fig. 4.25.

The wear coefficients are then calculated using the intercept (B) and the slope (A) as follows:

$$K_S = \frac{1}{B} \cdot \frac{\pi}{32d}$$

$$K_C = \frac{K_S}{A \cdot K_S + 1} = \frac{\frac{1}{B} \cdot \frac{\pi}{32d}}{A \cdot \left(\frac{1}{B} \cdot \frac{\pi}{32d} \right) + 1}$$

Some examples of ball craters on coated materials are shown in Fig. 4.26. In principal, the technique can be used to measure the wear coefficients of each independent coating, even in a complicated multilayer such as in Fig. 4.26b. It should be noted that the minimum coating thickness that can be measured in this manner is approximately 200–500 nm, depending on the quality of the interface and the optics used to measure the dimensions.

Commercially available equipment for measuring ball crater abrasion is shown in Fig. 4.27, in this case the Calowear Tester from CSM Instruments. The experimental arrangement is clearly shown in Fig. 4.27b and the load cell provides a direct acquisition of the normal load applied by the ball on the sample. In practice, this load can be varied by changing the lateral position of the motor drive shaft. The abrasive slurry is automatically fed to the ball/sample interface by a feed pump and flexible tubing. The resultant calottes are viewed through an integrated optical microscope which provides direct measurement of the ball crater dimensions.

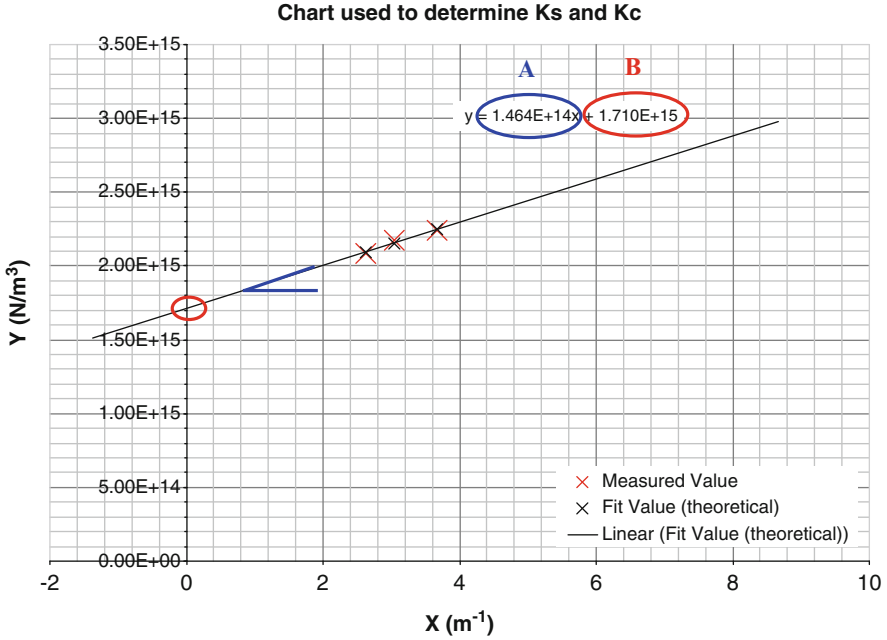


Fig. 4.25 Typical example of a plot from which the coating and substrate wear coefficients are derived for a TiN coating on a 440C steel substrate. The crosses show the actual experimental points made with a CSM Instruments Calowear Tester, to which the straight line has been fitted

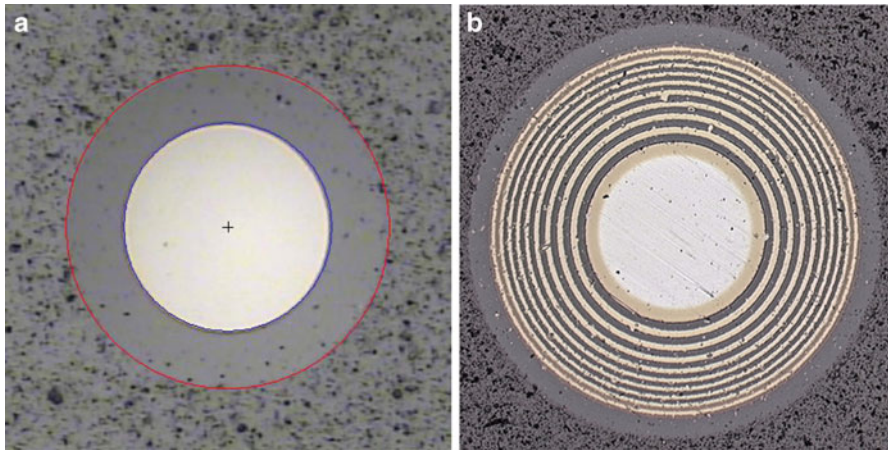


Fig. 4.26 Typical “calottes” made in (a) DLC monolayer coating on steel substrate and (b) multilayer of alternating TiN–TiCN coatings on steel substrate

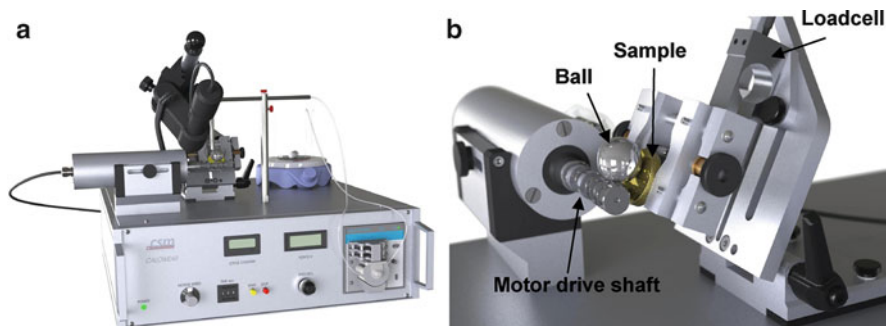


Fig. 4.27 Commercially available Calowear Tester (a) and detail of test setup (b)

Previous work [35] has shown that the ball crater wear behaviour of a wide range of Physical Vapour Deposition (PVD)-coated tool steels can be directly correlated to their performance as cutting tools. This means that the technique can be used to rank different cutting tool coatings for use in specific abrasive wear situations and also as a quality assurance tool in a production environment.

3 Examples of Tribology Testing Applications

The following examples are used to illustrate the use of some of the aforementioned tribology test methods in real applications.

3.1 High-Temperature Testing of TiN Coatings

Coatings used to extend the lifetime of cutting tools need to be tested at the temperatures at which they will be subjected in service.

In this study a CSM Instruments High Temperature Tribometer (capable of testing up to 1,000 °C) was used to carry out high-temperature wear testing of 2–3 μm thick TiN coatings applied on a steel K 110 steel substrate via Physical Vapour Deposition (PVD).

Figure 4.28 shows the High Temperature Tribometer which uses two linear variable differential transformer (LVDT) sensors for an accurate differential measurement of the tangential force without influence of temperature fluctuation (thermal drift). In practice, this means that the temperature gradient from the oven (surrounding the sample) to the measuring arm has no influence on the measurement of the coefficient of friction, even with significant temperature variations. A 6 mm diameter alumina ball was used as the static partner with a normal load 5 N

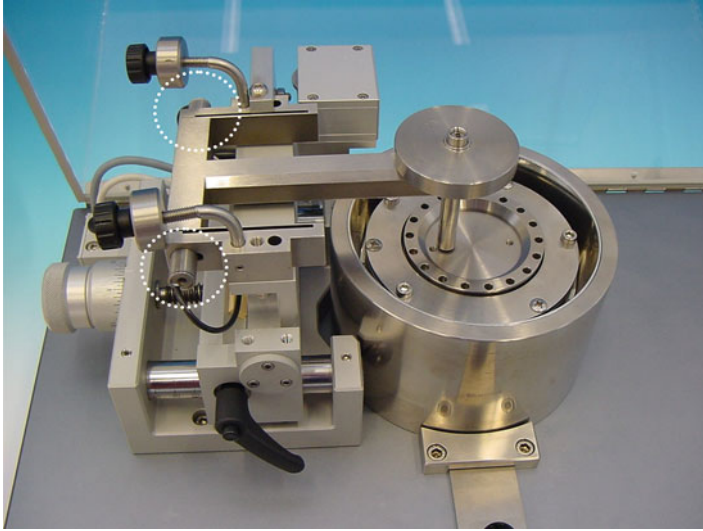


Fig. 4.28 CSM Instruments High Temperature Tribometer with two LVDT sensors (*circled*) which provide an accurate differential measurement of tangential force

Table 4.1 COF and wear measurements from high-temperature test of the TiN sample

	25 °C	150 °C	300 °C	500 °C	750 °C
Coefficient of friction (COF)	0.383	0.597	0.655	0.809	0.91
Wear of the ball (μm)	400	370	350	340	600
Wear of the disk (h in μm)	1.35	1.5	1.65	5.9	1.6
Wear of the disk (area in μm^2)	350	400	450	780	65

and linear velocity of 10 cm/s. Wear testing was carried out at 25, 150, 300, 500, and 750 °C on TiN-coated samples.

The results from the tests shown in Table 4.1 and Fig. 4.29a indicate an increase in coefficient of friction with an increase in temperature. Figure 4.29b shows that the wear on the ball steadily decreased until 500 °C. Once the temperature reached 750 °C, the wear on the ball increased to 600 μm . There was an increase in the area of wear until 500 °C to 780 μm^2 , but at 750 °C the wear area decreased to a minimal 65 μm^2 . The decrease in wear can be attributed to the fact that TiN oxidizes at 600 °C which is confirmed by Fig. 4.30 which shows the visible surface oxide present at 500 and 750 °C. The hard oxide layer therefore decreases the wear of the coating.

An interesting observation was made during the wear tests of the TiN-coated steel. Whilst the COF of the TiN increased with the rise in temperature, the wear decreased beyond 500 °C. This correlated to the oxidation of TiN which occurred around 600 °C. This would suggest that TiN is a valid coating for high-temperature cutting applications where the surface oxide can extend the service lifetime significantly.

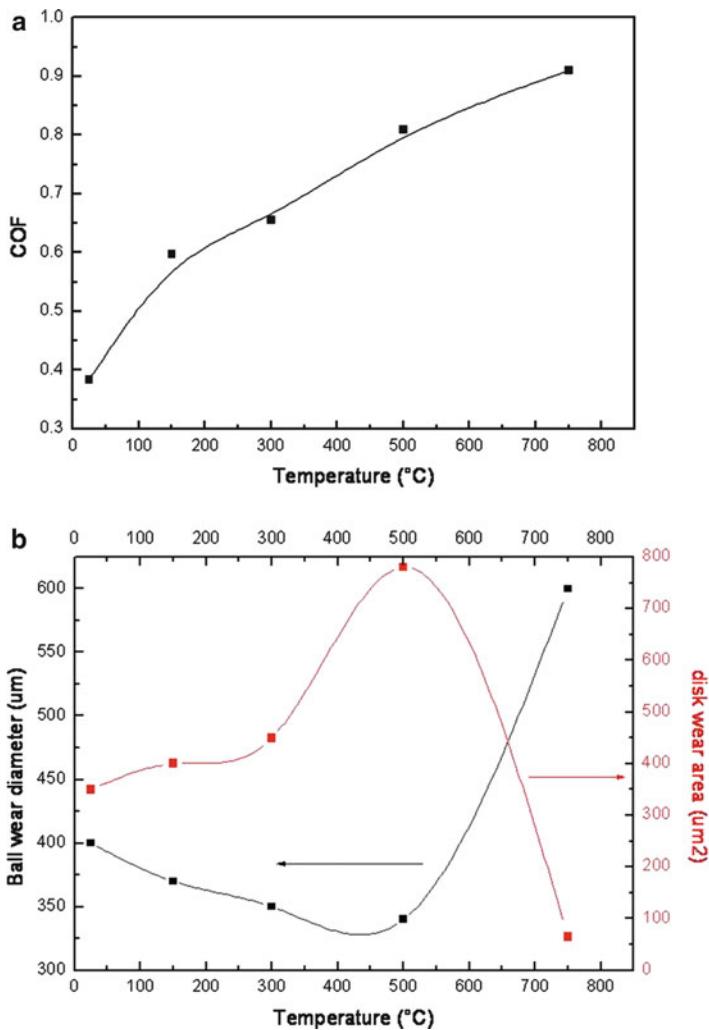


Fig. 4.29 (a) COF recorded during the high-temperature tests of the TiN-coated sample as a function of temperature. (b) Ball and disk wear recorded during the high-temperature tests of the TiN-coated sample as a function of temperature

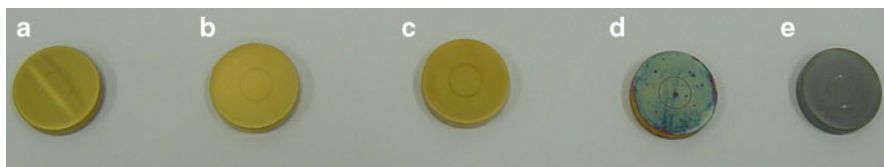


Fig. 4.30 TiN-coated samples after testing at temperatures of (a) 25 °C, (b) 150 °C, (c) 300 °C, (d) 500 °C, and (e) 750 °C

3.2 *Lifetime Study of Automotive Wheel Bearings*

In automotive applications, bearings form an integral part of many subassemblies, e.g. axle, engine, and gearbox, and their accurate characterization needs to take into account the final configuration of the bearing system. In the case of ball and tapered roller bearings, different types of loading may be applied at any one time, such as radial, axial, or other combination. The ratio of the radial to the axial load, the setting, and the bearing included cup angle determine the load zone in a given bearing. This load zone is defined by an angle which delimits the rollers or balls carrying the load. If all the balls are in contact and carry the load, then the load zone is referred to as being 360° .

Within the industry, the bearing life is defined as the length of time, or the number of revolutions, required to produce a fatigue spall of a size corresponding to an area of 6 mm^2 . Such a lifetime will depend on many factors such as applied load, speed, lubrication, fitting, setting, operating temperature, contamination, maintenance, as well as environmental considerations. Due to all these factors, the life of an individual bearing is impossible to predict precisely, and experience has shown that several bearings which appear identical can exhibit considerable life scatter when tested under identical conditions.

The pin-on-disk tribometer has proved ideal for investigating the evolution of friction and wear in a wide range of typical bearings as a function of the axial load. Figure 4.31 shows a typical friction trace for a single row bearing after 1 million revolutions. The friction coefficient, μ , soon stabilizes after running-in, after which it gradually decreases. Other studies have shown that the value stabilizes after several million laps.

Specially fabricated holders are used to mount the bearing and outer casings (see Fig. 4.32), and the complete “sandwich” is supported in a modified support shaft. A flat pin is used to apply the static 50 N load as shown in Fig. 4.33.

The required load zone of the bearing can be varied by changing the contact area and lateral position of the pin in order to simulate in-service conditions more accurately.

3.3 *In Vitro Testing of Orthopaedic Coatings*

The laboratory testing of biomaterials is often the first step in being able to rank a particular type of material within a specific wear application. Once a suitable material has been evaluated fully at the laboratory scale, in controlled environmental conditions, the next stage may often be a clinical trial in either an animal or human patient.

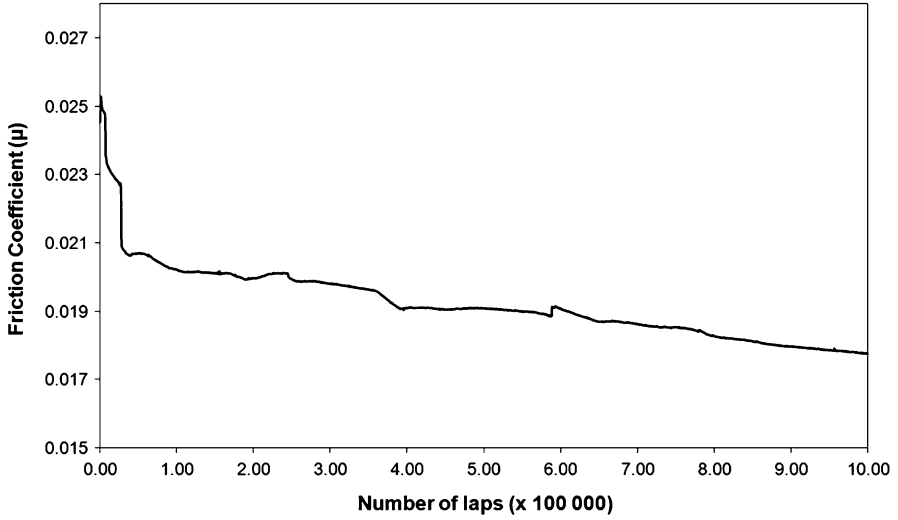


Fig. 4.31 Friction coefficient versus number of laps ($100,000\times$) for a single row bearing tested with the pin-on-disk tribometer. Note the initial running-in period and the gentle decrease in friction coefficient. Tests were carried out with an applied load of 50 N and speed 28 cm/s



Fig. 4.32 The component parts of a single row bearing: upper casing (a), inner bearing (b), and lower casing (c) which is located in a specially modified sample support shaft (d)

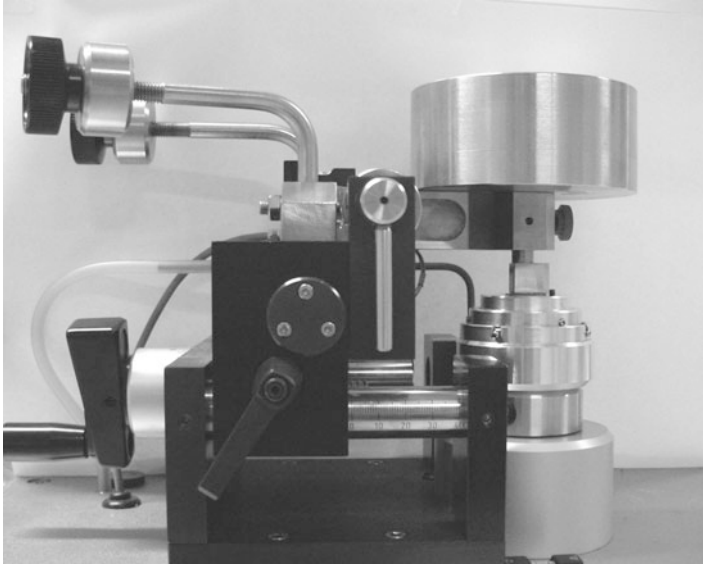


Fig. 4.33 The bearing shown was mounted on the tribometer for the test conditions summarized in Fig. 4.32

Tin oxide coatings are currently being developed for applications within the body where good adhesion and biocompatibility are the main considerations. Such coatings are spin coated onto standard stainless steel (316 L) substrates in a way that the coating thickness can be accurately controlled and the substrate roughness (R_{rms}) is less than 200 nm as verified by profilometry before deposition. The experimental setup consists of a pin-on-disk tribometer with a liquid cell and heating coil as shown in Fig. 4.34. The static partner is a 100Cr6 steel ball of diameter 6 mm and the materials in contact are submerged in BMF solution which is maintained at 37 °C for the duration of the test. The applied load is 2 N, linear speed 10 cm s⁻¹, and the wear radius is 3 mm.

The result of such a test is shown in Fig. 4.35 where an initial running-in period is followed by stabilization of the friction coefficient at a value of approximately 0.13 before increasing gradually until first failure of the coating occurs. As the coating starts to break down (after 2,730 revolutions), the friction coefficient drastically increases until at a value of 0.55 the substrate is reached and the coating no longer retains any integrity. Beyond about 4,000 revolutions the friction coefficient stabilizes at about 0.64. In this study, the test was paused at different points so that the sample could be imaged in a scanning electron microscope (SEM) to investigate the exact mode of failure and gain understanding about the amount of debris produced around the wear track.

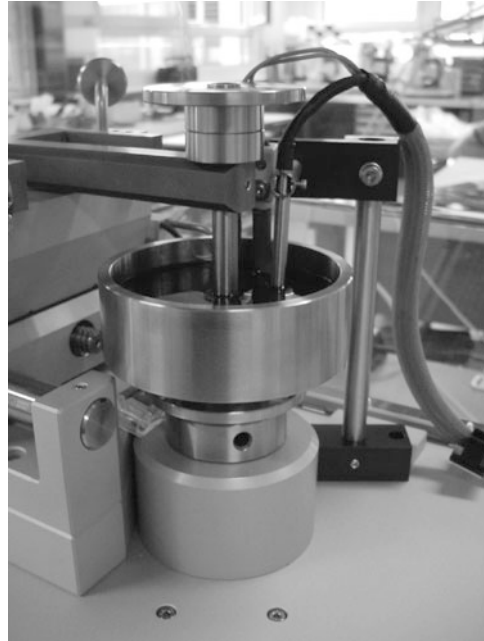


Fig. 4.34 Experimental setup for a tin oxide-coated 316 L steel disk in contact with a 100Cr6 steel ball, submerged in BMF and maintained at 37 °C with heating coil

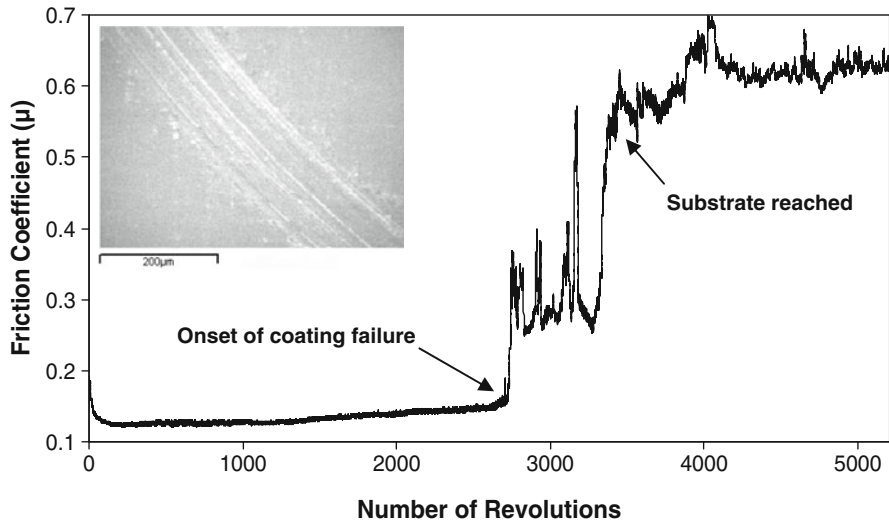


Fig. 4.35 Friction coefficient evolution for the test. The onset of coating failure and the point at which the substrate is reached are clearly denoted. SEM micrograph of the wear track confirms coating failure (*inset*)

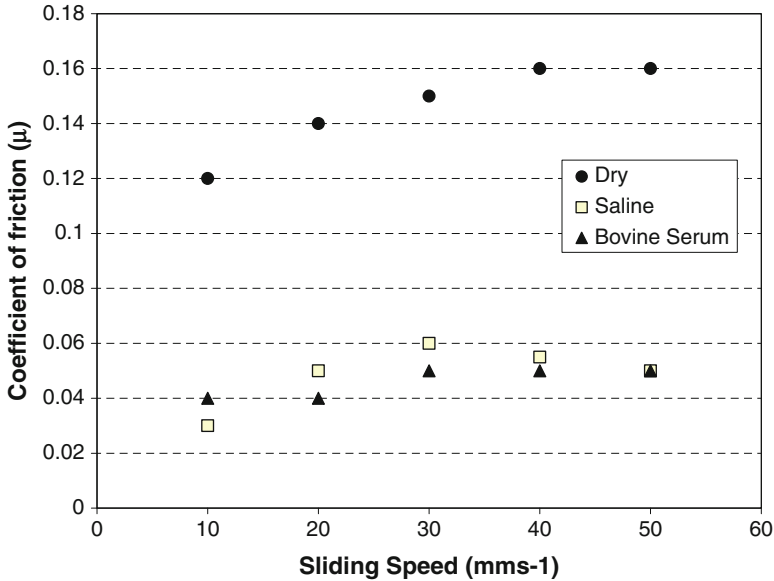


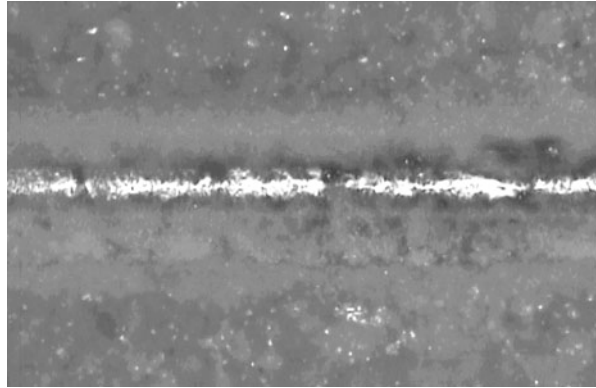
Fig. 4.36 Friction coefficients of a calcium phosphate coating (deposited on a steel substrate) when sliding against a UHMWPE pin at various different sliding speeds and in both dry and lubricated conditions

3.4 Dry and Wet Testing of Bone Biocompatible Coatings

Various biocompatible coatings have been developed in recent years for promoting fast healing between bone and a prosthetic implant material which may be ceramic, metallic, or polymeric (e.g. UHMWPE). Examples of such coatings are calcium phosphate and hydroxyapatite, both of which are found to have varying friction and wear properties when sliding in different environments. The results in Fig. 4.36 show the friction coefficients of a calcium phosphate coating (deposited on a steel substrate) when sliding against a UHMWPE pin at various different sliding speeds.

The experiment was repeated in dry and lubricated conditions. The two lubricants used were a standard saline solution (distilled water containing 0.1 % NaCl) and a commercially available bovine serum. Testing was performed on a pin-on-disk tribometer in unidirectional sliding (rotating) mode using an applied load of 2 N and a sliding speed from 10 to 50 mm s⁻¹, in 10 mm s⁻¹ increments. At each speed condition, the average friction coefficient was calculated from data acquired over 30 min. In the dry condition, the friction coefficient increases from 0.12 at 10 mm s⁻¹ up to 0.16 at 50 mm s⁻¹. In the saline and bovine serum lubricants, the friction coefficient drops to 0.03–0.06 with the bovine serum environment giving slightly lower values than the saline solution.

Fig. 4.37 Wear track of the calcium phosphate coating after 28 min of sliding at a speed of 40 mm s^{-1} in dry conditions



A typical wear track on the calcium phosphate coating is shown in the micrograph in Fig. 4.37, and the wear debris can be seen along the edges and the steel substrate has been reached.

3.5 Friction Study of Hydrogel Contact Lenses

The tribology testing of contact lens materials is usually performed under very low contact pressure conditions so as to simulate the effect of the eyelid during blinking which is of the order of 3.5–4.0 kPa with an average speed of approximately 12 cm s^{-1} [24–26]. Soft contact lenses are made of hydrogels which may contain up to 75 % water, and the contact pressure encountered in the human eye can cause redistribution and/or reduction of the water content, sometimes causing ocular discomfort, such properties also being related to the frictional characteristics. Testing of such soft contact lenses is therefore quite challenging as the applied loads tend to be only a few mN and so a high-resolution instrument is required, such as a CSM Instruments Nanotribometer 2. Contact lenses can be tested either with the lens acting as the static partner (see Fig. 4.38) or with the lens mounted flat and therefore operating as the dynamic partner (Fig. 4.39). In some cases, the lens may be mounted as the dynamic partner but using a spherical substrate which matches the curvature of the cornea. Typical experimental conditions might be an applied load of 4 mN, frequency 0.2 Hz, and stroke length of $100 \mu\text{m}$. The lens is usually tested completely submerged in saline solution in order to prevent it drying out and causing error in the measured friction coefficient.

Some experimental points which should be remembered when testing soft contact lenses are that the friction coefficient may differ between the two sides of the lens so it is important to always mount the lenses the same way. Secondly, there must be no air bubbles between the lens and its mounting. Often the lens can be secured to the substrate simply by capillary force, provided that the contact

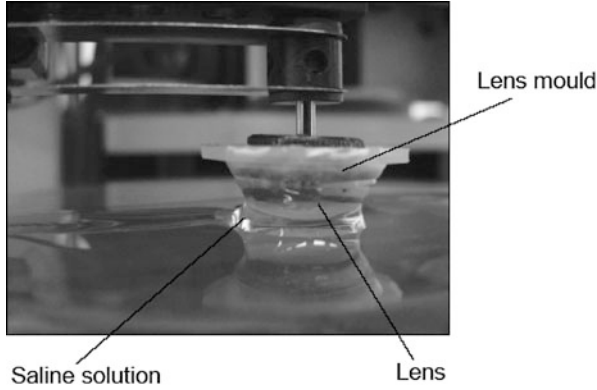


Fig. 4.38 Soft hydrogel contact lens mounted as the static partner on a nanotribo-meter and reciprocating linearly against a compliant substrate submerged in contact lens saline solution

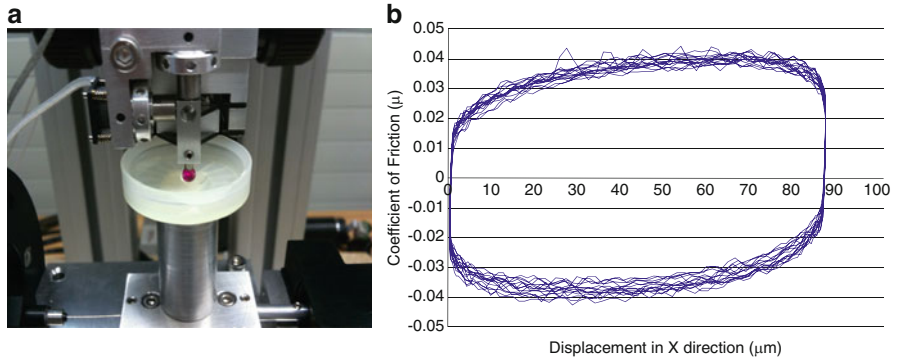


Fig. 4.39 Schematic view of a soft hydrogel contact lens mounted flat in a liquid cup (a) and reciprocating against a ruby ball of diameter 3 mm. The results after 20 cycles are shown in (b) where the average coefficient of friction was 0.03

pressures used are not too high. Sometimes, the lenses may need to be properly clamped down. Care should be taken not to stretch or deform them during the mounting process.

References

1. Bowden F, Tabor D (1973) Friction: an introduction to tribology. Anchor Press/Doubleday, Garden City, NY
2. Hutchings IM (1992) Tribology: friction and wear of engineering materials. Edward Arnold, London

3. Holmberg K, Matthews A (1994) *Coatings tribology: properties, techniques and applications in surface engineering*. Tribology Series 28, Elsevier Science
4. ASTM G99: standard test method for wear testing with a pin-on-disk apparatus
5. ASTM G133: standard test method for linearly reciprocating ball-on-flat sliding wear
6. Bowden F, Tabor D (1964) *The friction and lubrication of solids*, part I (1950) and part II. Clarendon Press, Oxford
7. Briscoe BJ, Tabor D (1978) *Friction and wear of polymers, polymer surfaces*. Wiley, New York
8. Buckley DH (1981) *Surface effects in adhesion, friction, wear and lubrication*. Tribology Series No. 5, Elsevier
9. Ling FF, Pan CHT (1988) *Approaches to modeling of friction and wear*. Springer, New York
10. Rabinowicz E (1965) *Friction and wear of materials*. Wiley, New York
11. *Fundamentals of Friction and Wear of Materials*. Rigney DA, ed. (1981) *Papers Presented at the 1980 ASM Materials Science Seminar, 4–5 October 1980, Pittsburgh, Pennsylvania*, ASM, Ohio, pp 235–289
12. Singer IL, Pollock HM (1992) *Fundamentals of friction*. Kluwer, Dordrecht
13. Landolt D (2006) *Electrochemical and materials aspects of tribocorrosion systems*. *J Phys D Appl Phys* 39:1–7
14. Yan Y (2006) *Biotribocorrosion—an appraisal of the time dependence of wear and corrosion interactions part II: surface analysis*. *J Phys D Appl Phys* 39:3206–3212
15. Landolt D (2007) *Corrosion and surface chemistry of metals*. EPFL Press, Lausanne, Switzerland, pp 227–274
16. Mischler S, Ponthiaux P (2001) *Wear* 248:211–225
17. Azzi M, Szpunar JA (2007) *Tribo-electrochemical technique for studying tribocorrosion behavior of biomaterials*. *Biomol Eng* 24(5):443–446
18. Azzi M, Benkahoul M, Szpunar JA, Klemberg-Sapieha JE, Martinu L (2009) *Tribological properties of CrSiN-coated 301 stainless steel under wet and dry conditions*. *Wear* 267 (5–8):882–889
19. Azzi M, Amirault P, Paquette M, Klemberg-Sapieha JE, Martinu L (2010) *Corrosion performance and mechanical stability of 316L/DLC coating system: role of interlayers*. *Surf Coatings Technol* 204(24):3986–3994
20. Jalota S, Bhaduri SB, Cuneys Tas A (2008) *Using a synthetic body fluid (SBF) solution of 2 mM HCO₃ to make bone substitutes more osteointegrative*. *Mater Sci Eng C* 28:129–140
21. Baboian R (2005) *Corrosion tests and standards: application and interpretation*, ASTM manual series, MNL 20 ISBN 0-8031-2098-2
22. Laing PG (1977) *Tissue reaction to biomaterials*, NBS Special Publication 472, Gaithersburg MD, pp 31–39
23. ASTM F-732: standard test method for wear testing of polymeric materials used in total joint prostheses
24. Nairn JA, Jiangizaire T (1995) *ANTEC '95*, 3384
25. Freeman ME, Furey MJ, Love BJ, Hampton JM (2000) *Wear* 241:129
26. Rennie AC, Dickrell PL, Sawyer WG (2005) *Friction coefficient of soft contact lenses: measurements and modeling*. *Tribol Lett* 18(4):499–504
27. ASTM D5183: standard test method for determination of the coefficient of friction of lubricants using the four-ball wear test machine
28. ASTM D4172: standard test method for wear preventive characteristics of lubricating fluid (four-ball method)
29. ASTM D2266: standard test method for wear preventive characteristics of lubricating grease (four-ball method)
30. ASTM G65: standard test method for measuring abrasion using the dry sand/rubber wheel apparatus
31. ISO EN-1071-2: determination of the abrasion resistance of coatings by a micro-abrasion wear test

32. Rabinowicz E, Dunn LA, Russel PG (1961) *Wear* 4:345
33. Rutherford KL, Hutchings IM (1996) *Surf Coat Tech* 79:231
34. Archard JF (1953) *J Appl Phys* 24:981
35. Rutherford KL, Bull SJ, Doyle ED, Hutchings IM (1996) *Surf Coat Tech* 80:176–180

Questions for Students

1. Name 6 typical tribometer configurations.
2. What is the difference between *steady state* and *static* friction coefficients?
3. Name 2 methods commonly used to determine the wear rate of a tested material.
4. What are the main components of a practical tribocorrosion setup and what are the 3 modes of operation?
5. What are the 3 most common parameters measured with the four-ball wear tester?
6. What is the main parameter measured with the ball crater abrader?

Chapter 5

Interface Temperature of Sliding Surfaces

R. Arvind Singh

Abstract The interface temperature between sliding surfaces plays an important role in the tribological performance of the surfaces. Temperature rise at the tribo-contacts can cause microstructural changes and tribo-chemical reactions, which in turn influence the operating wear mechanisms and wear transitions. Flash temperatures that arise at the tip of asperities are much higher than the surface bulk temperatures. Exact estimation of flash temperatures is rather difficult when compared to the surface bulk temperatures. However, calculations of surface bulk temperatures using models that are based on ab initio estimations, at the most, give values that are only indicative but not exact. The parametric uncertainties in these models give rise to either underestimates or overestimates of surface bulk temperatures. Estimation of surface bulk temperatures based on measurements can give temperature values closer to the real ones. This chapter presented a brief historical background on the subject of estimation of temperatures, earlier models based on ab initio calculations, and a new method to estimate surface bulk temperatures based on measurement of temperature at two points along a pin axis away from the sliding interface and in a realistic flow field of air around the pin. Discussion on the issues in the earlier models and comparison of temperature values obtained by these models with those estimated by measurements clearly indicate the importance of undertaking measurements to arrive at better estimates of temperature values that are closer to the real ones.

R.A. Singh (✉)
Energy Research Institute (ERIAN), Clean Tech One, Nanyang Technological University,
Singapore 637141, Singapore
e-mail: arvindsingh@ntu.edu.sg

1 Introduction

When bodies slid against each other, the interface temperature rises as a result of friction between the sliding surfaces. The rise in temperature at the interface reduces the yield strength, causes microstructural changes, and also promotes tribo-chemical reactions [1]. The contact surface temperature not only affects wear mechanisms but also affects the transition from mild to severe wear regime [2–4]. During sliding, heat is generated at the contact (asperities) of both the sliding surfaces. This area of contact being the real area constitutes a small fraction of the apparent (geometrical) area of contact. At the tip of asperities, the temperatures are high as the areas are small. This is generally designated as the “flash temperature.” The heat thus generated is conducted into the bulk, where it suffers losses due to convection and radiation. If we extrapolate the bulk temperature to the surface, by ignoring the asperities, the surface temperature so calculated may be termed as the “surface bulk temperature.” The estimation of surface temperature demands the consideration of all the three active processes of conduction, convection, and radiation. Many attempts, both analytical and experimental, have been undertaken in the past to arrive at estimating the bulk temperatures under various contact conditions.

2 Historical Background

Blok in 1937 conducted theoretical studies of the temperature rise at surface of actual contact under oiliness lubricating condition [5]. He defined the flash temperature as the asperity contact temperature above the bulk temperature. In 1942, J. C. Jaeger [6] in his work on analytical modeling of moving heat sources in semi-infinite solid defined a constant (ϕ -Jaeger’s dimensionless constant) that determines the onset of steady-state conditions. Carslaw and Jaeger [7] as an extension of previous work [6] arrived at the surface bulk temperature by considering thermophysical properties of the semi-infinite solid under moving heat source condition. These early theoretical models [5–7] are the base for the newer approaches [8–10] for estimating the surface temperatures.

3 Earlier Models

As a simple case, the estimation of surface temperature in the case of pin under sliding contact with a disc (pin-on-disc experiment) is considered throughout the chapter. In the pin-on-disc configuration, the sliding specimen (pin) is considered as a fin to estimate the temperature at its wearing end. The differential equation that is to be solved to estimate the surface temperature at the wearing end is given by

$$\frac{d^2\theta}{dz^2} - m^2\theta = 0 \quad (5.1)$$

where $\theta = (T - T_{\text{amb}})$ is the excess temperature over the ambient and “m” is given by

$$m = \sqrt{\frac{h_C P}{k_p A_c}} \quad (5.2)$$

and z = the distance from the wearing surface into the pin length.

Here, h_C , P , K_p , and A_c are the heat transfer coefficient (Newton’s cooling coefficient), perimeter area, thermal conductivity, and the cross-sectional area of the pin that is subjected to wear, respectively. The complete solution of (5.1) is given by

$$\theta = Ae^{mz} + Be^{-mz} \quad (5.3)$$

If A , B , and m are known, then (5.3) gives the temperature distribution in a pin as a function of depth (z).

3.1 Bowden and Tabor [9]

Bowden and Tabor [9] considered the pin to be an infinitely long cylinder and solved the fin equation (5.1) to estimate the surface temperature at the wearing end of the pin. In the solution (5.3), as $z \rightarrow \infty$, $\theta \rightarrow \infty$. This is unrealistic, so only one term is considered by them. For the temperature to be finite, the coefficient “A” should become zero. Hence, for an infinitely long pin, the solution given by them is

$$\theta = Be^{-mz} \quad (5.4)$$

In the case of a pin wearing on a disc, the heat input into the pin is given by

$$Q_p = f_p \mu W V \quad (5.5)$$

where f_p , μ , W , and V are the fraction of heat going into the pin, the friction coefficient, the normal load, and the sliding speed, respectively. From Fourier’s conduction law:

$$Q_p = -k_p A_c \left(\frac{d\theta}{dz} \right)_{z=0} \quad (5.6)$$

where “ θ ” is as given by (5.4). By equating the (5.5) and (5.6), the coefficient “B” is known, and the solution (5.4) is then given by

$$\theta = \left[\frac{f_p(\mu W)V_p}{k_p A_c \sqrt{\frac{\alpha P}{k_p A_c}}} \right] e^{-\sqrt{\frac{\alpha P}{k_p A_c}} z} \quad (5.7)$$

where f_p is the fraction of heat entering into the pin. For sliding surfaces of comparable conductivities, Bowden and Tabor [9] assumed the ratio of conductivities for the value of f_p . Thus, for an infinitely long pin, when $z = 0$, $\theta = \theta_b = B$ gives the temperature at the wearing end.

3.2 Lim and Ashby [8]

Lim and Ashby [8] solved the fin equation under an assumed condition of linear relation between the pin end temperatures and the pin length (“mean diffusion length,” l_b). They considered a hypothetical pin in which the temperature gradient is linear. This means that no heat is lost and the pin is insulated at its sides. This is the hypothetical pin whose length is “ l_b .” When the pin is insulated, no heat transfer occurs, and hence, the heat transfer coefficient (h_c) is absent in (5.2). Under such a condition, the fin equation (5.1) becomes

$$\left(\frac{d^2 \theta}{dz^2} \right) = 0 \quad (5.8)$$

whose solution is given by

$$\theta = Az + B \quad (5.9)$$

Invoking the following boundary conditions, A and B can be determined:

1. $z = 0 \rightarrow \theta = \theta_b$; $\theta_b = (T_b - T_{amb})$, where T_b is the surface temperature.
2. $z = l_b \rightarrow \theta = \theta_{sink}$; $\theta_{sink} = (T_{sink} - T_{amb})$, where T_{sink} is the sink temperature.

T_{sink} was assumed as the ambient temperature (T_{amb}) by them. Knowing A and B and considering the heat input into the pin (Q_p , 5.5) and the Fourier’s conduction law (5.6), the expression for the surface temperature was obtained by them as

$$T_b = \left(\frac{f_p \mu W V}{k_p A_c} \right) l_b + T_{amb} \quad (5.10)$$

Further, they considered the disc to be a semi-infinite solid and gave the expression for the bulk surface temperature generated at the interface as follows:

$$T_b = T_o + \left[\frac{\mu T^* \beta}{2 + \beta(\pi \bar{V}/8)^{1/2}} \right] \bar{F} \bar{V} \quad (5.11)$$

where T_o is the sink temperature (T_{amb}) and μ the friction coefficient. \bar{F} and \bar{V} are the dimensionless quantities. \bar{F} , \bar{V} , T^* , and β are defined below in (5.12a, 5.12b, 5.12c, 5.12d):

$$\bar{F} = \left[\frac{F}{A_p H_p} \right] \quad (5.12a)$$

$$\bar{V} = \left[\frac{V_p r_p}{a_d} \right] \quad (5.12b)$$

$$T^* = \left[\frac{H_p a_d}{k_p} \right] \quad (5.12c)$$

$$\beta = \left[\frac{l_b}{r_p} \right] \quad (5.12d)$$

where F , A_p , H_p , V_p , r_p , and k_p are the load, area, hardness, velocity, radius, and thermal conductivity of the pin material, respectively; a_d is the thermal diffusivity of the disc material. Here, l_b is the diffusion length of the pin under thermally insulated condition defined as $l_b = (\beta r_p)$. Lim and Ashby considered the value of β to be “6.” They arrive at the heat-partitioning coefficient f_p (fraction of the generated heat entering the pin surface) by considering the argument that the continuity at the interface requires the bulk temperature to be the same for the pin and the disc. They predicted the bulk surface temperature as in (5.13), considering the thermophysical quantities of the disc. Equation (5.14) is arrived by considering the thermophysical quantities of the pin:

$$T_b = T_o + \left[\frac{2(1 - f_p)q(a_d t_d)^{1/2}}{k_d(\pi)^{1/2}} \right] \quad (5.13)$$

where a_d , k_d , and t_d are the thermal diffusivity, conductivity, and interaction time of the disc, respectively. The interaction time $t_d = [(2r_p)/V_p]$ gives the time taken for a point on the disc to slide across the diameter of the pin, where V_p is the velocity of the pin:

$$T_b = T_o + \left[\frac{f_p \mu F V_p l_b}{A_n k_p} \right] \quad (5.14)$$

where A_n is the nominal contact area (πr_p^2) of the pin with the disc.

Lim and Ashby obtained f_p (heat partition coefficient) as

$$f_p = \frac{1}{2 + l_b \left(\frac{\pi V_p}{8 a_p r_p} \right)^{1/2}} \quad (5.15)$$

The disc having been considered as a semi-infinite solid has a very low contact interaction time (t_d) with the pin. Unlike the pin where heat is injected into it all the time, making it reach a steady state, the disc does not attain steady state due to the low interaction time. For the steady state to be attained in the disc, it is required that Jaeger's constant $\phi < 1$. When this is less than 1, f_p becomes 0.5, and when not, $f_p < 1/2$.

The Jaeger's constant ϕ is given by

$$\phi = \left(\frac{t_h}{t_d} \right) = \left(\frac{V_p r_p}{2a} \right) \quad (5.16)$$

where $t_h = \left(\frac{r_p}{a_p} \right)$ is the heat diffusion time.

4 Two-Point Method

In this section, a new model to estimate the surface bulk temperature based on temperature measurements conducted at two different places along the length of a pin sliding against a disc, in a pin-on-disc configuration, [11] is presented. In this model, the complete solution (5.3) of the fin equation (5.1) is considered to estimate the surface bulk temperature. "m" is referred from (5.2). Undertaking temperature measurements at two different places along the length of the pin (Fig. 5.1), the unknown coefficients "A" and "B" are obtained. The three active processes of conduction, convection, and radiation are considered as explained below. To note, in this model, the value of the fraction of heat entering into the pin (f_p) by itself is not required in estimating the surface temperature.

4.1 Conduction

Considering the pin to be a fin with a definite length, the one-dimensional equation of heat conduction in a pin and its solution are given by (5.1) and (5.3). Temperatures θ_1 and θ_2 at two different places, i.e., at two different heights along the length of the pin from the wearing end of the pin (Z_1 and Z_2), are measured. The value of "m" is obtained from the following correlation:

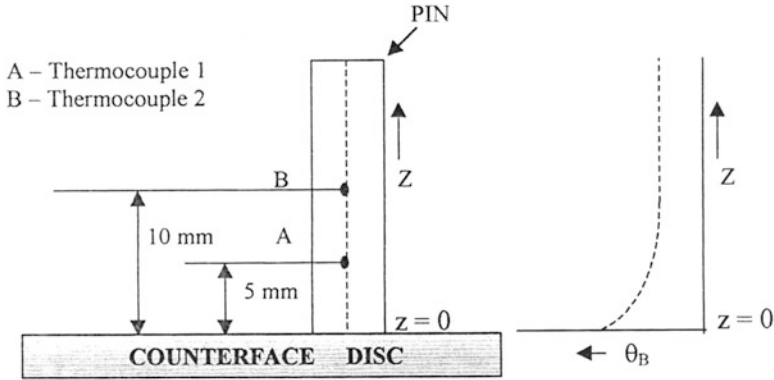


Fig. 5.1 Schematic showing a wear pin with thermocouples fixed in their position for temperature measurements at two different places along the length of the pin

$$m = \sqrt{\frac{h_T P}{k_p A_c}} \tag{5.17}$$

where $h_T = (h_C + h_R)$ is the total heat transfer coefficient; h_C and h_R are the heat transfer coefficients by convection and radiation, respectively. Having obtained the values of θ_1 , θ_2 , and m , using (5.3), the coefficients A and B are determined.

At $z = 0$, the surface bulk temperature is given by

$$\theta_b = (A + B) \tag{5.18}$$

4.2 Convection

The heat transfer coefficient due to convection (h_C) for the case of cross flow across a cylinder is obtained from the Churchill and Bernstein correlation [12]. The velocity (V_R) that affects this coefficient is obtained as a resultant velocity from the case of the flow in the neighborhood of a disc rotating in a fluid at rest [13] as discussed by Hermann Schlichting.

The convection term accounts for the loss of heat from the side of the pin along its length. The heat transfer coefficient by convection depends upon the velocity distribution of air along the pin length. The Bowden and Tabor model assumes a constant velocity profile along the length of the pin; the velocity of air is equal to that of the applied velocity. In reality, the velocity profile is not linear along the length, and the magnitude is equal to the applied velocity only at the wearing end of the pin. The magnitude of the velocity away from the wearing end is much lower than the applied velocity. This results at a lower heat transfer coefficient. The heat transfer coefficient by convection solely depends upon the flow properties of air and does not depend upon the pin materials.

4.3 Radiation

The heat transfer coefficient resulting from radiation (h_R) is estimated from the Stefan–Boltzmann law [14].

In the new model (two-point method), the temperatures θ_1 and θ_2 measured at the distances Z_1 and Z_2 (incorporating the height loss of the pin with appropriate wear rates), the coefficient of friction, and the conditions of sliding velocity (V_p) and normal load (L) are used in computing the surface bulk temperature (θ_b), as given below:

1. The properties of air which affect convection such as density (ρ_a), dynamic viscosity (η_a), specific heat (C_p), and thermal conductivity (k_a) can be evaluated at the average temperature between the pin surface and the ambient air using the following correlations:

$$\rho_a = \left(\frac{28.96(101.32 \times 10^3)}{8314.32(T + 273)} \right) \text{kg/m}^3 \quad (5.19a)$$

$$\eta_a = \left(\frac{1.48 \times 10^{-6}(T + 273)^{1.5}}{118 + (T + 273)} \right) \text{Pa} \quad (5.19b)$$

$$C_p = 10^3 \left(1 + 2.5 \times 10^{-10}(T + 273)^3 \right) \text{J/kgK} \quad (5.19c)$$

$$k_a = \left(\frac{1.19 \times 10^{-3}(T + 273)^{1.6}}{118 + (T + 273)} \right) \text{W/mK} \quad (5.19d)$$

2. The velocity of the air flowing over the pin, which occurs due to the flow field created by the rotating disc (counterface), is the resultant velocity (V_R) of the radial (V_r), tangential (V_θ), and axial (V_z) velocity components (Fig. 5.2). These can be estimated using the expressions as per the exact solution to the rotating disc problem [13]:

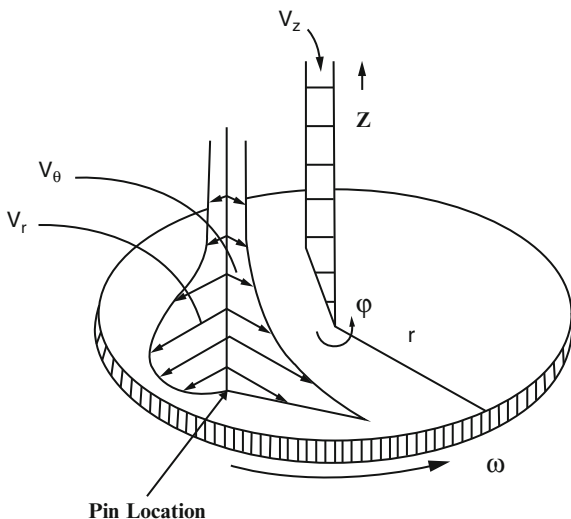
$$\begin{aligned} V_r &= r\omega F(z^*); & V_\theta &= r\omega G(z^*); & V_z &= (\omega\nu)^{1/2}H(z^*); \\ z^* &= z \left(\frac{\omega}{\nu} \right)^{1/2} \end{aligned} \quad (5.20)$$

ν and ω are the kinematic viscosity of the fluid (air) and the angular velocity of the disc.

“ r ” is the radial distance from the center of the disc (track position of the pin sample).

The values of the functions F , G , and H can be determined using the following relations:

Fig. 5.2 The velocity of air flowing over a pin, which occurs due to the flow field created by a rotating disc (counterface). V_r , V_θ , and V_z are the radial, tangential, and axial velocity components, respectively [11]



$$F(z^*) = -0.0002 + 0.5154z^* - 0.5214z^{*2} + 0.2427z^{*3} - 0.0668z^{*4} \quad (5.21a)$$

$$G(z^*) = 1.0098 - 0.7098z^* + 0.2059z^{*2} - 0.0301z^{*3} + 0.0021z^{*4} \quad (5.21b)$$

$$H(z^*) = -0.0014 - 0.0196z^* - 0.4584z^{*2} + 0.2834z^{*3} - 0.0841z^{*4} \quad (5.21c)$$

3. The convective heat transfer coefficient (h_c) can be determined from the correlation given by Churchill and Bernstein [12] for the cross flow across a cylinder as follows:

$$h_c = \left(\frac{k_a}{2r_p} \right) \left[0.3 + \frac{\text{Re}^{1/2} \text{Pr}^{1/3}}{(1 + 0.5429 \text{Pr}^{-2/3})^{1/4}} \left(1 + 3.9228 \times 10^{-4} \text{Re}^{5/8} \right) \right]^{4/5} \quad (5.22)$$

where Re and Pr are the Reynolds and Prandtl numbers, respectively:

$$\text{Re} = \left(\frac{2V_R r_p \rho_a}{\eta_a} \right)$$

and $\text{Pr} = \left(\frac{\eta_a C_p}{k_a} \right)$

The Reynolds number can be calculated using the resultant velocity, $V_R = \sqrt{(V_r^2 + V_\theta^2 + V_z^2)}$. However, since V_R varies along the length of the pin, h_c can be actually determined as a function of the axial distance along the pin length,

and an average value, numerically determined from the local values (typically 100) of h_C , can be used in the calculations.

4. The radiative heat transfer coefficient can be calculated using Stefan–Boltzmann law:

$$h_r = \frac{\sigma \varepsilon (T + 273)^4 - (T_s + 273)^4}{(T - T_s)} \quad (5.23)$$

where σ and ε are the Stefan–Boltzmann constant and emissivity of the pin. T and T_s are the temperature of the pin surface and the surrounding surfaces, respectively.

5. The total heat transfer coefficient is obtained as

$$h_T = (h_C + h_R) \quad (5.24)$$

6. The value of “ m ” can be estimated as from (5.17) using the above value of h_T . Using this value of “ m ,” (5.3) is solved to obtain the coefficients A and B. Using the boundary conditions $z = 0$, θ_b is obtained as in (5.18).

5 Certain Issues Regarding Earlier Models

The previous models [8, 9] do not consider any temperature measurements to estimate the surface bulk temperature. The new method relies on two measured temperature values along the axis of the pin specimen to estimate the same. Hence, the method may be called as “two-point” method. (Literature search revealed that earlier, Barber [15] used a two-point method, although no details were given.) In addition, the present two-point method provides the convenience of choosing any depths (excepting at depths very close to the surface) to undertake the temperature measurements. Some issues regarding the previous models [8, 9] are stated below.

Bowden and Tabor model demands that the value of the fraction of heat going into the pin (f_p) be known a priori to estimate the surface temperature. In Lim and Ashby’s model, heat partitioning involves the Jaeger’s constant (ϕ) for estimating the heat partition, when a transient temperature field exists in the disc. This time-dependent heat flow in the disc is considered by taking the thermal diffusivity into account. In the wake of being conformal with the Jaeger’s condition for the steady state, Lim and Ashby assume the value of the fraction of heat going into the pin as 0.5. Even though the components under sliding (both the pin and the disc) are for the same material, parameters such as the real area of contact, the geometry, and the thermophysical properties restrict the equal sharing of heat between the pin and the disc. In the present two-point method, this factor is estimated as a ratio of the heat flowing into the pin (Q_p) and that generated (Q_g) at the interface (5.25), although it is not required explicitly in obtaining the surface bulk temperature:

$$f_p = \left(\frac{Q_p}{Q_g} \right) = \left(\frac{k_p A_c \left(\frac{d\theta}{dz} \right)_{z=0}}{\mu W V_p} \right) \quad (5.25)$$

Lim and Ashby in their model introduced the quantity “ β ” under an assumed condition of thermal insulation to the pin. This dimensionless parameter “ β ” was used in obtaining the bulk diffusion length (l_b). The value of “ β ” which was taken to be equal to “6” by them has no explicit explanation.

6 Case Study

In this section, a case study of the estimation of surface bulk temperature of Ti–6Al–4V titanium alloy pin (cylindrical, 9 mm in diameter) slid against an alumina disc (roughness, CLA 0.2 μm) in a pin-on-disc machine [11, 16] has been presented. The surface bulk temperature was estimated using the two-point method. Temperature estimations using models proposed by Bowden and Tabor [9] and Lim and Ashby [8] have also been presented.

Alumel–chromel thermocouples were fixed at depths of 5 and 10 mm from the pin surface that is subjected to wear (Fig. 5.1). 1 mm diameter holes were drilled horizontally at those heights to reach the vertical axis of the pin. The thermocouples were set into the holes using silver paste. An adhesive bond was then applied over the setting so as to ensure the thermocouples are fixed in their position. A setting time of 4–6 h was permitted before conducting the experiments. Experiments were done with a stepwise increase in velocity from 1 to 11 m/s at the normal load of 110 N, each step lasting for about 2.5 min. Under all conditions of speeds, temperatures were measured in the steady state. It was found that both friction force and wear data become invariant with time (steady state) 1.5 min after each step increase in velocity.

Figure 5.3 shows the variation of surface bulk temperature with velocity at the normal load of 110 N estimated using (5.7), (5.14), and (5.18). The extrapolated predictions by the two-point method (5.18) are averages obtained from five repeated experiments. The nonlinearity with respect to sliding velocity is therefore real, whereas the non-extrapolated temperature predictions by Lim and Ashby are almost linear with velocity. The low values of temperature predicted by the Lim and Ashby’s method are due to the fact that their method gives a very low estimation of the “fraction of heat going into the pin” for the present configuration ($f_p \sim 0.0027$). On the other hand, the estimates of temperatures by the “long fin” model (5.7, Bowden and Tabor) can be considered to be overestimates.

To validate the two-point method, the temperature at an arbitrary “z,” referred to as the third point, along the pin axis of symmetry was estimated and was compared with that measured at that point. The third point is situated 2 mm away from the wearing surface. Table 5.1 shows a comparison of the estimates at three different sliding velocities (50 N normal load), with the experimentally obtained temperatures.

Fig. 5.3 Variation of surface bulk temperature with velocity at the normal load of 110 N estimated using (5.7), (5.14), and (5.18) [11] (present model refers to the temperature estimated using the two-point method)

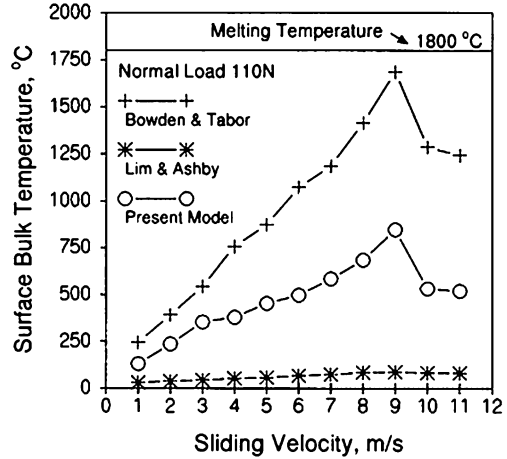


Table 5.1 Temperature at the pin axis, 2 mm away from the pin surface

Sliding velocity, m/s	Predicted temperature, °C	Measured temperature, °C
1	120	117
2	142	134
3	188	183

The estimation is seen to be in good agreement with the experimentally measured third point temperature. What has to be noted here is that the temperature measurements and validation of the two-point method were done at distances far away from the surface. This was dictated by the practical compulsion of putting thermocouples at locations, which will not be disturbed by the wear process.

In the case of Bowden and Tabor approach, although the heat partition factor evaluated by considering the ratio of thermal conductivities of the pin and the disc is close to that found in the present work (~0.133), the temperatures predicted are overestimations. The solution given by them (5.7) contains a single term that has the coefficient “B,” whereas the complete solution (5.3) for the fin (5.1) has two terms involving the coefficients A and B. The term having the coefficient “A” that is taken out by them moderates the temperature values. Thus, the absence of such a term in their solution (5.7) results at overestimation of temperatures.

In Lim and Ashby’s method, the Jaeger’s constant $\phi < 1$ ensures steady state in the disc. Here, for the present case, $\phi \gg 1$, and hence, the heat partition factor (f_p) estimated using (5.15) is found to be two orders less than that obtained by the two-point method. This leads to a gross underestimation of the surface bulk temperature as seen from Fig. 5.3.

Figure 5.4 shows the heat-partitioning factor obtained by the present two-point method to decrease with increasing sliding velocity (110 N normal load). Figure 5.5 however shows the experimentally obtained thermal conductivities [11, 16, 17] of

Fig. 5.4 Heat-partitioning factor (f_p) estimated using the two-point method (110 N normal load) [11]

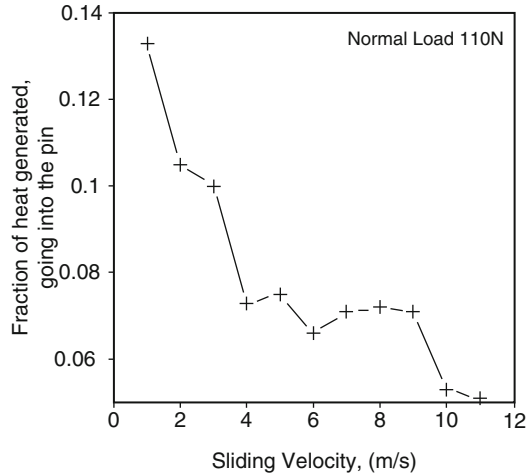
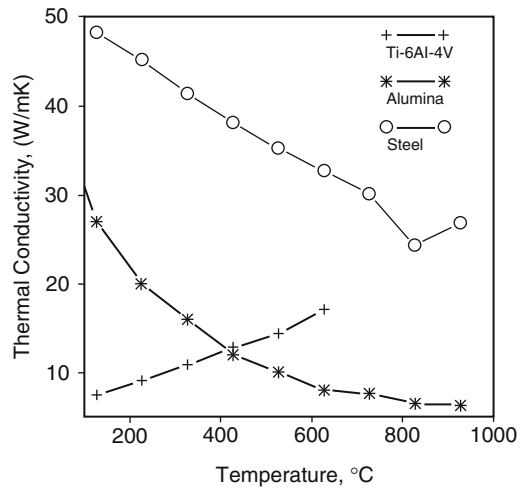
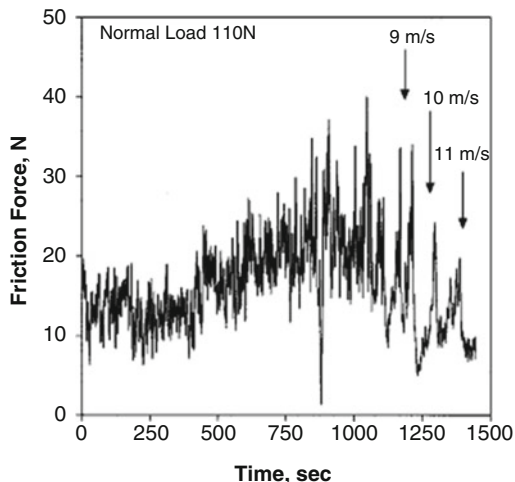


Fig. 5.5 Thermal conductivities of Ti-6Al-4V, alumina, and steel with increasing temperature [11, 16, 17]



Ti-6Al-4V to increase and that of alumina to decrease, with increasing temperature. As the pin and the disc temperatures increase with increasing sliding velocity (Fig. 5.3), the heat-partitioning factor may thus be expected to increase with increasing velocity. This would contradict the results presented in Fig. 5.4. A possible reason for this contradiction is that in the experiments, a small alumina disc (diameter 80 mm and thickness 5 mm) sits on a steel disc (diameter 200 and 15 mm thickness). The experimental schedule consisted of a stepwise increase in sliding velocity, once a steady-state temperature is reached at one velocity. Thus, as experiment progresses, the steel disc with its high thermal conductivity (Fig. 5.5)

Fig. 5.6 Variation of the friction force with time (increasing sliding velocities) at 110 N normal load [11, 16]



comes to play a major role as a heat sink, and the heat-partitioning factor is retained at a low level even at higher temperatures.

From Fig. 5.3, the estimate from the two-point method shows the temperature to reach about 775 °C at 9 m/s and then to decrease with increasing sliding velocity [11, 16]. This is in correspondence with the variation of friction force with the sliding velocity (Fig. 5.6). The friction force (Fig. 5.6) shows the friction to decrease with increasing sliding velocity as the sliding velocity exceeds 9 m/s. It is of interest to note that there are a few peaks in the friction force in this region (10–11 m/s) of speed. This may be due to one or both of the following effects [11, 16]:

- (a) Dynamic recrystallization of grains occurs, for Ti–6Al–4V [16], in the temperature range of 750–960 °C. This leads to spheroidization of acicular grains and consequent softening.
- (b) For acicular grained Ti–6Al–4V, the temperature of 970 °C [16] marks an $\alpha \rightarrow \beta$ phase transition. This transition is unstable and there is a tendency for the material to revert back to the α -phase cyclically with time. The periodic peaks in the friction trace reflect the unstable transition where the peaks correspond to the α -phase, while the low-friction level corresponds to the soft β -phase. The β -phase provides easy shear and causes low friction. This phenomenon gets initiated when the surface temperature reaches at ~900 °C, a temperature close to that estimated by the two-point method at 9 m/s sliding speed.

Figure 5.7a shows hairline cracks on the surface of the Ti–6Al–4V pin surface, caused due to the drastic lowering of the temperature at 110 N load and 10 m/s. Figure 5.7b shows melting on the pin surface at 110 N load and 11 m/s. It may be surmised that when there is surface melting, the coefficient of friction is much decreased (Fig. 5.6) [16, 18].

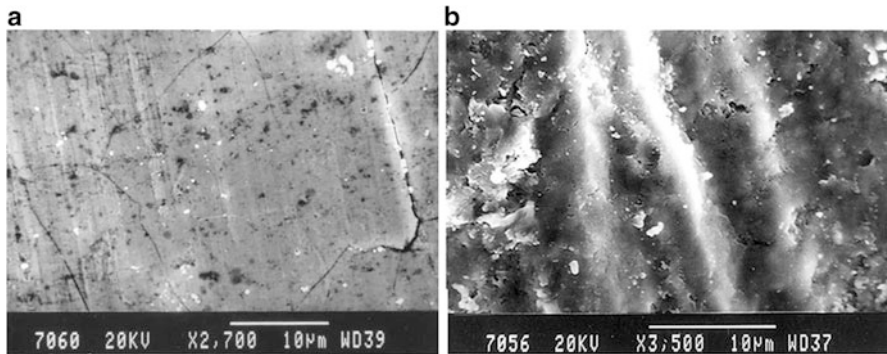


Fig. 5.7 (a) Hairline cracks on the surface of the Ti–6Al–4V pin surface, caused due to the lowering of the temperature at 110 N load and 10 m/s. (b) Melting on the pin surface at 110 N load and 11 m/s

7 Summary

Estimation of interface temperature of sliding surfaces is important as it plays an influential role in defining the tribological behavior of the sliding surfaces. Temperature estimations based on measurements are closer to the real values when compared to those estimated using other methods that are based on ab initio estimations, which have many parametric uncertainties.

References

1. Bhushan B (1998) Principles and applications of tribology. Wiley, New York, pp 431–478
2. Chen H, Alpas AT (2000) Wear 246:106–116
3. Wilson S, Alpas AT (1997) Wear 212:1–49
4. Yellup JM (1997) Comp Sci Technol 57:415–435
5. Blok M (1937) Gen Disn Lubn Inst Mech Eng 2:222–235
6. Jaeger JC (1942) J Proc Roy Soc New South Wales (Australia) 76:203–224
7. Carslaw HC, Jaeger JC (1959) Conduction of heat in solids, 2nd edn. Clarendon Press, Oxford
8. Lim SC, Ashby MF (1987) Acta Metallurgica 35(1):1–24
9. Bowden FP, Tabor D (1950) The friction and lubrication of solids, part I. Oxford Press, Cambridge
10. Ashby MF, Abulawi J, Kong HS (1991) Tribol Trans 34(4):577–587
11. Singh RA, Narasimham GSVL, Biswas SK (2002) Tribol Lett 12(4):203–207
12. Churchill SW, Bernstein M (1977) Trans ASME Ser C J Heat Transfer 99(2):300–306
13. Schlichting H (1979) Boundary layer theory, 7th edn. McGraw Hill Book Co., New York
14. Giedt WH (1957) Principles of engineering heat transfer. D. Vom Nostrand Company Inc, New York
15. Barber JR (1969) Proc Roy Soc A312:381–394

16. Arvind Singh R (2002) Sliding wear of metals: an approach based on strain rate response theory and mechanically mixed layer, Ph.D. Thesis, Department of Mechanical Engineering, Indian Institute of Science, Bangalore, India
17. Boyer R, Welsch G, Collings EW (1994) Materials properties handbook: Titanium Alloys, ASM International, Materials Park, Ohio
18. Biswas SK (2002) Proc Instn Mech Engrs Part J: J Eng Tribol 216:357–369

Questions and Answers

1. Is it really necessary to undertake temperature measurements in order to estimate surface bulk temperature of a body (e.g., pin) sliding against a counterface (e.g., disc)?

Yes, it is necessary to undertake temperature measurements in order to estimate surface bulk temperature of a body sliding against a counterface. Temperature estimations based on measurements (e.g., two-point method) are closer to the real values when compared to those estimated using other methods that are based on ab initio estimations (e.g., Bowden and Tabor, Lim and Ashby methods), which have many parametric uncertainties such as fraction of heat going into the pin. Further, all the three active processes of conduction, convection, and radiation should be considered to arrive at realistic temperature values.

2. In the case of the two-point method that estimates surface bulk temperature based on temperature measurements, should the value of the fraction of heat going into the pin (f_p) be known a priori to estimate the surface temperature?

No, it is not essential to know the value of f_p in order to estimate the surface temperature using the two-point method. However, f_p can be estimated as a ratio of the heat flowing into the pin (Q_p) and that generated (Q_g) at the interface (5.25).

3. Methods based on ab initio estimations (e.g., Bowden and Tabor, Lim and Ashby methods) estimate surface temperatures, whose values are either overestimates or underestimates (e.g., Sect. 6). What are the reasons for such occurrences?

Estimated surface temperature values show departure from realistic temperature values when methods based on ab initio estimations are used.

Considering the case study (Sect. 6), the values of the temperatures predicted by Bowden and Tabor approach are overestimates. The solution given by them (5.7) contains a single term that has the coefficient “B,” whereas the complete solution (5.3) for the fin (5.1) has two terms involving the coefficients A and B. The term having the coefficient “A” that is taken out by them moderates the temperature values. Thus, the absence of such a term in their solution (5.7) results at overestimation of temperatures. On the contrary, the surface temperature values predicted by Lim and Ashby’s approach shows lower values of temperatures, owing to the fact that their method gives a very low estimation of the fraction of heat going into the pin (f_p).

4. With increase in load and/or speed between two bodies sliding in relative motion, will the surface temperature during the steady-state sliding always show an increase?

During sliding, increase in load and/or speed increases the surface temperature. However, if the initial rise in temperature causes microstructural changes or tribo-chemical reactions, subsequently the surface temperature may decrease during the steady-state sliding. As an example, from the case study (Sect. 6), it could be seen that temperature drops when the sliding speed exceeds 9 m/s (Fig. 5.3) due to the decrease in friction (Fig. 5.6) caused by metallurgical transformations/microstructural changes.

5. In the case study of Ti–6Al–4V titanium alloy pin sliding against an alumina disc, presented in Sect. 6, why does the heat-partitioning factor decrease with the increase in sliding speeds (Fig. 5.4)?

In the experimental setup, the counterface alumina disc was fixed onto a steel disc. The experimental schedule consisted of a stepwise increase in sliding velocity, once a steady-state temperature was reached at one velocity. Thus, as the experiment progressed, the steel disc with its high thermal conductivity played a major role as a heat sink, and thereby the heat-partitioning factor remained at low levels. This example shows that it is important to consider the entire experimental setup/apparatus in understanding and estimating surface temperatures.

Part II
Tribology of Engineering Materials

Chapter 6

Tribology of Metals and Alloys

Sudeep P. Ingole

Abstract The surface properties of metals and alloys become important when these materials are used especially for tribological applications. Some basic concepts involved during wear of metals and alloys are briefly discussed in this chapter. Delamination theory of adhesive wear which is dominating wear mechanism for most metals and alloys is discussed. Most of the tribological joints are exposed to environmental oxygen when used in atmospheric conditions. Oxidation becomes problematic for such and high-temperature sliding applications when oxygen source is readily available at the interface. The debris formation mechanism and oxidation during sliding are included in this chapter. Information on oxidation and tribological behavior of 60NiTi is reviewed as it is a potential alloy for tribolelement applications. A brief description on phase transformation and high-temperature tribology of metallic materials is also included. The wear of materials at the interface depends on the interfacial strength of the sliding materials. In high-temperature oxidative wear, wear performance can be determined by the type of oxides formed on the sliding surfaces.

1 Introduction

Tribology has contributed to human culture as it evolved alongside of it; however, its formal study was not conducted for centuries. Sir Leonardo da Vinci's early work provided directions to the scientific study of tribology. Tribology is described in various sources such as "*The science of mechanisms of friction, lubrication, and wear of interacting surfaces that are in relative motion*" [1]. In another source, it is described as "*a branch of mechanical engineering that deals with the design, friction, wear, and lubrication of interacting surfaces (as bodily joints) in relative motion*" [2].

S.P. Ingole, Ph.D. (✉)
Curt G. Joa Inc., Sheboygan Falls, WI 53085, USA
e-mail: singole@joa.com

It is also described as “*the branch of engineering that deals with the interaction of surfaces in relative motion (as in bearings or gears): their design and friction and wear and lubrication*” [3]. In general, the purpose of tribological study is to design surfaces to reduce or regulate the friction. Despite extensive research efforts that have been made for decades, even today, the phenomenon of friction is not completely understood. It is empirically established that frictional force is directly proportional to applied load and the constant of proportionality is known as the coefficient of friction and represented as

$$\mu = \frac{F}{P} \quad (6.1)$$

where “ μ ” is the coefficient of friction, “ F ” is the frictional force, and “ P ” is the applied load. Experimental methods always face some difficulty understanding friction due to surface features such as asperities, surface roughness, and the scale of measurement such as micrometer length scale or nanometer length scale. Recent development in metrological techniques such as the atomic force microscope [4, 5], the surface force apparatus [6], and the quartz crystal balance [7, 8] enabled us to study surface forces at atomic length scales which are responsible for friction at that level.

2 Wear of Metallic Materials

Wear is defined as a process of material removal from the solid surface by means of mechanical, thermal, or chemical action. Writing with pencil on paper is an example of useful wear, whereas wear of machines is not useful wear. Wear takes place on the surface by one or combination of mechanisms like adhesion, sliding (delamination), fretting, abrasion, erosion, fatigue, or corrosion. Most of these types of wear involve the adhesion which is responsible for the surface damage. Among metals and alloys, adhesive wear is the most common. During sliding, metal from one sliding surface is transferred to another surface due to adhesive forces. This transfer stays on the surface or detaches from the surface in the form of debris [9].

2.1 Adhesive Wear Mechanism

The surface damage during relative motion of two surfaces could be due to the bombardment of one surface on the other, or due to the reaction between two surfaces, or with the surroundings. When two surfaces slide together, shear takes place at the junction. The shear strength of the interface and the type of metals involved in sliding determine the possibility of fragmentation. Different possibilities for shear to occur are [10]:

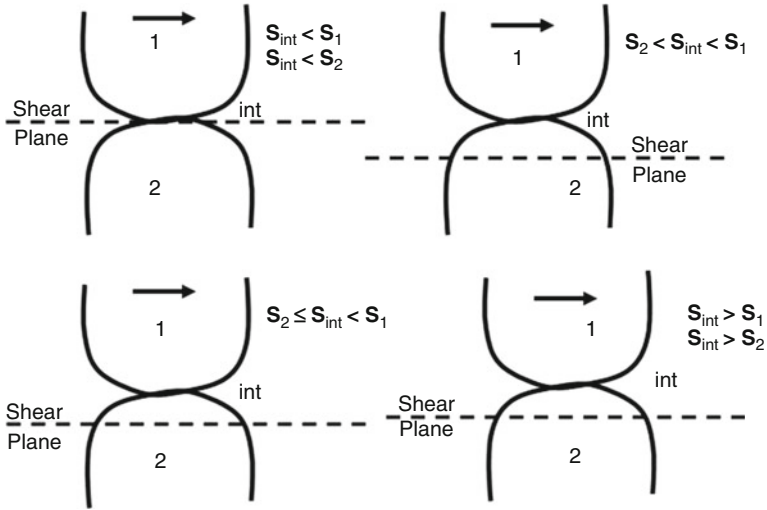


Fig. 6.1 Wear of metals due to shear [10]

- When the interface is slightly weaker than both the mating surfaces, shear occurs at the interface.
- When the interface is stronger than one of the mating surface and weaker than the other, shear occurs within the softer metal, and the detached fragments adhere to the harder sliding metal.
- When the interface is stronger than that of the mating surface but slightly harder than the other, severe shear occurs on the softer metal and a significant amount of metal transfers to the harder metal. The shear of the harder metals also occurs occasionally.
- When the interface is significantly stronger than both the sliding metals, shear occurs at some distance from the interface. In such a situation, transfer of metals occurs from both the surfaces and the surface damage encountered in this situation increases.

The schematic of all these possibilities is shown in Fig. 6.1 [10].

The delamination theory also explains adhesive wear [11, 12]. Adhesive wear occurs when cracks formed under the surface propagate under continuous loading conditions. These cracks upon reaching the surface lead to surface damage. During continuous sliding the dislocations pile up at a finite distance from the surface. As the sliding goes on, voids are formed at the pileup region. The rate of void formation is more if the sliding surface is an alloy with a hard second phase for dislocations to pile against. When there are large secondary-phase particles in the metal, voids are formed by a plastic flow of matrix around hard particles. Voids cluster together and result in a crack, which then propagate parallel to the surface and ultimately fragment the surface. The separated particle in this fashion is a platelike structure. The void formation at a distance from the surface is illustrated in Fig. 6.2 [11].

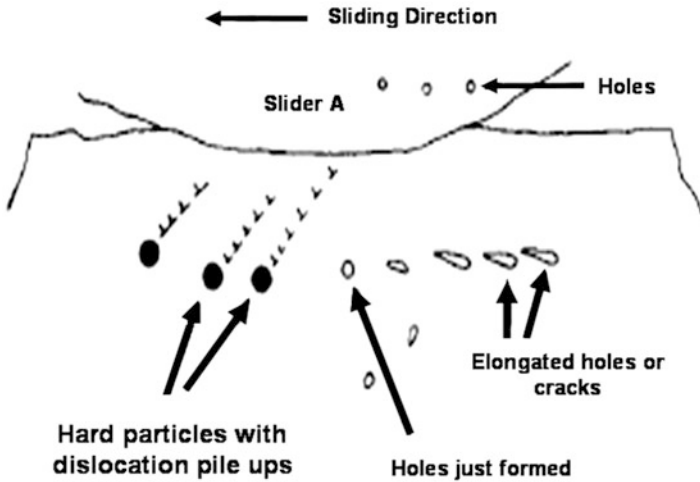


Fig. 6.2 Formation of debris by shear deformation [11]

Wear volume during adhesive wear can be expressed quantitatively [13, 14], i.e., the amount of wear is dependent on load, sliding distance, and hardness of the surface. The wear volume is given by

$$V = \frac{cLx}{p} \quad (6.2)$$

where “ c ” is a nondimensional constant, “ L ” is the load, “ x ” is the sliding distance, and “ p ” is the hardness of the surface.

3 Surface Reaction During Sliding: Tribo-oxidation

Frictional heat or external heat can affect the sliding wear of metallic materials significantly. The temperature rise facilitates the oxidation of the sliding surfaces. This can reduce the wear rate due to the transformation of metallic debris to oxide debris [15]. In metals such as Cu, Ni, Fe, Co, W, Mo, and Zn, surface oxide films form and grow as crystalline layers. However, in the case of Al, Si, Cr, Ge, Nb, and Ta, oxidation initially takes place forming amorphous films, and then these films transfer into crystalline depending upon temperature and time [16–20]. In aluminum alloys, an amorphous alumina oxide film can be thermodynamically more stable than the corresponding crystalline γ - Al_2O_3 film up to a certain critical oxide-film thickness. This amorphous film can also be more stable even for higher oxidation temperatures [17].

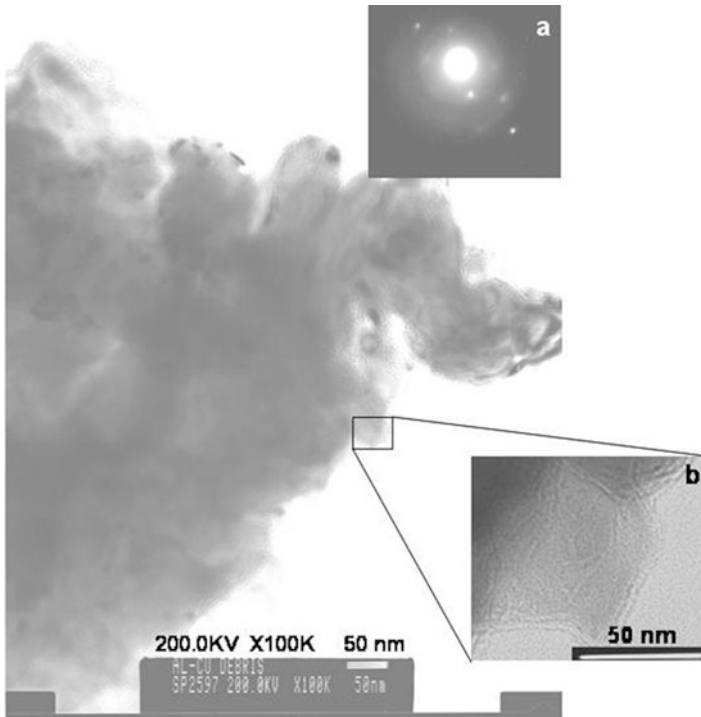


Fig. 6.3 TEM micrograph of Al-Cu debris [22]

3.1 Case Study: Aluminum-Copper Sliding

During sliding of Al and Cu in air, copper oxidizes to form a crystalline copper oxide layer, whereas aluminum forms amorphous and converts to crystalline aluminum oxide if sufficient time is permitted. Crystalline alumina can present on the surface from as-received sample or can form during the beginning of the sliding. The oxidation potential of Cu is $-0.34 \text{ E}^\circ\text{V}$ ($\text{Cu} \rightarrow \text{Cu}^{2+} + 2\text{e}^-$) and that of Al is $1.66 \text{ E}^\circ\text{V}$ ($\text{Al} \rightarrow \text{Al}^{3+} + 3\text{e}^-$) [21]. Copper oxidizes at a lower rate than aluminum. Initially, both oxide layers wear out. As wear continues, pure metals underneath those oxide layers expose to the atmosphere. As soon as the exposure of pure metals to the atmosphere, further oxidation commences. For Al, the initial oxide layer formed on the surface is amorphous alumina. Without sufficient time to crystallize, the amorphous alumina will be removed during sliding as amorphous debris. The TEM analysis of such debris formed during sliding of Cu-Al system showed the amorphous phase (Fig. 6.3) [22].

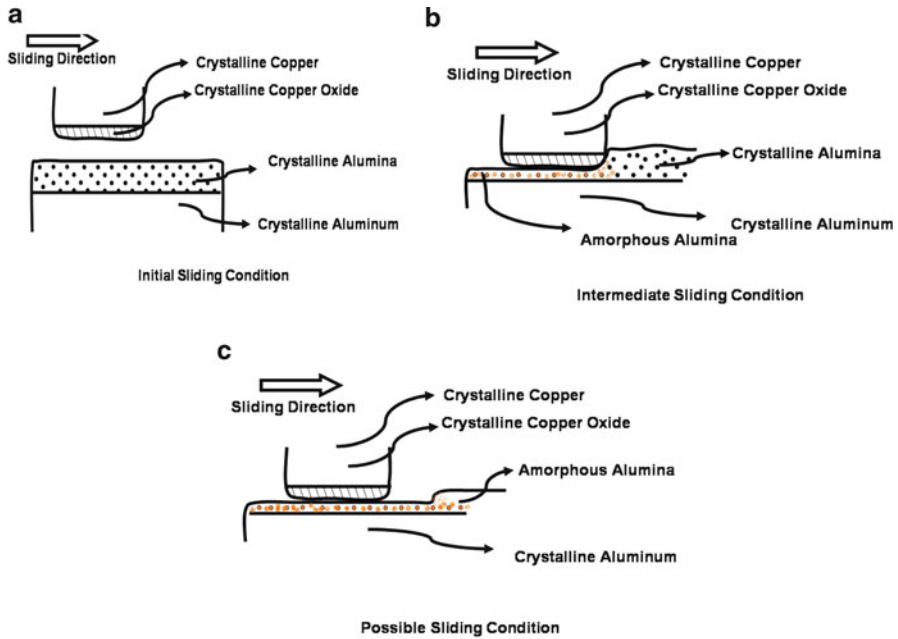


Fig. 6.4 Schematic of the tribo-oxidation wear process in Al-Cu sliding. (a) Pre-oxidation, (b) removal of initial oxide layer, (c) removal of newly formed oxide layer

This phenomenon of the tribo-oxidation wear is represented schematically in Fig. 6.4. There are three steps in this process: pre-oxidation, removal of the initial oxide layer, and removal of the newly formed oxide layer. Pre-oxidation is the natural oxidation of the surface of mating metals.

3.2 Oxidation and Tribological Properties of 60NiTi [23]

Oxidation and tribological behavior of two Ni-Ti alloys was recently reviewed [23]. Ni-Ti alloy with 55 wt% of Ni (50 at.% of Ni) has shape memory effect, superelasticity, and very good corrosion resistance and is recognized as 55NiTi. Another Ni-Ti alloy with 60 wt% of Ni (55 at.% of Ni) shows shape memory effect but has higher brittleness and is recognized as 60NiTi. 60NiTi is a promising material for tribological applications such as tribo-elements, bearings, gears, or tools. NASA's Engineering and Safety Center (NESC) is promoting 60NiTi as it showed shockproof, corrosion-resistant properties that can be used for aerospace bearing applications [24].

55NiTi has been studied for its oxidation behavior [25, 26]. Oxidation behavior of 60NiTi can be comparable to nitinol. At room temperature and 450 °C with low oxygen pressure 10^{-4} Torr, Ni did not oxidize but Ti was oxidized to TiO_2 [25].

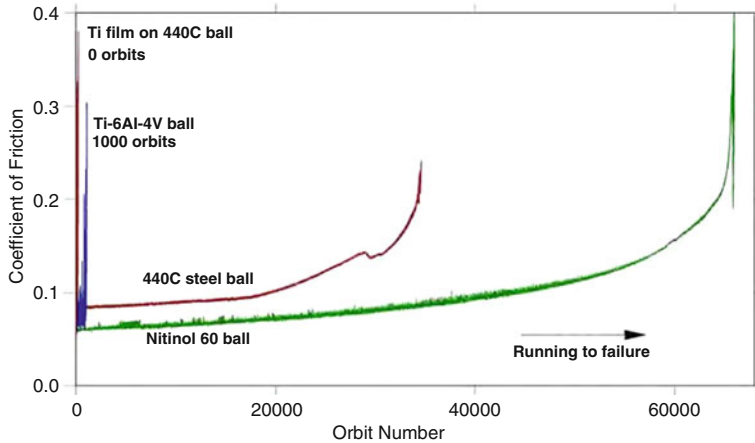


Fig. 6.5 Coefficient of friction of different bearing ball against 440C plate under Pennzane 2001A oil lubrication [29]

High-temperature oxidation (500 and 600 °C) of this alloy producing Ni-free zone with protective oxide coating of titanium oxide means Ni did not oxidize [26]. 60NiTi has high Ni content which might provide additional resistance to oxidation. NiTi alloys can be utilized for room and moderate temperature application as it showed good oxidation resistance up to 600 °C.

Study was conducted for tribological feasibility of 60NiTi for bearing applications in space using Spiral Orbit Tribometer (SOT) [27–31]. Powder metallurgical procedures were used to prepare the 60NiTi ball. In SOT the bearing ball slid between two parallel rotating disks. 60NiTi bearing ball was tested against 440C plates under boundary lubricated conditions using Pennzane 2001A oil. Under these conditions 60NiTi friction behavior (lower friction than 440C) was comparable to the high-performance 440C bearing balls which showed potential for these applications. No galling but mild abrasive wear on the tested was observed when the surface of 60NiTi ball was operated well beyond the lubricant life of the oil [27]. Tribological performance is compared with several other bearing materials in Fig. 6.5 which is adopted from the NASA/TM—2011-217105. The superiority of 60NiTi is evident from these results.

In our study of a typical dry sliding of thermally sprayed nitinol coating against 52100 bearing ball [32], it was observed that the friction was suddenly reduced after sometime during the test. This might be the indication of phase transformation of this shape memory alloy. The coefficient of friction was found to be very high (Fig. 6.6a) [32]. This behavior could limit nitinol's applications as tribo-element.

The topological study of the worn surface of nitinol depicts grain boundary failure. The hard Ni_3Ti phases along the grain boundary [33] might have influenced this failure. The debris generated was very fine due the brittle fracture of these particles (Fig. 6.6b) [32].

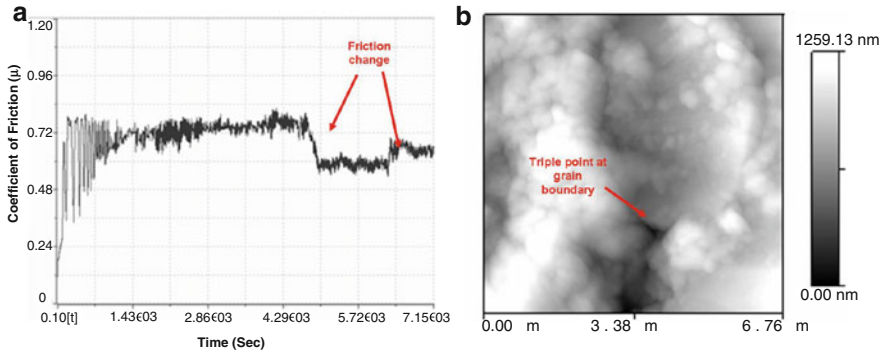


Fig. 6.6 (a) Friction coefficient with time plot for nitinol in dry test and (b) an atomic force microscopic image of worn nitinol surface [32]

4 Interface Phenomenon During Sliding of Metallic Materials: Debris Formation

The material behavior and the surface changes at the interface during the sliding of two different surfaces are a very complex process so as the debris formation. Materials used in tribological applications are mostly elastoplastic in nature. Due to continuous load and frictional forces on the surface, these materials deform plastically. The sliding also increases the interfacial temperature and is sudden at the asperities. It can reach the melting point of the mating surfaces. This temperature is termed as flash temperature [10, 34, 35]. When two metallic surfaces slide, deformation at the interface occurs. The severity of the deformation depends on the lubricating condition such as lubricated or unduplicated. The deformation is avoided only in ideal hydrodynamic conditions [36]. This results in plastic strains and the strain gradients near the severely deformed interfaces. The deformation is very well observed most of the time by visual observation in a form of wear scar. The strain decreases exponentially under the sliding surface. Therefore, at the sliding interface, the shear strain is very high and it diminishes rapidly under the sliding surface [36].

Hardness of the materials deformed or fragmented at the interface can be harder or softer compared to the interfaces. If “h” be the hardness of the layer material and “H” be the hardness of the highly deformed materials, the topology of the deformed surfaces or debris can be predicted. Debris flakes are generated when $h/H \leq 1$ and wear scar will be rough, whereas irregular debris formed when $h/H \geq 1$ and wear scar will be smooth [36, 37].

There are different possibilities for the debris particle to follow once it separates from the parent materials. These possibilities are explained in Fig. 6.7a. The detached particle can adhere to the other surface by adhesive interaction which is represented by “a.” It can react with the surrounding atmosphere and get oxidized

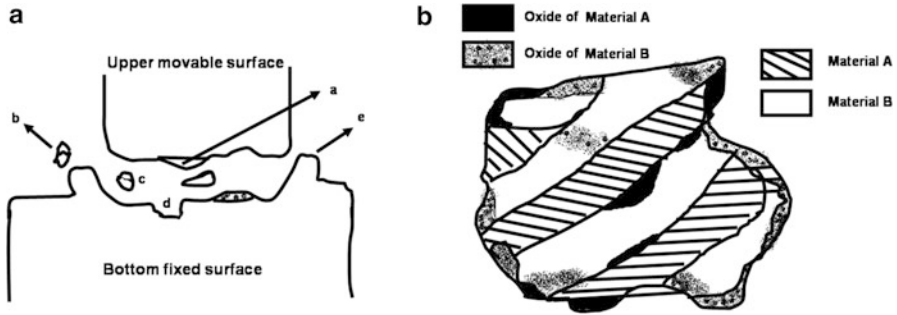


Fig. 6.7 Debris formation (a) possibilities of material behavior during sliding (b) schematic of debris particle formed during sliding

depending upon its reactivity with oxygen; this is represented by “b.” It can also roll in between two sliding surfaces as a third body which is represented by “c.” If the third-body rolling debris particle is hard, it will damage the softer surface and form groove on it which is represented by “d.” The deformation of the mating surface that can occur during sliding is represented by “e.” The debris formed during this process has a very complex structure. Figure 6.7b shows the schematic of the debris particle.

5 Phase Transformation During Sliding

Structural as well as chemical changes occur between the interfaces of two sliding bodies. Stable binary phases can form when alloying elements of binary alloys satisfy the criteria [38] given by the Hume–Rothery rules, i.e., (a) the ratio of atomic radii of constituent should not exceed 15 %, (b) the crystal structure of both the metals should be the same, (c) their electronegativity should be close, and (d) two metal ions must have the same valance. Most of the binary alloy system follows these rules.

On the other hand, the atomic radii of two constituent metals are important parameter that defines the amorphous structure [39, 40]. The difference between radii should be more than 15 %. Therefore, most of the binary alloys, which follow the Hume–Rothery rules, cannot be solidified as amorphous structures. These conventionally solidified alloys (in general, which follow the Hume–Rothery rules) show the long-range crystal structures. If this crystal structure is broken below the crystallization temperature, the alloys retain their metastable structure. Mechanical milling and mechanical alloying can produce such structures [41–47]. In these processes, the phase change occurs by interdiffusion and accumulation of lattice defects such as vacancies. During milling, amorphization can take place if the stored energy in the material exceeds the energy of the amorphous phase [48]. Mechanical deformation assists in interdiffusion to occur and subsequently to

form the homogeneous amorphous alloy [49]. The experimental conditions in mechanical milling are in many ways analogous to the sliding of two surfaces. Sliding of two metals and alloys provides all the necessary experimental parameters and driving forces for amorphization to occur such as plastic deformation, temperature rise, and the accumulation of the lattice defects. Temperature rise which is the driving force for the diffusion to occur speeds up the solid reaction and phase changes by interdiffusion between sliding metals; this mechanism is explained for the formation of an amorphous alloy from pure crystalline metals [50, 51]. Another example is the rail and wheel sliding. During the skid along the rail, the wheel material close to the contact surface undergoes excessive mechanical and thermal events. The frictional heat generated raises the temperature up to approximately 800–1,000 °C; this causes phase transformations in the wheel steel [52].

Material polishing produces a thin film on the surface that is different from its parent material. In the tribology community, this layer is known as the “Beilby Layer” [53]. This layer is amorphous and formed due to the rapid solidification of locally melted asperities [10, 54]. It is also possible that during sliding the nanocrystalline materials could develop [55, 56]. These experimental observations of nanocrystalline and amorphous material formation during sliding were also validated with Molecular Dynamics (MD) simulations [57–60]. Sliding of annealed nanocrystalline Zr–Ti–Cu–Ni–Be bulk metallic glass (BMG) in vacuum and in air produced a work-softened layer where the plastic deformation was highest and formed the amorphous layer. The debris formed during this process was re-amorphized [59].

Let’s consider another case of Cr and Fe; both crystals have body center cubic (BCC) structures. The bond lengths of Cr and Fe are 0.24980 and 0.24823 nm, respectively [61]. Fe–Cr is a typical binary alloy which, according to Hume–Rothery rules [53], forms a substitutional solid solution. Although this alloy system is not readily glass forming (RGF), the middle composition range formed an amorphous state by thermal evaporation at room temperature using very low deposition rates [62]. During sliding, the rise in temperature at interface will be the driving force for the interdiffusion of Fe and Cr. This diffusion can occur on one of the mating surfaces, on both surfaces, or on the debris after they detach from their parent surfaces. Plastic deformation which occurred due to the continuously applied load during sliding is another influencing factor for amorphization to occur.

6 Elevated Temperature Tribology of Metallic Materials

Elevated temperature tribology of metallic materials is even complicated than their tribological behavior at room temperature. These complications are due to more favorable thermodynamics conditions occurring particularly for oxidation of sliding partners. Excessive oxidation at elevated temperature results in loss of surface metals when the oxide formed on the surface is not adhesive to the surface and result in spalling. To improve the adhesiveness of the oxide, the oxide formed on

the surface is believed to be ductile. For example, the wear resistance of the Inconel 617 and Stellite 6 alloys at 750 °C is improved due to adhesive oxides growing slowly on Inconel 617 and Stellite 6 alloys. These oxides sustain the wear action and reduce spalling [63]. Some of the key points that contribute to high-temperature tribology are mentioned here [64]:

- Change in mechanical properties at elevated temperature coupled with the oxidation affects the friction behavior at the interface which will have varying effects at different temperatures.
- Tribo-chemistry at elevated temperature that is affected by other phenomenon such as diffusion between sliding surfaces and phase transformations.
- The performance of these sliding materials which is governed by mechanical properties of reaction products formed at elevated temperature, the surface layers formed, and the actual response of the subsurface materials to the applied forces (i.e., deformation and fracture).
- Geometry change at the sliding interface (scar formation) with possible wear phenomenon that took place at the interface.

7 Conclusions

The delamination theory can explain the wear and possibility of debris formation. Formation and type of oxide (amorphous or crystalline) on the surface of the sliding metals and alloys can influence the nature of debris formed. Whereas their adhesiveness to the surface on which they are formed influence further wear process, debris formed could be a complex composition than any sliding counterparts. Same as in milling, during sliding of metals and alloys, amorphization can take place if the stored energy in the material exceeds the energy of the amorphous phase.

References

1. In The American Heritage[®] Dictionary of the English Language, Houghton Mifflin Company
2. In Merriam-Webster Medical Dictionary© 2002, Merriam-Webster, Inc
3. In WordNet[®] 2.0 © 2003, Princeton University
4. Binnig G et al (1982) Surface studies by scanning tunneling microscopy. *Phys Rev Lett* 49(1):57–61
5. Binnig G, Quate CF, Gerber C (1986) Atomic force microscope. *Phys Rev Lett* 56(9):930–933
6. Israelachvili JN (1989) Techniques for direct measurements of forces between surfaces in liquids at the atomic scale. *Chemtracts Anal Phys Chem* 1:1–12
7. Krim J, Widom A (1988) Damping of a crystal oscillator by an adsorbed monolayer and its relation to interfacial viscosity. *Phys Rev B* 38(17):12184–12189
8. Krim J, Solina DH, Chiarello R (1991) Nanotribology of a Kr monolayer: a quartz-crystal microbalance study of atomic-scale friction. *Phys Rev Lett* 66(2):181–184
9. Rabinowicz E (1995) Friction and lubrication of materials. Wiley, New York

10. Bowden FP, Tabor D (1964) *The friction and lubrication of solids*, vol I and II. Clarendon Press, Oxford
11. Suh NP (1973) The delamination theory of wear. *Wear* 25(1):111–124
12. Suh NP (1986) *Tribophysics*. Printice-Hall, Englewood Cliffs, NJ
13. Holm R (1946) *Electric contacts*. Almqvist and Wiksells, Stockholm
14. Archard J (1953) Contact and rubbing of flat surfaces. *J Appl Phys* 24(8):981–988
15. Stott FH (1998) The role of oxidation in the wear of alloys. *Tribol Int* 31(1–3):61–71
16. Fehlner FP (1986) Low temperature oxidation, the role of vitreous oxides. OSTI ID: 5328041. Retrieved from <http://www.osti.gov/scitech/servlets/purl/5328041>
17. Jeurgens L et al (2000) Thermodynamic stability of amorphous oxide films on metals: application to aluminum oxide films on aluminum substrates. *Phys Rev B* 62(7):4707
18. Doherty P, Davis R (1963) Direct observation of the oxidation of Aluminum single crystal surfaces. *J Appl Phys* 34(3):619–628
19. Eldridge J et al (1988) Thermal oxidation of single-crystal aluminum at 550 °C. *Oxidation Metals* 30(5):301–328
20. Snijders P, Jeurgens L, Sloof W (2002) Structure of thin aluminium-oxide films determined from valence band spectra measured using XPS. *Surf Sci* 496(1):97–109
21. Francis E (1999) Standard oxidation potentials. ©1998 [cited 2012 Oct 30, 2012]; Accessed <http://dl.clackamas.cc.or.us/ch105-09/standard.htm>
22. Ingole SP (2005) Nanotribological characterization of dynamic surfaces. University of Alaska Fairbanks, Fairbanks, AK, USA
23. Ingole S (2013) 60NiTi alloy for tribological and biomedical surface engineering applications. *JOM* 65(6):792–798. doi:10.1007/s11837-013-0610-7
24. Industry updates (2011) *J Fail Anal Prev* 11(6):645–653. doi:10.1007/s11668-011-9515-3
25. Chan CM, Trigwell S, Duerig T (2004) Oxidation of an NiTi alloy. *Surf Interface Anal* 15(6):349–354
26. Firstov G et al (2002) Surface oxidation of NiTi shape memory alloy. *Biomaterials* 23(24):4863–4871
27. DellaCorte C et al (2009) Intermetallic Nickel–Titanium alloys for oil-lubricated bearing applications. NASA, Cleveland, OH
28. DellaCorte C, Glennon GN (2012) Ball bearings comprising nickel-titanium and methods of manufacture thereof, in Google Patents, The United States of America as represented by the National Aeronautics and Space Administration, Abbott Ball Company, USA
29. DellaCorte C et al (2011) Resilient and corrosion-proof rolling element bearings made from superelastic Ni-Ti alloys for aerospace mechanism applications. August 2011, NASA/TM—2011-217105, http://www.ntrs.nasa.gov/archive/nasa/casi.ntrs.nasa.gov/20110016524_2011017534.pdf
30. Pepper SV et al (2009) NITINOL 60 as a material for spacecraft triboelements. 2009. Proc. ‘13th European Space Mechanisms and Tribology Symposium – ESMATS 2009’, Vienna, Austria, 23–25 September 2009 (ESA SP-670, July 2009), <http://www.esmats.eu/esmatspapers/pastpapers/pdfs/2009/pepper.pdf>
31. Pepper SV, DellaCorte C, Glennon G (2010) Lubrication of Nitinol 60, June 2010, NASA/TM-2010: 215331-1-8, <http://www.grc.nasa.gov/WWW/StructuresMaterials/TribMech/highlights/documents/additional/TM-2010-216331.pdf>
32. Ingole S, Liang H, Mohanty P (2005) Tribology characteristics of thermal sprayed NiTi coatings. In presented at 4th ASM international surface engineering congress and 19th international conference on surface modification technologies. ASM International, Saint Paul
33. Stanford MK, Thomas F, DellaCorte C (2012) Processing issues for preliminary melts of the intermetallic compound 60-NITINOL. Nov 01, 2012, NASA/TM-2012-216044; E-18479; GRC-E-DAA-TN4035, Doc ID: 20130000580, http://ntrs.nasa.gov/archive/nasa/casi.ntrs.nasa.gov/20130000580_2012018813.pdf
34. Jaeger J (1942) Moving sources of heat and the temperature of sliding contacts. in. *J Proc Roy Soc NSW* 76:203–224

35. Cook N, Bhushan B (1973) Sliding surface interface temperatures (solid–solid interface temperature rise during sliding from model with surface topography statistics, frictional conditions, surface hardness and thermal parameters). *ASME Trans Ser F J Lubr Technol* 95:59–64
36. Rigney D et al (1986) Low energy dislocation structures caused by sliding and by particle impact. *Mater Sci Eng* 81:409–425
37. Don J, Sun TC, Rigney DA (1983) Friction and wear of Cu–Be and dispersion-hardened copper systems. *Wear* 91(2):191–199
38. Hume-Rothery W (1931) *The metallic state*. Oxford University Press, London
39. Davies H, Luborsky F (1983) *Amorphous metallic alloys*. Butterworths, London, pp 8–25
40. Giessen BC (1982) In: *Proceedings of 4th international conference on rapidly quenched metals*, Japan Institute of Metals, Sendai
41. Xia S et al (1999) Formation of disordered structures in Cr–Fe alloy by mechanical milling. *J Phys Condens Matter* 5(17):2729
42. Gaffet E et al (1988) Ball milling amorphization mechanism of Ni–Zr alloys. *J Less Common Metals* 145:251–260
43. Hellstern E, Schultz L (1988) Formation and properties of mechanically alloyed amorphous Fe–Zr. *Mater Sci Eng* 97:39–42
44. Koch C et al (1983) Preparation of “amorphous” Ni₆₀Nb₄₀ by mechanical alloying. *Appl Phys Lett* 43(11):1017–1019
45. Thompson J, Politis C (1987) Formation of amorphous Ti–Pd alloys by mechanical alloying methods. *EPL (Europhys Lett)* 3(2):199
46. Dolgin B et al (1986) Mechanical alloying of Ni, CO, and Fe with Ti. Formation of an amorphous phase. *J Non-Crystalline Solids* 87(3):281–289
47. Politis C, Johnson W (1986) Preparation of amorphous Ti_{1-x}Cu_x (0.10 ≤ x ≤ 0.87) by mechanical alloying. *J Appl Phys* 60(3):1147–1151
48. Schwarz RB, Koch CC (1986) Formation of amorphous alloys by the mechanical alloying of crystalline powders of pure metals and powders of intermetallics. *Appl Phys Lett* 49(3):146–148
49. Atzmon M et al (1984) Formation and growth of amorphous phases by solid-state reaction in elemental composites prepared by cold working. *Appl Phys Lett* 45(10):1052–1053
50. Schwarz R, Johnson W (1983) Formation of an amorphous alloy by solid-state reaction of the pure polycrystalline metals. *Phys Rev Lett* 51(5):415–418
51. Johnson WL (1986) Thermodynamic and kinetic aspects of the crystal to glass transformation in metallic materials. *Prog Mater Sci* 30(2):81–134
52. Ahlström J, Karlsson B (2002) Modelling of heat conduction and phase transformations during sliding of railway wheels. *Wear* 253(1–2):291–300
53. Beilby SG (1921) *Aggregation and flow of solids*. Macmillan, London
54. Bowden F, Hughes T (1937) Physical properties of surfaces. IV. Polishing, surface flow and the formation of the Beilby layer. *Proc Roy Soc Lon Ser A Math Phys Sci* 160(903):575–587
55. Rigney D, Hammerberg J (1999) Mechanical mixing and the development of nanocrystalline material during the sliding of metals. *Proc TMS Fall Meet* 465–474
56. Ganapathi S et al (1990) A comparative study of the nanocrystalline material produced by sliding wear and inert gas condensation. In *MRS proceedings*. Cambridge University Press, Cambridge
57. Rigney D et al (2003) Examples of structural evolution during sliding and shear of ductile materials. *Scripta Materialia* 49(10):977–983
58. Kim HJ, Karthikeyan S, Rigney D (2009) A simulation study of the mixing, atomic flow and velocity profiles of crystalline materials during sliding. *Wear* 267(5–8):1130–1136
59. Fu XY, Rigney D, Falk M (2003) Sliding and deformation of metallic glass: experiments and MD simulations. *J Non-Crystalline Solids* 317(1):206–214
60. Heilmann P et al (1983) Sliding wear and transfer. *Wear* 91(2):171–190

61. Weast R, Selby S, Hodgman C (1965/1966) Handbook of chemistry and physics, 46th edn. The Chemical Rubber Co, Cleveland, OH
62. Xia SK, Saitovitch EB (1994) Formation of an amorphous phase in $\text{Cr}(1-x)\text{FeX}$ films obtained by thermal evaporation. *Phys Rev B* 49(5):927
63. Birol Y (2010) High temperature sliding wear behaviour of Inconel 617 and Stellite 6 alloys. *Wear* 269(9–10):664–671
64. Blau PJ (2010) Elevated-temperature tribology of metallic materials. *Tribol Int* 43(7): 1203–1208

Exercise

1. Describe adhesive wear mechanism.
2. Discuss the delamination theory of adhesive wear.
3. Discuss debris formation during sliding of metallic materials.
4. Describe the oxidation and tribological properties of 60NiTi.
5. What factors do affect wear of metallic materials at high temperature?

Chapter 7

Tribology of Ceramics and Ceramic Matrix Composites

Prasanta Sahoo and J. Paulo Davim

Abstract Ceramic materials are well suited for tribological applications due to their superior hardness, high wear resistance, good chemical resistance, stability at high temperatures, etc. Ceramic pairs are commonly used in extreme environmental applications, such as high loads, high speeds, high temperatures and corrosive environments. This present chapter briefly discusses the friction and wear behaviour of ceramics and ceramic matrix composites. Friction of ceramics depends largely on fracture toughness besides normal load, sliding speed, temperature, etc. Wear mechanisms in ceramics involve fracture, tribo-chemical effects and plastic flow. In case of ceramic matrix composites, the incorporation of the secondary phase into ceramic matrix results in the improvement of both mechanical properties and friction performance. In nano-ceramics, reduction in microstructural scale yields significant improvements in wear resistance. Tribological behaviour of ceramics in biological environment is also highlighted.

1 Introduction

The word ‘ceramic’ owes its origin to the Greek term ‘keramos’, meaning ‘a potter’ or ‘pottery’. Keramos is related to an older Sanskrit root meaning ‘to burn’. A ceramic is an earthy material usually of silicate nature and is defined as a combination of one or more metals with a non-metallic element. According to the American Ceramic Society, ceramics are defined as inorganic, non-metallic

P. Sahoo (✉)
Department of Mechanical Engineering, Jadavpur University, Kolkata,
West Bengal 700 032, India
e-mail: psjume@gmail.com

J.P. Davim
Department of Mechanical Engineering, University of Aveiro, 3810-193 Aveiro, Portugal
e-mail: pdavim@ua.pt

materials, which are typically crystalline in nature, and are compounds formed between metallic and non-metallic elements such as aluminium and oxygen, calcium and oxygen, and silicon and nitrogen. Ceramics belong to a wide range of hard refractory inorganic materials. These are prepared by heating the base powder material to a high temperature such that sintering or solid state reaction takes place. As a result, the material so formed achieves a number of remarkable properties that make them well suited for tribological applications. These characteristics include superior hardness leading to high resistance to wear, low coefficient of expansion leading to high dimensional stability, low reactivity leading to good chemical resistance, and ability to maintain their physical properties at high temperatures.

Ceramics are categorized into oxides ceramics, non-oxide ceramics and ceramic-based composites. Oxide ceramics include alumina (Al_2O_3), sapphire (hard form of alumina), magnesium oxide (MgO), zirconia (ZrO_2) and yttrium oxide (Y_2O_3). The non-oxide group includes different nitrides (TiN , CrN , Si_3N_4 , cubic BN, etc.), carbides (TiC , SiC , ZrC , etc.) and diamond. Generally, oxide ceramics are oxidation resistant, chemically inert and electrically insulating while having low thermal conductivity. Non-oxide ceramics are low oxidation resistant, electrically conducting, thermally conductive and very hard. Ceramic-based composites are produced to combine the above to achieve better properties, i.e. sialon (solid solution of aluminium oxide and silicon nitride) and zirconia-toughened alumina composite. Table 7.1 presents the properties of some common ceramics used in tribological applications. Physical properties of the ceramics largely depend on the manufacturing process and thus the method of manufacturing (e.g. hot pressed or reaction bonded) is always included in material specifications. A ceramic component is produced by sintering a compacted ceramic powder. High-purity ceramic powder is an essential requirement for producing a dense ceramic part. The powder is milled properly to have an optimum particle size distribution. The large particles in the ceramic powder are avoided as they can introduce defects and act as regions of stress concentration under load leading to premature failures. Compacted ceramic powder, known as a green body, is sintered at an appropriate temperature for a certain period of time to obtain a dense part. The sintering process is vital since the amount and the method of applying energy as well as the sintering time determines the bonding properties between the powder particles and the amount of porosity in the component.

Each of the ceramics has their merits and demerits. Alumina-based ceramics are usually hard but brittle. These are commonly used in cutting tools, wear parts, grinding wheels, mechanical seals, supports for heating appliances, etc. Zirconia has exceptionally high fracture toughness, typically two to three times higher than that of alumina. Hence, it is very resistant to impacts and used in applications that require ductility. In such situations, alumina is unsuitable. Zirconia undergoes phase changes with temperature. Under normal atmospheric pressure and at ambient temperature, zirconia contains monoclinical crystalline structure that remains stable up to 1,100 °C. Then it converts to tetragonal between 1,100 and 2,300 °C, thereafter becomes cubic. These phase changes are reversible but accompanied

Table 7.1 Some physical properties of common ceramics

	Alumina	Sapphire	AlN	ZrO ₂ / Y ₂ O ₃	ZrO ₂ /BN MgO	BN hot pressed	B ₄ C hot pressed	SiC hot pressed (reaction bonded)	Si ₃ N ₄ hot pressed (reaction bonded)	Sialon	Diamond
Density [kg/m ³]	3,900	3,985	3,250	—	5,740	1,800	2,450	3,150 (3,100)	3,110 (2,400)	3,240	3,515
Hardness [Vickers]	1,800	2,500	1,200	1,200	1,200	—	3,200	2,400–2,800 (2,500–3,500)	1,700–2,200 (800–1,000)	1,650–1,800	7,000
Young's modulus [GPa]	300–400	–3,000	—	200	200	20–100	440–470	350–440 (410)	280–310 (170–220)	280–300	–10,000 1,054
Poisson's ratio	0.25–0.27	—	—	0.29	0.29	—	0.19	0.15	0.26–0.27	0.26	0.07–0.1
Fracture toughness [MPa m ^{1/2}]	3–5	—	—	8–13	6–10	—	—	3.5–4	4–5	5.4	—
Specific heat [J/kgK]	920	753	800	460	470	780	950	670–710	680–800 (690)	620–710	530
Thermal conductivity at 20 °C [W/mK]	28–35	41.9	165	1.9	1.9	15–33	27–36	90–160 (200)	15–43 (10–16)	20	2,000
Melting point [°C]	2,050	—	—	2,590	—	—	2,420	2,500	1,900	—	3,825
Max. service temperature [°C]	1,800	1,800	1,200	1,500	—	950–1,200	700–800	1,550	1,400–1,500	1,500	1,000

with significant variations in density. This puts a barrier to design and manufacture component parts with pure zirconia. In fact, such parts do crack during cooling. As a remedy, tetragonal or cubic zirconia is stabilized at low temperatures by doping the same with CaO, MgO or Y_2O_3 . This partially stabilized zirconia (PSZ) is a metastable state that recovers the monoclinical structure easily under the effect of mechanical or thermal stress.

Sialon (silicon aluminium oxynitride) has remarkable hardness and fracture toughness, high wear resistance and thermal conductivity. Thus it is used in cutting tools, wire die plates, extruders, etc. Silicon carbide and silicon nitride have good mechanical properties and excellent resistance to thermal stress. Thus these are particularly suitable for high-temperature applications. In oxidizing environment, they produce a coating of hydrated SiO_2 that enhances wear resistance. Silicon nitride is used to manufacture ball bearings for aeronautical applications, machine tools, engine valves, etc. due to their superior mechanical properties at high temperatures. However, the only drawback is that these require very high temperatures for processing.

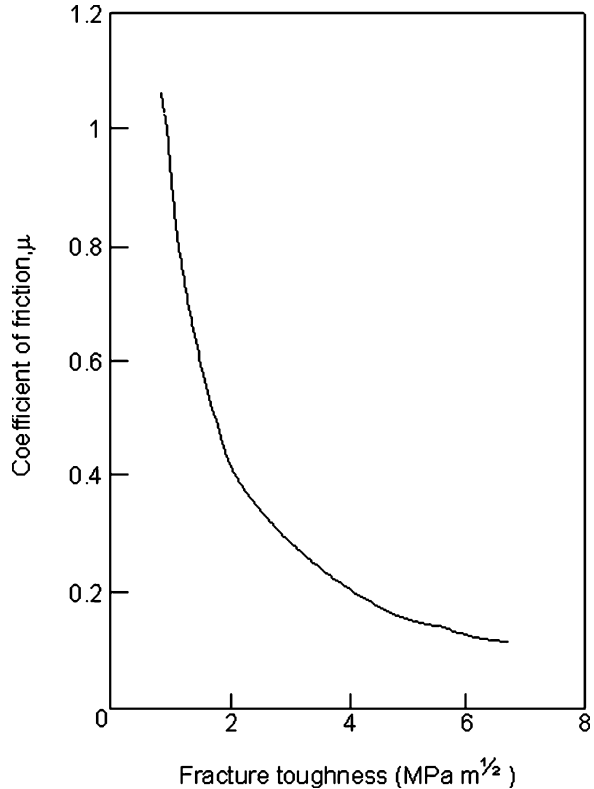
Boron nitride and diamond offer excellent hardness and high fracture toughness. Thus they are commonly used in cutting tools for machining hard and abrasive materials. Diamond is used for machining of non-ferrous materials since it gets oxidized at $700\text{ }^\circ\text{C}$ in contact with iron and its alloys. For high-speed machining of steel components, cubic boron nitride tool is used due to its stable chemical composition.

Ceramic materials contain strong ionic-covalent bonds resulting in good chemical stability and excellent mechanical properties. The strength of these interatomic bonds also leads to the fragility of ceramic materials. To avoid this, ceramic materials are often reinforced with a second phase in the form of whiskers. Whiskers are typically less than a micron in diameter and $5\text{--}20\text{ }\mu\text{m}$ in length. Whiskers improve the mechanical properties of the ceramic matrix by preventing crack propagation. Alumina when reinforced with tetragonal zirconia can prevent crack growth easily. If a crack nucleates within the material, the tetragonal zirconia grains undergo significant mechanical stress which in turn transforms tetragonal zirconia to its monoclinical form accompanied with an increase of material volume. This prevents crack propagation significantly. Another technique of crack arrest in a ceramic material is to introduce microcracks and voids in the ceramic during its manufacture.

2 Friction of Ceramics

Ceramics combine low density with excellent mechanical properties (e.g. high strength, stiffness, hardness) up to high temperatures. Ceramic pairs are commonly used in extreme environmental applications, such as high loads, high speeds, high temperatures and corrosive environments. The mechanical behaviour of ceramics differs from that of metals due to different nature of interatomic forces: covalent or

Fig. 7.1 Schematic variation of coefficient of friction as a function of fracture toughness (redrawn with data from [5])



ionic bonding in ceramics compared to metallic bonding in metals. Because of the different nature of bonds, ceramics show limited plastic flow at room temperature and correspondingly much less ductility than metals. Although adhesive forces are present between ceramic pairs, low real area of contact leads to relatively low friction in comparison to metallic pairs in the presence of oxide films. In clean environments, friction coefficients of ceramic couples do not reach the high values as observed in clean metals in high vacuum. Friction coefficients of polycrystalline ceramics in self-mated condition are usually high, 0.5–0.9, in vacuum and in dry gases. But in air, the values range from 0.3 to 1.0 [1–4].

Friction coefficient of ceramics decreases with an increase in fracture toughness. The occurrence of fracture leads to higher friction as it provides an additional mechanism for the dissipation of energy at the sliding contact. Figure 7.1 shows the coefficient of friction as a function of fracture toughness for a sharp diamond pin (5 μm tip radius) on SiC, Si₃N₄, Al₂O₃ and ZrO₂ disks produced with various hot-pressing conditions [5]. Fracture is readily produced in concentrated contacts, e.g. a sharp hard pin sliding against a flat.

Figure 7.2 shows results from experiments where a 60° diamond cone was slid over the (0001) face of a silicon carbide single crystal [6]. At low loads, no fracture

Fig. 7.2 Typical variation of coefficient of friction with normal load for diamond cone sliding on silicon carbide (adapted from [6], Copyright 1981, with permission from Elsevier)

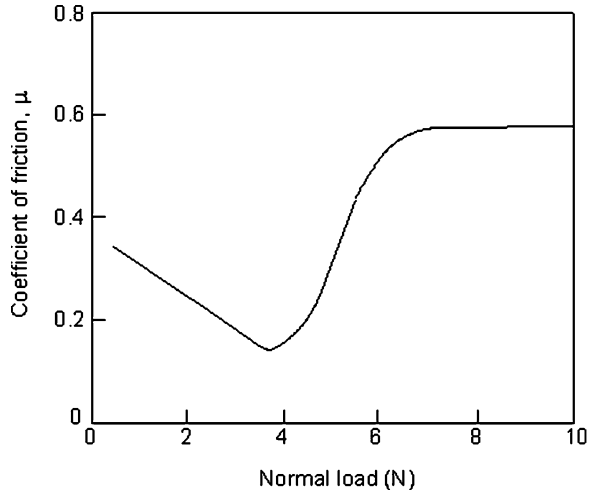
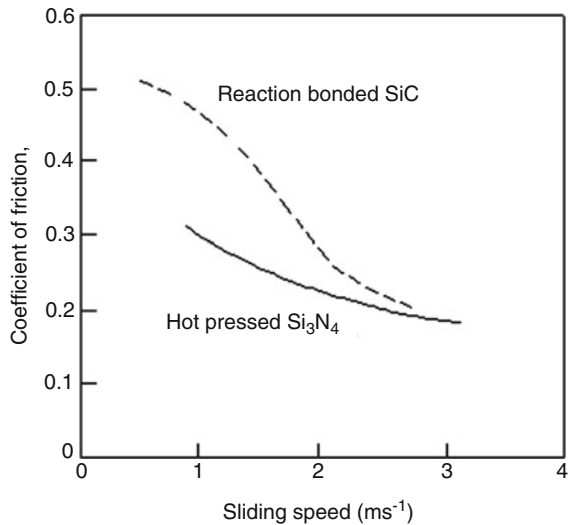


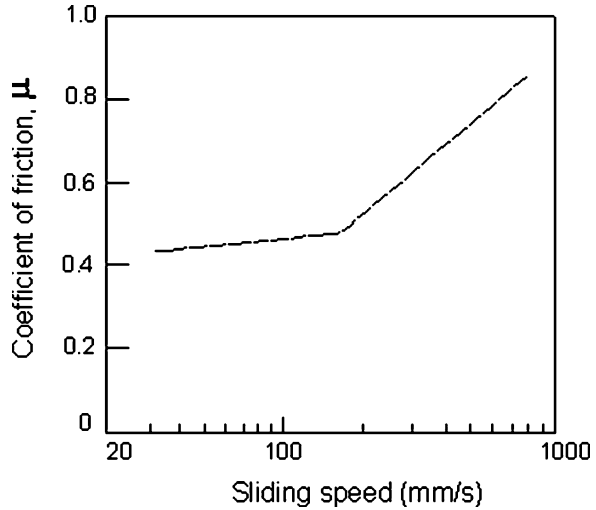
Fig. 7.3 Schematic variation of coefficient of friction with sliding speed for self-mated silicon carbide and silicon nitride (adapted from [7], Copyright 1985, with permission from Springer)



occurred with plastic grooving and friction was low. The increase for loads above ~ 4 N is associated with fracture along the sliding path. With increase in load, fracture occurred leading to higher friction.

The role of normal load, sliding speed, temperature and test duration on friction of ceramics may be interpreted in terms of changes in the tribo-chemical surface films and also the extent of fracture in the contact zone. Load and speed affect the temperature at the interface. Figure 7.3 shows the effect of sliding speed on friction coefficient of silicon carbide and silicon nitride in self-mated sliding in air [7]. The

Fig. 7.4 Schematic variation of friction with sliding speed of self-mated silicon nitride at low-speed range (redrawn with data from [5])



similar behaviour has been reported in alumina and zirconia also. With sliding speed, the interface temperature increases, and this enhances the tribological film formation on the sliding surfaces leading to a decrease in friction.

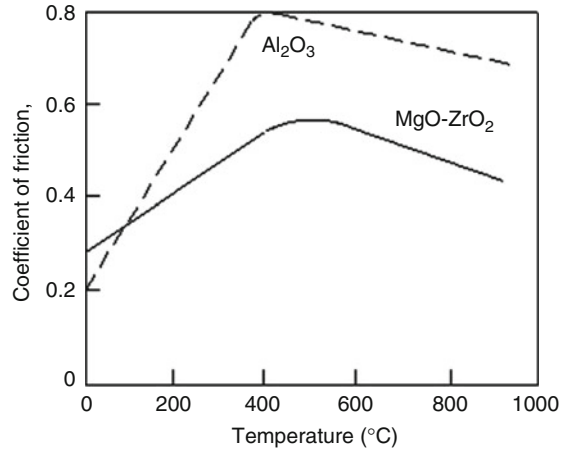
But at lower speed range, a different behaviour is observed. Figure 7.4 shows the effect of sliding speed on friction of hot-pressed silicon nitride on itself at a normal load of 10 N and ambient air in a pin-on-disk rig [5]. At low speeds, Si_3N_4 forms a surface layer in air containing water vapour. Since the shear strength of this layer is lower than the bulk ceramic, the coefficient of friction is lowered. As the speed is raised, the tribo-chemically reacted layer ceases to provide protection, and the coefficient of friction rises. The increased surface shear stress causes cracking and an increase in surface roughness resulting in the rise in the coefficient of friction.

Friction of ceramics usually increases at elevated temperatures. Figure 7.5 shows the variation of coefficient of friction as a function of temperature for alumina and magnesia–partially stabilized zirconia, sliding in self-mated pairs in air [8]. The removal of absorbed water from the interface results in the initial rise in friction with temperature.

3 Wear of Ceramics

Ceramic materials differ from metals in the nature of interatomic bonding, and this leads to very limited capacity for plastic flow at room temperature. Compared to metals, ceramics are more inclined to respond to stress by brittle fracture. In oxide ceramics, crack growth is sensitive to environmental factors, which affect the mobility of wear surface dislocations and hence influence plastic flow.

Fig. 7.5 Variation of coefficient of friction with temperature for self-mated magnesia–partially stabilized zirconia and alumina (adapted from [8], Copyright 1984, with permission from Elsevier)



Such chemo-mechanical effect is known as Rehbinder effect. Unlubricated sliding of ceramics results in significant tangential forces, which may lead to fracture rather than plastic flow. Sliding wear mechanisms in ceramics can involve fracture, tribo-chemical effects and plastic flow. Transitions between regimes dominated by each of these commonly lead to sharp changes in wear rate with load, sliding speed or environmental conditions. Mild wear in ceramics is associated with a low wear rate, smooth surfaces, finely divided wear debris, steady friction traces and mechanisms of wear dominated by plastic flow or tribo-chemical reactions. Severe wear causes higher wear rate along with a rougher surface, angular wear debris, a fluctuating friction trace and mechanisms of wear dominated by brittle intergranular fracture. Ceramic materials obey the Archard equation well enough. Typical values of non-dimensional wear coefficient for engineering ceramics undergoing severe wear are 10^{-4} to 10^{-2} , while for mild wear, 10^{-6} to 10^{-4} .

Figure 7.6 shows the effect of sliding speed on wear rate of hot-pressed silicon nitride on itself at a normal load of 10 N and ambient air in a pin-on-disk rig [5]. At low speeds, Si_3N_4 forms a surface layer in air containing water vapour, and this provides the source for wear debris. As the speed is raised, the tribo-chemically reacted layer ceases to provide protection. The increased surface shear stress causes cracking and a transition occurs from mild wear (tribo-chemical) to severe wear (extensive brittle fracture).

Figure 7.7 shows how transition in wear rate takes place in Si_3N_4 influenced by the change in humidity of the surrounding air [9]. In humid environment, Si_3N_4 forms silica and hydrated silica film is formed at the interface. The film being soft with low shear strength reduces the coefficient of friction and wear rate. Similar drop in wear rate as a function of relative humidity has been observed for SiC. In alumina and zirconia, strong sensitivity to water causes the wear rate to increase, typically tenfold in comparison with dry sliding. In the presence of water, the surface plasticity of these ceramics increases and crack growth is enhanced resulting in higher wear rate. Such chemically induced fracture phenomenon is

Fig. 7.6 Schematic variation of wear rate with sliding speed of self-mated silicon nitride (redrawn with data from [5])

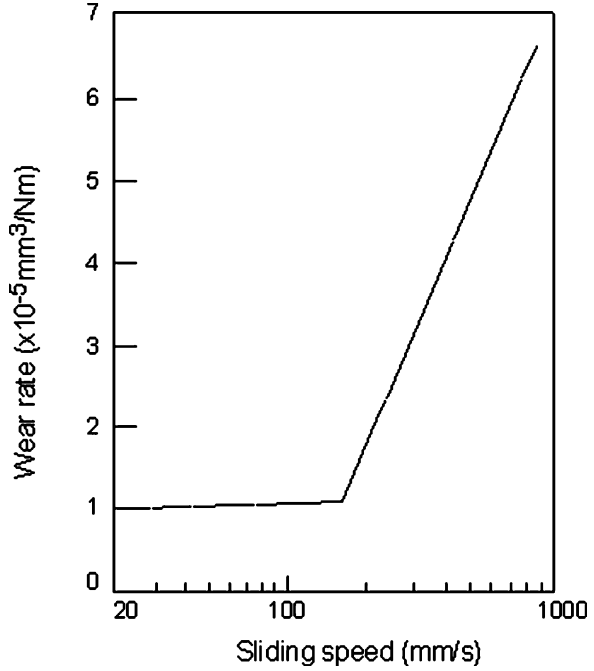
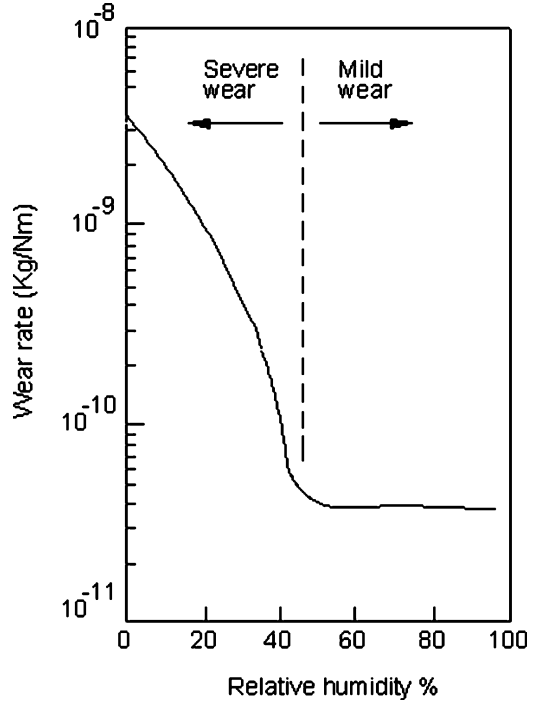


Fig. 7.7 Typical variation of wear rate with humidity for self-mated silicon nitride in a pin-on-disk test in air (redrawn with data from [9])



known as stress corrosion cracking or static fatigue, and the chemo-mechanical effect in which mechanical properties of many materials change as a result of exposure to many liquids is known as Joffe–Rehbinder effect. For different ceramics, the wear volume and the friction coefficient are found to be dependent on temperatures, but the trend of behaviour is not unique and varies from one ceramic material to another.

Ceramic materials respond to conventional lubricants in the same way as metals. Effective lubrication decreases wear rate. However, chemical effects play a significant role even under lubricated conditions. Surface oxidation of Si_3N_4 and SiC occurs even in mineral oils, and wear of these ceramics under lubricated conditions is due to tribo-chemical action. Boundary lubricants such as stearic acid function on ionic materials such as Al_2O_3 whereas SiC (with covalent bonding) is not effectively lubricated by stearic acid. Zirconia is susceptible to a phenomenon called thermo-elastic instability where contact between asperities in thin-film-lubricated sliding causes intense local power dissipation and consequent heating. The local temperature rise significantly distorts the topography of the surface and causes further asperity contact to be concentrated in the same area. This instability results in very high flash temperatures and rapid wear. Such phenomenon commonly occurs in the lubricated sliding of materials with low thermal conductivity and high thermal expansion coefficients. Poor performance of zirconia under some lubricated sliding conditions is attributed to this phenomenon.

4 Ceramic Wear Mechanisms

Ceramics being brittle solids wear by fracture. Fracture takes place when the applied mechanical stress exceeds the fracture strength which is a complex function of composition, grain boundary energy release rate, grain fracture energy release rate, defects, residual stresses, etc. Under mild wear regime, the macroscopic contact stresses remain below the fracture strength, but the asperity contact (determined by surface roughness) exceeds the fracture criteria leading to localized fracture. This results in grain boundary cracking and grain pull-outs. Thus surface roughness is a key parameter for ceramic wear. Ceramics in general possess high compressive strength and weak tensile strength. Thus in most cases tensile stresses cause the onset of wear particularly in a mild wear regime. Tensile stresses at an asperity cause microfracture at the surface as well as subsurface grain boundary dislocations. On the other hand, if contact pressure is sufficiently high to cause fracture, compressive stresses play a key role in causing wear.

Large body of wear data for ceramics are usually plotted as wear regime maps as a function of load and speed where wear transitions can be observed. Wear maps proposed by several researchers may be classified into two groups. The first group is the one that uses the experimental variables as the axes, the most obvious examples being normal load and sliding velocity, but can also include temperature, sliding distance and so on. These maps are in general straightforward to interpret but the

disadvantage is that the wear rate is system specific. Thus the wear rate read off a map is unlikely to be transferable to another wear geometry or engineering system and therefore cannot be used for design. The other group of map uses dimensionless axes. These tend to be more widely applicable and can cover a wide range of operating conditions. Accordingly, wear is classified into mild, severe and ultra-severe regimes. In mild wear regime, abrasion and microfracture are the two dominant wear mechanisms. In severe wear regime, brittle fracture in the form of intergranular cracking is observed as the dominant wear mechanism. In ultra-severe wear regime, gross fracture in the form of intragranular cracking and delamination cracks are seen. Typical wear maps for Al_2O_3 and Si_3N_4 under dry and paraffin oil-lubricated conditions are shown in Figs. 7.8 and 7.9. The results are from tests conducted by using a ball-on-three flats geometry on a four-ball wear tester with identical materials in air at room temperature. Wear volumes per unit time are listed in the figures. Various wear mechanisms are also listed in the figures. The interaction of lubricant with ceramics extends the pressure–velocity boundary towards the higher values for a transition from mild to severe wear. It is evident that the wear regime maps for ceramics are material specific.

Under high-speed, high-load conditions, accelerated cracking is attributed to thermal shock stresses which acts in addition to the mechanical induced tensile stress. A thermal shock stress is modelled as [10]

$$\sigma_{thermal} = \frac{E\alpha}{1-\nu} \exp \left[\frac{-4}{\sqrt{\pi}} \left(\frac{T}{T^*} - 5.3 \right) \right] \quad (7.1)$$

where E is the Young's modulus, α the linear expansion coefficient, ν the Poisson's ratio, T the flash temperature, and T^* the bulk temperature from nominal contact.

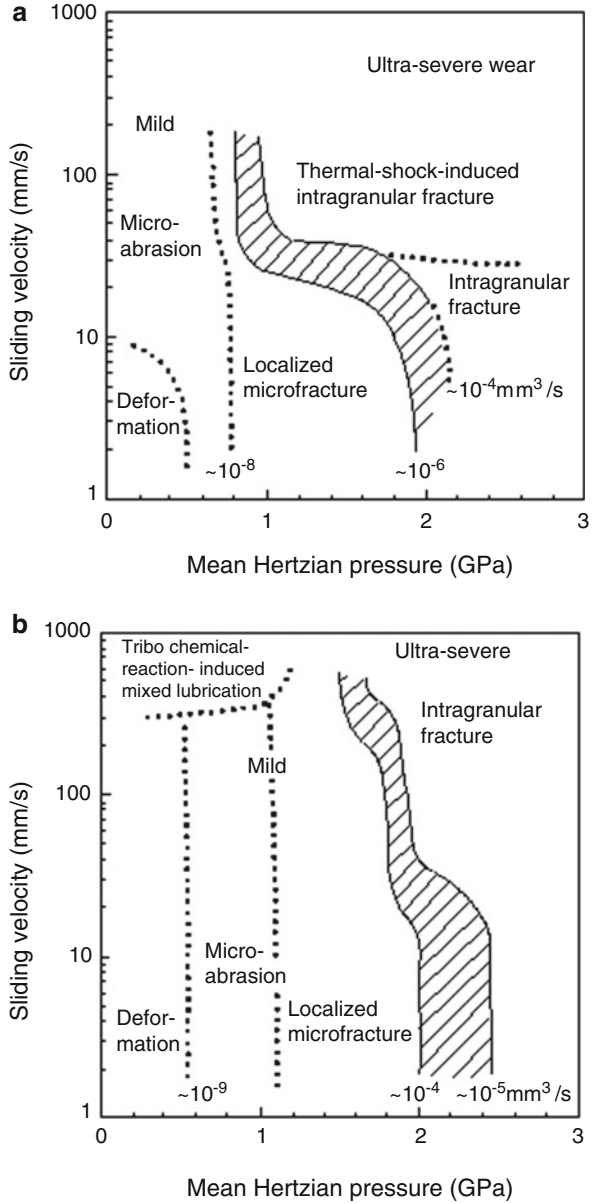
There are many wear studies and proposed wear models on ceramics in the literature. Evans and Marshall [11] proposed a wear volume model assuming sharp indenters. They presented a lateral fracture model based on the extension of lateral cracks due to the residual stresses caused by indentation. In this model, the wear volume is given by

$$V = \alpha_3 \frac{P^{9/8}}{K_c^{1/2} H^{5/8}} \left(\frac{E}{H} \right)^{4/5} l \quad (7.2)$$

where P is the normal load; K_c , E and H are the fracture toughness, elastic modulus and hardness, respectively, of the material; l is the distance slid; and α_3 is a material-independent constant.

Hsu and Shen [12] proposed an empirical model for wear volume calculation, in the case of blunt indenters, taking into account the presence of pre-existing cracks and third-body wear particles on asperity contacts and incorporating the effect of temperature on wear volume. The proposed proportionality relationship for wear volume is given by:

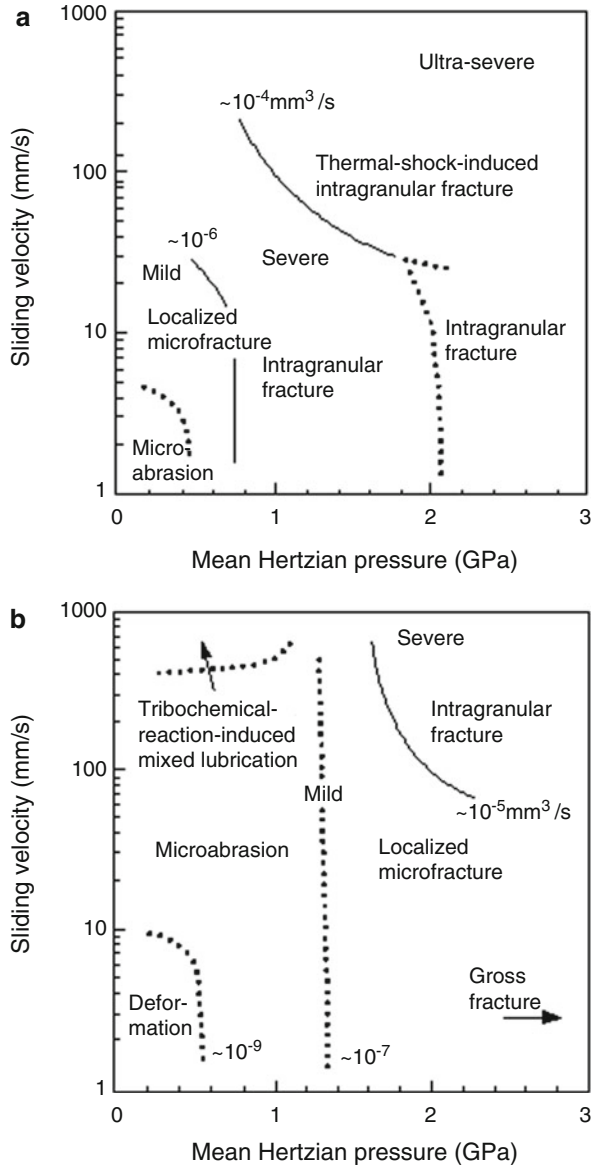
Fig. 7.8 Wear regime maps for Al_2O_3 sliding on itself at room temperature in a ball-on-three flats geometry on a four-ball wear tester (a) under dry conditions and (b) under paraffin oil-lubricated conditions (adapted from [10], Copyright 1996, with permission from Elsevier)



$$V \propto \frac{\sigma_{\max}(T^*/T_0)\sqrt{c}}{K_c} \frac{P}{H(T^*)} l \tag{7.3}$$

where T^* and T^0 are the temperatures of the interface and the ambient, respectively; σ_{\max} is the maximum tensile stress; and c is the cone crack length.

Fig. 7.9 Wear regime maps for Si_3N_4 sliding on itself at room temperature in a ball-on-three flats geometry on a four-ball wear tester (a) under dry conditions and (b) under paraffin oil-lubricated conditions (adapted from [10], Copyright 1996, with permission from Elsevier)



5 Ceramic–Metal Contacts

In case of ceramic–metal contacts, both the metal and the ceramic are found to contribute to the friction and wear behaviour. In dry conditions, the friction coefficient is influenced by the metallic counterface and the operating load–speed combination. This in fact controls the temperature at the interface and thus the

degree of oxidation at the metallic surface. For steels and cast irons, the coefficient of friction varies widely in the range 0.2–0.8, while for softer materials like brass, aluminium, copper and bronze, the same varies in the range 0.2–0.5 [8, 13–15]. These values usually increase at higher temperatures [15]. In general, metals adhere to the ceramic surface to form a transfer film since strong adhesion exists between clean metal and ceramic surfaces, and plastic flow stress of most metals is less compared to ceramics. The adhesion is hindered by the presence of contaminants and as a result lower friction is observed in such cases. At higher temperatures, the contaminants get removed and metals get softened enhancing the possibility of adhesion and transfer film formation resulting in an increase in friction.

Wear of metallic counterface depends on the type of ceramic materials. With softer ceramics like partially stabilized zirconia, wear is less while with harder ceramics like alumina, wear is more [16]. Sometimes the chemical reaction at the interface enhances the wear of the ceramic as in case of machining steel and cast iron using silicon-based cutting tools [17]. In some cases, cracks form in the ceramic due to the frictional heat generated at the interface and wear takes place both in the ceramic and the metal though large difference in the hardness exists between the two [15].

6 Ceramic–Polymer Contacts

Polymer–ceramic contacts yield low friction and wear characteristics as compared to polymer–metal contacts. The best known application of this type of contact is orthopaedic endoprostheses where alumina is used in prosthetic designs with a counterface of ultra high molecular weight polyethylene (UHMWPE). The low friction and wear behaviour in such applications is attributed to the chemical inertness, good wettability and high resistance against scratching for alumina [18, 19]. The good surface finish of alumina is retained for the lifetime of the prosthetic implant and this reduces the wear of the polyethylene. As the hardness of ceramic is higher than the polymer, it is expected that wear takes place mainly in the polymer. The surface finish and porosity of the ceramic control the wear rate of the polymer in such cases. Wear of the polymer increases with increase in surface roughness of the ceramic and is dominated by abrasive wear. The surface irregularities present on the ceramic surface get filled by polymer particles and the surface gets smoothened. Thus initial high wear rate is decreased with use.

7 Ceramic Matrix Composites

The majority of ceramic composites contain a ceramic matrix of alumina, silicon nitride, silicon carbide, glass or carbon with metallic or ceramic fibres or particulates as reinforcements. The incorporation of the secondary phase into

ceramic matrix results in improvement of both mechanical properties and tribological performance. Ceramics are resistant to high temperatures and have in general good wear resistance but poor friction performance often limits their application. Ceramic composites provide a solution in such cases. Graphite–fibre-reinforced glass offers reduced friction comparable to those of resins, while the wear resistance remains similar to that of ceramics and glasses [20]. Alumina matrix composite with silicon carbide whiskers reinforcements offers lower brittle wear rate in comparison to pure alumina which is brittle in nature [21]. In such cases, silicon carbide whiskers act as a mechanical barrier to the path of crack propagation, thereby leading to reduced brittle wear of the composite. Tribological behaviour of ceramic matrix composites strongly depends on the microstructure of the matrix, nature of inclusions, the bonding between the matrix and inclusions and test conditions along with the processing route used in the manufacturing of the composite [22–26].

Another class of ceramic composite is cermet which is a composite of ceramic and metallic materials. Cermets combine a hard phase (the ceramic) with a soft phase (the metallic binding). Hence, they possess both hardness and ductility. If a crack is formed within the ceramic, the propagation of the same to adjacent grains gets arrested by the more ductile metallic phase in contact. Cermets are classified into two groups: tungsten–carbide (WC)-based cermets and other carbide-based cermets. WC-based cermets are usually produced from WC powders of 1–10 μm grain diameter being mixed with a cobalt-binding agent (5–20 % by weight) through sintering at a temperature of around 1,500 °C. During initial stages of sliding of WC–Co cermets, preferential wear of the binding phase (Co) is observed and subsequently cracking and loosening of the carbide grains take place. The hardness and wear rate of WC–Co cermets strongly depend on the concentration of Co. With increase in Co concentration, hardness decreases and wear rate increases. It is also observed that the wear resistance of WC can be improved through the addition of other carbides such as TaC, TiC and NbC. Apart from WC-based cermets, other carbide-based cermets include TiCN–Ni, TiC–Ni, TiC–NiMo and TiCN–WC–N. These materials are in general harder than WC-based cermets and hence have greater wear resistance. For all the cermets, the wear rate linearly decreases with increase in hardness, irrespective of sintering conditions or starting powder, and follows the classical Archard's equation of wear given by $V = k \frac{Wx}{H}$, where V is the wear volume, k is the non-dimensional wear coefficient (which typically ranges from 10^{-6} to 10^{-1}), x is the sliding distance, W is the applied load (N), and H is the hardness of the material (GPa). Thus hardness is among the important parameters in determining the wear resistance of cermet materials. Such a strong dependence of hardness on wear rate implies that cermets behave more like a metallic material at the tribocontact situations. Also the mechanism of material removal is dominated by abrasive wear. However, Archard's model is valid for metallic materials that undergo plastic deformation during contact. In case of cermets, the amount of metallic binder is limited to 20 wt% and hence the wear cannot be controlled entirely by deformation-dominated abrasion. Moreover, the

wear behaviour of the cermets does not follow the material removal behaviour of classical brittle materials (brittle fracture and cracking). The high resistance of the cermets can be explained from the wear model proposed by Roberts [27]:

$$P^* = \frac{54.47\beta}{\pi\eta\theta} \left(\frac{K_{IC}}{H} \right)^3 K_{IC} \quad (7.4)$$

where P^* is the minimum load required to produce fracture from a point contact (N), β is the constant relating hardness to indentation diagonal (2.16 for Vickers indentation), η is a constant, θ is the geometrical constant (~ 0.2), K_{IC} is the fracture toughness of the material indented ($\text{MPa m}^{1/2}$), and H is the hardness of the material indented (GPa). Incorporating the typical material property for cermets yields an estimated load (P^*) of more than 100 N. This indicates that the material removal in cermets is highly unlikely to occur by severe brittle fracture under the tribological contact regime. Thus the cermets show high wear resistance.

8 Nano-ceramics

Nanostructured materials are defined as materials with structural units having a size scale of less than a 100 nm in any dimension, and such materials combine unique physical or functional properties that cannot be obtained in materials with structural units having length scale in microns or larger. The main challenge in nanoceramic development is the restriction in grain growth during processing, which is often difficult in conventional sintering techniques. New advanced sintering techniques, namely, spark plasma sintering and sinter-hot isostatic pressing are used for synthesizing bulk nanostructured ceramics. It is experimentally observed that reduction in microstructural scale yields significant improvements in the wear resistance of ceramics. This grain size dependence of wear resistance is attributed to two reasons. First, as hardness and yield strength improve considerably, the rate of accumulation of plasticity-controlled damage during the initial deformation-controlled wear reduces. Second, the smaller flaw sizes yield a considerable increase in the plasticity-induced critical stress that controls the subsequent brittle-fracture-controlled wear. Significantly lower material damage by pull-out is observed in ultra-fine-grained (400 nm) alumina ceramics compared with the coarser-grained (2.2 μm) counterpart [28]. Nanocomposite design leads to reduction in wear rate by reducing the dimension and rate of grain pull-out [29]. The fracture mode changes from intergranular to transgranular on reinforcing Al_2O_3 matrix by intergranular SiC nanoparticles, and the suppression of twins and dislocation pile-ups by the transgranular SiC nanoparticles leads to the improved wear behaviour of the Al_2O_3 -SiC nanocomposites. Wear resistance is found to improve on dispersing nanocrystalline SiC in Al_2O_3 during sliding wear [30] and erosive wear [31]. It has also been reported that the higher hardness of the nanostructured

cemented carbides leads to significant improvement in wear resistance. In general microstructural refinement in nanostructured ceramics or composites leads to better wear resistance, and nanoceramic composites can be used in the mild wear zone for wider spectrum of operating conditions than conventional micron-sized materials.

9 Bio-ceramics

Biomaterials are defined as synthetic materials that can be designed to perform a specific biological activity. The basic difference of biomaterials from structural materials is their ability to remain in a biological environment without causing damage to the surroundings and without getting damaged in the process. Biomaterials are classified into three groups: bioinert, bioactive and bioresorbable. Bioinert materials induce no interfacial biological bond with bone or cells. Al_2O_3 , ZrO_2 belong to this category. Bioactive materials attach directly to tissues and form biological bonds. Examples are 45S5 bioglass and calcium phosphates (e.g. hydroxyapatite, HA). Bioresorbable materials get gradually resorbed during post-implantation period and finally get replaced by new tissues. Examples are tricalcium phosphate (TCP) and bone cement. Sufficient knowledge about the tribological properties of biomaterials is essential. For example, the wear of orthopaedic alloys produces the wear debris particles that have to be assessed with respect to amount, size and shape. The surface properties along with the biological reactivity of biomaterials in simulated body fluids are important. Many bioceramic materials, particularly those based on calcium phosphate, form an apatite layer at the tribological contact, and thus the friction and wear properties depend on such an apatite layer. Biomaterials should not release wear debris particles to a significant extent and this requires extremely high wear resistance for these materials. Also friction coefficient values in articulating surfaces should be very low to minimize trauma to patients. Pure HA does not show acceptable wear resistance, even under water lubrication, and the value of wear factor lies in the range of 7×10^{-6} to 1×10^{-5} with high dependence on roughness properties [32]. CaP-based biocomposite with mullite ($3\text{Al}_2\text{O}_3 \cdot 2\text{SiO}_2$) reinforcement shows superior wear resistance though friction coefficient is on the higher side. For HA composites, the wear mechanism in dry contacts is mainly guided by microcracking, delamination, plowing and fatigue cracking. In simulated body fluids, the main wear mechanism for the mullite-containing HA composites is mild abrasion and/or plowing, subsequently leading to mild fracture and removal of the grains. Among HA–mullite composite materials, HA (30 wt%)–mullite ceramics possess the best combination of coefficient of friction and wear resistance under both dry and simulated body fluid conditions.

10 Summary

Ceramics are inorganic, non-metallic materials, typically crystalline in nature, and compounds formed between metallic and non-metallic elements such as aluminium and oxygen, calcium and oxygen, and silicon and nitrogen. Ceramics are prepared by heating the base powder material to a high temperature such that solid state reaction takes place. Ceramic materials contain strong ionic-covalent bonds resulting in good chemical stability and excellent mechanical properties along with the fragility of ceramic materials. To avoid this, ceramic materials are often reinforced with a second phase in the form of whiskers to prepare ceramic matrix composites. Ceramic pairs show low friction due to low real area of contact in presence of oxide films. Wear of metallic counterface depends on the type of ceramic materials, softer ceramics yielding low wear than harder ones. Polymer–ceramic contacts yield low friction and wear characteristics compared to polymer–metal contacts. Ceramic matrix composites provide good friction performance. Microstructural refinement in nanostructured ceramics or composites leads to better wear resistance. Bio-ceramics provide good tribological performance in biological environment.

Acknowledgements Authors gratefully acknowledge the publishers (ASME, Elsevier, Springer, etc.) of a number of technical/research papers used for preparation of this article.

References

1. Sasaki S (1989) The effects of the surrounding atmosphere on the friction and wear of alumina, zirconia, silicon carbide and silicon nitride. *Wear* 134:185–200
2. Fischer TE, Anderson MP, Jahangir S, Salher R (1988) Friction and wear of tough and brittle zirconia in nitrogen, air, water, hexadecane and hexadecane containing stearic acid. *Wear* 124:133–148
3. Yust CS, Carignan FJ (1985) Observation on the sliding wear of ceramics. *ASLE Trans* 28:245–253
4. Woydt M, Habig K-H (1989) High temperature tribology of ceramics. *Tribol Int* 22:75–87
5. Ishigaki H, Kawaguchi I, Iwasa M, Toibana Y (1985) Friction and wear of hot pressed silicon nitride and other ceramics. In: Ludema KC (ed) *Wear of materials*. ASME, New York, pp 13–21
6. Adewoye OO, Page TF (1981) Electron microscopy study of surface and subsurface friction damage in single crystal SiC. *Wear* 73:247–260
7. Cranmer DC (1985) Friction and wear properties of monolithic silicon based ceramics. *J Mater Sci* 20:2029–2037
8. Hannink RHJ, Murray J, Scott H (1984) Friction and wear of partially stabilized zirconia: basic science and practical applications. *Wear* 100:355–366
9. Fischer TE, Tomizawa H (1985) Interaction of tribochemistry and microfracture in the friction and wear of silicon nitride. In: Ludema KC (ed) *Wear of materials*. ASME, New York, pp 22–32
10. Hsu SM, Shen MC (1996) Ceramic wear maps. *Wear* 200:154–175

11. Evans AG, Marshall DB (1981) Wear mechanisms in ceramics. In: Rigney DA (ed) Fundamentals of friction and wear of materials. American Society for Metals, Metals Park, OH, pp 439–452
12. Hsu SM, Shen M (2004) Wear prediction of ceramics. *Wear* 256:867–878
13. Zum Gahr KH (1989) Sliding wear of ceramic-ceramic, ceramic-steel and steel-steel pairs in lubricated and unlubricated contact. *Wear* 133:1–22
14. Stachowiak GW, Stachowiak GB, Batchelor AW (1989) Metallic film transfer during metal-ceramic unlubricated sliding. *Wear* 132:361–381
15. Carter GM, Hooper RM, Henshall JL, Guillou MO (1991) Friction of metal sliders on toughened zirconia ceramic between 298 and 973 K. *Wear* 148:147–160
16. Cooper CV, Rollend CL, Krouse DH (1989) The unlubricated sliding wear behavior of a wrought cobalt-chromium alloy against monolithic ceramic counterfaces. *ASME J Tribol* 111:668–674
17. Bhattacharya SK, Ezugwu EO, Jawaid A (1989) The performance of ceramic tool materials for the machining of cast iron. *Wear* 135:147–159
18. Dowson D, Harding PT (1982) The wear characteristics of UHMWPE against a high density alumina ceramic under wet and dry conditions. *Wear* 75:313–331
19. Abdallah AB, Treheux D (1991) Friction and wear of ultrahigh molecular weight polyethylene against various new ceramics. *Wear* 142:43–56
20. Minford E, Prewo K (1985) Friction and wear of graphite-fibre-reinforced glass matrix composites. *Wear* 102:253–264
21. Yust CS, Leitnekar JM, Devore CE (1988) Wear of an alumina-silicon carbide whisker composites. *Wear* 122:151–164
22. Reis P, Davim JP, Xu X, Ferreira JMF (2005) Tribological behaviour of colloiddally processed sialon ceramics sliding against steel under dry conditions. *Tribol Lett* 18(3):295–301
23. Reis P, Filho V, Davim JP, Xu X, Ferreira JMF (2005) Wear behavior of advanced structural ceramics: α -sialon matrix reinforced with β -sialon fibers. *Mater Des* 26:417–423
24. Reis P, Davim JP, Xu X, Ferreira JMF (2006) Friction and wear behaviour of β -silicon nitride-steel couples under unlubricated conditions. *Mater Sci Technol* 22(2):247–252
25. Reis P, Davim JP, Xu X, Ferreira JMF (2007) A note on tribological behaviour of α -sialon/steel couples under dry conditions. *Mater Des* 28:1343–1347
26. Filho VXL, Davim JP, Cairo CA, Ferreira JMF (2009) Preparation and characterization of SiAlON matrix composites reinforced with combustion synthesis rod-like SiAlON particles. *Int J Refractory Metals Hard Mater* 27:647–652
27. Roberts SG (1999) Depth of cracks produced by abrasion of brittle materials. *Scripta Mater* 40(1):101–108
28. Wang X, Pature NP, Tanaka H, Ortiz AL (2005) Wear-resistant ultra-fine-grained ceramics. *Acta Mater* 53:271–277
29. Merino JLO, Todd RI (2005) Relationship between wear rate, surface pullout and microstructure during abrasive wear of alumina and alumina/SiC nanocomposites. *Acta Mater* 53(12):3345–3357
30. Rodrigues J, Martin A, Pastor JY, Llorca J, Bartolome JF, Moya JS (1999) Sliding wear of nanocomposites. *J Am Ceram Soc* 82(8):2252–2254
31. Davidge RW, Twigg PC, Riley FL (1996) Effects of silicon carbide nano-phase on the wet erosive wear of polycrystalline alumina. *J Eur Ceram Soc* 16:799–802
32. Kalin M, Jahangir S, Ives LK (2002) Effect of counterface roughness on abrasive wear of hydroxyapatite. *Wear* 252:679–685

Revision Questions

1. What makes ceramic materials well suited for tribological applications?
2. What is the main problem of design and manufacture of components with pure zirconia? How is it overcome?
3. How is fragility of ceramic materials reduced?
4. How does friction of ceramics vary with fracture properties? Explain the reason.
5. How does friction of ceramics depend on sliding speed?
6. Why does friction of ceramics usually increase with temperature?
7. How does wear of Si_3N_4 depend on humidity?
8. What is the effect of lubricant on wear of ceramics?
9. Why do cermets show high wear resistance?
10. What yields improvement in wear resistance of nano-ceramics?

Answers to Revision Question

1. Superior hardness leading to high resistance to wear, low coefficient of expansion leading to high dimensional stability, low reactivity leading to good chemical resistance, ability to maintain their physical properties at high temperatures, etc.
2. Zirconia undergoes phase changes with temperature. Under normal atmospheric pressure and at ambient temperature, zirconia contains monoclinical crystalline structure that remains stable up to 1,100 °C. Then it converts to tetragonal between 1,100 and 2,300 °C, thereafter becomes cubic. These phase changes are reversible but accompanied with significant variations in density. This puts a barrier to design and manufacture component parts with pure zirconia.

As a remedy, tetragonal or cubic zirconia is stabilized at low temperatures by doping the same with CaO, MgO or Y_2O_3 . This partially stabilized zirconia (PSZ) is a metastable state that recovers the monoclinical structure easily under the effect of mechanical or thermal stress.

3. Ceramic materials are often reinforced with a second phase in the form of whiskers that improve the mechanical properties of the ceramic matrix by preventing crack propagation. Another technique is to introduce microcracks and voids in the ceramic during its manufacture.
4. Friction coefficient of ceramics decreases with an increase in fracture toughness. The occurrence of fracture leads to higher friction as it provides an additional mechanism for the dissipation of energy at the sliding contact.
5. In general, friction of ceramics decreases with sliding speed. With increase in sliding speed, the interface temperature increases and this enhances the tribological film formation on the sliding surfaces leading to a decrease in friction.

6. The removal of absorbed water from the interface results in the rise in friction with temperature.
7. Wear rate of Si_3N_4 decreases with increase in humidity of the surrounding air. In humid environment, Si_3N_4 forms silica and hydrated silica film is formed at the interface. The film being soft with low shear strength reduces the coefficient of friction and wear rate.
8. Ceramic materials respond to conventional lubricants in the same way as metals. Effective lubrication decreases wear rate. However, chemical effects play a significant role even under lubricated conditions. In a wear regime map, the interaction of lubricant with ceramics extends the pressure–velocity boundary towards the higher values for a transition from mild to severe wear.
9. Material properties of cermets are such that these require a typically high load to produce fracture from point load. This indicates that the material removal in cermets is highly unlikely to occur by severe brittle fracture under the tribological contact regime. Thus the cermets show high wear resistance.
10. First, as hardness and yield strength improve considerably, the rate of accumulation of plasticity-controlled damage during the initial deformation-controlled wear reduces. Second, the smaller flaw sizes yield a considerable increase in the plasticity-induced critical stress that controls the subsequent brittle-fracture-controlled wear.

Chapter 8

Tribology of Metal Matrix Composites

Pradeep K. Rohatgi, Meysam Tabandeh-Khorshid, Emad Omrani,
Michael R. Lovell, and Pradeep L. Menezes

Abstract Metal matrix composites (MMCs) are an important class of engineering materials that are increasingly replacing a number of conventional materials in the automotive, aerospace, marine, and sports industries due to their lightweight and superior mechanical properties. In MMCs, nonmetallic materials are embedded into the metals or the alloys as reinforcements to obtain a novel material with attractive engineering properties, such as improved ultimate tensile strength, ductility, toughness, and tribological behavior. In this chapter, an attempt has been made to summarize the tribological performance of various MMCs as a function of several relevant parameters. These parameters include material parameters (size, shape, volume fraction, and type of the reinforcements), mechanical parameters (normal load and sliding speed), and physical parameters (temperature and the environment). In general, it was shown that the wear resistance and friction coefficient of MMCs are improved by increasing the volume fraction of the reinforcements. As the normal load and sliding speed increase, the wear rate of the composites increases and the friction coefficient of the composites decreases. The wear rate and friction coefficient decrease with increasing temperature up to a critical temperature, and thereafter both wear rate and friction coefficient increase with increasing temperature. The nano-composites showed best friction and wear performance when compared to micro-composites.

P.K. Rohatgi (✉) • M. Tabandeh-Khorshid • E. Omrani
Department of Materials Science and Engineering, University of Wisconsin-Milwaukee,
Milwaukee, WI 53201, USA
e-mail: prohatgi@uwm.edu

M.R. Lovell • P.L. Menezes
Department of Industrial Engineering, University of Wisconsin-Milwaukee,
Milwaukee, WI 53201, USA

1 Introduction

Composite materials are engineered or naturally occurring materials which contain two or more distinct materials with significantly different chemical, physical, and mechanical properties. Generally, the properties of composite materials are superior to those of the monolithic constituents. There are different classifications for composites. According to the most common classification which is based on the nature of the matrix, there are three kinds of composites. These are (a) metal matrix composites (MMCs), (b) polymer matrix composites (PMCs), and (c) ceramic matrix composites (CMCs).

MMCs are promising materials for a number of specific applications in the aerospace, sports, marine, and automotive industries. MMCs filled with nonmetallic fibers, particles, or whiskers and solid lubricants may have excellent mechanical and tribological properties. MMCs must be able to support heavy loads without distortion, deformation, or fracture during performance and maintain good tribological behavior over long periods without severe surface damages such as galling, scuffing, or seizure. The MMCs have gotten significant attention worldwide because of their superior mechanical and tribological properties.

Friction and wear are universal phenomena during sliding or rolling of solid surfaces and they usually cause energy dissipation and material deterioration. In general, the extent of friction and wear dramatically decreases by the application of lubricants between the solid surfaces. Some kinds of materials have a low coefficient of friction and wear rate during applications and no external lubricant is required. These kinds of materials are known as self-lubricating materials [1]. There are distinct methods to produce self-lubricating materials. They are (a) applying coatings like diamond-like carbon (DLC) [2] to the material and (b) embedding solid lubricants such as graphite [3] and molybdenum disulfide [4] into the matrix of a composite material. MMCs produced by embedding solid lubricants possess excellent tribological properties, good corrosion resistance, and higher fatigue life than the coated materials. These advantages cause an increase in the popularity of MMCs in comparison to the coated materials.

The amount, size, shape, and distribution of fibers or hard/soft particles embedded into the matrix have some effects on the wear and friction performance of the composites. In addition, the interfacial bonding between the reinforcements and the matrices is another important factor which affects the mechanical and tribological properties of the MMCs. Generally, it is an admissible opinion that the hard particles as reinforcements in the matrix increase the strength and wear resistance of MMCs; however, it decreases the ductility of the composites. On the other hand, soft particles usually act as a solid lubricant and hence decrease the friction coefficient of the MMCs. Sometimes, the reinforcements and solid lubricants have undesirable effects on the composites and lead to unexpected properties of MMCs [5]. An approach in SiC_p/Al (SiC particles embedded in Al matrix) composite production is to incorporate graphite particles as additional reinforcement into the SiC_p/Al composites. The graphite-embedded SiC_p/Al composites showed

better wear resistance and low coefficient of friction when compared to SiC_p/Al composites without graphite reinforcement [3, 6, 7].

There are three important factors which can determine the performance of MMCs: They are (1) the composition and the microstructure of MMCs; (2) the size, volume fraction, and distribution of particles in metal matrices; and (3) the properties of the interface between the metal matrices and the reinforcements. During manufacturing processes of MMCs, different types of defects including voids and porosities may form. These defects can influence the tribological properties such as friction and wear of the composite materials. It has been shown that increasing the porosity content in the composite materials leads to reduction of mechanical and tribological properties of MMCs. Additionally, tribological testing parameters such as sliding speed, applied load, sliding time, and surface roughness affect the wear and friction behavior of MMCs.

2 Wear and Friction Properties

Wear is the progressive loss of material during relative motion between a surface and the contacting substance or substances. Tribological properties of MMCs have been extensively investigated by various researchers [3, 6–14]. The results have shown that the wear performance of MMCs is higher than that of unreinforced matrices [10, 15–17] and is shown in Fig. 8.1. As an example, Al6061 MMC reinforced by SiC particles has better wear properties than Al6061 alloy [17]. However, under certain conditions, the wear resistance of MMCs is lower or comparable to that of unreinforced matrices.

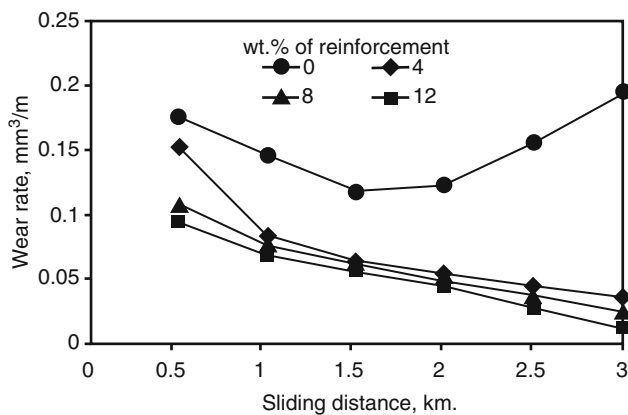


Fig. 8.1 Variations of wear rate with sliding distance for Al6061-based MMC at applied load of 10 N and sliding velocity of 1.85 m/s [17]

Different kinds of wear mechanisms may take place during the relative motion. These mechanisms include adhesive wear, abrasive wear, delamination wear, erosive wear, fretting wear, fatigue wear, and corrosive/oxidative wear. The common wear mechanisms of MMCs are adhesive wear, abrasive wear, fatigue wear, and corrosive/oxidative wear.

Adhesive wear occurs when two smooth metallic surfaces are made to slide against each other under an applied load. By applying normal pressure, the local pressure at the asperities increases to an extremely high value and often exceeds the material yield stress value. Then, the plastic deformation occurs at the asperities until the real area of contact has increased sufficiently to support the applied load. Consequently, the strong short-range forces come into action, and strong adhesive junctions may be formed at the real area of contact. During relative motion, the adhered junctions are sheared. The name “adhesive” is specified due to the formation of strong metallic bonds between the asperities on the surfaces of the contacting materials. Abrasive wear occurs when a hard rough surface slides across a softer surface. In some cases, abrasive wear occurs when hard particles trapped at the interface cause abrasive action against the surfaces in contact. Abrasive wear can be caused by both metallic and nonmetallic particles, but in most cases, the nonmetallic particles cause abrasion in MMCs. The dynamic interactions between the environment and mating material surfaces play an important role during the wear process. In corrosive wear, the contacting surfaces react with the environment and thus reaction products are formed on the surfaces at the asperities. Thus, during sliding interactions, wear of the reaction products occurs as a result of crack formation and/or abrasion. In fact, the corrosive wear occurs when reaction products on the surfaces of materials remove through physical interaction of the two surfaces in contact. Thus, corrosive wear requires corrosion and rubbing. Fatigue wear occurs at the surface of materials which experience cyclic loading. For example, the ball bearings and the gears normally experience fatigue wear due to existence of cyclic stresses during their applications.

Friction is the resistance an object encounters in moving over another. The coefficient of friction is a dimensionless scalar value which represents the ratio of the force of friction (F) between two bodies and the normal force (P) pressing them together. The symbol usually used for the coefficient of friction is μ and is expressed mathematically as follows:

$$\mu = \frac{F}{P} \quad (8.1)$$

Scientists and engineers are trying to employ an appropriate method to improve wear and friction behavior of metallic materials. One method which is used to decrease the coefficient of friction of materials is applying coating. DLC is a suitable coating which when applied to different metals such as aluminum decreases the coefficient of friction to less than 0.1 [2]. The other method to improve the tribological behavior of metals is embedding suitable reinforcements

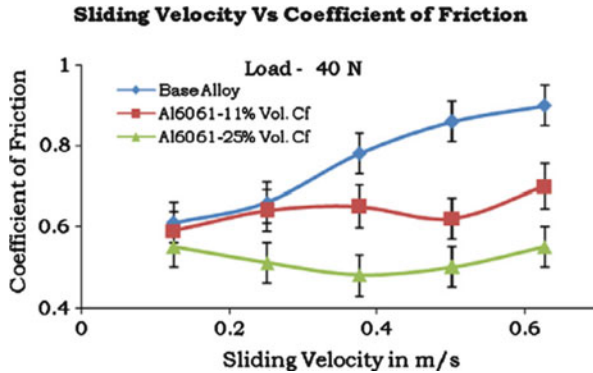


Fig. 8.2 Variation of coefficient of friction with sliding velocity for the Al6061 alloy and its carbon fiber (C_f)-reinforced composites [20]

into the metal matrices to produce composites. Different kinds of reinforcements are added to the metal matrices. Some kinds of reinforcements which are very common in MMCs are Al_2O_3 , SiC, and B_4C . They are usually added to the metal to improve the mechanical properties of the composites. These kinds of reinforcements have also improved the friction coefficient and wear resistance of the composites [14, 15, 18]. There are other types of reinforcements, known as solid lubricants, such as graphite, molybdenum disulfide, and hexagonal boron nitride. These particles are embedded into the metal matrices to improve the tribological behavior of MMCs. These kinds of reinforcements usually decrease the coefficient of friction of the composites significantly [19]. In general, the reinforcement particles improve the coefficient of friction of the composites [15–17]. Figure 8.2 shows the coefficient of friction of the aluminum alloy and the aluminum matrix composite [20]. It shows that the coefficient of friction of the aluminum MMC is less than that of unreinforced aluminum alloy [17].

Different factors can affect the wear and friction behavior of MMCs. The basic tribological parameters which can control the wear and friction behavior of MMCs can be classified into three categories [8]:

1. Material factors (intrinsic to the material undergoing surface interaction), such as type of reinforcement, reinforcement size, shape of reinforcement, reinforcement volume fraction, and microstructure of matrix.
2. Mechanical factors (extrinsic to the material undergoing surface interaction), such as normal load, sliding velocity, and sliding distance.
3. Physical factors (extrinsic to the material undergoing surface interaction), such as temperature and environmental conditions.

In this chapter, the influence of some of these parameters on tribological behavior of MMCs is discussed.

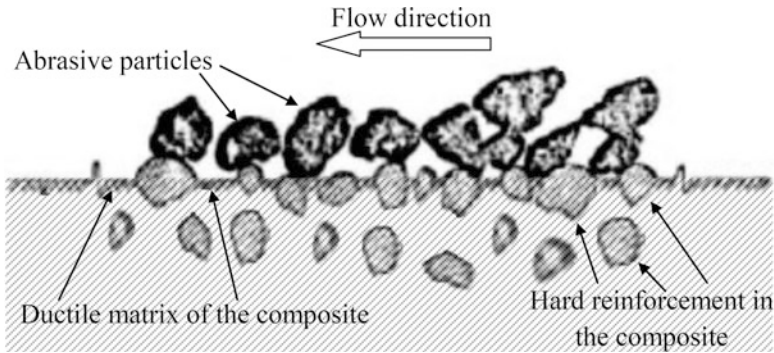


Fig. 8.3 Schematic illustration of hard second-phase particles protecting the ductile matrix from abrasion [35]

2.1 Volume Fraction

The volume fraction of particles has a strong effect on the wear resistance of MMCs [21, 22]. In general, increasing the reinforcement content enhances the wear resistance of composite materials [5, 23–30]. This is mainly due to the fact that the mechanical properties such as hardness and strength of MMCs increase with increase in the volume fraction of the reinforcements [31]. This trend was observed in different MMCs, such as Al–Fe composite [32], AZ91D–0.8 % Ce alloy reinforced by Al_2O_3 short fibers and graphite [33], nickel matrix composite reinforced by graphite and MoS_2 [19], and steel matrix composites reinforced with (W, Ti)C particles [34].

During sliding, the hard second phase particles resist the metal matrix against wear. Sometimes, these second phase particles might become dislodged from the matrix, and when this occurs the wear rate of matrix material increases due to abrasion of the second phase particles. At a certain critical volume fraction of the reinforcement, the metal matrix will be protected to a maximum extent. Figure 8.3 schematically illustrates the mechanism of protecting the ductile matrix by hard second-phase particles against abrasive particles. An increase in the volume fraction of reinforcement reduces the plastic deformation in the layer below the worn surface, which ultimately reduces the adhesive wear of the composite [35].

Figure 8.4 presents the wear rate of the aluminum MMC reinforced by micron-sized SiC particles as a function of volume fraction of SiC particles at different normal loads. It can be seen that when the volume fraction of SiC particles increases, the wear rate of the composite linearly decreases. This reveals that the volume fraction of the reinforcement is proportional to the wear resistance of the composite. The percentage improvement in the wear resistance of composites with respect to an alloy could be calculated from the measured wear rate values using the following equation [36]:

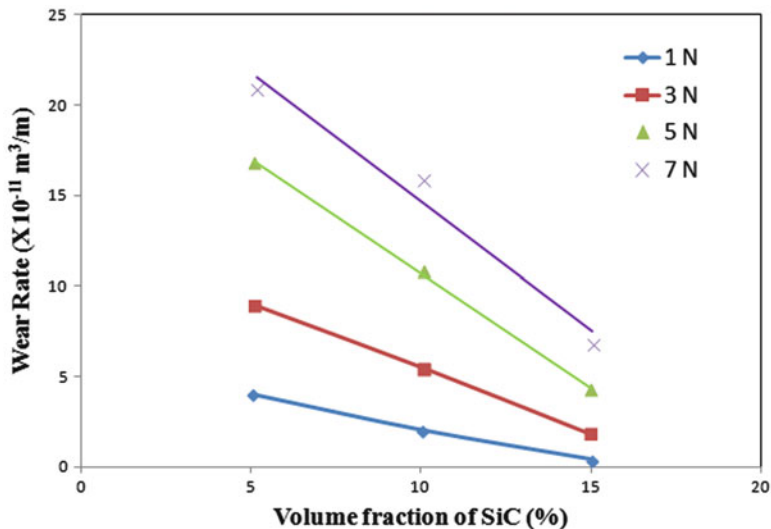


Fig. 8.4 Effect of volume fraction of SiC on the wear rate of aluminum metal matrix composite [36]

$$IWR_{ca}(\%) = \left(\frac{W_a - W_c}{W_a} \right) \times 100 \tag{8.2}$$

where IWR_{ca} is the percentage improvement in the wear resistance of the composite with respect to an alloy, W_a is the wear rate of an alloy, and W_c is the wear rate of the composite.

It is interesting to note that the improvement in the wear rate of the composite significantly diminished by increasing the volume fraction of micron-sized reinforcements over 20 vol%. As shown in Fig. 8.5, the aluminum alloy (Al-1080) reinforced by 10–50 % volume fraction of SiC with particle size of 20 μm indicates that weight loss is decreased by increasing the volume fraction of SiC particles. Until 20 vol% of the reinforcement, the weight loss decreases significantly. However, over 20 vol%, the weight loss decreases a negligible amount with increasing volume fraction of particles [37]. This trend has also been shown by other researchers [25, 35, 38]. Besides, it is commonly recommended for MMCs reinforced by ceramic particles that the volume fraction of ceramic should not be more than 30 vol% if the composite is proposed for structural applications [39].

Similar experiments have been carried out with nano-composites. A nano-composite is a multiphase solid material where the size of one of the phases or the constituents, at least in one dimension, is less than 100 nm or has a structure included with nano grains [40]. Metal matrix nano-composites (MMNCs) usually

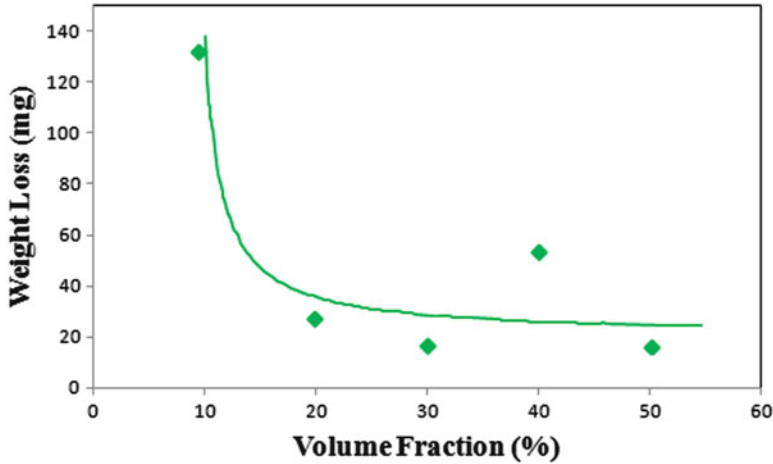


Fig. 8.5 Weight losses of the aluminum composite with vol% of SiC as reinforcement [37]

have better mechanical and tribological properties than those of MMCs reinforced by micron-sized particles [41–46].

Two factors have significant effects on the properties of MMNCs. They are (a) distribution of nanoparticles into the metal matrix and (b) deagglomeration of nanoparticles. Researchers have demonstrated that by having a good distribution of nanoparticles in the matrix [47, 48] and avoiding agglomeration of nanoparticles in the matrix [45, 49], the properties of MMNCs can be improved.

Among different nano reinforcements, such as Al_2O_3 and SiC, the recently developed nano reinforcement, such as carbon nano tubes (CNTs), has shown significant interest for researchers due to their excellent mechanical and physical properties. It is expected that the utilization of multi-wall carbon nano tubes (MWCNTs) will increase in the industrial applications due to their optimum cost. Thus, there have been many investigations to develop MMNCs reinforced with MWCNTs using various fabrication routes. One of the best methods for dispersion of CNTs in matrices is the frequently utilized powder metallurgy process [9, 19].

Some studies have explored the effect of volume fraction of CNTs as reinforcement in MMNCs on the wear rate of these composites [50–52]. The results illustrate a reduction of wear rate with an increase in the volume fraction of reinforcements up to 20 vol% as shown in Fig. 8.6. Nano-sized particles, when compared to the micron-sized particles, have more surface area than its volume. As a result, nanoparticles come together and tend to agglomerate so as to decrease their surface energy. This phenomenon has a negative effect on nano-composites and causes the properties of nano-composites to degrade. A good distribution of nanoparticles into the matrix and agglomeration prevention of nanoparticles are two important challenges during synthesizing of nano-composites. These challenges are much more difficult in larger volume fraction of nano-sized particles in the matrix. A study on aluminum matrix composites reinforced by MWCNTs has shown that the

Fig. 8.6 Effects of CNT volume fraction on the wear rate of the CNT/Al composite at a sliding velocity of 0.1571 ms^{-1} under a load of 30 N [50]

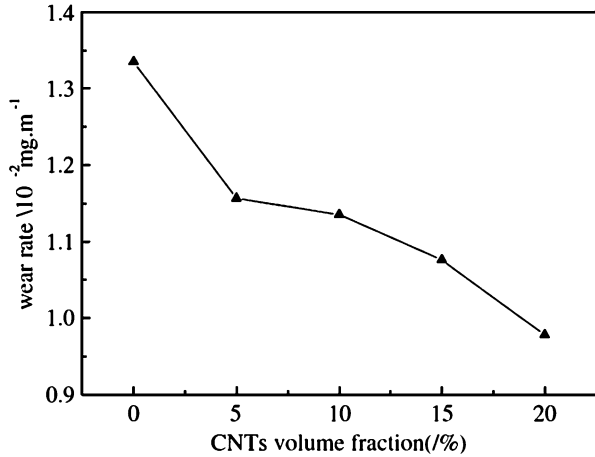
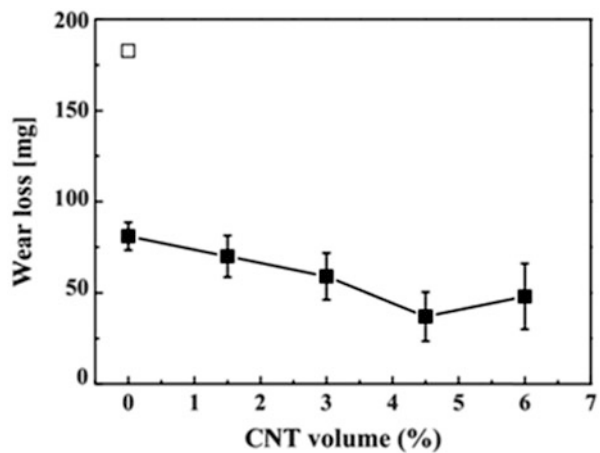


Fig. 8.7 The variation of wear rate with volume fraction of MWCNT [9]



composite with 4.5 vol% of CNTs has the minimum wear rate after 30 min of sliding at an applied load of 30 N and a sliding speed of 0.12 mm/s as shown in Fig. 8.7 [9]. According to this figure, by increasing the volume fraction of MWCNT up to 4.5 vol%, the wear loss of the composites gradually decreases and the wear resistance of the composites increases. However, when the volume fraction of the MWCNTs is more than 4.5 vol%, the wear resistance of the composite decreases. The decreasing tendency in wear resistance of the composites which contain the higher volume fraction of MWCNTs may due to the presence of voids, cracks, and agglomeration of nanoparticles. These kinds of defects could act as a source of weakening of the composites, and as a result the wear resistance of the composite decreases [9]. Moreover, many researchers [45, 53] have shown that when the volume fraction of nanoparticles in the composite is more than 4 vol%, the

mechanical properties of composite decrease due to the agglomeration of nano-sized particles. It is worth mentioning that the mechanical properties of MMCs have a great influence on wear resistance of the composites. A decrease in mechanical properties of the composites may lead to a decrease in wear resistance.

Hybrid metal matrix composites (HMMCs) are engineering materials reinforced with a combination of two or more different types of reinforcements. These composites have combined the properties of each reinforcement and exhibited an improvement in physical, mechanical, and tribological properties of the composites [54]. It has been reported that the hybrid composites have a lower wear rate than the composites which are reinforced by only one type of reinforcements. In general, the tribological properties of HMMCs are also increased by increasing the amount of reinforcements in the composites [55, 56].

As mentioned earlier, graphite is a solid lubricant which is used as reinforcement in metal matrices. Graphite usually increases the wear resistance of the composites by forming a protective layer between two contact surfaces of materials during sliding [7, 57]. In addition, it has been reported that by adding a hard ceramic particle like Al_2O_3 or SiC to the matrix the mechanical properties of the composites increase [45, 46]. Moreover, it has been shown that synthesizing an HMMC reinforced with hard ceramic particle and graphite at the same time increases the mechanical properties and also the wear resistance of the composite simultaneously [25]. In this regard, efforts have been made to study the mechanical behavior and wear resistance of two aluminum matrix composites. The results showed that hybrid aluminum alloy matrix composite reinforced by SiC and graphite (20 % SiC–3 % and 10 % Gr–Al) has a better mechanical properties and wear resistance than aluminum alloy matrix composite reinforced by SiC (20% SiC–A356) [6].

The wear behavior of a hybrid aluminum matrix composite reinforced by SiC and Al_2O_3 is also investigated. The results showed that the wear resistance of the hybrid composites reinforced by SiC and Al_2O_3 is higher than that of the aluminum matrix composite reinforced by SiC or Al_2O_3 alone [5, 54, 58–60]. Similar results are also observed in magnesium alloy hybrid composites. The magnesium alloy hybrid composite reinforced by Saffil short fibers and SiC particles has lower wear rate than magnesium alloy reinforced only with Saffil short fibers. In the hybrid composite, the SiC particles remain intact while retaining their load bearing capacity. The SiC particles also delay the fracturing of saffil short fibers at higher loads and cause an increase to the wear resistance of the hybrid composites [61].

Figure 8.8 shows a general variation of wear rate with volume fraction of reinforcement in the composites. The data for this plot was obtained from different references [22, 38, 62–66]. As indicated earlier, the wear rate of the composite decreases with increasing volume fraction of the reinforcement particles.

It has been indicated that the coefficient of friction of the composites decreased with increase in the volume fraction of reinforcements [25, 26, 50, 67, 68]. The coefficient of friction of aluminum matrix composite reinforced with CNTs decreases with increasing volume fraction of CNTs in the composite as shown in Fig. 8.9. It has been indicated that an increasing volume fraction of CNTs at the contact surfaces reduces the direct contact between the metal matrix and the

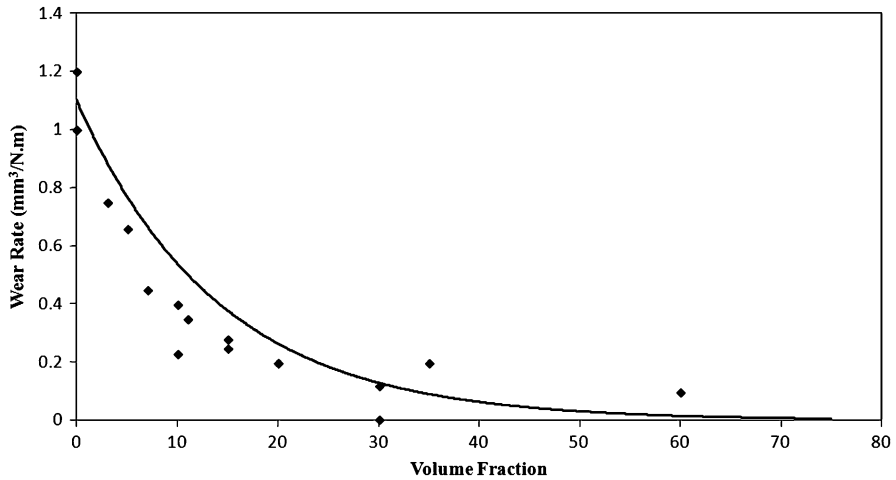
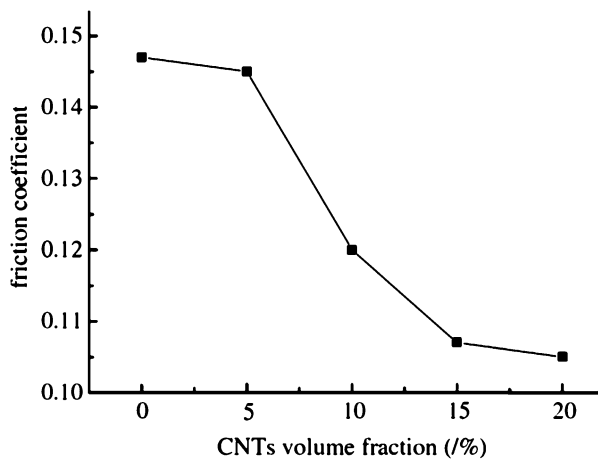


Fig. 8.8 Effect of volume fraction of reinforcement on wear rate of composites [22, 38, 62–66]

Fig. 8.9 Effects of CNT volume fraction on the friction coefficient of the CNT/Al composite at a sliding velocity of 0.15 ms^{-1} under a load of 30 N [50]



counterface [50, 52]. The CNTs have tube shape and also have the self-lubricating properties. Due to these characteristics, the CNTs can slide or roll easily between the mating metal surfaces; consequently, the coefficient of friction of the MMCs reinforced by CNTs decreases.

The coefficient of friction values of pure aluminum and aluminum matrix composite reinforced by MWCNTs with varying volume fraction is presented in Fig. 8.10. The coefficient of friction of the composite dramatically decreases with increasing volume fraction of MWCNTs up to 4.5 vol% because of the lubricating

Fig. 8.10 Variation of coefficient of friction with MWCNT volume fraction in the composite [9]

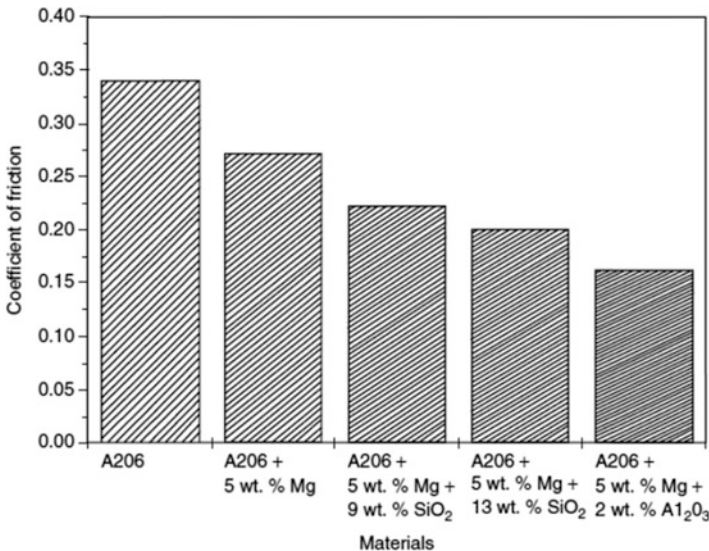
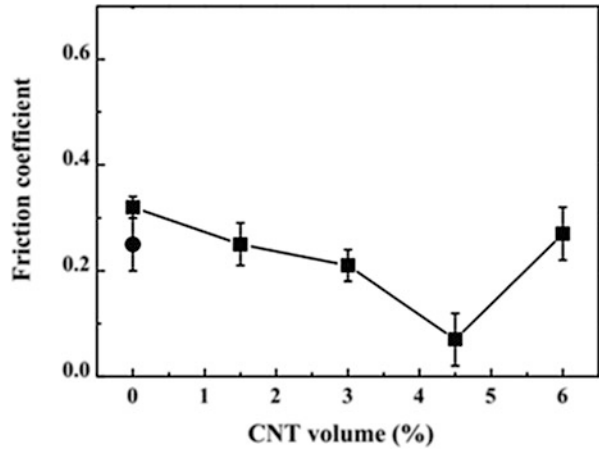


Fig. 8.11 Coefficient of friction values for various metal matrix composites reinforced by micron and nanoparticles [69]

effect of MWCNTs. Later on, the coefficient of friction of the composite increases with increasing volume fraction of MWCNTs. The composite that contains 4.5 vol % MWCNTs has the lowest coefficient of friction (about 0.1) [9].

As indicated earlier, the MMCs reinforced by nano-sized reinforcements usually have better wear resistance than the MMCs reinforced by micron-sized particles. Likewise, the MMNCs usually have lower coefficient of friction than the micron composites. Figure 8.11 shows the coefficient of friction values for aluminum

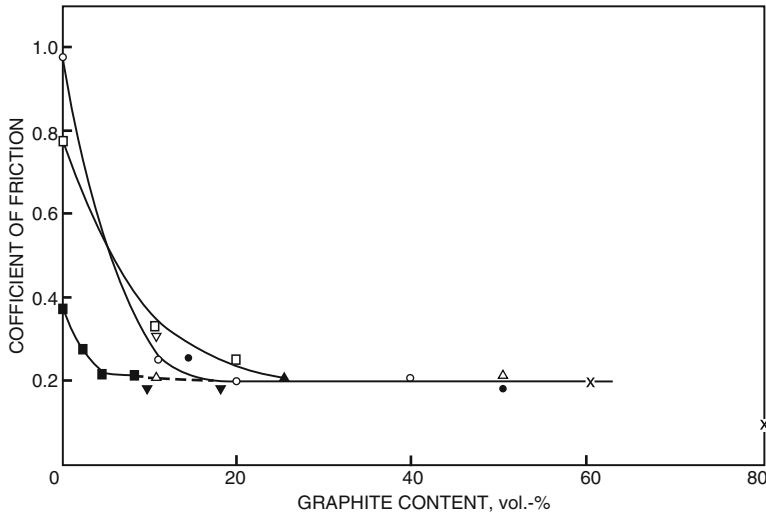


Fig. 8.12 Variation of coefficient of friction with graphite content for composites with different base alloys [70]

alloys and its composites. It can be observed that the A206 alloy shows the highest coefficient of friction values among other materials. Adding of 5 wt% magnesium to the A206 alloy decreased the coefficient of friction to a lower value. It can also be observed that the coefficient of friction values of the micro-composites is lower than that of aluminum alloys. The results show that by increasing the amount of reinforcement (SiO_2) from 9 to 13 wt% in the micro-composites, the coefficient of friction of the composites decreases. Moreover, it has been shown that by using 2 wt% nano-alumina instead of the micro- SiO_2 in the composite, the coefficient of friction of the nano-composite decreases to the lowest values among the materials tested. It is important to be mentioned again that the nano-composite showed the lowest coefficient of friction compared to that of the other micro-composites and unreinforced matrix materials [69].

Figure 8.12 presents the variation of friction coefficient with graphite volume fraction in the composites prepared using different base alloys. This figure shows that the coefficient of friction attains a constant value of close to 0.2 by increasing the amount of graphite in the composites over 20 vol%, and this is true for different composites. This means that the coefficient of friction is almost independent of the matrix and the graphite content over 20 vol%. The coefficient of friction of elemental graphite is about 0.18 and it increases with desorption of adsorbed vapors. Thus, when the content of graphite in the composites exceeds 20 vol%, both of the mating surfaces, including the composite reinforced by graphite and the counterface material like steel, are completely covered with the graphite, and a coefficient of friction value of 0.2, which is close to that of pure graphite against itself (i.e., 0.18), is observed regardless of the matrix material [70].

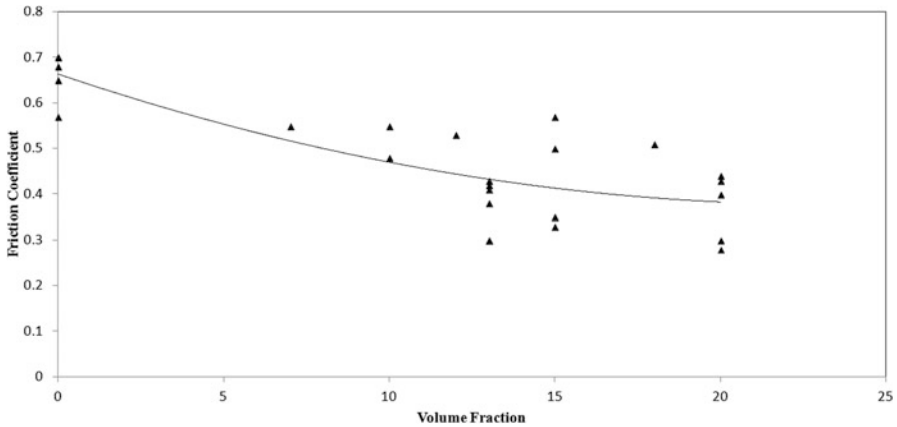


Fig. 8.13 Effect of volume fraction of reinforcements on friction coefficient of composites [13, 15, 38, 65, 71–78]

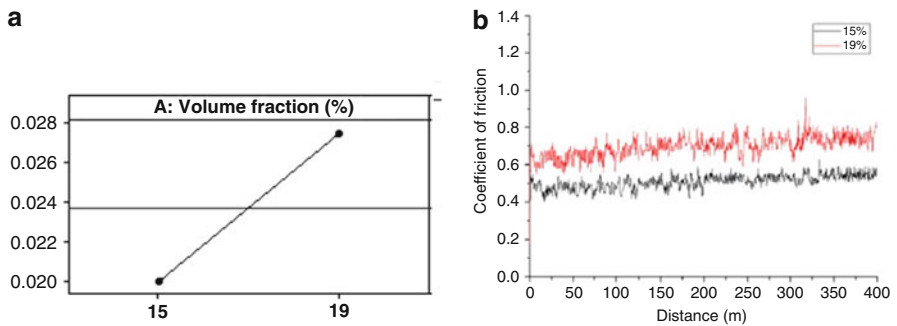
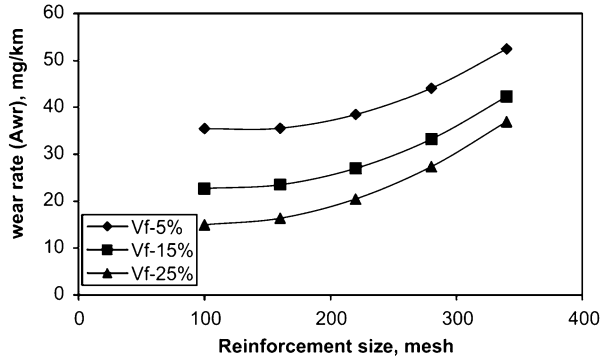


Fig. 8.14 The effect of increasing vol% of B_4C_p on (a) wear rate and (b) the friction coefficient of Al metal matrix composite [13]

Figure 8.13 shows the variation of the coefficient of friction with volume fraction of the reinforcements of composite materials. The data here is obtained from various research works [13, 15, 38, 65, 71–78]. The result shows that the coefficient of friction decreases with increasing volume fraction of the reinforcement in the composites.

It has been shown earlier that the wear rate of the composites generally decreases with increasing reinforcement volume fraction in the MMCs. However, the tribological behavior of the aluminum matrix composites reinforced by B_4C_p has showed different results [13]. It is important to note that the B_4C_p is an extremely hard particle when compared to other reinforcements, such as SiC or Al_2O_3 . The research results indicate that there is an increase in the values of the wear rate (see Fig. 8.14a) and the coefficient of friction (see Fig. 8.14b) of the composites with increasing volume fraction of B_4C particles from 15 to 19 vol%. The amount of

Fig. 8.15 The effect of reinforcement mesh size on the wear rate of MMCs [89]



abraded out B_4C particles at the interface between the counterface and the composite with 19 vol% B_4C in the wear test is higher than that at the interface between the counterface and the composite with 15 vol% B_4C . Consequently, the presence of higher amount of B_4C hard particles between two surfaces causes an increase in the wear rate and the coefficient of friction of the composite. This type of variations is very rare.

2.2 Particle Size

The mechanical and tribological properties of MMCs, such as hardness [79], ultimate tensile strength (UTS) [80], ductility [81], toughness [82], wear resistance [83], and coefficient of friction [84] depend strongly on the size of the reinforcement particles. The reinforcement which can affect the wear resistance of MMCs is an important parameter provided that a good interfacial bonding between the reinforcement and the matrix occurs.

MMC materials usually show a lower wear rate than the unreinforced alloys mainly due to the strength improvement of the composites caused by embedding the particles into the matrices. The particles act as load-bearing constituents in the composite materials and lead to an increase in the wear resistance of the metal matrices reinforced by particles in comparison with the unreinforced alloys [85].

It is well known that the nanoparticle-reinforced MMCs showed better wear resistance than the micro-particle-reinforced MMCs. Within the micro-composites, the effect of the particle size on the wear rate of the MMCs is not clear. Some researchers have indicated a decrease in the wear rate of the MMCs with an increase in the particle size of the reinforcements [6, 23, 86–88]. Efforts have been made to study the wear rate of 2014 Al matrix composite reinforced by SiC with different particle sizes. The results showed that the Al matrix composite reinforced by 15.8 μm SiC particle size has a superior wear resistance than the composite with the same volume fraction of 2.4 μm SiC particle size [23]. Figure 8.15 shows the wear rate of AA7075 Al matrix composite reinforced by SiC particles. The figure

Fig. 8.16 Effect of various SiC particle size (volume fraction of 12 %) on the wear rate of magnesium metal matrix composite [91]

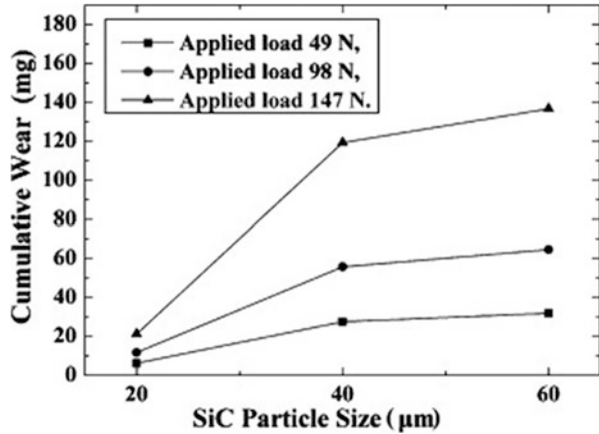
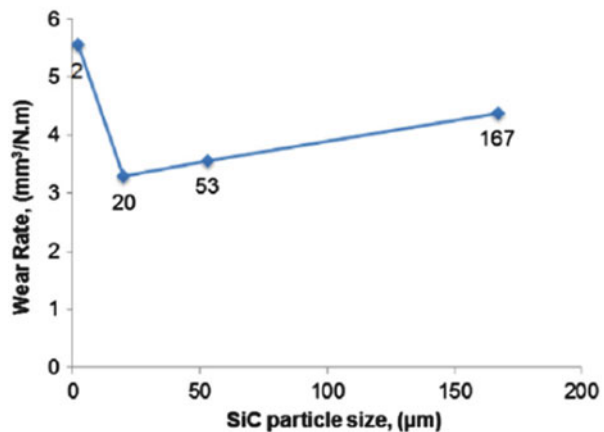


Fig. 8.17 The effect of particle size of reinforcement on the wear rate of the composite [66]



shows an increase in the wear rate of the MMCs with an increase in the mesh size of the reinforcements (increasing the mesh size means decreasing the particle size) [89]. However, other investigations have shown an increase in the wear rate of the MMCs by an increase in the size of the reinforcements [89, 90]. Figure 8.16 shows the wear rate of magnesium matrix composite reinforced by SiC particles. The figure shows an increase in wear rate of the MMCs with an increase in the size of the reinforcements [91]. Nevertheless, some studies show a critical particle size of reinforcements at which the wear rate of the composites changes considerably [66, 90]. Figure 8.17 shows the wear rate of the aluminum matrix composites reinforced by SiC particles (2–167 µm). The wear rate of the composites decreases with particle size up to 20 µm and later it increases with increasing particle size up to 167 µm. It has been observed that a critical particle size is important to determine the wear behavior of the composites. The 20 µm SiC particle size is the critical size for this composite at which the minimum wear rate is obtained [66].

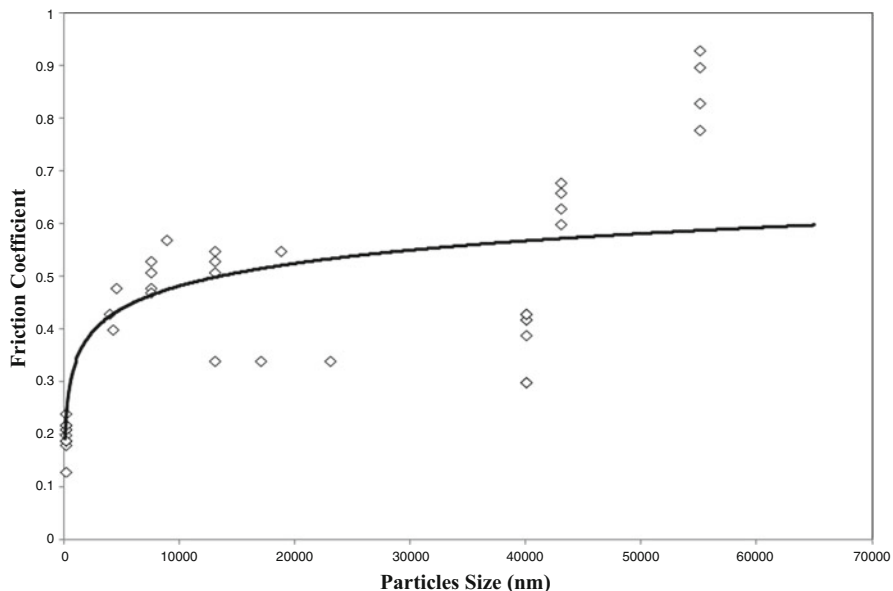


Fig. 8.18 The effect of particle size on coefficient of friction of the composites [14, 65, 72–75, 78, 85, 92, 93]

The effect of reinforcement particle size on the coefficient of friction has been studied. Figure 8.18 shows the variation of the coefficient of friction with particle size. The data presented here is considered from different references [14, 65, 72–75, 78, 85, 92, 93]. The results show that the friction coefficient increases with increasing particle size of the reinforcements.

Based on the above discussion, it is difficult to predict the wear behavior of the micro-composite reinforced by micron-size particles of varying sizes. However, a clear trend was observed when comparing the tribological properties between micron- and nano-composites. Figure 8.19a, b shows the wear rate and coefficient of friction of aluminum matrix composite reinforced by 15 vol% nano and micron Al_2O_3 particles. The results show a significant drop in the friction coefficient and wear rate of aluminum composites when the particle size is reduced below $1\ \mu m$ [94].

2.3 Shape of Particle

Shape of the reinforcements is another factor that may affect the tribological behavior of MMCs. The wear resistance of (a) hybrid aluminum matrix composites reinforced by 10 % Saffil fibers and 5 % graphite fibers, (b) hybrid aluminum matrix composites reinforced by 10 % Saffil fibers and 5 % graphite flake, (c) aluminum

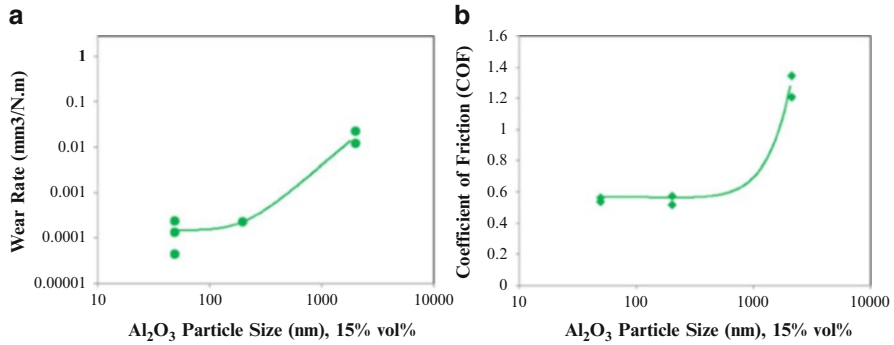


Fig. 8.19 Effect of particle size on (a) wear rate and (b) coefficient of friction of Al-15 vol% Al₂O₃ metal matrix composites [94]

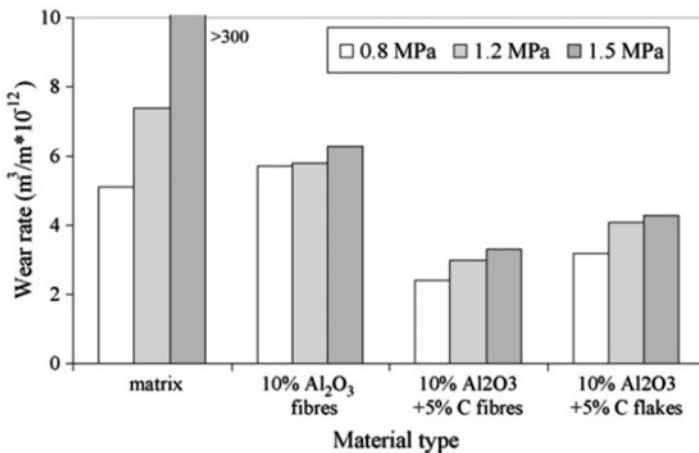


Fig. 8.20 The effect of normal load and graphite shape on the wear behavior of the composite at 0.8, 1.2, and 1.5 MPa contact pressures [10]

matrix composite reinforced by 10 % Saffil fibers, and (d) unreinforced aluminum alloy are compared in Fig. 8.20 [10]. The results showed that aluminum matrix composites reinforced by alumina fibers only prevent adhesion and seizure, especially under higher pressures, greater than 1 MPa. The aluminum matrix composites reinforced by alumina fibers and graphite (hybrid composites) showed a reduction in the wear rate when compared to Al/Saffil composites. Also, the shape of the graphite has an effect on the wear rate of the hybrid composites. The experimental results have indicated that the graphite fibers are more effective than the graphite flakes. This difference is much clear at low volume fraction of alumina fiber in the composites and at high pressure. In addition, the orientation of the alumina fibers affects the wear behavior of the composites, specifically at higher pressure. Parallel

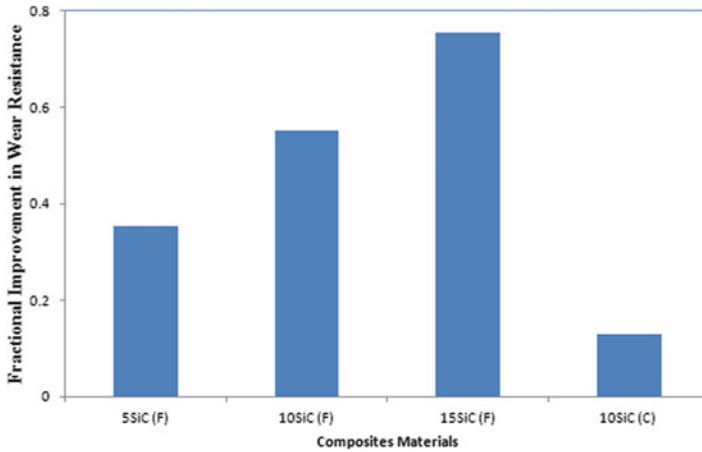


Fig. 8.21 Bar chart showing improvement in wear resistance of metal matrix composites reinforced by fine particles (F) and coarse particles (C) [36]

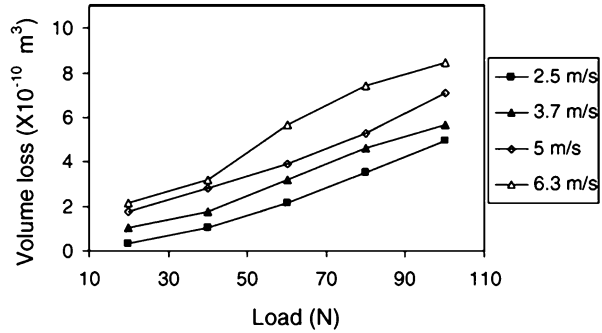
arrangement of the fibers to the friction surface has lower wear rate than the perpendicular arrangement [10].

Figure 8.21 compares the wear resistance of three different composites reinforced by fine particles and a composite reinforced by coarse particles. It was found that the percentage improvement in the wear resistance of the composites with respect to that of an alloy is 26, 55, and 75 % for 5, 10, and 15 vol% fine SiC reinforcements, respectively. On the other hand, the percentage improvement in the wear resistance of 10 vol% coarse SiC particle-reinforced composite is around 15 % as compared to 55 % improvement in 10 vol% fine SiC particle-reinforced composite [36].

2.4 Normal Load

Normal load is an important mechanical factor which affects the wear rate and friction coefficient of MMCs. With increasing applied normal load, especially at higher normal loads, fracture of the reinforcement particles in the matrix may occur. As a result, the mechanical properties of the composite decrease and hence the wear rate of the composites increases to the levels comparable to those of the unreinforced metallic matrix. It is generally accepted that the wear rate of MMCs increases with increasing normal loads during sliding [13, 14, 18, 26, 34–36, 89, 95, 96] as shown in Fig. 8.22. This type of trend has been observed in Al–Fe composite [32], Mg alloy matrix hybrid composite reinforced by Saffil short fibers (diameter 3–8 μm and length 200 μm) and SiC particles (40 μm) [61], AZ91D–0.8 % Ce alloy matrix hybrid composite reinforced by Al_2O_3 short fibers and graphite [86], and Cu/WC composites [97]. In addition to the increase of wear

Fig. 8.22 Variation of wear rate of MMCs with applied normal loads [14]



rate with increasing normal load, the wear mechanism of the composites changes with normal loads. It has been reported that the wear mechanism of the composites is usually by oxidation at lower normal loads. However, the wear mechanism of the composite materials at higher normal load is changed to adhesive wear and delamination wear [24]. It has been reported that a critical normal load would exist during wear test of MMCs [76]. Below this critical normal load, the wear rate is usually mild and steady. However, the wear rate increases and a severe wear occurs above this critical normal load during sliding. It has also been demonstrated that the temperature of the contact surfaces can influence the amount of the critical normal load, and at higher temperature the critical normal load decreases [98].

All flat surfaces and even those polished to a mirror finish are not perfectly flat on an atomic scale. Asperities or surface projections exist on all flat surfaces. When two flat surfaces come into contact, these two surfaces touch only at tops of highest asperity points. As a result, the contacts can be defined by (a) apparent area of contact (AAC) and (b) real area of contact (RAC). The RAC is the total area of asperities of two surfaces which are actually in contact. As a result, the RAC is always less than the AAC. When the surfaces are subjected to a normal load, the contacting asperities are plastically deformed and the RAC increases with increasing normal load and moves towards the amount of AAC. As a result of increasing RAC between two surfaces, the wear rate and also the temperature between these two surfaces usually increase during sliding.

As mentioned earlier, there is a critical normal load above which severe wear occurs and this is because of the increase in the RAC. When the RAC increases and reaches to an amount very close to AAC, it is very difficult for two contacting surfaces to slide over each other. This situation in tribology is referred to as seizure. The seizure occurs for both the unreinforced and reinforced composites. The seizure event is usually accompanied by a sudden increase in wear rate, heavy noise, and vibration [99].

Some studies [14, 33] have shown that at lower normal loads, the wear rates of the composite materials with different volume fraction of the reinforcement and the unreinforced matrices are comparable to each other. The reinforced and unreinforced matrices can tolerate the lower normal loads, and consequently the wear rate is low. However, the difference between the wear rates of the composites and the

Fig. 8.23 The variation of wear rate at low and high loads [14]

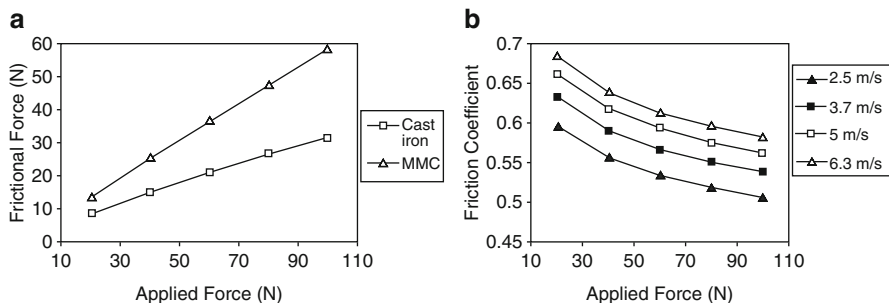
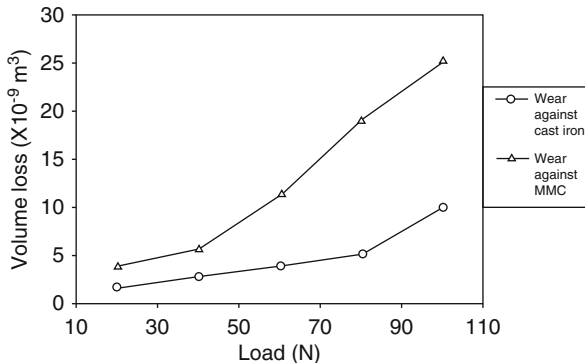


Fig. 8.24 Variation of (a) frictional force and (b) friction coefficient with different applied force [14]

unreinforced matrices is considerable at higher normal loads as shown in Fig. 8.23 [14]. At higher normal loads, the asperities of the unreinforced matrices plastically deform and the RAC increases; accordingly the wear rate also increases. The mechanical properties of the reinforced matrices are usually higher than the unreinforced one, and some amount of normal load is carried by the reinforcements during the wear tests. Thus, the plastic deformation of the asperities of reinforced matrices is delayed longer than the unreinforced one, and hence the reinforced matrices cause a lower wear rate. For example, as shown in Fig. 8.20, the wear rate of the unreinforced aluminum alloy was too high at a high contact pressure of 1.5 MPa, and the test was interrupted because of seizure. But, the wear rate of the composites at that contact pressure is much lower than the unreinforced one [10].

In general, an increment in the applied normal force increases the frictional force (see Fig. 8.24a). It has been reported that the coefficient of friction of MMCs decreases by increasing the normal load as shown in Fig. 8.24b [14, 18, 28, 57, 84, 95]. As an example, the tribological behavior of nickel matrix composites reinforced by graphite illustrates that the friction coefficient of the composites containing graphite decreases to about 0.3 by increasing the normal load [100].

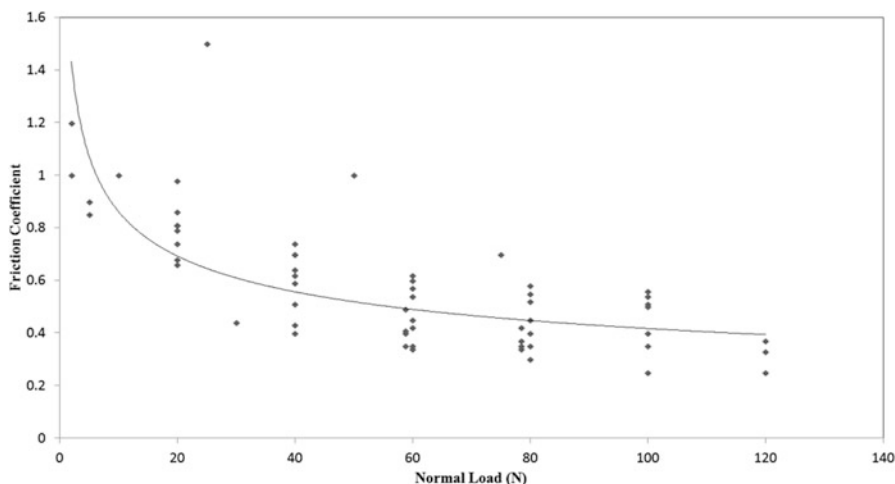


Fig. 8.25 The effect of normal load on friction coefficient [13, 14, 71, 101–104]

This is due to the formation of a transfer film during sliding, and this transfer film is found to be stable for longer duration and a broad range of normal loads. However, at very high normal loads, the transfer film may destroy [14], and as a result, the coefficient of friction may increase.

Figure 8.25 shows the results obtained from different resources demonstrating the effect of normal load on coefficient of friction of MMCs [13, 14, 71, 101–104].

2.5 Sliding Speed

Sliding speed is another important parameter which affects the tribological behavior of MMCs. It has been reported that an increase in the sliding speed causes an increase in the wear rate and decrease in the wear resistance of the MMCs [14, 26, 96, 105], and the variation between the wear rate and sliding speed is usually linear [106, 107]. As the sliding speed increases, the interface temperature also increases resulting in (a) the microthermal softening of matrix material [108], (b) oxide formation on the contact area [109], and (c) decrease in flow stress of the material [109]. In addition, there may be some changes in the microstructure, such as dissolution of precipitates which will also be reflected in the wear behavior. Since the physical and mechanical properties of different matrices in different composites are not the same, the microthermal softening, oxidation, and flow stress for different materials occur at distinct temperatures. As a result, the sliding speed may have different effects on the composites with different matrices.

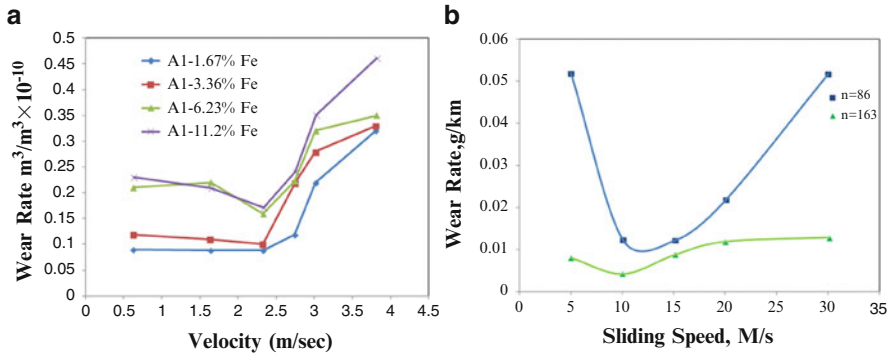


Fig. 8.26 Variation of the wear rate with sliding speed for (a) Al–Fe composites [32] and (b) aluminum matrix composite [5]

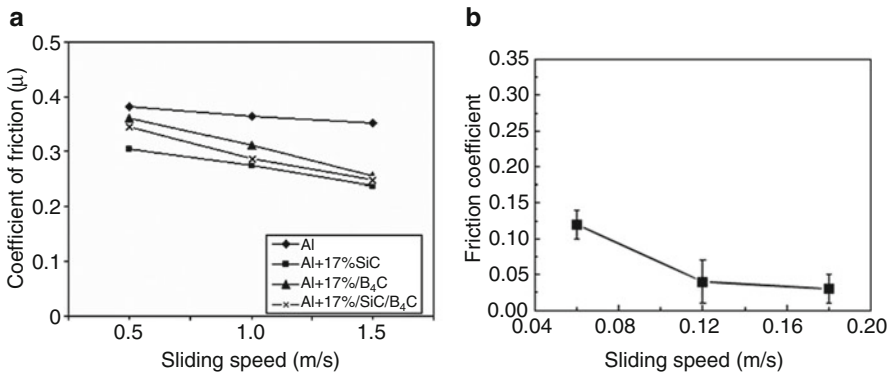


Fig. 8.27 Variation of coefficient of friction with sliding speed for (a) aluminum metal matrix composite reinforced by SiC and B₄C [110] and (b) aluminum metal matrix composite reinforced by CNT [9]

Several studies have shown that an increase in sliding speed leads to an increase in wear rate, especially at higher sliding speed ranges. For instance, Al–Fe and Al–SiC composite illustrate an initial decrease in the wear rate at lower sliding speeds; however, these composites showed a sharp increase in the wear rate at higher sliding speeds (see Fig. 8.26) [5, 32].

Generally, the friction coefficient of MMCs decreases with increasing sliding velocity [9, 13, 14, 18, 84, 110]. Figure 8.27a, b shows the dependency of the coefficient of friction of aluminum matrix composites reinforced by 17 % SiC and B₄C [110] and also 4.5 vol% CNTs [9] at different sliding speeds. It is obvious that the coefficient of friction decreases with increasing sliding speed. It can be observed in Fig. 8.27b that the coefficient of friction attains less than 0.05 with increasing sliding speed for the aluminum matrix nano-composite reinforced by CNTs.

2.6 Temperature

Temperature is another key parameter which affects the wear behavior of MMCs. The effect of temperature on tribological behavior of MMCs due to change in the normal loads and sliding speeds has been discussed in the previous sections. Investigations have demonstrated that the wear rate of MMCs initially decreases with increasing temperature and then increases with increasing temperature [19, 111, 112]. The thermal properties, such as thermal conductivity of the matrices and the reinforcements in the composites, may affect the wear resistance of MMCs at different temperatures. It has been reported that the higher thermal conductivity of the reinforcements in a composite can lead to an improvement in the wear resistance of the composites [113].

In general, there is a significant variation in the wear rate and coefficient of friction of MMCs by varying the temperature. These variations depend on the types of materials in the composites. Some studies have reported that a critical temperature exists which changes the wear rate and coefficient of friction of the MMCs [114, 115]. Below this critical temperature, the wear rate and coefficient of friction are either more or less constant or in some cases decrease inconsiderably with increasing temperature. Above this critical temperature, the wear rate and coefficient of friction increase significantly with increasing temperature. These variations are due to the change of mechanical properties of materials, such as hardness, at high temperatures. The critical temperature is generally higher for the MMCs when compared to the monolithic alloys. Figure 8.28 shows the variation of the wear rate and coefficient of friction with temperature for different aluminum matrix composites and monolithic aluminum alloys [114, 115]. In some composites a significant decrease in the wear rate and coefficient of friction with temperature below the critical temperature has been reported (Fig. 8.29) [116]. Hence, it can be inferred that the variation in tribological behavior of MMCs with temperature depends on the properties of the materials, such as mechanical properties of the materials at high temperatures.

The self-lubricating composites, such as Ni–Cr–W–Fe–C–MoS₂ composites, have excellent self-lubricating properties over a wide range of temperature due to the lubricating effect of graphite and molybdenum disulfide. The friction coefficient values of this composite are in the range of 0.14–0.27, and the wear rates are 1.0×10^{-6} – 3.5×10^{-6} mm³/(Nm) from room temperature to 600 °C (see Fig. 8.30). The results have shown that the wear rate of the composite varied slightly by increasing the amount of MoS₂ in the composite at low temperatures; however, at elevated temperatures, the wear rate and the coefficient of friction of the composite decreased by increasing the amount of MoS₂ in the composite. At temperature above 400 °C, graphite oxidation occurs, and the graphite oxide does not act as a good lubricant at that temperature. As a result, the MoS₂ is responsible for reduction of coefficient of friction and wear rate at elevated temperature [19]. The effect of temperature on the friction coefficient of self-lubricating MMCs is not the same as the effect of temperature on the wear rate of these

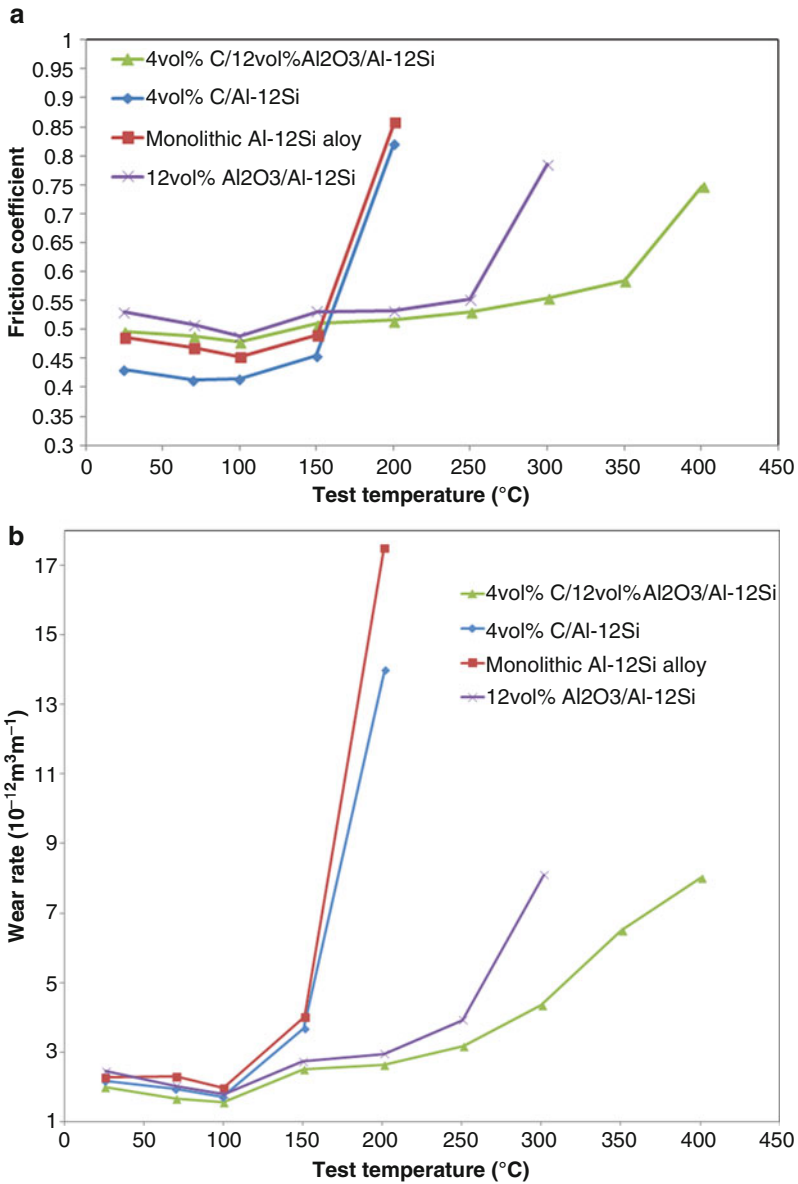


Fig. 8.28 Variations of (a) friction coefficient and (b) wear rate with test temperature for monolithic Al-12Si alloy, 4 vol% C/Al-12Si, 12 vol% Al₂O₃/Al-12Si composites, and 4 vol% C/12 vol% Al₂O₃/Al-12Si hybrid composites [114]

composites. Generally, increase in the temperature leads to a decrease in the coefficient of friction of the MMCs. Figure 8.30b shows the effect of temperature (from room temperature to 600 °C) on the coefficient of friction of nickel-based MMCs. In nickel-based MMCs reinforced by graphite, the friction coefficient in

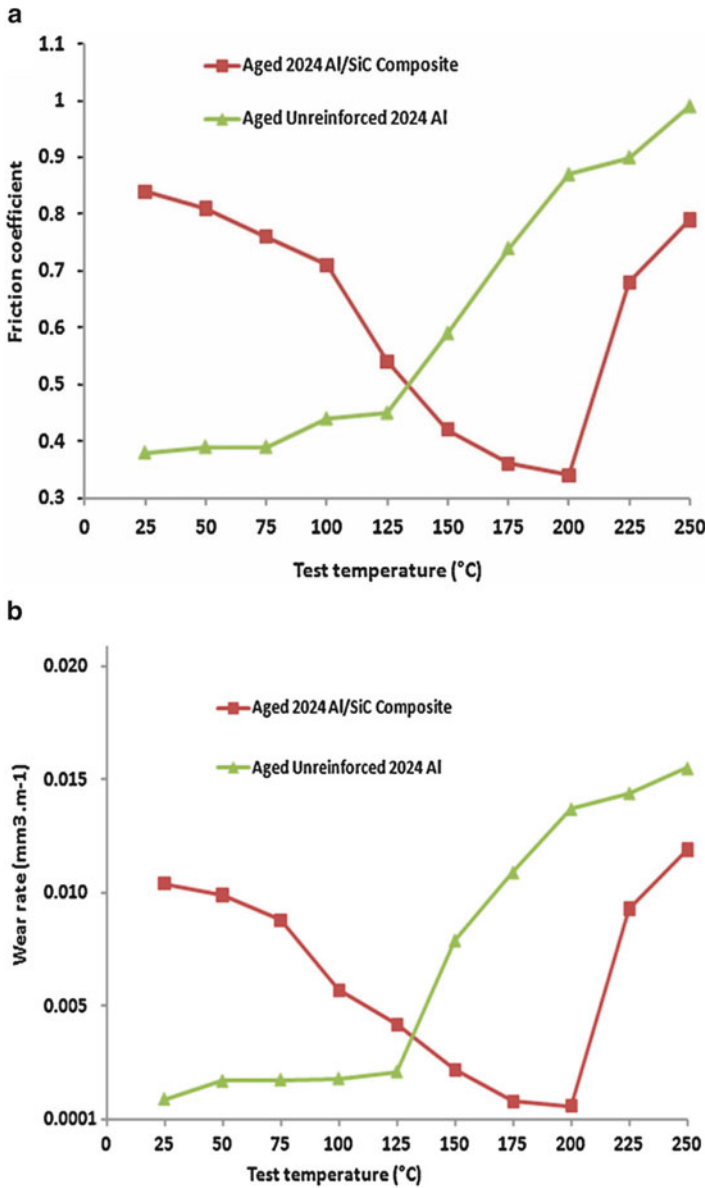
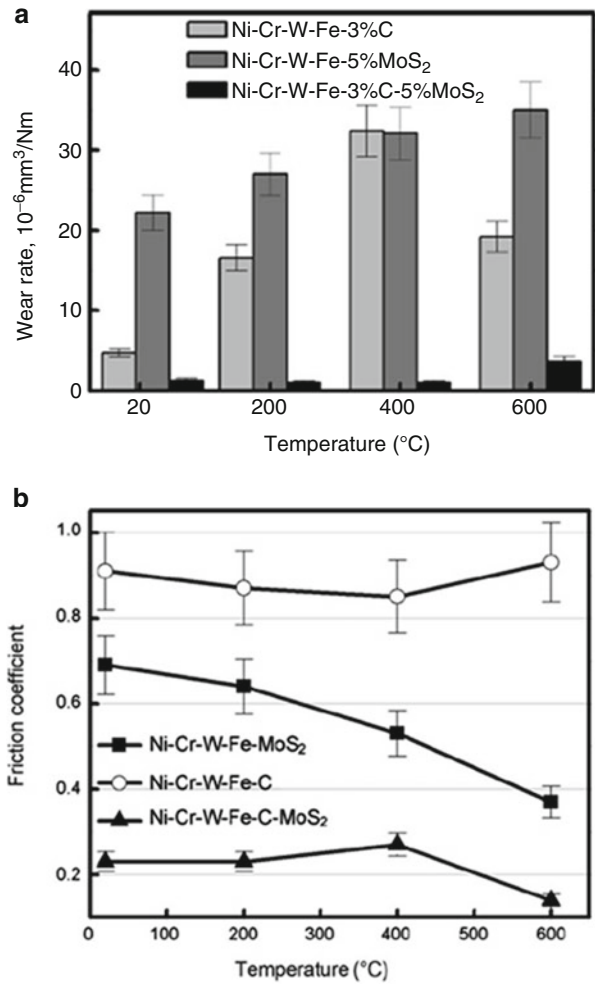


Fig. 8.29 Variations of (a) friction coefficient and (b) wear rate with test temperatures for aged 2024 Al/20 vol% SiC composite and aged unreinforced 2024 Al at the applied load of 20 N [116]

this range of temperature is about 0.8–1.0, while it is about 0.4–0.7 for nickel-based matrix composites reinforced by molybdenum disulfide. When graphite and MoS₂ are combined and used as reinforcement for nickel-based matrix, both the friction coefficient and the wear rate are reduced significantly. For instance, the coefficient

Fig. 8.30 The effect of temperature on the (a) wear rates and (b) friction coefficients of Ni matrix composite reinforced with graphite and MoS₂ lubricants [19]



of friction is reduced to about 0.2. In addition, the results have shown that at temperatures above 400 °C the oxidation of graphite occurs. At this temperature, the oxide layers form, and these layers play a key role of lubricant in the composites instead of graphite [19].

3 Summary

This chapter highlights the important parameters that affect wear and friction behavior of MMCs. More specifically, the influences of reinforcement size, volume fraction of reinforcement, shape of particles, normal load, sliding speed, and temperature on wear and friction behavior of MMCs have been discussed. As the

tribological parameters, such as normal load, sliding speed, and temperature, vary on a wide range and also the counterface materials differ in different experimental tests, comparing the results of tribological behavior of different composites is extremely difficult. Composite materials usually demonstrate enhanced tribological behavior such as wear rate and coefficient of friction than unreinforced alloys, and this is mainly due to the strength improvement of the composites achieved by adding the particles as reinforcement into the matrix. Moreover, hybrid MMCs demonstrate better tribological properties than the MMCs. The reinforcement has a significant effect on wear and friction behavior of MMCs than other parameters such as the normal load and the sliding speed.

The volume fraction, size, and shape of reinforcements are the material factors which affect the tribological behavior of the composites. The effect of volume fraction of reinforcements is that the wear resistance of composite materials is enhanced and the friction coefficient of composites decreased by increasing the micron- and nano-size reinforcement content in the composite. However, an increase in the volume fraction of micron-size reinforcements over 20 vol% has no significant improvement on the wear rate. It is commonly suggested that the volume fraction of reinforcements should not be more than 30 vol% if the composite is proposed for structural applications. Deagglomeration and distribution of nano-size particles in the composites are two key challenges during production of nano-composites. These challenges can restrict the usage of high volume fraction of nano-sized particles in the composite. Among micro-composites, the reinforcement particle size has no clear effect on the wear and friction behavior of the composites. Some studies have shown a decrease in the wear rate of the MMCs with an increase in the particle size of the reinforcements, and on the other hand, other studies have shown an increase in the wear rate of the MMCs with an increase in the particle size of the reinforcements. When comparing micro- and nano-composites, the MMNCs usually show lower coefficient of friction and wear rate than the micro-composites.

Normal load is an important mechanical factor that affects the tribological behavior of the composites. The results have shown that the wear rate increases and friction coefficient of MMCs decreases with increasing the normal load. Similar to the normal load, sliding speed also influences friction and wear performance. An increase in the wear rate and a decrease in the friction coefficient of the MMCs occur when sliding speed increases during the wear test. The relationship between the wear rate with the normal load and the sliding velocity is almost linear. Temperature is another important parameter that affects the tribological behavior of MMCs. The wear rate and friction coefficient decrease with increasing temperature up to a critical temperature, and thereafter both wear rate and friction coefficient increase with increasing temperature.

References

1. Nosonovsky M, Rohatgi PK (2012) *Biomimetics in materials science*. Springer, New York
2. Wei Y et al (2011) Characterizations of DLC/MAO composite coatings on AZ80 Magnesium alloy. *Acta Metall Sin* 47:1535–1540
3. Ted Guo ML, Tsao C-YA (2000) Tribological behavior of self-lubricating aluminium/SiC/graphite hybrid composites synthesized by the semi-solid powder-densification method. *Compos Sci Technol* 60(1):65–87
4. Wu Y et al (1997) A study of the optimization mechanism of solid lubricant concentration in Ni/MoS₂ self-lubricating composite. *Wear* 205:64–70
5. Kozma M (2003) Friction and wear of aluminum matrix composites. In: 3rd national tribology conference, Galati, Romania
6. Jinfeng L et al (2009) Effect of graphite particle reinforcement on dry sliding wear of SiC/Gr/Al composites. *Rare Metal Mater Eng* 38(11):1894–1898
7. Riahi AR, Alpas AT (2001) The role of tribo-layers on the sliding wear behavior of graphitic aluminum matrix composites. *Wear* 251(1–12):1396–1407
8. Sannino AP, Rack HJ (1995) Dry sliding wear of discontinuously reinforced aluminum composites: review and discussion. *Wear* 189:1–19
9. Choi HJ, Lee SM, Bae DH (2010) Wear characteristics of aluminum-based composites containing multi-walled carbon nanotubes. *Wear* 270:12–18
10. Naplocha K, Granat K (2008) Dry sliding wear of Al/Saffil/C hybrid metal matrix composites. *Wear* 265:1734–1740
11. Akhlaghi F, Pelaseyyed SA (2004) Characterization of aluminum/graphite particulate composites synthesized using a novel method termed “in-situ powder metallurgy”. *Mater Sci Eng A* 385:258–266
12. Kim I-Y, Lee Y-Z (2011) Tribological behavior of aluminum-CNT coated metal composite under dry and water lubricated conditions. *J Nanosci Nanotechnol* 11:335–338
13. Toptan F, Kerti I, Rocha LA (2012) Reciprocal dry sliding wear behavior of B₄C reinforced aluminum alloy matrix composites. *Wear* 290–291:74–85
14. Natarajan N, Vijayanarangan S, Rajendran I (2006) Wear behaviour of A356/25SiC_p aluminium matrix composites sliding against automobile friction material. *Wear* 261:812–822
15. Shafiei-Zarghani A, Kashani-Bozorg SF, Zarei-Hanzaki A (2009) Microstructures and mechanical properties of Al/Al₂O₃ surface nano-composite layer produced by friction stir processing. *Mater Sci Eng A* 500:84–91
16. Ghasemi-Kahrizangi A, Kashani-Bozorg SF (2012) Microstructure and mechanical properties of steel/TiC nano-composite surface layer produced by friction stir processing. *Surf Coat Technol* 209:15–22
17. Sharma SC (2001) The sliding wear behavior of Al6061–garnet particulate composites. *Wear* 249:1036–1045
18. Hemath Kumar G et al. (2010) The abrasive wear behaviour of Al-SiC_p composites for automotive parts In: *Frontiers in automobile and mechanical engineering 2010*. Chennai, India
19. Li JL, Xiong DS (2008) Tribological properties of nickel-based self-lubricating composite at elevated temperature and counterface material selection. *Wear* 265:533–539
20. Ramesh CS et al (2013) Tribological characteristics of innovative Al6061–carbon fiber rod metal matrix composites. *Mater Design* 50:597–605
21. Tu JP, Yang YZ (2000) Tribological behaviour of Al₁₈B₄O₃₃-whisker-reinforced hypoeutectic Al–Si–Mg-matrix composites under dry sliding conditions. *Compos Sci Technol* 60(9):1801–1809
22. Bindumadhavan PN, Wah HK, Prabhakar O (2001) Dual particle size (DPS) composites: effect on wear and mechanical properties of particulate metal matrix composites. *Wear* 248 (1–2):112–120

23. Alpas AT, Zhang J (1994) Effect of microstructure (particulate size and volume fraction) and counterface material on the sliding wear resistance of particulate-reinforced aluminum matrix composites. *Metall Mater Trans A* 25(5):969–983
24. Gul F, Acilar M (2004) Effect of the reinforcement volume fraction on the dry sliding wear behaviour of Al–10Si/SiC_p composites produced by vacuum infiltration technique. *Compos Sci Technol* 64(13–14):1959–1970
25. Prasad SV, Asthana R (2004) Aluminum metal–matrix composites for automotive applications: tribological considerations. *Tribol Lett* 17(3):445
26. Kumar KR et al (2012) Effect of particle size on mechanical properties and tribological behaviour of aluminium/fly ash composites. *Sci Eng Compos Mater* 19(3):247–253
27. Purohit R, Hemathkumar G, Sgar R (2002) Fabrication and wear testing of Aluminum based metal matrix composite automotive parts. In: National seminar on emerging trends in manufacturing, Varanasi, India
28. Hemath Kumar G et al. (2003) Abrasive friction and wear behaviour of Al-SiC_p composite for Valve guide. In: International conference, Delhi, India
29. Das S et al (2000) Influence of load and abrasive size on the two body abrasive wear of Al–SiC composites. *Aluminum Trans* 2:27–36
30. Das S, Mondal DP, Dixit G (2001) Mechanical properties of pressure die cast Al hard part composite. *Metall Mater Trans A* 32(3):633–642
31. Das S et al (2008) Synergic effect of reinforcement and heat treatment on the two body abrasive wear of an Al–Si alloy under varying loads and abrasive sizes. *Wear* 264:47–59
32. Srivastava S, Mohan S (2011) Study of wear and friction of Al-Fe metal matrix composite produced by liquid metallurgical method. *Tribol Industry* 33(3):128–137
33. Zhang M-J et al (2010) Effect of graphite content on wear property of graphite/Al₂O₃/Mg-9Al-1Zn-0.8Ce composites. *Trans Nonferrous Metals Soc China* 20:207–211
34. Degnan CC, Shipway PH (2002) Influence of reinforcement volume fraction on sliding wear behaviour of SHS derived ferrous based metal matrix composite. *Mater Sci Technol* 18 (10):1156–1162
35. Vencl A, Rac A, Bobic I (2004) Tribological behaviour of Al-based MMCs and their application in automotive industry. *Tribol Ind* 26(3–4):31–38
36. Mondal DP, Das S (2006) High stress abrasive wear behaviour of aluminium hard particle composites: effect of experimental parameters, particle size and volume fraction. *Tribol Int* 39:470–478
37. Cerit AA et al (2008) Effect of reinforcement particle size and volume fraction on wear behaviour of metal matrix composites. *Tribol Ind* 30(3–4):31–36
38. Uyyuru RK, Surappa MK, Brusethaug S (2006) Effect of reinforcement volume fraction and size distribution on the tribological behavior of Al-composite/brake pad tribocouple. *Wear* 260:1248–1255
39. Miserez A et al (2004) Particle reinforced metals of high ceramic content. *Mater Sci Eng A* 387–389:822–831
40. Ajayan PM, Schadler LS, Braun PV (2006) Nanocomposite science and technology. Wiley, New York
41. Yesil ZD et al (2008) Evaluation of the wear resistance of new nanocomposite resin restorative materials. *J Prosthet Dent* 99(6):435–443
42. Kim KT, Cha S, Hong SH (2007) Hardness and wear resistance of carbon nanotube reinforced Cu matrix nanocomposites. *Mater Sci Eng A* 449–451:46–50
43. Tu JP et al (2003) Dry sliding wear behavior of in situ Cu–TiB₂ nanocomposites against medium carbon steel. *Wear* 255(7–12):832–835
44. Shi L et al (2006) Mechanical properties and wear and corrosion resistance of electrodeposited Ni–Co/SiC nanocomposite coating. *Appl Surf Sci* 252(10):3591–3599
45. Tabandeh Khorshid M, Jenabali Jahromi SA, Moshksar MM (2010) Mechanical properties of tri-modal Al matrix composites reinforced by nano- and submicron-sized Al₂O₃ particulates developed by wet attrition milling and hot extrusion. *Mater Design* 31(8):3880–3884

46. Derakhshandeh Haghghi R et al (2012) A comparison between ECAP and conventional extrusion for consolidation of aluminum metal matrix composite. *J Mater Eng Perform* 21 (9):1885–1892
47. Torralba JM, da Costa CE, Velasco F (2003) P/M aluminum matrix composites: an overview. *J Mater Process Technol* 133:203–206
48. Prabhu B et al (2006) Synthesis and characterization of high volume fraction Al–Al₂O₃ nanocomposite powders by high-energy milling. *Mater Sci Eng A* 425:192–200
49. Suryanarayana C (2001) Mechanical alloying and milling. *Prog Mater Sci* 46:1–184
50. Zhou S-M et al (2007) Fabrication and tribological properties of carbon nanotubes reinforced Al composites prepared by pressureless in filtration technique. *Compos Part A Appl Sci Manufact* 38(2):301–306
51. Dong SR, Tu JP, Zhang XB (2001) An investigation of the sliding wear behavior of Cu-matrix composite reinforced by carbon nanotubes. *Mater Sci Eng A* 313(1–2):83–87
52. Wang LY et al (2003) Friction and wear behavior of electroless Ni-based CNT composite coatings. *Wear* 254:1289–1293
53. Kang YC, Chan SL (2004) Tensile properties of nanometric Al₂O₃ particulate-reinforced aluminum matrix composites. *Mater Chem Phys* 85:438–443
54. Dolata-Grosz A, Wiecek J (2007) Tribological properties of hybrid composites containing two carbide phases. *Arch Mater Sci Eng* 28(3):149–155
55. Mahendra KV, Radhakrishna K (2010) Characterization of Stir Cast Al–Cu–(fly ash + SiC) Hybrid Metal Matrix Composites. *J Compos Mater* 44(8):989–1005
56. Basavarajappa S et al (2006) Dry sliding wear behavior of Al 2219/SiC_p-Gr hybrid metal matrix composites. *J Mater Eng Perform* 15(6):668–674
57. Radhika N, Subramanian R, Venkat Prasat S (2011) Tribological behaviour of Aluminium/Alumina/Graphite hybrid metal matrix composite using taguchi's techniques. *J Miner Mater Character Eng* 10(5):427–443
58. Seyed Reihani SM (2006) Processing of squeeze cast Al6061–30vol% SiC composites and their characterization. *Mater Design* 27(3):216–222
59. Anandkumar R et al (2007) Microstructure and wear studies of laser clad Al-Si/SiC_p composite coatings. *Surf Coat Technol* 201(24):9497–9505
60. Fu HH, Han KS, Song J (2004) Wear properties of Saffil/Al, Saffil/Al₂O₃/Al and Saffil/SiC/Al hybrid metal matrix composites. *Wear* 256(7–8):705–713
61. Mondal AK, Kumar S (2009) Dry sliding wear behavior of magnesium alloy based hybrid composites in the longitudinal direction. *Wear* 267:458–466
62. Miyajima T, Iwai Y (2003) Effects of reinforcements on sliding wear behavior of aluminum matrix composites. *Wear* 255(1–6):606–616
63. Gurcan AB, Baker TN (1995) Wear behaviour of AA6061 aluminium alloy and its composites. *Wear* 188(1–2):185–191
64. Prasad SV, Rohatgi PK (1987) Tribological properties of Al alloy particle composites. *JOM* 39(11):22–26
65. Uyyuru RK, Surappa MK, Brusethaug S (2007) Tribological behavior of Al–Si–SiC_p composites/automobile brake pad system under dry sliding conditions. *Tribol Int* 40 (2):365–373
66. Karams MB et al (2012) The effects of different ceramics size and volume fraction on wear behavior of Al matrix composites (for automobile cam material). *Wear* 289:73–81
67. Zou XG et al (2003) Sliding wear behaviour of Al-Si-Cu composites reinforced with SiC particles. *Mater Sci Technol* 19(11):1519–1526
68. Zhan Y, Zhang G (2004) Friction and wear behavior of copper matrix composites reinforced with SiC and graphite particles. *Tribol Lett* 17(1):91–98
69. Rohatgi PK et al (2011) Tribological behavior of aluminum micro- and nano-composites. *Int J Aerospace Innov* 3(3):153–162
70. Rohatgi P, Ray S, Liu Y (1992) Tribological properties of metal matrix-graphite particle composites. *Int Mater Rev* 37:129–149

71. Maleque MA, Karim MR (2009) Wear behavior of as-cast and heat treated triple particle size SiC reinforced aluminum metal matrix composites. *Ind Lubr Tribol* 61(2):78–83
72. Korkut MH (2004) Effect of particulate reinforcement on wear behaviour of aluminium matrix composites. *Mater Sci Technol* 20(1):73–81
73. Shorowordi KM, Haseeb ASMA, Celis JP (2006) Tribo-surface characteristics of Al–B₄C and Al–SiC composites worn under different contact pressures. *Wear* 261(5–6):634–641
74. Tyagi R (2005) Synthesis and tribological characterization of in situ cast Al–TiC composites. *Wear* 259(1–6):569–576
75. Shorowordi KM, Haseeb ASMA, Celis JP (2004) Velocity effects on the wear, friction and tribochemistry of aluminum MMC sliding against phenolic brake pad. *Wear* 256(11–12):1176–1181
76. Wang Y et al (2001) Dry wear behaviour and its relation to microstructure of novel 6092 aluminium alloy–Ni₃Al powder metallurgy composite. *Wear* 251(1–2):1421–1432
77. Reddy GM, Rao KS, Mohandas T (2009) Friction surfacing: novel technique for metal matrix composite coating on aluminium–silicon alloy. *Surf Eng* 25(1):25–30
78. Zhang ZF, Zhang LC, Mai YW (1995) Particle effects on friction and wear of aluminium matrix composites. *J Mater Sci* 30(23):5999–6004
79. Montoya-Dávila M, Pech-Canul MA, Pech-Canul MI (2007) Effect of bi- and trimodal size distribution on the superficial hardness of Al/SiC_p composites prepared by pressureless infiltration. *Powder Technology* 176(2):66–71
80. Deng KK, Wang XJ, Wu YW, Hu XS, Wu K, Gan WM (2012) Effect of particle size on microstructure and mechanical properties of SiC_p/AZ91 magnesium matrix composite. *Mater Sci Eng A* 543:158–163
81. Cocen U, Onel K (2002) Ductility and strength of extruded SiC_p/Aluminium-alloy composites. *Comput Sci Technol* 62:275–282
82. Gong J, Miao H, Zhao Z (2001) The influence of TiC-particle-size on the fracture toughness of Al₂O₃-30 wt.% TiC composites. *Journal of the European Ceramic Society* 21(13):2377–2381
83. Matějka V, Lu Y, Jiao L, Huang L, Simha Martynková G, Tomášek V (2010) Effects of silicon carbide particle sizes on friction-wear properties of friction composites designed for car brake lining applications. *Tribol Int* 43(1):144–151
84. Zhang S, Wang F (2007) Comparison of friction and wear performances of brake material dry sliding against two aluminum matrix composites reinforced with different SiC particles. *J Mater Process Technol* 182(1–3):122–127
85. Habibnejad-Korayem M et al (2010) Tribological behavior of pure Mg and AZ31 magnesium alloy strengthened by Al₂O₃ nano-particles. *Wear* 268:405–412
86. Zhang M-J et al (2008) Effect of graphite particle size on wear property of graphite and Al₂O₃ reinforced AZ91D-0.8%Ce composites. *Trans Nonferrous Met Soc China* 18:273–277
87. Toshiro M, Tomomi H, Yoshiro I (2005) Effect of particle diameter and volume fraction on wear behaviour of SiC-particle reinforced aluminum matrix composites. *Trans Jpn Soc Mech Eng C* 71(710):3054–3060
88. Jo SK et al (2012) Effect of SiC particle size on wear properties of Al₂O₃. SiO₂/SiC/Mg hybrid metal matrix composites. *Tribol Lett* 45:101–107
89. Kumar S, Balasubramanian V (2010) Effect of reinforcement size and volume fraction on the abrasive wear behaviour of AA7075 Al/SiC_p P/M composites—a statistical analysis. *Tribol Int* 43(1–2):414–422
90. Baki Karamzş M, Nair F (2008) Effects of reinforcement particle size in MMCs on extrusion die wear. *Wear* 265(11–12):1741–1750
91. Zhang S, Jiang F, Ding W (2008) Microstructure and mechanical performance of pulsed current gas tungsten arc surface engineered composite coatings on Mg alloy reinforced by SiC_p. *Mater Sci Eng A* 490(1–2):208–220
92. Rodríguez J et al (2007) Dry sliding wear behaviour of aluminium–lithium alloys reinforced with SiC particles. *Wear* 262(3–4):292–300

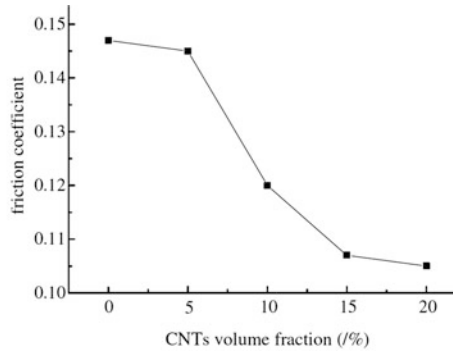
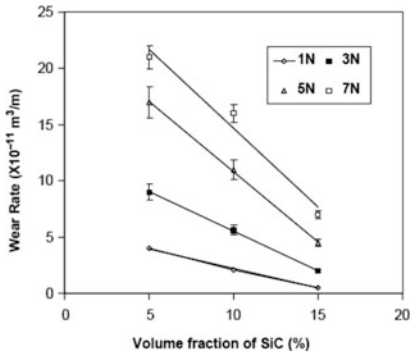
93. Rehman A, Das S, Dixit G (2012) Analysis of stir die cast Al–SiC composite brake drums based on coefficient of friction. *Tribol Int* 51:36–41
94. Jun Q, Linan A, Blau PJ (2006) Sliding friction and wear characteristics of Al₂O₃-Al nanocomposites. In: STLE/ASME IJTC
95. Umanath K, Selvamani TS, Palanikumar K (2011) Friction and wear behaviour of Al6061 alloy (SiC_p + Al₂O_{3p}) hybrid composites. *Int J Eng Sci Technol* 3(7):5441–5451
96. Sahin Y (2003) Wear behaviour of aluminium alloy and its composites reinforced by SiC particles using statistical analysis. *Mater Des* 24(2):95–103
97. Deshpande PK, Lin RY (2006) Wear resistance of WC particle reinforced copper matrix composites and the effect of porosity. *Mater Sci Eng A* 418:137–145
98. Yu SY et al (1997) Temperature dependence of sliding wear behavior in SiC whisker or SiC particulate reinforced 6061 aluminum alloy composite. *Wear* 213(1–2):21–28
99. Daoud A, Abou-Elkhair MT, Rohatgi P (2004) Wear and friction behavior of near eutectic Al–Si + ZrO₂ or WC particle composites. *Compos Sci Technol* 64(7–8):1029–1040
100. Li J, Xiong D (2009) Tribological behavior of graphite containing nickel-based composite as function of temperature, load and counterface. *Wear* 266:360–367
101. Mandal A, Chakraborty M, Murty BS (2007) Effect of TiB₂ particles on sliding wear behaviour of Al–4Cu alloy. *Wear* 262(1–2):160–166
102. Kumar S et al (2008) Tensile and wear behaviour of in situ Al–7Si/TiB₂ particulate composites. *Wear* 265(1–2):134–142
103. Mahmoud ERI et al (2010) Wear characteristics of surface-hybrid-MMCs layer fabricated on aluminum plate by friction stir processing. *Wear* 268(9–10):1111–1121
104. Zhiqiang S, Di Z, Guobin L (2005) Evaluation of dry sliding wear behavior of silicon particles reinforced aluminum matrix composites. *Mater Des* 26(5):454–458
105. Ranganath G, Sharma SC, Sharma SC (2001) Dry sliding wear of garnet reinforced zinc/aluminium metal matrix composites. *Wear* 251:1408–1413
106. Chaudhury SK et al (2005) Wear and friction behavior of spray formed and stir cast Al–2 Mg–11 TiO₂ composites. *Wear* 258:759–769
107. Hamid AA et al (2008) The influence of porosity and particles content on dry sliding wear of cast in situ Al(Ti)–Al₂O₃(TiO₂) composite. *Wear* 265(1–2):14–26
108. Qin QD, Zhao YG, Zhou W (2008) Dry sliding wear behavior of Mg₂Si/Al composites against automobile friction material. *Wear* 264(7–8):654–661
109. Menezes PL, Rohatgi PK, Lovell MR (2012) Self-Lubricating Behavior of Graphite Reinforced Metal Matrix Composites. In: *Green tribology*. Springer, Berlin, Heidelberg, pp 445–480
110. Soy U, Demir A, Findik F (2011) Friction and wear behaviors of Al-SiC-B₄C composites produced by pressure infiltration method. *Industrial Lubrication and Tribology* 63(5): 387–393
111. Martin A, Martinez MA, Llorca J (1996) Wear of SiC-reinforced Al matrix composites in the temperature range 20–200°C. *Wear* 193:169–179
112. Martin A, Rodriguez J, Llorca J (1999) Temperature effects on the wear behavior of particulate reinforced Al-based composites. *Wear* 225–229:615–620
113. Vissutipitukul P, Aizawa T (2005) Wear of plasma-nitrided aluminum alloys. *Wear* 259:482–489
114. Singh J, Alpas A (1996) High-temperature wear and deformation processes in metal matrix composites. *Metall Mater Trans A* 27(10):3135–3148
115. Yao-hui L et al (2004) High temperature friction and wear behaviour of Al₂O₃ and/or carbon short fibre reinforced Al–12Si alloy composites. *Wear* 256(3):275–285
116. Mousavi Abarghouie S, Seyed Reihani S (2010) Investigation of friction and wear behaviors of 2024 Al and 2024 Al/SiC_p composite at elevated temperatures. *J Alloys Compd* 501 (2):326–332

Problems

1. Mention the parameters which affect the wear and friction behavior of MMCs.
2. Explain the effect of the volume fraction of reinforcements on tribological behavior of MMCs and MMNCs with schematic diagrams.
3. How may the normal load affect the tribological (wear and friction) behavior of MMCs?
4. How can the interface temperature affect the tribological behavior of materials?
5. Different wear mechanisms occur during sliding of MMCs. Explain some of these mechanisms.
6. Tribological behavior of Al6061 and its composites reinforced by different weight percent of reinforcements have been investigated. The results are shown in Fig. 8.2. Calculate the percentage improvement in the wear resistance of composite reinforced by 12 wt% particles compared with Al6061 after 1 km sliding distance.
7. What is HMMC? Compare the tribological behavior of HMMC with MMC.

Answers

1. Different factors can affect the wear and friction behavior of MMCs. The basic tribological parameters which can control the wear and friction behavior of MMCs can be classified into three categories:
 - Mechanical factors (extrinsic to the material undergoing surface interaction), such as normal load, sliding velocity, and sliding distance.
 - Physical factors (extrinsic to the material undergoing surface interaction), such as temperature and environmental conditions.
 - Material factors (intrinsic to the material undergoing surface interaction), such as type of reinforcement, reinforcement size, shape of reinforcement, reinforcement volume fraction, and microstructure of matrix.
2. Tribology is a field of science and engineering which concentrates on interaction between surfaces of different materials in relative motion. This area of science includes the investigation and application of the principles of wear and friction. In general, increasing the reinforcement content enhances the wear resistance and the coefficient of friction of the composites of composite materials.
3. Normal load is another factor which affects wear rate and friction coefficient of MMCs. With increasing the applied load, especially in a high normal load, fracture of the reinforcement particles in the matrix may occur. As a result, the mechanical properties of the composite decrease and also wear rate of the composites increases to the levels comparable to those of unreinforced matrix alloys. It is generally accepted that when normal load increases, the wear rate also increases and the coefficient of friction of MMCs decreases during sliding.



- The effect of temperature changes on tribological behavior of MMCs as a result of changing the normal load and the sliding. The wear rate of MMCs increases with increasing temperature, and increase in the temperature leads to a decrease in the coefficient of friction of the MMCs.
- Different kinds of wear mechanisms may take place during the relative motion. These mechanisms include adhesive wear, abrasive wear, delamination wear, erosive wear, fretting wear, fatigue wear, and corrosive/oxidative wear. The common wear mechanisms of MMCs are adhesive wear, abrasive wear, fatigue wear, and corrosive/oxidative wear.

Abrasive wear occurs when a hard rough surface slides against a softer surface. Abrasive wear also occurs by abrading action of hard particles that are available as debris at the interface. Abrasive wear can be caused by both metallic and nonmetallic particles, but mostly nonmetallic particles cause abrasion. Adhesive wear is caused between two metallic components which are sliding against each other under an applied load and in an environment where no abrasive particles are present at the interface. By applying the normal pressure, local pressure at the asperities increases to an extremely high value and often the yield stress is exceeded. Then, the plastic deformation occurs in asperities until the RAC has increased sufficiently to support the applied load. Consequently, the strong short-range forces come into action, and strong adhesive junctions may be formed at the RAC. During relative motion the adhered junctions are sheared. The name “adhesive” is given due to the forming of a strong metallic bond between the asperities on the surface of the contacting materials. The dynamic interactions between the environment and mating material surfaces play an important role in corrosive wear. In corrosive wear, the contacting surfaces react with the environment, and reaction products are formed on the surface of asperities. In the contact interactions of materials during sliding, wear of the reaction products occurs as a result of crack formation and/or abrasion. Specifically, corrosive wear occurs when reaction products on the surfaces of materials are removed through physical interaction of the two surfaces in

contact. Fatigue wear can occur at the surface of materials which are cyclically stressed. For example, the ball bearings and the gears normally experience the fatigue wear due to the existence of cyclic stresses during their applications.

6. At first, according to Fig. 8.2, the wear rates of Al6061 and composites with 12 wt% particles are 0.15 and 0.07, respectively. So, the percentage improvement, according to (8.2), is

$$\text{IWR}_{\text{ca}}(\%) = \left(\frac{0.15 - 0.07}{0.07} \right) \times 100 \approx 115\%$$

7. HMMCs are engineering materials reinforced by a combination of two or more different types of reinforcements. These composites have combined the properties of each reinforcement and exhibited an improvement in physical, mechanical, and tribological properties of the composites. It has been reported in some studies that the hybrid composites have a lower wear rate than the composites which are reinforced by only one type of particles. In general, the tribological properties of HMMCs are also increased by increasing the amount of reinforcements in the composites.

Chapter 9

Coatings Tribology

Sudeep P. Ingole

Abstract Optimization of coefficient of friction in association with minimum wear is a general requirement to reduce energy consumption due to friction and wear losses. Lubrication such as solid and liquid is utilized to meet low friction and wear demands. Extreme environmental conditions such as space and high-temperature applications limit their usefulness. There is a need to design newer class of coatings for such applications. Design and selection parameters of coatings and their tribology are discussed in this chapter. These parameters include scale-dependent failure modes (nano- and micrometer length scale), state of stress at the interface, material properties, and chemical interactions at the interface. The requirements for selection of coating for friction applications are included. Tribology of low-friction coatings such as graphite, molybdenum disulfide, diamond-like carbon, chromium-based coatings, and polymeric coatings is discussed. Effects for service conditions such as load, nitrogen, humidity, and temperature for selected coatings are listed. Knowledge of the interfacial phenomena plays very important role in selection and development of coatings for tribological applications.

1 Introduction

Controlling the friction between sliding surfaces can enhance their useful life. Friction can be modified with physical or chemical properties of surfaces through surface treatments and/or coatings without jeopardizing the substrate properties. The growing environmental concerns also demand development of newer friction

A chapter contribution to Tribology for Scientists and Engineers.

S.P. Ingole, Ph.D. (✉)

Curt G. Joa Inc, Sheboygan Falls, WI 53085-0903, USA

e-mail: singole@joa.com

coatings (solid lubricants) to meet the service parameters and to minimize the usage of traditional lubrication methods (grease, oil) that pose higher environmental impacts. Friction, a surface phenomenon, is defined as the resistive effect to the relative motion. Friction can result in dry, lubricated, sliding, rolling, and other conditions during sliding. The basic information on friction is covered in Chap. 2. This chapter encompasses the overview of friction coatings, design, selection criteria, and friction properties of various coatings.

Low friction can easily be achieved by liquid lubrication. Engines are facilitated with liquid lubrication to minimize friction, wear, and increase service life and efficiency. However, there are several applications where liquid lubrication is not suitable or recommended. For example, in the food processing industry, liquid lubrication poses very high risk of contamination. It is not suitable in extreme environments, such as high temperature in the chemical and power generation industry and vacuum in space applications [1]. The foil bearing offers superiority over the rolling elements in high-speed and high-temperature applications that eliminate the liquid lubrication. Superior coatings for these bearings will extend their service life. Therefore, there is a need of coatings that perform at a high temperature and in extreme environments. These coatings will find applications in aircraft gas turbine engines, auxiliary power units, microturbines, pumps, compressors, cryogenic turboexpanders, and turbochargers [2–9].

Coatings adopted for surgical instruments are low-friction chromium, titanium-anodizing, aluminum-anodizing, electro-polishing, passivation, and various vapor deposition-type coatings [10]. Diamond-like carbon (DLC) coatings have potential applications in biomedical components, where high hardness, low friction, and biocompatibility are required [11, 12]. In the orthodontic applications, teeth need to move between surrounding wires and brackets. These movements can be facilitated by using low-friction materials. DLC films are suitable for these applications with high hardness, low coefficient of friction, and its biocompatibility [13–15]. Diamond-coated cutting tools are used for biomedical applications [16].

Friction of various sliding systems on the launch vehicle is important for positioning the spacecraft in its desired orbit. In addition, there are various other sliding mechanisms on the spacecraft, for example, deployment of antenna and solar panel, etc. Solid lubricants are used in these systems due to their merits over liquid lubrications. These merits include low vapor pressure and a wide range of operating temperature. The most important requirement in all these applications is the steady torque and friction [17].

Department of Health and Human Services (DHHS) of the Center for Disease Control and Prevention (CDC) reported that friction is one of the sources of fires in the mining industry. Friction of conveyor belts against pulleys, drives, rollers, idlers, and bearings resulted in 16 fires (18 %) with 4 injuries in the period of 1990–1999 [18]. Commercial fishing is one of the most hazardous occupations in the United States. The work is mostly performed in extreme weather conditions, such as extreme temperature, daylight, work hours, and on unstable platforms. The deck surfaces can be more slippery due to the presence of water, snow, ice, oils, fish/shellfish body tissues and fluids, and other potential deck contaminants.

Surface treatments and/or coatings are some of the most effective methods to address the friction requirement on such work surfaces [19]. A flooring (deck) surface that has a coefficient of friction high enough to avoid the slippery conditions can prevent accidents on these working surfaces. The maritime industry often addressed this challenge by the application of nonskid deck coatings on the steel surfaces [20]. Other examples where higher friction plays important roles are floor tile, grips of various tools, handheld equipment, seating places, electric contacts, and industrial applications where the sliding surfaces are exposed to the materials on conveyor belts.

2 Design of Coating for Friction Applications

Availability of advanced techniques for coating deposition makes it possible to develop coatings with desired properties. But there are no standard criteria that can be adopted for design of coatings for friction applications. Each method of deposition has some merits over the other. Friction performance of the coating at the sliding interface depends on sliding conditions, such as applied load, speed, interface chemistry, and the material's properties. Fundamental understanding of friction and wear behavior at these interfaces helps to develop the coatings and improve their performance. The primary failure mode at micro- and macroscale, and the crack initiation and propagation, depends on coating thickness, residual stress, and mechanical properties of the coating and the substrate. Considerable work has been carried out to optimize the coating parameters, such as deposition characteristics, deposition methods, and coating performance [21–35]. Failure mode, interface stress, and material properties are most important parameters which govern the process of coating design.

2.1 *Scale-Dependent Failure Modes*

Coating design parameter can be optimized with the understanding of friction and wear mechanisms of coatings at multi-scales. This includes the analysis of tribological changes (mechanical and chemical) and material transfer at multi-scales, i.e., nano, micro, and macro level [36].

2.1.1 **Nanoscale Friction and Wear**

Recent developments in surface observations and surface force measurement at molecular and atomic level have advanced knowledge of the origin of friction [37]. The surface force apparatus (SFA), scanning tunneling microscope (STM), atomic force microscope (AFM), friction-force microscopes (FFM), and quartz

crystal microbalance (QCM) techniques are used for topological observations and surface force measurements at nanometer length scale [38]. The origin of friction has been studied using QCM [37, 39, 40]. Adhesive forces influence the friction at nanometer scales. Studies by Bhushan et al. showed that insight of friction and wear behavior at nanoscales could extend the understating of failure mechanisms of materials. Authors used scratch tests and nano-indentation techniques to simulate conditions to create friction and wear at the nano level, which were then utilized to understand the tribological behavior. The friction at micro- and nanoscales was lower, and the mechanical property such as hardness of the corresponding materials was higher [38]. The technology advancements in computational techniques have enabled the study of the complex phenomenon of sliding at atomic level. A powerful atomistic computation technique, molecular dynamics, identified the origin and mechanisms of atomic scale interfacial behavior between sliding metals. The formation of eddies and flow resulted in nanoscale mixing. The friction at lower velocities is increased with velocity whereas for higher velocities it is reduced [41].

2.1.2 Micro- and Macro-Length-Scale Friction and Wear

Stress, strain, crack initiation, and propagation at microscale and asperity deformation, shear, and particle separation from parent materials at macroscale are studied [36]. The shear forces and strain generated at the surface initiate and propagate cracks and subsequently lead to failure of the surface [42, 43]. Tribo-chemical reactions take place at the interfaces that develop the tribo-films at sliding interfaces. These reactions and the reaction products have considerable influence on the friction and wear of the coatings [44]. The study of the effect of normal load on friction at microscale for pure silicon and its oxide pair showed that friction in the low-load region (less than about -15 mN) was lower than that in the high-load region. The increase in friction at critical load was related to the mechanical property, hardness. The higher friction was a result at higher load due to plowing. Figures 9.1 and 9.2 demonstrate the friction variation with applied load at microlevel [45]. Several studies have found that friction behavior of the surfaces at nanoscale [37–40] and microscale [45] are different. There is a necessity to correlate the understating of friction and wear mechanisms at multi-scale to get the insight of the overall sliding phenomenon.

2.2 *State of Stress Fields at the Interface*

Friction is a function of normal and tangential forces at the interface in the sliding system. These forces create the stress fields at the interface. Calculations of these stress fields are well studied using contact mechanics over a period of time [42, 43, 46, 47]. In coatings, these stresses are generated at the interfaces and at the coating/

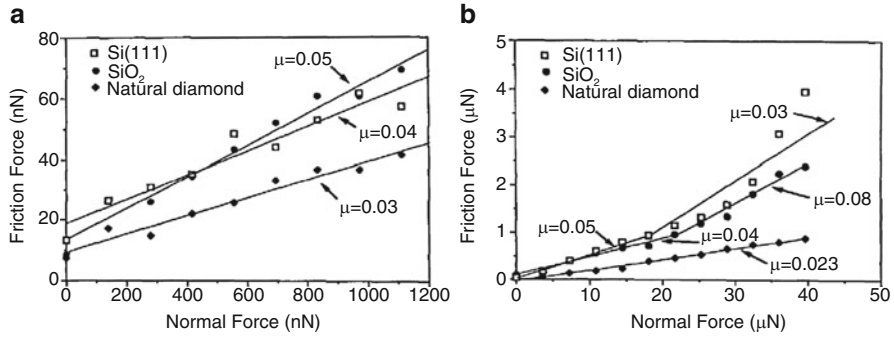


Fig. 9.1 Effect of applied load on friction at nano- and microlevel [45]

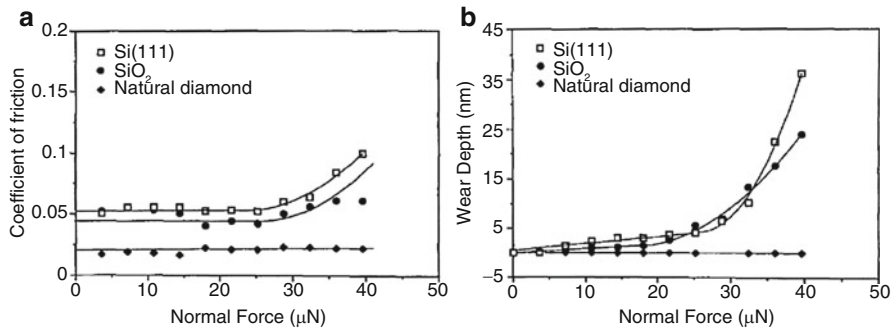


Fig. 9.2 Effect of applied load on friction and wear at microlevel [45]

substrate interfaces. Using computational [48–50] and indentation techniques [51], the state of stress fields at the interface provided information of yield and failure modes at the interface of coating and substrate [52, 53]. The stress generated in the coating can cause debonding from the substrate and influence the friction at the interface; therefore; the coating thickness optimization to increase the adhesion of the coating is important. The critical coating thickness as a function of stress field is calculated by [52]

$$\frac{t_b}{c_d} = \left[\frac{12(1 - \nu_f^2)\sigma_R}{\pi^2 E_f} \right]^{\frac{1}{2}} \tag{9.1}$$

where t_b is coating thickness, c_d is length of the interface crack, ν_f is the Poisson ratio, σ_R is the residual compressive stress, and E_f is elastic modulus of coating. The stress field at the interface is also influenced by friction and surface roughness [54, 55].

2.3 *Material Properties and Chemical Interaction at the Interface*

Hardness and elasticity on the interface materials can be related to the contact area during sliding. The plasticity index provided by Greenwood and Williamson relate the hardness and elasticity ratio (H/E) to plastic deformation of the asperity at the sliding interface [36, 56]:

$$\Psi = \frac{\dot{\epsilon}}{H} \sqrt{\frac{\sigma}{\beta}} \quad (9.2)$$

where $(E/(H))'$ is the ratio of modulus and hardness, “ β ” is the typical radius of an asperity, and “ σ ” is the standard deviation of the asperity height distribution.

The crack initiation and propagation can be controlled by the coating material toughness which determines the extent of wear particle generation and failure mode. The energy of repetitive and cyclic loading must be absorbed elastically without plastic deformation. This can be achieved with elastic resilient coatings with high hardness [36]. The thermodynamic conditions at the sliding interface become more feasible due to high temperature, pressure, and chemical nature of the coating materials. Therefore for durability and longer service life, coating materials should have high temperature, chemical stability, and corrosion resistance.

Matthews et al. [36] discussed the chemical reactions at the interface. These tribo-chemical reactions modify the surface properties and influence the friction and wear performance [36, 57].

3 Selection of Coatings for Friction Applications

Selection of the friction coating, based on the application requirements, can be divided as

- Low friction (wear rate is not priority)
- Low friction and low wear rate
- High friction but low wear rate
- Low wear rate (friction is not priority)

These requirements are considered during surface engineering to design coatings or modify the surfaces. In all of these requirements, factors that govern the decision making of friction coating or surface treatment selection are

- Cost-effectiveness, stability, cleanliness, and toxicity
- Wear during service life
- Stabilized friction coefficient
- Effects of service environment on the coefficient of friction

4 Surface Treatments and Coatings

Sliding interfaces of moving parts of machinery cause loss of energy due to friction and wear of materials that affect the efficiency of the machine. This loss can be minimized or eliminated by using friction surfaces using surface treatments or coatings. The advantages of friction surfaces include

- Control of friction
- Application over wide temperature ranges
- Operation without oil and grease
- Improvement of running-in of the machine (assists oil and grease lubrication) and support emergency running
- Protection against corrosion
- Reduction in cost due to surface modification
- Reduction of maintenance cost

Surface treatments available to produce friction surfaces include modification of the surface properties through thermochemical diffusion, ion implantation, laser surface treatment, and chemical conversion. Table 9.1 contains a partial list of these methods.

Recent developments in surface science and advanced tools made it feasible to develop newer coatings and rediscover the traditional ones. Friction coatings are also recognized as *solid lubricants* when the targeted applications are for friction reduction. The advantage of friction coatings over liquid lubrication is that the former can be engineered using their microstructure, compositions, and surface asperities to obtain the desired friction performance. The coatings consist of the solid materials at the interface which have lower vapor pressure and thus are less sensitive to the radiation effects for space applications [59]. Coatings also increase the application ranges in terms of temperature and service conditions.

Table 9.1 Surface treatment methods

		Ion implantation [36]	Laser surface treatment [36]	Chemical conversion [36, 58]
Diffusion [58]				
Nitriding	Boriding	Argon	Hardening	Anodizing
Tuftride	Tiduran	Nitrogen	Glazing	Phosphating
Sulfinuz	Tifran	Carbon	Surface alloying	Chromating
Sursulf	Tiodize	Chromium		Oxidizing
Sulf-BT	Delsum			Sulfurizing
Noskuff	Zinal			
Forez	Metalliding			
Carburizing	Siliconizing			

5 Low-Friction Coatings

Applications where low friction is required are automotive, aerospace engine, dies and die blocks (including CD dies), tapping, reaming, drilling, molding, punching, reduction of pickup, and galling of soft materials (Al, Cu, Ti, etc.), cutting, forming, electronics industry assembly, motor sports, marine hydropower, children's slides, and ice-skating.

The following examples provide the importance of friction coatings. Bearings can be found on line shafts, prop shafts, turbine shafts, pumps, machine tools, and axle bearings. In bearings, friction coatings are used [60]:

- As reserve or backup lubricants and to protect bearing surfaces during break-in period during machinery start-up and during reversing operations. When the overload is applied, the thin film of oil lubrication moves away from the sliding contact. This situation converts the hydrodynamic lubrication to mixed and sometimes to boundary lubrication.
- As lubricants in applications where fluid cannot be used (example: nonmetallic bearing synthesized using fiber, plastics, composites, and paper) in instrument and aircraft applications.

Low-friction coatings used on journal bearings can prevent contact between the journal and the shaft. It is recommended that when the length-to-diameter (l/d) ratio is lower than 0.4, a low-friction coating should be used as a precaution. When the l/d ratio in these bearings is less than 1 (typically 0.5 or less), the fluid push towards the side can be significant and can cause metal-to-metal contact, especially under severe loading conditions [60]. Traditionally, the materials selected for the low-friction coating are based on the layered structures. Some examples of these layered structures are graphite and transition metal dichalcogenides such as sulfides, selenides, tellurides [61], and PTFE.

5.1 Graphite

Graphite has a hexagonal structure with strong covalent bonding. The sp^2 bonding configuration of graphite provides layered structure with weak interlayer bonding. σ bonds are formed between carbon atoms when three valence electrons are given to trigonally oriented sp^2 hybrids. The weak π bond is formed when the fourth electron is placed in a π orbit which is perpendicular to the plane.

5.1.1 Effect of Load on Friction of Graphite

Jradi et al. [62] studied the effect of load on friction of graphite. The friction showed higher values against steel discs for lower loads (i.e., 2–5 N). Graphitic asperities were plastically deformed at increasing load, resulting in flattening,

spread-out, and increasing in true contact area. The adhesion junction increased and resulted in higher friction with increase in loads. At higher loads (i.e., 30–50 N), friction reduced to a point corresponding to “the critical applied load.” The friction is increased for loads higher than the critical loads. At the critical loads, the water vapor and oxygen presence at the interface were minimal, compared to other sliding and loading conditions. At critical loads, the reorientation of graphitic planes took place with low surface energy planes [62] and provided low friction [63]. When these planes were damaged, newer prismatic planes and dangling bonds formed [64]. The vapor and oxygen present at the sliding interface reacted with dangling bonds to produce the oxygenated groups which maintained low friction [65–67].

5.1.2 Effect of Nitrogen, Ambient Air (Oxygen), and Water Vapor on Friction of Graphite

Yen [68, 69] studied the effect of different environments on the friction of graphite. Graphite showed high and erratic/fluctuating friction in a dry nitrogen atmosphere. It is believed that this behavior is due to the dusting effect and lack of lubricating vapor in the environment at the interface. This effect was persistent when water vapors were added up to 100 ppm. When vapor concentration increased by adding wet nitrogen, friction suddenly dropped. This lubricating effect of water vapor is reversible.

Friction was reduced in the presence of dry nitrogen and oxygen. The oxygen in a dry atmosphere provided the lubrication at the interface. It also inhibited the dusting of graphite. This lubricating effect of oxygen disappeared when water vapor was introduced in the atmosphere. The friction was increased. Even in non-dusting conditions and in the presence of water at the interface, friction was not recovered, as oxygen modified the surface chemistry of graphite by chemisorptions and/or physisorption [68, 69].

In ambient air with increasing sliding distance, the asperities flattened and increased true contact area. It also formed a smooth contact surface and a third body layer (transfer film) on the counterface. The friction was increased with an increase in sliding distance. In the presence of water, the friction obtained was in the range of 0.13–0.18 [68, 69]. Initially, the low friction of graphite was explained on the basis of its crystal structure and shear in the adjacent basal planes [70]. Deacon and Goodman explained the low friction mechanism in graphite. The crystal structure of graphite consists of low-energy cleavage faces and edge faces [71]. The cleavage faces are formed by the basal planes [64]. The active dangling bonds from edge faces react with water and oxygen and develop new surfaces with oxygenated groups, which maintain low friction [65–67].

5.2 Molybdenum Disulfide (MoS_2) and MoS_2 -Based Multifunctional Coatings [72]

MoS_2 are dichalcogen of atoms surrounding the metal and form covalently bonded layer. These layers are held together with weak van der Waals bonds between them that require low shear during sliding. Low friction is resulted when most of these crystallites are aligned parallel to the sliding direction. MoS_2 is used as a solid lubricant in the presence of a vacuum and inert gases. MoS_2 coatings are developed using pressure vapor deposition and sputter coating technique. Sputter-coated multilayered MoS_2 consists of three distinct regions with a rigid formation region that is formed during the nucleation and growth. This layer is towards the substrate, an equiaxed transition zone, and a columnar fiber-like zone towards the surface of the coating [72].

5.2.1 Effect of Load on Friction of MoS_2 Coatings [73]

Singer et al. [73] studied the Hertzian stress contribution to the friction of MoS_2 films. The consistency of low friction of coatings relies on the transfer film formed through tribo-chemical reactions at the interface. The formation of transfer film depends on the environment and the contact pressure during sliding. The stresses developed during sliding contribute to the thermodynamic feasibility and defect-enhanced diffusion for phase transformations. For MoS_2 , the transfer film formed is MoS_2 when the sliding occurs in inert atmospheres and oxides in open air [73]. The Hertzian model is often used to show the effect of load on friction characteristics of materials, where the friction is related to the mechanical and material properties of interface materials [43]. The friction is defined as the function of applied force and resultant tangential generated at the sliding interface as

$$\mu = \frac{S}{P} \quad (9.3)$$

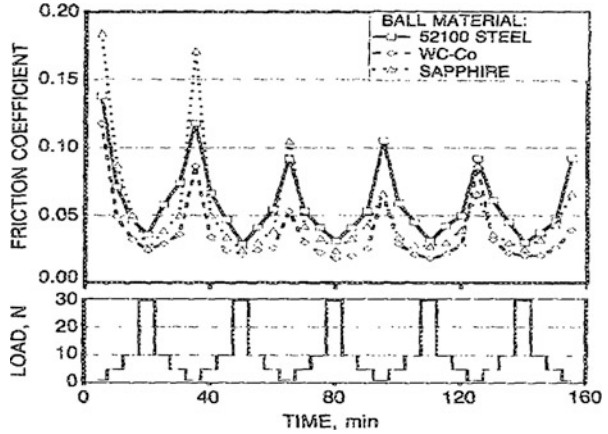
where S is shear strength and P is contact pressure. At high pressures, the shear strength showed the pressure dependence according to Bridgeman and is given by

$$S = S_0 + \alpha P \quad (9.4)$$

where S_0 and α are constants that control the friction. When the contact pressure is within the elastic limit of the sliding interfaces, the coefficient of friction is calculated as [74]

$$\mu = S_0 \pi \left(\frac{3R}{4E} \right)^{2/3} L^{-1/3} + \alpha \quad (9.5)$$

Fig. 9.3 Effect of load on friction of MoS₂ [73]



where E is the composite elastic modulus of sliding interface materials, R is the radius of the ball, and L is applied load. For the MoS₂ coatings against glass and steel, WC-Co showed that friction followed $\mu \propto L^{-1/3}$ (Fig. 9.3) within the elastic limits of the substrate.

5.2.2 Effect of Temperature and Relative Humidity on Friction of MoS₂ Coatings

Application of MoS₂ as a friction coating is still limited due to its poor performance properties in a humid environment. The environmental effect on the frictional properties of MoS₂ studied using atomic force microscope showed independence of humidity up to 40 % on friction, but above that, the friction was catastrophically increased (Fig. 9.4) [75]. The study of the effect of temperature and relative humidity on the friction of MoS₂ (Fig. 9.5) portrayed that the friction at 100 °C was three times lower than that of friction measured at room temperature with 50 % relative humidity. At 100 °C, the water dried out, which resulted in reduced friction. Friction was increased at higher temperatures due to the oxidation of MoS₂ (Fig. 9.6) [61]. Typically, MoS₂ films contain up to 20 atom % of substituted oxygen for sulfur. This oxygen contributes to the oxidation of MoS₂ and influences the friction. This substitutional oxygen interlocks or notches the basal plane surface, which further increases the friction. Also, increasing the percentage of substitutional oxygen decreases friction during sliding, but this friction is always higher, compared to pure MoS₂ films [76]. The friction coefficient of some MoS₂ coatings is listed in Table 9.2.

Fig. 9.4 Effect of temperature on friction of MoS₂ coatings [75]

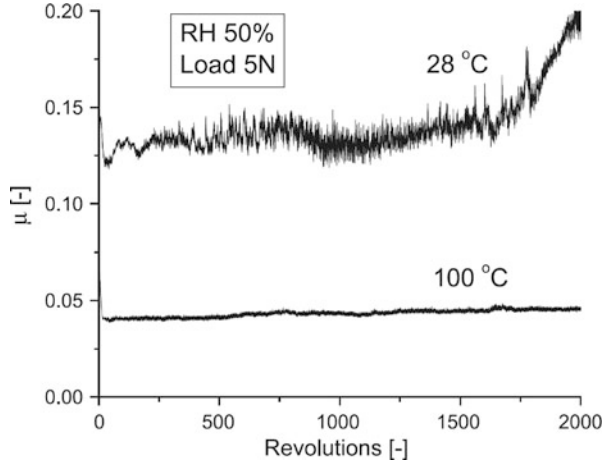


Fig. 9.5 Effect of humidity on friction of MoS₂ coatings [75]

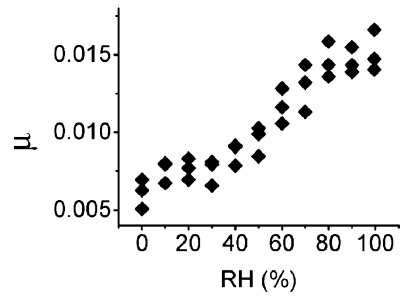


Fig. 9.6 Effect of temperature on friction of MoS₂ coatings [61]

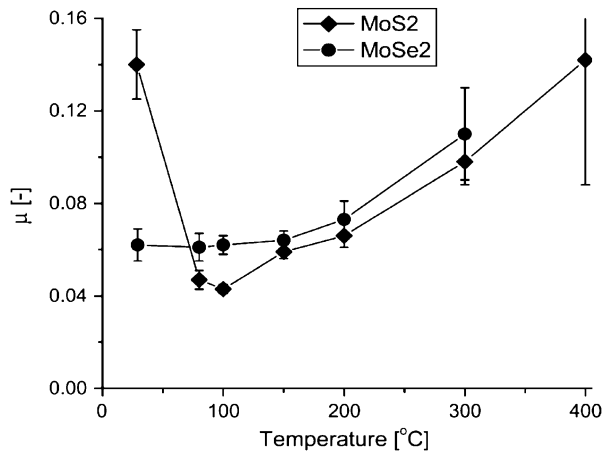


Table 9.2 Coefficient of friction of MoS₂ coatings

Deposition method	Structure (sliding pair)	COF	Ref
PVD closed-field unbalanced magnetron sputtering	MoS ₂ -Ti coating (WC-CO Ball)	0.05–0.08	[77, 78]
Radio-frequency magnetron sputtering of MoS ₂	MoS ₂ /52100 steel (52100 steel) in dry nitrogen (10 ⁵ Pa)	0.003	[79]
	MoS ₂ /52100 steel (52100 steel) in air (10 ⁵ Pa)	0.150	[79]
Closed-field unbalanced magnetron sputtering	TiN + MoS _x coating (tungsten carbide ball)	0.4–0.5	[80]
Radio-frequency magnetron sputtering of MoS ₂	MoS ₂ /52100 steel (52100 steel) in ultra-high vacuum (UHV) 5 × 10 ⁻⁸ Pa	0.002	[79]
	MoS ₂ /52100 steel (52100 steel) in high vacuum (HV) 10 ⁻³ Pa	0.013	[79]

Table 9.3 Coefficient of friction for TiN–MoS₂ systems

Synthesis method	Coefficient of friction	Counter surface (test method)	Ref
DC magnetron co-deposition	0.2	Steel (POD)	[86, 87]
Combined arc evaporation and magnetron sputter process	0.2	Steel (POD)	[88]
Physical vapor deposition (PVD) technique of E-gun evaporation and magnetron sputtering	0.2	Corundum ball (POD)	[81]
Magnetron sputtered	0.4–0.5	Tungsten carbide ball (POD)	[89]
Pulsed closed-field unbalanced magnetron sputtering	0.2–0.4	Cemented carbide ball (POD)	[85]

POD Pin-on-disk friction test

5.2.3 MoS₂-Based Multilayered and Multicomponent Coatings

Due the high industry demand, there is a growing trend to develop hard- and low-friction multilayer (multicomponent) systems based on MoS₂. Three primary approaches are taken to develop these hard- and low-friction coating systems: (1) solid lubricant top coats (these coatings have short life), (2) solid lubricant coatings with metal addition (due to the soft particle these do not fulfill requirements), and (3) hard wear-resistant layer, with lubricating phase dispersed. The PVD-deposited composite coating (TiN–MoS_x) showed reduced wear [81] (Table 9.3). The functionality of the multicomponent coating is increased by forming a nanoscaled multilayer [82] and inclusion of metal doping to form a nano-composite coating [83–85]. Examples of multicomponent systems that showed higher hardness and lower friction are listed in Table 9.1.

Other coatings that are used in industrial applications (dry machining) are TiAlN and TiN coating. The endurance of these coatings can further be increased by addition of MoS₂ layer. The thin MoS₂ film deposited on the top of TiAlN coating for dry machining applications was removed very quickly. The beneficial effects of MoS₂ were disappeared with the coating. The low-friction TiB₂ coating by incorporating MoS₂ showed low friction and better higher temperature (400 °C) performance [90]. The coefficient of friction was reduced with percentage of MoS₂ contents, i.e., μ was approx. 0.55 at 10 % MoS₂, whereas μ was approx. 0.1 at 40 % MoS₂.

5.3 Diamond-Like Carbon Coatings

Properties of diamonds, such as high hardness, elastic modulus, thermal conductivity at room temperature, low thermal expansion coefficient, and large bandgap, are due to its directional sp^3 bonding configuration [91–93]. sp^3 bonding can be obtained in noncrystalline carbon films (for example: hydrogenated amorphous carbon (a-C:H)) using a wide range of deposition methods, such as ion beam deposition, plasma deposition, magnetron sputtering ion beam sputtering, ion plating, and laser deposition. These films have structure between diamond (sp^3) and graphite (sp^2) and hydrocarbon polymers, with different amount of sp^3 and sp^2 carbon. Diamond (100 % sp^3) has the highest density and graphite with layered structure (100 % sp^2) has lower density than diamond and DLCs. In sp^3 configuration, σ bonds are formed between four neighboring carbon atoms when four valence electrons of a carbon atom are given to a tetrahedrally oriented sp^2 hybrid. The amorphous diamond-like coating is divided into two categories: hydrogen-free carbon films and hydrogenated carbon films (a-C:H). These films are deposited from carbon plasma or carbon ion beam source generated from a solid carbon. The density of the DLC is around 3 g/cm³, whereas hydrogenated DLC is reported to be 2 g/cm³. The mechanical properties of the DLCs vary with the deposition techniques.

The bond structure of the DLC coating can be characterized using electron energy loss spectroscopy (EELS) which detects sp^2 pi bond. Similarly, energy diffraction measurement and Raman spectroscopy can be used to study the bond structure [1, 94–96]. The density of atoms up to 100 nm thick films can be measured using Rutherford backscatter spectroscopy (RBS).

5.3.1 Friction Behavior of DLCs

The ratio of the hardness to elastic modulus of diamond-like coating is between 0.1 and 0.2, which makes these coatings far superior for low wear applications along with its coefficient of friction, 0.2, in humid air, and 0.05, in vacuum, under high load. This ratio for metals was between 0.003 and 0.03, for polymers between 0.2

Table 9.4 Coefficient of friction of DLC against different engineering materials

Test configuration	Temp. (°C)	Lubrication	Friction (μ)	Ref
DLC-Steel	RT	Dry	0.2	[99]
DLC-Ceramic	RT	Dry	0.1	[99]
DLC-PFTE	RT	Dry	0.1	[100]
DLC-PMMA	RT	Dry	0.1	[101]
DLC-Al alloys	RT	Dry	0.05–0.2	[102]
DLC-319 Al T6	RT		0.15	[103]
	200		0.06	[13]
	400		0.64	[13]
Ti-DLC-AISI 52100 steel ball	RT	Benzotriazole and borate esters	0.085–0.11	[104]
Ti/Al-DLC-AISI 52100 steel ball	RT	Benzotriazole and borate esters	0.075–0.105	[103]
DLC-AISI 52100 steel	RT	Dry	0.08	[105]
	40	SAE 5W-20	~0.14	
	80		~0.15	
	100		~0.15	
	120		~0.15	
DLC/SiC-SiC	23	Dry	0.8	[106]
	100		0.9	
	200		0.8	
	300		0.75	
	400		0.7	

and 0.5, and for ceramic inorganic coatings between 0.02 and 0.06 [97]. DLCs showed remarkably low coefficient of friction in dry sliding. The sliding performance of these coatings is influenced by the surrounding (operating) environment that affects the formation of transfer layer and interface chemistry [98]. The poor adhesion properties of DLCs to steel substrate can be improved by the addition of refractory metals (Nb, Ta, Ti, W, etc.) without jeopardizing its tribological properties [97]. The friction coefficient of DLC against different counter materials is reported (Tables 9.4 and 9.5).

5.3.2 DLC-Based Multifunctional Films

The friction properties of the DLC films are improved by developing multifunctional films. The multilayers or doping can integrate in one coating. The titanium addition or multilayer has increased the tribological performance of the DLCs [101, 113]. The DLC-based composite films TiC/a-C:H showed an ultralow coefficient of friction, 0.05, when the surface of the composite film was 0.4 rms rough.

Table 9.5 Friction of DLCs in different environment [98]

Method	Deposition source	Sliding counter face	Condition	Friction (μ)	Ref
PA CVD	Acetylene/ethylene	Steel ball	N ₂ > 1 % RH 10 % RH 100 % RH	0.01–0.02 0.05 0.19	[107]
Ion beam		Steel	After 10,000 passes in POD	0.19 0.04	[108]
RF-PACVD	Acetylene/toluene/benzene	Steel	UHV > 1%RH After 25 rotations N ₂ dry O ₂ dry Wet N ₂ and wet O ₂	0.02 0.2 0.02 0.6 0.25	[109]
RF-PA-CVD	Methane or butane	Silicon nitride	Dry N ₂ Lab air	0.1 0.18	[110]
RF-PA CVD	Methane/H ₂	Silicon nitride ball	5–100 % Humidity Ar Dry Ar	0.2 0.06	[111]
Magnetron sputtered		Ceramic Mn–Zn CaTiO ₃	Dry N ₂ for 50 h After 50 h and O ₂	0.2 1.2	[112]

5.4 Chromium-Based Coatings

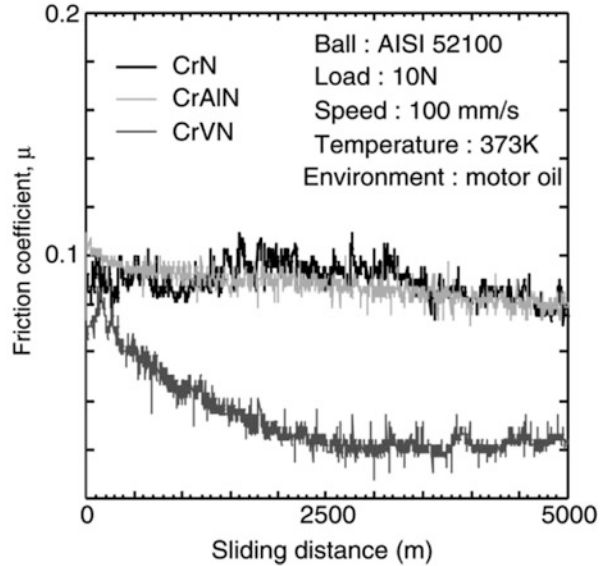
CrN possesses low friction, high hardness, and high toughness as compared to TiN. Still TiN has been commercially utilized as coating for machining tools for some time. Cathodic arc ion-plated CrN, CrAlN, and CrVN coatings showed the friction coefficient in the range of 0.5–0.8 (Fig. 9.7) when tested against AISI 52100 bearing ball [114]. A case study revealed that CrN showed lowest friction, as compared to TiN and MoS₂ coating on the P20 die steel at 85 °C [115], and could reduce the energy consumption and wear of the dies in plastic molding operations.

CrCN coating deposited using cathodic arc evaporation utilizing C₂H₂ flow of 24 standard cubic centimeters per minute (SCCM) showed friction ~0.55 at 700 °C against Si₃N₄ and ~0.3 when tested against Al₂O₃ [116].

5.5 Polymeric Coating Systems

In an application where very high strength is not required, polymeric systems pose a very good choice for the coating purposes. The polymeric coating systems are developed for both low- and high-friction applications. Polymeric coatings reinforced with low-friction compounds are used at low-temperature applications. These coatings are called as *antifriction* coatings or sometimes *bonded coatings*. These coatings are similar to the paints in many aspects such as application methods

Fig. 9.7 Coefficient of friction for Cr-based coatings [114]



and properties. Over a period of time, there are various approaches developed to prepare the polymeric *antifric*tion coating systems.

There are several applications where strength does not play a vital role but the friction coefficient does, for example, human-machine interfaces (sports equipment, etc.). In some applications customized (high) friction is required for skid-resistance, for example walking floors in rehabilitation centers and assisted living facilities, for accident prevention. A material with greater unidirectional coefficient of friction when attached to a raft and immersion suit would aide a survivor to enter a raft with reduced physical exertion. The National Institute for Occupational Safety and Health's (NIOSH) some initiatives focus on the coefficient of friction of footwear on walkway surfaces [117]. Industrial applications of polymeric coatings include o-rings and brake shoes in missile launch system.

Some of the advantages of the polymeric friction coatings are to

- Reduce and maintain coefficient of friction with very small variation.
- Use coatings in wide temperature range from -200 to $+650$ °C.
- Eliminate oil and grease usage.
- Improve the running-in of the machine, by assisting oil and grease lubrication and supporting the emergency running.
- Protect against corrosion.
- Reduce maintenance cost and application of thin coat possible.

The coatings can be applied to metallic as well as nonmetallic substrates. The coating materials consist of the curable polymeric system with friction modifier (particles that provide lower friction). In most cases the surface finish is required to apply the coating. The coating can be applied to the substrate using methods

like spraying and dipping. These coatings can also be applied by using paint drums. The polymeric coating can be applied to metallic, plastics, elastomers, wood, and ceramics.

6 Conclusions

Liquid lubrication can be used to achieve low friction requirements. Solid lubricant coatings are proved to be effective for certain applications. It is difficult to standardize the selection and design criteria for coatings. The service conditions vary with the applications. However, the factors influence coating selection, and surface treatment for friction coating includes cost-effectiveness, cleanliness, toxicity, and stability. Wear durability, stability of friction, and environmental effects on friction and wear factor in for the decision-making process. Yen's study showed that graphite has low friction due to the layered structure but it is load sensitive. It showed that higher friction in nitrogen environment reduced when oxygen was present but increased when water vapor was introduced. MoS₂ solid lubricant is load sensitive; the low friction is due to the weak van der Waals interaction between the covalently bonded layers. It showed poor performance in humid environment. Polymeric coating can meet friction requirement but has limitation for high-temperature applications.

References

1. Hirvonen JP et al (1996) Present progress in the development of low friction coatings. *Surf Coat Technol* 80(1–2):139–150
2. Heshmat H et al (2005) Low-friction wear-resistant coatings for high-temperature foil bearings. *Tribol Int* 38(11–12):1059–1075
3. Salehi M, Heshmat H (2002) Evaluation of large compliant foil seals under engine simulated conditions. In: *Proceedings of the 38th AIAA/ASME/SAE/ASEE joint propulsion conference*, Indianapolis, IN.
4. Salehi M, Heshmat H, Walton JF (2003) On the frictional damping characterization of compliant bump foils. *J Tribol Trans ASME* 125(4):804–813
5. Salehi M, Heshmat H (2001) Performance of a complaint foil seal in a small gas turbine engine simulator employing a hybrid foil/ball bearing support system. *Tribol Trans* 44(3):458–464
6. Salehi M, Swanson E, Heshmat H (2001) Thermal features of compliant foil bearings—theory and experiments. *J Tribol Trans ASME* 123(3):566–571
7. Salehi M et al (1999) The application of foil seals to a gas turbine engine. In: *Proceedings of the 35th AIAA/ASME/SAE/ASEE joint propulsion conference and exhibit*, Los Angeles, CA
8. Heshmat H, Hryniewicz P, Walton JF II, Willis JP, Jahanmir S, DellaCorte C (2006) Low-friction wear-resistant coatings for high-temperature foil bearings. *Tribol Int* 38(11–12):1059–1075, ISSN 0301-679X
9. Walton JF et al (2008) Testing of a small turbocharger/turbojet sized simulator rotor supported on foil bearings. *J Eng Gas Turb Power* 130(3):035001

10. Harris R, Roberts W (2006) Biomedical coatings and processes for surgical instruments—advantages and disadvantages. *Surface engineering, Proceedings*, pp 201–209, 220
11. Dearnaley G, Arps JH (2005) Biomedical applications of diamond-like carbon (DLC) coatings: a review. *Surf Coat Technol* 200(7):2518–2524
12. Catledge SA et al (2002) Nanostructured ceramics for biomedical implants. *J Nanosci Nanotechnol* 2(3–4):293–312
13. Huang T-H, Guo J-U, Kao C-T (2010) A comparison of the friction associated with diamond-like carbon (DLC) or titanium nitride (TiN) plating metal brackets. *Surf Coat Technol* 205(7):1917–1921
14. Kobayashi S et al (2005) Diamond-like carbon coatings on orthodontic archwires. *Diamond Relat Mater* 14(3–7):1094–1097
15. Muguruma T et al (2011) Effects of a diamond-like carbon coating on the frictional properties of orthodontic wires. *Angle Orthodontist* 81(1):141–148
16. Jackson MJ et al (2004) Diamond-coated cutting tools for biomedical applications. *J Mater Eng Perform* 13(4):421–430
17. Hilton MR, Fleischauer PD (1992) Applications of solid lubricant films in spacecraft. *Surf Coat Technol* 55(1–3):435–441
18. Rosa MID (2004) Analysis of mine fires for all U.S. underground and surface coal mining categories: 1990–1999. IC 9470 INFORMATION CIRCULAR/2004
19. Spitzer CJD (1999) Fishing Vessel Casualty Task Force—living to fish, dying to fish. In: *Fishing Vessel Casualty Task Force report*, U. S. Coast Guard
20. William English, CSP P.E (2003) *Pedestrian slip resistance: how to measure it and how to improve it*, 2nd edn. William English, Inc, Alva, FL
21. Gilmore R et al (1998) Low-friction TiN-MoS₂ coatings produced by dc magnetron co-deposition. *Surf Coat Technol* 109(1–3):345–351
22. Cselle T, Barimani A (1995) Today's applications and future developments of coatings for drills and rotating cutting tools. *Surf Coat Technol* 76–77(1–3):712–718
23. Spalvins T (1974) Structure of sputtered molybdenum-disulfide films at various substrate temperatures. *ASLE Trans* 17(1):1–7
24. Dimigen H, Hubsch H, Willich P (1979) Lubrication properties of Rf sputtered MoS₂ layers with variable stoichiometry. *Thin Solid Films* 64(2):221
25. Christy RI (1980) Sputtered MoS₂ lubricant coating improvements. *Thin Solid Films* 73(2):299–307
26. Haltner AJ, Oliver CS (1960) Frictional properties of molybdenum disulphide films containing inorganic sulphide additives. *Nature* 188(4747):308–309
27. Stupp BC (1981) Synergistic effects of metals Co-sputtered with MoS₂. *Thin Solid Films* 84(3):257–266
28. Spalvins T (1984) Frictional and morphological properties of Au-MoS₂ films sputtered from a compact target. *Thin Solid Films* 118(3):375–384
29. Wahl KJ et al (1995) Low-friction, high-endurance, ion-beam-deposited Pb-Mo-S coatings. *Surf Coat Technol* 73(3):152–159
30. Yu DY, Wang JA, Yang JLO (1997) Variations of properties of the MoS₂-LaF₃ cosputtered and MoS₂-sputtered films after storage in moist air. *Thin Solid Films* 293(1–2):1–5
31. Hilton MR et al (1992) Structural and tribological studies of MoS₂ solid lubricant films having tailored metal-multilayer nanostructures. *Surf Coat Technol* 53(1):13–23
32. Weise G et al (1997) Preparation, structure and properties of MoS_x films. *Thin Solid Films* 298(1–2):98–106
33. Teer DG et al (1997) The tribological properties of MoS₂/metal composite coatings deposited by closed field magnetron sputtering. *Surf Coat Technol* 94–5(1–3):572–577
34. Fleischauer PD (1984) Effects of crystallite orientation on environmental stability and lubrication properties of sputtered MoS₂ thin-films. *ASLE Trans* 27(1):82–88
35. Stewart TB, Fleischauer PD (1982) Chemistry of sputtered molybdenum-disulfide films. *Inorg Chem* 21(6):2426–2431

36. Matthews A, Franklin S, Holmberg K (2007) Tribological coatings: contact mechanisms and selection. *J Phys D Appl Phys* 40(18):5463–5475
37. Krim J (1996) Friction at the atomic scale. *Sci Am* 275(4):74–80
38. Bhushan B, Israelachvili JN, Landman U (1995) Nanotribology: friction, wear and lubrication at the atomic scale. *Nature* 374(6523):607–616
39. Krim J (1996) Atomic-scale origins of friction. *Langmuir* 12(19):4564–4566
40. Krim J (2002) Surface science and the atomic-scale origins of friction: what once was old is new again. *Surf Sci* 500(1–3):741–758
41. Kim HJ, Karthikeyan S, Rigney D (2009) A simulation study of the mixing, atomic flow and velocity profiles of crystalline materials during sliding. *Wear* 267(5–8):1130–1136
42. Suh NP (1977) Overview of delamination theory of wear. *Wear* 44(1):1–16
43. Suh NP (1986) *Tribophysics*. Prentice-Hall, Englewood Cliffs, NJ
44. Gee MG, Jennett NM (1996) High resolution characterisation of tribochemical films on alumina. *Wear* 193(2):133–145
45. Bhushan B, Kulkarni AV (1996) Effect of normal load on microscale friction measurements. *Thin Solid Films* 278(1–2):49–56
46. Johnson KL (1995) Contact mechanics and the wear of metals. *Wear* 190(2):162–170
47. Rosenfield AR (1980) A fracture-mechanics approach to wear. *Wear* 61(1):125–132
48. Wong SK, Kapoor A (1996) Effect of hard and stiff overlay coatings on the strength of surfaces in repeated sliding. *Tribol Int* 29(8):695–702
49. Diao DF, Kato K, Hayashi K (1993) The local yield map of hard coating under sliding contact. *Thin Films Tribol* 25:419–427
50. Diao DF, Kato K, Hayashi K (1994) The maximum tensile-stress on a hard coating under sliding friction. *Tribol Int* 27(4):267–272
51. Diao DF, Kato K, Hokkirigawa K (1994) Fracture mechanisms of ceramic coatings in indentation. *J Tribol Trans ASME* 116(4):860–869
52. Diao DF, Sawaki Y (1995) Fracture mechanisms of ceramic coating during wear. *Thin Solid Films* 270(1–2):362–366
53. Holmberg K, Matthews A (1994) Coatings tribology - properties, techniques and applications in surface engineering, vol 28, *Tribology and interface engineering series*. Elsevier Science, Amsterdam, p 442. ISBN 0444888705
54. Mao K, Sun Y, Bell T (1996) A numerical model for the dry sliding contact of layered elastic bodies with rough surfaces. *Tribol Trans* 39(2):416–424
55. Mao K et al (2010) Surface coating effects on contact stress and wear: an approach of surface engineering design and modelling. *Surf Eng* 26(1–2):142–148
56. Greenwood JA, Williamson JB (1966) Contact of nominally flat surfaces. *Proc R Soc Lond Ser A Math Phys Sci* 295(1442):300
57. Laukkanen A et al (2006) Tribological contact analysis of a rigid ball sliding on a hard coated surface, part III: fracture toughness calculation and influence of residual stresses. *Surf Coat Technol* 200(12–13):3824–3844
58. Lancaster JK (1984) Solid lubricants. In: Booser ER (ed) *Handbook of lubrication: theory and practice of tribology*. CRC Press, Inc, Boca Raton, FL, pp 269–290
59. King JP, Forster NH (1990) Synthesis and evaluation of novel high temperature solid lubricants. In: *Proceedings of the AIAA, SAE, ASME, and ASEE 26th joint propulsion conference*, Orlando, FL
60. Willis B (2002) Fighting friction with solid-film coatings. *Machine Des* 74(12):66
61. Kubart T et al (2005) Temperature dependence of tribological properties of MoS₂ and MoSe₂ coatings. *Surf Coat Technol* 193(1–3):230–233
62. Jradi K, Schmitt M, Bistac S (2009) Surface modifications induced by the friction of graphites against steel. *Appl Surf Sci* 255(7):4219–4224
63. Roselman IC, Tabor D (1976) Friction of carbon-fibers. *J Phys D Appl Phys* 9(17):2517
64. Skinner J, Gane N, Tabor D (1971) Micro-friction of graphite. *Nat Phys Sci* 232(35):195–196

65. Marchon B et al (1988) TPD and XPS studies of O₂, CO₂, and H₂O adsorption on clean polycrystalline graphite. *Carbon* 26(4):507–514
66. Carrott PJM (1992) Adsorption of water-vapor by nonporous carbons. *Carbon* 30(2):201–205
67. Harker H, Horsley JB, Robson D (1971) Active centres produced in graphite by powdering. *Carbon* 9(1):1
68. Yen BK (1995) Roles of oxygen in lubrication and wear of graphite in “dusting” and ambient conditions. *J Mater Sci Lett* 14(21):1481–1483
69. Yen BK (1996) Influence of water vapor and oxygen on the tribology of carbon materials with sp² valence configuration. *Wear* 192(1–2):208–215
70. Bragg WH (1929) An introduction to crystal analysis, vol 64. Van Nostrand, New York
71. Deacon RF, Goodman JF (1958) Lubrication by lamellar solids. *Proc R Soc Lond A Math Phys Sci* 243(1235):464–482
72. Spalvins T (1982) Morphological and frictional behavior of sputtered MoS₂ films. *Thin Solid Films* 96(1):17–24
73. Singer IL (1996) Mechanics and chemistry of solids in sliding contact. *Langmuir* 12(19):4486–4491
74. Singer IL et al (1990) Hertzian stress contribution to low friction behavior of thin MoS₂ coatings. *Appl Phys Lett* 57(10):995–997
75. Zhao XY, Perry SS (2010) The role of water in modifying friction within MoS₂ sliding interfaces. *ACS Appl Mater Interfaces* 2(5):1444–1448
76. Fleischauer PD, Lince JR (1999) A comparison of oxidation and oxygen substitution in MoS₂ solid film lubricants. *Tribol Int* 32(11):627–636
77. Arslan E et al (2005) The effect of deposition parameters and Ti content on structural and wear properties of MoS₂-Ti coatings. *Wear* 259:814–819
78. Arslan E, Bulbul F, Efeoglu I (2004) The structural and tribological properties of MoS₂-Ti composite solid lubricants. *Tribol Trans* 47(2):218–226
79. Donnet C et al (1996) Super-low friction of MoS₂ coatings in various environments. *Tribol Int* 29(2):123–128
80. Haider J et al (2005) Deposition and characterization of hard-solid lubricant coating by closed-field magnetron sputtering. *Surf Coat Technol* 200(1–4):1080–1083
81. Cosemans P et al (2003) Development of low friction wear-resistant coatings. In: *Surface and coatings technology, proceedings of the eight international conference on plasma surface engineering*, pp 416–420
82. Renevier NM, Fox VC, Teer DG, Hampshire J (2000) Coating characteristics and tribological properties of sputter-deposited MoS₂-metal composite coatings deposited by closed field unbalanced magnetron sputter ion plating. *Surf Coat Tech* 127(1):24–37
83. Simmonds MC, Savan A, Pflüger E, Van Swygenhoven H (2000) Mechanical and tribological performance of MoS₂ co-sputtered composites. *Surf Coat Tech* 126(1):15–24
84. Stupp BC (1981) Synergistic effects of metals co-sputtered with MoS₂. *Thin Solid Films* 84(3):257–266
85. Gangopadhyay S et al (2009) Composition and structure–property relationship of low friction wear resistant TiN–MoS_x composite coating deposited by pulsed closed-field unbalanced magnetron sputtering. *Surf Coat Technol* 203:1565–1572
86. Gilmore R, Baker MA, Gibson PN, Gissler W (1998) Preparation and characterisation of low-friction TiB₂-based coatings by incorporation of C or MoS₂. *Surf Coat Tech* 105(1–2):45–50
87. Gilmore R, Baker MA, Gibson PN, Gissler W, Stoiber M, Losbichler P, Mitterer C (1998) Low-friction TiN–MoS₂ coatings produced by dc magnetron co-deposition. *Surf Coat Tech* 109(1–3):345–351
88. Goller R, Torri P, Baker MA, Gilmore R, Gissler W (1999) The deposition of low-friction TiN–MoS_x hard coatings by a combined arc evaporation and magnetron sputter process. *Surf Coat Tech* 120–121:453–457
89. Rahman M, Haider J, Dowling DP, Duggan P, Hashmi MSJ (2005) Deposition of magnetron sputtered TiN+MoS_x coating with Ti-TiN graded interlayer. *Surf Coat Tech* 200(1–4):1071–1075

90. Gilmore R et al (1998) Preparation and characterisation of low-friction TiB₂-based coatings by incorporation of C or MoS₂. *Surf Coat Technol* 105(1–2):45–50
91. Robertson J (1992) *Surf Coat Technol* 50(3):185–203
92. Angus JC, Hayman CC (1988) Low-pressure, metastable growth of diamond and “diamondlike” phases. *Science* 241(4868):913–921
93. Geis MW, Efremow NN, Rathman DD (1988) Summary abstract: device applications of diamonds. *J Vac Sci Technol A Vac Surf Films* 6(3):1953–1954
94. Fallon PJ et al (1993) Properties of filtered-ion-beam-deposited diamondlike carbon as a function of ion energy. *Phys Rev B* 48(7):4777–4782
95. Green DC, McKenzie DR, Lukins PB (1989) Properties and characterization of amorphous carbon films. *Mater Sci Forum* 52–53:103–124
96. Dillon RO, Woollam JA, Katkanant V (1984) Use of Raman scattering to investigate disorder and crystallite formation in as-deposited and annealed carbon films. *Phys Rev B* 29(6):3482–3489
97. Dimigen H, Klages CP (1991) Microstructure and wear behavior of metal-containing diamond-like coatings. *Surf Coat Technol* 49(1–3):543–547
98. Grill A, Patel V (1993) Tribological properties of diamond-like carbon and related materials. *Diamond Relat Mater* 2(5–7):597–605
99. Holmberg K et al (1994) Tribological characteristics of hydrogenated and hydrogen-free diamond-like carbon coatings. *Diamond Films Technol* 4(2):113–129
100. Yang EL et al (1991) Friction and wear of polytetrafluoroethylene on diamond-like carbon film. *Thin Solid Films* 196(1):L25–L29
101. Koskinen J et al (1995) Proceedings of the 9th international conference on ion beam modification of materials, February 1995
102. Smith PL (2002) Reducing friction lets a new coating score in three ways for dry machining, in *American Machinist*. Penton Media, Inc., New York
103. Gharam AA et al (2010) High temperature tribological behaviour of carbon based (B₄C and DLC) coatings in sliding contact with aluminum. *Thin Solid Films* 519(5):1611–1617
104. Jia ZF et al (2011) Tribological behaviors of different diamond-like carbon coatings on nitrided mild steel lubricated with benzotriazole-containing borate esters. *Tribol Lett* 41(1):247–256
105. Gangopadhyay A et al (2011) Friction, wear, and surface film formation characteristics of diamond-like carbon thin coating in valvetrain application. *Tribol Trans* 54(1):104–114
106. Erdemir A, Fenske GR (1996) Tribological performance of diamond and diamondlike carbon films at elevated temperatures. *Tribol Trans* 39(4):787–794
107. Enke K, Dimigen H, Hubsch H (1980) Frictional-properties of diamond-like carbon layers. *Appl Phys Lett* 36(4):291–292
108. Weissmantel C et al (1982) Preparation and properties of hard I-C and I-Bn coatings. *Thin Solid Films* 96(1):31–44
109. Memming R, Tolle HJ, Wierenga PE (1986) Properties of polymeric layers of hydrogenated amorphous-carbon produced by a plasma-activated chemical vapor-deposition process. 2. Tribological and mechanical-properties. *Thin Solid Films* 143(1):31–41
110. Miyoshi K (1990) Studies of mechanochemical interactions in the tribological behavior of materials. *Surf Coat Technol* 43–44(Part 2):799–812
111. Kim DS, Fischer TE, Gallois B (1991) The effects of oxygen and humidity on friction and wear of diamond-like carbon films. *Surf Coat Technol* 49(1–3):537–542
112. Marchon B, Heiman N, Khan MR (1990) Evidence for tribochemical wear on amorphous-carbon thin-films. *IEEE Trans Magn* 26(1):168–170
113. Ronkainen H, Holmberg K (1995) International conference on metallurgical coatings and thin films, San Diego, CA
114. Uchida M et al (2004) Friction and wear properties of CrAlN and CrVN films deposited by cathodic arc ion plating method. *Surf Coat Technol* 177:627–630

115. Dearnley PA (1999) Low friction surfaces for plastic injection moulding dies—an experimental case study. *Wear* 229:1109–1113
116. Polcar T et al (2010) Effects of carbon content on the high temperature friction and wear of chromium carbonitride coatings. *Tribol Int* 43(7):1228–1233
117. Perkins P (1978) Measurement of slip between the shoe and ground during walking. *Am Soc Testing Mater* 649:71–87

Exercise

1. Describe different applications where friction coatings are used.
2. What are the design requirements for the friction coatings?
3. What factors affect the decision making of surface treatment to develop friction surfaces?
4. What are the advantages of friction surfaces?
5. What parameters govern the process of coating design? Briefly describe each.
6. What is the influence of environmental parameters on friction of graphite?
7. What is the influence of environmental parameters on friction of MoS₂?
8. What are the advantages of the polymeric friction coatings?
9. For alumina deposited on the cemented carbide, find the critical thickness using the relationship given below. $c_d = 2 \mu\text{m}$, $\nu_f = 0.25$, $E_f = 400 \text{ GPa}$, and $\sigma_R = 1 \text{ GPa}$:

$$\frac{t_b}{c_d} = \left[\frac{12(1 - \nu_f^2)\sigma_R}{\pi^2 E_f} \right]^{\frac{1}{2}}$$

Part III
Lubrication Science

Chapter 10

Fundamentals of Lubrication

Pradeep L. Menezes, Carlton J. Reeves, and Michael R. Lovell

Abstract Lubricants are substances used to minimize the friction and wear of moving parts. Additionally, they can serve to distribute heat, remove contaminants, and improve the efficiency and lifetime of mechanical systems. Lubricants can generally be categorized as liquid, solid, or gaseous. Liquid lubricants consist of base oils such as natural oils, mineral (petroleum) oils, and synthetic oils with combinations of additives that further enhance the properties of the lubricants. Solid or dry lubricants are generally powders or semisolids in the form of a grease or solid–liquid suspension. Gaseous lubricants have a much lower viscosity than liquid or solid lubricants and utilize gasses such as air under pressure. The selection of an appropriate lubricant for a mechanical system requires a thorough understanding of the rheology of lubricants, the effects of additive combinations, and the knowledge of lubrication theory. Lubrication theory is linked to numerous fields of expertise outside of tribology, and without this interdisciplinary aspect, the progression of lubricants and lubrication technologies within the vast array of applications may not have reached the necessary levels of success. The use of liquid lubricants is ubiquitous in most applications, ranging from automotive fluids, to industrial oils, and process oils. Within the lubrication industry, there are over 10,000 different lubricants used around the world. This chapter explores the many aspects of lubricants and lubrication technologies including lubrication fundamentals, rheology of liquid lubricants, liquid lubricant additives, and liquid lubrication theory.

P.L. Menezes (✉) • M.R. Lovell
Department of Industrial Engineering, University of Wisconsin-Milwaukee, Milwaukee,
WI 53201, USA
e-mail: menezesp@uwm.edu

C.J. Reeves
Department of Mechanical Engineering, University of Wisconsin-Milwaukee, Milwaukee,
WI 53201, USA

1 Lubrication Fundamentals

1.1 Introduction

A lubricant is a substance introduced between two moving surfaces to reduce friction, minimize wear, distribute heat, remove contaminants, and improve efficiency. The importance of lubricants and sustainable lubrication systems cannot be fully appreciated until understanding the implications of not using an appropriate lubricant or a lubricant at all. In 1979, it was estimated that over \$200 billion was spent in North America on machine maintenance [1]. Within the \$200 billion, approximately one-third (\$66.7 billion) could have been avoided with the use of adequate lubricants. More recently, estimates claim that the amount of energy wasted due to insufficient knowledge applied to the science of friction, lubrication, and wear resulted in roughly 0.4 % of the gross domestic product (GDP) being wasted [2]. In the United States, this means that over \$60.36 billion of the \$15.08 trillion GDP was wasted due to energy loss [3]. When considering the many applications that utilize lubricants such as internal combustion engines, turbines, hydraulic systems, compressors, vehicle and industrial gearboxes, and journal and thrust bearings, it becomes easy to understand the importance that lubricants play in the compliance, effectiveness, and operation of many of these applications.

Within the lubrication market, there are a vast number of applications which require specifically formulated lubricants that have given rise to the upwards of 10,000 different lubricants that satisfy more than 90 % of all lubricant applications worldwide [2]. Figure 10.1 dissects the global lubrication market as of 2004, which consumed roughly 37.4 million tons of lubricant [2]. This figure illustrates how automotive and industrial lubricants are the most prevalent. Industrial lubricants amount to 32 % and were composed of 12 % hydraulic oils, 10 % other industrial oils, 5 % metalworking fluids, 3 % greases, and 2 % industrial gear oils [4, 5].

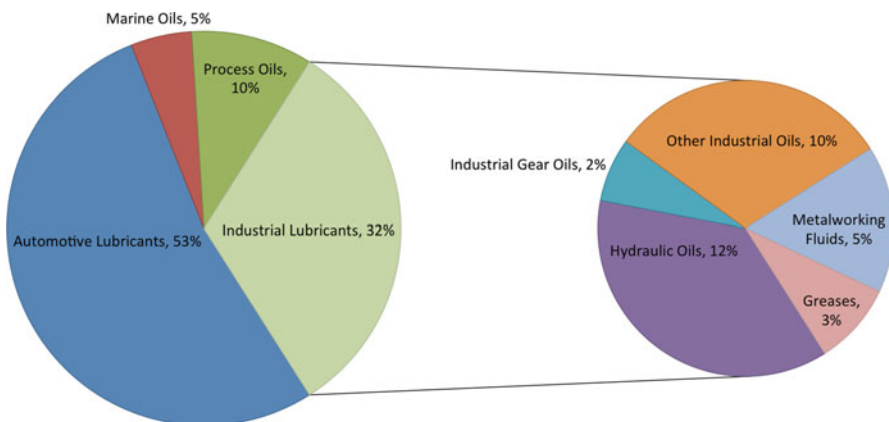


Fig. 10.1 2004 worldwide lubrication consumption [2]

The 10 % of other industrial oils within the industrial lubricants section consist of a wide range of lubricants such as air and gas compressor oils, bearing and circulating system oils, refrigerator compressor oils, and steam and gas turbine oils. In the automotive lubricants section, the most commonly used liquid lubricants were engine oils (petrol and diesel engine oils), automatic transmission fluids, gearbox fluids, brake fluids, and hydraulic fluids.

Lubricants originally consisted of natural oils and fats derived from plant- and animal-based raw materials which date back to 1400 BC. The modern lubrication market developed after the first oil well was drilled in 1959 in Titusville, PA. Since then, lubricants have evolved from mineral oils to petrochemically modified synthetic oils arriving in the 1960s to today's bio-based lubricants harvested from raw materials derived from the oleo-chemical industry. Recently, bio-based lubricants have begun to seek prominence for their environmental friendliness and superior tribological properties. The current trend in the lubrication industry is to develop more bio-based lubricants due to estimates indicating that nearly 50 % of all lubricants sold worldwide pollute the environment, through spillage, evaporation, and total loss applications [6]. An example of lubrication pollution is that of the diesel engine particulate emissions, where approximately one-third of the engine oil vaporizes, thus polluting the atmosphere. The large quantity of lubricant loss into the environment is the reason behind the development of environmentally friendly lubricants. Although the lubrication market is shifting to become more environmentally responsible by reducing the use of petroleum-based lubricants due to concerns of protecting the environment, depletion of oil reserves, and increases in oil price, mineral oil remains to be the largest constituent and the foundation to most lubricants [6].

Lubricants generally consist of about 90 % base oils, less than 10 % additives, and minute portions of other components. The exact formulation of a lubricant is typically linked to the specific application or intended use designated by the lubricant manufacture. Lubricants vary dramatically due to the wide functionality of a lubricant to dissolve or transport foreign particles, carrying away contaminants and debris, prevent corrosion or rust, seal clearances, dissipate heat, and minimize friction and wear of components. In general, there are three categories of lubricants: liquid, solid, and gaseous.

1.1.1 Liquid Lubricants

Liquid lubricants may be characterized in a variety of methods and the most common method is by the type of base oil used. Notable base oil types are lanolin (wool grease, a natural water repellent), water, mineral oils (derived from crude oil), vegetable oils (derived from plants and animals), and synthetic oils (consisting of oleo-chemical compounds synthesized from compounds other than crude oil) [7]. Liquid lubricants are often viscous fluids that require circulatory pumping systems or rotary mechanical systems such as bearings or gears to distribute the fluid through the various machine elements. The primary function of a liquid lubricant is to control friction, wear, and surface damage over the intended life of

a system. Secondary functions of liquid lubricants are to prevent corrosion and remove heat, dirt, and wear debris. In some instances, liquid lubricants are used to transfer either force or energy as in hydraulic systems.

1.1.2 Solid Lubricants

Solid or dry lubricants are generally powders or semisolids in the form of a grease or solid–liquid suspension. Some of the commonly known powder lubricant materials are graphite (C), molybdenum disulphide (MoS_2), tungsten disulphide (WS_2), and titanium dioxide (TiO_2) [8–14]. Solid lubricants offer lubrication at temperatures (up to 350 °C) that are higher than many liquid oil-based lubricants. Solid lubricants such as Teflon or PTFE (polytetrafluoroethylene) are typically used as a coating layer to provide a nonstick surface [15].

Solid–liquid suspensions consist of solid lubricants mixed into a liquid fluid such as water or oil to form a colloidal suspension. These slurry or two-phase lubricants are often utilized in metalworking processes such as forging and extrusion. Solid lubricants can also be used in a less viscous approach where they are applied as suspension in a carrier fluid such as vegetable oil [6, 16, 17].

Greases are complex semisolid lubricants consisting of liquid-base oils mixed with various thickening agents derived from soaps or other organic or inorganic substances [18]. Greases can also include a multitude of additives such as powder lubricants and their consistency closely resembles that of a paste [19]. They range in multiple viscosities and are available in semisolid (synonymous with semiliquid) form to solid form known as block greases. Greases are often processed in special grease-making facilities, as they require special equipment for their production.

1.1.3 Gaseous Lubricants

Gaseous lubricants have a much lower viscosity than liquid or solid lubricants. Gaseous lubricants also exhibit lower heat capacity and higher compressibility than liquid or solid lubricants [7]. Some examples of gaseous lubricants are air, technical gases, steam, and liquid-metal vapors. Gaseous lubricants can be found in foil bearings, where centripetal forces allow air to push the foil away from the shaft so that there is minimal contact. Another example is air hockey tables, a popular game at arcades, which utilizes compressed air to establish a thin air cushion on which the puck glides over allowing for a quasi-frictionless environment.

1.2 Lubricant Additives

Additives are substances used to improve the performance of lubricants. Additives are selected based on their ability to reduce friction and wear, increase viscosity, improve viscosity index, resist corrosion and oxidation, increase component and

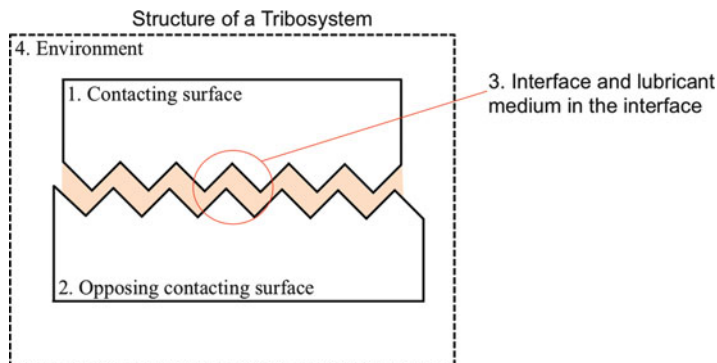


Fig. 10.2 Structure of a tribosystem: (1) contacting surface, (2) opposing contacting surface, (3) interface and lubricant medium in the interface, and (4) environment

lubricant lifetime, and minimize contamination [20]. The main categories of additives are antioxidants, antiwear formulations, antifoaming agents, corrosion inhibitors, detergents (demulsifying/emulsifying), extreme pressure, friction modifiers, metal deactivators, and viscosity index improvers [1].

1.3 Lubrication Regimes

Lubricants are used to reduce the frictional force between surfaces, known as a tribological system. A tribological system (or tribosystem) consists of four components as described in Fig. 10.2: (1) a contacting surface, (2) an opposing contacting surface, (3) the contacting interface along with the lubricant medium in the interface, and (4) the environment and all external properties [2, 21, 22]. Tribosystems can consist of numerous components and systems. For example, a plain bearing is a tribosystem. In this example, the material pair is the shaft and bearing shell, with the lubricant located in the annular gap. Other examples of material pairs that form tribosystems are in combustion engines such as the piston rings and cylinder wall and the camshaft lobes and tappets [7]. In metalworking, the tool and the workpiece also constitute as a material pair forming a tribosystem.

A lubricant functions by introducing a medium with a lower shear strength than the opposing surfaces. In some lubricated tribosystems, the lubricant may not completely prevent asperity contact between the surfaces. However, the lubricant will reduce the number of asperity contacts and it may also reduce the shear strength of the junctions formed during asperity contact. In other cases, the lubricant completely separates the surfaces and no asperity contacts are formed at all. Lubrication regimes are normally associated with dominant lubrication mechanisms involved in the mechanical system as illustrated in the Stribeck curve as shown in Fig. 10.3 [2] for liquid lubrication. The three main lubrication

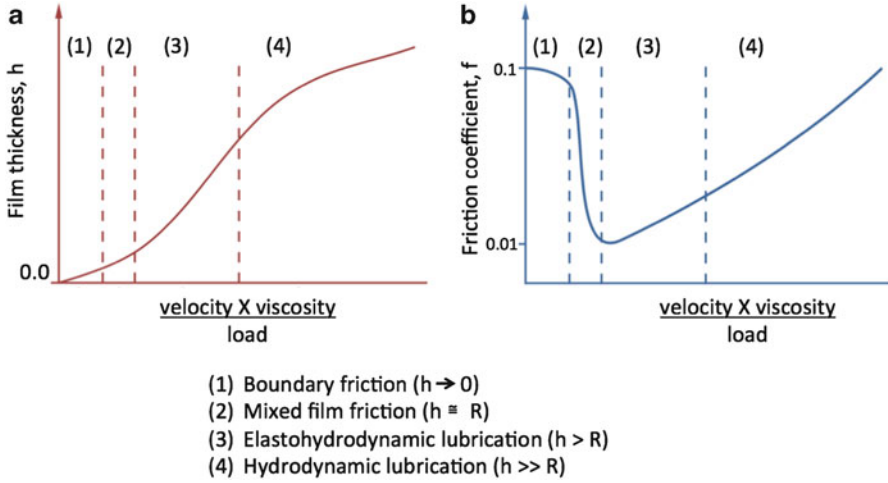
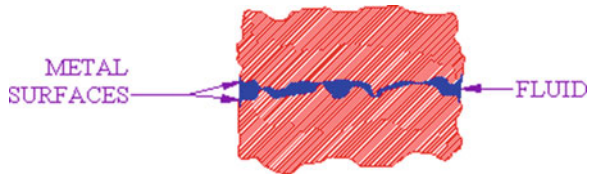


Fig. 10.3 Demarcation of lubrication regimes: (a) film thickness vs. Hersey’s number and (b) coefficient of friction vs. Hersey’s number (i.e., Stribeck curve)

Fig. 10.4 Boundary lubrication at the interface of a tribosystem

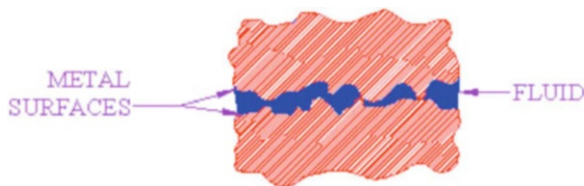


regimes can be referred to as boundary lubrication, mixed/elastohydrodynamic lubrication, and hydrodynamic lubrication.

1.3.1 Boundary Lubrication

Boundary lubrication or boundary friction is the lubrication regime with the most asperity contact between the surfaces occurring due the presence of a thin fluid film graphically depicted in Fig. 10.3a and illustrated in Fig. 10.4. Boundary lubrication is a complex process and is controlled by additives in the oil that form a thin molecular layer (monolayer) of fluid film through physical adsorption, chemisorption, and tribochemical reactions on the contacting surfaces [23]. One of the more common boundary lubrication additives are fatty acids which adhere to the metallic surfaces and form a tightly packed monolayer [24, 25]. This monolayer helps to reduce the asperity contacts that lead to high values of friction and wear. The development of a monolayer film is vital in boundary lubrication because in many practical applications, thick, long-lasting, lubricant films cannot be sustained between opposing surfaces and thus these monolayer films help to reduce the amount of surface interaction [20].

Fig. 10.5 Mixed lubrication/ elasto-hydrodynamic lubrication at the interface of a tribosystem



1.3.2 Mixed/Elastohydrodynamic Lubrication

Mixed film lubrication is the combination of full film hydrodynamic lubrication and boundary lubrication. In this lubrication regime, the surfaces are transitioning away from boundary lubrication into hydrodynamic lubrication where there may be frequent asperity contacts, but at least a portion of the bearing surface remains supported partially by a hydrodynamic film [23] as shown in Fig. 10.5. In mixed lubrication, the effects of monolayers formed by physical absorption, chemisorption, and chemical reaction remain critical to prevent unwanted adhesion during the asperity contacts [2].

Elastohydrodynamic (EHD) lubrication is a subset of hydrodynamic (HD) lubrication in which the elastic deformation of the contacting solids plays a significant role in the HD lubrication process. The film thickness in EHD lubrication is thinner (typically 0.5–5 μm) than that in HD lubrication and the load is still primarily supported by the EHD film [23]. In this transitional region, there is less asperity contact than that of mixed lubrication with more of the contacting surfaces being supported by the hydrodynamic fluid film.

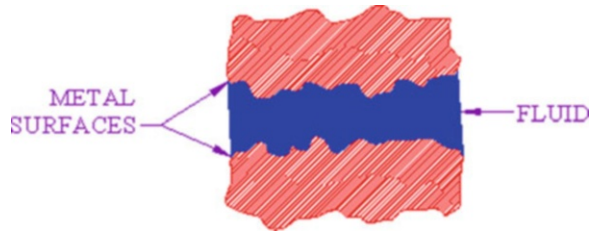
1.3.3 Hydrodynamic Lubrication

Hydrodynamic lubrication also known as fluid-film or thick-film lubrication involves two nonparallel surfaces in relative motion with a layer of fluid pulled in between the surfaces to develop adequate hydrodynamic pressure to support the load of the opposing surfaces and prevent asperity contact [2]. In this lubrication regime, the surfaces are no longer in contact as illustrated in Fig. 10.6 and the fluid has established itself in significant form to create a thick film.

1.4 Stribeck Curve

The Stribeck curve shown in Fig. 10.3b is a plot of the coefficient of friction against a nondimensional number known as Hersey's number (also referred to as the Stribeck number). Hersey's number was instrumental in demarcation of the aforementioned lubrication regimes [23]. Hersey's number is given by $(\eta v/p)$, where " η " is the lubricant viscosity, " v " is sliding velocity, and " p " is load per unit width.

Fig. 10.6 Hydrodynamic lubrication at the interface of a tribosystem



The values of the coefficient of friction that are depicted in the original Stribeck curve remain constant when Hersey's number approaches zero in the boundary lubrication regime. Experimental work done by Fischer et al. [26] led to the modification of the Stribeck curve. They showed that the coefficient of friction does not remain constant in the boundary lubrication regime, but reduces as the value of Hersey's number increases. The slope of this curve is determined by the efficiency of the boundary lubricant. At low values of Hersey's number, the thickness of the lubricant film, h , develops much less than the surface roughness, R . In boundary lubrication (illustrated in Fig. 10.4), thin monolayers develop causing the film thickness to approach zero, resulting in significant asperity contact and high friction. An increase in sliding speed or a decrease in load at constant viscosity can cause the film thickness to steadily increase therefore shifting the lubrication regime from boundary lubrication into mixed or elastohydrodynamic lubrication. This transition results in lower coefficient of friction values and thicker hydrodynamic fluid films. In the mixed lubrication regime, the fluid-film thickness can be on the same order of magnitude as the surface roughness ($h \cong R$), and in the elastohydrodynamic lubrication regime, the fluid-film thickness can be greater than the surface roughness ($h > R$). As the sliding speed continues to increase or the load decreases with a constant viscosity, this allows progress through the elastohydrodynamic regime allowing a full uninterrupted fluid film to develop that is significantly thicker than the surface roughness ($h \gg R$). When the fluid film is much greater than the surface roughness, then the hydrodynamic lubrication regime dominates. In this lubrication regime, internal friction in the lubricating film adds to external friction causing the coefficient of friction to increase as shown in Fig. 10.4.

Other methods have been proposed to quantify the various lubrication regimes. The Hamrock and Dowson model provided a formula for calculation of minimum film thickness in lubricated contacts [27–30]. The fluid-film thickness parameter, λ , decides the lubrication regime with boundary lubrication characterized by a value of λ less than 1, mixed or elastohydrodynamic lubrication described as $1 \leq \lambda \leq 3$, and hydrodynamic lubrication characterized by a value of λ greater than 3 [7, 20, 23, 31–34]. The fluid-film thickness parameter, λ , given in (10.1a), is the ratio of fluid-film thickness, h , and the composite surface roughness, σ :

$$\lambda = \frac{h}{\sigma} \quad (10.1a)$$

$$\sigma = \sqrt{\sigma_1^2 + \sigma_2^2} \quad (10.1b)$$

In (10.1a), the composite surface roughness is given in (10.1b) where σ_1 and σ_2 are RMS roughness of the two mating surfaces. The calculation of minimum film thickness for metals and polymers are presented in various publications throughout the literature [35–39].

2 Rheology of Liquid Lubricants

The characteristics of lubricants and their properties involve understanding the rheology of liquid lubricants. Many of the important characteristics of a lubricant include viscosity, consistency, flow properties, thermal stability, oxidative properties, and physiochemical properties.

2.1 Viscosity

Viscosity of a fluid may be defined as its resistance to flow. Different oils exhibit different viscosities. An example shown in Fig. 10.7 compares the viscosities of honey (~2,000 cP) and water (~1 cP) at 21 °C. If one examines honey in a jar and tries to pour it, the honey will move much more lethargically, whereas if one tries to pour water out of a jar, it readily pours. The difference between the two is that honey has a much higher viscosity and thus it is much more resistant to flow than water. Lubricant viscosity changes with temperature, load, shear rate, and pressure. Viscosity is important in the selection process of oils, because many oils have similar characteristics, but their viscosities differ. Viscosity directly relates to a lubricant's film strength and ability to keep moving parts separated.

The importance of proper viscosity selection is vital for the success of many lubrication systems. If an application operates at high speeds, low loads, and low temperatures, then it is generally accepted to use a low-viscosity lubricant.

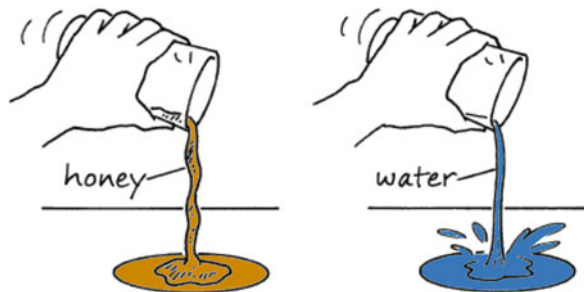
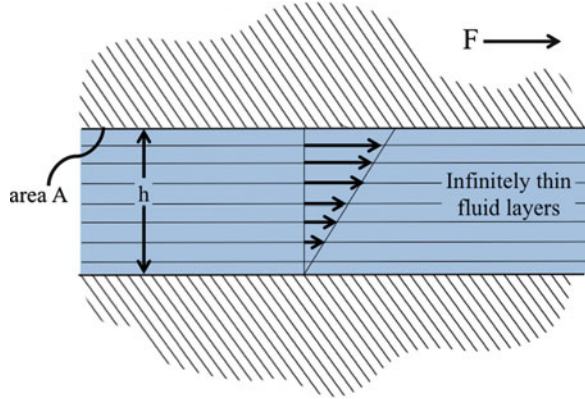


Fig. 10.7 Viscosity characteristics of honey and water. Honey is much more viscous than water

Fig. 10.8 Schematic of two parallel planes in relative motion with a velocity u , separated by a fluid film of thickness h with a linear velocity gradient [40]



Conversely, if an application operates at low speeds, high loads, and high temperatures, then higher viscous lubricants should be utilized [2]. Quantifying viscosity requires the use of two parameters, dynamic and kinematic viscosity, which will be addressed in the following sections.

2.2 Dynamic Viscosity

Dynamic viscosity can be explained by considering two parallel surfaces separated by a layer of fluid having a thickness h as demonstrated in Fig. 10.8. To move the upper surface, a force F is required which is proportional to the surface area A of the upper surface and the linear velocity s , as revealed in (10.2):

$$F \propto A \times u \quad (10.2)$$

Assuming that the fluid film separating the parallel surfaces is made up of a number of infinitely thin layers, the force needed to move the upper surface is thus proportional to

$$F \propto A \times \frac{u}{h} \quad (10.3)$$

Different fluids exhibit different proportionality constants η , known as the dynamic viscosity:

$$F = \eta \times A \times \frac{u}{h} \quad (10.4)$$

Rearranging (10.4) yields

$$\eta = \frac{F}{A} / \frac{u}{h} \quad (10.5a)$$

or

$$\eta = \tau / \frac{u}{h} \quad (10.5b)$$

where:

η is the dynamic viscosity (Pas),

τ is the shear stress acting on the fluid (Pa),

u/h is the shear rate, i.e., velocity gradient normal to the shear stress (s^{-1}).

Prior to the introduction of the international system (SI) of units of measure, the most commonly used dynamic viscosity unit was the Poise (P). However, for many practical applications, the Poise was far too large; thus a smaller unit, the centipoise (cP), was adopted as the standard unit. The SI unit for dynamic viscosity is Pascal-second (Pas). The relationship between Poise and Pascal-second is as follows: $1 \text{ (P)} = 100 \text{ (cP)} \approx 0.1 \text{ (Pas)}$.

2.3 Kinematic Viscosity

Kinematic viscosity is defined as the ratio of a fluid's dynamic viscosity divided by its density:

$$\nu = \frac{\eta}{\rho} \quad (10.6)$$

In (10.6), ν is the kinematic viscosity (m^2/s), η is the dynamic viscosity (Pas), and ρ is the fluid density (kg/m^3). Kinematic viscosity is often described in units of Stoke (S). This unit is also too large for many applications; thus a smaller unit, the centistoke (cS), is more commonly used. The SI unit for kinematic viscosity is m^2/s , with the following conversions: $1 \text{ S} = 100 \text{ cS} = 0.0001 \text{ m}^2/s$.

As previously mentioned, viscosity is dependent on temperature. Figure 10.9 profiles various lubricant viscosities over a broad range of temperatures revealing the relationship that as temperature increases, viscosity generally decreases [23, 40].

Ultimately, when choosing a lubricant based on viscosity, it is important that the lubricant is viscous enough to adequately provide a continuous fluid film in the contacting interface, but not too viscous as to create fluid friction due to viscous shearing. Viscous shearing is the phenomenon that occurs when the oil is too thick for a given application and the shear planes or layers of the fluid begin to drag over one another causing increased fluid friction also known as churning. As shown in

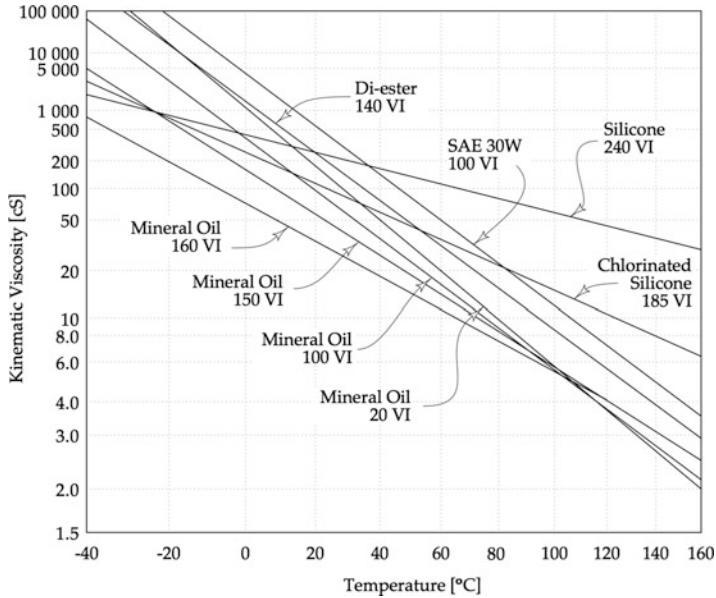


Fig. 10.9 Viscosity–temperature characteristics of selected oils [41, 42]

Fig. 10.9, viscosity is dependent on temperature. For example, on a cold morning, the engine of a car turns over much more slowly when starting up as compared to on a warm day, when the engine starts up immediately. This is an effect due to the cold ambient temperature causing the oil to thicken or become more viscous. When the engine warms up, the lubricant thins out or becomes less viscous, thus reverting back to its original design viscosity at operating temperature. Many multigrade lubricants such as automobile oils are designed to work in both cold and hot conditions. The vast majority of industrial lubricants are single-grade oils and are therefore much less resilient to volatile ambient and operating temperatures. Currently, there is no uniform standard for measuring viscosity; however in the following sections, some of the popular techniques will be explored.

2.4 Viscosity Index

Viscosity index (VI) is the rate of change in viscosity due to the change in temperature for a given fluid. The higher the VI of an oil, the less of a tendency for the oil's viscosity to change with fluctuations in temperature. Synthetic oils tend to have a better VI than petroleum-based oils. If two oils are being considered and they have the same properties, then the one with the higher VI should be the oil of choice.

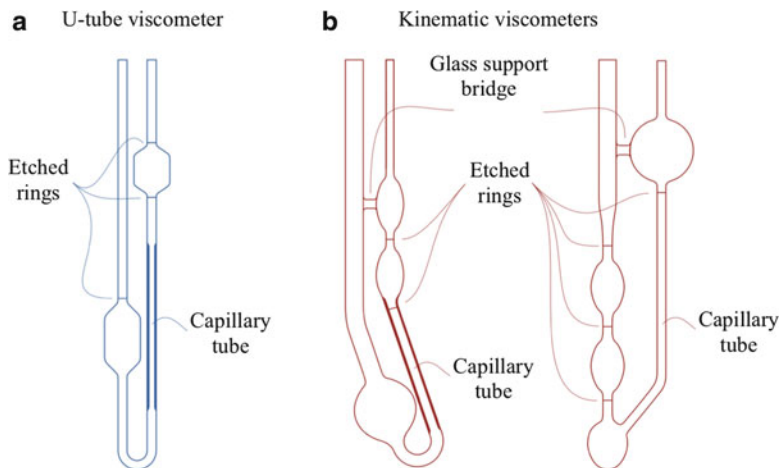


Fig. 10.10 Schematic of capillary viscometers: (a) British standard U-tube viscometer and (b) Ostwald kinematic viscometer [40]

2.5 Viscosity Measurement

The most commonly used apparatus in engineering applications for measuring viscosity is the capillary viscometer. Capillary viscometers are primarily used for measuring Newtonian lubricants with negligible end effects. Capillary viscometers are based on the principle that a specific volume of fluid will flow through a capillary and the time necessary for this volume of fluid to flow from one timing mark to another gives the kinematic viscosity. In these viscometers the fluid flow must be laminar to allow Poiseuille's law for steady viscous flow in a pipe to apply, allowing for the deduction of kinematic viscosity. Two of the more popular capillary viscometers are the British standard U-tube viscometer (Fig. 10.10a) and the Ostwald viscometer (Fig. 10.10b).

Capillary viscometers measure the kinematic viscosity of a fluid as defined by (10.7), which is derived from Poiseuille's law for steady viscous flow in a pipe:

$$v = \frac{\pi r^4 g l t}{8 L V} = k(t_2 - t_1) \quad (10.7)$$

where:

- v is the kinematic viscosity (m^2/s),
- r is the capillary radius (m),
- l is the mean hydrostatic head (m),
- g is the earth acceleration (m/s^2),
- L is the capillary length (m),
- V is the flow volume of the fluid (m^3),
- t is the flow time through the capillary, $t = (t_2 - t_1)$, (s),

k is the capillary constant which has to be determined experimentally by applying a reference fluid with a known viscosity or the manufacturer of the viscometer provides it.

2.6 Thermal Properties of Lubricants

Lubricants have three important thermal properties: specific heat, thermal conductivity, and thermal diffusivity. These parameters are important in evaluating the thermal effects during lubrication, such as the operating temperature of the surfaces and the cooling properties of the oil. The temperature characteristics are important in the selection process of a lubricant for a specific application. Other important thermal properties of a lubricant are pour point, cloud point, flash point, fire point, volatility and evaporation, oxidation and thermal stability, as well as surface tension. The temperature range over which a lubricant can be used is of extreme importance because at high temperatures, oils can decompose or degrade, while at low temperatures, oils may become solid or freeze. Oils can decompose by thermal and oxidative degradation. The decomposition of oil can cause a secondary effect where damage to the sensitive lubricated equipment may occur. A prime example of secondary damage is corrosion caused by the acidity of oxidized oils.

2.7 Pour Point

The pour point of a liquid is the lowest temperature at which it becomes semisolid and loses its flow characteristics. In order to determine the pour point, the oil is first heated to ensure solution of all ingredients. It is then cooled at a specific rate most commonly at decrements of 3 °C per minute; periodically, the container is tilted to check for any movement as illustrated in Fig. 10.11 [1]. The temperature 3 °C above the point at which the oil stops moving is recorded as the pour point. This property is important in the lubrication of any system exposed to low temperature, such as automotive engines, construction machines, military devices, and space applications, because it provides a lower bound for the operating temperature specification.

2.8 Cloud Point

The cloud point of a fluid is the temperature at which dissolved solids such as paraffin waxes are no longer soluble and begin to precipitate as a second phase giving the fluid a cloudy appearance during heating as shown in Fig. 10.12. The onset of a wax precipitation causes a distinct cloudiness or visible haze to appear in

Fig. 10.11 Illustration of a tilt check to verify if there is any movement for a lubricant during a pour test

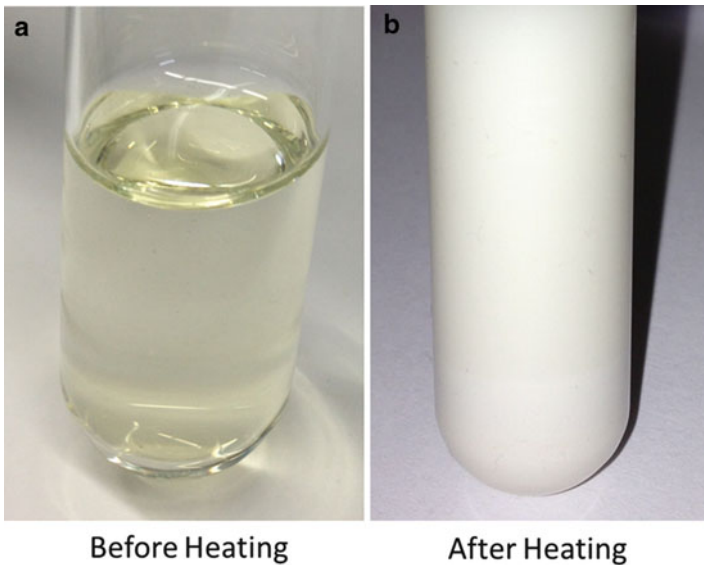


Fig. 10.12 Cloud point illustration of a transparent oil in a glass beaker: (a) before heating and (b) after heating

the beaker after heating. The cloud point has a practical application in capillary or wick feed lubrication systems in which the forming wax could potentially obstruct the oil flow. The cloud point is strictly limited to transparent fluids for the reason that measurement is based purely on observation through testing. If the cloud point of an oil is observed at a temperature higher than the pour point, the oil is said to have a “wax pour point.” On the contrary, if the pour point is reached without a cloud point, the oil is described as having a “viscosity pour point.”

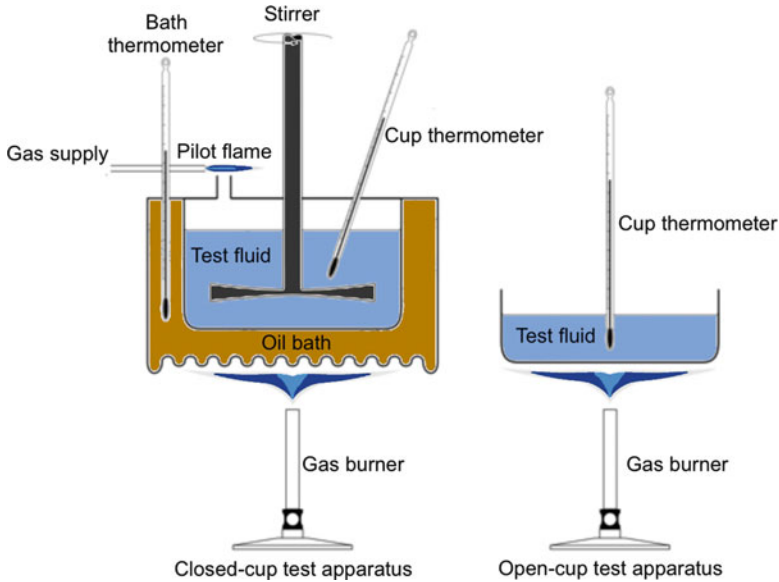


Fig. 10.13 Schematic diagram of the flash and fire point apparatus

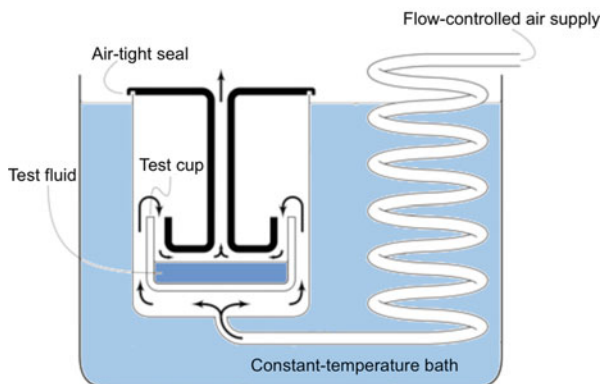
2.9 Flash and Fire Points

The only thermal properties, which define the fire hazard of a lubricant, are the flash and fire points. These properties are extremely important for safe application and use of a lubricant. The flash point of a lubricant is the temperature at which its vapor will flash ignite. Determination of the flash point requires oil to be heated at a standard pressure to a temperature high enough to produce sufficient vapor to form an ignitable mixture with air. Figure 10.13 illustrates two testing apparatuses: the closed-cup test and the open-cup test for measuring the flash and fire points. These tests work by heating a fluid and measuring its temperature at which the fluid's vapor is ignitable. The fire point of oil is the temperature at which enough vapor is produced to sustain burning after ignition. The fire point is always higher than the flash point. In general, the flash point and fire point of oils increase with increasing molecular weight. For a typical lubricating oil, the flash point is about 210 °C, whereas the fire point is about 230 °C [40].

2.10 Volatility and Evaporation

In many extended use or variable temperature applications, the loss of lubricant due to evaporation can be substantial. In particular, at elevated temperatures, oils may become more viscous and eventually dry out due to evaporation. The measure of

Fig. 10.14 Schematic diagram of an evaporation test apparatus



evaporation losses defines the volatility of a lubricant. In order to determine the lubricant volatility, a known quantity of lubricant is exposed in a vacuum thermal balance device. The evaporated material is then collected on a condensing surface and the decreasing weight of the original material is expressed as a function of time. Figure 10.14 shows an evaporation apparatus where a known quantity of oil is placed in a cup and aerated for a preset amount of time. The test cell is preheated to the required temperature in an oil bath. In this instrument, air enters through the periphery of the cup and flows across the surface of the oil and exits through the centrally located tube. At the completion of the test, the sample is cooled and weighed, revealing the percentage of lost mass, thus giving the evaporation rate. Recent advancements in lubricants have been through the use of ionic liquid lubricants for their composition of free flowing ions giving these fluids negligible vapor pressure and nonvolatility properties [43, 44].

2.11 Oxidation Stability

Oxidation stability is the resistance of a lubricant to molecular decomposition or reaction at elevated temperatures in an oxygen-enriched environment. Oxidation typically occurs in ambient environments where the air is composed of about 21 % oxygen. Lubricating oils rapidly oxidize when exposed to air at elevated temperatures, resulting in a strong impact on the useful life of an oil. Oxidation of oils is a complex process that includes thermally activated and physicochemical reactions that depend on the level of oil refinement, temperature, presence of metal catalysts, and operating conditions. Different compounds react at different temperatures and under different conditions [45, 46]. A lubricant that oxidizes rapidly requires more frequent maintenance or replacement resulting in higher operating costs.

Oils can be chemically modified to improve upon their oxidation stability by removing the hydrocarbon-type aromatics and molecules containing sulfur, oxygen, and nitrogen. More refined oils have a better oxidation stability; however, they have other shortcomings. Refined oils are typically more expensive to produce and they lead to a lubricant with poor boundary lubrication characteristics. For this reason, the oil selection for a particular application is always a compromise, depending on the type of job the oil is expected to perform. Blending antioxidant additives with oil can control oxidation. Details on antioxidants and the role of additives in lubricants will be discussed in a proceeding section.

2.12 Thermal Stability

All substances when heated above a certain temperature will naturally start to decompose, even if no oxygen is present. In this context, thermal stability is the resistance of a lubricant to molecular decomposition or reaction at elevated temperatures in the absence of oxygen. For example, when mineral oil is heated, it degrades to methane, ethane, and ethylene. Similarly, natural oils that are composed of fatty acids and esters have significant thermal instability due to the presence of double bonds in the unsaturated fatty acids. The presence of the double bonds in natural oils affects the thermal stability and causes the oil to breakdown at various temperatures into organic compounds, which adversely affect the functionality of the oil. Thermal stability of oils can often be improved through multiple types of refining processes such as epoxidation, metathesis, acylation, estolide formation, transesterification, and selective hydrogenation [47–60].

2.13 Surface Tension

Surface tension is a property of a liquid that allows it to resist an external force. Many lubricants show varying degrees of wettability and spreadability on surfaces. The wettability and spreadability characteristics of a lubricant are dependent on surface tension, which is especially sensitive to physicochemical changes. Depending on the degree of oxidation or the amount of additives present in a lubricant, the oils can have different wetting and spreading properties.

Surface and interfacial tension are related to the free energy of the surface and the attraction between the surface molecules, thus influencing the wetting and spreading characteristics. Surface tension refers to the free energy at a gas–liquid interface, while interfacial tension refers to interface between two immiscible liquids. A liquid with a large contact angle as shown in Fig. 10.15a has a high surface tension resulting in less physical spreading across the surface, thus acting as a poor lubricant. On the contrary, Fig. 10.15b illustrates a liquid with a small contact angle, having a low surface tension and thus spreading easily across the surface acting as a good

Fig. 10.15 Contact angle of a liquid droplet on a surface: (a) liquid with a large contact angle and (b) liquid with a small contact angle

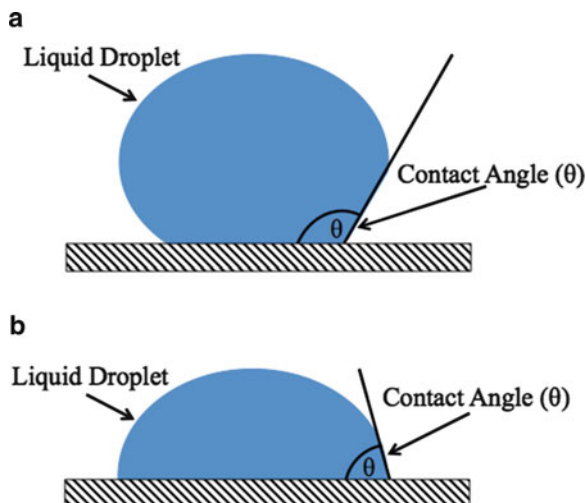


Table 10.1 Surface tension of various base oils [23]

Liquid	Surface tension (mN/m)
Water	72
Mineral oils	30–35
Esters	30–35
Methyl silicone	20–22
Perfluoropolyethers	19–21

lubricant. The surface tension of various base oils is presented in Table 10.1 [23]. As mentioned, surface tension for base oils is very sensitive to additives; for example, adding less than 0.1 % of methyl silicone to mineral oil reduces the surface tension by approximately 35 % to a value of about 21 mN/m.

3 Oil Additives

Base oils (vegetable oils, mineral oils, and synthetic oils) cannot always satisfy the demands of a high-performance lubricant by themselves [6]. For this reason, additives are blended with oils to enhance or modify the characteristics of a lubricant. Additives are synthetic chemical substances mixed with base oils to improve various characteristics of lubricants so the oils can placate the higher demand placed on them and satisfy specification requirements. Additives often improve existing properties, suppress undesirable properties, and introduce new properties to the base oils. One of the most important properties that additives enhance is a lubricant's ability to form protective films, which is especially important in boundary lubrication conditions.

Additives are classified based on their behavior, which takes into consideration the portion of the tribological system that the additive influences. For this reason, additives can be classified into two categories [2]:

1. Additives that influence the physical and chemical properties of the base oils:
 - (a) Physical effects: e.g., viscosity–temperature characteristics, demulsibility, and low-temperature properties
 - (b) Chemical effects: e.g., oxidation stability
2. Additives that influence the characteristics of the metal surfaces by modifying their physicochemical properties: e.g., reduction of friction, increase of extreme pressure behavior, wear protection, and corrosion inhibition

The use of additives has a large influence on the performance of lubricants that make it possible to fulfill the increasing complex demands placed on lubricants. Nevertheless, there are some properties that cannot be influenced by additives, such as volatility, air release properties, thermal stability, thermal conductivity, compressibility, and boiling point. Many of these properties require chemical modifications through various refinement processes. When blending additives with base oils, it is important to have a well-balanced and optimized composition to improve the performance of the lubricant. This usually requires the formulation of high-performance base oils that are derived from highly refined oils and then mixed with additives to further enhance the lubricant's properties.

3.1 Additive Compatibility and Solubility

Individual additives are generally added to base oils in small amounts between 0.1 and 0.5 % [23] with about 10 % of the total lubricant composition consisting of additives. When using multiple additives in a lubricant, they should be compatible with each other and soluble in the lubricant. Mixing additives with each other or with base oils can result in synergistic or antagonistic effects. For this reason, there are some additives that are multifunctional products that decrease the incompatibility of additives that would adversely interfere with each other. Two or more additives in an oil are generally considered compatible (1) if they do not react with each other and (2) if their individual properties are advantageous to the functioning of the lubricant. Often, a normal practice is to consider a mixture of additives to be compatible if they do not give visible evidence of reacting together, such as a change in color or smell.

Additive solubility requires that additives must dissolve or form colloidal mixtures in their base oils without settling out. Figure 10.16 shows several base oils of various colors with additives. In this figure, the additives are dissolved into the base oil, so they cannot be seen. Often, when an additive settles out of the base oil, it renders that specific additive ineffective; therefore it is important for additives to remain dissolved or mixed over the entire useful life of the lubricant. Separation



Fig. 10.16 Colors of several base oils with additives

of an additive in storage or in service is extremely detrimental and can pose a hazard in some systems because the lubricant may not function properly. For example, elemental sulfur could be used as an additive in extreme temperature and pressure applications; however it is insoluble in oil, separating during storage and service, thus rendering it unusable as an additive in oil [40].

3.2 Lubricant Additives

Lubricant additives are usually organic or organometallic chemicals that are added to oils to improve the lubricating capacity and durability of the oil. Specific purposes of lubricant additives are to [1, 2]:

1. Enhance the wear and friction characteristics
2. Improve the oxidation resistance
3. Minimize corrosion
4. Control contamination by reaction products, wear particles, and other debris
5. Reduce excessive decrease of lubricant viscosity at high temperatures
6. Decrease the pour point
7. Inhibit the generation of foam

Carefully selected additives are extremely effective in improving the tribological performance of a lubricant. Most additive manufacturers maintain complete secrecy over the details of their products. A result of this secrecy is that the supplier and end user of the lubricant may only know that a particular lubricant contains a “bundle” of additives without knowing the composition of each additive. Larger businesses very often produce many different brands and types of lubricants, which are effectively the same or have similar properties and composition. In this way, they can formulate their own lubricant recipes and protect them as trade secrets. This type of secrecy surrounding additives means that their formulation and the

exact properties of a bundle is partly an art rather than a purely scientific or technical process. This allows each company in the lubrication industry to have their own unique competitive advantage. Many of the most common additive bundles used in lubricant formulations are antiwear additives, extreme pressure additives, oxidation inhibitors, corrosion inhibitors, detergents and dispersants, viscosity improvers, pour point depressants, and foam inhibitors. In some instances other additives like dyes and odor improvers are also added to the oils.

3.2.1 Wear and Friction Improvers

Additives, which improve wear and friction properties, are the most important additives used in lubricant formulations. In machinery, when two surfaces engage in metal-to-metal contact and begin to move relative to each other, hydrodynamic lubrication does not occur at the onset or in the case of severe stress; hence, the lubricating system runs in the boundary or mixed lubrication regime. In this case, wear and friction improvers are necessary in any metalworking fluid, engine oil, hydraulic fluid, or lubricating grease to prevent welding of the moving parts, reduce wear, and lower friction. Wear and friction improvers consist of chemical additives that can be divided into three groups: adsorption or boundary additives, antiwear (AW) additives, and extreme pressure (EP) additives. “Boundary” additives are friction and wear modifiers such as fatty acids that are added to oil to minimize the asperity contact. The term “antiwear” commonly refers to wear reduction at moderate loads and temperatures whereas the term “extreme pressure” refers to high loads and temperatures. All of these additives control the lubricating performance of the oil, making their usage very important. If oil lacks its lubricating ability, excessive wear and friction will result, causing damage to the moving parts with usually an increase in energy consumption.

3.2.2 Adsorption or Boundary Additives

Adsorption or boundary additives, also known as “friction modifiers,” control the adsorption type of lubrication and are often used to prevent stick-slip phenomena [61]. Adsorption additives are vital in boundary lubrication. The additives currently used are mostly fatty acids, esters, and amines of the fatty acids. These types of additives generally consist of a polar carboxyl group ($-\text{OH}$) at one end of the molecule that reacts with the contacting surfaces through an adsorption (adherence) mechanism to form a surface film as shown in Fig. 10.17. The molecules attach to the charged surface by the polar group to form a layer of molecules, which reduces friction and wear by having low interfacial shear stress and minimized asperity contact. The surface films or monolayers produced are only effective in boundary lubrication at relatively low temperatures and low loads.

The important characteristic of these additives is their molecular structure consisting of an unbranched chain of carbon atoms with sufficient length to ensure

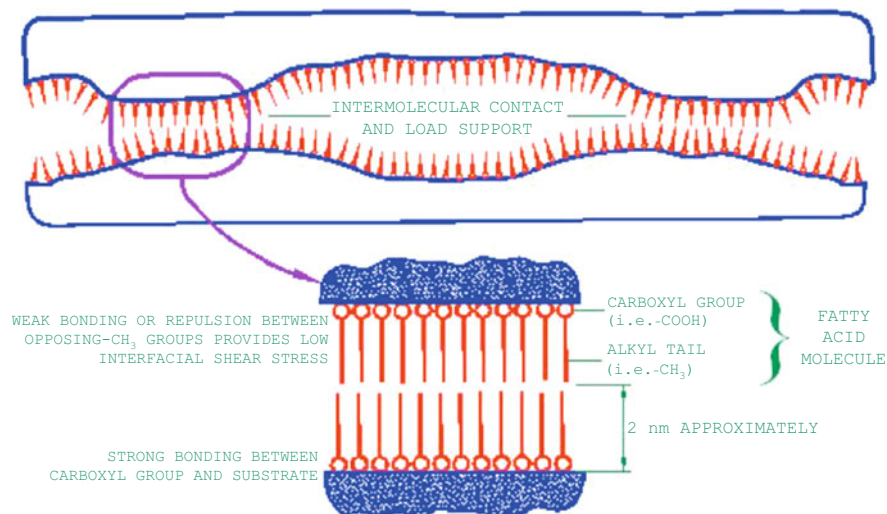


Fig. 10.17 Adsorbed molecules on a surface forming a monolayer

a stable and durable film that allows for the formation of close-packed monolayers. In natural oils, these molecules are generally unsaturated fatty acids have chain lengths of 18 or 16 carbon atoms consisting of oleic, linoleic, stearic, and palmitic acids [6]. In some specialized lubricants, unique additives are utilized which combine adsorption or boundary properties with corrosion protection or some other property for a specific application [61]. Depending on the type of additive used, adsorption additives are highly sensitive to the effects of temperature and can lose their effectiveness at temperatures between 80 and 150 °C. With increased temperature, these additives can reach a critical temperature threshold where the energy input to the surface is high enough to cause the additive to desorb rendering it inept. This critical temperature can be controlled by changing the additive's concentration, where a higher concentration results in a higher critical temperature. However, there is a downside to using a higher concentration as it also causes the lubricant to be more expensive; thus for specific applications, it is important to compare lubricant performance with cost.

3.2.3 Antiwear Additives

Antiwear (AW) additives are used when moderate stress is experienced between two surfaces in contact. In order to protect contacting surfaces at moderate loads and temperatures, antiwear additives are used. These additives function through chemisorption reactions with metal surfaces to form tribochemical reaction layers, which are protective surface layers that are much more durable than the adsorption monolayers. There are several different types of antiwear additives that are

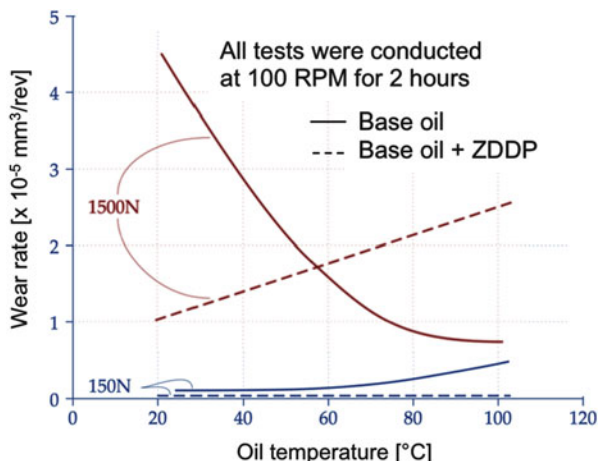
currently used in oil formulations typically in concentrations of 1–3 % by weight. The vast majority of antiwear additive are based on organic phosphorus compound such as diethylphosphate, dibutylphosphate, and tributylphosphate [2]. In engine oils, the most commonly used antiwear additive is zinc dialkyldithiophosphate (ZDDP), and in gas turbine oils, tricresylphosphate or other phosphate esters are used.

3.2.4 Extreme Pressure Additives

Extreme pressure (EP) compounds are designed to react with metal surfaces under extreme conditions of high load and temperature to prevent welding of the moving parts that would otherwise cause severe damage. Similar to antiwear additives, extreme pressure additives form layers on the metal surface by adsorption or chemisorption due to their polar molecules. Usually EP additives contain at least one aggressive nonmetal, such as sulfur, antimony, iodine, or chlorine molecules [40]. When hydrodynamic lubricating films are not present and a system runs under boundary lubrication, this can result in increased operating temperatures where exposed metal surfaces can become hot. The increase in temperature allows for EP additives to react with the warm metal surface forming tribochemical reaction layers composed of iron phosphides, sulfides, sulfates, oxides, and carbides that prevent direct contact between the sliding metals [2]. These reactions are designed to create protective low shear strength surface films that reduce friction and wear.

The use of EP additives results in a mild form of corrosion due to the reaction with the metallic surfaces; for this reason, the additive concentration is an important parameter. For example, if the EP additive concentration is too high, then excessive corrosion may occur resulting in increased wear. On the contrary, if the EP additive concentration is too low, then the surfaces may not be fully protected and failure could result. In some instances, EP additives contain sulfur or phosphorus, which is useful in suppressing oil oxidation; however, decomposition of these additives has been known to occur at even moderate temperatures. Therefore, EP additives containing sulfur or phosphorus are not recommended to extend the lubricant useful lifetime at high temperatures. There are several different types of EP additives currently used in oils, many of which are not considered toxic or carcinogenic. The most commonly used EP additives are dibenzyldisulphide, trichloroacetane and chlorinated paraffin, chlorinated wax, chlorinated paraffinic oils, and molybdenum disulfide [2, 10]. Dibenzyldisulphide is a mild EP additive with minimal reactivity and corrosion. Trichloroacetane and chlorinated paraffin are severe EP additives resulting in excessive corrosion, particularly in the presence of water. Molybdenum disulfide is a well-known solid lubricant that provides lubrication in extreme temperatures and contact pressures. It functions by depositing a solid lubricant layer on the contacting surfaces minimizing the potential surface contact. Molybdenum disulfide is noncorrosive, thus making it a popular additive despite being highly sensitive to humidity, which causes it to decompose.

Fig. 10.18 The influence of load and oil temperature on wear rate for base oil and base oil containing ZDDP at 150 N and 1,500 N



3.2.5 Zinc Dialkyldithiophosphate (ZDDP)

ZDDP is a well-known and commonly used antiwear additive primarily used in automotive lubricants. It was originally developed as an antioxidant and detergent, but was later revealed to exhibit superior antiwear properties and function as a mild EP additive [2]. By modifying the molecular structure, ZDDP derivatives can be produced such as zinc diphenyldithiophosphate; however many of these new compounds are less effective as ZDDP in reducing wear and friction. The presence of zinc in ZDDP plays an important role in minimizing the wear rate. The absence of zinc or replacing zinc with another metal substitute leads to an increase in wear rate. Experimental results indicate that ZDDP derivatives containing zinc alternatives have a higher wear rate in the following order: cadmium, zinc, nickel, iron, silver, lead, tin, antimony, and bismuth [62]. Cadmium offers the lowest wear rates but is too toxic for practical applications, making zinc the best alternative. Figure 10.18 shows the influence of load and temperature on wear rate for both base oil and a base oil containing ZDDP [63]. It can be seen that the wear rates increase with increasing temperature at a loads of 1,500 N for base oils containing ZDDP, but at low loads of 150 N, temperature has no effect on base oils containing ZDDP. For pure base oil, the trends are reversed. This figure demonstrates how ZDDP is most suitable for moderate loads with lower temperatures. For this reason, ZDDP is often used in valve trains of internal combustion engines to reduce friction and wear [64].

3.2.6 Tricresylphosphate

Tricresylphosphate (TCP) functions similar to ZDDP through chemisorption. It is a very effective antiwear additive that reduces wear and friction at temperatures up to approximately 200 °C. Beyond this temperature, TCP additives reach their critical

temperature threshold where the energy input to the surface causes the chemisorbed films to desorb. Desorption causes the additive to form less effective, much weaker, thick phosphate films with limited load-carrying capacity, resulting in high friction and wear [65, 66].

3.2.7 Antioxidants

Many of today's lubricants contain antioxidant additives to delay or minimize the onset of oxidation. Antioxidants or oxygen inhibitors are either natural or artificial additives that have the ability to suppress oxidation [67]. Natural antioxidants such as sulfur or nitrogen compounds can be naturally found in mineral oils. These compounds function by scavenging the radicals produced during the oxidation process. Phosphorus-based organic compounds found in extreme pressure and antiwear additives have been shown to function as artificial antioxidants [68]. Other common antioxidant additives are ZDDP, metal deactivators, and simple hydrocarbons such as phenol derivatives, amines, and organic phosphates [69–75]. Antioxidants are typically added to lubricants in quantities of approximately 1 % by weight.

Lubricants naturally oxidize or age during service. General characteristics of aged lubricants are discoloration and a burnt odor [76, 77]. Oxidation inhibitors prevent oxygen from attacking the base oils, thereby stabilizing the lubricant's viscosity and other properties [75, 78, 79]. This in turn prevents organic acid buildup that can cause corrosion. Antioxidants as their name suggests minimize the rate of oxidation occurring within a lubricant. This in turn improves the lifetime of the lubricant, resulting in significant decreases in friction and wear, which can lead to improved performance of machinery [69, 70, 74, 80, 81]. The main effect of oxidation is a gradual rise in the viscosity and acidity of a lubricant as shown in Fig. 10.19, which shows the variation of viscosity and acidity of a mineral oil as a function of oxidation time [82]. Both viscosity and acidity reach a critical oxidation time at approximately 120 h and 80 h, respectively, where their values increase tremendously. Beyond these durations, the oils have become extremely rancid through oxidation and should be replaced immediately.

A highly oxidized oil should be replaced promptly, since it can cause power losses due to increased viscous drag and difficulties in pumping of the oil through lubricant feed lines. It is important to realize that increases in viscosity are not only caused by oxidation but also by foreign contaminants entering the lubricant such as diesel soot. High levels of oil acidity can be problematic due to concerns of corrosion of vulnerable components such as lead, copper, and cadmium bearings.

3.2.8 Corrosion Control Additives

Corrosion control additives are classified as corrosion inhibitors and rust inhibitors. Corrosion inhibitors are used to protect nonferrous metal (i.e., copper, aluminum, tin, cadmium) surfaces against potential corrosive agents in the lubricant [83].

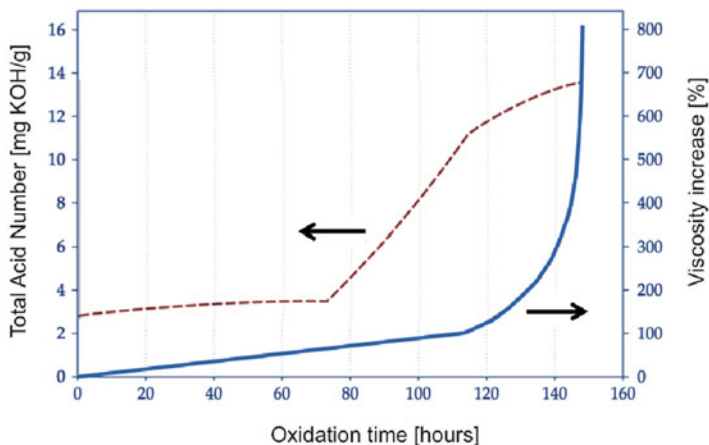
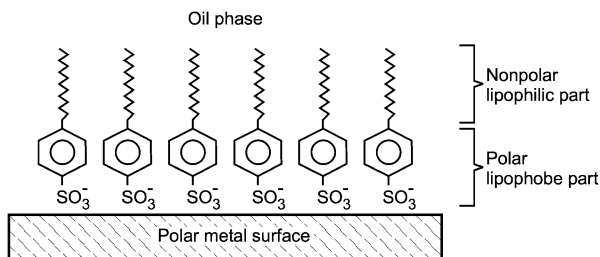


Fig. 10.19 The effect of oxidation times on viscosity and acidity for a typical base oil [40, 82]

Fig. 10.20 Function of corrosion control additives on a polar metal surface [2]



Rust inhibitors are used to protect ferrous metal (i.e., steel, iron, and iron alloys) surfaces against corrosion. The mechanism behind corrosion control additives is quite simple. Anticorrosion additives are molecules with long alkyl chains and polar groups that can be adsorbed on the metal surface forming densely packed, hydrophobic layers as shown in Fig. 10.20 [2]. The adsorption mechanism is based on either physical or chemical interaction of the polar anticorrosion additive with the metal surface [84]. However, due to the relatively high surface activity, anticorrosion additives compete with other polar additives such as EP and AW additives for the metal surface and can therefore reduce their efficiency. For this reason, it is important to use highly efficient and highly polar anticorrosion additives.

Corrosion Inhibitors

Corrosion inhibitors are used to protect the nonferrous surfaces of bearings, seals, and other vulnerable components against corrosive attacks by various additives. Highly corrosive additives generally contain sulfur, phosphorus, iodine, chlorine,

and oxidation by-products [84]. Corrosion inhibitors can be classified into three categories: film-forming compounds, complex-forming chelating agents, and sulfur scavengers [2]. The function of film-forming corrosion inhibitors consists of building protective layers on the nonferrous metal surface, thus preventing the surface reaction of metal ions that would work as prooxidants (chemicals that induce oxidation). Complex-forming chelating agents are able to build oil-soluble molecules with significantly reduced catalytic activity that have minimal influence on the nonferrous metal ions that would ordinarily oxidize the lubricant. Sulfur scavengers are corrosion inhibitors that are able to catch corrosive sulfur molecules by integrating sulfur into their molecular structure.

Corrosion attacks on nonferrous metallic parts can occur through a variety of mechanisms such as the presence of corrosive contaminants, oxidation by-products, and water present in the lubricant. Additionally, high-temperature effects can also instigate corrosion. Through the three types of corrosion inhibitors, many of the pro-corrosion products can be neutralized before they cause any damage to the operating parts of the machinery or to the lubricant. Commonly used corrosion inhibitors that operate through film-forming compound are benzotriazole, tolyltriazole, ZDDP, and trialkylphosphites. Complex-forming chelating agents can consist of *N,N*-disalicylidenealkylendiamines and sulfur scavengers can consist of 2,5-dimercapto-1,3,4-thiadiazole where sulfur is captured in the alkyl-sulfur-thiadiazol bonds.

Rust Inhibitors

Rust inhibitors are used to protect ferrous metal surfaces. Rust, the visible trace of corrosion, is often generated by the presence of dissolved oxygen or water in a lubricant. These contaminants in the lubricant can cause electrolytic attacks on the metal surfaces. These attacks can become severe and prevalent with increases in temperature. Rust inhibitors usually consist of long chain alkylarylsulfonic acids that can be neutralized with lyes. These compounds are typically known as petroleum sulfonates or mahogany sulfonates which are by-products from the production of white oils with oleum [2]. Rust inhibitors function by attaching themselves to the surface (see Fig. 10.21), severely reducing the mobility of water and thus minimizing the amount of corrosion that can occur [84]. Metal sulfonates, amine succinates, and other polar organic acids are additives used to control the corrosion of ferrous metals. The calcium and barium sulfonates are suitable for more severe conditions of corrosion, whereas the succinates and the other organic acids are used when corrosion is moderate. Low molecular weight sodium sulfonates have anticorrosion properties in water-based metalworking fluids, engine oils, and rust preventatives. High molecular weight sulfonates distinguish themselves as highly efficient corrosion inhibitors especially when used for divalent cations like calcium, magnesium, and barium. The use of the barium compounds has begun to decrease due to toxicological and environmental concerns.

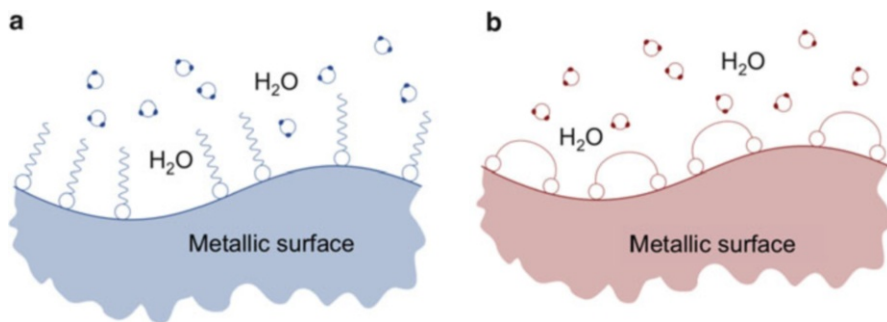


Fig. 10.21 Function of rust inhibitors on a metallic surface: (a) rust inhibitors as they first attach to the surface and (b) rust inhibitors after forming a protective layer

3.2.9 Detergents and Dispersants

Engine oils and other lubricants are repeatedly exposed to other functional fluids through leakage, combustion by-products, and other contaminants throughout their lifetime. Water adversely affects many lubricants because it aids in oxidation and can form an oil–water emulsion. When sulfur is present in the fuel during the combustion process, this causes the formation of sulfurous or sulfuric acid. These sulfur-based compounds can then be dissolved by water resulting in corrosion of the engine. Lubricants can face a multitude of contaminants such as wear debris, unburned fuel, by-products of the base oil, corrosion products, dust from the atmosphere, water, and other lubricants [40]. These contaminants deplete the lubricant by reducing its lubricating capacity and making the lubricant more corrosive, thus rendering it ineffective. The agglomeration of particles in engine oils, for instance, can cause oil supply pipelines or filters to become clogged and blocked, resulting in a very destructive situation for an engine. To minimize and help prevent these adverse effects, additives known as “detergents” and “dispersants” are used [85]. Detergents and dispersants are materials that chemically react with oxidation products and enable the oil to suspend dirt particles and debris, which can be removed through filtration [1]. They also help to neutralize acid buildup. The primary functions of these additives are to (1) neutralize any acids formed during the burning of fuel, (2) prevent varnish formation and corrosion on the operating parts of the engine, and (3) prevent the flocculation or agglomeration of particles and carbon deposits which may clog the oil flow path [40]. Table 10.2 presents some of the properties of commonly used dispersants.

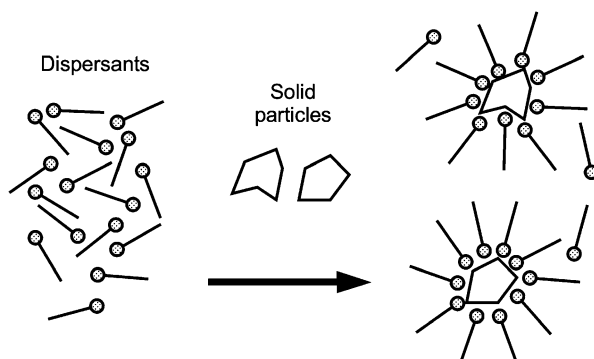
Detergents and dispersant (DD) additives usually consist of molecules having a large oleophilic hydrocarbon tail and a polar hydrophilic head. The tail section acts as a solubilizer in the base oil, while the head is attracted to contaminants in the lubricant. DD additives work by having multiple dispersant molecules attach to a single solid contaminant forming micelles whereby the nonpolar tail prevents

Table 10.2 Properties of commonly used dispersants [40]

Dispersant	Lacquer and varnish prevention	Acid neutralization	Coagulation prevention
Dispersants and over-based dispersants			
Calcium, barium, or zinc salts of sulfonic, phenol, or salicylic acid	Good, especially at high temperatures	Good	Fair
Carboxylic and salicylic type additives	Good	Fair	Poor (they can cause coagulation)
Mild dispersants (i.e., ashless compounds)			
Low-weight polymers of methacrylate esters or long chain alcohols	Fair ^a	Weak	Good
Polar vinyl compounds	Fair ^a	Weak	Good
Amines (e.g., triethylene amine)	Fair ^a	Fair	Good
Saturated succinimide	Fair ^a	Weak	Good

^aThese additives are only effective at low temperature

Fig. 10.22 Function of dispersants undergoing the peptization process [2]



adhesion of the polar soot particle on the metal surfaces as well as the agglomeration into larger particles as illustrated in Fig. 10.22 [2]. The process of DD additives attaching to colloid particles in the oil is known as peptization.

3.2.10 Viscosity Improvers

Additives that prevent the decrease in oil viscosity with temperature are known as viscosity index improvers. Viscosity index improvers are additives that consist of high molecular weight polymers, which are dissolved in the oil [86]. These molecules are chain-like molecules whose solubility depends on chain length, structure, and chemical composition [87]. Generally, the base oil solubility of these polymer chains deteriorates as the temperature falls and improves with increasing temperature so as to maintain the viscosity of the base oil. Due to the poor solubility at low temperatures, the chain-like viscosity improver molecules

Table 10.3 Types of polymeric viscosity modifiers and their most widely used applications [2]

VM type	Description	Main applications
OCP	Olefin copolymers	Engine and hydraulic oils
PAMA	Polyalkyl(meth)acrylates	Gear and hydraulic oils
PIB	Polyisobutylene	Gear oils, raw material for ashless dispersants
SIP	Hydrogenated styrene–isoprene copolymers	Engine oils
SBR	Hydrogenated styrene–butadiene	Engine oils

form coils of small volume, and as the temperature is increased, these molecules expand and unravel, resulting in an increasing beneficial effect on high-temperature viscosity [88]. The increase in viscosity and viscosity index depends on the polymer type, the molecular weight, and the concentration of viscosity improvers in the lubricant [89]. Depending on the projected application, molecular weights of the viscosity improver additives can range significantly. For example, viscosity index improvers such as polyalkylmethacrylates (PAMAs) can have molecular weights between 15,000 and 250,000 g/mol and polyisobutylene (PIBs) can have molecular weights between 2,000 and 5,000 g/mol. Some of the more commonly used viscosity improvers have found favor for certain applications. Table 10.3 shows the most important viscosity modifiers and their main applications. It can be seen that many viscosity modifiers find their use in engines followed by hydraulic and gear oils. Concentrations of viscosity improver additives are usually between 3 and 30 % mass fraction. As a result of their high molecular weight, viscosity modifiers are always dissolved in the base oil. Figure 10.23 describes various viscosity index improvers by polymer type, chain structure, and monomer makeup [2].

3.2.11 Pour Point Depressants

Pour point depressants (PPD) are similar to viscosity improvers. They help to keep the oil thin at low temperatures by preventing the generation of wax crystals. The major difference between the polymers used in viscosity improvers and PPD is their application concentration and the selection of monomer compounds [2, 90]. The molecular weight and thickening efficiency of PPDs are minor compared to that of viscosity improvers with mass fraction percentages that vary from 0.1 % to a




Polymer type	General structure	Chemical type
Homopolymer	A-A-A-A-A-A-A-A-A	PIB, PAO
Random	A-B-A-B-B-A-B-A-A-B	PMA, OCP
Alternating	A-B-A-B-A-B-A-B-A-B	MSC (Maleate Styrene Copolymer)
Random Block	A-A-A-B-B-A-A-B-B-B	SBR, SIP, OCP
Biblock (A-B block)	A-A-A-A-A-B-B-B-B-B 	SIP
Tapered Block		SBR
Graft copolymers	A-B-A-B-B-A-B-A-A-B X X	OCP-g-PMA or SBR-g-PMA
Star polymers		SBR, OCP

Fig. 10.23 Viscosity index improvers, chain structures, and monomer makeup [2]

maximum of 2 %. Generally, additional thickening effects occur, but are usually limited by solubility thresholds within the base oils.

3.2.12 Foam Inhibitors

The foaming of lubricants is a very undesirable effect that can cause increased oxidation by the intensive mixture with air, cavitation damage, and insufficient oil transport in circulatory lubrication systems that can cause lubrication starvation. Despite the negative mechanical influences, the foaming tendency is dependent on the lubricant itself and is influenced by the surface tension of the base oil and by the presence of surface-active substances such as detergents, corrosion inhibitors, and other ionic compounds. When describing the characteristics of lubricant foaming, there are two types: surface foam and the inner foam.

Surface foam refers to the foam at the surface of the lubricant that is usually visibly noticeable. This foam can be controlled by foam-inhibiting additives. Effective inhibitors possess a lower surface tension compared to the lubricant base oil, which are usually not soluble in the base oil, and therefore have to be finely dispersed in order to be sufficiently stable even after long-term storage or use. The particle size of the dispersed foam inhibitors for surface foam should be smaller than 100 μm . For enhanced performance, the particle size should be smaller than 10 μm [91].

The less innocuous inner foam refers to finely dispersed air bubbles within the lubricant that can form stable dispersions. Unfortunately, the vast majority of foam inhibitors used to control the surface foam tend to stabilize the inner foam dispersion. This makes the problem of removing the inner foam a challenge. On the

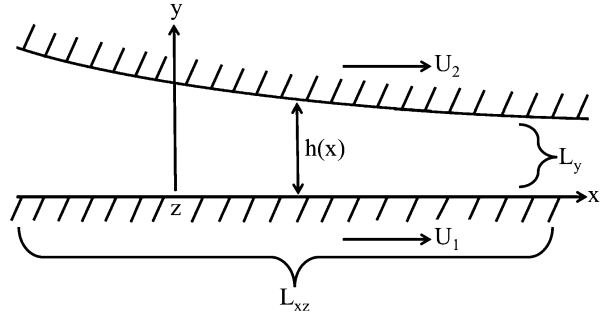
contrary, many of the additives used in lubricants have a negative influence on the inner foam stability thereby inadvertently minimizing the presence of the air bubbles [2]. Additives cannot improve lubricants that need excellent air release properties. Lubricants that need excellent air release properties operate as turbine oils which have to be formulated using specially selected base oils and additives. Air is not only present in the lubricants in the form of dispersed air bubbles as in surface and inner foam, but air can also be physically dissolved in the oil up to about 9 % volume fraction of the base oil. This type of air can cause severe problems like cavitation and cannot be controlled by additives.

The purpose of foam inhibitors is to destabilize foam generated during the lubricants operating cycle. Usually long chain silicone polymers are used in very small quantities of about 0.05–0.5 % by weight. Liquid silicones, such as linear and cyclic polydimethylsiloxanes, are very efficient antifoam additives at low concentrations. Silicone foam inhibitors are pre-dissolved in aromatic solvents to ensure stable dispersions when in use. When compared to other additives, silicone foam inhibitors have the disadvantage of settling out of the lubricant due to their insolubility and their strong affinity to polar metal surfaces. Recently, silicone-free foam inhibitors have been developed. These additives are being used extensively in metalworking processes as cutting fluids as well as hydraulic fluids. Silicone-free foam inhibitors consist of poly(ethylene glycols) (polyethers), polymethacrylates, tributylphosphate, and miscellaneous organic copolymers [2].

4 Fundamental Equations

This section discusses the basic equations that govern the application and science of lubricants and lubrication. In particular incompressible fluids will be assessed. The equations that describe lubrication with continuous fluid films are derived from the fundamental equations of fluid dynamics through specified geometry of the typical lubricant film as illustrated in Fig. 10.24 [7]. In the presented examples, lubricant films are described by their small thickness relative to their lateral size described as the “plane” of the film, as they would be in true application. In the derivations, L_y and L_{xz} denote the characteristic dimensions across the film thickness and the plane of the film, respectively, as indicated in Fig. 10.24. Typical industrial bearings experiencing liquid lubrication are characterized by $(L_y/L_{xz}) = O(10^{-3})$. This fact alone, and the assumption of laminar flow, permits the combination of the equations of motion and continuity into a single equation in lubricant pressure, revealing the infamous Reynolds equation. Much of the theory of lubrication is concerned with the solution of the Reynolds equation and in some instances the added solution of the equation of energy, under specified lubricating conditions. When surfaces are deformable, for example, in human and animal joints or rolling contact bearings, the equations of elasticity and the pressure dependence of lubricant viscosity must be included in the solution of a lubrication problem.

Fig. 10.24 Schematic of lubricant film



4.1 Equations of Motion

The basic equations that govern fluid flow of a lubricant begin with the Navier–Stokes equation [92], for an incompressible, constant viscosity fluid having a density ρ , velocity v , pressure p , viscosity μ , and body force f described in (10.8) [93]:

$$\rho \left[\frac{\partial v}{\partial t} + (v \cdot \nabla v) \right] = -\nabla p + \mu \nabla^2 v + \rho f \tag{10.8}$$

The corresponding equation of continuity for a constant density, incompressible fluid is as follows:

$$\text{div } v = 0 \tag{10.9}$$

These equations can be nondimensionalized by normalizing the orthogonal Cartesian coordinates (x,y,z) with the corresponding length scales and the velocities with the appropriate velocity scales, U^* in the x – z plane and V^* perpendicular to it [7]:

$$\text{Normalized } x, y, z \text{ terms : } x = L_{xz}\bar{x}, y = L_y\bar{y}, \text{ and } z = L_{xz}\bar{z} \tag{10.10a}$$

$$\text{Normalized velocity terms : } u = U^*\bar{u}, v = V^*\bar{v}, \text{ and } w = U^*\bar{w} \tag{10.10b}$$

It should be noted that the characteristic velocity in the y -direction V^* cannot be chosen independent of U^* , as the equation of continuity must always be satisfied. Substitution of (10.10a and 10.10b) into (10.9) yields

$$\frac{\partial \bar{u}}{\partial \bar{x}} + \frac{V^*L_{xz}}{U^*L_y} \frac{\partial \bar{v}}{\partial \bar{y}} + \frac{\partial \bar{w}}{\partial \bar{z}} = 0 \tag{10.11}$$

revealing that the terms of the equation of continuity are satisfied provided that

$$\frac{V^*L_{xz}}{U^*L_y} = O(1) \text{ or } V^* = \left(\frac{L_y}{L_{xz}} \right) U^* \tag{10.12}$$

From (10.12), the velocity scale in the y-direction has been established. The next step is to nondimensionalize the pressure and time terms [7]:

$$\text{Normalized pressure term : } \bar{p} = r_e \frac{P}{\rho U^{*2}} \quad (10.13a)$$

$$\text{Normalized time term : } \bar{t} = \Omega t \quad (10.13b)$$

In (10.13a), the reduced Reynolds number, r_e , and in (10.13b), the nondimensional frequency, $\bar{\Omega}$, are defined as

$$\text{Reduced Reynolds number : } r_e = \left(\frac{L_y}{L_{xz}} \right) \frac{L_y U^*}{\nu} \quad (10.13c)$$

$$\text{Nondimensional frequency : } \bar{\Omega} = \left(\frac{L_y}{L_{xz}} \right) \frac{L_y (L_{xz} \Omega)}{\nu} \quad (10.13d)$$

In (10.13b) and in (10.13d), Ω is the characteristic frequency of the system. For example, in journal bearings, the characteristic frequency is related to the rotational velocity of the journal. Taking the shaft surface velocity as the characteristic velocity, $U^* = R\omega$, and the journal radius as the characteristic length in the plane of the bearing, then $L_{xz} = R$, resulting in $r_e \approx \bar{\Omega}$. Making use of this approximation and substituting (10.10a), (10.10b) and (10.13a), (10.13b) into (10.8), the equations of motion and continuity can be rewritten in terms of the normalized quantities as follows:

$$r_e \left(\frac{\partial \bar{u}}{\partial \bar{t}} + \bar{u} \frac{\partial \bar{u}}{\partial \bar{x}} + \bar{v} \frac{\partial \bar{u}}{\partial \bar{y}} + \bar{w} \frac{\partial \bar{u}}{\partial \bar{z}} \right) = - \frac{\partial \bar{p}}{\partial \bar{x}} + \frac{\partial^2 \bar{u}}{\partial \bar{y}^2} + \left(\frac{L_y}{L_{xz}} \right)^2 \left(\frac{\partial^2 \bar{u}}{\partial \bar{x}^2} + \frac{\partial^2 \bar{u}}{\partial \bar{z}^2} \right) \quad (10.14a)$$

$$\left(\frac{L_y}{L_{xz}} \right)^2 \left[r_e \left(\frac{\partial \bar{v}}{\partial \bar{t}} + \bar{u} \frac{\partial \bar{v}}{\partial \bar{x}} + \bar{v} \frac{\partial \bar{v}}{\partial \bar{y}} + \bar{w} \frac{\partial \bar{v}}{\partial \bar{z}} \right) - \frac{\partial^2 \bar{v}}{\partial \bar{y}^2} - \left(\frac{L_y}{L_{xz}} \right)^2 \left(\frac{\partial^2 \bar{v}}{\partial \bar{x}^2} + \frac{\partial^2 \bar{v}}{\partial \bar{z}^2} \right) \right] = - \frac{\partial \bar{p}}{\partial \bar{y}} \quad (10.14b)$$

$$r_e \left(\frac{\partial \bar{w}}{\partial \bar{t}} + \bar{u} \frac{\partial \bar{w}}{\partial \bar{x}} + \bar{v} \frac{\partial \bar{w}}{\partial \bar{y}} + \bar{w} \frac{\partial \bar{w}}{\partial \bar{z}} \right) = - \frac{\partial \bar{p}}{\partial \bar{z}} + \frac{\partial^2 \bar{w}}{\partial \bar{y}^2} + \left(\frac{L_y}{L_{xz}} \right)^2 \left(\frac{\partial^2 \bar{w}}{\partial \bar{x}^2} + \frac{\partial^2 \bar{w}}{\partial \bar{z}^2} \right) \quad (10.14c)$$

$$\frac{\partial \bar{u}}{\partial \bar{x}} + \frac{\partial \bar{v}}{\partial \bar{y}} + \frac{\partial \bar{w}}{\partial \bar{z}} = 0 \quad (10.15)$$

4.2 Lubrication Approximations of Bearings

The normalization of (10.10a), (10.10b) and (10.13a), (10.13b) illustrates that each of the variable terms in 10.14a, 10.14b, 10.14c, and (10.15) is of the same order, e.g., $O(1)$. However, this indicates that the relative importance of the variable terms

is affected only by the magnitude of the dimensionless parameters $\left(\frac{L_y}{L_{xz}}\right)$ and r_e . In true applications, lubricant films are significantly thin relative to their lateral size. In a liquid lubricated bearing the $\left(\frac{L_y}{L_{xz}}\right)$ ratio can be on the order of 10^{-3} and for gas bearings a film thickness of $h \approx 2.5 \mu\text{m}$ is not unusual. The lubrication approximation of the Reynolds equation is established with the assumption that $\left(\frac{L_y}{L_{xz}}\right) \rightarrow 0$ and that $r_e \rightarrow 0$. Under these conditions, (10.14a, 10.14b, and 10.14c) indicate that

$$\frac{\partial \bar{p}}{\partial \bar{y}} = O(10^{-6}) \quad \text{and that} \quad \frac{\partial \bar{p}}{\partial \bar{x}} \approx \frac{\partial \bar{p}}{\partial \bar{z}} = O(1) \quad (10.16)$$

yielding new versions of (10.14a, 10.14b, and 10.14c) and (10.15), written in terms of the fundamental variables for a bearing

$$\frac{\partial p}{\partial x} = \mu \frac{\partial^2 u}{\partial y^2}, \quad \frac{\partial p}{\partial y} = 0, \quad \text{and} \quad \frac{\partial p}{\partial z} = \mu \frac{\partial^2 w}{\partial y^2} \quad (10.17)$$

$$\frac{\partial u}{\partial x} + \frac{\partial v}{\partial y} + \frac{\partial w}{\partial z} = 0 \quad (10.18)$$

4.3 The Reynolds Equation

Derivation of the Reynolds equation begins by first examining (10.17). Here, the pressure gradient in the y-direction, i.e., across the film, is zero, leaving only the pressure gradients in the x- and z-directions to be integrated to obtain

$$u = \frac{1}{2\mu} \frac{\partial p}{\partial x} y^2 A y + B \quad (10.19a)$$

$$w = \frac{1}{2\mu} \frac{\partial p}{\partial x} y^2 C y + D \quad (10.19b)$$

In (10.12), the integration constants A, B, C, and D can be solved using the boundary conditions for velocity from Fig. 10.24, where

$$u = U_1 \quad \text{and} \quad w = 0 \quad \text{at} \quad y = 0 \quad (10.20a)$$

$$u = U_2, \quad \text{and} \quad w = 0 \quad \text{at} \quad y = h \quad (10.20b)$$

Integration of (10.19a and 10.19b) with the conditions in (10.20a and 10.20b) yields the velocity components in the x- and z-planes of the bearing

$$u = \frac{1}{2\mu} \frac{\partial p}{\partial x} (y^2 - yh) + \left(1 - \frac{y}{h}\right) U_1 + \frac{y}{h} U_2 \quad (10.21a)$$

$$w = \frac{1}{2\mu} \frac{\partial p}{\partial x} (y^2 - yh) \quad (10.21b)$$

Equation (10.21a and 10.21b) reveals a pressure distribution that is not subjective. In fact, this pressure distribution must satisfy the equation of continuity in a similar manner to the normalized velocity terms previously demonstrated. For this, (10.21a and 10.21b) is substituted into (10.18). After performing the differentiation and integration, this calculation returns:

$$\begin{aligned} [v]_0^{h(x,t)} = & -\frac{\partial}{\partial x} \left[\frac{1}{2\mu} \frac{\partial p}{\partial x} \int_0^{h(x,t)} (y^2 - yh) dy \right] - \frac{\partial}{\partial z} \left[\frac{1}{2\mu} \frac{\partial p}{\partial z} \int_0^{h(x,t)} (y^2 - yh) dy \right] \\ & - \frac{\partial}{\partial x} \int_0^{h(x,t)} \left[\left(1 - \frac{y}{h}\right) U_1 + \frac{y}{h} U_2 \right] dy + U_2 \frac{\partial h}{\partial x} \end{aligned} \quad (10.22)$$

Realizing that

$$[v]_0^{h(x,t)} = -(V_1 - V_2) = \frac{dh}{dt} \quad (10.23)$$

where V_1 and V_2 are the normal or approach velocities also known as entraining velocities in bearing applications, the generalized Reynolds equation that governs the pressure distribution in a lubricant film can be determined as shown in (10.24) [7, 20, 92]:

$$\begin{aligned} \frac{\partial}{\partial x} \left(\frac{h^3}{\mu} \frac{\partial p}{\partial x} \right) + \frac{\partial}{\partial z} \left(\frac{h^3}{\mu} \frac{\partial p}{\partial z} \right) = & 6(U_1 - U_2) \frac{\partial h}{\partial x} + 6h \frac{\partial(U_1 + U_2)}{\partial x} \\ & + 12(V_2 - V_1) \end{aligned} \quad (10.24)$$

Now, to simulate a conventional thrust bearing where the relative motion between the surfaces in contact is pure translation and then by assuming that $\frac{\partial(U_1+U_2)}{\partial x} = 0$, (10.24) would simplify to

$$\frac{\partial}{\partial x} \left(\frac{h^3}{\mu} \frac{\partial p}{\partial x} \right) + \frac{\partial}{\partial z} \left(\frac{h^3}{\mu} \frac{\partial p}{\partial z} \right) = 6(U_1 - U_2) \frac{\partial h}{\partial x} + 12(V_2 - V_1) \quad (10.25)$$

In another example, to simulate a traditional journal bearing where relative motion of the surfaces in contact is not parallel, a component of the rotational velocity would augment the relative motion in the tangential direction. This would cause (10.24) to simplify to

$$\frac{\partial}{\partial x} \left(\frac{h^3}{\mu} \frac{\partial p}{\partial x} \right) + \frac{\partial}{\partial z} \left(\frac{h^3}{\mu} \frac{\partial p}{\partial z} \right) = 6(U_1 + U_2) \frac{\partial h}{\partial x} + 12(V_2 - V_1) \quad (10.26)$$

In these two examples, thrust bearings and the journal bearings differ by the velocities contributing to the pressure generated. In thrust bearings, the difference in tangential velocities creates pressure, whereas in journal bearings the sum of the tangential velocities creates pressure [23]. With this notation, in a journal bearing, if the journal and the bearing rotate in opposing directions with similar velocities, there would be no pressure generated. Furthermore, in both thrust and journal bearings, positive pressures are generated only when the fluid film is convergent in both space and time as indicated by (10.27):

$$U_0 \frac{\partial h}{\partial x} < 0, \frac{\partial h}{\partial t} < 0 \quad (10.27)$$

The Reynolds equation derived in (10.17) provides a relationship between the film thickness and the fluid pressure in a fluid-film liquid lubrication system. This equation forms the foundation of fluid-film lubrication theory and establishes the relationship between geometry of the surfaces, relative sliding velocity, the property of the fluid, and the magnitude of the normal load a bearing can theoretically support [94]. The first two terms on the left side of (10.24) represent the Poiseuille flow, the first and second term on the right side represent Couette flow, and the last term on the right side signifies the squeeze flow. Currently, there is no closed form solution to the Reynolds equation. Many solutions utilize boundary conditions and simplification techniques to solve this numerically.

5 Conclusion

The advancements in lubricants have become an integral part of the development of machinery and various corresponding technologies. Lubricants and lubrication techniques are linked to numerous fields of expertise, and without this interdisciplinary aspect, the progression of lubricants and many applications may have failed to achieve success. Lubrication is a vital segment of tribology with implications affecting world energy usage, system reliability, application feasibility, the environment, and financial stability. With more than 10,000 different types of lubricants and an abundance of additives, selecting the appropriate lubricant for a particular application is not obvious. Lubrication engineers must have an understanding of the performance demands of the application and the composition of the lubricating materials before selecting a lubricant that has appropriate physicochemical properties that are not detrimental to the system.

References

1. Bannister KE (1996) Lubrication for industry. Industrial Press, New York
2. Mang T, Dresel W (2006) Lubricants and lubrication. Wiley-VCH; John Wiley [distributor], Weinheim; Chichester
3. United States Central Intelligence Agency (2008) The CIA world fact book. New York, NY: Skyhorse Publishing
4. Bartz WJ, International Colloquium Tribology, and Technische Akademie Esslinge (2006) Automotive and industrial lubrication. 15th International Colloquium Tribology, TAE, Ostfildern, Jan 2006
5. Lingg G, Gosalia A (2008) The dynamics of the global lubricants industry—markets, competitors & trends. Tech Akad Esslingen Int Tribol Colloq Proc, p. 16
6. Reeves CJ, Menezes PL, Jen T-C, Lovell MR (2012) Evaluating the tribological performance of green liquid lubricants and powder additive based green liquid lubricants. Proceedings of 2012 STLE Annual Meeting & Exhibition, STLE
7. Bhushan B (2001) Modern tribology handbook. CRC, Boca Raton, FL
8. Miyoshi K (2001) Solid lubrication fundamentals and applications. Marcel Dekker, New York
9. Winer W (1967) Molybdenum disulfide as a lubricant: a review of the fundamental knowledge. Wear 10(6):422–452
10. Hu X (2005) On the size effect of molybdenum disulfide particles on tribological performance. Ind Lubr Tribol 57(6):255–259
11. Jamison WE (1972) Structure and bonding effects on the lubricating properties of crystalline solids. ASLE Trans 15(4):296–305
12. Petterson MB, Calabrese SJ, Stupp B, Wear Sciences Inc. Arnold MD (1982) Lubrication with naturally occurring double oxide films
13. Peterson MB, Li S, Murray SF (1997) Wear-resisting oxide films for 900C. J Mater Sci Technol 13(2):99–106
14. Scharf TW, Rajendran A, Banerjee R, Sequeda F (2009) Growth, structure and friction behavior of titanium doped tungsten disulphide (Ti-WS₂) nanocomposite thin films. Thin Solid Films 517:5666–5675
15. Blanchet TA, Kennedy FE (1992) Sliding wear mechanism of polytetrafluoroethylene (PTFE) and PTFE composites. Wear 153(1):229–243
16. Lovell MR, Menezes PL, Kabir MA, Higgs CF (2010) Influence of boric acid additive size on green lubricant performance. Philos Trans A Math Phys Eng Sci 368(1929):4851–4868
17. Menezes PL, Lovell MR, Kabir MA, Higgs CF III, Rohatgi PK (2012) Green lubricants: role of additive size. In: Nosonovsky M, Bhushan B (eds) Green tribology. Springer, Berlin, pp 265–286
18. Denton RM, Fang Z (1995) Rock bit grease composition. U.S. Pat. No. 5589443
19. Erdemir A, (1995) Lubrication from mixture of boric acid with oils and greases. U.S. Pat. No. 5431830A
20. Bhushan B (1999) Principles and applications of tribology. Wiley, New York
21. Czichos H (1978) Tribology a systems approach to the science and technology of friction, lubrication, and wear. Elsevier, Amsterdam
22. Czichos H (1992) Basic tribological parameters, friction, lubrication and wear technology. ASTM Handb 18:474
23. Bhushan B (2002) Introduction to tribology. Wiley, New York
24. Willing A (2001) Lubricants based on renewable resources—an environmentally compatible alternative to mineral oil products. Chemosphere 43(1):89–98
25. Fox NJ, Tyrer B, Stachowiak GW (2004) Boundary lubrication performance of free fatty acids in sunflower oil. Tribol Lett 16(4):275–281
26. Fischer TE, Bhattacharya S, Salher R, Lauer JL, Ahn YJ (1988) Lubrication by a smectic liquid crystal. Tribol Trans 31(4):442–448

27. Hamrock BJ, Dowson D, Lewis Research Center, United States. National Aeronautics and Space Administration, Scientific and Technical Information Office (1978) Minimum film thickness in elliptical contacts for different regimes of fluid-film lubrication. National Aeronautics and Space Administration, Scientific and Technical Information Office; For sale by the National Technical Information Service [Washington]; Springfield, VA
28. Hamrock BJ, Dowson D (1981) Ball bearing lubrication: the elastohydrodynamics of elliptical contacts. Wiley, New York
29. Hamrock BJ, Dowson D, United States. National Aeronautics and Space Administration, Scientific and Technical Information Office, Lewis Research Center, and University of Leeds (1978) Elastohydrodynamic lubrication of elliptical contacts for materials of low elastic modulus. National Aeronautics and Space Administration; For sale by the National Technical Information Service [Washington]; Springfield, VA
30. Hamrock BJ, Dowson D, Lewis Research Center, United States. National Aeronautics and Space Administration (1976) Isothermal elastohydrodynamic lubrication of point contacts: IV, starvation results. National Aeronautics and Space Administration; For sale by the National Technical Information Service [Washington]; Springfield, VA
31. Menezes PL, Kishore, Kailas SV (2006) Effect of roughness parameter and grinding angle on coefficient of friction when sliding of Al-Mg alloy over EN8 steel. *ASME J Tribol* 128(4):697–704
32. Pradeep KC, Menezes PL, Kailas SV (2008) Role of surface texture on friction under boundary lubricated conditions. *Tribol Online* 3(1):12–18
33. Menezes PL, Kishore, Kailas SV (2009) Study of friction and transfer layer formation in copper-steel tribo-system: role of surface texture and roughness parameters. *Tribol Trans* 52(5):611–622
34. Menezes PL, Kishore, Kailas SV (2009) Influence of roughness parameters and surface texture on friction during sliding of pure lead over 080 M40 steel. *Int J Adv Manuf Technol* 43(7–8):731–743
35. Menezes PL, Kishore, Kailas SV (2008) On the effect of surface texture on friction and transfer layer formation—a study using Al and steel pair. *Wear* 265(11–12):1655–1669
36. Menezes PL, Kishore, Kailas SV, Lovell M (2009) Studies on friction and formation of transfer layer in HCP metals. *J Tribol* 131(3):031604
37. Menezes PL, Kishore, Kailas SV (2009) Influence of surface texture and roughness parameters on friction and transfer layer formation during sliding of aluminium pin on steel plate. *Wear* 267(9–10):1534–1549
38. Menezes PL, Kishore, Kailas SV, Lovell M (2011) Response of materials during sliding on various surface textures. *J Mater Eng Perform* 20(8):1438–1446
39. Moore CT, Menezes PL, Lovell MR, Beschorner KE (2012) Analysis of shoe friction during sliding against floor material: role of fluid contaminant. *J Tribol* 134(4):041104
40. Stachowiak GW, Batchelor AW (2005) Engineering tribology. Butterworth-Heinemann, Dordrecht, Netherlands
41. Booser ER (1984) CRC handbook of lubrication. Theory and practice of tribology, vol II, Theory and design. CRC, Boca Raton, FL
42. Jones MH, Scott D (1983) Industrial tribology: the practical aspects of friction, lubrication, and wear. Elsevier Scientific Pub. Co.; Distributors for the U.S. and Canada, Elsevier Science Pub. Co., Amsterdam; New York; New York
43. Reeves CJ, Jen T-C, Garvey S, Dietz M, Menezes PL, Lovell MR (2012) Tribological performance of environmentally friendly ionic liquid lubricants. American Society of Mechanical Engineers, Tribology Division, TRIB. p 355–357
44. Reeves CJ, Jen T-C, Garvey S, Dietz M, Menezes PL, Lovell MR (2013) The effect of anion-cation moiety manipulation to characterize the tribological performance of environmentally benign room temperature ionic liquid lubricants. Proc. 2013 STLE annual meeting & exhibition (STLE 2013) Detroit, USA
45. Klaus EE, Ugwuzor DI, Naidu SK, Duda JL (1985) Lubricant-metal interaction under conditions simulating automotive bearing lubrication. Proceeding of JSLE international tribology conference, Elsevier, Tokyo, Japan, pp. 859–864

46. Colclough T (1987) Role of additives and transition metals in lubricating oil oxidation. *Ind Eng Chem Res* 26(9):1888–1895
47. Jayadas NH, Nair KP, Ajithkumar G (2005) Vegetable oils as base oil for industrial lubricants—evaluation oxidative and low temperature properties using TGA, DTA and DSC. Proc. 2005 world tribology congress III, American Society of Mechanical Engineers, 12 Sept 2005–16 Sept 2005, pp. 539–540
48. Birova A, Pavlovicov A, Cvenros J (2002) Lubricating oils based on chemically modified vegetable oils. *J Synth Lubr* 18(4):291–299
49. Meier MAR, Metzger JO, Schubert US (2007) Plant oil renewable resources as green alternatives in polymer science. *Chem Soc Rev* 36(11):1788–1802
50. King JW, Holliday RL, List GR, Snyder JM (2001) Hydrogenation of vegetable oils using mixtures of supercritical carbon dioxide and hydrogen. *J Am Oil Chem Soc* 78(2):107–113
51. Erhan SZ, Adhvaryu A, Sharma BK (2006) Chemically functionalized vegetable oils. *Chem Ind* 111:361–388
52. Doll KM, Sharma BK, Erhan SZ (2007) Synthesis of branched methyl hydroxy stearates including an ester from bio-based levulinic acid. *Ind Eng Chem Res* 46(11):3513–3519
53. Yunus R, Fakhru I-Razi A, Ooi TL, Iyuke SE, Perez JM (2004) Lubrication properties of trimethylolpropane esters based on palm oil and palm kernel oils. *Eur J Lipid Sci Technol* 106:52–60
54. Hwang H-S, Adhvaryu A, Erhan SZ (2003) Preparation and properties of lubricant basestocks from epoxidized soybean oil and 2-ethylhexanol. *J Am Oil Chem Soc* 80(8):811–815
55. Verkuijlen E, Kapteijn F, Mol JC, Boelhouwer C (1977) Heterogeneous metathesis of unsaturated fatty acid esters. *J Chem Soc* (7):198–199
56. Schmidt MA, Dietrich CR, Cahoon EB (2006) Biotechnological enhancement of soybean oil for lubricant applications. *Chem Ind* 111:389–398
57. Holser R, Doll K, Erhan S (2006) Metathesis of methyl soyate with ruthenium catalysts. *Fuel* 85(3):393–395
58. Erhan SZ, Bagby MO, Nelsen TC (1997) Drying properties of metathesized soybean oil. *J Am Oil Chem Soc* 74(6):703–706
59. Salih N, Salimon J, Yousif E (2011) The physicochemical and tribological properties of oleic acid based triester biolubricants. *Ind Crops Prod* 34(1):1089–1096
60. Jayadas NH, Nair KP (2006) Coconut oil as base oil for industrial lubricants—evaluation and modification of thermal, oxidative and low temperature properties. *Tribol Int* 39(9):873–878
61. Papay AG (1998) Antiwear and extreme-pressure additives in lubricants. *Lubr Sci* 10(3):209–224
62. Allum KG, Forbes ES (1968) The load-carrying properties of metal dialkyl dithiophosphates: the effect of chemical structure. Proceedings of the Institution of Mechanical Engineers, Conference Proceedings, 183(16), pp. 7–14
63. Jahanmir S (1987) Wear reduction and surface layer formation by a ZDDP additive. *J Tribol* 109(4):577–586
64. Rounds F (1985) Contribution of phosphorus to the antiwear performance of zinc dialkyldithiophosphates. *ASLE Trans* 28(4):475–485
65. Faut OD, Wheeler DR (1983) On the mechanism of lubrication by tricresylphosphate (TCP) the coefficient of friction as a function of temperature for TCP on M-50 steel. *ASLE Trans* 26(3):344–350
66. Faut OD, Wheeler DR, United States. National Aeronautics and Space Administration, Scientific and Technical Information Branch (1983) Mechanism of lubrication by tricresylphosphate (TCP). National Aeronautics and Space Administration, Scientific and Technical Information Branch; For sale by the National Technical Information Service [Washington, DC]; Springfield, VA
67. Ohkawa S, Konishi A, Hatano H, Ishihama K (1996) Oxidation and corrosion characteristics of vegetable-base biodegradable hydraulic oils. *Soc Automot Eng Trans* 104(4):737
68. Quinn TFJ, Winer WO (1985) The thermal aspects of oxidational wear. *Wear* 102(1–2):67–80

69. Ruger CW, Klinker EJ, Hammond EG (2002) Abilities of some antioxidants to stabilize soybean oil in industrial use conditions. *J Am Oil Chem Soc* 79(7):733–736
70. Brimberg UI, Kamal-Eldin A (2003) On the kinetics of the autoxidation of fats: influence of pro-oxidants, antioxidants and synergists. *Eur J Lipid Sci Technol* 105(2):83–91
71. Cermak SC, Isbell TA (2003) Improved oxidative stability of estolide esters. *Ind Crop Prod* 18(3):223–230
72. Sharma BK, Stipanovic AJ (2003) Development of a new oxidation stability test method for lubricating oils using high-pressure differential scanning calorimetry. *Thermochim Acta* 402(1–2):1–18
73. Cornils B, Herrmann WA (2004) *Aqueous-phase organometallic catalysis: concepts and applications*. Wiley-VCH, Weinheim
74. Petlyuk A, Adams R (2004) Oxidation stability and tribological behavior of vegetable oil hydraulic fluids. *Tribol Trans* 47(2):182–187
75. Schober S, Mittellbach M (2004) The impact of antioxidants on biodiesel oxidation stability. *Eur J Lipid Sci Technol* 106(6):382–389
76. Gordon MH, Kourimska L (1995) The effects of antioxidants on changes in oils during heating and deep frying. *J Sci Food Agr* 68(3):347–353
77. Becker R, Knorr A (1996) An evaluation of antioxidants for vegetable oils at elevated temperatures. *Lubr Sci* 8(2):95–117
78. Dunn RO (2005) Effect of antioxidants on the oxidative stability of methyl soyate (biodiesel). *Fuel Process Technol* 86(10):1071–1085
79. Aluyor EO, Obahiagbon KO, Ori-jesu M (2009) Biodegradation of vegetable oils: a review. *Sci Res Essays* 4(6):543–548
80. Yanishlieva NV, Marinova EM (2001) Stabilisation of edible oils with natural antioxidants. *Eur J Lipid Sci Technol* 103:752–767
81. Eisentraeger A, Schmidt M, Murrenhoff H, Dott W, Hahn S (2002) Biodegradability testing of synthetic ester lubricants—effects of additives and usage. *Chemosphere* 48(1):89–96
82. Stadtmiller WH, Smith AN (1986) ASTM Committee D-2 on Petroleum Products and Lubricants. In: *Aspects of lubricant oxidation: a symposium*. ASTM, Philadelphia, PA
83. Meade FS, Murphy JGP, Rock Island Arsenal IL (1962) *Dry lubricants and corrosion*
84. Rudnick LR (2009) *Lubricant additives chemistry and applications*. CRC Press, Boca Raton, FL
85. Borovaya MS, Krivenkova BD, Lepeshkina YS, Morozova IA, All-Union Sci-Res Inst. for Petroleum Processing (1983) Susceptibility of oils to detergent-dispersant additives (Engl. Transl.). *Chem Technol Fuels Oils* 19(4):196–198
86. Bartz WJ (1986) *Additives for lubricants and operational fluids*. 5th International colloquium: Papers. Technische Akademie Esslingen
87. Omeis J, Pennewiß H (1994) American Chemical Society, Division of Polymer Chemistry. *Polymer preprints*. *Polymer preprints* 35(2):714
88. Selby TW (1958) The non-Newtonian characteristics of lubricating oils. *ASLE Trans* 1(1):68–81
89. Schödel UF (1992) Automatic transmission. *Fluids Int Tribol Colloquium*, vol 3, Society of Automotive Engineers. Esslingen, 22.7–1
90. Böttcher W, Jost H (1991) Multifunctional pour point depressant, SAE Technical Paper 912410, doi:[10.4271/912410](https://doi.org/10.4271/912410)
91. Falbe JR, Hasserodt U (1978) *Katalysatoren. Tenside und Mineral ladditive*, Thieme, Stuttgart
92. Szeri AZ (1998) *Fluid film lubrication: theory and design*. Cambridge University Press, Cambridge, NY
93. White FM (1974) *Viscous fluid flow*. McGraw-Hill, New York
94. Williams JA (1994) *Engineering tribology*. Oxford University Press, Oxford, NY

Exercises

1. Define the term “lubricant” and explain its importance in tribology.
2. Define the term “additive.” Why are additives used in lubricants? List various families of additives.
3. Explain the various lubrication regimes.
4. What is the Stribeck curve? Define Hersey’s number.
5. Explain how lubrication regimes can be determined based on oil-film thickness and roughness of the contacting surfaces.
6. Explain various temperature characteristics of lubricants.
7. Explain:
 - (a) Pour point vs. cloud point
 - (b) Flash point vs. fire point
 - (c) Volatility vs. evaporation
 - (d) Oxidation vs. thermal stability
8. Write a note on:
 - (a) Boundary additives
 - (b) Extreme pressure additives
 - (c) ZDDP
 - (d) Oxidation inhibitors
 - (e) Corrosion inhibitors
9. What is the underlying difference between thrust bearings and journal bearings in regard to the Reynolds equation? Provide the Reynolds equation for both bearing types.

Answers

1. A lubricant is a substance introduced between two moving surfaces to reduce friction, minimize wear, distribute heat, and remove foreign contaminants to ultimately improve efficiency. Lubricants are important because they allow mechanical components to achieve the desired amount of work while minimizing the amount of energy required to perform the work.
2. Additives are substances used to improve the performance of lubricants. Additives are selected based on their ability to reduce friction and wear, increase viscosity, improve viscosity index, resist corrosion and oxidation, increase component and lubricant lifetime, and minimize contamination. The main families of additives are antioxidants, antiwear formulations, antifoaming agents, corrosion inhibitors, detergents, dispersants, extreme pressure, friction modifiers, metal deactivators, and viscosity index improvers.

3. The three main regimes of lubrication can be referred to as boundary lubrication, mixed/elastohydrodynamic lubrication, and full film hydrodynamic lubrication. Boundary lubrication or boundary friction is the lubrication regime with the most asperity contact between the surfaces occurring due the presence of a thin fluid film. Mixed film lubrication is the combination of full film hydrodynamic lubrication and boundary lubrication. In this lubrication regime, the surfaces are transitioning away from boundary lubrication into hydrodynamic lubrication where there may be frequent asperity contacts, but at least a portion of the bearing surface remains supported partially by a hydrodynamic film. Hydrodynamic lubrication also known as fluid-film or thick-film lubrication involves two nonparallel surfaces in relative motion with a layer of fluid pulled in between the surfaces to develop adequate dynamic pressure to support the load of the opposing surfaces and prevent asperity contact. In this lubrication regime, the surfaces are no longer in contact and the fluid has established itself in significant form to create a thick film.
4. The Stribeck curve is a plot of the variation of the coefficient of friction against a nondimensional number, known as Hersey's number (also referred to as the Stribeck number), which is instrumental in demarcation of the lubrication regimes. Hersey's number is given as $(\eta v/p)$, where "η" is the lubricant viscosity, "v" is sliding velocity, and "p" is load per unit width.
5. Lubrication regimes can be determined based on oil-film thickness and roughness of the contacting surface by using the Hamrock and Dowson formula given as

$$\lambda = \frac{h}{\sigma} \quad (10.28a)$$

$$\sigma = \sqrt{\sigma_1^2 + \sigma_2^2} \quad (10.28b)$$

Here, (10.28a) is the ratio of the fluid-film thickness, h , and the composite surface roughness, σ . In (10.28a), the composite surface roughness is given in (10.28b) where σ_1 and σ_2 are RMS roughness of the two mating surfaces. Equation (10.28a and 10.28b) allows for the calculation of the minimum film thickness in lubricated contacts. The fluid-film thickness parameter, λ , decides the lubrication regime with boundary lubrication characterized by a value of λ less than 1, mixed or elastohydrodynamic lubrication described as $1 \leq \lambda \leq 3$, and hydrodynamic lubrication characterized by a value of λ greater than 3.

6. The important thermal properties of lubricants are specific heat, thermal conductivity, and thermal diffusivity. These three parameters are important in assessing the heating effects in lubrication, i.e., the cooling properties of the oil and the operating temperature of the surfaces. The temperature characteristics are important in the selection of a lubricant for a specific application.

7. (a) The pour point of a liquid is the lowest temperature at which it becomes semisolid and loses its flow characteristics. The cloud point of a fluid is the temperature at which dissolved solids are no longer completely soluble, precipitating as a second phase giving the fluid a cloudy appearance.
(b) The flash point of a lubricant is the temperature at which its vapor will flash ignite. The fire point of oil is the temperature at which enough vapor is produced to sustain burning after ignition. The fire point is higher than the flash point.
(c) In many applications the loss of lubricant due to evaporation can be significant. At elevated temperatures, in particular, oils may become more viscous and eventually dry out due to evaporation. Volatility of lubricants is expressed as a direct measure of evaporation losses.
(d) Oxidation stability is the resistance of a lubricant to molecular breakdown or rearrangement at elevated temperatures in an open-air environment containing oxygen. Thermal stability is the resistance of the lubricant to molecular breakdown or molecular rearrangement at elevated temperatures in the absence of oxygen.
8. (a) Adsorption or boundary additives control the adsorption type of lubrication and are also known as “friction modifiers,” since they are often used to prevent stick-slip phenomena. Adsorption or boundary additives are vital in boundary lubrication. Examples of additives in current use are fatty acids, esters, and amines derived from fatty acids.
(b) Extreme pressure (EP) compounds are designed to react with metal surfaces under extreme conditions of load and velocity to prevent welding of the moving parts that would otherwise cause severe damage.
(c) ZDDP is a very important antiwear additive commonly used in engine oil formulations. It was originally developed as an antioxidant and detergent, but was later revealed to exhibit superior antiwear properties and function as a mild EP additive.
(d) Many lubricating oils contain antioxidant additives to delay the onset of severe oxidation of the oil. These are either natural antioxidants or artificially introduced additives that are able to suppress oxidation.
(e) Corrosion control additives are classified as corrosion inhibitors and rust inhibitors. Corrosion inhibitors are used for nonferrous metals and are designed to protect their surfaces against any corrosive agents present in the oil. Rust inhibitors are used for ferrous metals to protect ferrous surfaces against corrosion.
9. Thrust bearings and the journal bearings differ by the velocities contributing to the pressure generated. In thrust bearings, the difference in tangential velocities creates pressure, whereas in journal bearings the sum of the tangential velocities creates pressure.

To simulate a conventional thrust bearing where the relative motion between the surfaces in contact is pure translation, the equation of motion is

$$\frac{\partial}{\partial x} \left(\frac{h^3}{\mu} \frac{\partial p}{\partial x} \right) + \frac{\partial}{\partial z} \left(\frac{h^3}{\mu} \frac{\partial p}{\partial z} \right) = 6(U_1 - U_2) \frac{\partial h}{\partial x} + 12(V_2 - V_1)$$

To simulate a traditional journal bearing where relative motion of the surfaces in contact is not parallel, a component of the rotational velocity augments the relative motion in the tangential direction resulting in an equation of motion as follows:

$$\frac{\partial}{\partial x} \left(\frac{h^3}{\mu} \frac{\partial p}{\partial x} \right) + \frac{\partial}{\partial z} \left(\frac{h^3}{\mu} \frac{\partial p}{\partial z} \right) = 6(U_1 + U_2) \frac{\partial h}{\partial x} + 12(V_2 - V_1)$$

Chapter 11

Self-Lubricating Behavior of Graphite-Reinforced Composites

Pradeep L. Menezes, Carlton J. Reeves, Pradeep K. Rohatgi,
and Michael R. Lovell

Abstract Lubricants are extensively used between contacting surfaces to reduce friction and wear. Typically, liquid lubricants are used to achieve low friction and wear. However, these lubricants are not effective in elevated temperature applications or vacuum environments. For these reasons, solid lubricants are utilized to meet these operational needs, where liquid lubrication is impractical. Solid lubricants are only effective as long as they are present in the tribo-interface. Therefore, it is desirable to provide a constant supply of solid lubricant material to the contacting surface. This is often achieved by incorporating solid lubricants as a second phase in the base material. These composite materials have the ability to achieve low friction and wear at the contact surfaces without any external supply of lubrication during sliding. Metal matrix composites reinforced with lamellar solid lubricant particles such as graphite are being used as self-lubricating materials for various engineering applications. In this chapter, the tribological behavior of metal and ceramic matrix composites reinforced with graphite particles has been reviewed. More specifically, copper-graphite, nickel-graphite, magnesium-graphite, silver-graphite, aluminum-graphite, silicon nitride-graphite, and alumina-graphite composites are studied. The influence of various environmental and mechanical parameters on the friction coefficient and wear rate is discussed. It was found that the amount of graphite released on the worn surface forms a thin transfer film on the contact surfaces. This transfer film reduces the overall friction

P.L. Menezes (✉) • M.R. Lovell

Department of Industrial Engineering, University of Wisconsin-Milwaukee,
Milwaukee, WI 53201, USA
e-mail: menezesp@uwm.edu

C.J. Reeves

Department of Mechanical Engineering, University of Wisconsin-Milwaukee,
Milwaukee, WI 53201, USA

P.K. Rohatgi

Department of Materials Engineering, University of Wisconsin-Milwaukee,
Milwaukee, WI 53201, USA

coefficient and wear rate. The presence of the graphite-based transfer film increases the seizure resistance and enables the contacting surfaces to run under boundary lubrication without galling. The formation and retention of this transfer film on the sliding surface as well as its composition, area fraction, thickness, and hardness are important factors in controlling the friction and wear behavior of the material. The effectiveness of the transfer film also depends on the nature of the sliding surface, the test condition, environment, and the graphite content in the composite.

1 Introduction

A lubricant is a substance used to facilitate relative motion of solid bodies by minimizing friction and wear between contacting surfaces. A lubricant functions by introducing a layer of material between the contacting surfaces with a lower shear strength than the surfaces themselves [1]. In lubricated systems, a lubricant may either completely or partially prevent asperity contact, thus reducing the strength of the junctions formed [2]. In general, there are three categories of lubricants: liquid, solid, and gaseous.

Nearly all lubricants used in the automotive and manufacturing sectors are oil or grease based. These oils include engine oils, transmission fluids, hydraulic fluids, and gear oils. These products are not typically environmentally friendly or biodegradable and can introduce significant quantities of pollutants into the waste stream [3]. Thus, disposal of these large volumes of material obviously represents an environmental burden. Hence, it is very important to develop either green lubricants or composite materials, which have self-lubrication properties. Moreover, industrial applications are becoming more advanced with elevated temperatures or vacuum environments that are moving beyond the tolerable domain of liquid lubricants rendering liquid lubricants impractical. For these reasons, solid lubricants are utilized to meet the various extreme operational requirements of many advanced applications, where liquid lubricants are ineffective. Solid lubricants are most effective when they are continuously present in the tribo-interface; therefore, it is desirable to provide a constant supply of solid lubricant material at the contacting surface. This is often achieved by incorporating solid lubricants as a second phase material within the matrix material to create a composite.

1.1 Composite Materials

Composite materials are a special class of materials and are made from two or more constituent components with significantly different physical or chemical properties, which remain separate and distinct at the macroscopic or microscopic scale within the finished structure. In the case of two constituent components, the material with the highest volume fraction is considered as the matrix, whereas the other is the

reinforcement material that modifies the properties of the matrix. In metal matrix composites, the matrix is made of a metal and the reinforcement may be a different metal or another material, such as a ceramic or organic compound. Similarly, in ceramic matrix composites, the matrix is composed of silicon nitride, alumina, or another type of ceramic material and the reinforcement may be a different ceramic, metallic, or solid lubricant compound. When a composite has two or more second phase reinforcing materials, then it is called a hybrid composite. Composites are synthesized by dispersing a reinforcing material into a matrix. Sometimes, the reinforcement materials are coated to prevent a chemical reaction with the matrix. The matrix is the monolithic material into which the reinforcement is embedded and is completely continuous. The reinforcement material is embedded into the matrix usually in the form of particles, fibers, whiskers, or wires. The most common structurally reinforcing materials are alumina and silicon carbide, and the most common lubricating reinforcing materials are graphite and molybdenum disulfide. The reinforcement can be either continuous or discontinuous. Discontinuous matrix composites can be isotropic. The reinforcement does not always serve a purely structural task, but it is used to change physical properties such as friction coefficient, wear, or thermal conductivity. Metal and ceramic matrix composites have been used in the aerospace, aircraft, and automotive industries because they possess many potential advantages over monolithic materials, including higher specific strength and stiffness, higher wear resistance, higher thermal conductivity, and lower coefficient of thermal expansion.

1.2 Solid Lubricants

When lamellar solid lubricants such as graphite (C), molybdenum disulfide (MoS_2), boric acid (H_3BO_3), and hexagonal boron nitride (hBN) are introduced at the sliding interface, these often cause the friction and wear values to decrease. Lamellar solid lubricants are important because they have a layered structure [4]. The layers consist of flat sheets of atoms or molecules, and the structure is called a layer-lattice structure. The atoms are strongly bonded within the sheets by covalent bonds and are weakly bonded between the layers by van der Waals bonds. The importance of lamellar solid lubricants is their ability to shear more easily parallel to the layers than across them. They can therefore support relatively heavy loads at right angles to the layers while still being able to slide easily parallel to the layers in the direction of the relative motion. This property is effectively taken advantage of during the lubrication process. It is also important that the solid lubricant should adhere strongly to the contacting surface, otherwise it would be easily rubbed away which results in a short service life. Graphite, which consists of carbon atoms arranged in a layer-like structure, displays a low coefficient of friction ranging from 0.1 to 0.2 while sliding on a clean surface. With friction coefficients so low, this suggests that graphite can be used as a solid lubricant. It is reported that graphite is an effective lubricant additive for its anticorrosion,

high-temperature endurance, and self-lubricating properties derived from its lamellar structure [5]. The slippage between lamellar endows the graphite excellent lubricating properties under heavy loads [6].

One of the major issues in using solid lubricants is maintaining a continuous supply of lubricant between two sliding surfaces. A continuous supply of lubricant is more easily maintained in the case of fluid lubricants when compared to solid lubricants. An interesting innovation to ensure a supply of solid lubricant between sliding surfaces is to incorporate the solid lubricant into the matrix of one of the sliding components by forming a matrix composite. Thus, self-lubricating matrix composites are materials in which solid lubricants such as graphite or MoS_2 are introduced as reinforcing materials into the matrix during preparation that enable the self-lubricating properties.

During sliding contact, wear particles are often produced at the interface. Sometimes these wear particles act as a third body abrasive component causing the friction and wear rates to increase with sliding distance. For this reason, lubricants are generally used to reduce the friction coefficient and wear rate. Solid lubricants have been studied in the literature as a means to lubricate metals as solid films that are adsorbed, bonded, or deposited on the contacting surfaces [7–15]. Often solid lubricants are utilized as thin films on metallic substrates by burnishing [7, 8], sputtering [11, 12], or plasma spraying [13, 14]. Although, solid lubricant films can reduce the friction coefficient and the wear rate, they are only effective as long as they are present on the surface. Therefore, it is desirable to provide a constant supply of solid lubricant material in the tribo-contact. This is often achieved by incorporating solid lubricants as a second phase in the base material. Self-lubricating composites have a unique advantage in that the wear particles formed at the interface are comprised of the solid lubricant material initially used as the reinforcement material, which helps in decreasing the friction coefficient and wear rate. Under sliding conditions the composite becomes self-lubricating. Here, the solid lubricant embedded in the metal matrix transfers to the contacting surfaces and forms a thin film solid lubricant which prevents direct contact between the mating surfaces. Thus, friction and wear are reduced and this process eliminates the use of an external lubricant supply. The success of a matrix impregnated with lamellar solid particles relies on the ability of the solid particles to emerge from their embedded state in the matrix and spread evenly in the form of a solid lubricating film over the tribological surface to provide lubrication.

1.3 Self-Lubrication

A matrix composite impregnated with a solid lubricant combines the properties of strength, hardness, and abrasion resistance of the matrix alloy with the natural lubricity of the solid lubricant. The matrix alloy may also be chosen to impart good electrical and thermal conductivity to the composite. Much of the early work on metal matrix composites utilized graphite particles using powder metallurgy, which is expensive and limited in the sizes that can be produced. Rohatgi et al. [16–19]

first introduced graphite as a solid lubricant in aluminum matrices through casting routes, by mixing the molten alloy with graphite particles to make a uniform suspension that was then underwent a casting process. In many instances, the graphite is rejected by the liquid aluminum encountered in the casting due to the density differences and poor wettability between the metal matrix and the reinforcement material. These problems have been solved to a large extent at the laboratory scale by the use of metal coatings such as Ni and Cu on the particle of graphite and by the addition of reactive elements (e.g., Mg and Ti) to the melt. This work was subsequently extended to other solid lubricant dispersions but aluminum-graphite composite by far has the most potential for commercial applications. Cast aluminum-graphite composites for antifriction applications were initially developed in 1966. The cast aluminum-graphite composites have a unique structure, in which graphite particles are in the inter-dendrite regions. These composites have been reported to have superior tribological properties when compared with similar composites prepared by powder metallurgy techniques. These composites have been cast into tribological components using sand casting, pressure die casting, gravity die casting, and centrifugal casting. The particulate composites of graphite and a matrix alloy are characterized by (a) the composition and microstructure of the matrix alloy; (b) the size, volume fraction, and distribution of graphite particles; and (c) the nature of the interface between the matrix and the dispersed graphite. In addition, the composites may have defects such as voids and porosity, which, unless accounted for, will result in an erroneous estimate of area of contact and thereby influence friction and wear. Furthermore, the strength of the composite will reduce with increased porosity content, thus increasing the wear rate.

In composites, the reinforced solid lubricants enhance the tribological properties of the composite through the formation of a solid lubricant thin film on the tribo-surface [20, 21]. This lubricating film is formed as a result of shearing solid particles impregnated in the sliding surface of the composite. The solid particle-enriched lubricant film helps to reduce the magnitude of shear stress transferred to the material underneath the contact area, alleviate the plastic deformation in the subsurface region, minimize metal-to-metal contact, and act as a solid lubricant between two sliding surfaces. Therefore, it helps to reduce friction and wear and improve seizure resistance of the composite. The formation and retention of this tribo-layer on the sliding surface as well as its composition, area fraction, thickness, and hardness are important factors in controlling the wear behavior of the material and depend on the nature of the sliding surface, the test condition, environment, and solid particle content in the composite. The formation of the lubricating layer at the sliding surface becomes thicker with the addition of more solid particles to the base alloy. It is this lubricating layer that is responsible for playing an effective role for keeping the friction and wear behavior of the composite low. The formation of the solid lubricating film also depends on the matrix characteristics, for example, the deformability of matrix helps in the transfer of solid particles from the matrix to the tribo-surface. Additionally, the formation of the solid lubricating film also depends on the adhesion of the solid particle film to the matrix and the presence of

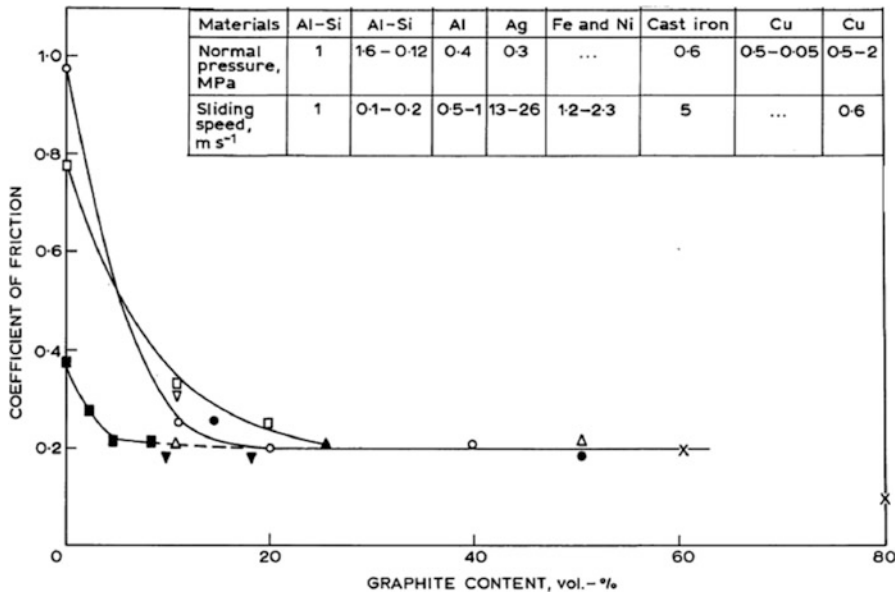


Fig. 11.1 Variation of coefficient of friction with graphite content for composites with different base alloys [21]

an environment, which permits the solid particles to spread in the form of a thin film thus acting as a lubricant. Earlier works have also identified that by increasing the solid particle content, the lubricating film formed on the tribo-surface lowers the wear rate [20, 21]. Several researchers [22, 23] have also observed the solid lubricating film formed on the wearing surface and reported that a solid lubricant particularly graphite particles in the composite helps in reducing the friction coefficient and increasing the anti-seizing quality, thus improving the tribological behavior of the base alloy.

In self-lubricating composites, solid particles such as graphite and MoS₂ are embedded in the matrix. Here, the formation of a thin film will occur by transferring the solid particles from the matrix to the tribo-surface during initial periods of sliding. The observed friction and wear behavior will, therefore, have two distinct stages: (a) transient state, while the thin solid lubricant film is being established, and (b) steady state, when a stable solid lubricant film (in the dynamical sense of being continuously replenished, i.e., “self-lubricating,” to make up for the wear loss) has formed. The variation of the coefficient of friction with graphite content for composites with different base alloys (aluminum, silver, iron, nickel, and copper) is shown in Fig. 11.1 [21]. The tests were carried out with different loads and sliding velocities. All the composites, with the exception of the silver matrix, were tested against a steel counter-surface, for the conditions indicated in the figure. It can be seen that when the graphite content in the composites exceeds 20 vol.%, the friction coefficients observed in different composites are virtually independent of the metal matrix and the graphite content and appear to attain a constant value of close to 0.2.

The elemental graphite has a friction coefficient of 0.18, and this increases with the desorption of adsorbed vapors. Thus, it appears that both the mating surfaces, including the graphitic composite and the counter-surfaces like steel, become completely smeared with graphite, and a friction coefficient close to that of pure graphite against itself is observed, regardless of the matrix.

In this chapter, the self-lubricating behavior of various graphite-reinforced metal matrix and ceramic matrix composites are reviewed. More specifically, metal matrix composites in the form of copper-graphite, nickel-graphite, magnesium-graphite, silver-graphite, and aluminum-graphite as well as ceramic-graphite composites in the form of silicon nitride-graphite and alumina-graphite composites are examined along with their tribological properties.

2 Self-Lubricating Behavior of Metal Matrix Composites

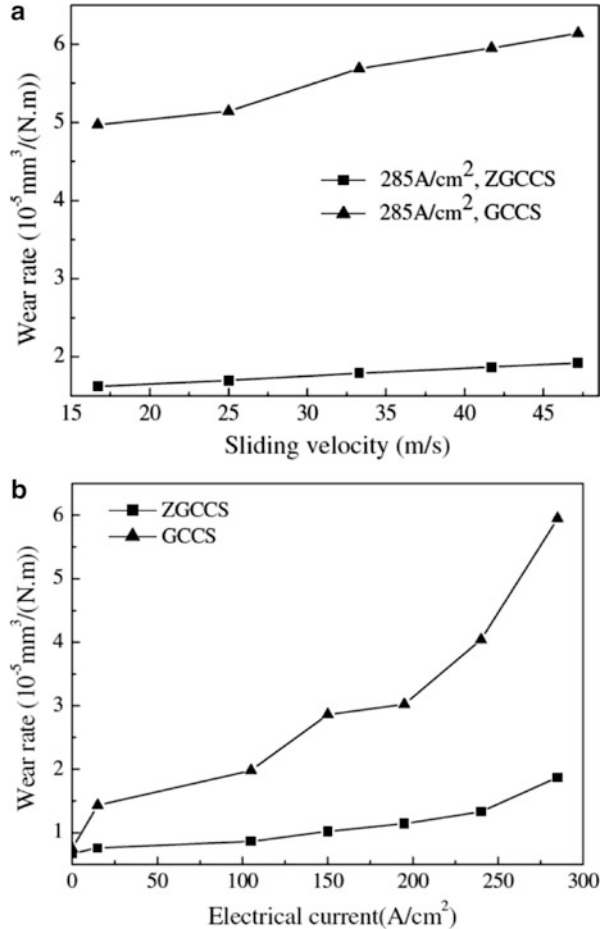
2.1 Introduction

Self-lubricating metal matrix composites have been extensively used in antifriction applications where liquid lubricants are impractical. The composites illustrate the mechanism of solid lubrication by graphite. In this section, selected examples of various metal-graphite composites are analyzed for their industrial potential and current application. The influence of the metal matrix alloy composition; graphite content, shape, and size; and test variables such as contact pressure, sliding velocity, temperature, current density, counterpart materials, and environment on the tribological behavior of the composites is discussed. The process of graphite-rich film formation on the tribo-surfaces of metal-graphite composites is analyzed. The superior tribological properties of graphite-reinforced composites are strongly dependent on the formation of a graphite-rich film. The friction and wear rate in the composites are significantly reduced due to the incorporation of graphite particles when compared to similar composites without graphite reinforcement.

2.2 Self-Lubricating Behavior of Copper-Graphite Composites

Metal matrix composites have a variety of uses and practical applications. Copper metal matrix composites, for example, are being investigated for their use in electromechanical applications. Copper, which is well known for its high thermal and electrical conductivity, is currently used in metal matrix composites reinforced with graphite particles for its use in electrical sliding contact applications such as brushes in electric motors and generators [24–31]. In welding machines, low voltage, high current densities, and sliding of critical components necessitate materials

Fig. 11.2 The variation of wear rate with (a) sliding velocity and (b) electrical current [32]



with a very high specific electrical conductivity, good thermal conductivity, and low friction coefficient. Copper–graphite composite materials are some of the few materials that can fulfill such conditions. Copper–graphite composites combine the properties of copper (i.e., excellent thermal and electrical conductivities) and graphite (i.e., superior lubricity and a low thermal expansion coefficient).

Considerable efforts have been made to study the tribological performance of copper–graphite composites. Tu et al. [32] studied the tribological behavior of a zinc-coated graphite–copper contact strip (ZGCCS) and a graphite–copper contact strip (GCCS) which were both derived from a graphite–copper matrix composite with self-lubricating properties. Figure 11.2 shows the variation of wear rate with sliding velocity and electrical current. It was observed that the wear rate of both the ZGCCS and the GCCS increased with the increment of the current density and the sliding velocity. However, the ZGCCS exhibited wear resistance superior to the GCCS, indicating the positive effect that the electroplating of zinc had on the graphite.

The zinc electroplating played an important role in improving the wear resistance and the wear rate of ZGCCS. In Fig. 11.2, it can be seen that the wear rate of the ZGCCS was only one-third of the GCCS at a sliding velocity of 41.7 m/s and with a current density of 285 A/cm². During the investigation of the graphite–copper contact strips, arc erosion wear, oxidative wear, and adhesive wear were the dominant mechanisms during the electrical sliding process. The arc erosion of the graphite–copper composite contact strip was reduced by the electroplating of zinc on graphite since the zinc-coated graphite particles were homogeneously distributed in the copper matrix. Kovačik et al. [33] investigated the effect of graphite composition on the friction coefficient of copper–graphite composites in the range of 0–50 vol.% of graphite at constant load. The study was specifically done to determine the critical graphite content above which the coefficient of friction of the composite remains almost composition independent and constant. Hence, an uncoated copper–graphite composite in the composition range of 0–50 vol.% of graphite and coated composites with 30 and 50 vol.% of graphite were prepared, and their tribological properties were measured. Figure 11.3 shows the composition dependence of the coefficient of friction for an (a) uncoated and (b) coated copper–graphite composite. It was found that with increasing concentration of graphite, the coefficient of friction of coated and uncoated composites at first decreased until a certain critical concentration threshold of graphite was reached. Then, the coefficient of friction of the composite becomes independent of the composition and corresponds to the dynamic coefficient of friction of used graphite material (0.15–0.16 for used graphite). In regard to the wear rate, it was seen to decrease continuously without stabilizing with an increasing concentration of graphite. The results were also compared with work done by Moustafa et al. [27] on copper–graphite composites as shown in Fig. 11.3.

Efforts have also been made to study the friction and wear performance of copper–graphite composites against different counterpart materials. Ma et al. [34] investigated tribological behaviors of copper–graphite composites sliding against different counterparts, specified as 2024 aluminum alloy, AZ91D magnesium alloy, and Ti6Al4V titanium alloy. Figure 11.4 shows the variation of friction coefficient and wear rate with sliding speed. It was found that the tribological performance of copper–graphite composite was strongly dependent on its counterpart materials. Copper–graphite composite could provide friction reduction in sliding against 2024 and Ti6Al4V. The copper–graphite composite was revealed to be an excellent self-lubricating material in sliding against AZ91D at low speeds. The authors described that the transfer layer of the copper–graphite composite on the counterface is the key to friction reduction. The wear mechanism of the copper–graphite composite was related to the transfer (from copper–graphite composite to counterpart alloys) and counter-transfer (from counterpart alloys to copper–graphite composite).

Studies were also made to investigate the influence of various self-lubricating particles on tribological behavior of copper–matrix composites. Chen et al. [35] studied the tribological properties of two solid lubricants, graphite and hexagonal boron nitride (hBN) dispersed within copper-based friction composites. Copper-based friction composites containing graphite at weight fractions in the range of 0 %, 2 %, 5 %, 8 %, and 10 %, corresponding to the hexagonal boron nitride at

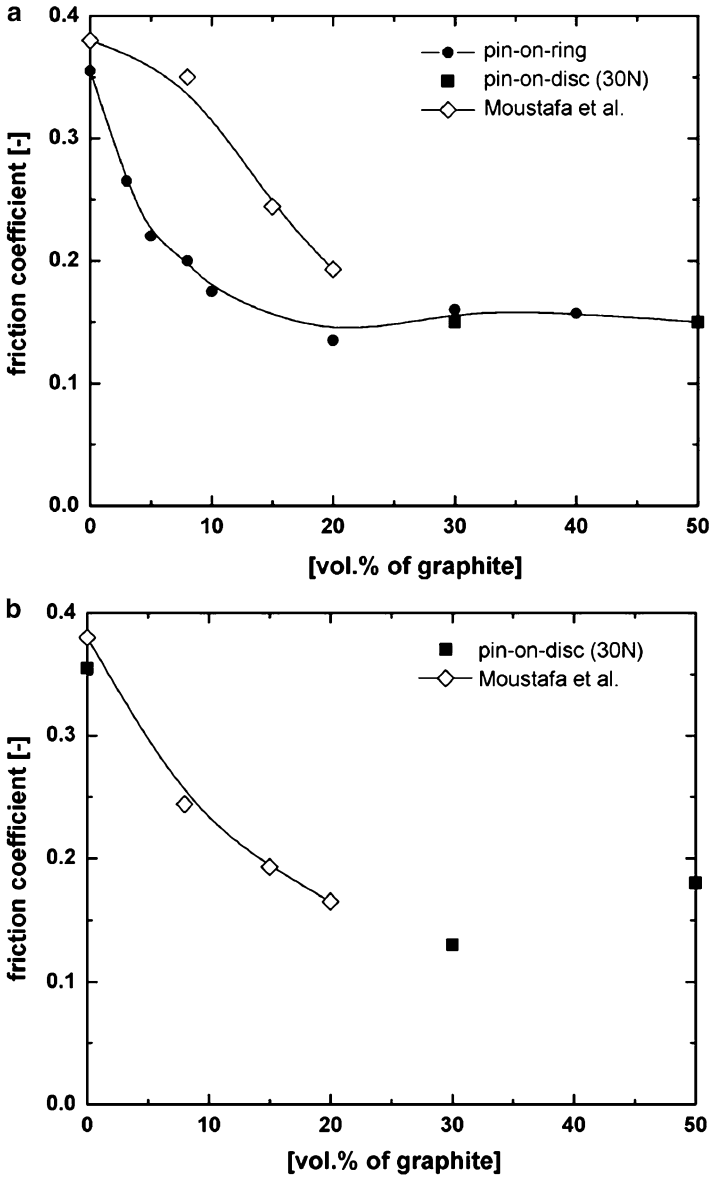


Fig. 11.3 Composition dependence of friction coefficient of (a) uncoated and (b) coated copper-graphite composites [33]

weight fractions in the range of 10 %, 8 %, 5 %, 2 %, and 0 %, were fabricated by a powder metallurgy hot press method, respectively. Figure 11.5 shows the variation of coefficient of friction and wear rates for different normal loads. The results indicate that the lubrication effects of graphite are superior to those of hBN. It was

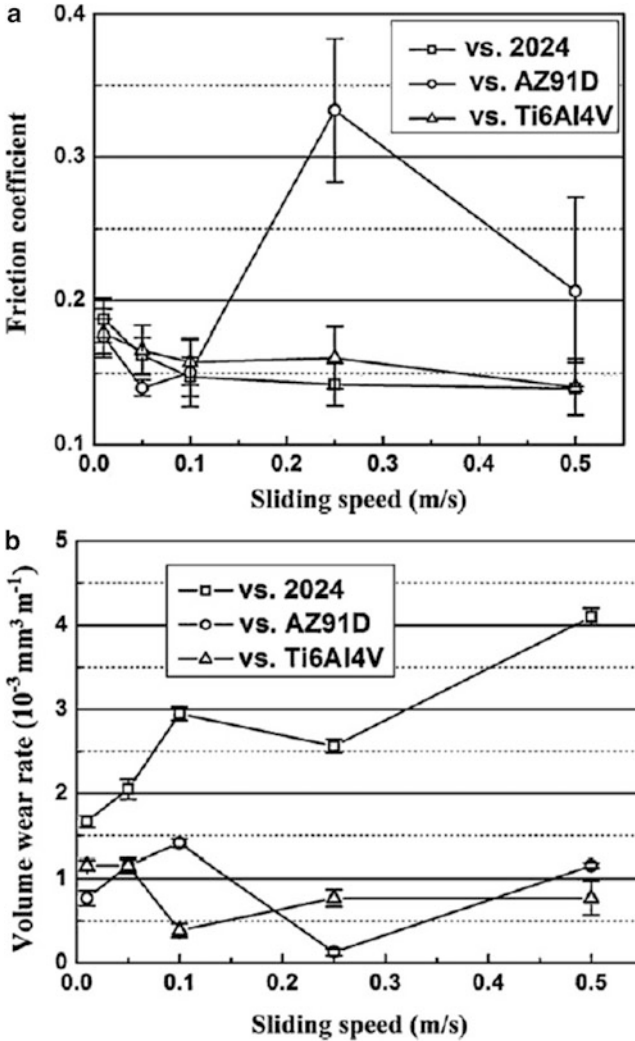


Fig. 11.4 (a) Friction coefficients and (b) wear rates of copper–graphite composite sliding against 2024 aluminum alloy, AZ91D, and Ti6Al4V [34]

also revealed that the wear rates and friction coefficients decreased with an increase in graphite content.

Different heat treatments were used to improve the tribological properties of copper–graphite composites. Rajkumar and Aravindan [36] studied friction and wear properties of microwave-heat-treated copper–5 wt% graphite composites and untreated copper–graphite composites. Figure 11.6 shows the variation of the coefficient of friction and the wear rates of untreated and microwave-heat-treated copper–graphite composites. It was found that the microwave-heat-treated

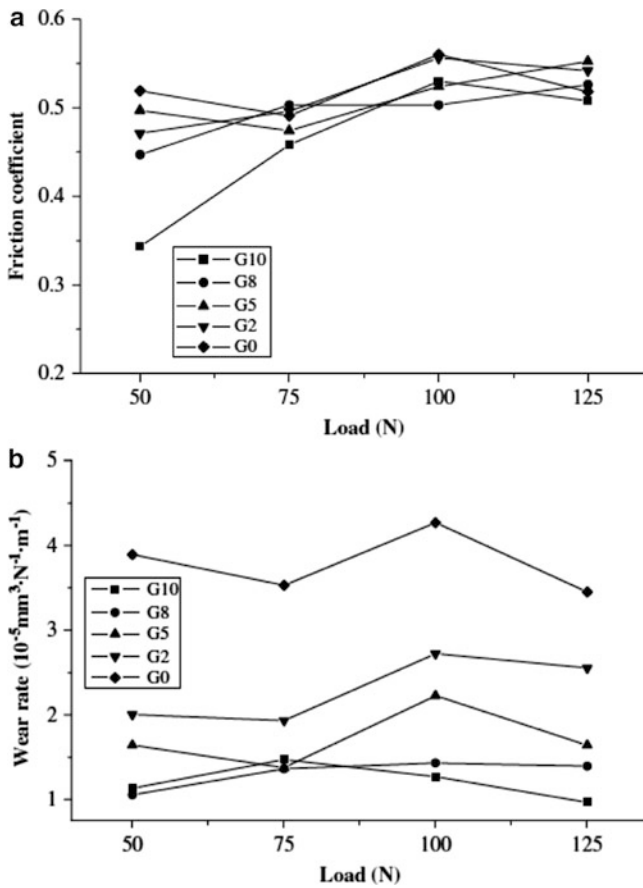


Fig. 11.5 Variation of (a) friction coefficient and (b) wear rates with loads for various copper-based composites [35]

composites exhibited a reduced coefficient of friction and specific wear rate when compared to the untreated ones. The untreated copper–graphite composites exhibited the highest coefficient of friction and specific wear rate due to weaker interface contact. Microwave-heat treating reduces the coefficient of friction and specific wear rate by facilitating the formation of a stable graphite layer at the contact region of the tribo-surface. Moreover, Rajkumar and Aravindan [37] studied the tribological performance of microwave-sintered copper–graphite hybrid composites reinforced with TiC. Figure 11.7 shows the variation of the coefficient of friction and wear rate of the hybrid composites with normal load. The coefficient of friction and wear rate of the copper–TiC–graphite hybrid composites and unreinforced copper material increased with an increase in the normal load. The coefficient of friction and the wear rate of the hybrid composites are lower than those of unreinforced copper. The wear rate of hybrid composites is reduced with an

Fig. 11.6 Variation of (a) coefficient of friction and (b) wear rates of untreated and microwave-treated copper-graphite composites [36]

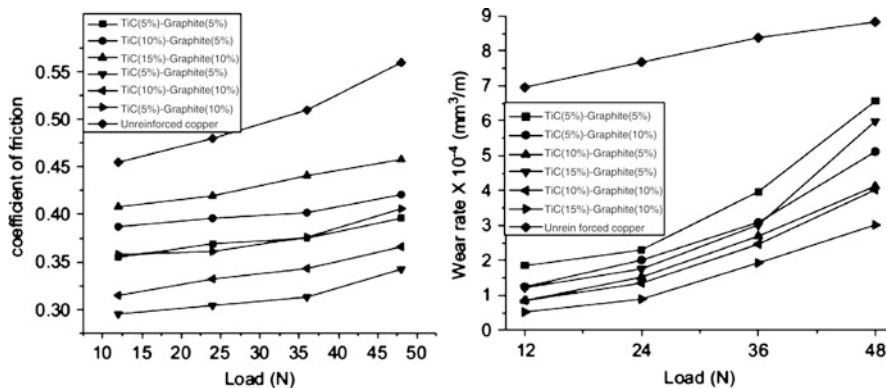
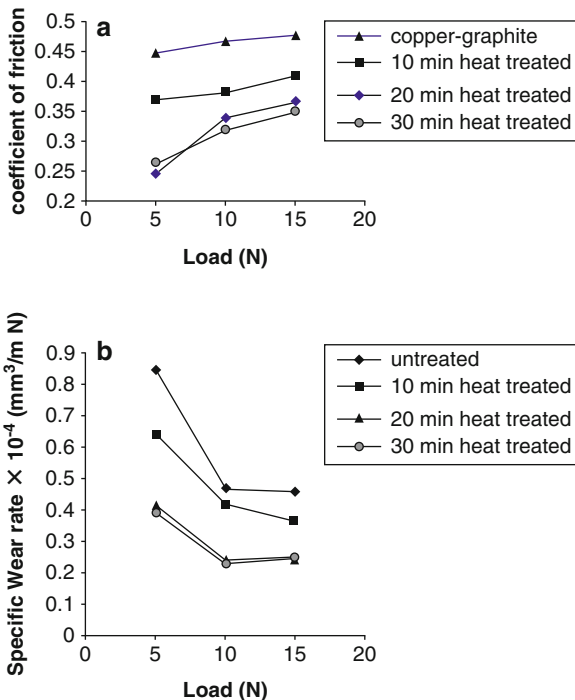


Fig. 11.7 Variation of friction coefficient and wear rate of hybrid composite with normal load [37]

increase in both the percentage of TiC and graphite, due to the cooperative effect offered for both reinforcement materials. An increased content of the TiC reinforcement for a given volume fraction of graphite leads to a higher coefficient of friction. The coefficient of friction of the hybrid composites decreases with an increase in the percentage of graphite reinforcement. The presence of a mixed layer

particularly in higher content graphite hybrid composites was found to influence the tribological properties. Increasing sliding velocity increased the coefficient of friction and wear rate of the hybrid composites. The wear mechanism involved in the copper–TiC–graphite hybrid composites for a given volume fraction of graphite and 5 % TiC was oxidative wear with plastic deformation. The wear mechanism occurring in the hybrid composites with 15 % TiC and the 5 % graphite hybrid composites were oxidative wear with high strained delamination. The wear mechanism involved in the 15 % TiC and 10 % graphite composite was oxidative wear with delamination. In another study, Ramesh et al. [38] analyzed the tribological performance of novel cast copper–SiC–graphite hybrid composites. The coefficient of friction of hybrid composites was higher than that of copper, and the wear rates of the hybrid composites were lower when compared to copper. These results revealed that an increased content of hard reinforcement material (SiC) for a given volume fraction of soft reinforcement material (graphite) in a metal matrix composite leads to a higher coefficient of friction and lower wear rate of the composite.

The influence of sliding speed on the tribological performance of copper–graphite composites was studied by Ma and Lu [39] to establish the effect of sliding speed on surface modification and tribological behavior of a copper–graphite composite. Figure 11.8 shows the variation of the coefficient of friction and wear rates for different sliding speeds. The results showed that the friction coefficient and wear rate of copper–graphite composites were largely dependent on sliding speed. When the speed exceeds the critical value, a transition of the friction and wear regime occurred. The formation of a lubricant layer on the contact surface is regarded as an important characteristic for enhanced tribological performance of copper–graphite composites. Due to a large strain gradient in the subsurface deformation zone, the graphite-rich lubricant layer can easily form on the sliding surface when the speed is lower than the critical value. At speeds exceeding the critical value, the formation of the lubricant layer is difficult due to the effects of delamination wear caused by the high strain rate. At speeds less than the critical value, the wear mechanism occurring tends to be mild wear caused by ratcheting, and at speeds exceeding the critical value, the wear mechanism is more severe induced by delamination wear. Ma and Lu [40] also studied the effect of surface texture on the transfer layer formation and tribological behavior of copper–graphite composites. Three kinds of texture were prepared on the surface of steel discs: parallel grooves (PG), random grooves (RG), and polished surfaces (PS). The influence of surface texture on the friction and wear behavior of copper–graphite composites was investigated under both low and high load conditions at a fixed speed. It was found that the textures had different ratcheting effects on the contact surface of the copper–graphite composite and thus influenced the friction and wear behaviors as shown in the Fig. 11.9.

Efforts have also been made to study the tribological performance of copper–graphite composites at high temperatures. Zhan and Zhang [41] studied the effect of graphite particles in a copper hybrid composite sliding against steel at high temperatures. Dry sliding wear properties of copper matrix composites

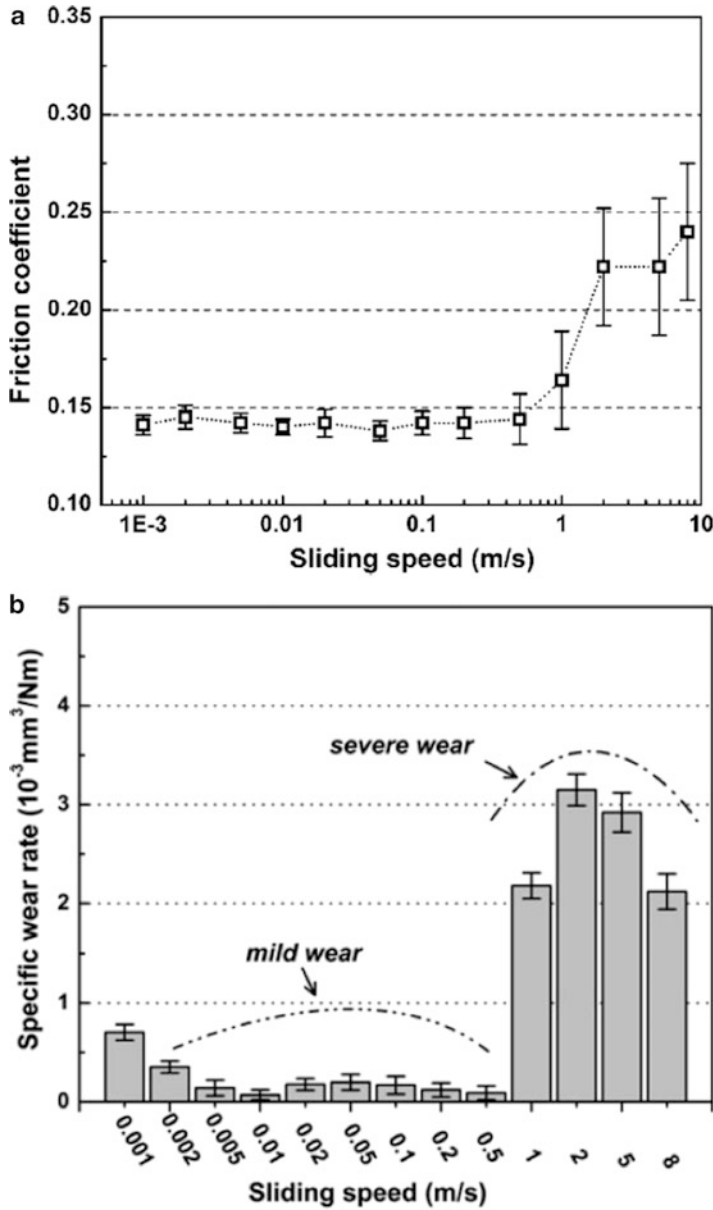


Fig. 11.8 Variation of (a) average friction coefficient and (b) wear rate of copper-graphite composites at different sliding speeds [39]

reinforced with SiC and graphite particles were tested at elevated temperatures ranging between 373 and 723 K. Figure 11.10 shows the variation of the coefficient of friction and wear rate for the two composites. It was found that the addition of graphite particles simultaneously decreased the wear rates of the composite and

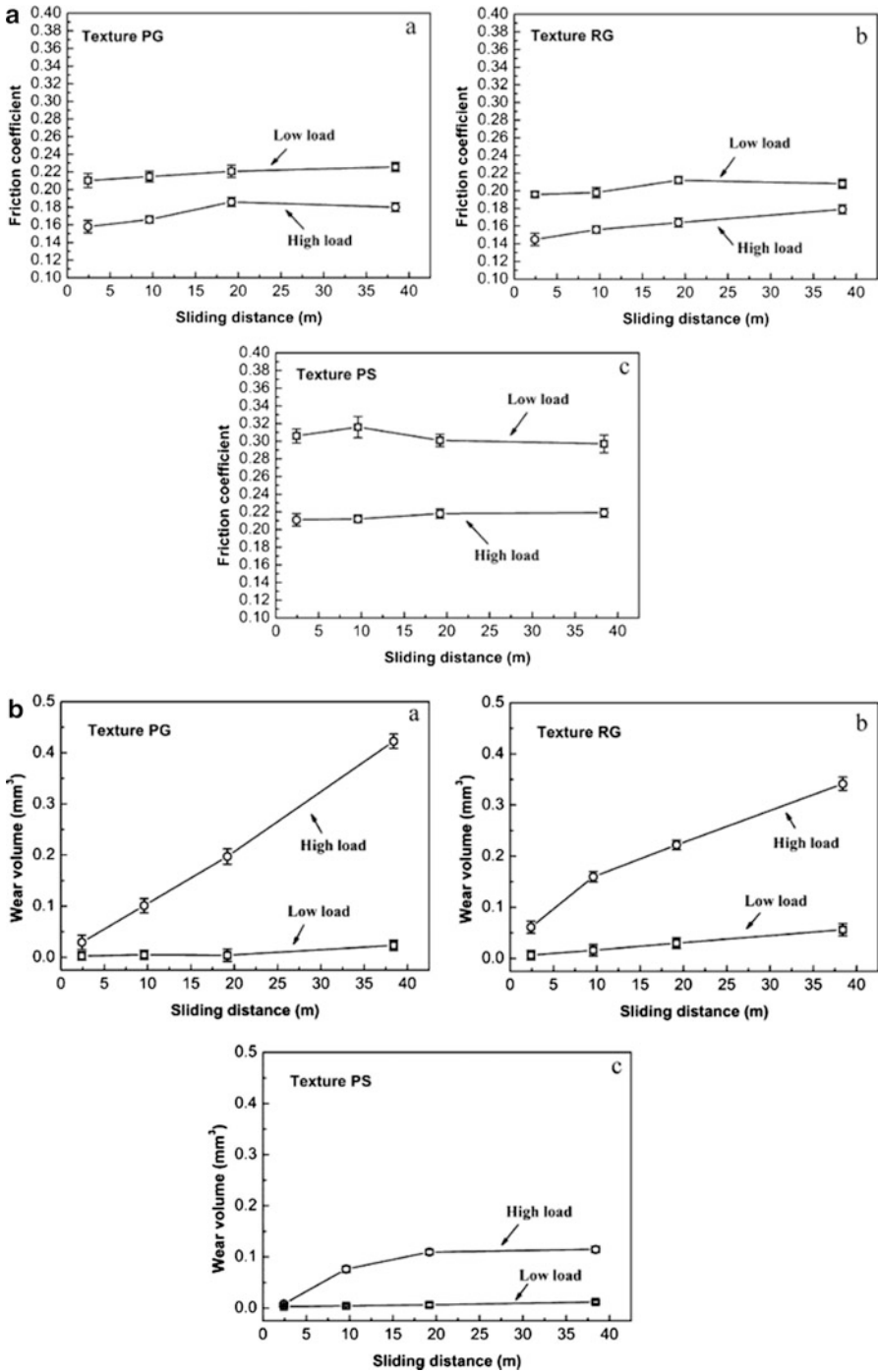
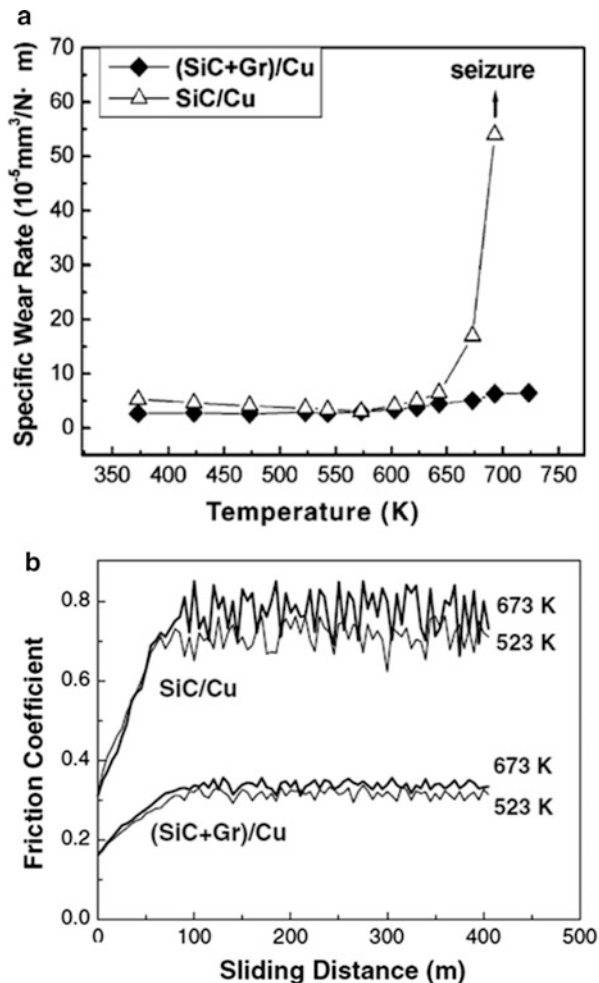


Fig. 11.9 Variation of average friction coefficient and wear rates with sliding distance for the pin sliding against various surface textures [40]

Fig. 11.10 (a) Variation of specific wear rate with temperature (b) variation of friction coefficient with sliding distance for various temperatures [41]



effectively avoided the occurrence of severe wear up to 723 K. The coefficient of friction of copper hybrid composites was more stable and lower than that of the SiC–copper composite. It was concluded that the graphite particles were an effective reinforcement material for copper matrix composites when subjected to high-temperature sliding wear conditions.

Various novel composites were developed to enhance self-lubricating properties of copper-based metal matrix composites for specific applications. Chen et al. [42] developed new composites with 1 and 2 wt% graphite for the use in frictional bearings under high speed and low-load sliding conditions. New copper-based self-lubricating composites with 1 and 2 wt% graphite were prepared using atomized Cu–10Ni–3Sn–3Pb (wt%) powder as the matrix alloy with 0.5 wt% Y₂O₃ as the matrix. Figure 11.11 shows the variation of friction and wear rate. It was found that

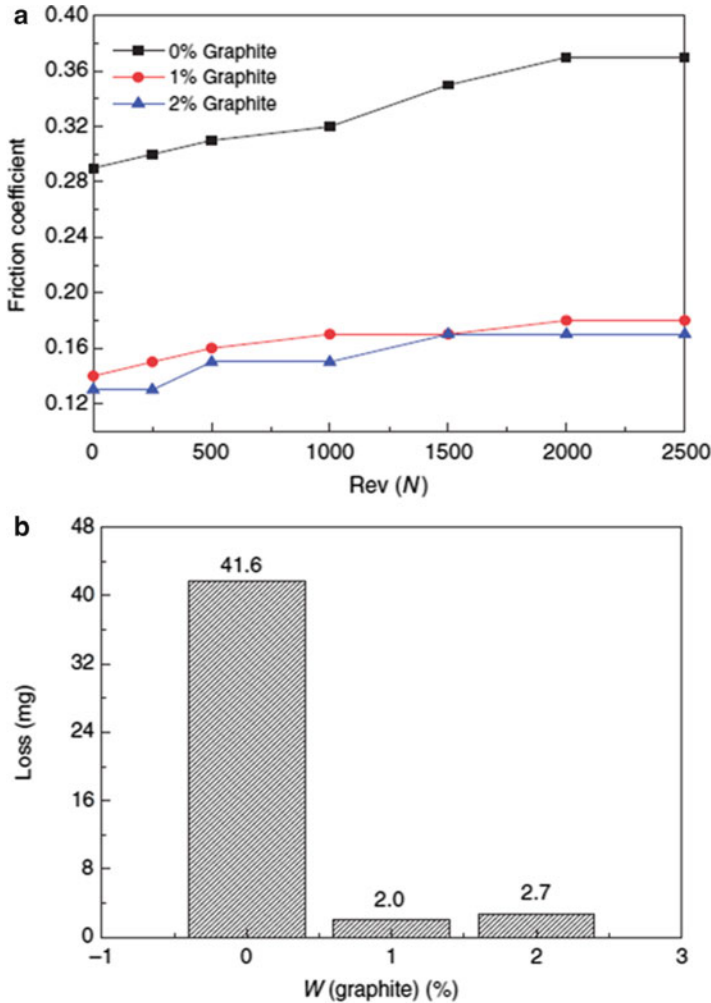


Fig. 11.11 (a) Friction coefficient and (b) wear loss of the composites with different graphite contents [42]

the composite with 1 wt% of graphite demonstrated improved mechanical and frictional properties, while the composite with a 2 wt% of graphite possessed better self-lubricating properties.

In another application of copper-based metal matrix composites, Ma et al. [43] studied the sliding wear behavior of copper-graphite composite material using a specially designed sliding wear apparatus. Here, the apparatus simulated the tribological conditions of sliding current collectors in a magnetic levitation (maglev) transportation system. The material was slid against a stainless steel band under unlubricated conditions. The investigation revealed that the wear loss increased

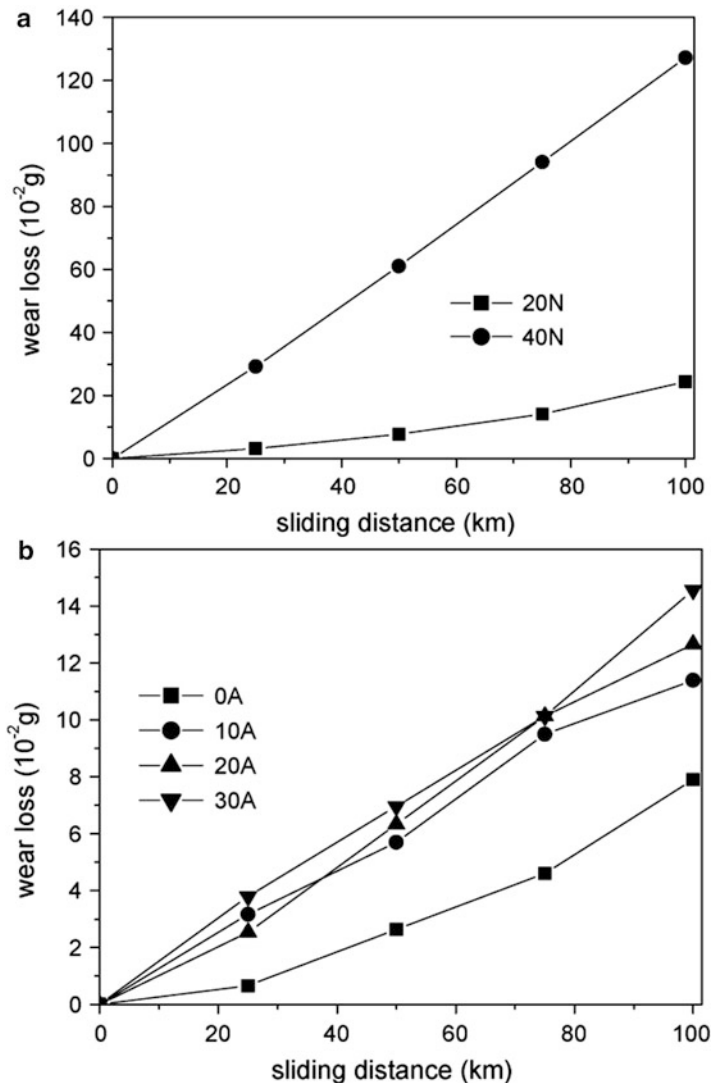


Fig. 11.12 Variation of wear loss with sliding distance as function of (a) normal load (b) current [43]

with the increasing normal pressure and electrical current. More specifically, at a sliding speed of 50 km/h and a cumulative sliding distance of 100 km without electrical current, the wear loss under a stress of 40 N is about five times to that with 20 N as shown in Fig. 11.12a. The wear loss almost doubled under electrical current, compared to the case without electrical current at an applied stress of 20 N and a sliding speed of 25 km/h as illustrated in Fig. 11.12b. Adhesive wear, abrasive wear, and electrical erosion wear are the dominant wear mechanisms

during the electrical sliding wear processes. The authors concluded that the results provide insight into understanding the governing principles that can add value to the design of sliding counterparts in the current collection device in magnetic levitation systems.

Copper–graphite composites have found use in various other applications such as in plane bearings for trucks, cranes, bulldozers, and automobiles; drive shafts and roller bearings for stoker chain feeds in boiler furnaces; screw conveyors; roller conveyors; spherical bushings for automotive transmissions; sliders for electric cars; overhead railways for dams and flood gates; slide bushings for discharge valves in hydraulic turbines; and electrical contacts and brushes. The complexity of each application of copper-based composites warrants unique and useful reinforcement materials that aid in achieving varying degrees of friction and wear necessary for system operation. As described these reinforcement materials can range from graphite particles dispersed in the metal matrix composite to zinc-coated graphite, hBN, TiC, and SiC.

2.3 Self-Lubricating Behavior of Nickel–Graphite Composites

Nickel–graphite composites are widely used in high-efficiency engines due to their excellent high-temperature performance. Considerable efforts have been made to study the effect of various operating parameters on the tribological behavior of nickel–graphite composites. Li and Xiong [44] studied the tribological performance of graphite-containing nickel-based composite as functions of temperature, load, speed, and counterface material. Figure 11.13 shows the variation of friction coefficients and wear rates for different graphite content, load, speed, and counterpart materials. It was observed that the friction and wear properties are significantly improved by adding graphite in a nickel-based alloy. The optimum addition of graphite is 6–12 wt% of the nickel-based alloy. The coefficient of friction of the nickel–graphite composite decreased with an increase of load and sliding speed. It was also revealed that the wear rates of the nickel–graphite composites increased with an increase of temperature and sliding speed. The lower friction coefficients and wear rates were obtained when the composites rubbed against nickel-based alloy containing molybdenum disulfide when compared to alumina and silicon nitride counterpart materials. Further, Li and Xiong [45] studied the tribological properties of nickel-based composites at various temperature conditions. More specifically nickel-based self-lubricating composites consisting of nickel (Ni), chromium (Cr), tungsten (W), and iron (Fe) with graphite and molybdenum disulfide as solid lubricant reinforcement materials were prepared. It was found that chromium sulfide and tungsten carbide were formed in the composite by adding molybdenum disulfide and graphite, which were responsible for low friction and

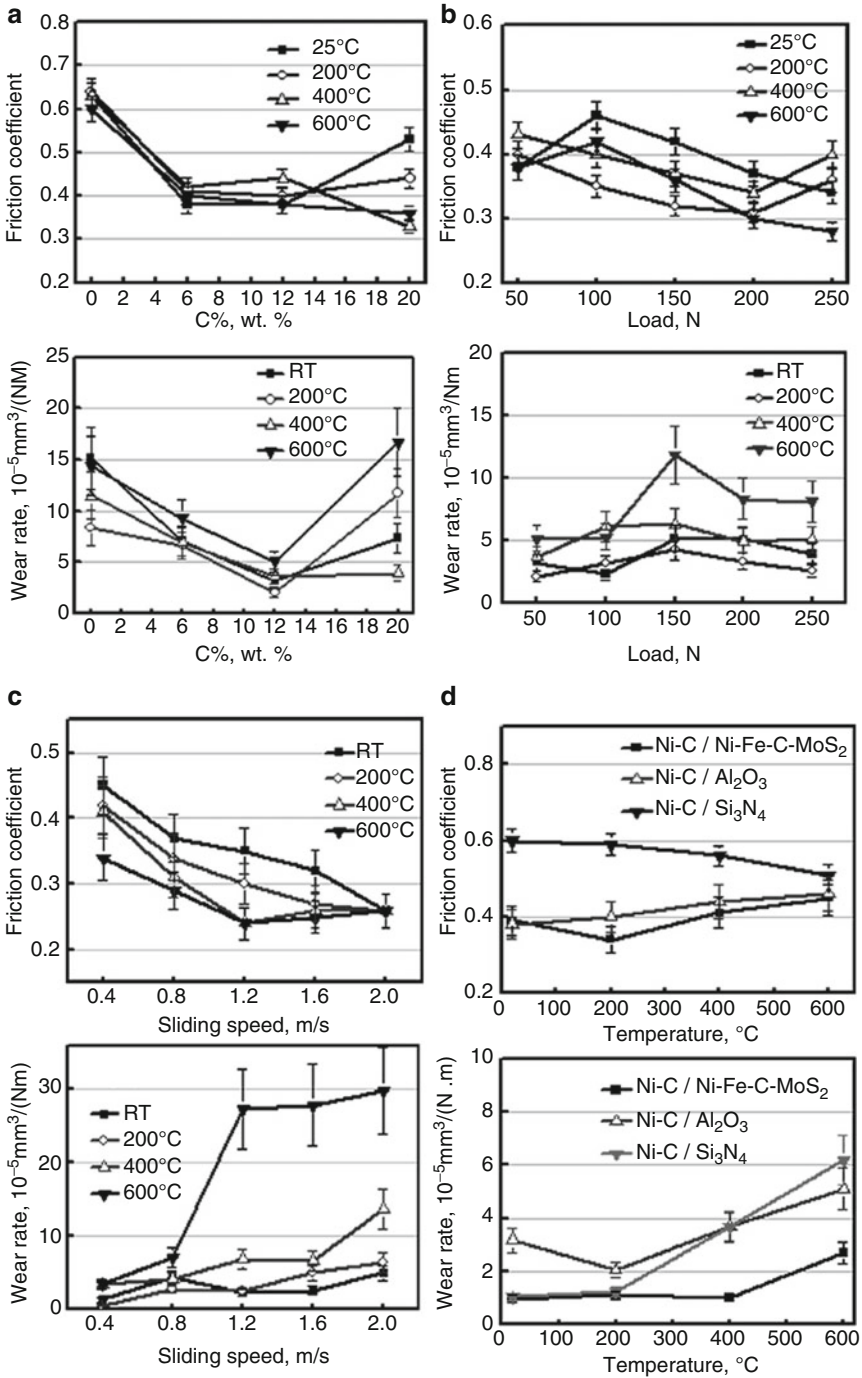


Fig. 11.13 Variation of friction coefficients and wear rates for different (a) graphite content, (b) load, (c) speed, and (d) counterpart materials [44]

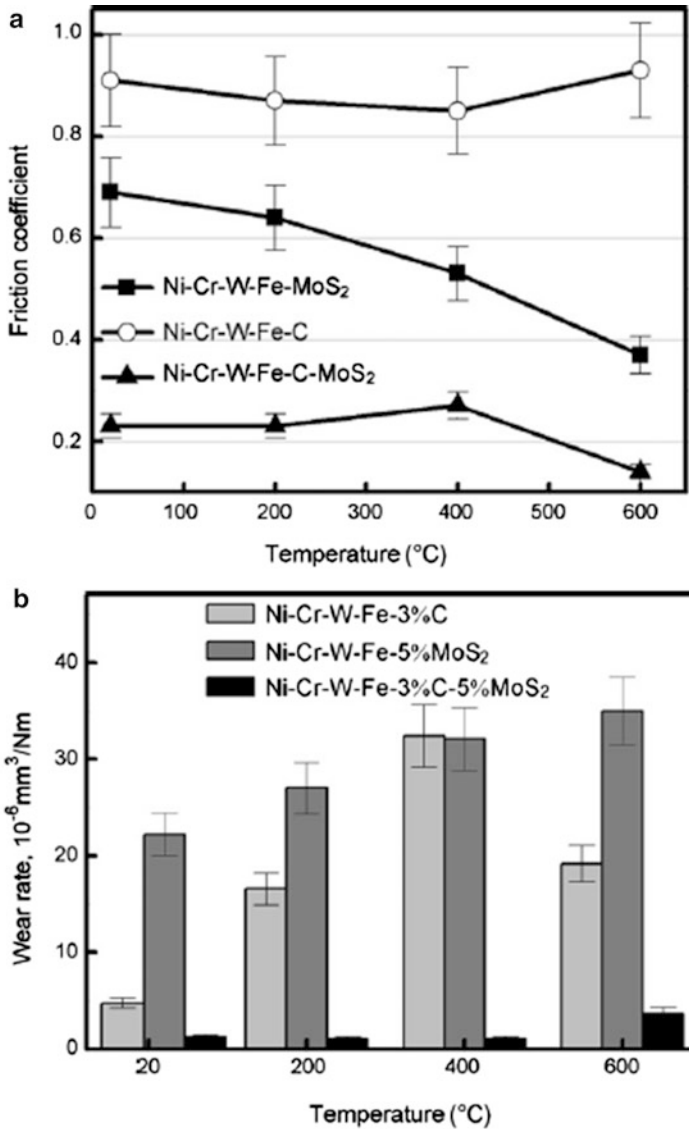


Fig. 11.14 Variation of (a) friction coefficients and (b) wear rates in the composites containing graphite and MoS₂ as lubricants [45]

high wear resistance at elevated temperatures, respectively. Figure 11.14 shows the variation of friction and wear rate for different composites containing graphite and MoS₂ as lubricants. The Ni-Cr-W-Fe-C-MoS₂ composite possessed excellent self-lubricating properties over a wide range of temperatures as a result of synergistic lubricating effect of graphite (C) and molybdenum disulfide (MoS₂). The graphite contributed to the dominant role of lubrication at room temperature, while

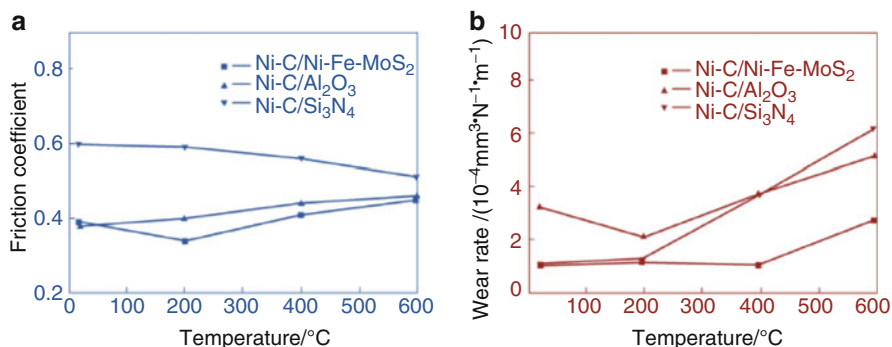


Fig. 11.15 Variation of (a) friction coefficient and (b) wear rate with temperature against different counterfaces [46]

the sulfides were responsible for low friction at high temperatures. Li et al. [46] studied the tribological properties of nickel–graphite composites against different counterfaces at elevated temperatures. Figure 11.15 shows the variation of coefficients of friction and wear rates of a 12 wt% graphite–nickel composite over various temperatures when rubbing against alumina (Al₂O₃) ceramic, silicon nitride (Si₃N₄) ceramic, and Ni–Fe–C–MoS₂ alloy under a load of 50 N and a velocity of 0.8 m/s. Compared with the counterface of alumina and silicon nitride, the friction coefficients and wear rates are lower when the composite rubs against the nickel-based alloy containing molybdenum disulfide. Wu et al. [47] studied the dry friction and wear behavior of Ni–P matrix composites with graphite (abbreviated Gr) and SiC particles. Figure 11.16 shows the variation of friction for the three composites. It was found that the Ni–P–Gr matrix composite had the lowest friction coefficient. The wear rates of the composites were found to be 0.5447, 0.0015, and 0.0152 (10⁻³ mm³/m) for Ni–P–Gr, Ni–P–SiC, and Ni–P–Gr–SiC, respectively. These results indicate that the Ni–P–SiC had the lowest wear rate. By comparison with Ni–P–Gr and Ni–P–SiC, the overall results indicate that the hybrid Ni–P–Gr–SiC composite had superior antifriction and wear resistance which is a result of the graphite-rich mechanical mixed layer (GRMML) formed on the contact surface. The graphite-rich mechanical mixed layer formed on the worn surface was responsible for enhanced lubricity, which allowed even the Ni–P–SiC to see improved results when graphite was added to the composite. When the SiC particles mixed with the graphite in the transfer layer, the SiC particles acted as a load-bearing support in protecting the graphite-rich mechanical mixed layer from easily shearing, thus maintaining improved friction reduction capabilities.

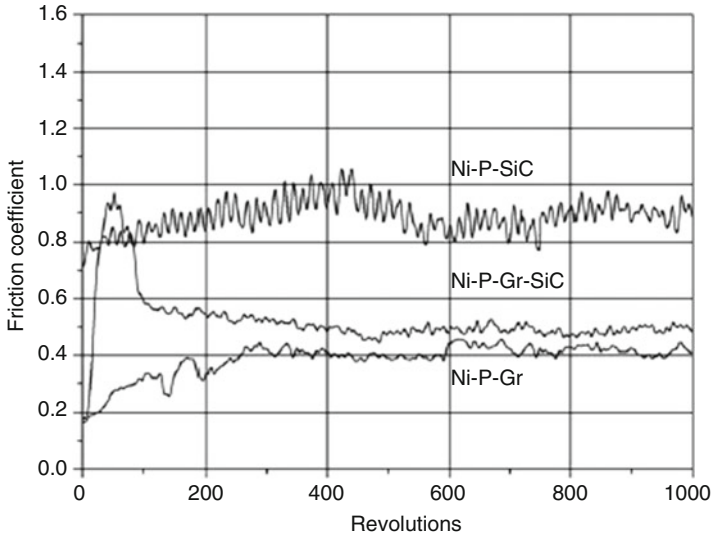


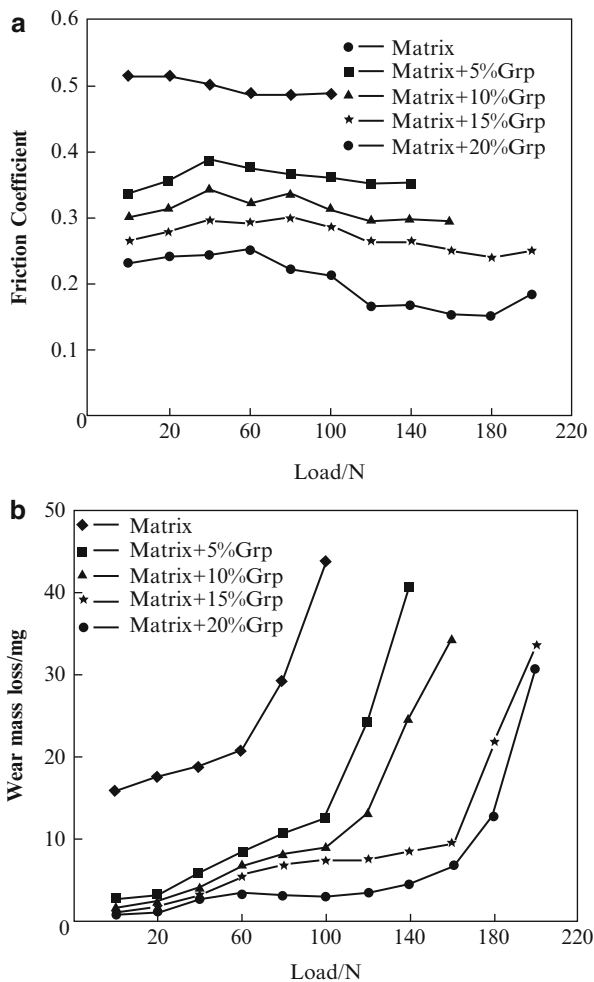
Fig. 11.16 The variation of friction coefficient of the Ni-P and Ni-P composites [47]

2.4 Self-Lubricating Behavior of Magnesium–Graphite Composites

Magnesium alloys are used in automobile and aerospace industries due to their low density, high specific strength, stiffness, good damping characteristic, excellent machinability, and ease of casting. Additionally, the poor corrosion and wear resistance of magnesium is a drawback that facilitates its primary use as an alloying agent to make aluminum–magnesium alloys. The most commonly used magnesium alloy is AZ91 alloy (consisting of 90 % magnesium, 9 % aluminum, and 1 % zinc). Magnesium alloy–graphite composites have found applications in pistons and space structural applications, thus expanding their versatility and use as self-lubricating metal matrix composites.

Attempts have been made to study the tribological performance of magnesium–graphite composites. Qi [48] studied the influence of graphite particle content on the friction and wear characteristics of an AZ91 magnesium alloy matrix composite. The variation of the friction coefficient of the composites normalized with respect to the base alloy as a function of the applied load against the hardened steel is shown in Fig. 11.17a. It can be seen that the coefficient of friction of the composites was much lower than that of the matrix alloy. The graphite content affects the friction coefficient of the composites, and the friction coefficients were revealed to reduce with increasing graphite content. In regard to the wear rate, the wear behavior of composites containing different contents of graphite particles has been determined and compared with that observed in the base alloy. Figure 11.17b shows the wear mass loss of the composites as well as the base alloy specimens as a

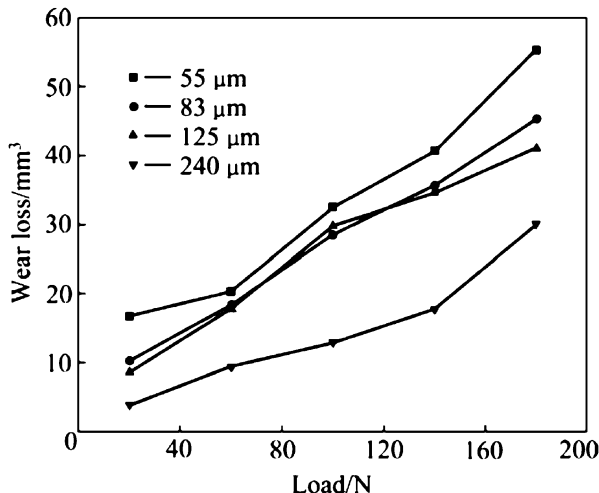
Fig. 11.17 Variation between (a) friction coefficient and (b) wear mass loss with load [48]



function of the applied load. The results showed that under similar testing conditions, the wear resistances of the graphite-containing composites are improved when compared to the based alloys that do not have graphite. The wear mass loss of each composite specimen reduces with the increase in graphite content. The investigations revealed that a continuous black lubricating film forms progressively on the worn surface during sliding, which effectively limits the direct interaction between the composite tribo-surface and the counterpart, and also remarkably delays the transition from mild wear to severe wear for the magnesium alloy graphite composites.

In regard to the influence of particle size on the tribological performance, Zhang et al. [49] studied the effect of graphite particle size on wear property of graphite

Fig. 11.18 Variations of wear loss with load of composites [49]

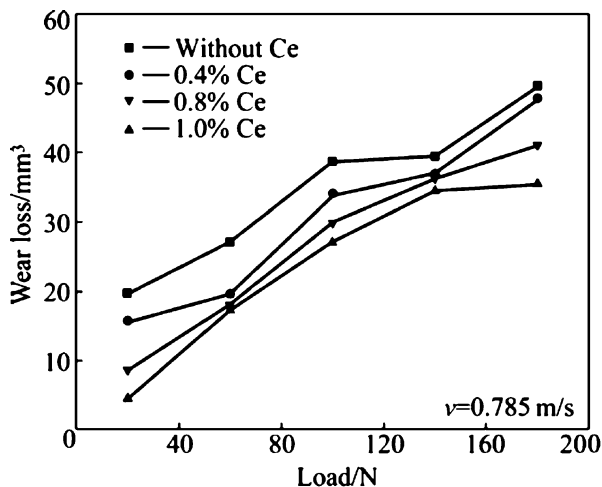


and alumina (Al_2O_3) ceramic-reinforced AZ91D–0.8 %Ce composite. Figure 11.18 shows the variation of wear loss with load. It was observed that the embedded graphite in the matrix acts as lubricant and decreases the wear loss. The wear resistance of the composite increased as the graphite particle size increased. At low loads, the composites have a low variation of wear loss; however, at high loads, the variations of wear loss of the composite are significant. It can be seen in the figure that the composite with the largest graphite particle size demonstrated superior wear resistance. The wear mechanism of all the composites at low load is abrasive wear and oxidation wear, and at high load, the wear mechanisms of the composites changed to delamination wear. In another study, Zhang et al. [50] investigated the effect of graphite content on the wear property of graphite/ Al_2O_3 /Mg–9Al–1Zn–0.8Ce composites. More specifically, the composites were studied for the influence of graphite content of 5, 10, 15, and 20 %. It was found that the wear resistance of the composites increased with increasing graphite content. Again, the wear mechanisms of the composites at low load were abrasive and oxidation wear, and at high loads the wear mechanism was delamination wear. Cerium (Ce) was found to play an important role in the magnesium–graphite composite. Zhang et al. [51] further investigated wear properties of graphite and Al_2O_3 -reinforced AZ91D–Cex composites. It was found that the wear resistance of the composites increased with an increasing Ce content as shown in the Fig. 11.19.

2.5 Self-Lubricating Behavior of Silver–Graphite Composites

Several metal matrix composites have been specifically designed for the use in electromechanical applications combining materials with excellent wear resistance and high electrical conductivity. These metal matrix composites are often

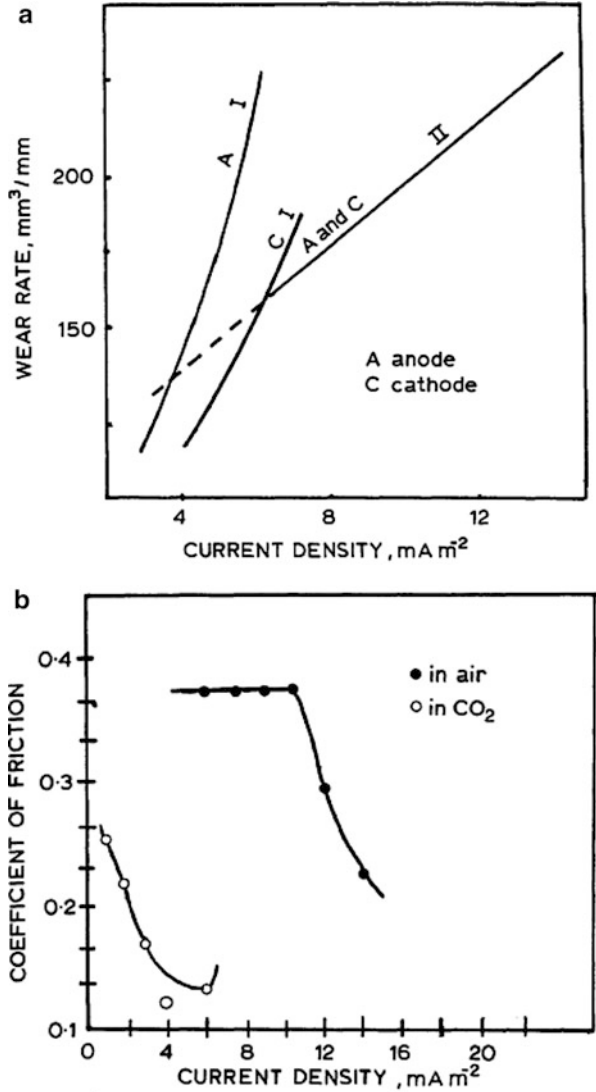
Fig. 11.19 Variations of wear loss of the composites with loads as a function of Ce content in the magnesium-graphite composite [51]



composed of copper-based metal matrices; however, in some applications, a silver based-graphite composite is used, especially for use in various electrical contacts. In electrical contact applications, the friction and wear behavior under sliding with electrical current flow can become quite complex when compared to that under purely mechanical sliding conditions. The amount of materials removed under sliding electrical contact is the sum of the contributions from purely mechanical wear in the absence of electrical current flow, arc erosion, and mechanical wear resulting from softening of the matrix by local heating caused by the electrical arcing. As reported in the literature [21, 52], in silver-graphite systems, the wear rate of composites increased with an increase of current density at both low and high temperatures, as shown in Fig. 11.20a. The figure shows that when there is a transition in the mode of sliding wear with temperature, the current density for the same wear is considerably higher while sliding at higher temperatures, compared with that observed during sliding at ambient temperature. The coefficient of friction decreased with the current density, as shown in Fig. 11.20b, both in air and in a CO₂ atmosphere.

The influence of pressure on the tribological behavior of the silver-graphite composites has been studied by Feng et al. [53] who investigated the effect of pressure on the friction and wear properties of carbon nanotube-silver-graphite composites with and without 10 A/cm² of current. The results showed that the mechanical wear of composites increased with an increase of pressure, but the electrical wear of composites varied in the shape of U with an increase of pressure (Fig. 11.21a). The electrical wear is shown to be significantly higher than mechanical wear by a factor of 6–20. The differences between the with-current electrical wear and without-current mechanical wear are due to the Joule heat released in the friction zone which leads to breakdown of the lubricating film, roughening of the surface, and intensification of the adhesive interaction at the contact spots. The coefficient of friction of metal matrix composites with electrical current is greater than metal matrix composite without electrical current as shown in Fig. 11.21b.

Fig. 11.20 (a) Variation of wear rate with current density at ambient and elevated temperatures; I is observed below 100 °C, but II is observed at elevated temperatures, above 100 °C. (b) Reduction in coefficient of friction of Ag-25 vol.% graphite composite with current density in air and CO₂ atmosphere [21]



Silver-graphite composite brushes are known for their low noise level, low and stable contact resistance, low friction, and high conductivity. In modern inertial energy storage devices (e.g., homopolar motor generators), a large amount of energy is stored and the energy is delivered in the form of low voltage, high current pulses. Silver-graphite brushes are suitable for such systems. Silver-graphite brushes suppress radio interference noise level and are useful for slip rings, segmented rings, and other applications where similar requirements justify the

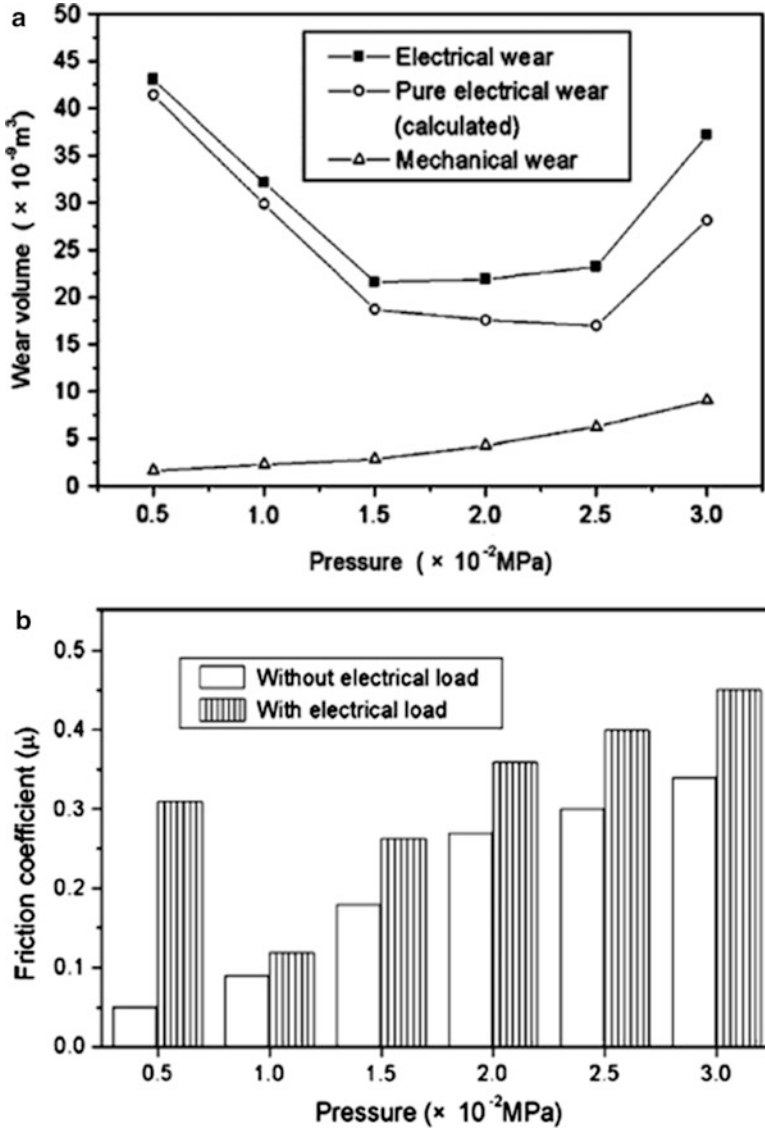


Fig. 11.21 Effect of pressure on (a) wear rate and (b) friction coefficient of carbon nanotube-reinforced silver-graphite composite under mechanical and electrical wear [53]

high material cost. Often silver-graphite composites are used in electromechanical applications that encounter severe detrimental effects caused by current erosion or electrical heating. Silver-based metal matrix composites can often minimize the effects of electrical current and maintain desirable tribological properties.

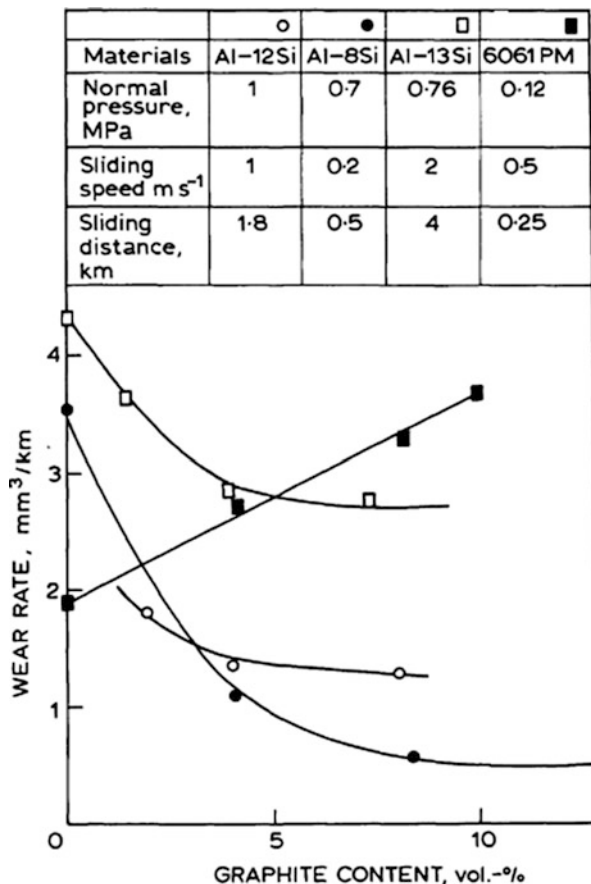
2.6 Self-Lubricating Behavior of Aluminum–Graphite Composites

Aluminum alloys are promising materials in high-technology automotive fields due to their excellent specific mechanical and physical properties such as low density, good resistance to corrosion, and low thermal expansion. However, their low resistance to wear under poor lubricating conditions and their severe seizure and galling under boundary lubrication conditions are major concerns for their use in high-performance tribological applications. With solid lubricant particle dispersion in the matrix of an aluminum alloy, this material can exhibit improved wear resistance and consequently become more suitable for high-performance tribological applications [54, 55].

Considerable efforts have focused on incorporating solid lubricating particles in aluminum alloy matrices to improve friction, wear, and anti-seizing properties. Researchers have identified graphite as a suitable solid lubricating material for the preferred applications. These self-lubricating aluminum alloy–graphite particulate composites have received attention because of their low friction and wear, reduced temperature rise in the tribo-interface, improved machinability, excellent anti-seizure effects, low thermal expansion, and high damping capacity. The variation of the coefficient of friction with graphite content for an Al–SiC–graphite composite is shown in Fig. 11.1. Figure 11.22 shows the variation of wear rate with graphite content for different Al–Si alloys reinforced with graphite. It can be seen that the coefficient of friction and the wear rate decrease with increasing graphite content as seen in Figs. 11.1 and 11.22, respectively. As the graphite content continues to increase, the friction and wear values plateau once the graphite film completely covers the sliding surface. It is speculated that the wear rate may increase when graphite content in the matrix exceeds a critically high value that can cause a decrease in the strength of the matrix. This scenario can lead to the formation of a thick graphite film, which in itself can wear by delamination within the film in a manner similar to that of bulk graphite. It is interesting to observe in Fig. 11.22 that for the case of 6061 alloy prepared by powder metallurgy method, a phenomenon occurs where the wear rate increases with increasing graphite content. Recently, Baradeswaran and Elayaperumal [56] studied this phenomenon by investigating the effect of graphite content on tribological behavior of aluminum alloy–graphite composites. The 6061 aluminum alloy–graphite composite with graphite particle dispersions up to 20 % was used. Here, the composites were prepared by a casting method. As illustrated in Fig. 11.23a, the wear rate of the composites decreased with an increasing graphite content which is in contrast to the result presented by the previous authors in Fig. 11.22 [21].

The coefficient of friction of 6061 aluminum alloy–graphite composite was also found to decrease with the addition of graphite particles as a reinforcement material and recorded a 2.5 times lower friction value than the base alloy (Fig. 11.23b). It was also revealed that the wear loss was found to decrease with increasing sliding speed. Like other Al–SiC alloy–graphite composites, the 6061 aluminum alloy

Fig. 11.22 Variation of wear rate with graphite content in aluminum alloy matrix [21]



exhibits its potential to act effectively as a matrix material for a self-lubricating composite under dry sliding conditions, due to the formation of the graphite-based transfer film.

It is reported earlier that the wear rate is also a function of sliding velocity in composites. Figure 11.24 shows the variation of wear rate with sliding velocity in Al-Si alloy-graphite composite and compares it with that of the respective base alloys without the presence of graphite. As the sliding speed increases, the interface temperature also increases resulting in (a) the formation of oxides on the sliding surface and (b) a decrease in the flow stress. In addition, there may be microstructural changes such as dissolution of precipitates, which would also be reflected in the wear behavior. In Fig. 11.24, it is interesting to note that the composite with only 5 vol.% of graphite retains relatively the same trend of wear rate with sliding speed as that of the base alloys. Conversely, the composite with 15 vol.% of graphite shows a drastically different trend to that of the base alloys. This trend is an indication that the sliding surface might have been largely covered by graphite film so that the wear rate

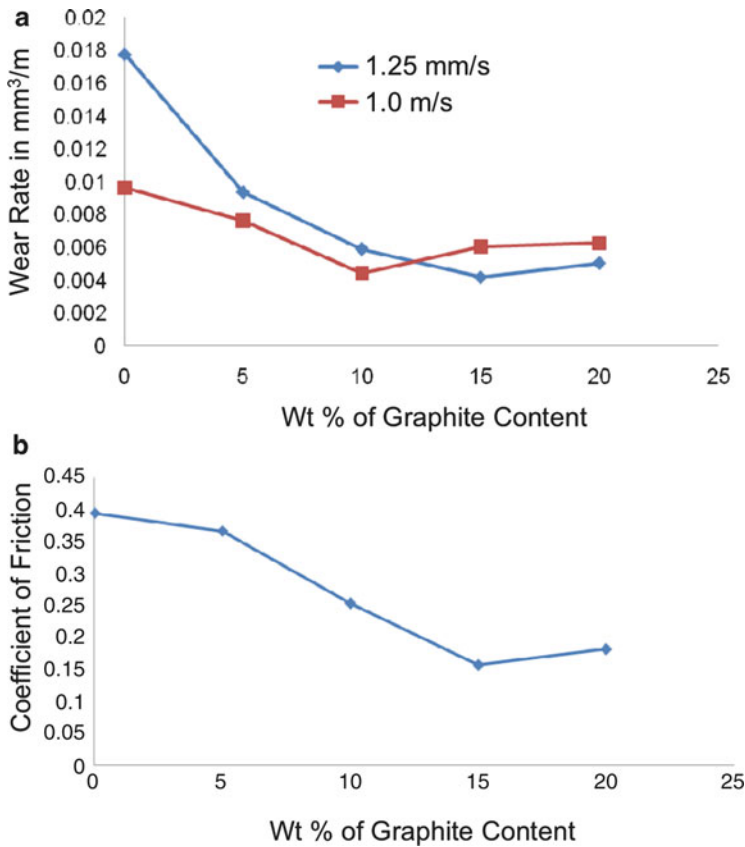


Fig. 11.23 Variation of (a) wear rate and (b) friction coefficient with graphite content [56]

becomes almost unaffected by changes in sliding speed under the given test conditions. When the graphite content is low, the sliding interface is insufficiently covered by the graphite-rich film, and the wear characteristics are similar to that of the matrix. Normal load is another important parameter that influences the wear rate of composites. The variation of wear rate with normal load in Al–Si alloys composites is shown in Fig. 11.25. Results demonstrated that the wear rate increases with increasing normal loads for all materials.

Efforts have been made to study various aluminum–graphite composites using different testing variables and conditions. For example, Akhlaghi and Zare-Bidaki [20] studied the influence of graphite content on wear behavior of Al 2024–graphite composites during dry sliding and oil-impregnated sliding. The variation in the measured coefficient of friction and wear rate with the weight percent of graphite in the composites for both dry sliding and oil-impregnated sliding are shown in Fig. 11.26. It was found that an increase in graphite content reduced the coefficient of friction for both dry and oil-impregnated sliding, but this effect was more

Fig. 11.24 Variation of wear rate with sliding speed for Al-Si alloy-graphite particle composites and corresponding base alloys [21]

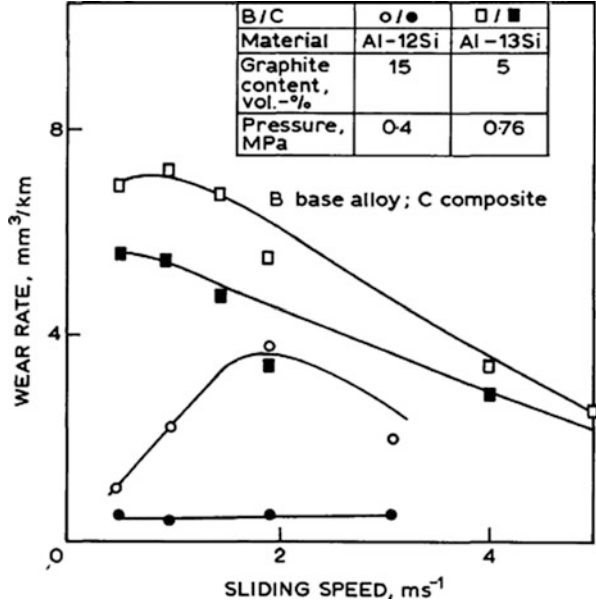
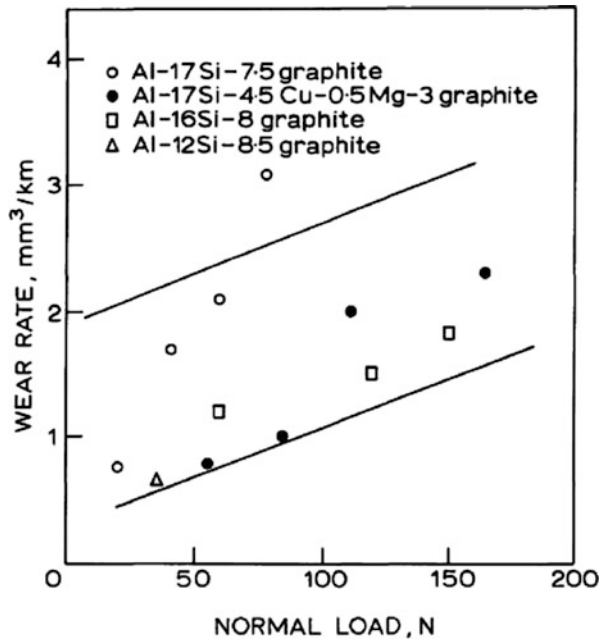


Fig. 11.25 Variation of wear rate with normal load for Al-Si alloy-graphite particle composites [21]



pronounced in dry sliding. Under dry sliding, the wear rate of the Al 2024-5 wt% graphite is about ten times lower than that for the base alloy. However, for composites with 10 wt% or more of graphite particle reinforcement material, the wear rate increased. The change in the wear rate for specific amounts of graphite

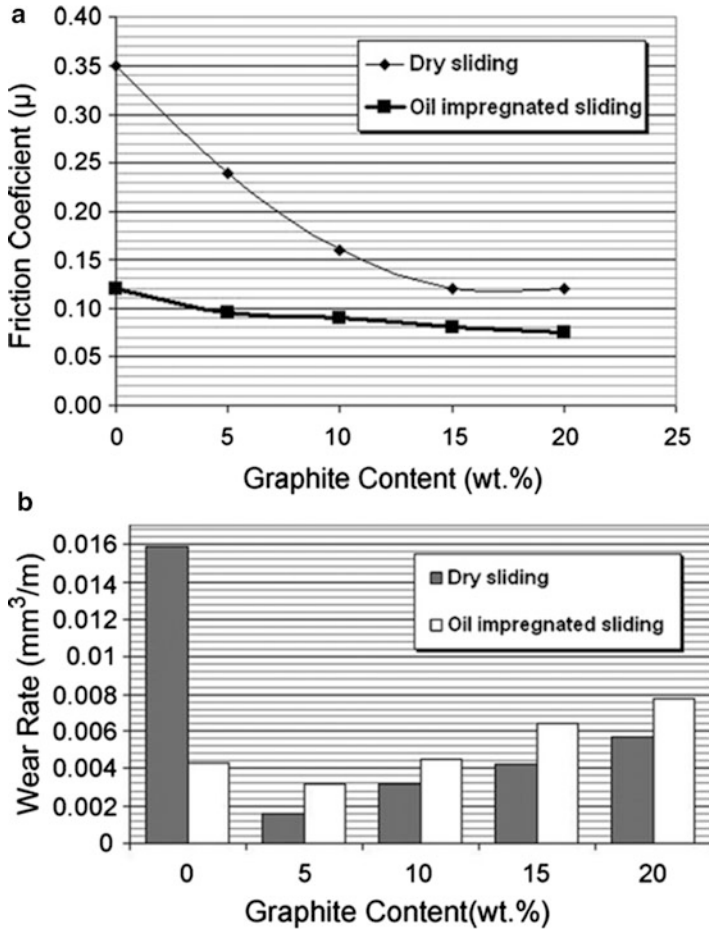
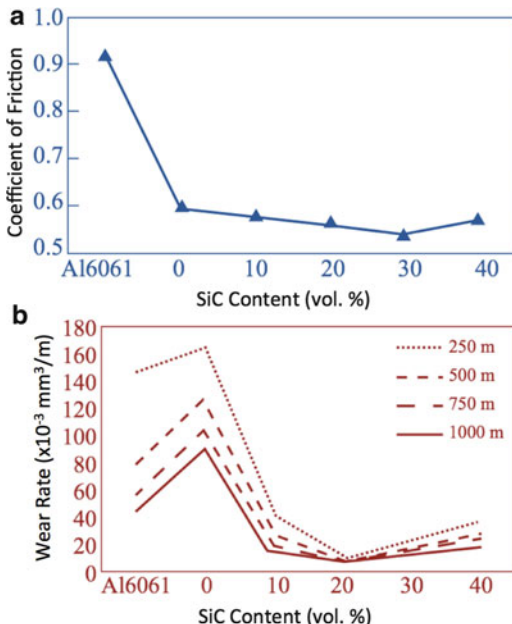


Fig. 11.26 The variation of (a) friction and (b) wear rate with the graphite content in the composites for both dry sliding and oil-impregnated sliding [20]

particle reinforcement material was caused by the following two competing factors: first, the beneficial effect of the graphite in reducing the wear of the composites due to formation of a thin lubricating graphite-rich film on the tribo-surface and second, the adverse effects of graphite in the formation of porosity and cracks as well as the deterioration of mechanical properties resulting in enhanced delamination. As shown in Fig. 11.26, for dry sliding, the coefficient of friction begins at 0.35 for the base alloy and decreases with an increasing graphite content reaching a final value of about 0.12 for composites containing 15 wt% graphite which is about one-third that of the base alloy. Additionally, the figure also shows that there is no significant difference in the friction coefficient between composites with 15 wt% and those with 20 wt% graphite content. The reason for this reduction in the coefficient of friction is attributed to the presence of the smeared graphite layer at the sliding

Fig. 11.27 Dependence between content of SiC in Al/SiC/Gr hybrid composites with 9 % graphite and (a) friction coefficient and (b) wear rate [59]



surface of the wear sample, which acts as a solid lubricant. This lubricant film prevents direct contact of the two surfaces.

Studies were also made to investigate the tribological behavior of hybrid aluminum–graphite composites. Suresha and Sridhara [57, 58] studied wear characteristics of hybrid aluminum matrix composites reinforced with graphite and silicon carbide particulates. In tribological applications demanding similar strength requirements, the authors [57, 58] reported that Al–SiC–graphite hybrid composites are better substitutes to Al–graphite or Al–SiC composites owing to an improved wear resistance and coefficient of friction as a result of the combined reinforcement of SiC and graphite particulates. Recently, Stojanovic et al. [59] investigated the tribological properties of aluminum matrices reinforced with SiC and graphite (Gr). In these studies, the hybrid composites showed that the friction coefficient and wear rate of the composite decreased with an increase in SiC and graphite content. Figure 11.27 shows the influence on the coefficient of friction and wear rate of the SiC content in the Al–SiC–Gr hybrid composite with 9 % of graphite. A maximum amount of SiC and graphite was permissible up to 20–30 %, before the effects of the reinforcement material became detrimental to the composite causing the coefficient of friction and wear rate to increase.

In another study, in contrast to previous research, Babic et al. [60] investigated the tribological characteristics of hybrid composites with aluminum-based A356 reinforced with silicon carbide and graphite material. Here, the hybrid composites consisted of 10 % SiC and 1 % graphite were subjected to various normal loads, speeds, and sliding distances to characterize their tribological performance. The results of this study revealed that the influence of the SiC and graphite

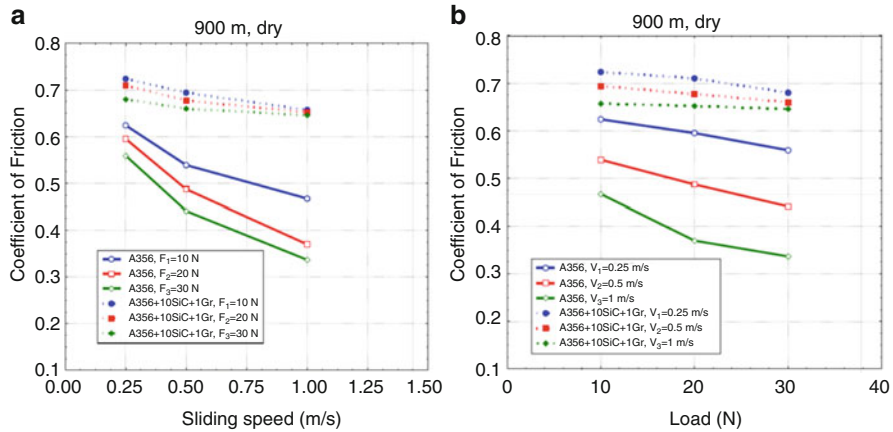


Fig. 11.28 Coefficient of friction dependence of sliding speed for different conditions of dry friction, (a) sliding speed and (b) normal load [60]

reinforcement material did not improve the coefficient of friction as seen in Fig. 11.28. In fact, the hybrid composites performed worse than the original matrix causing the friction values to increase with the addition of the reinforcement material. When a lubricious reinforcement material such as graphite is mixed with SiC, it can cause the coefficient of friction to increase for some aluminum matrices. These results could be due to the low quantity of graphite reinforcement material, the development of a poor graphite transfer layer, or the effects of wear debris.

Attempts were made to study the tribological behavior of the composites with higher graphite content under various environments. Goto and Uchijo [61] conducted wear tests of an Al–Si alloy impregnated with a high content (56 vol.%) of graphite reinforcement material. These Al–Si alloy matrix composites containing graphite were slid against bearing steel in various gas environments to investigate the wear mechanisms. The composites exhibited a decrease in wear at high loads in moist air. The wear rate was initially high at a low relative humidity (RH). The wear rate then decreased with an increasing RH to a minimum value at the median of the RH, and lastly, the wear rate increased slightly at a higher RH value. The wear rate in moist argon is approximately equal to one-third of the wear rate in moist oxygen. At the RH for the minimum wear, wide compacted transfer films consisting of graphite and metallic wear particles were formed on the disk sliding surface due to smearing of the graphite particles. These films prevent the sliding surfaces from metal-to-metal contact. The entrance of wear particles onto the contact surfaces causes the pin lifting, leading to an apparent decrease in wear.

The influence of graphite particle size on the tribological performance of the composites was also investigated. Jinfeng et al. [62] studied the effect of graphite (abbreviated Gr) particle reinforcement on dry sliding wear of SiC–Gr–Al composites. The aluminum alloy matrix composites composed of 40 % SiC, 5 % graphite, and 55 % Al with various sizes of graphite particles were fabricated by squeeze casting technology. The friction and wear properties of these aluminum matrix composites were

investigated as well. Results showed that after the addition of graphite, the coefficient of friction of the composites decreased and the wear resistance increased by 170–340 times. In addition, wear resistance was improved by increasing the graphite particle size, which is attributed to the enhancement of integrity of the lubrication tribo-layer composed of a complex mixture of iron oxides, graphite as well as fractured SiC particles and some fine particles containing aluminum.

It is well known that there have been a number of publications in the literature on the sliding wear and friction of aluminum alloy–graphite composites. Unfortunately, different researchers have used different experimental parameters for hardness and roughness of the counterface, sliding speed, normal load, and the test environment, making it difficult to quantify the effect of graphite content on the tribological performance of the composites. In addition, comparing empirical wear data to theoretical generalizations of wear behavior is often difficult because of the widely different test conditions employed by various researchers to characterize the tribological properties of the composites. Despite the lack of universal testing procedure, useful generalizations concerning wear behavior of different materials including composites have been applied by constructing wear mechanism maps. Wear maps serve as predictive tools to draw meaningful conclusions relative to wear behavior under different test conditions. Specifically, some of the variations between different studies can be overcome by utilizing normalized test parameters such as nondimensional wear rate, load, and sliding velocity. Hence, normalized wear rates (i.e., composite to the base matrix alloy) were introduced to analyze the data from different studies. Figure 11.29 is a compilation of the normalized friction coefficient and wear rate data of aluminum alloy–graphite composite showing the reduction in friction and wear volume due to graphite particle dispersion [63]. As shown in the figure, the aluminum alloy–graphite composites typically exhibit a much lower friction coefficient when compared with that of the matrix alloy. The coefficient of friction decreases considerably, up to about 3 % by weight of graphite, and thereafter remains constant at about 0.2 (0.5 on a normalized scale).

Although aluminum graphite composites possess a number of superior tribological properties, there are some drawbacks. For instance, graphite loses its lubricity in dry environments. In many aerospace applications where the tribo-components are expected to perform in a vacuum, this could be a limitation. Despite the few deficiencies of graphite, aluminum alloy composites reinforced with graphite have applications in cylinder blocks, journal bearings, connecting rods and pins, fan bushings, and internal combustion engines. Aluminum–silicon composites are used in pistons and liners in two stroke and four stroke engines in passenger cars as well as in race cars.

2.7 Conclusion

The self-lubricating behavior of various graphite-reinforced metal matrix composites was reviewed. The variety of applications and use of metal matrix composites stems from the variety of composite materials in the form of copper–graphite,

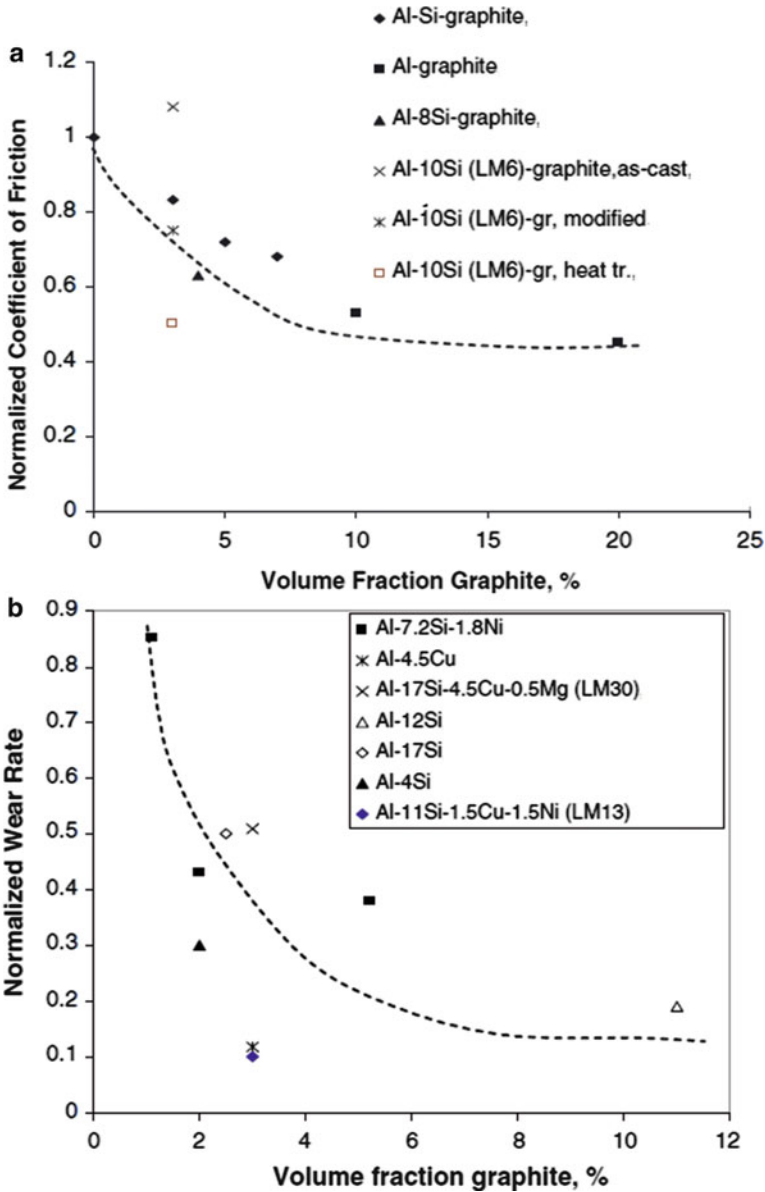


Fig. 11.29 Normalized (a) friction coefficient and (b) wear rate of aluminum–graphite composites [63]

nickel–graphite, magnesium–graphite, silver–graphite, and aluminum–graphite. Each of these composite materials presents a unique set of tribological properties and offers a unique application to take advantage of the self-lubricating properties of metal matrix composite. The complexities of each metal matrix composite achieve varying degrees

of friction and wear necessary for different systems to operate in environments where liquid lubricants are impractical. As described, the reinforcement materials can range from graphite particles dispersed in the metal matrix composite to zinc-coated graphite, hBN, TiC, alumina, and SiC. Ultimately, the incorporation of graphite-based reinforcement materials allowed the metal matrices to overcome friction and wear while achieving successful operation in the desired environments.

3 Self-Lubricating Behavior of Ceramic–Graphite Composites

3.1 Introduction

Self-lubricating composites are not only derived from metal matrices, but they can also be fabricated from ceramic matrices to produce self-lubricating ceramic composites reinforced with solid lubricant additives. Ceramic composites composed of silicon nitride and alumina are the most common of ceramic matrix materials and are used in a variety of specialized applications. Ceramics are often considered for engineering applications that require the use of advanced structural materials undergoing sliding or rolling behavior at elevated temperatures or in severe environments. Ceramics offer unique physical and mechanical properties such as low density, high hardness, high wear resistance, ability to retain strength and hardness at high temperatures, and corrosion resistance [64]. Investigations into the tribological performance of ceramic materials have shown that they exhibit high coefficients of friction between 0.5 and 0.8 in unlubricated sliding conditions [65–69]. In liquid lubricated conditions, ceramic materials have shown reductions in the coefficient of friction to significantly lower values of approximately 0.1 [70–75]. Many of the applications that require the use of ceramics (i.e., elevated temperatures or vacuum environments) are beyond the tolerable domain of liquid lubricants. For this reason, to achieve the desired levels of friction, solid lubricants are often utilized to meet the operational needs. The use of solid lubricants with metals is quite detailed in the literature through various applications as thin films on substrates by burnishing [7, 9], sputtering [11, 12], or plasma spraying [13, 14]. More recently, the use of solid lubricants with ceramic materials has garnered interest [76–79].

3.2 Self-Lubricating Behavior of Alumina–Graphite Composites

The study of friction and wear behavior of α -alumina coated with a thin film of silver by ion-assisted deposition techniques was investigated by Erdemir et al. [76]. This research demonstrated significant improvements in the wear

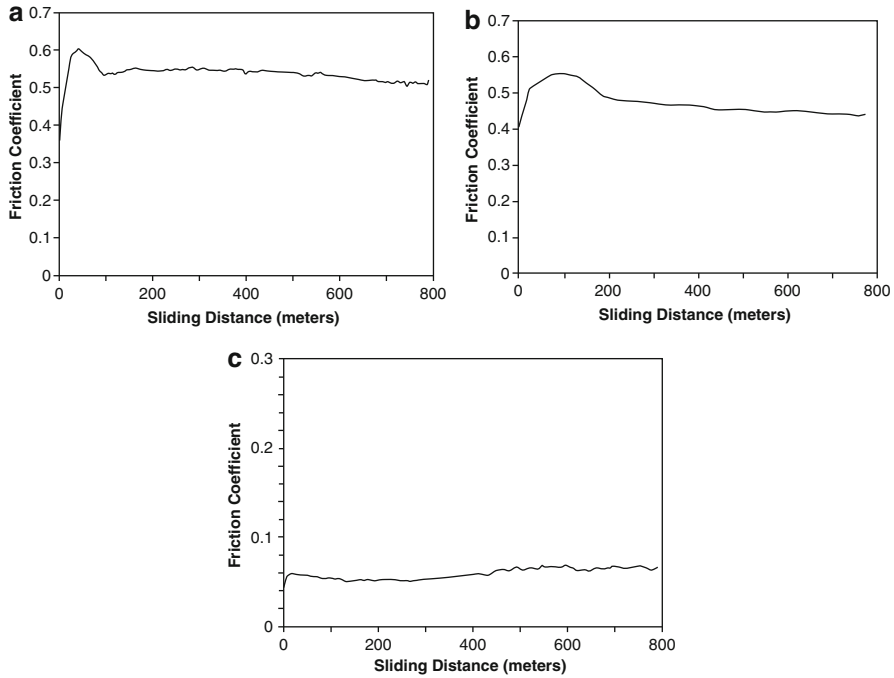


Fig. 11.30 Friction traces of (a) alumina, (b) alumina–graphite composite, and (c) graphite [64]

resistance for the silver-coated alumina but not for the steady-state coefficient of friction, which remained to be high, approximately 0.4. Although there was a slight improvement in the coefficient of friction when compared to the uncoated alumina material, the friction was still too high for practical applications. The tribological behavior of a glass–ceramic matrix reinforced with graphite fibers was studied [79]. It was revealed that the addition of the graphite fibers to the ceramic matrix did not provide adequate lubrication due to the high elastic modulus of the graphite fibers. Tests of alumina–graphite composites sliding on a 52100 steel ring revealed that the coefficient of friction was marginally reduced by the presence of the graphite reinforcement material as well. To further study the effects of graphite in alumina, another study by Gangopadhyay and Jahanmir [64] investigated the friction and wear characteristics of alumina–graphite matrix composites. In this study, alumina matrices were fabricated with small holes that were then mechanically filled with NiCl_2 intercalated graphite powder under high pressure to produce a self-lubricating composite. Friction tests were conducted and it was determined that the addition of graphite to the alumina matrix composite marginal reduced the coefficient of friction as seen in Fig. 11.30a, b. It can be seen in Fig. 11.30c, that graphite by itself has an extremely low coefficient of friction under similar conditions, illustrating the lubricious nature of the solid lubricant. The lack of a decrease in the coefficient of friction for the alumina–graphite composite can

be explained by the presence of steel wear particles that inhibited the formation of the graphite transfer layer. The steel wear debris physically covered the graphite regions within the composite thus retarding the lubricating properties of the graphite.

3.3 Self-Lubricating Behavior of Silicon Nitride–Graphite Composites

Wedeven et al. [77] and Pallini et al. [78] investigated the frictional behavior of solid lubricated silicon nitride balls sliding against silicon nitride disks. Here, solid lubrication was maintained by burnishing graphite-impregnated phosphate salts on both silicon nitride surfaces prior to testing. These studies have shown the success of deposited solid lubricant films on ceramics to minimize friction and wear. However, these lubricious protective films are only effective as long as they remain in the tribo-interface. For this reason, researchers have begun studying the effects of utilizing graphite reinforcement materials in ceramic matrices to establish a continuous supply of solid lubricant material at the tribo-interface [79–81]. Gangopadhyay et al. [80] investigated the use of a silicon nitride matrix reinforced with NiCl_2 -intercalated graphite pins pressed into the matrix to create a ceramic–graphite composite with improved lubricity. Tests of the silicon nitride–graphite composite sliding on a 52100 steel ring counter-surface revealed that the coefficient of friction of the silicon nitride–graphite matrix composite had a reduction from 0.45 to 0.17. Here, the presence of silicates was found in the transfer film. Unlike alumina–graphite composites that showed negligible improvements due to the presence of graphite, tests involving silicon nitride composite showed dramatic improvements due to the graphite reinforcement material being able to establish a transfer film. The highly lubricious graphite-based transfer films that developed were determined to be the underlying cause for the reduction of friction in the silicon nitride composites. To further study the effects of graphite in ceramics, another study by Gangopadhyay and Jahanmir [64] investigated the friction and wear characteristics of silicon nitride–graphite composites. In this study, silicon nitride was again reinforced with a NiCl_2 -intercalated graphite powder reinforcement material under high contact pressure from a tool steel die to produce a self-lubricating composite. Here, the NiCl_2 -intercalated graphite was pressed into two, three, and four predrilled holes on the contact surface of the silicon nitride matrix. Friction tests were conducted, and it was determined that the addition of graphite to the silicon nitride matrix composite drastically reduced the coefficient of friction as seen in Fig. 11.31a, b from 0.43 to 0.17. The decrease in the coefficient of friction for the silicon nitride–graphite composite is a result of the formation of the lubricious graphite transfer layer consisting of materials from both contacting surfaces (i.e., consisting of graphite, iron oxide, and the silicates).

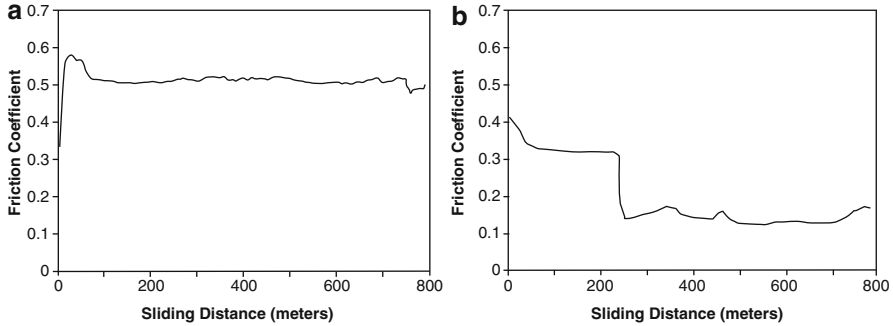


Fig. 11.31 Friction traces of (a) silicon nitride and (b) silicon nitride-graphite composite [64]

3.4 Conclusions

Research into the use of self-lubricating ceramic matrix composites has revealed that the selection of the ceramic matrix and the counterface material are as important as the selection of the solid lubricant reinforcement material. Selection of proper materials is important to (1) ensure the solid lubricant regions do not become covered by wear debris and (2) allow the formation of the lubricating transfer films in the tribo-interface. Ultimately, the advantage of self-lubricating composites over the deposition of thin solid lubricating films on ceramic substrates is the ability to have a constant supply of solid lubricant that is maintained as the matrix material wears. Self-lubricating matrix composites minimize the possibility of failure when compared to the material deposited by solid lubricant films that fail after the film has worn away.

4 Conclusions

Self-lubricating composite materials have the ability to sustain low friction and wear without any external supply of lubricants. The lubricants that are used for the tribological applications in automotive and manufacturing sectors are oil or grease based. These lubricants can introduce significant quantities of pollutants into the environment. In addition, friction and wear often lead to heat and chemical contamination to the environment. The development of self-lubricating composite materials is very important for green or environment-friendly tribology. Additionally, the use of self-lubricating composite materials allows for a practical lubrication mechanism in advanced application at elevated temperatures or vacuum environments that are beyond the tolerable domain of liquid or grease-type lubricants.

The tribological behavior of metal and ceramic matrix composites reinforced with graphite particles has been reviewed. More specifically, the tribological properties of copper–graphite, nickel–graphite, magnesium–graphite, silver–graphite, aluminum–graphite, silicon nitride–graphite, and alumina–graphite composites have been discussed. The influence of various parameters such as graphite content, particle size, normal pressure, sliding speed, sliding distance, surface texture, temperature, current density, environment, and counterpart materials on the friction coefficient and wear rate is discussed. The friction and wear rate in the metal and ceramic matrix graphite particle composites are significantly reduced when compared to similarly unreinforced material as a result of the incorporation of graphite particles. As the size of the particles increase, the friction and wear decrease in the composites. The friction and wear rate of the matrix composite decreases with an increasing graphite particle content. The graphite particles were found to be superior to other lubricant particles, and they provided effective lubrication when operating at elevated temperature. Additionally, heat treatment can improve the tribological performance of metal matrix graphite composites.

References

1. Ludema KC (1996) Friction, wear, lubrication: a textbook in tribology. CRC Press, Boca Raton
2. Stachowiak GW, Batchelor AW (2005) Engineering tribology. Butterworth-Heinemann, Boston, MA
3. Lovell MR, Kabir MA, Menezes PL, Higgs CF III (2010) Influence of boric acid additive size on green lubricant performance. *Philos Transact A Math Phys Eng Sci* 368(1929):4851–4868. doi:[10.1098/rsta.2010.0183](https://doi.org/10.1098/rsta.2010.0183)
4. Brudnyi AI, Karmadonov AF (1975) Structure of molybdenum disulphide lubricant film. *Wear* 33(2):243–249. doi:[10.1016/0043-1648\(75\)90279-3](https://doi.org/10.1016/0043-1648(75)90279-3)
5. Donnet C, Erdemir A (2004) Historical developments and new trends in tribological and solid lubricant coatings. *Surf Coat Technol* 180–181:76–84. doi:[10.1016/j.surfcoat.2003.10.022](https://doi.org/10.1016/j.surfcoat.2003.10.022)
6. Bryant PJ, Gutshall PL, Taylor LH (1964) A study of mechanisms of graphite friction and wear. *Wear* 7(1):118–126. doi:[10.1016/0043-1648\(64\)90083-3](https://doi.org/10.1016/0043-1648(64)90083-3)
7. Fusaro RL (1976) A comparison of the lubricating mechanisms of graphite fluoride and molybdenum films. In: ASLE proceedings of 2nd international conference on solid lubrication, Denver, CO, p 59
8. Fusaro RL (1984) Effect of substrate chemical pretreatment on the tribological properties of graphite films. In: ASLE proceedings 3rd international conference on solid lubrication, Denver, CO, p 1
9. Kato K, Osaki H, Kayaba T (1989) The lubricating properties of tribo-coating films of Pb-Sn alloys in high vacuum. *Tribol Trans* 32(1):42–46
10. Gardos MN (1988) The synergistic effects of graphite on the friction and wear of MoS₂ films in air. *Tribol Trans* 31(2):214–227
11. Hilton MR, Fleischauer PD (1989) Structural studies of sputter-deposited MoS₂ solid lubricant films. Defense Technical Information Center, Ft. Belvoir
12. Roberts EW, Price WB (1988) In-vacuo, tribological properties of high-rate sputtered MoS₂ applied to metal and ceramic substrates. *Mater Res Soc Symp Proc* 140:251–264

13. Sliney HE (1979) Wide temperature spectrum self-lubricating coatings prepared by plasma spraying. *Thin Solid Films* 64(2):211–217
14. Sliney HE (1986) Tribology of selected ceramics at temperatures to 900 C. National Aeronautics and Aerospace Administration, Washington, DC [For sale by the National Technical Information Service, Springfield, VA]
15. Shankara A, Menezes P, Simha K, Kailas S (2008) Study of solid lubrication with MoS₂ coating in the presence of additives using reciprocating ball-on-flat scratch tester. *Sadhana* 33(3):207–220
16. Pai BC, Rohatgi PK, Venkatesh S (1974) Wear resistance of cast graphitic aluminium alloys. *Wear* 30(1):117–125. doi:[10.1016/0043-1648\(74\)90061-1](https://doi.org/10.1016/0043-1648(74)90061-1)
17. Rohatgi PK, Pai BC (1980) Seizure resistance of cast aluminium alloys containing dispersed graphite particles of various sizes. *Wear* 59(2):323–332. doi:[10.1016/0043-1648\(80\)90190-8](https://doi.org/10.1016/0043-1648(80)90190-8)
18. Krishnan BP, Raman N, Narayanaswamy K, Rohatgi PK (1980) Performance of an Al-Si-graphite particle composite piston in a diesel engine. *Wear* 60(1):205–215. doi:[10.1016/0043-1648\(80\)90259-8](https://doi.org/10.1016/0043-1648(80)90259-8)
19. Biswas S, Rohatgi PK (1983) Tribological properties of cast graphitic-aluminium composites. *Tribol Int* 16(2):89–102. doi:[10.1016/0301-679x\(83\)90021-x](https://doi.org/10.1016/0301-679x(83)90021-x)
20. Akhlaghi F, Zare-Bidaki A (2009) Influence of graphite content on the dry sliding and oil impregnated sliding wear behavior of Al 2024-graphite composites produced by in situ powder metallurgy method. *Wear* 266(1–2):37–45. doi:[10.1016/j.wear.2008.05.013](https://doi.org/10.1016/j.wear.2008.05.013)
21. Rohatgi PK, Ray S, Liu Y (1992) Tribological properties of metal matrix-graphite particle composites. *Int Mater Rev* 37(3):129–152
22. Gibson PR, Clegg AJ, Das AA (1984) Wear of cast Al-Si alloys containing graphite. *Wear* 95(2):193–198. doi:[10.1016/0043-1648\(84\)90117-0](https://doi.org/10.1016/0043-1648(84)90117-0)
23. Das S, Prasad SV, Ramachandran TR (1989) Microstructure and wear of cast (Al-Si alloy)-graphite composites. *Wear* 133(1):173–187. doi:[10.1016/0043-1648\(89\)90122-1](https://doi.org/10.1016/0043-1648(89)90122-1)
24. He DH, Manory R (2001) A novel electrical contact material with improved self-lubrication for railway current collectors. *Wear* 249(7):626–636. doi:[10.1016/s0043-1648\(01\)00700-1](https://doi.org/10.1016/s0043-1648(01)00700-1)
25. Kato H, Takama M, Iwai Y, Washida K, Sasaki Y (2003) Wear and mechanical properties of sintered copper-tin composites containing graphite or molybdenum disulfide. *Wear* 255(1–6):573–578. doi:[10.1016/s0043-1648\(03\)00072-3](https://doi.org/10.1016/s0043-1648(03)00072-3)
26. Kestursatya M, Kim JK, Rohatgi PK (2003) Wear performance of copper-graphite composite and a leaded copper alloy. *Mater Sci Eng A* 339(1–2):150–158. doi:[10.1016/s0921-5093\(02\)00114-4](https://doi.org/10.1016/s0921-5093(02)00114-4)
27. Moustafa SF, El-Badry SA, Sanad AM, Kieback B (2002) Friction and wear of copper-graphite composites made with Cu-coated and uncoated graphite powders. *Wear* 253(7–8):699–710. doi:[10.1016/s0043-1648\(02\)00038-8](https://doi.org/10.1016/s0043-1648(02)00038-8)
28. Myshkin NK, Konchits VV (1992) Friction and wear of metal-composite electrical contacts. *Wear* 158(1–2):119–140. doi:[10.1016/0043-1648\(92\)90034-6](https://doi.org/10.1016/0043-1648(92)90034-6)
29. Kováčik J, Bielek J (1996) Electrical conductivity of Cu/graphite composite material as a function of structural characteristics. *Ser Mater* 35(2):151–156. doi:[10.1016/1359-6462\(96\)00121-2](https://doi.org/10.1016/1359-6462(96)00121-2)
30. García-Márquez JM, Antón N, Jimenez A, Madrid M, Martinez MA, Bas JA (2003) Viability study and mechanical characterisation of copper-graphite electrical contacts produced by adhesive joining. *J Mater Process Technol* 143–144:290–293. doi:[10.1016/s0924-0136\(03\)00476-x](https://doi.org/10.1016/s0924-0136(03)00476-x)
31. Stoessel CH, Withers JC, Pan C, Wallace D, Loutfy RO (1995) Improved hollow cathode magnetron deposition for producing high thermal conductivity graphite-copper composite. *Surf Coat Technol* 76–77(Pt 2):640–644. doi:[10.1016/0257-8972\(95\)02674-6](https://doi.org/10.1016/0257-8972(95)02674-6)
32. Tu CJ, Chen D, Chen ZH, Xia JT (2008) Improving the tribological behavior of graphite/Cu matrix self-lubricating composite contact strip by electroplating Zn on graphite. *Tribol Lett* 31(2):91–98. doi:[10.1007/s11249-008-9341-2](https://doi.org/10.1007/s11249-008-9341-2)
33. Kovacik J, Emmer S, Bielek J, Kelesi L (2008) Effect of composition on friction coefficient of Cu-graphite composites. *Wear* 265(3–4):417–421. doi:[10.1016/j.wear.2007.11.012](https://doi.org/10.1016/j.wear.2007.11.012)

34. Ma W, Lu J, Wang B (2009) Sliding friction and wear of Cu-graphite against 2024, AZ91D and Ti6Al4V at different speeds. *Wear* 266(11–12):1072–1081. doi:[10.1016/j.wear.2009.01.051](https://doi.org/10.1016/j.wear.2009.01.051)
35. Chen B, Bi Q, Yang J, Xia Y, Hao J (2008) Tribological properties of solid lubricants (graphite, h-BN) for Cu-based P/M friction composites. *Tribol Int* 41(12):1145–1152. doi:[10.1016/j.triboint.2008.02.014](https://doi.org/10.1016/j.triboint.2008.02.014)
36. Rajkumar K, Aravindan S (2009) Tribological performance of microwave-heat-treated copper-graphite composites. *Tribol Lett* 37(2):131–139. doi:[10.1007/s11249-009-9499-2](https://doi.org/10.1007/s11249-009-9499-2)
37. Rajkumar K, Aravindan S (2011) Tribological performance of microwave sintered copper-TiC-graphite hybrid composites. *Tribol Int* 44(4):347–358. doi:[10.1016/j.triboint.2010.11.008](https://doi.org/10.1016/j.triboint.2010.11.008)
38. Ramesh CS, Noor Ahmed R, Mujeebu MA, Abdullah MZ (2009) Development and performance analysis of novel cast copper-SiC-Gr hybrid composites. *Mater Design* 30(6):1957–1965. doi:[10.1016/j.matdes.2008.09.005](https://doi.org/10.1016/j.matdes.2008.09.005)
39. Ma W, Lu J (2010) Effect of sliding speed on surface modification and tribological behavior of copper-graphite composite. *Tribol Lett* 41(2):363–370. doi:[10.1007/s11249-010-9718-x](https://doi.org/10.1007/s11249-010-9718-x)
40. Ma W, Lu J (2011) Effect of surface texture on transfer layer formation and tribological behaviour of copper-graphite composite. *Wear* 270(3–4):218–229. doi:[10.1016/j.wear.2010.10.062](https://doi.org/10.1016/j.wear.2010.10.062)
41. Zhan Y, Zhang G (2006) The role of graphite particles in the high-temperature wear of copper hybrid composites against steel. *Mater Design* 27(1):79–84. doi:[10.1016/j.matdes.2004.08.019](https://doi.org/10.1016/j.matdes.2004.08.019)
42. Chen S, Wang J, Liu Y, Liang J, Liu C (2010) Synthesis of new Cu-based self-lubricating composites with great mechanical properties. *J Compos Mater* 45(1):51–63. doi:[10.1177/0021998310371542](https://doi.org/10.1177/0021998310371542)
43. Ma XC, He GQ, He DH, Chen CS, Hu ZF (2008) Sliding wear behavior of copper-graphite composite material for use in maglev transportation system. *Wear* 265(7–8):1087–1092. doi:[10.1016/j.wear.2008.02.015](https://doi.org/10.1016/j.wear.2008.02.015)
44. Li J, Xiong D (2009) Tribological behavior of graphite-containing nickel-based composite as function of temperature, load and counterface. *Wear* 266(1–2):360–367. doi:[10.1016/j.wear.2008.06.020](https://doi.org/10.1016/j.wear.2008.06.020)
45. Li J, Xiong D (2008) Tribological properties of nickel-based self-lubricating composite at elevated temperature and counterface material selection. *Wear* 265(3–4):533–539. doi:[10.1016/j.wear.2007.09.005](https://doi.org/10.1016/j.wear.2007.09.005)
46. Li J, Xiong D, Yi W (2007) Tribological properties of nickel-graphite composite against different counterfaces at elevated temperatures. *Trans Nonferrous Met Soc China* 17:99–104
47. Wu Y, Shen B, Liu L, Hu W (2006) The tribological behaviour of electroless Ni-P-Gr-SiC composite. *Wear* 261(2):201–207. doi:[10.1016/j.wear.2005.09.008](https://doi.org/10.1016/j.wear.2005.09.008)
48. Qi Q (2006) Evaluation of sliding wear behavior of graphite particle-containing magnesium alloy composites. *Trans Nonferrous Met Soc China* 16(5):1135–1140. doi:[10.1016/s1003-6326\(06\)60390-7](https://doi.org/10.1016/s1003-6326(06)60390-7)
49. Zhang M, Liu Y, Yang X, An J, Luo K (2008) Effect of graphite particle size on wear property of graphite and Al₂O₃ reinforced AZ91D-0.8%Ce composites. *Trans Nonferrous Met Soc China* 18(Suppl 1):S273–S277. doi:[10.1016/s1003-6326\(10\)60216-6](https://doi.org/10.1016/s1003-6326(10)60216-6)
50. Zhang MJ, Yang XH, Liu YB, Cao ZY, Cheng LR, Pei YL (2010) Effect of graphite content on wear property of graphite/Al₂O₃/Mg-9Al-1Zn-0.8Ce composites. *Trans Nonferrous Met Soc China* 20(2):207–211. doi:[10.1016/s1003-6326\(09\)60122-9](https://doi.org/10.1016/s1003-6326(09)60122-9)
51. Zhang MJ, Cao ZY, Yang XH, Liu YB (2010) Microstructures and wear properties of graphite and Al₂O₃ reinforced AZ91D-Cex composites. *Trans Nonferrous Met Soc China* 20:471–475
52. Johnson JL, Schreurs J (1982) High current brushes: VIII: Effect of electrical load. *Wear* 78(1–2):219–232. doi:[10.1016/0043-1648\(82\)90033-3](https://doi.org/10.1016/0043-1648(82)90033-3)
53. Feng Y, Wang J, Zhang M, Xu Y (2007) The influence of pressure on the electrical tribology of carbon nanotube-silver-graphite composite. *J Mater Sci* 42(23):9700–9706. doi:[10.1007/s10853-007-1939-5](https://doi.org/10.1007/s10853-007-1939-5)

54. Jha AK, Prasad SV, Upadhyaya GS (1989) Sintered 6061 aluminium alloy–solid lubricant particle composites: sliding wear and mechanisms of lubrication. *Wear* 133(1):163–172. doi:[10.1016/0043-1648\(89\)90121-x](https://doi.org/10.1016/0043-1648(89)90121-x)
55. Jha AK, Prasad SV, Upadhyaya GS (1989) Dry sliding wear of sintered 6061 aluminium alloy–graphite particle composites. *Tribol Int* 22(5):321–327. doi:[10.1016/0301-679x\(89\)90147-3](https://doi.org/10.1016/0301-679x(89)90147-3)
56. Baradeswaran A, Elayaperumal A (2011) Effect of graphite content on tribological behaviour of aluminium alloy–graphite composite. *Eur J Sci Res* 53(2):163–170
57. Suresha S, Sridhara BK (2011) Friction characteristics of aluminium silicon carbide graphite hybrid composites. *Mater Design*. doi:[10.1016/j.matdes.2011.05.010](https://doi.org/10.1016/j.matdes.2011.05.010)
58. Suresha S, Sridhara BK (2010) Wear characteristics of hybrid aluminium matrix composites reinforced with graphite and silicon carbide particulates. *Compos Sci Technol* 70 (11):1652–1659. doi:[10.1016/j.compscitech.2010.06.013](https://doi.org/10.1016/j.compscitech.2010.06.013)
59. Stojanovic B, Babic M, Mitrovic S, Miloradovic N, Pantic M, Vencel A (2013) Tribological characteristics of aluminium hybrid composites reinforced with silicon carbide and graphite. A review. *J Balkan Tribol Assoc* 19(1):83–96
60. Babic M, Stojanovic B, Mitrovic S, Bobic I, Miloradovic N, Pantic M (2012) The influence of lubricant on friction coefficient of hybrid Al-SiC-Gr composites. Paper presented at the international conference of Bulgarian tribologists, Sofia, 18–20 Oct 2012
61. Goto H, Uchijo K (2005) Wear mechanism of Al-Si alloy impregnated graphite composite under dry sliding. *Wear* 259(1–6):613–619. doi:[10.1016/j.wear.2005.02.024](https://doi.org/10.1016/j.wear.2005.02.024)
62. Jinfeng L, Longtao J, Gaohui W, Shoufu T, Guoqin C (2009) Effect of graphite particle reinforcement on dry sliding wear of SiC/Gr/Al composites. *Rare Met Mater Eng* 38 (11):1894–1898. doi:[10.1016/s1875-5372\(10\)60059-8](https://doi.org/10.1016/s1875-5372(10)60059-8)
63. Prasad SV, Asthana R (2004) Aluminum metal–matrix composites for automotive applications: tribological considerations. *Tribol Lett* 17(3):445–453
64. Gangopadhyay A, Jahanmir S (1991) Friction and wear characteristics of silicon nitride-graphite and alumina-graphite composites. *Tribol Trans* 34(2):257–265
65. Ishigaki H, Iwasa M, Toibana Y, Kawaguchi I (1986) Friction and wear of hot pressed silicon nitride and other ceramics. *J Tribol* 108(4):514
66. Bohmer M, Almond EA (1988) Mechanical properties and wear resistance of a whisker-reinforced zirconia-toughened alumina. *Mater Sci Eng A* 105–106:105–116
67. Yust C, McHargue C, Harris LA (1988) Friction and wear of ion-implanted TiB₂. *Mater Sci Eng A* 105–106:489–496
68. Zum Gahr KH (1989) Sliding wear of ceramic-ceramic, ceramic-steel and steel-steel pairs in lubricated and unlubricated contact. *Wear* 133(1):1–22
69. Miyoshi K, Buckley DH (1979) Friction, deformation and fracture of single-crystal silicon carbide. *ASLE Trans* 22(1):79–90
70. Holzhauser W, Johnson RL, Murray SF (1981) Wear characteristics of water lubricated Al₂O₃-metal sliding couples. *Wear of Materials* 676
71. Jahanmir S, Fischer TE (1988) Friction and Wear of Silicon Nitride Lubricated by Humid Air, Water, Hexadecane and Hexadecane + 0.5 Percent Stearic Acid. *Tribol Trans* 31(1):32–43
72. Tomizawa H, Fischer TE (1987) Friction and wear of silicon nitride and silicon carbide in water—hydrodynamic lubrication at low sliding speed obtained by tribochemical wear. *ASLE Trans* 30:41–46
73. Gangopadhyay AK, Janon FB, Fine ME, Cheng HS (1990) Enhanced wear resistance of α -alumina by surface modification with chromia and titania. *Tribol Trans* 33(1):96–104
74. Sasaki S (1989) The effects of the surrounding atmosphere on the friction and wear of alumina, zirconia, silicon carbide and silicon nitride. *Wear* 134(1):185–200
75. Fischer TE, Anderson MP, Jahanmir S, Salher R (1988) Friction and wear of tough and brittle zirconia in nitrogen, air, water, hexadecane and hexadecane containing stearic acid. *Wear* 124 (2):133–148

76. Erdemir A, Fenske GR, Erck RA, Cheng CC (1989) Ion-assisted deposition of silver films on ceramics for friction and wear control. Conference: 44 annual Stle meeting, A.G.A.U.S.A.M., Argonne National Lab, IL, United States
77. Wedeven LD, Pallini RA, Miller NC (1988) Tribological examination of unlubricated and graphite-lubricated silicon nitride under traction stress. *Wear* 122(2):183–205
78. Pallini RA, Wedeven LD (1988) Traction characteristics of graphite lubricants at high temperature. *Tribol Trans* 31(2):289–295
79. Minford E, Prewo K (1985) Friction and wear of graphite-fiber-reinforced glass matrix composites. *Wear* 102(3):253–264
80. Gangopadhyay A, Jahanmir S, Hegemann BE (1990) Paper III (i) Reduction in friction coefficient in sliding ceramic surfaces by in-situ formation of solid lubricant coatings
81. Ruff AW, Peterson MB, Gangopadhyay A, Whitenton E (1989) Wear and friction characteristics of self-lubricating copper-intercalated graphite composites. Ft. Belvoir: Defense Technical Information Center

Questions

1. What is a composite and describe two types of composites?
2. How does a self-lubricating matrix composite operate and what are the two stages?
3. Why is copper–graphite used as a self-lubricating metal matrix composite and what are some of its applications?
4. What are the dominant wear mechanisms during copper–graphite contact strip applications?
5. What is the effect of sliding speed on copper–graphite composites and how does this influence friction and wear?
6. What are the dominant wear mechanisms in the magnetic levitation transportation system?
7. In nickel–graphite composites, what compounds form to enhance the tribological properties when combining Ni, Cr, W, and Fe with graphite and molybdenum disulfide at high temperatures?
8. What contributed to the low- and high-temperature performance of the nickel alloy-based graphite–MoS₂-reinforced composite?
9. What are the mechanical properties that make magnesium alloys attractive? What are some of the drawbacks? What applications are magnesium alloys primarily used in? Provide an example of a magnesium alloy.
10. When using silver–graphite composites in electrical contact applications, the friction and wear behavior under sliding with electrical current flow can become quite complex when compared to that under purely mechanical sliding conditions. Briefly explain this behavior.
11. What are the drawbacks to aluminum matrix composites and what is the benefit to adding graphite to these composites?
12. What is the effect on the coefficient of friction when adding intercalated NiCl₂ graphite to silicon nitride and alumina ceramic matrices and what causes these phenomena?

Answers

1. Composite materials are a special class of materials and are made from two or more constituent components with significantly different physical or chemical properties, which remain separate and distinct at the macroscopic or microscopic scale within the finished structure. In the case of two constituent components, the material with the highest volume fraction is considered as the matrix, whereas the other is the reinforcement material that modifies the properties of the matrix. In metal matrix composites, the matrix is made of a metal and the reinforcement may be a different metal or another material, such as a ceramic or organic compound. Similarly, in ceramic matrix composites, the matrix is composed of silicon nitride, alumina, or another type of ceramic material, and the reinforcement may be a different ceramic, metallic, or solid lubricant compound.
2. In self-lubricating matrix composites, solid particle such as graphite and MoS_2 are embedded in the matrix. Here, the formation of a thin film will occur by transferring the solid particles from the matrix to the tribo-surface during initial periods of sliding. The observed friction and wear behavior will, therefore, have two distinct stages: (a) transient state, while the thin solid lubricant film is being established, and (b) steady state, when a stable solid lubricant film (in the dynamical sense of being continuously replenished, i.e., “self-lubricating,” to make up for the wear loss) has formed.
3. Copper–graphite is used as a metal matrix composite because it combines the properties of copper (i.e., excellent thermal and electrical conductivities) and graphite (i.e., superior lubricity and a low thermal expansion coefficient). These matrix composites are optimal for electromechanical applications such as in electrical sliding contact applications use in brushes in electric motors and generators. In welding machines, the low voltage, high current densities, and sliding of critical components necessitate copper–graphite metal matrix composites with a very high specific electrical conductivity, good thermal conductivity, and low friction coefficient.
4. In the copper–graphite contact strips, arc erosion wear, oxidative wear, and adhesive wear were the dominant mechanisms during the electrical sliding process.
5. When the sliding speed exceeds a critical value, a transition of the friction and wear regime occurs. The formation of a lubricant layer on the contact surface is regarded as an important characteristic for enhanced tribological performance of copper–graphite composites. Due to a large strain gradient in the subsurface deformation zone, the graphite-rich lubricant layer can easily form on the sliding surface when the speed is lower than the critical value. At speeds exceeding the critical value, the formation of the lubricant layer is difficult due to the effects of delamination wear caused by the high strain rate. At speeds less than the critical value, the wear mechanism occurring tends to be mild wear caused by ratcheting, and at speeds exceeding the critical value, the wear mechanism is more severe induced by delamination wear.

6. Adhesive wear, abrasive wear, and electrical erosion wear are the dominant wear mechanisms during the electrical sliding wear processes in the magnetic levitation transportation system.
7. Chromium sulfide and tungsten carbide were formed in the composite, and they were responsible for lowering the friction and improving the wear resistance at elevated temperatures.
8. The Ni–Cr–W–Fe–C–MoS₂ composite possessed excellent self-lubricating properties over a wide range of temperatures as a result of synergistic lubricating effect of graphite (C) and molybdenum disulfide (MoS₂). The graphite contributed to the dominant role of lubrication at room temperature, while the sulfides were responsible for low friction at high temperatures.
9. Magnesium alloys are used in automobile and aerospace industries due to their low density, high specific strength, stiffness, good damping characteristic, excellent machinability, and ease of casting. Additionally, the poor corrosion and wear resistance of magnesium is a drawback that facilitates its primary use as an alloying agent to make aluminum–magnesium alloys. The most commonly used magnesium alloy is AZ91 alloy (consisting of 90 % magnesium, 9 % aluminum, and 1 % zinc). Magnesium alloy–graphite composites have found applications in pistons and space structural applications, thus expanding their versatility and use as self-lubricating metal matrix composites.
10. In electrical contact applications, the amount of material removed under sliding electrical contact is the sum of the contributions from purely mechanical wear in the absence of electrical current flow, arc erosion, and mechanical wear resulting from softening of the matrix by local heating caused by the electrical arcing. In a purely mechanical sliding condition without current flow, only mechanical wear would result.
11. Aluminum alloys suffer from low resistance to wear under poor lubricating conditions, and their severe seizure and galling under boundary lubrication conditions are major concerns for their use in high-performance tribological applications. With solid lubricant particle dispersion in the matrix of an aluminum alloy, this material can exhibit improved wear resistance and consequently become more suitable for high-performance tribological applications. The inclusion of solid lubricating particles in aluminum alloy matrices improves friction, wear, and anti-seizing properties. Self-lubricating aluminum alloy–graphite particulate composites have received attention because of their low friction and wear, reduced temperature rise in the tribo-interface, improved machinability, excellent anti-seizure effects, low thermal expansion, and high damping capacity.
12. In silicon nitride–graphite composites, the decrease in the coefficient of friction is a result of the formation of a graphite transfer layer consisting of materials from both contacting surfaces (i.e., consisting of graphite, iron oxide, and the silicates). The lack of a decrease in the coefficient of friction for the alumina–graphite composite can be explained by the presence of steel wear particles that inhibited the formation of the graphite transfer layer. The steel wear debris physically covered the graphite regions within the composite thus retarding the lubricating properties of the graphite.

Chapter 12

Particle Tribology: Granular, Slurry, and Powder Tribosystems

C. Fred Higgs III, Martin Marinack Jr., Jeremiah Mpagazehe, and Randyka Pudjoprawoto

Abstract The purpose of this chapter is to give the reader a basic understanding of particles in sliding contact. First, we will describe granular flows (the flow of inelastic particles that transfer momentum primarily through collisions) from a tribology perspective, including modeling and experiments that have been conducted inside and outside of the tribology community. Second, slurry flow (particles in gas or liquids) tribosystems will be discussed including models and experiments related to the flow of particles in fluids. And finally, we conclude with a section on powder lubrication (soft particles which coalesce under load and coat surface asperities), where thick and thin film powder lubrication is discussed along with select modeling and experimental approaches.

1 Introduction

Particles in sliding contacts have always been a complex area of tribology. While tribology is a very broad field that is diffused into many areas of engineering and science, gaining an understanding of the interface between two sliding materials (i.e., a tribosystem) requires one to take a multidisciplinary perspective. When particles are introduced into the interface, the problem can quickly become intractable and thus highly empirical to compensate for the uncertainties involved with predicting the resulting tribology. Further, various particle flow communities are independent fields of science and engineering themselves, so few tribologists are trained to interpret the behavior of particulate systems and few classical particle engineers are trained to understand phenomena associated with sliding surfaces and the inherent friction, wear, and/or lubrication phenomena that emerge. For example, classical granular flow is a field mostly comprised of chemical engineers and

C.F. Higgs III (✉) • M. Marinack Jr. • J. Mpagazehe • R. Pudjoprawoto
Carnegie Mellon University (CMU), Pittsburgh, PA, USA
e-mail: higgs@andrew.cmu.edu

physicists; the mechanical engineer studying the flow of these inelastic grains is rarer, albeit not uncommon. The same situation exists with the flow of particles in fluids in sliding contacts, which we call slurry tribology. There is a strong slurry community, more commonly known as the multiphase flow community, which exists primarily to study fossil fuel-type energy systems such as circulating fluidized beds and flowing coal particles. This community routinely solves Navier–Stokes equations, not just for the fluid phase but for the solid phase comprised of flowing particles as well. The same cannot be said of powder lubrication however. Powder flows in sliding contacts remain an area rooted in tribology, and unlike granular and slurry (multiphase) flows, researchers outside of tribology reference papers within tribology journals when studying problems involving powders in sliding contacts. Even in areas such as earthquake science, powder lubrication works found in tribology journals are referenced to describe intriguing friction phenomena connected to shearing layers of earth.

2 Granular Flow Tribology

Granular flows are complex flows of solid, macroscopic, non-cohesive particulates (or granules), which collectively comprise the bulk flow. These granules are generally on the order of millimeters (mm) or larger, unlike powder flow particles (discussed in Sect. 4) which generally reside on the order of micrometers (μm). Granular flows are often characterized by the fact that they dissipate energy (unlike traditional liquid-based flows) through the inelastic collisions and interactions between the individual grains comprising the global flow. Granular flows can exhibit solid-, liquid-, and gaseous-like behavior under varying flow conditions. This display of nonlinear and multiphase flow behavior makes the prediction and study of granular flows challenging both locally (at the individual particle scale) and globally (at the bulk flow scale).

In tribology, liquid lubricants break down at extreme temperatures and can bring about stiction in micro-/nanoscale environments. This has led to the advent of alternative, dry lubrication mechanisms such as powder and granular flow. While powder tribology is described in detail in Sect. 4, the focus of this section remains granular tribology. Granular flow tribology focuses on the study of granular flows between relative sliding contacts, specifically focusing on the use of granular flows as a lubricant. Granular flows have been proposed as a particulate lubricant alternative to traditional oil-based lubricants [1–3] because of their hydrodynamic fluid behavior in sliding contacts, specifically their ability to carry loads and accommodate surface velocities. Typical sliding contact geometries, as summarized in Worniyoh et al. [4], include annular, parallel, and converging geometries, as shown in Fig. 12.1.

In their detailed review of dry particulate lubrication, Worniyoh et al. [4] define granular lubricants as “dry, ‘cohesionless,’ hard particles that essentially maintain their spherical geometry under load and accommodate surface velocity differences through sliding and rolling at low shear rates, and largely through collisions at high

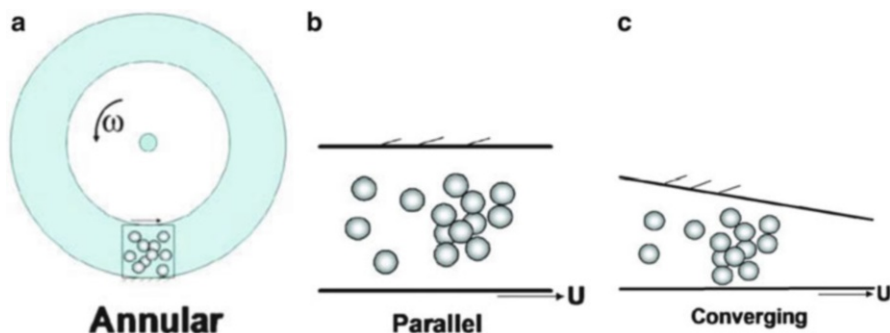


Fig. 12.1 Sliding contact geometries: (a) Annular, (b) parallel, and (c) converging [4]

shear rates.” In sliding contact geometries, granular lubrication mechanisms have shown that the particles inside the contact can enhance lubrication and lower friction beyond boundary lubrication levels. Granular flow lubricants also show a density distribution in sliding contacts, where a low-density region exists near the surfaces, while a high-density region exists near the center of the flow. Unlike hydrodynamic fluids, granular flow lubricants display a load-carrying capacity in static and parallel sliding (dynamic) contact regions, as well as a significant (measurable) amount of slip at the boundaries of macroscale geometries [4]. As an example of a specific granular lubrication application, McKeague and Khonsari [5] developed a model which predicts the behavior of a granular flow inside of a slider-bearing geometry.

Two modes of granular lubrication have been observed to exist. At lower shear rates or high loads, the load is supported by strong contact forces between compacted granules. This regime is known as granular *contact* lubrication; the classical granular flow community calls this the frictional regime. Global frictional forces are due to the continuous shearing of the beads, and the load-carrying capacity is due to elastic and plastic deformation of the granules in contact. At increased shear rates or small loads, the granules are more agitated and lubrication in this secondary regime is known as granular *kinetic* lubrication. There is also a *transition* regime which may be quasi-static [6, 7]. Load-carrying capacity in this mode is due to the shear and normal forces created by the colliding particles against the upper surface.

The scope of granular flows in tribology is not limited to the study of granular lubrication. Granular flow tribology also involves the more general examination of the role of friction, macroscale surface roughness, and the collision and contact mechanics of moving particles. Particularly important in characterizing and understanding granular flows from both a classical and tribological perspective is the study of the individual particles which comprise the bulk granular flow. This involves the study of individual particle collision parameters such as the coefficient of friction (COF) and coefficient of restitution (COR). Knowledge and understanding of all of these granular flow concepts (friction, roughness, contact

mechanics, COF, COR, etc.) can provide insight into areas, industries, and applications well beyond granular lubrication, including solids processing [8], pharmaceuticals [9], wheel and granular terrain interaction of planetary rovers [10], coal transportation [11], granular segregation [12, 13], and the design and operation of hoppers [14, 15] and silos [16, 17].

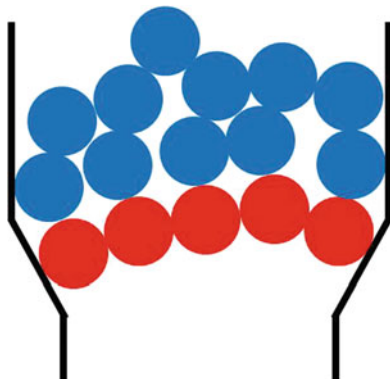
The following sections examine numerous aspects of granular flow tribology, beginning with a look at applications and phenomena such as segregation, jamming, and planetary rover–terrain interaction. Also discussed are key experimental geometries used to elucidate core granular flow science. This includes the study of individual particle physics as well as the study of global granular flow properties. Finally, modeling techniques in the study of granular flows are discussed, which includes an examination of both discrete (discrete element method (DEM), cellular automata (CA), and finite element method (FEM)) and continuum modeling approaches. Before moving forward, it should be noted that this section should not be viewed as an exhaustive examination of granular flows in tribology. Instead, it serves as a detailed overview of the major areas of study, concepts, experimental methods, and modeling methods in the study of granular flow tribology.

2.1 Applications and Phenomena

Granular flows display several unique behaviors and physical phenomena. Granular flow lubrication, which was already discussed in the granular introduction, is one such phenomenon. Other common granular flow phenomena include granular segregation and jamming, both of which are often witnessed in solids processing applications involving hoppers, silos, and/or mixers. Another interesting granular flow behavior involves the shear flow witnessed beneath a planetary rover wheel as it interacts with the granular terrain. The following section will highlight and discuss these three phenomena (segregation, jamming, and planetary rover–terrain interaction) in further detail.

It is well known that even small variations in granular properties and/or characteristics can lead to segregation in a granular flow. Granular segregation involves the separation (“unmixing”) of individual granular species inside of a bidisperse or polydisperse flow (i.e., a flow with two or more species). Bi/polydispersity in a granular flow can be due to differences in any number of granule properties or characteristics such as size, shape, material density, restitution, and friction coefficient. While granular flow segregation can be induced by variations in any number of these characteristics, perhaps the most prevalent characteristic inducing granular segregation is particle size. Ottino and Khakar [18] provide a detailed review of studies examining both density and size segregation for a range of granular flow geometries and situations. Particle size segregation is studied and witnessed in a wide variety of natural processes and industrial applications. Natural processes, such as avalanches, were studied by Gray and Ancey [19] who demonstrated that in an avalanche flow, the larger particles

Fig. 12.2 Schematic of a two-dimensional hopper exhibiting a jammed configuration (adapted from To et al. [15]). The *red* granules at the *bottom* display the formation of a granular arch which causes jamming of the flow



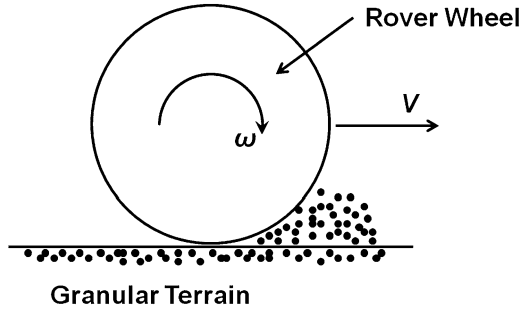
segregate at the top, where the flow velocity is largest, and move towards the flow front [19]. In terms of industrial applications, size segregation is displayed and has been studied in hoppers [20, 21] and silos [16, 22], as well as mixers [23], each of which is used extensively in the solids processing industries (e.g., pharmaceuticals and food processing).

Maintaining a tribological perspective, size segregation is a phenomenon which is also seen extensively in granular shear flows, such as those exemplified by the geometries shown in Fig. 12.1. Size segregation in a parallel-type geometry (Fig. 12.1b) has been studied extensively by Golick and Daniels [13] and May and her colleagues [12, 24]. In the work of Golick and Daniels [13], a bidisperse flow using glass particles with diameters of 4 and 6 mm was initially placed between two disks such that the smaller particles resided at the top, while the larger particles resided at the bottom. As the flow was sheared between parallel disks, the larger particles began to segregate to the top creating a mixed flow for a period of time. However, by the end of the experiment, the flow was fully segregated, with the larger particles now residing at the top of the flow and the smaller particles at the bottom. This classic trend of larger particles segregating to the top occurs because the smaller particles tend to fall through the gaps between the large particles in a sievelike fashion.

Jamming is another relevant and important granular flow phenomenon which has been studied extensively in the literature [15, 25–31]. Jamming involves the granular flow becoming rigid and stagnating. Figure 12.2, adapted from the work of To et al. [15], shows an example of jamming occurring inside of a hopper flow. At the local level, jamming is related to the forces and force distribution among the individual particles and particle chains [26–28]. Jamming in granular flows has been likened to the jamming of certain other complex fluids like glass which is rigid (jammed) but can transition to a flowing state at higher temperatures [26]. Granular flows have likewise demonstrated the ability to transition between a flowing state and a jammed (stagnate) state based on the properties of the so-called granular temperature, solid fraction, and shear stress, as exemplified in the works of Zhang et al. [28] and Liu and Nagel [31].

A third granular flow application is the interaction between planetary rover wheels and granular regolith (terrain). As described by Higgs et al. [10], wheeled

Fig. 12.3 Schematic of the planetary rover wheel–terrain interaction geometry, showing the individual granules becoming entrained in the converging gap at the wheel’s leading edge (adapted from [33])



mobile robots, also known as rovers, are the primary vehicles for transporting scientific instrumentation across rough planetary terrain while being controlled remotely. Since there is a finite lifetime for which scientific information can be obtained, it is important that the rovers are reliably built to transverse the rough terrain without mechanical failure [10]. One of the most important mechanical operations of the rover is the ability of the rover wheel to negotiate the granular-type Martian surface, which requires sufficient traction between the wheel surface and granular terrain [10]. The planetary rover wheel and granular terrain display a geometry which is detailed in the works of Shibly et al. [32] and Liu et al. [33]. Figure 12.3 (adapted from Liu et al. [33]) displays a schematic for a rover wheel being driven on a granular surface in which the granular material enters the converging gap at the front end of the driven wheel [33]. The key thing to notice from the diagram in Fig. 12.3 is that the geometry of the rover wheel–terrain interaction is that of a converging-type sliding contact as depicted in Fig. 12.1c. Thus, this application/phenomenon becomes a granular flow tribology problem in that the wheel–terrain interface serves as a converging gap flow bounded by the wheel on one side and the bulk granular material on the other. This situation also shows the development of different granular flow regimes at different locations. The portion of the granules near the surface flows due to the shear being applied by the wheel, while the base of the granular terrain remains stationary. A more detailed summary and review of specific theoretical, simulation, and experimental work performed on wheel–terrain interaction mechanics for planetary rovers can be found in the work of Ding et al. [34].

2.2 Experiments

2.2.1 Single-Particle Experiments: Coefficient of Restitution

Granular flow experimentation takes place at both the single-particle (microscopic) level and the global (macroscopic) bulk flow level. At the single-particle level, individual particle and collision properties are examined, as these properties

ultimately drive the behavior of the bulk flow. Granular collision properties, such as coefficient of restitution (COR) and coefficient of friction (COF), are of particular importance, as they influence the granular flow characteristics, such as velocity, spin, solid fraction, and granular temperature. The following section details the experimental examination of the COR. COF is studied through the use of pin-on-disk testing of individual granules to characterize friction inside of granular flows.

The coefficient of restitution (COR) is a parameter which defines the ratio of relative post-collision velocity to pre-collision velocity when two materials collide. Mathematically, the coefficient of restitution between colliding materials can be written as seen in (12.1), where e , $v_{reb,1}$, $v_{reb,2}$, $v_{imp,2}$, and $v_{imp,1}$ represent the COR, the rebound velocity of object 1, the rebound velocity of object 2, the impact velocity of object 2, and the impact velocity of the object 1, respectively:

$$e = \frac{v_{reb,1} - v_{reb,2}}{v_{imp,2} - v_{imp,1}} \quad (12.1)$$

The coefficient of restitution can also be understood to indicate the fraction of the pre-collision kinetic energy present after the collision, where $e = 1$ represents a perfectly elastic collision with no kinetic energy loss and $e = 0$ represents a perfectly inelastic collision where all kinetic energy is dissipated during the collision. When examining the COR as it relates to granular flows, several collision cases (geometries) are of significant importance.

The first of these cases is granules (spheres) colliding with thick plates (blocks) and thin plates, which represent the boundaries of many granular systems. In the case of sphere–plate collisions, most of the experimental rigs are relatively simple in their construction and design, with spheres being dropped (under the influence of gravity) on a plate [35–39]. In these setups, the plates (like most granular boundaries) remain stationary (in the normal direction) during the collision. Thus, the expression in (12.1) can be reduced to that of (12.2). The subscripts in (12.2) are dropped since both values are now for the moving sphere, which impacts and rebounds from its collision with the plate/block:

$$e = \frac{-v_{reb}}{v_{imp}} \quad (12.2)$$

When the sphere (granule) is undergoing free fall under the influence of gravity, it is often useful to write the COR in terms of the impact (H_I) and rebound (H_R) height of the sphere for post-processing purposes. Through the use of kinematics and the inclusion of air drag effects, (12.2) can be written as (12.3), where the coefficient of restitution is now a function of heights instead of velocities. In (12.3), g , m_s , $F_{D,I}$, and $F_{D,R}$ represent the acceleration due to gravity, mass of the sphere, the drag force during the particle's free fall before impact, and the drag force during the particle's rebound to its maximum height, respectively:

$$e = \left(\frac{g + \left(\frac{F_{D,I}}{m_s}\right)}{g - \left(\frac{F_{D,R}}{m_s}\right)} \right) \sqrt{\frac{H_R}{H_I}} \quad (12.3)$$

However, in most instances air drag effects can be neglected. This eliminates the first term in (12.3), reducing the coefficient of restitution equation (for a falling sphere impacting a stationary boundary) to the much simpler expression shown in (12.4):

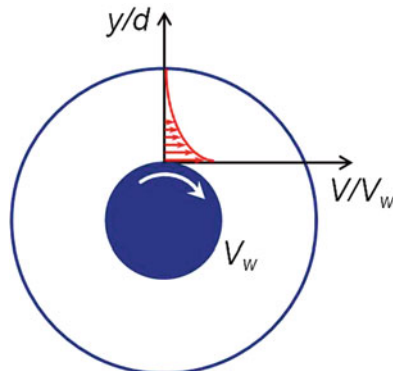
$$e = \sqrt{\frac{H_R}{H_I}} \quad (12.4)$$

A large body of experiments has been performed to examine the coefficient of restitution between spheres and stationary plates. Tabor [40], Kharaz and Gorham [37], and others [38, 39, 41] performed experiments studying the coefficient of restitution between spheres and thick plates (large blocks) for various material combinations and impact velocities. Results from the work of Kharaz and Gorham [37], for 5 mm (diameter) aluminum oxide particles colliding against thick steel and aluminum plates, show a decrease in coefficient of restitution with increased impact velocity. This trend is well documented in other experimental works [36, 39, 40] as well as in theory development. For example, K.L. Johnson [42] developed an analytical formulation of e , for the plastic impact of rigid small spheres colliding with elastic-plastic bodies (i.e., blocks, spheres) at what the author termed “moderate” speeds (up to ~500 m/s). This formulation is shown in (12.5), where p_d , E^* , v_{imp} , and R represent the dynamic pressure (hardness) of the softer material, the composite elastic (contact) modulus, the impact velocity, and the reduced radius of curvature ($1/R = 1/R_1 + 1/R_2$), respectively. The dynamic hardness can be related to the more commonly well-known static hardness of the material through a material-specific factor, as shown in the works of Tabor [40, 43]. As can be seen, e varies with $v_{imp}^{-1/4}$ [42], demonstrating the trend of decreasing COR for increased impact velocity:

$$e = 1.88 \left(\frac{p_d}{E^*} \right)^{\frac{1}{2}} \left(\frac{\frac{1}{2} m_s v_{imp}^2}{p_d R^3} \right)^{-\frac{1}{8}} \quad (12.5)$$

There are many other collision situations such as repeated impacts [44], spheres colliding with thin plates (as compared to sphere diameter) [36, 45–47], sphere–sphere collisions [48–50], oblique impacts [51–53], and the collision of spheres and boundaries in fluids. Gondret et al. [54], Joseph et al. [55], and Ruiz-Angulo and Hunt [56] have studied the COR for these fluid-based collisions extensively. However, this work goes beyond the scope of the current section on dry granular flows.

Fig. 12.4 Schematic of an annular geometry with a velocity profile (adapted from MiDi [61])

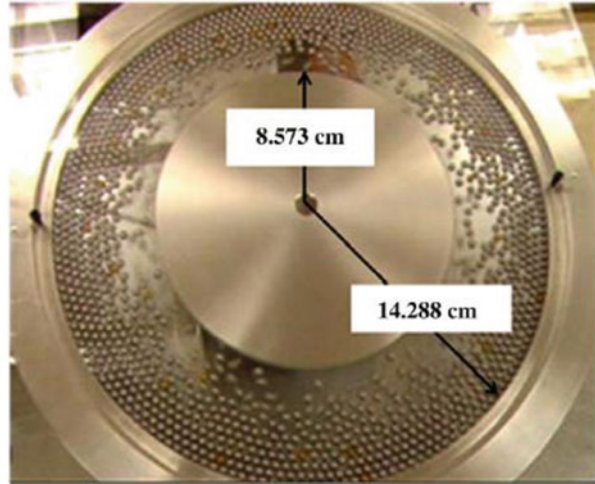


2.2.2 Granular Flow Experiments

The previous section detailed experiments performed at the local (single-particle) level, namely, COR. At the global (bulk) flow level, a number of experimental studies have been performed to gain insight into the behavior of granular flows inside of tribosystems, such as those seen in Fig. 12.1. As such, this section focuses specifically on experimental work performed using the annular, parallel, and converging geometries shown in Fig. 12.1. These tribologically relevant sliding contact geometries are discussed in detail, with their examination being adapted from the work of Wornyo et al. [4]. Other common, but less (non-)tribologically relevant, granular flow geometries are briefly highlighted at the end of the section.

Annular geometry refers to the concentric cylinder setup shown in Fig. 12.1a, where the granular flow resides in the annular gap between the cylinders which slide relative to one another. The pioneering experiments of Bagnold [57] were the first to study the flow of granules under shear. He sheared a dispersion of uniform-sized, solid spherical grains in Newtonian fluid in annular space between two concentric drums. Two distinct regions, grain-inertia region and macroviscous region, were identified, and empirical relations for shear stress were formulated. He also established a third transition region. Representative results for a number of granular experiments [58–60] performed using the annular geometry can be found in the detailed review of MiDi [61]. MiDi [61] summarized experiments and simulations conducted on dense (high solid fraction) granular flows and classified them into six geometric configurations. Figure 12.4 (adapted from MiDi [61]) shows a schematic of the annular flow geometry and velocity profile. In Fig. 12.4, the velocity profile displays an exponential decrease in velocity when moving from the inner rotating wheel to the outer stationary wheel (cylinder). This is typical of many experimental velocity profiles, as detailed in MiDi [61]. It is also shown that for annular geometries, volume fraction shows a slight increase when moving away from the inner wall, while velocity fluctuations (when plotted on a log scale) show a relatively linear decrease when moving across the annular gap [61].

Fig. 12.5 Granular shear cell (GSC) [35]



Other annular-type experiments include the work of Tardos et al. [62] which sheared a bed of fine glass beads between concentric rough vertical cylinders and measured the shear and normal stresses. Veje et al. [63] sheared photoelastic disks at slow rates in a two-dimensional annular setup with a rough rotating inner wheel. Velocity, spin, and solid fraction distributions were measured by means of digital particle tracking. Howell et al. [64] used the same annular setup as Veje et al. [63] to measure the stress fluctuations using photoelasticity. Mueth et al. [59] combined three noninvasive techniques—magnetic resonance imaging (MRI), x-ray tomography, and high-speed-video particle tracking—to obtain the particle velocity, spin, and solid fraction data in three dimensions. They sheared mustard and poppy seeds between concentric rough cylinders. Losert et al. [65] sheared black glass beads between a rotating inner cylinder and outer cylindrical frame. Mean particle velocities and velocity fluctuations were measured as a function of distance from the rotating wall [65]. The inner and the outer cylinder walls were coated with glass beads to make them rough. These experimental results [65] were compared to a continuum model developed by the same researchers in the work of Bocquet et al. [60].

Higgs et al. [10], Jasti and Higgs [66], and Marinack et al. [35] made use of the granular shear cell (GSC) shown in Fig. 12.5 to study granular material in an annular configuration (Fig. 12.1a). The GSC is unique in that it provides a variable and quantifiable macroscopic roughness on its inner driving wheel as shown in Fig. 12.6. These works [10, 35, 66] obtained data for the granular velocity, solid fraction, granular temperature, and slip velocity by averaging discrete particle data gathered in radial bins. Representative results from the GSC [35] are shown in Fig. 12.7 for granular velocity, solid fraction, and granular temperature. Slip velocity at the boundary of the inner wheel can also be obtained as the difference between the wheel's linear surface velocity and the velocity of the granules in the bin adjacent to the inner rotating wheel.

Fig. 12.6 Macroscopic roughness factor on the GSC in the form of granules glued at fixed distances along the wheel's outer edge [66]

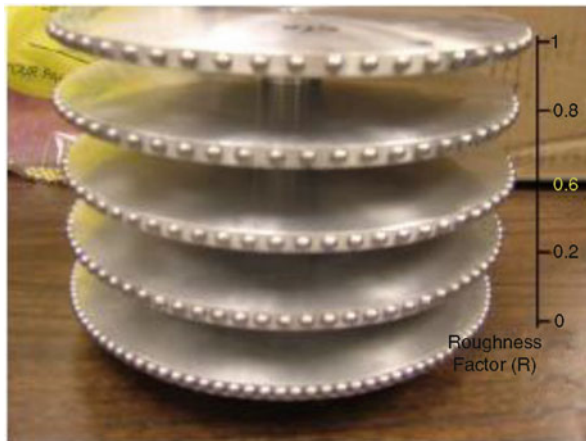


Figure 12.7a displays one of the interesting behaviors from these experiments [35, 66], which is the development of two distinct regions inside the flow. The region near the inner rotating wheel is termed the kinetic region, where the flow is sparsely populated, and characterized by high-speed collisions with short contact times. In these types of collisions, extended sliding between granules, in which frictional effects become more significant, is unlikely. As a result, the coefficient of friction (COF) between colliding particles tends to have a much smaller influence on the flow characteristics than does the coefficient of restitution (COR). In contrast, the contact region (region adjacent to the outer wall) is densely populated and depicted by extended frictional (sliding) contacts. This leads to the COF, as opposed to the COR, being more influential on the characteristics and properties of the contact region [35].

The tangential velocity profile in Fig. 12.7b shows a decrease in velocity when moving from the inner wheel to the outer rim. A distinct transition between the two regions (regimes) is witnessed, where velocities in the contact region approach zero. The velocity profile (Fig. 12.7b) also displays a significant amount of slip at the driving (wheel) surface, which is a common difference between granular and traditional fluid flows. The solid fraction is a minimum near the wheel (Fig. 12.7c) and increases while moving outward to the contact region. The granular temperature (Fig. 12.7d) follows a similar trend as the velocity (Fig. 12.7b).

Parallel geometry (see Fig. 12.1b), often called “parallel type,” refers to horizontal plates or “racetrack” geometries, which are commonly studied for first-order predictions and as idealistic conditions. Savage and Sayed [67] developed and performed experiments on annular shear cells with various granular materials, at rapid shear rates. Though the setup was annular, the shear zone was parallel type. They determined the effects of shear rates and solid fraction on shear and normal stresses. Similar to the annular shear cell, a parallel-plate shear cell was used to shear glass spheres mixed with water or air at high speeds by Hanes and Inman [68]. They observed two types of flows. At high shear rates, all the granules in the

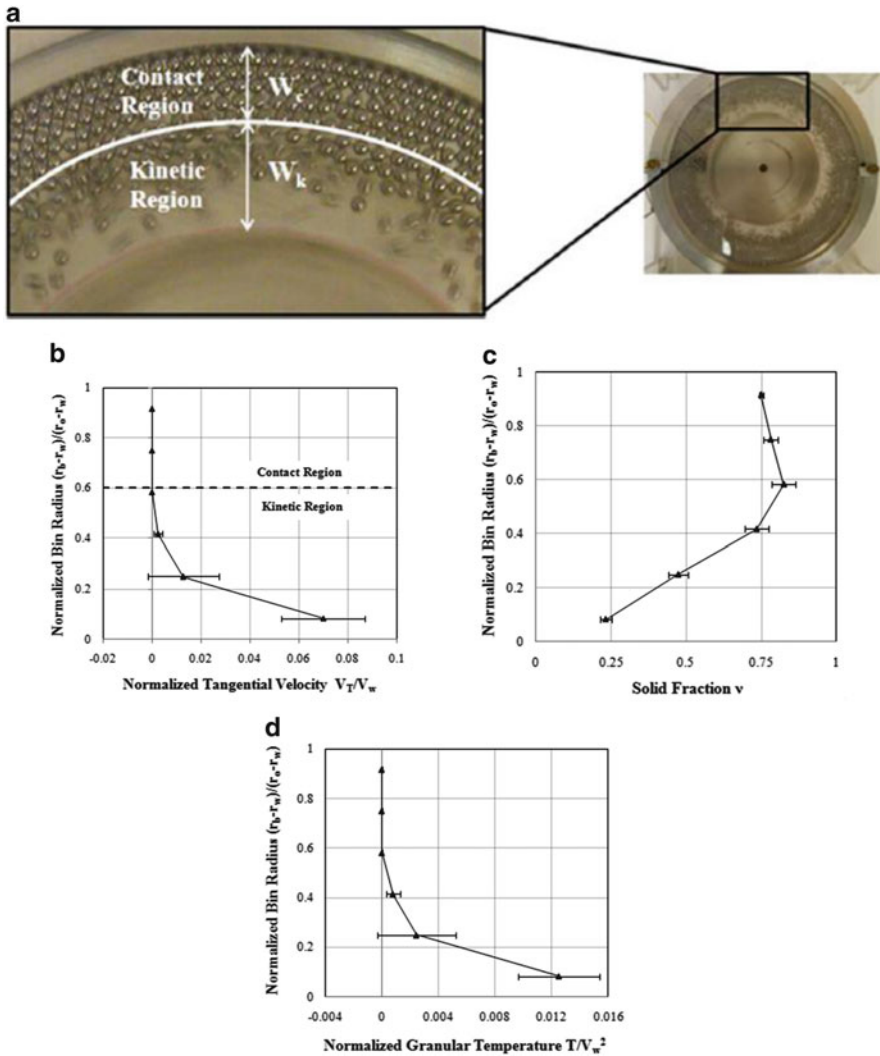


Fig. 12.7 Experimental results for the granular shear cell (GSC) [35]: (a) image of experiment displaying kinetic and contact flow regions, (b) velocity profile, (c) solid fraction profile, and (d) granular temperature profile

shearing gap were mobile. On the other hand, in the second type of flow, some granules remained stationary and others were sheared rapidly creating an internal boundary.

Miller et al. [69] performed experiments on variable-sized glass beads by shearing them in a Couette parallel geometry. They measured the fluctuations in normal stress. Yu et al. [2] sheared glass beads in a parallel shear cell apparatus in order to measure normal and shear stresses. This is the first experimental work that refers to

normal stress as load and shear stress as a frictional stress. They also proposed the idea of granular kinetic lubrication in this paper. Effects of surface roughness, particle size, and solid fraction are further elaborated using the same setup as Craig et al. [70, 71]. Elkholy and Khonsari [3] performed experiments to investigate the characteristics of granular collision lubrication by using a rig similar to that of Yu et al. [2]. In their work [3], three regions were witnessed along the width of the flow. The first region consisted of the granules adjacent to the upper moving wall; the second was the “locked” (or jammed) granules adjacent to the bottom stationary wall; and the third region was the transitional region in between [3].

Converging-type geometry, also called bearing type, usually refers to a geometry that has a converging region that the particulate materials are entrained in during operation to produce a lubrication effect, as seen in Fig. 12.1c. The shear cell apparatus developed by Yu et al. [2] was adjustable such that it could have a flat shear surface or a surface containing three sloping regions with a step. This geometry created a converging gap between shearing surfaces. They confirmed that lubrication wedge effect exists and that the (lubrication) normal stress is roughly proportional to the square of the surface slope. Additional experimental studies into converging gap geometries can be seen in the experimental investigations into the behavior of planetary rover wheel–terrain interactions, which have already been mentioned and discussed in Sect. 2.1.

2.3 Modeling

Granular flow modeling can be divided into two categories or factions. These categories are discrete and continuum modeling. Discrete modeling treats each individual particle within the flow as a single entity while discretizing time into individual time steps at which the particles can move and interact with each other and the boundaries. In a discrete modeling approach, all the granules are tracked at every time step and simulations are driven by the collisions and interactions of the individual granules. Flow parameter results are obtained by means of averaging discrete particle data from the individual granules in the flow. In contrast, continuum modeling treats the granular flow as a fluid-like continuum through the use of mass, momentum, and energy conservation equations, with granular modifications, to describe the flow. These conservation equations can be paired with constitutive relations and boundary and initial conditions to effectively solve for the flow parameters of interest, in the same manner that the Navier–Stokes equations might be solved for a fluid. This section will discuss the three main discrete modeling approaches as well as continuum modeling.

2.3.1 Discrete Modeling

There are three major discrete modeling approaches which will be discussed in this section. These three approaches include the discrete element method (DEM),

lattice-based cellular automata (CA), and the explicit finite element method (FEM). As will be detailed in the following sections, these discrete approaches differ in significant ways such as their particle physics, spatial discretization, and/or processing algorithms.

Discrete Element Method (DEM)

The discrete element method (DEM) of particle modeling, originally introduced by Cundall and Strack [72], treats each particle as an individual and singular entity which moves freely through space (at fixed time intervals), participating in interactions with other particles and boundaries. DEM modeling can be split into two main classifications: the hard-sphere (body) model and the soft-sphere (body) model.

Hard-Sphere DEM: The hard-body model assumes that particle collisions are instantaneous, nonoverlapping, and binary, meaning that one particle may only interact with one other particle in a given time step. As a result of not having to incorporate multi-particle contacts, the hard-body model can utilize a larger time step and is better suited for dilute flows. Particle collisions are generally solved through the use of coefficient of restitution (COR), coefficient of friction (COF), and coefficient of rotational (tangential) restitution (CORR) interaction parameters. Walton [73] provides a friction-inclusive hard-sphere collision model which is essentially an extension of the works of Hawkins [74] or Hopkins and Shen [75]. This model [73] serves as a good representation of collision processing within hard-sphere collision models and is thus presented in detail. The hard-sphere model presented in Walton [73] is based on the use of the three previously mentioned parameters: COR (e), COF (μ), and CORR (β_0). Conserving linear momentum and making use of the definitions of the coefficient of restitution ($e = v'_n/v_n$) and the coefficient of rotational restitution ($\beta = -v'_s/v_s$) result in (12.6) and (12.7) for the changes in normal direction velocities (Δv_{na} and Δv_{nb}) of two colliding spheres (denoted a and b):

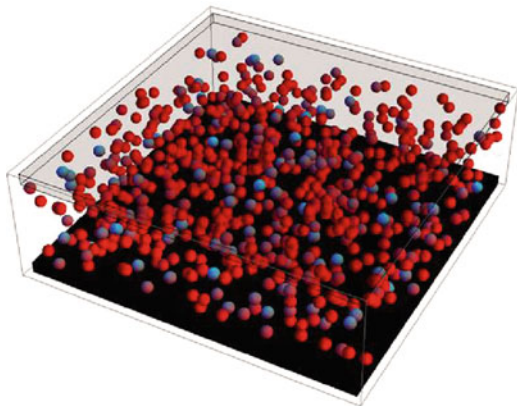
$$\Delta \vec{v}_{na} = \frac{m_b(1+e)}{m_a+m_b} \vec{v}_n \quad (12.6)$$

$$\Delta \vec{v}_{nb} = \frac{-m_a(1+e)}{m_a+m_b} \vec{v}_n \quad (12.7)$$

where m and v_n represent the mass of the particles and the relative normal velocity, respectively.

In terms of application of the hard-sphere model, Campbell and Brennen [76] compared their two-dimensional simulations of collisional granular flows to experiments by Savage and Sayed [67] and Bagnold [57]. Hopkins and Louge [77] developed a two-dimensional computer simulation for rapidly shearing uniform smooth inelastic disks. They compared the results to the theoretical

Fig. 12.8 Couette shear cell simulation domain (similar to that of Louge [81])



model of Jenkins and Richman [78] with good agreement. Sawyer and Tichy [79] performed numerical and particle dynamic simulations to generate results that were compared to the granular experiments of Yu and Tichy [80]. Louge [81] examined the interaction of a rapid granular flow with a flat, frictional wall, by means of a simulation domain similar to the one shown in Fig. 12.8, with the addition of hemispheres along the upper wall. In this same work, Louge [81] also displays results for the dynamic friction coefficient vs. normalized slip at the wall at varying friction coefficients. Louge [81] compares numerical simulation results against theoretical predictions from Jenkins [82].

Soft-Sphere DEM: In contrast to the hard-body approach, the soft-body particle collision model treats the granules as deformable spheres which allows for enduring (over multiple time steps) and multiple particle contacts. This requires the soft-body approach to employ a relatively small time step. In the soft-body collision approach, particle interactions are governed by force laws which determine the sum of the forces acting on the particles and hence dictate the resultant motion of the interacting particles. As a result, the soft-body approach is well suited for modeling dense granular flows where multi-body contact is prevalent.

Examples of force models and equations used in the soft-body modeling approach are provided by McCarthy et al. [83]. This set of force models (equations) is presented as merely a sampling of the types of equation used in the soft-body approach. There are certainly a wide range of other force equations and models available. In terms of normal forces, two separate force models are examined. The first normal force (F_n) model is a spring–dashpot model shown in (12.8):

$$F_n = k_n \alpha^{3/2} - \beta \alpha \dot{\alpha} \quad (12.8)$$

The first term acts as the “spring” term, where α and k_n represent the particle overlap and the normal force constant from Hertz theory [42], respectively. The second term acts as the “dashpot,” where β and $\dot{\alpha}$ define the damping parameter and the relative normal velocity of the colliding particles, respectively. A plastic normal

force model is also examined in the work of McCarthy et al. [83] and is shown in (12.9):

$$F_n = F_y + k_y(\alpha - \alpha_y) \quad (12.9)$$

The variables F_y and k_y respectively define the yield force and plastic stiffness ($k_y = (3/2)(F_y/\alpha_y)$). The variable α_y is the deformation at the point of yield. A tangential force (F_t) model is shown in (12.10):

$$F_t = F_{t_0} - k_t \Delta s \quad (12.10)$$

In (12.10), F_{t_0} , k_t , and Δs define the initial tangential force during the previous time step, the tangential stiffness, and the tangential displacement during the current time step. The quantity $k_t \Delta s$ gives the incremental change in tangential force during the current time step based on relative particle motion. Finally, a rolling friction model is also included, where the torque resisting the rolling motion (M_r) is calculated as shown in (12.11):

$$M_r = -\frac{3\gamma}{16} a F_n \frac{\omega}{|\omega|} \quad (12.11)$$

In (12.11), γ , a , and, ω define the fraction of energy lost in a single rotation, the radius of the contact spot, and the angular velocity of the particle, respectively. By defining a coefficient of rolling friction as $\mu = 3\gamma a/16R$, this (12.11) can be reduced to (12.12):

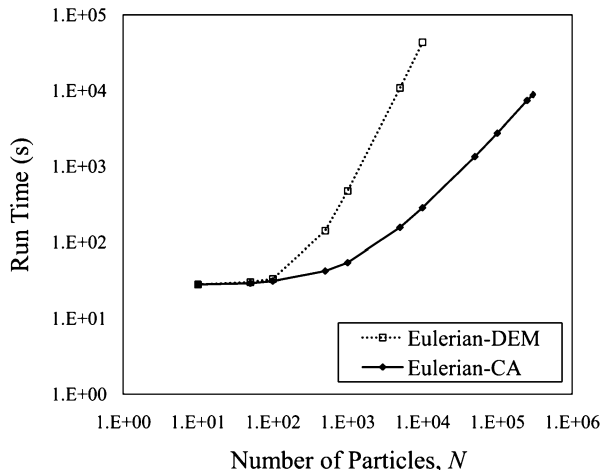
$$M_r = -\mu_r R F_n \frac{\omega}{|\omega|} \quad (12.12)$$

Overall, the discrete element method provides for a large amount of accuracy in the simulation of granular flows. The development and use of numerous force and particle interaction models allows for rigorous modeling of granule interactions at the local level. This results in DEM being able to provide good quantitative and qualitative predictions for a number of flow situations. As a result, DEM is often considered the “gold standard” in granular flow modeling. The one major drawback of the discrete element method is its computational cost. As a result of its rigorous modeling, DEM simulations tend to be extremely computationally demanding and costly. This becomes particularly concerning as the number of particles being simulated is increased.

Cellular Automata (CA)

Cellular automata (CA), originally introduced by von Neumann [84] in his study of biological systems, is a discrete modeling platform for obtaining fast first-order

Fig. 12.9 Time study for CA vs. DEM at increasing particle counts, as presented in Marinack et al. [86]



approximations of the properties of many physical systems, such as local granular flow properties. CA modeling uses either rule-based mathematics or physics-based equations to model physical processes (such as granular flow). It does this on a lattice, where space is divided into cells and each cell exists in one of a defined number of states.

CA is based on several fundamental principles, which are common among CA modeled systems. These principles, outlined in Ilachinski [85], include:

1. Space is represented by a uniform grid made up of discrete cells.
2. Each cell should be in one of a finite number of fixed states.
3. Cells may change states only at fixed, regular intervals of time.
4. States are updated in accordance with fixed local rules operated on an interaction neighborhood.

The major advantage of using a CA model is its computational efficiency. For example, a multiphase (solid particle–fluid) flow model, which combined computational fluid dynamics to model the fluid phase and CA to model the particle phase [86], has demonstrated the potential computational advantages of using a CA approach over DEM. It did so by comparing the CA model’s run times for simulating ten real-time seconds of a low solid fraction multiphase flow between parallel plates against run times for a model using DEM for the particle phase. As shown in Fig. 12.9, as the number of particles in the simulation domain increased, CA provided for an increasingly large amount of time savings. Another advantage of the CA model is that because the particles are on a lattice and only move based on neighbor interactions, no particle interaction behavior is missed. Additionally, the spatial lattice is inherently comprised of neighborhoods, which can each be processed in parallel.

The disadvantages of the CA model include an accuracy trade-off and some simulation limitations. While CA is a fast first-order modeling approach, the computational efficiency of CA leads to a trade-off in accuracy as compared to

the DEM approach. Additionally, the lattice-based spatial discretization scheme makes it impossible to model length scales smaller than the size of a lattice cell. Additional comments and details on the strengths and limitations of a CA framework are given by Jasti and Higgs [87].

CA has been used to model a wide array of granular behavior, including segregation [88–90], heap formation [91–93], and flow down silos and hoppers [94, 95]. Particle interactions in a CA model can be derived from empirically based rules (often from lookup tables), rule-based mathematics, or physics-based equations. The Higgs' group began employing physics-based particle interaction equations to granular tribology problems through the CA modeling framework [87, 96]. Other works [89, 91, 93, 94] consider the dissipative nature of COR and COF in processing particle interactions. However, they do not apply them directly through the solving of physics conservation equations, but rather through rules based on probability.

Jasti and Higgs [97] applied a CA modeling approach to granular flow lubrication and compared results from the CA simulations to the granular kinetic lubrication (GKL) model [1]. The GKL model is a continuum approach that applies rheological constitutive equations for stress, conduction and dissipation to thin granular shear flows, as well as rigorous boundary conditions for momentum and energy transport [1]. Particles in the CA model from Jasti and Higgs [97] were processed primarily with a rule-based approach as shown in Fig. 12.10. Figure 12.10 displays the rules for processing particle–particle interactions inside of the parallel-type shear cell geometry. The results from the CA simulations were promising as they showed a favorable match to results from the GKL continuum model [1] for the prediction of slip at the wall of a shear cell. Other uses of CA in granular tribology include Osterle et al. [98], who used a CA modeling approach to examine the flow of third bodies during dry sliding in automotive braking technology.

Jasti and Higgs [87] applied CA modeling to annular-type geometries (see Fig. 12.1a), namely, the granular shear cell (see Fig. 12.5). Marinack and Higgs [96] extended this CA framework to include interparticle friction and spin. In this work [96], particles which collided on the CA grid were processed using the full model from Walton [73], as presented previously during the discussion of hard-sphere DEM. The simulation representation of the GSC and velocity profile results from this work [96] are shown in Fig. 12.11. For relatively dilute flows (see Fig. 12.11a), results showed that the CA model which accounted for friction compared much more favorably to the experiment than the frictionless CA model.

Finite Element Method (FEM)

The finite element method (FEM) has become widely used in the tribology community to study complex contact, thermal, fluid, and structural interaction. In the finite element analysis arena, two distinct methods, the implicit and explicit time integration techniques, have emerged for simulating engineering and scientific problems. Although both of these methods are used to solve the same basic set of

Fig. 12.10 Rules for processing particle–particle interactions in the model of Jasti and Higgs [97]

Input	Output	Input	Output

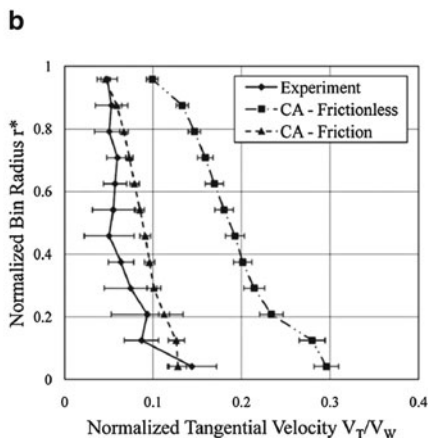
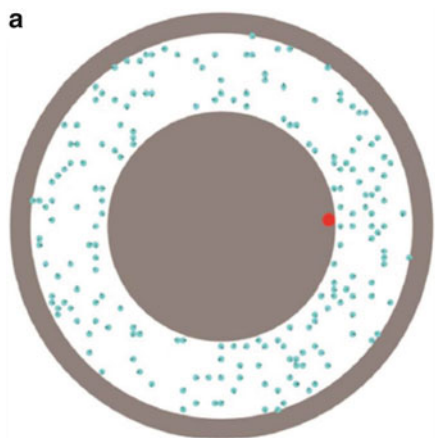


Fig. 12.11 CA simulation of the GSC (Fig. 12.7) from Marinack et al. [96]. (a) The simulation domain. (b) Velocity profile results for experiment and CA simulation

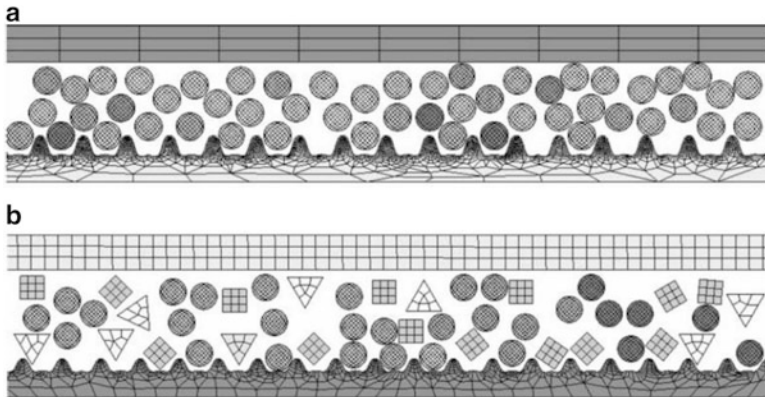


Fig. 12.12 Meshed finite element models [100] with (a) round particles and (b) multi-shaped particles

governing equations, the primary applications for which each method obtains a robust accurate solution are vastly different. Explicit FEM was originally developed to solve problems in wave propagation and impact engineering, but more recently, it has been applied to diverse areas that include sheet metal forming, underwater simulations, failure analyses, glass forming, metal cutting, pavement design, and earthquake engineering [99]. Since the method is good for highly transient events, the explicit FEM approach has been employed in granular flow tribology.

Kabir et al. [100, 101] first introduced the explicit FEM approach for granular modeling. In these works [100, 101], the explicit FEM method (using LS-DYNA software) was applied to modeling parallel (Couette) shear cells where the top wall remained stationary while the rough bottom wall moved at a fixed velocity. Figure 12.12 shows examples of two meshed finite element models [100], one of which contains round particles (Fig. 12.12a), while the other contains multi-shaped particles (Fig. 12.12b). In both cases, the roughness bumps on the bottom wall can be seen. As can be seen in Fig. 12.12, the particles themselves are meshed and thus comprised of a number of elements. This is in contrast to the previously examined discrete element method (DEM) and cellular automata (CA) approaches, which treat each particle as a single entity. As a result of individual particle meshing, the stress distributions inside of the particles can be obtained. This ability allows for many interesting phenomena to be witnessed in explicit FEM simulations, such as the breaking and forming of force chains. Figure 12.13 [100] displays an example of this behavior where a chain of particles spans the gap from the upper to lower wall. The stress distribution is easily viewed, obviating the formation of a force chain throughout these particles.

There are several advantages that make FEM uniquely suited to model granular flow tribosystems. First, FEM allows deformations of the grains to happen in silico (i.e., during the simulation), which means that the surrounding particles have to

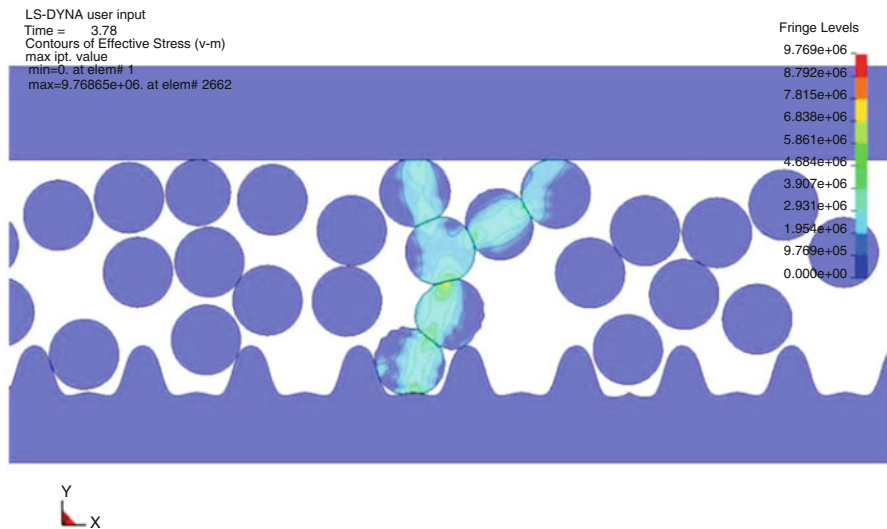


Fig. 12.13 Stress and deformation plot from an explicit FEM study of a shear cell, performed in the work of Kabir et al. [100]

react to a newly deformed geometry, where particles have modified shapes and contact behavior. Secondly, the explicit FEM approach can handle complex boundaries and aspherical particles (as shown in Fig. 12.12b), since the FEM framework meshes all solid objects with a finite set of elements that can be assigned varying material behavior. This also enables FEM to accommodate heterogeneous materials with varying mechanical properties or material behavior. Third, the main material information needed to simulate the contact and collision behavior of grain flow is the mechanical properties, since the FEM framework is fundamentally solving the continuum equations of solid mechanics. Thus, collisional system parameters such as the coefficient of restitution can be predicted in FEM whereas it is normally required as input in the DEM and CA approaches. As such, FEM work to predict COR has been done to consider elastic and elastic–plastic impact of spheres against substrates of varied thickness [102], repeated impacts [44], and many other collision situations [49, 103–105]. There are two major disadvantages of the explicit FEM approach with application to discrete grain simulations. First, as it is not an implicit approach (i.e., unconditionally stable for large time steps), smaller time steps have to be used to maintain stability. The time step in the explicit FEM approach must not exceed $\Delta t = L_e/c$, where L_e is a mesh element length and c is the wave propagation velocity through the material [106], which is often the speed of sound. Therefore, the time step scales down with increased FEM mesh resolution. Second, as the FEM particles are meshed (as opposed to a single element per particle in DEM or CA), computational costs per contact event are higher than the mesh-free particles.

2.3.2 Continuum Modeling

This section is adapted from the detailed review performed by Wornyo et al. [4]. Since granular flows exhibit fluid-like behavior, continuum approaches for modeling granular flows have used the conservation equations for mass, momentum, and granular energy, which take into account velocity fluctuations and the inelastic collisions of particles. Once obtained, the governing equations are solved for parameters such as velocity, solid fraction (or density), friction coefficient, and load-carrying capacity. Constitutive relations are also needed to describe the behavior of dry particulates, in addition to describing the behavior of the particulates at the surface boundaries.

The granular tribology community [1, 79, 107, 108] has employed granular forms of the conservation equations as described by either Haff [109] or Lun et al. [110]. The conservation of mass equation for granular flows is of the form

$$\frac{D\rho}{Dt} = -\rho \left(\vec{\nabla} \cdot \vec{U} \right) \quad (12.13)$$

where the granular flow density ρ and granular mixture velocity U are the key parameters. The granular conservation of momentum equation is

$$\rho \frac{D\vec{U}}{Dt} = \rho \vec{g} - \nabla \cdot \vec{\pi} \quad (12.14)$$

where $\vec{\pi}$ is the stress tensor and \vec{g} is the body force vector. The granular conservation of energy equation is also known as the pseudoenergy equation. It is similar to the conventional energy equation for fluids except that the rate of change of the granular temperature is balanced against the energy added and dissipated from the system due to friction and inelastic particle collisions. The granular temperature is a measure of the fluctuating component of the granular particles relative to the mean granular velocity field [111]. Thus, it is written as

$$\frac{3}{2} \frac{D(\rho T)}{Dt} = -\vec{\nabla} \cdot \vec{q} - \varphi^f - \varphi^c \quad (12.15)$$

where \vec{q} is the molecular energy transport, φ^f is the work rate of momentum, and φ^c is the inelastic work rate (dissipation due to inelastic particle collisions). Details on (12.13)–(12.15) can be found in Higgs and Tichy [1].

Haff's continuum theory and constitutive relations [109] for describing the motion of granular material are used frequently by granular tribologists ever since Elrod took the "first look" in his granular tribology review paper [112], which focused largely on granular flows. Adopting Haff's constitutive relations, Dai et al. [113] worked to determine the capability of granular flows to be viable mechanisms for lubrication in slider bearings. Subsequently, McKeague and

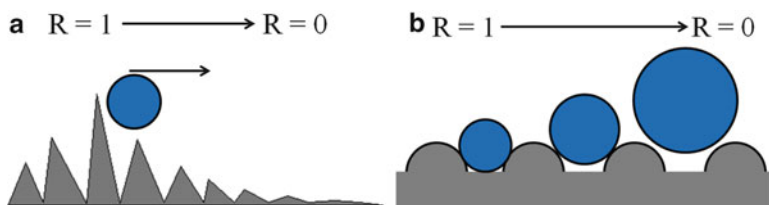


Fig. 12.14 Roughness factor schematic (adapted from [4]). The roughness factors are defined as: (a) the fraction of lateral momentum imparted to the granule by the surface and (b) the fraction of a granular particle that fits between wall hemispheres

Khonsari [5] used his theories to perform parametric studies with granular flows and also to predict the hydrodynamic pressure profiles from the well-known powder lubrication experiments of Heshmat [114]. Tribologists have also used constitutive relations by Lun et al. [110] to model granular flows in parallel sliding contacts under load [1, 79, 108, 110] and granular slider bearings [115].

Developing relations to describe the behavior of granular materials around the boundaries is also important. The boundary equations in the granular tribology community are often derived from the work of Jenkins and Richman [116] and Hui et al. [117]. In these works, the macroscopic roughness factor R varies as $0 \leq R \leq 1$, where $R = 0$ corresponds to a fairly (macroscopically) smooth surface and $R = 1$ corresponds to a very (macroscopically) rough surface. It has been characterized in Fig. 12.14 as the fraction of lateral momentum transferred to the granular flow by the walls [118] and the fraction of a granule that fits exactly between the cylindrical wall disks [119]. The roughness factor affects the slip at the boundary, which ultimately affects the granular film's ability to accommodate velocity and carry load.

3 Slurry Tribology

“Slurry tribology” is the study of particle–fluid suspensions as they relate to friction, lubrication, and wear. In tribology, slurries are often used to remove materials from surfaces in a controlled manner [120–123]. However, oftentimes, engineering solutions are sought to reduce the amount of material removed from surfaces due to slurry wear mechanisms such as abrasion and erosion [124]. In other scenarios, slurries formed by adding lubricious particulates to fluid lubricants can actually increase bearing life [125]. Though the behavior of a slurry in a tribological environment is complex, many people are already familiar with natural processes that are dominated by slurry tribology. The erosion of riverbeds due to small rocks suspended in the flow is also a slurry tribological phenomenon.

In one of their most familiar tribological applications, slurries are used as lapping and polishing compounds for the preparation of test specimen surfaces. The micron- and submicron-sized particles used in these polishing applications are

essential for achieving the desired surface finishes. Though there are many different particle types in slurries, a few of the most common ones used in slurry polishing are silica, alumina, and synthetic diamond. The specific abrasive particle type is chosen based upon parameters such as the material being polished, the base fluid in which the particles are suspended, the polishing load and speed, and the desired surface finish. Typically, the smaller the particle size, the better the surface finish (i.e., lower surface roughness) as large particles may remove more material and produce unwanted scratches. This type of slurry polishing has been used for years with much success. Currently, there are many new and exciting applications of slurry tribology.

3.1 Slurry Tribology Applications

In this section, three important uses of slurry tribology in relation to nanofabrication, lubrication, and energy production are discussed.

3.1.1 Slurry Tribology in Nanofabrication

Over the last several decades, chemical mechanical polishing (CMP) has become a fundamental application of slurry tribology [126]. CMP is used to fabricate computer chips or integrated circuits (ICs) because of its ability to planarize and polish the large wafers on which ICs are built. During CMP, the wafer is pressed into a soft rotating polishing pad. Between the pad and the wafer, a chemically-active slurry, containing abrasive nanoparticles, is entrained. Though there is still discussion in the literature regarding the details of the wear mechanisms in CMP, it is generally accepted that the nanoparticles in the slurry abrade the wafer to remove unwanted material from its surface. In Fig. 12.15, an image of the G&P Poli-300 CMP machine is displayed.

Though widely used in the IC fabrication industry, improper CMP is known to impart defects on the IC's [122]. As the IC is built, nano-sized trenches are etched into the dielectric materials (mostly silicon dioxide) on the surface of the wafer. Conductive copper is deposited into these trenches to form copper lines which serve as the wires in the IC. To ensure that the trenches are filled, it is easier to deposit copper over the entire wafer and remove the excess using CMP. Once much of the excess copper has been removed, the resulting wafer surface is a heterogeneous combination of soft copper and hard dielectric materials. The difference in material properties between the copper and the dielectric can result in differential wear rates as CMP is performed. Two defects which occur during this CMP process are commonly known as "dishing," which is unwanted material removal from the copper line, and "erosion," which is unwanted material removal of the dielectric. Moreover, contact stresses and fluid pressures in the slurry can cause changes in material removal rates at the edge of the wafer. This unwanted material removal can

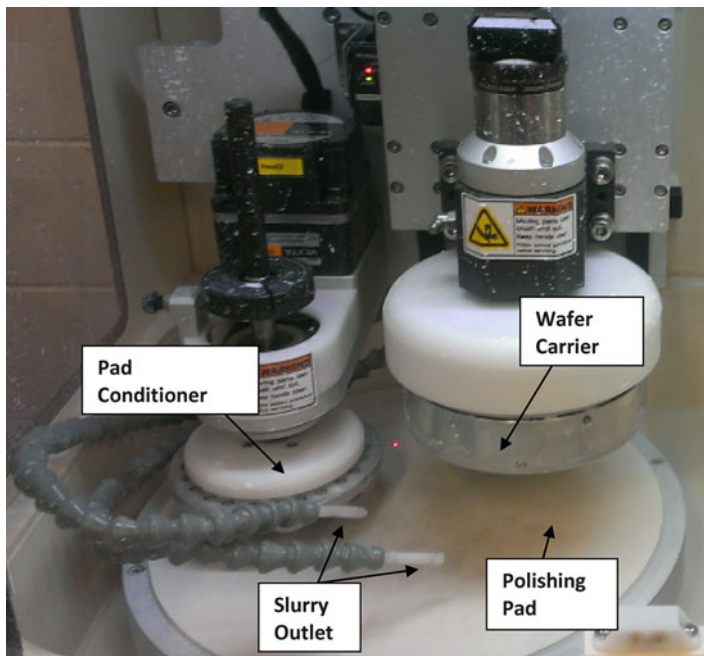


Fig. 12.15 An image of the G&P Poli-300 CMP machine

result in electrical shorts or open circuits which may ultimately require the IC to be discarded. Understanding the mechanics of the slurry during CMP can lead to a reduction of such defects [126].

3.1.2 Slurry Tribology in Lubrication

Greases and oils provide essential lubricant films for machine components such as bearings, gears, chains, and seals. However, when tiny particulate matter is entrained into these lubricants, a slurry is formed which, in many cases, exacerbates wear and reduces the lifetime of the hardware [127]. Once the particles get into the interfacial film, they can disrupt the load-carrying capacity of the film and reduce the lubricant's effectiveness. If the particles are so large that they transmit load between the surfaces, stresses on the surfaces can result in unwanted wear.

There are several examples of this phenomenon. In the internal combustion engine, the air filter helps to prevent particulate matter from entering the engine. However, when sand or dirt particles in the air intake make it past the air filter, these particles can enter the combustion cylinder and make their way into the lubricant system. Notably, they can become trapped in the lubricant film on the piston rings and cause abrasive wear damage to the cylinder walls [127]. In internal combustion

engines, particulates are also generated as a result of the combustion process itself. Soot particles can be formed which affect the lubricant's performance. Finally, a third example is the generation of particulate matter due to wear debris. During startup and shutdown, bearings are particularly vulnerable to wear as they transition into the mixed and boundary lubrication regimes. Once this happens, wear debris can be introduced into the lubrication system. Oil filters in engines are used to help remove particulate debris from the lubricant to minimize the effect of these wear particles.

Artificial Joints

Another example of slurry formation in lubricants occurs in the human body. When hip and knee replacements are performed, cements, such as polymethyl methacrylate (PMMA), are used to bind materials together. Over time, the PMMA can chip generating sharp fragments which make their way into the synovial fluid forming a slurry. This slurry of synovial fluid and PMMA fragments can be detrimental to joints and cause unwanted wear to them [128].

Particle Additives

It should be noted that not all slurries are detrimental to lubricated interfaces. Particle additives such as polytetrafluoroethylene (PTFE) and molybdenum disulfide (MoS_2) have been discussed in the literature for years. Some studies indicate that the effect of such additives may increase bearing performance [129] and this practice has been adopted commercially. There is, however, a balance between particulate additives acting to increase the bearing performance and the potential for them to clog the interface reducing the entrainment of lubricant into the bearing. That has led to the emerging and exciting new field of nano-fluid slurry lubricants. Nano-fluid slurry lubricants are fluid lubricants to which nanoparticles have been added. The particles in nano-fluid slurries may be large enough to help lubricate the interface during boundary and mixed lubrication but small enough to reduce the potential for clogging [125, 130]. Additionally, because of their fine size, nanoparticles may form a more uniform protective layer on the surfaces as compared to larger micron-sized particle [131].

There have been several studies which have investigated the use of nanoparticles as lubricant additives which show great promise in improving bearing performance. In a recent work, boric acid particles were added to environmentally-friendly lubricants, such as canola oil, and displayed a reduction in friction [130].

As a final example of the potential benefits of particles in lubricants, there is a class of bearings called "two-phase porous" bearings which rely on the presence of particles, advected by the lubricant, to clog pores in the bearing surfaces reducing their porosity. Once the porosity of the bearing is reduced, sufficient film pressures are generated to carry the bearing loads [132].

3.1.3 Slurry Tribology in Energy Production

Slurry tribology is an important component in energy production. There are several examples of the role of slurry tribology in the petroleum industry. Petroleum and natural gas reserves are found deep under the Earth's surface. When drilling for these fuel reserves, it is common to use a slurry to lubricate the drill bit as it cuts into the rock formation [133]. This slurry, called a drilling fluid (often referred to as a drilling "mud" in the field), is an important component in the drilling process. The drilling fluid (1) lubricates the drill bit, (2) removes heat from the rock–drill bit interface, (3) transports rock cuttings away from the well bore, and (4) helps to prevent well blowouts by keeping formation fluids from prematurely entering the well bore.

Typically, the drilling fluid slurry is either oil based or water based and contains particles such as calcium carbonate. By adjusting the concentration of particles and the particle type, the drill operator or "mud engineer" responsible for the drilling fluid can "tune" the drilling fluid's properties to better perform its tasks.

A closely related application of slurry tribology is a process called hydraulic fracturing. During hydraulic fracturing (often called "fracking"), fracturing fluid is pumped into fissures and cracks in the rock formation. The high pressure of the fracturing fluid fractures the rock formation releasing pockets of trapped gas. Much like drilling fluid slurries, fracturing fluid slurries are comprised of a base fluid and loaded with particulates to enhance their performance.

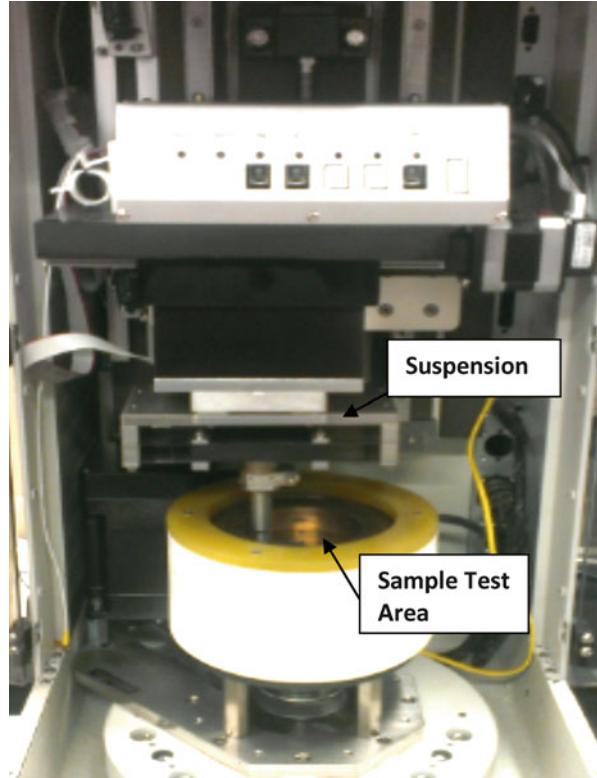
Finally, after the petroleum fluids have been taken from the ground, sand and dirt in raw petroleum fluids create a slurry which can cause erosive wear to pipe surfaces as it is being transported long distances to refineries. This erosion is particularly severe at areas where the fluid changes directions or velocities sharply such as pipe elbows, tees, and valves [124].

3.2 Slurry Tribology Experiments

Before using a slurry in tribological applications, it is important to test its performance. There are many devices that have been created which can assess the performance of slurries. One such device is a multipurpose tribometer. These types of instruments can be configured to conduct experiments such as pin-on-disk tests in which a slurry can be introduced into the interface. Additionally, some of the machines can be configured to do benchtop CMP to test the performance of different CMP slurries. Moreover, 4-ball tests can be run with contaminated lubricants to test their effect on potential ball-bearing applications. In Fig. 12.16, an image of the CETR UMT multipurpose tribometer is displayed.

In addition to these multipurpose slurry tribometers, there are also a host of highly specialized tribometers which are used to test slurries in extreme conditions using specialized materials. An example of this is the spiral orbit tribometers

Fig. 12.16 CETR UMT multipurpose tribometer

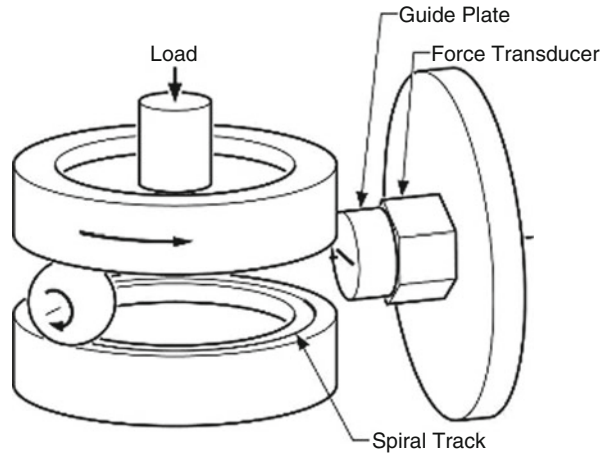


(SOTs) used by the US National Aeronautics and Space Administration (NASA) to evaluate the performance of nano-fluid slurry lubricants under a high vacuum [125]. A schematic of the SOTs used by the NASA Glenn Research Center is shown in Fig. 12.17 [134].

3.3 *Slurry Tribology Modeling*

Many techniques have been developed to model the behavior of slurries in tribological applications. The challenge in modeling slurries is that particle–particle interaction and particle–fluid interaction usually play a significant role in the slurry behavior. Slurry tribology modeling has benefited from decades of fluid modeling and particle modeling from the well-developed fields such as fluid mechanics, colloid science, and granular flow.

Fig. 12.17 Schematic of spiral orbit tribometer used by the NASA Glenn Research Center to test nano-fluid slurry lubrications on ball-bearing components in extreme vacuum (Courtesy NASA/GRC [134])



3.3.1 Fluid Modeling

Typically in tribology, fluids are modeled using the Reynolds equation. The Reynolds equation (12.16), derived from the more general Navier–Stokes equations, is suitable for predicting fluid pressures in thin interfaces at low Reynolds numbers [135–137]:

$$\frac{\partial}{\partial x} \left(h^3 \frac{\partial p}{\partial x} \right) + \frac{\partial}{\partial y} \left(h^3 \frac{\partial p}{\partial y} \right) = 12\eta U \frac{dh}{dx} \quad (12.16)$$

To derive the Reynolds equation, from the Navier–Stokes equations, there are several assumptions which must be made [138]:

1. Body forces are negligible.
2. Pressure is constant through the lubricant film.
3. No slip at the bounding surfaces.
4. The lubricant flow is laminar (low Reynolds number).
5. Inertial and surface tension forces are negligible compared with viscous forces.
6. Shear stress and velocity gradients are only significant across the lubricant film.

The advent of increased computing power on modern personal computers and supercomputers has led to increased usage of computational fluid dynamics (CFD) as a means to predict fluid behavior in tribological interfaces. Because CFD is a numerical approximation of the Navier–Stokes equations (12.17 and 12.18), it is applicable for more general slurry modeling. Moreover, it is better suited for incorporating the effect of the slurry particles on the fluid:

$$\rho \left(\frac{\partial u}{\partial t} + u \frac{\partial u}{\partial x} + v \frac{\partial u}{\partial y} + w \frac{\partial u}{\partial z} \right) = - \frac{\partial p}{\partial x} + \mu \left(\frac{\partial^2 u}{\partial x^2} + \frac{\partial^2 u}{\partial y^2} + \frac{\partial^2 u}{\partial z^2} \right) \quad (12.17a)$$

$$\rho \left(\frac{\partial v}{\partial t} + u \frac{\partial v}{\partial x} + v \frac{\partial v}{\partial y} + w \frac{\partial v}{\partial z} \right) = - \frac{\partial p}{\partial y} + \mu \left(\frac{\partial^2 v}{\partial x^2} + \frac{\partial^2 v}{\partial y^2} + \frac{\partial^2 v}{\partial z^2} \right) \quad (12.17b)$$

$$\rho \left(\frac{\partial w}{\partial t} + u \frac{\partial w}{\partial x} + v \frac{\partial w}{\partial y} + w \frac{\partial w}{\partial z} \right) = - \frac{\partial p}{\partial z} + \mu \left(\frac{\partial^2 w}{\partial x^2} + \frac{\partial^2 w}{\partial y^2} + \frac{\partial^2 w}{\partial z^2} \right) \quad (12.17c)$$

$$\frac{\partial u}{\partial x} + \frac{\partial v}{\partial y} + \frac{\partial w}{\partial z} = 0 \quad (12.18)$$

In CFD, the momentum equations (12.17a–12.17c) are discretized, and pressure–velocity coupling is achieved by seeking to satisfy the continuity equation (12.18). The variables u , v , w , and p represent the x , y , z components of the fluid velocity and the pressure, respectively. The increased modeling fidelity and flexibility gained by using CFD comes at the price of computational time. As a result, when applicable, the Reynolds equation is still widely used today. As computers become faster, it is expected that CFD usage will increase in slurry tribology. Computational processing speeds may become so fast that widespread simulation of fluids in slurry tribology can be performed using molecular dynamics (MD). In MD, the fluid is not modeled as a continuum. Instead the behavior of the atoms that comprise the fluid is simulated. It is currently unfeasible to perform macroscale slurry tribology simulations using MD due to the computational resources required. However, much progress has been made in the study of nano-fluids using MD simulations at nanoscales. In the not-too-distant future, it may be possible to run an MD simulation to predict the slurry behavior at the macroscale.

3.3.2 Particle Modeling

Particle modeling in slurry tribology has benefited from a number of other fields such as contact mechanics [42] and granular flow. It is typically assumed that the behavior of the particle in the absence of the fluid will be the same as when the fluid is present except for specific forces which are introduced by the fluid. There are many numerical methods now used to predict particle behavior in slurry tribology. One of the most commonly used techniques is the discrete element method (DEM). Details about the DEM and finite element method (FEM) for particle modeling in slurry tribology are provided in the granular flow tribology section 2.3.1.

3.3.3 Particle–Fluid Interaction

The fundamentals of particle modeling in slurry tribology were developed with little consideration for the particle’s effect on the fluid. Unlike classical multiphase flow mechanics where there are advanced treatments of particle dynamics, it was assumed that the particles would generally follow the path of the fluid and their

effect on the system would be to do the tribological work of removing material. This type of modeling, called one-way particle–fluid coupling, has been successful in predicting many phenomena such as material removal rates during CMP [139].

A desire to model the scenario with higher fidelity has led to the use of two-way coupling in particle tribology. In two-way coupling, the fluid is affected by forces from the particle, and the particle is affected by forces from the fluid [140]. Such interaction is necessary, especially when predicting the effect of particulates on the entrainment of lubricants into the interface between surfaces.

Typically, the momentum between the fluid and the particle is coupled by calculating the force of drag and the force of pressure gradients in the fluid (buoyancy) on the particle. In some of the earliest models, and in many models used today, Stokes drag was used to calculate the drag force. Stokes drag is applicable for spherical-particle slurry flows with low solid fractions (so that the effect of other particles can be neglected) and very low Reynolds numbers in areas where the fluid boundary has little effect on the flow around the particle. When these criteria are satisfied, Stokes drag can be calculated by 12.19:

$$F_{drag} = 6\pi\eta Ua \quad (12.19)$$

When these criteria are not satisfied, it may become necessary to take into account phenomena such as the shearing of the fluid through a collection of particles and the effect of wakes generated in the fluid as it flows around the particles. For the former, there have been methods derived based on empirical predictions for the flow through packed beds of particles [141]. For the latter, more detailed modeling may be necessary, and fine CFD meshes around particles have been created to elucidate this behavior. Empirical relations, such as the COR of immersed particles [55], have also been used in slurry modeling when such relations adequately describe the dominant physics [140].

Finally, slurry tribology has benefitted largely from the field of colloid science. The understanding of forces such as Magnus forces, Saffman forces, and Brownian forces gleaned from colloid science has helped in the modeling of slurry tribology. Notably, the attractive dispersion forces (such as van der Waals forces) and the repulsive electrostatic forces (such as electric double-layer forces) are important in modeling the stability of slurries and interactions between particles.

3.4 Future Trends in Slurry Tribology

Though slurry tribology has been studied for many years, advances in the understanding of nano-fluids have opened many new applications. As discussed earlier, the introduction of nanoparticles into lubricants can help to protect bearing surfaces during boundary and mixed lubrication. Additionally, smart slurries such as magneto-rheological fluids (MR) show great promise for future implementation as their properties can be tuned based upon external magnetic fields. This property

has much potential and has already been utilized in magnetically activated suspensions. Additionally, there is a need for much analysis and modeling to be performed for these novel applications and others such as two-phase porous bearings.

4 Powder Tribology

4.1 Introduction

Powder lubricants suggest dry, cohesive, soft particles that accommodate surface velocity differences by deforming under load and adhering to surfaces. Powder lubricants can reduce friction and wear between two surfaces below boundary lubrication levels, in a manner similar to granular lubricants because of their abilities to allow interlayer motion. These similarities include the generation of lift in sliding contacts, the existence of particle density distributions, the dependence of pressure on the mixture properties, and the demonstration of slip at the boundaries in macroscale geometries [4]. However, there must be distinguishing features in the flow of powder lubricants that separate themselves from granular lubricants. One of the main differences between powder and granular lubricants is the fact that powder lubricants adhere and coat surfaces while granular lubricants slip, roll, and collide with the surfaces at their boundaries. Because granular lubricants slip, roll, and collide, granular particles experience nearly elastic collisions. On the other hand, powder particles experience entirely inelastic collisions since they adhere to surfaces after colliding with them. Another difference between powder and granular flow lies in the size of their particles (powder particles are typically on the order of 1 μm or less, while granular particles are on the order of 1 mm). This is a weaker delineation since cohesionless powders which are on the order of microns can still transfer momentum between surfaces through collisions. There are also similarities and differences between hydrodynamic fluids and powder lubricants. Similar to hydrodynamic fluids, they shear in the bulk medium, where lubrication can be attained by steady velocity accommodation. Powder lubricants can achieve this lubrication process due to their lamellar structures. However, they are different in that powder lubricants can sustain load in not only static contacts but also in flows that include parallel geometries, where the “wedge” effect is absent [4].

To understand the physics of powder lubrication, it is important to acknowledge the macroscopic and microscopic interactions of powder lubricants. Some microscopic quantities that influence powder flows are the small forces between particles, individual particle size, and porosity [142]. The interlayer bonding between the lamellar structures affects the lubrication processes of powder lubricants as supported by friction data and results gathered from an electron microscope [143]. These characteristics play a role in some important macroscopic properties,

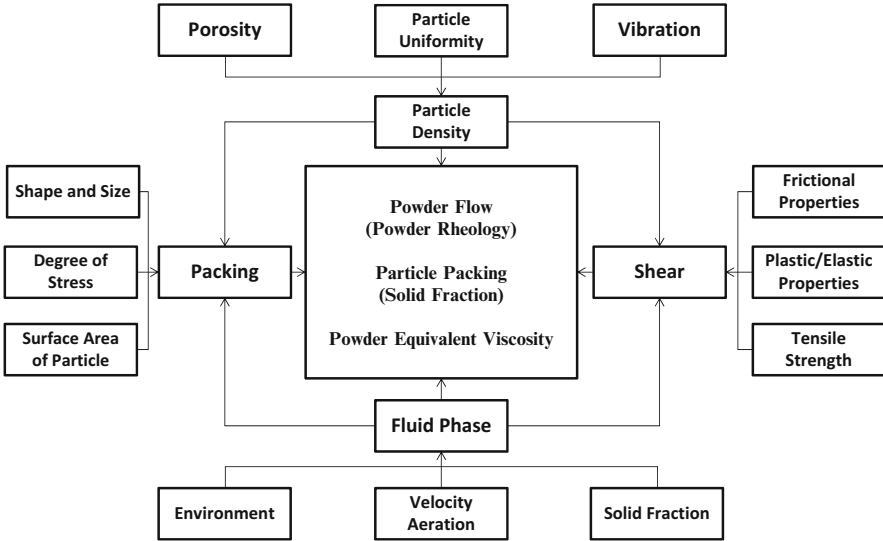


Fig. 12.18 Properties that affect powder lubricants

such as hardness and compaction. In powder lubrication, cohesive powder particles amalgamate, shear, and coat surfaces to improve lubrication performance by providing velocity accommodation and load-carrying capacity while reducing wear and friction. Figure 12.18 presents the intricacy of the dispositions that determine the circumstances of powder materials as reported by Higgs and Heshmat [144]. Some typical examples of lamellar powder lubricants include molybdenum disulfide [145, 146], titanium dioxide [147], boric acid [148], and tungsten disulfide [149].

4.2 Application and Phenomenon

Powder lubrication schemes have been proposed as innovative candidates for lubrication in extreme environments (i.e., temperature and/or loads), where conventional lubricants cannot perform adequately. For example, the increased capacity of turbine engines will result in high temperatures on the order of 800 °C, posing serious problems on modern cooling technology. At temperatures greater than 500 °C, conventional liquid lubricants are unable to sustain loads, hence, the advent of solid/particulate lubrication [4]. Kaur and Heshmat developed an oil-free journal bearing, capable of supporting significant rotor loads of 445 N (100 lb.) operating at 815 °C and 30,000 rpm that was lubricated by in situ powder film transfer. The dry particulate powders, which are pelletized, provide a long-lasting, low-power-loss backup bearing. Some applications that may use such bearings are ground- and space-based flywheel energy storage systems, auxiliary and integrated

power units, and gas turbine engines [150]. Similar concepts have been adopted by companies that manufacture several different types of self-lubricating bearings that utilize reservoirs containing polytetrafluoroethylene (PTFE) solid lubricants for aerospace, hydropower, industrial, and offshore applications.

Powder lubricant applications extend beyond the bearing domain. Heshmat designed a powder lubricant piston ring for adiabatic diesel engines and coal–water slurry-fueled diesel engines [151]. The heat transfer between the cylinder walls and the cooling system must be minimized in order to achieve an adiabatic cycle in an internal combustion engine such as a diesel engine. The heat transfer normally makes up for 30–35 % of the total fuel energy of a diesel cycle. An increase in surface temperatures at the piston is observed in this configuration during the compression stage. As the surface temperatures exceed the limit of the operational temperature for the engine oil, current adiabatic diesel cycles are reduced to keep the temperature of the process below the limit of the operational temperature of the hydrocarbon lubricant. The reduction of the engine's capacity results in lower fuel efficiency and lower power per unit weight.

Consequently, a powder-lubricated piston ring was proposed for an adiabatic cycle diesel engine that can operate at temperatures above the hydrocarbon lubrication limit of 600 °C, thus, permitting the engine to function with higher fuel efficiency and higher power output [151]. There are two embodiments of the patent. The first includes powder-lubricated piston rings in conjunction with hydrodynamic compliant-mounted bearings, and the second includes powder-lubricated piston rings in conjunction with oil-lubricated hydrodynamic rings. Quasi-hydrodynamic lubricant film between the piston and the cylinder is formed to provide a separation between the two surfaces. The flow of powder particles is similar to the motion of liquid molecules, such as hydrocarbon lubricant; the powder particulates provide a load-carrying capacity and film thickness.

Powder lubrication can also be seen as an important factor in the fault weakening of earthquake phenomenon [152]. For a long time, earthquake instability has been accredited to fault weakening during accelerated slip, and the main question of earthquake physics has revolved around identifying the weakening mechanisms. During experiments with dry solid-granite blocks, fine rock powder, known as gouge, quickly forms and is responsible for the reduced fault strength due to its organization into a thin deforming layer. When the gouge ages, which happens soon after slip, the fault would regain its strength rapidly, thereby, suggesting that only newly formed gouge can weaken the experimental faults. It can be observed that dynamic gouge formation is a common and causal mechanism for an earthquake due to the behavior similarity between a fault gouge and industrial powder lubricants.

4.3 Experiments

The evaluation of powder lubrication based on its frictional behavior and wear characteristics has been studied extensively. Various powder lubrication parameters such as materials, surface conditions, load, speed, temperature, environment,

contact area, and particle size are the main subjects of studies [153–155]. This section will explore some of the experimental approaches to determine the relationship between some of the mentioned parameters in both thick film (i.e., hydrodynamic lubrication) and thin film (i.e., boundary lubrication) types of powder lubrication.

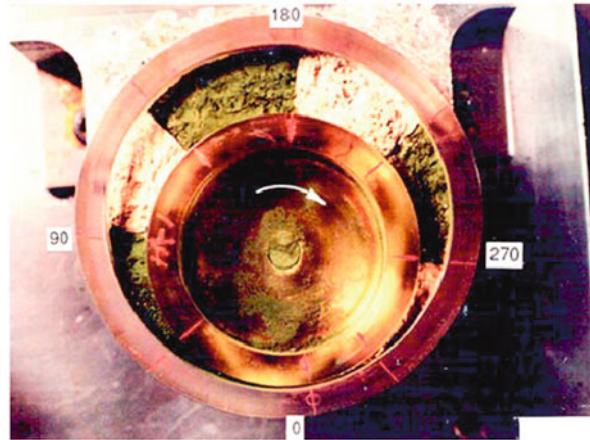
4.3.1 Thick Film Powder Lubrication

One of the earliest thick film experimental investigations was carried out by Heshmat to present a visual documentation of the fluid-like flow of certain powders [119]. It can be observed that a number of basic features of powder flow in narrow interfaces exhibit the characteristics of fluid film lubrication. These characteristics are also called the “quasi-hydrodynamic” nature of powder lubricants. The test rig assembly designed for flow visualization included a variable speed electric motor and a cup-shaped transparent journal bearing. The test rig and journal were made of a transparent thermoplastic synthetic resin (methyl methacrylate). A steel shaft was connected at the journal’s center. An outboard grease-lubricated bushing radially provided the support for the rotating shaft. A transparent cup-shaped cover was positioned over the journal bearing to minimize the powder loss during the test [119]. Figure 12.19 shows the general experimental setup.

The test rig was utilized to conduct a series of experiments to explore several features of powder flow in eccentrically convergent spaces. The transparent bearing clearance was filled with titanium dioxide (TiO_2) and molybdenum disulfide (MoS_2) powders in a layered manner. To provide a reference frame for the powder testing, the basic pattern of fluid flow in the interface of a journal bearing was demonstrated. Viscosity was the main fluid property that was responsible for the behavior of a hydrodynamic film; thereby, paint, due to its high viscosity that is equivalent to SAE 40 oil, was chosen to compare to the hydrodynamic flow of the powder lubricant. In comparing the results between powder flow and fluid flow in a journal bearing, the following was inferred for powder flow [119]:

- A boundary layer-like flow can be observed along the moving surface, and there is a distribution of shear stress across the film.
- Due to the journal rotation, compressive and tensile stresses in the radial direction are generated in the film. The converging region of the film forms compressive stresses, and the diverging region produces tensile stresses.
- There was an evidence of the formation of hydrodynamic pressure profiles in powder lubricants.
- The original circumferential flow of powder assumes an axial motion as the powder moves towards the smallest gap in the converging section. This occurrence suggests an axial pressure distribution, which is analogous to hydrodynamic lubrication.
- After the powder particulates flow passed the smallest gap of the converging section, a powder film shows chaotic motion similar to turbulent flow.

Fig. 12.19 Thick film powder-lubricated journal bearing



- There was adhesion of a thin powder layer to the two mating surfaces that was responsible for the low-friction behavior of the tribological process of powder lubrication.

A follow-on series of work to the powder-lubricated bearing visualization studies led Heshmat to develop what he called “quasi-hydrodynamic theory of powders” in converging contacts [156].

4.3.2 Thin Film Powder Lubrication

Heshmat and his collaborators studied powders in pin-on-disk tests to evaluate the performance of molybdenum disulfide (MoS_2) in bearings [150, 157]. The “pellet-on-disk” tests were performed using a modified pin-on-disk tribometer where compacted MoS_2 powder was run against a titanium carbide (TiC) disk. The two major technology components for the experimental setup consisted of the pelletized powder lubricant delivery system and the compliantly mounted slider type. The tests helped to establish the optimum geometries and system parameters to make MoS_2 lubricant pellets [147]. From this work, a self-contained solid-/powder-lubricated auxiliary hydrodynamic bearing was developed. This bearing was operated at 30,000 rpm and at loads up to 445 N (100 lb) [150].

Similar to the pellet-on-disk with slider tribometer developed by Heshmat, Higgs and Wornyo developed a tribometer setup to study thin powder transfer films from compacted powder pellets [158], as shown in Fig. 12.20. In wear tests, MoS_2 pellets were sheared against the surface of the rotating titanium carbide (TiC) disk forming a transfer film which was then depleted by the downstream loaded slider pad [158]. The resulting friction coefficient between the slider and disk was a function of the amount of lubricant that remained on the disk.

During the tests, a pellet was loaded against the disk, as it rotated. Since the pellet is pressed against the disk with a weight F_p , the thin film is transferred to the

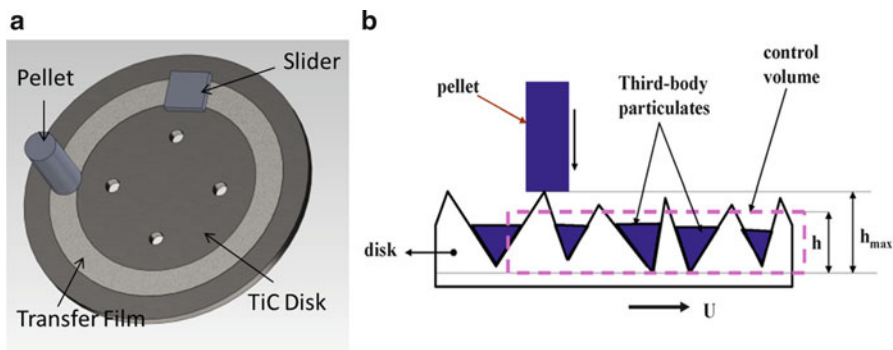


Fig. 12.20 (a) Pellet-on-disk with slider setup. (b) Diagram of the pellet–disk and slider/disk interfaces

disk which has a linear speed U . The transfer film supports the normal load F_s on the slider. Lastly, the wear rate of the pellet and the frictional behavior at the pellet–disk and pad/disk interfaces were measured with load cells [158].

Figure 12.21 shows typical experimental results from the pellet-on-disk with slider tribometer. In Fig. 12.21a, the friction coefficients for an MoS_2 pellet with an average particle size of $7.4 \mu\text{m}$ and slider riding atop the rotating disk are shown. The friction coefficient for the solid MoS_2 compact is generally higher than a hard metal slider pad riding on a lubricious transfer film of MoS_2 likely because the slider pad shears the lamellar MoS_2 film similar to a fluid. Figure 12.21b shows a typical wear graph for the pellet in terms of mass loss in grams. In Fig. 12.21c, the friction coefficients for an MoS_2 pellet with an average particle size of $1.56 \mu\text{m}$ and slider are shown. The friction coefficients reach steady-state values in approximate range of 0.13 and 0.15. The distance that it takes for these friction coefficients to reach the steady-state values corresponds to the distance that indicates where a steady-state wear rate starts to occur, and the approximate distance falls at 1 km as shown in Fig. 12.21d.

4.4 Modeling

The nonexistence of a clear-cut fundamental equation of motion for powder lubrication led researchers to adopt a variety of forms [4]. For example, some authors have favored the rheological study or the study of material as a reasonable assumption in modeling powder lubrication [4]. Rheology combines the theories of continuum mechanics with ideas obtained by considering the microstructure of the objects being studied. This section will examine three different modeling approaches such as thick film modeling, thin film modeling, and discrete element method (DEM) modeling.

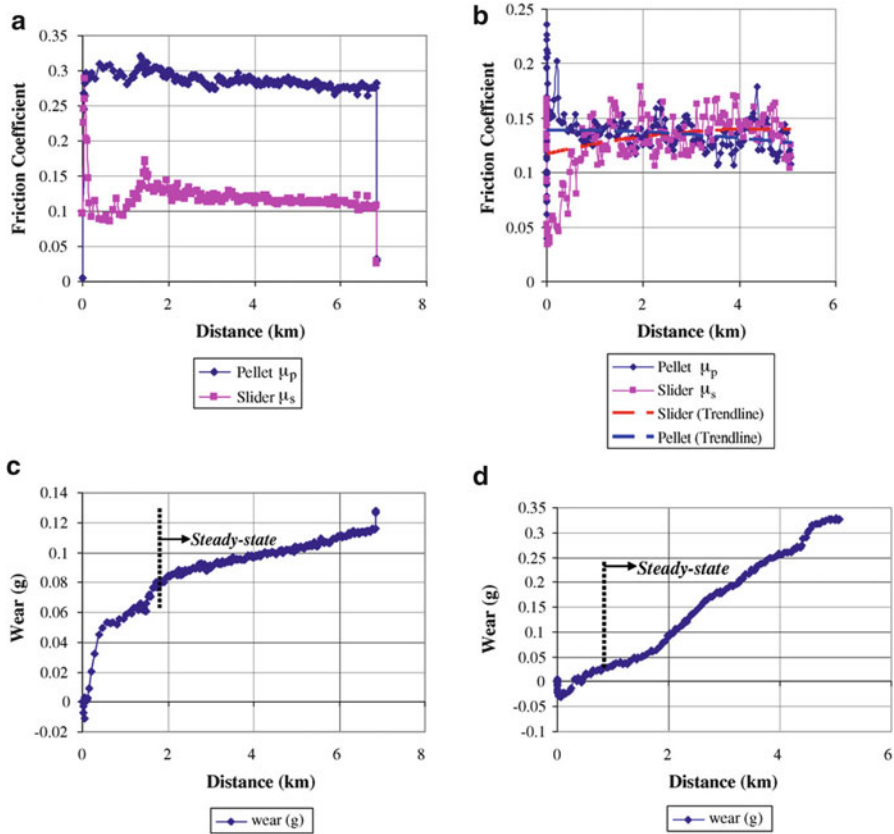


Fig. 12.21 Test results from pellet-on-disk test. (a, c) Pellet and slider pad friction coefficient. (b, d) Cumulative pellet wear. (a, b) Test results for average MoS₂ powder particle size of 7.4 μm. (c, d) Test results for average MoS₂ powder particle size of 1.56 μm

4.4.1 Thick Film Powder Lubrication Modeling

For thick film powder films, Heshmat [159] used a continuum approach to develop a semiempirical model to predict the behavior and performance of powders, which he said behaved as “quasi-hydrodynamic” lubricant films. Figure 12.22 shows his phenomenological description of the velocity accommodation provided by lamellar powders between sliding surfaces. Lamellar powders such as MoS₂, graphite, and tungsten disulfide are called “powder lubricants” because they inherently have layered shearing. Heshmat developed a rheological model for powder lubricants which related the shear rate (du/dy) of the powder to an odd fifth-order function of the shear stress τ as seen in (12.20) [159]. Powder lubrication or layered shearing was shown to only occur when the film is sheared with a stress between the powder’s shear-based yield strength τ_0 and its limiting shear stress τ_1 ; both are values which he measured experimentally [159]:

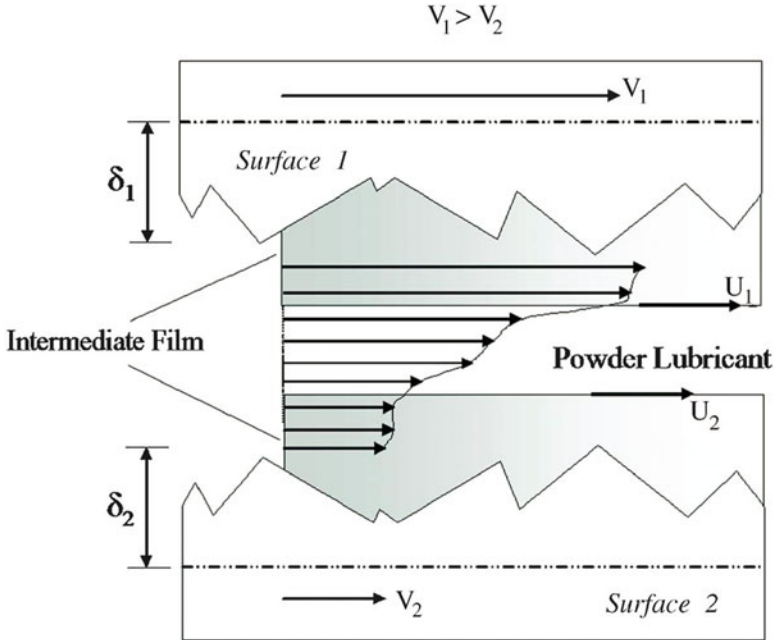


Fig. 12.22 Powder lubricant as a third body

$$\mu \left(\frac{du}{dy} \right) - \tau_0 = \tau + C_1 \tau^3 + C_2 \tau^5 \tag{12.20}$$

where μ is the powder viscosity, u is the velocity, τ_0 is the yield shear strength, τ is the shear stress, and C_1 and C_2 are empirical constants. An effective powder viscosity could be measured in rheological-type experiments, and a one-dimensional momentum equation taken from the Navier–Stokes fluid equations was used to determine the hydrodynamic pressure numerically.

4.4.2 Thin (Transfer) Film Powder Lubrication Modeling

The transfer film approach of modeling powder lubrication assumes the powder film thickness does not exceed the height of the surface asperities and, in most cases, is less than the tallest asperities (see Fig. 12.20b). In order to develop a tribology model of the lubrication process, the asperity domain was assumed to be the control volume [158]. Figure 12.20b showed a simplified schematic of the pellet as it is sheared against the disk and as the slider pad depletes the lubricant off the disk with exaggerated asperity heights; for simplicity, the slider is not shown. A control volume fractional coverage (CVFC) model [158] was developed with the following assumptions:

- The slider/disk and pellet–disk interface topographies are represented by a nominally flat or slider surface in contact with a rough disk.
- The disk topography varies little relative to the maximum asperity height h_{\max} .
- The frictional response in the pellet–disk and slider/disk interfaces is predominantly a function of the height of the transfer film covering the disk surface.

The fractional coverage, X , is dimensionless and is defined as the fraction of lubricant that covers the asperities of the disk surface. That is,

$$X = h/h_{\max} \quad (12.21)$$

where h is the local height of third body film. The film height when the disk asperities are completely covered is $h = h_{\max}$ and in that case, $X = 1$. Similarly, $X = 0$ represents the case of no lubricant coverage. Referring to Fig. 12.20b, consider the control volume that encloses asperities and valleys. The rate at which the amount of lubricant can be stored on the disk is equal to the difference between the amount of lubricant entering the control volume and the amount of lubricant exiting the control volume. This is expressed as (12.22) as a conservation of mass flow rate or volume flow rate if density is assumed constant as in this case:

$$\begin{aligned} (\textit{Third Body Storage Rate}) &= (\textit{Third Body Input Rate}) \\ &\quad - (\textit{Third Body Output Rate}) \end{aligned} \quad (12.22)$$

To mathematically interpret (12.21), a generalized wear law is used to describe the rates of material being input or output from the control due to wear mechanisms:

$$\dot{V} = KF_N U \quad (12.23)$$

where \dot{V} is the volume wear rate, K is the dimensional wear coefficient, F_N is the normal load applied, and U is the sliding velocity. K is an empirical constant that describes the probability of wear occurring between two different materials such as TiC on MoS₂, although in some cases, K could just be between the same kinds of material (e.g., MoS₂ pellet riding on MoS₂ third body). Applying Archard's wear law from (12.23) on each of the interacting interfaces, (12.22) becomes

$$A \frac{dh}{dt} = K_p F_p U (1 - X) - K_{ep} F_p U (X) - K_{es} F_s U (X) \quad (12.24)$$

where A is the cross-sectional area and F_p and F_s are pellet and slider loads, respectively. Additionally, K_p is the wear coefficient for the pellet–disk interface, while wear coefficients for the third body wear due to the shearing from the pellet and slider pad are K_{ep} and K_{es} . The fractional coverage X coefficients in each of the three terms on the right side of (12.24) act as “switches.” For example, if the disk is fully covered ($X = 1$), the pellet switches off from wearing which means the first term goes to zero. When the disk has no lubricant film on it ($X = 0$), the second and

third output wear terms on the right side of the equation go to zero, and the equation reduces back to the general wear equation just for the pellet.

Equation (12.24) is the governing equation which together with the initial condition $X(0) = 0$ completely define the problem for the CVFC model. The solution to (12.24) is given by

$$X(t) = \frac{(K_p F_p)}{(K_{ep} + K_p)F_p + K_{es}F_s} \left[1 - \exp\left(-\frac{t}{\tau}\right) \right] \quad (12.25)$$

where τ is the time constant defined by

$$\tau = \frac{Ah_{\max}}{\left((K_{ep} + K_p)F_p + K_{es}F_s\right)U} \quad (12.26)$$

After a long time has elapsed, the steady-state fractional coverage is

$$X_{ss} = \frac{(K_p F_p)}{(K_{ep} + K_p)F_p + K_{es}F_s} \quad (12.27)$$

Assuming a linear rule of mixture can be used to predict the friction coefficient between unlubricated and fully lubricated conditions, the pellet and slider friction coefficients can be defined as (12.28) and (12.29):

$$\mu_p = X\mu_{lub,p} + (1 - X)\mu_{dry,p} \quad (12.28)$$

$$\mu_s = X\mu_{lub,s} + (1 - X)\mu_{dry,s} \quad (12.29)$$

where μ_p and μ_s are friction coefficients at the pellet–disk and slider/disk interfaces, respectively. The pellet and slider friction coefficients for unlubricated conditions are $\mu_{dry,p}$ and $\mu_{dry,s}$, while those for lubricated conditions are indicated by $\mu_{lub,p}$ and $\mu_{lub,s}$.

Lastly, Iordanoff et al. [160] suggest the use of a discrete element method (DEM) modeling approach. They studied mechanisms operating in sliding contacts and outline the influence of external parameters. The proposed unified approach considers the following conventional modeling:

- The quasi-hydrodynamic model developed by Heshmat [159]
- The kinetic model developed by Haff [109] and extensively modified by tribologists, such as Dai et al. [161], McKeague and Khonsari [5, 162], Yu, et al. [163], and Zhou and Khonsari [108]

The authors' [160] discrete model was based on the principles of DEM proposed by Cundall and Strack [72] for geotechnical applications. Recently, simulations involving solid third bodies, similar to pelletized powder, have been conducted by Fillot et al. [164].

5 Conclusion

The purpose of this chapter was to expose readers to the tribology of particles interacting with other particles, fluids, and external or internal surfaces. The topic of particle tribology is much broader than the three tribosystems—granular, slurry, and powder—presented in this chapter. However, most fundamental issues concerning particle tribology and its associated applications likely have been addressed within the sections of this chapter. For example, granular flows can be a broad description of particulate systems where the particles primarily interact through collisions resulting in dissipative momentum transfer. An application of this might be the flow of coal down long pipelines where vast amounts of power are needed to pump these solids which are constantly losing kinetic energy due to particle–particle and particle–surface interactions. Slurry flows which are multi-phase particle–fluid flows exhibit behavior that is often difficult to predict because one must first understand the fluid mechanics and particle dynamics occurring between sliding surfaces. And finally, the most classical of the particle tribology areas is powder lubrication which refers to particles that often exhibit dual lubrication behavior. They either accommodate surface velocity differences by shearing, or they lower frictional performance by coating surface asperities during sliding. The student aiming to study broad particle engineering and science problems such as earthquake prediction, flow stoppage during solids processing, and the erosion susceptibility of surfaces during processing or basic operation should greatly benefit from the concepts presented in this chapter.

References

1. Higgs CF, Tichy J (2004) Granular flow lubrication: continuum modeling of shear behavior. *J Tribol* 126(3):499–510
2. Yu C-M, Craig K, Tichy J (1994) Granular collision lubrication. *J Rheol* 38(4):921–936
3. Elkholy KN, Khonsari MM (2007) Granular collision lubrication: experimental investigation and comparison to theory. *J Tribol* 129(4):923
4. Worniyoh EYA, Jasti VK, Fred Higgs C (2007) A review of dry particulate lubrication: powder and granular materials. *J Tribol* 129(2):438
5. McKeague KT, Khonsari MM (1996) An analysis of powder lubricated slider bearings. *J Tribol* 188(1):206–214
6. Jordanoff I, Khonsari MM (2004) Granular lubrication: toward an understanding of the transition between kinetic and quasi-fluid regime. *J Tribol* 126(1):137
7. Lu K, Brodsky EE, Kavehpour HP. Tribological aspects and fluidity of dense granular flow. In: 2005 ASME international mechanical engineering congress and exposition 2005. American Society of Mechanical Engineers: Orlando, FL, United States. pp 181–190
8. Roberts AW, Ooms M, Wiche SJ (1990) Concepts of boundary friction adhesion and wear in bulk solids handling. *Bulk Solids Handling* 10(2):189–198
9. Lee T, Jia L (2003) Particle attrition by particle-surface friction in dryers. *Pharm Technol* 27(5):64–72

10. Higgs III CF, Jasti V, Racusen C, Heller C, Cohen N, Tichy J (2006) On the behavior of granular materials in rough wheel contacts on mars. In: Tenth biennial ASCE aerospace division international conference on engineering, construction, and operations in challenging environments 2006, American Society of Civil Engineers. p. 32
11. Elliott KE, Ahmadi G, Kvasnak W (1998) Couette flows of a granular monolayer—an experimental study. *J Non-Newtonian Fluid Mech* 74(1):89–111
12. May LBH, Golick LA, Phillips KC, Shearer M, Daniels KE (2010) Shear-driven size segregation of granular materials: modeling and experiment. *Phys Rev E* 81(5):051301
13. Golick L, Daniels K (2009) Mixing and segregation rates in sheared granular materials. *Phys Rev E* 80(4):042301
14. Wambaugh J, Behringer R, Matthews J, Gremaud P (2007) Response to perturbations for granular flow in a hopper. *Phys Rev E* 76(5):051303-1–051303-8
15. To K, Lai P-Y, Pak H (2001) Jamming of granular flow in a two-dimensional hopper. *Phys Rev Lett* 86(1):71–74
16. Samadani A, Pradhan A, Kudrolli A (1999) Size segregation of granular matter in silo discharges. *Phys Rev E* 60(6):7203–7209
17. Dhoriyani M, Jonnalagadda K, Kandikatla R, Rao K (2006) Silo music: sound emission during the flow of granular materials through tubes. *Powder Technol* 167(2):55–71
18. Ottino JM, Khakhar DV (2000) Mixing and segregation of granular materials. *Annu Rev Fluid Mech* 32:55–91
19. Gray JMNT, Ancey C (2009) Segregation, recirculation and deposition of coarse particles near two-dimensional avalanche fronts. *J Fluid Mech* 629:387
20. Arteaga P, Tuzun U (1990) Flow of binary mixtures of equal-density granules in hoppers—size segregation, flowing density and discharge rates. *Chem Eng Sci* 45(1):205–223
21. Ketterhagen W, Curtis J, Wassgren C, Kong A, Narayan P, Hancock B (2007) Granular segregation in discharging cylindrical hoppers: a discrete element and experimental study. *Chem Eng Sci* 62(22):6423–6439
22. Samadani A, Kudrolli A (2001) Angle of repose and segregation in cohesive granular matter. *Phys Rev E* 64(5):051301
23. Conway SL, Lekhal A, Khinast JG, Glasser BJ (2005) Granular flow and segregation in a four-bladed mixer. *Chem Eng Sci* 60(24):7091–7107
24. May LBH, Shearer M, Daniels KE (2010) Scalar conservation laws with nonconstant coefficients with application to particle size segregation in granular flow. *J Nonlinear Sci* 20(6):689–707
25. Hong DC, McLennan JA (1992) Molecular dynamics simulations of hard sphere granular particles. *Physica A* 187(1):159–171
26. Corwin EI, Jaeger HM, Nagel SR (2005) Structural signature of jamming in granular media. *Nature* 435(7045):1075–1078
27. Garcimartín A, Zuriguel I, Maza D, Pastor JM, Pugnaloni LA. Jamming in granular matter. In: 8th Experimental Chaos Conference 2004, AIP Conference Proceedings, American Institute of Physics, Florence, Italy. pp 279–288
28. Zhang J, Majmudar TS, Sperl M, Behringer RP (2010) Jamming for a 2D granular material. *Soft Matter* 6(13):2982
29. Mailman M, Schreck C, O’Hern C, Chakraborty B (2009) Jamming in systems composed of frictionless ellipse-shaped particles. *Phys Rev Lett* 102(25):255501
30. Schreck CF, Xu N, O’Hern CS (2010) A comparison of jamming behavior in systems composed of dimer- and ellipse-shaped particles. *Soft Matter* 6(13):2960
31. Liu AJ, Nagel SR (1998) Jamming is not just cool any more. *Nature* 396:21–22
32. Shibly H, Iagnemma K, Dubowsky S (2005) An equivalent soil mechanics formulation for rigid wheels in deformable terrain, with application to planetary exploration rovers. *J Terramech* 42(1):1–13
33. Liu J, Tang S, Cheng P, Liu S (2012) Influence analysis and evaluation of wheel parameters on motion performance of lunar rover. *Inform Technol J* 11(2):225–232

34. Ding L, Deng Z, Gao H, Nagatani K, Yoshida K (2010) Planetary rovers' wheel–soil interaction mechanics: new challenges and applications for wheeled mobile robots. *Intell Serv Robot* 4(1):17–38
35. Marinack MC Jr, Jasti VK, Choi YE, Higgs CF (2011) Couette grain flow experiments: the effects of the coefficient of restitution, global solid fraction, and materials. *Powder Technol* 211(1):144–155
36. Sondergaard R, Chaney K, Brennen CE (1990) Measurements of solid spheres bouncing off flat plates. *J Appl Mech Trans ASME* 57(3):694–699
37. Kharaz AH, Gorham DA (2000) A study of the restitution coefficient in elastic-plastic impact. *Philos Mag Lett* 80(8):549–559
38. Koller MG, Kolsky H (1987) Waves produced by the elastic impact of spheres on thick plates. *Int J Solid Struct* 23(10):1387–1400
39. Reed J (1985) Energy losses due to elastic wave propagation during an elastic impact. *J Phys D Appl Phys* 18(12):2329–2337
40. Tabor D (1948) A simple theory of static and dynamic hardness. *Proc R Soc A* 192:247
41. Vincent JH (1900) Experiments on impact. *Proc Camb Philos Soc* 10:332–357
42. Johnson KL (1985) *Contact mechanics*. Cambridge University Press, Cambridge, UK
43. Tabor D (1951) *The hardness of metals*. Oxford University Press, London
44. Seifried R, Schiehlen W, Eberhard P (2005) Numerical and experimental evaluation of the coefficient of restitution for repeated impacts. *Int J Impact Eng* 32(1):508–524
45. Raman CV (1920) On some applications of Hertz's theory of impact. *Phys Rev* 15:249–343
46. Marinack Jr MC, Gaudio BG, Musgrave RE, Rizzo CE, Lovell M, Higgs III CF (2010) Coefficient of restitution testing: explicit finite element modeling and experiments. In: *ASME/STLE 2010 International Joint Tribology Conference 2010, Conference Proceedings*, San Francisco, CA
47. Marinack Jr MC, Musgrave RE, Higgs III CF (2012) Experimental investigations on the coefficient of restitution of single particles. *Tribol Trans*. Accepted for publication
48. Minamoto H, Hagawa T, Kawamura S (2010) Direct central impact between two spheres made of dissimilar materials. *Nihon Kikai Gakkai Ronbunshu, C Hen (Trans Jpn Soc Mech Eng C)* 76(768):1988–1995
49. Minamoto H, Kawamura S (2011) Moderately high speed impact of two identical spheres. *Int J Impact Eng* 38(2):123–129
50. Goldsmith W (1960) *Impact*. E. Arnold Pub, London, pp 249–307
51. Dong H, Moys M (2006) Experimental study of oblique impacts with initial spin. *Powder Technol* 161(1):22–31
52. Foerster SF, Louge MY, Chang H, Allia K (1994) Measurements of the Collision Properties of Small Spheres. *Phys Fluids* 6(3):1108–1115
53. Kharaz AH, Gorham DA, Salman AD (2001) An experimental study of the elastic rebound of spheres. *Powder Technol* 120(3):281–291
54. Gondret P, Lance M, Petit L (2002) Bouncing motion of spherical particles in fluids. *Phys Fluids* 14(2):643
55. Joseph GG, Zenit R, Hunt ML, Rosenwinkel AM (2001) Particle-wall collisions in a viscous fluid. *J Fluid Mech* 433:329–346
56. Ruiz-Angulo A, Hunt ML (2010) Measurements of the coefficient of restitution for particle collisions with ductile surfaces in a liquid. *Granular Matter* 12(2):185–191
57. Bagnold RA (1954) Experiments on a gravity-free dispersion of large spheres in a newtonian fluid under shear. *Proc R Soc Lond A Math Phys Sci* 225(1160):49–63
58. da Cruz F (2004) *Friction and jamming in granular flows*. Ecole Nationale des Ponts et Chaussees, Marne la vallee
59. Mueth DM, Debregeas GF, Karczmar GS, Eng PJ, Nagel SR, Jaeger HM (2000) Signatures of granular microstructure in dense shear flows. *Nature* 406(6794):385–389
60. Bocquet L, Losert W, Schalk D, Lubensky T, Gollub J (2001) Granular shear flow dynamics and forces: experiment and continuum theory. *Phys Rev E* 65(1):011307

61. MiDi G (2004) On dense granular flows. *Eur Phys J E* 14(4):341–365
62. Tardos GI, Khan MI, Schaeffer DG (1998) Forces on a slowly rotating, rough cylinder in a couette device containing a dry frictional powder. *Phys Fluids* 10(2):335–341
63. Veje CT, Howell DW, Behringer RP (1999) Kinematics of a two-dimensional granular Couette experiment at the transition to shearing. *Phys Rev E* 59(1):739–745
64. Howell DW, Behringer RP, Veje CT (1999) Fluctuations in granular media. *Chaos* 9(3):559–572
65. Losert W, Bocquet L, Lubensky TC, Gollub JP (2000) Particle dynamics in sheared granular matter. *Phys Rev Lett* 85(7):1428–1431
66. Jasti V, Higgs C (2008) Experimental study of granular flows in a rough annular shear cell. *Phys Rev E* 78(4):041306
67. Savage SB, Sayed M (1984) Stresses developed by dry cohesionless granular materials sheared in an annular shear cell. *J Fluid Mech* 142:391–430
68. Hanes DM, Inman DL (1985) Observations of rapidly flowing granular-fluid materials. *J Fluid Mech* 150:357–380
69. Miller B, O’Hern C, Behringer RP (1996) Stress fluctuations for continuously sheared granular materials. *Phys Rev Lett* 77(15):3110–3113
70. Craig K, Buckholz RH, Domoto G (1986) Experimental study of the rapid flow of dry cohesionless metal powders. *J Appl Mech Trans ASME* 53(4):935–942
71. Craig K, Buckholz RH, Domoto G (1987) Effect of shear surface boundaries on stress for shearing flow of dry metal powders—an experimental study. *J Tribol* 109(2):232–237
72. Cundall PA, Strack ODL (1979) Discrete numerical model for granular assemblies. *Geotechnique* 29(1):47–65
73. Walton OR (1994) Numerical simulation of inelastic. Frictional particle-particle interactions. In: Roco MC (ed) *Particulate two-phase flow*. Butterworth-Heinemann, Stoneham, pp 884–911
74. Hawkins GW (1983) Simulation of granular flow. In: Jenkins JT, Satake M (eds) *Mechanics of granular materials: new models and constitutive relations*. Elsevier Science Publications, Amsterdam, pp 305–312
75. Hopkins MA, Shen HH (1988) A Monte Carlo simulation of a simple shear flow of granular materials. In: Satake M, Jenkins JT (eds) *Micromechanics of granular materials*. Elsevier Science Publications, Amsterdam
76. Campbell CS, Brennen CE (1985) Computer simulation of granular shear flows. *J Fluid Mech* 151:167–188
77. Hopkins MA, Louge MY (1991) Inelastic microstructure in rapid granular flows of smooth disks. *Phys Fluids A* 3(1):47–57
78. Jenkins JT, Richman MW (1988) Plane simple shear of smooth inelastic circular disks: the anisotropy of the second moment in the dilute and dense limits. *J Fluid Mech* 192:313–328
79. Sawyer WG, Tichy JA (2001) Lubrication with granular flow: continuum theory, particle simulations. *Comp Exp J Tribol* 123(4):777
80. Yu C-M, Tichy J (1996) Granular collision lubrication: effect of surface roughness, particle size and solids fraction. *Tribol Trans* 39(3):537–546
81. Louge MY (1994) Computer simulations of rapid granular flows of spheres interacting with a flat, frictional boundary. *Phys Fluids* 6(7):2253
82. Jenkins JT (1992) Boundary conditions for rapid granular flow: flat frictional walls. *J Appl Mech* 59(1):120–127
83. McCarthy JJ, Jasti V, Marinack M, Higgs CF (2010) Quantitative validation of the discrete element method using an annular shear cell. *Powder Technol* 203(1):70–77
84. Von Neumann J (1966) Theory of self-reproducing automata. In: Burks AW (ed.) *University of Illinois Press, Urbana*
85. Ilachinski A (2001) *Cellular automata a discrete universe*. World Scientific Publishing Co. Pte. Ltd., Singapore

86. Marinack MC Jr, Mpagazehe JN, Higgs CF III (2012) An Eulerian, lattice-based cellular automata approach for modeling multiphase flows. *Powder Technol* 221:47–56
87. Jasti VK, Higgs CF (2010) A fast first order model of a rough annular shear cell using cellular automata. *Granular Matter* 12(1):97–106
88. Fitt AD, Wilmott P (1992) Cellular-automaton model for segregation of a two-species granular flow. *Phys Rev A* 45(4):2383
89. Karolyi A, Kertesz J, Havlin S, Makse HA, Stanley HE (1998) Filling a silo with a mixture of grains: friction-induced segregation. *Europhys Lett* 44(3):386–392
90. Cizeau P, Makse HA, Stanley HE (1999) Mechanisms of granular spontaneous stratification and segregation in two-dimensional silos. *Phys Rev E* 59(4):4408–4421
91. Alonso JJ, Herrmann HJ (1996) Shape of the tail of a two-dimensional sandpile. *Phys Rev Lett* 76(26):4911–4914
92. Goles E (1992) Sand pile automata. *Ann l'Institut Henri Poincare Phys Theor* 56(1):75–90
93. Karolyi A, Kertesz J (1998) Lattice-gas model of avalanches in a granular pile. *Phys Rev E* 57(1):852–856
94. Kozicki J, Tejchman J (2005) Application of a cellular automaton to simulations of granular flow in silos. *Granular Matter* 7(1):45–54
95. Baxter WG, Behringer RP (1990) Cellular automata models of granular flow. *Phys Rev A* 42(2):1017–1020
96. Marinack MC Jr, Higgs CF III (2011) The inclusion of friction in lattice-based cellular automata modeling of granular flows. *J Tribol* 133(3):031302
97. Jasti VK, Higgs CF (2006) A lattice-based cellular automata modeling approach for granular flow lubrication. *J Tribol* 128(2):358
98. Österle W, Dmitriev AI, Kloß H (2012) Possible impacts of third body nanostructures on friction performance during dry sliding determined by computer simulation based on the method of movable cellular automata. *Tribol Int* 12(48):128–136
99. Tavares FA (2001) Simulation behavior of composite grid reinforced concrete beams using explicit finite element methods. University of Wisconsin-Madison, Madison, WI
100. Kabir MA, Lovell MR, Higgs CF (2008) Utilizing the explicit finite element method for studying granular flows. *Tribol Lett* 29(2):85–94
101. Kabir MA, Jasti VK, Higgs CF, Lovell MR (2008) An evaluation of the explicit finite-element method approach for modelling dense flows of discrete grains in a Couette shear cell. *Proc Inst Mech Eng J J Eng Tribol* 222(6):715–723
102. Wu C-Y, Li L-Y, Thornton C (2005) Energy dissipation during normal impact of elastic and elastic-plastic spheres. *Int J Impact Eng* 32(1):593–604
103. Seifried R, Minamoto H, Eberhard P (2010) Viscoplastic effects occurring in impacts of aluminum and steel bodies and their influence on the coefficient of restitution. *J Appl Mech* 77(4):041008
104. Li L-y, Thornton C, Wu C-y (2000) Impact behaviour of elastoplastic spheres with a rigid wall. *Proc Inst Mech Eng C J Mech Eng Sci* 214(8):1107–1114
105. Katta RR, Polycarpou AA, Hanchi JV, Crone RM (2009) High velocity oblique impact and coefficient of restitution for head disk interface operational shock. *J Tribol* 131(2):021903
106. ANSYS (2005) *Ansys, LS-DYNA user's guide* (release 10). Ansys, Inc., Livermore, CA
107. Tsai H-J, Jeng Y-R (2006) Characteristics of powder lubricated finite-width journal bearings: a hydrodynamic analysis. *J Tribol* 128(2):351
108. Zhou L, Khonsari MM (2000) Flow characteristics of a powder lubricant sheared between parallel plates. *J Tribol* 122(1):147–154
109. Haff PK (1983) Grain flow as a fluid-mechanical phenomenon. *J Fluid Mech* 134:401–430
110. Lun CKK, Savage SB, Jeffrey DJ, Chepurmiy N (1984) Kinetic theories for granular flow: inelastic particles in couette flow and slightly inelastic particles in a general flowfield. *J Fluid Mech* 140:223–256
111. Higgs CF III (2001) *Particulate flow lubrication: continuum modeling of shear behavior*. Department of Mechanical Engineering, Rensselaer Polytechnic Institute, Troy, NY

112. Elrod HG (1988) Granular flow as a tribological mechanism—a first look. In: *Interface Dynamics, Proc. of the Leeds-Lyon Conference*, Butterworth, Oxford, England. p. 75
113. Dai F, Khonsari MM, Lu ZY (1994) On the lubrication mechanism of grain flows. *STLE Tribol Trans* 37(3):516–524
114. Heshmat H (1992) The quasi-hydrodynamic mechanism of powder lubrication. Part II: lubricant film pressure profile. *Lubr Eng* 48(5):373–383
115. Pappur M, Khonsari MM (2003) Flow characterization and performance of a powder lubricated slider bearing. *J Tribol* 125(1):135
116. Jenkins JT, Richman MW (1985) Kinetic theory for plane flows of a dense gas of identical, rough, inelastic, circular disks. *Phys Fluids* 28(12):3485
117. Hui K, Haff PK, Ungar JE, Jackson R (1984) Boundary conditions for high-shear grain flows. *J Fluid Mech* 145:223–233
118. Wyszynski ML, Bridgewater J (1993) Effect of solid lubricants on powder attrition and breakage. *Tribol Int* 26(5):311–317
119. Heshmat H (1992) The quasi-hydrodynamic mechanism of powder lubrication. I. Lubricant flow visualization. *Lubr Eng* 48(2):96–104
120. Boning D, Lee B, Oji C, Ouma D, Park T, Smith T, Tugbawa T (1999) Pattern dependent modeling for CMP optimization and control. *Materials Research Society (MRS) Spring Meeting*, San Francisco, CA.
121. Runnels SR (1996) Advances in physically based erosion simulators for CMP. *J Electron Mater* 25(10):1574–1580
122. Nguyen V, VanKranenburg H, Woerlee P (2000) Dependency of dishing on polish time and slurry chemistry in Cu CMP. *Microelectron Eng* 50(1–4):403–410
123. Mpagazehe JN, Thukalil GA, Higgs III CF (2009) A study to estimate the number of active particles in CMP. *Materials Research Society Spring Meeting*, San Francisco, CA.
124. Edwards JK, McLaury BS, Shirazi SA (2001) Modeling solid particle erosion in elbows and plugged tees. *J Energy Resour Technol* 123:277–284
125. Street KW, Marchetti M, Wal RLV, Tomasek AJ (2004) Evaluation of the tribological behavior of nano-onions in Krytox 143AB. *Tribol Lett* 16(1–2):143–149
126. Zantye PB, Kumar A, Sikder AK (2004) Chemical mechanical planarization for microelectronics applications. *Mater Sci Eng R Rep* 45(3–6):89–220
127. Nikas GK (2010) A state-of-the-art review on the effects of particulate contamination and related topics in machine-element contacts. *Proc Inst Mech Eng J J Eng Tribol* 224 (J5):453–479
128. Wang A, Essner A (2001) Three-body wear of UHMWPE acetabular cups by PMMA particles against CoCr, alumina and zirconia heads in a hip joint simulator. *Wear* 250:212–216
129. Chinas-Castillo F, Spikes HA (2003) Mechanism of action of colloidal solid dispersions. *J Tribol* 125(3):552–557
130. Lovell MR, Kabir MA, Menezes PL, Higgs CF III (2010) Influence of boric acid additive size on green lubricant performance. *Philos Trans R Soc A* 368:4851–4868
131. Duan B, Lei H (2001) The effect of particle size on the lubricating properties of colloidal polystyrene used as water based lubrication additive. *Wear* 249:528–532
132. Nikas GK, Sayles RS (2008) A study of lubrication mechanisms using two-phase fluids with porous bearing materials. *Proc Inst Mech Eng J J Eng Tribol* 222:771–783
133. Darley HCH, Gray GR (1988) *Composition and properties of drilling and completion fluids*, 5th edn. Butterworth-Heinemann, Houston, TX
134. Pepper S (2011) Effect of test environment on lifetime of two vacuum lubricants determined by spiral orbit tribometry. NASA, Cleveland, OH
135. Higgs CF, Ng ISH, Borucki L, Yoon I, Danyluk S (2005) A mixed-lubrication approach to predicting cmp fluid pressure modeling and experiments. *J Electrochem Soc* 152(3): G193–G198
136. Shan L, Levert J, Meade L, Tichy J, Danyluk S (2000) Interfacial fluid mechanics and pressure prediction in chemical mechanical polishing. *J Tribol* 122(3):539–543

137. Park S-S, Cho C-H, Ahn Y (2000) Hydrodynamic analysis of chemical mechanical polishing process. *Tribol Int* 33(10):723–730
138. Gohar R (1988) *Elastohydrodynamics*. Wiley, New York
139. Luo J, Dornfeld DA (2001) Mechanical removal mechanism in chemical mechanical polishing: theory and modeling. *IEEE Trans Semicond Manuf* 14(2):112–133
140. Terrell EJ, Higgs CF (2009) A particle-augmented mixed lubrication modeling approach to predicting chemical mechanical polishing. *J Tribol* 131(1):012201
141. Li Q, Rudolph V, Wang FY, Horio M (2005) A study of particle packing compression under fluid drag force by DEM simulations. *Dev Chem Eng Miner Process* 13(5–6):693–708
142. Mei R, Shang H, Walton OR, Klausner JF (2000) On the improved flowability of cohesive powders by coating with fine particles. *Proc. of 1997 TMS Annual Meeting*. pp. 225–236
143. Erdemir A (1994) Crystal chemistry and solid lubricating properties of the monochalcogenides gallium selenide and tin selenide. *STLE Tribol Trans* 37(3):471–478
144. Higgs CF, Heshmat H (2001) Characterization of pelletized MoS₂ powder particle detachment process. *ASME J Tribol* 123(3):455–461
145. Higgs CF, Heshmat CA, Heshmat HS (1999) Comparative evaluation of MoS₂ and WS₂ as powder lubricants in high speed, multi-pad journal bearings. *J Tribol Trans ASME* 1–121(3):625–630
146. Kaur RG, Higgs CF, Heshmat HS (2001) Pin-on disk tests of pelletized molybdenum disulfide. *Tribol Trans* 44(1):79–87
147. Heshmat H, Heshmat CA (1999) The effect of slider geometry on the performance of a powder lubricated bearing. *Tribol Trans* 42(3):640–646
148. Sawyer WG, Ziegert JC, Schmitz TL, Barton A (2006) In situ lubrication with boric acid: Powder delivery of an environmentally benign solid lubricant. *Tribol Trans* 49(2):284–290
149. Johnson VR, Lavik MT, Vaughn GW (1957) Mechanism of WS₂ lubrication in vacuum. *J Appl Phys* 28(7):821
150. Kaur RG, Heshmat H (2002) 100 mm diameter self-contained solid/ powder lubricated auxiliary bearing operated at 30,000 rpm. *Lubr Eng* 58(6):13–20
151. Heshmat H (1992) Powder-lubricant piston ring for diesel engines. U.S. Patent, Editor E. Rollins Cross, United States
152. Reches Z, Lockner DA (2010) Fault weakening and earthquake instability by powder lubrication. *Nature* 467:452–455
153. Ettles CM (1985) The thermal control of friction at high sliding speed. *ASME Paper* 85
154. Heshmat H, Pinkus O, Godet M (1989) On a common tribological mechanism between interacting surfaces. *Tribol Trans* 32(1):32–41
155. Heshmat H, Godet M, Berthier Y (1995) On the role of and mechanism of dry triboparticulate lubrication. *Lubr Eng* 51(7):557–564
156. Heshmat H (1995) The quasi-hydrodynamic mechanism of powder lubrication: Part III On the theory and rheology of triboparticulates. *Tribol Trans* 38(2):269–276
157. Higgs CF, Heshmat H (1999) Characterization of pelletized MoS₂ powder particle detachment process. *ASME J Tribol* 123(3):640–646
158. Higgs CF, Worniyoh EYA (2007) An in situ mechanism for self-replenishing powder transfer films: Experiments and modeling. *Wear* 264:131–138
159. Heshmat H (1991) The rheology and hydrodynamics of dry powder lubrication. *Tribol Trans* 34(3):433–439
160. Iordanoff I, Berthier Y, Descartes S, Heshmat H (2002) A review of recent approaches for modeling solid third bodies. *ASME J Tribol* 124(4):725–735
161. Dai FL, Khonsari MM, Lu ZY (1994) On the lubrication mechanism of grain flows. *Tribol Trans* 37(3):516–524
162. Mckeague KT, Khonsari MM (1996) Generalized boundary interactions for powder lubricated couette flows. *ASME J Tribol* 118(3):580–588
163. Yu CM, Craig K, Tichy J (2005) Granular collision lubrication. *J Rheol* 38(4):921–936
164. Fillot N, Iordanoff I, Berthier Y (2005) Simulation of wear through mass balance in a dry contact. *ASME J Tribol* 127(1):230–237

Problems

12.1 *Single Particle Coefficient of Restitution Analysis*

Understanding granular flow tribology hinges on an understanding of the interactions of individual particles at the local level. As discussed in the chapter, one of the key parameters at the local particle interaction level is the coefficient of restitution. Evaluate each of the following problems related to the coefficient of restitution:

- (a) Find e for the collision of a sphere falling from rest at an initial height of 18 in., which collides with a stationary plate and rebounds at a velocity of 2.43 m/s.
- (b) Assuming a sphere colliding with a stationary block, derive an expression for the coefficient of restitution (e), in terms of the pre-collision (KE_i) and post-collision kinetic energy (KE_f) of the sphere.
- (c) In experiments, it is impossible to study the effects of certain individual particle properties, such as material density (ρ), due to the inability to experimentally vary them in isolation. This is where modeling, theoretical and/or FEM, can become particularly useful. Consider a sphere (granule) being dropped from rest against a stationary block. Under a certain set of collision conditions, the coefficient of restitution (e_1) between the sphere and the block is found to be 0.85. Now consider a second collision case, where *only* the material density of the sphere (ρ_s) was to change and be increased by a factor of 1.5. Assuming all other parameters of the collision remain the same, use the theoretical formulation (12.5) to predict the coefficient of restitution (e_2) for this second collision case.

12.2 *Particle Settling*

You are a tribologist working for a chemical plant and are responsible for a new process. During this process, a small amount of nickel catalyst particles (100 μm in diameter) are placed into a 15 m-tall vat of vegetable oil to encourage a chemical reaction. Though the suspension is very dilute, it has been found that the catalyst particles cause substantial erosive and abrasive wear to downstream equipment. As a result, the oil must be particle-free before it can be sent to downstream processing equipment. Using gravitational settling would be significantly less expensive than filtering the catalyst particles out of the oil. The maximum amount of time the plant operators can wait for the particles to settle is 2 h. Calculate whether or not gravitational settling will be a viable method of separating the catalyst particles from the vegetable oil given the time constraints of the plant operators.

12.3 *Derivation of Powder Equation*

Derive (12.25) starting from (12.22).

12.4 *Powder Film Classification*

What is the difference between thick film powder lubrication and thin film powder lubrication?

Solutions

12.1 Part a.: *Solution.*

$$v_{imp}^2 = v_I^2 + 2gH_I = 0^2 + 2(9.81\text{m/s})(18\text{in.})(0.0254\text{m/in.}) = 8.970\text{m}^2/\text{s}^2$$

$$v_{imp} = -2.995\text{m/s}$$

From (12.2):

$$e = \frac{-v_{reb}}{v_{imp}} = \frac{-2.43\text{m/s}}{-2.995\text{m/s}}$$

$$e = 0.81$$

Part b.: Starting from (12.1)

$$e = \frac{v_{reb,1} - v_{reb,2}}{v_{imp,2} - v_{imp,1}}$$

Assuming the stationary block is object 1 and the sphere is object 2, this can be reduced to

$$e = \frac{0 - v_{reb,2}}{v_{imp,2} - 0} = \frac{-v_{reb,2}}{v_{imp,2}} \quad (1)$$

Just before impact the sphere's kinetic energy is given by

$$KE_{imp,2} = \frac{1}{2}mv_{imp,2}^2$$

Solving for the impact velocity gives

$$v_{imp,2} = \sqrt{\frac{2KE_{imp,2}}{m}} \quad (2)$$

Similarly the rebound velocity of the sphere can be derived in terms of kinetic energy as

$$v_{reb,2} = \sqrt{\frac{2KE_{reb,2}}{m}} \quad (3)$$

Substituting (2) and (3) into (1) yields

$$e = \frac{-\sqrt{\frac{2KE_{reb,2}}{m}}}{\sqrt{\frac{2KE_{imp,2}}{m}}} = -\sqrt{\frac{KE_{reb,2}}{KE_{imp,2}}}$$

Using KE_i and KE_r to represent the pre-collision and post-collision kinetic energy of the sphere and since the positive or negative root can be obtained, this can simply be written as

$$e = \sqrt{\frac{KE_r}{KE_i}}$$

Part c.: First, derive e as a function of ρ_s . Start from (12.5):

$$e = 1.88 \left(\frac{p_d}{E^*} \right)^{\frac{1}{2}} \left(\frac{\frac{1}{2} m_s v_{imp}^2}{p_d R^3} \right)^{-\frac{1}{8}} \quad (1)$$

Consider the equation for the reduced radius of curvature between the sphere and block:

$$\frac{1}{R} = \frac{1}{R_s} + \frac{1}{R_{block}},$$

where $R_{block} \rightarrow \infty$
Solving for R yields

$$\frac{1}{R} = \frac{1}{R_s} + \frac{1}{\infty} = \frac{1}{R_s} + 0 = \frac{1}{R_s}$$

$$R = R_s \quad (2)$$

Substitute (2) into (1) to obtain

$$e = 1.88 \left(\frac{p_d}{E^*} \right)^{\frac{1}{2}} \left(\frac{\frac{1}{2} m_s v_{imp}^2}{p_d R_s^3} \right)^{-\frac{1}{8}} \quad (3)$$

The density of the sphere (ρ_s) can be written as

$$\rho_s = \frac{m_s}{V_s} = \frac{m_s}{\frac{4}{3} \pi R_s^3}$$

Rearranging this expression yields

$$\frac{m_s}{R_s^3} = \frac{4}{3} \pi \rho_s \quad (4)$$

Substitute (4) into (3) to obtain

$$e = 1.88 \left(\frac{p_d}{E^*} \right)^{\frac{1}{2}} \left(\frac{\frac{1}{2} \frac{4}{3} \pi \rho_s v_{imp}^2}{p_d} \right)^{-\frac{1}{8}} = 1.88 \left(\frac{p_d}{E^*} \right)^{\frac{1}{2}} \left(\frac{\frac{2}{3} \pi \rho_s v_{imp}^2}{p_d} \right)^{-\frac{1}{8}}$$

Since no parameters (besides ρ_s) change between the two collision cases (1 and 2) defined in the problem, this expression can be written for the two collision cases as

$$e_1 = C\rho_{s1}^{-1/8}$$

$$e_2 = C\rho_{s2}^{-1/8}$$

In these equations, C is a constant which is equivalent in the two equations. From this, it can be obtained that

$$C = \frac{e_1}{\rho_{s1}^{-1/8}} = \frac{e_2}{\rho_{s2}^{-1/8}} \quad (5)$$

It is given in the problem that

$$e_1 = 0.85 \quad (6)$$

$$\rho_{s2} = 1.5\rho_{s1} \quad (7)$$

Substitute (6) and (7) into (5) to obtain

$$\frac{0.85}{\rho_{s1}^{-1/8}} = \frac{e_2}{(1.5\rho_{s1})^{-1/8}}$$

Solve for e_2 :

$$0.85(1.5\rho_s)^{-1/8} = e_2\rho_{s1}^{-1/8}$$

$$0.85(1.5)^{-1/8}\rho_{s1}^{-1/8} = e_2\rho_{s1}^{-1/8}$$

$$0.85(1.5)^{-1/8} = e_2$$

$$e_2 = 0.81$$

12.2 The particles in the suspension will have a number of different forces acting on them. By using Newton's second law (12P.1), it is possible to estimate when they will fall out of suspension.

$$\mathbf{F} = m\mathbf{a} \quad (12P.1)$$

Because a clue is provided in the problem that the suspension is very dilute, surface forces between particles are neglected. As a result, the primary forces acting on the particles are gravity, buoyancy, and drag. The force of gravity \mathbf{F}_g is calculated from (12P.1) where ρ_p is the particle density, V is the particle volume, and \mathbf{g} is the gravitational acceleration.

$$\mathbf{F}_g = \rho_p \mathbf{g}V \quad (12P.2)$$

The force of buoyancy on the particle is based on the particle volume and can be calculated using (12P.3), where ρ_f is the fluid density.

$$\mathbf{F}_b = \rho_f \mathbf{g}V \quad (12P.3)$$

The force of drag acting on the particles can be calculated using a Stokes drag formulation based on the assumption that the Reynolds number, Re , is significantly less than unity. If this is the case, the force of drag can be calculated from (12.19)

$$\mathbf{F}_{drag} = 6\pi\eta Ua \quad (12.19)$$

It is important to note here that U is equal to the difference between the particle velocity and the fluid velocity.

$$U = U_p - U_f$$

Because the fluid is mostly stationary, the fluid velocity will be considered zero. Particles falling out of suspension will reach a constant terminal velocity in which the sum of all forces on them is zero. Using this information to populate (12P.1), (12P.4) can be generated.

$$\begin{aligned} \mathbf{F}_{drag} &= \mathbf{F}_g - \mathbf{F}_b \\ 6\pi\eta Ua &= \rho_p \mathbf{g}V - \rho_f \mathbf{g}V \\ U_p &= \frac{V\mathbf{g}(\rho_p - \rho_f)}{6\pi\eta a} \end{aligned} \quad (12P.4)$$

Continuing the assumption that the particles are spherical, the volume can be calculated as

$$V = \frac{4}{3}\pi a^3$$

The resulting equation can be used to calculate the terminal velocity of the particle

$$U_p = \frac{4\mathbf{g}(\rho_p - \rho_f)}{18\eta} a^2 \quad (12P.5)$$

Inserting values for the variables

Gravitational acceleration $\mathbf{g} = -9.81 \text{ m/s}^2$

Density of the particles $\rho_p = 8,908 \text{ kg/m}^3$
 Density of the fluid $\rho_f = 918.8 \text{ kg/m}^3$
 Viscosity of the fluid $\eta = 0.0523 \text{ Pa s}$
 Radius of the particles $a = 50\text{E}-6 \text{ m}$
 yields a terminal velocity of -0.00083 m/s

This velocity is based upon the assumption that Stokes drag (12.19) would be valid for this scenario. To check the validity of this assumption, we check the Reynolds number using of the calculated particle velocity:

$$Re = \frac{\rho_f U_p 2a}{\eta}$$

$$Re = 0.00147$$

It is seen, that the Reynolds number is significantly less than unity and the use of the Stokes drag formulation was appropriate. Dividing the height of the tank, 15 m, by the terminal velocity of the particles means that the particles will take a minimum of approximately 5 h to fall out of suspension. The particles will actually take longer due to the time needed for them to accelerate to their terminal velocity. This time frame will be too long for the chemical plant and a different type of particle separation will be desired:

12.3 Start with $\dot{S} = \dot{I} - O$

$$\dot{S} = \frac{dV}{dt} \text{ and } V = A \text{ (area)} \times h \text{ (height) so, } \dot{S} = A \frac{dh}{dt}$$

$$\dot{I} = K_p F_p U \text{ (applying Eq.(12.23) at pellet/disk interface)}$$

$$\dot{O} = K_{es} F_s U \text{ (applying Eq.(12.23) at slider/disk interface)}$$

There is one more output rate which is caused by the pellet at the pellet/disk interface.

$$\text{So, } \dot{O} = K_{ep} F_p U + K_{es} F_s U$$

After applying the linear rule of mixture, we arrive at Eq. (12.24)

$$A \frac{dh}{dt} = K_p F_p U (1 - X) - (K_{ep} F_p U + K_{es} F_s U) (X)$$

We know that $X = \frac{h}{h_{\max}}$ from Eq.(12.21). We can substitute h with X

in the storage rate.

Eq.(12.24) becomes :

$$A h_{\max} \frac{dX}{dt} = K_p F_p U (1 - X) - (K_{ep} F_p U + K_{es} F_s U) (X)$$

Solving the differential equation using integrating factor method:

$$X(t) = \frac{K_p F_p}{K_p F_p + K_{ep} F_p + K_{es} F_s} - \frac{K_p F_p}{K_p F_p + K_{ep} F_p + K_{es} F_s} \exp\left(-\frac{(K_p F_p + K_{ep} F_p + K_{es} F_s) U t}{A h_{\max}}\right)$$

Simplify and define τ (time constant), we arrive at Eq. (12.25)

- 12.4 Thick film powder lubrication is when the powder film separates the two interacting surfaces completely so that no contact occurs between them. The film height extends beyond the highest asperity. Typically, this phenomenon is associated with hydrodynamic lubrication, and that is when the rubbing surfaces are separated due to the hydrodynamic lift generated by the film flowing through a converging gap. Thin film powder lubrication is when the powder film does not extend beyond the highest asperity, and there is a constant contact between the two interacting surfaces. This phenomenon is often associated with boundary lubrication.

Chapter 13

Tribology of Solid Lubricants

Carlton J. Reeves, Pradeep L. Menezes, Michael R. Lovell,
and Tien-Chien Jen

Abstract Over the last seven decades, extreme operating conditions encountered in many industrial and engineering applications—particularly those within the aerospace industry—have driven the evolution of more advanced commercial lubricants. While many long-standing lubrication techniques utilize liquid or grease-type lubricants, new tribological applications have developed over the last 70 years that have led to the development of lubricants derived from solid materials and coatings with self-lubricating properties. Many tribological applications require two surfaces to slide over one another in relative motion, resulting in friction and wear, such as in cutting and forming operations, gears, bearings, and engine parts. Increasingly, more of these applications are operating in extreme environments (such as high vacuum, microgravity, high/low temperatures, extreme pressure, space radiation, and corrosive gas environments) that are beyond the tolerable and usable domain of liquid and grease-based lubricants. This has propelled the development of dry/solid lubricants that are nonvolatile and can withstand such extreme environmental conditions. In this chapter, a review of the state of solid lubrication and the utilization of solid lubricants as powder transfer films, thin film coatings, colloidal mixtures, and composite matrices are presented for the field of tribology.

C.J. Reeves • T.-C. Jen
Department of Mechanical Engineering, University of Wisconsin-Milwaukee,
Milwaukee, WI 53211, USA

P.L. Menezes • M.R. Lovell (✉)
Department of Industrial Engineering, University of Wisconsin-Milwaukee,
Milwaukee, WI 53211, USA
e-mail: mlovell@uwm.edu

1 Introduction

Solid lubricants were first introduced as commercial products in the 1940s to meet the demands of the aerospace industry to control friction and wear. As many of the applications became specialized and oriented towards conditions of extreme environments (e.g., high or low temperatures, vacuum, radiation, and high contact pressures), they began reaching beyond the tolerable domain of conventional liquid and grease-type lubricants. In the early developments of solid lubricants, much of the research was performed by government organizations such as the National Aeronautics and Space Administration (NASA) and was under proprietary restrictions. However, as solid lubricants have become more prevalent and understood by commercial lubrication engineers, much of the research and data has become readily available and the technology has become commercialized with the information being disseminated through the scientific community. Solid lubricants offer a variety of advantages when compared to conventional liquid or grease-type lubricants. As described in Table 13.1, they have a high resistance to abrasion, lower rates of deterioration, and are less volatility than conventional lubricants. Applications of solid lubricants involve their use as dry lubricants, thin films, and as dispersants in water, oils, and greases. Combinations of solid and liquid lubricants also play an important role in the synergetic effect of controlling friction and wear performance in specialized sliding interfaces where

Table 13.1 Advantages and disadvantages of solid lubricants [8]

Advantages	Disadvantages
<ul style="list-style-type: none"> • Are highly stable in high-temperature, cryogenic temperature, vacuum, and high-pressure environments • Have high heat dissipation with high thermally conductive lubricants, such as diamond films • Have high resistance to deterioration in high-radiation environments • Have high resistance to abrasion in high-dust environments • Have high resistance to deterioration in reactive environments • Are more effective than fluid lubricants at intermittent loading, high loads, and high speeds • Enable equipment to be lighter and simpler because lubrication distribution systems and seals are not required • Offer a distinct advantage in locations where access for servicing is difficult • Can provide translucent or transparent coatings, such as diamond and diamond-like carbon films, where desirable 	<ul style="list-style-type: none"> • Have higher coefficients of friction and wear than for hydrodynamic lubrication • Have poor heat dissipation with low thermally conductive lubricants, such as polymer-base films • Have poor self-healing properties so that a broken solid film tends to shorten the useful life of the lubricant (however, a solid film, such as a carbon nanotube film, may be readily reapplied to extend the useful life.) • May have undesirable color, such as with graphite and carbon nanotubes

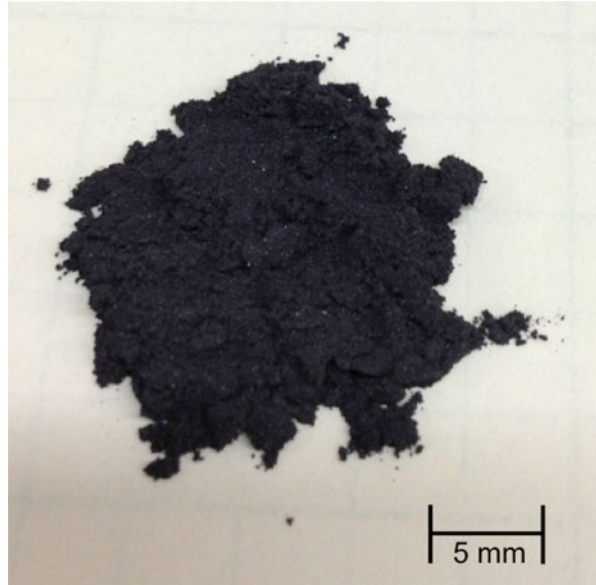
the combined properties enhance the lubricant performance [1]. Solid lubricants behave and function similar to liquid or grease type lubricants in sliding contact, by adhering to the lubricating surfaces and forming a protective boundary layer that minimizes contact between opposing surface asperities to prevent wear. The protective boundary layer acts as a lubricant in sliding contact by easily shearing and accommodating the relative surface velocities. This allows the lubricious protective layers or coatings to provide low friction and minimal wear thus facilitating lubrication. Solid lubricants are often used in environments where their ability to resist the detrimental factors that render conventional liquid or grease-type lubricants ineffective—such as operation within cryogenic temperatures. The advantages to using solid lubricants include their ability to lubricate components for the duration of their life; perform dry lubrication; maintain non-volatility; lubricate where the presence of vapors from fluids or greases are unacceptable; and resist attraction to dust or dirt. Despite the many accolades received by solid lubricants, there are still some limitations, where environmental conditions such as atmospheric conditions, temperature, radiation, and load can influence their performance. In this chapter, the many contributing factors to the rise in solid lubricant usage as well as their lubricating performance are discussed in detail.

2 History of Solid Lubrication

2.1 Introduction to Solid Lubricants

The history of solid lubricants dates back to the invention of the wheel and has since grown into one of the largest industries in the world. Even now, it is estimated that one-third to one-half of all the energy produced is still lost through friction due to inefficient lubrication practices. Early applications of lubricants include the use of animal fats and vegetable oils until the first oil well was drilled in Titusville, PA, USA in 1859. This brought rapid advances in lubrication technology with the advent of petroleum-based oils. During the mid-1930s, the use of petroleum-based oils was significantly improved through the use of additives (some being solids) to enhance the load carrying capacity, lubricity, corrosive protection, and thermal-oxidative stability of the oils. As industrial applications became more complex, this required the use of lubricating components at higher temperatures and extreme environments. In many applications petroleum oils became inept, which led to the development of synthetic lubricants in the late 1930s. However, even synthetic lubricants encountered problems involving extremely high temperatures of supersonic aircraft, spacecraft, and other advanced industrial applications. This problem forced lubrication engineers to develop lubricants that do not evaporate at high temperatures and can withstand the various environmental and operational conditions, thus the solid lubricant was born in the 1940s. Solid lubricants are often

Fig. 13.1 Photograph of 50 nm graphite powder

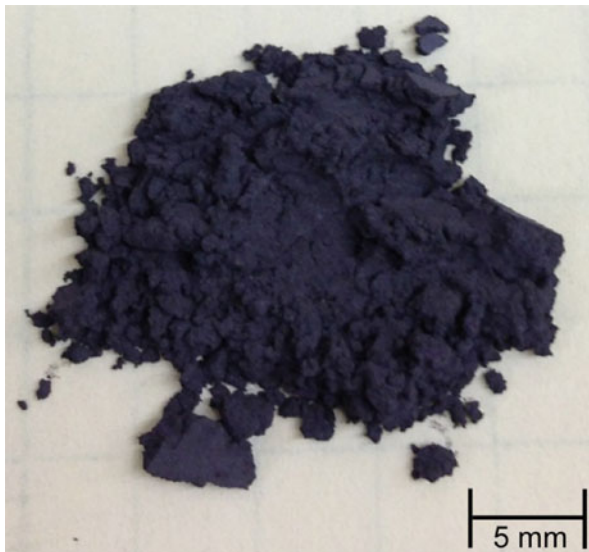


described as substances that provide lubrication between two surfaces in relative motion under dry conditions. In preliminary studies, solid lubricants were effective at providing adequate lubrication of bearing surfaces at high temperatures and low pressures. The two best known and most popular solid lubricants are graphite and molybdenum disulfide. This is due to their slippery nature and low friction qualities. Photographs of graphite and molybdenum disulfide powders are shown in Figs. 13.1 and 13.2, respectively. Graphite is one of the oldest solid lubricants and has been used as a lubricant for centuries. Molybdenum disulfide was first used as a solid lubricant when travelers in Colorado employed pulverized rock to lubricate their wagon wheels. Coincidentally, this also happens to be where the world's largest mineral deposit of molybdenite is located at Climax, CO, USA. Other types of solid lubricants consist of soft metals, metallic oxides, sulfides, selenides, tellurides, polymers, and composite materials, all of which have differing properties making them advantageous in various applications. A brief history of solid lubricants and their applications can be seen in the literature [2–4].

2.2 Advantages and Disadvantages of Solid Lubricants

Solid lubricants offer many advantages over liquid lubricants in applications (see Table 13.1) involving high vacuum, high temperature, cryogenic temperature, radiation, extreme dust, or corrosive environments [2, 3, 5, 6]. Figure 13.3 depicts the many operating conditions in which fluid lubricants are undesirable or ineffective, thus requiring the use of solid lubricants [7]. More specifically, Fig. 13.3 illustrates the

Fig. 13.2 Photograph of 2 μm molybdenum disulfide (MoS_2) powder



environmental applicability of solid and liquid lubricants in radiation, extreme temperature, and vacuum environments. In extreme pressure applications (i.e., high to ultrahigh vacuum conditions—a vacuum of $\sim 10^{-2}$ Pa or higher or a gas density of $\sim 10^{-12}$ molecules/cm³ or lower) liquid lubricants can vaporize [2]. For example, in space, a liquid lubricant would vaporize, thus contaminating the device it is lubricating and potentially damaging it. This example could occur in the case of an optical or electronic equipment application. On the contrary, if a solid lubricant were used this problem would no longer exist. In high temperature applications extending beyond 523 K, liquid lubricants often vaporize or decompose, limiting their use as a lubricant. In contrast, when compared to liquid lubricants, solid lubricants at these temperatures can maintain relatively low coefficients of friction. Liquid lubricants can also solidify or become highly viscous and may not be effective at cryogenic temperatures. For this reason, solid lubricants are used when operating at temperatures as low as 0 K. In radiation environments, liquid lubricants tend to decompose at 10^6 rads (radiation dose absorbed of 10^4 J/kg), whereas solid lubricants demonstrate better radiation resistance and relatively low friction. In extreme dust areas, dust particles would ordinarily adhere to liquid lubricants, forming a grinding paste. This paste can cause abrasive wear and damage surfaces and sensitive equipment. In such a case, hard solid lubricants, such as diamond-like carbon and boron nitride films are preferred. In aerospace applications (e.g., weight-limited spacecraft and rovers) where weight limits are critical, solid lubrication is advantageous. Solid lubricants weigh substantially less than liquid lubricants and their use eliminates the need for recirculatory oil systems with pumps and heat exchangers [2, 3]. Moreover, the limited use of liquid lubricants and their replacement by solid lubricants would reduce spacecraft weight and therefore, have a dramatic impact on mission extent and spacecraft

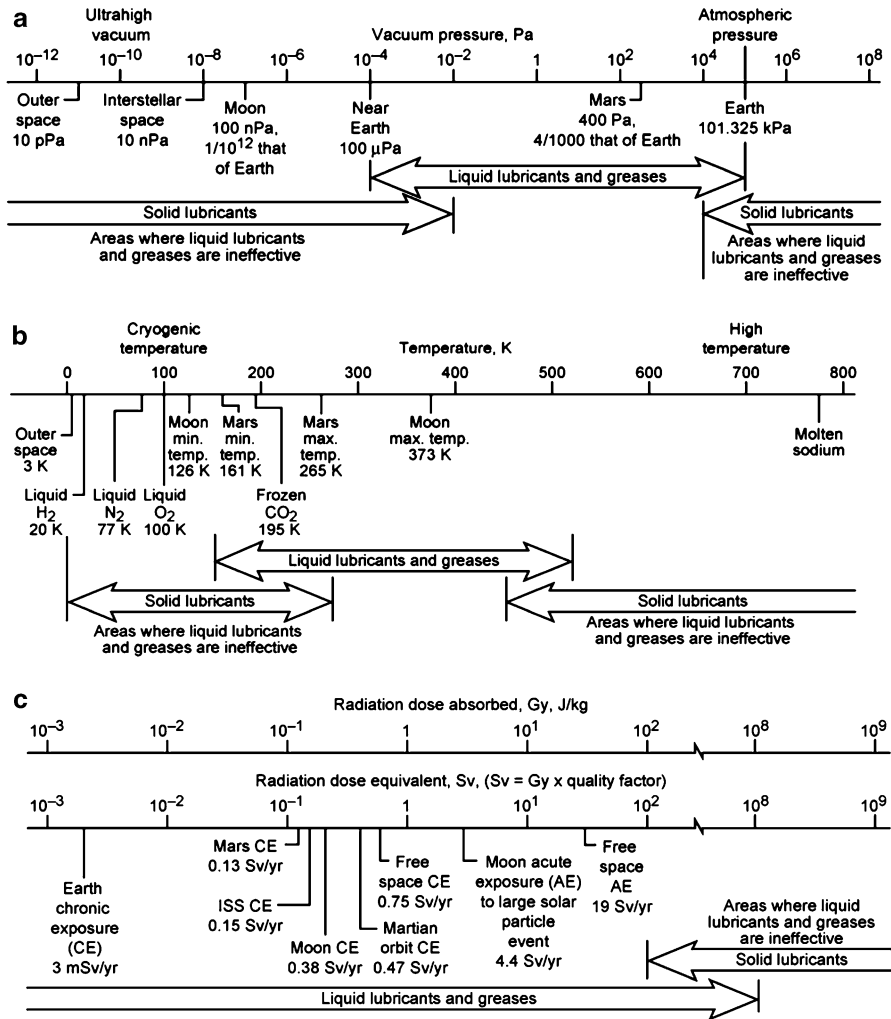


Fig. 13.3 Variations in environmental conditions for adequate usage for liquid, solid, and grease type lubricants: (a) vacuum environments; (b) cryogenic and high temperature environments, (c) radiation environments [7]

maneuverability. Under intermittent loading conditions or in corrosive environments, liquid lubricants can become contaminated, lose their lubricity, and lead to seizure of components. Changes in critical service and environmental conditions such as loading, time, contamination, pressure, temperature, and radiation, also affect liquid lubricant efficiency. When equipment is stored or is idle for extended periods, solid lubricants provide permanent satisfactory lubrication by maintaining their physico-chemical attributes unlike liquid lubricants.

Some of the disadvantages of solid lubricants are their higher coefficient of friction and wear rates when used in hydrodynamic lubrication processes. Many solid lubricants maintain poor heat dissipation with low thermal conductivity when compared to liquid lubricants. For this reason, applications that require heat dissipation generally resort to liquid lubricants that can be pumped or circulated to remove heat. In cases where a solid lubricant is used and minimal heat generation is required, alternative techniques must be implemented to dissipate the heat. Additionally, solid lubricants have poor self-healing properties in the sense that a broken solid film can cause a decrease in the useful life of particular mechanical components.

2.3 Applications of Solid Lubrication

When solid materials were first being used as lubricants, much of the industry knowledge was primarily constrained to individuals within the lubrication industry and commissioned by government agencies such as the National Aeronautics and Space Administration (NASA), the Department of Defense (DOD), and the Department of Energy (DOE). As solid lubricants gained acceptance, other aerospace and commercial industries began utilizing them. Currently, knowledge of the applicability and use of solid lubricants is widespread and disseminated through publications in numerous scientific journals and conferences worldwide. The acceptance of solid lubricants to become a viable lubricant in the larger lubrication market was slow and encountered much reluctance, because of the frequent misuse and lack of knowledge in their early days. As more information was learned in the last several decades, their potential has been fully realized. Table 13.2 lists applications of solid lubricants that are utilized in various environments and operating conditions.

Solid lubricants received their start in the aircraft industry on both military and commercial aircraft as indicated by the numerous aerospace applications in Table 13.2. Solid lubricants were used in missiles and space vehicles as well as being exploited in these industries for their ability to lubricate under extreme conditions. Solid lubricants were initially used in only a few components in the 1900s fighter planes, however with time solid lubricants were eventually adopted and utilized in over 1,000 components on the North American Rockwell XB-70 bomber. Here, over 95 % of the plain bearings were lubricated with a plastic or thin-film-ceramic solid lubricant. The North American Rockwell Corporation was well known for its ceramic-bonded lubricant, “Vitrolube” which was used on bushings or plain spherical type bearings in applications from room temperature up to 644 K [3]. Aircraft components that require solid lubrication are ejection seat parts, canopy linkages, and control lever components. In these safety devices the movement is limited but it is critical that these mechanisms perform when needed. Other aerospace applications of solid lubricants include missiles, satellites, and spacecraft components [8]. Solid lubricant coatings have also been used in space

Table 13.2 Applications of solid lubricants [2, 7]

(a) Areas where fluid lubricants are undesirable	
Requirements	Applications
Resist abrasion in dirt-laden environments	Space vehicles (rovers) Lunar base Martian base Aircraft Automobiles Agricultural and mining equipment Off-road vehicles and equipment Construction equipment Textile equipment Dental implants
Avoid contaminating product or environment	Space telescopes Equipment in lunar base Equipment in Martian base Microscopes and cameras Spectroscopes Medical and dental equipment Artificial implants Food-processing machines Optical equipment Metalworking equipment Surface-mounted equipment Hard disks and tape recorders Textile equipment Paper-processing machines Business machines Automobiles
Maintain servicing or lubrication in inaccessible or hard-to-access areas	Space vehicles Satellites Aerospace mechanisms Nuclear reactors Consumer durables Aircraft
Provide prolonged storage or stationary service	Space telescope mounts Space antenna mounts Aircraft equipment Railway equipment Missile components Nuclear reactors Heavy plants, buildings, and bridges Furnaces

(continued)

Table 13.2 (continued)

(b) Areas where fluid lubricants are ineffective			
Environment		Applications	
High vacuum	Room temperature or cryogenic temperatures	Vacuum products Space mechanisms Satellites Space telescope mounts Space platforms Space antennas	
	Cleanroom	Biomedical equipment Analytical tools Coating equipment Semiconductor manufacturing equipment	
	High temperature	Space nuclear reactors X-ray tubes X-ray equipment Furnaces	
High temperature	Lunar environments	Space vehicles Space mechanisms Lunar bases	
	Air atmosphere	Furnaces Metalworking equipment Compressors	
	Molten metals (sodium, zinc, etc.)	Nuclear reactors Molten metal plating equipment	
Cryogenic temperatures		Lunar and Martian bases Space mechanisms Satellites Space vehicles Space propulsion systems Space telescope mounts Space platforms Space antennas Turbo pumps Liquid nitrogen pumps Butane pumps Freon pumps Liquid natural gas pumps Liquid propane pumps Refrigeration plants	
	Radiation (gamma rays, fast neutrons, X-rays, beta-rays, etc.)		Lunar and Martian bases Nuclear reactors Space mechanisms Satellites Space vehicles Space platforms Space antennas

(continued)

Table 13.2 (continued)

(b) Areas where fluid lubricants are ineffective	
Environment	Applications
Corrosive gases (chlorine etc.)	Maneuvering Semiconductor manufacturing equipment
High pressures or loads	Metalworking equipment Bridge supports Plant supports Building supports
Fretting wear and corrosion (general)	Space antennas Space platforms Aircraft engines Turbine blades Landing gear Automobiles

vehicle components such as the gimbal bearings, tie-down clamps, camera parts, gears, bearings, sliding tracks, and valves.

In military applications, the US Army utilizes tremendous amounts of solid lubricants in a variety of forms for weapons and ground-handling equipment such as ball sockets, sliding covers, hand wheels, bearing-support points, slide dust covers, hand brakes, chain and sprocket drives, plungers, screw threads, telescoping-tube assemblies, warhead-mating fixtures, trailer elevating mechanisms, torsion bar suspensions, bearing areas, rifle mounts, rocket launchers, ammunition, firing mechanisms, breech mechanisms, and Trunnion bearings [9]. The US Army also utilizes solid lubricants in helicopter gearboxes and antifriction bearings. In these applications, the solid lubrication system serves as an auxiliary backup lubrication system in the event that the liquid oil lubrication system failed during an aircraft's flight. Other branches of military also utilize solid lubricants, such as the US Navy for applications involving aircraft and ships where greases with molybdenum disulfide additives are used to prevent seizure of gears, bearings, and joints.

The secondary adoption of solid lubricants began when commercial industries such as automotive, heavy electrical, metalworking, marine, household-appliance, toy, farming, and solid-waste disposal industries realized the value of such lubricants. Their applications are vast with some applications shown in Table 13.2. Other applications of solid lubricants include convex draw dies, solenoids, arc-furnaces guides, core-oven wheel bearings, conveyor wheels, railroad centerplates, helicopter gear boxes, cold extruder (wire), roller chains, turntable 45 rpm spindle (music), air-cooled four cylinder engines, cold hobbing (with steel dies), rolling mills, conveyor parts, brake air cylinders, oil pipeline valves, bullets, boat hulls, roll-extruded cylinders, wire rope (wire strand), aircraft landing gear, oxygen-furnace bearings, pressurized tee connectors on gas mains, small arms, ball joints and front suspensions (automobiles), air cylinder tubing, three-jaw chucks, plug valves, racecar axle threads, timing mechanisms, fuel pump mechanisms, rear axle assemblies (tractors), electrical

connectors (space), cylinder walls (gasoline engines), gear trains, clutch brakes, hinge bolts, pylon-hinge pins (copters), rocket bellows, bearing-link assemblies, clock springs, camera shutters (space flight), root ribs (aircraft), rocket engines, fasteners, valves, bushings, rolling-mill couplings, self-aligning ball bushings, composite brushes, thrust bearings, draw and blanking punches, drilling and tapping machines, wheel bearings and kingpins (truck fleets), and sliding-tandem trailers (trucks) [3].

3 Quantification of Lubricants

3.1 Classifications

Lubricants are classified into two categories by (1) lubricating film type and (2) physiochemical properties. When categorizing lubricants as lubricating films, they are organized into three types: solid films, fluid films, and thin films. Solid films can be adsorbed, bonded, or deposited on lubricating surfaces. Solid lubricants are generally classified as solid films because of their ability to adhere to surfaces through various adsorption and deposition processes. Fluid films are thick films that completely separate two surfaces moving in relative motion with each other, whereas thin films only provide partial separation. Both fluid and thin films are typically composed of liquid lubricants. Table 13.3 shows the classification according to lubrication film with the addition of gas films, which consist of a pressured mass of gaseous atoms. In Table 13.3, fluid films are subclassified into several categories:

- (a) Hydrodynamic films, which are defined as films formed by the motion of the lubricating surfaces through a convergent zone creating sufficient (hydrodynamic) pressure to support a normal load and thus maintaining separation of the surfaces without the aid of an external pumping apparatus;
- (b) Hydrostatic films, which are fluid films that occur when pumping a fluid or film between the two lubricating surfaces that are in relative motion; and
- (c) Squeeze films, which are fluid films that occur when lubricating surfaces move towards each other.

The second method of quantifying lubricants is through their physiochemical properties. This method classifies them based on their chemistry, crystal structure, and lubricity. Table 13.4 presents the most widely used and most recently developed lubricants by their subclasses as well as providing their coefficient of friction range. The ranges in the coefficient of friction are due to the fact that friction is a system dependent property that is dependent upon test environment, operating conditions, and surface geometrical configuration. Ambient conditions such as temperature and humidity as well as the type of counter face materials and surface texture also affect the friction coefficient of a given solid lubricant. Moreover, even the physical nature (i.e., powder, thin film, bulk, composite, and crystalline or amorphous state), deposition method, and/or application method of the solid lubricant can cause variations in the friction and wear properties.

Table 13.3 Types of lubricating films [2, 7]

Type	Lubricating film	
Solid films	Nanotubes, nano-onions, and other nanoparticles (C, BN, MoS ₂ , and WS ₂)	
	Nanocomposite coatings (WC/C, MoS ₂ /C, WS ₂ /C, TiC/C, and nanodiamond)	
	Diamond and diamond-like carbon coatings (diamond, hydrogenated carbon (a-C:H), amorphous carbon (a-C), carbon nitride (C ₃ N ₄), and boron nitride (BN) films)	
	Superhard or hard coatings (VC, B ₄ C, Al ₂ O ₃ , SiC, Si ₃ O ₄ , TiC, TiN, TiCN, AlN, and BN)	
	Lamellar film (MoS ₂ and graphite)	
	Nonmetallic film (titanium dioxide, calcium fluoride, glasses, lead oxide, zinc oxide, and tin oxide)	
	Soft metallic film (lead, gold, silver, indium, copper, and zinc)	
	Self-lubricating composites (nanotubes, polymer, metal-lamellar solid, carbon, graphite, ceramic, and cermets)	
	Lamellar carbon compound film (fluorinated graphite and graphite fluoride)	
	Carbon	
	Polymers (Polytetrafluoroethylene (PTFE), nylon, and polyethylene)	
	Fats, soap, wax (stearic acid)	
	Ceramics and cermets	
	Fluid film	Hydrodynamic films: Thick hydrodynamic film Elastohydrodynamic film
		Hydrostatic film
Squeeze film		
Thin film		Mixed lubricating film
	Boundary lubricating film	
Gas film	Hydrodynamic film	
	Hydrostatic film	

3.2 Lamellar Solid Lubricants

Lamellar or layered solid lubricants are some of the most widely used class of lubricants by engineers. A significant amount of research and development has been performed to understand the tribological characteristics of these lubricants as well as determining the optimal lubricant for specific applications. A few examples of lamellar lubricants are graphite (shown in Fig. 13.1), transition metal dichalcogenides (compounds consisting of at least two molecules from Group 16 of the periodic table) such as MoS₂ (Fig. 13.2) or WS₂ (Fig. 13.4), hexagonal boron nitride (hBN) (Fig. 13.5), and boric acid (H₃BO₃) (Fig. 13.6). These lamellar solid powders all have similar molecular structures composed of layers of atoms bonded together with covalent bonds. These layers are held together by the weak

Table 13.4 Solid materials with self-lubricating capabilities [16]

Classification	Key examples	Typical range of friction coefficient
Lamellar solids	MoS ₂	0.002–0.25
	WS ₂	0.01–0.2
	hBN	0.150–0.7
	Graphite	0.07–0.5
	Graphite fluoride	0.05–0.15
	H ₃ BO ₃	0.02–0.2
	GaSe, GaS, SnSe	0.15–0.25
Soft metals	Ag	0.2–0.35
	Pb	0.15–0.2
	Au	0.2–0.3
	In	0.15–0.25
	Sn	0.2
Mixed oxides	CuO–Re ₂ O ₇	0.3–0.1
	CuO–MoO ₃	0.35–0.2
	PbO–B ₂ O ₃	0.2–0.1
	CoO–MoO ₃	0.47–0.2
	Cs ₂ O–MoO ₃	0.18
	NiO–MoO ₃	0.3–0.2
	Cs ₂ O–SiO ₂	0.1
Single oxides	B ₂ O ₃	0.15–0.6
	Re ₂ O ₇	0.2
	MoO ₃	0.2
	TiO ₂ (sub-stoichiometric)	0.1
	ZnO	0.1–0.6
Halides and sulfates or alkaline earth metals	CaF ₂ , BaF ₂ , SrF ₂	0.2–0.4
	CaSO ₄ , BaSO ₄ , SrSO ₄	0.15–0.2
Carbon-based solids	Diamond	0.02–1
	Diamond-like carbon	0.003–0.5
	Glassy carbon	0.15
	Hollow carbon nanotubes	–
	Fullerenes	0.15
	Carbon-carbon and carbon-graphite-based composites	0.05–0.3
Organic materials/polymers	Zinc stearite	0.1–0.2
	Waxes	0.2–0.4
	Soaps	0.15–0.25
	PTFE	0.04–0.15
Bulk or thick-film (>50 μm) composites	Metal-, polymer-, and ceramic-matrix composites consisting of graphite, WS ₂ , MoS ₂ , Ag, CaF ₂ , and BaF ₂	0.05–0.04
Thin-film (<50 μm) composites	Electroplated Ni and Cr films consisting of PTFE, graphite, diamond, B ₄ C, etc., particles as lubricants	0.1–0.5
	Nanocomposite or multilayer coatings consisting of MoS ₂ , Ti, DLC, etc.	0.05–0.15

Fig. 13.4 Photograph of 0.6 μm tungsten disulfide (WS_2) powder

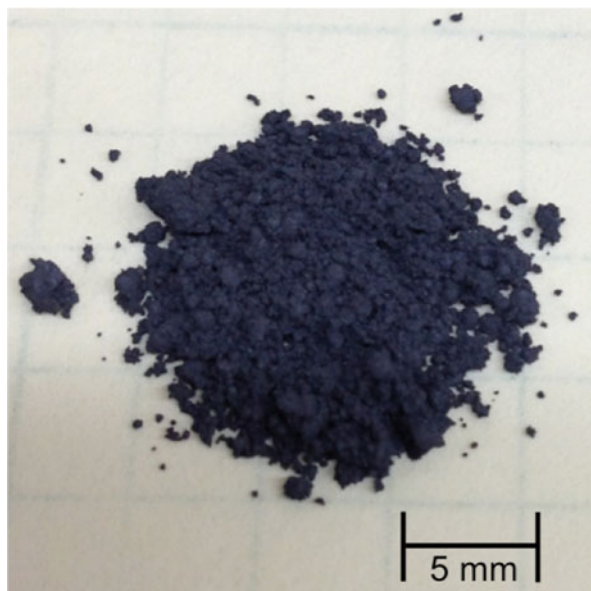


Fig. 13.5 Photograph of 70 nm hexagonal boron nitride (hBN) powder

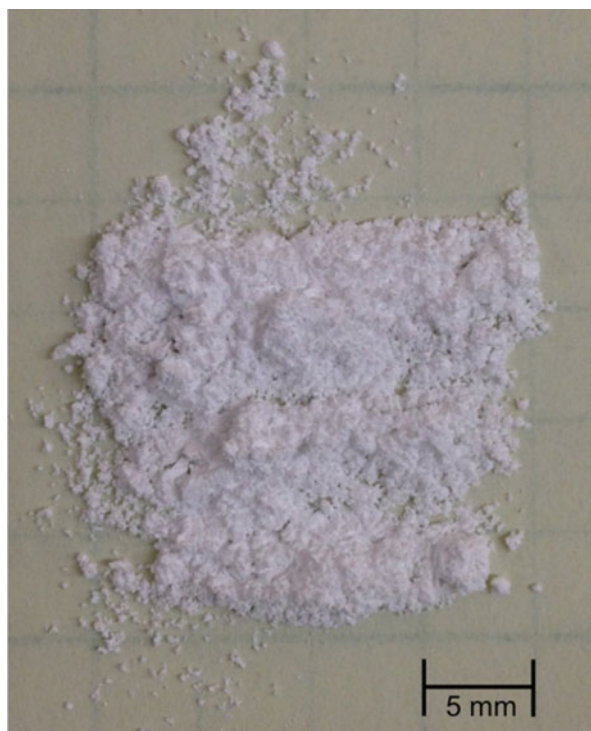


Fig. 13.6 Photograph of micron-sized boric acid (H_3BO_3) powder



van der Waals force and maintain different distances between the layers for different molecules. Figures 13.7, 13.8, 13.9, and 13.10 show a schematic representation of the layered crystal structure of graphite, MoS_2 , hBN, and H_3BO_3 molecules, respectively. Some of the more widely used solid lubricants are derived from natural minerals, extracted from deposits found in the earth such as MoS_2 , graphite, and boric acid. Other solid lubricants are synthetic, for example WS_2 , hBN, fluorinated graphite, and transition metals diselenides (consist of two selenide molecules) and ditellurides (consist of two telluride molecules). The use of diselenides and ditellurides as solid lubricants is significantly less common than the use of graphite and MoS_2 . As with many lamellar lubricants, transition metal dichalcogenides gain their lubricity from their layered crystal structure caused by the low intra-layer shear resistance due to the weak van der Waals force.

In the case of lamellar solids such as molybdenum disulfide (MoS_2), the friction coefficient varies from 0.002 to 0.25 due to the film microstructure, chemistry, test environment, ambient temperature, contact pressure, film thickness, stoichiometry, and purity. Due to the porous columnar structure, MoS_2 films deposited by conventional sputtering methods such as physical vapor deposition tend to exhibit higher friction and lower wear rates than films deposited by ion-beam-assisted deposition (IBAD) or closed-field unbalanced magnetron sputtering techniques. The effect of the different film deposition methods results in some films having near perfect

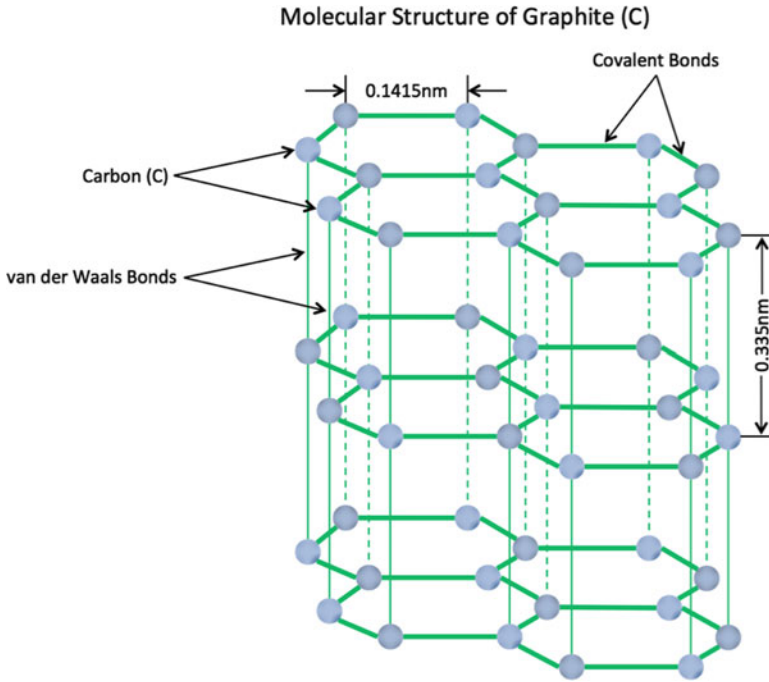


Fig. 13.7 Illustration of the layered crystal molecular structure of graphite (C)

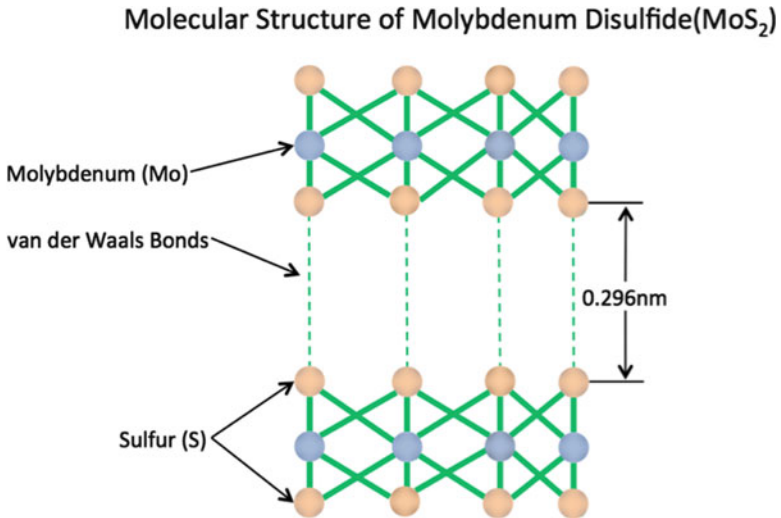


Fig. 13.8 Illustration of the layered crystal molecular structure of molybdenum disulfide (MoS_2) a dichalcogenide

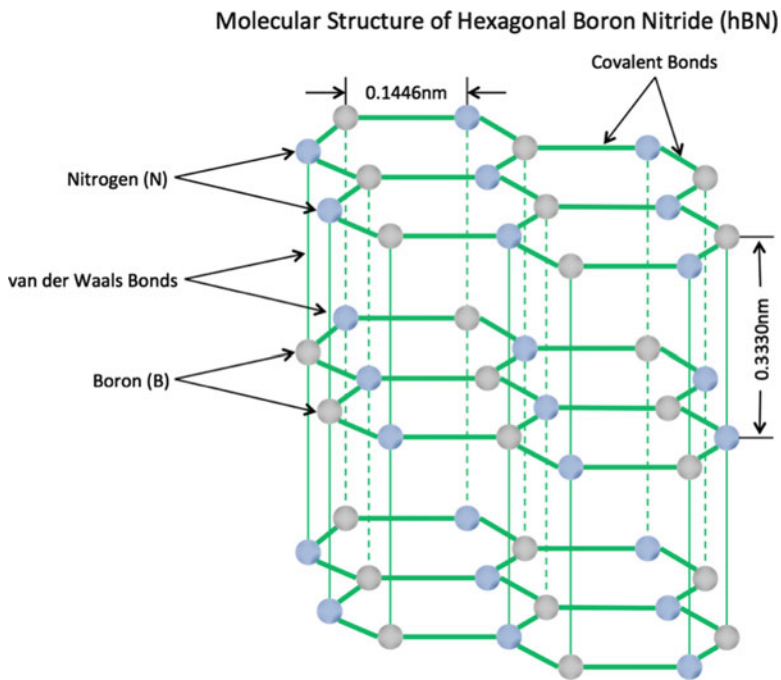


Fig. 13.9 Illustration of the layered crystal molecular structure of hexagonal boron nitride (hBN)

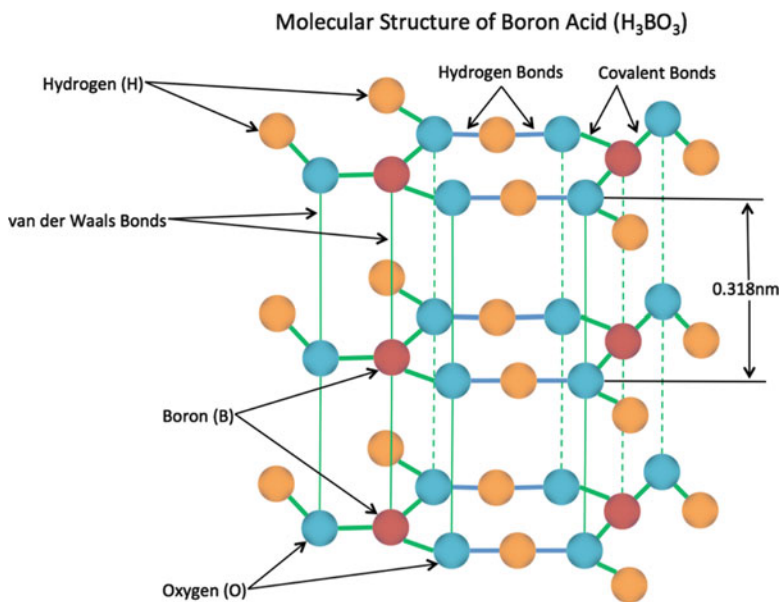


Fig. 13.10 Illustration of the layered crystal molecular structure of boric acid (H_3BO_3)

stoichiometry, purity, and basal plane orientation to the lubricating surface and the direction of motion, thus facilitating extremely low friction coefficients. In fact, in the presence of an ultrahigh vacuum, these deposited MoS₂ films can have friction values as low as 0.002 [10, 11]. All of the aforementioned factors affect the shear rheology and frictional properties of MoS₂, as the coefficient of friction is test dependent. Furthermore, not a single lubricant, including solid lubricants, can provide both low and consistent friction coefficients over a wide variety of test conditions, temperatures, environments, and deposition methods. Therefore, it is customary for lubrication engineers to optimize a lubricant for a specific application with a defined set of operational and environmental conditions.

Due to the sensitivity of each lubricant to its environment, many techniques have been developed to optimize a particular lubricant for a specific application. In extreme environments consisting of vacuum or high/low temperatures MoS₂, WS₂, and hBN are preferred as solid lubricants [12, 13]. Graphite and H₃BO₃ are superior lubricants in moist air environments; however, they are poor lubricants in dry or vacuum environments. As a modification, tribologists have learned that if graphite is fluorinated through a process of electrolysis in a solution of hydrogen fluoride, this creates graphite fluoride. Graphite fluoride has larger spacing between the carbon–carbon layers in graphite resulting in easier shear and hence better lubricity in dry environments. Among the lamellar solids, MoS₂ and WS₂ have some of the best overall load-carrying capacities when used as thin films. Most lamellar solids have good wetting capability and chemical affinity for ferrous surfaces [14]. On a rough or porous sliding surface, MoS₂ and WS₂ accumulate in the valleys between asperities, thus providing a smoother surface finish. When applied properly, these solid lubricants can withstand extreme contact pressures without being squeezed out of the load-bearing surfaces. WS₂ is preferred over MoS₂ when applications involve relatively higher temperatures [15]. However, WS₂ is a synthetic lubricant and therefore it is more expensive than MoS₂, which is derived from a natural mineral known as molybdenite. Selenides of molybdenum (Mo), tungsten (W), and niobium (Nb) can provide even higher temperature capabilities than their sulfide counterparts, and have demonstrated greater electrical conductivity, however, they too are expensive and hence they are used less frequently [16].

3.3 Transition-Metal Dichalcogenides

Transition-metal dichalcogenides are among the lowest-friction materials known for their use in dry, vacuum, and cryogenic environments. They comprise of MX₂ structure, where M is a transition metal consisting of molybdenum (Mo), tungsten (W), niobium (Nb), or tantalum (Ta) and X₂ refers to a chalcogenide consisting of two atoms from Group 16 in the periodic table, most notably consisting of sulfur (S), selenium (Se), or tellurium (Te). MoS₂ and WS₂ are among the most widely used transition-metal dichalcogenides and photographs of

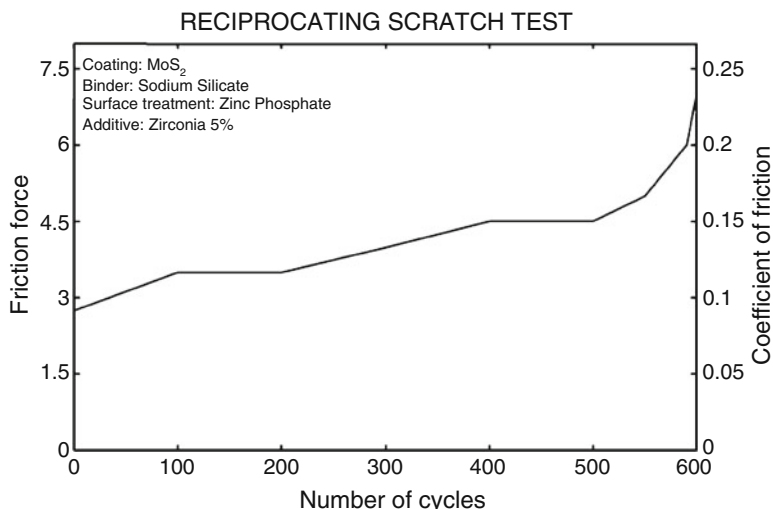


Fig. 13.11 Variation of friction force and coefficient of friction with number of cycles when a steel ball is slid against a zinc phosphated steel specimen coated with the MoS₂ and 5 % zirconia additive [19]

these powder particles are shown in Figs. 13.2 and 13.4, respectively. Dichalcogenides are chemically stable and resist attack by most acids with the exception of aqua regia (also known as nitro-hydrochloric acid), hydrochloric acid (HCL), sulfuric acid (H₂SO₄), and nitric acid (HNO₃). At room temperature in ultrahigh vacuum, these solid lubricants can provide the lowest coefficient of friction values ranging from 0.002 to 0.2. Their shortcomings occur in the presence of moisture environments, which have a detrimental effect on their lubricity [17, 18]. Oxidation of MoS₂ begins when temperatures reach about 648 K and at approximately 773 K, rapid oxidation occurs resulting in MoO₃ and SO as byproducts. The thermal-oxidative stability of WS₂ is better than that of MoS₂ and thus it is used in higher temperature application.

An investigation of MoS₂-based solid lubricant mixtures containing zirconia and graphite on the contact surface during sliding against a steel ball was made [19]. In this study, Zirconia, a ceramic material, was studied because it offers superior tribological properties such as a high resistance to wear. Experiments were conducted to measure the friction force for various numbers of cycles using a reciprocating scratch tester. Figure 13.11 shows the variation of friction force and coefficient of friction with number of cycles when a steel ball is slid against a zinc phosphated steel specimen coated with the MoS₂ and 5 % zirconia additive. The MoS₂-based lubricant with a 5 % zirconia additive has an average wear rate of 0.018 μm/cycle and an initial coefficient of friction value of 0.1. A similar coating containing 8 % of zirconia in the lubricant demonstrated an average wear rate of 0.0125 μm/cycle with an initial coefficient of friction value of 0.11.

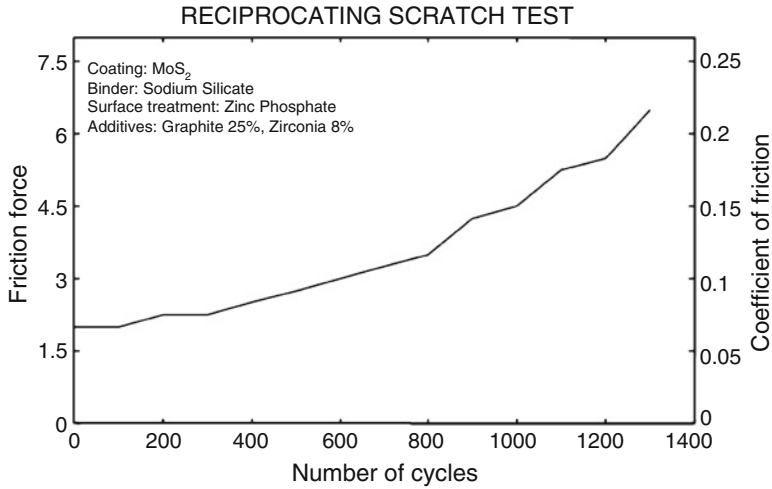


Fig. 13.12 Variation of the friction force and the coefficient of friction with the number of cycles when a steel ball is slid against a zinc phosphated steel specimen coated with MoS_2 , 8 % zirconia, and 25 % graphite as additive [19]

Although the addition of zirconia improved the wear properties, it also increased the initial friction value when changing from 5 to 8 % of zirconia. This problem of an increased coefficient of friction value was overcome by the addition of graphite into the lubricant. Graphite, as previously discussed, is an excellent solid lubricant to use in humid conditions because it maintains its low-friction behavior when it is contaminated by water vapor or other condensable vapors. Here, the MoS_2 -based lubricant was prepared with a combination of 25 % graphite and 8 % zirconia as additive material. Figure 13.12 shows the variation of the friction force and the coefficient of friction with the number of cycles when a steel ball is slid against a zinc phosphated steel specimen coated with MoS_2 , 8 % zirconia, and 25 % graphite as additive. The experiment revealed an average wear rate of $0.003 \mu\text{m}/\text{cycles}$ and an initial coefficient of friction value of 0.06. The addition of 8 % of zirconia and 25 % of graphite to the lubricant increased the wear resistance of the film by about 72 % and reduced the friction coefficient from 0.11 to 0.06.

To understand the influence of moisture on friction and wear, the tests were conducted at a high temperature of 473 K. Figure 13.13, shows the variation of friction force and coefficient of friction with number of cycles when a steel ball is slid against manganese phosphated steel specimens coated with MoS_2 and 8 % zirconia and 25 % graphite as additive at 473 K. The behavior of the MoS_2 film in the presence of moisture at ambient temperatures was found to be poor. On the contrary, at high temperatures, the moisture evaporated and thus enhanced the film performance. The results of scratch tests conducted for 5,500 cycles at 473 K had not shown any signs of failure and maintained a friction coefficient of 0.05. The temperature of the specimen that were maintained at 473 K, were then decreased to room temperature. The results showed a failure of the films occurring as low as

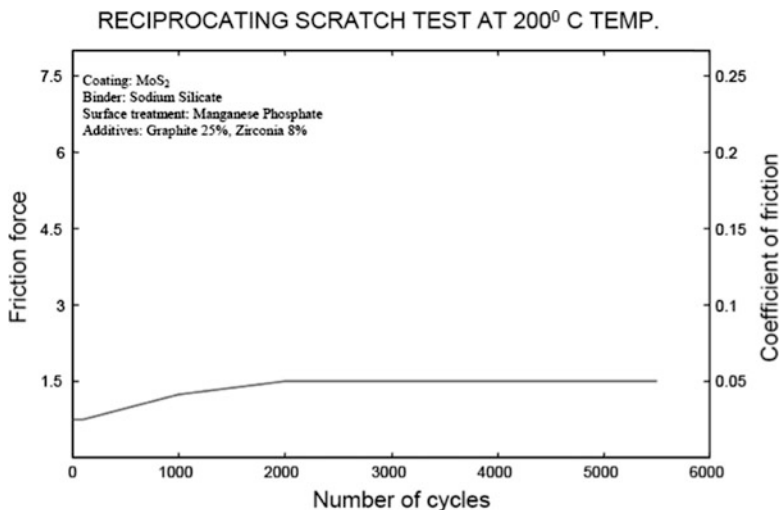


Fig. 13.13 Variation of friction force and coefficient of friction with number of cycles when a steel ball is slid against manganese phosphated steel specimens coated with MoS₂ and 8 % zirconia and 25 % graphite as additive at 473 K [19]

600 cycles and as high as 3,000 cycles. These tests demonstrate the effect of moisture on MoS₂ film. In summary, the results showed that the addition of zirconia and graphite into the MoS₂-based lubricant has improved its properties in terms of both friction and wear. In addition, it was observed that the presence of moisture in the air affects the life of the lubricating film increasing the coefficient of friction and wear rate. It was shown that at high temperatures the moisture evaporation enhanced the coating performance of the film.

3.4 *Metal-Monochalcogenides*

Metal-monochalcogenides, such as GaS, GaSe, or SnSe are similar to transition-metal dichalcogenides by nature of their crystal structures. Monochalcogenides are composed of a MX structure, where the M is a metal consisting of gallium (Ga) or tin (Sn) and the X refers to a single chalcogenide atom such as sulfur (S) or selenium (Se). These solid lubricants are well-known sandwich semiconductors in solid-state physics for their superior electrical and optical properties [20]. Tin and germanium-based monochalcogenides represent a group of layered compounds that also consist of sulfides (SnS and GeS) and selenides (SnSe and GeSn). Similarly, another class of layered metal-monochalcogenides consist of an indium metal-base and have been explored with sulfides (InS) and selenides (InSe). Pin-on-disk experiments, as well as electron microscopy inspection of metal-monochalcogenides, have revealed that the interlayer bonding and the crystal chemistry are responsible for the lubricity and

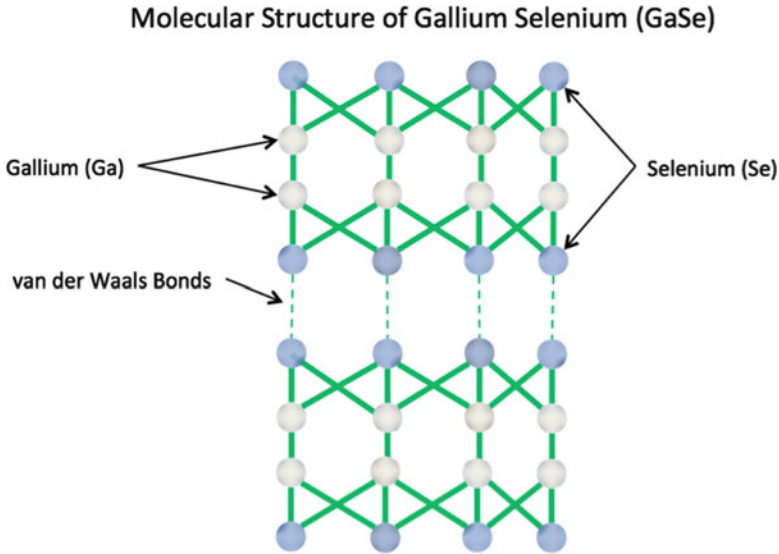


Fig. 13.14 Illustration of the layered crystal molecular structure of Gallium Selenium (GaSe) a Monochalcogenide

self-lubricating mechanisms [21]. Chalcogenide are known for obtaining their low friction and high wear resistance to sliding surfaces due to their lamellar structure in which strongly bonded atoms form extensive rigid sheets. Unlike dichalcogenides such as MoS_2 or MoSe_2 whose crystal structure creates a monolayer of Mo ions trapped between layers of S or Se ions, monochalcogenides such as GaS or GaSe have a crystal structure composed of a double layer of Ga sandwiched between S or Se ions. Figure 13.14 illustrates a schematic of the layered crystal structure of GaSe molecules.

3.5 Graphite

Another lamellar solid that offers superior friction reduction and wear resistance properties is graphite. A photograph of graphite powder is shown in Fig. 13.1. Graphite occurs naturally from deposits in the earth and can be synthesized by heating petroleum coke to temperatures of 2,973 K beyond that of graphitization, which converts carbon to graphite. Graphite has been used in many industrial applications due to its good lubricity, abundance, low cost, and resistance to both acids and bases. Graphite can be used as a lubricant in a variety of forms such as a powder, bulk, thin film, colloidal dispersion, solid, and composite forms to combat friction and wear. In some applications, it is used as a dispersant in water, solvents, oils, and greases to achieve better lubricity under extreme application conditions

such as lubrication of molds and dies in metal forming; flange on rails; and railcar wheels. Graphite has even found uses as a self-lubricating filler in various metal, ceramic, and polymer matrix composites used in various engines, aircraft components, and seal applications [22–24]. Graphite is one of the softest materials with a relatively poor thermal conductivity but a good electrical conductor. The structure of graphite is sheet-like crystals where carbon atoms are strongly bonded in a plane to form a layer and the layers are weakly held together by van der Waals forces. The layered crystal molecular structure of graphite is shown in Fig. 13.7. In dry air, inert atmospheres, or vacuum, the lubricity of graphite degrades quickly, causing it to be removed from the contacting surfaces. In contrast, the tribological properties of graphite are superior in moist or humid environments. Research has shown that the lubricity of graphite is not solely due to its layered crystal structure, but depends strongly on the quantity of water vapor in the environment. Graphite requires a small amount of condensable vapor to allow the atomic layers to slide with ease thus improving its lubricity. The thermal-oxidative stability of graphite allows it to lubricate in open-air environments where the temperature is below 773 K, however the friction does tend to increase as the temperature rises. Beyond this temperature threshold, graphite begins to rapidly oxidize and lose its lubricity. In vacuum environments, the trends are reversed for graphite. For example, it has an initially higher coefficient of friction of 0.4 at lower temperatures in vacuum, however when the temperature increases, the coefficient of friction decreases. At a maximum temperature of 1,573 K, the coefficient of friction decreases to about 0.2 and beyond this temperature, graphite begins to decompose and lose its lubricity.

3.6 Hexagonal Boron Nitride

A lamellar solid with similar structural and lubricating properties as graphite is hexagonal boron nitride (hBN), also referred to as “white graphite” [25]. A photograph of hBN powder particles is shown in Fig. 13.5 and the layered crystal structure is shown in Fig. 13.9. It can be seen that the molecular structure resembles other lamellar solid lubricants such as graphite. This soft, white, lubricious powder is derived from the reaction of boric oxide or boric acid with urea or ammonia at high temperatures ranging between 1,073 and 1,273 K. There are two crystal structures of boron nitride, cubic and hexagonal. Cubic boron nitride is extremely hard and wear resistant like diamond and is very abrasive. Hexagonal boron nitride, a synthetic inorganic solid lubricant, is a highly refractory and thermochemically stable material that maintains its lubricious qualities at high temperatures with negligible oxidation occurring below 1,273 K. Moreover, hBN is chemically inert and resists attack by molten metals, oxides, glasses, slags, and fused salts. It is environmentally friendly and displays excellent electrical insulating properties, even under vacuum. The lubricating properties of hBN arise from its graphitic-like crystal structure where atomic planes arranged in two-dimensional arrays of

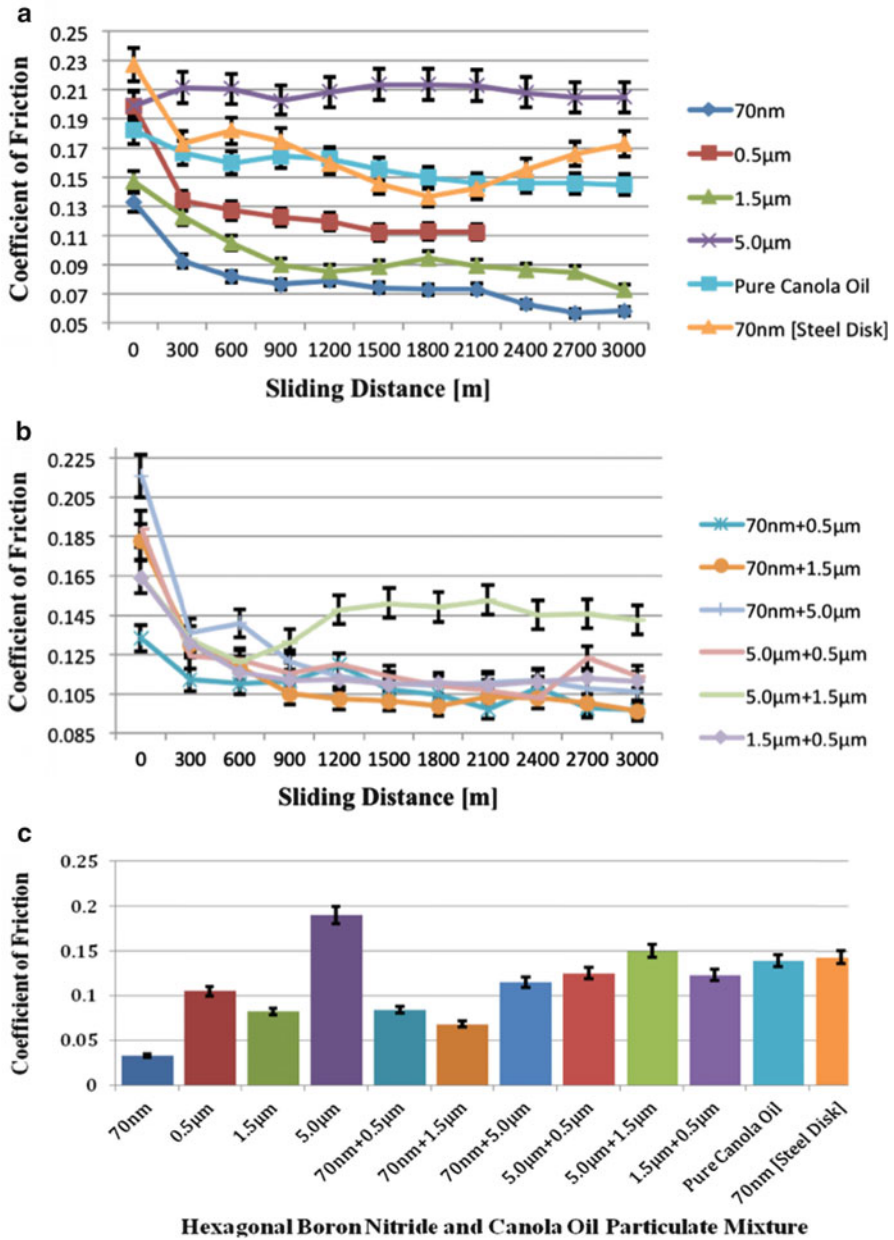


Fig. 13.15 (a) Variation of coefficient of friction with sliding distance for single particle-size particulate mixtures, (b) Variation of coefficient of friction with sliding distance for multiple particle-size particulate mixtures, (c) Coefficient of friction for various particulate mixtures at the end of the experiments

boron and nitrogen atoms, configure in a honeycomb lattice as illustrated in Fig. 13.9. The bonding between atoms in a plane is the strong covalent bond and the bonding between each planar layer is the weak van der Waals bond.

Lubrication applications of hBN include compaction through hot pressing to create dense solid pieces or prepared as a solid polymer composite structure. Hexagonal boron nitride has been used as a dispersed additive to oils and greases to improve antiwear and antifriction properties as well as a self-lubricating coating where it is plasma/thermal-sprayed with ceramics [1, 26–28]. It can be used as metal–ceramic electro-deposition coatings, constituent in epoxy coatings, and has found uses in aqueous and oil dispersions as release agents in metalworking operations. The physical and chemical properties of hBN are similar to graphite, which allows it to function in a variety of similar applications under sliding contact in conditions involving high-load, high-temperature, and extreme pressure [29, 30].

In a recent study, the size effect of hBN particles in canola oil was investigated using a pin-on-disk apparatus [1]. Here, various sizes of hBN particles were combined into colloidal mixtures containing canola oil and 5 % by weight of hBN particles. The sizes investigated were 70 nm and 0.5, 1.5, and 5.0 μm . Figure 13.15a shows the variation of coefficient of friction with sliding distance for the single particle-size particulate mixtures; Fig. 13.15b illustrates the variation of coefficient of friction with sliding distance for multiple particle-size particulate mixtures; and Fig. 13.15c shows the coefficient of friction for all the particulate mixtures at the end of the study. Figure 13.16(a) shows the variation of the pin wear volume with sliding distance for the all the particulate mixtures and Fig. 13.16(b) depicts the variation of pin wear volume for various particulate mixtures at the completion of the test. It was determined that the nanometer-sized particulate mixtures outperformed micron- and submicron-sized particulate mixtures in terms of friction and wear performance, and provided a smoother surface finish to the metallic substrates. Furthermore, the tribological response of canola oil containing micron- and submicron-sized particles was found to be significantly enhanced by the addition of nanometer sized particles, where friction and wear rates were reduced by 40 % and 70 % respectively.

Furthermore, this research study [1] revealed that the tribological performance was influenced by the particle shape. In this study, the larger particles had a plate-shaped geometry and the smaller particles exhibited a spherical geometry. The scanning electron micrographs of the various sized hBN particles are shown in Fig. 13.17. Figure 13.18 demonstrates the size and shape effects that the various hBN particles have on the tribological properties. Larger particles behave more abrasively than smaller particles due to their plate-shaped geometry. Additionally, particles having a size on the same order of magnitude as the initial surface roughness resulted in high stress concentration scenarios (Fig. 13.18), which diminished their tribological performance.

Figures 13.17 and 13.18, illustrate the importance of choosing an appropriately sized solid particle lubricant to enhance the lubricity and minimize wear of the tribo-interface. By optimizing the particle size and by selecting an appropriate carrier fluid, a sustainable lubricant can be developed that has properties that will lower friction and wear, thereby improving system efficiency and ultimately conserving energy.

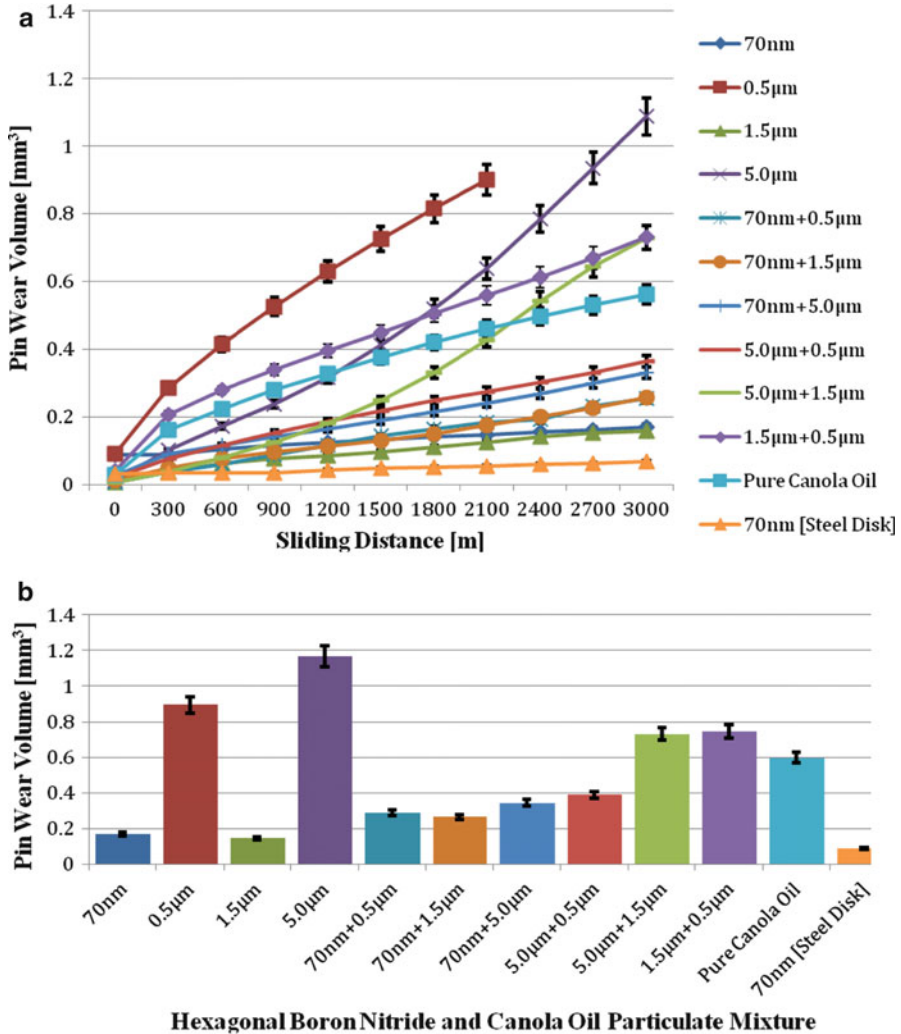


Fig. 13.16 (a) Variation of pin wear volume with sliding distance for particulate mixtures, (b) Variation of pin wear volume for various particulate mixtures at the end of the experiments

3.7 Boric Acid

Boric acid (H_3BO_3) is another lamellar solid lubricant with a layered crystal structure closely related to that of graphite and hBN [31]. Figure 13.6 shows a photograph of boric acid crystals in a powder form and Fig. 13.19 shows scanning electron micrographs of the lamellar structure of the boric acid powder. Boric acid has a triclinic crystal structure and is composed of boron, oxygen, and hydrogen atoms arranged to form atomic layers parallel to the basal plane. Figure 13.10 is an

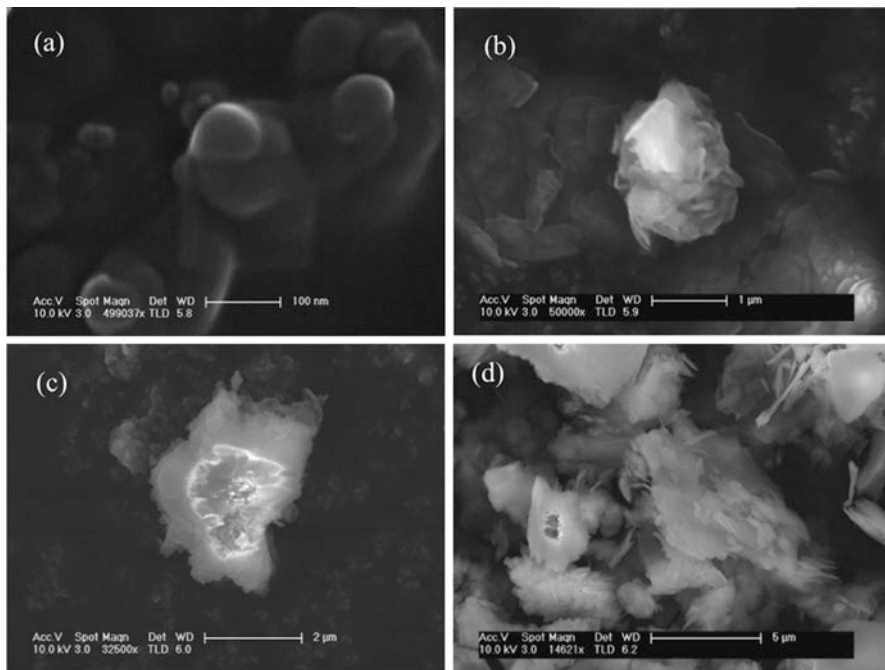


Fig. 13.17 SEM micrographs of hexagonal boron nitride (hBN) particles with size (a) 70 nm, (b) 0.5 μm, (c) 1.5 μm, (d) 5.0 μm

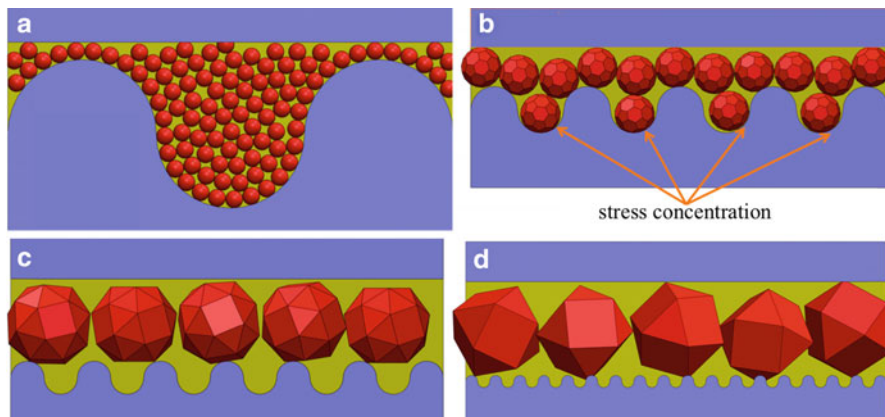


Fig. 13.18 Schematic diagram of boron nitride and canola oil particulate mixtures with size (a) 70 nm, (b) 0.5 μm, (c) 1.5 μm, (d) 5.0 μm at the tribo-interface

Fig. 13.19 SEM micrograph of the lamellar structure of boric acid

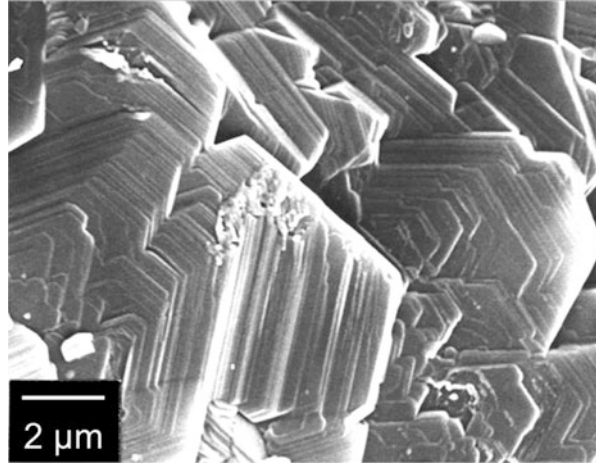


illustration of the layered crystal structure of the boric acid. Atoms on the same plane are closely packed and the bonding between the atoms is of the strong covalent type for boron and oxygen and of the hydrogen type. The weak van der Waals force holds adjacent planes together. The bonding types present in boric acid allow it to dissolve in water and other solvents, making it a useful additive in many lubricants. Two forms of boric acid that exhibit the layered crystal structure are the orthoboric and orthorhombic metaboric acids. The lubricious nature of boric acid arises from its ability to align its plate-like crystals parallel to the direction of relative motion under shear stress [32]. Once aligned, these layers can slide over one another with relative ease, thus providing the low friction and self-lubricating properties similar to that of MoS_2 , graphite, and hBN. The limitation of boric acid is that it decomposes at temperatures over 443 K, turning into B_2O_3 , losing its layered structure, and thus its lubricious nature. At temperatures over 723 K, B_2O_3 begins to melt where it can possibly react with the surfaces of the underlying substrate. If the underlying substrate is metallic, the reactions can be negligible and low friction can be maintained due to viscous-flow lubrication. On the contrary, if the underlying substrate is ceramic, the liquid B_2O_3 produces an oxide film that worsens the tribological properties due to high corrosive wear and high friction. Despite minimal drawbacks, boric acid has found a place in various applications, for example in metal-forming, boric acid films have been shown to bond to metallic surfaces to provide excellent lubricity [33]. Boric acid has also been used as fillers in polymers and dispersed in oils and greases to enhance lubricity, wear resistance, and extreme pressure capabilities [34–36].

An investigation by Lovell et al. studied the size effect of boric acid powder particles used as a performance enhancing additive when mixed with canola oil to form a multifunctional biolubricant [35]. The effect of nano- (20 nm), submicron- (600 nm), and micron-sized (4 μm) boric acid powder additives combined with canola oil in a vortex generator to establish a colloidal mixture were investigated for

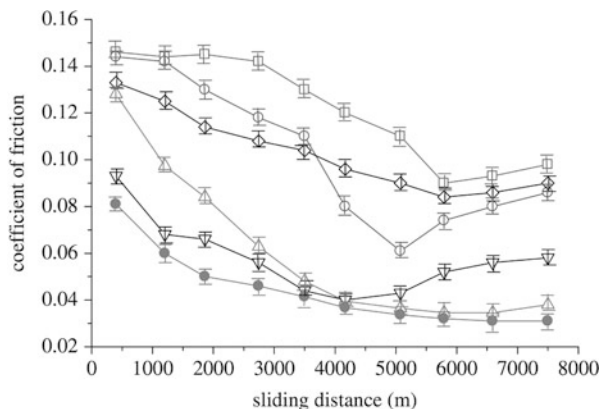


Fig. 13.20 Variation of coefficient of friction with sliding distance for various lubricants (*open square*, boric acid 4 nm; *open circle*, boric acid 600 nm; *open triangle*, boric acid mix (4 nm and 600 nm); *open inverted triangle*, MoS₂ 5 nm; *open diamond*, canola oil; *filled circle*, boric acid 20 nm) [35]

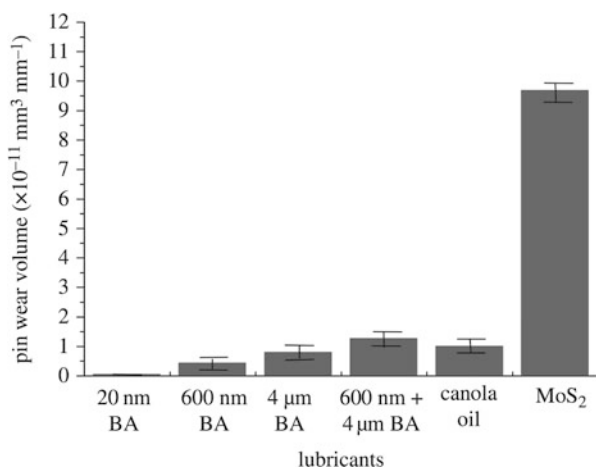


Fig. 13.21 Variation of wear rate of the Cu pins slid against Al disks in the presence of various additives in canola oil-based lubricants at the interface. BA boric acid [35]

their influence on tribological properties. As a basis for comparison, lubricants of pure canola oil and canola oil mixed with MoS₂ powder (ranging from 0.5 to 10 μm) were also prepared. Friction and wear experiments were carried out on the prepared lubricants using a pin-on-disk apparatus under ambient conditions. Figure 13.20 shows the variation of coefficient of friction with sliding distance for lubricants containing various particulate additives. Figure 13.21 shows the variation of wear rate of the Cu pins slid against Al disks in the presence of various sized boric acid additives in canola oil-based lubricants at the interface. Based on the experiments,

the lubricant mixtures containing the nano-sized boric acid particulate additive significantly outperformed all of the other lubricants with respect to friction and wear performance. In this study, the nano-sized boric acid powder-based lubricants exhibited a wear rate more than an order of magnitude lower than the MoS₂ and larger sized boric acid additive-based lubricants. It was also discovered that the oil mixed with a combination of submicron- and micron-sized boric acid powder additives exhibited better friction and wear performance than the canola oil mixed with submicron- or micron-sized boric acid additives alone.

3.8 *Soft Metals*

Soft metals such as silver, gold, platinum, indium, tin, and lead are used as lubricants because of their low shear strength, rapid recovery, and recrystallization properties that allow them to exhibit low friction in sliding contacts [37, 38]. Many soft metals are used in place of typical solid lubricants because they offer properties that are not offered by many solid lubricants such as excellent electrical and thermal conductivity, oxidation resistance, good transfer-film-forming tendency, and relatively high melting point than liquid lubricants. Soft metals traditionally have low hardness values between 1 and 3 in the Mohs hardness scale and coefficients of friction between 0.1 and 0.4 depending on material and testing conditions as shown in Table 13.4. The applications of soft metals are limited by their physical properties; lead (Pb), indium (In), and tin (Sn) have lower friction coefficients than silver (Ag), gold (Au), and platinum (Pt). However, in applications involving high temperatures, lead, indium, and tin tend to oxidize and melt, for this reason silver, gold, and platinum are more commonly used in high temperature applications due to their high melting points and thermal-oxidative stability [39–41].

Soft metals are applied to substrates as thin films through various deposition techniques. During these processes, the film-to-substrate adhesion is important for long-term durability, improved lubricity, and antiwear properties [42, 43]. Electroplating and vacuum evaporation processes can be used to deposit most soft metals on substrates as thin self-lubricating films. However, to obtain high density and strong adherent soft metal films, ion plating, sputtering, and ion-beam-assisted deposition techniques are utilized [44]. The thickness of a deposited soft metal film is critical to friction and wear performance. The optimal thickness of a soft metal film is between 0.5 and 1.0 μm , where the film can maintain a low coefficient of friction and minimize the wear rate under a high contact pressure [38, 45, 46]. If the film is too thin ($<0.5 \mu\text{m}$), it can degrade quickly and become ineffective at lowering friction and minimizing wear. In contrast, a thick film ($>1.0 \mu\text{m}$) exhibits a higher coefficient of friction and wear rate due to an increase in contact area caused by plastic deformation as a result of softening of the film. In some instances, the physical and mechanical properties of soft metals change due to environmental interactions that result in variations in the tribological performance. The coefficient of friction decreases in

most soft metals as the ambient temperature increases due to initial softening of the material and rapid recovery from strain hardening [5]. At very high temperatures, the coefficient of friction increases due to softening of the material causing the material to flow with increased ductility and a larger real area of contact, which results in stronger adhesion between the surfaces. In instances of high frictional or ambient heating, silver and gold are ideal solid lubricants due to their high thermal conductivity, low shear strength, and chemical inertness, resulting in lower adhesion and a lower coefficient of friction when compared to other soft metals. Moreover, when highly thermally conductive films are used such as silver and gold, the wear rate tends to decrease because frictional heat is dissipated rapidly from the sliding interface.

Applications of soft metals consist primarily of dry and oil-lubricated sliding contact conditions where effective dissipation of frictional heating is necessary. Extensive usage of soft metals is limited by their affinity to react with sulfur and chlorine and undergo corrosive wear. Despite this deficiency, soft metals do have their optimal applications. Silver, for instance, is often used to lubricate the high-speed ball bearings of rotating anode X-ray tubes, satellite parts, ball bearings, bolts, and sliding parts in nuclear reactors. Bronze and Babbitt components prepared by alloying soft metals with aluminum, zinc, and copper have been used to lubricate bushings, bearings, and many other mechanical components.

3.9 Polymers

Polymers are a common solid lubricants in tribology because they are lightweight, inexpensive, easy to produce, corrosion resistance, and biocompatible. They are often combined with other solid lubricants to create self-lubricating composite materials that can be used in bulk and thin-film forms as well as binding agents for other solid lubricants [5, 47–49]. Some of the better-known polymers are ultrahigh-molecular-weight polyethylene (UHMWPE), polyimide, nylon, and polytetrafluoroethylene (PTFE). Polymer coatings can be deposited on surfaces by spraying or dusting a powder form on a substrate, then curing it at high temperatures. UHMWPE is a popular polymer for its use in joint replacements, because it has long entangled molecular chains that provide improved wear resistance [50, 51]. Polyimide is a polymer known for having low friction and good thermal stability. It can be combined with self-lubricating inorganic fillers at high temperatures to enhance the mechanical and tribological properties of composite structures [52, 53]. PTFE is the most well known polymer by its trade name Teflon (an E.I. DuPont de Nemours and Company product). PTFE is a “nonstick” surface coating that is commonly used in cookware, seals, and gaskets to facilitate release and separation in applications below 523 K. Less common forms of PTFE are powder, composite, and colloidal dispersion in oils and greases to lower friction [54]. Its coefficient of friction ranges between 0.04 and 0.2 depending on the materials and testing conditions.

4 Lubrication Mechanisms of Layered Solids

The lubrication mechanisms that govern solid lubricants are controlled by intrinsic and extrinsic parameters. There are no solid lubricants that can provide both low friction and wear in all environments. The friction and wear performance of solid lubricants is influenced by inherent properties, environmental parameters, and application usage. Solid lubricants can be used as dry lubricants by themselves in which their physiochemical properties are dominant. They are used as additives in oils and greases where their physical properties prevail and in coatings in which physiochemical reactions and adherence become critical. This section discusses the viability of solid lubricants based on their lubrication mechanisms and the lubricating environment.

Layered solid lubricants include lamellar solids (i.e., graphite, hBN, and H_3BO_3), transition-metal dichalcogenides (i.e., MoS_2 and WS_2), and metal-monochalcogenides (i.e., GaS, GaSe, or SnSe). The lubrication mechanisms of these various solid lubricants are controlled by their affinity for interfilm sliding, intrafilm flow, and interface slip, which are all dependent on the material's interlayer shear properties. As previously discussed in this chapter, all of these solids have layered crystal structures where atoms lying on the same plane are closely packed and strongly bonded through ionic, covalent, or hydrogen bonds and the layers themselves are bonded through weak van der Waals forces. The lubricity, wear resistance, and durability of these solid lubricants are derived from their strong interatomic bonding and packing within each layer that allows for the high in-plane strength. Furthermore, when these lubricants are entrained between two surfaces in relative motion, they are able to align themselves parallel to the relative motion and slide over one another with relative ease providing lubrication. Moreover, many of these layered solids coalesce in surface asperities (see Fig. 13.18), creating a thin smooth transfer film that is able to accommodate the relative sliding velocity and dissipate frictional energy affording longer wear lives and greater performance.

When discussing solid lubricants, layered crystal structure is of interest, because layers can be composed of single or multiple atomic planes. Lubricants with single atomic planes per layer include graphite (Fig. 13.7), hBN (Fig. 13.9), and H_3BO_3 (Fig. 13.10), while transition-metal dichalcogenides consist of three atomic planes per layer such as MoS_2 (Fig. 13.8) and WS_2 ; and metal-monochalcogenides consist of four atomic planes in each layer, for example GaSe (Fig. 13.14). The three atomic planes in the transition-metal dichalcogenides are arranged where the metal atom is sandwiched between the chalcogen atoms in a planar array. For example in MoS_2 , the atoms are arranged as S–Mo–S (Fig. 13.8), similarly, for WS_2 , the planar array is arranged as S–W–S. The monochalcogenides atomic plane array differs slightly from dichalcogenides where the interior is composed of two metal atomic planes sandwiched between the chalcogen atoms. For example, GaSe has the atomic planar sequence of Se–Ga–Ga–Se (Fig. 13.14), likewise SnSe and GaS follow a similar atomic planar sequence of Se–Sn–Sn–Se and S–Ga–Ga–S, respectively.

The lubricity of solid lubricants is controlled by intrinsic properties, such as the layered crystal structure, interlayer distance, electrostatic attraction, and extrinsic parameters such as humidity, temperature, and environment. The intrinsic properties contribute to the tribological performance of solid lubricants because the layered crystal structure allows the solids to shear with minimal resistance. The interlayer distance between layers is also important because as the interlayer distance increases, the ability of the van der Waals force to hold adjacent layers together decreases, thus the shearing resistance between layers weakens enhancing lubricity. For graphite and MoS₂ the interlayer distances are 0.335 nm and 0.296 nm respectively. In humid air, graphite can have a lower friction coefficient than MoS₂; however, in dry and vacuum environments MoS₂ has the lower coefficient of friction [16]. This shows how the lubricity and tribological performance of solid lubricants are largely controlled by extrinsic factors. Electrostatic attraction between layers is another intrinsic parameter that affects the lubricity of solid lubricants. For this reason, when choosing metals and transition metals that could function as possible solid lubricants, one must consider the electrostatic attraction, which significantly reduces the number of potential options. For example, there are many dichalcogenides that have a layered crystal structure such as NbS₂, TiS₂, VS₂, TaS₂, MoS₂, and WS₂. However, based on molecular orbital and valence bond theories, it is speculated that NbS₂, TiS₂, VS₂, and TaS₂, are poor lubricants. The inferior lubricity is a result of these dichalcogenides having a region of negative electrical charge that is concentrated between the chalcogen atoms on a specific layer and in between chalcogen atoms of adjacent layers [55]. This affects the lubricity, because the spaces between atoms are positively charged due to the exposed ion cores surrounding the atoms. As a result, in these solids, there is an electrostatic attraction between layers that strengthens the shear resistance. To the contrary, MoS₂ and WS₂ exhibit superior lubricity because they have a region of negative electrical charge between the chalcogen atoms on a specific layer. Thus, the surfaces of the chalcogen atoms are positively charged, causing an electrostatic repulsion between neighboring layers that lowers the shear resistance and improves the lubricity.

The electronic states of atoms in each layer are important because they can affect the shear resistance of the solid lubricant. Graphite and hBN are similar in that they each have single atomic planes per layer and have similar electronic states. A major difference between the two is the bonding configuration. Graphite's π -bonding and π -antibonding bands overlap weakly at the Brillouin-zone boundary, providing it with good electrical conductivity [16]. In contrast, the hBN's π -bonding and π -antibonding bands are separated by an energy gap of several electron volts, thus causing it to be an insulator. Both graphite and hBN are examples of lamellar solid lubricants where high friction and wear occur if the π attractions between the atomic layers are not eliminated or reduced. Eliminating the π -bond interactions is performed in graphite through intercalation, the process of increasing the interlayer distance by incorporating another atom or molecule such as fluoride, thus creating graphite fluoride. Intercalation can be achieved through the use of alkali metals (known as donor) and metal chlorides (known as acceptor) [56, 57]. As a result of intercalation, the interlayer distance of graphite can expand from 0.335 nm to approximately 0.8 nm, thus decreasing the effectiveness of the weak van der Waals forces and reducing the shear resistance,

thus minimizing friction and enhancing the lubricity [58]. Attempts to perform intercalation to hBN have been unsuccessful.

The dominating factor limiting friction and wear performance of solid lubricants in all environments are the detrimental effects caused by extrinsic factors such as humidity, temperature, and environment. The presence of humidity in the atmosphere plays a large role when selecting a lubricant for a particular application. As previously noted, graphite functions best in humid air, while MoS₂ performs best in dry and vacuum environments. Boric acid and hBN have similar properties to graphite. The presence of water molecules in the atmosphere is speculated to cause a weakening of the π -bonds between layers in hBN and graphite, thus increasing the lubricity. The poor lubricating property of MoS₂ in humid environments is related to the reaction of the water molecules, which alter the interatomic array bonding causing an increase in friction.

Solid lubricants can be applied as dry lubricants or as additives in oils or greases. In either case, the physical mechanisms that control their lubricity and wear resistance are the same. Lamellar solids are able to coalesce in the valleys between asperities on rough or porous sliding surfaces while withstanding extreme contact pressures without being squeezed out of the contacting interface. In these situations, the solid lubricant develops into a thin lubricating transfer film that can protect a surface by accommodating the relative motion by easily shearing and carrying a portion of the asperity contact load, thus decreasing friction and minimizing wear. This physical behavior allows lamellar solids to be used as solid lubricants whether they are in the form of a granular powder, compressed pellet, or colloidal solution.

5 High-Temperature Solid Lubricants

Many of the solid lubricants discussed in this chapter lose their lubricious qualities in open air and at temperatures above 773 K. Furthermore, most sliding metal surfaces and non-oxide ceramic surfaces become oxidized in these high temperature environments [59]. During oxidation, thin oxide films can develop on the sliding surfaces that can affect the friction and wear properties. Multiple oxide films can develop if the two opposing surfaces differ chemically or if there is a third body particulate in the sliding interface. When abrasive wear particles become trapped in the sliding interface, high wear can result. Investigations into the shear rheology of oxide films has focused on the development of lubricious oxides through the use of metal alloys and metallic composite structures that induce low shear strength oxide formation [60].

5.1 Oxides, Fluorides, and Sulfates

At elevated temperatures, various oxides, fluorides, and sulfates can become soft with minimal shear resistance and thus used as a lubricant. These oxide (e.g., Re₂O₇,

MoO₃, PbO, B₂O₃), fluoride (e.g., CaF₂, BaF₂, SrF₂, LiF, and MgF₂), and sulfate (e.g., CaSO₄, BaSO₄, SrSO₄,) solid layers can be deposited as highly lubricious thin films or coatings by plasma vapor, plasma spraying, and fusion bonding deposition techniques to provide lower friction coefficients and promote longer component lifetimes at higher temperatures [61–65]. Solid films can be mixed with themselves (for example in the case of oxides CuO–Re₂O₇, CuO–MoO₃, PbO–B₂O₃, PbO–MoO₃, CoO–MoO₃, Cs₂O–MoO₃, NiO–MoO₃) or with other solid lubricants to broaden the lubricants operable temperature range and durability [66, 67]. The drawbacks of oxide films are their inherently brittle nature and ease of fracture. Additionally, oxide films suffer from thermal instability as their tribological properties, particularly their lubricity, is dependent on temperature. At temperatures below room temperature (296 K) or if frictional heating is negligible, oxide films can develop defectively resulting in thin films that can wear out quickly or result in high shear resistance. Oxide films develop high shear resistance due to lack of heat causing them to solidify thereby retarding their lubricating properties. To remedy these low temperature problems, a zinc oxide film was synthesized by pulsed-laser deposition and has been shown to provide effective lubrication and wear resistance at room temperature due to its stoichiometry and microstructure [68]. Oxide, fluoride, and sulfate lubricants tend to find uses in high temperature seal, bearing, gear, valve, valve seat, variable stator vane, and foil bearing applications. At high temperatures, the oxide layer that forms on alloy surfaces is advantageous and desirable in comparison to traditional solid lubricant coatings, which have finite lifetimes. The extended lifetime of oxide layers is a result by the process where previously formed oxide layers are depleted from a surface due to wear and normal operation. The alloying ingredients within the material diffuse to the surface of the material where the oxygen potential is higher and begin to reoxidize. Thus, the surface is replenished with a new oxide layer that offers low shear strength and surface energy, which play a role in decreasing friction [60, 67].

5.2 Composites

Alternative approaches to combat friction and wear at high temperatures have been investigated through the use of plasma-sprayed composites and adaptive lubricants. Composite coatings consist of a self-lubricating component composed of silver or an alkaline halide such as calcium fluoride (CaF₂) or barium fluoride (BaF₂) and a wear resistant component composed of chrome carbide or oxide [69–72]. Deposited self-lubricating composite coatings can be as thick as 0.2 mm and have a coefficient of friction ranging between 0.2 and 0.5 depending on testing parameters and chemical composition. These composite coatings have demonstrated superior durability and frictional performance in high speed sliding bearing surfaces, such as foil bearing applications [73]. Composite coatings have a broad temperature range, as they are able to lubricate from room temperature to high temperatures due to their adaptive nature allowing them to chemically change with temperature

variations. The ability of these coatings to adapt to their environment thermally is a result of their composition of multiple ingredients. At low temperatures, adaptive composites provide low friction, however, as the temperature increases, their ingredients begin to react with each other and with oxygen to form a new lubricious solid lubricant that provides low friction at high temperatures [74]. The largest concern with such a lubricant is that the reaction is not reversible, thus once oxidation has taken place and the composite has transformed, it cannot provide effective lubrication at low temperatures again. In an attempt to solve this problem, some tribologists have used thin diffusion-barrier layers to limit the extent of oxidation to the surface layers, thus allowing the bulk composite coating material to remain unreacted. An alternate solution utilizes capsules of high temperature adaptive lubricants in a low-temperature matrix. Here, the low temperature matrix can dominate the friction properties at low temperatures, while the capsules provide a protective shell on the surface reacting with the oxygen to produce a high-temperature lubricant.

5.2.1 Self-Lubricating Composite Structures

Self-lubricating composite structures thwart friction and reduce wear in sliding, rolling, and rotating applications. These composites are derived by dispersing self-lubricating solids (known as fillers) in a powder form into a metal, polymer, or ceramic matrix. Powder metallurgy processes are used to mix, compact, and sinter the fillers and matrix materials into functional parts that can be extruded, rolled, or hot/cold-pressed into various forms [16]. These techniques have been available for a long time and are extensively used in industrial applications. In some instances, parts are made to undergo centrifugal processes in which compositional gradients occur within the composite structure. Here, the core can be nearly a pure matrix material to yield high strength, hardness, and durability, while the exterior perimeter is enriched with the self-lubricating powder. In effect, the area where the sliding and relative motion takes place has enhanced lubricity due to the high concentrations of lubricating material on the exterior. Composite structures prepared in this manner are advantageous because of their ability to be used in a wide variety of applications such as bushings, bearings, gears, and traction devices. The increase in performance of self-lubricating composite structures is a result of the formation of a thin transfer layer on the exterior sliding surface caused by the rubbing against a counter material. This transfer layer is continuously replenished by the embedded self-lubricating lubricious powders dispersed in the composite matrix material that enter the area of sliding contact as a result of surface wear and subsurface deformation [22]. In some instances, when self-lubricating composite structures are used with polymers an increase in mechanical strength occurs yielding high wear resistance.

Copper-graphite and silver-graphite used in electrical brushes and contact strips and aluminum-graphite used in bearings, pistons, and cylinder engines are among the many examples of these self-lubricating metal-matrix composite

structures [75, 76]. Investigations into composite structures have revealed that when the filler is mixed at the optimal concentration and particle size, there is a substantial enhancement to the mechanical and tribological properties of the matrix material. This has been shown with graphite, MoS_2 , and boric acid fillers used with a nylon and PTFE-type polymer matrix material where an increase in wear resistance was observed [48, 53]. Moreover, aluminum-graphite composites have been shown to exhibit superior lubricity, durability, and resistance to galling in both lubricated and non-lubricated applications [22]. Transition-metal dichalcogenides such as WS_2 used as fillers have also shown to reduce the effects of galling as well as exhibit excellent lubricity and durability under high-vacuum environments, thus increasing component resistance to seizure and facilitating operation in higher loading conditions.

Self-lubricating polymer–matrix and ceramic–matrix composite structures have successfully exhibited properties that reduce friction, minimize wear, and decrease galling under extreme conditions for use in industrial applications [24, 77]. Alumina–graphite composites have been shown to minimize friction by more than 50 % in comparison to alumina–alumina composites and are being explored for the utilization in sealing applications [78]. Ceramic composites were created by drilling small holes in alumina and silicon nitride ceramics and filling them with NiCl_2 intercalated graphite under high pressure. The silicon nitride composites exhibited substantial friction coefficient reduction in comparison to the alumina composite due to the formation of a graphite-rich transfer film, which cannot be formed in the case of the alumina composite [24]. In more advanced self-lubricating composite structures, mixtures of fillers containing Sb_2O_3 and MoS_2 were shown to greatly improve friction and wear performance. There, the MoS_2 particles on the surface established the thin transfer layer and were influenced by oxidation. The presence of the Sb_2O_3 particles in the composite structure protected the subsurface MoS_2 particles from thermal and environmental degradation. Thus by minimizing the effects of tribo-oxidation the tribological properties can be improved [79].

In a new and expanding field, self-lubricating nanocomposite films and coatings are being developed due to the improvements in the tribological performance brought upon by using physical vapor and chemical vapor deposition techniques. These nanocomposites are based on self-lubricating solids (such as MoS_2 , WS_2 , DLC, graphite, and PTFE) that are deposited onto metal, ceramic, and metal nitride or carbide surfaces (such as Ti, TiN, TiC, Pb, PbO, ZnO, Sb_2O_3) as thin films or multilayered coatings. They have been shown to exhibit improved hardness, wear resistance, lower friction, and resistant to extrinsic parameters such as humidity in the most demanding tribological conditions [80–82]. These composite coatings have been proposed in various milling, drilling, and tapping processes; cold-forming dies and punches; stamping applications; bearings; and gears for aerospace and vacuum applications, among many other dry sliding and machine applications [16, 83, 84]. Furthermore, nanocomposite films have been shown to exhibit adaptive properties where they can provide superior lubrication in oxidizing environments both at room temperature and high temperature. In these

environments the nanocomposite films react with atmospheric oxygen to produce lubricious oxide films that aid in minimizing friction [74, 85–87].

6 Methods of Evaluating Solid Lubricants

Characterizing the tribological properties and evaluating the surface properties are imperative to understanding the success and applicability of solid lubricants and coatings. Many of their properties such as friction, adhesion, bonding, abrasion, erosion, oxidation, corrosion, fatigue, and cracking are all affected by surface properties [2, 3, 5]. Lubrication engineers and tribologists can enhance the performance of solid lubricants by lowering their surface energy, adhesion, and friction, and increasing their resistance to abrasion, erosion, oxidation, corrosion, and cracking. Additionally, improving solid lubricants' compatibility with extraterrestrial environments by having a working knowledge and understanding of deposition techniques of thin films, production methods of multilayered coatings, and modification procedures of surfaces also improves their tribological performance [6, 88, 89]. The multidisciplinary knowledge required to understand the interaction between surfaces and lubricants demands an understanding of physical and chemical characteristics of a material surface and the lubricant. Many of these studies are performed using friction and wear testers and surface analysis tools.

6.1 *Friction and Wear Testers*

Methods of evaluating the tribological properties of solid lubricants are extensive. Many of the methods used in research laboratories, industries, and commercial applications try to replicate the physical contact geometry that the lubricant is going to be operated in by the use of a tribometer. A tribometer is an experimental apparatus used to evaluate wear-life, wear rate, coefficient of friction, and friction force of a lubricant or material pair over a broad set of parameters as well as examine lubricant film adhesion, fluid resistance, heat resistance, and corrosion resistance. Many of the methods to test solid lubricants are designed based on the intended application specifications of the lubricant. However, some of these testing procedures are standardized through the American Society for Testing and Materials (ASTM) International. Due to the wide variation in test results of solid lubricants the Coordinating Research Council (CRC) conducted a round-robin test program to determine a correlation between the most widely accepted tribometers. Their results indicated that there was no correlation between different machines and that little repeatability exists between identical tribotesters (due to the fact that friction is a system property). Table 13.5 is a brief compilation of tribotesters that are frequently used in the tribological characterization of solid lubricants.

Table 13.5 Examples of friction and wear test apparatus for solid lubricants [3]

Name	Specimen
Plain bearing tester	H-11 test shaft, M-2 steel bushing
Friction tester	Metal disk and rider
High temperature, high speed bearing performance apparatus	20 mm rolling contact bearing
Vacuum friction and wear apparatus	Metal disk and rider
Lubricant vacuum environment apparatus	20 mm rolling contact bearing
Modified 4-ball wear machine	½ in. diameter balls
High temperature, high speed rubbing wear apparatus	Rotating washer vs. stationary
Pellet friction machine	Pellet vs. tool steel track
Press-fit tester	Pin and bushing
Lubricant tester model LFW-1	Test block and 1 3/8 in. Timken® bearing outer race
Falex lubricant tester	Cylindrical pin and V-Blocks
Timken tester	Cylindrical cup rotating against a stationary rectangular block
Oscillating tester	Rotating ring vs. stationary blocks
Dry-film lubricant tester	Cylindrical pin and V-blocks
Sliding friction test apparatus	Cylindrical sleeve slider sliding on a cylindrical rod
Bearing test apparatus	20 mm rolling contact bearing
Fretting corrosion apparatus	Steel flat vibrating against steel flat
High temperature bearing radial and thrust rig	20 mm rolling contact bearing
Modified lubricant tester	Rotating ring vs. rectangular block
Modified Falex tester	Rotating ring vs. stationary V-blocks
Crossed cylinders friction apparatus	Vertical cylinder-carbon tool steel, horizontal cylinder-solid section
Model A-3 friction and wear tester	Timken test cup T-54148 and AISI-4130 steel blocks
Stick–slip slow-speed friction apparatus	½ in. diameter ball vs. flat block
Rolling and sliding contact specimen test machine	Ball and plate
A-6 friction and wear tester	Rotating ring vs. rectangular blocks
Galling machine	Flat plate vs. test cup

6.2 Surface Characterization

Surface analysis techniques are becoming more prevalent and necessary in the characterization process of solid lubricants. There are a number of ways to perform a surface analysis of any solid lubricant, thin film, or coating [90, 91]. Table 13.6, lists many of these surface analysis techniques that are being incorporated in scientific, industrial, and commercial fields [2, 7, 92–100]. Of these techniques, the most widely used for examining solid lubricants, thin films and coatings are optical microscopes, scanning electron microscopy, energy-dispersive X-ray spectroscopy, Fourier transform infrared spectroscopy, surface profilometry, X-ray

Table 13.6 Surface analysis techniques [2]

Technique	Main information	Use (popularity)
Light microscopy	Defects image and morphology	Extensive
Scanning electron microscopy (SEM)	Defects image and morphology	Extensive
Scanning tunneling microscopy (STM) and atomic force microscopy (AFM)	Structure defects image and morphology	Medium
Transmission electron microscopy (TEM)	Phase structure defects image and morphology	Medium
Energy-dispersive X-ray spectroscopy (EDS)	Element composition image	Medium
Electron energy-loss spectroscopy (EELS)	Element composition chemical state image	Not common
Cathodoluminescence (CL)	Element composition defects	Not common
Electron probe X-ray microanalysis (EPMA)	Element composition image	Medium
X-ray diffraction (XRD)	Phase structure defects	Extensive
Low-energy electron diffraction (LEED)	Structure defects	Medium
Reflection high-energy electron diffraction (RHEED)	Structure defects	Medium
X-ray photoelectron spectroscopy (XPS)	Element composition chemical state image	Extensive
Auger electron spectroscopy (AES)	Element composition chemical state image	Extensive
X-ray fluorescence (XRF)	Element composition	Extensive
Photoluminescence (PL), or fluorescence spectrometry	Chemical state defects image	Medium
Variable-angle spectroscopic ellipsometry (VASE)	Film thickness	Not common
Fourier transform infrared spectroscopy (FTIR) chemical state defects	Chemical state defects	Extensive
Raman spectroscopy	Chemical state defects	Medium
Solid-state nuclear magnetic resonance (NMR)	Chemical state phase structure	Not common
Rutherford backscattering spectrometry (RBS)	Element composition structure defects	Medium
Elastic recoil spectroscopy (ERS)	Hydrogen content	Not common
Ion-scattering spectroscopy (ISS)	Element composition	Not common
Secondary ion mass spectrometry (SIMS)	Element composition chemical state image	Extensive
Mass spectrometries Sputtered neutral (SNMS) Laser ionization (LIMS) Spark source (SSMS) Glow discharge (GDMS) Inductively coupled plasma (ICPMS)	Element composition chemical state	Extensive to medium
Profilometers Stylus profiler Optical profiler	Surface roughness image	Extensive
Adsorption	Surface areas chemisorption	Medium

diffraction, Auger electron spectroscopy, ellipsometry, scanning probe microscopy, transmission electron microscopy, thermogravimetric analysis (TGA), X-ray photoelectron spectroscopy, confocal microscopy, and secondary ion mass spectroscopy. As industrial applications become more complex, the need to properly verify the surface preparation, coating, or treatment process will become imperative for understanding the performance of a solid lubricant. In many applications, these procedures are vital for identifying surface contaminants that can be detrimental to the performance of a solid lubricant or coatings. For this reason, it is imperative to select the correct surface analysis tool to gain the appropriate information for a particular application. The selection process depends on specific criteria such as specimen size, sampling area, sampling depth, spatial resolution, and detection sensitivity as well as quantitative or qualitative data acquired through destructive or nondestructive analysis [7]. Although there is no single tool that can provide a complete analysis, it is becoming more common to utilize a variety of tools to assess the performance of a lubricant.

7 Conclusion

The technology of solid lubricants has advanced rapidly over the last seven decades, primarily to meet the demands of the industrial and aerospace industries. Solid lubricants are used in environments that are beyond the tolerable domain of conventional petroleum-based and synthetic lubricants where temperatures and pressures are extremely high or low. In these environments, solid lubricants thrive, due to their resistance to many of the environmental issues that would ordinarily render an oil or grease type lubricant ineffective. Solid lubricants generally consist of materials with low shear strength and high wear resistance. When solid lubricants enter the gap between interacting surfaces in relative motion, they achieve lubrication by accommodating the relative surface velocities by easily shearing; coalesce in the surface asperities; carry a portion of the asperity contact load; and form a protective transfer layer. Solid lubricants can be applied as dispersants in oils and greases, as loose powders, or as coatings where they establish thin protective films on surfaces reducing friction and wear thus preventing unwarranted damage to the lubricating surfaces. As tribosystems continue to advance, the use of solid lubrication is expected to increase in the near future to meet the demands of these future systems. Although solid lubricants meet many of the necessary demands of a traditional lubricant, there is no one solid lubricant that provides both low friction and high wear resistance over a broad set of environments. Solid lubricants are severely influenced by intrinsic and extrinsic parameters and are used in a wide variety of lubricant application. When solid lubricants are used as coating or thin films, their performance is related to the thickness of the film and adherence of the film to the surface. This makes the study of deposition techniques critical for adequate usage of solid lubricant thin films. As technology evolves and industrial applications become more advanced, having a

multidisciplinary approach to understanding the physical and chemical interactions that affect the tribological performance of solid lubricants will become increasingly more important. Additionally, the use of surface analysis tools will aid in the successful utilization of solid lubricants in the future.

References

1. Reeves CJ, Menezes PL, Jen T-C, Lovell MR (2012) Evaluating the tribological performance of green liquid lubricants and powder additive based green liquid lubricants. Proceedings 2012 STLE annual meeting & exhibition, STLE
2. Miyoshi K (2001) Solid lubrication fundamentals and applications. Marcel Dekker, New York
3. Campbell ME, Loser JB, Sneegas E, Midwest Research, I (1966) Solid lubricants. National Aeronautics and Space Administration; for sale by the Superintendent of Documents, U.S. Govt. Print. Off., Washington, DC
4. Dowson D (1978) History of tribology. Longman, London; New York
5. Booser ER (1984) CRC handbook of lubrication. Theory and practice of tribology: volume II: theory and design. CRC, Boca Raton, FL, USA
6. Lince JR, Fleischauer PD (1997) Solid lubrication for spacecraft mechanisms. Defense Technical Information Center, Ft. Belvoir
7. Miyoshi K (2007) "Solid lubricants and coatings for extreme environments: state-of-the-art survey," Program (January)
8. Lockheed M, Space C, Goetzel CG, Rittenhouse JB, Singletary JB (1965) Space materials handbook. Addison-Wesley, Reading, MA
9. Meade FS, Murphy GP Jr (1962) Dry lubricants and corrosion. Rock Island Arsenal, IL
10. Martin JM, Pascal H, Donnet C, Le Mogne T (1994) Superlubricity of MoS₂: crystal orientation mechanisms. Surf Coat Technol 68/69(COM):427
11. Donnet C (1993) Superlow friction of oxygen-free MoS₂ coatings in ultrahigh vacuum. Surf Coat Technol 62(1-3):406-411
12. Donnet C, Erdemir A (2004) Solid lubricant coatings: recent developments and future trends. Tribol Lett 17:389-397
13. Bhattacharyya S, Schwartzbart H, Iit Research Inst, C (1969) Wear and friction of fiber-metal molybdenum bodies impregnated with molybdenum disulfide. Am Soc Metals Trans Quart 62:318-323
14. Bhushan B (2001) Modern tribology handbook. CRC, Boca Raton, FL
15. Scharf TW, Rajendran A, Banerjee R, Sequeda F (2009) Growth, structure and friction behavior of titanium doped tungsten disulphide (Ti-WS₂) nanocomposite thin films. Thin Solid Films 517:5666-5675
16. Bhushan B (2001) Modern tribology handbook. CRC, Boca Raton, FL
17. Peterson MB, Johnson RL, United States National Advisory Committee for Aeronautics (1953) Friction and wear investigation of molybdenum disulfide. 1 - Effect of moisture. National Advisory Committee for Aeronautics, Washington, DC
18. Fusaro RL, United States National Aeronautics and Space Administration, Scientific and Technical Information Office (1978) Lubrication and failure mechanisms of molybdenum disulfide films. National Aeronautics and Space Administration, Scientific and Technical Information Office; For sale by the National Technical Information Service, Washington, DC; Springfield, VA
19. Shankara A, Menezes P, Simha K, Kailas S (2008) Study of solid lubrication with MoS₂ coating in the presence of additives using reciprocating ball-on-flat scratch tester. Sadhana 33(3):207-220

20. Phillips J (1969) Excitonic instabilities and bond theory of III-VI sandwich semiconductors. *Phys Rev* 188(3):1225–1228
21. Erdemir A, Argonne National Lab, IL (1993) Crystal chemistry and self-lubricating properties of monochalcogenides gallium selenide and tin selenide. American Society of Mechanical Engineers/Society of Tribologists, and Lubrication Engineers joint tribology conference, N. O. L. A. O., 1993, United States
22. Rohatgi PK, Ray S, Liu Y (1992) Tribological properties of metal matrix-graphite particle composites. *Int Mater Rev* 37(3):129–149
23. Prasad SV, McConnell BD (1991) Tribology of aluminum metal-matrix composites. Lubrication by graphite. Proceedings of international conference on wear of materials, 7–11 Apr 1991, ASME, pp 149–157
24. Gangopadhyay A, Jahanmir S (1991) Friction and wear characteristics of silicon nitride-graphite and alumina-graphite composites. *Tribol Trans* 34(2):257–265
25. Rabinowicz E, Imai M (1964) Frictional properties of pyrolytic boron nitride and graphite. *Wear* 7(3):298–300
26. Denton RM, Fang Z (1995) Rock bit grease composition, U.S. Pat. No. 5589443
27. Kimura Y, Wakabayashi T, Okada K, Wada T, Nishikawa H (1999) Boron nitride as a lubricant additive. *Wear* 232(2):199–206
28. Menezes PL, Lovell MR, Kabir MA, Higgs CF III, Rohatgi PK (2012) Green lubricants: role of additive size. In: Nosonovsky M, Bhushan B (eds) *Green tribology*. Springer, Berlin; Heidelberg, pp 265–286
29. Funatani K, Kurosawa K (1994) Composite coatings improve engines. *Adv Mater Process* 146(6):27–34
30. Westergard R, Ahlin A, Axen N, Hogmark S (1998) Sliding wear and friction of Si 3N - 4SiC-based ceramic composites containing hexagonal boron nitride. *J Eng Tribol* 212(J5):381–387
31. Erdemir A, Argonne National Lab, IL (1990) Tribological properties of boric acid and boric acid forming surfaces: Part I, Crystal chemistry and self-lubricating mechanism of boric acid. Conference: 45. Annual meeting of the Society of, T., and Lubrication Engineers, D. C. O. M., 1990, United States
32. Erdemir A, Fenske GR, Nichols FA, Erck RA, Busch DE, Argonne National Lab, IL (1990) Self-lubricating boric acid films for tribological applications. Japan international tribology conference, N. O. N., United States.
33. Erdemir A, Bindal C (1996) Formation and self-lubricating mechanisms of boric acid on borided steel surfaces. *Surf Coat Technol* 76–77:443
34. Erdemir A (1995) Lubrication from mixture of boric acid with oils and greases. U.S. Pat. No. 5431830A
35. Lovell MR, Menezes PL, Kabir MA, Higgs CF III (2010) Influence of boric acid additive size on green lubricant performance. *Phil Trans R Soc A Math Phys Eng Sci* 368(1929):4851–4868
36. Deshmukh P, Lovell M, Sawyer WG, Mobley A (2006) On the friction and wear performance of boric acid lubricant combinations in extended duration operations. *Wear* 260(11–12):1295–1304
37. Wells A, De Wet DJ (1988) The use of platinum in thin tribological coatings. *Wear* 127(3):269–281
38. Sherbiny MA, Halling J (1977) Friction and wear of ion-plated soft metallic films. *Wear* 45(2):211–220
39. Erdemir A, Erck RA (1996) Effect of niobium interlayer on high-temperature sliding friction and wear of silver films on alumina. *Tribol Lett* 2(1)
40. Maillat M, Chattopadhyay AK, Hintermann HE (1993) Preparation of silver coatings to obtain low friction in alternating sliding at 570C. *Surf Coat Technol* 61(1–3):25–29
41. Seki K, Suzuki M, Nishimura M (1995) Performance of ball bearings operated at temperatures up to 500C in vacuum. *Lubr Eng* 51(9):753–763

42. Spalvins T, Sliney HE, United States National Aeronautics and Space Administration (1994) Frictional behavior and adhesion of Ag and Au films applied to aluminum oxide by oxygen-ion assisted screen case ion plating (SCIP). National Aeronautics and Space Administration, Washington, DC
43. Spalvins T, United States Aeronautics and Space Administration, Lewis Research Center (1998) The improvement of ion plated Ag and Au film adherence to Si and SiC surfaces for increased tribological performance. National Aeronautics and Space Administration, Lewis Research Center, Cleveland, OH
44. Erdemir A, Fenske GR, Erck RA, Cheng CC, Argonne National Lab, IL (1989) Ion-assisted deposition of silver films on ceramics for friction and wear control. Conference: 44. Annual Stle meeting, A. G. A. U. S. A. M., United States.
45. Dayson C (1971) The friction of very thin solid film lubricants on surfaces of finite roughness. *ASLE Trans* 14(2):105–115
46. El-Sherbiny M, Salem F (1986) Tribological properties of PVD silver films. *ASLE Trans* 29(2):223–228
47. Fusaro RL (1988) Evaluation of several polymer materials for use as solid lubricants in space. *Tribol Trans* 31(2):174–181
48. Fusaro RL, United States National Aeronautics and Space Administration (1990) Self-lubricating polymer composites and polymer transfer film lubrication for space applications, NASA; for sale by the National Technical Information Service, Washington, DC; Springfield, VA
49. Booser ER, American Society of Lubrication Engineers, Society of Tribologists, Lubrication Engineers (1983) CRC handbook of lubrication: theory and practice of tribology. CRC, Boca Raton, FL
50. Kurtz SM, Muratoglu OK, Evans M, Edidin AA (1999) Advances in the processing, sterilization, and crosslinking of ultra-high molecular weight polyethylene for total joint arthroplasty. *Biomaterials* 20(18):1659–1688
51. Wang A, Sun DC, Stark C, Dumbleton JH (1995) Wear mechanisms of UHMWPE in total joint replacements. *Wear Usure Verschleiss* 181/183(1):241
52. Fusaro RL, Sliney HE (1973) Lubricating characteristics of polyimide bonded graphite fluoride and polyimide thin films. *ASLE Trans* 16(3):189–196
53. Blanchet TA, Kennedy FE (1992) Sliding wear mechanism of polytetrafluoroethylene (PTFE) and PTFE composites. *Wear* 153(1):229–243
54. Willson B (1992) PTFE as a friction modifier in engine oil. *Ind Lubr Tribol* 44(2):3–5
55. Clauss FJ (1972) Solid lubricants and self-lubricating solids. Academic, New York
56. LÈvy F (1979) Intercalated layered materials. Reidel, Dordrecht, Holland; Boston
57. Dresselhaus MS (1986) Intercalation in layered materials. Plenum Press, New York
58. Fusaro RL, Sliney HE (1970) Graphite fluoride (CF_x)_nA new solid lubricant. *ASLE Trans* 13(1):56–65
59. Quinn TFJ, Winer WO (1985) The thermal aspects of oxidational wear. *Wear* 102(1–2):67–80
60. Peterson MB, Li S, Murray SF (1997) Wear-resisting oxide films for 900 °C. *J Mater Sci Technol* 13(2):99–106
61. Ling FF (1985) Fundamentals of high temperature friction and wear with emphasis on solid lubrication for heat engines. Industrial Tribology Institute, Troy, NY
62. Kanakia MD, Peterson MB, Southwest Research Institute, San Antonio, TX, Belvoir Fuels, Lubricants Research F (1987) Literature review of solid lubrication mechanisms. Defense Technical Information Center, Ft. Belvoir
63. Sliney H, Strom T, Allen G (1965) Fluoride solid lubricants for extreme temperatures and corrosive environments. *Tribol Trans* 8(4):307–322
64. Sliney HE (1969) Rare earth fluorides and oxides: an exploratory study of their use as solid lubricants at temperatures to 1800°F (1000 °C). National Aeronautics and Space Administration, Washington, D.C

65. John PJ, Zabinski JS (1999) Sulfate based coatings for use as high temperature lubricants. *Tribol Lett* 7(1):31–37
66. Peterson MB, Murray SF, Florek JJ (1959) Consideration of lubricants for temperatures above 1000 F. *Tribol Trans* 2(2):225–234
67. Petterson MB, Calabrese SJ, Stupp B (1982) Lubrication with naturally occurring double oxide films. Defense Technical Information Center, Ft. Belvoir
68. Zabinski JS, Corneille J, Prasad SV, McDevitt NT, Bultman JB (1997) Lubricious zinc oxide films: synthesis, characterization and tribological behaviour. *J Mater Sci* 32(20):5313
69. DellaCorte C, Sliney H, Lewis Research Center (1989) Tribological properties of PM212 a high-temperature, self-lubricating, powder metallurgy composite. Lewis Research Center, Cleveland, OH
70. Dellacorte C, Sliney HE, Nasa LRCCOH (1987) Composition optimization of self-lubricating chromium-carbide-based composite coatings for use to 760 C. *ASLE Trans* 30:77–83
71. DellaCorte C, Fellenstein JA, United States National Aeronautics and Space Administration (1996) The effect of compositional tailoring on the thermal expansion and tribological properties of PS300 a solid lubricant composite coating. National Aeronautics and Space Administration, National Technical Information Service, distributor, Washington, DC; Springfield, VA
72. A. S. M. H. Committee, A. S. M. I. H. Committee (1978) *Metals handbook*. American Society for Metals, Metals Park, OH
73. DellaCorte C, Lewis Research Center (1998) The evaluation of a modified chrome oxide based high temperature solid lubricant - coating for foil gas bearing. National Aeronautics and Space Administration, Lewis Research Center; National Technical Information Service, distributor, Cleveland, OH; Springfield, VA
74. Zabinski JS, Donley MS, Dyhouse VJ, McDevitt NT (1992) Chemical and tribological characterization of PbOMoS₂ films grown by pulsed laser deposition. *Thin Solid Films* 214(2):156–163
75. Kumar R, Sudarshan TS (1996) Self-lubricating composites: graphite-copper. *Mater Technol* 11(5):191–194
76. Basu B, Kalin M (2011) *Tribology of ceramics and composites a materials science perspective*. Wiley, Hoboken, NJ
77. Friedrich K, Lu Z, Hager AM (1995) Recent advances in polymer composites' tribology. *Wear Usure Verschleiss* 190(2):139
78. Yu C-Y, Kellet BJ (1996) Tribology of alumina-graphite composites. *Ceramic Eng Sci Proc* 17(3):220
79. Zabinski JS, Donley MS, McDevitt NT (1993) Mechanistic study of the synergism between Sb₂O₃ and MoS₂ lubricant systems using Raman spectroscopy. *Wear* 165(1):103–108
80. Moonir-Vaghefi SM, Saatchi A, Hedjazi J (1997) Tribological behaviour of electroless Ni-P-MoS₂ composite coatings. *Zeitschrift fur Metallkunde* 88(6):498–501
81. Voevodin AA, Bultman J, Zabinski JS (1998) Investigation into three-dimensional laser processing of tribological coatings. *Surf Coat Technol* 107(1):12–19
82. Simmonds MC, Savan A, Van Swygenhoven H, Pflueger E, Mikhailov S (1998) Structural, morphological, chemical and tribological investigations of sputter deposited MoS_x/metal multilayer coatings. *Surf Coat Technol* 108/109(1/3):340–344
83. Gilmore R, Baker MA, Gibson PN, Gissler W, Stoiber M, Losbichler P, Mitterer C (1998) Low-friction TiN - MoS₂ coatings produced by dc magnetron co-deposition. *Surf Coat Technol* 108/109(1/3):345–351
84. Gilmore R, Baker MA, Gibson PN, Gissler W (1998) Preparation and characterisation of low-friction TiB₂-based coatings by incorporation of C or MoS₂. *Surf Coat Technol* 105(1–2):45
85. Walck SD, Zabinski JS, McDevitt NT, Bultman JE (1997) Characterization of air-annealed, pulsed laser deposited ZnO-WS₂ solid film lubricants by transmission electron microscopy. *Thin Solid Films* 305(1–2):130

86. Wahl KJ, Dunn DN, Singer IL (1999) Wear behavior of Pb-Mo-S solid lubricating coatings. *Wear Usure Verschleiss* 230(2):175
87. Walck SD, Donley MS, Zabinski JS, Dyhouse VJ (1994) Characterization of pulsed laser deposited PbO/MoS₂ by transmission electron microscopy. *J Mater Res* 9(01):236–245
88. United States Congress, Office of Technology Assessment (1991) Exploring the moon and mars: choices for the nation. Congress of the U.S., Office of Technology Assessment: For sale by the Supt. of Docs., U.S. G.P.O, Washington, DC
89. Space Mechanisms Technology Workshop (2002) Space Mechanisms Technology Workshop. National Aeronautics and Space Administration, Glenn Research Center, Cleveland, OH
90. Miyoshi K, Center, N. G. R (2002) Surface characterization techniques an overview. National Aeronautics and Space Administration, Glenn Research Center; Available from NASA Center for Aerospace Information, Cleveland, OH; Hanover, MD
91. Miyoshi K, Center, N. G. R (2002) Surface analysis and tools. National Aeronautics and Space Administration, Glenn Research Center; Available from NASA Center for AeroSpace Information, Cleveland, OH; Hanover MD
92. DS, Otto FV (1970) Glossary of terms and definitions in the field of friction, wear and lubrication (Tribology) *Wear* 15(6):456
93. Great Britain (1966) Lubrication (tribology), education and research; a report on the present position and industry's needs. H.M. Stationery Off, London
94. Czichos H (1978) Tribology a systems approach to the science and technology of friction, lubrication, and wear. Elsevier; distributors for the U.S. and Canada, Amsterdam, North Holland; New York
95. Peterson MB, Winer WO (1980) Wear control handbook. American Society of Mechanical Engineers, New York, NY (345 East 47th St., New York, N.Y. 10017)
96. Devine MJ (1970) Proceedings of a workshop on wear control to achieve product durability. Analytical Rework/Service Life Project Office, Naval Air Development Center, Warminster, PA
97. United States National Bureau of S, Bennett LH, Battelle Memorial Institute, Columbus, L (1978) Economic effects of metallic corrosion in the United States: a report to the Congress. The Bureau: For sale by the Supt. of Docs, U.S. Govt. Print. Off, Washington, DC
98. United States Congress Office of Technology Assessment (1979) Technical options for conservation of metals: case studies of selected metals and products. Congress of the U.S., Office of Technology Assessment: for sale by the Supt. of Doc. U.S. Govt. Print. Off, Washington, DC
99. Jost HP (1990) Tribology origin and future. *Wear* 136(1):1–17
100. Pinkus O, Wilcock DF (1977) Strategy for energy conservation through tribology. American Society of Mechanical Engineers, New York

Exercises

1. What is a lamellar solid lubricant? Give an example and explain its lubrication mechanism.
2. Why are oxides, fluorides, and sulfates important? When are they applicable lubricants?
3. List five methods of surface analysis.
4. What are the subcategories when classifying solid lubricants as lubricating films and by physiochemical properties?
5. List five environments that solid lubricants thrive in and possible applications.
6. Explain the evolution of lubricants and why we began utilizing solid lubricants.

7. What are five apparatuses for evaluating the friction and wear of a solid lubricant?
8. Give three examples of a transition-metal dichalcogenides, metal-monochalcogenides, and a soft metal lubricant.
9. Provide examples of intrinsic and extrinsic parameters that affect the lubricity of solid lubricants.
10. Explain how self-lubricating composite structure function.
11. Explain how solid lubricant composites function.

Answers

1. A lamellar solid lubricant is a layered solid lubricant where the atoms on a single layer are held together via covalent, ionic, or hydrogen bonds and the layers are held together by the weak van der Waals force. Examples of lamellar solids are graphite, hexagonal boron nitride, boric acid, molybdenum disulfide, and tungsten disulfide. These lubricants function by coalescing within surface asperities, accommodating relative velocities, and establishing a thin monolayer that protects the surfaces with high lubricity.
2. At elevated temperatures, oxides, fluorides, and sulfates can act as high temperature solid lubricants. They function by softening at high temperatures that result in a lubricant with minimal shear resistance. Examples of oxide are Re_2O_7 , MoO_3 , PbO , and B_2O_3 ; examples of fluoride are CaF_2 , BaF_2 , SrF_2 , LiF , and MgF_2 ; and examples of sulfates are CaSO_4 , BaSO_4 , and SrSO_4 .
3. (1) Optical microscopes, (2) scanning electron microscopy, (3) energy-dispersive X-ray spectroscopy, (4) Fourier transform infrared spectroscopy, and (5) surface profilometry.
4. Solid lubricants are classified in two types by quantifying them as lubricating films and by physiochemical properties. When describing solid lubricants by lubricating films they are classified as three categories: solid films, fluid films, and thin films. When quantifying solid lubricants through their physiochemical properties, they are categorized based on chemistry, crystal structure, and lubricity.
5. (1) High vacuums environments with applications in satellites, space antennas, semiconductor manufacturing, or X-ray tubes. (2) High temperatures environments with applications in space vehicles, furnaces, and nuclear reactors. (3) Cryogenic temperature environments with applications such as space propulsion systems, turbo pumps, and liquid propane pumps. (4) Radiation environments with applications such as Lunar and Martian base stations, nuclear reactors and satellites. (5) Corrosive environments with applications such as maneuvering systems, semiconductor manufacturing, and all-purpose equipment.
6. Lubricants came into existence with animal fats and oils and were soon replaced with petroleum-based oils during the industrial revolution. Since the development of the aerospace industry, solid lubricants have been developed because many applications were requiring lubricants to operate in

environments that were beyond the tolerable domain of many petroleum-based lubricants. Currently, solid lubricants are becoming more prevalent as they are beginning to find uses in many more terrestrial applications such as additives to conventional automotive lubricants and gear oils.

7. (1) Plain Bearing Tester, (2) 4-Ball Wear Machine, (3) Pellet Friction Machine, (4) Dry-Film Lubricant tester, (5) Vacuum Friction and Wear Apparatus.
8. Transition-metal dichalcogenides: MoS₂, WS₂, and hBN
Metal-monochalcogenides: GaS, GaSe, and SnSe
Soft metals: Ag, Pb, and Au
9. The lubricity of solid lubricants is controlled by intrinsic properties such as the layered crystal structure, interlayer distance, electrostatic attraction, and extrinsic parameters such as humidity, temperature, and environment. These properties contribute to the tribological performance of solid lubricants because the layered crystal structure allows the solids to shear with minimal resistance, thus establishing their high lubricity.
10. Self-lubricating composite structures function by having solid lubricant powders known as fillers dispersed into a metal, polymer, or ceramic matrix allowing them to have superior lubricity and antiwear properties. The increase in performance of self-lubricating composite structures is a result of the formation of a thin transfer layer on the exterior sliding surface caused by rubbing against a counter material. This transfer layer is continuously replenished by the embedded self-lubricating lubricious powders dispersed in the composite matrix material that enter the area of sliding contact as a result of surface wear and subsurface deformation. In some instances, when self-lubricating composite structures are used with polymers an increase in mechanical strength occurs yielding high wear resistance.
11. Conventional composites consist of a self-lubricating component composed of silver or an alkaline halide such as calcium fluoride or barium fluoride and a wear-resistant component composed of chrome carbide or oxide. Composite coatings have a broad temperature range, where they are able to lubricate from room temperature to very high temperatures. The ability of these coatings to adapt and continually provide low friction despite a change in temperature environment is a result of their composition of multiple ingredients. At low temperatures, adaptive composites provide low friction and at high temperatures, their ingredients begin to react with each other and with oxygen in the atmosphere to form a new lubricious solid lubricant that provides low friction at high temperatures.

Chapter 14

Tribology of Green Lubricants

Jagadeesh K. Mannekote, Pradeep L. Menezes, Satish V. Kailas,
and Sathwik Chatra K.R.

Abstract Increased demand to protect the environment from mineral oil based lubricants has necessitated replacing them with products derived from natural resources. In addition to this a combination of environmental, health, and economic challenges has also renewed interest in the development and use of green lubricants over the last two decades. This chapter gives an overview of green lubricants beginning from their ancient use to the challenges prospective of the lubricant industry. The review includes structural and chemical properties of important vegetable oils and chemical modification of vegetable oils. Tribological behavior of products based on vegetable oils, green additives, and ionic liquids under varied testing conditions is also presented. This study also gives an insight into the testing procedures and sustainability aspects of green lubricants and additives.

1 Introduction

The phenomenon of friction has been observed since early civilization. Friction is a primary cause of energy loss. Considerable savings can be made by better understanding of the phenomenon. The use of natural products to reduce friction dates back to antiquity. The histories of Herodotus and Pliny indicate the use of oils for many applications such as hubs on wheels, axles, and bearings in addition to non-tribological applications. The artifacts and weaponries of early civilizations of Mesopotamia, Egypt, Greek, and Roman indicate the use of lubricants. The earliest evidence is available in the art decorations on the inner wall of the Egyptian

J.K. Mannekote • S.V. Kailas (✉) • S.C. K.R.
Department of Mechanical Engineering, Indian Institute of Science,
Bangalore, Karnataka 560012, India
e-mail: satvk@mecheng.iisc.ernet.in

P.L. Menezes
Department of Industrial Engineering, University of Wisconsin-Milwaukee,
Milwaukee, WI 53211, USA

tomb of Tehuti-Hetup (ca. 1650 B.C.) indicating the use of olive oil on wooden planks to facilitate the sliding of building materials, in addition to the evidence of ancient inscriptions dating back to 1400 B.C. demonstrating the use of lubrication with animal fats to reduce friction on chariot wheel axles [1–3].

Use of tallow oil was a common practice during Leonardo da Vinci's time as illustrated in one of his designs for an internal grinding machine. Extensive use of plain bearing of iron, steel, brass, and bronze during the renaissance clearly indicates the use of animal or plant based lubricants during that time [4]. The first record of grinding operation can be seen in the Utrecht Psalter of 850 A.D. with water as a grinding fluid. Use of water as "hydraulic oil" was also evident from Joseph Bramah for his historic press in 1795. It was also utilized as the hydraulic medium in subterranean power transmission network of London's factories towards the end of the nineteenth century. The colloidal chemistry work of William Hardy paved the way for the development of water-soluble cutting fluids [5].

1.1 Mineral Oil Based Lubricants

Lubricants based on vegetable oils are in use since ancient times, but mineral oil based products have become prominent ever since the discovery of petroleum. Mineral oils are complex mixtures of C_{20} – C_{50} hydrocarbons that are commonly known as Paraffinic, Paraffinic–Naphthenic, and Aromatic species composed of basically Carbon and Hydrogen. They also contain small concentrations of hetero atoms, mainly sulfur.

In a lubricant, base oil primarily provides a fluid layer separating the moving surfaces. In addition it also dissipates heat from the contacting interface. Other functional properties of the lubricants can be achieved by virtue of the addition of special chemical additives. The main families of additives are antioxidants, antiwear formulations, antifoaming agents, corrosion inhibitors, detergents, demulsifying/emulsifying agents, extreme pressure, friction modifiers, metal deactivators, and viscosity index improvers. They have been discussed in detail in the later part of the chapter.

1.2 Limitations of Mineral Oil Based Lubricants [6]

- Mineral oil based lubricants are derived from Petroleum, which is nonrenewable.
- Mineral oil based lubricants cause environmental concerns for air quality as they produce oxides of Carbon, Nitrogen, Sulfur. Further they produce substances like Benzene, Xylene, Ethane during the manufacturing, use, recycling, and disposal processes.

- The direct contact with mineral oils may also lead to skin irritation, oil acne, and contact eczema. Further, it is also found to cause irritation in the mucous membranes.
- It has been found that a drop of mineral oil can contaminate ten million liters of water and takes close to 100 years for ultimate degradation. Even small amounts of mineral oil can inhibit the growth of trees and can be toxic to aquatic life. For example, as little as 0.1 % contamination can reduce the life of shrimp by 20 %.
- Mineral oil based lubricants are not biodegradable and their disposal is hazardous to the environment.
- Mineral oils used in ink can get into foods when they are packed in recycled cardboard. Manufacturers in Europe and USA have stopped using recycled cardboard in food packaging because they are carcinogenic.

2 Green Lubricants

At present worldwide bulk of the used lubricants end up in the environment through usage, spill, volatility, or improper disposal causing immense damage to the environment. Hence, government agencies all over the world have started to impose increasingly stringent regulations on the use and disposal of lubricants due to their negative impacts. These regulations have changed the landscape of the lubrication marketplace especially over the last two decades resulting in the appearance of new environment friendly lubricants in the market. Since the disposal costs of traditional lubricants based on petroleum are also increasing exponentially, it has become essential to develop and use lubricants that come from natural resources. The increased use of renewable resources for lubricant applications will have a remarkable impact on our society in terms of conserving the environment.

The development of green lubricants to replace the conventional products is presently attaining interest all over the world due to its significance in conserving the environment. The term “green lubricants” is generally used for lubricants where the base oil is derived from the renewable sources or from its derivatives. The other common names for green lubricants are “environmentally acceptable,” “environmentally benign,” and “environmentally friendly” lubricants. The use of biodegradable lubricants is required to be more prevalent in the areas of agriculture, forestry, and water treatment. The vegetable oils have become the primary choice in formulating green lubricants as they are renewable, nontoxic, and readily biodegradable. In addition the following factors also play a significant role in forming green lubricants.

- Chemical and physical properties of vegetable oils
- Cost, performance, and technological compatibility
- Adoptability to environment, recycling, and disposal of the used lubricants
- Health and safety concerns

2.1 Sustainability and Its Importance

The concept of “Sustainable Development” has become a key issue in forming environmental policy and industrial development in the recent past as unrestrained use of resources for economic development results in ecological imbalance. Thus, sustainability refers to the maintenance of integrity of the ecology. Hence, sustainable development can be defined as “Development which meets the needs of the current generation without compromising the future generation to meet their own needs” The phrase “Environmentally Sound and Sustainable Development (ESSD)” is also in use in place of “Sustainable Development” in the recent past.

Lubricants in the backdrop of complexity of production and usage have become the subject of life cycle analysis as their production, use, and disposal have significant impact on the environment. Sustainability of lubricant materials has two aspects. The first aspect refers to the origin of resources. For example, mineral oil is a finite resource and fossil raw material formed over millions of years ago; the process took thousands of years. They are being consumed at an alarming rate and even available deposits cannot be guaranteed for a long term, whereas the vegetable oils and the products derived thereof are renewable raw materials [7, 8]. The second aspect is related to the CO₂ cycle; as in the case of oleo chemicals, the CO₂ liberated is equal to the CO₂ that is originally taken up by the plants and the cycle is closed. By contrast the CO₂ cycle of petrochemicals is not closed but open, leading to increase in atmospheric CO₂ level and thus contributing to global warming. This is in addition to the effects of pollution caused by the exposition of petroleum derivatives into the environment. Since bulks of used lubricants are unaccounted, lubricants have significantly high environmental relevance [9].

2.2 Structure and Composition of Vegetable Oils

Vegetable oils are the liquid or semisolid plant products composed of glycerides of the fatty acids. A schematic structure of triglyceride is shown in Fig. 14.1. The chemical structure of vegetable oils is relatively uniform as opposed to that of mineral oils. The composition of vegetable oil is expressed in terms of its building blocks “fatty acids,” which are plant specific. The fatty acids are linked to glycerol with an ester bond to form triglycerides. The naturally available fatty acids exist only in *cis* configuration. There is a possibility of variation in the fatty acid proportion for a given oil with reference to the region, climatic conditions, and availability of nutrients for growth. The fatty acids are composed of straight chain carbon molecules ranging from 8 to 24 carbon atoms. A brief note on different kinds of fatty acids is presented in the following section.

- (a) Saturated fatty acids: The fatty acids which do not have carbon–carbon double bond in their backbone structure, like Lauric acid, Palmitic acid, and Stearic acid, are identified as saturated fatty acids. They are resistant to oxidation and

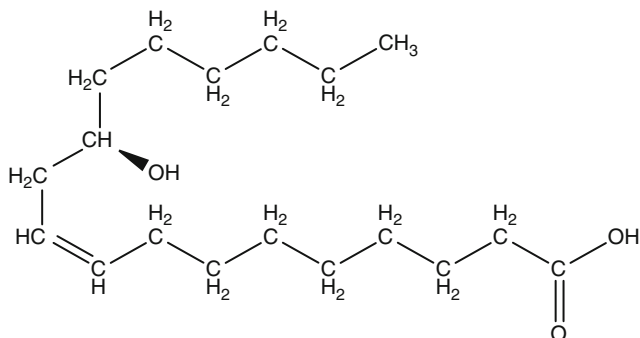


Fig. 14.4 Schematic representation of a hydroxy fatty acid

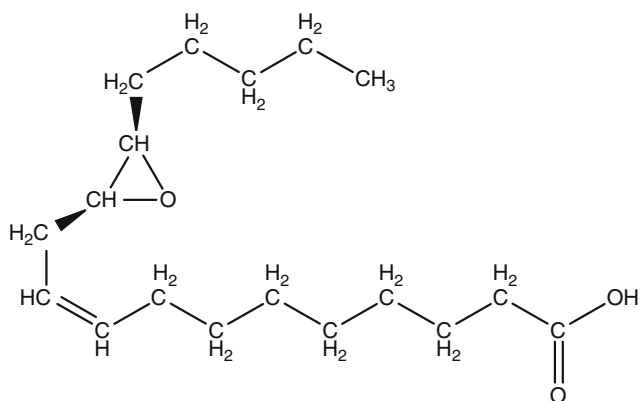


Fig. 14.5 Schematic representation of an Epoxy fatty acid

- (d) Hydroxy fatty acid: The fatty acids which have one hydroxyl group ($-OH$) in their backbone structure, e.g., Ricinoleic acid in Castor oil, are considered as hydroxy fatty acids. Due to the presence of hydroxyl group, they exhibit relatively low pour point and offer multiple reactive sites for chemical modification. A schematic representation of a hydroxyl fatty acid is shown in Fig. 14.4.
- (e) Epoxy fatty acid: This is a special kind of fatty acid present in the seed oil of *Vernonia anthelmintica* and the fatty acid is called as vernolic acid. A schematic representation of an epoxy fatty acid is shown in Fig. 14.5.

2.3 *Benefits of Using Vegetable Oils as Base Oil in Green Lubricants [10–17]*

- High flash point of esters results in lesser emission of oxides of carbon in comparison to mineral oil. It also benefits in higher safety on a shop floor.
- They are totally free from aromatics.
- They deliver higher tool life when used as metal cutting oils because of higher wetting tendency of polar esters resulting in reduced friction.
- They exhibit better skin compatibility, lesser dermatological problems when used as metal working fluids.
- Their higher viscosity index is an advantage when developing lubricants for use over a wide range of temperatures.
- Vegetable oils are renewable, biodegradable, and nontoxic to the ecosystem.

2.4 *Limitations of Vegetable Oils as Base Oil in Green Lubricants*

- The important issue is related to their low temperature limitations. As most of the vegetable oils have considerable amount of saturated fatty acids in their composition, it restricts their use to limited applications.
- Their compatibility with sealing is not good, and they also exhibit flushing tendency because of lower viscosity.
- They have poor oxidation and hydrolytic stability.
- Filter clogging, foaming, and poor corrosion protection are the other issues which limit their application.

2.5 *Chemical Modification of Vegetable Oils*

The inherent limitations are restricting the use of vegetable oils for lubricant applications. The poor oxidative stability of vegetable oils is primarily due to the presence of bisallylic protons as shown in Fig. 14.6, which are highly susceptible to radical attack and subsequently undergo oxidation, resulting in deposits making vegetable oils unusable. Further, the vegetable oils are easily susceptible to hydrolytic breakdown, and their low temperature properties are also of concern.

Chemical modification of vegetable oils can overcome these shortcomings. One of the ways to perform this task is by splitting the vegetable oils into their constituents before they are modified according to the requirement. The other way is to modify the vegetable oils directly by reacting it with an appropriate reagent, to transform the reactive groups into various products suitable for different applications. From chemistry point of view, triglycerides generally have two

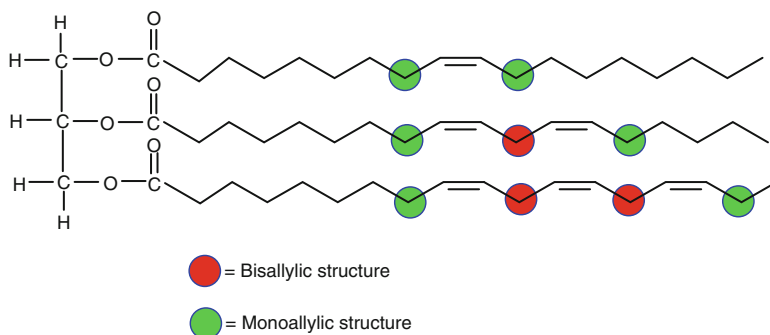


Fig. 14.6 Schematic representation of bisallylic and monoallylic sites in triglyceride molecule

Table 14.1 Chemical modification of vegetable oils—reactions of ester [18–21]

Nature of reaction	Definition	Reagents used	Products obtained
Hydrolysis	It is a process of splitting of triglycerides into fatty acids and glycerol by breaking ester bond	Acid/base/enzyme	Fatty acids and glycerol
Trans-esterification/esterification	The reaction between an ester of one alcohol and a second alcohol to form an ester of the second alcohol	<i>p</i> -toluene sulfonic acid, phosphoric acid, sulfuric acid, sodium hydroxide, sodium ethoxide and sodium methoxide	Monoesters, diesters, polyesters, and complex esters
Saponification	A chemical reaction, where a triglyceride reacts with strong alkali to form glycerol and fatty acid soap	Alkali/metallic salts	Soluble and insoluble soaps
Amidation	The process of forming amides, through the reaction of triglycerides and alkyl amines	Alkyl amines	Amine salts and amides

reactive sites, the double bond in the unsaturated fatty acid chain and the carboxyl group of the fatty acid chain. The most important modifications are related to the transformation of the carboxyl group of the fatty acids which accounts for about 90 % of the products. Tables 14.1 and 14.2 give important chemical modifications of vegetable oils.

Table 14.2 Chemical modification of vegetable oils—reactions of carbon–carbon double bond [21–26]

Nature of reaction	Definition	Reagents used	Products obtained
Selective hydrogenation	It is a reduction reaction, which results in the formation of monounsaturated fatty acids from polyunsaturated fatty acids	Hydrogen in presence of catalyst	Hydrogenated oils
Epoxidation	It is a reaction in which an oxygen atom is binding to the region of unsaturation in fatty acids to form cyclic, three-membered compounds	Hydrogen peroxide	Epoxidized oils
Oligomerization	The process involves the attachment of two or more fatty acids at the site of unsaturation.	Layered aluminosilicate catalysts	Dimmer/trimer derivative fatty acid
Cooligomerization	It is the process of forming alkyl branched fatty acid derivatives	Rh based homogeneous catalysis	Branched fatty acid derivatives with different terminal functional groups
Hydroformylation	It is the reaction of adding hydrogen and the –CHO group to the carbon atoms across a double bond to yield oxygenated derivatives	Co or Rh based complex catalysts	
Friedel–Crafts reaction	A substitution reaction, in which an alkyl group replaces a hydrogen atom to produce a ketone	$\text{Et}_3\text{Al}_2\text{Cl}_3$ as catalyst	

3 Lubricants Testing

Testing of lubricants in general is very essential as the lubricant oils formulated for wide range of applications require fulfilling specific properties and functions. A laboratory test method has to be meaningful and should simulate the test conditions of the lubricant operation. Most of the test methods used across the industrial fields described today are developed by the following bodies.

- American Society for Testing and Materials (ASTM) International—<http://www.astm.org>

- American Association of State Highway and Transportation Officials (AASHTO)—<http://www.transportation.org/>
- American National Standards Institute (ANSI)—<http://www.ansi.org>
- American Petroleum Institute (API)—<http://www.api.org>
- British standards (BS)—<http://www.bsigroup.com/>
- Bureau of Indian standards (BIS)—<http://www.bis.org.in>
- Coordinating Research Council Inc. (CRC)—<http://www.crcao.com>
- Deutsches Institut fur Normung e.V. (DIN)—<http://www.normung.din.de>
- Institute of Petroleum(IP)—<http://www.energyinst.org.uk>
- International Standards Organization (ISO)—<http://www.iso.org>
- National Lubricating Grease Institute (NLGI)—<http://www.nlgi.org>
- Society of Automotive Engineers (SAE)—<http://www.sae.org>

Among these, ASTM, IP, and DIN standards aim at testing various lubricant properties. A few important test methods are demonstrated in the following section with reference to lubricant testing. These standards are used to test the specification requirements and also to evaluate the performance of new oils.

3.1 Wear Prevention Properties (ASTM D2670, ASTM D4172, ASTM D5182, ASTM D7043) [27–30]

ASTM D2670 method determines wear properties of lubricants using Falex pin on V block machine. This test uses a steel pin rotating at 290 ± 10 rpm against a pair of V blocks immersed in lubricant sample for a period of 15 min. The wear on the pin and V blocks are interpreted to determine the lubricants' wear properties.

ASTM D4172 method is used to evaluate the antiwear properties of lubricants using a four ball tester. The test utilizes a steel ball fixed to a collet rotating at 1,200 rpm against three stationary balls locked in a ball pot filled with oil. The sample temperature is controlled at 75 °C, the applied load is 392 N, and the test duration is of 60 min. The results are expressed in terms of average value of wear scar diameter.

ASTM D5182 (IP 334, IP 166, and DIN 51354) method is used to evaluate the scuffing load capacity of oil used to lubricate hardened steel gears. The test uses Forschungsstelle fur Zahnrad und Getriebebau (FZG) visual method. In this method, FZG gear machine is operated at constant speed for a predefined time at increasing loads until failure criteria are reached.

ASTM D7043 method is used to evaluate the wear properties of hydraulic oils using constant volume pump. The test uses a rotary vane pump that pumps test fluid through a standardized circuit at 1,200 rpm, 13.8 MPa for 100 h and the results are expressed in terms of total weight loss of the pump cam ring and vanes.

3.2 *Extreme Pressure Properties of Lubricants (ASTM D2782, ASTM D2783, ASTM D3233, ASTM D6121, and ASTM D6425) [31–35]*

ASTM D2782 (IP 240) method uses the Timkin apparatus to evaluate the extreme pressure properties of lubricants and is useful for the test fluids having viscosity less than 5,000 cSt at 40 °C. The test machine uses a steel cup rotating at 123.71 ± 0.77 rpm against a steel block lubricated with the test sample. The test fluid is preheated before starting the test. The test is evaluated in terms of two parameters: (a) The maximum load (OK load) at which no scoring occurs between the rotating cup and the stationary block and (b) The minimum load (Score value) at which seizure occurs.

ASTM D2783 (IP 239) method uses a four ball tester where the top steel ball rotates at 1,760 rpm against three stationary balls lubricated with oil. The results are expressed in terms of minimum load corresponding to the seizure or welding.

ASTM D3233 (IP 241) method is used to evaluate the load carrying capacity of lubricants using Falex pin on V block machine. This test uses a steel pin rotating at 290 ± 10 rpm against a pair of V-blocks immersed in lubricant sample for a period of 15 min. The load is increased to 1,112 N in steps, and the load at which the pin fails is taken as the end point.

ASTM D6121 method is also referred as L-37 used to evaluate the load carrying capacity of test samples under low speed and high torque conditions.

ASTM D6425 (DIN 51834) method uses SRV (Schwingung–Reibung–Verschleiss) test rig in which the test ball oscillates at constant frequency, stroke amplitude, and load against test disk and the results are interpreted in terms of mean wear scar diameter.

3.3 *Biodegradability and Toxicity of Lubricants*

Biodegradability is the most important aspect with reference to the environmental fate related to the residual life of a component, its decomposition mechanisms, and the possible environmental impact it can cause at any stage during the course of the deterioration. Biodegradability is an environmental characteristic by the action of natural population of microorganisms; carbonaceous materials are removed from soil and water. The Organisation for Economic Co-operation and Development (OECD) is a prominent body which promotes policies to improve the economic and social well-being of people around the world. It facilitates common forums in which governments can work together to share experiences and seek solutions to common problems. Thus, formulating and using environment friendly lubricants have attained significant importance in the recent times [36–39]. A few important test methods along with the standards set by OECD for testing the chemicals which are applicable to lubricants are provided in Table 14.3.

Table 14.3 Standard test systems for biodegradability of organic matter [40]

Test method	Name of the test	Parameters evaluated and standard adopted
OECD screening tests	DOC die-away test	DOC* (OECD 301 A)
	Modified Sturm test	CO ₂ (OECD 301 B)
	MITI test	BOD (OECD 301 C)
	Closed Bottle test	BOD/COD (OECD 301 D)
	MOST	DOC (OECD 301 E)
	Manometric respirometry	BOD/COD (OECD 301 F)

Table 14.4 International standard ecotoxicological test methods [43, 44]

Test method	Species used	Duration of the test-Standard followed
Short-term tests (acute tests)	Algae	72 h-OECD 201
	Daphnia	48 h-OECD 202/1
	Fish	96 h-OECD 203
	Bacteria	30 min-OECD 209
Long-term tests (chronic tests)	Daphnia	21 (Days)-OECD 202/2
	Fish	≥4 weeks-OECD 210

In the Table 14.3, DOC refers to Dissolved Organic Carbon, BOD refers to Biological Oxygen Demand, and COD refers to Chemical Oxygen Demand.

Chemicals consumed in the form of food in general can have a wide range of effects on our health. It is also essential to understand the adverse effects of chemicals which are used for non food applications. Since toxic effects can vary depending on the composition, comparing the toxicity of one with another would be unwise. Therefore, one way to compare the toxic potency or intensity of different chemicals is to measure the lethality testing (the LD₅₀ tests). The term LD stands for “Lethal Dose.” LD₅₀ is the amount of a material, given all at once, which causes the death of 50 % (one half) of a group of test species and LC stands for “Lethal Concentration,” referring to the concentration of a chemical in air, but in environmental studies it can also mean the concentration of a chemical in water [41, 42]. The term Effective Concentration (EC) is also sometimes used. Since it is not always feasible to investigate the effect on different species in the laboratory, only certain species which represent the natural food chain are evaluated and for aquatic toxicity; Fish, Daphnia, Algae, and Bacteria are the most relevant species. A few important toxicity test methods are provided in Table 14.4.

1. The acute tests investigate the effects of high concentrations of test chemical during a relatively short period of time of exposure to evaluate the LC₅₀ or EC₅₀ concentration.
2. The subchronic tests investigate long-term effects at low concentrations to find out NO Observed Effect Concentration (NOEC).

In general, for a readily biodegradable substance, if the acute test indicates no toxicity, chronic tests are done, whereas for high volume chemicals like lubricants, determination of chronic tests is necessary to evaluate a reliable risk assessment.

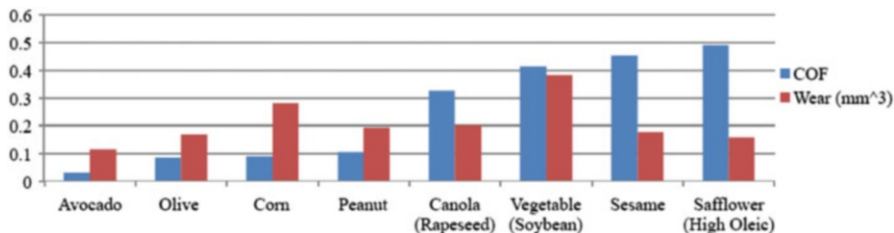


Fig. 14.7 Variation of coefficient of friction and wear rate for vegetable oils [45]

4 Tribology and Applications of Vegetable Oils

The triglyceride structure of vegetable oils essentially provides many qualities desirable in a lubricant. The chain length of the fatty acids plays a very important role in controlling wear rate and coefficient of friction. The presence of adsorbed surface film of long polar fatty acids resists the penetration of asperities and inhibits the metal-to-metal contact and thereby reduces the friction and wear. The strong intermolecular interactions among the fatty acid molecules are also responsible for the high viscosity index observed with vegetable oils.

Efforts were made to evaluate the tribological performance of green liquid lubricants using a pin-on-disk apparatus [45]. More specifically, various green liquid lubricants such as avocado, canola (rapeseed), corn, olive, peanut, safflower, sesame, and vegetable oil are considered. Figure 14.7 shows the variation of friction and wear rate for these lubricants. It was found that the avocado oil showed the best friction and wear performance when compared to other green lubricants. It was concluded that the natural oils with high percentages of monounsaturated fatty acids particularly oleic acid, present in oils develop tightly packed carbon chains that better protect the pin-disk interface, resulting in lower friction and wear.

4.1 Hydraulic Oils

The term “hydraulics” is generally used to describe the transmission and control of forces and movement by means of a functional fluid. Liquids used for this purpose are termed “hydraulic fluids.” The first-generation biodegradable hydraulic oils were based on vegetable oils. The limitations of vegetable oil based hydraulic oils, such as oxidation and hydrolytic stability, poor low temperature performance, and an average service life, paved way to synthetic ester based hydraulic oils having high viscosity index, excellent oxidation, and thermal stability. With the use of synthetic products, the service life is increased along with the improved reliability. These products are typically used in the following applications

- Construction cranes
- Commercial elevators
- Earth-moving excavators
- Rock-drilling equipment
- Sewage treatment plants
- Water treatment equipment

The disposal of the vegetable based hydraulic oils will be economically less expensive and also of no concern to the environment as they are completely biodegradable. A detailed study was conducted using soybean oil to develop the baseline for use in hydraulic and other applications. Soybean oil showed sufficient lubricating property to perform in hydraulic systems. Change in color (darkening) was also observed with time when aged oil was exposed to extremely high temperatures of 200 °C or higher resulting in a strong odor in oil which in time became rancid. The soybean oil showed compatibility with most materials, including seals and rubber hoses. The presence of highly polyunsaturated fatty acids in its composition was responsible for the formation of polymeric film on the oil when it was exposed to air. Although a slight swelling of hoses was observed, the soybean oil had similar compatibility with rubber hoses as that of other oils [46, 47].

Studies were also conducted on two vegetable oil based formulations where the first formulation was based on rapeseed oil, while the second was high oleic sunflower oil. In the experiments, the same additive system was used for comparison. The results have revealed that Ester based oils show low friction coefficient than higher additive containing mineral based lubricant. The Forschungsstelle für Zahnräder und Getriebekonstruktion (FZG) gear test results showed that gear protection properties of the vegetable based oils are better than or equivalent to that of the mineral oil based lubricant [48].

4.2 Metal Cutting Fluids

Cutting fluids are used in machining operations to provide adequate lubrication, to perform cooling operation, and to carry away the generated chips. The mineral oil based metal cutting fluids cause high degree of environmental contamination due to spillages, mist formation, and evaporation in cutting operations. In order to be environment friendly, cutting fluids should be readily biodegradable after disposal without being toxic to the ecosystem. The use of vegetable oils allows making possible development of a new generation cutting fluid, where high performance in machining combined with good environment compatibility could be achieved. Compared to mineral oil, vegetable oil can even enhance the cutting performance, extend tool life, and improve the surface efficiency.

The machinability of ferrous alloys is a challenging task as they have high strength, low thermal conductivity, high ductility, and high work hardening tendency. Poor surface finish of the work materials, high cutting force, and high

tool wear are associated with the machining of these materials. Research and development in the application of vegetable oil based cutting fluids have witnessed a great attention in the recent past as they are widely used in medium to heavy-duty machining and grinding processes of ferrous based metals due to their improved performance [49].

Studies were conducted to evaluate the influence of different cutting fluids on tool wear and surface roughness during turning of AISI304 austenitic stainless steel with carbide tool. It was found that coconut oil was relatively effective in reducing the tool wear and improving the surface finish compared to conventional mineral oil based formulation. This study also showed that increase in cutting tool temperatures was less when coconut oil was used for lubrication during the turning of AISI1040 steel with cemented carbide tool and improved surface finish in presence of 0.5 % nano boric acid suspensions [50, 51]. Further, studies were conducted on canola and sunflower oil based cutting fluids and compared with commercial type semi-synthetic cutting fluids to determine the optimum conditions for tool wear and forces during milling of AISI304 austenitic stainless steel with carbide tool material. Research was also carried out in the past on the effect of coconut oil, palm kernel oil, and groundnut oil on cutting forces during cylindrical turning of mild steel, copper, and aluminum using tungsten carbide tool [52, 53]. The results showed that these oils were suitable for metalworking processes, but the effects of these oils on cutting force were material dependent. They observed that groundnut oil exhibited the highest reduction in cutting force while turning operation with aluminum. Palm kernel oil exhibited the best performance when copper was turned at lower feed rate. However, at higher feeds, groundnut oil had the best performance for copper. Further, coconut oil recorded the highest cutting force in all the three materials machined [54–56]. It was observed that there has been a gap using vegetable oil based metal cutting fluids in machining applications of nonferrous and super alloy materials, which exhibit a combination of mechanical strength and resistance to surface degradation [57].

4.3 Two-Stroke and Four-Stroke Engine Oil

The use of mineral oil based lubricants which are nonbiodegradable and their disposal emphasize the need for environment friendly two- and four-stroke engine oils. A study on snowmobile engine emissions was conducted in Yellowstone National Park, USA to determine potential emission benefits of use of bio-based fuels and lubricants in snowmobile engines. The biodegradable lubricants in use have shown reduced carbon monoxide by as much as 38 % [58]. Assessment of tribological and emission performance of vegetable and mineral oil based lubricants were carried out using a universal wear and friction testing machine and a two-stroke engine. These studies conducted on Yamaha generator, two-stroke ET950 engine with palm oil based lubricant showed the effectiveness in reducing the emission levels for CO and HC compared to conventional lubricants. The wear

studies conducted on piston ring and liner pair of the same engine with palm oil based lubricant have shown better wear resistance compared to mineral oil based lubricants [59]. The performance evaluation of the coconut and palm oils in four-stroke engines have also shown reduction in exhaust emission in terms of oxides of carbon and nitrogen and improved fuel efficiency when compared to the standard mineral oil based four-stroke engine oil. The tribological evaluation of the oil samples, collected at different intervals from the engine, carried out by means of four ball tester. The results revealed that the mineral oil based lubricant was better in terms of reducing the wear compared to vegetable oils which was possibly due to the absence of the performance enhancing additives in the vegetable oil based formulations [60, 61].

5 Lubricant Additives

Lubricating oil additives form essential components of modern lubricants. They are defined as compounds which impart new characteristics to the base oil or strengthen desirable properties. The concentration of additives in oil is variable depending on the application. For example, the compressor oil will have few tenths of percentage of additives while special motor and gear oils show an additive content up to 40 %. A fully formulated lubricant shows range of properties which are absent in the base oil. Properties of different additives and their mode of action have been provided in Table 14.5.

The additive selection for a given application depends on the following factors.

- Solubility in base oil and effective concentration required
- Reactions with metals and seals
- Tolerance of other additives and synergic effects
- Availability of raw materials, cost, and patent situation

It is important to note that many properties of lubricating oils are practically unaffected by additives, while few properties show improvement by virtue of additives, whereas the other lubricant properties are solely due to the presence of additives as indicated in the Table 14.6.

6 Additives for Green Lubricants [62, 63]

The performance of any lubricant depends on base oil, additives and the overall formulation. The commercial additives which are in use today are derived from a variety of elements. Most of them have phosphorus, sulfur, nitrogen, and zinc as the active elements. However, due to environmental restrictions, phosphorus is expected to be phased out. In addition, it is expected that environmentally friendly

Table 14.5 Properties of different additives and their mode of action

Additive	Function	Mode of action
Antiwear agent	Minimizes wear caused by metal-to-metal contact	Additive reacts chemically and forms a film on metal surfaces
Corrosion inhibitor	Prevents corrosive attack on nonferrous metallic surfaces	It forms a film on nonferrous metallic parts and protects them from attack by contaminants in the oil
Detergent and dispersant	Prevents oxidation products by removing deposits already formed on metallic components Keeps oxidation products separated and suspended in the oil	By chemical reaction—oxidation products (sludge) remain soluble in the oil and do not stick to the metal surfaces By chemical reaction—oxidation product particles are kept small enough to allow them to float in the oil
Extreme pressure (EP) agent	Prevents welding of contacting metal parts under extreme or shock load conditions	When metal-to-metal contact occurs the heat generated causes the additive to react chemically with the metal resulting in reduced friction and prevents welding
Emulsifier	Promotes mixing of water and oil resulting in the formation of a stable emulsion	Permits mixing of oil and water by reducing the interfacial tension
Foam inhibitor	Facilitates foam to dissipate more rapidly	Protects combination of small bubbles into large bubbles and further prevents foaming
Oxidation inhibitor	Prevents sludge formation	Reacts readily with oxygen than the base oil itself, and retards oxidation of the base oil
Pour depressant	Lowers the pour point	Keeps small wax crystals apart and facilitates the flow of oil
Rust inhibitor	Prevents rusting of ferrous components	Protects metallic parts by forming a film
Viscosity index (VI) improver	Reduces rate of change of viscosity with temperature	Additive thickens with increasing temperature and preventing oil from thinning out too rapidly

Table 14.6 Effect of additives on different properties of base oils

Properties of base oils not affected by additives	Heat transfer Viscosity–pressure relationship Temperature effects
Properties of base oils improved by additives	Low temperature properties Ageing stability Viscosity–temperature relations Corrosion protection
Properties exclusively imparted by additives	Detergency Dispersion Extreme pressure Foam inhibition

lubricants must not contain any chlorine and nitrites. The following section focuses on the different additives suitable for green lubricants.

The oxidative degradation or ageing is an important process in a lubricant which reduces lubricant performance due to the formation of acids, varnish, and deposits. Antiwear and EP additives are used to protect metal surface from mechanical damage under critical conditions by inducing tribochemical reactions. Zinc dialkyl dithio phosphate (ZDDP), the most commonly used Antiwear/EP additive in the industry, cannot be used in environment friendly green lubricants due to presence of Zinc; hence, for green lubricants ashless phosphites and thioesters are preferred.

Pour Point Depressants (PPD) and Viscosity Index (VI) improvers are used to improve the rheological or flow properties of lubricants. Natural esters require PPDs as they have poor low temperature properties compared to synthetic ester based lubricants; further, the quantity of PPDs used also varies according to the requirement. The VI improvers are very rarely used in the vegetable oil based formulations, as the vegetable oils have high viscosity index.

Antihydrolysis additives are used only for ester class lubricants, which act as acid scavengers to remove the catalyst. The corrosion inhibitors which protect the metals against attack of moisture and oxygen can also catalyze the hydrolysis of esters. The additives are to be balanced in a careful manner to minimize such effects.

7 Tribology of Green Additives

Water-based lubricants have been in use even in ancient times and today they are mainly used in applications like fire-resistant hydraulic fluids and metal working fluids. They have number of disadvantages like insufficient lubricating properties and high corrosive activity limiting their use. There is an ever increasing demand for water compatible additives to improve the performance of water-based lubricant formulations.

The performance of Alkyl polyglucosides were tested as additives in water where improved performance was observed even at the concentration levels of 0.1 % with reference to the antiwear properties [64, 65]. In another study, novel fullerene–styrene sulfonic acid copolymer of particle size 3–40 nm was synthesized by typical free radical polymerization followed by sulfonation. The performance of the water-soluble additive was evaluated in triethanolamine aqueous solution base stock. Improved wear resistance, load carrying capacity, and antifriction properties with the addition of fullerene–styrene sulfonic acid copolymer to the base stock were noticed [66]. Studies on O,O-poly ethoxy glycol diester of dithio phosphoric acid as a additive in water at different concentrations showed improved initial seizure loads and weld loads and similar effect was noticed with *S*-(carboxylpropyl)-*N*-dialkyl dithiocarbamic acid in water as an additive [67].

As biodegradability and toxicity are of most extensive concern for environment friendly lubricants, the most widely used commercial additives like ZDDPs are facing strong environmental challenges; hence, there is a tremendous interest in the

development of new additives for the environment friendly lubricants. Several compounds including the fatty acids and alcohols have been tested. The results revealed that addition of fatty acids in sunflower oil showed improved boundary lubrication properties under sliding conditions. It was also found that the stearic acid was effective in improving the boundary lubrication of sunflower oil. However, the increased level of unsaturation in the fatty acid has a negative effect on the performance [68]. The performance of fatty acids in sunflower oil deteriorated with temperatures approaching 150 °C. In addition, it was observed that these compounds have very poor extreme pressure properties. Combining sulfur and fatty acid can provide a synergistic effect as fatty acids are effective in reducing the antiwear properties where as sulfur can be effective in improving the extreme pressure properties. This prompted to study the effect of sulfurized fatty acids as additives. It was observed that the sulfurized additives have very good extreme pressure and antiwear properties [69].

Efforts have been made to develop and use environment friendly powder lubricants that come from natural resources. As reported in literature, solid lubricants such as boric acid and hexagonal boron nitride (hBN) have excellent lubrication properties [65, 70, 71]. These additives are readily available and environmentally safe. The Environmental Protection Agency (EPA) has established that these additives do not classify as pollutants. In fact, a dilute water solution of boric acid is also used as a mild antiseptic and eyewash. Hence, efforts have been made to evaluate the tribological performance of the green powder lubricants. Green additive such as Boric acid or hBN when used alone are forced out of the contact zone during sliding contact. A logical alternative is to use these powders with an environmentally friendly liquid lubricant that carries the solid boric acid or hBN crystals.

Tribological evaluation of green lubricant such as canola oil and green additive such as boric acid with varying particle size were made. More specifically, nano size (20 nm), submicron size (average size 600 nm), micron size (average size 4 μm), and combined submicron and micron boric acid additives in base canola oil are considered. As a basis for comparison, 5 μm size MoS₂ powder additives mixed with canola oil was also studied. Experiments were conducted using pin-on-disk with Copper pin and Aluminum disk. Figures 14.8 and 14.9 show the variation of coefficient of friction and wear rate with sliding distance for all the lubricant mixture, respectively. It was found that the nano size boric acid additives in canola oil lubricants significantly outperformed all of the other lubricants with respect to frictional and wear performance. In fact, the nano size boric acid powder based lubricants exhibited a wear rate more than an order of magnitude lower than the MoS₂ and larger sized boric acid additive based lubricants. It was also discovered that the oil mixed with a combination of submicron and micron size boric acid powder additives exhibited superior friction and wear performance than the canola oil mixed with submicron or micron-size boric acid additives alone [72].

Similar results can also be obtained when the green lubricant (canola oil) mixed with green additives such as hexagonal Boron nitride (hBN) particle additives. Figure 14.10 shows the variation of coefficient of friction and wear rate when hBN particles of different size and their combinations mixed with canola oil in the

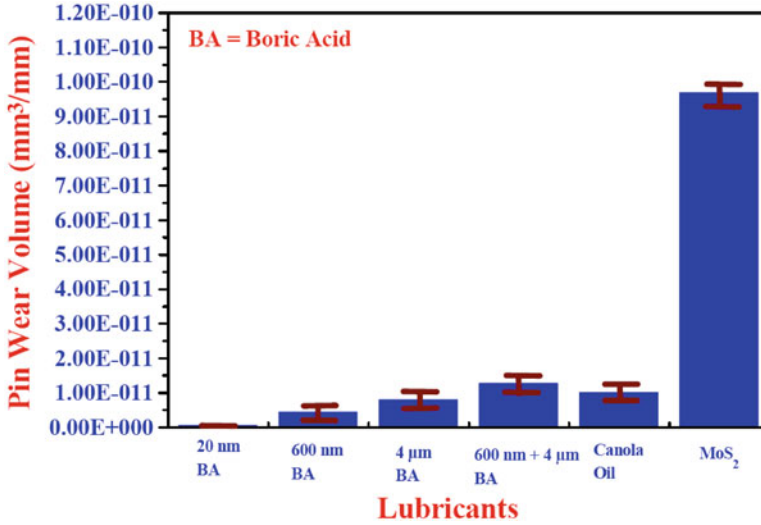


Fig. 14.8 Variation of wear rate for various lubricant combinations [71]

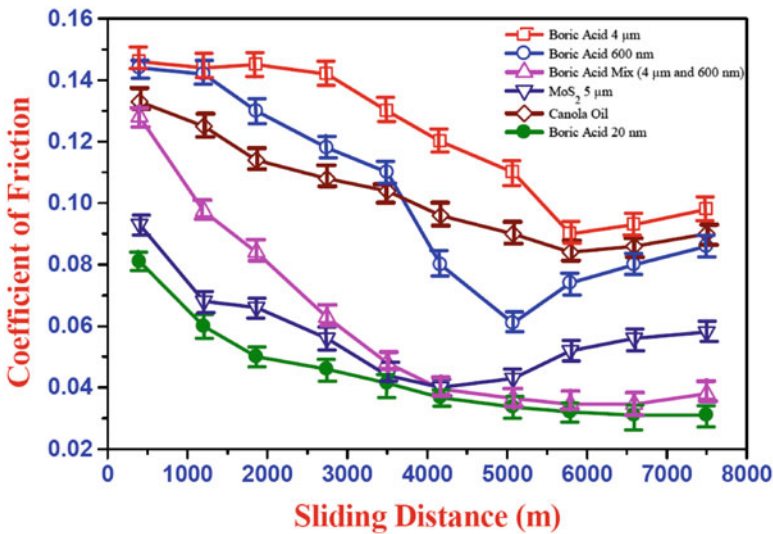


Fig. 14.9 Variation of coefficient of friction with sliding distance for various lubricant combinations [73]

pin-on-disk experiment. It was demonstrated that the hBN additives that are larger than the asperities carry a portion of the load between the contacting asperities, resulting in a decrease of friction. However, these larger particles are also more abrasive causing higher wear rates. The nano sized particles in canola oil coalesce in the asperity valleys, creating a superior protective film between the contacting surfaces that thwarts friction and wear.

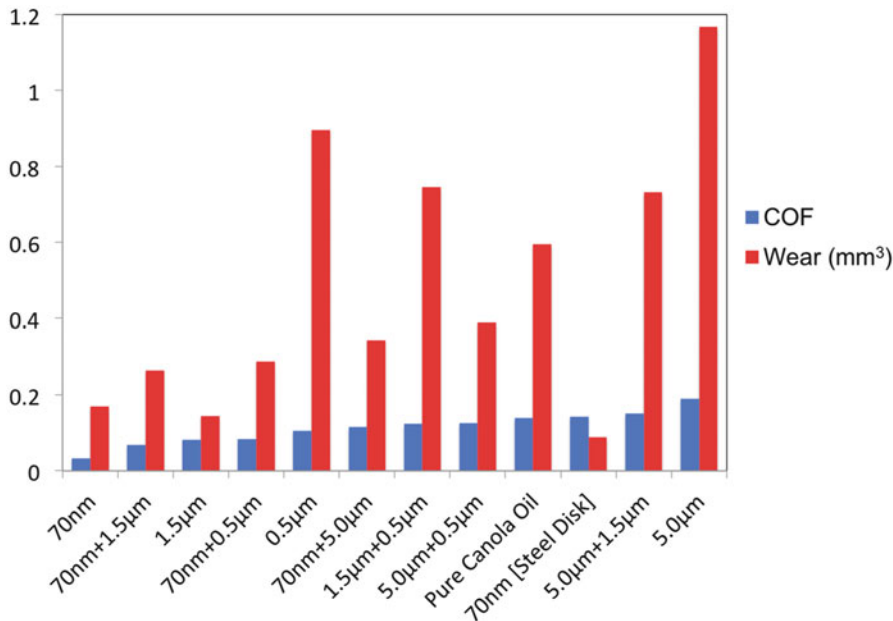


Fig. 14.10 Variation of coefficient of friction and wear rate when hBN particles of different size and their combinations mixed with canola oil [65]

8 Ionic Liquids

A “new class” of lubricant, namely, ionic liquids (IL), which are fluid at ambient conditions, represent a promising solution to the problems associated with both conventional lubricants as well as lubricants based on natural oils. They typically have a bulky and asymmetric organic cation and an appropriate organic anion, exhibiting number of unique properties making them as promising lubricants. The application of ILs as lubricants becomes more apparent as they have several advantages over conventional lubricants [74, 75].

- They have broad liquid range with negligible vapor pressure
- Nonflammability and superior thermal stability
- High viscosity and better miscibility/solubility
- Environmentally safe, very economical
- Lamellar-like liquid crystal structure providing improved lubricity and
- Consistent physicochemical properties

Tribological studies with pin-on-disk apparatus using Aluminum pin sliding against stainless steel disk was carried out for selected green ionic liquids (salicylate, saccharinate, and benzoate), convention ionic liquid ($C_{10}mimTf_2N$). For comparison, natural (Canola, SoyGold, Safflower, Vegetable) oils and petroleum-based

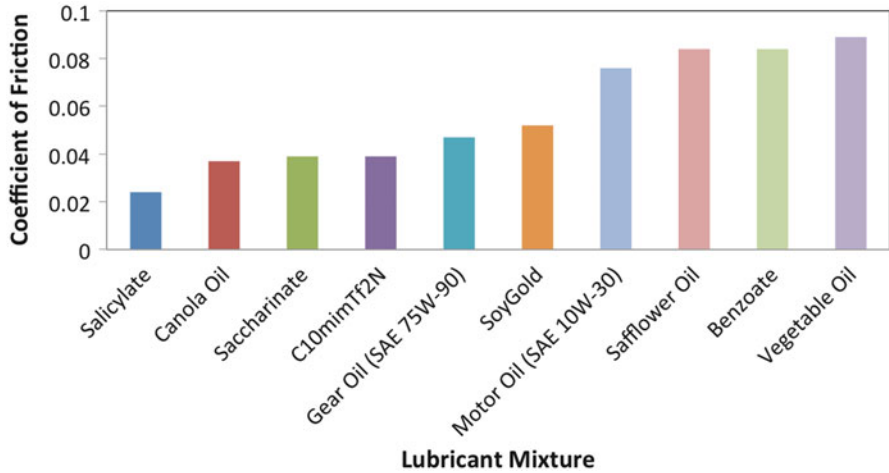


Fig. 14.11 Variation of coefficient of friction for various ionic liquids, natural oils, and petroleum based lubricants

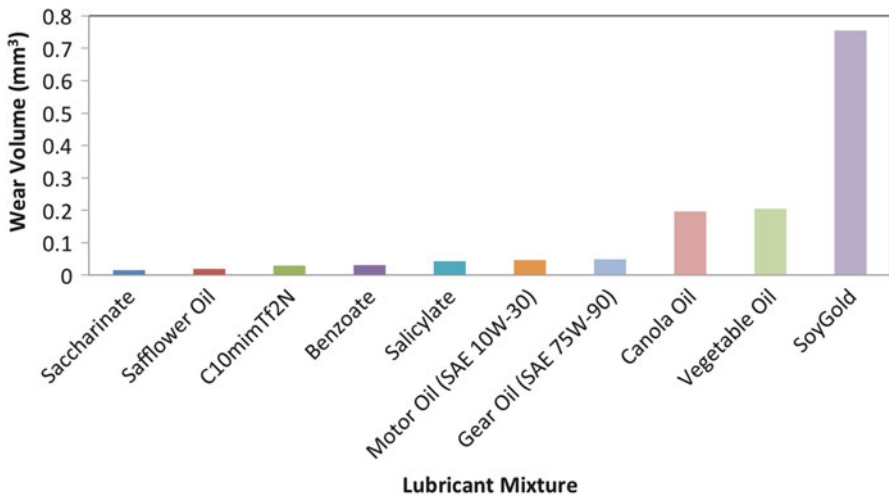


Fig. 14.12 Variation of wear rate for various ionic liquids, natural oils, and petroleum based lubricants

(Gear and Motor) oils are considered. Figures 14.11 and 14.12 shows the variation of coefficient of friction and wear rate for these lubricants.

In general, it was observed that the green ionic liquids have shown promising tribological performance when compared to other natural and petroleum based lubricants tested. The superior boundary lubrication property of ionic liquids was attributed to the development of a monolayer film formed by the anion adhering to the positively charged worn metal surface providing antiwear properties [76].

It has been anticipated that the new class of green ionic liquid lubricants will have a significant role in the fields ranging from aerospace, manufacturing, mining and mineral processing, marine equipment to magnetic storage devices in the near future [77].

9 Conclusions

Lubricants based on vegetable oils have become more relevant in the present scenario as they are derived from renewable sources. The production and usage of environment friendly lubricants will have significant impact on the society and environment, as they are completely biodegradable, significantly reducing the pollution when compared to petroleum based oils. The major drawback of vegetable oil based lubricants is their limited thermal and oxidative stability. Chemical modification of base oil can be made to overcome this problem to prepare base oils having improved thermal and oxidative stabilities. In addition to this, several green additives have also been tested under varied conditions; though few are promising, there is a long way to go in order to replace ZDDP. Further testing of lubricants or the base oils is very essential to evaluate the suitability and success of a product for a wide range of applications. The biodegradability and toxicity tests are of primary importance when the products are labeled as “Environment Friendly.” Various test methods are available to evaluate the biodegradability and toxicity of the green products, which are to be selected based on the requirement.

References

1. Wills JG (1980) Lubrication fundamentals. Marcel Dekker, New York, pp 1–2
2. Bastian ELH (1968) *Lubr Eng* 25(7):278
3. Dowson D (1979) History of tribology. Longmans Green, New York, pp 125–254
4. Woodbury RS (1959) History of the grinding machine. MIT Press, Cambridge, MA, pp 13–23
5. McCoy JS (2006) Introduction: tracing the historical development of metal working fluids. In: Jerry PB (ed) Taylor and Francis group boca raton, CRC Press, FL. Metal working fluids, CRC, pp 1–18
6. Boyde S (2002) Green lubricants, environmental benefits and impacts of lubrication. *Green Chem* 4:293–307. doi:[10.1039/b202272a](https://doi.org/10.1039/b202272a)
7. ANSI/ISO 14043:2000 (E), Environmental management - Life cycle assessment—Life cycle interpretation, First Edition (2000), NSF International
8. International Organization for Standardization. ISO 14040
9. Anastas PT, Lankey RL (2000) Life cycle assessment and green chemistry: the yin and yang of industrial ecology. *Green Chem* 2:289. doi:[10.1039/B005650M](https://doi.org/10.1039/B005650M)
10. Goyan RL, Melley RE, Wissner PA, Ong WC (1998) Biodegradable lubricants. *Lubr Eng* 54(7):10–17
11. Lea CW (2002) European development of lubricants from renewable sources. *Ind Lubr Tribol* 54(6):268–274. doi:[10.1108/00368790210445632](https://doi.org/10.1108/00368790210445632)

12. Pettersson A (2007) High-performance base fluids for environmentally adapted lubricants. *Tribol Int* 40:638–645. doi:[10.1016/j.triboint.2005.11.016](https://doi.org/10.1016/j.triboint.2005.11.016)
13. Erhan SZ, Asadauskas S (2000) Lubricant basestocks from vegetable oils. *Ind Crop Prod* 11(2–3):277–282. doi:[10.1016/S0926-6690\(99\)00061-8](https://doi.org/10.1016/S0926-6690(99)00061-8)
14. Bartz WJ (1998) Lubricants and the environment. *Tribol Int* 31:35–47. doi:[10.1016/S0301-679X\(98\)00006-1](https://doi.org/10.1016/S0301-679X(98)00006-1)
15. Anand ON, Chhibber VK (2006) Vegetable oil derivatives: environment-friendly lubricants and fuels. *J Synth Lubr* 23:91–107. doi:[10.1002/jsl.14](https://doi.org/10.1002/jsl.14)
16. Wilson B (1998) Lubricants and functional fluids from renewable resources. *Ind Lubr Tribol* 50:6–15. doi:[10.1108/00368799810781274](https://doi.org/10.1108/00368799810781274)
17. Schneider MP (2006) Plant-oil-based lubricants and hydraulic fluids. *J Sci Food Agric* 86:1769–1780. doi:[10.1002/jsfa.2559](https://doi.org/10.1002/jsfa.2559)
18. Schuchardt U, Ricardo S, Rogerio MV (1998) Transesterification of vegetable oils: a review. *J Braz Chem Soc* 9(3):199–210. doi:[10.1590/S0103-50531998000300002](https://doi.org/10.1590/S0103-50531998000300002)
19. Grylewicz S (2000) Synthesis of dicarboxylic and complex esters by transesterification. *J Synth Lubr* 17(3):191–200. doi:[10.1002/jsl.3000170303](https://doi.org/10.1002/jsl.3000170303)
20. Behr A, Westfechtel A, Gomes JP (2008) Catalytic processes for the technical use of natural fats and oils. *Chem Eng Technol* 31(5):700–714. doi:[10.1002/ceat.200800035](https://doi.org/10.1002/ceat.200800035)
21. Wagner H, Luther R, Mang T (2001) Lubricant base fluids based on renewable raw materials their catalytic manufacture and modification. *Appl Catal Gen* 221(1–2):429–442. doi:[10.1016/S0926-860X\(01\)00891-2](https://doi.org/10.1016/S0926-860X(01)00891-2)
22. Johansson LE, Lundin ST (1979) Copper catalysts in the selective hydrogenation of soybean and rapeseed oils: I. The activity of the copper chromite catalyst. *J Am Oil Chem Soc* 56(12):974–980. doi:[10.1007/BF02674147](https://doi.org/10.1007/BF02674147)
23. Hwang H-S, Erhan SZ (2001) Modification of epoxidized soybean oil for lubricant formulations with improved oxidative stability and low pour point. *J Am Oil Chem Soc* 78(12):1179–1184. doi:[10.1007/s11745-001-0410-0](https://doi.org/10.1007/s11745-001-0410-0)
24. Johnson RW, Fritz E (1988) *Fatty acids in industry*. Marcel Dekker, New York, p 667
25. Pryde EH (1984) Hydroformylation of unsaturated fatty acids. *J Am Oil Chem Soc* 61(2):419–425. doi:[10.1007/BF02678807](https://doi.org/10.1007/BF02678807)
26. Metzger JO, Biermann U (1993) Alkylaluminium dichloride induced Friedel-Crafts acylation of unsaturated carboxylic acids and alcohols. *Liebigs Annalen der Chemie* 1993(6):645–650. doi:[10.1002/jlac.1993199301105](https://doi.org/10.1002/jlac.1993199301105)
27. ASTM D2670 Standard test method for measuring wear properties of fluid lubricants (Falex Pin and Vee Block Method). ASTM International, West Conshohocken, 2011
28. ASTM D4172 Standard test method for wear preventive characteristics of lubricating fluid (Four-Ball Method). ASTM International, West Conshohocken, 2011
29. ASTM D5182 Standard test method for evaluating the scuffing load capacity of oils (FZG Visual Method). ASTM International, West Conshohocken, 2011
30. ASTM D7043 Standard test method for indicating wear characteristics of non-petroleum and petroleum hydraulic fluids in a constant volume vane pump. ASTM International, West Conshohocken, 2011
31. ASTM D2782 Standard test method for measurement of extreme-pressure properties of lubricating fluids (Timken Method). ASTM International, West Conshohocken, 2011
32. ASTM D2783 Standard test method for measurement of extreme-pressure properties of lubricating fluids (Four-Ball Method). ASTM International, West Conshohocken, 2011
33. ASTM D3233 Standard test methods for measurement of extreme pressure properties of fluid lubricants (Falex Pin and Vee Block Methods). ASTM International, West Conshohocken, 2011
34. ASTM D6121 Standard test method for evaluation of load-carrying capacity of lubricants under conditions of low speed and high torque used for final hypoid drive axles. ASTM International, West Conshohocken, 2011
35. ASTM D6425 Standard test method for measuring friction and wear properties of extreme pressure (EP) lubricating oils using SRV test machine. ASTM International, West Conshohocken, 2011

36. Battersby NS (2000) The biodegradability and microbial toxicity testing of lubricants: some recommendations. *Chemosphere* 41:1011–1027. doi:10.1016/S0045-6535(99)00517-2
37. Battersby NS, Ciccognani D, Evans MR, King D, Painter HA, Peterson DR, Starkey M (1999) An inherent biodegradability test for oil products: description and results of an international ring test. *Chemosphere* 38:3219–3235. doi:10.1016/S0045-6535(98)00552-9
38. ASTM D6139 Standard test method for determining the aerobic aquatic biodegradation of lubricants or their components using the gledhill shake flask. ASTM International, West Conshohocken
39. ASTM D6139 (2011) Standard test method for predicting biodegradability of lubricants using a bio-kinetic model. ASTM International, West Conshohocken
40. http://www.oecd-ilibrary.org/environment/oecd-guidelines-for-the-testing-of-chemicals-section-2-effects-on-biotic-systems_20745761. Accessed 3 Oct 2013
41. Schmitz RPH, Eisentrager A, Lindvogt T, Moller M, Dott W (1998) Increase in the toxic potential of synthetic ester lubricant oils by usage: application of the aquatic bioassays and chemical analysis. *Chemosphere* 36:1513–1522. doi:10.1016/S0045-6535(97)10049-2
42. Willing A (2001) Lubricants based on renewable resources—an environmentally compatible alternative to mineral oil products. *Chemosphere* 43:89–98. doi:10.1016/S0045-6535(00)00328-3
43. ASTM D6081-04 (2011) Standard test method for aquatic toxicity testing of lubricants: sample preparation and results interpretation. ASTM International, West Conshohocken
44. http://www.oecd-ilibrary.org/environment/oecd-guidelines-for-the-testing-of-chemicals-section-2-effects-on-biotic-systems_20745761. Accessed 3 Oct 2013
45. Reeves CJ, Menezes PL, Jen T-C, Lovell MR (2012) Evaluating the tribological performance of green liquid lubricants and powder additives based green liquid lubricants, 2012 STLE annual meeting & exhibition (STLE2012), St. Louis, USA
46. Honary LAT (1996) An investigation of the use of soybean oil in hydraulic systems. *Bioresour Technol* 56:41–47. doi:10.1016/0960-8524(95)00184-0
47. Arnsek A, Vizintin J (2000) Lubrication properties of rapeseed-based oils. *J Synth Lubr* 16(4):281–296. doi:10.1002/jsl.3000160402
48. Krzan B, Vizintin J (2003) Tribological properties of an environmentally adopted universal tractor transmission oil based on vegetable oil. *Tribol Int* 36:827–833. doi:10.1016/S0301-679X(03)00100-2
49. Lawal SA, Choudhury IA, Nukman Y (2012) Application of vegetable oil-based metal working fluids in machining ferrous metals—a review. *Int J Mach Tool Manuf* 52:1–12. doi:10.1016/j.ijmactools.2011.09.003
50. Xavier MA, Adithan M (2009) Determining the influence of cutting fluids on tool wear and surface roughness during turning of AISI304 austenitic stainless steel. *J Mater Process Technol* 209:900–909. doi:10.1016/j.jmatprotec.2008.02.068
51. Kuram E, Ozcelik B, Demirbas E, Sik E (2010) Effects of the cutting fluid types and cutting parameters on surface roughness and thrust force. *Proceedings of the WCE 2010, London, UK, vol II*, 30 Jun–2 Jul 2010
52. VamsiKrishna P, Srikant RR, Nageswara Rao D (2010) Experimental investigation on the performance of nano boric acid suspensions in SAE-40 and coconut oil during turning of AISI 1040 steel. *Int J Mach Tool Manuf* 50(10):911–916. doi:10.1016/j.ijmactools.2010.06.001
53. Khan MMA, Mithu MAH, Dhar NR (2009) Effects of minimum quantity lubrication on turning AISI9310 alloy steel using vegetable oil-based cutting fluid. *J Mater Process Technol* 209:5573–5583. doi:10.1016/j.jmatprotec.2009.05.014
54. Avila RF, Abrao AM (2001) The effect of cutting fluids on the machining of hardened AISI 4340 steel. *J Mater Process Technol* 119(1–3):21–26. doi:10.1016/S0924-0136(01)00891-3
55. Rahim EA, Sasahara H (2011) A study of the effect of palm oil as MQL lubricant on high speed drilling of titanium alloy. *Tribol Int* 44(3):309–317. doi:10.1016/j.triboint.2010.10.032
56. Anthony Xavier M, Adithan M (2009) Determining the influence of cutting fluids on tool wear and surface roughness during turning of AISI 304 austenitic stainless steel. *J Mater Process Technol* 209:900–909. doi:10.1016/j.jmatprotec.2008.02.068

57. Belluco W, DeChiffre L (2004) Performance evaluation of vegetable-based oils in drilling austenitic stainless steel. *J Mater Process Technol* 148(2):171–176. doi:[10.1016/S0924-0136\(03\)00679-4](https://doi.org/10.1016/S0924-0136(03)00679-4)
58. White JJ, Carroll JN, Haines HE (1997) SETC Paper 972108 and JSAE 9734412 presented at the small engine technology conference-1997, Yokohama, Japan
59. Masjuki HH, Maleque MA, Kubo A, Nonaka T (1999) Palm oil and mineral oil based lubricants—their tribological and emission performance. *Tribol Int* 32:305–314. doi:[10.1016/S0301-679X\(99\)00052-3](https://doi.org/10.1016/S0301-679X(99)00052-3)
60. Mannekote JK, Kailas SV (2009) Performance evaluation of vegetable oils as lubricant in a four stroke engine. World tribology conference, Kyoto, Japan, 12–15 Sept 2009, D-215, 331
61. Mannekote JK, Kailas SV (2011) Experimental investigation of coconut and palm oils as lubricants in four stroke engines. *Tribol Online* 6(1):76–82. doi:[10.2474/trol.6.76](https://doi.org/10.2474/trol.6.76)
62. Habereeder T, Moore D, Lang M (2009) Eco requirements for lubricant additives. In: Rudnick LR (ed) *Lubricant additives chemistry and applications*, 2nd edn., CRC Press, Taylor and Francis Group Boca Raton, FL pp 647–666
63. Becker R, Knorr A (1996) An evaluation of antioxidants for vegetable oils at elevated temperatures. *Lubr Sci* 8(2):95–116. doi:[10.1002/ls.3010080202](https://doi.org/10.1002/ls.3010080202)
64. Farnig LO (2009) Ashless antiwear and extreme-pressure additives. In: Rudnick LR (ed) *Lubricant additives chemistry and applications*, 2nd edn, CRC Press, Taylor and Francis Group Boca Raton, FL, pp 213–249
65. Sulek MW, Wasilewski T (2006) Tribological properties of aqueous solutions of alkyl polyglucosides. *Wear* 260:193–204. doi:[10.1016/j.wear.2005.02.047](https://doi.org/10.1016/j.wear.2005.02.047)
66. Platz G, Polike J, Thuning C, Hofmann R, Nickiel D, vonRybinski W (1995) Phase behavior lyotropic phases and flow properties of alkyl glycosides in aqueous solution. *Langmuir* 11:4250–4255. doi:[10.1021/la00011a015](https://doi.org/10.1021/la00011a015)
67. Lei H, Guan W, Luo J (2002) Tribological behavior of fullerene–styrene sulfonic acid copolymer as water-based lubricant additive. *Wear* 252(3–4):345–350. doi:[10.1016/S0043-1648\(01\)00888-2](https://doi.org/10.1016/S0043-1648(01)00888-2)
68. Huang W, Dong J, Li F, Chen B (2002) Study of the tribological behavior of S-(carboxylpropyl)-N-dialkyl dithiocarbamic acid as additives in water-based fluid. *Wear* 252(3–4):306–310. doi:[10.1016/S0043-1648\(01\)00887-0](https://doi.org/10.1016/S0043-1648(01)00887-0)
69. Fox NJ, Tyrer B, Stachowiak GW (2004) Boundary lubrication performance of free fatty acids in sunflower oil. *Tribol Lett* 16(4):275–281. doi:[10.1023/B:TRIL.0000015203.08570.82](https://doi.org/10.1023/B:TRIL.0000015203.08570.82)
70. Cao Y, Yu L, Liu W (2000) Study of the tribological behavior of sulfurized fatty acids as additives in rapeseed oil. *Wear* 244(1–2):126–131. doi:[10.1016/S0043-1648\(00\)00445-2](https://doi.org/10.1016/S0043-1648(00)00445-2)
71. Lovell MR, Kabir MA, Menezes PL, Higgs F (2010) Influence of boric acid additive size on green lubricant performance. *Phil Trans R Soc A* 368:4851–4868. doi:[10.1098/rsta.2010.0183](https://doi.org/10.1098/rsta.2010.0183)
72. Sawyer WG, Ziegert JC, Schmitz TL, Barton T (2006) In situ lubrication with boric acid: powder delivery of an environmentally benign solid lubricant. *Tribol Trans* 49(2):284–290. doi:[10.1080/05698190600639939](https://doi.org/10.1080/05698190600639939)
73. Menezes PL, Lovell MR, Kabir MA, Higgs F, Rohatgi PK (2012) Green lubricants: role of additive size. In: *Green tribology*, Springer, pp 265–287; doi: [10.1007/978-3-642-23681-5](https://doi.org/10.1007/978-3-642-23681-5)
74. Freemantle M (2010) *An introduction to ionic liquids*. RSC, Cambridge, UK
75. Canter N (2005) Evaluating ionic liquids as potential lubricants. *Tribol Lubr Technol* 61:15–17
76. Reeves CJ, Garvey S, Menezes PL, Dietz M, Jen T-C, Lovell MR (2012) Tribological performance of environmentally friendly ionic liquid lubricants. *Proceedings of the ASME/STLE 2012 international joint tribology conference IJTC2012*, Denver, Colorado, USA, 8–10 Oct 2012
77. Bermúdez MD, Jiménez AE, Sanes J, Carriñán FJ (2009) Ionic liquids as advanced lubricant fluids. *Molecules* 14(8):2888–2908. doi:[10.3390/molecules14082888](https://doi.org/10.3390/molecules14082888)

Questions

1. What are mineral oils? What are the limitations of mineral oil based lubricants?
2. Define green lubricants and enlist the advantages with green lubricants.
3. What are fatty acids and how are they classified?
4. What are the advantages and disadvantages of vegetable oil based lubricants?
5. Write a note on chemical modification and explain it with an example.
6. What are the different applications of vegetable oil based lubricants?
7. What are ionic liquids? What are the benefits associated with them in comparison to conventional lubricants?
8. Name a few international organizations that develop standards for lubricant testing procedures.
9. What is the significance of the biodegradability and toxicity of lubricants?
10. What are the different methods used for testing biodegradability and toxicity of the lubricants?
11. What are lubricant additives? Give one or two examples and explain their function and mode of action.

Part IV
Tribology at Nanometer Length Scale

Chapter 15

Nanotribology

Seung Ho Yang and Eui-Sung Yoon

Abstract Nanotribology is a study on friction phenomena occurring at nanometer scale. The distinction between nanotribology and conventional tribology is primarily due to the effect of surface forces in the determination of the adhesion and friction behavior of the system. Commercial bearings and lubricating oils reduce friction in the macroscopic machines; however, the tribological issues on small devices such as microelectromechanical systems and nanoelectromechanical systems require other solutions. Their high surface-to-volume ratio leads to severe adhesion and friction issues, which dramatically reduce their reliability and lifetime. This chapter reviews the basic concepts for handling the adhesion and friction issues at nanoscale. A brief summary on analytical models of single-asperity contact as well as the basic concepts on the surface forces occurring at nanometer gap are discussed in the first two sections, followed by three case studies: (1) experimental measurements on adhesion and friction at single-asperity contact, (2) experimental measurements on adhesion at multi-asperity contact, and (3) biomimetics: controlling nano-adhesion and nano-friction.

1 Introduction

Nanotribology is a study on [friction](#) phenomenon at the nanometer scale. The distinction between nanotribology and conventional tribology is primarily due to the effect of surface forces in the determination of the adhesion and friction behavior of the system. Figure 15.1 depicts an example of the adhesion failure of

S.H. Yang (✉)

Head Disk Interface, Seagate Technologies, 1200 Disc Dr, Shakopee, MN 55379, USA
e-mail: seung.yang@nist.gov

E.-S. Yoon

Center for BioMicrosystems, Korea Institute of Science and Technology, Hwarangno 14-gil
5, Seongbuk-gu, Seoul 136-791, Republic of Korea

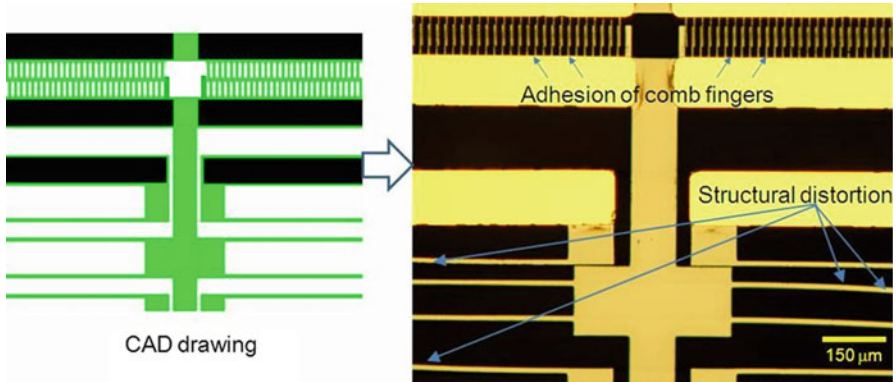


Fig. 15.1 Adhesion failure of MEMS comb drive

microelectromechanical system (MEMS) comb actuator. The strong adhesion between combs distorts the whole MEMS comb actuator.

For the conventional macroscopic machine elements, friction can be reduced using bearings and liquid lubricants, but smaller machines, such as MEMS and nanoelectromechanical systems (NEMS), require other solutions. Despite their sub-nanometer-scale accuracy, MEMS and NEMS have high surface-to-volume ratio leading to severe friction and wear issues, which dramatically reduce their reliability and lifetime [1].

For the small-scale elements, such as MEMS and NEMS, the mass and the applied load are usually negligibly small. Instead, the contact between rubbing surfaces is usually originated by surface forces. Capillary force, electrostatic force, and van der Waals forces are the known surface forces, which hold the elements from moving [2].

At nanoscale, every interaction starts at the tip of a single asperity, and the force interaction at the single-asperity contact has been given lots of intentions. Therefore, understanding the adhesion, contact, and friction phenomenon at the single-asperity contact has been a good start for investigating the real tribological issues occurring at multi-asperity contacts [3].

Over the past few decades, analytical models have been established for the single-asperity contact. Hertz [4], Johnson, Kendall, and Roberts (JKR) [5] and Derjaguin, Muller, and Toporov (DMT) [6] models are the representative ones which delivered reasonable answers on this single-asperity contact.

In these days, researchers are not only performing simulations with the mentioned analytical models but also experimentally measuring the interaction forces at the single-asperity contact [7] at nanoscale. Atomic force microscope (AFM) opened a new era for tribologists to perform direct tribological experiments using a nano sharp tip.

This chapter reviews the basic concepts for handling the adhesion and friction issues at nanoscale. Several analytical models on single-asperity contact as well as the basic concepts on the surface forces occurring at nanogap are reviewed, and the

brief summary is given in the front two sections. Then three case studies performed with AFM are given: (1) experimental measurements on adhesion and friction at single-asperity contact, (2) experimental measurements on adhesion at multi-asperity contact, and (3) biomimetics: controlling nano-adhesion and nano-friction.

2 Analytical Contact Models on Single-Asperity-On-Flat Elastic Half Space

The first analytical solution on the single-asperity contact is reported by Heinrich Hertz. In the year of 1882 Hertz [4] solved the contact problem between two elastic lenses with curved surfaces. This solution delivered a fundamental understanding on the single-asperity contact. On deriving his analytical solution, Hertz made the following assumptions: (1) the strains are small and within the elastic limit of the contacting bodies, (2) the contact area is much smaller than the characteristic radius of the contacting body, (3) the surfaces are nonconforming, (4) the contacts are frictionless, and (5) the influence of surface forces on contact formation is disregarded. For the ball-on-elastic half space contact, the Hertzian model delivered the radius of the contact area, a , and is given in (15.1):

$$a^3 = \frac{3FR}{4E^*} \quad (15.1)$$

where F is the applied load, R is the radius of the ball, and the E^* is given in (15.2):

$$\frac{1}{E^*} = \frac{1 - \nu_1^2}{E_1} + \frac{1 - \nu_2^2}{E_2} \quad (15.2)$$

where E_1 and E_2 are the elastic moduli and ν_1 and ν_2 are the Poisson's ratios of the contacting bodies. Until now, Hertzian analytical contact model has been successfully used to solve many industrial contact problems.

In the early 1970s, JKR [5] reported a similar analytical solution on the elastic contact that includes the effect of surface forces on the contact formation. In order to incorporate the effect of surface force interaction on the elastic contact into Hertzian model, they reported the JKR contact model by taking the balance between the stored elastic energy and the surface energy loss. For taking into account the effect of the surface force interaction, JKR model considered the effect of the surface force interaction only inside the contact area. The given solutions on the pull-off force, F_c , of the contacting bodies and the radius, a , of the contact area for the ball-on-elastic half space are given in (15.3) and (15.4):

$$F_c = -3\gamma\pi R \quad (15.3)$$

$$a^3 = \frac{3R}{4E^*} \left(F + 6\gamma\pi R + \sqrt{12\gamma\pi R F + (6\gamma\pi R)^2} \right) \quad (15.4)$$

where γ is the surface energy per unit area.

A competing theory was reported by DMT in the 1970s [6]. They proposed a different analytical solution of adhesion, and the model came to be known as the DMT model for adhesive elastic contact. DMT model assumed that the contact regime is the same with Hertzian contact but added attractive surface force interactions outside the contact area. The given solutions on the pull-off force, F_c , of the contacting bodies and the radius, a , of the contact area for the ball-on-elastic half space are given in (15.5) and (15.6):

$$F_c = -2\Delta\gamma\pi R \quad (15.5)$$

$$a^3 = \frac{3R}{4E^*} (F + 2\Delta\gamma\pi R) \quad (15.6)$$

where $\Delta\gamma = \gamma_1 + \gamma_2 - \gamma_{12}$ is the work of adhesion between the materials, γ_1 and γ_2 are the surface energies of the materials of the contacting bodies, and γ_{12} is the interfacial energy. The contradiction between JKR and DMT models has been studied, later, by Tabor [8]. He found a parameter which correlates the JKR and DMT models. Maugis' model [9] refined the effect of the surface force interaction by adopting Dugdale cohesive zone approximation.

3 Surface Forces

3.1 Capillary Force

Capillary condensation is the process of filling the gap with condensed liquid from the vapor. The vapor condensation occurs below the saturation vapor pressure of the pure liquid, and once the condensation occurs, a meniscus forms at the liquid-vapor interface.

This meniscus formation depends upon the surface tension of the liquid and the shape of the capillary. The size of the meniscus is governed by the Kelvin equation, which relates the Kelvin radius, R_k , of the bridge to the relative humidity (ratio of the vapor pressure, p , to the saturated vapor pressure, p_s) as [10]

$$\frac{1}{R_k} = \frac{1}{R_1} + \frac{1}{R_2} = \frac{RT \ln\left(\frac{p}{p_s}\right)}{\gamma V} \quad (15.7)$$

where V is the molar volume of water, RT is the temperature times the gas constant, γ is the surface tension of liquid water, and R_1 and R_2 are the principal radii of the capillary bridge [2].

Once the meniscus is developed at the gap, pressure difference is generated by the meniscus and is given by the Young–Laplace equation [2]

$$\Delta p = \gamma \left(\frac{1}{R_1} + \frac{1}{R_2} \right) \quad (15.8)$$

where Δp is the pressure difference across the fluid interface, γ is the surface tension (or wall tension), and R_1 and R_2 are the principal radii of curvature.

3.2 *Electrostatic Force*

The electrostatic force arises by the cumulated charges at the adjacent bodies. The electrostatic interaction between electrically charged bodies was first published in 1785 by Coulomb. He established a solution on dependence of the force between charged bodies.

Charge accumulation may also occur due to the potential difference, V . In this case, the electrostatic force per unit area is given by Maboudian and Howe [11]:

$$F_{el} = \frac{\epsilon_0 V^2}{2d^2} \quad (15.9)$$

where ϵ_0 is the permittivity of the air gap and d is the separation distance between two bodies.

3.3 *van der Waals Force*

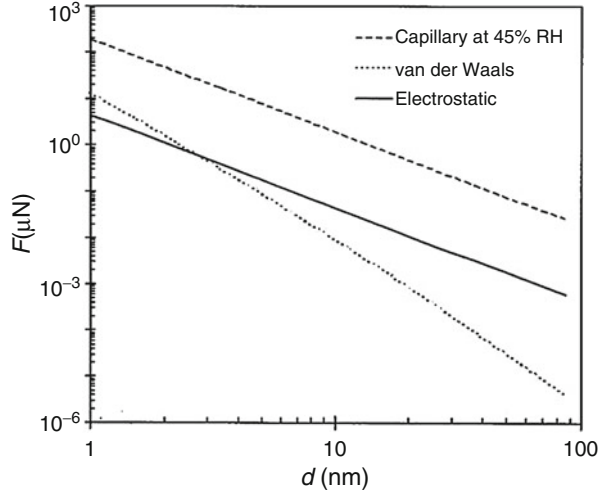
van der Waals (vdW) attraction is originated from the interaction between instantaneous dipole moments of atoms. The ability of geckos to climb on sheer surfaces has been attributed to the vdW forces between these surfaces and the spatula, or microscopic projections, which cover the hairlike setae found on their footpads [12].

Hamaker [2] reported the energy of the vdW interaction between two bodies by summing the interactions between all molecular pairs. The vdW energy for the interaction between a sphere and a flat surface separated by a distance, D , is given by Israelachvili [2]:

$$V_{vdW}(D) = -\frac{AR}{6D} \quad (15.10)$$

where R is the radius of a sphere and A is the Hamaker constant [2], which is defined as

Fig. 15.2 Comparison of attractive forces per $1 \mu\text{m}^2$ area existing at the dimensions of microstructures as a function of the separation (d) between two perfectly smooth surfaces of silicon [11]



$$A = \pi^2 C \rho_1 \rho_2 \quad (15.11)$$

where ρ_1 and ρ_2 are the number of atoms per unit volume in the two bodies and C is the coefficient in the atom–atom pair potential.

3.4 Comparison of the Surface Forces

The capillary, vdW, and electrostatic forces per $1 \mu\text{m}^2$ area are depicted in Fig. 15.2 [11]. Figure 15.2 shows that capillary forces dominate at close separation range and are thus the major contributor to the attractive forces present between two bodies.

4 Experimental Measurements on Adhesion and Friction at Single-Asperity Contact

In this section, nano-adhesion and nano-friction between a single asperity and flat samples are reported. Measurements on adhesion and friction were performed in an atomic force microscope (AFM, Multimode IIIa, Veeco).¹ In order to study the effect of radius of the single asperity on the nano-adhesion, three different AFM

¹ Certain instruments and materials are identified to adequately specify the experimental procedure. Such identification does not imply recommendation or endorsement by the National Institute of Standards and Technology, nor does it imply that the materials or the instruments identified are necessarily the best available for the purpose.

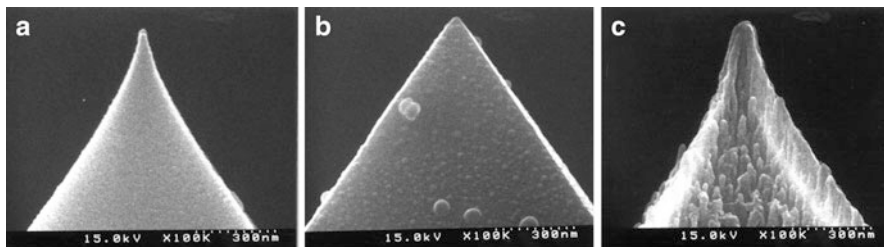


Fig. 15.3 SEM micrographs of scanning probe microscope (SPM) tips: (a) $R = 15$ nm, (b) $R = 22$ nm, (c) $R = 50$ nm [16]

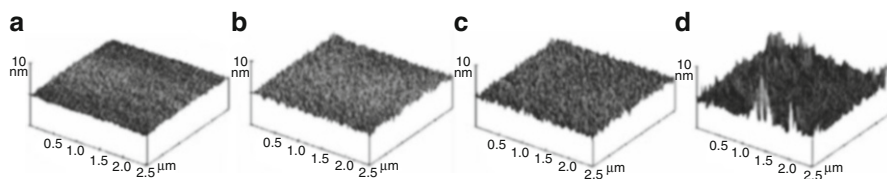


Fig. 15.4 3D surface images of Si wafer, W-DLC, DLC, and OTS SAM surfaces measured by AFM: (a) Si wafer, (b) W-DLC, (c) DLC, (d) OTS SAM [16]

tips, made of silicon nitride, whose radii of curvature are 15, 22, and 50 nm, were prepared. The AFM tips of radius 15 nm (NPS, Veeco) and 22 nm (NP, Veeco), commercial tips, are used. For preparing the tip of radius 50 nm, a commercial silicon nitride tip (tip radius of 22 nm, NP, Veeco) was wet-etched with hydrofluoric acid solution. Figure 15.3 shows the scanning electron microscope (SEM) micrographs of the tips used.

Bare Si wafer and three different flat samples are prepared; diamond-like carbon (DLC), tungsten-incorporated diamond-like carbon (W-DLC), and octadecyltrichlorosilane (OTS) self-assembled monolayer (SAM) films are deposited on Si wafers. The DLC and W-DLC films are formed on the Si wafers by a radio-frequency plasma-assisted chemical vapor deposition (rf-PACVD) method. The films are formed using benzene (C_6H_6) gas at the bias voltage of 400 V and chamber pressure of 1.33 Pa. OTS SAM was deposited on Si wafer by a series of wet etching, oxide forming, and SAM coating process. Figure 15.4 depicts the AFM images of Si wafer-, DLC-, W-DLC-, and OTS SAM-coated surfaces.

In order to study the effect of wetting on nano-adhesion, water contact angles were measured with Contact Angle meter (ERMA, goniometer type) after the deposition processes. The measured water contact angles of Si wafer, W-DLC, DLC, and OTS SAM surfaces were 22° , 55° , 62° , and 100° , respectively, and they are depicted in Fig. 15.5a.

Figure 15.5b depicts the measured adhesion forces plotted as a function of the tip radii under a relative humidity of 30 %. The adhesion force increased almost linearly as a function of the AFM tip radius. OTS SAM revealed the lowest

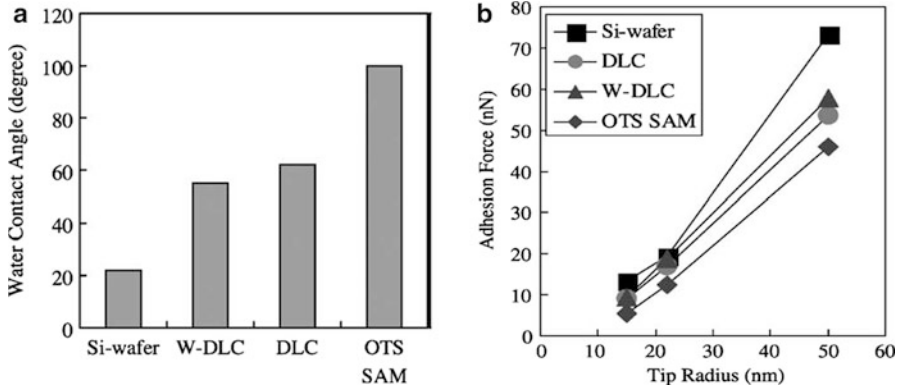


Fig. 15.5 Water contact angles of flat samples and adhesion forces: (a) Water contact angles of Si wafer, W-DLC, DLC, and OTS SAM surfaces; (b) adhesion forces of Si wafer, W-DLC, DLC, and OTS SAM surfaces plotted as a function of AFM tip radii [16]

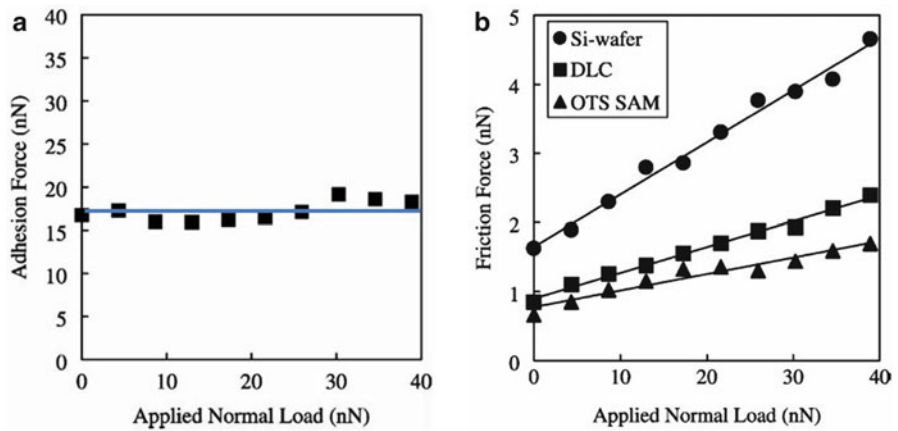


Fig. 15.6 Adhesion forces and friction forces plotted as a function of applied load: (a) Adhesion force measured at a Si wafer surface, (b) friction forces measured on Si wafer, DLC, and OTS SAM surfaces plotted as a function of the applied normal loads [16]

adhesion force among the flat samples. Also the adhesion force decreased with the water contact.

Figure 15.5b shows that there could be two key factors that affected the adhesion: contact stress and wetting characteristics. In order to study how the contact stress affected, adhesion measurements were performed at various normal loads. Also, the adhesion measurements were carried out under various relative humidity conditions in order to study how the wetting characteristic affected. Figure 15.6a shows the adhesion force between an AFM tip, whose radius is 15 nm, and the Si wafer at various normal loads under the relative humidity of 30 %. The results showed that

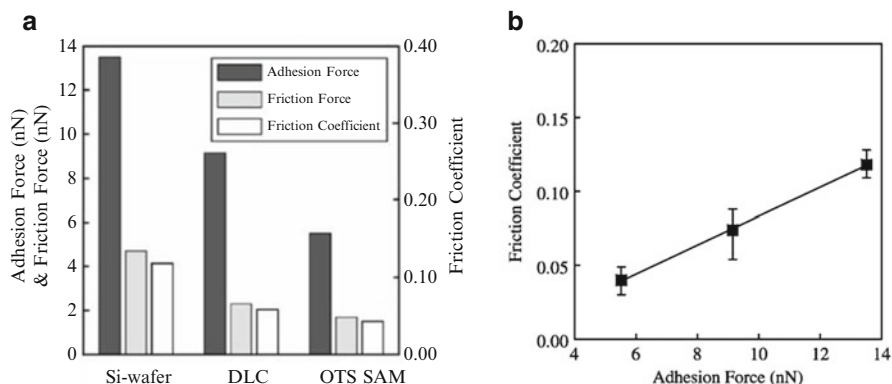


Fig. 15.7 Adhesion force, friction force, and friction coefficient of Si wafer, DLC, and OTS SAM (applied normal load, 40 nN; relative humidity, 30 %) (a); adhesion force plotted as a function of friction coefficient (b) [16]

the adhesion force is not a function of the applied load since it shows that the adhesion force did not change when increasing the normal load from 0 to 40 nN.

Friction forces were measured with the applied loads under the relative humidity of 30 %, and the results are depicted in Fig. 15.6b. It revealed that OTS SAM showed the lowest friction force, and DLC showed lower friction force than that of Si wafer. Therefore, the water wetting characteristics also played a very important role on the nano-friction. Figure 15.6b also revealed two interesting natures of single-asperity friction: (1) friction increased linearly with the applied load and (2) friction forces were found to have nonzero values even at a zero applied load.

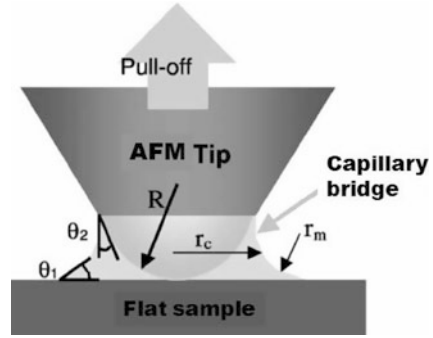
The abovementioned results showed that the capillary force is mainly responsible for this nonzero friction force at the zero applied loads.

Figure 15.7a depicts that the adhesion force, friction force, and friction coefficients decrease as the flat sample is coated with DLC and further decrease at the OTS SAM surface. It implies that the capillary force is the key to understand how the nano-adhesion and nano-friction vary.

Figure 15.7b depicts the linear increase of friction coefficient with the adhesion force. From Fig. 15.7a, b, it is found that capillary force is a major factor and governs the nano-adhesion and nano-friction between the single asperity and flat samples.

The results shown in this section clearly reveal the roles of mechanical deformation and capillary force on nano-adhesion and nano-friction. Israelachvili [2] mentioned that the micro- and nano-adhesion is affected by the short-range surface forces such as vdW force, long-range interaction forces such as capillary force, and mechanical deformation force. For the short-range interaction and mechanical deformation, several investigators [13–15] worked on the energy of adhesion and Hertzian deformation theory. The adhesion predicted based on the JKR theory [5] considered the above two concepts altogether. According to the JKR theory, the

Fig. 15.8 A schematic view of the capillary bridge between AFM tip and flat [16]



adhesion force is affected by the energy of adhesion and the tip radius as shown in (15.12):

$$F_{\text{ad}} = \frac{3}{2}\pi R\gamma \quad (15.12)$$

where F_{ad} is the adhesion force, R is the AFM tip radius, and γ is the work of adhesion between the tip and flat sample. Therefore, the results shown in Fig. 15.5b are consistent with the given JKR model. The results showed that, however, the adhesion force increased with the relative humidity when using the same surface and tip radius. It implies that the capillary force also affected greatly the adhesion interaction. The capillary formed between an AFM tip and a flat sample is depicted schematically in Fig. 15.8. If the radius of curvature of the meniscus (r_m) is negligibly smaller than the tip radius (R), the radius of capillary (r_c) could be given as (15.13) [1]

$$r_c = \sqrt{2Rr_m(\cos\theta_1 + \cos\theta_2)} \quad (15.13)$$

where θ_1 and θ_2 represent the water contact angles of flat sample and the tips. The area under the Laplace pressure is πr_c^2 . Therefore, the adhesion force generated by the meniscus can be represented as (15.14) [1], where the γ_L is the surface energy of water–air interface:

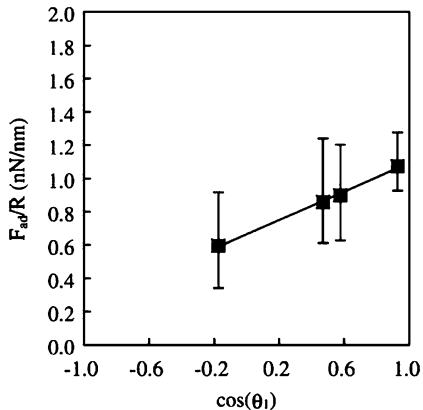
$$F_{\text{ad}} = 2\pi R\gamma_L(\cos\theta_1 + \cos\theta_2) \quad (15.14)$$

Another important parameter which must be included in the above equation (15.14) is the solid–solid adhesion force generated by the contact, and the adhesion force can be given as follows:

$$F_{\text{ad}} = 2\pi R\{\gamma_L(\cos\theta_1 + \cos\theta_2) + 2\gamma_{\text{SL}}\} = 4\pi R\gamma_{\text{SV}} \quad (15.15)$$

where γ_{SL} is the adhesion energy of solid–liquid interface and γ_{SV} is the adhesion energy of solid–air (vapor) interface. In fact, adhesion force is dependent on the

Fig. 15.9 Normalized adhesion forces of various surfaces with the water contact angle (F_{ad} : adhesion force, θ_1 : water contact angle between flat and moisture layer) [16]



adsorbed vapors from the experimental atmosphere, and the adhesion force in air may increase with the relative humidity if γ_{SV1} (moist air) > γ_{SV2} (dry air). The adhesion force in vapor must exceed $2\pi R\gamma_L(\cos \theta_1 + \cos \theta_2)$, if the value of $\gamma_L(\cos \theta_1 + \cos \theta_2)$ greatly exceeds γ_{SL} . Therefore, adhesion force can be determined by the surface energy of the liquid as it is given by (15.14) [2].

The adhesion force could be represented as the sum of the JKR adhesion force contribution and the capillary force as represented in (15.16). This adhesion force could be normalized with the tip radius (R), and then it may be possible to eliminate the tip radius effect. Equation (15.17) represents the adhesion force normalized with the tip radius:

$$F_{ad} = 2\pi R\gamma_L(\cos \theta_1 + \cos \theta_2) + \frac{3}{2}\pi\gamma R \tag{15.16}$$

$$\frac{F_{ad}}{R} = 2\pi\gamma_L(\cos \theta_1 + \cos \theta_2) + \frac{3}{2}\pi\gamma \tag{15.17}$$

In (15.17), if the capillary force dominates the adhesion, F_{ad}/R may increase linearly with $\cos \theta_1$. Measured results are normalized with the tip radius and are summarized in Fig. 15.9. F_{ad}/R increased linearly with $\cos \theta_1$ as seen in Fig. 15.9. That means when the surface becomes more hydrophobic, the adhesion force would decrease.

The nano-adhesion and nano-friction between a single asperity and flat samples, Si wafer- and W-DLC-, DLC- and OTS SAM-coated ones, were experimentally measured in various applied loads and humidities. The summary of the results are the following:

1. The adhesion force increased with the radius of the single asperity and the relative humidity. If the contact is under elastic regime, the adhesion force is not a function of the applied load.
2. Friction force showed linear increase as a function of the applied load. And the nonzero friction forces were observed at zero applied loads.

3. OTS SAM showed the highest water contact angle and revealed the lowest adhesion force. The adhesion force decreased as the flat sample became hydrophobic.
4. The adhesion force normalized with the single-asperity tip radius increase linearly with the cosine value of water contact angles of flat samples.

5 Experimental Measurements on Adhesion at Multi-Asperity Contact

Adhesion phenomenon at nanoscale between multi-asperities is receiving increased attention due to rapid deployment of small-scale devices. For the solid–solid contacts, adhesion force is proportional to the real contact area. Therefore the perturbations in the area of contact such as surface roughness would significantly alter the adhesion force. Recently, many researchers are using AFM to measure the interaction forces at nanoscale. The commercial AFM tips are usually nano sharp and could be used for measuring force interactions for the single-asperity contact. However, for the MEMS, the actual size of the elements is in microscale and the multi-asperity contact in nature. Therefore the need for attaching microscale element at the end of the AFM arises.

Ducker [17] introduced the concept of colloidal probe which is made by gluing a microsphere at the end of the cantilever. The spherical shape of the tip permits the use of elastic contact mechanic models such as JKR [5] and DMT [6] for data analyses if the glued spheres are smooth. Fuller and Tabor [18], however, suggested that roughness affects the adhesion force. Briscoe [19] also reported similar results on the effect of roughness on adhesion.

This section reports the effect of surface roughness on adhesion between glass beads of various radii and a flat silicon surface. In order to determine the exact contact spot on the colloidal probe, the reverse AFM imaging method developed by Neto and Craig [20] is adopted. By scanning regularly located nano sharp peaks with the colloidal probe, the shape of the colloidal probe is measured. Then, the surface of the colloidal probes is directly imaged by a compliant AFM cantilever which has a sharp tip to provide detailed three-dimensional surface topography of the contacting spot. The measured adhesion forces are normalized by the real area of contact which is calculated based on the digitized image of the colloidal probe.

Colloidal probes were prepared by gluing (Loctite, QuickSet Epoxy) glass beads (NIST, SRM 1003C) of various radii (3.3–17.4 μm) onto AFM cantilevers (Veeco, NPS). A typical colloidal probe is shown in Fig. 15.10.

The stiffness of each probe was individually calibrated using the added mass method [21]. The radii of colloidal probes were measured by scanning a silicon grating sample (TGT01, NT-MDT), with the colloidal probes. The measured stiffnesses and the radii are listed in Table 15.1.

Adhesion forces between the colloidal probes and the cleaned silicon (100) surface were measured under applied loads of 6–82 nN using an AFM (Multimode,

Fig. 15.10 SEM image of the colloidal probe [25]

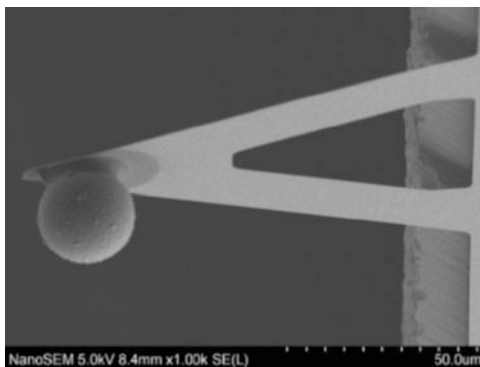
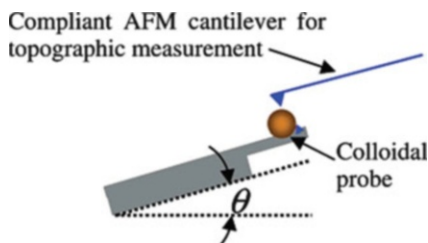


Table 15.1 Measured radii and bending stiffness of colloidal probes (at a level of confidence of approximately 95 %) [25]

Radii of glued glass balls (μm)	Bending stiffness in z-direction of AFM cantilevers (nN/nm)
3.3 (± 0.192)	0.19 (± 0.012)
7.5 (± 0.258)	0.29 (± 0.020)
8.0 (± 0.192)	0.30 (± 0.012)
8.9 (± 0.252)	0.33 (± 0.024)
9.4 (± 0.100)	0.34 (± 0.012)
10.3 (± 0.252)	0.28 (± 0.012)
11.7 (± 0.326)	0.27 (± 0.012)
13.2 (± 0.490)	0.28 (± 0.012)
17.4 (± 1.144)	0.25 (± 0.020)

Fig. 15.11 A schematic illustration of the method of measuring topography of colloidal probes [25]



Nanoscope IIIa, Veeco) in a vibration-isolated temperature and humidity-controlled environment. The silicon surface was electrically grounded by using a conducting silver paste (Three Bond, CNX-005) to avoid electrostatic charge interference. After the adhesion force measurement, the surface topographies of the silicon surface and the colloidal probes were scanned with a 0.06 nN/nm cantilever and a silicon nitride tip under contact mode. In order to scan only the contact area of the probe, a specially designed tilting holder was used to hold the colloidal probe at a specific inclined angle, and the contact surface was scanned, as shown in Fig. 15.11.

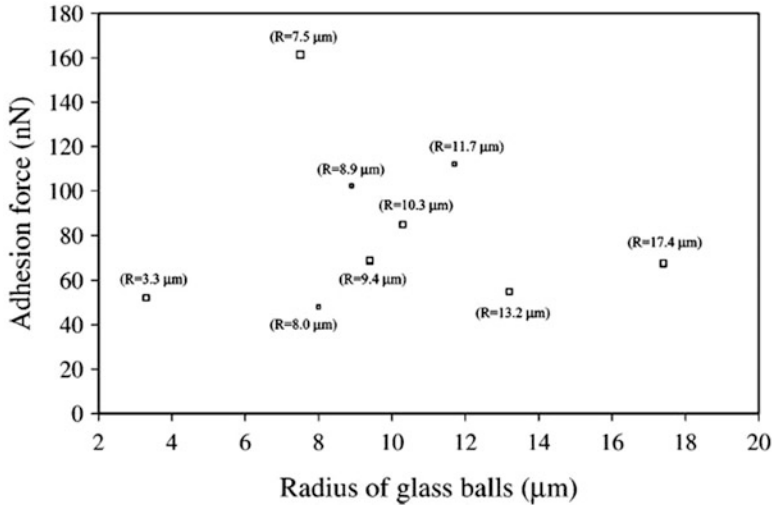


Fig. 15.12 Measured adhesion forces plotted as a function of the radii of colloidal probes (size of symbol represents uncertainty ($<5\%$) of data points) [25]

Figure 15.12 shows the measured adhesion forces as a function of the colloidal probe radii. In order to measure the topography of colloidal probes at the spot where the contact is made, a new method is developed. First, the grating sample (TGT1, NT-MDT) is scanned with the colloidal probe to identify the contact spot location. Then, the colloidal probe is mounted on an inclinable stage and scanned with a compliant AFM cantilever which has a sharp tip. The exact contact spot is located by changing the sample stage inclination angle.

According to the data in Fig. 15.12, it is not possible to find a correlation between the measured adhesion forces and the radii of the colloidal probes. In order to understand why the adhesion forces did not correlate with the probe radii, the colloidal probe surfaces are precisely examined. Figure 15.13 depicted the three-dimensional surface topography of the colloidal probes.

The AFM surface topographies showed that some of the random surface features are more than 50 times the height of the probe substrate surface roughness features. The measured root mean square (rms) roughness values of these colloidal probes range from 20.6 to 45.4 nm, and they are tabulated in Table 15.2. The silicon surface used as a counter surface for the adhesion force measurements has an rms roughness of 0.5 nm; therefore, the colloidal probe roughness tends to dominate the contact condition.

For understanding the adhesion at nanoscale, the area of contact is important. The basic concept of load-bearing area is that, when a rough surface compressed, the asperities will be deformed down to an equilibrium height at which the total compressive load is equal to the sum of the material reaction forces generated by the compressed asperities. The degree of elastic deformation may be characterized by a , the radius of contact. According to the JKR theory, the adhesion force at zero

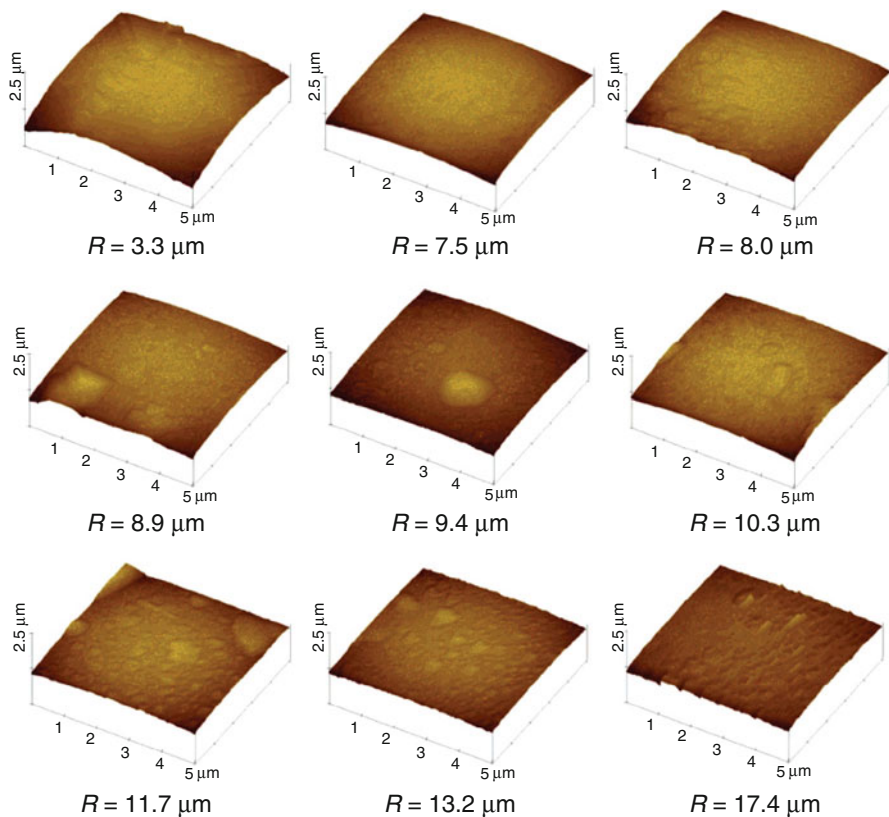


Fig. 15.13 AFM topographies of the colloidal probe tip surfaces [25]

Table 15.2 Measured rms roughness values of colloidal probes [25]

Radii of glued glass balls (μm)	rms (nm)
3.3	42.5 (± 7.8)
7.5	20.9 (± 6.8)
8.0	20.6 (± 15.4)
8.9	40.1 (± 48.6)
9.4	45.4 (± 51.2)
10.3	27.4 (± 12.4)
11.7	31.8 (± 7.8)
13.2	27.3 (± 3.4)
17.4	40.0 (± 5.2)

load leads to a radius of contact the same as that of the Hertzian contact under a load of the same amount as the adhesion force, i.e.,

$$a = \left(\frac{3NR}{4E'} \right)^{1/3} \tag{15.18}$$

where N is the normal force (the Hertzian contact load or adhesion force with no load applied), R is the radius of glass sphere, and E' is the combined elastic modulus of glass sphere and silicon surface and is given by

$$E' = \left(\frac{1 - \nu_1^2}{E_1} + \frac{1 - \nu_2^2}{E_2} \right)^{-1} \quad (15.19)$$

where E_1 and E_2 are the Young's moduli of the colloidal probe and silicon, respectively, and ν_1 and ν_2 are their Poisson's ratios. For each of these probes, (15.18) may provide the nominal radius of contact as a function of the measured adhesion force.

Since the penetration depth of the colloidal probe is much smaller than the radius of the probe, the volume under elastic deformation can be determined as follows [4]:

$$V_e = \int_0^\delta 2\pi R(\delta - z)dz = \pi R\delta^2 \quad (15.20)$$

where δ is the nominal penetration depth

$$\delta = a^2/R \quad (15.21)$$

For the multi-asperity contact, the elastic energy is stored in the compressed asperities as illustrated in Fig. 15.14. The deformed depth can be estimated by (15.20).

Figure 15.15 presents the adhesion forces normalized by the load-bearing areas. If the effect of the roughness is fully accounted by the load-bearing area, then the normalized adhesion forces should be a straight line against the probe radii. However, Fig. 15.15 showed that there is no straight-line relationship. This suggests that the multi-asperity contact is not being adequately corrected by the use of the load-bearing areas.

The failure of the load-bearing area correction leads to a more in-depth analysis on the contact. The rough surface contact at nanoscale involves multiscale behavior [22, 23]. The radii of curvature of the colloidal probes at different resolutions are determined by finding the least squares best-fit semi-ellipsoids to the data around distributed peaks. Figure 15.16 depicted the average radius of curvature obtained as a function of the resolution of discretization for the 8.0 μm radius colloidal probe. In this log-log plot, the radius of curvature is linearly dependent on the size of the discretization.

For the random multi-asperity contact, the contact may undergo sequential multiscale process migrating from one scale to another. This suggests that one asperity comes into contact first, and if the load instability occurs, the contact will expand to find other asperities to support the load. This process continues until the contact reaches deformation equilibrium. Here, the degree of compression of the asperities at the highest is examined by calculating the surface contact pressure using a numerical method based on elastic contact models:

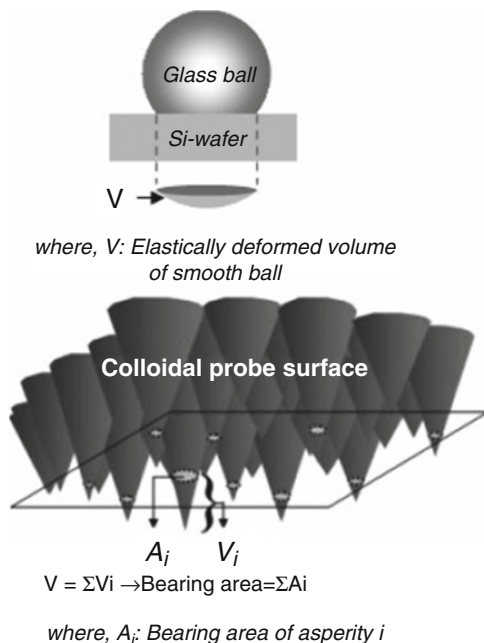


Fig. 15.14 A schematic illustration of how the elastic deformation of glass ball was calculated [25]

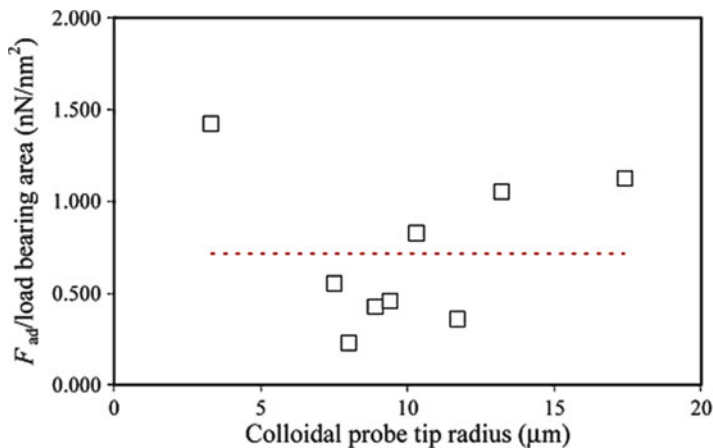


Fig. 15.15 Normalized adhesion forces plotted as a function of colloidal probe radii (size of symbol represents uncertainty (<5 %) of data points) [25]

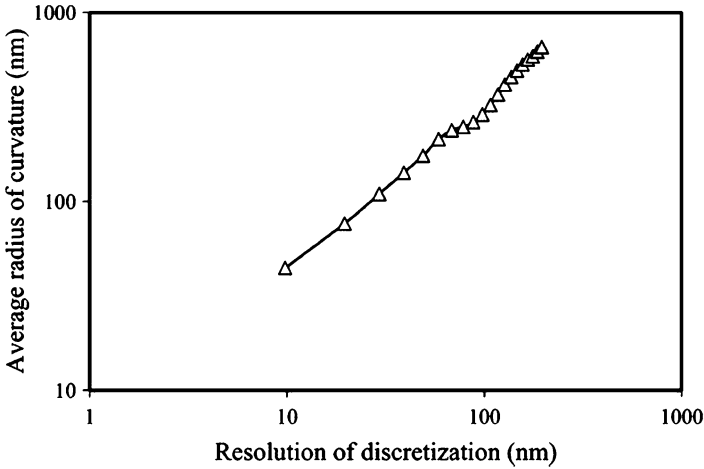


Fig. 15.16 The average radius of curvature as a function of the discretization size (for the sphere of $R = 8.9 \mu\text{m}$) [25]

$$P_m(\delta) = \frac{4E'}{3\pi} \left(\frac{\delta}{R_c}\right)^{1/2} \tag{15.22}$$

$$A_1(\delta) = \pi R_c \delta \tag{15.23}$$

$$W_1(\delta) = \frac{4E'}{3} (R_c \delta)^{1/2} \delta \tag{15.24}$$

where E' is the reduced elastic modulus, δ is the local interference, and R_c is the asperity radius of curvature.

For the numerical solution algorithm, additional characteristics are taken into account. When one asperity is compressed, the surrounding asperities are taken into the calculation; the degree of interlinking in terms of compressibility is defined as the influence coefficient. With the digitized topography over a square grid at a grid size, the corresponding numerical solution to solve the elastic contact problem of all the asperities in contact at the corresponding scale is based on the following equations [24]:

$$\sum_i \sum_j p_{ij} = P_0 \text{ or } \mathbf{q}^T \mathbf{p} = P_0 \tag{15.25a}$$

$$g_{ij} = h_{ij} + u_{ij} - u_0 \text{ or } \mathbf{g} = \mathbf{h} + \mathbf{u} - u_0 \tag{15.25b}$$

$$u_{ij} = \sum_l \sum_k K_{ik,jl} p_{kl} \text{ or } \mathbf{u} = \mathbf{A} \mathbf{p} \tag{15.25c}$$

where \mathbf{h} is the gap before the deformation, \mathbf{u} is the composite surface displacement under the applied force F_0 , \mathbf{g} is the gap after the deformation, \mathbf{p} is the interfacial pressure, u_0 is the rigid normal approach of one body to the other, P_0 is defined by

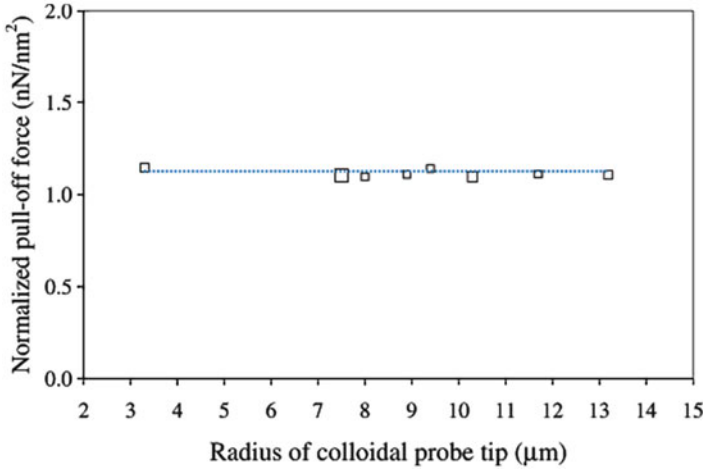


Fig. 15.17 The measured pull-off forces normalized by the real area of contact vs. the radii of glass spheres [25]

$F_0 = \Delta x \Delta y P_0$, Δx and Δy are element sizes in rectangular grid, \mathbf{q} is a vector of ones, $K_{ik,jl}$ are the influence coefficients, and \mathbf{A} is the influence coefficient matrix. The above three equations show interface conformity, elastic deformation, and equilibrium equation. The influence coefficient $K_{ik,jl}$ is the normal displacement at the center of element (i, j) due to a unit pressure acting on the element (k, l) . They are determined by integrating the Boussinesq relationship between the concentrated force and the surface normal deflection:

$$K_{ik,jl} = \frac{1}{\pi E'} \int_{y_l - a_y/2}^{y_l + a_y/2} \int_{y_k - a_x/2}^{y_k + a_x/2} \frac{dx \, dy}{\sqrt{(x_i - x)^2 + (y_i - y)^2}} \quad (15.26)$$

By solving (15.25a–15.25c), the area of contact can be determined by summing up the areas of each element (i, j) . Figure 15.17 presents the adhesion forces normalized by the real contact areas estimated by the multiscale numerical sequential contact model. In this figure, the 17.4 μm radius probe is not included, since it was not possible to define its scale of equilibrium elastic contact because of its sharp edges in the digitized topography. It is shown that the normalized adhesion force falls onto a horizontal straight line. This result suggests that the adhesion force is a function of the real contact area.

On the basis of the results described above, the conclusion is summarized as follows:

1. Measured adhesion force data scattered a lot and did not show any correlation on the radii of the colloidal probe. This is because of the nanoscale features which led to the multi-asperity contact.
2. The load-bearing area correction did not deliver reasonable correction in terms of the deviation normalized by the mean value.

3. The use of a multiscale contact model provides estimation of the contact areas which proves to be a more effective correction model for adhesion.

6 Biomimetics: Controlling Nano-Adhesion and Nano-Friction

The topographical and chemical modifications of engineering surfaces are newly emerging technologies that could control the nano-adhesion and nano-friction issues. Topographical modifications, such as laser texturing and dimple formation, have been investigated to reduce the real area of contact [26].

Biomimetics is the study on imitating the nature's own solution to engineering objects [27]. Research work on the Lotus effect [28] is such an example. It is characterized by the unique surface patterns as well as the hydrophobic properties of the epicuticular waxes. Neinhuis and Barthlott [28] characterized the water-repellent and self-cleaning nature of the lotus leaf. Recently, Watanabe et al. [29, 30] reported an ultrahydrophobic nature of a polymeric thin film that was prepared by combining a phase separation of tetraethyl orthosilicate induced by the addition of an acrylic polymer and subsequent fluoroalkylsilane coating. In this section, the effect of topography on wetting, adhesion, and friction was studied experimentally with various ion beam-treated polymeric surfaces.

Polytetrafluoroethylene (PTFE; Teflon, Dupont) surfaces were modified by irradiating the accelerated argon ion beam. Figure 15.18 shows the schematic diagram of the ion beam-assisted surface modification device.

The main concept of the surface modification by the ion beam irradiation is shown in Fig. 15.19. Under the energetic ion bombardment, surface defects in the PTFE are formed. During the further bombardment, the defects grow and the surface layer becomes filament-like structures [31]. The conditions for the modification of PTFE surfaces and the average roughness are summarized in Tables 15.3 and 15.4.

The surface topography, adhesion, and friction were measured with an AFM (Multimode AFM, NanoScope IIIa, Digital Instruments), using an AFM tip (Veeco, NPS). The static water-wetting angle was measured with a contact anglemeter (ELMA, Goniometer Type) to evaluate the hydrophobic characteristics.

The microscale adhesion forces were measured with a custom-made ball-on-flat micro-adhesion tester as is shown in Fig. 15.20a. The adhesion force between a Si_3N_4 ball and the PTFE sample was measured under a load of 100 μN . Micro-friction tests were performed with a custom-made ball-on-flat micro-tribotester under reciprocating motion, and the close-up photo of the micro-tribotester is shown in Fig. 15.20b. The friction force between a Si_3N_4 ball and a PTFE sample was measured under a normal load of 100 μN and a sliding speed of 1 mm/s. All of the tests were performed under an ambient condition of 20–24 °C and 27–33 % RH.

Fig. 15.18 A schematic view of the ion beam-assisted surface modification device used for the modification of PTFE samples

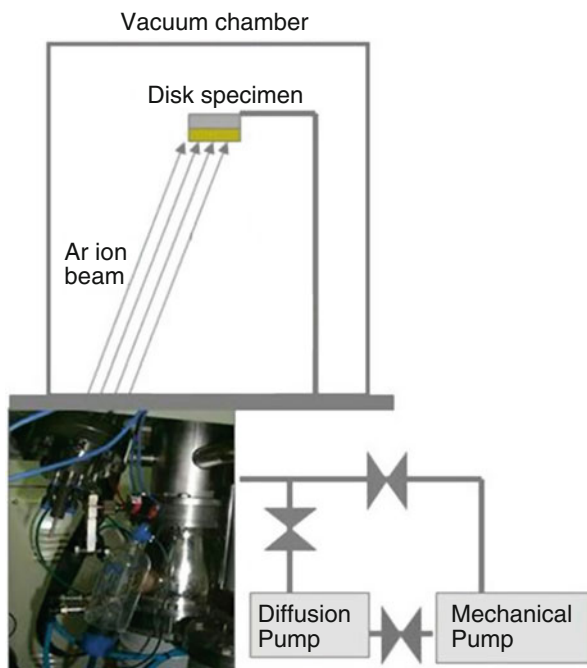


Figure 15.21 depicts the surface topography of the ion beam-treated PTFE samples as a function of the argon-ion dose. The shapes of surface asperities were changed from dull to sharp as a function of argon-ion dose.

The water-wetting angles increased as a function of the argon-ion dose as shown in Fig. 15.22, and an ultrahydrophobic nature [32] was observed when the argon-ion dose was over 10^{17} ions cm^{-2} .

Figure 15.23 depicts the nano-adhesion force and nano-friction force of the PTFE samples measured with AFM. The nano-adhesion force revealed no change as a function of the argon-ion dose as shown in Fig. 15.23a, even though the water-wetting angle had increased. It was considered that the nano-scale surface topography of these samples did not affect the nano-scale adhesion.

The nano-friction coefficient increased as a function of the ion dose as shown in Fig. 15.23b. This result could be explained by the local increase of friction force resulting from the ratcheting mechanism proposed by Bhushan [26]. He noted that the ratcheting mechanism is valid when the tip is assumed to be small compared to the size of the asperity in the ratcheting mechanism. In this study, the asperity scale on the ion beam-treated PTFE surfaces is relatively large compared to the Si_3N_4 tip. Therefore, in order to take into account the effect of scale on adhesion and friction, the microscale surface roughness was introduced.

The micro-roughness of the four PTFE samples was measured with a profilometer, and the results are depicted in Fig. 15.24. The average micro-roughness increased as a function of the ion dose, and the water-wetting angle

Fig. 15.19 A schematic illustration of the surface-roughening method of PTFE samples using argon-ion bombardment [34]

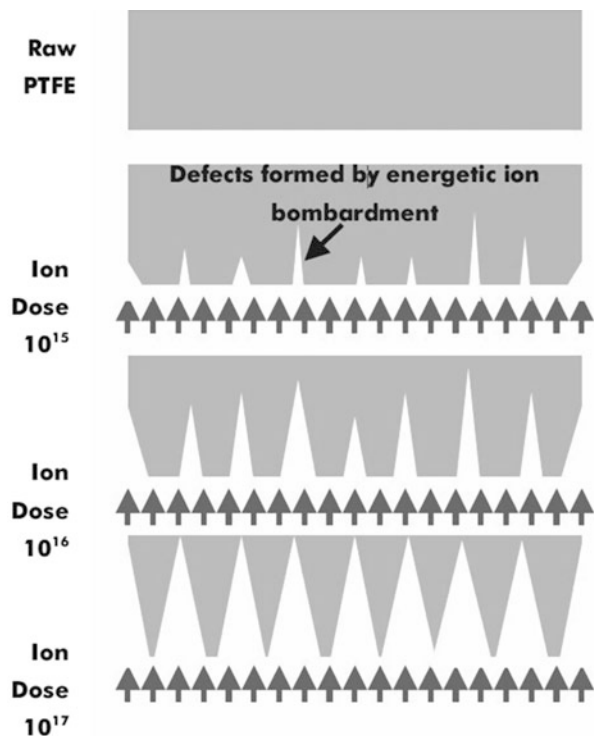


Table 15.3 Treatment conditions and static wetting angles of PTFE samples [34]

Specimens	Surface treatments	Static wetting angles (θ) ($^{\circ}$)	Max. deviation in wetting angle ($\Delta\theta$) ($^{\circ}$)
PTFE plate modified by argon-ion beam	Raw PTFE	105	+8/-12
	Ar^+ 10^{15} ions cm^{-2}	119	+12/-12
	Ar^+ 10^{16} ions cm^{-2}	138	+20/-11
	Ar^+ 10^{17} ions cm^{-2}	160	+12/-20

Table 15.4 Difference of surface roughness (R_a) of PTFE samples at the cutoff length [34]

Specimens	Average roughness, R_a (nm)	
	Cutoff length 0.8 mm	Cutoff length 0.2 μm
Raw PTFE	290	41
Ar^- ion dose 10^{15}	670	43
Ar^+ ion dose 10^{16}	740	18
Ar^+ ion dose 10^{17}	1,520	38

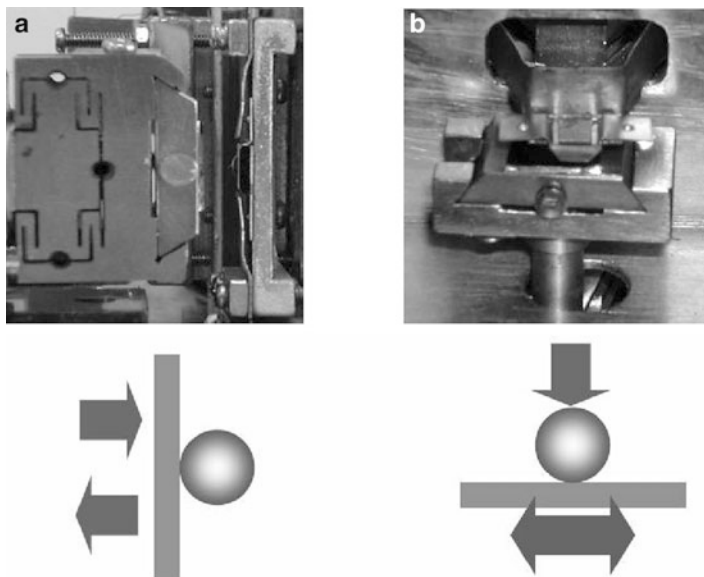


Fig. 15.20 Close-up view of (a) a ball-on-flat-type micro-adhesion tester and (b) a ball-on-flat-type reciprocating micro-tribotester [34]

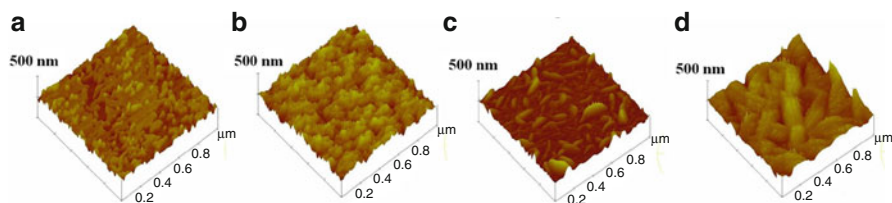


Fig. 15.21 Three-dimensional surface topographies of the ion beam-treated PTFE samples as a function of the argon-ion dose: (a) Raw PTFE, (b) ion dose 10^{15} ions/cm², (c) ion dose 10^{16} ions/cm², (d) ion dose 10^{17} ions/cm² [34]

increased with the ion dose. These results revealed a good agreement with other works [32, 33], in which it was stated that the ultrahydrophobic nature mainly results from topographic changes, although the bombardment of PTFE ($-\text{CF}_2-\text{CF}_2-$) by argon ions can result in both chain scission and cross-linking [33]. Therefore, it could be explained that the ion beam changed not only the nano-roughness but also the micro-roughness of those PTFE samples and resulted in the increase of the water-wetting angle.

The micro-adhesion force decreased as a function of the ion dose, as depicted in Fig. 15.25a, which is different from that of nano-adhesion. Figure 15.25a suggests that the capillary force acting between a Si_3N_4 ball and the PTFE surfaces decreases as the surface becomes hydrophobic as a function of the argon ion. Therefore, it

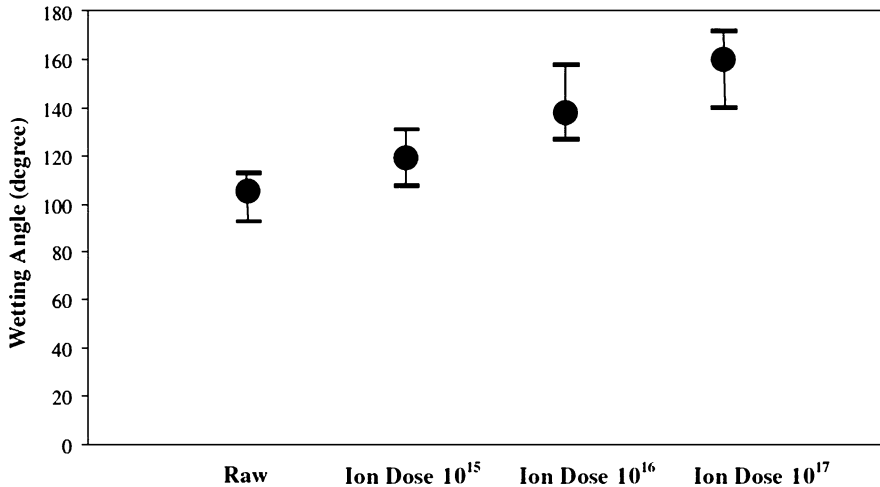


Fig. 15.22 Static water-wetting angles of the ion beam-treated PTFE samples as a function of the argon-ion dose (in ions cm⁻²) [34]

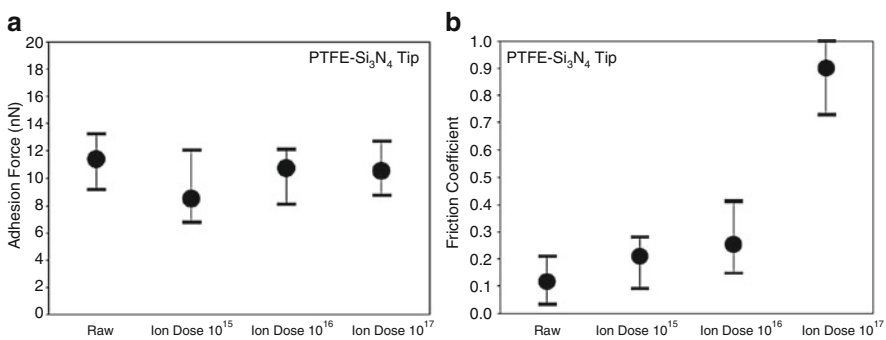


Fig. 15.23 (a) Nanoscale adhesion forces and (b) friction coefficients of the ion beam-treated PTFE samples measured with AFM as a function of the argon-ion dose (in ions/cm²) [34]

could be argued that the topographical changes of PTFE samples greatly affected the microscale adhesion. The micro-friction decreased as a function of the ion dose, as shown in Fig. 15.25b. It was thought that the real contact area between the Si₃N₄ ball and ion beam-treated PTFE surfaces decreased as the surfaces became rough as a function of the ion dose, so the micro-friction force decreased, and this result was different from that of nano-friction, too. Therefore, it could be concluded that the tribological characteristics are greatly affected by the real scale of the rubbing bodies.

When measuring the surface roughness, important information on the micro- and nano-tribological characteristics could be missed, if the scale effect of surface roughness is not considered. The ratio of the radius of tip or ball to the average

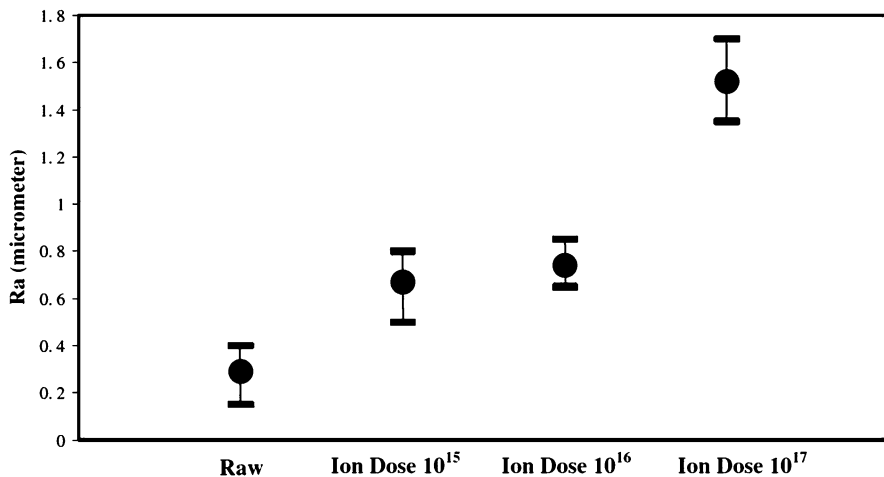


Fig. 15.24 Microscale surface roughness (R_a) values of the ion beam-treated PTFE samples as a function of the argon-ion dose (in ions/cm²) [34]

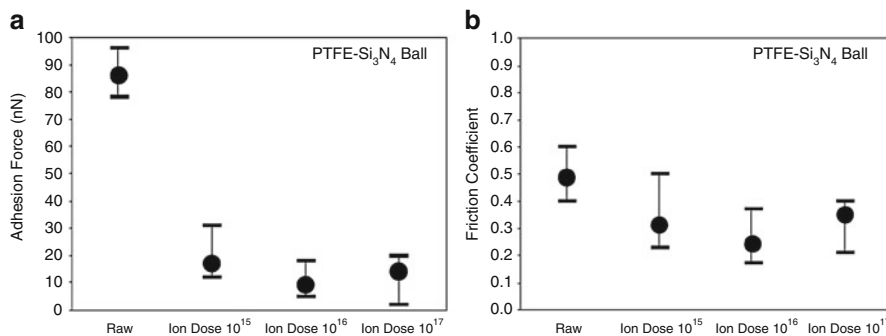


Fig. 15.25 Microscale adhesion forces and friction coefficients of the ion beam-treated PTFE samples measured with (a) micro-adhesion tester and (b) micro-friction tester as a function of the argon-ion dose [34]

surface roughness, the contact size ratio, at a standard cutoff length should be considered in order to obtain better test results between the micro- and nanoscale tribo testing:

$$\text{contact-size ratio} = \frac{\text{radius of tip}}{\text{surface roughness}(R_a)} \tag{15.27}$$

In this section, the contact size ratio of the PTFE samples was on the order of 10³ for the micro-tribotesting and 10⁻¹ for the nano-tribotesting. The contact size ratios of the samples are summarized in Fig. 15.26. In the case of the plasma-treated, thin polymer films, the contact size ratio was on the order of 1–10 for nano-tribo testing.

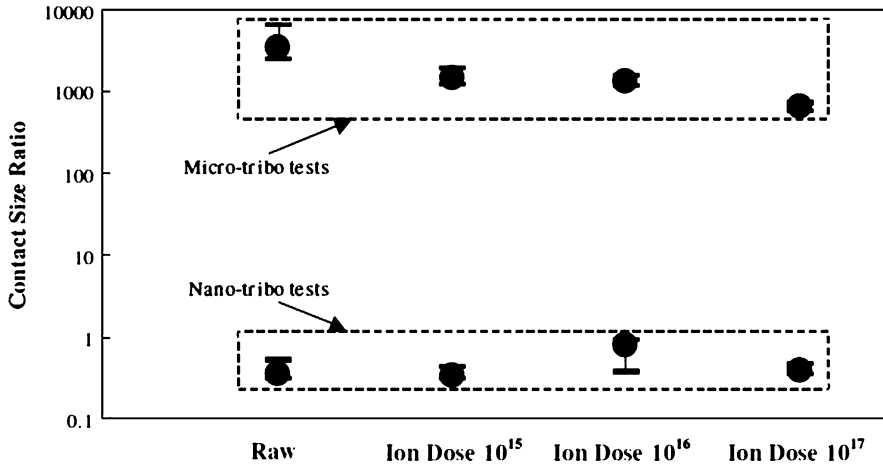


Fig. 15.26 Contact size ratios of the ion beam-treated PTFE samples and calculated using the contact configuration of the micro-adhesion tester and atomic force microscope [34]

It is found that the tribotests could provide misleading results, if the contact size ratio is less than 1. This happens when the surface roughness is larger than the radius of the tip or the ball of the specimen.

The experimental results can be summarized as follows:

1. Ion beam-treated PTFE samples were rendered increasingly hydrophobic as a function of the ion dose. The variations in surface topography affected the water wetting greatly.
2. The wetting characteristics of the PTFE samples were strongly dependent upon the micro-roughness. The asperity sharpness affected the apparent water-wetting characteristics.
3. Micro-adhesion and micro-friction of the ion beam-bombarded PTFE depend on the wetting characteristics. However, nano-tribological characteristics revealed almost no dependency on the wetting characteristics and surface roughness, i.e., the tribological characteristics on the nanoscale showed different results from those on the microscale.
4. The ion beam-bombarded PTFE samples are roughened as a function of ion dose. The effect of contact size ratio must be taken into account when tribotesting on the micro- and nanoscale.

Acknowledgement This work was supported by the Next Generation Robotics and Automation program and was performed in part in the NIST Center for Nanoscale Science and Technology Nano Fabrication Clean Room.

References

1. Maboudian R (1998) *MRS Bull* 23:47–51
2. Israelachvili JN (1992) *Intermolecular and surface forces*. Academic, Boston, MA
3. Bowden FP, Tabor D (2001) *The friction and lubrication of solids*. Oxford University Press, Oxford
4. Johnson KL (1985) *Contact mechanics*. Cambridge University Press, Cambridge
5. Johnson KL, Kendall K, Roberts AD (1971) *Proc R Soc Lond A* 324:301–313
6. Derjaguin BV, Muller VM, Toporov YP (1975) *J Colloid Interface Sci* 53:314–326
7. Bhushan B (1999) *Handbook of micro/nanotribology*, 2nd edn. CRC, Boca Raton, FL
8. Tabor D (1977) *J Colloid Interface Sci* 58(1):2–13
9. Maugis D (1992) *J Colloid Interface Sci* 150:243–269
10. Rowlinson JS, Widom B (1982) *Molecular theory of capillarity*. Clarendon, Oxford
11. Maboudian R, Howe RT, Vac J (1997) *Sci Technol B* 15(1):1–20
12. Autumn K, Sitti M, Liang YA, Peattie AM, Hansen WR, Sponberg S, Kenny TW, Fearing R, Israelachvili JN, Full RJ (2002) *PNAS* 99(19):12252–12256
13. Yamada S, Israelachvili JN, Phys J (1998) *Chem B* 102:234–244
14. Myshkin NK, Petrokovets MI, Chizhik SA (1999) *Tribol Int* 32:379–385
15. Ando Y, Ino J (1997) *J Tribol* 119:781–787
16. Yoon E-S, Yang SH, Han H-G, King H (1991) *Wear* 254:974–980
17. Ducker WA, Senden TJ, Pashley RM (1991) *Nature* 353:239–241
18. Fuller KNG, Tabor D (1975) *Proc R Soc Lond Ser A* 345:327–342
19. Briscoe BJ, Panesar SS (1992) *J Phys D Appl Phys* 25:A20–A27
20. Neto C, Craig VSJ (2001) *Langmuir* 17:2097–2099
21. Cleveland J, Manne S (1993) *Rev Sci Instrum* 64:403–405
22. Bora CK, Flater EE, Street MD, Redmond JM, Starr MJ, Carpick RW, Plesha ME (2005) *Tribol Lett* 19:37–48
23. Greenwood JA (1992) Problems with surface roughness. In: Singer IL, Polack HM (eds) *Fundamentals of friction, macroscopic and microscopic processes*. Kluwer, Dordrecht, pp 57–76
24. Allwood J (2005) *ASME J Tribol* 127:10–23
25. Yang SH, Zhang H, Hsu SM (2005) *Langmuir* 23:1195–1202
26. Bhushan B (1999) *Wear* 225:465–492
27. Spencer ND, Lee S, Perry SS, Lim MS (2002) *Proceedings of the second international workshop on Microtribology, Ishigaki Island, Japan, 16–19 April 2002*
28. Neinhuis C, Barthlott W (1997) *Ann Bot* 79:667–677
29. Nakajima A, Abe K, Hashimoto K, Watanabe T (2000) *Thin Solid Films* 376:140–143
30. Nakajima A, Saiki C, Hashimoto K, Watanabe T, Mater J (2001) *Sci Lett* 20:1975–1977
31. Michael R, Stulik D (1986) *J Vac Sci Technol A* 4:1861–1865
32. Extrand CW (2002) *Langmuir* 18:7991–7999
33. Cho JS, Choi WK, Koh SK, Yoon KH (1998) *J Vac Sci Technol B* 16:1110–1114
34. Yoon E-S, Yang SH, King H, Kim K-H (1998) *Tribol Lett* 15(2):145–154

Problems

1. For a ball-on-flat elastic half space contact, discuss the difference in the radii of contact for the Hertz, JKR, and DMT models.
2. Explain why the capillary force under single-asperity contact depends on the water-wetting angles of the surfaces.

3. If an AFM tip made of conductive silicon is approaching onto a gold surface in vacuum, jump-to-contact usually occurs. Explain this using the surface force interaction between the AFM tip and the gold surface.
4. Explain the origin of the nonzero friction at zero applied load.
5. Suppose you are designing a micro-ball. If you know the material properties, you may calculate the adhesion force with the 3D drawings by using Hertz, JKR, and DMT models. Can you estimate the accuracy of the calculated values?
6. Define the meaning of biomimetics.

Solutions

1. Hertzian model: $a^3 = \frac{3FR}{4E^*}$
where F is the applied load, R is the radius of the ball, and the E^* is given by

$$\frac{1}{E^*} = \frac{1 - \nu_1^2}{E_1} + \frac{1 - \nu_2^2}{E_2}$$

where E_1 and E_2 are the **elastic moduli** and ν_1 and ν_2 are the **Poisson's ratios** of the contacting bodies.

$$\text{JKR model: } a^3 = \frac{3R}{4E^*} \left(F + 6\gamma\pi R + \sqrt{12\gamma\pi R F + (6\gamma\pi R)^2} \right)$$

where γ is the surface energy per unit area.

$$\text{DMT model: } a^3 = \frac{3R}{4E^*} (F + 2\Delta\gamma\pi R)$$

2. The adhesion force could be represented as the sum of the JKR adhesion force contribution and the capillary force as represented in (15.16). This adhesion force could be normalized with the tip radius (R), and then it may be possible to eliminate the tip radius effect. Equation (15.17) represents the adhesion force normalized with the tip radius:

$$F_{\text{ad}} = 2\pi R\gamma_L (\cos\theta_1 + \cos\theta_2) + \frac{3}{2}\pi\gamma R \quad (15.16)$$

$$\frac{F_{\text{ad}}}{R} = 2\pi\gamma_L (\cos\theta_1 + \cos\theta_2) + \frac{3}{2}\pi\gamma \quad (15.17)$$

In (15.17), if the capillary force dominates the adhesion, F_{ad}/R may increase linearly with $\cos\theta_1$. Measured results are normalized with the tip radius and are summarized in Fig. 15.9. Figure 15.9 shows that F_{ad}/R increased linearly with $\cos\theta_1$. That means when the surface becomes more hydrophobic, the adhesion force would decrease.

3. Jump-to-contact in AFM usually occurs when F_s/z (where F_s is the surface force, and z is the gap distance) becomes greater than the stiffness of AFM cantilever. The surface force usually increases with decreasing gap distance. Thus, when the

AFM tip is far out from the sample surface, $k_c > F_s/z$ and the AFM tip do not exhibit jump-to-contact. When approaching the AFM tip onto the surface, the cantilever stiffness, k_c , is constant but F_s/z increases. At a threshold point where $F_s/z = k_c$, jump-to-contact occurs.

4. Figure 15.6b shows that the friction at zero applied load is not zero. The friction occurs when there is load on it. That means some other, nonmechanical load is already given onto the AFM tip. Figures 15.8 and 15.9 clearly show that it is capillary force.
5. Only a rough estimate of the force can be obtained. This is because the real contacting surfaces including the micro-ball are inherently rough. One example is shown in Fig. 15.12 where it is seen that the deviation range is unbelievably large.
6. Biomimetics is an interdisciplinary subject which involves the study of the structure and function of biological systems as models for the design and engineering of materials and machines.

Chapter 16

Surface Probe Techniques

K. Anantheshwara and M.S. Bobji

Abstract Study of surface properties is of significance in tribology since interaction between objects takes place at surface level and also surface properties are different than the bulk of the material. This chapter discusses about different surface probe techniques which are used to characterize the surface at nanoscale. Depending upon the interaction of the probe (electron/mechanical) with the sample, different techniques are developed. In case electron probe, scanning electron microscope and transmission electron microscope are used to study surface as well as subsurface information. In case of mechanical probes, atomic force microscope and nanoindentation techniques are widely used in nanoscale tribology. Each of the above techniques is discussed in this chapter with the working principle to application along with the limitations. Finally, recent developments in real-time tribological studies or in situ techniques are discussed.

1 Introduction

Surface of an object delimits its volume and defines the region of interaction with its environment. Contact of two objects in relative motion, be it is rolling, sliding, or combination of two, involves the interaction of number of surfaces and interfaces. The physical and the chemical properties of the surfaces determine the friction and wear behavior of the surfaces. Properties of the surfaces will be different than that of the bulk due to the different physiochemical environment. Tribological behavior relies on the surface properties of materials that come into contact. So studies of surface properties are important in tribology.

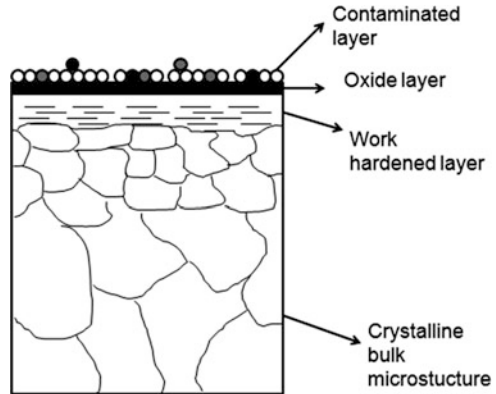
A solid surface irrespective of the method of formation contains irregularities or deviations in both physical and chemical nature. Further, the physiochemical

K. Anantheshwara (✉) • M.S. Bobji

Department of Mechanical Engineering, Indian Institute of Science, Bangalore 560012, India

e-mail: anantheshwara.k@gmail.com

Fig. 16.1 Schematic representation of a surface



interaction of the surface with its surroundings or with other surfaces leads to its modification in case of metals, alloys, ceramics, and polymers. This leads to formation of highly modified region close to the surface and can be thought of being composed of different layers. These surface layers have different zones, each with different physiochemical properties.

Figure 16.1 shows the cross-sectional view of a typical surface of metals with different layers present in it. The outermost layer consists of adsorbed gases such as water vapor, hydrocarbons, and atmospheric pollutants like dust particles. The second layer is made up of products arising from the interaction with the environment and generally consists of oxides whose composition depends on both the base metal and the environment. The third layer corresponds to an amorphous layer formed due to mechanical contact interactions with other surfaces called as “Beilby layer” [1, 2]. The fourth zone is the mechanically deformed layer due the residual stresses. Fifth zone corresponds to the unmodified structure of the bulk material.

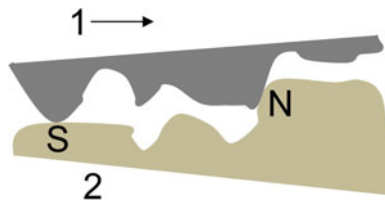
In case of ceramic materials, oxide layer may or may not be present. However, adsorbents (water, hydrocarbons) may be still present on the surface from the environment. In case of polymers, much similar to ceramics, the outermost surface layer may not be oxide as it is in case of metals and alloys. But adsorbents are certainly present on the solid surface.

In addition to this surface layers in different types of material, whole texture of the surface layer has a geometric property characterized by a series of irregularities having different amplitudes and frequency of occurrence. This particular property, the surface roughness/texture, is the fundamental importance in the study of friction and wear and lubrication.

1.1 Why Surface Properties Are Important in Tribology?

Why surfaces are so important in the study of tribology? First of all, the properties of surface atoms are generally different from those of the same atoms in the bulk;

Fig. 16.2 Schematic representation of two surfaces coming into contact



and second, in any interaction of a solid with another phase, the surface atoms are the first to be encountered.

When two solid surfaces come into contact (Fig. 16.2), the contact happens at the tips of irregularities which are called as asperities. Even the smoothest surface contains roughness at atomic scale. Surface roughness has a huge influence on many important physical phenomena such as contact mechanics, sealing, adhesion, and friction. As the top surface is moved against the bottom surface (Fig. 16.2), interaction between the asperities takes place, at some places the asperities may slide against each other (point S) and in some other places the asperities indent with each other (point N). So the macroscopic contact can be summarized as the contact interaction taking place at the asperity level. So it is important to study the interaction at the asperity level.

During the interaction of the asperities, asperity region can deform either elastically or plastically depending on the local contact pressure. With the deformation of the asperity, the adsorbed layers, and oxides, worked area also gets deformed. In some cases depending upon the mechanical properties of the surface layers, they may deform with the material, in other cases the films get disrupted or dislodged, and contact between the clean surfaces takes place. At this point the basic material properties of solids themselves become extremely important in determining friction and wear characteristics of the materials.

From experiments [3] it is evident that the presence of something as simple as hydrogen on a surface can influence the friction behavior of materials. Tribological properties of surface and surface films are extremely sensitive to the adsorbed species, surface texture, and orientation of the solid surface. This extreme sensitivity brings out the importance of the use of surface characterization tools to understand the tribological mechanisms.

1.2 Why at Nanoscale?

The important question needs to be answered now is “why we have to study tribology at nanometer length scale?” When surfaces come into contact, the contact happens between the asperities. There will be wide distribution in the size of asperities, across many length scales. A variety of phenomena take place in any practical contact. In reality, friction is a complex multiscale phenomenon that depends both on the atomic interactions inside the contacts and on the

macroscopic-scale, elastic, and plastic deformation around the regions surrounding the contact that determine the morphology and stress distribution within these contacts. Atomic interactions will depend upon the atomic properties of interacting material. Understanding the atomistic mechanisms within the contact is fundamental to many basic and applied problems, such as wetting, capillarity, adhesion, lubrication, sealing, hardness, micro-/nanoindentation, atomic-scale probing, surface modification, and manipulation. Although micro-/nanotribological studies are inevitable in study of micro-/nanostructures, these studies are also valuable in fundamental understanding of interfacial phenomena in macrostructures to provide a bridge between science and engineering. Exploring these phenomena at the nanoscale regime often requires experimental probes. This chapter will discuss about the different surface probe techniques to characterize the surfaces at nanometer length scale from tribology point of view.

2 Different Probes

Numerous surface diagnostic techniques are available that provide direct information on surface morphology, surface composition, chemical state, molecular identity of adsorbents, and structure. A surface can also be characterized by its topographic physiochemical and mechanical properties. Three different kinds of probes are used for surface characterization, namely, photon (optical and X-rays), electron, and mechanical probes. Optical probe techniques (profilometer, spectroscopy) are discussed in other chapter of this book. In this chapter the different surface characterization techniques using electron and mechanical probes are discussed.

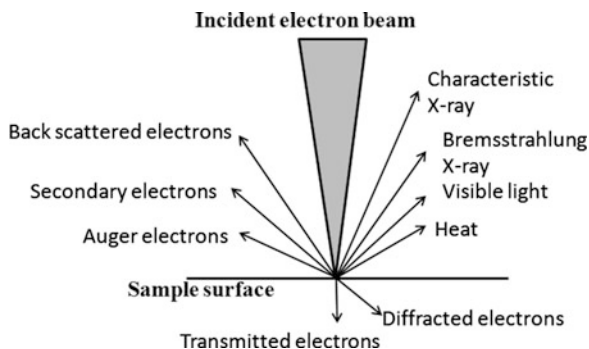
2.1 Electron Probe

Optical microscopes, frequently used to study the friction and wear of the materials, suffer with the limit of optical resolution. The resolving power of an optical microscope is given by

$$d = \frac{\lambda}{2NA}$$

Where “ λ ” is the wavelength of light used, “ NA ” is numerical aperture, and “ d ” is the resolving power. Usually a wavelength of 550 nm is assumed, which corresponds to green light. With air as the external medium, the highest practical NA is 0.95. So theoretically, the highest resolving power can be achieved is close to half of the wavelength which is about 200 nm. In practice it is always less than this because of the aberrations present in the lenses.

Fig. 16.3 Schematic of electron interaction with the sample

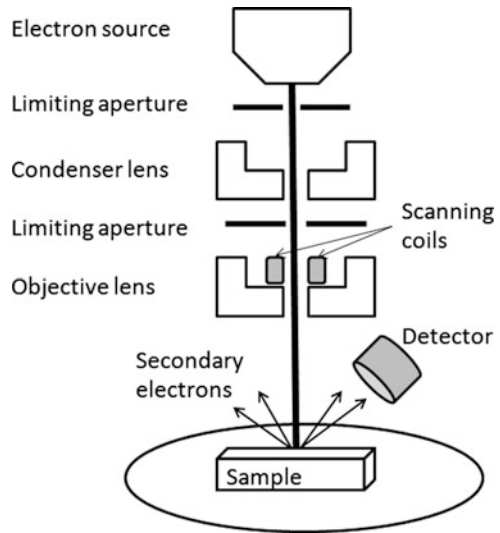


The interaction between the asperities taking place at nanometers scale cannot be resolved using optical microscope. So, one has to think of other alternative methods to observe the surfaces at high resolutions. To overcome this limit of resolution present in the optical technique, electron probe which are having wavelengths about 10,000 times shorter than visible light are used.

To understand the principle of the electron probe techniques, one needs to understand the interaction between accelerated electrons and the sample. When high-energy electrons hit the sample, some portion get back scattered while the rest get transmitted into the sample as schematically shown in Fig. 16.3 [4].

When the high-energy accelerated electrons incident on the sample, they undergo both elastic scattering and inelastic scattering carrying the signature of the sample material with them. These scattered electrons are used in a variety of ways for imaging, for obtaining quantitative and semiquantitative information of the target sample. The incident electron can get reflected back which are called as backscattered electrons (BSE), or it can knock out the electrons from the sample which are called as secondary electrons (SE). Typical signals used for imaging in scanning electron microscope (SEM) include secondary electrons and backscattered electrons. The incident beam can remove the electron from the inner shell of the sample, and an electron from higher orbit can jump into the energy level occupied originally by the ejected electron by emitting a photon. This results in the generation of X-rays having characteristic wavelengths that give information about the energy levels of the atoms. These X-rays are being used for the compositional studies called as energy-dispersive X-ray spectroscopy (EDX or EDS). Electron jumping from a higher energy level to a lower one can be associated with an emission of electron instead of a photon, and this emitted electron is known as Auger electrons. Interaction of the electrons results in bremsstrahlung (continuum) X-ray radiation that is a continuous spectrum. The electron interaction also results in the emission of visible light, which is known as cathodoluminescence (CL). Inelastic interaction results in the heating up of the sample. When the sample is very thin, the incident beam can pass through the sample which is called as transmitted beam, and also it can get diffracted by the sample called as diffracted beam, which is used in transmission electron microscope (TEM) for imaging.

Fig. 16.4 Schematic of scanning electron microscope



2.1.1 Scanning Electron Microscope

Scanning electron microscope uses secondary electrons and backscattered electrons for imaging samples. Secondary electrons are most valuable for showing morphology and topography on samples, and backscattered electrons are most valuable for illustrating contrasts in composition in multiphase samples. Compositional analysis can also be done detecting the X-rays produced during the interaction (Fig. 16.4).

Instrumentation

SEM consists of various subsystems such as the following: a vacuum chamber allowing free passage of electrons with minimum loss of energy to ionization of gas molecules, an electron source filament (electron gun), a system of electromagnetic lenses to control the electron beam, and a secondary electron detector to collect the secondary electrons emitted after interaction of the beam with a specimen. The electron beam is made to focus on the sample with the help of electromagnetic lenses and raster over the sample using scanning coils. Electron detectors are used to collect either SE or BSE and the image formed from the collected signal. Apart from the secondary electron detector, most SEMs have additional detectors that collect other signals such as BSE and X-rays. The X-ray detectors help to determine the compositional analysis of the sample. Since an ultrahigh vacuum is necessary to collect low-energy Auger electrons, a separate instrument, scanning Auger microscope, is devoted to this purpose.

Sample Preparation

Sample preparation can be minimal or elaborate for SEM analysis, depending on the nature of the samples and the data required. Minimal preparation includes acquisition of a sample that will fit into the SEM chamber and some accommodation to prevent charge buildup on electrically insulating samples. Most electrically insulating samples are coated with a thin layer of conducting material, like carbon or gold. The choice of material for conductive coatings depends on the data to be acquired: carbon is most desirable if elemental analysis is a priority, while metal coatings are most effective for high-resolution electron imaging applications.

Applications

The SEM is routinely used to generate high-resolution images of shapes of objects and to show spatial variations in chemical compositions: (1) acquiring elemental maps or spot chemical analyses using EDS, (2) discrimination of phases based on mean atomic number (commonly related to relative density) using BSE, and (3) compositional maps based on differences in trace element. The SEM is also widely used to identify phases based on qualitative chemical analysis and/or crystalline structure. Precise measurement of very small features and objects down to 50 nm in size can also be accomplished using the SEM equipped with field emission sources. Backscattered electron (BSE) images can be used for rapid discrimination of phases in multiphase samples. SEMs equipped with backscattered electron detectors can be used to examine crystallographic orientation in many materials, and the technique is known as electron backscattered diffraction (EBSD).

During the SEM examination, in most cases, secondary electrons are used as this gives good surface detail on almost any object. Secondary electron SEM images of worn surfaces have provided critical data, which helped to formulate the basic theories of wear and friction mechanisms.

Backscattered electron (BSE) imaging has been found to be extremely useful in the studies of worn metallic surfaces as this mode of imaging is less easily disrupted by poor surface quality than secondary electron imaging. Worn metallic surfaces are often covered with nonconducting deposits (oxides) and particles, which tend to gather electric charge during observation and disrupt photographic recording of the secondary electron image. Fretting wear often presents severe imaging difficulties because of the accumulations of nonconducting iron oxide or oxidized debris on the surface of the wear scar. In this instance, BSE imaging is particularly useful since it provides a reliable means of obtaining a high-quality photographic record of the worn surface.

Advantages

The critical advantage of an SEM compared to a light microscope is the combination of finer resolution and larger depth of field [4]. In an SEM the resolution depends on the diameter of the incident electron beam, or more exactly the sampling volume. The minimum diameter of an electron beam is typically 4 nm for a heated tungsten filament [4]. In some more advanced instruments with much brighter LaB₆ or field emission filaments, this diameter might be as small as 3 nm and 1 nm, respectively. The limiting resolution of a typical SEM is about twice the beam diameter, i.e., about 7 nm. In contrast, the resolution of best white-light microscopes is about 0.5 μm (500 nm).

The depth of field for SEM is typically 10–100 times larger than that for the optical microscope [4]. It is this characteristic of SEM which makes it so important tool for tribological investigations. A further advantage of SEM is that the wear damage in optically transparent materials like glass or polymethacrylate can be studied by SEM which is difficult with optical microscopes.

High resolution and large depth of field of SEM are the main reasons that this technique is almost exclusively used nowadays for determining wear mechanisms on the worn or failed tribological surfaces.

Limitations

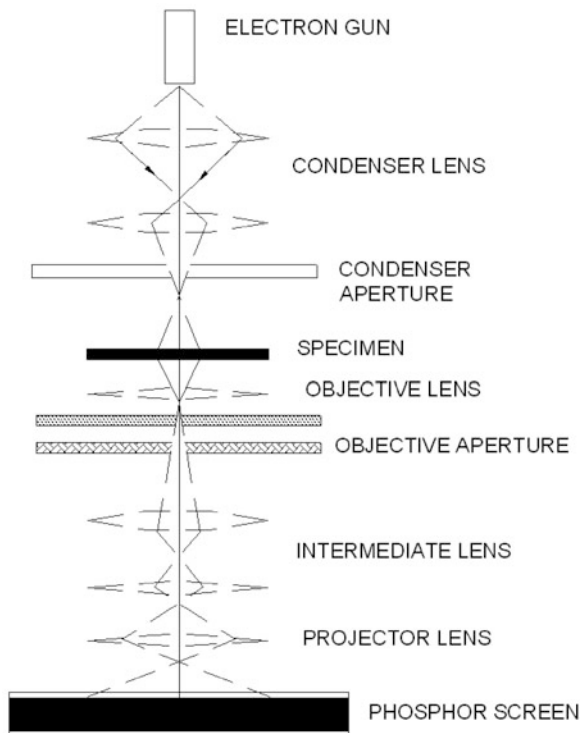
The limitation of a conventional SEM is that examination occurs only under a high vacuum which precludes the observation of liquids or wetted objects, e.g., oily layers on worn surfaces. A recently developed related technique, the environmental scanning electron microscope (ESEM), allows the observation of wet objects, e.g., biological samples [5]. ESEM has been used to investigate wear processes on the cartilage of knee joints [6] where dehydration under a vacuum by conventional SEM would destroy the original cartilage surface structure.

2.1.2 Transmission Electron Microscope

A TEM works much like a slide projector; it uses transmitted electrons from the electron sample interaction. A projector shines a beam of light through (transmits) the slide, as the light passes through it is affected by the structures and objects on the slide. This transmitted beam is then projected onto the viewing screen, forming an enlarged image of the slide. TEM works in the same way except that a beam of electrons transmitted through the specimen is used to form the image [7].

Figure 16.5 shows a schematic of TEM. An electron gun placed at the top of the microscope produces a stream of monochromatic electrons. The electron beam is then passed through a condenser lens, which focuses the beam to a small, thin, coherent beam. The beam strikes the specimen and part of it is transmitted. This transmitted portion beam carrying the information of the specimen is focused by the

Fig. 16.5 Schematic of transmission electron microscope



objective lens to form an image. The image is then enlarged by passing the beam down the column through the intermediate and projector lenses. As it falls on phosphor image screen, the information contained in the beam is converted into visible image allowing the user to see the image. The darker areas of the image represent those areas of the specimen where fewer electrons were transmitted through (specimen is thicker or denser or has higher atomic number). The lighter areas of the image represent those areas of the specimen where more electrons were transmitted through. The whole TEM column is maintained under high-vacuum environment to prevent unwanted scatter of electrons from gaseous molecules, as well as to prevent local deposition of the contaminants in the imaging area of the sample.

Imaging Methods

Different imaging methods are used to modify the electron beam exiting the sample in a form that is useful to obtain information about the sample or the beam itself. The most common mode of operation for a TEM is the bright-field imaging mode as shown in Fig. 16.6a. In this mode the contrast formation, when considered classically, is formed directly by occlusion and absorption of electrons in the sample.

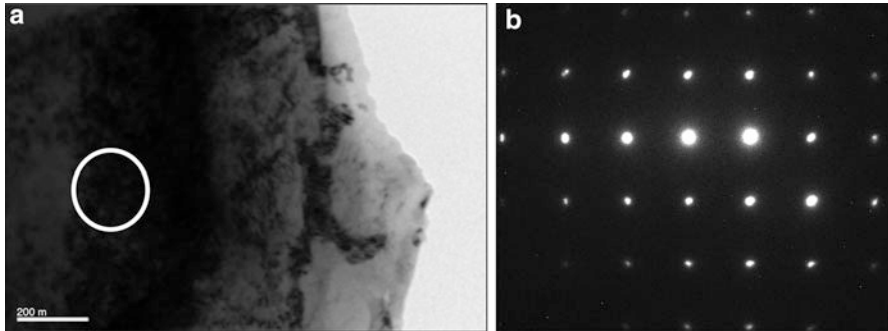


Fig. 16.6 (a) Bright-field image of aluminum sample and (b) diffraction pattern obtained from the encircled region showing [001] orientation

Thicker regions of the sample, or regions with a higher atomic number, will appear dark, while regions with no sample in the beam path will appear bright—hence, the term “bright field.” The image is in effect assumed to be a simple two-dimensional projection of the sample down the optic axis and to a first approximation may be modeled via Beer’s law.

Periodic structure of crystalline solid acts as a grating for the beam of electrons, and diffraction of the electrons takes place. This results in the formation of diffraction pattern as shown in Fig. 16.6b. To form the diffraction pattern, all the electrons leaving the specimen at a particular angle are brought to focus at a point in the image plane, whereas in bright-field mode, all the electrons leaving the sample at a particular point in the specimen are brought to focus at a point in the image. By obtaining diffraction pattern from the specific region of the sample, crystallographic orientation can be determined.

Sample Preparation

Sample preparation in TEM is a complex procedure. TEM specimens are required to be at most few hundreds of nanometers thick. Preparation of TEM specimens is specific to the material under analysis and the desired information to obtain from the specimen. As such, many generic techniques have been used for the preparation of the required thin sections. In material science and metallurgy, the specimens tend to be naturally resistant to vacuum but still must be prepared as a thin foil or etched so some portion of the specimen is thin enough for the beam to penetrate. Constraints on the thickness of the material may be limited by the scattering cross section of the atoms from which the material is comprised.

Chemical Etching

Certain samples may be prepared by chemical etching, particularly metallic specimens. These samples are thinned using a chemical etchant, such as an acid, to prepare the sample for TEM observation. Devices to control the thinning process may allow the operator to control either the voltage or current passing through the specimen and may include systems to detect when the sample has been thinned to a sufficient level of electron transparency.

Ion Etching

Ion etching is a sputtering process that can remove very fine quantities of material. This is used to perform a finishing polish of specimens polished by other means. Ion etching uses an inert gas passed through an electric field to generate a plasma stream that is directed to the sample surface. Acceleration energies for gases such as argon are typically a few kilovolts. The sample may be rotated to promote even polishing of the sample surface. The sputtering rate of such methods is on the order of tens of micrometers per hour, limiting the method to only extremely fine polishing.

Focused Ion Beam (FIB) Microscope Method

More recently focused ion beam (FIB) methods have been used to prepare samples. FIB uses high-energy gallium ions for site-specific milling of the sample. FIB is a relatively new technique to prepare thin samples for TEM examination from larger specimens. Because FIB can be used to micromachine samples very precisely, it is possible to mill very thin membranes from a specific area of interest in a sample, such as a semiconductor or metal. Unlike inert gas ion sputtering, FIB makes use of significantly more energetic gallium ions and may alter the composition or structure of the material through gallium implantation. Figure 16.7 shows the micrographs of TEM samples prepared using FIB.

Advantages of TEM

TEM exclusively allows the internal structure and composition of materials to be investigated at scales continuously ranging from micrometers to Angstroms. This has resulted in TEM becoming an important tool for characterization of materials at nanoscale and is being recently used in the study of wear particles and worn surfaces.

TEM studies of wear particles and worn surfaces have helped in understanding deformation taking place in the material. Further, very recently, in situ TEM

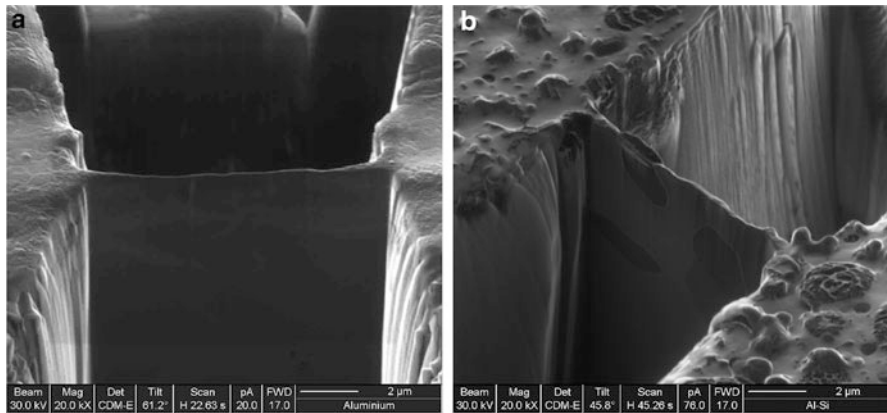


Fig. 16.7 Micrograph of electron transparent region of the sample prepared using FIB. (a) Aluminum and (b) Al-Si alloy

tribology has become promising tool for the real-time observation of interaction taking place during rubbing.

Limitations of TEM

For TEM study, sample should be very thin and electron transparent and it should be vacuum compatible. In case of tribology, the deformed surface study is of significance to understand the interaction that has taken place. Surface protection is very important during sample preparation; otherwise, important information will be lost. Also, sample preparation technique should not affect the wear damage which is of interest.

2.1.3 Auger Electron Spectroscopy (AES)

The Auger effect is a phenomenon in which the filling of an inner-shell vacancy of an atom is accompanied by the emission of an electron from the same atom. When high-energy electrons (2–50 keV) are made to incident on the material, a core state electron can be removed leaving behind a hole. As this high-energy state is unstable, the core hole can be filled by an outer-shell electron. The electron moving to the lower energy level loses an amount of energy equal to the difference in orbital energies. This difference in the energies is emitted as a photon. If this photon is then absorbed by an outer-shell electron and subsequently gets emitted from the atom, then these electrons are referred to as Auger electrons (Fig. 16.8). Since the energy of the Auger electron is specific to chemical element, the Auger electron spectroscopy (AES) provides information about the elemental composition of a surface under examination.

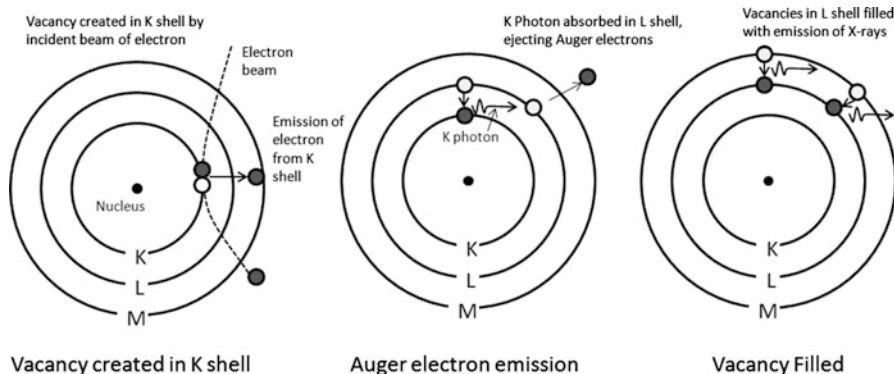
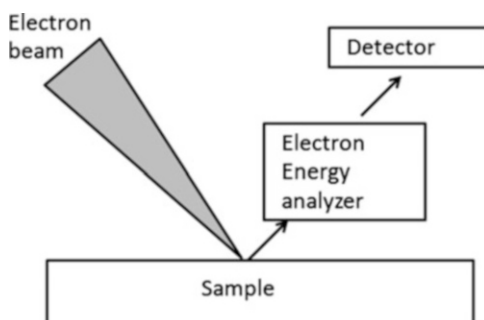


Fig. 16.8 Principle of Auger electron emission

Fig. 16.9 Auger electron microscope working principle



A schematic of Auger electron microscope is shown in Fig. 16.9. Electron beam is focused on the sample, and the energy of the Auger electrons emitted is detected using electron analyzer. The function of an electron energy analyzer is to disperse the secondary emitted electrons (Auger) from the sample according to their energies. The dispersed Auger electrons are received in the electron detector. Detector communicates the energy with respect to time data to the computer attached with it. The data is analyzed to find out the Auger peak.

Applications

There are a number of electron microscopes that have been specifically designed for use in Auger spectroscopy. Auger spectrum can produce high-resolution, spatially resolved chemical images of the surfaces, which is used for determining surface composition. The technique allows for the investigation of the variation in surface film composition generated during wear process. In addition, sputtering is sometimes used with Auger spectroscopy to perform depth profiling experiments.

Sputtering removes thin outer layers of a surface so that AES can be used to determine the underlying composition.

Limitation

Though AES has high spatial resolution and precise chemical sensitivity, this technique can be used only in solids. One of the most common limitations with Auger spectroscopy is charging effects in case of nonconducting samples.

Auger electron detectors are sometimes fitted to SEM as an accessory, but this practice is not very popular as Auger spectroscopy requires a higher vacuum and more intense electron source than usually used in the SEM. In most instances, Auger spectroscopy is installed as a separate apparatus.

2.2 Mechanical Probes

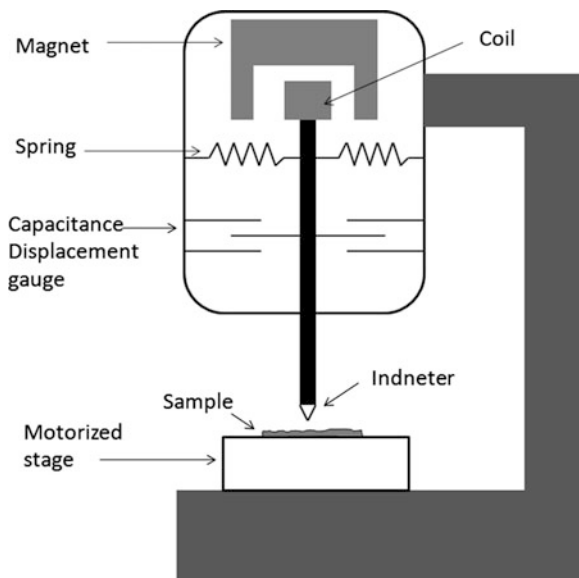
In case of mechanical probe techniques, a sharp tip of known geometry is used to probe the sample. Nanoindentation and atomic force microscopy (AFM) are widely used mechanical probes techniques in tribology. Nanoindentation is one such technique that can be used to determine the mechanical properties of small volume of the materials. AFM is used to get the topographic information of the surface in nanometer length scale.

2.2.1 Nanoindentation

Nanoindentation is one of the techniques with which mechanical properties of small volumes like thin films and nanostructures can be determined. In nanoindentation experiments a geometrically well-characterized indenter of a material with known properties (usually diamond) is brought into contact with the sample surface. The material response to penetration is characterized by continuously measuring the load on the indenter and its penetration into the sample. Compared to other conventional indentation techniques, nanoindentation does not need subsequent imaging. This enables probing to very small penetrations and automation of the measurement process. Since the indentation imprint is of extremely small size and the automated measurements enables large number of measurements, nanoindentation allows the surface to be probed at various locations and spatially map its mechanical properties.

Nanoindentation not only enables measurement of the hardness of very thin films, but it can also be used to determine the elastic modulus. In conventional microhardness testing, the elastic modulus cannot be measured while the hardness of very thin films is difficult to measure due to substrate effects. To eliminate the

Fig. 16.10 Schematic of nanoindenter



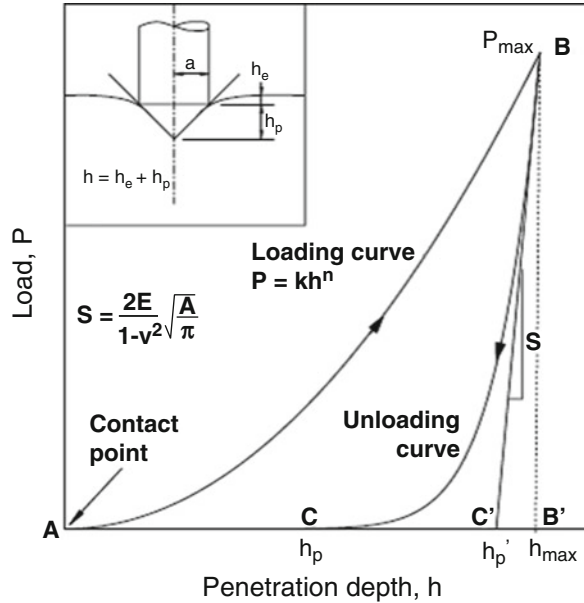
substrate effect during indentation, a conservative rule has been followed, i.e., the depth of the imprint should be less than 10 % of the film thickness.

Instrumentation

Main requirements of nanoindenters are the ability to produce and measure very small loads and displacements. From the measurement of load and displacement as a function of time, material's mechanical properties are obtained. Figure 16.10 shows a schematic of a typical nanoindenter instrument. Load is applied through a coil and magnet assembly. The load is determined directly from the current flowing through the coil, while in the piezoceramic case specially designed load cells are employed. Displacement is generally measured using capacitance sensors. Indentations can be carried out on the desired locations of the sample using motorized stage. The whole system is mounted on vibration isolation system to minimize the effect of vibrations during the experiment.

As the indenter is driven into the sample, both elastic and plastic deformations occur. Test involves continuous measurement of load supported by the material and the displacement of the indenter as the indenter penetrates the material. A typical load displacement curve obtained during indentation is shown in Fig. 16.11. The indenter establishes contact with the sample at A, and as the load increases along AB, the loading curve, the indenter penetrates the material. After reaching the desired maximum load or displacement at B, typically the sample is held at position B for a finite time. The load is then decreased along BC—the unloading curve. If the

Fig. 16.11 Typical load–displacement curve [8]



material is perfectly elastic and has no hysteresis, then AB and BC will be identical. If the material is not elastic, then AC gives a measure of permanent deformation.

The area ABB' gives the total work done on the material, the area CBB' represents the amount of energy that has been recovered elastically, and the area ABC gives the energy that has been absorbed by the material resulting in the permanent impression. For a perfectly plastic material, there is very little elastic recovery; hence, area CBB' \rightarrow 0, while for a perfectly elastic material area ABC \rightarrow 0.

Hardness of material is defined as the ratio of the load to the projected area of the residual impression. This hardness usually termed as Meyer's hardness [9] is different from other definition of Brinell or Vickers which usually uses the surface area of the impression for obtaining hardness. From the load–displacement curve (Fig. 16.11), the plastic depth of penetration h_p is obtained by extending the initial portion of the unloading curve as shown. In literature different methods have been used in estimating this depth; however, a method suggested by Oliver and Pharr [10] is most popular. Once the plastic depth is obtained, the residual projected area of the indent is obtained by using area function of the indenter used. Area function gives the area of the cross section of the indenter at different penetration depths. This is purely a means of describing the geometry of the indenter and is given by $24.5 h^2$ for an ideal Berkovich indenter. Actual indenters used will deviate from the ideal shape, and hence the area function is generally defined as a series whose coefficients are obtained by well-established calibration procedures.

Hardness measured from the nanoindentation is thus directly obtained from the definition of Meyer's hardness. Using appropriate theoretical models, other

properties of the materials such as elastic modulus, fracture toughness, and creep can be obtained [11]. It should be noted that these models involves many assumptions and the validity of these for the particular test condition and sample has to be established before obtaining quantitative data. Usually such measurements are considered in relative sense. For example, while evaluating two thin films under identical conditions, nanoindentation can be used to find out which one has higher modulus rather than obtaining an absolute modulus for the thin film. The elastic deformation occurs over a large area of the sample unlike the plastic deformation.

More advanced instruments allow a continuous measurement of contact stiffness “S” during the nanoindentation test [12]. The continuous stiffness measurement technique offers a way of continuous measurement of the contact areas of nanometer size contacts during the nanoindentation test [12].

Applications

Using nanoindenters, local properties like hardness and modulus can be determined. In addition instrument can be used for nanoscratch and wear tests. Mostly, nanoindenters are used to evaluate the relative properties of thin films used in various industries.

Limitations

Modulus of elasticity is being calculated based on the unloading curve which is limited to linear, isotropic materials. Errors will be introduced when materials exhibit “pileup” or “sink-in” during the indentation. Roughness on the sample also has the impact on the measured properties, so one should be careful while interpreting the data of worn samples from nanoindentation experiments.

2.2.2 Atomic Force Microscope

Atomic force microscope (AFM) consists of a cantilever with a sharp tip (probe) at its end that is used to scan the specimen surface. The cantilever is typically silicon or silicon nitride with a tip radius of curvature on the order of nanometers. When the tip is brought into proximity of a sample surface, forces between the tip and the sample cause the cantilever to deflect. This deflection is measured with the help of optical beams and is used for obtaining surface topographic images in AFM.

The interaction between the sample and the tip can be understood with the help of force distance curve as shown in Fig. 16.12. When the distance between the surfaces is large, interaction force is close to zero. As the surfaces are brought closer, van der Waals attractive interaction takes place. These are longer range attractive forces, which may be felt at separations of up to 10 nm or more. They

Fig. 16.12 Force–distance curve between two surfaces

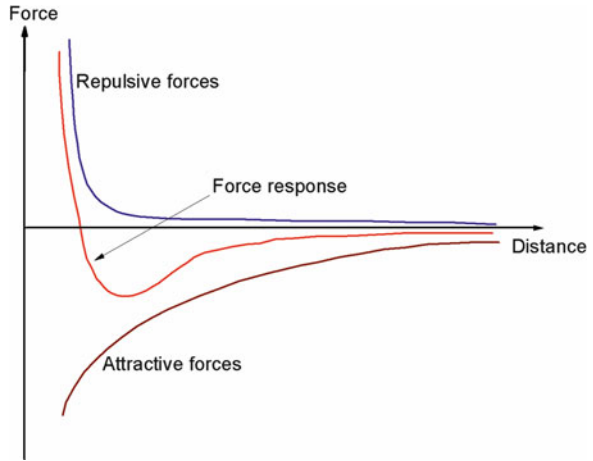
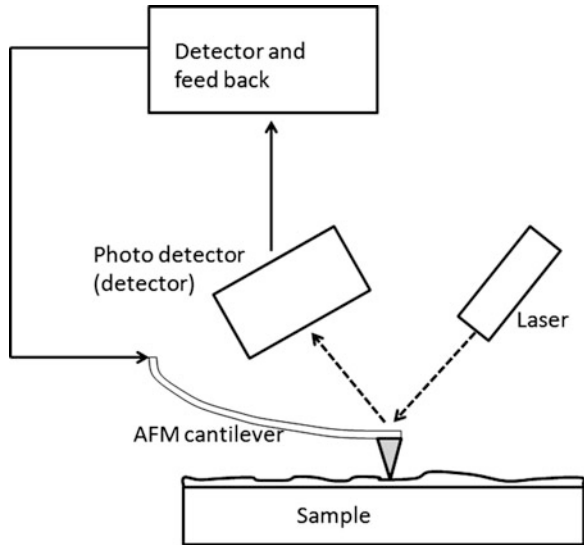


Fig. 16.13 Schematic diagram of AFM



arise due to interaction of the electrical dipoles of the atoms. At separation distance comparable to interatomic spacings, short range repulsive force arises from steric hindrance resulting from Pauli's exclusion principle that inhibits electrons from having same energy. The repulsion increases sharply as the separation decreases. The combination of these interactions results in a force–distance curve as shown in Fig. 16.13. So interaction force is a function of distance.

Instrumentation

In most AFMs optical lever techniques are employed to measure the deflection of the cantilever to obtain the force interaction between the tip and the sample (Fig. 16.13: schematic). A mirrorlike surface at the back of the cantilever is used to reflect a laser beam onto a position-sensitive photodetector. Depending on the force experienced by the tip, the cantilever deflection varies, and hence the beam shifts its position in the detector. The tip is raster scanned over the surface in both the lateral directions (x and y). Depending on the specific designs, AFMs either scan the tip over a stationary surface or scan the surface beneath a stationary cantilever. In both the cases, the displacements of the tip are obtained as a function of “ x ” and “ y ” coordinates resulting in a topographical image of the sample surface. Sometimes this image is called a “force map” since the displacements of the tip can be related to force, i.e., $F = -kz$, where “ k ” is the spring constant of the cantilever and “ z ” is the displacement [13].

Depending on the location of the force region in which the tip–sample interaction is measured, AFM can operate in three different modes: contact, noncontact, and tapping.

Contact mode: In contact mode the tip makes the direct contact with the surface examined. As the tip scans the surface, the cantilever bends to accommodate the changes in surface topography due to the contact forces acting upon it.

Noncontact mode: In noncontact mode, the tip is separated from the sample by a distance between 50 and 100 Å. In noncontact mode a stiff cantilever must be used since the soft cantilever could flop onto the surface of a sample because of the attractive van der Waals force. Since the attractive forces from the sample are substantially weaker, the tip must be given a small oscillation so that AC detection methods can be used to detect the small forces between the tip and the sample by measuring the change in amplitude, phase, or frequency of the oscillating cantilever in response to force gradients from the sample.

Tapping mode: This technique overcomes problems associated with friction, adhesion, electrostatic forces, and other difficulties that can be observed in conventional AFM scanning methods by alternately placing the tip in contact with the surface to provide high resolution and then lifting the tip off the surface to avoid dragging the tip across the surface. Tapping mode imaging is implemented in ambient air by oscillating the cantilever assembly at or near the cantilever’s resonant frequency using a piezoelectric crystal. The reduction in oscillation amplitude is used to identify and measure surface features. During tapping mode operation, the cantilever oscillation amplitude is maintained constant by a feedback loop. When the tip passes over a bump in the surface, the cantilever has less room to oscillate and the amplitude of oscillation decreases. Conversely, when the tip passes over a depression, the cantilever has more room to oscillate and the amplitude increases (approaching the maximum free air amplitude). The oscillation amplitude of the

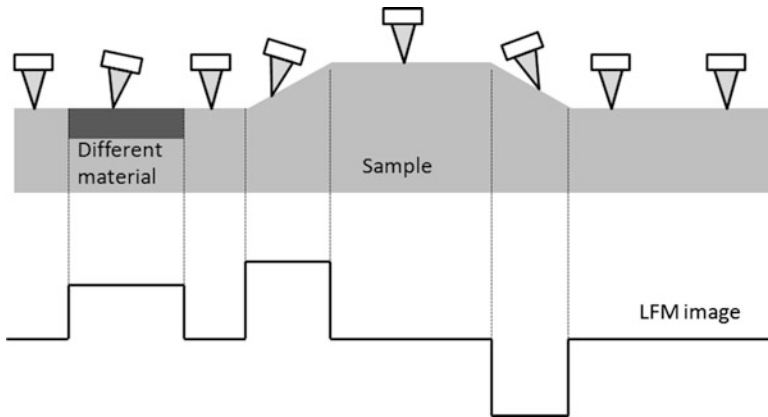


Fig. 16.14 Principle of lateral force microscopy

tip is measured by the detector. The digital feedback loop then adjusts the tip-sample separation to maintain constant amplitude and force on the sample.

Lateral force microscope (LFM): LFM is also known as friction force microscope (FFM) [13]. These instruments allow one to measure local variations in surface friction, which can arise from inhomogeneity in surface material and changes in the slope as illustrated in Fig. 16.14.

As the tip traverses the surface, it is subjected to lateral forces, which are related to local coefficients of friction, i.e., ratio of the lateral force to the normal force acting on a tip is a coefficient of friction. This view of friction is naturally a simplification as it avoids considerations such as contact stress, which would normally be included in a more rigorous analysis of friction. These forces are transmitted to a cantilever, which twists along its length. The cantilever deflections and twists, i.e., lateral deflections, are monitored in the same manner as in a traditional AFM using position-sensitive photodetectors. The operating principles of LFM are illustrated in Fig. 16.14. As a result of this refinement, the LFM can provide a frictional map of the surface with nanometer resolution together with the surface topography data in one scan.

3 In Situ Techniques

In spite of 300 years of attention, the reason why we know so little about friction and wear process is that “we cannot see what is taking place at the interface during sliding” [14]. The main limitation in the conventional tribological studies is that the interface is hidden by contacting bodies and the interaction taking place cannot be seen in real time. So it is important to visualize the interface during sliding in real time. The real-time studies are called as “in situ” studies. Initially in situ optical techniques were developed, to study the friction and wear of the materials, suffer

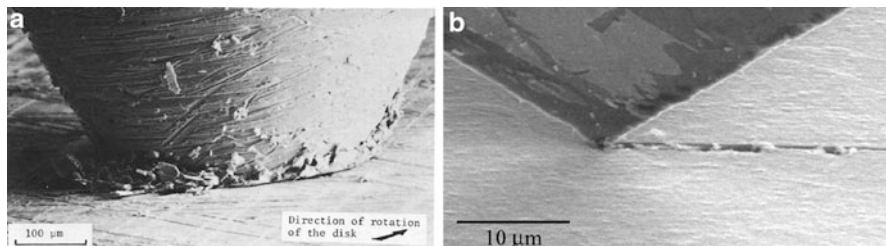


Fig. 16.15 In situ tribology using SEM (a) pin-on-disk wear rig [15] and (b) nanoindentation scratch stage [16]

with the limit of optical resolution. Also this technique cannot be used for all the materials; one of the contacting surfaces should be optically transparent.

To achieve high resolution, in situ SEM techniques have been developed, which have the ability to provide a greater magnification with a greater depth of field than optical microscope and make it particularly suitable for use in the study of wear. A pin-on-disk wear rig has been constructed by Lim et al. [15] to operate inside the scanning electron microscope to allow direct, high-magnification observation of wear as it occurs. Sheet or flake-like debris were observed in the wear of high purity copper pins on case-hardened mild steel disks (Fig. 16.15a)

Rabe et al. [16] developed a miniaturized nanoindentation and nanoscratch device for use inside a scanning electron microscope. During the experiment the sample is directly observed with sub-micrometer resolution and linked to the simultaneously recorded load–displacement data. The indentation response of nanocomposite TiN/SiN_x coatings and indentation and scratching of hard diamond-like carbon (DLC) films studied using the setup (Fig. 16.15b).

Though the SEM has better resolution than the optical microscope, it can only give the surface information but cannot give subsurface information. Any deformation includes both surface and subsurface changes, and the macroscopic friction or wear is net effect of interaction of the asperities which results at surface as well as subsurface [17, 18]. So one needs to go for the advanced microscope which is TEM, in which both the surface and subsurface of an electron transparent sample can be seen at a time. Different analytical techniques employed for the in situ tribology have been listed in following Table 16.1, with examples of measurement application, resolution, and limitation.

From the table, it can be seen that TEM could be an ideal tool, which gives both surface and subsurface information, for the study of in situ tribology at asperity level. TEM has additional advantages like one can use diffraction to determine the crystallographic orientation, EDX (energy-dispersive X-ray spectroscopy) or EELS (electron energy-loss spectroscopy) for the chemical composition of the material.

The effort for development of in situ TEM contact holder was started in 1970 itself [19]. Though it has a long history, the progress was sporadic, mostly because of numerous engineering challenges in designing these instruments. All the electrical connections and movement mechanisms must be incorporated in to the holder.

Table 16.1 Comparison of different analytical techniques used for the study of in situ tribology

Technique	Observation capability	Resolution	Limitations
Optical spectroscopy	Tribofilm, wear particles	$\sim 1 \mu\text{m}$	One of the surfaces should be optically transparent, no subsurface information
Scanning electron microscope (SEM)	Indentation, scratch, wear particles	$\sim 1 \text{nm}$	Subsurface information in real time not available
Transmission electron microscope (TEM)	Microstructural transformation during indentation sliding and reciprocation	$\sim 0.1 \text{nm}$	Sample should be electron transparent and vacuum compatible

The materials used should be high-vacuum compatible and free from internal magnetism. Magnetic field of the pole pieces excludes a certain type of actuating and sensing devices which further restricts the choice of construction materials. Most importantly very thin region of the sample holding portion ($\sim 3 \text{mm}$) requires precision manufacturing capabilities.

Different in situ TEM contact probes were built by different groups recently. Wall et al. [20] have described the development of an in situ nanoindenter that uses a piezoceramic actuator to indent a specimen using a sharp diamond tip. Sharp diamond tip is mounted onto a long, stiff metal rod. Coarse positioning of the indenter tip in all three axes is accomplished with manual screw. Fine motion of the tip is controlled in all three axes with piezoceramic tube, and they have carried out indentation experiments on aluminum. Minor et al. [21, 22] have measured the force on the indenter by observing the difference in the piezoelectric translator's displacements under no load and loaded conditions.

Kizuka et al. [23] have described the study of atomic-scale contact and noncontact scanning on gold surfaces by gold tips in time-resolved high-resolution transmission electron microscopy (HRTEM), using a piezo-driven specimen holder. In the design the coarse displacement is by means of micro-screw motor and fine displacement by means of tube piezoceramic. The needle for indentation is initially positioned by means of a motorized micro-screw drive mechanism, then fine positioning by tube piezoceramic.

Erts et al. [24] have investigated force interactions between two gold samples using a combination of atomic force microscope (AFM) and a transmission electron microscope (TEM). The size and shape of the tip and sample, as well as size of contact area and interactions type (elastic-plastic), are observed directly. They have reported two different designs of TEM-STM as well as an extension with an atomic force microscope (TEM-AFM). In the first TEM-STM (scanning tunneling microscope) design, a stepper motor, combined with a one-dimensional inertial slider, is used as coarse positioner. The advantage of this design is the strong pulling force

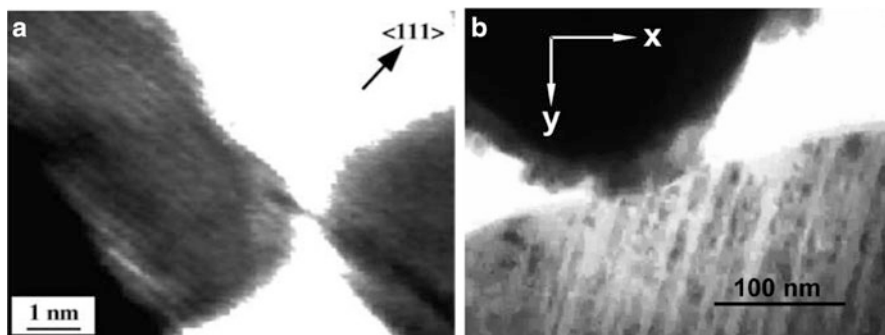


Fig. 16.16 (a) Still frame from in situ TEM gold contact by Erts et al. [24]. (b) Indentation on Cu-Be alloy by Bobji et al. [26]

that enabled notched metallic (gold) wires to be broken inside TEM (Fig. 16.16a), resulting in clean sample surfaces.

Bobji et al. [25] developed an in situ indentation stage, with which the deformation mechanics of Cu-Be alloy was studied (Fig. 16.16b) [26]. This stage uses inertial slider-based coarse positioning system and 4-quadrant tube piezoceramic as fine positioner. The main advantage with this design is the high stiffness which is $>1,800$ N/m. The whole compact positioning system is inside the vacuum, which helps to improve the stiffness as well as it minimizes the vibrations during the experiments.

Anantheshwara et al. [27] designed and developed a triboprobe, based on Bobji et al. [25] design, capable of carrying out indentation, sliding, and reciprocation experiments. It is desired to have high stiffness to carry out the tribological experiments.

Reciprocation experiments were carried out using diamond probe on an Al-Si alloy sample [28]. It is observed that different mechanisms of friction and wear operate at different contact pressures. Sample surface starts wearing out at higher contact pressures and generates wear debris by abrasive action of the diamond probe (Fig. 16.17). These nanoscale wear debris get trapped between the rubbing surfaces and undergo complex interactions involving agglomeration, rolling, and disassociation. Some of the trapped particles roll between the contacting surfaces leading to a considerable increase in the reciprocation amplitude. Repeated deformation of the trapped particles leads to the formation of tiny liquid drops on some of the wear debris [29]. Further liquid bridge pulling experiments were carried out to observe interaction of the liquid droplet at the interface (Fig. 16.18).

Advantage of in situ TEM tribology technique is that it overcomes the hidden-interface problem existing in the conventional studies. This technique will provide important information and insight to a range of tribological phenomena taking place at the interface, which will be useful for materials development as well as modeling wear behavior. This technique enables real-time studies on the formation and interaction of the nanoparticles by observing them inside TEM at high resolutions.

Fig. 16.17 Formation of the nanoscale wear particle [28]

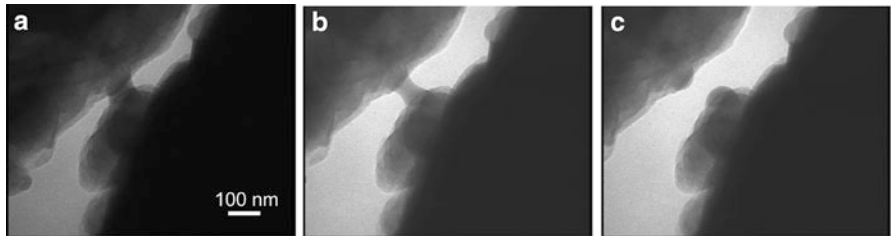
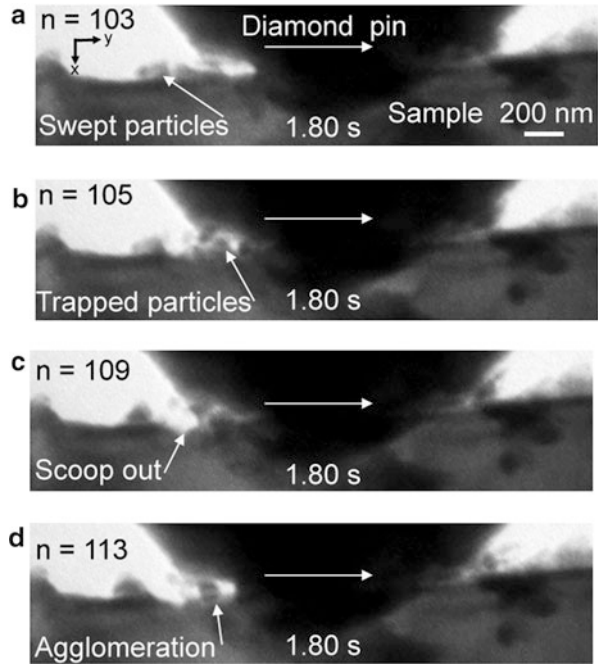


Fig. 16.18 Liquid bridge pulling experiment

The capability of this technique, allowing the tribological processes to be observed dynamically in real time and at high magnifications, makes it an indispensable tool in fundamental understanding tribological interactions.

4 Summary

In this chapter, different surface probe techniques available for the study of surfaces at nanometer length scale have been discussed from the tribology point of view. Each technique has its own advantages and limitations. Recently, in situ techniques are becoming more popular tools in the fundamental study of tribological interactions.

References

1. Beilby G (1921) *Aggregation and flow of solids*. Macmillan, London
2. Bowden F, Hughes TP (1937) Physical properties of surfaces. IV. Polishing, surface flow and the formation of the Beilby layer. *Proc Roy Soc Lond A* 160:575–587
3. Bhushan B (2003) Adhesion and stiction: mechanisms, measurement techniques, and methods for reduction. *J Vac Sci Technol B* 21:2262
4. Goldstein J et al (2003) *Scanning electron microscopy and x-ray microanalysis*. Springer Science + business media, New York, NY
5. Donald AM (2003) The use of environmental scanning electron microscopy for imaging wet and insulating materials. *Nat Mater* 2:511–516
6. Crockett R, Roos S, Rossbach P, Dora C, Born W, Troxler H (2005) Imaging of the surface of human and bovine articular cartilage with ESEM and AFM. *Tribol Lett* 19(4):311–317
7. Williams DB, Carter CB (2009) *Transmission electron microscopy. A textbook for materials science*. Springer Science + business media, New York, NY
8. Bobji MS (1999) *Studies in depth sensing indentation*, Ph.D. Thesis, Indian Institute of Science, Bangalore
9. Tabor D (1951) *Hardness of metals*. Oxford University Press, New York, NY
10. Oliver WC, Pharr GM (1992) An improved technique for determining hardness and elastic modulus using load and displacement sensing indentation experiments. *J Mater Res* 7(06):1564–1583
11. Fischer-Cripps AC (2004) *Nanoindentation*. Springer, New York, NY
12. Li X, Bhushan B (2002) A review nanoindentation continuous stiffness measurement technique and its applications. *Mater Charact* 48(1):11–36
13. Bhushan B (1999) *Handbook of micro/nanotribology*, 2nd edn, CRC Press LLC, Boca Raton, FL
14. Singer L, Pollock HM (1992) *Fundamentals of friction: macroscopic and microscopic processes*. Kulwer Academic Publishers, Netherlands
15. Lim SC, Brunton JH (1985) A dynamic wear rig for the scanning electron microscope. *Wear* 101:81–91
16. Rabea R, Bregueth JM, Schwallerer P, Staussa S, Hauga FJ, Patscheidera J, Michlera J (2004) Observation of fracture and plastic deformation during indentation and scratching inside the scanning electron microscope. *Thin Solid Films* 469–470:206–213
17. Suh NP (1986) *Tribophysics*. Prentice-Hall, Inc, Englewood Cliffs, NJ
18. Rigney DA (1981) *Fundamentals of friction and wear of materials*. American Society for metals, Metals Park, OH
19. Gane N (1970) The direct measurement of strength of metals on a sub-micrometer scale. *Proc Roy Soc Lond A* 317:367–391
20. Wall MA, Dahmen U (1998) An in situ nanoindentation specimen holder for a high voltage transmission electron microscope. *Microsc Res Tech* 42:248–254
21. Wall MA, Stach EA, Freeman T, Minor AM, Owen DK, Cumings J, Chraska T, Hull R, Morris JW Jr, Zettl A, Dahmen U (2001) Development of a nanoindenter for in situ transmission electron microscopy. *Microsc Microanal* 7:507–517
22. Minor AM, Morris JW Jr, Stach EA (2001) Quantitative in situ nanoindentation in an electron microscope. *Appl Phys Lett* 79(11):1625–1627
23. Kizuka T (1998) Atomic visualization of deformation in gold. *Phys Rev B* 57:158–163
24. Erts D, Lohmus A, Lohmus R, Olin H (2001) Instrumentation of STM and AFM combined with transmission electron microscope. *Appl Phys A* 72(suppl):S71–S74
25. Bobji MS, Ramanujan CS, Pethica JB, Inkson BJ (2006) A miniaturized TEM nanoindenter for studying material deformation in situ. *Meas Sci Technol* 17:1–6
26. Bobji MS, Pethica JB, Inkson BJ (2005) Indentation mechanics of Cu–Be quantified by an in situ transmission electron microscopy mechanical probe. *J Mater Res* 20(10):2726–2732

27. Anantheshwara K, Bobji MS (2010) In-situ transmission electron microscope study of single asperity sliding contacts. *Tribol Int* 43(5–6):1099–1103
28. Anantheshwara K, Lockwood AJ, Mishra RK, Inkson BJ, Bobji MS (2012) Dynamical evolution of wear particles in nanocontacts. *Tribol Lett* 45(2):229–235
29. Lockwood AJ, Anantheshwara K, Bobji MS, Inkson BJ (2011) Friction formed liquid droplets. *Nanotechnology* 22:105703

Questions

1. Explain any five ways in which the electron interact with the materials and how each one of these is exploited to characterize the materials
2. What is an atomic force microscope? How is it used to obtain atomic resolution images? Sketch the displacement of the cantilever as a function of the separation distance between the tip atom and the surface, assuming an ideal case of a tip consisting of a single atom.
3. Explain the principle behind the Auger electron spectroscopy.
4. What is a transmission electron microscope? How is it used to characterize the materials?
5. What are the different material properties that can be determined by nanoindentation? Explain how any two properties are measured.
6. Describe the significance of in situ techniques. Explain how these techniques became useful in the study of surface interactions.

Part V
Tribology in Nature

Chapter 17

Biotribology and Human Tribology

Kurt E. Beschorner

Abstract In biotribology and human tribology, tribological theories are applied to biological systems and human interactions, respectively. This chapter focuses on the human tribology fields, slip and fall accidents and hand-object interaction, and the biotribology fields, ocular and oral tribology. Slip and fall accidents are caused by low friction between the shoe and floor surface, frequently due to a fluid contaminant. Experimental methods of evaluating shoe-floor friction are most relevant to human slips when mimicking the dynamics of human stepping and the environmental conditions (using common shoes, floors, and/or contaminants). The tribological mechanisms affecting shoe-floor friction are adhesion, hysteresis, boundary lubrication, and hydrodynamic lubrication. Modeling efforts have shown that certain floor roughness parameters correlate well with shoe-floor friction, that adhesion and hysteresis can be simulated with finite element analysis, and that models using Reynolds equation can simulate the hydrodynamic effects. Skin friction is essential for everyday activities such as gripping and manipulating objects. The friction of the outermost layer of the skin, the stratum corneum, is modulated by hydration allowing the body to optimize skin friction through perspiration. Increasing skin friction leads to improved performance by increasing grip strength and fine motor speed. The tribological interaction in the eye, with or without a contact lens, contributes significantly to comfort. Eye discomfort and the disorder dry eye syndrome occur when abnormalities occur to any of the three tear film layers that protect and lubricate the eye. Low friction is essential to the comfort of contact lens. Experiments and models have implicated that adhesion, hysteresis, boundary lubrication, and elastohydrodynamic lubrication may all contribute to eye lens friction. Tooth wear due to abrasion and corrosion is a major threat to healthy teeth and dental restorative surfaces. Tribological principles such as two-body wear, three-body wear, and corrosion along with innovative modeling

K.E. Beschorner, Ph.D. (✉)
Industrial and Manufacturing Engineering, University of Wisconsin-Milwaukee,
PO Box 784, Milwaukee, WI 53201, USA
e-mail: beschorn@uwm.edu

and experimental techniques have revealed personal risk factors and the effects of behavior on dental wear. Another application of oral tribology is creaminess perception in the mouth. Creaminess of a food is largely dependent on its ability to lubricate the mouth surfaces. Replication of this sensation using low-fat alternatives to traditional high-fat creamy foods has the potential to achieve reductions in obesity. This chapter demonstrates the applications of tribology to biological systems.

1 Overview

Biotribology is known as the application of tribological principles to biological systems. The field has a broad set of applications including total joint arthroplasty (see Chap. 22 for “Wear of Biomedical Implants”), preventing slip and falling accidents, developing consumer products that appeal to tactile sensations, and manipulating objects and tools by hand. Human tribology, a subset of biotribology, can be used to describe the application of tribology to human interactions with their surrounding environment. Such interactions include the shoe-floor interface during walking or hand-object interface when handling or manipulating objects. This chapter will provide an overview for how to apply tribological principles to medical and human systems.

Biotribology and human tribology are different from other tribological disciplines such as lubrication or contact mechanics because they represent the *application* of tribological theories from specific tribological disciplines on to biological problems. Biotribology, therefore, does not inherently have its own set of theory. Applying tribology principles to biological systems requires an understanding of the biological system being studied and the relevant tribological theory. For example, studying the tribological interaction between the eye lens and eyelid requires understanding the biological composition of the tear film lubricant, the speed and loading patterns of the eyelid during blinking, and the material properties of the eye lens and eyelid, which are dependent on structure in the tissue, cellular, and subcellular layers. Furthermore, the research questions should be driven by the biological concern that is being considered. For example, wear particles formed during use of prosthetic joints can cause an immune response that ultimately causes the joint to fail, which means the tribological research questions should focus on enhancing the wear resistance of these joints. Alternatively, low friction causes slipping accidents, which means that tribological research should focus on enhancing friction between a person’s foot or shoe and the floor. Thus, an aspiring biotribologist must be equally diligent in learning the underlying biological issues that are related to their subject as they are in learning the applicable tribology theory.

Applying tribological principles to biological systems can present several unique challenges that are not typical in other tribology disciplines. The human body is a highly complex system with unusual geometries, biochemical immune responses that are particularly aggressive to foreign substances, sophisticated non-Newtonian

biofluids, and movement and loading patterns that are highly transient and variable. Therefore, scientists must also consider these other factors when applying tribological principles to the human body.

This chapter will provide an introduction for applying tribology to biological systems in order to gain better understanding in human tribology topics (slip and fall accidents, interaction between the hand and objects) and biotribology topics (ocular tribology and oral tribology). Special focus will be made to point out specific biological issues that interact or affect the tribological interactions. Many of the biotribology issues include relevant tribological theory such as lubrication or wear. The reader is referred to the other chapters of this book to gain this specific tribology theory as it will not be repeated in this chapter.

2 Human Tribology

The primary effectors in which humans transport themselves throughout their environment and manipulate their environment are the feet and hands, respectively. A nonoptimal interface can lead to a failure in locomotion (i.e., a falling accident) or difficulty in handling objects (e.g., trouble operating a wrench). Tribologists can bring a unique perspective to these areas by implementing the most sophisticated tribological methods to the relevant ergonomic and rehabilitation research questions. This approach has the potential to identify optimal frictional characteristics that can reduce falling accidents and enhance a person's ability to use their hands.

2.1 *Slip and Fall Accidents*

The safety of each step that we take relies on the tribological interaction between the foot or shoe and the ground or floor surface. In order to maintain walking, the friction between the foot/shoe and the floor/ground must be sufficiently high. The forces between a shoe and floor surface can be recorded using a 6 degree of freedom force platform that is embedded in the floor (Fig. 17.1a). By normalizing the shear forces to the vertical force, we can determine the amount of friction that is utilized throughout the gait cycle. The maximum amount of friction that is used during a step is called the Required Coefficient of Friction (RCOF) (Fig. 17.1b). Shoe-floor friction that is below the RCOF typically leads to a slip. RCOF values are typically between 0.17 and 0.22 for level ground and are higher when walking on sloped surfaces [1]. Using tribological principles to increase these friction values has tremendous potential as slip, trip, and falling accidents cause 24.5 % of nonfatal injuries in the workplace [2] and cause 1 in 3 adults over the age of 65 to fall each year [3].

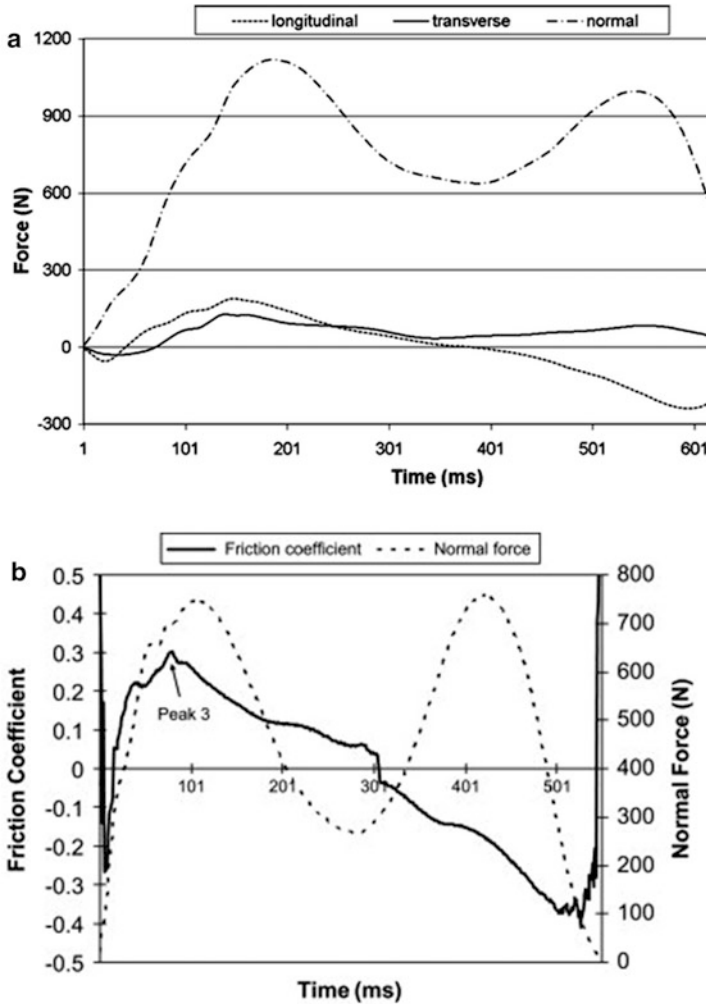


Fig. 17.1 (a) Time-series plot of ground reaction forces during normal walking [4]. The longitudinal forces represent shear forces in the direction of walking, transverse forces are shear forces perpendicular to the direction of walking, and normal forces are normal to the ground surface. (b) Time-series plot of the required friction during gait [5]. The Required Coefficient of Friction (RCOF) is shown as *Peak 3* on the graph

2.1.1 Experimental Methods to Evaluate Shoe-Floor Friction

Experimental measurements of shoe-floor friction are commonly used to compare the slip potential of different shoe and floor surfaces. These measurements can be used to select the safest materials, particularly in environments where slipping accidents might be expected like in restaurant kitchens or outdoor steps at a ski resort. The friction results from a measurement can significantly depend on the

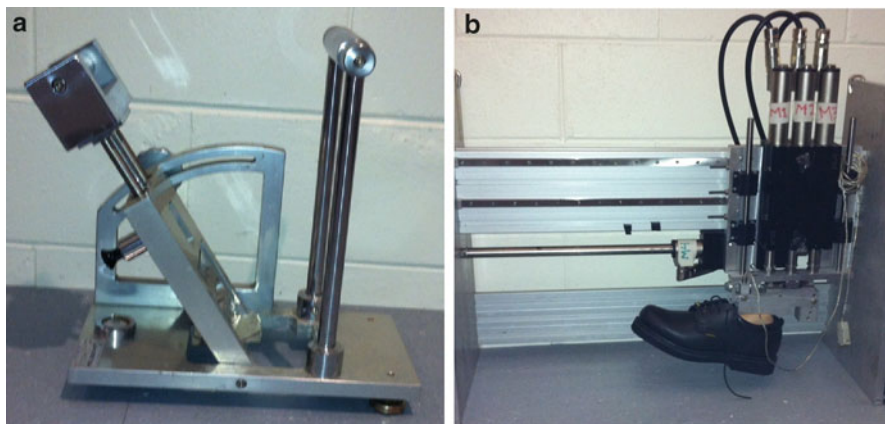


Fig. 17.2 Devices used to test the friction coefficient of floor surfaces including a portable device (a) and a laboratory device that tests entire shoe samples (b)

testing methods [6]. Thus, mimicking conditions that would be experienced during a typical slip is critical to get values that are relevant to slipping. The parameters used during testing can roughly be divided into three categories: testing parameters, environmental conditions, and shoe-floor samples. Testing parameters such as the vertical loading and kinematics of the foot are known to tremendously influence the slipperiness. During human slipping events, normal pressures are approximately 400 kPa [7], shoe-floor angles are usually between 0 and 20°, and sliding speeds are typically between 0 and 1 m/s [1]. While all of these parameters are known to affect friction, an increase in sliding speed has the most pronounced effect and typically causes a reduction in friction [6]. The testing parameters of portable devices (Fig. 17.2a) are typically defined by the design of the apparatus, while laboratory devices (Fig. 17.2b) often have more flexibility to specify exact testing parameters [8]. In addition to the testing parameters, another critical component in evaluating shoe-floor friction is the environmental conditions [9]. The level of friction between two surfaces is highly dependent on whether a fluid contaminant is present and the composition of the fluid parameter [10]. Therefore, examining the slipperiness of floor tiles that are likely to be used in a restaurant kitchen might require identifying contaminants that are most likely to be found in that environment like vegetable oil, floor detergent, and flour, whereas floor tiles that are used on uncovered outside services should be tested with precipitation hazards that are relevant to a certain region (rain, ice, snow, etc.). The last critical parameter is the choice of shoe and floor materials. Floor materials should be tested against shoe samples that are typically worn on that floor surface, while shoe materials should be tested against the floor surfaces that are typical. For example, work boots would be appropriate when testing scaffolding standing surfaces because construction and maintenance workers who wear construction boots are most likely to use that surface.

2.1.2 The Tribology of Shoe-Floor-Liquid Contaminant Friction

Friction of dry shoe and floor surfaces is typically high enough to prevent slipping. Slips commonly occur when a liquid contaminant lubricates the shoe and floor surfaces, which causes a reduction in friction. Hydrodynamic lubrication can cause friction levels to go extremely low (<0.01) and is highly likely to cause a slipping accident [11]. Boundary lubrication, however, can also reduce friction to the point of causing slips. This section will describe the relevance of boundary and hydrodynamic lubrication to slipping and how an understanding of the underlying tribology theory can be used to prevent slipping accidents.

Hydrodynamic effects can cause large reductions in shoe-floor-contaminant friction by generating a fluid layer that separates the shoe and floor surfaces and causes a reduction in their interaction. The two primary mechanisms that cause these hydrodynamic effects are the squeeze-film effect and the wedge-term effect. The squeeze-film effect is most severe directly after heel contact when fluid underneath the shoe must be squeezed out of the interface. The film thickness, h , due to the squeeze-film effect can be approximated with a plate that is squeezing fluid from between a counter-surface (K is a constant based on the shape of the plate, η is the viscosity, A is the area of the plate, F_N is the normal force and t is the time) [12]:

$$h^2 = \frac{K^* \eta^* A^2}{F_N^* t} \quad (17.1)$$

The contact area can be interpreted as the area of each tread. Increasing the number of tread channels can divide the shoe sole into several “plates” that each has a smaller area, A , than the shoe as a whole. Therefore, tread is capable of reducing the squeeze-film thickness that separates the shoe and the floor, while increasing viscosity will increase the film thickness. Squeeze film is also dependent on the normal force and dissipates over time. The other component contributing to the hydrodynamic effect, the wedge term, can be approximated by considering a slider bearing with incline angle of 10° [13]. In this equation, the film thickness (h) is dependent on the viscosity (η), characteristic length (l), velocity (v), and normal force (F_N):

$$h^2 = \frac{0.066^* \eta^* l^3 * v}{F_N} \quad (17.2)$$

This equation demonstrates that the wedge effect is facilitated by high-viscosity fluids, length, and sliding speed and inhibited by high normal forces. Once again, the characteristic length can be interpreted to mean the tread size indicating that more tread channels can reduce the film thickness of the fluid during slipping by reducing l . Experiments that measured hydrodynamic pressures during a simulated slip showed that a small amount of shoe tread is capable of completely eliminating

hydrodynamic pressures [11]. These findings indicate that shoe tread is an effective method of addressing hydrodynamic lubrication in the shoe-floor interface.

Even in the absence of hydrodynamic effects, the friction of lubricated shoe-floor surfaces can be low enough to cause a slip due to boundary lubrication. The primary sources of shoe-floor friction in boundary lubrication are adhesion and hysteresis [14]. Adhesion forces are the intermolecular attractive forces that occur between two dissimilar surfaces. Adhesion forces between rubber materials and hard surfaces are proportional with the true shear stress, σ_s , and the real area of contact, A_c , which is closely linked with normal force [15]. The true shear stress, σ_s , is highest under dry and clean conditions causing high dry adhesion friction. It is typically reduced by the presence of contaminants and fluids, causing lower lubricated adhesion values. Fluids affect adhesion by forming a thin boundary lubrication, which can block the adhesional junctions between the shoe and floor asperities. High-viscosity fluids such as oil or grease typically result in a greater reduction of adhesion friction than lower-viscosity fluids like water [14]. In environments where high-viscosity fluids are present, a high level of hysteresis friction is needed to prevent a slip. Hysteresis is defined as the friction caused by viscoelastic deformation in the elastomer material as asperities from another material move across its surface. In shoe-floor friction, hysteresis friction is caused by the harder floor asperities deforming the softer shoe asperities. Hysteresis is unaffected by boundary lubricants [15]. Hysteresis friction can be increased by increasing the size of the asperities in the floor or by increasing the relative hardness between the floor and shoe material. Thus, identifying and designing shoe and floor combinations with high hysteresis are effective strategies for preventing slipping accidents.

2.1.3 Modeling Shoe-Floor-Contaminant Friction

Models of shoe-floor friction have been developed to further elucidate the mechanisms that contribute to shoe-floor friction. These models are based on measurable and controllable properties of the shoe surface, floor surface, and fluid contaminant. While experimental methods are useful in comparing existing shoes and flooring modeling shoe-floor friction can be useful in optimizing parameters that lead to superior designs of slip-resistant materials and environments. Models can also lead to a priori predictions of friction (i.e., predictions made before installing and testing the floor) in order to select slip-resistant flooring during the design phase of a workplace. Shoe-floor friction models can be broadly broken into two categories: deterministic models and physics-based models. In deterministic modeling, friction coefficient is regressed against certain shoe or floor properties such as floor roughness to determine whether a relationship exists and the nature of the relationship between the variables (e.g., positive linear correlation, negative linear correlation, parabolic correlation). Physics-based models typically use a combination of constitutive equations to predict shoe-floor friction such as the Reynolds equation to evaluate fluid pressure

or contact mechanics to predict hysteresis friction. Deterministic models are typically limited to the set of conditions used during the experiments, whereas physics-based models are more generalizable.

Deterministic models of shoe-floor friction have established relationships between floor roughness and lubricated friction, dry adhesion on lubricated adhesion, and testing conditions such as normal force/sliding speed and lubricated friction. Higher shoe-floor roughness values have consistently been found to positively correlate with lubricated friction although some roughness measures demonstrate better correlation than others. For example, short cutoff lengths are correlated with friction when using low-viscosity fluids, while waviness measurements are associated with long cutoff lengths and are better correlated with friction coefficient for high-viscosity fluids [16]. Roughness (R) parameters are representative of surface deviations on length scales that are shorter than a given cutoff length (i.e., calculated using a high-pass filter with a cutoff frequency of $1/\text{cutoff length}$), while waviness parameters are representative of surface deviations on length scales that are longer than a given cutoff length (i.e., calculated using a low-pass filter with a cutoff frequency of $1/\text{cutoff length}$). In addition, the method used to quantify roughness is also important. Specifically, roughness (cutoff length = 0.8 mm) and waviness parameters (cutoff length = 2.5 mm), R_{pm} and W_{pm} , that calculate the average height of each asperity peak have been shown to demonstrate the best correlation to coefficients with friction when compared with other roughness and waviness parameters (such as root mean square roughness, R_q , or average roughness parameters, R_a) [16]. Roughness parameters (such as R_{pm}) are calculated by high-pass filtering surface profiles, while waviness parameters are filtered with a low-pass filter. The “pm” subscript indicates that the maximum peak height above the mean line in each cutoff length is measured and averaged. Thus, the R_{pm} and W_{pm} terms are calculated by high-pass or low-pass filtering the profile, respectively, dividing the surface profile into separate equal sections using the cutoff length, calculating the maximum peak height in each of these sections, and averaging the peak heights [16]. The roughness term, R_z , calculates the total peak to valley roughness by averaging highest peak to lowest valley height within each of the different cutoff lengths. The two primary components to boundary-lubricated friction, adhesion and hysteresis, can be individually modeled based on floor roughness and testing parameters. Wet adhesion friction forces are dependent on the dry adhesion, and their relationship can be described with just two fluid-specific coefficients [14]. Strong correlations have also been found between floor roughness, R_z , and hysteresis friction coefficient ($r = 0.88\text{--}0.90$) and dry adhesion ($r = -0.80$ to -0.87) [17]. Deterministic models have also revealed a positive either linear or parabolic relationship between wet friction and normal force although this affect is modified by both the fluid and shoe-floor angle [6]. An exponential decay model is appropriate when describing the effects of speed on friction when a fluid is present [10]. Because of the interactions that occur between several of the contributing factors to shoe-floor friction, deterministic models have a limited ability to predict friction outside of the range of experimental conditions used to establish these relationships. Therefore, the generalizability of these models is somewhat limited.

Physics-based models, once validated against experimental data, have significant potential for predicting shoe-floor friction in novel environments and in optimizing parameters to enhance frictional properties. These models can also be used to explain the mechanisms that are behind the relationships of deterministic models. For example, consider the exponential decay relationship between sliding speed and shoe-floor friction. In the presence of hydrodynamic lubrication, exponential decay in friction coefficient occurs due to an increase in hydrodynamic pressures. This phenomenon can be modeled by considering the Reynolds equation, contact mechanics, and load balance. The hydrodynamic pressures increase the film thickness and reduce contact forces between the shoe and floor asperities [18]. This exponential decay effect can also be described in boundary lubrication by using finite element analysis. Modeling the interaction between viscoelastic materials (like shoes) and hard materials (like flooring) reveals that increasing speed causes a reduction in contact area and subsequently adhesion friction [19]. This finite element model also explains that increasing roughness leads to more viscoelastic deformation and a reduction in contact area, which describes the positive correlation between roughness and hysteresis and negative correlation between roughness and dry adhesion, respectively [19]. This kind of physics-based model can be applied to many different situations by changing the viscoelastic material properties to simulate different shoes, asperity heights to simulate different roughness flooring, and different loading parameters to simulate different testing conditions. Thus, physics-based models are highly versatile.

2.2 *Hand Function*

Many everyday activities involving the hands (e.g., picking up objects, grasping a railing, or climbing a ladder) would be nearly impossible without the presence of friction. Understanding the role of friction in hand-object interaction has wide benefits including improving the function of stroke patients or reducing falling accidents by increasing a person's capacity to hold on to a railing or ladder rung. The gripping technique used to interact with objects can be broadly categorized as power grips and precision grips (Fig. 17.3). A power grip is capable of producing high forces and typically involves using most or all of the hand and wrapping fingers around an object. Precision grips will often only use a few fingers and involve fine motor control. Typical power grip actions would be carrying a glass of water or grasping the rung of a ladder, while precision grip activities include writing with a pencil, using a fork and knife, and tying a knot. Friction affects both the capacity of power grips and the precision at which a person can manipulate an object. The friction between a person's skin and another object is affected by a large number of factors including properties of the skin and the material of the object being handled.

The coefficient of friction of skin can vary from less than 0.1 to well over 2 and is dependent on the state of the skin (hydration, location of the body), the counter-surface (i.e., what the skin is touching), and the interaction conditions between the

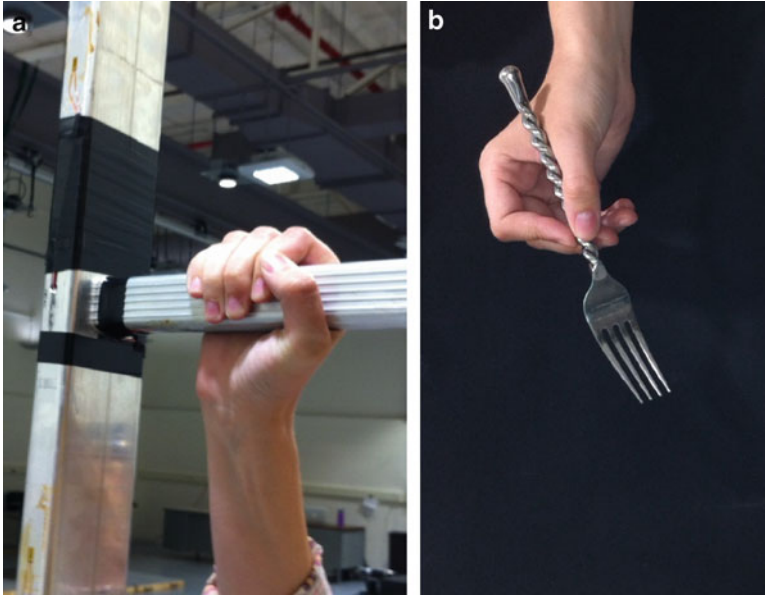
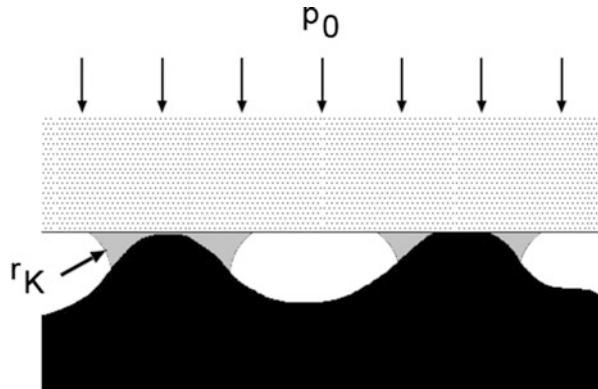


Fig. 17.3 Examples of a power grip (a) in which all five fingers are involved in grasping the object and a precision grip (b) in which just a few of the fingers are involved in grasping the object

surfaces (e.g., contact pressure) as explained in a thorough review by Derler and Gerhardt [20]. The skin is a nonlinear viscoelastic material caused, in part, by its multiple layers, which layer from deep to superficial in the following order: subcutis, dermis, epidermis, and stratum corneum. While the stratum corneum is the thinnest layer, it plays a major role in generating friction between the hand and other objects. Hydration of this layer causes capillaries in the skin to dilate and increases the contact area and subsequently adhesion friction [21] (Fig. 17.4). Adhesion is thought to be the primary source of skin friction although hysteresis may also contribute to the total friction [21]. When the skin becomes wet as opposed to hydrated, however, the friction coefficient will begin to decrease [22, 23]. Skin friction can become further reduced when soap is introduced to the wet skin [22]. In addition to the hydration condition of the skin, the counter-surface has a large effect on the overall friction. Rubber counter-surface materials have greater friction coefficients than metal, whereas cardboard/paper has a lower friction coefficient than metal [24]. Even within metal surfaces, friction coefficients vary across different types of metal surfaces [22]. Lastly, the loading and sliding speed affect the overall friction. The friction coefficient reduces towards an asymptote with increasing contact pressure under most conditions [20]. The wide variations in skin friction due to several different factors tremendously affect our ability to handle and interact with other objects.

Fig. 17.4 Hydration (gray) on the skin surface increases the contact area between the skin (black) and another object (dotted surface) [25]. This adhesion generates a force in addition to the average applied pressure, p_0 , between the surfaces. The radius of curvature or Kelvin radius, r_K , formed by the hydration remains constant under thermal equilibrium



Skin friction is critical to handling objects and changes in friction due to the above mentioned factors can affect this interaction. For example, the outer layer of the skin adapts itself when manipulating objects by achieving the optimal hydration level which maximizes friction and reduces grip effort [21]. In fact, enhancing the friction between the hand and an object can lead to less effort as gripping forces are inversely proportional to the friction coefficient during grasping. Higher-friction surfaces can lead to increased productivity as the fingers are able to more quickly lift and move objects with higher-friction surfaces like rubber compared with wood and paper surfaces [26]. This effect is particularly important for stroke participants who have impaired fine motor control [27, 28]. In fact, even the maximum force exerted during pinching is influenced by the friction of the surface with higher-friction surfaces leading to larger pinch forces, possibly indicating that hand-object friction is an important part of tactile feedback when performing fine motor tasks [29]. Power grips that involve the entire hand are also dramatically affected by friction. For example, the maximum force that a person can generate to hold on to a ladder rung is higher when wearing high-friction rubber gloves compared with moderate-friction skin and low-friction polyester gloves [30]. This indicates that wearing low-friction gloves may impede a person's ability to hold on to the rung, particularly when attempting to recover from a ladder falling event. When gripping cylindrical objects, each of the fingers exerts shear forces that range from 9 to 51 % of the normal force, which indicates that a coefficient of friction of 0.51 or greater is required to prevent the fingers from slipping [31]. Lower friction objects may cause the fingers to slip, which is likely to reduce the amount of control that a person has during the handling of the object. Increasing the friction between the hands and objects that are commonly used, therefore, seems to have several potential benefits ranging from typical holding and manipulation of objects to fall prevention and stroke rehabilitation.

3 Biomedical Tribology

While the oldest and most active research area in biomedical tribology is knee and hip replacement implants, the overlap between tribology and biomedical sciences is quickly growing. Other emerging areas include ocular tribology, cellular tribology, and developing therapies for patients with severe dermal conditions. There is also active research being pursued in dental tribology and cardiovascular tribology. Biomedical tribology can be studied *in vivo*, *in vitro*, and *in silico*, which means conducted inside the living organism, conducted outside the living organism, and conducted using computer simulation, respectively. The term *in situ* is sometimes also used when neither *in vivo* nor *in vitro* terms completely apply. Examples may include temporarily inserting specimens into a living organism and then removing them for analysis. In this section, tribological issues related to the function of the human body including ocular and oral tribology will be covered.

3.1 *Ocular Tribology*

While the blinking of the eye is an effortless and automatic action for most people, it represents an interesting tribological interaction between the cornea of the eye and the eyelid, particularly for individuals wearing contact lenses. Contact lenses are placed directly on the eye and alter the curvature of the eye to provide vision correction. Friction between the contact lens and the eye is thought to be a potential source of eye discomfort and irritation. Therefore, identifying contact lens materials and properties that reduce friction is critical to developing contact lenses that are more comfortable and can be used by more people.

The eye contains structures that serve different purposes such as the retina where light is sensed; the eye lens, which bends light so that images are focused properly on the retina; and the cornea, which is the outermost surface that protects the eye. In order to keep the eye adequately hydrated, a tear film separates the cornea surface from the eyelid, contact lens, or surrounding environment. The tear film can be thought of as three distinct layers: a mucous or mucin layer adjacent to the cornea, an aqueous layer above the mucous layer, and a lipid layer that is adjacent to the eyelid during blinking. The mucin layer modifies the surface of the corneal epithelium to enhance interaction with the aqueous layer. The mucin layer is an oily layer that allows it to fill in the gaps of the hydrophobic cornea surface, which creates a very smooth surface. Enhancing the smoothness of the epithelial layer leads to reduced friction and better refractive properties of the cornea [32]. The aqueous layer represents the bulk of the tear film and is the main lubricating film during blinking. The outer lipid layer slows the evaporation of the aqueous layer [32]. Improperly functioning tear films, in any of the three layers, can cause discomfort and a loss of function in the eye. The most common disorder is dry eye syndrome (DES) or keratitis sicca, which can cause dryness and stinging

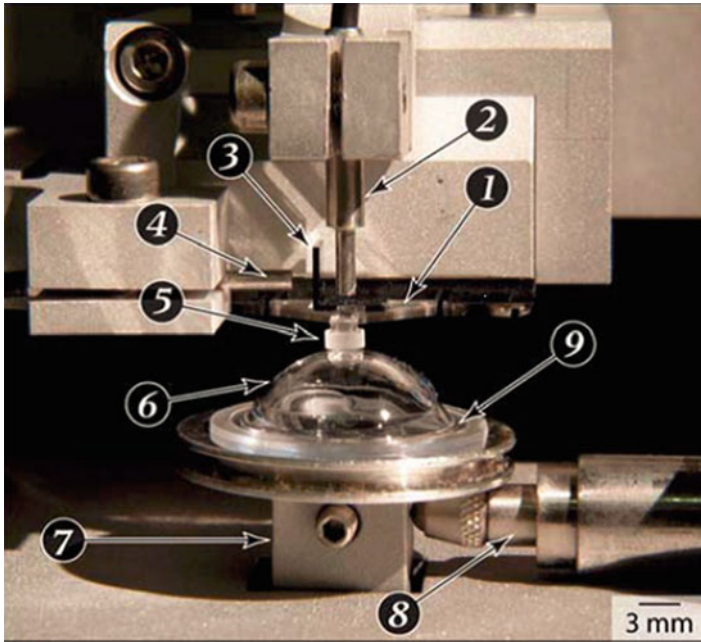


Fig. 17.5 Micro-tribometer setup for testing frictional properties of contact lens [35]. A reciprocating stage (7) moves a hydrogel contact lens (6) relative to a curved glass pin (5). Other components in this micro-tribometer include the glass flexure (1), optical sensors to measure deflections (2 and 4), mirrors (3), linear variable displacement transducer (8) and base to hold contact lens (9)

sensations and can lead to damage to the corneal surface. This disorder can be caused by any of the three layers including a lack of production of the aqueous layer [32] or an improper lipid layer that causes excessive evaporation of the aqueous layer [32]. Even an inadequate mucin layer has negative effects in DES animal models [33], perhaps because the aqueous layer is unable to properly form over dysfunctional mucin film. Clearly the function of the eye is dependent on a properly functioning tear film layer.

Experimental studies have been used to better understand the interaction between hydrogel contact lenses and the eye (Fig. 17.5). The order of magnitude for friction coefficient is known to typically be in the range between 0.01 and 0.1 [34]. The overall friction force can be thought of as the sum of friction due to material deformation (hysteresis), friction due to adhesion, and the friction due to the interfacial shear stress between contacting regions of the eye and contact and fluid shearing (Couette flow). Rennie et al. [35] found good agreement between such a model and experimental results over a variety of testing speeds and normal loads. Friction forces increase nonlinearly with normal force in these lenses and friction forces are higher for faster sliding speeds. Over time, the friction coefficient can increase due to damage to the endothelial layer if this layer is not renewed.

Researchers have proposed different arguments regarding the dominant mechanism during blinking, which has varied between boundary lubrication [36] and elastohydrodynamic lubrication mechanisms [37, 38]. Certainly when the eyelid begins to move and is at a very low velocity, the system is dominated by boundary lubrication, but evidence has suggested at high speeds, the film thickness demonstrates characteristics of elastohydrodynamic lubrication by exceeding the roughness of the epithelium. When identifying the lubrication mechanism, it is important to consider the operating condition. The eye is unusual in that the low sliding speeds (0.15 m/s) and viscosity (4–10 mPa s) [39] suggest boundary lubrication. Yet low normal forces (0.2–0.25 N) and a relatively smooth endothelial layer (0.5 μm) do not require high sliding speeds and viscosity in order to achieve elastohydrodynamic lubrication [38]. The lubrication mechanism, however, may be different during transitional effects at the start or end of the blink when sliding speeds would be close to 0. Jin and Dowson [38] suggest that the spherical form of Reynolds equation is most appropriate for modeling the eye joint based on its spherical geometry (17.3). The spherical Reynolds equation defines the relationship between the film thickness, h ; fluid pressure, p ; fluid viscosity, μ ; and velocities, ω_x , ω_y , and ω_z , across the spherical coordinates of R , θ , and ϕ . The sliding velocities are Cartesian velocities where the z -coordinate is defined as the direction from the center of the lens towards the spherical coordinate system pole and the y -velocity is the velocity perpendicular to the center of the lens' surface. This equation demonstrates that the lubrication of the fluid is highly dependent on the orientation of the lens ($dh/d\theta$ and $dh/d\phi$):

$$\sin\theta \frac{d}{d\theta} \left(h^3 \sin\theta \frac{dp}{d\theta} \right) + \frac{d}{d\phi} \left(h^3 \frac{dp}{d\phi} \right) = 6\mu R^2 \sin\theta^* \left[\left(-\omega_x \sin\phi + \omega_y \cos\phi \right) \sin\theta \frac{dh}{d\theta} + \left(-\omega_x \cos\phi \cos\theta - \omega_y \sin\phi \cos\theta + \omega_z \sin\theta \right) \frac{dh}{d\phi} \right] \quad (17.3)$$

3.2 Oral Tribology

Oral tribology primarily refers to the application of tribology methods to either the teeth or other oral tissues (like the tongue). Oral tribology helps to guide the development and selection of oral restoration implants like veneers, crowns, and implants and can also be used to understand the perception of certain taste sensations like creaminess and roughness of food. Performing tribological simulations of the mouth can be difficult due to the high variation of the conditions that the mouth experiences.

Tooth wear is a pervasive problem that can cause loss of the hard and protective outer surface, called the enamel. Tooth wear affects around 3 % of young adults and approximately 17 % of older adults [40]. Dental wear commonly occurs on the

surface between the upper and lower sets of teeth, called the occlusal surface, although it can occur on other dental surfaces as well. Tooth wear typically occurs at a rate of $0.6 \mu\text{m}/\text{month}$ but can occur at higher rates in certain cases [41]. Identifying personal habits that increase this process is critical to developing interventions that modify behaviors to promote dental health, while identifying individual risk factors is important to targeting those in need of interventions. The main theory that is relevant to the tribology of teeth is two-body wear, three-body wear, and corrosion. In the dental community, the terms abrasion, attrition, and corrosion are typically used to mean two-body wear, three-body wear, and corrosion, respectively. In addition, abfraction is also used to refer to cracking in the teeth caused by bending moment loads that can occur vertically across the tooth and can lead to excessive tension stresses in the outside portion of the tooth.

Tribological theory from three-body wear (see Chap. 2 for theory related to three-body wear) can be applied to the teeth to understand how different conditions, food, and cleaning processes can lead to pathological wear of the teeth. In three-body wear during *mastication*, which is the act of chewing, the food that is being chewed can act as an abrasive slurry and cause wear on the teeth. In this condition, the lubricating fluid is saliva, while hard particles within the food can act as the abrasive. The mechanical action of the teeth moving together and sliding next to each other generates the necessary dynamics to cause this wear. Another relevant three-body wear problem occurs when brushing the teeth, where small particles suspended in toothpaste are pushed into the enamel by the toothpaste and wear the material away. In certain cases, excessive toothbrushing has been identified to cause significant wear [42] although the benefits of normal toothbrushing far outweigh the wear effects.

Evaluating three-body wear is critical to understanding the performance of dental restoration materials. For example, composite materials are commonly used for fillings to the back molar teeth due to the fact that they blend in with the teeth and have minimal toxicity compared to some metal fillings. Unfortunately, composite materials have traditionally worn at a higher rate, which may lead to a person replacing these restorations multiple times over their lifetime. Therefore, experiments simulating three-body wear have been used to measure the relative wear between different composite materials and identify the most wear-resistant materials [43].

Two-body wear and corrosion can also cause the teeth to wear, and thus their understanding may contribute to the understanding for why certain individuals experience excessive wear in their teeth. Two-body wear can occur when two surfaces such as the top and bottom sets of teeth directly contact and shear relative to each other. Individuals who grind their teeth during sleep may therefore experience a higher wear rate of their tooth enamel. Two-body wear can also occur during cleaning when a dentist uses a scaler or sickle to scrape tartar and plaque from the tooth surface. This type of tooth wear occurs infrequently for most people, and the health benefits of having tartar and plaque removed likely offset the negative effects of tooth wear.

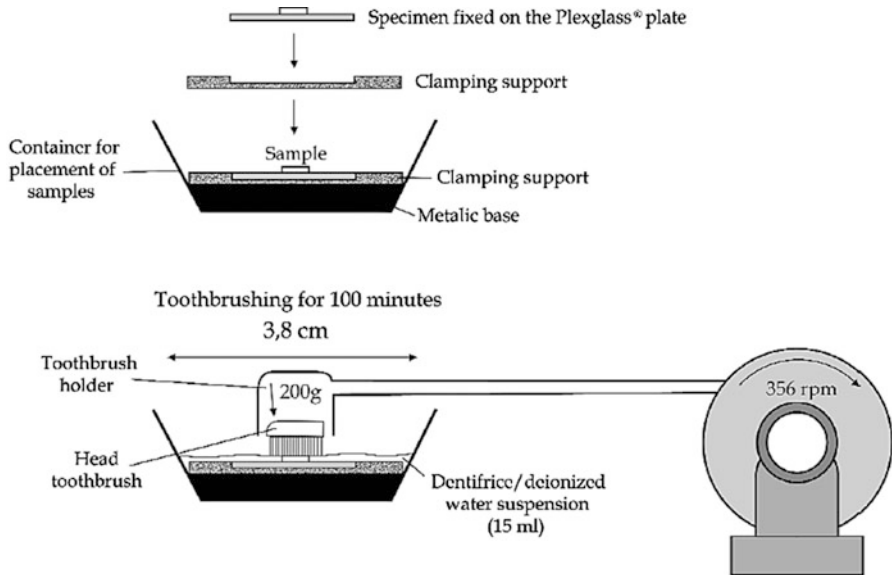


Fig. 17.6 Schematic for simulated toothbrushing apparatus. The head of the toothbrush reciprocates over the dental specimen with toothpaste and water slurry present. This represents a method for *in vitro* testing of dental materials. The dental sample is attached to a plate, which is fastened to a base using a clamping support (*top*). After applying a toothpaste/water suspension, the toothbrush reciprocates over the surface during the experiment (*bottom*) [48]

Corrosion is another major cause of tooth wear. Corrosion commonly occurs when the mouth becomes acidic due to acidic beverages or acid reflux. Acidity in the mouth can cause demineralization of the enamel, which causes it to soften [44]. The softening of the enamel due to corrosion can also alter the rate of two- and three-body wear in a process analogous to chemical mechanical polishing [45]. Therefore, changing the composition of soda in order to reduce its acidity may improve the dental hygiene of soda drinkers. In addition, drinking acidic beverages and acid reflux may target people at risk for corrosion who are in need of interventions such as fluoride, which enhances enamel.

Several techniques have been created to simulate wear on teeth, restorations, and dentures *in vitro*. Brushing simulators have been developed to analyze the effects of brushing technique, toothbrushes, and toothpaste on wear (Fig. 17.6). These simulators typically simulate the loading and movement patterns of brushing and then measure the amount of lost wear. These devices can be used to quantify the effects of toothpaste on tooth wear using the relative enamel abrasivity [46]. Several other three-body wear devices have been developed for simulating wear during mastication (chewing). It is critical that these devices simulate the *in vivo* conditions as closely as possible including the material composition and shape of the tooth and antagonist tooth surfaces: loading, number of cycles, chewing frequency, shear sliding speed, temperature, food bolus, lubricant and friction, pH, and enzymes included in saliva [47].

The tribological interaction between mouth surfaces and the tongue has a major effect on the way that certain foods are perceived. While sensations related to sweet, sour, salty, bitter, and savory are sensed by very specific tasting receptors, other sensations such as creaminess and smoothness are affected by the mechanical interactions between the tongue and other oral surfaces. Certain properties of the *food bolus*, a mass of food and saliva that has been or is being chewed, can affect the mechanical interaction between the tongue and other surfaces and thus lead to certain sensations. In particular, fats or oils in food typically serve as a lubricant and cause a reduction in friction. The reduction in friction eases the effort to move the bolus around and swallow it, which leads to a perception of creaminess. The viscosity of the food bolus is inversely proportional to the friction value although this effect is not linear [49]. Different tribological methods have been used to simulate the effects of fluid and fat content on friction. When testing the effects of different food contents on tongue friction, it is critical to properly simulate the chemical interactions between the food and saliva. Specifically, including amylase in the simulated saliva is critical because it breaks down lipids and causes an increase in friction [49]. Implementing lubrication principles to reduce friction between the tongue and surrounding surfaces may provide an opportunity to preserve the creaminess sensation of certain foods when identifying appropriate substitutes for fats and oils.

3.3 Other Biotribology Topics

There are several other biotribology topics such as adhesion at the cellular level and skin disorders that this chapter does not cover in detail. Cells in the body develop adhesive bonds that allow them to stick to specific other cells and to move relative to other cells. For example, leukocytes (white blood cells) roll across the endothelium of blood vessels under normal circumstances because the blood pressure flow exceeds the adhesive force between those surfaces. When an inflammation response is triggered, however, the leukocytes generate large enough adhesive forces so that the leukocyte sticks to the endothelium even though blood is flowing around it [50]. Understanding of the mechanism that allows this selective adhesion is critical to controlling autoimmune disorders and developing selective-adhesive technology. Another application of tribology to biology relates to the role of skin friction in blistering. Blistering commonly occurs when the friction forces are transmitted through the top layer of skin (the stratum corneum) causing delamination of the skin layers [51]. This can occur due to interactions between the hands and tools (e.g., from pushing a lawn mower) or between the skin and clothing (e.g., after running a marathon in bad socks). Blistering can be clinically significant in the case of the genetic disorder epidermolysis bullosa, where the skin is exceptionally sensitive to blistering. In this disorder, even typical activities such as wearing clothing can cause the entire body to become covered in blisters. Reducing the coefficient of friction between the skin and the surface is critical to reducing blistering and can be

accomplished by applying lubricants such as cornstarch or skin glide sticks to the skin [52]. As friction and wear is critical to most biological systems, the potential to apply tribology to areas beyond the topics covered in this chapter is extensive. Significant opportunities exist for improving medical therapies and for engineering products that mimic some of the exceptional tribological properties of materials and fluids that are observed in the human body and in nature.

4 Conclusions

In this chapter, we have demonstrated the value of tribologists to several biological problems. Applying advanced tribological techniques has led to improved understanding of shoe-floor friction, handling of objects, eye discomfort, and oral health. Many more tribology problems exist in biological systems. Performing biotribology research requires understanding the underlying biological principles relevant to a problem, identifying the most relevant tribology theory, and applying this theory to understand and optimize the biological system. By adopting this approach of considering both the biological responses and tribological interactions, the next generation of biotribologists has an opportunity to make significant advancements in medicine, ergonomics, and rehabilitation.

References

1. Redfern MS, Cham R, Gielo-Perczak K, Gronqvist R, Hirvonen M, Lanshammar H, Marpet MI, Pai YC (2001) Biomechanics of slips. *Ergonomics* 44:1138–1166
2. US Bureau of Labor Statistics (2011) Table 1: Number, percent distribution, and median days away from work for nonfatal occupational injuries and illnesses involving days away from work by selected worker and case characteristics and gender. Department of Labor, Washington, DC
3. Hausdorff J, Rios DA, Edelberg HK (2001) Gait variability and fall risk in community-living older adults: a one-year prospective study. *Arch Phys Med Rehab* 82:1050–1056
4. Chang WR, Chang CC, Matz S, Lesch MF (2008) A methodology to quantify the stochastic distribution of friction coefficient required for level walking. *Appl Ergon* 39(6):766–771
5. Chang WR, Chang CC, Matz S (2012) Comparison of different methods to extract the required coefficient of friction for level walking. *Ergonomics* 55(3):308–315
6. Beschoner KE, Redfern MS, Porter WL, Debski RE (2007) Effects of slip testing parameters or measured coefficient of friction. *Appl Ergon* 38:773–780
7. Harper FC, Warlow WJ, Clarke BL (eds) (1961) The forces applied to the floor by the foot in walking. National building studies: research paper 32. HMSO, London
8. Chang WR, Gronqvist R, Leclercq S, Brungraber RJ, Mattke U, Strandberg L, Thorpe SC, Myung R, Makkonen L, Courtney TK (2001) The role of friction in the measurement of slipperiness, Part 2: survey of friction measurement devices. *Ergonomics* 44(13):1233–1261
9. Chang W, Courtney TK, Grönqvist R, Redfern M (2003) Measuring slipperiness—discussions on the state of the art and future research. Taylor and Francis, London
10. Moore CT, Beschoner K, Menezes PL, Lovell M (2012) Analysis of shoe friction during sliding against floor material: role of fluid contaminant. *J Tribol* 134(4):041104

11. Beschoner K, Singh G (2012) A novel method for evaluating the effectiveness of shoe-tread designs relevant to slip and fall accidents. Paper presented at the Human Factors and Ergonomics Society, Boston, MA
12. Strandberg L (1985) The effect of conditions underfoot on falling and overexertion accidents. *Ergonomics* 28(1):131–147
13. Proctor TD, Coleman V (1988) Slipping, tripping and falling accidents in Great Britain—present and future. *J Occup Accid* 9:269–285
14. Strobel CM, Menezes PL, Lovell MR, Beschoner KE (2012) Analysis of the contribution of adhesion and hysteresis to shoe–floor lubricated friction in the boundary lubrication regime. *Tribol Lett* 47:341–347
15. Heinrich G, Klüppel M (2008) Rubber friction, tread deformation and tire traction. *Wear* 265:1052–1060
16. Chang WR, Grönqvist R, Hirvonen M, Matz S (2004) The effect of surface waviness on friction between Neolite and quarry tiles. *Ergonomics* 47(8):890–906
17. Cowap M (2012) The effects of floor roughness on shoe-floor friction adhesion and hysteresis. In: ASME/STLE International Joint Tribology Conference, Los Angeles, CA, 2012
18. Beschoner K, Lovell M, Higgs CF III, Redfern MS (2009) Modeling mixed-lubrication of a shoe-floor interface applied to a pin-on-disk apparatus. *Tribol Trans* 52(4):560–568
19. Singh G (2012) Analysis of shoe-floor slipperiness through computational modeling and measurements of hydrodynamic pressures with robotic slip simulator. University of Wisconsin, Milwaukee, WI
20. Derler S, Gerhardt LC (2011) Tribology of skin: review and analysis of experimental results for the friction coefficient of human skin. *Tribol Lett* 45:1–27
21. André T, Lefèvre P, Thonnard JL (2010) Fingertip moisture is optimally modulated during object manipulation. *J Neurophysiol* 103(1):402–408
22. O'Meara D, Smith R (2002) Functional handgrip test to determine the coefficient of static friction at the hand/handle interface. *Ergonomics* 45(10):717–731
23. Tomlinson S, Lewis R, Liu X, Texier C, Carré M (2011) Understanding the friction mechanisms between the human finger and flat contacting surfaces in moist conditions. *Tribol Lett* 41(1):283–294
24. Seo NJ, Armstrong TJ, Drinkaus P (2009) A comparison of two methods of measuring static coefficient of friction at low normal forces: a pilot study. *Ergonomics* 52(1):121–135
25. Persson B (2008) Capillary adhesion between elastic solids with randomly rough surfaces. *J Phys Condens Matter* 20:315007
26. Enders LR (2010) Effect of hand-object friction on grip force application and hand function. University of Wisconsin, Milwaukee, WI
27. Hermsdörfer J, Hagl E, Nowak D, Marquardt C (2003) Grip force control during object manipulation in cerebral stroke. *Clin Neurophysiol* 114(5):915–929
28. Scott JO, Brandenburg AR, Allard BM, Seo NJ (2011) Identification and improvement of difficult hand grip movement components for stroke survivors using the box and block test. American Society of Biomechanics, Long Beach, CA
29. Seo NJ, Shim JK, Engel AK, Enders LR (2011) Grip surface affects maximum pinch force. *Hum Factors* 53(6):740–748
30. Hur P, Motawar B, Seo NJ (2012) Hand breakaway strength model—effects of glove use and handle shapes on a person's hand strength to hold onto handles to prevent fall from elevation. *J Biomech* 45:958–964
31. Enders LR, Jin Seo N (2011) Phalanx force magnitude and trajectory deviation increased during power grip with an increased coefficient of friction at the hand-object interface. *J Biomech* 44(8):1447–1453
32. Lens A, Nemeth SC, Ledford JK (2007) Ocular anatomy and physiology. Slack Incorporated, Thorofare, NJ

33. Viau S, Maire MA, Pasquis B, Grégoire S, Fourgeux C, Acar N, Bretillon L, Creuzot-Garcher CP, Joffre C (2008) Time course of ocular surface and lacrimal gland changes in a new scopolamine-induced dry eye model. *Graefe's Arch Clin Exp Ophthalmol* 246(6):857–867
34. Dunn AC, Cobb JA, Kantzios AN, Lee SJ, Sarntinoranont M, Tran-Son-Tay R, Sawyer WG (2008) Friction coefficient measurement of hydrogel materials on living epithelial cells. *Tribol Lett* 30(1):13–19
35. Rennie A, Dickrell P, Sawyer W (2005) Friction coefficient of soft contact lenses: measurements and modeling. *Tribol Lett* 18(4):499–504
36. Ehlers N (1965) The precorneal film. *Biomicroscopical, histological and chemical investigations. Acta ophthalmologica. Supplementum*, vol 81. Munksgaard, Copenhagen, pp 1–136
37. Dowson D (2009) A tribological day. *Proc IME J J Eng Tribol* 223(3):261
38. Jin Z, Dowson D (2005) Elastohydrodynamic lubrication in biological systems. *Proc IME J J Eng Tribol* 219(5):367–380
39. Tiffany JM (1991) The viscosity of human tears. *Int Ophthalmol* 15(6):371–376
40. Van't Spijker A, Rodriguez JM, Kreulen CM, Bronkhorst EM, Bartlett DW, Creugers N (2009) Prevalence of tooth wear in adults. *Int J Prosthodont* 22(1):35
41. Zhou Z, Zheng J (2008) Tribology of dental materials: a review. *J Phys D Appl Phys* 41:113001
42. Addy M, Hunter M (2003) Can tooth brushing damage your health? Effects on oral and dental tissues. *Int Dent J* 53(S3):177–186
43. Schultz S, Rosentritt M, Behr M, Handel G (2010) Mechanical properties and three-body wear of dental restoratives and their comparative flowable materials. *Quintessence Int* 41(1):e1
44. Bartlett DW (2005) The role of erosion in tooth wear: aetiology, prevention and management. *Int Dent J* 55(S4):277–284
45. Eisenburger M, Addy M (2002) Erosion and attrition of human enamel in vitro part I: interaction effects. *J Dent* 30(7):341–347
46. Hefferen JJ (1976) A laboratory method for assessment of dentifrice abrasivity. *J Dent Res* 55(4):563–573
47. Lambrechts P, Debels E, Van Landuyt K, Peumans M, Van Meerbeek B (2006) How to simulate wear?: overview of existing methods. *Dent Mater* 22(8):693–701
48. Takeuchi C, Flores VHO, Dibb RGP, Panzeri H, Lara E, Dinelli W (2003) Assessing the surface roughness of a posterior resin composite: effect of surface sealing. *Oper Dent* 28(3):281–286
49. de Wijk RA, Prinz JF (2005) The role of friction in perceived oral texture. *Food Qual Prefer* 16(2):121–129
50. Gebeshuber IC, Drack M, Scherge M (2008) Tribology in biology. *Tribol Mater Surf Interf* 2(4):200–212
51. Naylor P (1955) Experimental friction blisters. *Br J Dermatol* 67(10):327–342
52. Guerra C, Schwartz C (2012) Investigation of the influence of textiles and surface treatments on blistering using a novel simulant. *Skin Res Technol* 18:94–100

Review Questions

1. Choose the modeling type (physics-based or deterministic) that would be most appropriate for the following slip-prevention situations. Support the rationale of your choice by considering whether that model is the most efficient means of achieving the stated objective:
 - (a) You are developing guidelines for a fast-food chain on when they need to replace their tile flooring based on the roughness. The chain would like to

replace their tiles when the coefficient of friction goes below a level of 0.30. All employees wear the same type of footwear and only two fluids are ever present in the kitchen (cooking oil and water).

- (b) You work for a shoe design company and are in charge of developing a tread pattern for a new type of footwear. The footwear is meant to have exceptional friction characteristics and is intended for elderly adults. You would like to ensure that the tread size and type is optimal. The shoes will be worn in several different locations and will be exposed to several different conditions.
2. During a slipping event, a foot accelerates to a peak speed of about 2 m/s. The normal forces are approximately 500 N. Consider a treadless shoe with a width of 110 mm and a treaded shoe with treads that have a width of 15 mm. How high would floor roughness asperities need to be to break through the fluid films of water and oil? Do not consider the effects due to squeeze film.
 3. You have been hired by a tool manufacturer to suggest a redesign of pipe wrenches. Customers complain that they have trouble generating enough force to break apart seized pipes. How would you redesign the tool in order to optimize the tribological interaction between the tool and the hand? Specifically focus on solutions that would assist the user in increasing the force they can exert on the tool? Provide at least one suggestion for redesigning the tool and another suggestion for what the person using the tool could do to improve their grip force.
 4. Consider the tribological differences between contact lens that are hydrophobic and hydrophilic. How would each of these surfaces interact with the lipid and aqueous layer of the tear film? How would a hydrophobic lens act differently than a hydrophilic lens when the lens is initially put in the eye and when trying to take the lens out of the eye?
 5. Typical wear rates for teeth are 0.6 $\mu\text{m}/\text{month}$. Drinking acidic beverages is thought to increase this wear. Determine the approximate enamel thickness of the teeth by searching the relevant literature. Assuming that drinking acidic beverages increases this wear rate by a factor of 8, how long would it take to wear through the enamel of teeth for a person who drinks a lot of acidic beverages compared to a person who did not drink acidic beverages? How would the wear rate be affected by eating food simultaneously to drinking acidic beverages? Therefore, what would you tell a person who insists on drinking acidic beverages but is also concerned with reducing tooth wear?
 6. You are evaluating several different low-fat substitute ingredients to replace the cream in ice cream. Describe experimental methods that could be used to evaluate how each of the replacement ingredients would be perceived. How would you determine the best replacement ingredient so that the new low-fat ice cream “tastes” similar to regular ice cream?
 7. Identify a biological problem that is caused in part or whole by friction, lubrication, or wear. Learn about the relevant biological principles and identify the appropriate tribological techniques to study the biological issue in more depth.

Chapter 18

Green and Biomimetic Tribology

Michael Nosonovsky, Vahid Hejazi, and Vahid Mortazavi

Abstract Green Tribology is a new area of tribology studying ecological approaches, methods, and applications in tribology. The major premise of green tribology is minimization of friction and wear, and reduction or elimination of lubrication. It includes eco-friendly materials and coating, green lubricants (biodegradable lubricants) and biomimetic surfaces used in tribological application. Using sustainable chemistry and engineering principles, biomimetic approaches and surface texturing are other concerns of green tribology. The area also takes degradation of surfaces, coatings, and components into consideration during design stages. The tribology of renewable sources of energy can also be considered as a relatively new challenge. We discuss areas and principles of green tribology and current developments in biomimetic materials and surfaces.

1 Introduction

Green and biomimetic tribology constitute new areas of tribology which emerged in the twenty-first century. Tribology (from the Greek word τριβω “tribo” meaning “to rub”) is defined by the Oxford dictionary as “the branch of science and technology concerned with interacting surfaces in relative motion and with associating matters (as friction, wear, lubrication, and the design of bearings).” The word “tribophysics” was used already in the 1940s by David Tabor and Philip Bowden for the name of their laboratory in Melbourne University, Australia [61, 70]. The term “tribology” was officially introduced and defined at the governmental level in 1966 by Prof. H. Peter Jost, chairman of a working group of lubrication engineers, in his published report for the UK Department of Education and Science. The group

M. Nosonovsky (✉) • V. Hejazi • V. Mortazavi
College of Engineering and Applied Science, University of Wisconsin,
Milwaukee, WI 53201, USA
e-mail: nosonovs@uwm.edu

recommended uniting multidisciplinary scientific and engineering efforts in the areas of friction, wear, and lubrication, so that they can benefit from one another. Since the emergence of the word tribology almost 50 years ago, many new areas of tribological studies have developed which are at the interface of various scientific disciplines, and various aspects of interacting surfaces in relative motion have been the focus of tribology. These areas include, for example, nanotribology, biotribology, the tribology of magnetic storage devices and micro/nanoelectromechanical systems (MEMS/NEMS), and adhesive contact. The research in these areas is driven mostly by the advent of new technologies and new experimental techniques for surface characterization. Ecotribology or green tribology is one of such areas.

Even prior to 2010, when the first scientific volume on green tribology appeared [89], a number of economists and leaders responsible for the scientific policy and planning paid attention to the need for ecological or “green” tribology. Bartz [8] stated that “Savings of resources of energy and reducing the impact on the environment are the most important aspects of ecotribology. In the course of relevant practices savings of basic resources and materials, optimum design, optimum operation, reduced energy consumption, and the protection of the environment have to be covered. Using environmentally acceptable lubricants is the key factor for this” He suggested a diagram which he called “ECO-Balance-Sheet-Tree” which summarized all of these aspects. Sasaki [100] has emphasized the need for ecological Tribology, which he considered a response to the World economic and financial crisis of 2008 as well as the global warming crisis as reflected by the “Kyoto Protocol.” Si-wei Zhang, past chairman of the Chinese Tribology Institution, suggested Green Tribology as an international concept in June 2009. After that, H. Peter Jost emphasized the economic need for Green Tribology during his address to the Fourth World Tribology Congress, in Kyoto in September 2009. The new concept of “green tribology” has been defined as “the science and technology of the tribological aspects of ecological balance and of environmental and biological impacts.” Jost [73] elaborated on the need for green tribology and has mentioned that “the influence of economic, market, and financial triumphalisms have retarded tribology and could retard ‘Green Tribology’ from being accepted as a not-unimportant factor in its field. Therefore, by highlighting the economic benefits of tribology, tribology societies, groups and committees are likely to have a far greater impact on the makers of policies and the providers of funding than by only preaching the scientific logic. Tribology societies should highlight to the utmost the economic advantage of tribology. It is the language financial oriented policy makers and markets, as well as governments, understand.”

These earlier works by research administrators and economists called scientists to pay attention to Green Tribology; however, they did not define the field in a rigorous scientific or academic manner. The first scientific volume on Green Tribology emerged in 2010, when *Philosophical Transactions of the Royal Society*, the oldest (published since 1666) and one of the most prestigious research journals in the world, decided to devote a theme issue to Green Tribology, edited by Nosonovsky and Bhushan [88]. In that volume, the editors defined Green Tribology

in quite a broad way, so that it encompasses biomimetic tribology (which follows the ways of living nature to solve engineering problems, as it will be described below), eco-friendly lubrication and clean and sustainable energy applications. The presumption was that combination of these areas under the umbrella of Green Tribology could enhance them all and help to benefit from one another by establishing new links. Another volume on Green tribology was published by Nosonovsky and Bhushan [90]. A number of workshops, conference sections, and symposia took place after that, which confirmed the inclusive approach, as well as the interest to Green Tribology in general. Since 2009, a relatively large group of tribologists works at the University of Wisconsin-Milwaukee (UWM). Several of them are involved into the topics related to Green Tribology, so currently UWM can be called the main center of Green Tribology research in the USA.

The specific field of green or environment-friendly tribology emphasizes the aspects of interacting surfaces in relative motion, which are of importance for energy or environmental sustainability or which have impact upon today's environment. This includes tribological technology that mimics living nature (biomimetic surfaces) and thus is expected to be environment-friendly, the control of friction and wear that is of importance for energy conservation and conversion, environmental aspects of lubrication and surface modification techniques, and tribological aspects of green applications, such as wind-power turbines, tidal turbines, or solar panels. It is clear that a number of tribological problems could be put under the umbrella of "green tribology" and is of mutual benefit to one another.

Green tribology can be viewed in the broader context of two other "green" areas: green engineering and green chemistry. The US Environmental Protection Agency (EPA) defined green engineering as "the design, commercialization and use of processes and products that are technically and economically feasible while minimizing (i) generation of pollution at the source (ii) risk to human health and the environment". Besides that, the three tiers of green engineering assessment in design involve: (i) process research and development, (ii) conceptual/preliminary design, and (iii) detailed design pollution prevention, process heat/energy integration, process mass integration [2].

Another related area is green chemistry, also known as sustainable chemistry, which is defined as "the design of chemical products and processes that reduce or eliminate the use or generation of hazardous substances". The focus of green chemistry is on minimizing the hazard and maximizing the efficiency of any chemical choice. It is distinct from environmental chemistry which focuses on chemical phenomena in the environment. While environmental chemistry studies the natural environments as well as pollutant chemicals in nature, green chemistry seeks to reduce and prevent pollution at its source. Green chemistry technologies provide a number of benefits, including reduced waste, eliminating costly end-of-the-pipe treatments, safer products, reduced use of energy and resources, and improved competitiveness of chemical manufacturers and their customers. Green chemistry consists of chemicals and chemical processes designed to reduce or eliminate negative environmental impacts. The use and production of these

chemicals may involve reduced waste products, nontoxic components, and improved efficiency.

Anastas and Warner [3] formulated The 12 Principles of Green Chemistry which provided a road map for chemists to implement green chemistry. A number of green chemistry metrics have been suggested to quantify the environmental efficiency of a chemical process. These metrics include the Environmental Factor (“E-factor”), which is equal to the total mass of waste divided by mass of product [103], the atom economy [110], the effective mass yield [69], the carbon efficiency, reaction mass efficiency [24], etc.

Attempts are made not only to quantify the “greenness” of a chemical process but also to factor in other parameters such as chemical yield, the price of reaction components, safety in handling chemicals, hardware demands, energy profile and ease of product workup and purification. Green chemistry is increasingly seen as a powerful tool that researchers must use to evaluate the environmental impact of nanotechnology. As nanomaterials are developed, the environmental and human health impacts of both the products themselves and the processes to make them must be considered to ensure their long-term economic viability. While many scientists use the term “green chemistry,” there are also critics who argue that green chemistry is no more than a public relations label, since some chemists use the term green chemistry without relating it to the green chemistry principles proposed by Anastas and Warner [3], as it was pointed out by Linthorst [78]. Green Tribology may have to deal with the same problem.

2 Principles and Areas of Green Tribology

Nosonovsky and Bhushan [88, 90] suggested that 12 principles of Green Tribology can be formulated, similar to the principles of Green Chemistry. Some principles are related to the design and manufacturing of tribological applications (iii–x), while others belong to their operation (i–ii and xi–xii). We followed the tradition and limited the number of principles to 12.

- (i) *Minimization of heat and energy dissipation.* Friction is the primary source of energy dissipation. According to government estimates, about one-third of the energy consumption in the USA is spent to overcome friction. Most energy dissipated by friction is converted into heat and leads to the heat pollution of atmosphere and the environment. The control of friction and friction minimization, which leads to both the energy conservation and prevention of the damage to the environment due to the heat pollution, is a primary task of tribology. It is recognized that for certain tribological applications (e.g., car brakes and clutches) high friction is required; however, ways of effective use of energy for these applications should be sought as well.

- (ii) *Minimization of wear* is the second most important task of tribology which has relevance to green tribology. In most industrial applications wear is undesirable. It limits the lifetime of components and therefore creates the problem of their recycling. Wear can lead also to catastrophic failure. In addition, wear creates debris and particles which contaminate the environment and can be hazardous for humans in certain situations. For example, wear debris generated after human joint replacement surgery is the primary source of long-term complications in patients.
- (iii) *Reduction or complete elimination of lubrication and self-lubrication*. Lubrication is a focus of tribology since it leads to the reduction of friction and wear. However, lubrication can also lead to environmental hazards. It is desirable to reduce lubrication or achieve the self-lubricating regime, when no external supply of lubrication is required. Tribological systems in living nature often operate in the self-lubricating regime. For example, joints form essentially a closed self-sustainable system.
- (iv) *Natural lubrication* (e. g., vegetable oil based) should be used in cases when possible, since it is usually environmentally friendly.
- (v) *Biodegradable lubrication* should also be used when possible to avoid environmental contamination. In particular, water lubrication is an area which attracted researchers in recent years. Natural oil (such as canola) lubrication is another option, especially discussed in the developing countries.
- (vi) *Sustainable chemistry and green engineering principles* should be used for the manufacturing of new components for tribological applications, coatings, and lubricants.
- (vii) *Biomimetic approach* should be used whenever possible. This includes biomimetic surfaces, materials, and other biomimetic and bio-inspired approaches, since they tend to be more ecologically friendly.
- (viii) *Surface texturing* should be applied to control surface properties. Conventional engineered surfaces have random roughness, and the randomness is the factor which makes it extremely difficult to overcome friction and wear. On the other hand, many biological functional surfaces have complex structures with hierarchical roughness, which defines their properties. Surface texturing provides a way to control many surface properties relevant to making tribosystems more ecologically friendly.
- (ix) *Environmental implications of coatings* and other methods of surface modification (texturing, depositions, etc.) should be investigated and taken into consideration.
- (x) *Design for degradation* of surfaces, coatings, and tribological components. Similar to green chemistry applications, the ultimate degradation/utilization should be taken into consideration during design.
- (xi) *Real-time monitoring*, analysis, and control of tribological systems during their operation should be implemented to prevent the formation of hazardous substances.
- (xii) *Sustainable energy applications* should become the priority of the tribological design as well as engineering design in general.

The following three focus areas of tribology have the greatest impact on environmental issues, and, therefore, they are of importance for green tribology: (i) biomimetic and self-lubricating materials/surfaces, (ii) biodegradable and environment-friendly lubricants, coatings, and materials, and (iii) tribology of renewable and/or sustainable sources of energy. Below we briefly discuss the current state of these areas and their relevance for the novel field of green tribology.

3 Biomimetics in Tribology

Biomimetics (also referred to as bionics or biomimicry) is the application of biological methods and systems found in nature to the study and design of engineering systems and modern technology. It is estimated that the 100 largest biomimetic products generated approximately US \$1.5 billion over the years 2005–2008 and the annual sales are expected to continue to increase dramatically [90]. Many biological materials have remarkable properties which can hardly be achieved by conventional engineering methods. For example, a spider can produce huge amounts (comparing with the linear size of his body) of silk fiber, which is stronger than steel, without any access to the high temperatures and pressures which would be required to produce such materials as steel using conventional human technology. These properties of biomimetic materials are achieved due to their composite structure and hierarchical multiscale organization [45]. The hierarchical organization provides biological systems with the flexibility needed to adapt to the changing environment. As opposed to the traditional engineering approach, biological materials are grown without the final design specifications, but by using the recipes and recursive algorithms contained in their genetic code. The difference of natural versus engineering design is the difference of growth versus fabrication [44, 82, 83, 85]. Hierarchical organization and the ability of biological systems to grow and adapt also provides a natural mechanism for the repair or healing of minor damage in the material.

The remarkable properties of the biological materials serve as a source of inspiration for materials scientists and engineers indicating that such performance can be achieved if the paradigm of materials design is changed. While in most cases it is not possible to directly borrow solutions from living nature and to apply them in engineering, it is often possible to take biological systems as a starting point and a source of inspiration for engineering design. Molecular scale devices, superhydrophobicity, self-cleaning, drag reduction in fluid flow, energy conversion and conservation, high adhesion, reversible adhesion, aerodynamic lift, materials, and fibers with high mechanical strength, biological self-assembly, antireflection, structural coloration, thermal insulation, self-healing and sensory-aid mechanisms are some of the examples found in nature that are of commercial interest [83, 84].

Biomimetic materials are also usually environmentally friendly in a natural way, since they are a natural part of the ecosystem. For this reason, the biomimetic approach in tribology is particularly promising. In the area of biomimetic surfaces, a number of ideas have been suggested [6, 12, 43, 83–85, 103].

Superhydrophobic or highly hydrophobic (hydro/water + phobic/fearing) surfaces are surfaces which repel water and it is extremely difficult to wet their surfaces. In other words, when the water contact angle (primary parameter which characterizes the wetting property of a surface) is between 150° and 180° , the surface is called superhydrophobic. There are a large number of biological surfaces such as plant leaves which are known to be superhydrophobic and self-cleaning.

The self-cleaning property of plant leaves is due to especially textured topography of the surface as well as the chemical constituents of the cuticle covering their surface [7, 35, 81, 114]. These surfaces have been fabricated in the lab with comparable performance [74]. While self-cleaning property is present in many plant surfaces, the self-cleaning behavior of lotus leaves has drawn iconic interest. Water drops on lotus leaves readily roll upon the surface, picking up the dirt particles along the way, in a mechanism known as self-cleaning. Therefore the phenomenon of self-cleaning and water repellency was called “Lotus effect”.

The static contact angle is determined by the interactions across the three interfaces. Most often the concept is illustrated with a small liquid droplet resting on a smooth horizontal solid surface. The shape of the droplet is determined by the Young–Laplace equation, with the contact angle playing the role of a boundary condition. The Young–Laplace equation shows the pressure difference of a spherical surface and is given by

$$P_a - P_b = \frac{2\gamma}{R} \quad (18.1)$$

where P_a and P_b are the pressures inside and outside of the spherical surface, respectively. γ is surface tension and R is radius of the spherical surface.

When a liquid droplet or air bubble comes in contact with a smooth solid surface under the angle θ_0 (Fig. 18.1), the net energy change for propagation of the liquid front for a small distance dx is equal to $(\gamma_{SL} - \gamma_{SV} + \gamma_{LV} \cos \theta_0) dx$. Thus, for the liquid front being at equilibrium, the Young’s equation should be satisfied [99], and the contact angle is given by

$$\cos \theta_0 = \frac{\gamma_{SV} - \gamma_{SL}}{\gamma_{LV}} \quad (18.2)$$

where γ_{SL} , γ_{SV} , and γ_{LV} are solid–liquid, solid–vapor, and liquid–vapor interfacial energies, respectively.

From (18.2), it is obvious that three situations are likely to exist. If $(\gamma_{SV} - \gamma_{SL})/\gamma_{LV} > 1$, the surface is completely wetted with the liquid fully absorbed by the solid surface ($\theta_0 = 0$), if $(\gamma_{SV} - \gamma_{SL})/\gamma_{LV} < -1$, the liquid is completely repelled by the

Fig. 18.1 A water-vapor surface coming to the solid surface at the contact angle of θ

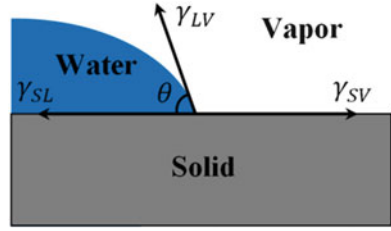
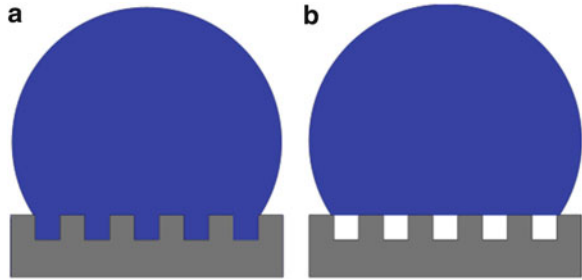


Fig. 18.2 Wetting of a rough surface (a) Wenzel model, (b) Cassie-Baxter model



solid surface ($\theta_0 = 180^\circ$), and the last situation is when $-1 < (\gamma_{SV} - \gamma_{SL})/\gamma_{LV} < 1$ in which $0 < \theta_0 < 180^\circ$.

In Young’s equation, the solid surface is assumed to be smooth and chemically homogeneous, whereas in practice the surfaces are rough and heterogeneous. Consider a water droplet on a rough surface with a homogeneous interface. Comparing to smooth surface, the interface area for a rough surface is increased. Using the surface force balance and empirical considerations, the contact angle of a water droplet upon a rough solid surface, θ , is related to that upon a smooth surface, θ_0 , for a homogeneous interface (Fig. 18.2a), through the nondimensional surface roughness factor, $R_f > 1$, equal to the ratio of the surface area, A_{SL} , to its flat projected area, A_F [117]

$$R_f = \frac{A_{SL}}{A_F} \tag{18.3}$$

This is called Wenzel model and is given by

$$\cos \theta = \frac{dA_{LA}}{dA_F} = \frac{dA_{SL}}{dA_F} \frac{dA_{LA}}{dA_{SL}} = R_f \cos \theta_0 \tag{18.4}$$

As it is observed in Fig. 18.2a, in Wenzel model it is assumed that the liquid retains contact with the solid surface at all points and wetting is homogeneous.

For a surface composed of two fractions, one with the fractional area f_1 and the contact angle θ_1 and the other with f_2 and θ_2 , respectively (so that $f_1 + f_2 = 1$), the contact angle for the heterogeneous interface is given by the Cassie equation [21]

$$\cos \theta = f_1 \cos \theta_1 + f_2 \cos \theta_2 \quad (18.5)$$

For the case of a composite interface (Fig. 18.2b), consisting of a solid–liquid fraction ($f_1 = f_{SL}$, $\theta_1 = \theta_0$) and liquid–air fraction ($f_2 = f_{LA} = 1 - f_{SL}$, $\cos \theta_2 = -1$), combining (18.3) and (18.5) yields the Cassie-Baxter equation [21]

$$\cos \theta = R_f f_{SL} \cos \theta_0 - 1 + f_{SL} = R_f \cos \theta_0 - f_{LA} (R_f \cos \theta_0 + 1) \quad (18.6)$$

As it is observed in Fig. 18.2b, in Cassie-Baxter model it is assumed that the liquid only bridges across the protrusions, and there are air pockets trapped between protrusions under the water droplet.

Adhesion is a general term for several types of attractive forces that act between solid surfaces, including the van der Waals force, electrostatic force, chemical bonding, and the capillary force due to the condensation of water at the surface. Adhesion is a relatively short-range force, and its effect (which is often undesirable) is significant for microsystems which have contacting surfaces. The adhesion force strongly affects friction, mechanical contact, and tribological performance of such systems surface, leading, for example, to “stiction” (combination of adhesion and static friction), which precludes microelectromechanical switches and actuators from proper functioning. It is therefore desirable to produce nonadhesive surfaces, and applying surface microstructure mimicking the Lotus effect (as well as its modifications, e.g., the so-called petal effect) has been successfully used for the design of nonadhesive surfaces, which are important for many tribological applications.

The so-called rose petal effect [13] characterized by high contact angle and simultaneously strong adhesion (a droplet can be suspended to a horizontal surface upside down) is related to the Lotus effect.

The Gecko effect which stands for the ability of specially structured hierarchical surfaces to exhibit controlled adhesion. Geckos are known for their ability to climb vertical walls due to a strong adhesion between their toes and a number of various surfaces. They can also detach easily from a surface when needed. This is due to a complex hierarchical structure of gecko feet surface. The Gecko effect is used for applications when strong adhesion is needed (e.g., adhesive tapes). The Gecko effect can be combined with the self-cleaning abilities [82, 91].

Microstructured surfaces for underwater applications, including easy flow due to boundary slip, the suppression of turbulence (the shark-skin effect), and anti-biofouling (the fish-scale effect). Biofouling and biofilming are the undesirable accumulation of microorganisms, plants, and algae on structures which are immersed in water. Conventional antifouling coatings for ship hulls are often toxic and environmentally hazardous. On the other hand, in living nature there are ecological coatings (e.g., fish scale), so a biomimetic approach is sought [23, 28, 54, 75, 86].

Oleophobic surfaces capable of repelling organic liquids. The principle can be similar to superhydrophobicity, but it is much more difficult to produce an oleophobic surface, because surface energies of organic liquids are low, and they

tend to wet most surfaces [85, 110, 111]. Underwater oleophobicity can be used also to design self-cleaning and antifouling surfaces.

Microstructured surfaces for various optical applications, including non-reflective (the Moth-eye effect), highly reflective, colored (in some cases, including the ability to dynamically control coloration), and transparent surfaces. Optical surfaces are sensitive to contamination, so the self-cleaning ability should often be combined with optical properties [56, 82–84].

Microtextured surfaces for de-icing and anti-icing. De-icing (the removal of frozen contaminant from a surface) and anti-icing (protecting against the formation of frozen contaminant) are significant problems for many applications that have to operate below the water freezing temperature: aircrafts, machinery, road and runway pavements, traffic signs, traffic lights, etc. The traditional approaches to de-icing include mechanical methods, heating, the deposition of dry or liquid chemicals that lower the freezing point of water. Anti-icing is accomplished by applying a protective layer of a viscous anti-ice fluid. All anti-ice fluids offer only limited protection, dependent upon frozen contaminant type, and precipitation rate, and it fails when it no longer can absorb the contaminant. In addition to limited efficiency, these de-icing fluids, such as propylene glycol or ethylene glycol can be toxic and raise environmental concerns. Anti-icing on roadways is used to prevent ice and snow from adhering to the pavement, allowing easier removal by mechanical methods.

Ice formation occurs due to condensation of vapor phase water and further freezing of liquid water. For example, droplets of supercooled water that exist in stratiform and cumulus clouds crystallize into ice when they are struck by the wings of passing airplanes. Ice formation on other surfaces, such as pavements or traffic signs also occurs via the liquid phase. It is therefore suggested that a water repellent surface can also have de-icing properties [19]. When a superhydrophobic surface is wetted by water, an air layer or air pockets are usually kept between the solid and the water droplets. After freezing, ice will not adhere to solid due to the presence of air pockets and will be easily washed or blown away. However, recent studies have indicated that not all superhydrophobic surfaces are necessary icephobic, since the mechanisms of water adhesion and wetting/dewetting differ from the mechanisms of ice adhesion, cracking, and fracture [92].

1. Microelectromechanical system (MEMS)-based dynamically tunable surfaces for the control of liquid/matter flow and/or coloration (for example, mimicking the coloration control in cephalopods), used for displays and other applications, the so-called origami [17, 104].
2. Various biomimetic microtextured surfaces to control friction, wear, and lubrication [113].
3. Self-lubricating surfaces, using various principles, including the ability for friction-induced self-organization [87].
4. Self-repairing surfaces and materials, which are able to heal minor damage (cracks, voids) [87, 88].

5. Various surfaces with alternate (and dynamically controlled) wetting properties for micro/nanofluidic applications, including the Darkling beetle effect, e.g., the ability of a desert beetle to collect water on its back using the hydrophilic spots on an otherwise hydrophobic surface of its back [82–84, 94, 98].
6. Water strider effect mimicking the ability of insects to walk on water using the capillary forces. The hierarchical organization of the water strider leg surface plays a role in its ability to remain dry on water surface [47].
7. The “sand fish” lizard effect, able to dive and “swim” in loose sand due to special electromechanical properties of its scale [82–84, 98].
8. Composite and nanocomposite materials tailored in such way that they can produce required surface properties, such as self-cleaning, self-lubrication, and self-healing. Metal-matrix composites, polymeric composites as well as ceramics (including concrete) have been recently used for this purpose. Natural fiber-reinforced composites are among these materials. The difference between microstructured surfaces and composite materials is that the latter have hydrophobic reinforcement in the bulk and thus can be much more wear-resistant than microstructured surfaces, which are vulnerable even to moderate wear rates.
9. Green biomimetic nanotribology, including cell adhesion, nanoornamentics, and biochemistry is another new area associated with Green Tribology.

Environmental engineers have only just started paying attention to biomimetic surfaces. Raibeck et al. [98] investigated the potential environmental benefits and burdens associated with using the Lotus effect-based self-cleaning surfaces. They found that while the use phase benefits are apparent, production burdens can outweigh them when compared with other cleaning methods, so a more thoughtful and deliberate use of bio-inspiration in sustainable engineering is needed. Clearly, more studies are likely to emerge in the near future.

In living nature, various organisms face tribological challenges since they have surfaces in relative motion, e.g., in joints, in the blinking of an eye, and so on. While engineers have researched the field of tribology for centuries, nature has been producing lubricants and adhesives, as well as optimizing materials and junctions, for millions of years [52].

Biomimetic has been investigated by engineers, researchers, and scientists for decades. Gorb and his research group [72] studied the interactions and adhesion forces between the insects attachment systems and the surfaces. They investigated how the insects attach to the surfaces in vertical or even upside-down position. They studied the adhesion of an attachment pad of the cricket’s leg on a horizontal surface. These insects can stand and walk on a smooth vertical surface, even upside down under the surface. They used a recently developed force tester and conducted experiments to measure the adhesive properties of the pad. They applied normal force to separate the attachment pad from the surface and measured the force with force tester which sensed the force in the range of centi- to micronewton. They studied the adhesive properties of the secretion, adhesion of the pad, and the relationship between adhesion and deformation of the pad. They concluded that

the adhesive secretion is essential for the attachment of the pad, and the attachment is achieved by deformation of the pad. After that in 2001, they studied the adhesion force between attachment pads of legs of various syrphid flies and a horizontal surface [57]. There are stiff hairs on fly legs called setose. They studied the role of setose shape, size, density, and weight of species in the generation of friction force on a surface of polyvinylchloride using light and scanning electron microscopy. They used a centrifugal force tester to measure friction force. This device is commonly used for the measurement of friction and adhesive forces for a variety of insects. They concluded that the friction force was greater in heavier insects, whereas the acceleration at which an insect loses contact with the surface was greater in lighter species. One year later, in 2002, they worked on groups of friction-based attachment devices in insects and gave an overview of the functional design of them. They found the geometry of the surface, load forces, at which the system operates, and mechanical properties of material play essential roles in the design of particular system. In addition, chemistry of surfaces, presence and nature of secretory fluids affect surface forces [58]. They also studied the friction force generated by the beetle (*Pachnoda marginata*) claws during the walking on a sand paper surface and investigated the role of claw tip shape and size and the substrate texture on this force. They selected this beetle for experiments because this species does not possess any specialized attachment devices for smooth substrate. They used a load cell force transducer to find the force range by which the claw interact with a substrate. To measure forces generated by walking beetles on different textures, they used a force sensor and a beam which transmitted the beetle force to the sensor. They proposed a theoretical model explaining the friction force with increased texture roughness. They found the friction force increases rapidly by increasing the grain size of the sand paper [25]. Gorb and his group investigated the attachment ability of varying body weight animals such as flies, spiders, and geckos and the effect of dimensions and scales of attachment pad's setose on adhesion force. They studied the setae of these animals down to μm and sub- μm levels. They found that the weight of the animal increases more rapidly than the area of the foot-to-substrate contact, and it should be compensated by a simultaneous increase in the setae density. They showed that in heavier animals within a given lineage, the adhesion is improved by increasing the setae density slightly [4].

In 2003, Gebeshuber et al. [49] studied the adhesion properties of living diatoms (common types of phytoplankton) in ambient temperature using atomic force microscopy. They did phase-imaging experiments to understand the characteristics of these natural adhesives. They used phase imaging because it highlights edges and is not affected by large-scale height differences, and therefore it provides clearer observation of fine features that can be hidden by rough topography. They found that diatoms produce adhesives which are extremely strong and robust both in fresh- and in seawater environments. After that in 2004, they investigated diatoms as tribological systems. They found several diatom species can actively move (e.g., *Bacillaria paxillifer* forms colonies in which the single cells move along each other) or can be elongated a major fraction of their original

length (e.g., *Ellerbeckia arenaria* colonies can reversibly be elongated by one-third of their original length). Therefore, they assumed that some sort of lubrication may be present in these species.

One year later in 2005, Gorb et al. theoretically studied the adhesive systems of spiders, lizards, and other animals with dry adhesive systems. They found that the micromechanisms of adhesion in animals such as insects, spiders, and lizards are different. In animals producing secretions like flies and beetles, adhesion is apparently enhanced by capillary forces, whereas in animals with dry adhesion systems such as spiders and geckos, it relies entirely on van der Waals forces between the feet and a substrate [107]. They investigated the effect of contact shape on attachment system and described a single-contact element with spherical contact using the classical Johnson-Kendall-Roberts (JKR) model. Finally, they concluded the other shapes, such as a toroidal contact geometry observed in beetles and flies should lead to better attachment. Inspiring geckos, [26] designed a small robot which had the ability to walk on vertical surfaces overcoming the gravity force. They used a Mini-Whegs, small prefabricated quadruped robot, and reduced its weight and modified its legs to better attach and detach from the wall mimicking the same action done by geckos. After that they studied the nanoscale adhesion of individual spatula of gecko using atomic force microscopy and found the adhesion force for this smallest element of gecko's attachment system is about 10 nN. The gecko footpad areas are covered with hundreds of thousands of setae and each seta is branched into hundreds of spatulas with dimensions of 100 nm [68]. In 2006, Beutel and Gorb [12] investigated the attachment systems of various hexapods such as Hexapoda, Ellipura, Diplura, Dicondylia, and so on. They used light and scanning electron microscopy to study the surface structure of a tarsi (part of insect's leg) of various species. They found these insects have the hairy soles structure which increases the adhesion between their feet and the substrate.

In the same year, Gebeshuber et al. [50] studied the effect of biotribological systems on advancements in micro- and nanotechnology. They discussed that since the biological systems had millions of years to adapt, therefore novel approaches can be expected from natural systems which help us to design new lubricants, materials, and processes. A year later in 2007, they reviewed the dry adhesive biotribological systems like gecko foot, certain insect attachment pads and single molecules which serves as adhesives (Diatoms in seawater, fresh water, or moist surfaces) and showed that biotribology may be a path to design smart, dynamic, environmentally friendly, self-healing, and multifunctional lubricants and adhesives. In the same year, Nosonovsky and Bhushan [81] discussed various mechanisms of solid–solid and solid–liquid friction and their relation to the surface roughness hierarchy. They used nature evidences such as lotus leaf and gecko foot to demonstrate how hierarchical textured engineering surfaces lead to reduced or increased adhesion and friction. They concluded that in order to achieve a high or low adhesion or friction, the surfaces should be hierarchical, because the friction mechanisms are multiscale and such surfaces can be found in biological objects. In 2008, Nosonovsky and Bhushan theoretically studied the effect of roughness on

superhydrophobicity of biomimetic surfaces. Roughness is an important property in surface mechanics, physics, chemistry, and biology, and it is critical for many tribological applications. They explained that the traditional roughness parameters such as the root mean square, correlation length, or fractal dimensions are not always appropriate to analyze the wetting, and a successful design of superhydrophobic surfaces requires a correct assessment of the surface roughness effect on wetting.

Sidorenko et al. [105] studied the wetting behavior of biomimetic surfaces with hydrogel-supported nanostructures. Hydrogels are responsive (smart) materials composed of cross-linked polymeric chains which are flexible. They applied a hydrophobic coating (monolayers of silane) and observed the nanostructured surface shows remarkable superhydrophobicity and superoleophobicity. They demonstrated such surfaces can be designed in two ways. The first design shows reversible transitions from superhydrophobicity to hydrophilicity and the second shows reversible transitions from hydrophilicity to superhydrophobicity. Gebeshuber et al. [53] investigated the relation between tribology and biology. They presented different examples for biological tribosystems to exemplify the hierarchical nature of biomaterials and introduce possible biomimetic scenarios to overcome current tribological challenges. They discussed the major concerns in designing tribosystems which are minimizing friction, saving energy, and reducing wear [1].

One year after that in 2010, Nosonovsky and Bhushan discussed the concept of green tribology and its relation to other areas of tribology as well as other “green” disciplines such as green engineering and green chemistry. They formulated principles of green tribology (minimization of friction and wear, reduction of lubrication, sustainable chemistry) and discussed the challenges of green tribology and future directions of research [89]. They also studied the self-healing in biological and technical surfaces. They used the ability of biological surfaces and tissues for self-healing, to mimic engineered self-healing materials. They concluded that special efforts should be made in order to apply self-healing property from the nature into engineered materials. For example from thermodynamic point of view, the self-healing is a result of decreasing entropy. Another example is preventing of crack propagation by embedding of the microcapsules with a healing liquid into the bulk of materials [90].

4 Green Lubrication

The terms “green lubrication” and “green lubricants” are generally used for lubricants manufactured from vegetable or other natural sources. The other common names for green lubricants are “environmentally acceptable,” “environmentally benign,” and “environmentally friendly”. In recent years, there has been an increasing interest on the development of green lubricants to displace petroleum-based lubricants. It should also be noted the term “green lubrication” by some

researchers [14] has been used in assessing the environmental impact of lubricants, i.e., friction reduction, wear reduction, and lubricant stability. Green lubricants, by this definition, have a unique capability to deliver environmental benefits in use, mainly through their role in reducing friction in machinery, which improves energy efficiency, thereby conserving fuel resources and reducing emissions of CO₂ and acid gases.

4.1 *Natural Oils*

Natural oils have a long history of use as lubricants as they dominated the lubrication industry before the petroleum age [62]. Problems of limited oxidative stability and poor low temperature performance gradually led to their replacement by fossil oils and later by synthetic oils [79].

Natural oils are renewable, biodegradable, have relatively low manufacturing and process energy requirements, and show some good lubricant properties. Their polar nature gives them a better affinity for metal surfaces than nonpolar mineral oils [14]. Natural oils also show improved thermal properties due to the presence of a large number of carboxylate groups in the ester molecules. Such structure gives them the capability of maintaining a thicker lubricating film in highly loaded and high slip contacts. Low volatility, higher load carrying capacity, and high viscosity index are some other advantages of the natural oils.

However natural oils also have performance deficiencies which mean that their use is not necessarily an environmentally preferable option. The poor thermo-oxidative stability of natural oils reduces operational lifetime and increases the amount of lubricant required to be manufactured and disposed off [14, 40]. Compared to mineral and synthetic oils, natural oils have a number of distinct advantages including poor low temperature fluidity, higher pour point, higher shear stability, detergency, and dispersancy [79]. Also, in applications where a closely specified viscosity is required for optimum energy efficiency, the narrow range of viscosities available from natural oils may not be optimal, with consequent energy inefficiencies [14].

Because of their particular combination of properties, natural oils are a good option for total loss, once-through applications like chainsaw lubricants and railroad greases, where stability is not an issue and ready biodegradability is a requirement. Natural oils such as rapeseed, canola, and soybean oils are already widely used in such applications [14]. Today, Natural oils represent a nearly inexhaustible source of raw materials for lubricants. In 2004, the world production of natural oil exceeded 100 million tons and most of this oil was used by the food industry [9]. Recent reports [79] show that presently, the highest volume of natural oil production is for hydraulic applications.

Considerable effort is being applied for modifying the properties of natural oils in order to make them more suitable for use in other applications. Conventional plant breeding and genetic modification of oil producing crops has been undertaken

in order to alter the composition of the oils that they produce, for example, by controlling polyunsaturation in order to improve oxidative stability [29], and introducing branching to improve low temperature flow properties or increase viscosity [34]. However, the performance improvements achieved so far are marginal when compared to mineral oil or synthetic lubricant formulations.

4.2 Solid Lubrication (Boric Acid)

Over the past 30 years, solid (dry powder) lubricants have been employed in a variety of sliding contacts as an alternative to conventional liquid lubricants. Several of these lubricants—molybdenum disulfide, tungsten disulfide, titanium oxide, and boron nitride—were evaluated for their lubrication behavior at a variety of sizes and found to exhibit excellent tribological performance without requiring expensive disposal [37–39, 115].

Solid lubricants have some interesting attributes such as [79]:

- They adhere to surfaces to form a protective boundary layer that prevents wear [27, 65].
- They act as a lubricant in sliding contacts by accommodating relative surface velocities [16, 55].
- They lubricate at high temperatures [22, 66].

Boric acid has been identified as an effective solid lubricant due to its lamellar molecular structure. Boric acid is the common term for orthoboric (or boracic) acid H_3BO_3 , which is a hydrate of boric oxide B_2O_3 . When in contact with water, boric oxide will readily hydrate, converting to boric acid. Boric acid is a weakly acidic white powder that is soluble in water (about 27 % by weight in boiling water and about 6 % at room temperature), soft, ductile, stable, free flowing, and easily handled [108].

The effectiveness of boric acid can be attributed to its low friction and shear strength values. The shear strength of boric acid has been experimentally determined to be 23 MPa by Gearing et al. [48]. This is almost the same as the experimentally determined shear stress of molybdenum disulfide, which was found to be 24 MPa by Singer et al. [106]. The coefficient of friction of boric acid lowers with increased contact pressure and is well below 0.1 for average pressures above 100 MPa [48].

Different studies [36, 39, 115] have indicated that boric acid's unique layered inter-crystalline structure makes it a very promising solid lubricant because of its relatively high load carrying capacity and low steady-state friction coefficient. In metal forming applications [15, 77, 97], it was shown that boric acid powder provided very low coefficient of friction (0.04) between aluminum workpiece and a steel forming tool. In drilling experiments with Sapphire tools [77], results indicated that the addition of boric acid to distilled water increased the rate of drilling of polycrystalline alumina by a factor of 2.

Despite its known benefits, it is demonstrated that there are difficulties associated with utilizing boric acid alone as a lubricant in repeated or extended duration contacts [30]. These drawbacks are due to the fact that boric acid powder can be dehydrate or forced out the contact zone during sliding contact. Thus, it must be continues replenished, which requires the development of spray and recovery systems that would significantly change the present manufacturing process; it may be one reason that boric acid lubrication has had limited application by industry [79].

4.3 *Water Lubrication*

To reduce the friction and wear, bearings need adequate hydrodynamic film lubrication between their sliding surfaces. Oil has been a common lubricant, but other liquids such as water can be used. The increasing environmental awareness in recent decades leads bearing designers to consider more reliable design solutions with water as a lubricant. It should be mentioned that use of water as a lubricant is not merely a new idea. Early shaft-driven propellers on ships used water, but development of more reliable oil-lubricated bearings dominated the industry from 1940s [93]. However, concerns about increasing oil pollution from the ships—most due to the routine operations, and discarded lubricants—has made very strong global interest in water-based lubrication technologies in recent three decades. Water's natural abundance, non-compressibility, cooling properties, and low coefficient of friction suggest it as a perfect lubricant for bearings of ships, boats, and submarines. Water-lubricated bearings can also be used in mining industry and water conditioning stations.

Pai and Hargreaves [93] summarized water-lubrication advantages over oil-lubrications:

- Oil-based bearings are hazardous to the environment. Potential oil release into the waterways and the land for mechanical malfunction, spillage, or leakage is the main issue, but the problems associated with safe disposal following use should be considered too.
- Cooling is required in many systems that contain bearings, e.g., a turbine compartment, and unlike oil, water can function as both a coolant and a lubricant. This is because of the low frictional drag coefficient due to the low viscosity of water. Furthermore, if required, by appropriate design of the lubrication system water can control the temperature of a mechanical assembly within a very narrow temperature range.
- Water lubrication is simple in design and the cost of equipment can kept low due to the elimination of any special design features to accommodate the lubricant. More important, water lubrication removes the need for complex oil sealing arrangements. This allows bearings shafts to be shorter and stiffer, eliminating problems of misalignment.

- Water-lubricated bearings are uniquely suited to many common applications such as marine, pumps, and hydroelectric turbines because lubricant (water or process fluid) is supplied at one end flows through the bearing along the multiple axial grooves. When marine vessels travel through the water the speed of the vessel forces water through the axial grooves keeping the bearing lubricated.

5 Tribology of Eco-Friendly Energy Devices

5.1 Wind Turbines

As an environmental-friendly source of renewable energy, and due to its wide availability, wind power is of increasing interest in industry. The use of wind turbines to extract electrical energy from wind can be dated back to the late-1800s, with 12 kW windmill generator by Charles Brush [5], as well as the mid-1900s, with the 1,250 kW Smith-Puntnam wind turbine [109]. From early developments to present day, wind turbine designs have made significant developments in complexity, size, and power capacity. Nevertheless they had various limitations to their mechanical system reliability owing to the tribological problems over the past few decades [76]. The tribological components in a wind turbine include rotor support bearings, intermediate gearbox rotor bearings, high-speed bearings, pitch bearings in the hub, epicyclic and parallel gears in gearbox, a mechanical brake, a roller bearing system in the yaw mechanism, and slip rings in generator [109].

Although current turbine designs have addressed and solved a number of the problems plaguing their predecessors, tribological issues still exist [76]. Bell [10] reported that the number of failures per turbine per year in Denmark and Germany dropped from 1 and 2.5, respectively, in 1994 to 0.5 and 0.8 in 2004. This represents a significant improvement in wind turbine reliability over the course of a decade; however, this number still indicates one failure per turbine every 15 months to 2 years. Furthermore, it is evident from this report that systems containing tribological components experience less than 0.2 failures per year. Considering that the gearbox, pitch, yaw, and generator systems are very large, have great mass, and require large cranes and expensive rigging equipment when undergoing repair or replacement, and including the lost production owing to downtime, the crane rental costs, and the system replacement costs, it becomes clear that a tribological failure in one of these systems becomes very expensive [76]. These maintenance, reliability, and operating expenses significantly affect the overall generating cost per kilowatt-hour and, therefore, the competitiveness of wind in the overall energy marketplace. In the following, the tribological challenges facing the primary systems of wind turbines will be summarized.

5.1.1 Main Shaft Bearings

Rolling-element bearings are used to support the rotor and rotor shaft, the gearbox shafts, and the generator input shaft because of their ability to accommodate misalignment between the shaft and the bearing housing. These bearings are experiencing damage from wear that reduces their serviceable life to much less than that for which they were designed. This life-limiting wear leads to expensive downtime and excessively high maintenance and warranty costs [76].

One of the most common wear modes is rolling contact fatigue, whose occurrence can often be attributed to the relatively large stresses that tend to appear below the surface of the rolling elements. These subsurface stresses can produce cracks that form beneath the surface of the rolling elements or raceways, which then propagate to the surface, causing material to be removed from the surface and leaving behind small pits [63]. However, the wear that limits the life of main shaft spherical roller bearings is not classical rolling contact fatigue, but predominately micropitting wear. Micropitting is caused by interaction of the raceway and roller residual finishing marks, or asperities, leading to high stresses in the part [76]. Fretting wear can also occur within bearings, as wind gusts can cause the bearings to have low-amplitude motion while the system is shutdown for maintenance [109].

Surface engineering has been an extremely well practice at reducing and eliminating wear in rolling element bearings by altering the chemical and/or topographical properties of the surfaces of the elements [76]. An engineered surface that has been shown by Doll and Osborn [32] and Doll et al. [33] to work satisfactory in rolling element bearings is an amorphous carbon coating applied to superfinished rolling elements.

5.1.2 Gearboxes

Gearboxes are employed in wind turbines to transfer the torque from a slowly rotating input shaft (25–35 r.p.m.) to a high-speed output (1,500–1,800 r.p.m.) suitable for the AC generator. Handling of the large amounts of torque causes wind turbine gearboxes operate in conditions that are rather unusual for industrial gearboxes. While the electrical systems in wind turbine systems are generally most prone to failure, gearbox and components tend to be the costliest to maintain and replace [71, 100].

Studies [64, 76, 95, 109] show that less reliability of wind turbine gearboxes can be attributed to different factors, some of them described in the following:

- Wind gusts and generator connection/disconnection from the electrical grid may cause undesired load reversals in gearbox, which can lead to excessive contact stresses in gear flanks.
- Undesired movements of the main shafts, which can be caused by deformations within the bed plate, can cause misalignment of the gearbox with the generator shafts. This misalignment results in unexpected damage to the high-speed bearings, which leads to damage in the high-speed gears.

- The gearbox may be subject to particulate contamination, which may lead to surface pitting in the gears.
- Excessively high oil temperature may result in scuffing wear in the gears, thus necessitating the use of oil coolers and filters in lubricant delivery system.

5.1.3 Lubrication System

Lubrication of the main shaft bearings is done using either pressure-fed oil or grease lubrication. The pressure-fed oil lubrication method uses a circulating oil delivery system including pumps, valves, and pipes for supplying oil to the bearings. While this system is considered to be most effective for the regulating the oil temperature and filtering contaminants and metallic wear particles, the complexity of the system and possibility of lubricant leakage makes it not practically the best choice [109]. Though grease lubrication is preferred since it needs low maintenance and does not require any delivery system.

5.2 Marine Energy Systems

Marine energy devices including tidal power turbines, water current energy extractors, and water energy collectors are another important way of producing renewable energy, which involve certain tribological problems. In the following, we briefly review these devices and their tribological challenges.

Underwater horizontal-axis tidal turbines (HATT) extract kinetic energy from the tidal flow through moving a lifting surface (blade or foil) connected to an electrical power generator. Tidal flow is originated from the Earth's oceanic tides; tidal forces are periodic variations in gravitational attraction exerted by celestial bodies. Tides are more predictable than wind energy over long timescales and are not subject to very high random excursions as wind velocity is [46]. In recent years, a considerable experience and knowledge is being transferred from wind turbines [18] as well as from the understanding of ship propellers [20]. Furthermore, several tribological approaches are also borrowed from wind turbines. However, Wood et al. [117] pointed out that there are many differences between wind and tidal turbines. Typically, there are only two tidal directions, which are usually 180° apart. Topography constraints due to a finite path, channel width, as well as the presence of the free surface constrain the tidal flow rate. Furthermore, the vapor pressure of water limits the rotational speed of the blade before significant cavitation effects cause a rapid increase in blade drag and loss of lift. Centripetal loads dominate in the long and slender blades of wind turbines, and these restrict bending. In water turbines, however, bending loads dominate. For a 1 MW tidal turbine, the thrust is perhaps 100 tones, which is about double that on a similarly rated wind turbine [117]. Corrosiveness of the working environment of the tidal

turbine with suspended solids leads to the possibility of erosive damage over the lifetime of the device.

Water current energy extractor is another device that collects the energy of water currents. This can be either a horizontal-axis turbine or vertical-axis turbine. Gorlov helical turbine (GHT) is a famous example of the vertical-axis turbine which was invented in the 1990s by Gorlov [60]. The main difference between GHT and conventional turbines is the orientation of the axis in relation to current flow. Unlike conventional turbines, in GHT, the axis is positioned perpendicular to current flow. It uses helical blades designed in such a manner that one component of force acting from water current upon the blade create torque in the same direction, independent of the direction of the current [59]. This makes the GHT a convenient tool to operate in the conditions where water current direction can change including rivers, lakes, and seas. The GHT is an example of damless hydropower technology, which is considered safer and more environmental-friendly than traditional methods [46].

Another type of hydropower devices is the wave energy collector (WEC). The energy inherent in the orbital motion and pressure field beneath a wave present a significant challenge to extract efficiently while being able to survive extreme storm conditions [117]. It has been demonstrated that capturing wave energy in offshore locations is possible [46]. Falnes [42] reviewed wave energy extraction methods, showing that the power flow intensity is up to five times larger for ocean waves than for the wind that generates the waves. Optimum wave interference, for a single oscillating system, occurs at the resonance (whereby the excitation force and the velocity of the device are in phase frequency) and for specific amplitude of the motions of the oscillator. In order to extract the maximum energy, the shape of the immersed volume has to be carefully designed and control strategies used to keep the phase between excitation and velocity close to zero for different wave periods [117].

The tribological components within such energy conversion machines are typically hydraulic systems, pistons/cylinders, hinge bearings, sliding and rotating seals, and embedded turbines. These must be compatible with the complex loadings and harsh marine environment of wave surface operation [117]. Furthermore, access is limited to these components and therefore maintenance of them is difficult.

5.3 Other (Geothermal)

First commercial delivery of geothermally generated electric power occurred in 1914 when a 250 kW unit at Larderello (in the Tuscany region of Italy) provided electricity to the nearby cities [31]. Since then, installation of geothermal plants has been increased in the geographical areas at the edges of tectonic plates [11]. For instance, there are over 843 MW installed at Larderello and the other nearby geothermal fields in the Tuscany region. The largest group of geothermal power plants in the world is located at The Geysers, a geothermal field in California,

United States with 3.4 GW. Philippines (1.9 GW), Indonesia (1.2 GW), and Mexico (0.96 GW) are other major countries with considerable installed capacity of geothermal power plants [67].

Geothermal power plants are not dissimilar to other steam turbine thermal power plants—heat from a fuel source (in this case, the earth's core) is used to heat water or another working fluid. The working fluid is then used to turn a turbine of a generator, thereby producing electricity. The fluid is then cooled and returned to the heat source. Geothermal power plants can be categorized into as following [31]:

- Direct steam plants are used at vapor-dominated (or dry steam) reservoirs. Dry, saturated, or slightly superheated steam is produced from wells and then transmitted to powerhouse.
- Flash steam power plants are used at reservoirs producing a two-phase mixture of liquid and vapor. These plants separate the phases and use the resulting flashed steam to drive turbines. This is the most common type of plant in operation today.
- Binary cycle power plants are the most recent development and can accept fluid temperatures as low as 57 °C [41]. The thermal energy of geofluid is transferred via a heat exchanger to a secondary working fluid for use in a conventional Rankin cycles.

Water contamination, wear of the main shaft and gearbox bearings and erosion are some of the tribological problems need to be investigated more in geothermal power plants.

6 Challenges

In the preceding sections we have outlined the need for green tribology, its principles, and primary areas of research. As a new field, green tribology has a number of challenges. One apparent challenge is the development of the above-mentioned fields in such a manner that they could benefit from each other. Only in the case where such a synthesis is performed, it is possible to see green tribology as a coherent and self-sustained field of science and technology, rather than a collection of several topics of research in tribology and surface engineering. There is apparently potential synergy in the use of biomimetic approach, microstructuring, biodegradable lubrication, self-lubrication, and other novel approaches as well as in developing methods of their applications to sustainable engineering and energy production.

Environmental effect of wear particles is another field of interest. Philip and coworkers suggested that environmental aspects should become an integral part of brake design [118]. Preliminary data obtained with animal experiments revealed that the inhaled metallic particles remain deposited in lungs of rats 6 months after the exposure. The presence of inhaled particles had negative impact on health and

led to emphysema (destroyed alveoli), inflammatory response and morphological changes of lung tissue.

More research should be done for the integration of these fields. Some ideas could be borrowed from the related field of green chemistry, for example, developing quantitative metrics to assess the environmental impact of tribological technologies.

The creator of the Periodic table of elements, chemists D. Mendeleev used to say that science starts when the measurement begins. This saying should apply to Green Tribology as well. It is important to develop quantitative measures and metrics which would allow to compare which tribological material, technology, or application is “greener,” i.e., produces smaller carbon footprint, less chemical or thermal pollution of the environment.

Green tribology should be integrated into world science and make its impact on the solutions for world-wide problems, such as the change of climate and the shortage of food and drinking water. Jost [73] mentioned the economical potential of the new discipline: “The application of tribological principles alone will, of course, not solve these world-wide problems. Only major scientific achievements are likely to be the key to their solution, of which I rate Energy as one of the most important ones. For such tasks to be achieved, the application of Tribology, and especially of Green Tribology can provide a breathing space which would enable scientists and technologists to find solutions to these, mankind’s crucial problems and allow time for them to be implemented by governments, organizations and indeed everyone operating in this important field. Consequently, this important—albeit limited—breathing space may be extremely valuable to all working for the survival of life as we know it. However, the ultimate key is science and its application. Tribology—especially Green Tribology can and—I am confident—will play its part to assist and give time for science to achieve the required solutions and for policy makers to implement them.”

7 Conclusions

Green tribology is a novel area of science and technology. It is related to other areas of tribology as well as other “green” disciplines, namely, green engineering and green chemistry. We formulate the 12 principles of green tribology and defined three areas of tribological studies most relevant to green tribology. The integration of these areas remains the primary challenge of green tribology and defines future directions of research.

References

1. Abdel-Aal HA, El Mansori M, Gebeshuber IC (2010) Python Regius (Ball Python) shed skin: biomimetic analogue for function-targeted design of tribo-surfaces. arXiv e-print (arXiv:1007.4419)
2. Allen DT, Shonnard DR (2001) Green engineering: environmentally conscious design of chemical processes. Prentice-Hall, Upper Saddle River, NJ
3. Anastas PT, Warner JC (1998) Green chemistry: theory and practice. Oxford University Press, New York, NY
4. Arzt E, Gorb S, Spolenak R (2003) From micro to nanocontacts in biological attachment devices. *Proc Natl Acad Sci U S A* 100:10603–10606
5. Babu BC, Mohanty KB (2010) Doubly-fed induction generator for variable speed wind energy conversion systems—modeling and simulation. *Int J Comput Electr Eng* 2(1):141–147
6. Bar-Cohen Y (2006) Biomimetics: biologically inspired technologies. Taylor & Francis, Boca Raton, FL
7. Barthlott W, Neinhuis C (1997) Purity of the sacred lotus, or escape from contamination in biological surfaces. *Planta* 202:1–8
8. Bartz WJ (2006) Ecotribology: environmentally acceptable tribological practices. *Tribol Int* 39(8):728–733
9. Battersby N (2005) Environmentally acceptable lubricants: current status and future opportunities. In: Proceedings of the world tribology congress III, Washington, DC, USA, pp 483–484
10. Bell B (2006) Wind turbine reliability workshop, Albuquerque, NM, 3–4 October 2006, Wind turbine reliability and service improvements. Albuquerque, NM, Sandia National Laboratories
11. Bertani R (2007) World geothermal generation in 2007. Proceedings of the European geothermal congress, Unterhaching, Germany, 11 p
12. Beutel RG, Gorb SN (2006) A revised interpretation of the evolution of attachment structures in Hexapoda (Arthropoda), with special emphasis on Mantophasmatodea. *Arthropod Syst Phylogeny* 64:3–25
13. Bhushan B, Nosonovsky M (2010) The rose petal effect and the modes of superhydrophobicity. *Phil Trans R Soc A* 21:4713–4728
14. Boyde S (2002) Green lubricants. Environmental benefits and impacts of lubrication. *Green Chem* 4:293
15. Branneen WT, Burt GD, McDonald RA (1990) Phosphite amine lubricant for metal working and machining. US Patent No 4965002
16. Brendle M, Turgis P, Lamouri S (1996) A general approach to discontinuous transfer films: the respective role of mechanical and physicochemical interactions. *Tribol Trans* 39(1):157–165
17. Bucaro MA, Kolodner PR, Taylor A, Sidorenko A, Aizenberg J, Krupenkin TN (2009) Tunable liquid optics: electrowetting-controlled liquid mirrors based on self-assembled janus tiles. *Langmuir* 25:3876–3879. doi:10.1021/la803537v
18. Burton T, Sharpe D, Jenkins N, Bossanyi E (2001) Wind energy handbook. Chichester, Wiley Blackwell
19. Cao L, Jones AK, Sikka VK, Wu J, Gao D (2009) Anti-icing superhydrophobic coatings. *Langmuir* 25:12 444–12 448. doi:10.1021/la902882b
20. Carlton JS (2007) Marine propellers and propulsion. Butterworth-Heinemann, London
21. Cassie A, Baxter S (1944) Wettability of porous surfaces. *Trans Faraday Soc* 40:546–551
22. Centers PW (1987) The role of oxide and sulfide additions in solid lubricant compacts. *Tribol Trans* 31(2):149–156
23. Chambers LD, Stokes KR, Walsh FC, Wood RJK (2006) Modern approaches to marine antifouling coatings. *Surf Coat Technol* 201:3642–3652. doi:10.1016/j.surfcoat.2006.08.129

24. Constable DJC et al (2001) Green chemistry measures for process research and development. *Green Chem* 3:7–9. doi:[10.1039/b0078751](https://doi.org/10.1039/b0078751)
25. Dai ZD, Gorb SN, Schwarz U (2002) Roughness-dependent friction force of the tarsal claw system in the beetle *pachnoda marginata* (coleoptera, scarabaeidae). *J Exp Biol* 205(16):2479–2488
26. Daltorio K, Horchler A, Gorb S, Ritzmann R, Quinn R (2005b) A small wall-walking robot with compliant, adhesive feet. In: *Proceedings of the international conference on intelligent robots and systems*, pp 4018–4023
27. Dareing DW, Atluri S (1997) Traction behavior and physical properties of powder graphite lubricants compacted to Hertzian pressure levels. *Tribol Trans* 40(3):413–420
28. Dean B, Bhushan B (2010) Shark-skin surfaces for fluid-drag reduction in turbulent flow: a review. *Phil Trans R Soc A* 368:4775–4806. doi:[10.1098/rsta.2010.0201](https://doi.org/10.1098/rsta.2010.0201)
29. Debonte LR, Fan Z, Kodali DR (2000) New triacylglycerol oils with high 1,3-dierucoyl-2-oleoylglycerol content. *PCT Pat. Appl.*, WO-200007432 A
30. Deshmukh P, Lovell MR, Sawyer WG, Mobley A (2006) On the friction and wear performance of boric acid lubricant combinations in extended duration operations. *Wear* 260(11–12):1295–1304
31. DiPippo R (1999) Small geothermal power plants: design, performance and economics. *GHC Bull* 20:1–8
32. Doll GL, Osborn BK (2001) Engineering surfaces of precision steel components. *Proc Annu Tech Conf Soc Vac Coaters* 44:78–84
33. Doll GL, Ribaud CR, Evans RD (2004) Engineered surfaces for steel rolling element bearings and gears. *Mater Sci Technol* 2:367–374
34. Duhot P, Gontier E, Menard M, Thomas D, Thomasset B (1999) Transgenic plants producing branched fatty acids. *Fr. Pat. Appl.*, FR-2769320 A
35. Eadie L, Ghosh TK (2011) Biomimicry in textiles: past, present and potential. An overview. *J R Soc Interface* 8:761–775
36. Erdemir A, Eryilmaz OL, Fenske GR (1999) Self-replenishing solid lubricant films on boron carbide. *Surf Eng* 15(4):291–295
37. Erdemir A (1991) Tribological properties of boric acid and boric-acid-forming surfaces: part II: mechanisms of formation and self-lubrication films on boron- and boric oxide-containing surfaces. *Lubr Eng* 47(3):179–184
38. Erdemir A, Fenske GR, Erck RA, Nicholas FA, Busch DE (1991) Tribological properties of boric acid and boric-acid-forming surfaces: part 1: crystal chemistry and mechanism of self-lubrication of boric acid. *Lubr Eng* 47(3):168–178
39. Erdemir A, Halter M, Fenske GR (1997) Preparation of ultralow-friction surface films on vanadium diboride. *Wear* 205:236–239
40. Erhan SZ, Asadauskas S (2000) Lubricant basestocks from vegetable oils. *Ind Crops Prod* 11:277–282
41. Erkan K, Holdmann G, Benoit W, Blackwell D (2008) Understanding the Chena Hot Springs, Alaska, geothermal system using temperature and pressure data. *Geothermics* 37(6):565–585
42. Falnes J (2007) A review of wave-energy extraction. *Mar Struct* 20(4):185–201
43. Favret E, Fuentes NO (eds) (2009) *Functional properties of bio-inspired surfaces: characterization and technological applications*. World Scientific Publishing Co., Hackensack, NJ
44. Fratzl P (2007) Biomimetic materials research: what can we really learn from nature's structural materials? *J R Soc Interface* 4:637–642. doi:[10.1098/rsif.2007.0218](https://doi.org/10.1098/rsif.2007.0218)
45. Fratzl P, Weinkamer R (2007) Nature's hierarchical materials. *Prog Mater Sci* 52:1263–1334. doi:[10.1016/j.pmatsci.2007.06.001](https://doi.org/10.1016/j.pmatsci.2007.06.001)
46. Fronck A, Nosonovsky M, Barger B, Avdeev I (2012) Tribological and mechanical design considerations for wave energy collecting devices. In: Nosonovsky M, Bhushan B (eds) *Green tribology*. Springer, Berlin, pp 607–619
47. Gao XF, Jiang L (2004) Biophysics: water-repellent legs of water striders. *Nature* 432:36. doi:[10.1038/432036a](https://doi.org/10.1038/432036a)

48. Gearing B, Moon H, Anand L (2001) A plasticity model for interface friction: application to sheet metal forming. *Int J Plasticity* 17:237–271
49. Gebeshuber IC, Kindt JH, Thompson JB, Del Amo Y, Stachelberger H, Brzezinski M, Stucky GD, Morse DE, Hansma PK (2003) Atomic force microscopy study of living diatoms in ambient conditions. *J Microsc* 212(Pt3):292–299
50. Gebeshuber IC, Pauschitz A, Franek F (2006) Biotribological model systems for emerging nanoscale technologies. In: *Proceedings of the 2006 I.E. conference on emerging technologies—nanoelectronics*, Editors, pp 396–400
51. Gebeshuber IC, Stachelberger H, Drack M (2004) Surfaces in relative motion: bionanotribological investigations. In: Boblan I, Bannasch R (eds) *First international industrial conference Bionik*. *Fortschr.-Ber. VDI Reihe 15*(249), VDI Verlag, Düsseldorf, pp 229–236
52. Gebeshuber IC (2007) Biotribology inspires new technologies, invited article. *Nano Today* 2(5):30–37. doi:[10.1016/S1748-0132\(07\)70141-X](https://doi.org/10.1016/S1748-0132(07)70141-X)
53. Gebeshuber IC, Majlis BY, Stachelberger H (2009) Tribology in biology: biomimetic studies across dimensions and across fields. *Int J Mech Mater Eng* 4(3):321–327
54. Genzer J, Efimenko K (2006) Recent developments in superhydrophobic surfaces and their relevance to marine fouling: a review. *Biofouling* 22:339–360
55. Godet M (1984) The third-body approach: a mechanical view of wear. *Wear* 100:437–452
56. Gombert A, Blasi B (2009) The moth-eye-effect—from fundamentals to commercial exploitation. In: Favret E, Fuentes NO (eds) *Functional properties of bio-inspired surfaces: characterization and technological applications*. World Scientific Publishing Co., Hackensack, NJ, pp 79–102. doi:[10.1142/9789812837028_0004](https://doi.org/10.1142/9789812837028_0004)
57. Gorb SN, Gorb E, Kastner V (2001) Scale effects on the attachment pads and friction forces in syrphid flies (Diptera, Syrphidae). *J Exp Biol* 204:1421–1431
58. Gorb SN, Beutel RG, Gorb EV, Jiao Y, Kastner V, Niederegger S, Popov VL, Scherge M, Schwarz U, Vötsch W (2002) Structural design and biomechanics of friction-based releasable attachment devices in insects. *Integr Comp Biol* 42:1127–1139
59. Gorban' AN, Gorlov AM, Silant'ev VM (2001) Limits of the turbine efficiency for free fluid flow. *ASME J Energy Res* 123:311–317
60. Gorlov AM (1995) Unidirectional helical reaction turbine operable under reversible fluid flow for power systems. United States Patent 5,451,137, Sept 19
61. Greenwood NN, Spink JA (2003) An antipodean laboratory of remarkable distinction. *Notes Rec R Soc Lond* 57:85
62. Grusheow J (2005) [High oleic plant oils with hydroxy fatty acids for emission reduction](#). In: *Proceedings of the world tribology congress III*, pp 683–684
63. Harris TA, Kotzalas MN (2007) *Essential concepts of bearing technology*. Taylor and Francis, Boca Raton
64. Hau E (2006) *Wind turbines*. Springer, Berlin
65. Heshmat H (1995) Quasi-hydrodynamic mechanism of powder lubrication: part III: on theory and rheology of triparticulates. *Tribol Trans* 38(2):269–276
66. Heshmat H (1991) High-temperature solid-lubricated bearing development-dry powder lubricated traction testing. *J Propul Power* 7(5):814–820
67. Holm A (2010) *Geothermal energy: international market update*. Geothermal Energy Association, Washington, DC, p 7
68. Huber G, Gorb SN, Spolenak R, Arzt E (2005) Resolving the nanoscale adhesion of individual gecko spatulae by atomic force microscopy. *Biol Lett* 1:2–4. doi:[10.1098/rsbl.2004.0254](https://doi.org/10.1098/rsbl.2004.0254)
69. Hudlicky T, Frey DA, Koroniak L, Claeboe CD, Brammer LE (1999) Toward a reagentfree synthesis. *Green Chem* 1:57–59. doi:[10.1039/a901397k](https://doi.org/10.1039/a901397k)
70. Hutchinson JW (2000) Plasticity at the micron scale. *Int J Solid Struct* 37:225–238
71. Hyers RW, McGowan JG, Sullivan KL, Manwell JF, Syrett BC (2006) Condition monitoring and prognosis of utility scale wind turbines. *Energy Mater Mater Sci Eng Energy Syst* 1(3):187–203

72. Jiao Y, Gorb SN, Scherge M (2000) Adhesion measured on the attachment pads of *Tettigonia viridissima* (Orthoptera, Insecta). *J Exp Biol* 203:1887–1895
73. Jost HP (2009) 30th anniversary and “green tribology”. Report of a Chinese Mission to the United Kingdom, Tribology Network of the Institution of Engineering & Technology, 7–14 Jun 2009
74. Jung YC, Bhushan B (2009) Wetting behavior of water and oil droplets in three-phase interfaces for hydrophobicity/philicity and oleophobicity/philicity. *Langmuir* 25:14 165–14 173
75. Jung YC, Bhushan B (2010) Biomimetic structures for fluid drag reduction in laminar and turbulent flows. *J Phys Condens Matter* 22:035104. doi:[10.1088/0953-8984/22/3/035104](https://doi.org/10.1088/0953-8984/22/3/035104)
76. Kotzalas MN, Doll GL (2010) Tribological advancements for reliable wind turbine performance. *Phil Trans Royal Soc A Math Phys Eng Sci* 368(1929):4829–4850
77. Liang H, Jahanmir S (1995) Boric acid as an additive for core-drilling of alumina. *J Tribol* 117(1):65–73
78. Linthorst JA (2010) An overview: origins and development of green chemistry. *Found Chem* 12:55–68
79. Menezes PL, Rohatgi PK, Lovell MR (2012) Self-Lubricating Behavior of Graphite Reinforced Metal Matrix Composites. In: Nosonovsky M, Bhushan B (eds) *Green tribology*. Springer, Berlin, Heidelberg, pp 445–480
80. Nosonovsky M (2007) Multiscale roughness and stability of superhydrophobic biomimetic interfaces. *Langmuir* 23:3157–3161. doi:[10.1021/la062301d](https://doi.org/10.1021/la062301d)
81. Nosonovsky M, Bhushan B (2007) Multiscale friction mechanisms and hierarchical surfaces in nano and bio-tribology. *Mater Sci Eng R* 58:162–193
82. Nosonovsky M, Bhushan B (2008) Biologically-inspired surfaces: broadening the scope of roughness. *Adv Funct Mater* 18:843–855
83. Nosonovsky M, Bhushan B (2008) Superhydrophobicity for energy conversion and conservation applications. *J Adhes Sci Technol* 17:2105–2115
84. Nosonovsky M, Bhushan B (2008) Energy transitions in superhydrophobicity: low adhesion, easy flow and bouncing. *J Phys Condens Matter* 20:395005
85. Nosonovsky M, Bhushan B (2009) Multiscale effects and capillary interactions in functional biomimetic surfaces for energy conversion and green engineering. *Phil Trans R Soc A* 367:1511–1539. doi:[10.1098/rsta.2009.0008](https://doi.org/10.1098/rsta.2009.0008)
86. Nosonovsky M, Bhushan B (2009) Superhydrophobic surfaces and emerging applications: non-adhesion, energy, green engineering. *Curr Opin Colloid Interface Sci* 14:270–280. doi:[10.1016/j.cocis.2009.05.004](https://doi.org/10.1016/j.cocis.2009.05.004)
87. Nosonovsky M, Bhushan B (2009) Thermodynamics of surface degradation, self-organization, and self-healing for biomimetic surfaces. *Phil Trans R Soc A* 367:1607–1627. doi:[10.1098/rsta.2009.0009](https://doi.org/10.1098/rsta.2009.0009)
88. Nosonovsky M, Bhushan B (2010) Surface self-organization: from wear to self-healing in biological and technical surfaces. *Appl Surf Sci* 256:3982–3987. doi:[10.1016/j.apsusc.2010.01.061](https://doi.org/10.1016/j.apsusc.2010.01.061)
89. Nosonovsky M, Bhushan B (2010) Green tribology: principles, research area, and challenges. *Phil Trans R Soc A* 368:4677–4694
90. Nosonovsky M, Bhushan B (2010) Surface self-organization: from wear to self-healing in biological and technical surfaces. *Appl Surf Sci* 256:3982–3987
91. Nosonovsky M, Bhushan B (eds) (2012) *Green tribology: biomimetics, energy conservation and sustainability*. Springer, Berlin
92. Nosonovsky M, Hejazi V (2012) Why superhydrophobic surfaces are not always icephobic. *ACSNano* 6(10):8488–8491
93. Pai R, Hargreaves DJ (2012) Water lubricated bearings. In: Nosonovsky M, Bhushan B (eds) *Green tribology*. Springer, Berlin, pp 347–391
94. Parker AR, Lawrence CR (2001) Water capture by a desert beetle. *Nature* 414:33–34. doi:[10.1038/35102108](https://doi.org/10.1038/35102108)

95. Ragheb A, Ragheb M (2010) Wind turbine gearbox technologies. In: International nuclear and renewable energy conference (INREC10), Amman, Jordan
96. Raibeck L, Reap J, Bras B (2009) Investigating environmental burdens and benefits of biologically inspired self-cleaning surfaces. *CIRP J Manuf Sci Technol* 1:230–236. doi:[10.1016/j.cirpj.2009.05.004](https://doi.org/10.1016/j.cirpj.2009.05.004)
97. Rao KP, Wei JJ (2000) Performance of a new dry lubricant in the forming of aluminum alloy sheets. *Wear* 249(1–2):85–92
98. Rechenberg I, El Khyeri AR (2007) The sandfish of the Sahara. A model for friction and wear reduction. Department of Bionics and Evolution Techniques, Technical University of Berlin. <http://www.bionik.tu-berlin.de/institut/safiengl.htm>
99. Rowlinson JS, Widom B (1982) Molecular theory of capillarity. Clarendon, Oxford
100. Ribrant J, Bertling L (2007) Survey of failures in wind power systems with focus on Swedish wind power plants during 1997–2005. IEEE Power Engineering Society general meeting
101. Sasaki S (2010) Environmentally friendly tribology (Eco-tribology). *J Mech Sci Technol* 24:67–71
102. Scherge M, Gorb S (2001) Biological micro- and nanotribology: nature's solutions. Springer, Heidelberg
103. Sheldon RA (1992) Organic synthesis: past, present and future. *Chem Ind* 23:903–906
104. Sidorenko A, Krupenkin T, Taylor A, Fratzl P, Aizenberg J (2007) Reversible switching of hydrogel-saturated nanostructures into complex micropatterns. *Science* 315:487–490. doi:[10.1126/science.1135516](https://doi.org/10.1126/science.1135516)
105. Sidorenko A, Krupenkin T, Aizenberg J (2008) Controlled switching of the wetting behavior of biomimetic surfaces with hydrogel-supported nanostructures. *J Mater Chem* 18:3841–3846
106. Singer I, Bolster R, Wegand J et al (1990) Hertzian stress contribution to low friction behavior of thin MoS₂ coatings. *Appl Phys Lett* 57:995–997
107. Spolenak R, Gorb S, Gao H, Arzt E (2005) Effects of contact shape on the scaling of biological attachments. *Proc R Soc Lond Ser A* 461(2054):305–319
108. Sawyer WG, Ziegert JC, Schmitz TL, Barton T (2006) In situ lubrication with boric acid: powder delivery of an environmentally benign solid lubricant. *Tribol Trans* 49(2):284–290
109. Terrell EJ, Needelman WM, Kyle JP (2012) Wind turbine tribology. In: Nosonovsky M, Bhushan B (eds) Green tribology. Springer, Berlin, Heidelberg, pp 483–530
110. Trost BM (1991) The atom economy—a search for synthetic efficiency. *Science* 254:1471–1477. doi:[10.1126/science.1962206](https://doi.org/10.1126/science.1962206)
111. Tuteja A, Choi W, Ma M, Mabry JM, Mazzella SA, Rutledge GC, McKinley GH, Cohen RE (2007) Designing superoleophobic surfaces. *Science* 318:1618–1622. doi:[10.1126/science.1148326](https://doi.org/10.1126/science.1148326)
112. Tuteja A, Choi W, Mabry JM, McKinley GH, Cohen RE (2008) Robust omniphobic surfaces. *Proc Natl Acad Sci U S A* 105:18 200–18 205
113. Varenberg M, Gorb SN (2009) Hexagonal surface micropattern for dry and wet friction. *Adv Mater* 21:483–486
114. Wagner P, Furstner R, Barthlott W, Neinhuis C (2003) Quantitative assessment to the structural basis of water repellency in natural and technical surfaces. *J Exp Bot* 54:1295–1303
115. Wei J, Erdemir A, Fenske G (2000) Dry lubricant films for aluminum forming. *Tribol Trans* 43(3):535–541
116. Wenzel RN (1936) Resistance of solid surfaces to wetting by water. *Ind Eng Chem* 28:988–994
117. Wood RJK, Bahaj AS, Turnock SR, Wang L, Evans M (2010) Tribological design constraints of marine renewable energy systems. *Phil Trans R Soc A* 368:4807–4827
118. Yun R, Lu Y, Filip P (2010) Application of extension evaluation method in development of novel eco-friendly brake materials. *SAE Int J Mater Manuf* 2:1–7

Questions

1. Green tribology can be viewed in the broader context of two green areas, describe them?
2. What are the principles of Green Tribology?
3. Define the term “Biomimetics.”
4. Describe the two famous wetting models?
5. What is oleophobicity? Why it is hard to produce oleophobic surfaces?
6. Describe three attributes of the solid lubricants.

Answers

1. Green tribology can be viewed in the broader context of two other “green” areas: green engineering and green chemistry.
 Green engineering: the design, commercialization, and use of processes and products that are technically and economically feasible while minimizing (i) generation of pollution at the source and (ii) risk to human health and the environment.
 Green chemistry: the design of chemical products and processes that reduce or eliminate the use or generation of hazardous substances.
2. (i) Minimization of heat and energy dissipation
 (ii) Minimization of wear
 (iii) Reduction or complete elimination of lubrication and self-lubrication
 (iv) Natural lubrication
 (v) Biodegradable lubrication
 (vi) Sustainable chemistry and green engineering principles
 (vii) Biomimetic approach
 (viii) Surface texturing
 (ix) Environmental implications of coatings
 (x) Design for degradation
 (xi) Real-time monitoring
 (xii) Sustainable energy applications
3. Biomimetics (also referred to as bionics or biomimicry) is the application of biological methods and systems found in nature to the study and design of engineering systems and modern technology.
4. In Wenzel model it is assumed that the liquid retains contact with the solid surface at all points and the wetting is homogeneous.
 In Cassie-Baxter model it is assumed that the liquid only bridges across the protrusions and there are air pockets trapped between protrusions under the water droplet, therefore the wetting is heterogeneous.
5. The ability of a surface to repel oil or any organic liquid is called oleophobicity. It is much more difficult to produce an oleophobic surface, because surface energies of organic liquids are low, and they tend to wet most surfaces.

6. (a) They adhere to surfaces to form a protective boundary layer that prevents wear.
- (b) They act as a lubricant in sliding contacts by accommodating relative surface velocities.
- (c) They lubricate at high temperatures.

Problem 1 (Laplace Equation). $\Delta P = 2\gamma/R$

There are two hemispherical water droplets with the diameter of 10 μm

1. Calculate the pressure inside the droplets using the Laplace equation (assume water surface tension $\gamma = 0.072 \text{ N/m}$)
2. Calculate the total free surface energy (the surface area times surface energy) $E_{\text{Surf}} = \gamma A$.
3. The two droplets join together forming one single large droplet. Calculate the radius of the single droplet and pressure inside it. By how much the pressure changed?
4. Calculate the total free surface energy of the large droplet. What is the change in the surface energy ΔE_{Surf} ? Compare with the change of the volume energy (pressure times the droplet volume $\Delta E_{\text{vol}} = \Delta PV$). Discuss.

Problem 2 (Young, Wenzel, and Cassie-Baxter Equation)

Given $\gamma_{\text{WaterAir}} = 72$, $\gamma_{\text{SolidAir}} = 20$, $\gamma_{\text{SolidWater}} = 30$, $\gamma_{\text{OilWater}} = 40$, $\gamma_{\text{SolidOil}} = 25$, $\gamma_{\text{OilAir}} = 40$ (in mN/m)

1. Calculate contact angles for the (1) solid–water–air system, (2) solid–oil–air system, (3) solid–oil–water system (flat surface)
2. The 2D solid surface is roughened by rectangular asperities of height $H = 20 \mu\text{m}$, length $L = 20 \mu\text{m}$, and pitch $P = 40 \mu\text{m}$. Calculate the roughness factor R_f for the Wenzel model and the solid–liquid fractional area, f_{SL} for the Cassie-Baxter model
3. Calculate the contact angle for the (1) solid–water–air system, (2) solid–oil–air system, (3) solid–oil–water system with the rough surface (for both Wenzel and Cassie-Baxter models). Discuss.

Solutions

Problem 1 (Laplace Equation). $\Delta P = 2\gamma/R$

1.

$$\Delta P = P_{inside} - P_{outside} = \gamma \left(\frac{1}{R_1} + \frac{1}{R_2} \right)$$

$$R_1 = R_2 = R = 5 \mu m$$

$$P_{inside} = \Delta P + P_{outside} = \frac{2\gamma}{R} - \frac{\gamma}{R} = \frac{\gamma}{R} \rightarrow P_{inside} = \frac{0.072}{5 \times 10^{-6}} = 14.4 kPa$$

2.

$$A = 4\pi R^2 = 4\pi \times (5 \times 10^{-6})^2 \approx 3.14 \times 10^{-10} m^2$$

$$E_{Surf} = \gamma A = 0.072 \times 3.14 \times 10^{-10} = 0.226 \times 10^{-10} N.m$$

3. Volume of single large droplet: $V = \frac{8}{3}\pi R^3 = \frac{8}{3}\pi \times (5 \times 10^{-6})^3 \approx 1046.7 \times 10^{-18} m^3$

$$\text{Radius of single large droplet: } R = \sqrt[3]{\frac{3}{4\pi}V} \approx 6.3 \times 10^{-6} m = 6.3 \mu m$$

$$P_{inside} = \frac{\gamma}{R} = \frac{0.072}{6.3 \times 10^{-6}} \approx 11.4 kPa$$

$$\Delta P = P_2 - P_1 = 11.4 - 14.4 = -3 kPa$$

The pressure is decreased by 3 kPa.

4.

$$A = 4\pi R^2 = 4\pi \times (6.3 \times 10^{-6})^2 \approx 4.99 \times 10^{-10} m^2$$

$$E_{Surf} = \gamma A = 0.072 \times 4.99 \times 10^{-10} = 0.359 \times 10^{-10} N.m$$

$$\rightarrow \Delta E_{Surf} = 0.359 \times 10^{-10} - 0.226 \times 10^{-10} - 0.133 \times 10^{-10} N.m$$

$$E_{Vol,1} = P_1 V_1 = 14400 \times 523.35 \times 10^{-18} \approx 0.075 \times 10^{-10} N.m$$

$$E_{Vol,2} = P_2 V_2 = 11400 \times 1046.7 \times 10^{-18} \approx 0.119 \times 10^{-10} N.m$$

$$\rightarrow \Delta E_{Vol} = 0.119 \times 10^{-10} - 0.075 \times 10^{-10} = 0.044 \times 10^{-10} N.m$$

Problem 2 (Young, Wenzel, and Cassie-Baxter Equation)

1. (1) $\cos \theta = \frac{\gamma_{SA} - \gamma_{SW}}{\gamma_{WA}} = \frac{20-30}{72} \approx -0.139 \rightarrow \theta \approx 98^\circ$

(2) $\cos \theta = \frac{\gamma_{SA} - \gamma_{SO}}{\gamma_{OA}} = \frac{20-25}{40} = -0.125 \rightarrow \theta \approx 97^\circ$

(3) $\cos \theta = \frac{\gamma_{SW} - \gamma_{SQ}}{\gamma_{OW}} = \frac{30-25}{40} = +0.125 \rightarrow \theta \approx 83^\circ$

2. Roughness factor is the ratio of the real substrate area to the projected area.

$$R_f = \frac{A_S}{A_P} = \frac{4 \times 20 \times 20}{2 \times 20 \times 20} = 2$$

Solid–liquid fractional area is the ratio of the solid–liquid projected area to the total projected area.

$$f_{SL} = \frac{A_{SL}}{A_T} = \frac{20 \times 20}{2 \times 20 \times 20} = \frac{1}{2}$$

3. Wenzel:

$$(1) \cos \theta_W = R_f - \frac{\gamma_{SA} - \gamma_{SW}}{\gamma_{WA}} \approx -0.278 \rightarrow \theta \approx 106.1^\circ$$

$$(2) \cos \theta_W = R_f - \frac{\gamma_{SA} - \gamma_{SO}}{\gamma_{OA}} = -0.250 \rightarrow \theta \approx 104.5^\circ$$

$$(3) \cos \theta_W = R_f - \frac{\gamma_{SW} - \gamma_{SO}}{\gamma_{OW}} = +0.250 \rightarrow \theta \approx 75.5^\circ$$

Cassie-Baxter:

$$(1) \cos \theta_{CB} = f_{SL} R_f \frac{\gamma_{SA} - \gamma_{SW}}{\gamma_{WA}} - (1 - f_{SL}) \approx -0.639 \rightarrow \theta \approx 129.7^\circ$$

$$(2) \cos \theta_{CB} = f_{SL} R_f \frac{\gamma_{SA} - \gamma_{SO}}{\gamma_{OA}} - (1 - f_{SL}) = -0.625 \rightarrow \theta \approx 128.7^\circ$$

$$(3) \cos \theta_{CB} = f_{SL} R_f \frac{\gamma_{SW} - \gamma_{SO}}{\gamma_{OW}} - (1 - f_{SL}) = -0.375 \rightarrow \theta \approx 112^\circ$$

According to Wenzel model, for an intrinsically hydrophobic surface, the contact angle increases with increasing roughness, whereas for an intrinsically hydrophilic surface, it decreases with increasing roughness. According to Cassie-Baxter model, the contact angle increases with increasing roughness.

Chapter 19

Fundamentals of Linking Tribology and Corrosion (Tribocorrosion) for Medical Applications: Bio-tribocorrosion

V.A. Barão, C. Sukotjo, and M.T. Mathew

Abstract Metal/alloys have been used in orthopedic and dental implants for many years. In a physiological environment, they are susceptible to materials degradation affecting its performance and lead to gradual and early failures due to the continuous exposure to the variation in in vivo mechanical and chemical conditions. Tribocorrosion is a new area of research that links tribology and corrosion, which can be defined as the irreversible material degradation process resulting from the synergistic interaction of wear and corrosion phenomena on surfaces subjected to a relative contact movement in biological environments. This book chapter describes some fundamental aspects about this new research area and focused on its significances in biomedical application, namely, orthopedics and dentistry.

1 Introduction

Earlier in the decade, the application of tribocorrosion was predominantly focused in the mining and petroleum industries. Recently, there has been a growing interest in the subject of “tribocorrosion” as it pertains to biomedical applications due to the urgent need to improve implants in the fields of orthopedics and dentistry [1–5]. Tribocorrosion is a subject that deals with two separate scientific domains,

V.A. Barão

Department of Prosthodontics and Periodontology, Piracicaba Dental School,
University of Campinas (UNICAMP), Piracicaba, SP 13414-903, Brazil
e-mail: barao@fop.unicamp.br

C. Sukotjo

Restorative Dentistry, College of Dentistry, University of Illinois at Chicago (UIC), Chicago,
IL 60612, USA
e-mail: csukotjo@uic.edu

M.T. Mathew (✉)

Department of Orthopedic Surgery, Rush University Medical Center, Chicago, IL 60612, USA
e-mail: mathew_t_mathew@rush.edu

“tribology” and “corrosion.” An established branch of mechanical engineering, tribology is the science of two contacting surfaces in relative motion and the consequences of wear, friction, and lubrication at this interface. In fact, the prefix “tribo” originated from the Greek word “tribos,” which means rubbing. Otherwise known as an electrochemical process, *corrosion* is the disintegration of a metal into its constituent atoms due to chemical reactions with its surroundings. This leads to the development of a simple definition of *tribocorrosion*, which could be stated as “a science related to the surface degradation mechanisms and processes when mechanical wear and chemical/electrochemical reactions interact with each other” [6]. Further, bio-tribocorrosion is directly related to the application of the tribocorrosion to the biological environments, particularly implants in orthopedics and dentistry [6].

This chapter addresses some of the fundamental aspects of bio-tribocorrosion and highlights its relevance to orthopedics and dentistry. In addition, this chapter also includes a case study on the bio-tribocorrosive nature of the most commonly used implant metal, titanium (Ti), under physiological conditions.

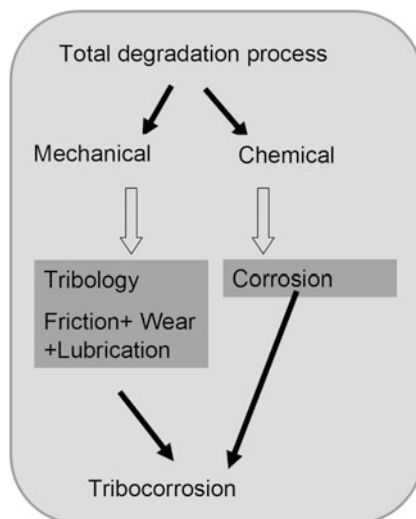
2 Tribocorrosion: An Overview

2.1 Linking Tribology and Corrosion

Tribocorrosion has recently made significant progress as an area of research. Solely, the tribological mechanism already exhibits high complexity in its focus on the degradation process and its time-dependant nature and nonlinear behavior, but including the component of corrosion to the system further increases its complexity [7]. Often a tribological event is characterized by the movement, or articulation, between two bodies. Corrosion is typically distinguished by an electrochemical process that generally takes place under a stable environment with an exposed surface [8–11]. Implementing the synergistic interaction of tribology and corrosion is the novel aspect of the area of tribocorrosion research. Generally, there are two types of events that are influenced by tribocorrosion: (1) the increase in damage from combined the effect of tribology and corrosion (synergy) and (2) the inhibition of the tribological effect on corrosion and vice versa leading to the reduction of the total loss (antagonism).

Linking tribology and corrosion presents many challenges as the material and degradation process exhibit different behaviors under combined exposure. In other words, tribological events are affected by corrosive mechanisms, and likewise, there may be significant variation in the corrosion process under the tribological exposure. It has already been reported that the total degradation loss is not a simple summation of wear loss or corrosion loss, but much more multifactorial [12–14]. This indicates the need to clearly distinguish the pathways of the degradation mechanisms.

Fig. 19.1 Flow chart of a total degradation process induced by the combined effect of corrosion and wear (tribocorrosion)



Tribological events can be divided into the following categories: erosion, abrasion, adhesion, fretting, and fatigue. Hence, tribocorrosion will be used to cover the much broader area and all wear and corrosion interactions. Common types of tribocorrosion are abrasion-corrosion, sliding wear-corrosion, and microabrasion-corrosion [6]. A condition of microabrasion is defined when small particles of less than 10 μm are employed between interacting surfaces.

From an industry perspective, understanding of the tribocorrosion process can assist in developing a system that will mitigate the material loss and improve the performance of the tribological systems. This achievement can enhance the function and durability of artificial joints and dental implants with a direct impact on the patient's quality of life. Figure 19.1 shows the flow chart of a total degradation process induced by the combined effect of corrosion and wear (tribocorrosion).

2.2 History

Although "tribocorrosion" is a relatively new subject, it has a long history. In the eighteenth century, Faraday observed the potential changes of the surface under applied friction, while the material surface was exposed to mechanical sliding. Some investigators in 1960 onwards called it as tribo-oxidation or tribochemistry. In 1992, Celis et al. [16] reported that sliding and corrosion influenced the coating of a thin film on the surface, which brought this area of research to the forefront. He called it tribo-electrochemistry. During last 20 years the subject has since developed and was first highlighted in industrial applications. Further, the contribution of the Tribocorr network (www.tricor.network.com) by Dr. Stack and collaborators has made a significant impact to the growth of the subject.

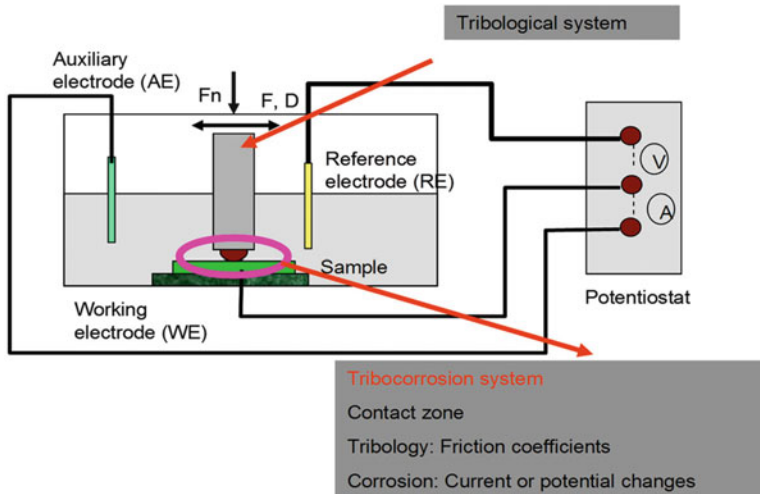


Fig. 19.2 A schematic diagram exhibits the principle of tribocorrosion. Tribo system—two bodies are in contact and involved in tribological event (sliding or fretting). Potentiostat is connected to the tribo system to monitor the electrochemical response or variations. In situ monitoring is the essential feature of the tribocorrosion system

The application of tribocorrosion in the biomedical field has since created bio-tribocorrosion as a critical area of research that has made significant progress during the last 5 years. The strong efforts by Mischler et al. [1, 7, 9, 10, 17, 18], Geringer et al. [19–24], Rocha et al. [4, 25–30], and Yan et al. [2, 5, 31, 32] have provided a clear direction for scientists and clinicians. Currently, tribocorrosion is being studied by many research groups in Europe and is becoming prominent in other countries including the USA and Brazil.

2.3 Fundamentals

The fundamental principles behind tribocorrosion are explained in Fig. 19.2. It provides an integrated protocol to study the material degradation mechanisms as mechanical movements combined with environmental effects. For example, a dental implant is exposed to a constantly changing oral environment, which due to the patient's diet can have sudden changes in pH levels [33, 34]. Additionally, mechanical movements of the mouth play a role during the mastication process (2,000 mastication cycles/day) [3].

The effective way to monitor the tribological response is to measure the friction coefficient. Electrochemical variation could be monitored by the evolution of current or potential. The electrochemical noise technique provides a way to monitor current and potential over time [6].

2.4 Synergistic Approach

The results will be used to construct tribocorrosion maps, based on the extensive work of Stack et al. [12, 13, 15]. There are some variables used in studying the synergistic effects in tribocorrosion interactions. The total wear volume loss (K_{wc}) can be expressed as

$$K_{wc} = K_w + K_c,$$

where K_w is the individual contribution of wear to the total weight loss and K_c is the individual contribution of corrosion to the total weight loss.

This can be further subdivided into two groups:

$$K_{wc} = (K_{wo} + \Delta K_w) + (K_{co} + \Delta K_c),$$

where K_{wo} = wear volume loss in the absence of corrosion, ΔK_w = change in the wear rate loss due to corrosion, K_{co} = volume loss due to corrosion in the absence of wear, and ΔK_c = change in the corrosion rate due to wear.

The K_{wc} value can be calculated by metrology. The K_c is estimated using Faraday's Law:

$$K_c = M \times i \times t / n \times F$$

and

$$i \times t = Q$$

where "M" is the atomic mass of the material or equivalent weight in g/mol; "i" is the total current; "t" is the total exposure time; "n" is the number of electrons involved in the corrosion process which can be 2⁺, 3⁺, and 4⁺; "F" is Faraday's constant (96,500 C/mol⁻¹); and "Q" is the charge passed through the working electrode (in coulombs).

The synergistic effects and dominating tribocorrosion mechanisms can be identified based on the ratio of corrosion loss to wear loss (K_c/K_w) [12, 13, 15]. The major criteria are:

- (i) $K_c/K_w \leq 0.1$ (wear)
- (ii) $0.1 < K_c/K_w \leq 1$ (wear-corrosion)
- (iii) $1 < K_c/K_w \leq 10$ (corrosion-wear)
- (iv) $K_c/K_w > 10$ (corrosion)

Based on the above methodology and polarization curves (changes in the corrosion mechanisms), a mechanism map or model can be developed. Interplay of corrosion (passivation and dissolution) and wear mechanisms could be clearly demonstrated as electrochemical parameters (pH, electrode potential) and mechanical conditions.

The advantage of tribocorrosion is in the analysis of estimating synergistic component between wear and corrosion [15]. The effect could be synergistic or antagonistic [15]. The best example of such synergistic effect is the removal of passive film under sliding or mechanical motion. The antagonistic effects are clear in metal-on-metal hip joints, where a tribolayer forms due to the sliding action of protein content solution [4].

The synergistic interactions between wear and corrosion can be evaluated by the ratio $\Delta K_w/\Delta K_c$ (enhancement of wear due to corrosion to enhancement of corrosion due to wear) and are classified into three groups (antagonistic, antagonistic-synergistic, and synergistic) [15] as follows:

$$\begin{aligned} \Delta K_w/\Delta K_c < 0.1 & \text{ Antagonistic} \\ 1 > \Delta K_w/\Delta K_c \geq 0.1 & \text{ Antagonistic-synergistic} \\ \Delta K_w/\Delta K_c > 1 & \text{ Synergistic} \end{aligned}$$

where ΔK_w is the effect of corrosion on the weight loss due to wear and ΔK_c is the effect of wear on the corrosion rate.

Generally, an antagonistic behavior is defined when the interplay of corrosion and wear reduces the total material weight loss (beneficial effect). On the other hand, synergistic behavior is defined when corrosion enhances the wear, hence the total weight loss [15].

One of the important features of tribocorrosion is the interdisciplinary nature. The investigation of tribocorrosion includes the disciplines of tribology, corrosion, material science, and clinical science. This provides a common platform for experts from the above areas to explore the material degradation mechanisms.

3 Clinical Problems in Orthopedics

3.1 General Problems: Metal-Based Implants

In the USA, more than 200,000 total hip replacements are conducted annually, with an average life-span of 10–15 years [35]. In this scenario, around 10 % of the patients who received hip prosthesis have implant failure within the first 5 years [35]. The most common metallic materials used in orthopedics are stainless steel, titanium, and Co-Cr-Mo alloys [36]. A spontaneously passive film forms on their surface, which confers their ability to be used clinically as a biocompatible material; however, this passive oxide layer may break down under in vivo conditions (i.e., sliding, fretting wear, and corrosion), and further clinical problems could result [37]. These wear particles, also known as third bodies, may increase degradation of metallic orthopedic prosthesis and also infect human body fluid, which in turn could induce cell necrosis (osteolysis) [38]. Retrieved orthopedic implants have shown discoloration and metal ions present on the peri-implant bone tissue. Figure 19.3 displays a scheme of an orthopedic implant.

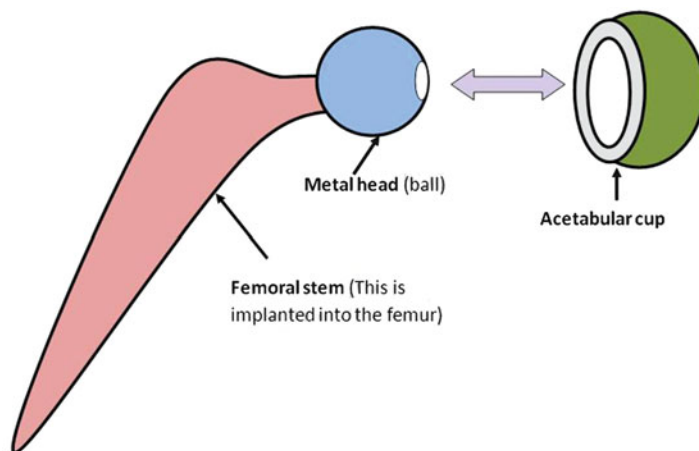


Fig. 19.3 Scheme of an MoM retrieved hip orthopedic implant. The femoral stem inserted into the femur and ball is fitted at the top part. The acetabulum cup creates tribological contact with ball during walking. There are also possibilities of micromotion (fretting) at the tapered modular junction femoral neck and inner surface of the ball. Further, the metal and bone interface at the femoral bottom sides could suffer from fretting corrosion

The material breakdown mechanism is complex due to the interaction of mechanical parameters (contact pressure, sliding velocity, and lubrication), surface chemistry (metal oxidation and dissolution, adsorption of organic molecules), and material properties (composition, microstructure, hardness) [9]. In this situation, the material degradation process is governed by the interaction and possible synergism between corrosion and wear, which characterizes tribocorrosion [5]. Lomholt et al. [39] examined the *in vivo* degradation mechanism of Ti-6Al-4V alloy implants during the articulating movements of the hip joint in the human body. Authors observed a combined effect of corrosion and wear on the degradation process of retrieved hip implants. The formation and accumulation of wear debris are greater than 100 μm and smaller than 5 μm . Smaller particles seem to be more harmful in the hip joint owing to their stronger biochemical interaction with the peri-prosthetic tissue. These small particles may cause inflammation in the peri-implant region and lead implant failure. Furthermore, they may also circulate through the body.

3.2 *Metal-on-Metal Hip Implant*

In total hip replacement procedures, metal-on-metal (MoM) bearings have been widely used. Nevertheless, several studies attempted to show that metal ions and wear debris caused by the wear and corrosion of such joints promote tissue

degradation with consequent local bone resorption and toxicological risk [40–43]. During human body motion, a sliding contact in the femoral articulation occurs [8]. For this reason, in case of hip implants, the metallic components of such artificial joint are prone to be tribocorroded [8]. The metallic wear debris affects bone cell (i.e., osteoblast) integrity, which could decrease the osseointegration between bone and metal implant [44].

For this reason, several studies have focused on the tribocorrosion behavior of metallic orthopedic materials used in hip prosthesis to overcome this problem. Mathew et al. [4] evaluated the tribocorrosion behavior of a low-carbon Co-Cr-Mo alloy as a function of loading in two different tribometer configurations. In the first configuration, “System A,” a linearly reciprocating alumina ball slid against the flat metal immersed in a phosphate-buffered solution (PBS). In the second configuration, “System B,” the flat end of a cylindrical metal pin was pressed against an alumina ball that oscillated rotationally, using bovine calf serum (BCS) as the lubricant and electrolyte. The tribocorrosion tests were performed under potentiostatic conditions at -0.345 V, with a sliding duration of 1,800 s and a frequency of 1 Hz. In System A, the applied loads were 0.05, 0.5, and 1 N (138, 296, and 373 MPa, respectively), and in System B, they were 16, 32, and 64 N (474, 597, and 752 MPa, respectively). An attempt was made to compare both systems in their tribochemical responses and formulate some insights in the total degradation processes. The authors observed that the proteins in the serum lubricant assisted in the generation of a protective layer against corrosion during sliding. The tribocorrosion behavior of the Co-Cr-Mo alloy was influenced by the test system. The study highlights the need of adequate methodology/guidelines to compare the results from different test systems and translating in solving the practical problems.

Another study [45] examined the tribocorrosion of high-carbon Co-Cr-Mo alloy in phosphate-buffered solution (PBS) alone and PBS mixed with bovine serum albumin under the influence of sliding velocity and applied potential. Under anodic potential, the anodic current density increases with sliding velocity, but wear rate does not change; however, the presence of bovine serum albumin enhanced the mechanical wear volume of the samples. Under cathodic conditions, the current density also increased, but the wear rate decreased with sliding velocity and presence of bovine serum albumin, which in turn reduced the total wear volume of the samples.

The use of different coatings has been shown to improve the wear-corrosion behavior of certain biomaterials. Vangolu et al. [46] coated Ti-6Al-4V alloy samples with hydroxyapatite and observed improved wear properties of titanium alloy in addition to enhanced bone bonding ability. Another study [47] observed that the nitrided Ti-6Al-4V alloy presented significantly increased tribocorrosion resistance compared to bare Ti-6Al-4V alloy. Other surface modifications have also been proposed such as thermal oxidation and anodic oxidation. Kumar et al. [48] compared the fretting-corrosion resistance of untreated, anodized, and thermally oxidized commercially pure titanium in simulated body fluid and observed that regardless of the surface modification type, the tribocorrosion resistance of titanium

improved. The performance of thermally oxidized, commercially pure titanium was superior to the anodized one.

4 Clinical Problems in Dentistry

4.1 Artificial Implant Replacing Teeth: Oral Environment

Dental implants have become a broadly used alternative to replace missing teeth in partial and total edentulous patients [49]. In the USA, more than 300,000 patients currently receive dental implants per year [50]. The use of dental implants has improved the quality of life of many people, mainly the elderly population. Titanium is the most common material used to fabricate dental implants because of its mechanical properties, excellent corrosion resistance, and biocompatibility [51]. The spontaneous ability of titanium to form a stable and dense oxide layer (TiO_2) is responsible for its corrosion resistance and the reason for wide acceptance, particularly in biomedical application [52].

In the oral cavity, dental implants are exposed to a complex degradation process, which involves mechanical, chemical, and microbiological actions. During mastication, implants are subjected to different forces which create micromovements at several interfaces, such as implant/crown, implant/abutment, abutment/crown, and implant/bone [30]. In these situations, fretting corrosion can induce wear and corrosion of the system. Every time the two surfaces rub against each other, their protective passive film can be removed leading to surface corrosion, and release of corrosion products into the system occurs. According to Kumar et al. [48], fretting corrosion is one of the most important factors for the failure of prosthesis made of titanium and titanium alloys under in vivo conditions. Figure 19.4 displays a photograph of a retrieved titanium dental implant. Additionally, implants are subjected to chemical and microbiological attack such as saliva, fluoride, changes in temperature and pH, and bacterial biofilm [53]. All these events promote the release of inflammatory mediators from various cells which contribute to bone



Fig. 19.4 Photograph showing titanium dental implant loss

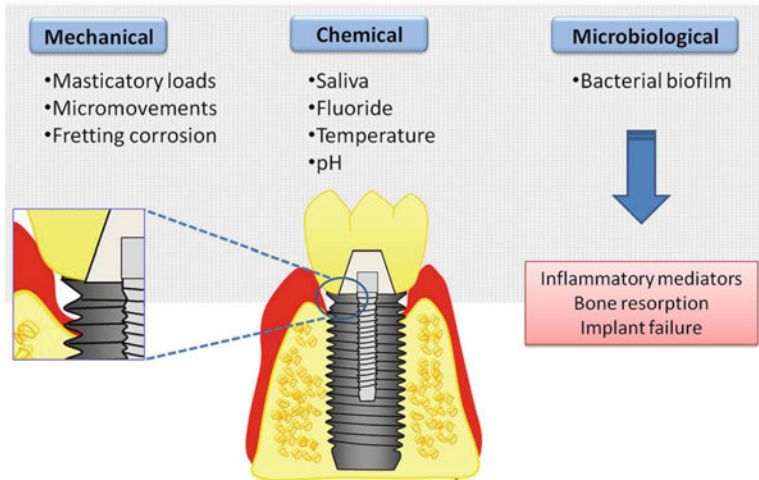


Fig. 19.5 Complex degradation process of dental implants into oral cavity

resorption and the encapsulation of the implant by fibrous tissue with subsequent failure of the implant [54, 55] (Fig. 19.5).

Numerous studies have attempted to investigate the chemical corrosion of titanium surfaces [33, 34, 51–53, 56–64]; however, very few have reported on the effect of combined chemical and mechanical actions, which resemble the clinical oral environment [3]. Vieira et al. (2006) [30] investigated the tribocorrosion behavior of commercially pure titanium in contact of artificial saliva with different levels of pH (3.8, presence of citric acid, and 5.5) and the presence of inhibitors included in the content of tooth-cleaning agents or medicines (sodium nitrite, anodic inhibitor; calcium carbonate, cathodic inhibitor; and benzotriazole, organic inhibitor). Authors noted that both the acidic saliva (presence of citric acid) and anodic inhibitor slightly improved the tribocorrosion of titanium material. This phenomenon may be explained by the nature of the oxidation and reduction reactions occurring in the contact area during tribological sliding. The tribolayers become more stable after 7,000 cycles in acidic artificial saliva and artificial saliva contacting anodic inhibitor as exposed by the lower friction coefficient and the reduced corrosion current.

When the tribocorrosion occurs in a biological environment, such as in the oral system, the presence of biological species creates further complexity in understanding the materials degradation pathways and dominant driving mechanisms generated by the interplay of wear and corrosion [65]. One previous study [26] investigated the tribocorrosion behavior of titanium in the presence of mixed oral biofilms. Although biofilms induced low friction on titanium during tribocorrosion test, its corrosion resistance was reduced probably due to the reduction of pH caused by the presence of microorganisms and their secreted products. The reduction of friction could affect the mechanical integrity and stability (elastic

deformation, rupture, and irreversible shear) of internal connections of dental implants [25].

4.2 Temporomandibular Joint

Temporomandibular disorder is related to injuries to the jaw, temporomandibular joint (i.e., disc displacement and osteoarthritis), or muscles of the head and neck [66]. It is normally observed among people ages 20–40 and presents greater prevalence in women. Around one-quarter of population worldwide shows some symptoms of temporomandibular disorder [67].

In severely damaged conditions (advanced degenerative diseases, tumors, and developmental anomalies), a total joint replacement is the only available treatment of choice [68]. It has been estimated that approximately 1,000–2,000 patients undergo some kind of temporomandibular joint implant surgery annually, which may indicate that temporomandibular joint implant surgery is still not a well-established/predictable surgical procedure. The implants used to replace the temporomandibular joint are made of titanium, cobalt chromium, or a combination of both due to their strength, ductility, corrosion resistance, and rigidity [69] characterizing a metal-on-metal joint. The temporomandibular joint implant system is a ball-and-socket device, which is similar to the hip joint implant. In orthopedics, several failures of total hip implants occur owing to the material breakdown from wear and corrosion. Although temporomandibular joint implants present more active tribocorrosion behavior when compared to orthopedic implants, they have been scarcely evaluated and need further investigation. The overall performance of such joints is the result of a system response to the combined effect of both wear and corrosion. In other words, their synergistic interactions have a direct influence on the life-span of the implants and subsequently impact the host body system. The temporomandibular joint motion is unique to any other joint surface in that sliding occurs with varying linear speed and is subjected to functional load and pH variations of synovial fluid.

5 Case Study: Lipopolysaccharide Influence on Tribocorrosion

This case study is used to explain a typical investigation method to study the pathways of tribocorrosion nature of a metal exposed to a biological environment.

6 Background

Lipopolysaccharides (LPS), also called as endotoxins, are component of membrane of gram-negative bacteria [70] and have marked effects on cells like macrophages, lymphocytes, fibroblasts, and osteoblasts [71]. When associated with the gingival crevicular fluid, they could induce inflammation, inhibition of cell growth, osteoclasts, and delayed healing [72]. Into the peri-implant area, this endotoxin can promote inflammation with consequent influence in the implant prognosis [73]. Our previous study [33] showed that different concentrations of LPS increased the corrosion kinetics of commercially pure titanium in a simulated oral environment containing saliva with different levels of pH.

6.1 Objectives/Hypothesis

Based on these previous results, we evaluated the role of such LPS on the corrosion and wear (tribocorrosion) nature of titanium dental implants material (commercially pure titanium and titanium alloy—Ti-6Al-4V) in artificial saliva at normal pH (6.5) [3]. We hypothesized that LPS would induce high wear/corrosion regardless of the titanium type.

6.2 Experimental Details

In this experiment we simulated different concentrations of *Escherichia coli* LPS (0, 0.15, 15, and 150 µg/ml) in artificial saliva, in order to mimic an oral inflammation. A ceramic ball was used to rub the flat titanium sample, creating a tribological contact into an electrolyte chamber. Previously, basic corrosion tests were conducted to investigate the potential of titanium in artificial saliva. In this way, an anodic potential (−0.3 V vs. SCE) was used to conduct the tribocorrosion experiment. Aiming to mimic the mastication function, a total of 2,000 cycles in a frequency of 1.2 Hz at 20 N of load were employed during the test. The changes in terms of corrosion kinetics before and after tribocorrosion test were measured using electrochemical impedance spectroscopy. The total weight loss of the samples was calculated.

7 Results and Discussion

The corrosion kinetics and resistance of titanium materials were affected by the presence of LPS into the artificial saliva. In a simpler way, we could say that LPS increased the ion exchange between titanium and electrolyte solution (artificial

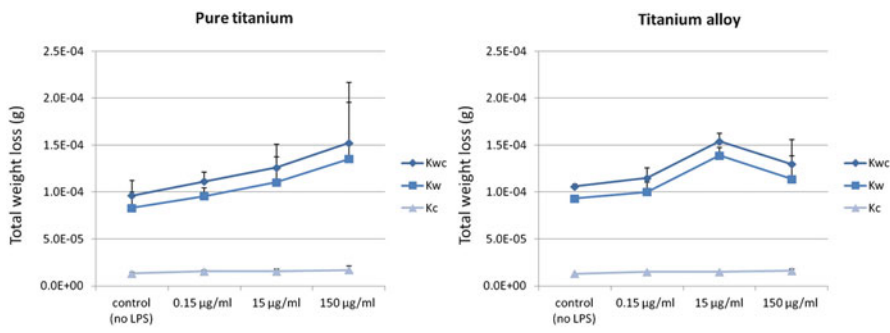


Fig. 19.6 Variation of weight loss of pure Ti and Ti alloy as a function of different LPS concentrations. The individual contribution of corrosion (K_c) and wear (K_w) to the weight loss and the combined effect of corrosion and wear (K_{wc}) are expressed in grams

saliva) with consequent reduction of the corrosion resistance of titanium surface. In addition, the tribological contact between the ceramic ball and titanium reduced the protection of the titanium oxide film. Although the corrosion behavior of both titanium materials was dissimilar, they had comparable total weight loss. It was possible to note that the corrosion performance of Ti-6Al-4V alloy was superior when compared with pure titanium. The endotoxin also enhanced the total weight loss of titanium materials (Fig. 19.6). The titanium oxide film in environment containing LPS is less protective which might explain the greater weight loss of titanium samples. The wear and corrosion seem to have an interaction herein which induces a synergistic effect (i.e., corrosion and wear are enhancing each other) that in this case is considered a detrimental effect.

7.1 Clinical Outcomes

The outcomes of the present experiment highlighted the possible negative influence of oral infection for titanium implant prognosis, since the titanium materials were more prone to corrode and wear in environment containing LPS.

8 Concluding Remarks

This book chapter provides some fundamental concepts of bio-tribocorrosion. The highlights of the chapter are summarized as follows:

- Bio-tribocorrosion is a relatively new research area that deals with the application of tribocorrosion (tribology and corrosion) to biomedical problems.

- The interdisciplinary approach is essential in the study of bio-tribocorrosion, particularly in the areas of tribology, corrosion, materials science, and clinical science.
- The application of tribocorrosion in the fields of orthopedics and dentistry is highlighted including specific examples in total hip replacements and temporomandibular joint replacement.
- A recent research study on influence of LPS on the tribocorrosion nature is included as a case study.

Acknowledgements Authors would like to express their sincere gratitude to Dr. Wimmer MA (Director, Tribology section, Rush University Medical Center) for the support. Special thanks go to Nagelli CN and Royhan D (Rush University Medical Center) for the valuable suggestions.

References

1. Mischler S (2008) Triboelectrochemical techniques and interpretation methods in tribocorrosion: a comparative evaluation. *Tribol Int* 41:573–583
2. Yan Y, Neville A, Dowson D, Williams S, Fisher J (2008) Tribo-corrosion analysis of wear and metal ion release interactions for metal-on-metal and ceramic-on-metal contacts for the application in artificial hip prostheses. *Proc Inst Mech Eng Part J J Eng Tribol* 222:483–492. doi:10.1243/13506501jet366
3. Mathew MT, Barao VA, Yuan JC, Assunção WG, Sukotjo C, Wimmer MA (2012) What is the role of lipopolysaccharide on the tribocorrosive behavior of titanium? *J Mech Behav Biomed Mater* 8:71–85
4. Mathew MT, Runa MJ, Laurent M, Jacobs JJ, Rocha LA, Wimmer MA (2011) Tribocorrosion behavior of Co-Cr-Mo alloy for hip prosthesis as a function of loads: a comparison between two testing systems. *Wear* 271:1210–1219. doi:10.1016/j.wear.2011.01.086
5. Yan Y, Neville A, Dowson D, Williams S (2006) Tribocorrosion in implants—assessing high carbon and low carbon Co-Cr-Mo alloys by in situ electrochemical measurements. *Tribol Int* 39:1509–1517. doi:10.1016/j.triboint.2006.01.016
6. Mathew MT, Srinivasa Pai P, Pourzal R, Fischer A, Wimmer MA (2009) Significance of tribocorrosion in biomedical applications: overview and current status. *Adv Tribol Article ID 250986:250912* pages
7. Vieira AC, Rocha LA, Papageorgiou N, Mischler S (2012) Mechanical and electrochemical deterioration mechanisms in the tribocorrosion of Al alloys in NaCl and in NaNO₃ solutions. *Corros Sci* 54:26–35. doi:10.1016/j.corsci.2011.08.041
8. Diomidis N, Mischler S, More NS, Roy M, Paul SN (2011) Fretting-corrosion behavior of beta titanium alloys in simulated synovial fluid. *Wear* 271:1093–1102. doi:10.1016/j.wear.2011.05.010
9. Munoz AI, Mischler S (2011) Effect of the environment on wear ranking and corrosion of biomedical Co-Cr-Mo alloys. *J Mater Sci Mater Med* 22:437–450. doi:10.1007/s10856-010-4224-0
10. More NS, Diomidis N, Paul SN, Roy M, Mischler S (2011) Tribocorrosion behavior of beta titanium alloys in physiological solutions containing synovial components. *Mater Sci Eng C Mater Biol Appl* 31:400–408. doi:10.1016/j.msec.2010.10.021
11. Equey S, Houriet A, Mischler S (2011) Wear and frictional mechanisms of copper-based bearing alloys. *Wear* 273:9–16. doi:10.1016/j.wear.2011.03.030

12. Stack MM, Mathew MT, Hodge C (2011) Micro-abrasion-corrosion interactions of Ni-Cr/WC based coatings: approaches to construction of tribo-corrosion maps for the abrasion-corrosion synergism. *Electrochim Acta* 56:8249–8259. doi:[10.1016/j.electacta.2011.06.064](https://doi.org/10.1016/j.electacta.2011.06.064)
13. Stack MM, Huang W, Wang G, Hodge C (2011) Some views on the construction of bio-tribo-corrosion maps for Titanium alloys in Hank's solution: particle concentration and applied loads effects. *Tribol Int* 44:1827–1837. doi:[10.1016/j.triboint.2011.07.009](https://doi.org/10.1016/j.triboint.2011.07.009)
14. Eddoumy F, Addiego F, Celis JP, Buchheit O, Berradja A, Muller R et al (2011) Reciprocating sliding of uniaxially-stretched ultra-high molecular weight polyethylene for medical device applications. *Wear* 272:50–61. doi:[10.1016/j.wear.2011.07.013](https://doi.org/10.1016/j.wear.2011.07.013)
15. Stack MM, Abdulrahman GH (2010) Mapping erosion-corrosion of carbon steel in oil exploration conditions: some new approaches to characterizing mechanisms and synergies. *Tribol Int* 43:1268–1277
16. Celis JP, Franck M, Roos JR, Kreutz EW, Gasser A, Wehner M et al (1992) Potential of photon and particle beams for surface-treatment of thin ceramic coatings. *Appl Surf Sci* 54:322–329
17. Mischler S, Debaud S, Landolt D (1998) Wear-accelerated corrosion of passive metals in tribocorrosion systems. *J Electrochem Soc* 145:750–758
18. Vieira AC, Rocha LA, Mischler S (2011) Influence of SiC reinforcement particles on the tribocorrosion behaviour of Al-SiC(p) FGs in 0.05M NaCl solution. *J Phys D Appl Phys* 44. doi:[10.1088/0022-3727/44/18/185301](https://doi.org/10.1088/0022-3727/44/18/185301)
19. Geringer J, Tatkiwicz W, Rouchouse G (2011) Wear behavior of PAEK, poly(aryl-ether-ketone), under physiological conditions, outlooks for performing these materials in the field of hip prosthesis. *Wear* 271:2793–2803. doi:[10.1016/j.wear.2011.05.034](https://doi.org/10.1016/j.wear.2011.05.034)
20. Geringer J, Boyer B, Farizon F (2011) Understanding the dual mobility concept for total hip arthroplasty. Investigations on a multiscale analysis-highlighting the role of arthrofibrosis. *Wear* 271:2379–2385. doi:[10.1016/j.wear.2011.02.027](https://doi.org/10.1016/j.wear.2011.02.027)
21. Pellier J, Geringer J, Forest B (2011) Fretting-corrosion between 316L SS and PMMA: influence of ionic strength, protein and electrochemical conditions on material wear. Application to orthopaedic implants. *Wear* 271:1563–1571. doi:[10.1016/j.wear.2011.01.082](https://doi.org/10.1016/j.wear.2011.01.082)
22. Geringer J, Atmani F, Forest B (2009) Friction-corrosion of AISI 316L/bone cement and AISI 316L/PMMA contacts: Ionic strength effect on tribological behaviour. *Wear* 267:763–769. doi:[10.1016/j.wear.2008.12.087](https://doi.org/10.1016/j.wear.2008.12.087)
23. Geringer J, Forest B, Combrade P (2007) Wear of poly (methyl methacrylate) against a metallic surface in dry conditions. *Polymer Eng Sci* 47:633–648. doi:[10.1002/Pen.20736](https://doi.org/10.1002/Pen.20736)
24. Geringer J, Forest B, Combrade P (2006) Wear analysis of materials used as orthopaedic implants. *Wear* 261:971–979. doi:[10.1016/j.wear.2006.03.022](https://doi.org/10.1016/j.wear.2006.03.022)
25. Souza JC, Henriques M, Oliveira R, Teughels W, Celis JP, Rocha LA (2010) Biofilms inducing ultra-low friction on titanium. *J Dent Res* 89:1470–1475. doi:[10.1177/0022034510378428](https://doi.org/10.1177/0022034510378428)
26. Souza JCM, Henriques M, Oliveira R, Teughels W, Celis JP, Rocha LA (2010) Do oral biofilms influence the wear and corrosion behavior of titanium? *Biofouling* 26:471–478
27. Mathew MT, Ariza E, Rocha LA, Vaz F, Fernandes AC, Stack MM (2010) Tribocorrosion behaviour of TiC(x)O(y) thin films in bio-fluids. *Electrochim Acta* 56:929–937. doi:[10.1016/j.electacta.2010.08.067](https://doi.org/10.1016/j.electacta.2010.08.067)
28. Mathew MT, Novo J, Rocha LA, Covas JA, Comes JR (2010) Tribological, rheological and mechanical characterization of polymer blends for ropes and nets. *Tribol Int* 43:1400–1409. doi:[10.1016/j.triboint.2010.01.011](https://doi.org/10.1016/j.triboint.2010.01.011)
29. Kanagaraj S, Mathew MT, Fonseca A, Oliveira MSA, Simoes JAO, Rocha LA (2010) Tribological characterisation of carbon nanotubes/ultrahigh molecular weight polyethylene composites: the effect of sliding distance. *Int J Surf Sci Eng* 4:305–321
30. Vieira AC, Ribeiro AR, Rocha LA, Celis JP (2006) Influence of pH and corrosion inhibitors on the tribocorrosion of titanium in artificial saliva. *Wear* 261:994–1001

31. Yan Y, Neville A, Dowson D, Williams S, Fisher J (2009) Effect of metallic nanoparticles on the bio-tribocorrosion behaviour of Metal-on-Metal hip prostheses. *Wear* 267:683–688. doi:[10.1016/j.wear.2008.12.110](https://doi.org/10.1016/j.wear.2008.12.110)
32. Yan Y, Neville A, Dowson D (2007) Tribo-corrosion properties of cobalt-based medical implant alloys in simulated biological environments. *Wear* 263:1105–1111. doi:[10.1016/j.wear.2007.01.114](https://doi.org/10.1016/j.wear.2007.01.114)
33. Barao VA, Mathew MT, Assuncao WG, Yuan JC, Wimmer MA, Sukotjo C (2011) The role of lipopolysaccharide on the electrochemical behavior of titanium. *J Dent Res* 90:613–618. doi:[10.1177/0022034510396880](https://doi.org/10.1177/0022034510396880)
34. Barao VA, Mathew MT, Assuncao WG, Yuan JC, Wimmer MA, Sukotjo C (2011) Stability of cp-Ti and Ti-6Al-4V alloy for dental implants as a function of saliva pH—an electrochemical study. *Clin Oral Implants Res*. doi:[10.1111/j.1600-0501.2011.02265.x](https://doi.org/10.1111/j.1600-0501.2011.02265.x)
35. Faghihi S, Li D, Szpunar JA (2010) Tribocorrosion behaviour of nanostructured titanium substrates processed by high-pressure torsion. *Nanotechnology* 21:485703. doi:[10.1088/0957-4484/21/48/485703](https://doi.org/10.1088/0957-4484/21/48/485703)
36. Milosev I (2011) Metallic materials for biomedical applications: laboratory and clinical studies. *Pure Appl Chem* 83:309–324. doi:[10.1351/Pac-Con-10-07-09](https://doi.org/10.1351/Pac-Con-10-07-09)
37. Kumar S, Narayanan TSNS, Raman SGS, Seshadri SK (2010) Evaluation of fretting corrosion behaviour of CP-Ti for orthopaedic implant applications. *Tribol Int* 43:1245–1252. doi:[10.1016/j.triboint.2009.12.007](https://doi.org/10.1016/j.triboint.2009.12.007)
38. Milosev I, Remskar M (2009) In vivo production of nanosized metal wear debris formed by tribochemical reaction as confirmed by high-resolution TEM and XPS analyses. *J Biomed Mater Res A* 91A:1100–1110. doi:[10.1002/Jbm.A.32301](https://doi.org/10.1002/Jbm.A.32301)
39. Lomholt TC, Pantleon K, Somers MAJ (2011) In-vivo degradation mechanism of Ti-6Al-4V hip joints. *Mater Sci Eng C Mater Biol Appl* 31:120–127. doi:[10.1016/j.msec.2010.08.007](https://doi.org/10.1016/j.msec.2010.08.007)
40. Jacobs JJ, Skipor AK, Patterson LM, Hallab NJ, Paprosky WG, Black J et al (1998) Metal release in patients who have had a primary total hip arthroplasty. A prospective, controlled, longitudinal study. *J Bone Joint Surg Am* 80:1447–1458
41. Doorn PF, Campbell PA, Worrall J, Benya PD, McKellop HA, Amstutz HC (1998) Metal wear particle characterization from metal on metal total hip replacements: transmission electron microscopy study of periprosthetic tissues and isolated particles. *J Biomed Mater Res* 42:103–111
42. DiCarlo EF, Bullough PG (1992) The biologic responses to orthopedic implants and their wear debris. *Clin Mater* 9:235–260
43. Hallab N, Merritt K, Jacobs JJ (2001) Metal sensitivity in patients with orthopaedic implants. *J Bone Joint Surg Am* 83-A:428–436
44. Lenz R, Mittelmeier W, Hansmann D, Brem R, Diehl P, Fritsche A et al (2009) Response of human osteoblasts exposed to wear particles generated at the interface of total hip stems and bone cement. *J Biomed Mater Res A* 89:370–378. doi:[10.1002/jbm.a.31996](https://doi.org/10.1002/jbm.a.31996)
45. Gil RA, Munoz AI (2011) Influence of the sliding velocity and the applied potential on the corrosion and wear behavior of HC Co-Cr-Mo biomedical alloy in simulated body fluids. *J Mech Behav Biomed Mater* 4:2090–2102. doi:[10.1016/j.jmbbm.2011.07.008](https://doi.org/10.1016/j.jmbbm.2011.07.008)
46. Vangolu Y, Alsaran A, Yildirim OS (2011) Wear properties of micro arc oxidized and hydrothermally treated Ti6Al4V alloy in simulated body fluid. *Wear* 271:2322–2327. doi:[10.1016/j.wear.2010.12.039](https://doi.org/10.1016/j.wear.2010.12.039)
47. Manhabosco TM, Tamborim SM, dos Santos CB, Muller IL (2011) Tribological, electrochemical and tribo-electrochemical characterization of bare and nitrided Ti6Al4V in simulated body fluid solution. *Corros Sci* 53:1786–1793. doi:[10.1016/j.corsci.2011.01.057](https://doi.org/10.1016/j.corsci.2011.01.057)
48. Kumar S, Narayanan TSNS, Raman SGS, Seshadri SK (2010) Surface modification of CP-Ti to improve the fretting-corrosion resistance: thermal oxidation vs. anodizing. *Mater Sci Eng C Mater Biol Appl* 30:921–927. doi:[10.1016/j.msec.2010.03.024](https://doi.org/10.1016/j.msec.2010.03.024)

49. Heuer W, Elter C, Demling A, Neumann A, Suerbaum S, Hannig M et al (2007) Analysis of early biofilm formation on oral implants in man. *J Oral Rehabil* 34:377–382. doi:[10.1111/j.1365-2842.2007.01725.x](https://doi.org/10.1111/j.1365-2842.2007.01725.x)
50. Ratner BD, Hoffman AS, Schoen FJ, Lemon JE (2004) *Biomaterials science: a multidisciplinary endeavor. An introduction to materials in medicine.* Elsevier Academic Press, San Diego
51. Nakagawa M, Matsuya S, Shiraishi T, Ohta M (1999) Effect of fluoride concentration and pH on corrosion behavior of titanium for dental use. *J Dent Res* 78:1568–1572
52. Huang HH (2003) Effect of fluoride and albumin concentration on the corrosion behavior of Ti-6Al-4V alloy. *Biomaterials* 24:275–282
53. Mabileau G, Bourdon S, Joly-Guillou ML, Filmon R, Basle MF, Chappard D (2006) Influence of fluoride, hydrogen peroxide and lactic acid on the corrosion resistance of commercially pure titanium. *Acta Biomater* 2:121–129. doi:[10.1016/j.actbio.2005.09.004](https://doi.org/10.1016/j.actbio.2005.09.004)
54. Azzi M, Szpunar JA (2007) Tribo-electrochemical technique for studying tribocorrosion behavior of biomaterials. *Biomol Eng* 24:443–446. doi:[10.1016/j.bioeng.2007.07.015](https://doi.org/10.1016/j.bioeng.2007.07.015)
55. Jones FH (2001) Teeth and bones: applications of surface science to dental materials and related biomaterials. *Surf Sci Rep* 42:79–205
56. Schiff N, Grosgeat B, Lissac M, Dalard F (2002) Influence of fluoride content and pH on the corrosion resistance of titanium and its alloys. *Biomaterials* 23:1995–2002
57. Popa MV, Vasilescu E, Drob P, Vasilescu C, Demetrescu I, Ionita D (2008) Long-term assessment of the implant titanium material–artificial saliva interface. *J Mater Sci Mater Med* 19:1–9. doi:[10.1007/s10856-007-3271-7](https://doi.org/10.1007/s10856-007-3271-7)
58. Mareci D, Chelariu R, Gordin DM, Ungureanu G, Gloriant T (2009) Comparative corrosion study of Ti-Ta alloys for dental applications. *Acta Biomater* 5:3625–3639. doi:[10.1016/j.actbio.2009.05.037](https://doi.org/10.1016/j.actbio.2009.05.037)
59. Souza ME, Lima L, Lima CR, Zavaglia CA, Freire CM (2009) Effects of pH on the electrochemical behaviour of titanium alloys for implant applications. *J Mater Sci Mater Med* 20:549–552. doi:[10.1007/s10856-008-3623-y](https://doi.org/10.1007/s10856-008-3623-y)
60. Messer RL, Tackas G, Mickalonis J, Brown Y, Lewis JB, Wataha JC (2009) Corrosion of machined titanium dental implants under inflammatory conditions. *J Biomed Mater Res B Appl Biomater* 88:474–481. doi:[10.1002/jbm.b.31162](https://doi.org/10.1002/jbm.b.31162)
61. Messer RL, Seta F, Mickalonis J, Brown Y, Lewis JB, Wataha JC (2010) Corrosion of phosphate-enriched titanium oxide surface dental implants (TiUnite) under in vitro inflammatory and hyperglycemic conditions. *J Biomed Mater Res B Appl Biomater* 92:525–534. doi:[10.1002/jbm.b.31548](https://doi.org/10.1002/jbm.b.31548)
62. Joska L, Fojt J (2010) Corrosion behaviour of titanium after short-term exposure to an acidic environment containing fluoride ions. *J Mater Sci Mater Med* 21:481–488. doi:[10.1007/s10856-009-3930-y](https://doi.org/10.1007/s10856-009-3930-y)
63. Joska L, Fojt J, Hradilova M, Hnilica F, Cvrcek L (2010) Corrosion behaviour of TiN and ZrN in the environment containing fluoride ions. *Biomed Mater* 5:054108. doi:[10.1088/1748-6041/5/5/054108](https://doi.org/10.1088/1748-6041/5/5/054108)
64. Nakagawa M, Matsuya S, Udoh K (2002) Effects of fluoride and dissolved oxygen concentrations on the corrosion behavior of pure titanium and titanium alloys. *Dent Mater J* 21:83–92
65. Landolt D, Mischler S, Stemp M (2001) Electrochemical methods in tribocorrosion: a critical appraisal. *Electrochim Acta* 46:3913–3929
66. Ingawale S, Goswami T (2009) Temporomandibular joint: disorders, treatments, and biomechanics. *Ann Biomed Eng* 37:976–996. doi:[10.1007/s10439-009-9659-4](https://doi.org/10.1007/s10439-009-9659-4)
67. van Loon JP, de Bont LG, Stegenga B, Spijkervet FK, Verkerke GJ (2002) Groningen temporomandibular joint prosthesis. Development and first clinical application. *Int J Oral Maxillofac Surg* 31:44–52. doi:[10.1054/ijom.2001.0175](https://doi.org/10.1054/ijom.2001.0175)
68. Mercuri LG (2000) The use of alloplastic prostheses for temporomandibular joint reconstruction. *J Oral Maxillofac Surg* 58:70–75

69. Chaturvedi TP (2009) An overview of the corrosion aspect of dental implants (titanium and its alloys). *Indian J Dent Res* 20:91–98
70. Simon BI, Goldman HM, Ruben MP, Baker E (1969) The role of endotoxin in periodontal disease. I. A reproducible, quantitative method for determining the amount of endotoxin in human gingival exudate. *J Periodontol* 40:695–701
71. Wilson M (1995) Biological activities of lipopolysaccharides from oral bacteria and their relevance to the pathogenesis of chronic periodontitis. *Sci Prog* 78(Pt 1):19–34
72. Knoernschild KL, Tompkins GR, Lefebvre CA, Griffiths LL, Schuster GS (1996) Effect of pH on *Porphyromonas gingivalis* endotoxin affinity for resins. *Int J Prosthodont* 9:239–247
73. Nelson SK, Knoernschild KL, Robinson FG, Schuster GS (1997) Lipopolysaccharide affinity for titanium implant biomaterials. *J Prosthet Dent* 77:76–82

Questions

1. Define tribocorrosion and bio-tribocorrosion.
2. Explain how tribocorrosion can affect the survival rate of orthopedic implants.
3. Based on the tribocorrosion principle, how can the oral environment be harmful to the survival of dental implants?
4. How can oral biofilms damage the integrity of dental implants?
5. In relation to the synergistic approach between corrosion and wear, define K_{wc} , K_w , and K_c .

Answers

1. Tribocorrosion is a degradation phenomenon of a material's surface (wear, cracking, corrosion) affected by the combined action of mechanical loading (friction, abrasion, erosion) and corrosion attack caused by the environment (chemical and/or electrochemical interaction). When this phenomenon occurs into the biological system, it characterizes a bio-tribocorrosion principle (e.g., orthopedic implants and dental implants).
2. As the human body moves, the hip and knee joint implants suffer oscillatory and friction movements at the contact region between the implant and bone. This situation can cause fretting corrosion and consequently inflammatory tissue reaction. The metallic wear debris, also called third body, may increase degradation of metallic orthopedic prosthesis and also infect human body fluid, which in turn could induce cell necrosis with direct implication on the osseointegration between bone and metal implant. Additionally, the metal ions and wear debris caused by the wear and corrosion of such joints promote tissue degradation with consequent local bone resorption and toxicological risk.
3. During mastication, which is a unique mechanical action, implants are subjected to both axial and oblique forces which create micromovements at several interfaces, i.e., implant/prosthetic crown, implant/abutment, abutment/prosthetic crown, and implant/bone interfaces. In such situations, fretting corrosion, a

surface damage mode caused by low-amplitude oscillatory sliding motion between two contacting surfaces, can induce wear and corrosion. Particles created from wear (surface damage) of implants promote the release of inflammatory mediators from various cells which contribute to bone resorption and the encapsulation of the implant by fibrous tissue with subsequent failure of the implant. Additionally, dental implants are exposed to an aggressive environment including agents such as bacterial biofilm and saliva. The thermal, ionic, microbiological, and enzymatic properties of this environment are ideal to induce the biodegradation of metals, which could reduce the fatigue life and ultimate strength of the material, leading to mechanical failure of dental implants.

4. The presence of biofilms and their secreted products reduce the pH of the oral environment. It has been shown that acidic medium decreases the corrosion resistance of dental materials. Additionally, the induced low friction coefficient promoted by the presence of biofilm on the “tribo” region could affect the mechanical integrity and stability (elastic deformation, rupture, and irreversible shear) of internal connections of dental implants.
5. K_{wc} is the total weight loss of a material due to the combined effect of corrosion and wear. K_w is the individual contribution of wear to the total weight loss, and K_c is the individual contribution of corrosion to the total weight loss.

Chapter 20

Wear of Biomedical Implants

P.S. Rama Sreekanth and S. Kanagaraj

Abstract Total joint arthroplasty (TJA) is one of the major successes of the twentieth century changing the lives of millions of people, both younger and older generations. However, critical problems like wear, loosening, and osteolysis still remain in the process of realizing its capabilities to the fullest extent. The change in the lifestyle of the people has further aggravated the seriousness of the problem. Thus, the present chapter is focused on the “Wear of biomedical implants,” which introduces the various possibilities, causes and concerns, critical issues and solutions to the above-said problems enabling a neophyte to understand the current scenario. It briefly discusses the basic tribological aspects involved in a typical synovial joint, its structure, and wear mechanism involved. The discussion then turns towards highlighting the primary causes and concerns of wear debris, various tools and techniques to estimate the wear in specific relevance to artificial joint materials. It also highlights the various implant materials and techniques for reduction of wear in the implants.

1 Introduction

Tribology is defined as “the science and technology of interacting surfaces in relative motion and of related subjects and practices” [1]. It includes technologically relevant phenomena such as friction, wear, and lubrication. Interacting surfaces in relative motion essentially produce friction and consequently wear of the counterfaces, while

P.S.R. Sreekanth
Department of Mechanical Engineering, National Institute of Science and Technology,
Bherampur 761008, Orrisa, India

Department of Mechanical Engineering, Indian Institute of Technology Guwahati,
North Guwahati 781 039, Assam, India

S. Kanagaraj (✉)
Department of Mechanical Engineering, Indian Institute of Technology Guwahati,
North Guwahati 781 039, Assam, India

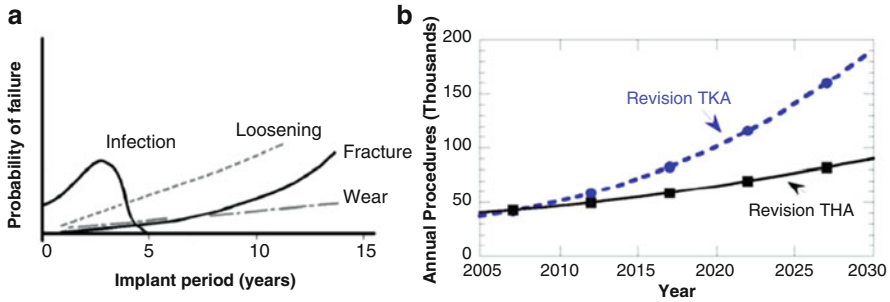


Fig. 20.1 (a) Possible reasons for implant failure [4] (b) Projected revisions in THA and TKA [3]

lubrication is a preventive measure to restrict the consequences thereof. Wear is the progressive loss of a material from solid surfaces in contact, which occurs as a result of friction. It is a slow and continuous process of removal of particles from one or more materials. Wear is not an intrinsic property of a material but rather it is complex response of a material induced by the system such as load, speed, temperature, hardness, surface finish, presence of foreign materials, etc. In this chapter, an emphasis is laid on the relevance of Tribology and related phenomena to biomedical implants such as hip and knee joint implants. Research studies covering wear of bearing couple, influencing factors, different types of bearing materials, characterization and other related issues are discussed elaborately to provide a basic and firm understanding of the wear of biomedical implants.

1.1 Necessity to Study Tribology in Relevance to Human Joints

Success of Total joint replacements (TJR)s is a landmark achievement in the orthopedic history of the twentieth century. However, the number of revised surgeries being performed due to wear of an implant is a major concern among the material science community. Revision surgeries represent a heavy burden to patients, surgeons, and also health care systems. It was estimated that the number of replacement surgeries in the USA amounts to approximately 2 million per year [2]. Kurtz et al. [3] reported that a dramatic increase in the number of TJRs (both primary and revision) likely to be performed between 2005 and 2030 will grow by a colossal 673 % in the USA. Figure 20.1a shows the possible reason for failure of implant [4] and Fig. 20.1b shows projected revisions in total hip arthroplasty (THA) and total knee arthroplasty (TKA) in the USA alone. THA revisions are projected to grow from 40,400 in 2005 to 90,000 in 2030 corresponding to an increase of 123 %. TKA revisions are expected to increase from 37,300 in 2005 to 191,000 in 2030 corresponds to 412 % increase.

Davidson et al. [5] reported that the total number of revisions resulting from the wear of an acetabular was more than 10,000 per year. It clearly reflects the severity of the problem, and thus it strongly demands the necessity of proper understanding

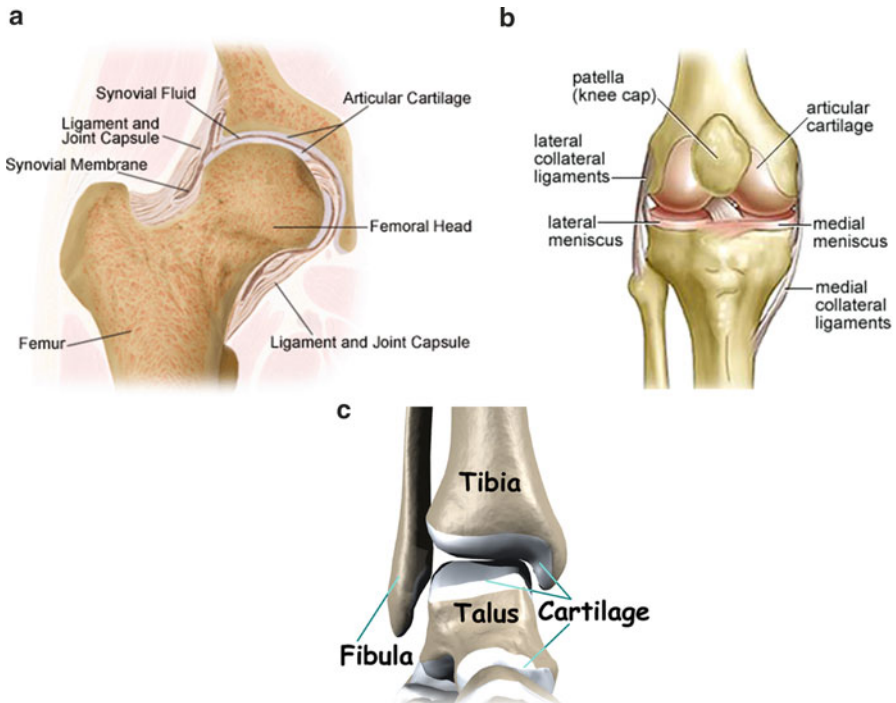


Fig. 20.2 Anatomy of load bearing joints (a) hip joint [6] (b) knee joint [7] (c) ankle joint [8]

the possible mechanisms and seriously finding a solution for the same. In addition to that the design goals have been advanced from simply alleviating pain and discomfort for elderly patients to returning the more physically demanding lifestyles for young active patients including sports activities with a promising life of about 20–25 years. These demands and challenges have kept the research activity still open with “enhanced longevity of the implant” as an ultimate goal.

1.2 Understanding Structural Anatomy of Human Joints

Human joints have a crucial role to play in the overall functioning of the body and carry out routine activities allowing bones to articulate on one another. Joints allow a wide variety of stability and motion options which vary depending on their location, position, and function. For example, the hip joint can be compared to a ball-on-socket joint allowing motion in three axes, while knee joint acts as a disk-on-plate allowing very restricted type of motion. Besides, the human joints are also classified as load bearing joints and non-load bearing joints. Hip, knee, and ankle joints are among the primary load bearing joints and these are also called synovial joints. Most of the other joints such as elbow, wrist, and shoulder pertain to non-load bearing class. Typical anatomy of synovial joints is shown in Fig. 20.2.

The joints may vary in their shape, size, and loading pattern but the typical lubrication mechanism remains the same.

The articulating surfaces of the bones are covered with articular cartilage preventing their direct physical contact. The assembly is encapsulated by ligament and joint capsule, which is lined with synovial membrane and filled with synovial fluid [9]. Tribology of the natural joints is extremely good due to the presence of synovial fluid which allows the joints to work under a wide range of loading conditions without causing damage to the bones. The excellent lubrication of joints is due to very low friction coefficient of bone, (0.003–0.015) which usually lasts for over 70 years [10]. However, due to accident or some degenerative joint diseases like arthritis or due to excessive wear, the joint may lose its natural lubricating function leading to severe pain in the joint location paving a way for Total joint replacement (TJR). Although TJRs are common in case of knee, shoulder, elbow, wrist, ankle, and finger joints, they are recent developments compared to that of hip. Hence, the present chapter mainly focuses on the various developments highlighting the major breakthroughs in Total Hip Arthroplasty (THA) to reduce the wear and enhance the prosthesis longevity.

1.3 Hip Joint Prosthesis and Wear in Medical Prosthesis

The objective of total hip replacement (THR) is to relieve the pain in the joint location and restore its original mobility. The shape, size and design of the implant depend primarily on the location of it in the body. The hip joint prosthesis, shown in Fig. 20.3, usually consists of three components, namely, acetabular cup—a hemispherical cup fitted in metallic back up fixed into the pelvis, femoral stem—fitted into the femur, and a femoral head, which articulates in the acetabular cup. The typical arrangement of different material combination used for THR is shown in Fig. 20.4.

Based on different combinations from the above mentioned materials, the prosthesis can be a metal-on-metal or ceramic-on-ceramic or metal-on-polyethylene or any other suitable combination.

The artificial hip prosthesis implanted in the patient is not once in a lifetime procedure, the chances of revised surgery vary depending on the lifestyle, activities, and other postoperative care of the patient. Various factors that enforce revision surgery are given in Fig. 20.5, which illustrates that the primary reasons for material related revision surgeries are aseptic loosening, implant breakage and wear of acetabular, which amount to 58 %. During hip surgery, the synovial membrane needs to be cut to access the joint and it is not known from the available literature that whether the synovial membrane functions correctly or not after surgery [13]. If it does not function properly it usually leads to direct mechanical contact of the articulating surfaces and causes asperity contacts, which generates heat and wear debris. Local bone resorption resulting from polyethylene wear debris is one of the primary causes for loosening of component in hip replacement surgery.

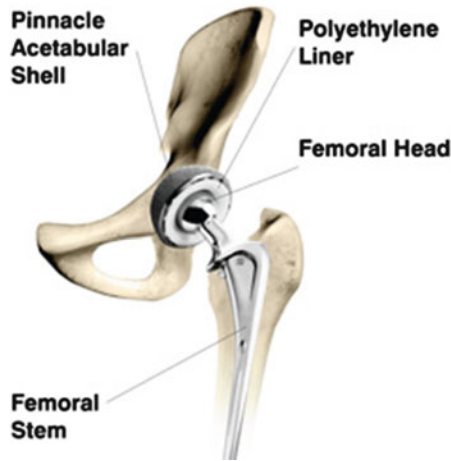


Fig. 20.3 Assembly of artificial hip prosthesis [11]

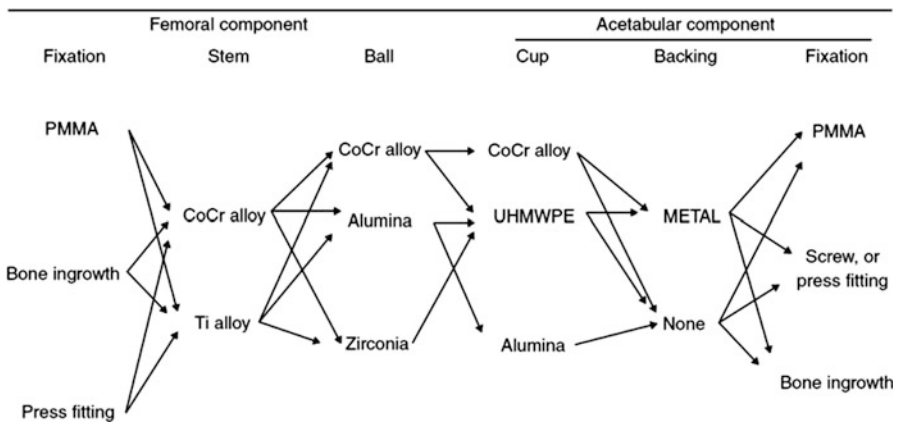


Fig. 20.4 Possible combinations of different materials used in total hip replacement [12]

1.4 Wear: Causes and Concerns

Concerns have risen about the biological influence and lifetime effects of the wear debris. Wear has been accepted as a major cause of osteolysis in total hip arthroplasty. Submicron particles migrate into the effective joint space and stimulate a foreign-body response resulting in bone loss [14]. In many patients, the bone around the implant becomes worn away leading to reduced joint function, which is caused by wear debris induced osteolysis in the implant [15]. In a normal metal-on-polymer bearing couple, wear debris is generated from the acetabular cup against

Diagnosis - revision hip replacement

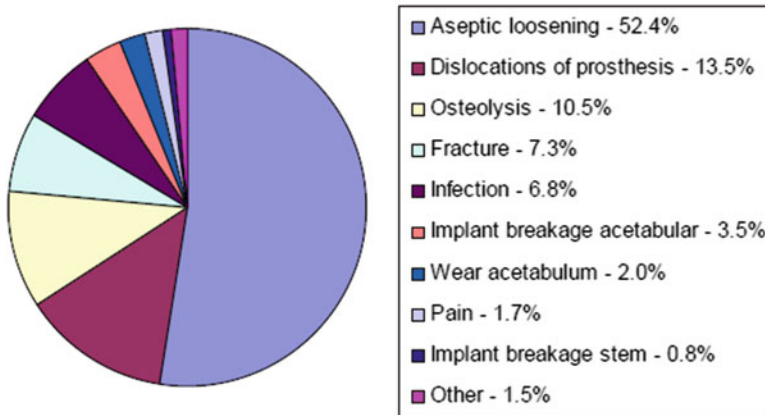


Fig. 20.5 Statistics of various factors leading to the revision of Hip surgery [5]

femoral head and it can cause serious damage to living tissues. Though ultra high molecular weight polyethylene (UHMWPE) is biologically inert material, presence of large amounts of biologically inactive particulate material can trigger an exceptionally strong macrophage response, which leads to the osteolysis around the implant in general and bone–implant interfaces in particular [16]. From the clinical studies, it is revealed that no apparent osteolytic response was observed in an articulation of total hip replacement [17]. It was also observed that metal-on-metal articulation appeared to be effective in order to reduce wear and loosening when compared with metal-on-polyethylene in a 4–7-year follow-up [18]. However, metal debris generated during usage can become ionized and can travel anywhere in the body. While there is no strong link between metal ions and health problems, patients with metal-on-metal implants have shown high metal levels in their blood and organs, and there is a lot of concern about systemic health effects [15]. As such there has been increased focus on the development of alternative materials or improvement of wear resistance of existing materials for the total joint replacements in order to avoid the necessity of costly revision surgery often necessitated by the osteolysis triggered by the wear debris.

1.5 Basic Wear Mechanisms in Total hip Replacements

From the literature, it was observed that there was a little chance of developing protective lubricant films in total joint replacements by hydrodynamic action. It became clear that wear would play a major role in determining the success or failure of any implant. Initially attention was focused upon friction, but basic studies on

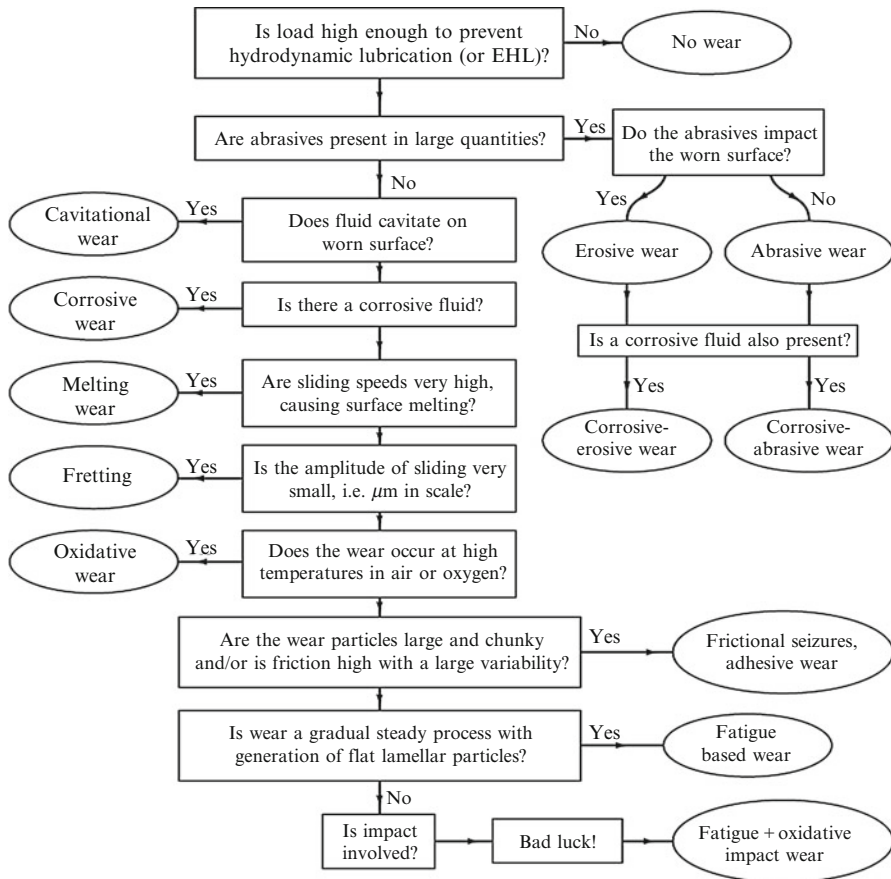


Fig. 20.6 Flowchart illustrating relation between operating conditions and types of wear [20]

wear of the implant in the laboratory and in vivo have enriched the knowledge about phenomenological and quantitative aspects of wear of implants [19]. Human joints are a typical example of elasto-hydrodynamic lubrication (EHL) in iso-viscous regime. A schematic flowchart shown in Fig. 20.6 gives an overall picture of different types possible wear mechanism in an EHL bearing couple [20].

There are three main processes involved in the wear of UHMWPE in total joints replacements: [21, 22]; abrasive wear associated with the scales of irregularities on the hard counter faces, adhesive wear associated with the surface features of the polymer, and fatigue wear with the overall geometrical conformity of the mating components.

Wear in orthopedic joints is expected to occur in four different modes. Mode 1 is an articulation between intended bearing surfaces (femoral head and the acetabular cup), Mode 2 is an articulation between a primary bearing surface and a surface that was never intended to be a bearing surface (the femoral head and the metal backing

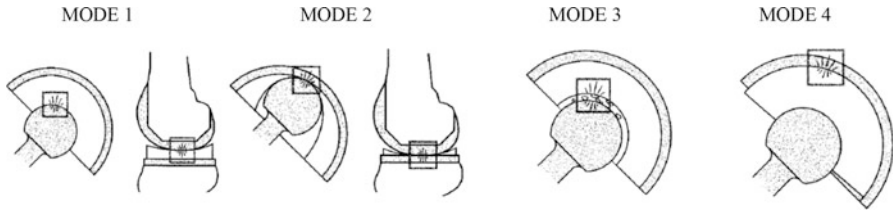


Fig. 20.7 Modes of wear in orthopedic joints [23]

of an acetabular cup (i.e., through a worn polyethylene acetabular liner), Mode 3 is an articulation between intentional bearing surfaces in the presence of third body components (femoral head and the acetabular cup in the presence of wear debris), and Mode 4 is an articulation between two nonbearing secondary surfaces (motion between the back of a polyethylene insert and the metallic tray). The four modes of wear are graphically shown in Fig. 20.7.

The need to solve or reduce wear problems in orthopedic joints is of primary importance. The purpose of research in Tribology is the minimization and elimination of losses resulting from friction and wear at all levels of technology where the rubbing of surfaces is involved [24], which leads to improved implant efficiency and better performance.

1.6 Estimation of Wear: “Tools and Techniques”

Clinical wear of implants is usually measured in two ways [19]:

1. Radiographic measurements of penetration of the femoral head into the acetabulum.
2. Measurement of dimensional changes in the retrieved prosthesis.

In the laboratory, wear of a pair of implant materials or complete prostheses is usually recorded by either:

1. Measurement of weight loss using a sensitive balance.
2. Monitoring dimensional changes of the polymeric components.

Table 20.1 briefly describes advantages and limitations of each technique suggested above.

Estimation of wear of a new material or after modifying an existing material is an essential stage before it can be tested under *in vitro* and *in vivo* condition. Several wear testing equipments are now available starting from basic wear test rigs like pin-on-disk, ball-on-disk, ball-on-plate, etc. There are another category of wear testing equipments, called simulators, which simulate the complex physiological loading patterns, anatomical position and *in vivo* environmental

Table 20.1 Relative merits of different methods of estimating wear [24]

Techniques	Advantages	Disadvantages
Weighing	Simple and accurate	Data corrupted by displaced or transferred materials
In situ measurement of change in length of worn surfaces	Accurate and allows continuous record of wear rates	No discrimination between wear of either specimens
Stylus profilometry	Very accurate; gives distribution of wear between specimens	Slow and mostly suitable for the end of the test; expensive equipment is required
Laser scanning profilometry	Very accurate and fast; gives distribution of wear between specimens	Expensive equipment is required
Optical profilometry	Simple and rapid	Method impossible when specimen has complex shape or its shape is distorted by wear or creep under load
Surface activation	In situ measurements of wear in closed machinery; possibility of simultaneous measurements of wear rates of various parts	Inaccurate and difficult to ensure safety of personnel
Ultrasonic interference	Sensitive to small changes in dimension	Specialized technique that requires expertise

conditions. Figure 20.8 shows the various wear test rigs and simulators that are commonly used to study the wear behavior of test materials.

It has been reported that pin-on-disk or pin-on-plate type of wear testers do not correlate with joint simulators that are based on multidirectional motion [27, 28]. Linear motion wear testers not only underestimate the wear rate by orders of magnitude compared with joint simulators and clinical results, but also produce incorrect wear rate rankings for linear and cross-linked UHMWPE [26]. Bragdon et al. [28] and Wang et al. [29] have emphasized that the motion of the wear tester or the joint simulator must be multidirectional in order to produce a wear rate that is comparable to average clinical wear rate with undamaged femoral heads.

1.7 Techniques for Reduction of Wear

Several techniques are being employed to enhance the wear resistance of the implant materials, such as irradiation cross-linking of UHMWPE, oxidation prevention and loss of material properties using vitamin E, UHMWPE composites with fillers, and surface modification by ion implantation techniques.

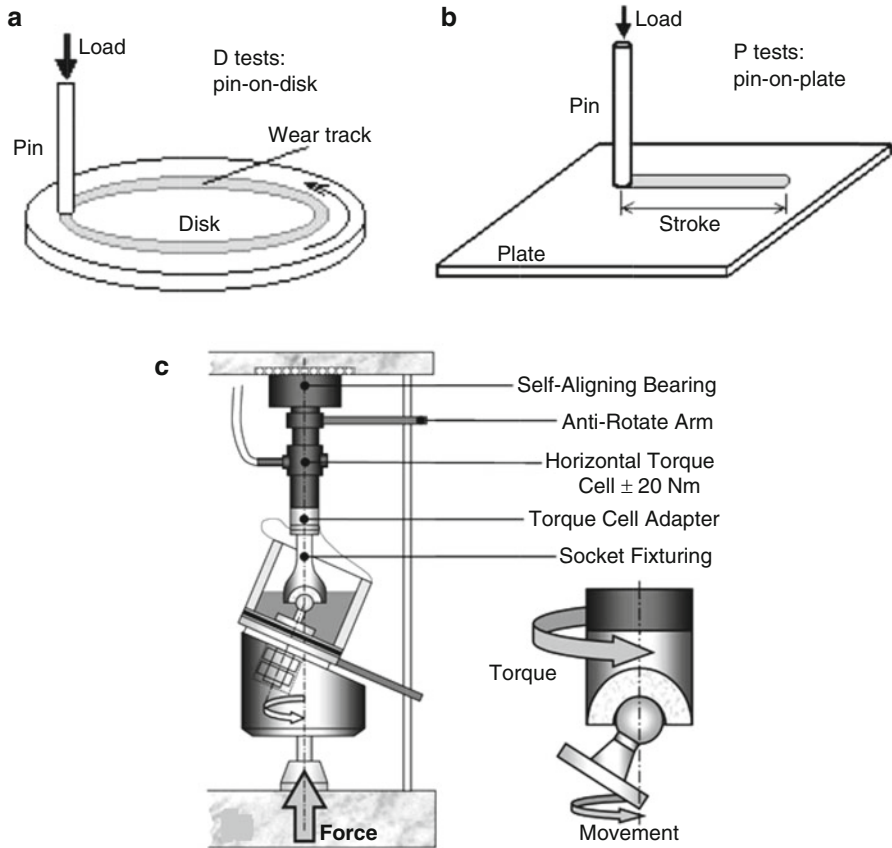


Fig. 20.8 Geometric configuration of a (a) rotating pin-on-disk [25] (b) reciprocating pin-on-plate [25] (c) typical hip simulator along with environmental chamber [26]

1.7.1 Radiation Cross-linking of UHMWPE

The molecular chain architecture of a polymer imparts many unique attributes, including crystallinity, toughness, wear resistance, etc. Over the years, a good amount of expertise has been invested in studying the wear phenomenon of UHMWPE and developing strategies for reducing the *in vivo* wear of virgin UHMWPE bearing components. However, it does not stand up to the high demands of “zero wear” and hence necessitating structural modification of UHMWPE in order to improve its characteristics. Cross-linking of the polymer chain is the first step in the direction. Researchers have attempted to improve wear resistance of UHMWPE for orthopedic applications by the introduction of a highly cross-linked UHMWPE by over 1,000 kGy of gamma irradiation in air. Since then much of the recent literature explicitly reported on the enhancement of wear resistance [30, 31]. Though irradiation is used to improve the wear resistance of UHMWPE, it

Table 20.2 Wear rate of cross-linked UHMWPE results from selected literature

Irradiation process and dosage	Wear		Type of wear tester	Reference
	Virgin	Irradiated		
Lupersol 130	23.3 mm ³ /year	1.1 mm ³ /year	Hip joint simulator	Shen et al. [31]
Gamma ; 75 kGy	51 mm ³ /year	5.62 mm ³ /year	Hip joint simulator	Essner [32]
Electron-beam; 50 kGy	0.375 mm ³ /250,000 cycles	0.225 mm ³ /250,000 cycles	Two axis simulator	Schwartz et al. [33]
Gamma; 10 Mrad	0.649 × 10 ⁻⁶ mm ³ /Nm	0.449 × 10 ⁻⁶ mm ³ /N-m	Multidirectional pin-on-disk	Burroughs et al. [34]
Gamma; 100 kGy	0.04 × 10 ⁻⁶ mm ³ /Nm	0.03 × 10 ⁻⁶ mm ³ /Nm	A six-station multidirectional tribometer	Kilgour [35]
Gamma 10 MRad	6.8 × 10 ⁻⁷ mm ³ /N-m	3.94 × 10 ⁻⁷ mm ³ /Nm	Six-station pin-on-plate	Lu Kang et al. [36]
Electron-beam; 72 kGy	14.2 mg/year	4.1 mg/year	Knee simulator	Stoller [37]

has deteriorating effects on other material properties such as decrease of chain mobility and chain stretch, which leads to decrease of mechanical properties of the polymer. As the radiation dose increases, there is a monotonic decrease in ductility and toughness of the polymer, both of them saturate beyond 100 kGy along with cross-link density [38]. Reduced ductility makes the implant brittle and more vulnerable for failure and reduced toughness generates more implant wear debris.

From Table 20.2, it is observed that cross-linking has tremendous effects on the wear resistance of the polyethylene ensuring the longevity of the implant. The optimum radiation dosage for increasing wear resistance is found to be in the range of 50–100 kGy. However, literature reports that mechanical properties of UHMWPE are degraded due to the oxidation of the polyethylene resulted from the cross-linking. The beneficial effect of radiation cross-linking in terms of increased wear resistance can be sufficiently extracted only if the problem of oxidation is counteracted.

1.7.2 Vitamin E Doped UHMWPE

The use of vitamin E as an antioxidative and biocompatible additive for normal and cross-linked UHMWPE has been suggested as an alternative method to improve wear resistance of polymer without altering its mechanical strength. This section briefly describes the rationale of using vitamin E as an additive for UHMWPE and its possible use in the orthopedic field.

The addition of vitamin E (0.3 wt.%) to normal or cross-linked UHMWPE is reported to prevent oxidation and delamination [39]. Oral et al. [40] studied the fatigue and wear resistance of vitamin E doped irradiated UHMWPE. They have reported that wear of test material at 100 kGy decreased by 20.26 % compared to that of 100-kGy irradiated/melted UHMWPE. However, the fatigue strength was improved by 58 %. Shibata et al. [41] performed bidirectional sliding fatigue tests for (1) γ -irradiated (25 kGy) UHMWPE, and (2) γ -irradiated (25 kGy) with 0.3 wt% vitamin E added UHMWPE specimens. It was reported that UHMWPE has shown severe fatigue fracture and wear rate compared to vitamin doped polyethylene. Oral et al. [42] reported that the hip simulator wear rate of irradiated vitamin E doped UHMWPE has decreased by fourfold to tenfold when compared with 100 kGy-irradiated and melted UHMWPE. The mechanical properties and fatigue resistance of vitamin E-doped and irradiated UHMWPE were significantly higher than that of 100 kGy-irradiated and melted UHMWPE.

Though manufacturers are now developing cross-linked UHMWPE inserts containing vitamin E, the method by which the antioxidant is introduced into the polymer is still a concern. It can be added either before the irradiation process [43], i.e., during melt processing state or by diffusion after irradiation process [44]; each having its own merits. However, the use of vitamin E does not completely suppress the oxidation during high-energy radiation but it only retards the oxidation process. Vitamin E diffused, radiation cross-linked UHMWPE was given food and drug administration (FDA) clearance for clinical use in total joint replacements [45]. Based on the preclinical studies for the period of 5 years, it shows promising improvement in the longevity of highly cross-linked UHMWPE implants due to improved fatigue strength while maintaining the wear and oxidation resistance of irradiated and melted UHMWPE.

1.7.3 UHMWPE Composites

Even though cross-linking has shown its influence on reduction of wear rate of UHMWPE, it causes the reduction of various mechanical properties. UHMWPE-doped with vitamin E has good wear resistance comparable to that of irradiation-cross-linked polymer. Further enhancement of the mechanical properties of UHMWPE can be achieved by reinforcing the polymer with different fillers.

Plumlee et al. [46] used Zirconium particles of 3 μm diameter and studied wear of composites on dual axis wear simulator for 250,000 cycles. They observed a reduced wear with the increased concentration of Zirconium, and it was found to be 66 % reduction of wear for 10 % Zr composite without sacrificing the impact toughness of material. Morley et al. [47] studied tribological characteristics of UHMWPE/Ag nanocomposites using a horizontal Tribometer under synovial fluid condition with different sliding velocities varying from 10 mm/s to 80 mm/s for 3 h. They reported negligible mass loss for both counterbodies and the composite disks. In addition, no detectable variation of either temperature or friction coefficient was observed over the range of sliding velocity. Ge et al. [48] used

5–30 wt.% of natural coral (NC) particles as a reinforcement for UHMWPE to increase the wear resistance. The wear of the said composites was studied using a hip simulator lubricated with bovine serum against CoCrMo femoral head. They reported a 70 % increase of wear resistance for 30 % natural coral composite as compared to virgin UHMWPE. Tong et al. [49] reinforced UHMWPE with wollastonite fibers having the aspect ratio of 10:1, 15:1 and 20:1. It was observed that the addition of wollastonite fibers up to 20 wt.% significantly improved the abrasive wear resistance of the composites. Guofang et al. [50] reported that the wear rate was much lower for the polymerization based UHMWPE/kaolin composites than the melt mixing one. Hashmi et al. [51] studied sliding wear of polypropylene (PP) and UHMWPE blends. The wear volume of PP reduced significantly by adding UHMWPE. At 0.28 m/s sliding speed, wear rate of PP was observed to be reduced by 98 % with the addition of 15 wt.% of UHMWPE. A very few works have been reported so far in the direction of multi-walled carbon nanotubes (MWCNT) and UHMWPE composites [52], and a lot more is still awaited to explore the full potentiality of carbon nanotubes (CNT) as a reinforcing material for UHMWPE.

1.7.4 Surface Modification of UHMWPE

Surface modification of UHMWPE is yet another technique reported in the literature, which is very promising to enhance the longevity of the acetabular cup. Literature has reported about improving the tribological behavior as well as surface mechanical properties of polymeric materials by ion implantation technique without changing the bulk properties [53].

Valenza et al. [54] modified the surface of UHMWPE by implanting H^+ , He^+ , Ar^+ , and Xe^+ ion by 300 keV energy beam. The irradiation was performed using an ion flux ranging between 10^{14} and 10^{17} ions/cm². The wear testing of pure and ion irradiated UHMWPE samples was performed in a pin-on-disk machine and observed that the surface wear resistance increased with irradiation dose. A reduction of about 76 % of wear was noticed after 72 h in a UHMWPE sample irradiated with 3×10^{15} Xe^+ ions/cm². Strbac et al. [55] modified high density polyethylene (HDPE) surface by Ag^+ ion with the energy of 60 keV at varying dosage level. It was observed from the surface topography by atomic force microscope (AFM) that the average surface roughness of implanted HDPE was decreased, which indicates the flattening of the surface. It led to the reduction of surface roughness and wear volume of the polymer. Laura et al. [56] studied the effect of swift heavy ion irradiation that uses N^{+2} ions, energy of 33 MeV and dosage of 1×10^{12} ions/cm² on UHMWPE. An improvement in wear performance was reported without detrimental effect on elastic modulus and yield stress, unlike modifications induced by γ or e-beam irradiation. Ge et al. [57] implanted UHMWPE disk with three nitrogen ion doses to study its wear behavior against ZrO_2 . The obtained results were 1.8–4.5 times reduced wear rate compared to that of untreated UHMWPE. They also reported that the hardness of N^+ implanted UHMWPE surface was found to be

55–155 % higher than that of untreated one. Grosso et al. [58] characterized the surface of UHMWPE implanted with swift heavy ions with 6.77 MeV helium and 12.5 MeV carbon beams where ion flux ranged from 10^{11} to 10^{13} and 2×10^{10} to 5×10^{13} ions/cm², respectively. It was observed that the wear resistance of ion implanted sample was increased by 85 % compared to that of an unirradiated polymer. The results observed from the above studies confirmed that an ion implantation of UHMWPE enhanced the wear resistance and longevity of the implants.

1.8 Conclusions and Future Scope

The complete replacement of joints has been a resounding medical success, improving the quality of lives of many patients. However, the nanoparticulate wear debris occurring in many implants is a cause of significant problems. UHMWPE has undergone much technological advancement in improving its physical, physiological and mechanical properties. However, potential areas discussed in this chapter are in their very nascent stages. It can be well explored to extract the best from UHMWPE in realizing the “zero wear effect” to improve the longevity of implants and quality of life of patients.

Acknowledgements The authors duly acknowledge the researchers and working scientists whose contributions are referred herein.

Check Your Understanding

1. Define the terms: Tribology and wear
2. Explain the necessity to study Tribology of human joints. Discuss some facts and figures supporting your arguments.
3. Elucidate how load, speed, temperature, hardness, surface finish, and the presence of foreign materials influence the wear of human joints.
4. What is a synovial joint?
5. Discuss the mechanism of load bearing joints.
6. What are the components in a hip prosthesis?
7. Discuss the primary causes leading to the revision of total hip replacement surgeries.
8. Briefly discuss the different material combinations used for the total hip replacement. Compare among them.
9. What are the primary wear mechanisms associated with elasto-hydrodynamic lubrication systems such as human joints?

10. How does the wear debris generated from the artificial joint materials influence the recipient? Explain clearly the concerns associated with metallic implants in relevance to this discussion.
11. What are the main processes involved in the wear of UHMWPE implants?
12. What are different types of wear modes associated with hip joints?
13. How is wear of the implant measured in hospitals and laboratories?
14. Briefly discuss the advantages and limitations associated with various techniques employed to estimate wear of the implants.
15. What are the specific advantages that UHMWPE possesses over its counterpart materials like ceramics and metals for THR applications?
16. What are the various types of wear testing equipments used to evaluate the candidacy of a newly developed material for joint replacements?
17. What are the specific advantages that hip simulators possess over the conventional wear testing equipment?
18. What are the techniques employed to reduce the wear rate of UHMWPE?
19. Explain the mechanism of enhancement of wear resistance of UHMWPE by irradiation process.
20. What is the significant effect of oxidation of UHMWPE due to irradiation? How it could be avoided?
21. What is the mechanism of prevention of oxidation in a medical grade UHMWPE?
22. What are the different methods followed to introduce antioxidant in polymers? Compare among them.
23. How does addition of vitamin E in UHMWPE help to reduce the oxidation problem caused due to irradiation process?
24. What are the primary parameters to be considered before any material considered for successful in vivo application?
25. What are the advantages of using composites for total hip replacement applications?
26. What is ion implantation technique?
27. What are the advantages of ion implantation technique in comparison with other techniques followed to improve the properties of implant materials?

References

1. Majumdar BC (1986) Introduction to tribology of bearings. A.H. Wheeler & Co, Allhabad
2. Huo MH, Cook SM (2001) What's new in hip arthroplasty. *J Bone Joint Surg Am* 83-A:1598–1610
3. Kurtz SM, Ong K, Lau E, Mowat F, Halpern M (2007) Projections of primary and revision hip and knee arthroplasty in the United States from 2005 to 2030. *J Bone Joint Surg Am* 89:780–785
4. Park J, Lakes RS (2007) Biomaterials-an introduction. Springer, New York, NY
5. Davidson D, Graves S, Batten J, Cumberland W, Harris J, Morgan (2003) National Joint Replacement Registry, Australian Orthopaedic Association

6. http://caretipsvilla.com/tips/exercises-for-loosening-the-hip-joint-hamstring-calf_muscles, referred on 27/11/11.
7. http://lifepositiveayurveda.com/joint_pain.html referred on 27/11/11.
8. http://advancedpt.patientsites.com/Injuries-Conditions/Ankle/Ankle_Anatomy_/a-47/article.html referred on 27/11/11.
9. Sokoloff L (1978) *The Joints and synovial fluid—Volume 1*. Academic Press inc, New York, NY
10. Dumbleton JH (1981) *Tribology of natural and artificial joints*, Tribology series-3. Elsevier, New York, NY
11. <http://www.hipreplacement.com/DePuy/technology/implants/basics>
12. Wong JY, Bronzino JD (2007) *Biomaterials*. CRC press, USA
13. Burger NDL, de Vaal PL, Meyer JP (2007) Failure analysis on retrieved ultra high molecular weight polyethylene (UHMWPE) acetabular cups. *Eng Fail Anal* 14:1329–1345
14. Zhu YH, Chiu KY, Tang WM (2001) Review article: polyethylene wear and osteolysis in total hip arthroplasty. *J Orthop Surg* 9:91–99
15. Amstutz H, Campbell P, Kossovsky N, Clarke I (1992) Mechanism and clinical significance of wear debris-induced osteolysis. *Clin Orthop Relat Res* 276:7–18
16. Peter DF, Campbell PA, Amstutz HC (1996) Metal versus polyethylene wear particles in total hip replacements: a review. *Clin Ortho Relat Res* 329:S206–S216
17. Sedel L, Nizard RS, Kerboul L, Witvoet J (1994) Alumina-alumina hip replacement in patients younger than 50 years old. *Clin Orthop* 298:175–83
18. Dorr LD, Wan Z, Longjohn DB, Dubios B, Murken R (2000) Total hip arthroplasty with use of the metasul metal-on-metal articulation. *J Bone Joint Surg* 82-A:789–798
19. Dowson D (1995) A comparative study of the performance of metallic and ceramic femoral head components in total replacement hip joints. *Wear* 190:171–183
20. Stachowiak GW, Batchelor AW (2001) *Engineering tribology*, 2nd edn. Butterworth-Heinemann, Boston, MA
21. Brown KJ, Atkinson JR, Dowson D, Wright V (1975) The wear of ultra-high molecular weight polyethylene with reference to its use in prostheses. *Plastics in Medicine and Surgery*, London, pp 2.1–2.8
22. Dowson D (1978) Tribological characteristics of polymers with particular reference to polyethylene, *Polymer Surfaces*, vol 19. Wiley, Chichester, pp 399–424
23. Wright TM, Goodman SB (2001) Implant wear in total joint replacement. *American Academy of Orthopaedic Surgeons*, USA, pp 3–12
24. Affatato S, Spinelli M, Zavalloni M, Mazzega-Fabbro C, Viceconti M (2008) Tribology and total hip joint replacement: current concepts in mechanical simulation. *Med Eng Phys* 30:1305–1317
25. Stachowiak GW, Batchelor AW, Stachowiak GB (2004) 'Experimental methods in tribology', in Dowson D, *Tribology series*, vol 44. Elsevier, Amsterdam
26. Maru MM, Tanak DK (2006) Influence of loading, contamination and additive on the wear of a metallic pair under rotating and reciprocating lubricated sliding. *J Braz Soc Mech Sci Eng* 28:3
27. Bowsher JG, Shelton JC (2001) A hip simulator study of the influence of patient activity level on the wear of crosslinked polyethylene under smooth and roughened femoral conditions. *Wear* 250:167–179
28. Bragdon CR, O'Connor DO, Lowenstein JD, Jasty M, Syniuta WD (1996) The importance of multidirectional motion on the wear of polyethylene. *Proc Inst Mech Eng J Eng Med* 210:157–165
29. Wang A, Sun DC, Yau S-S, Edwards B, Sokol M, Essner A, Polineni VK, Stark C, Dumbleton JH (1997) Orientation softening in the deformation and wear of ultra-high molecular weight polyethylene. *Wear* 203:204–230
30. Dorr LD, Wan Z, Shahrardar C, Sirianni L, Boutary M, Yun A (2005) Clinical performance of a Durasul highly cross-linked polyethylene acetabular liner for total hip arthroplasty. *J Bone Joint Surg Am* 87:1816–18621

31. Shen FW, McKellop HA, Salovey R (1996) Irradiation of chemically crosslinked ultrahigh molecular weight polyethylene. *J Polym Sci Part B: Polym Phys* 34:1063–1077
32. Essner A (2005) Hip simulator wear comparison of metal-on-metal, ceramic-on-ceramic and crosslinked UHMWPE bearings. *Wear* 259:992–995
33. Schwartz CJ, Bahadur S, Mallapragada SK (2007) Effect of crosslinking and Pt–Zr quasicrystal fillers on the mechanical properties and wear resistance of UHMWPE for use in artificial joints. *Wear* 263:1072–1080
34. Borrighs B, Blanchet TA (2006) The effect of pre-irradiation vacuum storage on the oxidation and wear of radiation sterilized UHMWPE. *Wear* 261:1277–1284
35. Kilgour A, Elfick A (2009) Influence of crosslinked polyethylene structure on wear of joint replacements. *Tribol Int* 42:1582–1594
36. Kang L, Galvin AL, Thomas D, Jina Z, Fisher J (2008) Quantification of the effect of cross-shear on the wear of conventional and highly cross-linked UHMWPE. *J Biomech* 41:340–346
37. Stoller AP, Johnson ST, Popoola OO, Humphrey MS, Blanchard RC (2011) Highly Crosslinked polyethylene in posterior-stabilized total knee arthroplasty. *J Arthroplasty* 26:483–491
38. McKellop H, Shen FW, Lu B, Campbell P, Salovey R (1999) Development of an extremely wear resistant ultra-high molecular weight polyethylene for total hip replacements. *J Orthop Res* 17(2):157–167
39. Wolf C, Lederer K, Muller U (2002) Tests of biocompatibility of alpha tocopherol with respect to the use as a stabilizer in ultrahigh molecular weight polyethylene for articulating surfaces in joint endoprostheses. *J Mater Sci Mater Med* 13:701–705
40. Oral E, Wannomae KK, Hawkins N, Harris WH, Muratoglu OK (2004) α -Tocopherol-doped irradiated UHMWPE for high fatigue resistance and low wear. *Biomaterials* 24:5515–5522
41. Shibata N, Tomita N (2005) The anti-oxidative properties of α -tocopherol in γ -irradiated UHMWPE with respect to fatigue and oxidation resistance. *Biomaterials* 26:5755–5762
42. Oral E, Christensen DS, Malhi AS, Wannomae KK, Muratoglu OK (2006) Wear resistance and mechanical properties of highly cross-linked, ultrahigh-molecular weight polyethylene doped with vitamin E. *J Arthroplasty* 21(4):580591
43. Burton G, Ingold K (1981) Autoxidation of biological molecules. 1. The antioxidant activity of vitamin E and related chain-breaking phenolic antioxidants in vitro. *J Am Chem Soc* 103:6472–6477
44. Wolf C, Maninger J, Lederer K, Frühwirth-Smounig H, Gamse T, Marr R (2006) Stabilisation of crosslinked ultrahigh molecular weight polyethylene (UHMWPE)- acetabular components with alpha-tocopherol. *J Mater Sci Mater Med* 17(12):1323–1331
45. Kurtz SM (2009) UHMWPE biomaterials hand book, 2nd edn. Academic press, London, pp 221–236
46. Plumlee K, Schwartz CJ (2009) Improved wear resistance of orthopaedic UHMWPE by reinforcement with zirconium particles. *Wear* 267:710–717
47. Morley KS, Webb PB, Tokareva NV, Krasnov AP, Popov VK, Zhang J, Roberts CJ, Howdle SM (2007) Synthesis and characterisation of advanced UHMWPE/silver nanocomposites for biomedical applications. *Eur Polym J* 43:307–314
48. Ge S, Wang S, Huang X (2009) Increasing the wear resistance of UHMWPE acetabular cups by adding natural biocompatible particles. *Wear* 267:770–776
49. Tong J, Ma Y, Ren L (2006) Free abrasive wear behavior of UHMWPE composites filled with wollastonite fibers. *Composites: Part A* 37:38–45
50. Guofang G, Huayong Y, Fu X (2004) Tribological properties of kaolin filled UHMWPE composites in unlubricated sliding. *Wear* 256:88–94
51. Hashmi SAR, Neogi S, Pandey A, Chand N (2001) Sliding wear of PP/UHMWPE blends: effect of blend composition. *Wear* 247:9–14
52. Rama Sreekanth PS, Naresh Kumar N, Kanagaraj S (2012) Effect of MWCNT on mechanical properties of γ -irradiated UHMWPE during shelf ageing process. *Adv Mat Res* 410:160–163

53. Chen J, Zhu F, Pan H, Cao J, Zhu D, Xu H, Cai Q, Shen J, He Z (2000) Surface modification of ion implanted ultra high molecular weight polyethylene. *Nucl Inst Methods Phys Res B* 16:26–30
54. Valenza A, Visco AM, Torrisi L, Campo N (2004) Characterization of ultra-high-molecular-weight polyethylene modified by ion implantation. *Polymer* 45:1707–1715
55. Strbac S, Nenadovic M, Rajakovic L, Rakocevic Z (2010) Chemical surface composition of the polyethylene implanted by Ag⁺ ions studied by phase imaging atomic force microscopy. *Appl Surf Sci* 256:3895–3899
56. Laura F, Cura J, del Grosso M, Bermúdez GG, Frontini P (2010) Effect of nitrogen ion irradiation on the nano-tribological and surface mechanical properties of ultra-high molecular weight polyethylene. *Surf Coat Technol* 204:3887–3894
57. Ge S, Wang Q, Zhang D, Zhu H, Xiong D, Huang C, Huang X (2003) Friction and wear behavior of nitrogen ion implanted UHMWPE against ZrO₂ ceramic. *Wear* 255:1069–1075
58. Grosso MF, Chappa VC, Bermúdez GG, Forlerer E, Behar M (2008) Surface characterization of ultra high molecular weight polyethylene modified by swift heavy ion beam bombardment. *Surf Coat Technol* 202:4227–4232

Part VI
Tribology in Manufacturing

Chapter 21

Tribology in Metal Cutting

Valentino Anok Melo Cristino, Pedro Alexandre Rodrigues Carvalho Rosa,
and Paulo António Firme Martins

Abstract This chapter revisits tribology tests in metal cutting in order to obtain new fundamental knowledge on friction and to understand which technical modifications and operating parameters need to be developed and implemented in order to obtain good estimates of the coefficient of friction. The methodology draws from the development of new equipment and testing procedures focused on the interaction between surrounding medium, surface roughness and freshly formed surfaces to the independent determination of the coefficient of friction.

The assessment of the coefficient of friction obtained from experimentation with two of the most commonly utilized simulative tribology tests in metal working (pin-on-disc and ring compression tests) against that determined in orthogonal metal cutting conditions allows concluding that the former, performed in dry friction conditions with adequate control of surface morphology and under a protective shield of Argon, is capable of modeling contact with friction in close agreement with real metal cutting.

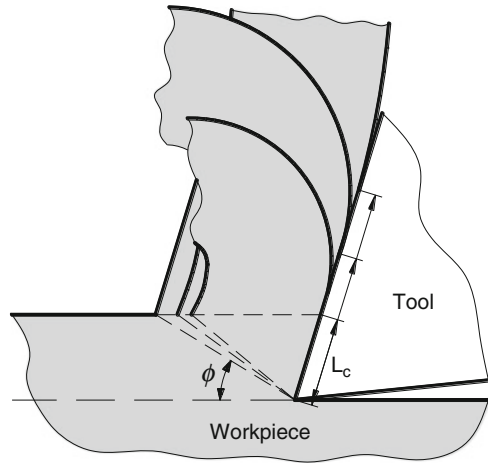
The identification of operative testing conditions that are capable of merging the estimates of the coefficient of friction provided by the different tribology tests ensures a unified view of tribologists and metal cutting experts on the accuracy, reliability, and validity of simulative tribology tests for metal cutting applications.

1 State of the Art

The knowledge of the mechanics of chip flow has been motivated by the study of metal cutting fundamentals, as reported in the state-of-the-art review paper by Jawahir and van Luttervelt [1]. The investigation started in the 50s when chip

V.A.M. Cristino (✉) • P.A.R.C. Rosa • P.A.F. Martins
Instituto Superior Técnico, University of Lisbon,
Av. Rovisco Pais, 1049-001 Lisbon, Portugal
e-mail: valentino.anok@ist.utl.pt; pedro.rosa@ist.utl.pt; pmartins@ist.utl.pt

Fig. 21.1 Influence of the frictional conditions on the contact length and chip curling. Chip curling increases and the contact length decreases when the coefficient of friction diminishes



curling was studied in connection with tool–chip contact length, restricted contact tools and clamped-on chip formers and, ever since then, there has been an enormous amount of research work in the area because the mechanics of chip flow is the basis for developing analytical and numerical models to predict cutting forces, chip curling, chip breaking, tool-wear, and surface integrity.

Friction is also found to significantly influence the mechanics of chip flow. In fact, by reducing the coefficient of friction, the shear plane angle ϕ increases, the chip thickness reduces and chip curling increases. Because the area of the shear plane decreases as well as the contact length and the applied pressure, the cutting force required for the process will decrease [2–10] (Fig. 21.1).

Despite the efforts performed by leading researchers over approximately 50 years, the explanation how chips are formed, what is the role played by friction and what causes chips to curl are not clearly understood. Some of the most significant contributions in the field were systematized in Jawahir and van Luttervelt [1] and van Luttervelt and coauthors [11] with the aim of saving fragmented and scattered experimental and theoretical knowledge in the mechanics of chip flow for further development.

In what concerns chip formation, the commonly accepted view considers (1) that new surfaces in metal cutting are formed by plastic flow around the tool edge, (2) that the energy required for cutting is overwhelmingly due to plasticity and friction, and (3) that any energy required for the formation of new surfaces is negligible. This view is referred as the “plasticity and friction only” approach and is inherent in the most significant contributions to the understanding of metal cutting fundamentals made by Zorev [12], Shaw [13], and Oxley [14], among others (Fig. 21.2).

The mechanics of metal cutting based on the “plasticity and friction only” approach considers the existence of three main zones; (1) the primary shear zone, (2) the secondary shear zone, and (3) the sliding zone along the clearance surface.

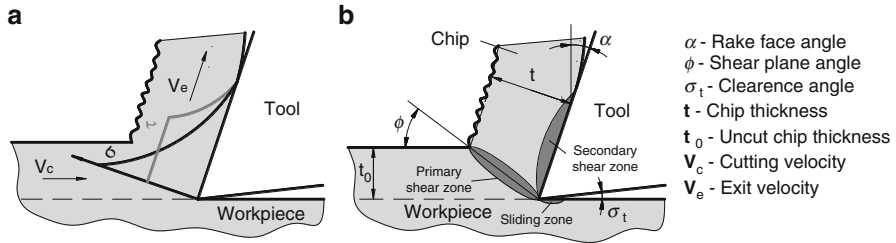


Fig. 21.2 Schematic representation of the mechanism of chip formation: (a) Distribution of normal and shear stresses proposed by Zorev [12]; (b) Representation of the three main zones of interest

The primary shear zone, shown in Fig. 21.2a, extends from the cutting edge to the surface of the workpiece, and is the zone where the material is plastically deformed under high values of the shear strains and stresses. The secondary shear zone occurs on the rake face of the cutting tool and results from plasticity and friction acting along the chip–tool contact interface. As originally developed by Zorev [12], the distribution of the normal and shear stresses on the rake surface gives rise to a region of seizure (or sticking) close to the cutting edge and to a region of sliding in the remaining contact interface (Fig. 21.2b).

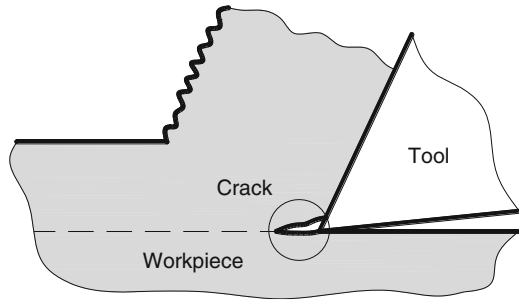
The sliding zone along the clearance surface is caused by friction, increases with the area of contact between the tool and the workpiece, and is mainly responsible for producing flank wear in the cutting tools.

A recent breakthrough in the mechanics of chip formation was made by Atkins [15, 16] by extending traditional analysis to include the work involved in the formation of new surfaces at the tip of the tool (Fig. 21.3). The combination of plasticity and friction with ductile fracture mechanics proved effective for obtaining good estimates of the cutting forces and to solve a longstanding incompatibility problem of the metal cutting theory concerning the specific cutting pressure and the state-of-stress resulting from the stress–strain/strain rate behavior of the materials [17].

In addition to what was mentioned previously, there is a common believe among researchers and practitioners that active gases (such as Oxygen) acting on the freshly cut surfaces may influence friction, chip compression factor, chip curling and forces to a level that goes significantly beyond what has been said and written in the commonly accepted fundamentals of metal cutting. Despite early experiments conducted by Poletica (Astakhov [18]) on copper and Armco iron indicated that the surrounding medium does not show any influence, there is a necessity of revisiting the subject by identifying and quantifying the type of contaminants films as a function of the surrounding medium and the average surface roughness of the cutting tool.

In what concerns chip curling, several models have been emphasized but they are not widely applicable. Therefore, contrary to chip formation there has never been a commonly accepted view to explain what causes chips to curl. In general

Fig. 21.3 Schematic representation of the crack formation at the tip of the cutting tool



terms, results available in the literature estimate the radius of curvature to decrease with increasing uncut chip thickness, with decreasing cutting velocity and decreasing friction and contact length at the rake face of the tool [1]. Some of these dependencies have been properly modeled by means of finite elements and artificial intelligence [11]. However, investigations by other authors also claim the distribution of stresses in the primary and secondary shear zones, thermal effects and work-hardening characteristics of the workpiece material to influence chip curl [19] and side-curl to be produced when machining dry and inhibited when using a lubricant [20].

Despite its technical and economic importance, friction remains one of the least understood phenomena in metal cutting because of poor characterization of the key influential parameters, low predictive capability of the existing theoretical models, and difficulties in undertaking an independent evaluation that ensures agreement between the reported values of the coefficient of friction obtained with different experimental techniques.

This underlies the reason for the well-known mismatches between theory and experimentation in metal cutting and also explains the reason why several authors suggest friction to be utilized as a function allowing the adjustment of the numerical estimates in order to fit the experimental results [21, 22]. In line with this modeling practice, Astakhov [23] noticed that results from finite element simulation of metal cutting reported in literature always seem to be in good agreement with experimentation regardless of the particular value of the coefficient of friction that had been utilized in the simulation. Astakhov also noticed that although the experimental values of the coefficient of friction are commonly reported in the range $\mu > 0.577$ (the limiting value to suit the sliding condition in metal forming), the values used in finite element modeling were in most of the cases considerably below 0.577.

The discrepancies between theory and experimentation have been comprehensively analyzed by Bil and coauthors [24] who compared the estimates provided by commercial finite element computer programs with experimental data and concluded that although individual parameters (such as the cutting force, the thrust force and the shear plane angle) may be made to match experimental results, none of the numerical simulation models was able to achieve a satisfactory correlation with all the measured process parameters all of the time. Differences between

numerical predictions and experimental results were attributed to friction, among other reasons.

More recently, Özel [25] investigated friction characterization at the tool–chip contact interface and concluded that finite element predictions of metal cutting based on the measured normal and frictional stresses on the tool rake face were more accurate than those based on alternative models and characterization procedures.

It is apparent from the above state-of-the-art review that frictional conditions in metal cutting should be reexamined with the objective of selecting the most adequate tribology tests and identifying the most significant dependences and interactions between process variables, surrounding medium and surface morphology of the cutting tool. This is because friction is not directly measurable, nor is it really an independent parameter as it depends on the contact pressure, area expansion, relative sliding velocity, and interface temperature, among other factors [26].

2 Tribology Tests

A great number of tribology tests have been suggested in the literature for modeling the frictional conditions in metal working processes [27]. They can be broadly grouped into two different types: process tribology tests and simulative tribology tests [28]. Process tribology tests apply typical metal cutting operations without changing the basic process kinematics while simulative tribology tests make use of cheap but effective laboratory equipment and procedures to evaluate friction without losing relevance to real metal cutting applications.

2.1 Process Tribology Tests

The most widespread process tribology tests in metal cutting simplifies the three-dimensional (oblique) geometry, which typifies most industrial processes, to a two dimensional (orthogonal) geometry, where the cutting motion is perpendicular to the cutting edge (refer to Fig. 21.4).

Orthogonal metal cutting conditions can be obtained by: (1) end cutting a tube wall by turning (Fig. 21.5a) or (2) machining a parallelepiped specimen as shown in Fig. 21.5b.

When process tribology tests based on orthogonal metal cutting are carried out with a rake angle of the cutting tool equal to 0° , the coefficient of friction results directly from the ratio $\mu = F_t/F_c$ between the experimental values of the cutting F_c and the thrust F_t forces. However, when tests are performed with rake angles different from 0° , it is necessary to relate the cutting F_c and thrust forces F_t with

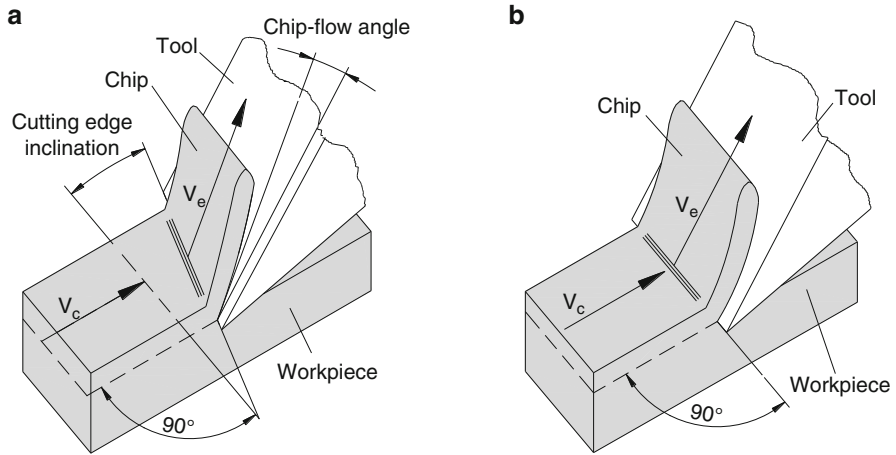


Fig. 21.4 Schematic representation of: (a) Oblique metal cutting and (b) Orthogonal metal cutting

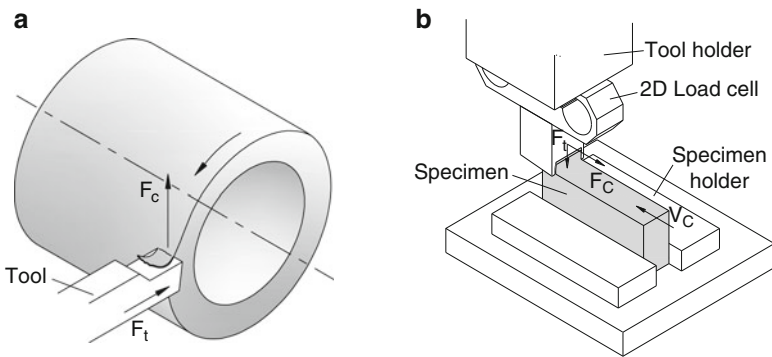


Fig. 21.5 Commonly utilized apparatuses for the orthogonal cutting test: (a) Turning a tube with large diameter; (b) Machining a parallelepiped specimen

the normal F_n and tangential F_t forces applied on the cutting tool. This is done by the following analytical relationships (Fig. 21.6):

$$\begin{aligned}
 F_f &= F_c \sin \alpha + F_t \cos \alpha \\
 F_n &= F_c \cos \alpha - F_t \sin \alpha \\
 \mu &= \frac{F_f}{F_n} = \frac{F_t + F_c \tan \alpha}{F_c - F_t \tan \alpha}
 \end{aligned}
 \tag{21.1}$$

where α is the rake face angle and β , commonly named as the friction angle, is the angle between normal force F_n and the resultant force F_r .

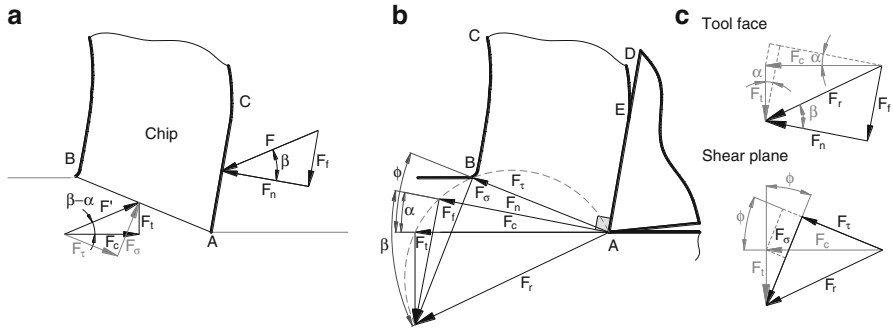


Fig. 21.6 Applied forces in orthogonal metal cutting: (a) Free body diagram of the chip; (b) Circle of composite cutting forces; (c) Diagrams of the acting forces in the shear plane and on the tool face

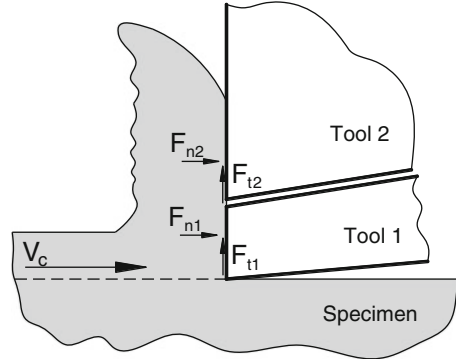
In an effort to better understand the frictional conditions along the rake surface of the cutting tool researchers like Usui and Takeyama [29] and Chandrasekaran and Kapoor [30] utilized photoelasticity to evaluate the distribution of stresses and assess the model that had been previously proposed by Zorev [12] (Fig. 21.2b). They observed that the normal stress is found to decrease exponentially from a maximum value at the tool edge to zero at the point where the chip separates from the rake face, whereas the frictional shear stress remains constant for a distance, from the tool edge and subsequently decreases rapidly.

Different results were obtained by Ahmad and coauthors [31], where the normal stress presents a similar trend to the distribution proposed by Zorev, the frictional stress does not exhibit a constant value near the tool edge and, instead, presents a trend similar to that of the normal stress.

Another approach in the investigation of the stress distribution makes use of the split tool technique [32–34], where the tool rake face is divided into two parts (Fig. 21.7). During the experiments, the forces acting only on the part labeled as “Tool 1” were measured and the length of the part labeled as “Tool 2” was incrementally increased from the smallest possible value up to L_c (refer to Fig. 21.1). Kato and coauthors [32] showed that when cutting aluminum, copper, lead and steel both the frictional and normal stresses remain constant near the tool edge and then fall off towards the tool–chip separation point. In the case of zinc as a work material, it was observed that the frictional and normal stresses decrease monotonically from the tool edge. Experimental evidences show that there is not a universal solution for the stress distribution on the tool, depending on the investigated material and technique.

Although the general accuracy and reliability of the coefficient of friction determined in process tribology tests based on metal cutting conditions is high, there are several reasons for considering the approach as inadequate. In fact, these tests require the availability of machine tools (preferentially not enrolled in production), are greatly influenced by operating variables (which may be difficult to

Fig. 21.7 Schematic representation of the split tool technique utilized for analyzing the distribution of stresses on the tool rake face



control), fail to provide quantitative local information about the coefficient of friction [23] and sometimes require complex experimental apparatuses. Moreover, process tribology tests based on metal cutting experiments cannot be classified either as independent calibration techniques or laboratory tests for the determination of the coefficient of friction. This is the reason why researchers have long been seeking for alternative procedures based on simulative tribology tests.

2.2 Simulative Tribology Tests

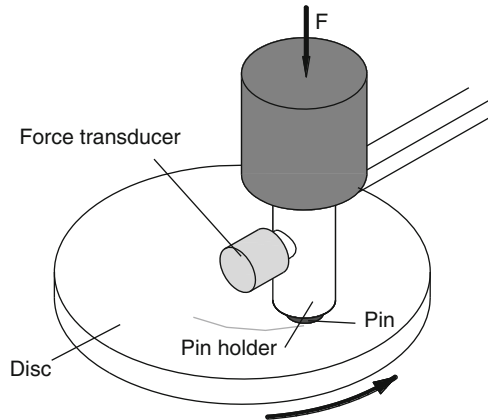
2.2.1 Pin-on-Disc

One of the most commonly utilized simulative tests for evaluating friction in local plastic or elastic deformation is the pin-on-disc. The pin-on-disc simulative test consists essentially of a pin in contact with a rotating disc and the coefficient of friction is determined by measuring the tangential and normal forces acting on the pin with a dynamometer (Fig. 21.8). In case of analyzing friction characteristics of sliding contacts in metal cutting, the pin is made of the work material to be machined and the disc is made of the material and coating of the cutting tool, or vice-versa.

The utilization of pin-on-disc test to evaluate friction in metal cutting has always been controversial because several authors argue that pin-on-disc testing is not adequate for analyzing friction in metal cutting because it is not capable of reproducing the contact pressure, temperature, and material flow conditions that are commonly found in real metal cutting applications [35]. In case of material flow it is also claimed that chip flows on the rake face and never comes back again, whereas the pin always rubs the disc on the same track during pin-on-disc testing.

As a result of this, several alternatives to pin-on-disc have been proposed by Olsson and coworkers [36], Hedenquist and Olsson [37], and Zemzemi and coworkers [38], among others. However, although the alternative tests are successful in reproducing real metal cutting conditions, they are more expensive, more

Fig. 21.8 Schematic representation of the pin-on-disc simulative tribology test



time consuming and demand a more accurate control of the operating parameters than conventional pin-on-disc tests. It is further worth noticing that very often pin-on-disc tribometers work under exaggerating contact pressures and sliding velocities with the aim of deliberately increasing or accelerating the wear rate of a test in order to speed up the overall evaluation. This is not necessary for evaluating the coefficient of friction and the test can be performed in a single turn of the rotating disc in order to avoid pin rubbing on the same track.

Taking into account what has been said in the previous paragraphs it can be concluded that pin-on-disc needs revisiting in order to identify which technical modifications may be included and which operating parameters need to be carefully controlled in order to successfully employ this easy, quick, and cheap simulative test (available in the vast majority of manufacturing laboratories worldwide) for the independent determination of the coefficient of friction in metal cutting applications.

2.2.2 Ring Compression Test

The ring compression test is a very widespread experimental technique for evaluating friction in metal forming [39]. The test method was developed to provide a measurement of the interface friction between a flat ring specimen and two parallel compression platens. The evaluation of the coefficient of friction is performed by measuring the change in the specimen's internal diameter with the reduction in height during compression.

Over the years, the ring compression test has gained wide acceptance as a reliable tribology test, particularly for bulk metal forming applications such as forging. The test consists of plastically compressing a ring specimen between two flat parallel platens. As its height is reduced, the ring expands radially outward and the change in dimensions depends on the amount of compression in the thickness direction and on the frictional conditions at the contact interfaces between ring

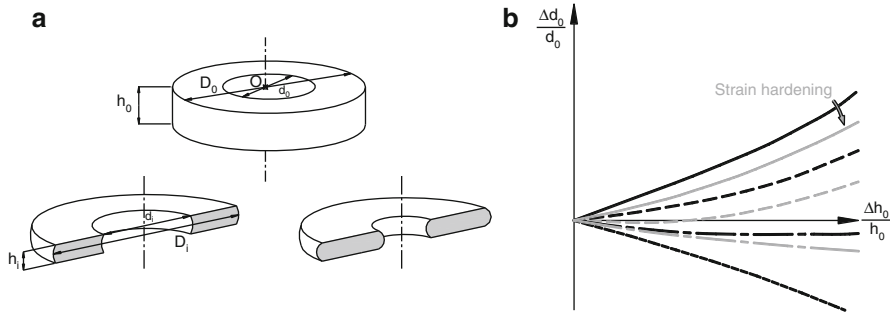


Fig. 21.9 Fundamentals of the ring compression test: (a) Basic kinematics showing that if friction is small, both the inner and outer diameters increase as the specimen is compressed, whereas if friction is high the inner diameter decreases; (b) Schematic plot of the friction calibration curves

and platens. If friction is small, both the inner and the outer diameter expand but, because friction resists expansion, the inner diameter expands less as friction increases and becomes actually smaller than the original diameter at higher values of friction (Fig. 21.9a).

The evaluation of the coefficient of friction is performed by measuring the change in the specimen's inner diameter with the reduction in height and making use of friction calibration curves generated by theoretical or numerical procedures (Fig. 21.9b).

Nowadays, most researchers consider the ring compression test as textbook knowledge due to three main periods of development that extended over the past five decades. The first period (1954–1970) draws from the pioneer experimental studies by Kunogi [40] and Male and Cockcroft [39] to the early mathematical modeling by Kudo [41, 42], Hawkyard and Johnson [43], and Avitzur [44]. In this period most attention was given to the development of theoretical models based on the slab and upper bound methods for predicting the position of the neutral surface which divides the regions of radial inward and outward material flow and for generating the friction calibration curves. Some of the investigations performed in this period already pointed out the dependence of friction calibration curves on the amount of strain hardening, temperature, morphology, and oxide films covering the contacting surfaces, but only after the advent of modern computers and finite elements it was possible to fully understand and analyze some of these dependencies.

The second period (1970–1990) was greatly influenced by the development and application of the finite element method (FEM). The utilization of finite elements stimulated many researchers to properly evaluate the influence of strain hardening, strain rate, temperature, and lubrication in friction and to successfully narrowing down the discrepancy between theory and experimentation. Each ring specimen made from a specific material and tested under controlled conditions of strain rate and temperature could now have its own specific set of friction calibration curves instead of resorting to curves built upon slab and upper bound methods with

rigid-perfectly plastic material assumptions. Some of the most significant contributions to knowledge in this period are systematized in the state-of-the-art review paper by Rao and Sivaram [45].

The third period (1990–until now) has been mainly driven by research objectives that were not properly taken into consideration during the two earlier periods. For example, the development of new complementary geometries of the ring compression test so as to allow for characterization of friction under low and high normal pressure conditions [46] and the enhancement of friction mechanics by taking into consideration the influence of surface topography and roughness [47–49].

The utilization of the ring compression test for the evaluation of friction in metal cutting is considered not an option within metal cutting researchers because it is claimed that generation of new contacting surfaces during upsetting, results from plastic material flow throughout the entire work material while in metal cutting formation of new contacting surfaces and plastic deformation is limited to the tip of the tool and adjacent regions of the shear plane. Moreover, it is also argued that plastic deformation in metal cutting is always combined with sliding of the new surfaces along the rake and relief faces of the cutting tools. However, there are two research works that justify further investigation on the validity, accuracy, and reliability of the ring compression test for calibration of the coefficient of friction in metal cutting. The first work was performed by Male in 1966 [50], reporting that friction, in ring compression testing, varies whenever a layer of contaminants is present on the surface of freshly prepared specimens. The second work was published by Rosa in 2007 [51] and shows that the coefficient of friction provided by means of the ring compression tests can be utilized as input data in finite element analysis of orthogonal metal cutting.

2.2.3 Other Tests

Although friction is a major issue in metal cutting, the available experimental tests for the calibration of the coefficient of friction are limited and most of the times focused on the phenomena generated by friction such as heat generation and wear, among others. Komanduri and Hou [52] present an overview of the experimental techniques utilized for this purpose, which include: (1) the chip–tool thermocouple, (2) infrared photography; (3) infrared optical pyrometers, (4) materials of known melting temperatures, either in the powder form or, as a thin film, (5) thermal paints, and (6) change in microstructure with temperature in the case of high-speed steel tools. Each technique presents its own advantages and disadvantages, and its selection depends on the situation under consideration, such as the accessibility, dynamics of the situation, accuracy, and cost of instrumentation. Despite the progress that has been made in temperature measurement, it is difficult to accurately measure localized temperatures during the cutting process, and this has led many investigators to rely on analytical and numerical methods for the determination of the contact temperature.

The following sections present a comprehensive investigation that reexamines process and simulative tribology tests in order to understand the above mentioned friction mechanisms in metal cutting. The utilization of the simulative tribology tests based on pin-on-disc and ring upset compression for the evaluation of friction in metal cutting has been subject of controversy in the metal cutting community for many years. Some researchers claim that these tests are not adequate for evaluating the coefficient of friction in metal cutting because they are not capable of reproducing the contact pressure, temperature, and material flow conditions that are found in real metal cutting applications. However, this discussion also points out the necessity of analyzing and identifying the operative testing conditions that ensure the accuracy, reliability, and validity of simulative tribology tests for metal cutting applications.

3 New Developments in Equipment and Methods

The present section focuses on laboratory testing equipment and procedures that aim at providing a new level of understanding for the tribological conditions at the tool–chip contact interface that arise from the interaction between cutting medium, surface roughness and freshly cut metal surfaces. The section starts by describing the orthogonal metal cutting testing apparatus that was specifically designed and fabricated for assessing the coefficient of friction in laboratory process conditions close to real metal cutting and follows with the presentation of the testing apparatuses that were developed to carry out the simulative tribology tests based on pin-on-disc and ring compression. The last part of this section presents the experimental work plan.

3.1 Orthogonal Cutting Test

The orthogonal cutting experimental setup (Fig. 21.10) was installed in a *Deckel-Maho DMC 63V* machining center and is essentially composed by a cutting tool, a cutting specimen, a three-dimensional piezoelectric dynamometer and a Grinding and Polishing Unit (GPU).

The cutting specimen is fixed directly on the three-dimensional piezoelectric dynamometer and the experiments were performed in orthogonal conditions that is, the cutting edge of the tool was straight and perpendicular to the direction of motion (refer to Fig. 21.13b). The three-dimensional piezoelectric dynamometer (*Kistler 9257B*) is attached to a signal amplifier (*Kistler 5011B*) and allows measuring the cutting forces during testing. The system is linear across its entire range, measures forces with an accuracy of 1 % and its resolution allows measuring almost any dynamic changes in the forces of great amplitude. A personal computer data logging system based on a multifunction data acquisition card (*National*

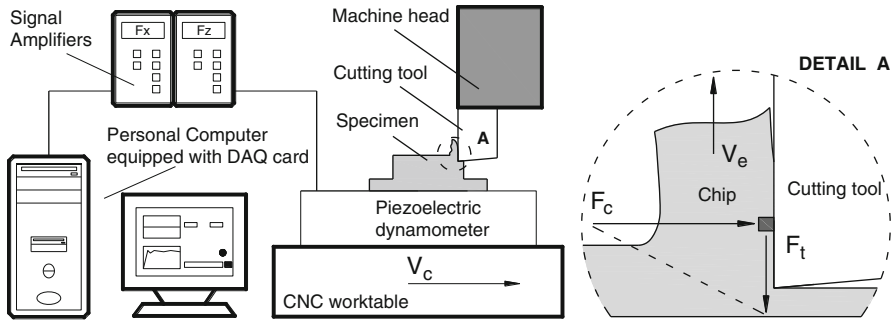


Fig. 21.10 Schematic representation of the orthogonal cutting test

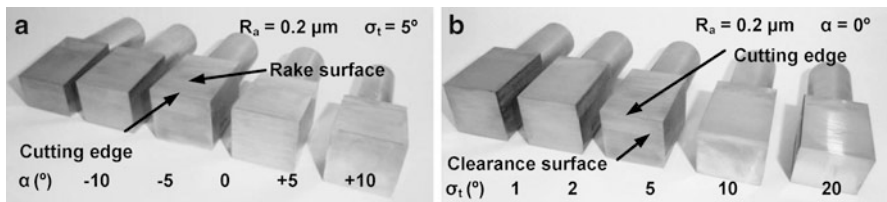


Fig. 21.11 Cutting tools utilized to analyze the influence of tool geometry on friction: (a) Tools with different rake angles; (b) Tools with different clearance angles under similar surface roughness

Instruments PCI-6025E) combined with a special purpose LabVIEW software controls testing, and acquires and stores the experimental data.

The cutting tools were manufactured from the same material as the other simulative tribology tests and are composed by two sets. The first set of tools has the objective of analyzing the influence of the tool geometry on friction under the same surface texture (Fig. 21.11). Tools belonging to this set have a fixed clearance angle σ_t of 5° and the rake face angle α ranges from -10° to $+10^\circ$ (Fig. 21.11a). The second set of tools has a fixed rake angle α of 0° and the clearance angles σ_t varies from 1° to 20° (Fig. 21.11b).

The GPU is schematically shown in Fig. 21.12a and is a custom-built piece of equipment that serves the purpose of producing and regenerating the desired texture and roughness in the surface of the cutting tools after completion of each test. The GPU consists of two separated blocks, each one for a respective tool's surface, with a well-defined geometry (rake and clearance angle) guarantying not only the reconditioning of the cutting tool, but also the cutting edge sharpness. As seen in Fig. 21.12a, the movement of the cutting tool during self-grinding and polishing operations is accomplished by the CNC machining center together with the utilization of sand paper and polishing clothes.

It is worth to notice that the GPU is designed to ensure the directionality of the predominant surface pattern to closely match those of the discs and platens of the

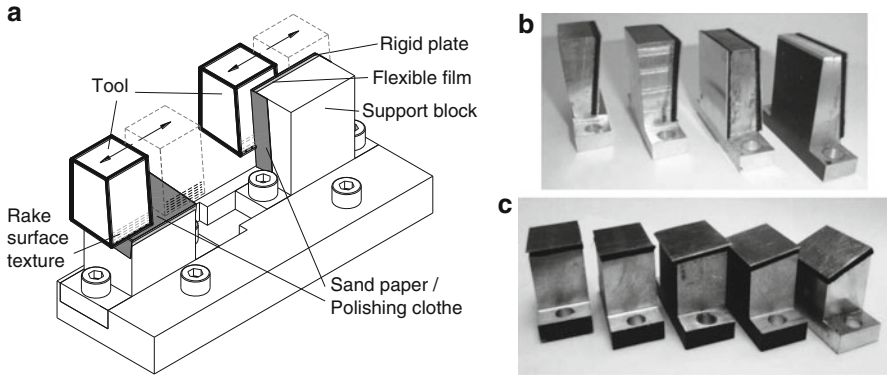


Fig. 21.12 (a) Schematic representation of the Grinding and Polishing Unit (GPU) and photographs of the support blocks for reconditioning the (b) rake and (c) clearance surfaces

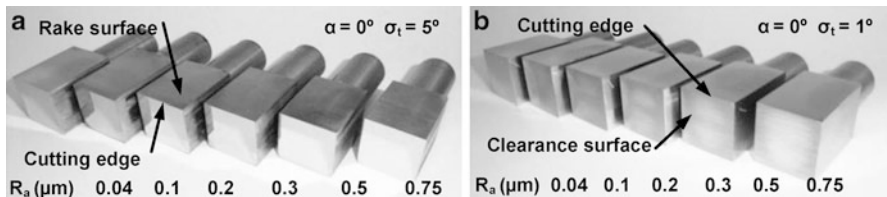


Fig. 21.13 Cutting tools utilized to analyze the influence of surface roughness on friction: (a) Tools with $\alpha = 0^\circ$ and $\sigma_t = 5^\circ$; (b) Tools with $\alpha = 0^\circ$ and $\sigma_t = 1^\circ$

simulative tribology tests because patterns aligned in different directions will inevitably influence the coefficient of friction [53–55].

A second assortment of cutting tools was manufactured for analyzing the influence of surface texture under the same geometry (Fig. 21.13). The first group of these tools is expected to evaluate the influence of the rake surface texture. The tools have a rake face angle $\alpha = 0^\circ$ and a clearance angle $\sigma_t = 5^\circ$ for minimizing the contact with the clearance surface (where the surface is the smoothest possible, with an arithmetical mean roughness R_a of $0.04 \mu\text{m}$). The second group aims at evaluating the influence the clearance surface texture. The tools have a rake face angle $\alpha = 0^\circ$ and a clearance angle $\sigma_t = 1^\circ$, for maximizing the contact on the clearance surface, and a very good surface finish of the rake surface ($R_a = 0.04 \mu\text{m}$).

As mentioned previously, surface texture and geometry of the cutting tools were carefully controlled. The same applies to the radius of the cutting edge, which in turns greatly affects the minimum value of the uncut chip thickness. In other words, a higher cutting edge radius can only remove layers of higher thicknesses. The manufactured cutting tools present a value of cutting edge radius below $2 \mu\text{m}$ depending on the geometry of the tools (Fig. 21.14).

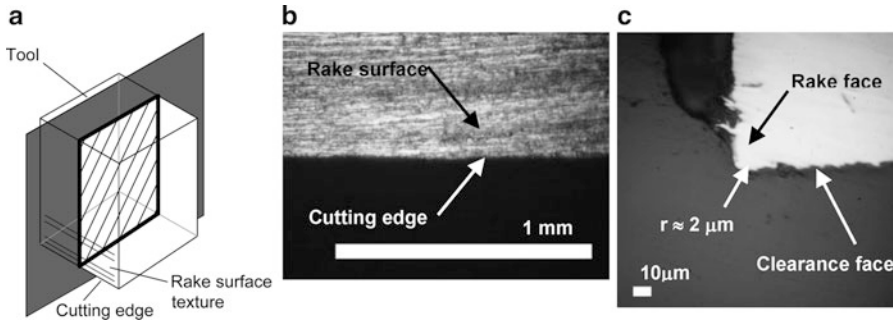


Fig. 21.14 Control of the cutting edge radius: (a) Schematic representation of the cross section of a tool; (b) Microscopic photograph of the rake surface next to the cutting edge; (c) Detail of the tip of the tool showing the radius of the cutting edge

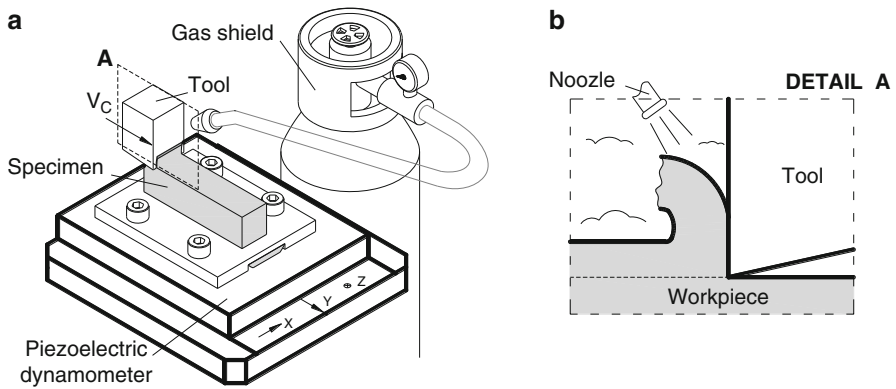


Fig. 21.15 Orthogonal cutting test performed under gas shields: (a) Schematic representation of the apparatus; (b) Detail of the cutting region

The influence of the surrounding medium was analyzed by cutting in the presence of air and by shielding the cutting region by means of active and inert gases. The gases were supplied from an external source and applied through a nozzle on to the cutting region, at a low pressure, in order to avoid turbulent flow (Fig. 21.15).

3.2 Pin-on-Disc Test

Figure 21.16 presents the pin-on-disc simulative test apparatus that was developed and fabricated by the authors [56]. The main components of the equipment can be divided into four different groups: (1) Basic structural parts; (2) Specific electrical

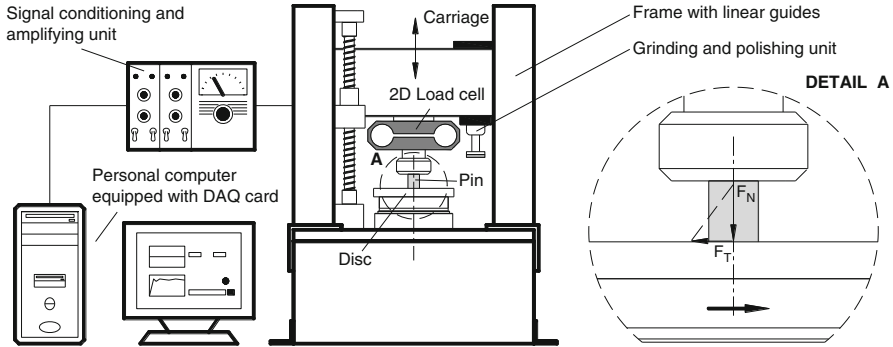


Fig. 21.16 Schematic representation of the pin-on-disc simulative tests

and mechanical parts; (3) Control and measurement appliances; (4) Grinding and polishing unit (GPU).

The basic structural parts provide support to electrical and mechanical components, to control and measurement appliances as well as to the GPU. They are independent of the type of testing (e.g., wear or friction), operation conditions and materials, coatings and lubricants to be analyzed. Specific electrical and mechanical parts comprise the electrical motor, the disc holder, the pin holder, the position and guiding systems, the pins and the discs. The electrical motor is equipped with a frequency inverter for a precise control of the rotational velocity of the disc. The disc holder is mounted to the rotating shaft of the electrical motor by means of a tapered roller bearing that takes radial and axial combined loadings resulting from the interaction between the pin and the disc. Since the pin-on-disc tests that were performed in this investigation were specially designed for testing friction in metal cutting it follows that the pin is simulating the workpiece material, whereas the disc is replicating the rake face of the cutting tool. The design of the pin holder deviates from traditional architecture of commercial pin-on-disc tribometers in order to increase stiffness and reduce the deformation caused by weight and applied loads. The new design also eliminates the need for a counterweight.

A precision ball screw driven by a motor and coupled with a linear guiding system is utilized for controlling the position of the pin holder. The utilization of linear guides reduces the axial gaps of the screw, improves the parallelism of the overall positioning system and allows the applied loads to reach maximum values up to 10 kN. Pins and discs are dependent on the type of testing, operation conditions, and materials, coatings, and lubricants to be analyzed.

The control and measurement appliances include a two-dimensional load cell, a multifunction data acquisition system and a personal computer. The load cell was specially manufactured for this work and is fixed to the pin holder and connected to a signal amplifier unit (*Vishay 2100*). A personal computer data logging system based on a data acquisition (DAQ) card (*National Instruments PCI-6025E*) combined with a special purpose *LabVIEW* software controls testing, and acquires and stores the experimental values of the normal and tangential forces.

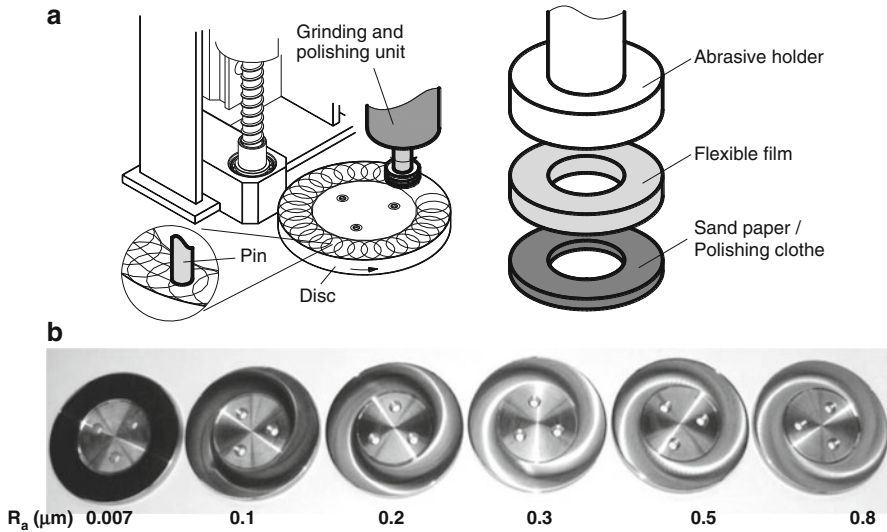


Fig. 21.17 (a) Schematic representation of the Grinding and Polishing Unit (GPU) utilized in the pin-on-disc simulative tests. (b) Photograph showing stainless steel discs prepared with different values of average surface roughness (R_a)

It is worth noticing that its design allows two different methods of applying loads in the pin; (1) the standard procedure of loading calibrated weights on a slot and (2) an innovative procedure that makes use of the precision ball screw (driven by a motor) for controlling both position and load applied on the pin. This new procedure of applying loads is different from what is commonly found in commercial pin-on-disc machines and allows simulative tests to be carried out under variable loading conditions.

The GPU is a custom-built piece of equipment that serves the purpose of producing and regenerating the desired texture and roughness in the surface of the discs after the completion of each test. As seen in Fig. 21.17, the unit combines the rotational velocity of the sand paper or polishing clothes with the rotation of the disc in order to ensure average values of the surface roughness R_a in the range 0.007–0.8 μm . These values are measured by a roughness tester (from 0.8 to 0.2 μm) and an Atomic Force Microscope (below 0.2 μm) along a direction perpendicular to the rotation of the discs (Fig. 21.17b). The inner diameter of the sand paper or polishing clothe is about 2–2.5 times bigger than the pin's diameter.

After each test, the discs are polished and followed by roughness measurements in order to guarantee repeatability and an analogy of the surface topography of the discs irrespective of the friction test case.

Several innovations were added to the pin-on-disc test apparatus in order to replicate the surface conditions observed in real metal cutting conditions. The first innovation is the inclusion of a cutting blade for shaving the bottom of the pin and

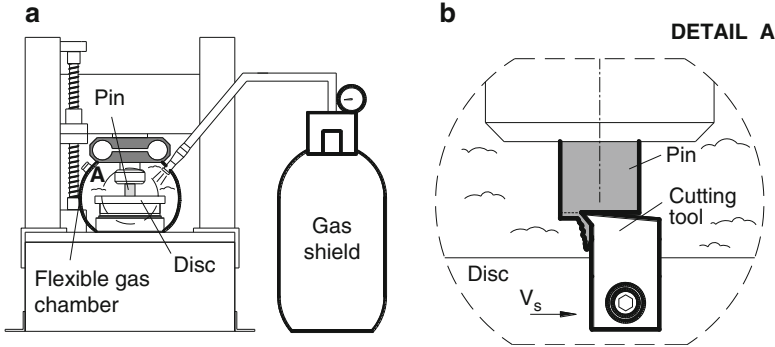


Fig. 21.18 Pin-on-disc test performed under gas shield: (a) Schematic representation of the apparatus; (b) Detail of the testing region

exposes new freshly cut surfaces for the evaluation of the coefficient of friction (Fig. 21.18). The test is performed in a single turn of the rotating disc in order to avoid contamination due to pin rubbing on the same track.

The second innovation is the utilization of the flexible gas chamber presented in Fig. 21.18, in order to perform the pin-on-disc experiments under protective shields of inert and active gases. The chamber works by forcing gas through a nozzle at an applied rate of approximately 5 l/min.

3.3 Ring Compression Test

As explained in Sect. 2.2, the ring compression test is a tribology simulative test commonly utilized in metal forming, namely, forging. Due to its simplicity and acceptance among metal forming researchers, the authors decided to evaluate its performance in metal cutting.

The test was performed in the *Instron 1200 KN* universal testing machine. The specimen was centered between the platens and compression was performed to several predetermined height reductions (Detail A in Fig. 21.19). At the end of each compression stage, the values of its height, inner and outer diameter were measured accordingly utilizing a digital caliper, and checked against calibration curves obtained by means of finite element based simulations. All the tests were performed in room temperature at quasi-static conditions.

The platens were manufactured from AISI 316L stainless steel and the desired texture and roughness of the surfaces were accomplished by means of polishing procedures that combines the utilization of sand paper or polishing clothes with the rotation of the compression platen in order to ensure predominant circular

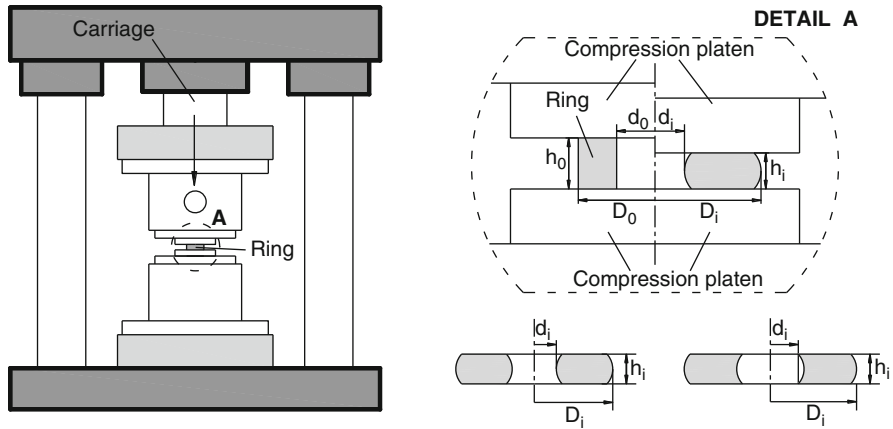


Fig. 21.19 Schematic representation of the ring compression test

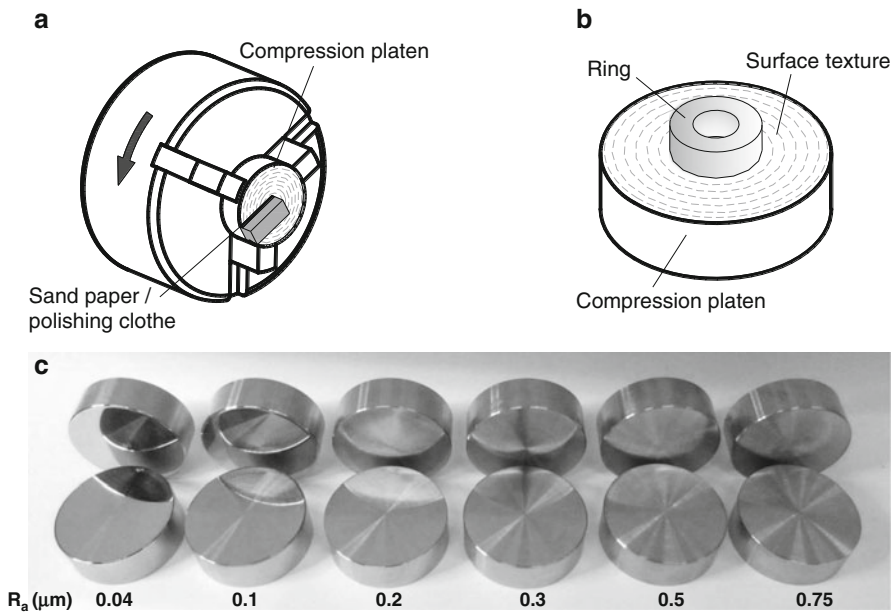


Fig. 21.20 Surface preparation for the ring compression tests: (a) Schematic representation of the polishing procedure and (b) surface texture of the platen; (c) Photograph showing stainless steel compression platens prepared with different values of average surface roughness (R_a)

patterns and average values of surface roughness R_a in the range 0.04–0.75 μm (Fig. 21.20c), which is schematically shown in Fig. 21.20. These values were measured by a contact roughness tester (*Kosaka Lab SE 1200*) along the direction of the material flow during the compression of the specimens.

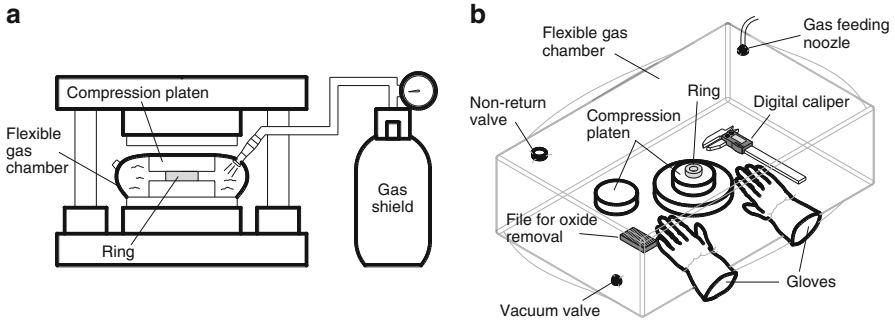


Fig. 21.21 Ring compression test performed under gas shields (a) Schematic representation of the apparatus; (b) Detail of the flexible gas chamber

As it is impossible to put into practice the regeneration of the surface texture after each compression stage, the platens were cleaned and degreased with ethanol in order to avoid deposition of the testing material on the platen, compromising the overall results.

The new proposed methodology for performing ring compression testing draws from the original observations by Male [50] to the development of an experimental apparatus that enables the combined analysis of freshly cut surfaces, oxide films, and surface roughness in the evaluation of friction (Fig. 21.21). The chamber was designed and fabricated by the authors and works by forcing active or inert gas through a nozzle at an applied rate of approximately 5 l/min. The chamber is able to maintain the pressure during the test due to a non-return valve installed in the apparatus.

The preparation procedures are necessary to remove oxides and contaminant films that may have been originated by exposure of freshly machined surfaces to atmosphere during preparation and handling of the rings during the fabrication. This is essential to ensure clean surface conditions and is accomplished by polishing the rings and degreasing both the rings and platens inside the gas chamber where the ring compression tool is mounted.

3.4 Experimental Work Plan

The choice of work material was crucial due to the need to ensure narrow zones of intense plastic shearing under low cutting velocities, as required by the ideal orthogonal cutting conditions. This requirement is important for reducing the effect of strain-hardening, eliminating the influence of strain-rate sensitivity and keeping temperature rise, induced by energy dissipation due to plasticity and friction, low enough to allow the investigation to be exclusively focused on the influence of the surrounding medium in the mechanics of chip flow.

Unfortunately, commonly used engineering materials are unable to fulfill the above mentioned requirement in real cutting velocity conditions due to combined interactions between strain-hardening, strain-rate sensitivity, and temperature that will stimulate the shear plane to broaden into a larger plastic shearing zone called the primary shear zone.

Technically pure Lead (99.9 %) was chosen because its mechanical behavior under low cutting velocities is very close to that of an ideal rigid-plastic material. In addition, the choice of technically pure Lead makes possible to simulate at room temperature and at low strain rates the material flow behavior of conventional steels at the usual manufacturing temperatures [57].

The stress–strain/strain rate relationship of the technically pure Lead was determined by means of compression tests carried out at room temperature under three different strain-rate conditions ($\dot{\epsilon} = 0.02, 0.2$ and 2 s^{-1}). The tests were performed on cylindrical specimens with an initial diameter of $D_c = 24$ mm and a height-to-diameter ratio $H_c/D_c = 1.5$. The specimens were lubricated with PTFE (polymer based lubricant) to ensure homogeneous deformation.

The mechanical behavior of technically pure Lead is given by the following stress–strain/strain rate relationship developed from the well-known stress–strain model due to Voce, $\sigma = A - b \cdot e^{(-c \cdot \epsilon)}$.

$$\bar{\sigma} = 19.2\dot{\epsilon}^{0.042} - 12.0\dot{\epsilon}^{0.052}e^{(0.68\dot{\epsilon}-7.34)\epsilon} \quad (21.2)$$

The evaluation of the coefficient of friction by means of the ring compression test was based on friction calibration curves that were generated by means of the in-house finite element computer program I-form2.

The cutting tools utilized in the process tribology tests were manufactured from the same material as the rotating discs and compression platens (AISI 316L stainless steel). The reason for choosing stainless steel was due to its superficial properties that can easily ensure good surface finishing and to its almost chemically inert features in practically any environment. Another important aspect for picking up the AISI 316L was due to its stress response being much higher than that of Lead.

The elimination of lubrication, temperature, and strain-hardening from the experimental work plan was crucial for reducing the number of parameters that influence friction. Otherwise, the number of possible combinations of variables would become quite large. The experiments were done in a random order and at least two replicates were produced for each test configuration in order to provide statistical meaning.

Another important factor involved in designing friction experiments was related with specimen preparation and cleaning procedures. This is because surfaces contain contaminants such as hydrocarbons, adsorbed moisture, and oxides that, although are usually invisible to the naked eye, can greatly affect the overall friction value, as these contaminants present mechanical and chemical properties different from those of the testing material. The cleaning process took place after

Table 21.1 Experimental work plan for the orthogonal cutting tests: influence of the geometrical and kinematical conditions

α (°)	σ_t (°)	t_0 (mm)	Rake surface R_a (μm)	Clearance surface R_a (μm)	Cutting velocity (m/min)
-10	5	0.015, 0.03, 0.05,	0.20	0.20	0.6, 6, 15, 30
-5		0.075, 0.1, 0.15, 0.2			
5					
10					
0					
0	1				
	2				
	10				
	20				

manufacturing the specimens, in order to remove the lubricants utilized during the fabrication process. The specimens were cleaned with an ultrasonic cleaner and before each test they were further degreased with ethanol.

The work plan for the orthogonal cutting tests was designed to match the pin-on-disc and ring compression experiments with the same tribo-pair in order to ensure that the comparison between the various types of tests was performed under similar operating conditions. The experiments were designed in order to isolate the influence of the process parameters that are considered more relevant for metal cutting: (1) the tool geometry, (2) the velocity, (3) the uncut chip thickness, (4) texture and surface roughness, and (5) surrounding medium. Before each test, the rake and clearance surfaces were reconditioned by the polishing unit in order to ensure that the tests were conducted under the same operational conditions.

The specimens had a prismatic shape and the dimension of the testing area was 80 mm \times 20 mm (length \times width). All the experiments were performed in orthogonal conditions that is, the cutting edge of the tool was straight and perpendicular to the direction of motion and the ratio of the uncut chip thickness to the width of the specimens (1/100) was small enough for width changes to be neglected (plane strain conditions).

Eliminating the influence of lubrication (dry cutting conditions), temperature, and strain-hardening and maintaining the cutting velocity (below 30 m/min) revealed crucial for analyzing the mechanics of chip flow. The influence of size effects was also removed from experimentation because the ratio of the uncut chip thickness to the edge radius of the cutting tools was equal to 100. Otherwise, the number of possible combinations of variables and phenomena would become very large for a comprehensive interpretation of the obtained test results. Table 21.1 presents the first set of the orthogonal cutting tests to evaluate the influence of the cutting tool geometry and kinematics conditions on friction.

Tables 21.2 and 21.3 present the two sets of orthogonal cutting tests that were specially designed in order to analyze the impact of the surface roughness and surrounding medium when employing cutting tools having different surface textures under the same geometry (refer to Fig. 21.13).

Table 21.2 Experimental work plan for the orthogonal cutting tests: influence of the rake surface texture and surrounding medium

α (°)	σ_t (°)	t_0 (mm)	Rake surface R_a (µm)	Clearance surface R_a (µm)	Cutting velocity (m/min)	Gas Shield
0	5	0.2	0.04	0.04	0.6	Air, Argon, Nitrogen, and Oxygen
			0.1			
			0.2			
			0.3			
			0.5			
			0.75			

Table 21.3 Experimental work plan for the orthogonal cutting tests: influence of the clearance surface texture

α (°)	σ_t (°)	t_0 (mm)	Rake surface R_a (µm)	Clearance surface R_a (µm)	Cutting velocity (m/min)
0	5	0.2	0.04	0.04	0.6
				0.1	
				0.2	
				0.3	
				0.5	
				0.75	

Table 21.4 Experimental work plan for the pin-on-disc simulative tests

R_a (µm)	Velocity (m/min)	Gas shield
≤0.1	4, 13, 26, and 40	Air, Argon, and Oxygen
0.2		
0.3		
0.4		
0.5		
0.8		

Note: Tests under Argon and Oxygen gas shields were only performed at 4 m/min

Table 21.4 presents the experimental work plan for the pin-on-disc simulative tests, where the pin has a cylindrical shape with 8 mm diameter. The experiments were designed in order to isolate the influence of the process parameters that were considered more relevant for the frictional behavior: (1) the applied forces, (2) the velocity, and (3) the texture and surface roughness of the tools. The forces were measured by the two-dimensional load cell with a frequency rate of 300 Hz.

Table 21.5 presents the experimental work plan for the ring compression tests. The ring test specimens have a geometrical ratio $D_0 : d_0 : h_0$ (refer to the detail on Fig. 21.19a) of 6:3:2, with the following dimensions 24:12:8 mm.

Table 21.5 Experimental work plan for the ring compression tests

R_a (μm)	Increment (mm)	Velocity (m/min)	Gas shield
0.04	0.5 (incremental) and 1.6, 3.2,	0.05	Air, Argon, and
0.1	and 4.8 (continuous)		Oxygen
0.2			
0.3			
0.5			
0.75			

4 Results and Discussion

This section presents the contribution to knowledge derived from the innovative experimental apparatuses and testing procedures that were addressed in previous sections of this chapter. Broadly, this section is structured into three different parts. Firstly, a new fundamental level of understanding about process tribology tests based on orthogonal metal cutting that include analysis of its performance across the useful range of process conditions. Secondly, the evaluation of operative parameters related to surface texture, roughness and surrounding medium on simulative tribology tests based on pin-on-disc and ring compression. Finally, it is performed a comparison between the coefficient of friction obtained with simulative tribology tests and that obtained by orthogonal metal cutting with the aim of determining if these tests are capable of providing a good characterization of the frictional conditions in metal cutting applications.

4.1 Process Tribology Test Based on Orthogonal Cutting

4.1.1 Thrust and Cutting Forces

The experimental apparatus described in Sect. 3.1 (Fig. 21.11) and the experimental work plan described in Tables 21.1, 21.2, and 21.3 allowed determining the thrust F_t and cutting F_c forces for a wide range of operative testing conditions. Figure 21.22a presents a typical evolution of the thrust force F_t and the cutting force F_c for $\alpha = 0^\circ$, $\sigma_t = 5^\circ$, $R_a = 0.04 \mu\text{m}$, $t_0 = 0.2 \text{ mm}$, $V_c = 0.6 \text{ m/min}$ of Table 21.2, in air. As seen in the figure, the cutting and thrust forces increase sharply at the beginning of the test (refer to “A” in Fig. 21.22) and remain almost constant throughout subsequent steady-state cutting conditions (refer to “B” in Fig. 21.22).

As a results of this, the plot of the thrust force as a function of the cutting force depicted in Fig. 21.22b, allows identifying two linear trends with different slopes corresponding to distinct values of the coefficient of friction. The coefficient of friction is lower at the initial non-steady-state conditions and higher in the steady-state cutting regime. The sharp decrease on the evolution of the thrust

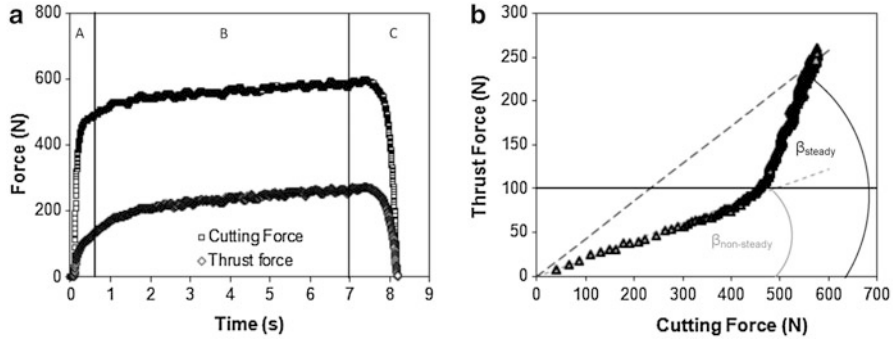


Fig. 21.22 (a) Evolution of the cutting and thrust forces during an orthogonal cutting test; (b) F_t as a function of F_c (in air, $\alpha = 0^\circ, \sigma_t = 5^\circ, R_a = 0.04 \mu\text{m}, t_0 = 0.2 \text{ mm}, V_c = 0.6 \text{ m/min}$)

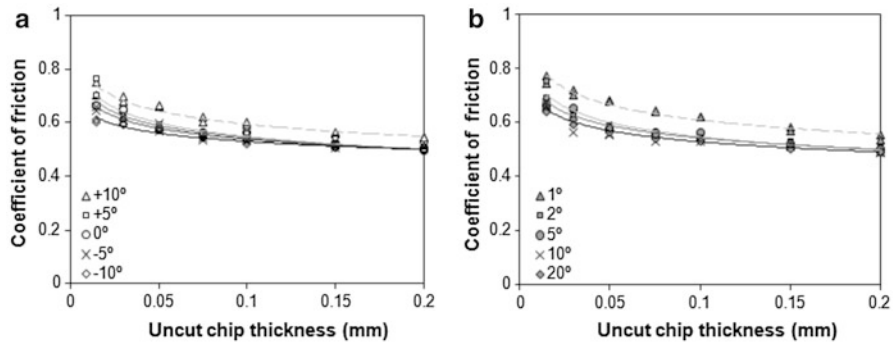


Fig. 21.23 Coefficient of friction as a function of the uncut chip thickness for the orthogonal metal cutting tests performed in air, under dry friction conditions, with $R_a = 0.2 \mu\text{m}$ and $V_c = 0.6 \text{ m/min}$: (a) for rake face angles α varying from -10 to 10° ($\sigma_t = 5^\circ$); (b) for clearance angles σ_t varying from 1 to 20° ($\alpha = 0^\circ$)

force F_t against the cutting force F_c that was registered at the end of the orthogonal metal cutting test (C in Fig. 21.22a) will not be addressed here due to its small relevance for the overall discussion.

4.1.2 Geometrical and Kinematical Operative Conditions

After performing the entire set of process tribology tests based on orthogonal metal cutting that are listed in Tables 21.1, 21.2, and 21.3 and calculating the coefficient of friction from the ratio $\mu = F_t/F_c$ between the experimental values of the cutting F_c and thrust F_t forces in steady-state conditions (refer to region “B” in Fig. 21.22a) it is possible to conclude that the coefficient of friction is influenced by the uncut chip thickness, the geometry of the cutting tool and the cutting velocity (Figs. 21.23 and 21.24).

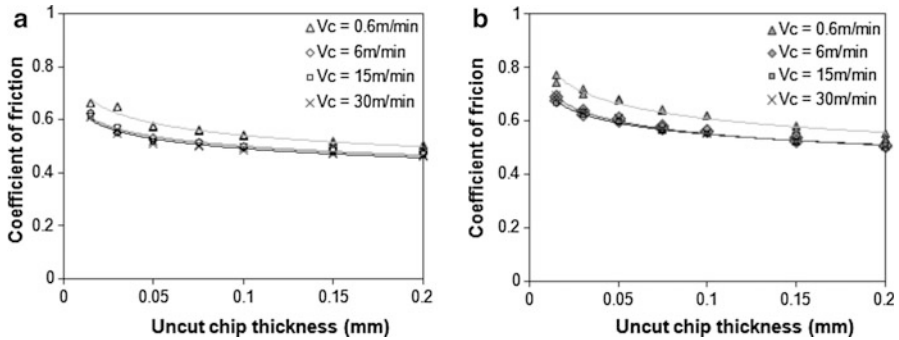


Fig. 21.24 Coefficient of friction as a function of the uncut chip thickness for the orthogonal metal cutting tests performed in air, under dry friction conditions, and with cutting speeds in the range between 0.6 and 30 m/min: (a) For $\alpha = 0^\circ$, $\sigma_t = 5^\circ$, and $R_a = 0.2\mu\text{m}$; (b) for $\alpha = 0^\circ$, $\sigma_t = 1^\circ$, and $R_a = 0.2\mu\text{m}$

The increase of the coefficient of friction with the decrease of the uncut chip thickness (Fig. 21.23) is commonly observed in the literature and usually attributed to the influence of the cutting edge radius. In fact, as the uncut chip thickness approaches the cutting edge radius in size, plowing forces will significantly contribute to the overall cutting forces making the overall coefficient of friction to increase. The effect is, however, limited for the entire set of test cases that are listed in Table 21.1 because the cutting edge radius utilized in the experiments is very sharp (around $2\mu\text{m}$, refer to Fig. 21.14).

The increase of the coefficient of friction with the rake face angle (Fig. 21.23a) has long been reported in the literature. Well-known authors like Shaw [13] considered the increase of the coefficient of friction with the increase of the rake face angle as one of the paradoxes associated with metal cutting because the cutting force decreases as the rake angle increases. Others like Rajput [58] consider this to happen because the normal force on the rake face decreases a great extent compared to the friction force. Thus, although there is an overall decrease in the forces, the coefficient of friction increases.

The increase of the coefficient of friction with the decrease in the clearance angle (Fig. 21.23b) is straightforwardly attributed to the enlargement of the flank face, which will increase frictional contact with the newly formed surfaces of the work material. Observation of Figs. 21.23a, b also allow concluding that the rate of change of the coefficient of friction with both rake and clearance angles is more pronounced for the highest and smallest values of the rake and clearance angles, respectively, and less pronounced when the uncut chip thickness is larger.

However, despite limiting values of the rake face angle equal to 10° and of the clearance angle equal to 1° , it can be concluded that friction shows little dependence on the geometry of the cutting tools. The above figures justify the reason why process geometry variables consisting of an uncut chip thickness of 0.2 mm, a rake face angle $\alpha = 0^\circ$, a clearance angle $\sigma_t = 5^\circ$ and a sharp tool edge of approximately $2\mu\text{m}$ (to limit the effect of the flake-face contact in friction, refer to

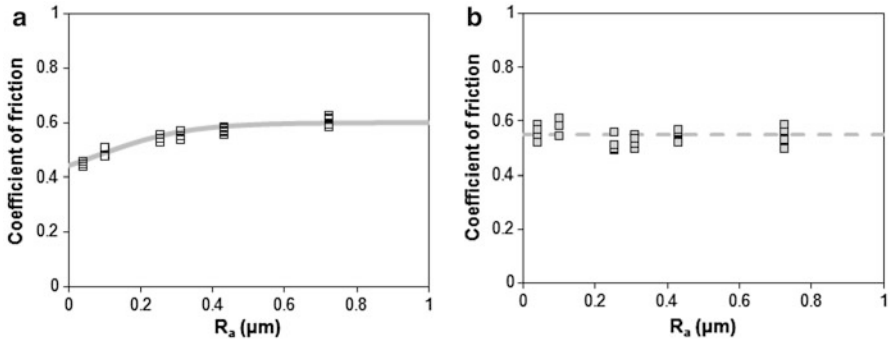


Fig. 21.25 Coefficient of friction as a function of surface roughness for the orthogonal cutting tests (dry friction, $t_0 = 0.2$ mm, in air): (a) Rake surface ($\alpha = 0^\circ$, $\sigma_t = 5^\circ$ with $V_c = 0.6$ m/min); (b) Clearance surface ($\alpha = 0^\circ$, $\sigma_t = 1^\circ$ with $V_c = 0.6$ m/min)

Fig. 21.14), will not influence the value of the coefficient of friction obtained from tribology tests based on orthogonal metal cutting. This will allow extending the above set of observations to kinematic conditions (Fig. 21.24) where variations in the cutting speed between 0.6 and 30 m/min are seen to influence the estimate of the coefficient of friction.

The reason why low cutting speeds may lead to higher values of friction under dry friction conditions is due to longer exposure of freshly cut surfaces to air, as will be discussed later in the presentation.

4.1.3 Surface Morphology

The experimental results presented on previous subsections helped identifying the geometrical and kinematical conditions that are best suited for the evaluation of the influence of surface morphology on friction. The resulting experimental work plan is listed in Table 21.2 and 21.3 of Sect. 3.4.

Figure 21.25 presents the evolution of the coefficient of friction with the surface roughness (R_a), of the rake (Fig. 21.25a) and clearance (Fig. 21.25b) surfaces. Figure 21.25a reveals that surface roughness of the rake surface produces changes in the resulting coefficient of friction of nearly 40 % when cutting in the presence of air under dry conditions. The amount of these changes will be influenced by the surrounding medium, as will be seen later when cutting in the presence of Oxygen rich or inert atmospheres.

It is clear from Fig. 21.25a that roughness of the rake surface influences the overall value of the coefficient of friction. In fact, the coefficient of friction increases progressively with the increase of surface roughness ($R_a < 0.3$ μm), and then becomes almost independent of surface roughness to provide the maximum value of 0.6. In the rightmost region of the graphic, because surface roughness

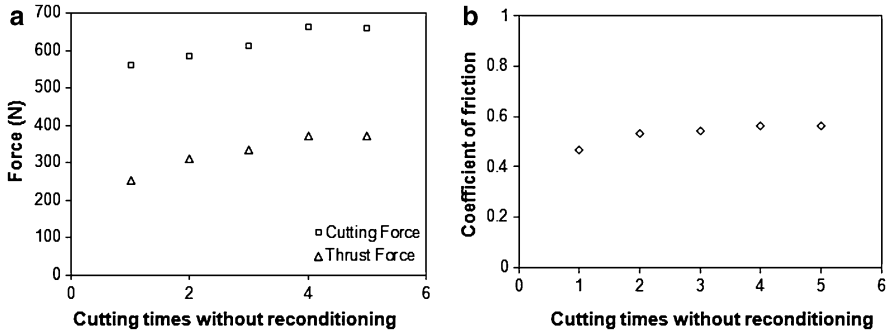


Fig. 21.26 Reconditioning the cutting tool in process tribology tests based on orthogonal metal cutting (dry friction, in air $\alpha = 0^\circ$, $\sigma_t = 5^\circ$, $R_a = 0.04 \mu\text{m}$, $t_0 = 0.2 \text{ mm}$, $V_c = 0.6 \text{ m/min}$):(a) Influence on the cutting and thrust forces; (b) Influence on the coefficient of friction

is large, the interaction between the tips of the asperities on the rake surface and the chip is also large and, therefore, the coefficient of friction takes the highest values.

Conversely, one would expect adhesion to be the basic source of friction in the leftmost region of Fig. 21.25a (where surface roughness is very small). However, this is not the case, because the cutting experiments were performed in the presence of air and, therefore, the newly formed surfaces reacted with the surrounding medium (mainly with Oxygen) to form oxides that influence friction as well as the overall mechanism of chip formation. Adhesion and the influence of surrounding medium in cutting will be addressed later in the presentation.

The results included in Fig. 21.25b indicate that, even with a geometry that maximizes the contact between tool and workpiece, the roughness of the clearance surface will not influence the coefficient of friction. This allows concluding that the major contribution to friction in metal cutting derives from the rake surface. The roughness of the clearance surface only seems to affect the overall surface finish of the workpiece.

Another important subject in the experimental work plan is the influence of surface preparation in the calibration of friction by means of process tribology tests based on orthogonal metal cutting. This subject is particularly relevant for two main reasons: firstly, because in real metal cutting there is never a truly clean cutting tool, and secondly, because research work published in literature, often do not explain if the active surfaces of the cutting tools were clean from contaminants and reconditioned after each test. Figure 21.26 shows the importance of reconditioning the cutting tool after each test for preventing surface contaminant films formed on the rake and flank faces of the cutting tools to influence the experimentally determined coefficient of friction. As seen in Fig. 21.26b, dry cutting with the same tool without reconditioning both the rake and clearance faces, will allow the coefficient of friction to reach values that are 25 % above those obtained with a clean cutting tool.

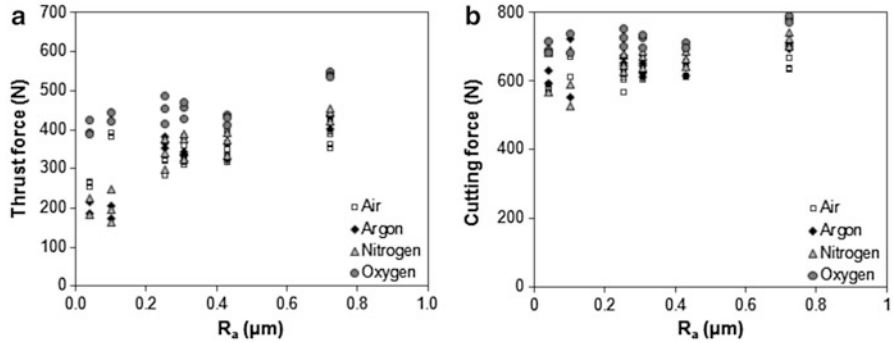


Fig. 21.27 Forces acting on a cutting tool as a function of surface roughness and surrounding medium: (a) Thrust force F_t as a function of surface roughness and surrounding medium; (b) Cutting force F_c as a function of surface roughness and surrounding medium

4.1.4 Surrounding Medium

The influence of the surrounding medium was evaluated by utilizing the test apparatus illustrated on Fig. 21.15. Figure 21.27 which shows the forces acting on the cutting tool under different active and inert gas shields as a function of surface roughness for the entire set of test cases presented on Table 21.2.

As seen, dry cutting under an Oxygen-rich atmosphere may require cutting and thrust forces up to 30 % higher than those needed in the presence of air or under an Argon atmosphere. This is attributed to chemical reactions of Oxygen with Lead to form oxide films (PbO , the expected product of the chemical reaction between Lead and Oxygen) on the upper and lower surface boundaries of the chip and unveils the importance of the interactions between active gases and the freshly formed surfaces of the work materials. Figure 21.27 also shows that cutting in the presence of air generally provides higher forces than those obtained under atmospheres of Nitrogen or Argon. This is because the low affinity of Lead for Nitrogen and the inert characteristics of Argon avoid the formation of surface films on the freshly formed surfaces.

Figure 21.28 shows the coefficient of friction as a function of the surface roughness of the cutting tool for the entire set of test cases listed on Table 21.2. The results obtained for Nitrogen and Argon allowed the identification of three different regions; (1) a leftmost region ($R_a < 0.1 \mu\text{m}$) where the coefficient of friction is constant and takes the smallest value among all the test cases, (2) a rightmost region ($R_a > 0.3 \mu\text{m}$) where the coefficient of friction is constant and reaches the largest value among all the test cases and (3) a region in between where the coefficient of friction progressively grows from the smallest to the largest measured values.

In the leftmost region of the graphic the basic source of friction is adhesion ($\mu \cong \mu_{adh}$) and the friction force resulting from the relative sliding movement between the chip and the cutting tool should be roughly equal to the force that is

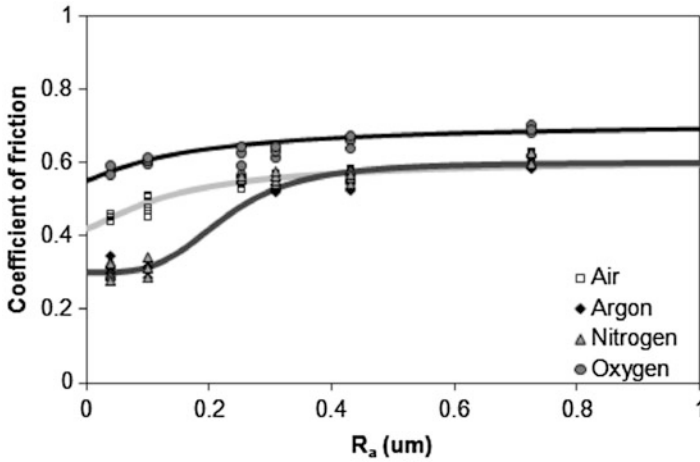


Fig. 21.28 Coefficient of friction as a function of surface roughness and surrounding medium

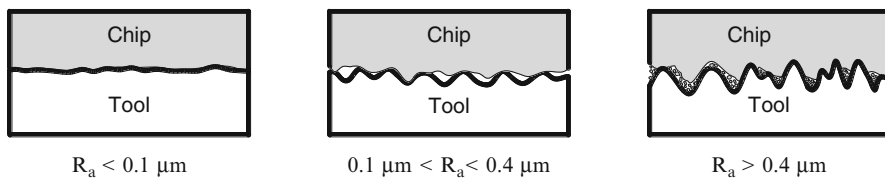


Fig. 21.29 Illustration showing the interaction between the specimen and the cutting tool for different values of surface roughness

needed for shearing the junctions formed by localized pressure welding (cold welding) at the asperities. This is because surface roughness is very small and because the low affinity of Lead for Nitrogen and the inert characteristics of Argon avoid the formation of surface films, allowing the chip to slide smoothly along the rake surface of the cutting tool.

On the contrary, in the rightmost region of the graphic (where the surface roughness of the cutting tool is very large) there is a more pronounced interaction between the asperities. A possible explanation considers the tips of the asperities on the tool to penetrate and plastically deform the boundary surfaces of the chips and, in some cases, debris also to be produced from micro-cutting in the asperity level (Fig. 21.29). The increase of plowing and the extra resistance to sliding caused by loose debris raises the friction force and, therefore, the coefficient of friction for rougher tools is larger than for smoother tools (Fig. 21.29).

The results obtained from the orthogonal cutting tests in the presence of air or under an Oxygen-rich atmosphere do not show evidence of the aforementioned first and second regions of the graphic (Fig. 21.28). In fact, both cases show a monotonic increase of the coefficient of friction from smaller to larger values of surface roughness. This is attributed to the oxide films of PbO formed in the upper and

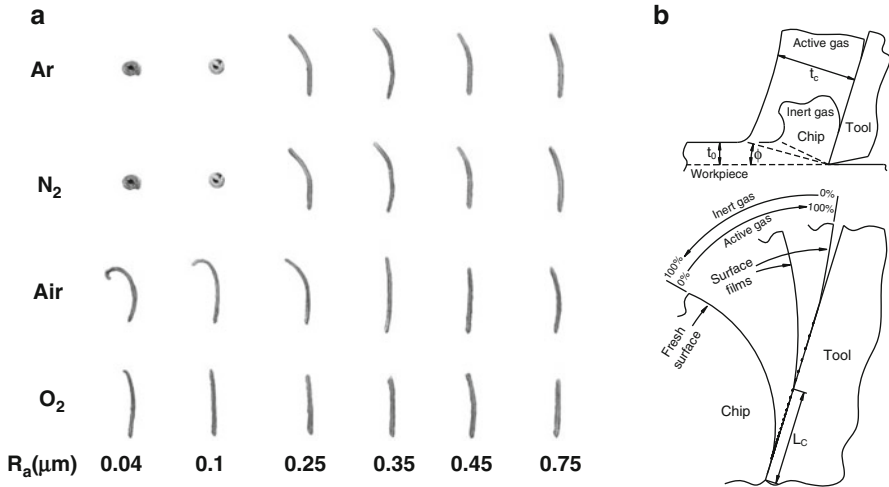


Fig. 21.30 Influence of surface roughness R_a of the tool and surrounding medium in chip curling: (a) Photographs of chip cross sections obtained in different cutting tests; (b) Basic types of chip flow as a function of the surrounding medium

lower surface boundaries of the chips, which do not allow material to slide smoothly along the rake surface of the cutting tools, even when roughness is very small. Finally, it is worth notice that the affinity of Lead for Oxygen is responsible for increasing the overall level of friction even when cutting with tools having large surface roughness. The above observations turn out evident that the surrounding medium does not influences only on the value of the coefficient of friction but also the chip flow, and consequently the chip curling mechanism, which will be discussed in what follows.

4.1.5 Chip Curling

Although the influence of the surrounding medium in metal cutting is often resumed to its primary function of cooling and lubricating, one important aspect of the cutting medium on the tribological conditions at the tool–chip contact interface is the protection against active gases in air. Figure 21.30a presents the cross section of the chips obtained from cutting under active and inert gas shields for the entire test cases listed on Table 21.2. Figure 21.30a shows that cutting under Nitrogen or Argon atmospheres allow chips to curl naturally within the normal range of surface roughness currently found in cutting tools, whereas the exposure to Oxygen causes the chip curl radius to become larger. In fact, the exposure to Oxygen causes the chips to flow along the rake surface of the cutting tools, increasing the contact length L_c (Fig. 21.30b), and promoting its curvature away from the cutting edge.

The contact length L_c in steady-state cutting conditions (Fig. 21.30b) is due to an energy compromise between the plastic work, a quantity inversely proportional to

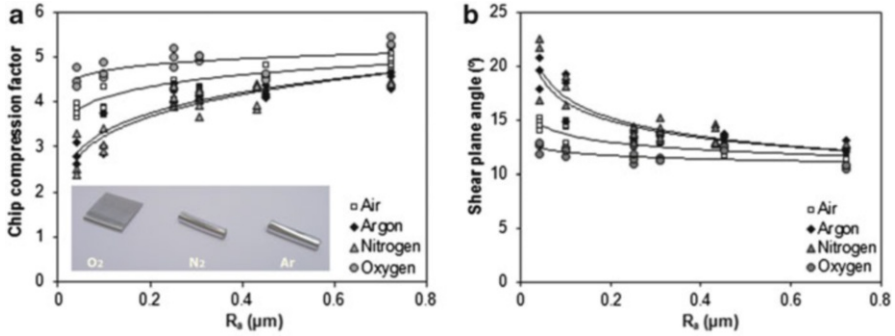


Fig. 21.31 Chip-compression factor and shear plane angle for different surrounding medium:(a) Chip-compression factor as a function of R_a ; (b) Shear plane angle as a function of R_a . Inset shows pictures of chips produced by cutting in the presence of different gas shields

the radius of curvature of the chip, and the amount of frictional work which is directly proportional to the contact length and, therefore, to the radius of curvature of the chip. Because, cutting in the presence of Oxygen increases the coefficient of friction (Fig. 21.28), it follows that frictional work will also increase with the formation of oxide films on the new freshly cut surfaces of Lead. The exposure of Lead to Oxygen also results in larger chip curl radius (Fig. 21.30).

The influence of the surrounding medium in the mechanics of chip flow can be further understood by analyzing the evolution of the chip-compression factor t/t_0 and of the primary shear plane angle ϕ as a function of surface roughness R_a for the cutting tests performed in the presence of different gas shields (Fig. 21.31):

$$\frac{t}{t_0} = \frac{\overline{AB} \cdot \cos(\phi - \alpha)}{AB \cdot \sin \phi} = \cot \phi \cos \alpha + \sin \alpha \quad (21.3)$$

where α is the rake angle, t_0 is the uncut chip thickness and t is the chip thickness.

Two different patterns of behavior can be distinguished; in case of inert gas shields the chip-compression factor t/t_0 and the primary shear plane angle ϕ are very sensitive to the surface roughness R_a , whereas in case of cutting in the presence of active gases the aforementioned sensitivity is less important.

In the first pattern type of behavior, chip thickness decreases (using the original uncut chip thickness as reference) as surface roughness R_a diminishes due to an increase of the shear plane angle ϕ . As a result of this, the contact length L_c at the rake tool surface is diminished and curling of the chip is promoted when cutting in the presence of Argon and Nitrogen, as shown in the photographs included in Fig. 21.31. The second pattern type of behavior in Fig. 21.31 is similar to that of cutting under dry conditions. The curling radius is much larger than that experimentally observed in case of cutting in the presence of inert gas shields and the acquired data points towards the influence of oxide films of PbO to be more

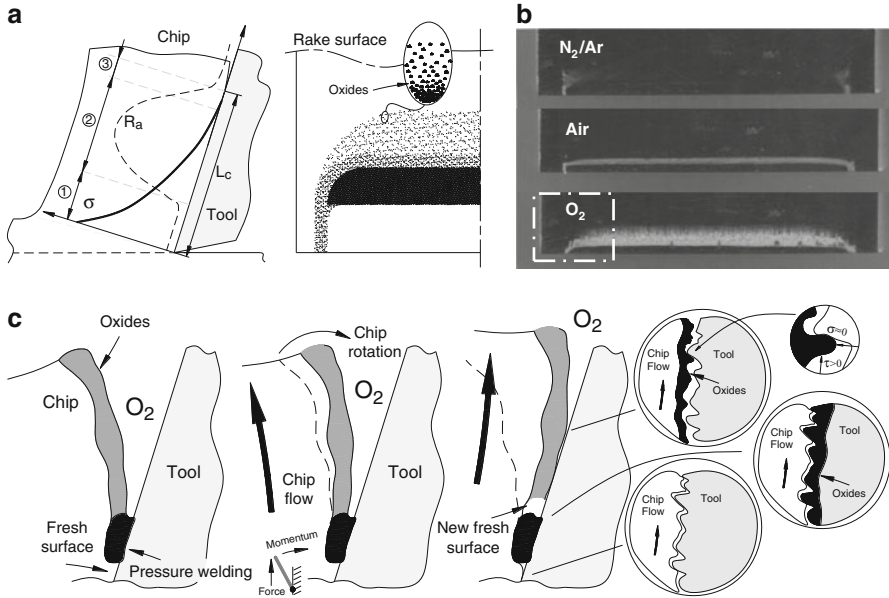


Fig. 21.32 Cutting under inert and active gas shields: (a) Schematic representation of the oxide films that were formed on the freshly cut surface of the chip and are pressure welded onto the rake face of the cutting tool; (b) Photographs showing evidence of oxide films on the tool rake face when cutting in the presence of air or under an Oxygen gas shield; (c) The proposed mechanism for explaining the influence of oxide films in chip curl

important than the diminishing of the surface roughness R_a . As expected, the influence of oxide films in the mechanics of chip flow reaches a maximum when cutting in the presence of an Oxygen gas shield.

The influence of surface roughness in chip curling can be further analyzed in Fig. 21.30. As seen, the larger the roughness, the smaller is the influence of the surrounding medium and the greater are the difficulties for the chips to curl away from the rake face (Fig. 21.30), this is due to a more pronounced interaction between the asperities of the chip and tool. It is possible to conclude that cutting in the presence of active gases will diminish the magnitude of the shear plane angle φ and will produce thicker chips than in case of cutting under low-affinity or inert atmospheres.

The results supporting these conclusions are in line with common beliefs among researchers and practitioners that Oxygen may significantly influence the mechanics of chip flow and go against published research work in the field claiming no influence of the surrounding medium, that was listed in the state-of-the-art review included in the introduction of this chapter. The proposed mechanism for explaining the influence of Oxygen in the mechanics of chip flow is shown in Fig. 21.32 and requires contact length L_c to be divided into three main regions; (1) the bottom newly cut surface of the chip (denoted as region “1” in Fig. 21.32a),

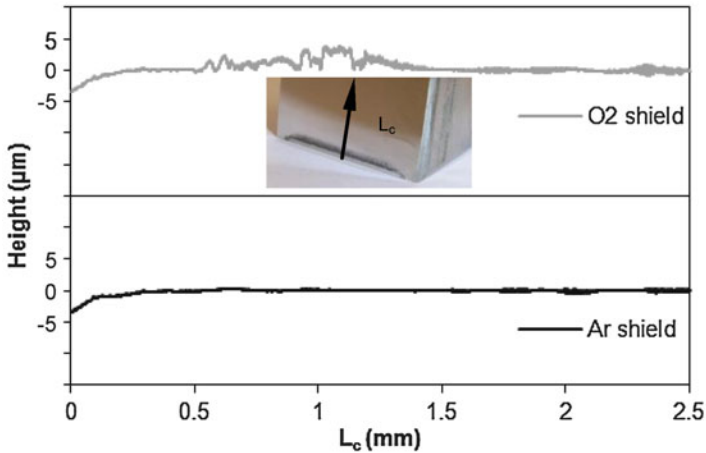


Fig. 21.33 Profile of the rake surface after cutting in the presence of different gas shields: (*top*) Oxygen gas shield; (*bottom*) Argon gas shield

(2) the intermediate surface of the chip (region “2”) and (3) the upper surface (region “3”) that extends up to the point where chip separates from tool.

Region “1” is in immediate and intimate contact with the rake face of the tool, is submitted to high normal pressures and is uncontaminated by Oxygen. Because its length is small (approximately or slightly greater than t_0) and its roughness R_a is also small (refer to the leftmost values in Fig. 21.33, which are identical to the original R_a values in Fig. 21.13a), the basic source of friction in region “1” is expected to be adhesion.

Region “2” experiences less significant normal pressures than previous region “1” but its exposure to Oxygen results in the formation of oxide films in the lower surface boundary of the chip. Figure 21.32a, b show a schematic representation and a photograph of the oxide films that were formed on the surface boundary of the chip and were subsequently smeared over the rake face of the tool (refer to the light colored strips in Fig. 21.32a) when cutting in the presence of air or under an Oxygen-rich atmosphere. Because the average thickness of the oxide films was found to be $3\ \mu\text{m}$ (Fig. 21.33), which is a value significantly larger than the average surface roughness of the rake face of the cutting tool, it is possible to conclude that the interaction between cutting medium and freshly formed surfaces is strong and penetrates deep into the metallic substrate. It is worth notice that in case of cutting under Nitrogen or Argon atmospheres there is no evidence of surface films left on the rake face of the tool (Fig. 21.32b) and, therefore, roughness after cutting is similar to that before cutting (Fig. 21.33).

As seen, the oxide films that are pressure welded onto the rake face of the cutting tool are spread throughout a larger area in case of cutting under an Oxygen-rich atmosphere than in the presence of air. The increase in surface roughness due to the oxides (Figs. 21.32b) in conjunction with the extra force that is needed for shearing

the junctions formed between the oxide particles and the asperities gives rise to higher values of friction in region “2”. Material flow behavior approaches sticking conditions, due to a more pronounced interaction between the oxide particles and the asperities and this creates difficulties for the chips to curl away from the rake face of the cutting tools, thereby, increasing its overall contact length L_c (Fig. 21.32c). This explains the differences observed in the chip cross sections that are pictured in Fig. 21.30.

Region “3” experiences the lowest normal pressures. Scattered oxide films, if present, are likely washed away during sliding of the chip along the rake face of the cutting tools and this explains the reason why Fig. 21.32b shows no signs of contamination arising from the lower surface boundaries of the chips.

The above conclusion helps clarifying the role of cutting fluids in metal cutting. In fact, besides cooling the working area, thereby reducing its temperature, distortion and improving tool life, cutting fluids are also responsible for protecting the freshly formed surfaces of the work material from active gases such as Oxygen.

The following sections present a comprehensive analysis of the experimental results obtained from the simulative tribology tests based on pin-on-disc and upsetting ring compression under operative parameters that are intended to replicate real metal cutting conditions.

4.2 *Simulative Tribology Test Based on Pin-on-Disc*

4.2.1 **Physical and Kinematical Operative Conditions**

The innovative features of the new tribometer described in Sect. 3.2 (Fig. 21.16) allows experiments to be performed under variable loading conditions with exposure of freshly cut surfaces to surrounding medium for a wide range of operative testing conditions (Table 21.4).

Figure 21.34a shows a typical plot of the normal F_N and tangential (friction) F_T forces as a function of time retrieved from a test performed with a sliding velocity of $V_s = 4$ m/min and a Lead-stainless steel tribo-pair. By extending the analysis to the entire set of velocities that are included in the experimental work plan it is possible obtain the result depicted in Fig. 21.34b.

As a result of this, Fig. 21.34 allows two different types of conclusions to be drawn. Firstly, it shows the friction force to be directly proportional to the normal force applied on the pin and the coefficient of friction not being affected by the contact pressure. Secondly, it reveals friction not to be significantly influenced by the sliding velocity. In fact, the maximum deviation of the coefficient of friction observed in the whole range of velocity testing conditions is below 5 %.

The first conclusion is in close agreement with the fundamental laws of friction. The second conclusion may be surprising when analyzed in the light of previous works in tribology but falls right in-line with the experimental results published by Sedlacek and coworkers [55].

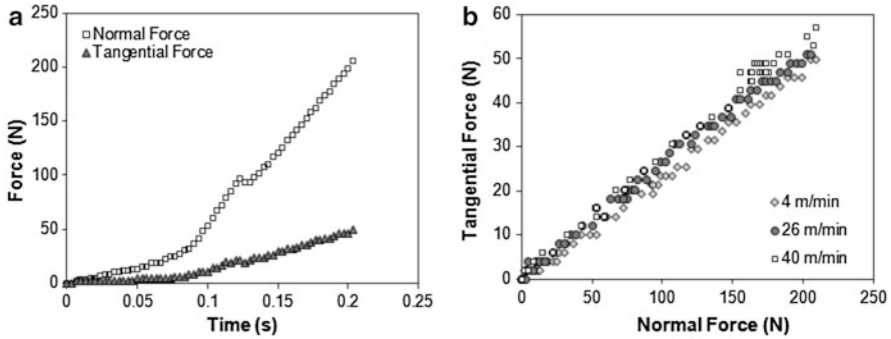


Fig. 21.34 Experimental results for pin-on-disc tests (dry friction, in air, $R_a = 0.007 \mu\text{m}$): (a) F_N and F_T as a function of time for $V_s = 4 \text{ m/min}$; (b) F_T as a function of the F_N

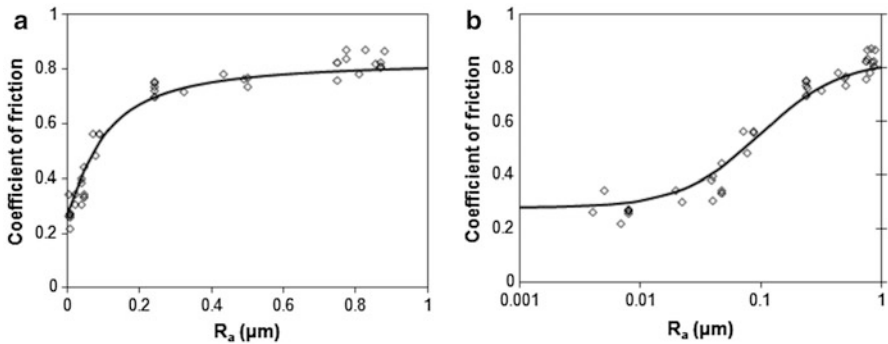


Fig. 21.35 (a) Coefficient of friction as a function of the average surface roughness R_a on pin-on-disc simulative tests; (b) Same as in (a) but showing the leftmost region of the graphic in greater detail

It may, however, be argued that the range of velocities employed in the pin-on-disc tests was not sufficiently large enough to support the aforementioned conclusion but, for the testing conditions under investigation, it seems that surface morphology and surrounding medium will play the key role in the frictional behavior of the tribo-pair.

4.2.2 Surface Morphology and Surrounding Medium

Figure 21.35 shows the variation of the coefficient of friction with surface roughness for the tribotests performed in the presence of air that are listed in the experimental work plan (Table 21.4). The main differences between Fig. 21.35a, b are due to the fact that the latter employs a logarithmic scale instead of the usual linear one on the horizontal axis in order to facilitate reading of the results obtained for the discs with smoother surfaces.

Like in case of process tribology tests based on orthogonal metal cutting, the combined analysis of both graphics allows the identification of three different regions: (a) a leftmost region ($R_a < 0.1 \mu\text{m}$), where the coefficient of friction is constant and takes the smallest value among all the test cases, (b) a rightmost region ($R_a > 0.5 \mu\text{m}$), where the coefficient of friction is constant and reaches the largest value among all the test cases, and (c) a region in-between where the coefficient of friction progressively grows from the smallest to the largest measured values. In the leftmost region of the graphic, the surface roughness of the stainless-steel discs is very small and, for that reason, the sliding between the pin and the discs is smooth. The main source of friction is adhesion ($\mu \cong \mu_{adh}$) and the friction force resulting from the relative movement between the pin and the disc is roughly equal to the force that is needed for shearing the junctions formed by localized pressure welding (cold welding) at the asperities. However, the role of adhesion will be further investigated at the end of this section by performing pin-on-disc experiments under an inert gas shield that avoids chemical reactions with the Oxygen in the air.

On the contrary, in the rightmost region of the graphics (where the surface roughness of the discs is very large) there is a more pronounced interaction between the asperities. The result is similar to that previously obtained in process tribology tests performed with orthogonal metal cutting and the mechanism may also be explained by the tips of the asperities on the discs that will penetrate and plastically deform the surfaces of the pins, and in some cases by debris that may also be produced from micro-cutting in the asperity level (Fig. 21.29). The increase of plowing and the extra resistance to sliding caused by loose debris at the interface will raise the friction force. As a consequence, the coefficient of friction for rough discs is larger than for smooth discs (Fig. 21.35).

In what concerns the influence of surrounding medium, Fig. 21.36 presents the evolution of the coefficient of friction with surface roughness R_a under different gas shields. As seen, the presence of an active atmosphere promotes higher values of the coefficient of friction that, in some cases, may increase up to 100 %. This is attributed to the oxide films of PbO formed on the surface of the pin that will not allow material to slide smoothly on the rotating disc. By eliminating the presence of Oxygen and employing an inert atmosphere of Argon the coefficient of friction is reduced and the transition between the regions that were previously identified in Sect. 4.1 becomes smoother.

4.3 Simulative Tribology Test Based on Ring Compression

4.3.1 Compressive Testing Procedures

It is a common believe among researchers that friction conditions may vary during the upset compression of a ring test specimen [50]. This is observed in Fig. 21.37 for the different continuous and sequential compression testing procedures that were listed in Table 21.5. The calibration curves included in this figure were built

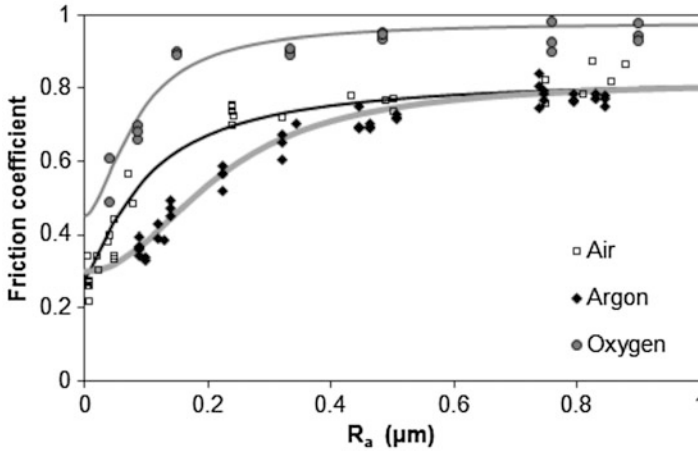


Fig. 21.36 Coefficient of friction as a function of the average surface roughness R_a for different types of exposure to surrounding medium in simulative tribology tests based on pin-on-disc

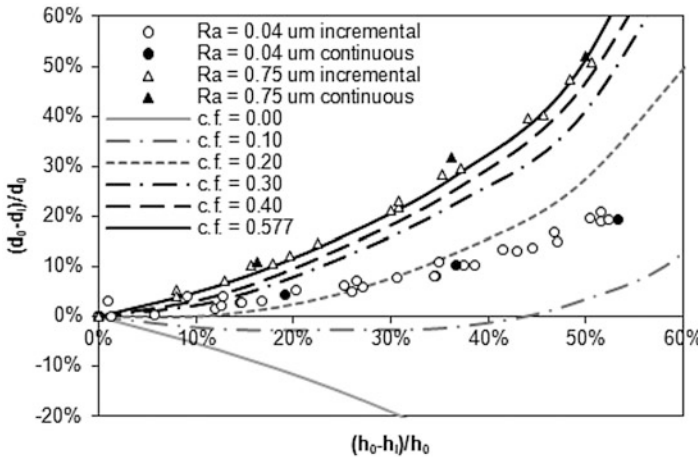


Fig. 21.37 Experimental results and friction calibration curves for ring compression tests using flat compression platens with various surface roughness R_a and different compression procedures

with the in-house finite element computer program I-form and the first conclusion to be taken from results is that there is no variation of the coefficient of friction with the compression testing procedure.

As will be seen in what follows, the surface morphology and the surrounding medium will play the key role in the frictional characterization of the tribo-pair by means of the ring compression test.

4.3.2 Surface Morphology and Surrounding Medium

The combined investigation on the influence of surface roughness and surrounding medium in friction is exclusively focused on the morphology of the compression platens. The approach followed by the authors was different from the actual research trends in the field, which tends to be centered on analyzing the influence of different types of surface preparation of the ring test specimens in the coefficient of friction. This is because the surface asperities of the ring specimens are flattened by the compression platens, made from a high strength and harder material, and make difficult to conclude whether or not the coefficient of friction is influenced by surface roughness. In fact, some authors conclude on a small variation of the coefficient of friction for different types of surface preparation of the ring specimens [49], while others conclude that surface preparation only influence the values of the coefficient of friction at low compression ratios [47].

By placing the analysis on the differences in surface preparation of the compression platens it is possible to conclude that low values of surface roughness reduce the coefficient of friction, whereas high values of surface roughness R_a cause the coefficient of friction to increase (Fig. 21.38). In fact, when surface roughness is very small and the preparation and testing of the ring specimens are protected by an inert gas shield of Argon, the sliding between the ring and the platen is smooth and the basic source of friction is adhesive bonding at the junctions of the asperities. On the contrary, when the surface roughness of the compression platens is large, the basic source of friction is due to interaction between the asperities, for all types of atmospheres.

Although interactions between asperities may be more or less significant, it is known and shown in Fig. 21.38 that ring compression tests experience difficulties in reproducing variations in the coefficient of friction when friction approaches limiting values.

Figure 21.39 presents the geometry of the ring test specimens after performing the experiments. As seen, technically clean surfaces resulting from preparation and testing, with low surface roughness, and under an inert atmosphere of Argon give rise to an increase of the inner diameter of the specimens and provides the lowest values of friction. On the other hand, rough surfaces covered by oxide films provide the highest values of friction and lead to a decrease of the inner diameter of the ring test specimens.

Figure 21.40 summarizes the variation of the coefficient of friction with surface roughness obtained from the experimental measurements and calibration curves that are plotted in Fig. 21.38. A brief observation of Fig. 21.40 allows the identification of the same type of regions that had been described in the other tribology tests (Sects. 4.1 and 4.2); (1) a leftmost region where the coefficient of friction is constant and takes the smallest value among all the test cases (basic source of friction in this region is adhesion), progressively growing to (2) a rightmost region where the coefficient of friction is constant and reaches the largest value.

The observation of Fig. 21.40b allows understanding the combined influence of oxide films and surface roughness. In general terms, oxide films of PbO play an important role when surface roughness is small because they do not allow material

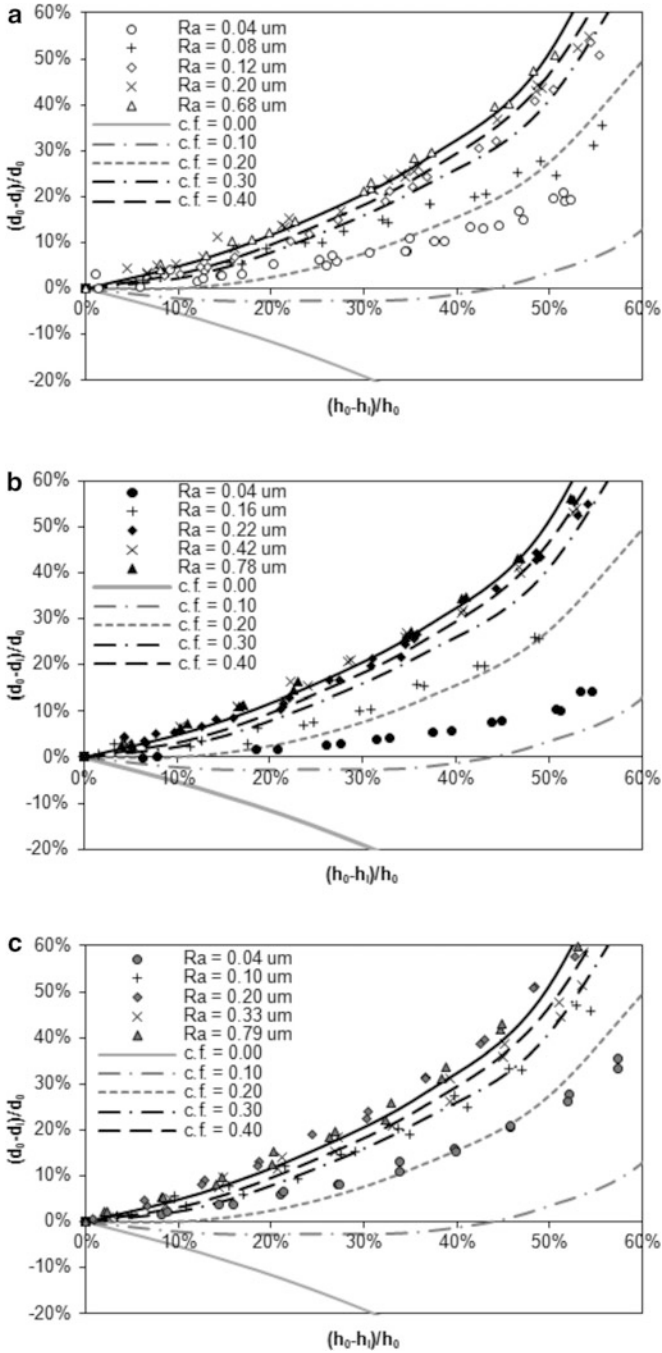


Fig. 21.38 Experimental results and friction calibration curves obtained for ring compression tests prepared and performed under different gas shields: (a) Air; (b) Argon, and (c) Oxygen

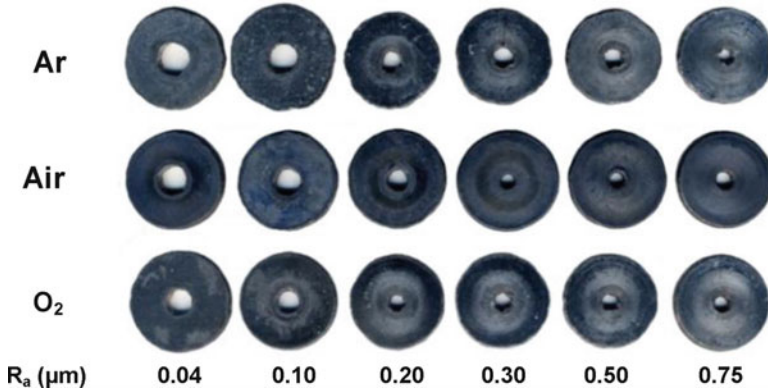


Fig. 21.39 Ring specimens prepared and tested under inert and active gas shields with compression platens having different values of surface roughness

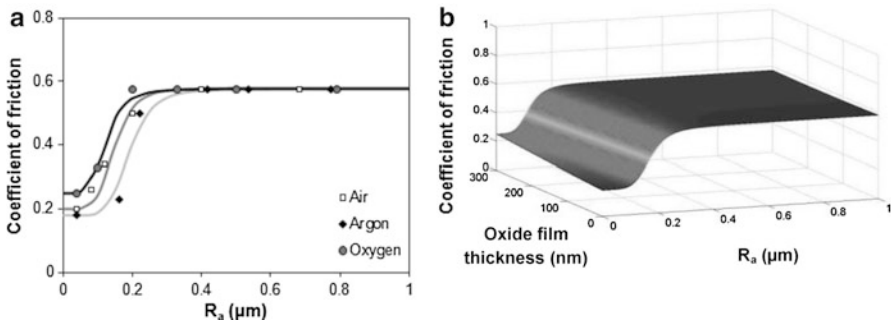
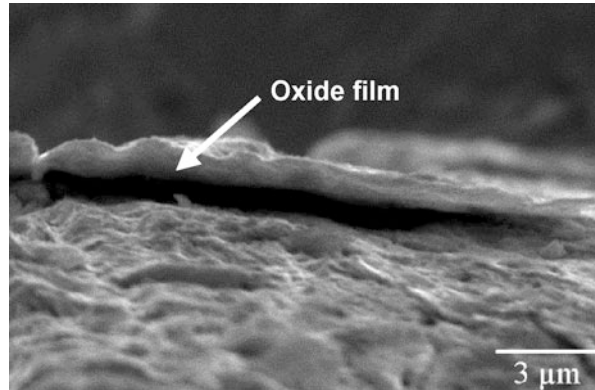


Fig. 21.40 Coefficient of friction as a function of surface roughness R_a and surrounding medium in the ring compression test: (a) Experimental results and the best fit for the experimental data obtained by means of sigmoid curves; (b) 3D representation of the best fitted sigmoid surface for the experimental results

to slide smoothly, even when roughness is very small. On the contrary, oxide films almost have no influence in the resulting coefficient of friction when surface roughness is large due to predominant interaction between the asperities and the previously mentioned difficulty of the ring compression test in reproducing high friction conditions.

The thickness of the oxide films (PbO) that are formed through exposure to active atmospheres on the ring specimens was experimentally measured by means of a Scanning Electron Microscope (SEM). The procedure required specimens to be removed from the gas chamber where ring compression tests were performed, immediately immersed into liquid Nitrogen and subsequently separated into two halves so that the oxides come off the surface. The separation between the layer of oxides and the surface of the ring specimens is clearly seen in Fig. 21.41 for a specimen that was compressed between flat platens with an average value of surface

Fig. 21.41 Detail of the PbO layer of oxides in the surface of a ring test sample that was compressed between flat platens with an average value of surface roughness $R_a = 0.04 \mu\text{m}$ in a rich atmosphere of Oxygen



roughness $R_a = 0.04 \mu\text{m}$ in a rich atmosphere of Oxygen. Additional measurements at different ring compression testing conditions revealed that the thickness of the PbO oxide films is between 10 and 100 nm when tests were performed in air and above 300 nm when tests were carried out in a rich atmosphere of Oxygen.

4.3.3 Assessing Simulative Tribology Tests Against Orthogonal Cutting

Figure 21.42 shows the coefficient of friction as a function of surface roughness derived from experimentation with orthogonal metal cutting, pin-on-disc, and ring compression tests. All the tests were performed in air under dry friction conditions.

The nearly identical estimates of the coefficient of friction provided by orthogonal metal cutting and ring compression testing in the rightmost region of the graphic shown in Fig. 21.42 may be attributed to interaction between asperities, instead of relative sliding, being the driving force of contact with friction between tribo-pairs. In the leftmost region of the graphic the basic source of friction should be adhesion but the experimental values determined by means of the three different tribology tests display significant differences.

The disagreements in the coefficient of friction obtained by means of the different tribology tests appear to be in line with common beliefs among metal cutting researchers that calibration of friction is only accurate, reliable, and valid by measuring normal and tangential forces on the tool rake face. If this were true, then one might be tempted to conclude that differences between the results provided by ring compression and orthogonal metal cutting in the leftmost region of the graphic should come from different tribological conditions on the contact interfaces between workpiece and tooling in metal cutting and metal forming.

However, as can be seen from Fig. 21.43, the explanation for the above mentioned discrepancies relies in the surrounding medium where tools (discs or platens) and test samples are prepared and where experiments are to be performed. In fact, calibration of the coefficient of friction under an active atmosphere of Oxygen enlarges the differences between the results provided by each tribology test

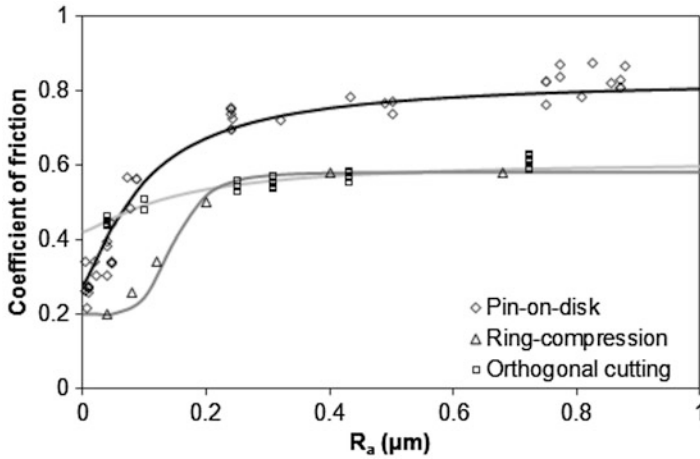


Fig. 21.42 Coefficient of friction as a function of surface roughness for the tribology tests under investigation (dry friction, in air)

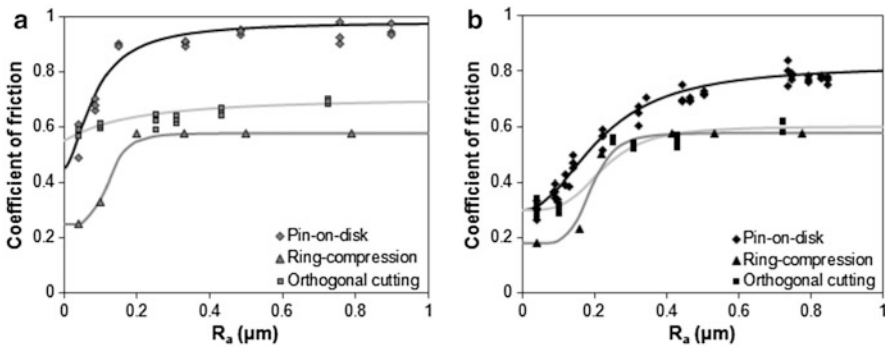


Fig. 21.43 Coefficient of friction as a function of surface roughness for two different gas shields (dry friction): (a) Active atmosphere of Oxygen; (b) Inert atmosphere of Argon

(Fig. 21.43a), whereas calibration under an inert atmosphere of Argon changes the values towards a closer similarity (Fig. 21.43b).

The oxide films of PbO that are formed in the upper and lower surface boundaries of the work material, when cutting in the presence of Oxygen, do not allow material to slide smoothly along the cutting tools (discs or platens), even when roughness is very small. Figure 21.44a, b, and c shows evidence of the oxide films that were formed on the surface boundary of the chip, pin, and ring and were subsequently smeared over the rake face of the tool, disc and platen (refer to the oval mark in Fig. 21.44d) when performing tests under an Oxygen-rich atmosphere.

Because the average thickness of the oxide films in the cutting tool was found to be approximately equal to 3 μm , which is a value significantly larger than the

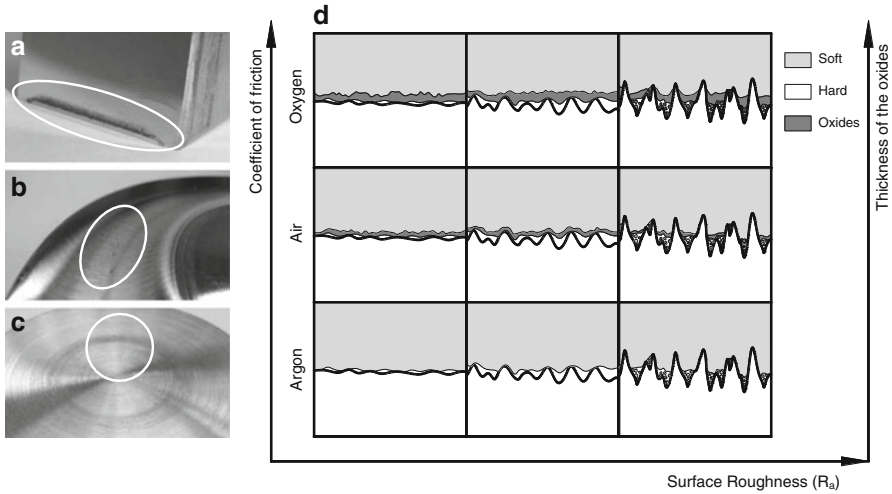


Fig. 21.44 Interaction between cutting tool, disc or compression platen (hard), and the work material (soft). Photographs showing evidence of the oxide films in the presence of an Oxygen gas shield after each test: (a) The rake face of the cutting tool; (b) The disc surface; (c) The compression platen; (d) Schematic variation of the coefficient of friction as a function of surface roughness for different thicknesses of the oxide films

original surface roughness of the rake face of the cutting tools (Fig. 21.13a), it is possible to conclude that the interaction between Oxygen and freshly formed surfaces is strong and penetrates deep into the metallic substrate.

It is worth notice that in case of performing tribology tests under an inert gas shield there is no evidence of surface films left over the rake face of the cutting tools, discs or platens, and therefore roughness after testing should be similar to that before testing. However, the overall quality of the results is very encouraging and allows concluding that simulative tribology tests, when performed with an adequate control of texture, surface roughness and surrounding medium, are capable of providing a good estimate of the average coefficient of friction in metal cutting applications.

5 Conclusions

This chapter presents two contributions to knowledge in tribology of metal cutting. Firstly, the identification of a new level of understanding on the influence of geometry, kinematics, surface morphology, surrounding medium, and contaminant oxide films on the mechanics of chip flow and friction. Secondly, the development of innovative technical solutions and experimental methodologies for the determination of the coefficient of friction by means of process and simulative tribology tests based on orthogonal metal cutting, pin-on-disc, and ring compression.

Process tribology tests based on orthogonal metal cutting show that cutting in the presence of Oxygen leads to higher values of friction, chip compression factor, and chip curl radius and to lower values of the shear plane angle. This indicates that surface oxide films formed on freshly cut surfaces will significantly influence the mechanics of chip flow.

The proposed model for explaining the aforementioned influence is based on the interaction between chip and tool rake face and allow us to understand the reason why cutting in the presence of Oxygen will increase the contact length and promote curvature away from the cutting edge.

The overall results are in line with common believes among researchers and practitioners that Oxygen has a significant influence on the cutting conditions. In fact, if the interaction between chip and tool in real cutting processes do not take into consideration the chemical reactions with active gases in air, there is room for misunderstanding the mechanics of chip flow, the sources of friction along the rake surface of the cutting tools, and the role of cutting fluids, if used. In connection to this, researchers engaged in numerical modeling of metal cutting must be aware that surrounding medium has a substantial influence in the distribution of the coefficient of friction along the rake face of the cutting tool. The utilization of data from simulative tests that are performed under operative conditions different from those of metal cutting often gives rise to the necessity of tuning friction during modeling in order to obtain good estimates of the chip flow and cutting forces.

This chapter is also a step towards clarification of the feasibility and validity of simulative tribology tests based on pin-on-disc and ring compression for modeling the frictional conditions at the tool–chip contact interface in metal cutting that arise from the interaction between cutting medium, surface morphology, and freshly cut surfaces.

In both simulative tribology tests, results show that experiments performed in dry friction conditions, with adequate control of surface morphology and under a protective shield of Argon, are capable of providing estimates of the coefficient of friction in close agreement with those found in process tribology tests based on orthogonal metal cutting. Thus, surface morphology together with the existence of contaminant oxide films due to different exposures to atmosphere during preparation and testing of samples seems to be the main reason for the discrepancies that are commonly found between the coefficient of friction determined by simulative and process tribology tests.

References

1. Jawahir IS, van Luttervelt CA (1993) Recent developments in chip control research and applications. *Ann CIRP* 42:659–693
2. Nakayama K, Ogawa M (1978) Basic rules on form of chip in metal cutting. *Ann CIRP* 27(1):17–21
3. Kfuft W, Konig W, Luthukelt CA, Nakayama K, Pekelkuing AJ (1979) Present Knowledge of chip control. *Ann CIRP* 28(2):441–455

4. Henriksen EK (1953) Chip braking—a study of three dimensional chip flow. ASME Paper No. 53-S-9
5. Ten Horn BL, Shkermann RA (1954) Chip control—How to determine tool feed to obtain desirable chip form. *Tool Eng* 32(4):37–44
6. Spaans C (1954) The fundamentals of the dimensional chip curl, chip braking and chip control, PhD Thesis, TH Delft
7. Pekelharing AJ (1963) Why and how does the chip curl and break. *Ann CIRP* 12(1):144–147
8. Nakayama K (1962). A study on chip-braking. *Bull JSME* 5(7):142–150
9. Bhattacharyya A (1965) Mechanics of chip-Breakers. *Int J Product Res* 4(1):37–49
10. Okushime K, Hoshi T, Tujirawe T (1960) On the behaviour of the chip in steel cutting. *Bull JSME*
11. van Luttervelt CA, Childs THC, Jawahir IS, Klocke F, Venuvinod PK (1998) Present situation and future trends in modelling of machining operations—progress report of the CIRP working group ‘modelling of machining operations’. *Ann CIRP* 47:587–626
12. Zorev N (1966) *Metal cutting mechanics*. Pergamon Press, Oxford
13. Shaw MC (1984) *Metal cutting principles*. Clarendon, Oxford
14. Oxley PLB (1989) *Mechanics of machining: An analytical approach to assessing machinability*. Wiley, New York, NY
15. Atkins AG (2003) Modelling metal cutting using modern ductile fracture mechanics: quantitative explanations for some longstanding problems. *Int J Mech Sci* 45:373–396
16. Atkins AG (2009) *The science and engineering of cutting*. Butterworth-Heinemann, Oxford
17. Rosa PAR, Martins PAF, Atkins AG (2007) Revisiting the fundamentals of metal cutting by means of finite elements and ductile fracture mechanics. *Int J Mach Tools Manuf* 47:607–617
18. Astakhov VP (2006) *Tribology of metal cutting*. Elsevier, Oxford
19. Kalpakjian S (1997) *Manufacturing processes for engineering materials*. Addison-Wesley, Boston, MA
20. De Chiffre L (1990). *Metal cutting mechanics and applications*. DSc. Thesis, Technical University of Denmark
21. Özel T, Altan T (2000) Determination of workpiece flow stress and friction at the chip–tool contact for high-speed cutting. *Int J Mach Tool Manuf* 40:133–152
22. Zemzemi F, Rech J, Ben Salem W, Dogui A, Kapsa P (2009) Identification of a friction model at tool/chip/workpiece interfaces in dry machining of AISI4142 treated steels. *J Mater Process Technol* 209:3978–3990
23. Astakhov VP (2005) On the inadequacy of the single-shear plane model of chip formation. *Int J Mech Sci* 47:1649–1672
24. Bil H, Kiliç SE, Tekkaya AE (2004) A comparison of orthogonal cutting data from experiments with three different finite element models. *Int J Mach Tools Manuf* 44:933–944
25. Özel T (2006) The influence of friction models on finite element simulations of machining. *Int J Mach Tools Manuf* 46:518–530
26. Bay N (2002) Modelling of friction in cold metal forming processes. *Proceedings of the 2nd Workshop on Process Simulation in Metal Forming Industry, DIMEG, Padova, Italy*
27. Schey JA (1983) *Tribology in metalworking: friction, lubrication and wear*. American Society for Metals, Metals Park, OH
28. Bay N, Wibom O, Martins PAF (1998) Testing of friction and lubrication in bulk metal forming. *Proceedings of the IMECE98—International Mechanical Engineering Conference and Exhibition, Anaheim, USA*
29. Usui E, Takeyama H (1960) A photoelastic analysis of machining stresses. *Trans ASME J Eng Ind* 82:303–308
30. Chandrasekaran H, Kapoor DV (1965) Photoelastic analysis of tool-chip interface stresses. *Trans ASME J Eng Ind* 87:495–502
31. Ahmad MM, Draper WA, Derricot RT (1989) An application of the finite element method to the prediction of cutting tool performance. *Int J Mach Tools Manuf* 29(2):197–206
32. Kato S, Yamaguchi K, Yamada M (1972) *Trans ASME J Eng Ind* 94:683
33. Barrow G, Graham W, Kurimoto T, Leong YF (1982) Determination of rake face stress distribution in orthogonal machining. *Int J Mach Tool Des Res* 22(1):75–85

34. Childs THC, Mahdi MI (1989) On the stress distribution between the chip and tool during metal turning. *Ann CIRP* 38:55–58
35. Grzesik W, Zalisz Z, Nieslony P (2002) Friction and wear testing of multilayer coatings on carbide substrates for dry machining applications. *Surf Coat Technol* 155:37–45
36. Olsson M, Soderberg S, Jacobson S, Hogmark S (1989) Simulation of cutting pin-on-disc test. *Int J Mach Tools Manuf* 29:377–390
37. Hedenquist P, Olsson M (1991) Sliding wear testing of coated cutting tool materials. *Tribol Int* 23:143–150
38. Zemzemi F, Rech J, Ben Salem W, Kapsa P, Dogui A (2007) Development of a friction model for the tool–chip–workpiece interface during dry machining of AISI4142 steel with TiN coated carbide cutting tools. *Int J Mach Machinability Mater* 2:361–367
39. Male AT, Cockcroft MG (1964) A method for the determination of the coefficient of friction of metals under conditions of bulk plastic deformation. *J Inst Metals* 93:38
40. Kunogi M (1954) On plastic deformation of hollow cylinders under axial compressive loading. *J Sci Res Inst* 2:63–92
41. Kudo H (1995) An analysis of plastic compressive deformation of lamella between rough plates by energy method. *Proceedings of the 5th. Japan National Congress Applied Mechanics, Japan*
42. Kudo H (1960) Some analytical and experimental studies of axisymmetric cold forging and extrusion. *Int J Mech Sci* 2:102–127
43. Hawkyard JB, Johnson W (1967) An analysis of the changes in geometry of a short hollow cylinder during axial compression. *Int J Mech Sci* 9:163–182
44. Avitzur B (1968) *Metal forming: processes and analysis*. McGraw-Hill, New York, NY
45. Rao KP, Sivaram K (1993) A review of ring-compression testing and applicability of the calibration curves. *J Math Proc Tech* 37:295–318
46. Petersen SB, Martins PAF, Bay N (1998) An alternative ring-test geometry for the evaluation of friction under low normal pressure. *J Math Proc Tech* 79:14–24
47. Hu ZM, Dean TA (2000) A study of surface topography, friction and lubricants in metal forming. *Int J Mach Tools Manuf* 40:1637–1649
48. Mahrenholtz O, Bontcheva N, Iankov R (2005) Influence of surface roughness on friction during metal forming processes. *J Math Proc Tech* 159:9–16
49. Sahin M, Çetinarşlan CS, Akata HE (2007) Effect of surface roughness on friction coefficients during upsetting processes for different materials. *Mat Design* 28:633–640
50. Male AT (1966) Variations in friction coefficients of metals during compressive deformation. *J Inst Metals* 94:121–125
51. Rosa PAR (2007) *Theoretical and experimental modelling of orthogonal metal cutting*. Universidade Técnica de Lisboa, Portugal
52. Komanduri R, Hou ZB (2001) A review of the experimental techniques for the measurement of heat and temperatures generated in some manufacturing processes and tribology. *Tribol Int* 34:653–682
53. Svahn F, Kassaman-Rudolph A, Wallen E (2003) The influence of surface roughness on friction and wear of machine element coatings. *Wear* 254:1092–1098
54. Menezes PL., Kishore and Kailas SV (2009), Role of surface texture of harder surface on subsurface deformation. *Wear* 266, 103–109
55. Sedlacek M, Podgornik B, Vizintin J (2009) Influence of surface preparation on roughness parameters, friction and wear. *Wear* 266:482–487
56. Cristino VAM, Rosa PAR, Martins PAF (2008), Método e aparelho para a determinação do coeficiente de atrito em interfaces de contacto com superfícies recém-geradas, Patent no. PT103935, INPI, Portugal
57. Altan T, Henning HJ, Sabroff AM (1970) The use of model materials in predicting forming loads in metalworking, *Journal Engineering for Industry*. *Trans ASME* 92:444–452
58. Rajput RK (2007) *Manufacturing technology*. Laxmi Publications, New Delhi

Exercises

Process Tribology Test Based on Orthogonal Metal Cutting

A process tribology test based on orthogonal metal cutting (Chap. 21, Sect. 2.1) is being carried out under the following operative conditions (Fig. 21.45):

Rake angle $\alpha = 0^\circ$
 Clearance angle $\sigma_t = 5^\circ$
 Uncut chip thickness $t_0 = 0.2$ mm
 Width of cut $w = 20$ mm
 Cutting velocity $V_c = 0.6$ m/min

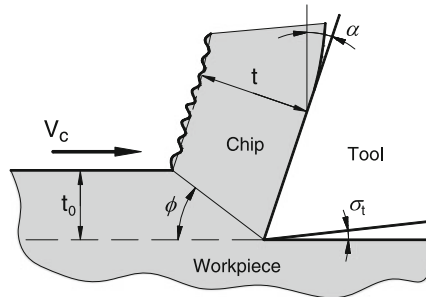


Fig. 21.45 Process tribology test based on orthogonal cutting experiment

The experimental measurements of the chip thickness, cutting and thrust forces provided the following data:

Chip thickness $t = 0.795$ mm
 Cutting force $F_c = 613$ N
 Thrust force $F_t = 320$ N

- Find the coefficient of friction μ .
- Determine the percentage change in the chip compression factor if the coefficient of friction is reduced by 20 %.

Simulative Tribology Tests Based on Pin-on-Disc

Figure 21.46 shows the plot of the normal F_N and tangential F_T forces as a function of time obtained from an experimental pin-on-disc test (Chap. 21, Sect. 2.2) that was carried out under dry conditions, without protective gas shield.

- Plot the tangential force F_T as a function of the normal force F_N and find the coefficient of friction μ .
- Provide an estimate of the surface roughness R_a of the disc.
- Explain how many rotations of the disc are necessary for calibrating the coefficient of friction μ .
- Assuming that the contact area between the pin and the rotating disc is constant during the test, plot the coefficient of friction μ as a function of the contact pressure.

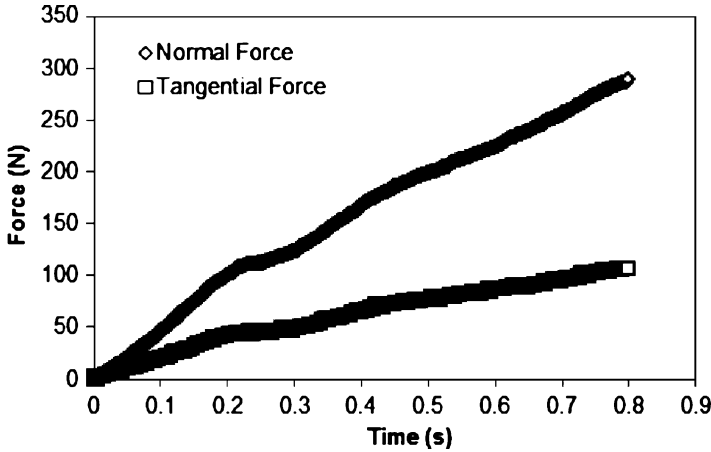


Fig. 21.46 Experimental forces measured on a pin-on-disc test performed with a Lead-stainless steel tribo-pair

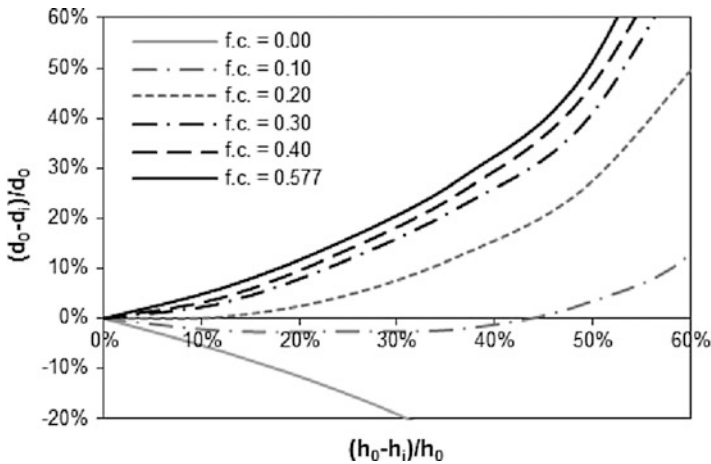


Fig. 21.47 Friction calibration curves obtained with the finite element computer program I-form

Simulative Tribology Tests Based on Ring Compression

The simulative tribology tests based on ring compression that were described in Chap. 21, Sect. 2.2 utilize specimens that have a geometrical ratio $D_0: d_0: h_0$ (refer to the detail on Fig. 21.19a) with the following dimensions 24:12:8 mm.

- (a) Find the coefficient of friction μ of the tribo-pair if the change in inner diameter of the specimen is equal to 15 % after 40 % reduction in height. Make use of the friction calibration curves shown in Fig. 21.47.

- (b) Ignore barrelling and determine the outer diameter of a ring test specimen after 45 % reduction in height if the coefficient of friction $\mu = 0.1$.

Solutions to Exercises

Process Tribology Test Using Orthogonal Metal Cutting

- (a) The coefficient of friction is obtained from (21.1),

$$\mu = \frac{F_t + F_c \tan \alpha}{F_c - F_t \tan \alpha} = \frac{320 + 613 \tan 0}{613 - 320 \tan 0} = 0.522$$

- (b) The original chip compression factor is obtained dividing the chip thickness by the uncut chip thickness:

$$\frac{t}{t_0} = \frac{0.795}{0.2} = 3.975$$

The coefficient of friction μ is expressed as a function of the friction angle β ,

$$\mu = \tan \beta$$

Therefore, when the coefficient of friction μ is reduced by 20 % the friction angle becomes,

$$\beta = \tan^{-1}(0.8 \cdot 0.522) \approx 0.396$$

Applying the well-known shear-angle relationship of orthogonal metal cutting due to Merchant,

$$\varphi = \frac{\pi}{4} + \frac{\alpha}{2} - \frac{\beta}{2} \rightarrow \varphi = \frac{\pi}{4} + \frac{0}{2} - \frac{0.396}{2} \approx 0.587$$

This result allows determining the new value of the chip compression factor as (21.3):

$$\frac{t}{t_0} = \cot \varphi \cos \alpha + \sin \alpha, \alpha = 0^\circ \rightarrow \frac{t}{t_0} = \cot \varphi$$

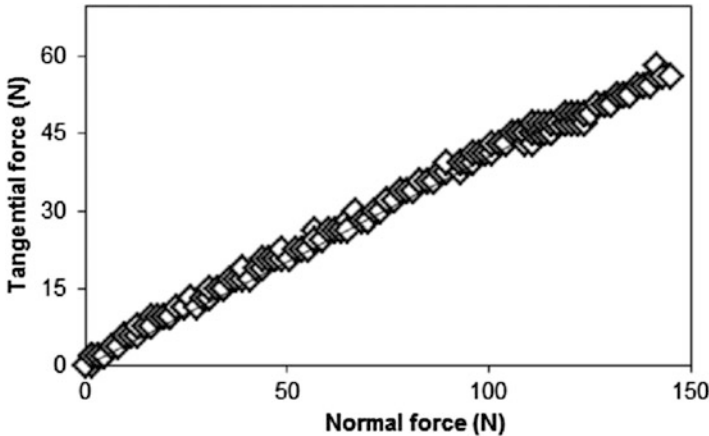
$$\frac{t}{t_0} = \cot \varphi = \cot(0.587) \approx 1.501$$

Under these circumstances, the percentage change in the chip compression factor is obtained from,

$$\frac{3.975 - 1.501}{3.975} \cdot 100 \approx 62.2\%$$

Simulative Tribology Tests Based on Pin-on-Disc

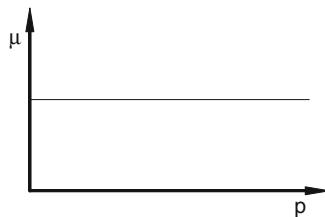
- (a) From the plot of the normal F_N and tangential F_T forces as a function of time it is possible to obtain the following evolution of the tangential force with the normal force applied on the pin:



The resulting coefficient of friction μ is obtained from the slope of the interpolation line that passes through the experimental data points,

$$\mu = \frac{F_T}{F_N} \approx 0.406$$

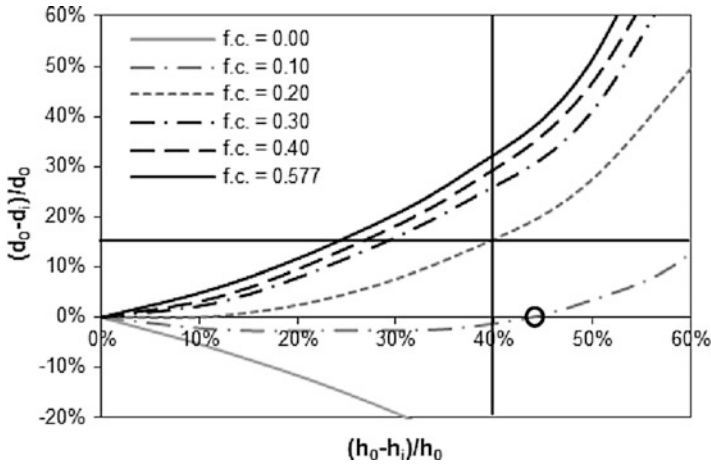
- (b) The surface roughness $R_a \cong 0.04 \mu\text{m}$ from Fig. 21.35.
- (c) Only a single turn, in order to avoid contamination due to the pin rubbing the disc on the same track.
- (d) Because the experimental data points in a) can be interpolated by a line it follows that the coefficient of friction μ is constant and independent of the applied normal force F_N .



If the contact area between the pin and the rotating disc is constant during the pin-on-disc test it follows that μ is constant and independent of the applied normal pressure p

Simulative Tribology Tests Based on Ring Compression

(a) The auxiliary (vertical and horizontal) lines included in the following figure allow determining the coefficient of friction $\mu = 0.2$



(b) Observation of the previous figure allow us to conclude that the change in the inner diameter of the ring test specimen for a coefficient of friction $\mu = 0.1$ after 45 % reduction in height is zero (refer to the open circular mark in the above figure),

$$\frac{d_0 - d_i}{d_0} = 0 \rightarrow d_i = d_0$$

The corresponding height of the specimen is obtained from,

$$\frac{h_0 - h_i}{h_0} = 0.45 \rightarrow h_i = 0.55 h_0$$

Thus, applying volume conservation, the outer diameter is obtained from,

$$\frac{\pi}{4} (D_0^2 - d_0^2) \cdot h_0 = \frac{\pi}{4} (D_i^2 - d_i^2) \cdot 0.55 \cdot h_0 \rightarrow D_i = 30.487 \text{ mm}$$

Chapter 22

Tribo-chemistry and Tribo-corrosion

Sudeep P. Ingole and John Valdes*

Abstract Tribological losses at interfaces can cost important recourses such as time and money. Knowledge of interface chemistry is vital to understand fundamentals of tribological parameters. Sliding of two surfaces provide favorable thermodynamic parameters for chemical reactions to take place at these interfaces. The study of these reactions primarily studied under special fields of tribology, i.e., tribo-chemistry and tribo-corrosion. It is difficult to separate these two fields. Usually, study of tribo-corrosion deals with surface deterioration due to the synergism of tribological factors, electrical stimulus, and corrosion. The thermodynamics approach can be utilized to understand the tribo-chemical reactions. This chapter provides different approaches taken to study these two fields. In this chapter, some of the mechanisms responsible for and applications of tribo-chemical interactions are discussed for example tribo-emission, tribo-chemical polishing, tribo-chemistry of magnetic media drive. Tribo-corrosion of coatings and metallic materials is briefly discussed. The case study of complex tribo-chemistry in sugarcane roller mill is included.

*John Valdes retired from British Petroleum's Refining Centre, Texas City as Senior Chemist after 37 years of service

S.P. Ingole, Ph.D. (✉)
Department of Mechanical Engineering Texas A&M University, Galveston, TX, USA
e-mail: singole@joa.com

J. Valdes
College of the Mainland, Texas City, TX, USA

1 Introduction

The study of tribology is advanced to the extent that the sliding at the interfaces is no more simply a mechanical interaction. The two terms (i.e., tribo-chemistry and tribo-corrosion) are well known in the tribology community and applied in the wide range of applications for fundamental understanding of sliding interfaces. It is difficult to distinguish these two areas. This chapter provides some of the aspects of these two areas in tribology. Section 2 provides simple and advanced approaches in studying the sliding interfaces and its usefulness in different applications such as magnetic media drives and polishing. Tribo-corrosion primarily is of concern when reaction products at the sliding interfaces are deteriorating effects such as in gear, bio-joints, dental implants etc. A case study of sugarcane mill roller shaft is presented. The tribo-corrosion in medical applications is discussed in a separate chapter.

2 Tribo-chemistry

The study of chemistry of surface interactions during sliding is commonly known as tribo-chemistry. This is a specialized field of chemistry which deals with the chemical and physio-chemical interactions of mating surfaces [1, 2]. It is highly inter-disciplinary that encompasses fields like mechanical engineering, surface chemistry, physics, mechanics, and biomedical, among others. The conditions present at the interfaces become extremely complex during sliding, which involve high contact stress, temperature increase, and chemical reactions between sliding materials. It becomes further complicated when external stimuli are present such as lubricant, corrosive environment etc.

2.1 *Chemical Reaction Between Lubricant and the Substrate (Simplified Approach)*

The chemical reaction depends on thermodynamic variables such as time, concentration of reactant species, temperature, pressure, characteristics of surfaces involved such as chemical activity, reactivity, and surface energies etc. The complex reaction/chemical process takes place at sliding interfaces with the lubricant environment and sliding materials under extreme conditions (i.e., high speed, high temperature, etc.). In a simple approach to study complex processes at the interface could be the approach of thermodynamics. This concept was utilized by Orcutt et al. [3] to understand the interfacial reaction during sliding. In general, the interfaces can be formed between:

1. Metallic–metallic system
2. Metallic–ceramic system
3. Metallic–polymeric system
4. Ceramics–ceramics system
5. Ceramics–polymeric system
6. Polymeric–polymeric system

and combinations with composites formed by these systems.

The free energy change will be an indication of the possibility of the occurrence of reaction. The positive free energy change will indicate that no reaction has taken place at the interface and the negative free energy change will indicate the possibility of the reaction to take place [3].

The typical equation for the free energy formation of a reactant is:

$$\Delta F_{\text{Reaction}}^{\circ} = \sum (\Delta F_{\text{Product}}^{\circ} - \Delta F_{\text{Reactant}}^{\circ}) \quad (22.1)$$

In this simplified approach, the assumptions made were [3]:

1. The effect of alloying element of the sliding surfaces are eliminated
2. No reaction occurs between surrounding gas with either lubricant or sliding surfaces and
3. Reaction between lubricant and sliding surfaces forms a simple binary compound

The possibility of the reaction at sliding interface is governed by the free energy change (ΔF) of the accompanying reaction between the interacting species. For example, this approach can be applied to the reaction between mercuric sulfide and nickel at 1200°F which gives -21 kcal (ΔF of HgS is $+5$ kcal/mol, ΔF of NiS is -16 kcal/mol, and ΔF of Ni and Hg is 0 kcal/mol). However, this approach is not very useful as in realistic sliding where alloying elements can influence tribo-chemical reactions involved and surrounding gases can participate in the reactive environment at the interfaces.

Authors also used this approach for selection of lubricant for rolling disk elevation. They used the solid lubricants such as solid binary sulfides, selenides, tellurides, oxides, chlorides, and other commonly used compounds as high temperature solid lubricants. The two sliding interfaces used were titanium carbide–nickel cermets and cast cobalt–chromium–tungsten alloy. Nickel and Cobalt were used as substrate reactants to calculate ΔF . Based on these calculations Ag_2S , Bi_2S_3 , HgS , PbO , CuO , and graphite were the most promising candidates.

2.2 Thermochemical Reaction at the Sliding Interface

Approach of Orcutt et al. [3] was practical but over simplified. There are more complexities that need to be understood. Usually surfaces are protected to reduce the friction and wear rate. Therefore, the materials removal has decreased

drastically resulting in mild surface wear. In case of mild wear, the surface chemistry becomes increasingly important. During mild wear process only a single layer is removed during each sliding cycle. The removed surface can transfer to the counter part of freely available at the sliding interface. The freshly exposed surfaces become available for surrounding therefore the chemistry becomes important for lower wear rates [4]. Singer developed the model to explain the thermochemical wear for mild wear rates [4]. He utilized second law of thermodynamics to describe the possibilities of reaction at the interface.



A and B are reactants and C and D are products. The number of products formed can be determined by the Gibb's Phase rule. At constant temperature and pressure, number of products of reaction is less or equal to the number of elements involved in the reaction. The possibility of product formed is determined by Gibb's free energy (G). The lower the value of G higher the possibility of product to be formed involving those elements. Therefore, for reaction in (22.2), the energy equation can be written as [4]:

$$\partial G = (cG_T^C + dG_T^D) - (aG_T^A + bG_T^B) \quad (22.3)$$

where

$$\partial G_T = \partial H_{298}^o - T \partial S_{298}^o \quad (22.4)$$

For the case of Mo-S-O system, author represented the calculations in the graphical form (Fig. 22.1) [4].

Based on the tie line shown by dashed line in Fig. 22.1a, and using Lever rule (Fig. 22.2b), for 30 % concentration of Oxygen, the predicted phases were 55 % MoS₂, 30 % SO₂, and 15 % MoS₂ (Point A). 20 % SO₂, 67 % O, and 13 % MoO₃ were predicted for 90 % oxygen concentration (point B) [4].

2.3 *Tribo-emission*

The emission of electrons, ions, photons, and neutral particles during tribological surface damage is called tribo-emission [5]. Tribo-emission is a specific case of exo-electrons in which these negatively charged particles become available when two surfaces slide together. It is believed that these electrons play a significant role in tribo-chemical reactions under boundary lubrication conditions. These electrons can be emitted in both metal and nonmetal sliding [6].

Charges and photons were emitted simultaneously from the sliding surface of semiconductor and insulators. In conducting surface sliding, only charges were emitted. Mechanical properties such as hardness of the surface have an influence on

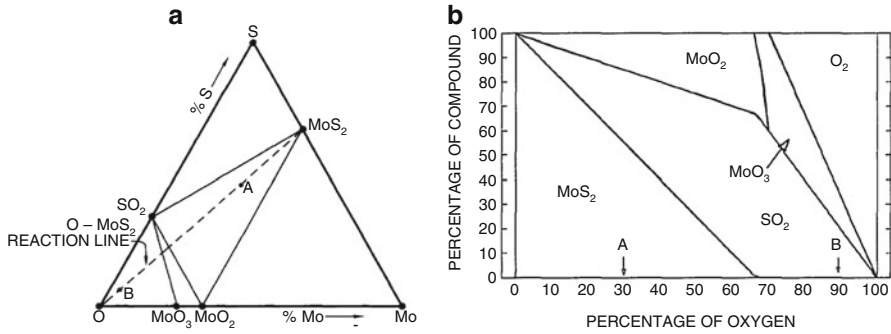


Fig. 22.1 Equilibrium phase diagram for Mo-S-O system (with permission from Elsevier Limited) [4]

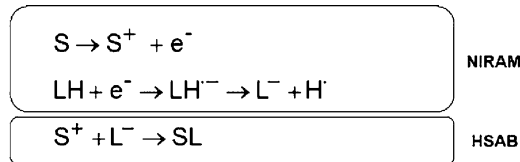


Fig. 22.2 NIRAM–HSAB mechanism, *S* surface site, *LH* lubricant molecule, e^- electron emitted under boundary lubrication conditions [14, 15]

the emission of negative charges. Higher hardness of the sliding surface resulted in lower intensity of emission of negative charges. Additionally, increased applied load and sliding speed increase intensities of both charges and photon emission. The mechanisms of these emissions in conductor and insulators are different. In the case of metals, exo-electrons are emitted by interaction of the fresh metals surface and the surrounding gas molecules [5].

The tribo-emission effect was demonstrated in carbon dioxide formation from carbon monoxide and oxygen in presence of sliding between aluminum oxide and palladium. The reaction between two chemi-sorbed gases (i.e., carbon monoxide and oxygen) was enhanced due to friction particularly the formation of carbon dioxide from carbon monoxide and oxygen was enhanced. The activation energy of this reaction related to friction was found to be 2.49 kJ/mol. The contribution of friction in order to speed up the chemical reaction is called tribo-catalysis. The exo-electrons associated with friction attach themselves to the chemisorbed species and make the negative-ion-radicals. These radical react with each other and form carbon dioxide [7].

2.3.1 Tribo-chemistry of Ceramics

The energy presence (as a result of operating conditions such as temperature) at the interface during the sliding of ceramics surfaces plays a vital role to determine the

chemical reactions and products formed during sliding. Some examples are listed below: The high reactivity of ceramics with water when tribo-tested in air environment causes to formation of oxide and hydroxides [8]. Low temperature (below 200 °C) sliding of alumina is primarily dominated by tribo-chemical reactions between water vapor and the formation of hydroxide film on the sliding surface [8, 9]. Low temperature sliding of silicon carbide is dominated by the tribo-chemical reactions between water vapors and silicon carbide. At higher temperature surface oxidation governs the friction [8, 10]. Low temperature (below 400 °C) sliding of silicon nitride is dominated by the tribo-chemical reaction and formation of silicon hydroxide. Surface oxidation of silicon nitride controls the surface phenomenon at temperature greater than 900 °C [8, 11]. The tribo-chemically formed oxide layer provides the lubrication [12, 13]. The inter-facial chemistry depends on the reactions with water and other organic lubricants. The enhanced activity of silicon nitride is explained based on the active sites formed on the surface and the activation of tribo-emission. The radical active sites found on the surface of silicon are divided into two categories viz. homolytic cleavage of Si bond, and heterolytic bond cleavage [14].

The tribo-chemical reactions are explained based on the Negative-Ion-Radical-Mechanism (NIRAM)-HSAB (Hard and soft acid bases) theory [15]. According to this theory, low energy tribo-emitted electrons with 1–4 eV initiate tribo-chemical reactions. The lubricant reacts with the activated sliding surface by the frictional work. The surface forms cations and emits low energy electrons which then react with lubricant a molecule which is primarily hydrocarbon. The radical-ion formed during this reaction split into the hydrogen radical H^+ and the anion L^- . L^- recombines with the cation to produce new species (Fig. 22.2).

During tribo-chemical reactions of silicon nitride, flat surfaces decreased the stresses at the interface as the water or alcohol based insoluble products acted as lubricants and serve as a protective film [14]. Silicon nitride reinforced with hexagonal boron nitride under distilled water lubrication reduced the coefficient of friction drastically. The worn surface showed SiO_2 and B_2O_3 formation on the surfaces. These tribo-chemical reaction products are formed due to the oxidation of debris and form a uniform film on the surface. These surface films made the sliding surfaces very smooth and lead to reduced coefficient of friction [16].

2.4 *Tribo-chemistry in Magnetic Storage Devices*

Magnetic disk drives and slider (head) must fly and land during each operation of switch on and off, which is also termed as contact start–stop (CSS) of disk drive. During this operation physical contact between drive and slider occurs [17]. Magnetic surface of drive is protected with lubricant layer to avoid wear. Further, environmental conditions such as temperature and humidity affect this lubrication characteristic.

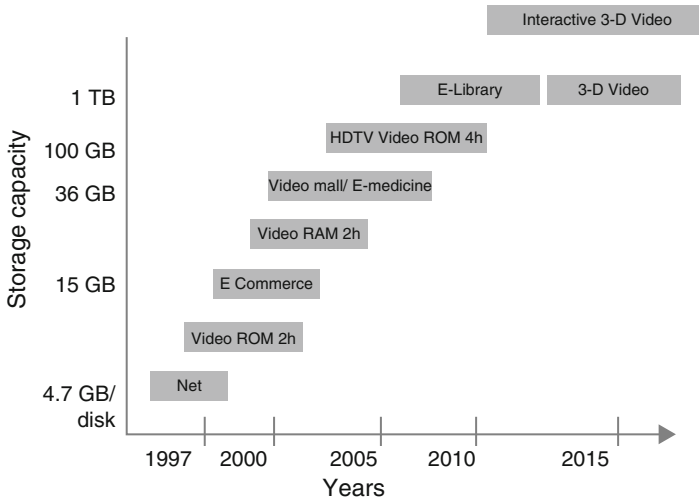
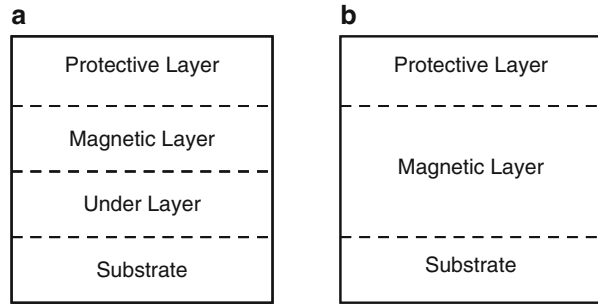


Fig. 22.3 Capacity demand of information storage on magnetic disk (With permission from Elsevier) [26]

As the importance was pointed out by Feynman [18, 19], the underline theme of nanotechnology is to miniaturization [20]. For example, these developments are required to meet the growing demand for higher capacity of information storage on magnetic disk drives (Fig. 22.3). However, the principle of magnetic disk drive has not changed much over a very long period of time. Magnetic recording was invented in 1898 by Valdemar Paulsen [21]. During its historical development [21], the surface area of disks has shrunk and its storage capacity increased. It experienced the tremendous increase in the areal density [22, 23]. The areal density is growing about 100 % per year with steady reduction in head media interface (HDI) [24] and increase in the frequency of head–disk contacts [25]. This has implications not only on recording device modeling, materials, fabrication, metrology, characterization, but also on tribology of the head–disk interface [26]. Menon and Gupta described that the head width, gap length and the magnetic and mechanical spacing are the limitations for these devices. The transducer width governs the track density whereas bit density depends on the gap length and magnetic spacing [26]. Along with the cost reduction, non-computer markets also opened up for the magnetic disk storage [23]. For higher data storage, smaller track width (microns) and even smaller bit length (nanometers) are required [27, 28]. To develop the newer technologies, the tribology of HDI becomes very important as with the increasing storage capacity, reduced track and bit length, and writing and reading magnetic information is a near field process [17]; the small separation and optimum lubrication on the surface are necessary.

Fig. 22.4 Schematic of cross section of (a) magnetic disk (b) magnetic tape [31]



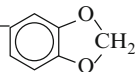
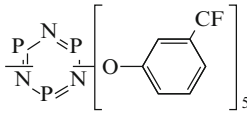
2.4.1 Lubrication Criteria for Head–Disk Interface (HDI)

The landing zone is usually textured to reduce wear. To reduce wear the friction (i.e., static and kinetic) needs to be low [29–31]. As discussed by Mate [17] and Bhushan's group [32, 33], a good HDI requires, (a) good boundary lubrication, (b) mobility of lubricant molecule, (c) good surface affinity of lubricant molecules for disk surfaces, (d) low volatility, (e) low surface tension, and (f) thermal and chemical stability. Klaus and Bhushan [32] included other criteria such as (a) chemical inertness to metals, glasses, plastics, and non deposit forming to insure no damage to heads, guides, and devices, (b) Solubility in organic solvents [30]. When the slider strike the disk surface with speed higher than 10 m/s, shearing, interface heating [17, 34], and tribo-emission of electron [17, 35] can damage the lubricant film. Additionally, the particulates at HDI increases the friction can cause error writing and reading the information [24]. The schematic of cross section of magnetic disk and magnetic tape is provided in Fig. 22.4 [31].

2.4.2 Ultrathin Carbon Lubricant Over-Layer

Wear resistant carbon coating is applied to head and disk for corrosion and protection from environmental exposure. This film also provides wear resistance when dry contact occurs during flying and landing. The coating is about 5–10 nm thick [26]. The growth in storage density of magnetic media will demand the thickness of overcoat reduced to 2 nm [36]. Advantages of Diamond like Carbon (DLC) are its cost-effectiveness, chemical immunity, and engineering mechanical properties. Its adhesion and failure due to delamination is a cause of concern which can jeopardize the functionality of the disk media [26]. Under decreased spacing, temperature and humidity becomes extremely important for the lubrication performance. The high speed of the disk drives also put higher stresses on the lubrication film at HDI [25]. The water interaction with the PFPE showed that $\text{CF}_3\text{CH}_2\text{OH}$ adsorbs on the amorphous carbon overcoat (i.e., $\alpha\text{-CH}_x$) and $(\text{CF}_3\text{CF}_2)_2\text{O}$ has weak interaction in presence of water. This suggests the higher mobility of lubricant in humid conditions [25].

Table 22.1 PFPE Lubricants list adopted from [30, 31]

	$X - CF_2(OCF_2CF_2)_n(OCF_2)_mOCF_2 - X(0.5 < n/m < 1)$
Z	$X = - OCF_3$
Z-DO1	$X = - CH_2OH$
Z-DIAC	$X = - COOH$
Z-Tetraol	$X = - CH_2 OCH_2 \underset{\substack{ \\ OH}}{CH} CH_2 OH$
AM2001	$X = - CH_2OCH_2$ 
A20H	$HOCH_2CF_2(OCF_2CF_2)_n(OCF_2)_mOCF_2CH_2O$ 
Mono	$F - (CF_2CF_2CF_2O)_1 - CF_2CF_2CH_2 - N(C_3H_7)_2$

2.4.3 Perfluoropolyether (PFPE) Lubricants

Lubrication selection depends on the viscosity especially for hydrodynamic lubrication. Ionic liquids can be engineered for their viscosity based on the anions and cations combination. Due to their low vapor pressure and high thermal stability, ionic liquids are suitable for hydrodynamic lubrication [37]. Halogen containing ionic liquids showed low friction and wear when operate in boundary lubrication. The metal fluoride formed due to tribo-chemical reaction provide low friction [37]. Ionic liquids are traditionally used as lubricant in magnetic media over 25 years due to its better lubrication properties [30, 31]. The commercial PFPE lubricants are listed in Table 22.1. The list is adopted from [30] and [31].

Typical PFPE has a linear backbone structure with end group. The nature of end group determines the interaction with solid surface and subsequently the lubrication properties [29]. A thin layer of PFPE is applied on the drive surface to provide lubrication at HDI [29]. Kondo [30, 31] studied lubrication properties of modified PFPE. Carboxylic acids ammonium salt showed more stable friction due to its stronger adsorption (adhesive interaction). Author suggested that the ammonium salt end group can be used in commercial PFPE what makes the friction independent on the PFPE backbone. Hydrocarbon chains increased the cohesive interaction. The olefinic end groups increased the friction due to weaker cohesion [30, 31]. The bonding between lube and drive surface increased the wear durability; however, lube bonding increased coefficient of friction [38]. Coefficient of friction and wear were observed to be high for slower speed but the values decreased at high speeds [38].

2.5 *Tribo-chemical Polishing*

Tribo-chemical polishing (TCP) is an abrasive free materials removal process in which chemical reaction is facilitated by friction and contact stresses at the sliding interface [39]. The polishing fluid used in this process plays an important role as a driving force for reaction rates. This process is different from the Chemical Mechanical Polishing (CMP) which is predominantly used in semiconductor industry. CMP involves the abrasive media embedded in pH controlled solution. The removal rates and surface finish are functions of size of abrasive particles, and pH of the solution. It also requires polishing pads (polyurethane or polyethylene). More information on CMP can be found in the separate chapter on CMP of this textbook.

TCP utilize the chemical reactivity of the solution and polishing media. This chemical reaction is stimulated by friction between the asperity contacts [40]. The stress inducted chemical reaction control the removal rate and surface finish. There is no mechanical deformation involved, therefore the surface resulted from TCP is free of defects such as cracks, pores, etc. TCP is carried out by rubbing target surfaces against the suitable surface in present of suitable chemical solution (pH controlled). Hah and Fischer explained the polishing kinetics using Preston's equation [39].

$$\frac{\Delta H}{\Delta t} = K_p \frac{L}{A} \frac{\Delta S}{\Delta t} \quad (22.5)$$

where ΔH is the thickness of materials removed, t is the time elapsed, L is applied load, A is contact area (macroscopic), S is the sliding distance, K_p is the polishing rate (Preston's constant).

3 **Tribo-corrosion**

Tribo-corrosion is the phenomenon which in the presence of mechanical, chemical, and electrical stimulus deteriorates the sliding system. The individual processes viz., mechanical, chemical, and electrical provide the enriched environment and thermodynamically feasible conditions for this deterioration to occur. The possibilities of combinations that can experience tribo-corrosion [41] are (a) solid particles erosion, (b) abrasion, (c) cavitation erosion, (d) fretting, (e) biological solutions, and (f) sliding wear and tribo-oxidation. Tribo-corrosion is a multidisciplinary field of study that clarifies the in situ durability of interacting materials surfaces with the synergetic approach of materials surface, an environment, and a mechanical contact. Therefore, tribo-corrosion is of interest to researchers in cross-disciplines ranging from materials science, surface engineering, electrochemistry, tribology, biology, and medicine [42].

There are several examples where tribo-corrosion is responsible for the failure of the surfaces. The gear failure due to wear and corrosion is one example of the tribo-corrosion. Tribo-corrosion in real life occurs in dynamic conditions, for example bio-tribo-corrosion of the human joints. Tribology plays a vital role alongside the corrosive effects of the fluids present at the interface. Therefore, the shortening of life span of bio-joints due to the tribo-corrosion in presence of bio-fluids is of prime concern [43]. In metal-on-metal total hip replacements, the tissue responses are susceptible to the reaction products generated during sliding. These products form due to the combined effects of wear and corrosion [44, 45]. In the case of austenitic cobalt-chrome-molybdenum (CoCrMo) alloys, the tribological layer in metal-on-metal hip replacements was primarily graphitic carbon. Graphite reduced the friction and subsequently less wear and corrosion were observed [44]. At the sliding contact, failure is observed primarily due to surface fatigue; carbides of Mo and Cr were fractured and failed at the surface due to indentation and caused abrasion which subsequently resulted in weight loss. At the same time, the tribo-chemical reactions between proteins present at the joint and sliding materials also contributed to the surface deterioration. However, the tribo-chemical layer on the surface avoided the adhesion; therefore, the main contributing mechanism for failure was surface fatigue and abrasion along with the tribo-chemical reactions [46].

Deterioration of tooth structure is also an example of tribo-corrosion. The failure is typical a tribo-corrosive phenomenon, which includes a combination of adhesion, abrasion, attrition, chemical degradation, and fatigue. These processes take place almost simultaneously [47–49]. Readers are further advised to refer to the comprehensive reviews on tribo-corrosion of different sliding systems which are discussed by several authors [41, 43, 50].

Corrosion and wear processes are complementary to each other during deterioration. The corrosion at the interface increases the wear rate, and wear enhances the corrosion rate. The materials selected for tribo-systems are immune to the corrosion if used alone in a harsh environment, but due to wear at the interface tribo-corrosion takes place [50]. Furthermore, high stresses at the interface create favorable conditions for mechanical deterioration. A temperature raise stimulates chemical reactions between sliding components and the surrounding. These conditions are enhanced when the sliding systems are open to the external environment or in contact with lubrication. Corrosion reactions are also triggered by the electrical stimuli. The passive film is normally damaged or removed by tribological contact (e.g., sliding or rolling) and, as a result, the corrosion rate likely increases [51–53].

The tribo-corrosion can be explained in a simple way by studying the effects of surface interaction under applied load to the electro-potential behavior. Electro-potential behavior provides the information of corrosive behavior of the interaction surfaces. During sliding, the passive film is fractured and is exposed to new surface and new galvanic cell [54, 55]. This behavior can further be correlated to the sliding frequency and the time available to re-passivate the new surface formed [54, 55]. Pourbaix diagram [56] is the representation of the passive, active, and immune behavior of metallic elements in aqueous solutions. It is plotted as E-pH. It however does not provide information on the corrosion rate of materials, and

kinetic aspects of corrosion processes. The modified Ponthiaux diagram can be created by considering the mechanical load and sliding parameters to analyze the tribo-corrosion processes for metals and alloys [57].

3.1 *Tribo-corrosion of Coatings*

Replacement of expensive solid alloy component with coating on cheaper carbon steel is a potential cost-effective method. If the application is just for corrosion protection, organic coating performs better. It will not be an efficient option when high energy solid particles impingement is present. Ceramics are an option for high priority applications. Metallic coatings pose a potential and cost-effective method for tribo-corrosive applications. For cost-effective applications, aluminum, copper, nickel, and zinc alloys, and their composites are a suitable choice. In aggressive sliding environment Co and Ni based coating are suitable. For very high energetic flow WC-CoCr or WC-NiCr cermets are also suitable [41, 58–60].

The tribo-corrosion controlling parameters for coatings are coating composition, microstructure, defect level, and its interfacial strength (adhesion and cohesion) with the substrate. Metallic surfaces can be protected using metallic or hard oxide coatings from tribo-corrosion [41]. Most thermally sprayed cermet coatings for tribo-corrosion applications are hard particle embedded in metallic matrix as binder. The dissolution of binder at the interface of hard particles is a key mechanism for corrosion contribution. The porosity also plays a role as penetration of the electrolyte in the porous coating increases the corrosion [41].

3.2 *Tribo-corrosion of Metallic Materials [61]*

Passivated metallic materials are susceptible for tribo-corrosion in unidirectional sliding contacts in presence of an electrolyte. The material loss of components during wear tests is calculated using the unit area per cycle based on the materials loss and surface area and the frequency of the sliding (number of cycles) as [62]:

$$W_i^j = \frac{W_i^i}{NA_i} \quad (22.6)$$

“i” is “repass” or “act” and “j” is “c” or “m” where “c” represent corrosion and “m” represents mechanical action.

When we compare W_{repass}^c and W_{act}^c

Then the tribo-corrosion of passivating materials can be predicted by the ratio K_C [62]

$$K_C = \frac{W_{act}^c + W_{repass}^c}{W_{act}^m + W_{repass}^m} \quad (22.7)$$

where

W_{act}^c = Loss of material in wear tract due to the corrosion in active area

W_{repass}^c = Loss of material in wear tract due to the corrosion of re-passivated materials

W_{act}^m = Loss of material in wear tract due to the mechanical wear in active area

W_{repass}^m = Loss of material in wear tract due to the mechanical wear of re-passivated materials

When $K_C > 1$ the tribo-corrosion is primarily controlled by the materials loss due to corrosion and depends on the reactivity of the materials

$K_C < 1$ the mechanical wear predominates the tribo-corrosion process.

$K_C < < 1$ the tribo-corrosion is dominated by the passivated film destruction.

3.3 Case Study: Laboratory Simulation of Tribo-corrosion of the Sugar Mill Roller Shaft [63]

Three-roller mill [64] is often used to crush sugarcane for juice extraction and is an important equipment in sugar manufacturing globally (Fig. 22.5a). Top roll shaft of journal surface often indicates the wear damage. Wear on the surface of the shaft and initiation of crack leads to the crack propagation. Consequently the shaft fails due to low cycle fatigue (Fig. 22.5b). Untimely failure of the shaft can drastically reduce productivity and has a financial negative effect due to downtime and unusually high maintenance costs. Therefore, roller shaft failure in the sugarcane mill industry is a major cause of concern. This failure also affects the reliability of the system. In most cases service life of the roller shaft is reduced by 50 % due this failure. These shafts are made up of EN8 steel.

In laboratory simulated tests, the coefficient of friction of EN8 was decreased in lubricating oil when contaminated with sugarcane juice, bagasse. The coefficient of friction during lubricated with contamination friction test was less than dry, contaminated test, and lubricated test conditions alone. This might have happened due to the presence of reaction products. There are possibilities of reactions to occur between sugarcane juice, bagasse, lubricating oil, and sliding materials.

Material is subjected to stress corrosion cracking when exposed to corrosive environment. It has been seen that surface damage occurs due to the material subjected to the simultaneous action of wear and corrosion. In this study it was found that the movement of the bagasse particles over the surface caused abrasion

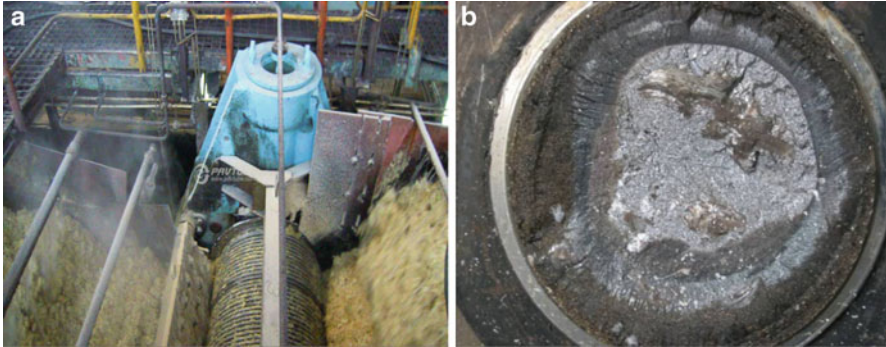


Fig. 22.5 (a) Sugar mill stand, (b) Failed shaft surface showing the crack flow pattern from surface to interior (with permission from Elsevier Limited) [63]

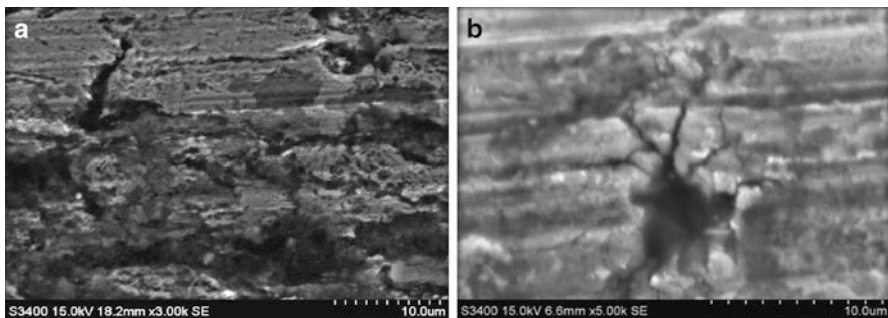


Fig. 22.6 Scanning electron micrographs showing the worn surface morphologies of EN8. (a) Contaminated condition, (b) Lubricated with contaminated condition (with permission from Elsevier Limited) [63]

and which might have resulted in the removal of material. Worn surfaces after contaminated condition friction tests showed deeply indented and rough surface. When lubricant oil was contaminated with sugarcane juice, bagasse, and water, it was observed that the deep grooves caused by abrasion were formed which can be realized from Fig. 22.6a, b. In this condition, wear is dominated by abrasion.

During sliding, surface damage and the rate of materials removal were severe. Surface cracks grew perpendicularly to the sliding direction. Contamination converted the wear from mild to severe. The worn surfaces have clearly shown large amount of cracks which indicate abrasive nature of wear and the dominating wear mechanism. Abrasive wear or abrasion was caused by the displacement of material from a solid surface due to hard particles or protuberances sliding along the surface. Severe and continuous abrasive wear along with corrosion over time can reduce the size and destroy the shape of a shaft.

4 Conclusions

Tribo-chemistry is one of the latest and important specializations of tribology. Tribo-chemical conditions generated at the sliding interfaces can be used for useful applications for example materials removal in tribo-chemical polishing. The understanding of tribo-chemistry is vital for lubrication of magnetic drives which must last during the life of the drive. In the thermodynamics approach of tribo-chemistry, the free energies of reactants determine the possibilities of the product of tribo-chemical reactions. Lever rule can be used to calculate the phases. In a process of tribo-emission, electrons, photon, ions, and natural particles can emit and can alter the surface chemistry. Surface coatings are cost-effective methods to mitigate corrosion but are not universal solution for deterioration of surfaces when present during sliding along with corrosion. Organic coatings can be used for corrosion only and can fail when surface stress due to tribological parameters present. Thermally sprayed ceramic coatings are alternative for extreme environment applications but have their own limitations in corrosive environment due to porosity.

References

1. Heinicke G (1985) *Tribochemistry*, Carl Hanser Verlag, Munich
2. Fischer T (1988) *Tribochemistry*. *Annu Rev Mater Sci* 18(1):303–323
3. Orcutt F, Krause H, Allen C (1962) The use of free-energy relationships in the selection of lubricants for high-temperature applications. *Wear* 5(5):345–362
4. Singer I (1991) A thermochemical model for analyzing low wear-rate materials. *Surf Coat Technol* 49(1):474–481
5. Nakayama K, Suzuki N, Hashimoto H (1992) Triboemission of charged particles and photons from solid surfaces during frictional damage. *J Phys D Appl Phys* 25(2):303
6. Dante R, Kajdas C, Kulczycki A (2010) Theoretical advances in the kinetics of tribochemical reactions. *React Kinet Mech Catal* 99(1):37–46
7. Hiratsuka KI, Kajdas C, Yoshida M (2004) Tribo-catalysis in the synthesis reaction of carbon dioxide. *Tribol Trans* 47(1):86–93
8. Jahanmir S (2002) Wear transitions and tribochemical reactions in ceramics. *Proc IME J J Eng Tribol* 216(6):371–385
9. Jahanmir S, Dong X (1994) Wear mechanisms of aluminum oxide ceramics. *Friction and wear of ceramics*, vol 6, *Materials Engineering*. Marcel Dekker, Inc., New York, NY, pp 15–49
10. Dong X, Jahanmir S, Ives LK (1995) Wear transition diagram for silicon carbide. *Tribol Int* 28(8):559–572
11. Jahanmir S, Fischer T (1988) Friction and wear of silicon nitride lubricated by humid air, water, hexadecane and hexadecane + 0.5 percent stearic acid. *STLE Trans* 31(1):32–43
12. Fischer TE, Liang H, Mullins WM (1988) Tribochemical lubricious oxides on silicon nitride MRS proceedings. 140: 339, doi: [10.1557/PROC-140-339](https://doi.org/10.1557/PROC-140-339)
13. Fischer TE, Tomizawa H (1985) Interaction of tribochemistry and microfracture in the friction and wear of silicon nitride. *Wear* 105(1):29–45
14. Dante RC, Kajdas CK (2012) A review and a fundamental theory of silicon nitride tribochemistry. *Wear* 288:27–38
15. Kajdas CK (2006) Physical and chemical phenomena related to tribochemistry, Chapter 12. In: Buzio R, Valbusa U (eds) *Advances in contact mechanics: implications for material science, engineering and biology*. Transworld Research Network, Kerala, pp 383–412

16. Chen W et al (2010) Tribochemical behavior of Si 3N 4-hBN ceramic materials with water lubrication. *Tribol Lett* 37(2):229–238
17. Mate CM (1998) Molecular tribology of disk drives. *Tribol Lett* 4(2):119–123
18. Feynman R (1961) Miniaturization. Reinhold, New York, NY, pp 282–296
19. Feynman RP (1960) There's plenty of room at the bottom. *Eng Sci* 23(5):22–36
20. Rao C, Cheetham A (2001) Science and technology of nanomaterials: current status and future prospects. *J Mater Chem* 11(12):2887–2894
21. Wood R, Takano H. Prospects for magnetic recording over the next 10 years. in *Proc. IEEE Int. Magnetics Conf.* 2006, San Diego, CA
22. Hayes B (2002) Computing science: terabyte territory. *Am Sci* 90(3):212–216
23. Coughlin TM (2001) High density hard disk drive trends in the USA. *J Magnet Soc Jpn* 25(3/1):111–120
24. Khurshudov A, Waltman RJ (2001) Tribology challenges of modern magnetic hard disk drives. *Wear* 251(1):1124–1132
25. Lei RZ, Gellman AJ (2000) Humidity effects on PFPE lubricant bonding to a-CH x overcoats. *Langmuir* 16(16):6628–6635
26. Menon AK, Gupta B (1999) Nanotechnology: a data storage perspective. *Nanostruct Mater* 11(8):965–986
27. Lambeth D et al (1996) Media for 10 Gb/in. < sup > 2</sup > hard disk storage: issues and status. *J Appl Phys* 79(8):4496–4501
28. Lambeth DN et al (1997) Present status and future magnetic data storage, in *Magnetic hysteresis in novel magnetic materials*. Springer, New York, NY, pp 767–780
29. Jhon MS, Choi HJ (2001) Lubricants in future data storage technology. *J Ind Eng Chem* 7(5):263–275
30. Kondo H. Ionic liquid lubricant with ammonium salts for magnetic media liquids in science and technology. In: Scott Handy (ed.) ISBN: 978-953-307-605-8, InTech http://cdn.intechopen.com/pdfs/20221/InTech-Ionic_liquid_lubricant_with_ammonium_salts_for_magnetic_media.pdf
31. Kondo H (2012) Tribochemistry of ionic liquid lubricant on magnetic media. *Adv Tribol* 2012:1
32. Klaus E, Bhushan B (1985) Lubricants in magnetic media—a review. *Tribol Mech Magnet Stor Syst* 2:7–15
33. Bhushan B (1996) *Tribology and mechanics of magnetic storage devices*. Springer, New York, NY
34. Novotny VJ, Pan X, Bhatia CS (1994) Tribochemistry at lubricated interfaces. *J Vac Sci Technol A* 12(5):2879–2886
35. Homola A (1996) Lubrication issues in magnetic disk storage devices. *IEEE Trans Magnet* 32(3):1812–1818
36. Robertson J (2001) Ultrathin carbon coatings for magnetic storage technology. *Thin Solid Films* 383(1–2):81–88
37. Kondo Y, Koyama T, Sasaki S (2013) Tribological properties of ionic liquids, ionic liquids: new aspects for the future. 127–141 <http://dx.doi.org/10.5772/52595>
38. Sinha SK et al (2003) Wear durability studies of ultra-thin perfluoropolyether lubricant on magnetic hard disks. *Tribol Int* 36(4–6):217–225
39. Hah S, Fischer T (1998) Tribochemical polishing of silicon nitride. *J Electrochem Soc* 145(5):1708–1714
40. Muratov VA, Fischer TE (2000) Tribochemical polishing. *Annu Rev Mater Sci* 30(1):27–51
41. Wood RJK (2007) Tribo-corrosion of coatings: a review. *J Phys D Appl Phys* 40(18):5502
42. Celis J-P, Ponthiaux P (2006) Editorial. *Wear* 261(9):937–938
43. Yan Y, Neville A, Dowson D (2006) Biotribocorrosion—an appraisal of the time dependence of wear and corrosion interactions: I. The role of corrosion. *J Phys D Appl Phys* 39(15):3200
44. Liao Y et al (2011) Graphitic tribological layers in metal-on-metal hip replacements. *Science* 334(6063):1687–1690

45. Langton DJ et al (2011) Adverse reaction to metal debris following hip resurfacing: the influence of component type, orientation and volumetric wear. *J Bone Joint Surg* 93-B (2):164–171
46. Wimmer MA et al (2001) The acting wear mechanisms on metal-on-metal hip joint bearings: in vitro results. *Wear* 250(1–12):129–139
47. Lambrechts P et al (2006) Degradation of tooth structure and restorative materials: a review. *Wear* 261(9):980–986
48. Lim B-S et al (2002) Effect of filler fraction and filler surface treatment on wear of microfilled composites. *Dent Mater* 18(1):1–11
49. Pallav P. Occlusal wear in dentistry, fundamental mechanisms, clinical implications, and laboratory assessment, in *Academisch Proefschrift*. 1996, ACTA, VU University Amsterdam.
50. Landolt D (2006) Electrochemical and materials aspects of tribocorrosion systems. *J Phys D Appl Phys* 39(15):3121
51. Buford A, Goswami T (2004) Review of wear mechanisms in hip implants: paper I-general. *Mater Des* 25(5):385
52. Dowson D et al (2004) A hip joint simulator study of the performance of metal-on-metal joints: part II: design. *J Arthroplasty* 19(8):124–130
53. Contu F, Elsener B, Böhni H (2004) A study of the potentials achieved during mechanical abrasion and the repassivation rate of titanium and Ti6Al4V in inorganic buffer solutions and bovine serum. *Electrochim Acta* 50(1):33–41
54. Pokhmurs'kyi V, Dovhunyk V (2010) Tribocorrosion of stainless steels (Review). *Mater Sci* 46(1):87–96
55. Chen G, Zhou Z (2005) Experimental observation of the initiation process of friction-induced vibration under reciprocating sliding conditions. *Wear* 259(1):277–281
56. Pourbaix M (1963) *Atlas d'équilibres électrochimiques*. Gauthier-Villars, Paris
57. Celis JP, Ponthiaux P, Wenger F (2006) Tribo-corrosion of materials: interplay between chemical, electrochemical, and mechanical reactivity of surfaces. *Wear* 261(9):939–946
58. Wheeler DW, Wood RJK (2005) Erosion of hard surface coatings for use in offshore gate valves. *Wear* 258(1–4):526–536
59. Allen C, Ball A (1996) A review of the performance of engineering materials under prevalent tribological and wear situations in South African industries. *Tribol Int* 29(2):105–116
60. Wood RJK, Mellor BG, Binfield ML (1997) Sand erosion performance of detonation gun applied tungsten carbide/cobalt-chromium coatings. *Wear* 211(1):70–83
61. Henry P, Takadoum J, Berçot P (2011) Depassivation of some metals by sliding friction. *Corros Sci* 53(1):320–328
62. Diomidis N et al (2009) A methodology for the assessment of the tribocorrosion of passivating metallic materials. *Lubri Sci* 21(2):53–67
63. Kakade AB et al (2013) Tribological behavior of sugar mill roller shaft in laboratory simulated conditions. *Wear* 302:1568–1572
64. Hugot E (1986) *Handbook of cane sugar engineering*. Elsevier, Amsterdam

Exercise

1. Describe briefly
 - (a) Tribo-chemistry
 - (b) Tribo-corrosion
 - (c) Exo-electrons

2. What is NIRAM–HSAB mechanism?
3. What are the criteria for lubrication in magnetic storage devices? Why is it necessary?
4. What are the factors affecting lubrication in magnetic storage devices?
5. Describe tribo-chemical polishing.
6. Describe one example of tribo-corrosion you have seen in everyday life apart from those are described in this book.

Chapter 23

Tribology in Chemical–Mechanical Planarization

Sukbae Joo and Hong Liang

Abstract Chemical–mechanical planarization (CMP) is one of the most important process steps in making integrated circuits. Tribology plays significant roles in material removal, polishing, and planarization. This chapter provides an introduction to CMP and discusses evolution, roles, and effects of tribology in this important industrial process. Tantalum and copper CMP are discussed here as two examples in understanding mechanisms of CMP.

1 Chemical–Mechanical Planarization (CMP)

1.1 Introduction to CMP

1.1.1 Brief History of CMP

Since the first invention of transistors by Bell Laboratory in 1947, integrated circuit (IC) technology has brought numerous benefits to humankind such as the personal computer, cellular phone, GPS (global positioning system), spaceship, smart implants that dose medicine on demand, and many other electronic devices [1]. These marvels of the IC technologies have improved the quality of our life. Since the early 1960s when Gordon Moore (cofounder of Intel) noticed that the number of transistors per die doubles every 18 months (Fig. 23.1), microelectronic devices have evolved with shrinkage in minimum feature size and increasing complexity of the circuit in the wafer level. The feasibility of feature size reduction and complication predominantly depends on the photolithography process. To obtain desired features and patterns across the wafer, each step of photolithography

S. Joo • H. Liang (✉)

Mechanical Engineering, Texas A&M University, College Station, TX, USA

e-mail: hliang@neo.tamu.edu

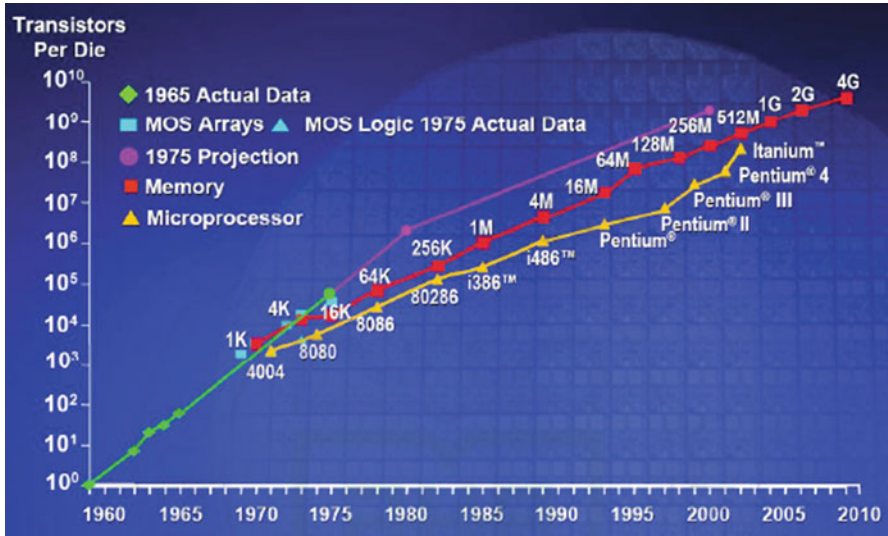


Fig. 23.1 Complexity of integrated circuits; Moore's law (Courtesy of Intel Corporation)

has to be accurately performed. For the formation of minute interlayers and multilevel structures, the depth of focus (DOF), a description of photolithography margin, becomes more critical [2]. The resolution of the DOF can be improved using either short-wavelength lights or large numerical apertures. However, this makes the DOF shallow and a much higher planarity is required to avoid fatal defects to the multilayer formation (Fig. 23.2). To overcome these challenges, it is essential to produce a flat surface by using viable and unique planarization methods.

In the early stages, various planarization methods such as reflow, spin-on-glass (SOG), and etch back had been used; however, these methods are not appropriate for interconnect structures which have more than three metal layers and provide only a limited local planarity (Fig. 23.3) [3]. To meet this strict requirement, CMP technology was invented by IBM in the early 1980s.

The first practical application of CMP was the planarization of interlayer dielectric (ILD) which is commonly known as oxide CMP, starting in 1989 [4]. The planarization of ILD enabled the fabrication of next levels such as the interconnection of metal in logic or dynamic random-access memory (DRAM) devices in 0.8 μm of the technology node [5]. Afterwards, the technology node was shifted to 0.35 μm with the application of shallow trench isolation (STI) CMP which enables compact isolation between transistors [6] and polysilicon CMP [7] as well as tungsten (W) CMP in the back-end-of-line (BEOL) process. W CMP gave the possibility of a technology node of under 0.18 μm and the necessity of copper (Cu) arose as the replacement of aluminum due to better conductivity and manufacturability. Since the dual damascene process has been introduced as Cu

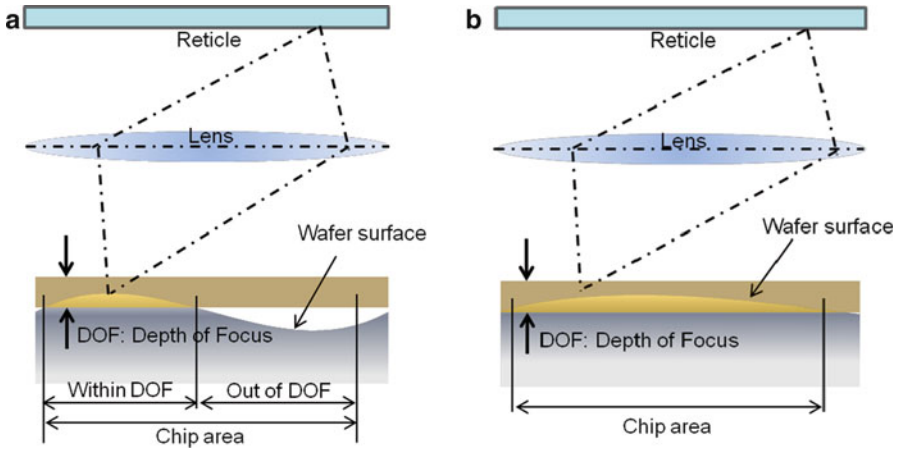


Fig. 23.2 Planarization requirements for the lithography process. (a) Poor planarization, (b) good planarization

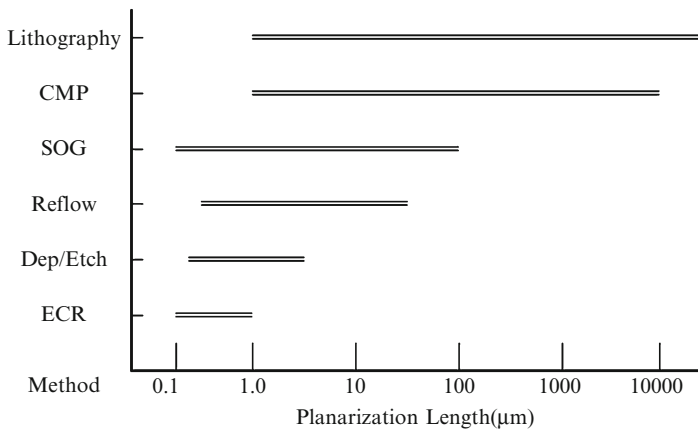


Fig. 23.3 Comparison of planarization length of various planarization methods [3]

metallization technology, the point of interest in CMP has been moved to Cu CMP [8, 9]. In the past 30 years, CMP has been widely used in back-end-of-line (BEOL) process and considered as long-term increasing item in semiconductor market. In 2007–2008, there was a stagnation in the demand of CMP consumables; however, recently the semiconductor wafer pass demand has increased by 20 % in 2010, and the CMP consumables market has been expected to increase from \$2.8 billion in 2008 to \$5.5 billion in 2013 (Fig. 23.4) for a compound annual growth rate (CAGR) of 14.7 % [10].

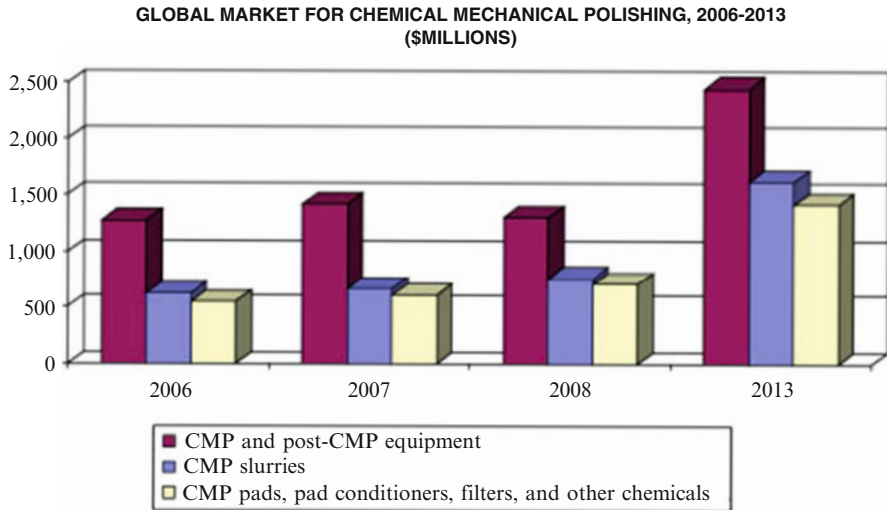


Fig. 23.4 Global market for chemical mechanical polishing [10]

1.1.2 Basics of CMP

Wafers

As a multilevel device wafer involves various materials and features in each level, there are different types of CMP processes depending on the target material, such as Si CMP, STI CMP, W CMP, Cu CMP, and ILD CMP. All of these CMP processes are very important and contribute to the successful production of electronic devices.

The CMP process in semiconductor manufacturing starts with bare silicon wafers. In the past, single-sided polishing was the general case. However, as the device feature size shrinks, a silicon wafer which has an ultrafine surface (nanotopography) is necessary for the good connection of STI, which is the following step. Simultaneous polishing of both sides for mirror surfaces is used recently for the preparation of front-end-of-line (FEOL) process. In this process, silicon wafer surfaces need to have a high-precision finishing which is haze-free and contamination-free [11]. After undergoing silicon wafer CMP, the wafers can be ready for the next step and be transferred to the device fabrication process.

Shallow trench isolation (STI) is another important microstructure in the FEOL process. The STI process can be defined as a method for electrical isolation by locating the insulator between each transistor. Conventionally, Local Oxidation of Si (LOCOS) has been used as an isolation method; however, due to the limit of bird's beak encroachment (Fig. 23.5 [12]), the field oxide thinning effect results in current leakage and is not allowed for the minimum feature under $0.25\ \mu\text{m}$ [13]. To meet the requirements of high packing densities and minimum feature size, the STI process has been introduced.

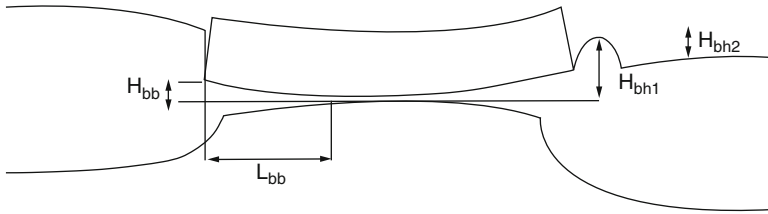


Fig. 23.5 LOCOS structure and bird’s beak and bird’s head [12]

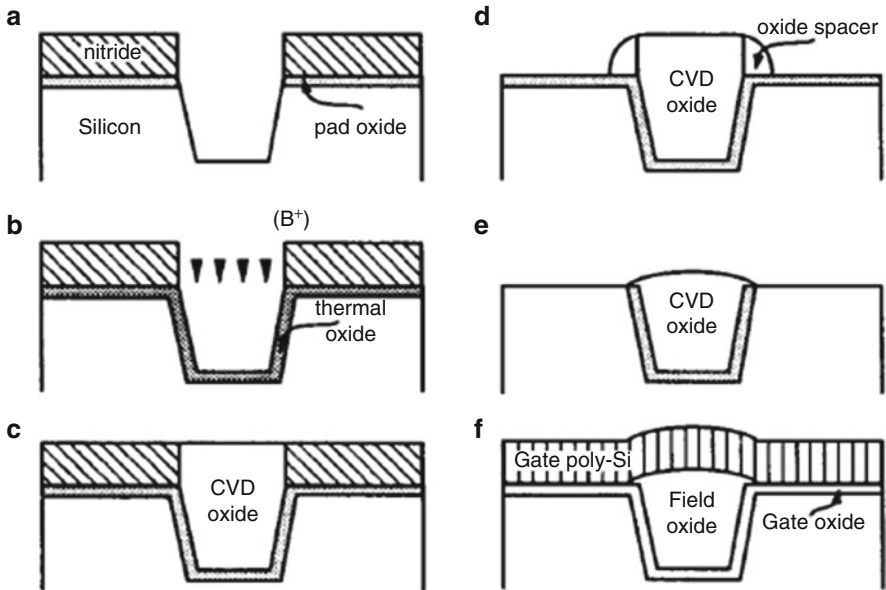


Fig. 23.6 The summary of shallow trench isolation (STI) process flow: (a) definition of the mask and trench, (b) B doping and trench oxidation, (c) CVD oxide and CMP planarization, (d) formation of oxide spacer, (e) pad oxide wet etch, (f) gate deposition and oxide growth [14]

Since the planarity of the STI structure directly affects the connection between BEOL and FEOL process, the STI CMP is significant enough to determine other patterning processes. Figure 23.6 shows the STI process sequences [14]. During the process, STI CMP participates in the leveling over oxide and nitride layers prior to the oxide spacer formation and provides a much tighter control over device and isolation dimensions.

The initial CMP step in the BEOL process is tungsten (W) CMP. The major application of W CMP is to create a W plug that plays an important role of a vertical bridge through each level in-line wiring. As seen in Fig. 23.7 [15], the W plug is located in between two metal lines by the damascene process (which will be explained later) and there are adhesion and diffusion layers such as Ti and TiN.

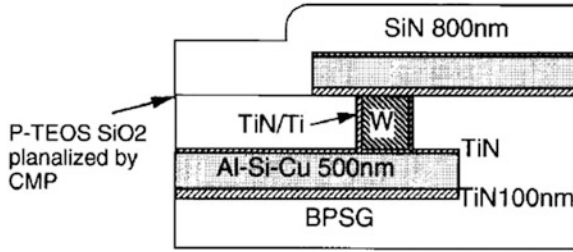


Fig. 23.7 The tungsten stud via structure of TiN/Al-Si-Cu/TiN layered metallic lines [15]

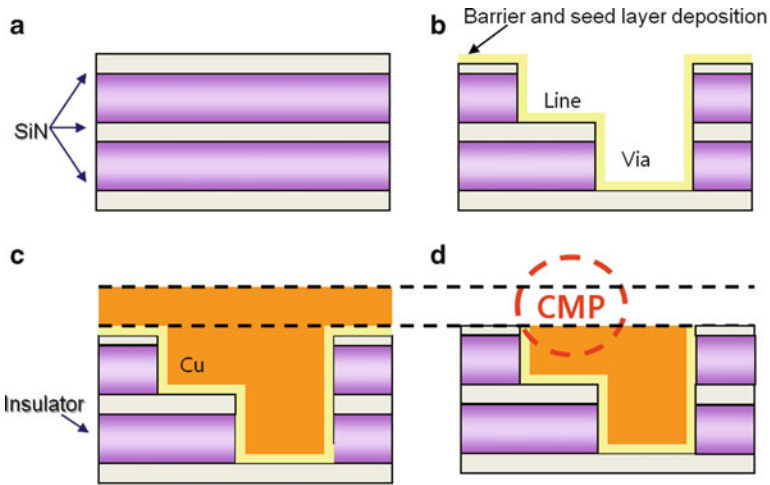


Fig. 23.8 Dual damascene process: (a) insulator deposition, (b) line and via definition, (c) metallization, (d) CMP process

Thus, W CMP actually encompasses a planarization of tungsten, titanium, and titanium nitride in the same level.

Along with W CMP, Cu CMP is the major process for the metallization in the entire multilevel structure. Cu has been considered as the best metal which can replace aluminum (Al) as an interconnect metal for the minute feature size because Cu has lower resistivity and a high electromigration resistance than Al. In Cu metallization, however, Cu cannot be dry etched due to the lack of a volatile component; thus, semiconductor industries adopted the dual damascene procedure [16] whereby Cu is deposited by electroplating (EP) or chemical vapor deposition (CVD) into via and trench formed by insulator etching (Fig. 23.8). Between Cu and the interlayer dielectric (ILD), there are barrier and seed layers which are usually tantalum (Ta)/tantalum nitride (TaN) and thin Cu layer, respectively.

Table 23.1 The components of CMP slurry and examples

Component	Major role	Example
Oxidizer	Formation of metal oxide layer	Nitric acid [18], hydrogen peroxide [19–21], ferric nitrate [22–24], potassium periodate [25, 26], sodium periodate [27, 28], potassium permanganate [29]
Chelating agent	Ion dissolution via complexing	Ammonia [18, 30], organic acids [31–34]
Corrosion inhibitor	Controlling reaction process	BTA [31, 35–38], ADS [39, 40], ATA [41]
Surfactant	Dispersion of particle	SDS [42, 43], PAA [44]

In the damascene process, Cu deposition method such as CVD or EP does not conform the exact outline of via and trench; therefore, the over-deposition of a Cu film is inevitable and an extra process is required for the removal thereof. This over-deposited Cu can be removed most effectively by using CMP, which is believed to be the only technique that provides global planarization over interconnection.

As known by its name, the interlayer dielectric (ILD) is located among the metal parts such as the W plug and Cu interconnection. Due to its location, ILD CMP is also important and cannot be explained without selectivity issues with nearby metals. ILD CMP normally deals with polishing silicon oxide such as plasma-enhanced tetraethyl orthosilicate (PETEOS) or high-density plasma chemical vapor deposition (HDCVD) film [17]. With the development of the integrated circuit (IC), the number of levels in the structure increases and ILD CMP, along with metal CMP, plays an important role in planarization on each level.

Slurries

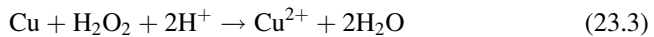
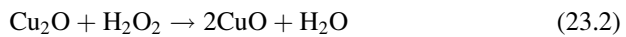
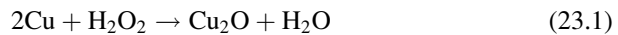
CMP slurries can be categorized into two groups based on their applications in metal and nonmetal CMP slurries. Since the material removal mechanism is different based on the target material, slurry components vary depending on each property of material. Especially for metal CMP, the slurry consists of three major components: deionized (DI) water, additive agents, and abrasive particles. DI water is used as a vehicle for abrasive particles and additive agents as well as lubricant and cooling agents during polishing. The additive agents play roles of surface modification for effective removal and low defect probability. Typically, there are several components in additive agents depending on their roles in CMP: an oxidizer, a chelating (or complexing) agent, a corrosion inhibitor, and surfactants. The role of each component and example are shown in Table 23.1.

Here BTA is benzotriazole, ADS is ammonium dodecyl sulfate, ATA the aurintricarboxylic acid, SDS the sodium dodecyl sulfate, and PAA the poly (acrylic acid).

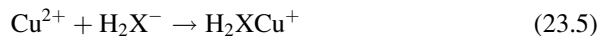
The oxidizer reacts with the surface and forms different oxide states of metal depending on pH values. Metal oxides are usually porous in nature which are

relatively easy to be removed through mechanical sweeping between a pad and wafer. Since the CMP process is a nonequilibrium process, there are many kinetic factors changing the formation of surface oxide films and subsequent removal. In such, it is crucial to select a proper oxidizer and concentration thereof. As shown in Table 23.1, there are various types of oxidizers depending on the metals and polishing conditions. It is known that oxidizers can provide the controllability of material removal rates (MRR) as well as within-wafer nonuniformity (WIWNU) during polishing because it can change the corrosion and passivation state of metal [45]. Therefore, the oxidizer is regarded as one of the most critical components for a CMP slurry.

When the material is chemically dissolved and mechanically removed, the dissolved metal ion might dwell around the surface. This causes ion redeposition which hinders the continuous dissolution and overall material removal rate because of the equilibrium tendency on the metal surface [46]. To solve this problem, there has to be an additional transportation media to move the dissolved ions into the exit stream. A chelating agent, as its name implies, is a ligand which binds to a metal ion and forms a metal ion–ligand complex. Gorantla and coworkers [33] investigated the role of citric acid and its complex during Cu CMP. When copper is in the peroxide and acid based slurry, copper dissolution happens, as shown below:



As a result of the copper reaction (23.3), Cu^{2+} can be chelated by the citric acid existing in the slurry as shown below:



where HX^{2-} and H_2X^- are the most stable forms of citric acid H_3X ($\text{X} \equiv -\text{OOCCH}_2\text{OHCOO}-\text{CH}_2\text{CCOO}-$) in acidic slurry. Thus, reactions (23.4) and (23.5) affect the equilibrium of the copper surface and continuous depletion of Cu^{2+} in reaction (23.3) can drive higher copper dissolution and, consequently, higher removal of copper with the assistance of mechanical force.

The most desirable operation of CMP is to provide sufficient material removal and, at the same time, an excellent surface finish with the least defects. While the chelating agent triggers the chemical dissolution of metal and, thus, high MRR, the corrosion inhibitor is for controlling the reaction process. The corrosion inhibitor is used to generate a passivation layer to protect the copper film from aggressive chemical attacks and to enhance the surface finish and uniformity. For the patterned

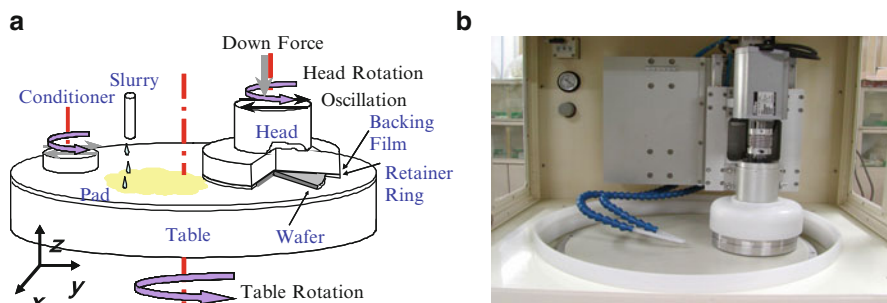


Fig. 23.9 (a) The schematic illustration of a CMP equipment and (b) a polisher GnP POLI 400 (G&P Technology Inc.)

geometry, it also protects the recessed area from the corrosion and only the protruded area is selectively removed by mechanical abrasion [37]. As shown in Table 23.1, there are several organic compounds which are used as the corrosion inhibitor in CMP. Among these, benzotriazole (BTA) is the most widely used inhibitor, especially in Cu CMP. Tromans [47] established aqueous potential–pH equilibria in Cu–BTA systems by thermodynamic analysis and showed the stability region of Cu–BTA films. It is reported that BTA can also be a good additive for ionic liquid lubricants which can enhance the tribological performance during polishing [48]. In this way, the corrosion inhibitor is an important chemical constituent for slurry designs.

Surfactants are molecules that have at least one hydrophobic and one hydrophilic part. These compounds lower surface tension in liquids, and when they collaborate with other molecules in solutions, they hinder interaction between each molecule. Thus, surfactants may increase the dispersibility of abrasive particles and also prevent surface contamination by organic residues.

In addition to the chemical components mentioned above, abrasive particles also play important roles. One of the major functions of abrasive particles is to assist mechanical removal. Another role of abrasive particles is to adsorb reaction by-products as well as transfer debris generated during polishing. Various materials have been used as abrasive particles during CMP. For example, alumina [49, 50], ceria [51, 52], silica [34, 43], diamond [53], and mixed abrasives [54, 55] have been reported. Since abrasive particles directly interact with material surfaces, both the bulk and particle surfaces play important roles in polishing. This aspect has been a hot issue in the CMP industry and, until now, most industries have maintained efforts in developing new particles.

Polishers

Figure 23.9a and b respectively show typical schematic illustrations and real images of a polisher for CMP. A brief demonstration of a polisher is as follows. The wafer is held by the head and the polishing pad is located on the table. During the process,

the target material on the wafer is removed via the friction force generated at the interface between the rotating head and the polishing pad. At the same time, polishing slurry is continuously supplied through the nozzle as a chemical reactor to enhance the material removal rate and stability. The surface of the pad is maintained using a conditioner.

In the polishing head, it is extremely important to know how to apply uniform pressure to the wafer because uniform distribution of pressure definitely determines WIWNU and MRR. There are three features which compose the polishing head [3]: a backing film that delivers pressure to the back side of the wafer uniformly, a retainer ring that keeps the wafer from coming out of it, and the wafer-retaining chuck for holding the wafer.

The polishing pad is adhered to the polishing platen. Since the wafer is expected to be extremely flat after polishing, it is important that the polishing platen be leveled with the polishing head and precisely flat. In addition, a large bearing has to be used for the platen in order to be rigid enough to endure very high loads being applied to it during polishing. As polishing proceeds, pad asperity deteriorates due to the continuous friction and wear and this can cause lower MRR and higher defect probability. Thus, the in situ (in time) or ex situ (after polishing) conditioning is required for the polishing pad. Normally, diamond abrasives embedded on the round disk are used and they get rid of the polishing by-products clogging pad pores and, simultaneously, pad asperity recovers.

Since the CMP process is an important step in the entire device wafer manufacturing process and the actual polishing time is very short and precise, all of these equipment parts have to be smoothly interacting with each other to guarantee high repeatability and productivity.

2 Tribology in CMP

2.1 Friction and Wear in Tribo-CMP

2.1.1 Friction

The surface finishing process which gives rise to friction and wear has long been a case of tribology. The chemical–mechanical polishing process, as its name indicates, cannot be explained without friction and wear. Friction can be defined as the resistance of two tangentially sliding bodies in contact [56]. In dry sliding conditions, there are three factors affecting the frictional behavior: the real contact area between two bodies, the bond strength in the contact region, and shearing and rupturing characterizations of the sliding material. In a viewpoint on nanoscale, Bowden and Tabor [57] claimed that the real contact area (A) is the contact area at which the asperities touch a counterpart. The friction force can be explained as shown below:

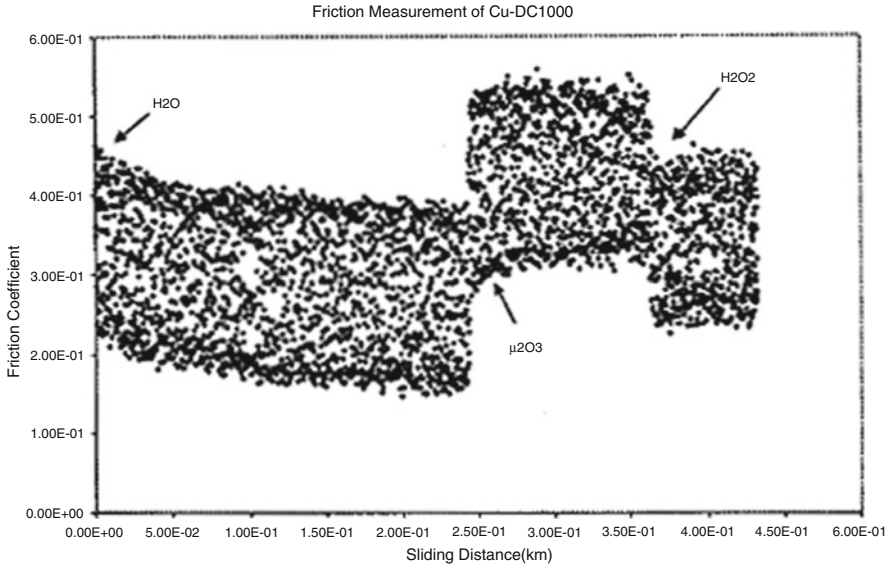


Fig. 23.10 Friction coefficient measured under a different polishing media [58]

$$F_f = \tau A \quad (23.6)$$

where F_f is the friction force and τ is the critical shear strength. In terms of the friction coefficient (μ), the friction force can also be represented as

$$F_f = \mu L \quad (23.7)$$

where L is the normal force through the contact. Thus, the friction coefficient (μ) can be a useful indicator for explaining the tribological phenomenon.

In the CMP process, friction happens through the interaction between wafers, pads, and abrasive particles in slurries. Friction behaviors have been reported by researchers with those interaction components. As mentioned earlier, the contact condition of two counterparts (wafer and pad in this case) strongly affects the tribological behavior during CMP. For this reason, the surface structure, such as roughness and asperity, and the surface hardness are worth researching.

The relationship between the wafer surface property and friction has been reported [58]. This research has shown that the modified copper surface by different slurries resulted in different friction coefficients. During the copper polishing with the Rodel IC1000 pad, as shown in Fig. 23.10, the friction coefficients changed when deionized (DI) water, alumina abrasives, and hydrogen peroxide (H_2O_2) were added, respectively. Copper is known to form different copper oxide states (CuO and Cu_2O) depending on the electrochemical conditions, i.e., pH and potential [59]. Cu_2O has been verified to be a predominant surface during polishing with alumina slurry and CuO during polishing with DI water or H_2O_2 . When alumina

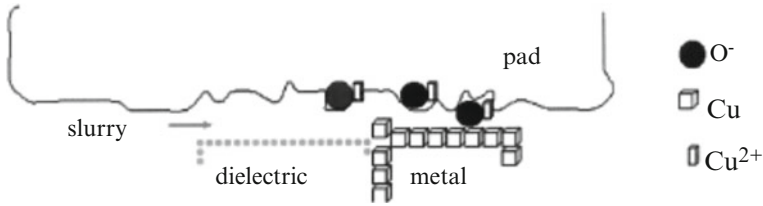


Fig. 23.11 The illustration of transfer of copper atoms to urethane chains [60]

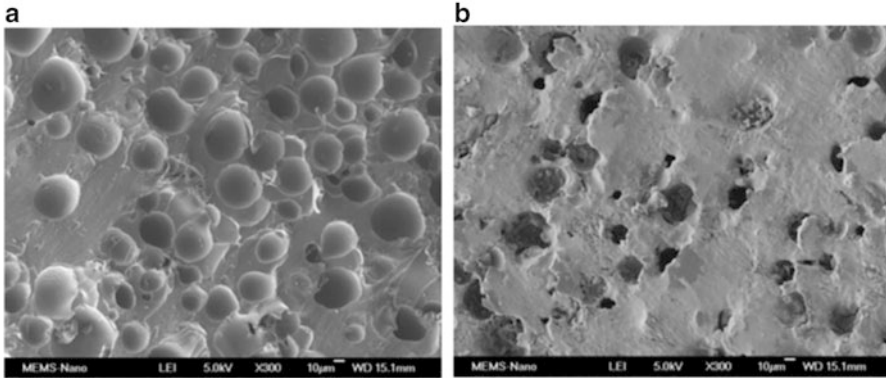


Fig. 23.12 SEM image of polishing pads. (a) Before polishing and (b) after polishing [61]

slurry was added during polishing, the friction coefficient promptly increased due to the surface change from CuO to Cu_2O . These changes indicate that the frictional behavior of Cu CMP can be affected by the nature of oxide films.

Besides wafer surface properties, the pad property is also a significant factor affecting the friction coefficient. Polishing pad materials are usually composed of polyurethane and/or polyester and these polymers have viscoelastic property and, thus, strong time dependence. During CMP, chemical interaction is known to occur between the wafer surface and polymeric pad because of the stimulation of friction [60]. As shown in Fig. 23.11, metal oxide can be transferred to the polymeric pad, and the molecular structure of the pad can also be transferred to the wafer surface. In addition, by-products from slurry can also be transferred to the pad. When the pad pores are clogged with these by-products and debris (Fig. 23.12), there is a drop of the friction coefficient, which indicates pad degradation. Figure 23.13 shows the different frictional behaviors under different conditioning methods [61]. As shown, the friction coefficient decreases without conditioning, which indicates the degradation of pad asperity. In situ conditioning can maintain the friction coefficient at a high level by continuous recovery of pad asperity. The conclusion is that the friction coefficient is the useful method for monitoring pad conditions during the CMP process.

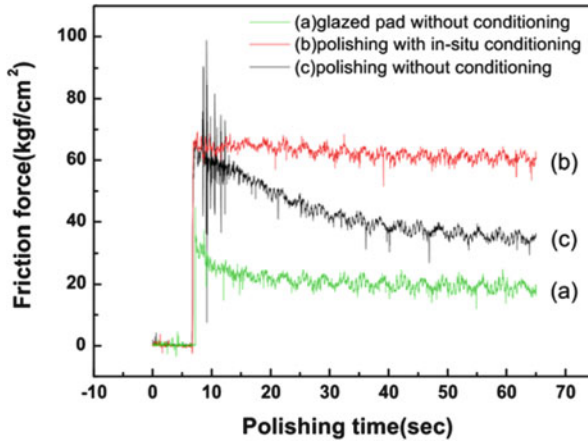


Fig. 23.13 Friction force signals of the glazed pad in the absence of the in situ conditioning process and the conditioned pad with the in situ conditioning process. (a) Glazed pad without conditioning, (b) polishing with in situ conditioning, and (c) polishing without the conditioning process [61]

2.1.2 Wear

Along with friction, wear is another important factor in the CMP process. It normally explains the material removal rate (MRR). In the CMP process, there are various wear mechanisms depending on the contact theory as shown below:

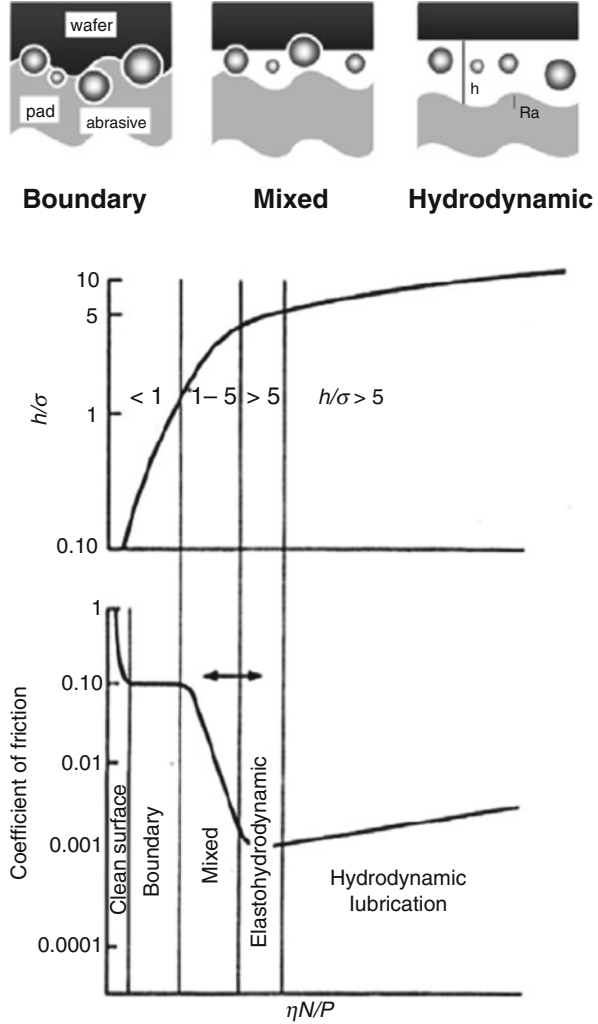
- Adhesive wear
- Abrasive wear
- Tribochemical wear
- Fatigue wear

Adhesive wear occurs in poorly lubricated sliding surfaces and has linear relationship with contact force [62]. When two surfaces are in contact under a high load, adhesion of two asperity contacts (which is called “cold welding”) begins and then under the shearing stress, materials transfer between two bodies inducing fragments.

Abrasive wear occurs when harder parts (abrasive particles in CMP) abrade softer counterparts, normally in the two- or three-body systems. The two-body abrasion happens when those abrasive particles are pushed into the soft pad and then into the wafer surface, removing material similar to plowing. The three-body abrasion is considered when loose abrasive particles roll and slide at the interface between a pad and wafer. Generally, both adhesive and abrasive wear mechanisms are related to the three-body interaction (wafer–pad–abrasive particles).

Tribochemical wear involves a chemical reaction of the surface forming passivation layer and removal thereof. Therefore, this type of wear is caused by two simultaneous removal mechanisms: surface passivation and mechanical wear [63]. The effect of slurry chemistry and surface modification on material removal is usually related to tribochemical wear.

Fig. 23.14 Lubricant film parameter (h/σ) and coefficient of friction as a function of $\eta N/P$ (Stribeck curve) showing different lubrication regimes observed in fluid lubrication [64]

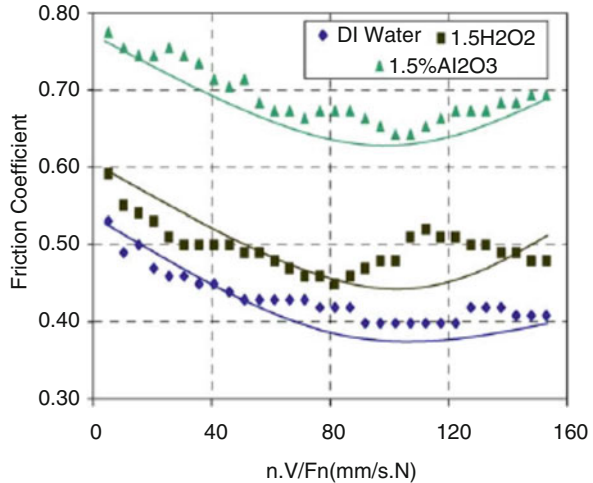


Fatigue wear occurs after many cycles of high-stress flexing of materials. In CMP, this type of wear usually happens to the polishing pad after the cyclic process. Fatigue wear can be reduced by increasing slurry film thickness and this can increase the pad life.

2.2 Lubrication

Along with friction and wear, lubrication is also an important part of tribology in CMP. Lubrication regimes have been explained by the Stribeck curve illustrated in Fig. 23.14 [64]. This curve was firstly obtained by Stribeck in 1902 in his research

Fig. 23.15 Stribeck curve in Cu CMP under different lubricant media [65]



about fluid lubrication of journal bearings. It presents the friction coefficient as a function of operating parameters including lubricant viscosity (η), rotational speed (N), and contact pressure (P). The lubrication regimes are sometimes explained by the ratio of the mean film thickness to a composite standard deviation of the distance between two surfaces facing each other. There are typically four types of lubrication: boundary, mixed, elasto-hydrodynamic, and hydrodynamic. Boundary lubrication is characterized by the film thickness which is smaller than the height of asperity contact. Mixed lubrication is the transition between boundary and elasto-hydrodynamic lubrication in which these two lubrications occur simultaneously. Elasto-hydrodynamic lubrication is characterized by the film thickness which is greater than the height of an asperity contact. In this case, elastic deformation of the contacting solid determines the lubrication condition. Hydrodynamic lubrication occurs when the film thickness is substantially greater than the height of the asperity contact and, thus, two surfaces are fully separated by the film.

During CMP, lubrication regimes may vary depending on the slurry property, applied load, and speed. There are several studies about the lubrication regime for CMP. An example of a Stribeck curve was obtained during Cu CMP (Fig. 23.15) [65]. This figure shows that the addition of hydrogen peroxide increased the friction coefficient, and an even larger increase of the friction coefficient was obtained after adding alumina particles. Another example, shown in Fig. 23.16, illustrates that the abrasive particles predominantly increase the friction coefficient. The pH value of a lubricant changes the friction coefficient as well. At a pH value of around 7, the friction coefficient is higher, meaning that the CuO film was generated on the surface of copper affecting frictional behavior in the boundary and mixed lubrication regimes. Accordingly, surface interactions between slurries, pads, and chemically modified surfaces behave synergistically and affect the frictional behavior during CMP.

Lubrication behavior was also studied for the post-CMP cleaning process [66]. Figure 23.17 shows a modified Stribeck curve for a soft brush sliding against

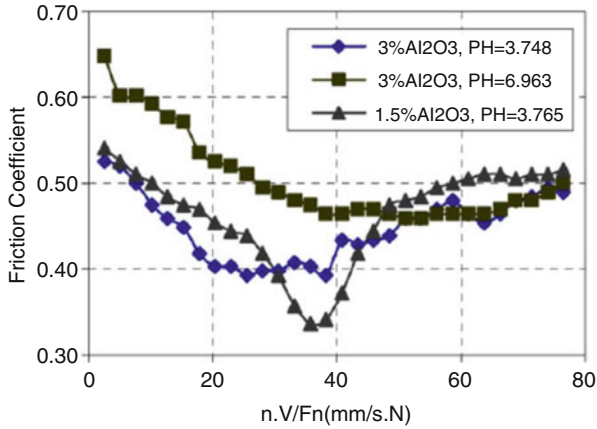


Fig. 23.16 Effect of particle concentration and pH on lubrication in Cu CMP [65]

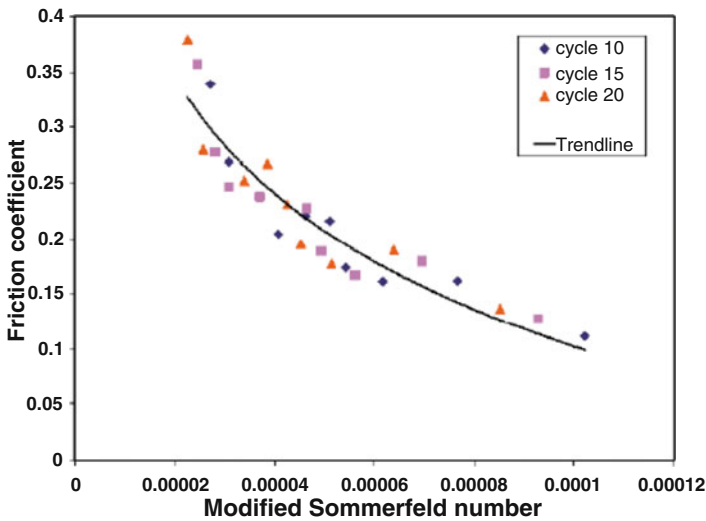


Fig. 23.17 Modified Stribeck curve for a soft material sliding against solid surface [66]

a solid surface. Since the polymeric brush used for post-CMP cleaning is soft, it is hard to obtain the contact pressure and, thus, the classic lubrication theory is not appropriate to this case. The modified Stribeck curve encompassing the bulk modulus of brush and the variation of brush height under compression was obtained as a function of friction coefficient. From this soft-on-hard lubricating system, it was verified that elastic modulus of the soft brush is significant factor in lubricating behavior, and effective particle removal can be obtained in the boundary and mixed lubrication regimes.

3 Tantalum CMP

As mentioned earlier, tantalum (Ta) is one of the materials most used as a diffusion barrier layer in Cu damascene structure. Along with Cu CMP, Ta CMP is also important in order to obtain a planarized surface over the interconnect and insulator area. Due to the inertness of tantalum, an exact understanding of electrochemistry and reaction kinetics of tantalum will help the process optimization of Ta CMP.

3.1 Effects of Applied Potential on Friction and CMP

Due to the nature of Ta CMP performed in an aqueous solution, electrochemical reactions of tantalum have to be investigated to understand the material removal mechanism of Ta CMP. Kar et al. [67] have researched nonequilibrium oxidation kinetics of tantalum with mechanical force and electropotential. They measured the frictional behavior of tantalum polishing in a 5 % hydrogen peroxide-based solution with and without external electropotential in order to study the effects of electropotential on friction. As shown in Fig. 23.18, the friction coefficient jumped when a potential of 2.4 V was applied after 9 min.

The increase of a friction coefficient can be correlated with the different states of tantalum oxide and the further XPS analysis of tantalum oxide was performed as shown in Fig. 23.19. Figure 23.19a shows different peaks of three samples with friction and electropotential, friction only, and electropotential only. Obviously, when electropotential is applied to the sample, the peak shows shifting compared to other conditions. This indicates that the different tantalum suboxides can be formed under electropotential–mechanical interaction. By the comparison between Fig. 23.19b and c, the difference in the electrochemical–mechanical reaction and mechanical reaction is the Ta_2O in the latter case (Ta^{1+} peak). With electropotential, the friction shows prompt jump, meaning that more mechanical

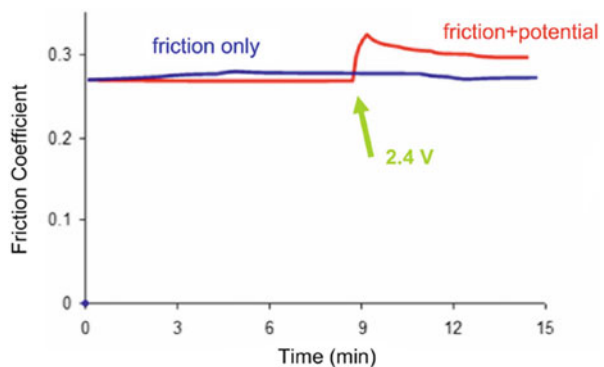


Fig. 23.18 Friction coefficient variation of the tantalum sample when potential was applied [67]

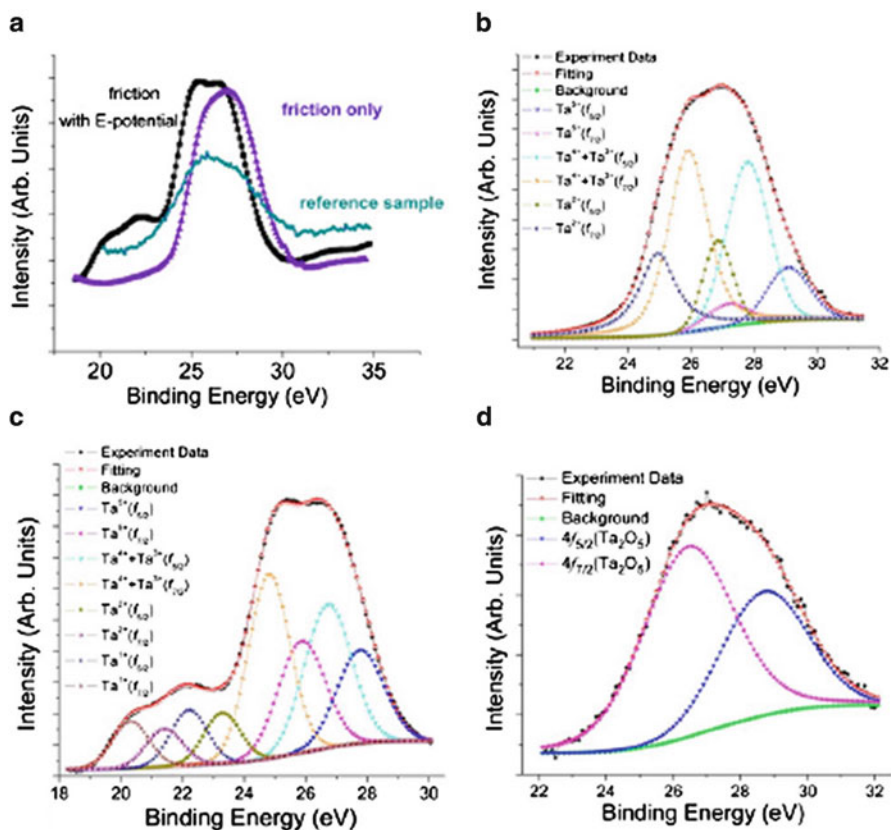


Fig. 23.19 (a) XPS spectra of Ta sample surfaces obtained after immersion in 5 wt% H_2O_2 solution with friction and electropotential, friction only, and electropotential only. (b) Deconvoluted Ta 4f XPS envelope obtained from the Ta surface after immersion in a solution with 5 wt% H_2O_2 with both friction and electropotential. (c) Deconvoluted Ta 4f XPS envelope obtained from the Ta surface after immersion in a solution with 5 wt% H_2O_2 with friction only. (d) Deconvoluted Ta 4f XPS envelope obtained from the Ta surface after immersion in a solution with 5 wt% H_2O_2 with electropotential only and as the reference sample with pentoxide Ta_2O_5 [67]

energy is introduced and brings back the least stable Ta_2O_5 , reverting back to a more stable status. The existence of suboxide products, Ta^{2+} , Ta^{3+} , and Ta^{4+} , indicates the reverse reaction from Ta_2O_5 to other suboxides, meaning that electrochemical–mechanical oxidation is dynamic and a nonequilibrium process. The notable peak shifting of an oxidation state to lower binding energy with the assistance of friction and electropotential indicates that the transition from Ta_2O_5 to TaO/Ta_2O requires external energy, as illustrated in Fig. 23.20. During the electrochemical reaction, tantalum is anodized by anodic potential and its surface energy is lowered.

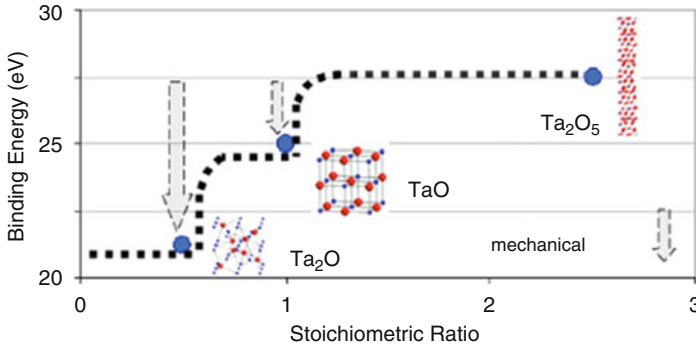


Fig. 23.20 The relationship between the binding energy and the stoichiometric ratio of tantalum oxides [67]

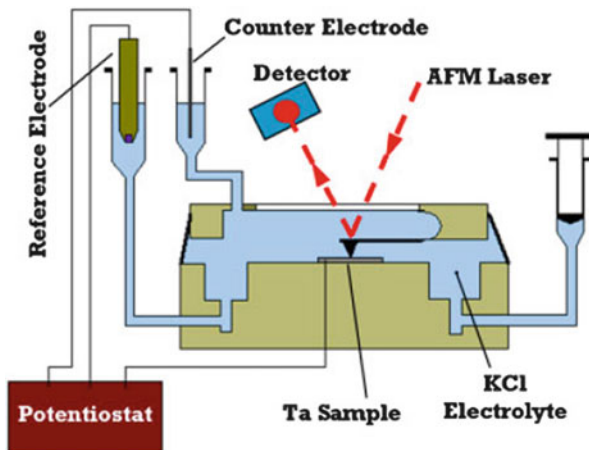


Fig. 23.21 Dynamic surface monitoring AFM (DSM-AFM) [68]

3.2 Surface Evolution During CMP

The interactions between contact forces and frictional surfaces are some of the most fundamental aspects of tribology. Evolutionary change of surfaces by these interactions under electrochemical environments can give deeper understanding of CMP. A scanning-probe-based technique was introduced for observation of tribo-electrochemically modified surfaces by Huitink et al. [68]. They used their own developed atomic force microscope (AFM) technique combined with electrochemical cells, so-called dynamic surface monitoring AFM (DSM-AFM) as shown in Fig. 23.21.

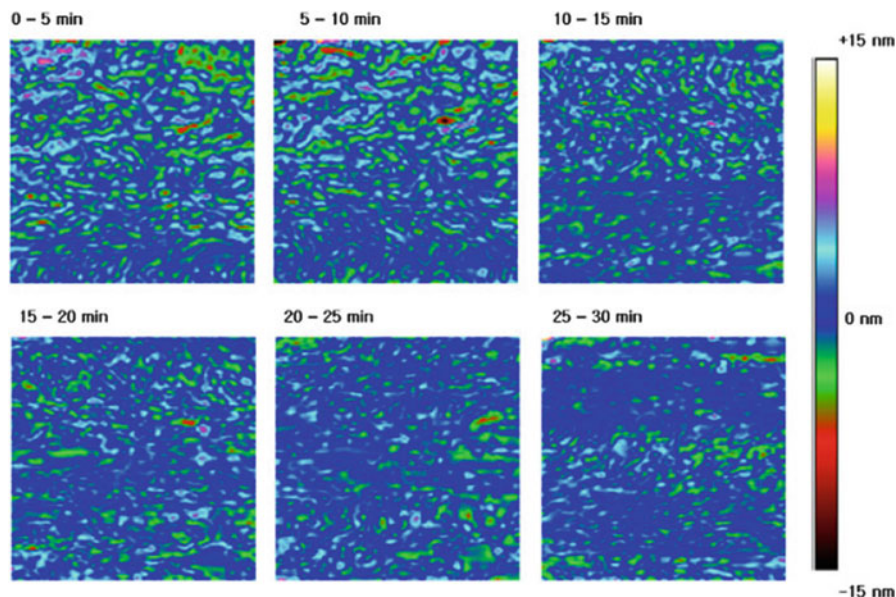


Fig. 23.22 Directly observed surface transformations during testing with 2 V potential [68]

In this experimental setup, nonconductive polyoxymethylene and environmental cell were used and a potentiostat system was attached for the electrochemically controllable atmosphere. A contact mode silicon tip (spring constant: 0.2 N/m) was used to scan a polycrystalline Ta sample immersed in 0.4 wt% KCl electrolyte. To observe surface changes from one image to the next, a scanning from one image to another image occurred over a 5 min time period. Figures 23.22 and 23.23 show the time-dependent surface change through a tribo-electrochemical reaction under 2 V potential and no potential, respectively. Different colors are based on the height of the scanned surface. A close comparison of the image sequences reveals the surface modification by moderate surface growth and removal and it is more pronounced in the case of a potential of 2 V. In the case of 2 V and no potential, the surfaces are seen to be affected by tribo-electrochemical reaction, while the 4 V potential shows no outstanding changes (not shown here). Additionally, the surface roughness change during the sequential scanning for ~1 h is shown in Table 23.2. It is obvious that the overall change of the surface under the 4 V potential is less than the other cases.

The evolutionary surface roughness change is evaluated by using the bearing ratio curve (BRC) during the scanning period and is shown in Fig. 23.24. This figure indicates that the variation range of the bearing ratio decreases under different external potentials. The different electrochemical conditions affect the oxidation kinetics of tantalum. Under a higher potential, anodization of tantalum triggers the oxidation process of tantalum and can be somehow resistant to mechanical stimuli by the scanning tip, meaning that the electrochemical reaction dominated the

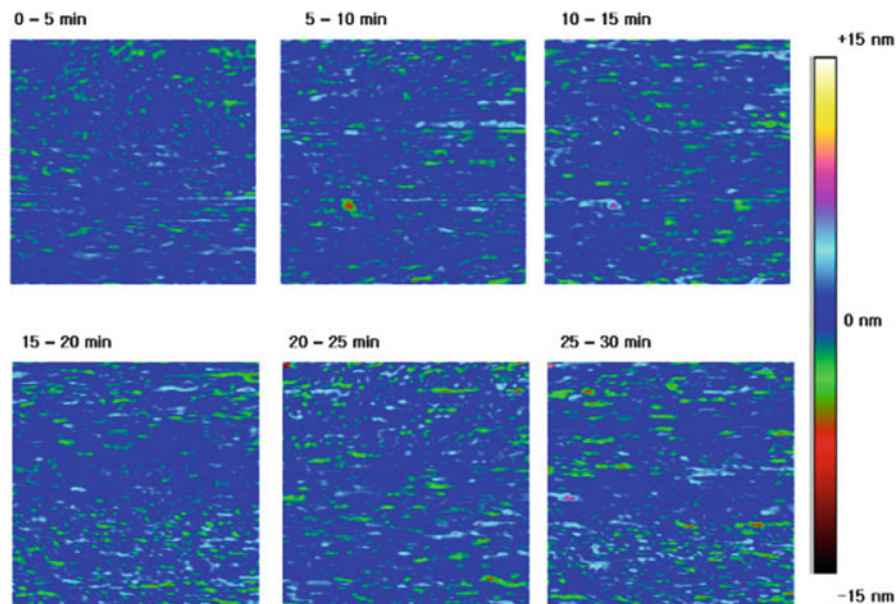


Fig. 23.23 Directly observed surface transformations during testing with 0 V potential [68]

Table 23.2 Comparison of average surface roughness (R_a) on tribo-electrochemically activated region versus only electrochemically activated region [68]

Applied potential	Roughness inside test area, R_a (nm)	Roughness outside test area, R_a (nm)
None	2.88 ± 0.51	1.82 ± 0.13
2 V	1.89 ± 0.46	2.53 ± 0.22
4 V	1.38 ± 0.40	1.58 ± 0.28

surface transformation. On the other hand, without any potential, the surface reaction appeared to be ruled by the tribological reaction, indicating that the surface transforms much more as the scanning proceeds.

As mentioned in the previous section, the tribo-electrochemical reaction causes tantalum oxide and its transformation to suboxides. This phenomenon is also depicted in DSM-AFM. Figure 23.25 illustrates the surface phenomena under the AFM tip in an electrochemical environment. The top left inset image shows the tribo-electrochemically modified area revealing a new frictional behavior due to the presence of suboxides. In the existence of electrolytes and potential, the electric double layers (indicated by \pm) form around both surface and polishing material (tip) and this can be disturbed by mechanical contact. There are mechanical interactions inducing surface stress (color gradient) to form oxides and subsequent removal of the same. This competing mechanism can provide new understanding of metallic oxidation and direct observation of evolutionary change of surface during CMP.

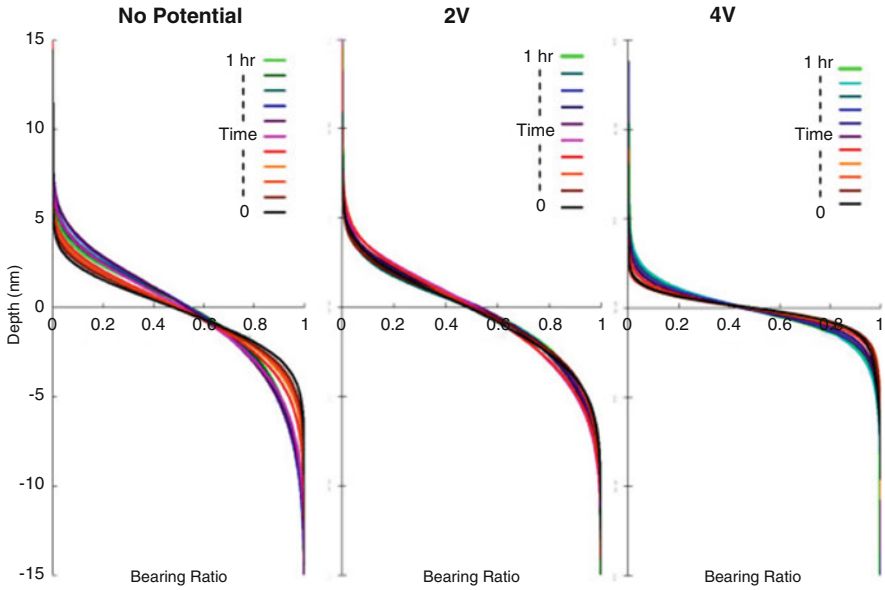


Fig. 23.24 Direct comparison of bearing ratio curves revealing net difference as a result of electrochemical potentials [68]

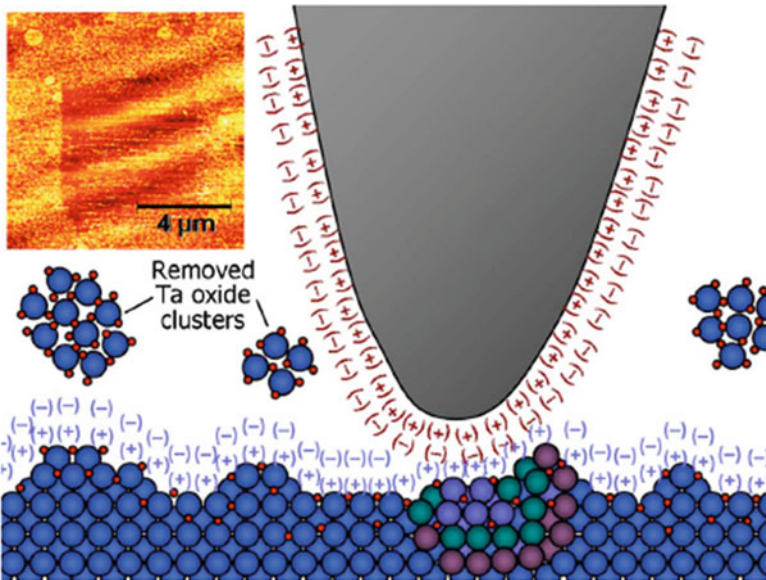


Fig. 23.25 Lateral force microscopy image (top left) of DSM-AFM test area revealing new frictional behavior due to suboxide presence and schematic illustrating surface phenomena during tribo-electrochemical activation [69]

3.3 *Materials Removal Mechanisms*

Since the previous two sections delivered the basic and fundamental study of the metastable oxide formation and removal, this section will shed light on a practical evaluation of the material removal mechanisms during Ta CMP. Ever since CMP has been developed, the material removal mechanisms have been reported, such as the metal passivation [70], chemical wear [58, 60], boundary lubrication [65], and synergistic behavior [71, 72]. The predominant theory is that CMP mechanism is in a balance between chemical and mechanical interactions. More empirical and practical proof of the quantitative analysis of the material removal mechanism has been performed by Gao et al. [73]. For the material removal mechanism of CMP, the metal oxide formation is the key factor and this oxide film is well known to have an insulating property. From this point of view, the single-frequency electrochemical impedance spectroscopy (EIS) technique can enable an in situ analysis of oxide formation and removal mechanism. Basic principles of single-frequency EIS are discussed in the following. Unlike potentiostatic EIS, which involves a wide frequency range, an AC potential is applied to an electrode at a certain frequency. Then, impedance change can be recorded against time. For single-frequency EIS, the impedance can be explained as shown below:

$$Z = a + jb = a + j \frac{1}{2\pi fc} \quad (23.8)$$

where Z is the impedance, a is the real part which can be regarded as the resistance of the oxide film and b is the imaginary part which can be denoted as $1/2\pi fc$, and c is the capacitance of the oxide film [74]. The magnitude of Z can be expressed as

$$|z| = \sqrt{a^2 + b^2} \quad (23.9)$$

It can be known that the impedance depends on the resistance and capacitance of the oxide film and, thus, the variation of impedance during polishing can represent the dynamics of the surface state of Ta CMP. Figure 23.26 shows impedance responses under different loads at 60 rpm of pad rotation speed. The period of sinusoidal curve, T , and the average value of impedance, A , were obtained by the calculation using the sine function. As mentioned previously, impedance is proportional to the resistance of the film and inversely proportional to the capacitance. Based on the well-adopted theory that resistance increases and capacitance decreases with the increase of the oxide layer thickness [75, 76], the impedance is governed by oxide thickness. Consequently, the sinusoidal change of the impedance curve reflects the oxide formation (curve-up) and removal (curve-down) during CMP. From the figure, it is seen that the impedance and the period pattern decreases as the applied load increases. This means that more efficient oxide removal and faster oxide formation/removal occur under higher mechanical energy. The material removal during CMP has appeared to be governed by the oxide film

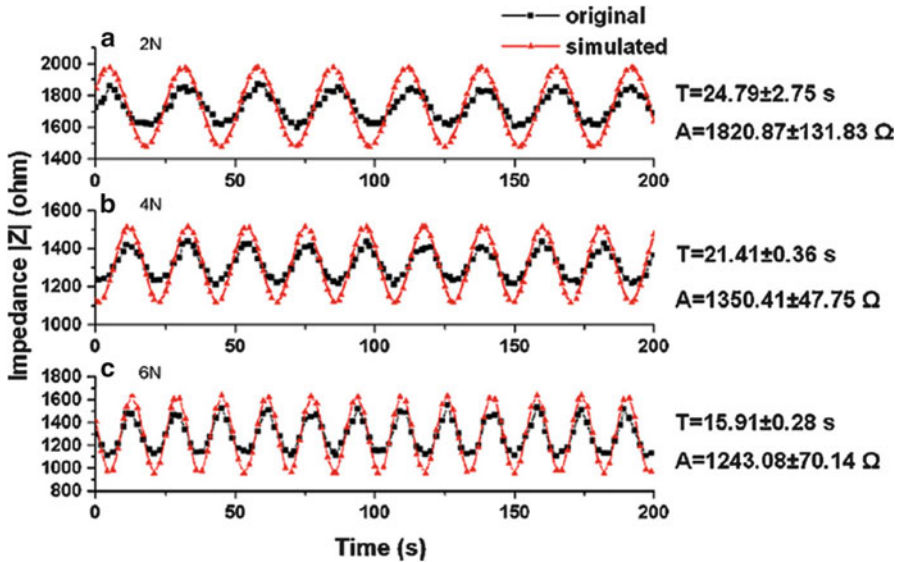


Fig. 23.26 The impedance and sinusoidal simulation curves under different load at 60 rpm and 1 V: (a) 2 N, (b) 4 N, and (c) 6 N [73]

states, and the single-frequency EIS method can provide direct observation of cyclic formation as well as removal of the metal oxide film.

4 Copper CMP

The largest portion of metal parts in a multilevel device wafer is copper (Cu). It has been used mainly for multilayer interconnection. In Cu CMP, chemical reaction between copper and slurry is one of the most important factors ruling the material removal mechanism. As mentioned in earlier sections of friction and wear, monitoring friction and its correlation with wear can provide useful analysis of Cu CMP. In this section, we will investigate the frictional behavior and wear mechanism of CMP in various electrochemical conditions and the characterization of a copper patterned wafer CMP.

4.1 Friction Monitoring During CMP

Due to the nonequilibrium process of CMP, it is hard to see what is happening on the interface between pad and wafer. Figure 23.27 shows the Pourbaix diagram of the Cu–water system in a different pH and electropotential indicating that a copper surface exists in its different states depending on the various electrochemical conditions.

Fig. 23.27 Pourbaix diagram of copper–water system [59]

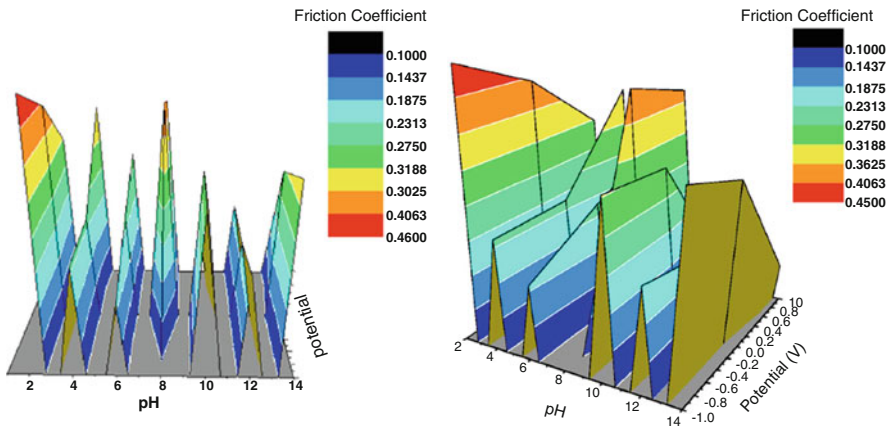
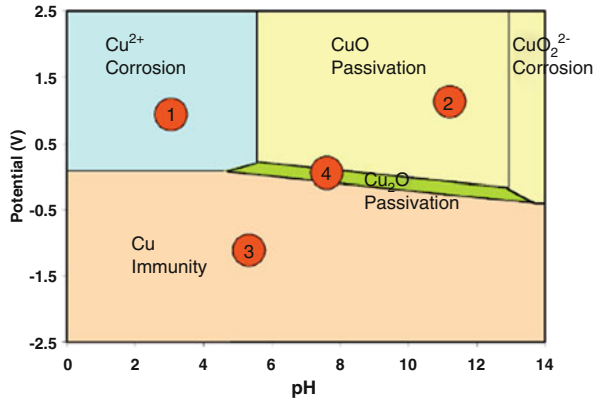


Fig. 23.28 Friction coefficient superimposed on the Pourbaix diagram of the Cu system at room temperature [77]

Since friction force depends on the copper surface property during sliding, the friction monitoring is an effective method for monitoring Cu CMP. The friction during Cu CMP in different electrochemical conditions has been investigated by Ng et al. [77]. As shown in Fig. 23.27, four different regions were chosen and friction and surface roughness results superimposed on the Pourbaix diagram are shown in Fig. 23.28 and in Table 23.3, respectively.

In reference to Table 23.3, Region 1 (pH 1–6) represents the acidic slurry and anodic potential. In this region, dissolved Cu²⁺ ion is the predominant factor. Any Cu oxide formation is depressed in this area and continuous dissolution causes poor balance between chemical and mechanical removal resulting in a loss of surface planarity. The surface roughness in this region appears to be the highest among all regions shown in Table 23.3. Thus, this poor planarization is the culprit in the high friction distribution. Region 2 (pH 6–14) represents the alkaline slurry and anodic

Table 23.3 Typical surface roughness and its associated friction coefficient [77]

	Polishing condition	R_a (nm)	Friction coefficient
Region 1	pH 2, 1 V	47.55	0.3091 ± 0.0077
Region 2	pH 14, 1 V	4.6	0.1387 ± 0.0095
Region 3	pH 6, 0 V	11	0.2412 ± 0.0066
Region 4	pH 10, 0 V	20.12	0.3028 ± 0.0098

potential. In this region, copper reacts with oxygen in a solution and forms a cupric oxide (CuO) layer on the surface. This oxide layer serves as a sacrificial layer which can be easily removed by friction force and subsequently reforms at a synergistic rate. Thus, this layer is handled in the balance between chemical and mechanical removal, resulting in a good surface planarity ($R_a = 4.6$ nm in Table 23.3) and low friction distribution. Further oxidation at a pH value up to 14 introduces continued precipitation of copper ions on the surface, which can cause a thermodynamically unstable surface. Friction coefficients were high around this region due to the formation of nonequilibrium oxide by the tribochemical mechanism. Region 3 (pH 1–14) shows the entire pH range and cathodic potential range. Since the chemical reaction of copper is depressed under the cathodic potential, there is no oxidation activity and material removal is mainly dominated by mechanical abrasion. The friction distribution in this region is somewhat inconsistent, depending on the pH values. It is high particularly in pH 2, 10, and 14. A highly mechanical abrasive atmosphere brings unstable removal conditions and the formation of grooves is considered to be the reason of high a friction coefficient. Region 4 shows the neutral and alkaline slurry and either cathodic or anodic potential near 0 V. In this region, cuprous oxide (Cu₂O) is a predominant form. A weak and unstable oxide layer with an incomplete passivation might form at low potentials giving high surface roughness and subsequently a high friction coefficient.

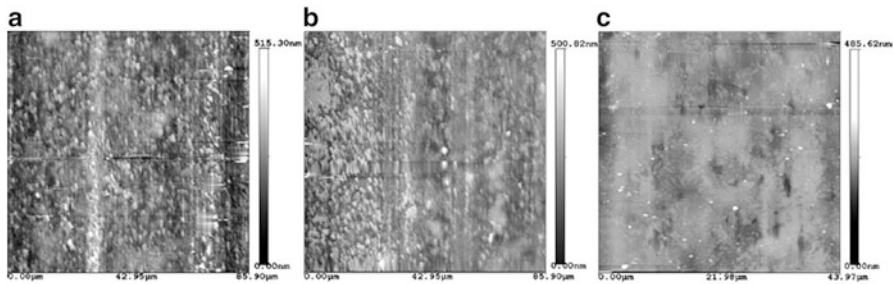
4.2 Wear Mechanisms in Cu CMP

In the previous section, frictional behavior appeared to depend on the various electrochemical conditions. Wear, as an indicator of material removal, is also an important factor in which the mechanism is yet to be carefully understood. Kulkarni et al. [78] investigated wear mechanisms during Cu CMP by applying various potentials to study the behavior of electrons, ions, and atoms. The wear amount in Cu CMP with various potentials such as 2 V, -2 V, and pulsating ± 2 V is shown in Table 23.4.

As listed in Table 23.4, the total material removal rate is highest when anodic potential is applied during CMP. However, the rate under cathodic potential is almost four times lower. It is known that the chemical reaction of copper under anodic potential is more favorable than that under cathodic potential. This is obviously observed in the large difference in the electrochemical material removal

Table 23.4 Material removal rates and average friction coefficients (R_a) values of copper surface after CMP [78]

Applied potential (V)	Electrochemical material removal rate (nm/min)	Mechanical material removal rate (nm/min)	Total material removal rate (nm/min)	Friction coefficient, μ	R_a (nm)
+2	34.2 ± 0.7	9.6 ± 5.3	43.6	0.43 ± 0.05	46 ± 13
-2	9.3 ± 0.5	7.3 ± 0.2	16.3	0.50 ± 0.03	36 ± 20
± 2 pulsating	5.5 ± 0.4	8.0 ± 1.4	13.5	0.37 ± 0.03	10 ± 5

**Fig. 23.29** AFM images of Cu after CMP under applied potential of (a) anodic 2 V, (b) cathodic 2 V, and (c) pulsating 2 V dc [78]

rate. On the other hand, the friction coefficient under anodic potential is lower than that under cathodic potential and pulsating potential resulted in the lowest friction coefficient. For the average surface roughness, anodic potential resulted in the poorest surface finish and, interestingly, pulsating potential brought the best surface finish result. The surface finish results by using AFM are well illustrated in Fig. 23.29.

The following explains how these results can be correlated with wear mechanisms. As shown in Fig. 23.29a, polished under anodic potentials, the grain structures are distributed randomly on the surface. When this random distribution contacts electrolytes, the dissolution rate can vary depending on the locations and asperities due to the different ion concentrations. During polishing, the Cu oxide layer is continuously removed and the different ion dissolution rate results in the rough surface. This high dissolution of copper ions and decreasing tendency in formation of oxide layers induce wear in an abrasive mode. In CMP with cathodic potential, electrons continuously move into the Cu surface such that metal ions are not dissolved, causing a suppressed Cu chemical reaction. With the assistance of an oxidizer in the slurry, the oxidation–passivation reaction of copper is stabilized by providing electrons, and subsequently, a more uniform oxide layer with good planarization (lower surface roughness) can be obtained. As seen in Table 23.4, the mechanical material removal rate of cathodic polishing is slightly lower than that of anodic polishing, indicating that a uniformly formed oxide film is harder than pure copper film. The suppressed oxidation, controlled Cu chemical reaction,

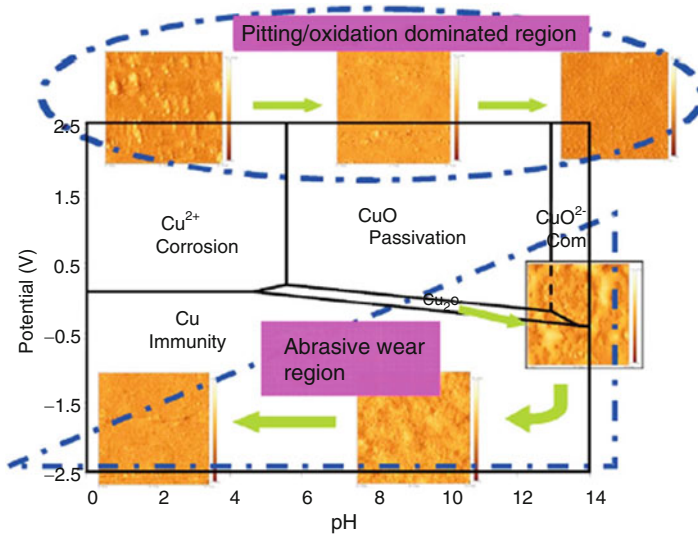


Fig. 23.30 Summary of wear mechanisms based on Pourbaix diagram [77]

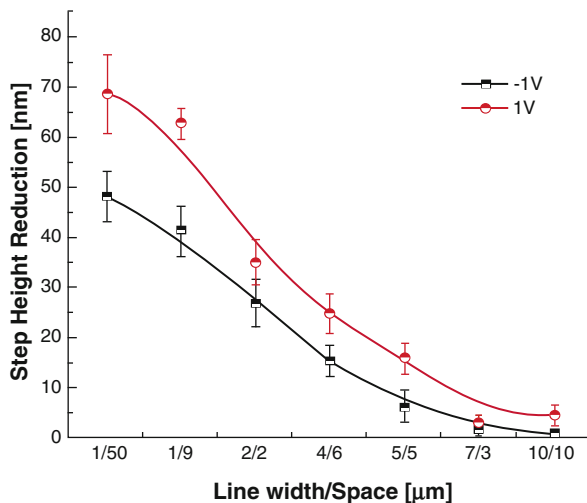
and reduced mechanical removal resulted in a better surface finish. A pulsating potential has the combined aspect of anodic and cathodic potential. As seen in the previous two cases, the kinetics of ionic dissolution and/or deposition is nonuniform and this causes uneven current distribution on the surface. By applying pulsating current to the electrode, one can control the mass transfer over diffusion. Under the balanced dynamics of ion dissolution and deposition, a good surface finish can be obtained, however; this causes a low material removal rate compared with the removal from peaks in the anodic cycle while redeposited in the valley sites.

As shown in Fig. 23.30, wear mechanisms are dominated by the surface chemical states in various electrochemical conditions. The wear mechanisms are composed of two major competing mechanisms: mechanical abrasion and chemical abrasion. These two have to be balanced to obtain a desirable material removal rate as well as a good surface finish.

4.3 *Tribo-electrocharacterizations of CMP*

In this section, a more practical analyzing strategy for a Cu patterned wafer as a real application in industry will be demonstrated. Since a device wafer has many various shapes of patterns and the density thereof, the contact pressure applied to each pattern and chemical reactivity might be different. These different processing conditions cause nonuniform removal on the patterns, resulting in several defects such as dishing and erosion. Thus, it is important to understand the mechanisms of

Fig. 23.31 Step height reduction versus pattern density plot for each condition; after CMP at -1 V and after CMP at 1 V [46]



step height reduction. A tribo-electrochemical approach has been performed by Joo et al. [46]. Figure 23.31 shows the step height reduction depending on the line width/space after CMP at -1 and 1 V. It is obvious that the amount of the step height reduction after CMP at 1 V is larger than that after CMP at -1 V through all pattern densities.

Under anodic potential, copper surface easily forms a copper oxide layer which is passive film. As shown in Fig. 23.32, such a layer acts as a sacrificial layer which is easily removed by mechanical abrasion on a protruded area and a passivation layer that protects the copper surface on a recessed area. Under cathodic potential, the formation of a passivation layer is suppressed, and the recessed area is continuously attacked by chemical slurry during polishing, resulting in a less effective step height reduction.

Due to the synergistic mechanisms of CMP, both the mechanical and electrochemical approaches are necessary to analyze the step height reduction. The contact pressure applied to each pattern is directly related to the mechanical aspect. It can be explained by Hertzian contact pressure (as illustrated in Fig. 23.33). As seen, the contact pressure applied to a single pattern decreases inverse proportionally to the width of the single pattern, which shows a similar trend in step height reduction as shown in Fig. 23.31.

Due to the nature of chemically reactive copper, electrochemical analysis is also important. When copper is in the electrolyte, an equilibrium state is established between the tendency of Cu ion dissolving from the surface and the opposing tendency of Cu ion redepositing on the surface (Fig. 23.34). From this equilibrium state, when there are different sizes of patterns, the gradient of local ion concentration can exist between the different patterns. Thus, as can be seen in Fig. 23.35, there is a larger number of ions around the larger pattern while observing less ions

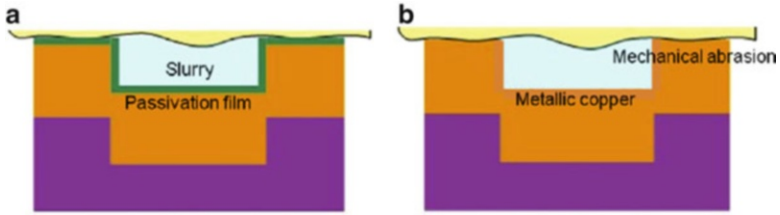


Fig. 23.32 The schematic diagram of step height reduction; (a) anodic CMP and (b) cathodic CMP [46]

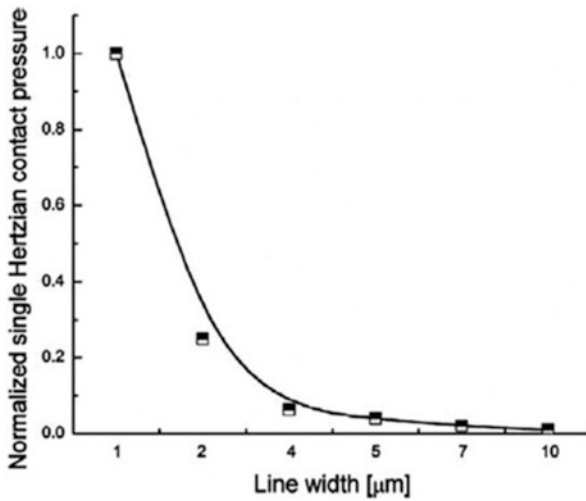


Fig. 23.33 Normalized single Hertzian contact pressure at a different line width [46]

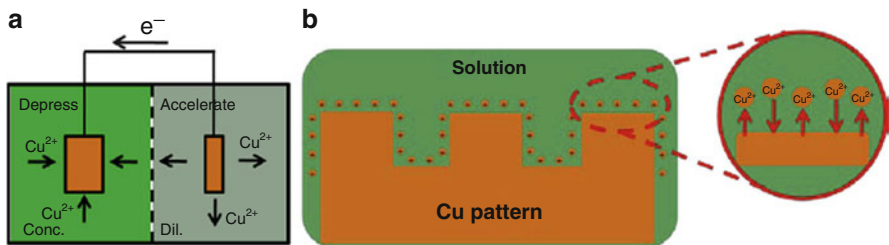


Fig. 23.34 The schematic diagram of (a) concentration cell and (b) equilibrium state of copper pattern and solution [46]

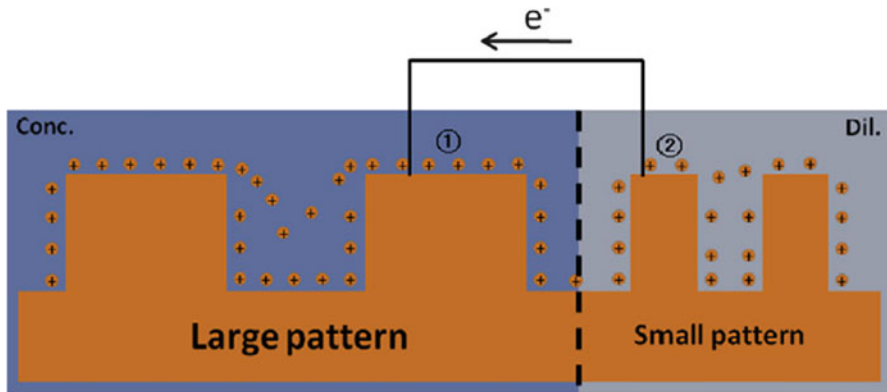


Fig. 23.35 The schematic diagram of metal ion concentration cell effect on different patterns [46]

Table 23.5 Properties of a large pattern and a small pattern [46]

	1. Large pattern	2. Small pattern
Cu ion density	High	Low
Potential of Cu	High	Low
As a concentration cell	Cathode (anticorrosion)	Anode (corrosion)
Cu reactivity	Low	High

around the smaller pattern. The small ones might act as an anode. In this case, the reactivity is higher than that of the larger ones, as shown in Table 23.5. Considering patterns 2/2, 5/5, and 10/10 μm in Fig. 23.31, even with same pattern density, the amount of the step height reduction is different due to the different electrochemical characteristics in each pattern.

This combinatorial approach of mechanical and electrochemical study elucidates the complexity of the Cu patterned wafer CMP and provides a useful and promising analyzing method for the mechanism of the step height reduction.

5 Summary

This chapter discussed the history, development, and emerging approaches in chemical–mechanical polishing (CMP). The latest development has been focused on tribo-electrochemical polishing, which is particularly important for soft materials. Polishing and material removal mechanisms have been discussed in order to understand roles of tribological principles in CMP. As the interconnect size reaches the manufacturing limit, high-precision polishing under the control of friction and material removal through wear becomes extremely important. Tribology will continually play dominating roles in CMP development in the near future.

References

1. Xiao H (2001) Introduction to semiconductor manufacturing technology. Prentice Hall, Upper Saddle River, NJ
2. Oliver MR (2004) Chemical-mechanical planarization of semiconductor materials. Springer, Berlin
3. Marinescu ID, Uhlmann E, Doi T (2006) Handbook of lapping and polishing. CRC, Boca Raton, FL
4. Banerjee G, Rhoades RL (2008) Chemical mechanical planarization historical review and future direction. Chemical Mechanical Polishing 9—213th ECS Meeting, 18–23 May 2008 (13), pp 1–19. doi:[10.1149/1.2912973](https://doi.org/10.1149/1.2912973)
5. Li Y (2007) Microelectronic applications of chemical mechanical planarization. Wiley, Hoboken, NJ
6. Davari B, Koburger CW, Schulz R, Warnock JD, Furukawa T, Jost M, Taur Y, Schwittek WG, DeBrosse JK, Kerbaugh ML, Mauer JL (1989) A new planarization technique, using a combination of RIE and chemical mechanical polish (CMP). 1989 international electron devices meeting—technical digest, 3–6 December 1989, pp 61–64
7. Jeong Deog K, Dae Won S, Dong Won H, Jin Woong K, Nae Hak P, Sang Beom H (1999) Investigations in polysilicon CMP to apply in sub-quarter micron DRAM device. ICVC'99 6th international conference on VLSI and CAD, 26–27 Oct 1999, pp 214–217. doi:[10.1109/icvc.1999.820881](https://doi.org/10.1109/icvc.1999.820881)
8. Edelstein D, Heidenreich J, Goldblatt R, Cote W, Uzoh C, Lustig N, Roper P, McDevitt T, Motsiff W, Simon A, Dukovic J, Wachnik R, Rathore H, Schulz R, Su L, Luce S, Slattery J (1997) Full copper wiring in a sub-0.25 μ m CMOS ULSI technology. International electron devices meeting IEDM technical digest, 7–10 Dec 1997, pp 773–776. doi:[10.1109/iedm.1997.650496](https://doi.org/10.1109/iedm.1997.650496)
9. Goldblatt RD, Agarwala B, Anand MB, Barth EP, Biery GA, Chen ZG, Cohen S, Connolly JB, Cowley A, Dalton T, Das SK, Davis CR, Deutsch A, DeWan C, Edelstein DC, Emmi PA, Faltermeier CG, Fitzsimmons JA, Hedrick J, Heidenreich JE, Hu CK, Hummel JP, Jones P, Kaltalioglu E, Kastenmeier BE, Krishnan M, Landers WF, Liniger E, Liu J, Lustig NE, Malhotra S, Manger DK, McGahay V, Mih R, Nye HA, Purushothaman S, Rathore HA, Seo SC, Shaw TM, Simon AH, Spooner TA, Stetter M, Wachnik RA, Ryan JG (2000) A high performance 0.13 μ m copper BEOL technology with low-k dielectric. Proceedings of the IEEE 2000 international interconnect technology conference, 5–7 Jun 2000, pp 261–263. doi:[10.1109/iitc.2000.854342](https://doi.org/10.1109/iitc.2000.854342)
10. BCC Research (2008) Chemical mechanical polishing (CMP) equipment and materials. A Market Research Report by BCC Research. <http://www.bccresearch.com/report/chemical-mechanical-polishing-cmp-avm047b.html> Accessed 20 June 2012
11. Liu Y, Zhang K, Wang F, Di W (2003) Investigation on the final polishing slurry and technique of silicon substrate in ULSI. IUMRS-ICEM 2002, 10–14 June 2002(66), pp 438–444. doi:[10.1016/s0167-9317\(02\)00908-5](https://doi.org/10.1016/s0167-9317(02)00908-5)
12. Smeys P (1996) Local oxidation of silicon for isolation. Dissertation, Stanford University
13. Hui J, Vande Voorde P, Moll J (1985) Scaling limitations of submicron local oxidation technology. In: International electron devices meeting. Technical Digest (Cat. No. 85CH2252-5), 1–4 Dec 1985, New York, NY, USA. IEEE, pp 392–395
14. Fazan PC, Mathews VK (1993) Highly manufacturable trench isolation process for deep submicron DRAMs. Proceedings of the 1993 I.E. international electron devices meeting, 5–8 Dec 1993, pp 57–60
15. Kageyama M, Hashimoto K, Onoda H (1999) Electromigration performance of Al-Si-Cu filled vias with titanium glue layer. Microelectron Reliab 39(11):1697–1706. doi:[10.1016/s0026-2714\(99\)00175-4](https://doi.org/10.1016/s0026-2714(99)00175-4)

16. Lakshminarayanan S, Steigerwald J, Price DT, Bourgeois M, Chow TP, Gutmann RJ, Murarka SP (1994) Contact and via structures with copper interconnects fabricated using dual damascene technology. *IEEE Electron Device Let* 15(8):307–309. doi:[10.1109/55.296225](https://doi.org/10.1109/55.296225)
17. Broomfield MC, Spooner TA (1996) HDP dielectric BEOL gapfill: a process for manufacturing. Advanced semiconductor manufacturing conference and workshop, 1996 ASMC 96 Proceedings IEEE/SEMI 1996, pp 255–258. doi:[10.1109/asmc.1996.558013](https://doi.org/10.1109/asmc.1996.558013)
18. Ein-Eli Y, Starosvetsky D (2007) Review on copper chemical–mechanical polishing (CMP) and post-CMP cleaning in ultra large system integrated (ULSI)—an electrochemical perspective. *Electrochim Acta* 52(5):1825–1838. doi:[10.1016/j.electacta.2006.07.039](https://doi.org/10.1016/j.electacta.2006.07.039)
19. Wang MT, Tsai MS, Liu C, Tseng WT, Chang TC, Chen LJ, Chen MC (1997) Effects of corrosion environments on the surface finishing of copper chemical mechanical polishing. *Thin Solid Films* 308–309:518–522. doi:[10.1016/s0040-6090\(97\)00500-2](https://doi.org/10.1016/s0040-6090(97)00500-2)
20. Stavreva Z, Zeidler D, Ploetner M, Drescher K (1997) Characteristics in chemical-mechanical polishing of copper: comparison of polishing pads. *Appl Surf Sci* 108(1):39–44. doi:[10.1016/s0169-4332\(96\)00572-7](https://doi.org/10.1016/s0169-4332(96)00572-7)
21. Du T, Tamboli D, Desai V, Seal S (2004) Mechanism of copper removal during CMP in acidic H₂O₂ slurry. *J Electrochem Soc* 151(4):G230–G235. doi:[10.1149/1.1648029](https://doi.org/10.1149/1.1648029)
22. Stein DJ, Hetherington D, Guilinger T, Cecchi JL (1998) In situ electrochemical investigation of tungsten electrochemical behavior during chemical mechanical polishing. *J Electrochem Soc* 145(9):3190–3196
23. Subramanian RS, Zhang L, Babu SV (1999) Transport phenomena in chemical mechanical polishing. *J Electrochem Soc* 146(11):4263–4272. doi:[10.1149/1.1392626](https://doi.org/10.1149/1.1392626)
24. Bernard P, Valette S, Daveau S, Abry JC, Tabary P, Kapsa P (2008) Nature and removal of the modified layer in Cu CMP with ferric nitrate as oxidizer. *Tribol Int* 41(5):416–424. doi:[10.1016/j.triboint.2007.09.009](https://doi.org/10.1016/j.triboint.2007.09.009)
25. Peethala BC, Babu SV (2011) Ruthenium polishing using potassium periodate as the oxidizer and silica abrasives. *J Electrochem Soc* 158(3):H271–H276. doi:[10.1149/1.3528942](https://doi.org/10.1149/1.3528942)
26. Peethala BC, Roy D, Babu SV (2011) Controlling the galvanic corrosion of copper during chemical mechanical planarization of ruthenium barrier films. *Electrochem Solid-State Lett* 14(7):H306–H310. doi:[10.1149/1.3589308](https://doi.org/10.1149/1.3589308)
27. Kim I-K, Cho B-G, Park J-G, Park J-Y, Park H-S (2009) Effect of pH in Ru slurry with sodium periodate on Ru CMP. *J Electrochem Soc* 156(3):H188–H192. doi:[10.1149/1.3058594](https://doi.org/10.1149/1.3058594)
28. Kim I-K, Kang Y-J, Kwon T-Y, Cho B-G, Park J-G, Park J-Y, Park H-S (2008) Effect of sodium periodate in alumina-based slurry on Ru CMP for metal-insulator-metal capacitor. *Electrochem Solid-State Lett* 11(6):H150–H153. doi:[10.1149/1.2901544](https://doi.org/10.1149/1.2901544)
29. Cui H, Cho J-Y, Hwang H-S, Lim J-H, Park J-H, Park HS, Hong K, Park J-G (2010) Potassium permanganate as oxidizer in alkaline slurry for chemical mechanical planarization of nitrogen-doped polycrystalline Ge₂ Sb₂Te₅ Film. *J Electrochem Soc* 157(11):H1036–H1041. doi:[10.1149/1.3486886](https://doi.org/10.1149/1.3486886)
30. Steigerwald JM, Duquette DJ, Murarka SP, Gutmann RJ (1995) Electrochemical potential measurements during the chemical-mechanical polishing of copper thin films. *J Electrochem Soc* 142(7):2379–2385
31. Wu Y-F, Tsai T-H (2007) Effect of organic acids on copper chemical mechanical polishing. *Microelectron Eng* 84(12):2790–2798. doi:[10.1016/j.mee.2007.01.123](https://doi.org/10.1016/j.mee.2007.01.123)
32. Seal S, Kuiry SC, Heinmen B (2003) Effect of glycine and hydrogen peroxide on chemical-mechanical planarization of copper. *Thin Solid Films* 423(2):243–251. doi:[10.1016/s0040-6090\(02\)00989-6](https://doi.org/10.1016/s0040-6090(02)00989-6)
33. Gorantla VRK, Assiongbon KA, Babu SV, Roy D (2005) Citric acid as a complexing agent in CMP of copper investigation of surface reactions using impedance spectroscopy. *J Electrochem Soc* 152(5):G404–G410. doi:[10.1149/1.1890786](https://doi.org/10.1149/1.1890786)
34. Gorantla VRK, Babel A, Pandija S, Babu SV (2005) Oxalic acid as a complexing agent in CMP slurries for copper. *Electrochem Solid-State Lett* 8(5):G131–G134. doi:[10.1149/1.1883873](https://doi.org/10.1149/1.1883873)

35. Luo Q, Babu SV, Campbell DR (1996) Stabilization of alumina slurry for chemical-mechanical polishing of copper. *Langmuir* 12(15):3563–3566. doi:[10.1021/la960062w](https://doi.org/10.1021/la960062w)
36. Brusic V, Frisch MA, Eldridge BN, Novak FP, Kaufman FB, Rush BM, Frankel GS (1991) Copper corrosion with and without inhibitors. *J Electrochem Soc* 138(8):2253–2259
37. Carpio R, Farkas J, Jairath R (1995) Initial study on copper CMP slurry chemistries. *Thin Solid Films* 266(2):238–244. doi:[10.1016/0040-6090\(95\)06649-7](https://doi.org/10.1016/0040-6090(95)06649-7)
38. Cohen SL, Brusic VA, Kaufman FB, Frankel GS, Motakef S, Rush B (1990) X-ray photoelectron spectroscopy and ellipsometry studies of the electrochemically controlled adsorption of benzotriazole on copper surfaces. *J Vac Sci Technol A Vac Surf Films* 8(3):2417–2424
39. Hong Y, Roy D, Babu SV (2005) Ammonium dodecyl sulfate as a potential corrosion inhibitor surfactant for electrochemical mechanical planarization of copper. *Electrochem Solid-State Lett* 8(11):G297–G300. doi:[10.1149/1.2042618](https://doi.org/10.1149/1.2042618)
40. Philipossian A, Lee H, Babu SV, Patri U, Hong Y, Economikos L, Goldstein M, Zhuang Y, Borucki L (2006) Study of inhibition characteristics of slurry additives in copper CMP using force spectroscopy. In: 10th International symposium on silicon materials science and technology—209th meeting of the Electrochemical Society, 7–12 May 2006, Denver, CO, United states, 2006. ECS Transactions. Electrochemical Society Inc., pp 515–522
41. Ying L, Tianbao D, Desai V (2003) Chemical-mechanical planarization of copper: the effect of inhibitor and complexing agent. In: Chemical-mechanical planarization. Symposium, 22–24 April 2003, Warrendale, PA, USA, 2003. (Mater. Res. Soc. Symposium Proceedings vol.767). Mater. Res. Soc. pp 297–302
42. Palla BJ, Shah DO (2000) Correlation of dispersion stability with surfactant concentration and abrasive particle size for chemical mechanical polishing (CMP) slurries. *J Disper Sci Technol* 21(5):491–509
43. Pan Y, Lu X, Pan G, Liu Y, Luo J (2010) Performance of sodium dodecyl sulfate in slurry with glycine and hydrogen peroxide for copper-chemical mechanical polishing. *J Electrochem Soc* 157(12):H1082–H1087. doi:[10.1149/1.3494159](https://doi.org/10.1149/1.3494159)
44. Kang H-G, Katoh T, Lee M-Y, Park H-S, Paik U, Park J-G (2004) Effect of molecular weight of surfactant in nano ceria slurry on shallow trench isolation chemical mechanical polishing (CMP). *Jpn J Appl Phys 2 Lett* 43(8B):L1060–L1063. doi:[10.1143/jjap.43.l1060](https://doi.org/10.1143/jjap.43.l1060)
45. Seo Y-J, Lee W-S (2005) Effects of different oxidizers on the W-CMP performance. In: EMRS 2004, symposium D: functional oxides for advanced semiconductor technologies, 2005. Materials Science and Engineering B: Solid-State Materials for Advanced Technology. Elsevier Ltd, pp 281–284. doi:[10.1016/j.mseb.2004.12.064](https://doi.org/10.1016/j.mseb.2004.12.064)
46. Joo S, Liang H (2012) Tribo-electrochemical characterization of copper with patterned geometry. *Microelectron Eng* 98:12–18. doi:[10.1016/j.mee.2012.05.023](https://doi.org/10.1016/j.mee.2012.05.023)
47. Tromans D (1998) Aqueous potential-pH equilibria in copper-benzotriazole systems. *J Electrochem Soc* 145(3):L42–L45
48. Liu X, Zhou F, Liang Y, Liu W (2006) Benzotriazole as the additive for ionic liquid lubricant: one pathway towards actual application of ionic liquids. *Tribol Lett* 23(3):191–196. doi:[10.1007/s11249-006-9050-7](https://doi.org/10.1007/s11249-006-9050-7)
49. Song M-G, J-h L, Lee Y-G, J-h K (2006) Stabilization of gamma alumina slurry for chemical-mechanical polishing of copper. *J Colloid Interface Sci* 300(2):603–611. doi:[10.1016/j.jcis.2006.04.046](https://doi.org/10.1016/j.jcis.2006.04.046)
50. Jui-Chin C, Wen-Ta T (2004) Effects of hydrogen peroxide and alumina on surface characteristics of copper chemical-mechanical polishing in citric acid slurries. *Mater Chem Phys* 87(2–3):387–393. doi:[10.1016/j.matchemphys.2004.06.007](https://doi.org/10.1016/j.matchemphys.2004.06.007)
51. Zefang Z, Lei Y, Weili L, Zhitang S (2010) Surface modification of ceria nanoparticles and their chemical mechanical polishing behavior on glass substrate. *Appl Surf Sci* 256(12):3856–3861. doi:[10.1016/j.apsusc.2010.01.040](https://doi.org/10.1016/j.apsusc.2010.01.040)
52. Zefang Z, Weili L, Jingkang Z, Zhitang S (2010) Synthesis, characterization of ceria-coated silica particles and their chemical mechanical polishing performance on glass substrate. *Appl Surf Sci* 257(5):1750–1755. doi:[10.1016/j.apsusc.2010.09.009](https://doi.org/10.1016/j.apsusc.2010.09.009)

53. Zhu H, Tessaroto LA, Sabia R, Greenhut VA, Smith M, Niesz DE (2004) Chemical mechanical polishing (CMP) anisotropy in sapphire. *Appl Surf Sci* 236(1–4):120–130. doi:[10.1016/j.apsusc.2004.04.027](https://doi.org/10.1016/j.apsusc.2004.04.027)
54. Jindal A, Hegde S, Babu SV (2002) Chemical mechanical polishing using mixed abrasive slurries. *Electrochem Solid-State Lett* 5(7):G48–G50. doi:[10.1149/1.1479297](https://doi.org/10.1149/1.1479297)
55. Suzuki K, Saitou T, Korezawa T, Khajornrungruang P, Kimura K (2010) Study on sapphire chemical mechanical polishing using mixed abrasive slurry with fullereneol. In: *Advanced metallization conference 2010, 5–7 Oct 2010, Albany, NY, United States*. Advanced Metallization Conference (AMC). Materials Research Society, pp 294–295
56. Liang H, Craven DR (2005) Tribology. In: *Chemical-mechanical planarization*. Taylor & Francis, Boca Raton, FL
57. Bowden FP, Tabor D (1958) *The friction and lubrication of solids*. Clarendon, Oxford
58. Liang H, Martin JM, Lee R (2001) Influence of oxides on friction during Cu CMP. *J Electron Mater* 30(4):391–395
59. Pourbaix M (1974) *Atlas of electrochemical equilibria in aqueous solutions*. National Association of Corrosion Engineers, Houston, TX
60. Liang H, Mogne TL, Martin J-M (2002) Interfacial transfer between copper and polyurethane in chemical-mechanical polishing. *J Electron Mater* 31(8):872–878
61. Park KH (2008) Investigation of pad surface topography for material removal uniformity in CMP process. Dissertation, Pusan National University
62. Bozkaya D, Muftu S (2009) A material removal model for CMP based on the contact mechanics of pad, abrasives, and wafer. *J Electrochem Soc* 156(12):H890–H902. doi:[10.1149/1.3231691](https://doi.org/10.1149/1.3231691)
63. Mischler S, Spiegel A, Landolt D (1999) The role of passive oxide films on the degradation of steel in tribocorrosion systems. In: *12th international conference on wear of materials, 25–29 April 1999, Switzerland*. Wear (Switzerland). Elsevier, pp 1078–1087. doi:[10.1016/S0043-1648\(99\)00056-3](https://doi.org/10.1016/S0043-1648(99)00056-3)
64. Bhushan B (1999) *Principles and applications of tribology*. Wiley, New York
65. Liang H (2005) Chemical boundary lubrication in chemical-mechanical planarization. In: *Boundary lubrication, 2005*. Tribology International. Elsevier Ltd, pp 235–242. doi:[10.1016/j.triboint.2004.08.006](https://doi.org/10.1016/j.triboint.2004.08.006)
66. Ng D, Liang H (2008) Comparison of interfacial forces during post-chemical-mechanical-polishing cleaning. *J Tribol* 130(2):1–5. doi:[10.1115/1.2908896](https://doi.org/10.1115/1.2908896)
67. Kar P, Wang K, Liang H (2008) Oxidation of tantalum with mechanical force. *Electrochem Solid-State Lett* 11(2):C13–C17. doi:[10.1149/1.2820616](https://doi.org/10.1149/1.2820616)
68. Huitink D, Feng G, Hong L (2010) Tribo-electrochemical surface modification of tantalum using in situ AFM techniques. *Scanning* 32(5):336–344. doi:[10.1002/sca.20197](https://doi.org/10.1002/sca.20197)
69. Huitink D, Feng G, Ke W, Hong L (2010) In situ monitoring of tantalum during electrochemical-mechanically induced oxidation. *Electrochem Solid-State Lett* 13(9):F16–F19. doi:[10.1149/1.3457845](https://doi.org/10.1149/1.3457845)
70. Xu G, Liang H, Zhao J, Li Y (2004) Investigation of copper removal mechanisms during CMP. *J Electrochem Soc* 151(10):G688–G692. doi:[10.1149/1.1787497](https://doi.org/10.1149/1.1787497)
71. Liang H, Kaufman F, Sevilla R, Anjur S (1997) Wear phenomena in chemical mechanical polishing. *Wear* 211(2):271–279. doi:[10.1016/S0043-1648\(97\)00124-5](https://doi.org/10.1016/S0043-1648(97)00124-5)
72. Larsen-Basse J, Liang H (1999) Probable role of abrasion in chemo-mechanical polishing of tungsten. In: *International Conference on Erosive and Abrasive Wear (ICEAW). Incorporating the 9th international conference on erosion by liquid and solid impact (ELSI IX), 13–17 Sept 1998, Switzerland*. Wear (Switzerland). Elsevier, pp 647–654. doi:[10.1016/S0043-1648\(99\)00248-3](https://doi.org/10.1016/S0043-1648(99)00248-3)
73. Gao F, Liang H (2009) Material removal mechanisms in electrochemical-mechanical polishing of tantalum. *Electrochim Acta* 54(27):6808–6815. doi:[10.1016/j.electacta.2009.06.093](https://doi.org/10.1016/j.electacta.2009.06.093)

74. Walter GW (1990) A comparison of single frequency and wide frequency range impedance tests for painted metals. *Corros Sci* 30(6–7):617–629. doi:[10.1016/0010-938x\(90\)90027-3](https://doi.org/10.1016/0010-938x(90)90027-3)
75. Wosu SN (2007) Anodic oxidation of tantalum in water and biological solutions using current limiting constant voltage method. *J Mater Sci* 42(11):4087–4097
76. Li YM, Young L (1998) Effect of incorporated electrolyte species on the ac response of the high field ionic conduction process in anodic oxide films on tantalum. *Electrochim Acta* 44(4):605–611. doi:[10.1016/s0013-4686\(98\)00183-2](https://doi.org/10.1016/s0013-4686(98)00183-2)
77. Ng D, Sen T, Gao F, Liang H (2008) Friction and wear-mode comparison in copper electrochemical mechanical polishing. *J Electrochem Soc* 155(7):H520–H524
78. Kulkarni M, Dedy N, Baker M, Hong L, Her R (2007) Electropotential-stimulated wear of copper during chemical mechanical planarization. *Wear* 263(7–12):1470–1476. doi:[10.1016/j.wear.2006.12.028](https://doi.org/10.1016/j.wear.2006.12.028)

Questions and Answers

1. What is CMP? Chemical–mechanical planarization or chemical–mechanical planarization.
2. What is patterned wafer?
3. What are roles of tribology in CMP?
4. Discuss difference in material removal between Ta and Cu CMP.

Chapter 24

Tribology in Metal Forming

Pradeep L. Menezes, Carlton J. Reeves, Satish V. Kailas,
and Michael R. Lovell

Abstract The ability to produce a variety of shapes from a block of metal at high rates of production has been one of the real technological advances of the current century. This transition from hand-forming operations to mass-production methods has been an important factor in the great improvement in the standard of living, which occurred during the period. With these forming processes, it is possible to mechanically deform metal into a final shape with minimal material removal. The use of metal forming processes is widely spread over many different industries. In metal forming processes, friction forces between metal and forming tools play an important role because of their influence on the process performance and on the final product properties. In many instances, this frictional behavior is often taken into account by using a constant coefficient of friction in the simulation of metal forming processes. Several different types of instruments are constructed to measure the coefficient of friction for different materials. In this chapter, the fundamental concept of forming processes and the influence of friction in metal forming are discussed. A case study on the influence of friction based on surface texture during metal forming is also presented.

P.L. Menezes (✉) • M.R. Lovell
Department of Industrial Engineering, University of Wisconsin-Milwaukee,
Milwaukee, WI 53211, USA
e-mail: menezesp@uwm.edu

C.J. Reeves
Department of Mechanical Engineering, University of Wisconsin-Milwaukee,
Milwaukee, WI 53211, USA

S.V. Kailas
Department of Mechanical Engineering, Indian Institute of Science,
Bangalore 560 012, India

1 Introduction

The basic understanding of sliding friction at dry contacts has been relatively well known since the early work of Coulomb in the seventeenth and eighteenth centuries. Friction is caused by the shearing of asperity junctions, by asperity interlocking between two surfaces, and by plastic deformation of the soft surface by hard asperity.

Friction has an important influence in metal forming operations. Friction arises during sliding of the workpiece against the tool. Friction between the tool and workpiece has a significant effect on material deformation, forming load, component surface finish, and die wear. It is also an essential input parameter for the ever-increasing use of finite element (FE) simulation for metal forming. The frictional conditions prevailing at the tool–workpiece interface greatly influence distribution of stresses and thereby the material flow. As friction plays a crucial role in metal forming, it is important to determine the friction as accurately as possible. Although a tremendous amount of work and discussion has gone into this subject over the decades, friction in metal forming is still not completely understood [1–3].

1.1 Fundamentals of Metal Forming

Metals can be formed into useful shapes, such as tubes, rods, and sheets, during metalworking. Useful shapes may be formed in three basic ways:

1. *By casting processes:* Here, the molten liquid is poured into a mold that holds the required shape, and allowing hardens the metal with or without external pressure. This process occurs in the liquid state.
2. *By plastic deformation or forming processes:* Here, the volume and mass of metal are preserved, and the metal is displaced from one location to another location by applying pressure. This process occurs in the solid state.
3. *By metal removal or machining processes:* Here, the material is removed in order to give it the required shape. This process also occurs in the solid state.

1.2 Classification of Metal Forming

Since the discovery of metal forming, hundreds of processes have been developed for specific metalworking applications. However, these processes may be classified into only a few classes on the basis of the type of forces applied to the workpiece as it is deformed into a particular shape as shown in Fig. 24.1 [4]. The classes are:

1. Direct-compression-type processes
2. Indirect-compression-type processes
3. Tension-type processes
4. Bending processes
5. Shearing processes

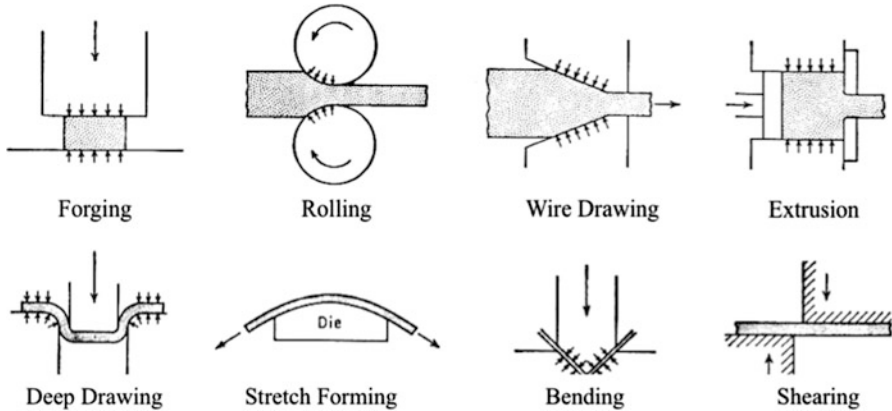
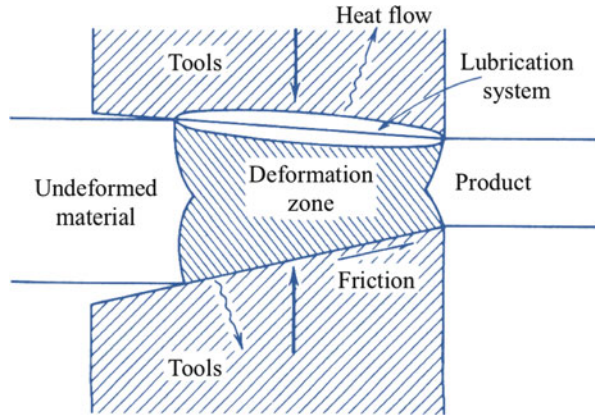


Fig. 24.1 Typical forming operations [4]

1. *Direct-compression-type processes*: In direct-compression-type processes, the force is applied to the surface of the workpiece, and the metal flows at right angles to the direction of the compression, for example, forging and rolling processes (see Fig. 24.1).
2. *Indirect-compression-type processes*: In indirect-compression-type processes, the primary applied forces are frequently tensile, but indirect compressive forces are developed by the reaction of the workpiece with the die. Therefore, the metal flows under the action of a combined stress state, which includes high compressive forces in at least one of the principal directions. Examples: wire drawing, tube drawing, deep drawing, and extrusion.
3. *Tension-type processes*: The best example of a tension-type forming process is stretch forming, where metal sheet is wrapped to the contour of a die under the application of tensile forces.
4. *Bending processes*: Bending involves the application of bending moments to the sheet.
5. *Shearing processes*: Shearing involves the application of shearing forces of sufficient magnitude to rupture the metal in the plane of shear.

The deformation processing system can be best viewed as shown in Fig. 24.2. The deformation zone can be analyzed with the distribution of stress, strain, particle velocities, and the overall pressure required to perform the operation. Foremost, the applied forces must develop yielding in the workpiece material, but the stresses must not locally create any fracture. During this process, the metallurgical phenomena, such as strain hardening, recrystallization, and fracture, are important. Often, other phenomena, such as strain rates and temperature, are also important under specialized process conditions. During the metalworking process, the workpiece will be in contact with the nondeforming tools or dies. The friction between the tool and the workpiece interface and the heat transfer from the workpiece to the tool are

Fig. 24.2 Deformation processing system [4]



important considerations [4]. This is because tool wear and change in surface finish of the workpiece may occur during metal processing.

2 Metal Forming Processes

2.1 Manufacturing Processes

Metal manufacturing processes are those processes that are done to manipulate the size, shape, or appearance of materials. Many of the today's products require various manufacturing techniques to form, shape, and fabricate the necessary components. Raw materials are seldom useable immediately as they must be refined to separate impurities or unwanted materials from the more desirable materials, for example, iron ore must be refined to make steel. Secondary processes are procedures where prepared materials are used to manufacture more complex items. Most secondary processes result in products that are eventually bought and used by consumers or original equipment manufacturers to undergo more processes before being used by consumers.

In regard to metal forming processes, most metals, which are not used in cast form, are reduced to standard shapes for subsequent processing. Companies that manufacture metals often supply metals in the form of ingots, which are obtained by casting liquid metals into square cross sections known as slabs, billets, or blooms. Sometimes continuous casting methods are used to cast liquid metals into their appropriate shape. These shapes are further processed through rolling, forging, extrusion, or drawing to produce metal materials that are in standard form for distribution such as plates, sheets, tubes, rods, and various structural sections. Figure 24.3 details the sequence of operations for obtaining different shapes and the transformation from billets, blooms, and slabs to the final shapes often found by customers. In general, metal forming processes are carried out under hot-working or cold-working conditions. Hot-working is defined as the process of deformation of

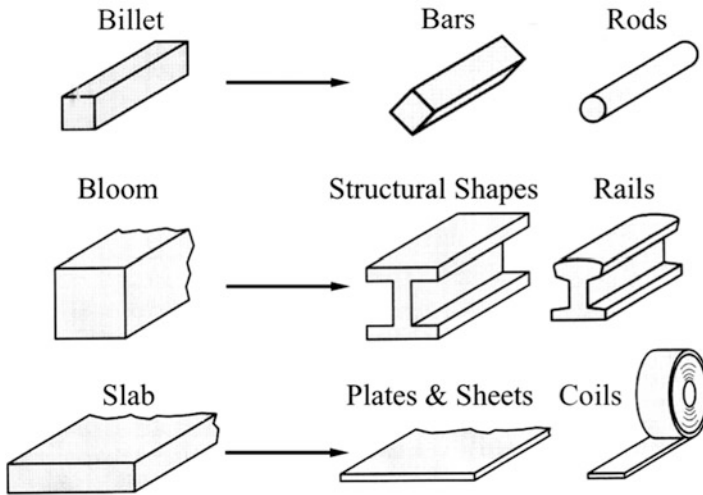


Fig. 24.3 Visualization from a billet, bloom, or slab to its final form

the workpiece under conditions of high temperature and strain rate such that the recovery process takes place along with the deformation of the workpiece. Cold-working is defined as the process of deformation under conditions where the recovery process is ineffective [4]. In hot-working, the strain hardening and distorted grain structure in the workpiece produced by deformation are transforming into new strain-free grains due to the recrystallization processes. For these reasons, very large deformations are possible in hot-working because the recovery processes occur simultaneously with the deformation. Hot-working processes occur at a constant flow stress within the workpiece, and these flow stresses decrease with an increase in temperature; thus, the energy required to deform the material is generally much less for hot-working than for cold-working [4]. Since the strain hardening is not relieved in cold-working, the flow stress increases with the deformation, therefore limiting the amount of deformation to the point of fracture. In cold-working, these limitations can be relieved by the process of annealing in between successive cold-working processes. It is important to note that the distinction between hot-working and cold-working is not an arbitrary temperature, but rather the processes occur at material-dependent temperature where recrystallization will occur. The primary metal forming processes that will be discussed are rolling, forging, extrusion, tube and wire drawing, and deep drawing.

2.2 Rolling

Rolling is the most widely used metal forming process with nearly all metals undergoing this process because it allows for high production and close control of the final product [4]. Rolling is the process where a sheet or plate is drawn by means

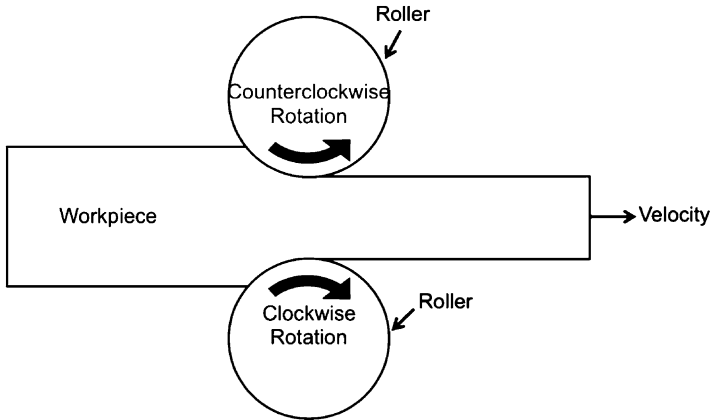


Fig. 24.4 Schematic of the rolling process for sheet and plates

of friction in between two rollers as shown in Fig. 24.4 [5]. The compressive forces applied by the rollers reduce the thickness of the workpiece while minimizing the cross-sectional area and causing the rolled material of the workpiece to elongate and spread. The final geometry of the workpiece depends on the contour of the roll gap, i.e., the distance between the rollers. Often the roller materials are cast iron, cast steel, or forged steel because of the high strength and wear resistance required. Generally, plates, sheets, rods, bars, pipes, rails, and other structural shapes undergo hot rolling, while sheets, strips, and foils with a good surface finish and increased mechanical strength undergo cold rolling [4]. Cold rolling also allows for a high degree of control over the final products dimensions and specifications. If the temperature of the workpiece is above its recrystallization temperature, then the process is termed as hot rolling. If the temperature of the workpiece is below its recrystallization temperature, the process is termed as cold rolling. In hot rolling, the rolls are generally rougher than in cold rolling, so that they can grasp the incoming workpiece and pull it through the roll gap. In cold rolling, the rolls are ground and polished for a smooth finish. During the rolling process, the grain size and structure change due to compression and the crystals of the rolled material become elongated in the rolling direction as shown in Fig. 24.5. In cold rolling, the crystals of the rolled material maintain the elongated shape, but in hot rolling, the crystals start reforming (due to recrystallization process) after coming out from the deformation zone (see Fig. 24.6).

As with many tribological applications, velocity and friction have an impact on the rolling process. If the peripheral velocity of rolls at entry exceeds that of the material to be rolled, which is dragged into the gap roll, this will cause the interface friction to be high. If in the deformation zone, the thickness of the material gets reduced, this elongates the material, thus increasing the linear speed at the exit, when leaving the gap roll. Within these variations, there exists a neutral point where roll speed and strip speeds are equal. At this point, the direction of the friction reverses.

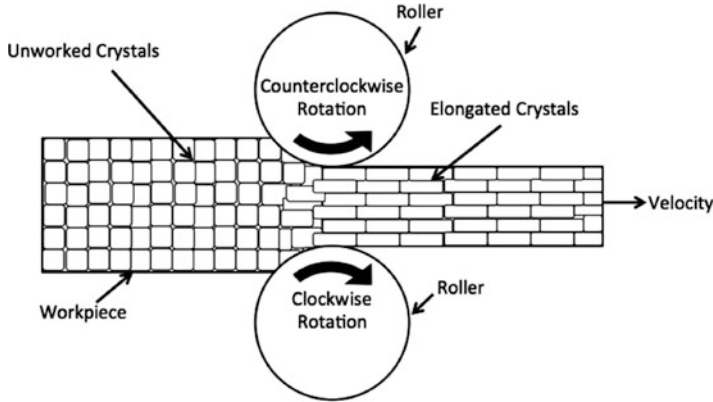


Fig. 24.5 Schematic of the grain or crystal elongation during the rolling process due to the compression and elongation of the rolled material

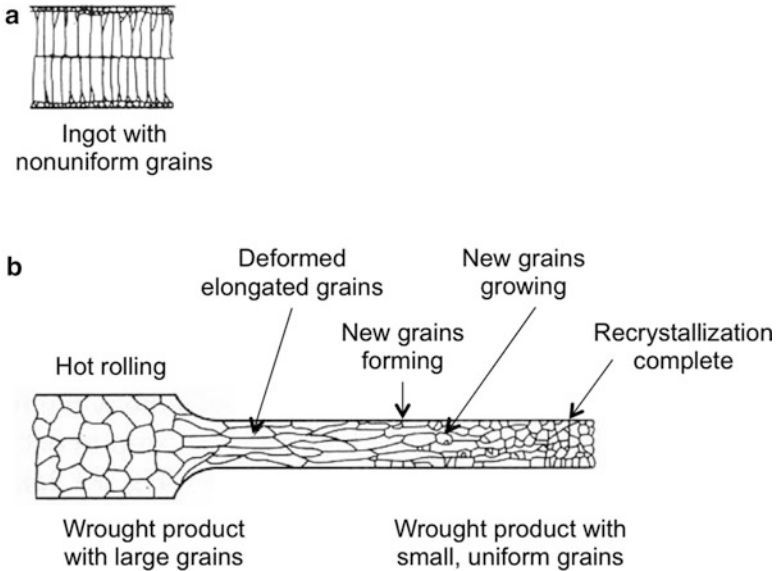


Fig. 24.6 Grain orientation in (a) ingot with nonuniform grains and (b) rolled material undergoing hot rolling

When the angle of contact α exceeds the friction angle λ , the rolls cannot draw fresh material, causing the roll torque and power input to increase with an increase in roll work contact length or roll radius. The pressure during rolling varies along the contact length in flat rolling. The peak pressure is often located at the neutral point. The friction in rolling is dependent on lubrication, work material, and also on the temperature. In cold rolling, the value of the coefficient of friction is around 0.1, and

Table 24.1 Typical lubricants and their coefficient of friction values in hot and cold rolling operations of various metals [6]

Material	Hot rolling— lubricant	Hot rolling— COF	Cold rolling— lubricant	Cold rolling— COF
Cu and Cu alloys	Emulsion, 2–8 % of mineral oil	0.3	2–10 % concentration of mineral oil with fat	0.01–0.03
Refractory metals	Dry	0.3	Mineral oil with boundary and EP additives	0.01–0.03
Steel	Water emulsion of fat + EP additive fat (ester) + EP	Sticking 0.4 0.3	3–6 % emulsion of palm oil	0.01–0.03
Ti alloys	Fat and water	Sticking	Esters or soap Castor oil, compounded mineral oil	0.2 0.2 0.2
Al and Mg alloys	Emulsion, 2–15 % of mineral oil	0.4	Mineral oil with 1–5 % fatty acid	0.01–0.03

in warm rolling, the coefficient of friction is around 0.2. In either case, the use of lubricants is kept at a minimum to control friction and satisfy various surface finish requirements. In hot rolling, the coefficient of friction is around 0.4. In some instances of hot rolling, a friction condition occurs due to adhesion, which causes the coefficient of friction to increase to 0.7. Here, the hot rolling material surface adheres to the roller; thus, the central part of the material undergoes severe deformation. Lubricants are used extensively in hot rolling processes to control the adhesion between the workpiece and the rollers. Commonly, lubricants used in rolling processes are oil or water based with plenty of extreme pressure additives to aid in the lubrication process through a mixed-film lubricating mechanism [6]. Some of the common lubricants used in hot and cold rolling operations are presented in Table 24.1.

2.3 Forging

Forging is one of the oldest metalworking processes dating back many centuries to ancient times when metallic tools were made by blacksmiths who hammered heated metals against an anvil to form various shapes. Forging is the process of hammering or pressing material between two dies to achieve the desired shape and structure through plastic deformation. Since the Industrial Revolution, the development of machinery has replaced the physical presence of a blacksmith with a variety of forging machinery that is capable of forming anything from a bolt to a turbine rotor, to an entire airplane wing [4]. Forging operations generally occur through hot-working; however, some metals and metal alloys require cold-working. Forging

Fig. 24.7 Schematic of open-die forging of a billet

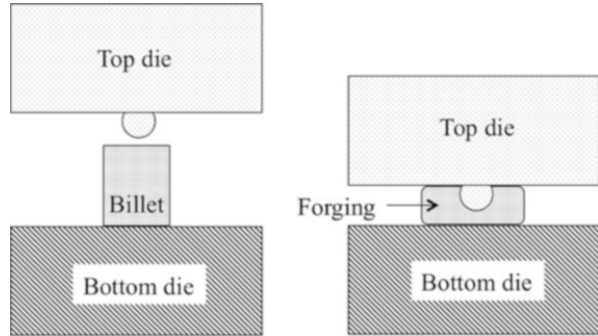
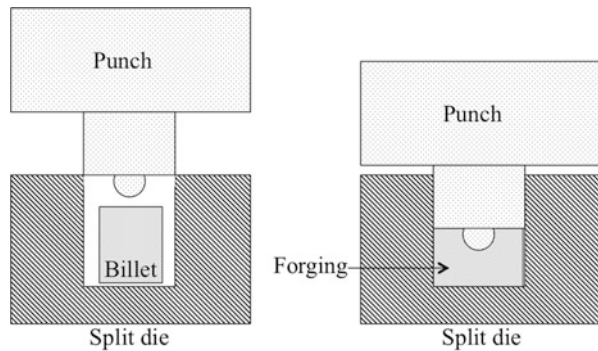


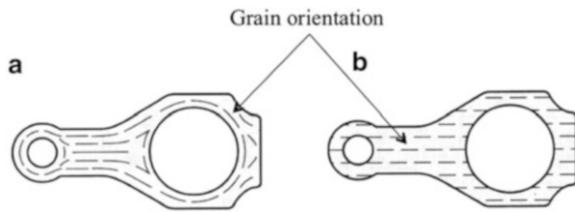
Fig. 24.8 Schematic of closed-die forging of a billet



can be classified into two classes of equipment: (1) the forging hammer or drop hammer, which delivers rapid impact blows to the surface of the workpiece, and (2) the forging press, which delivers slow-speed compressive forces to the workpiece. Depending upon the complexity of the part, forging is carried out as open-die forging or closed-die forging operation. Open-die forging, shown in Fig. 24.7, is the process where metal is compressed by hammering or pressing between flat or contoured dies either mechanically or manually, and the shape of the material is deformed through plastic deformation [5]. Open-die forging gets its name from the fact that the dies (the surfaces that are in contact with the workpiece) do not enclose the workpiece entirely, allowing the metal to flow except where contacted by the dies. Closed-die forging is the process where the metal is compressed between a shaped die and a hammer that presses the metal deforming it within the die causing the metal to flow and fill the die cavities as illustrated in Fig. 24.8 [5]. Two popular types of closed-die forging are drop forging and press forging. Drop forging is the repeated process of closed-die forging, where the hammer is dropped onto the metal workpiece and many successive strikes occur. In press forging, the metal is squeezed slowly by a hydraulic or mechanical press and the metal component is produced in a single strike. Open- and closed-die forging can be carried out as hot (temperatures above recrystallization temperature) or cold (temperatures below

Table 24.2 Typical lubricants and their coefficient of friction values in hot and cold forging operations of various metals [6]

Material	Hot forging— lubricant	Hot forging— COF	Cold forging— lubricant	Cold forging— COF
Cu and Cu alloys	Graphite in water	0.15	Fat: wax (lanolin),	0.07
			zinc stearate (soap),	0.05
			graphite or MoS ₂ in grease	0.07
Refractory metals	Glass and graphite	0.05	N/A	N/A
Steel	Soap	0.3	Lime and oil	0.1
	Graphite in water	0.2	Copper and oil	0.1
	Salt solution	0.2	Phosphate and soap	0.05
Ti alloys	MoS ₂	0.2	Zinc fluoride phosphate and soap	0.1
				0.05
Al and Mg alloys	Graphite in water	0.3	Lanolin	0.07
			Phosphate and soap	0.05

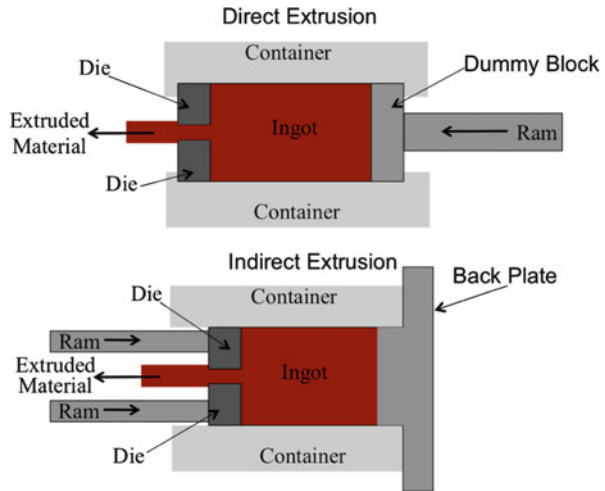
Fig. 24.9 Grain orientation in a (a) forged part and in a (b) machined part

recrystallization temperature) processes. In either hot or cold forging, lubricants are used to ensure proper material flow. Lubricants in forging are advantageous to prevent unwanted die wear and reduce local forging pressures on the die and forging material. Lubricants in cold forging typically consist of compounded oils and semi-solids such as fats, soaps, and waxes. In high-contact-pressure situations, MoS₂ is used as an extreme pressure additive. In hot forging, lubricants are composed of oil-based graphitic solutions or graphite-free solutions. Table 24.2 shows the typical lubricants used in hot and cold forging operations [6]. A benefit of forging, especially with the use of lubricants, is that the flow of material due to the plastic deformation produces desirable grain orientation of the metal when compared to standard machining processes. Figure 24.9 compares the grain orientation due to forging to the grain orientation produced by machining.

2.4 Extrusion

Extrusion is the process where a material is compressed in a chamber and the deformed material is forced to flow through a die orifice under high pressure.

Fig. 24.10 Schematic of the tooling and metal flow for direct and indirect extrusion process



The die opening corresponds to the cross section of the required product. Extrusion is a relatively new process and its commercial exploitation started in the nineteenth century with the extrusion of lead pipes and later to copper, brass, and steel. The extrusion of steel became available in the 1930s, when extrusion chambers could be designed to withstand high temperatures and pressures. Extrusion is primarily a hot-working process due to the large forces and high amounts of deformation; however, for softer materials, cold extrusion is also performed and it has become an important commercial process. There are a few types of extrusion processes that are used extensively in industry: direct extrusion, indirect extrusion, impact extrusion, and hydrostatic extrusion. Direct extrusion illustrated in Fig. 24.10 is the process where the metal flows in the same direction as that of the ram. Due to the relative motion between the heated billet and the chamber walls, friction is severe and is reduced by using molten glass as a lubricant in the case of steels and high-temperature alloys at higher temperatures [5]. At lower temperatures, oils with graphite powder are used for lubrication. The indirect extrusion process shown in Fig. 24.10 allows the metal to flow in the opposite direction of the ram. It is more efficient since it reduces friction losses considerably [5]. The process, however, is not used extensively because it restricts the length of the extruded component. Impact extrusion is similar to indirect extrusion. Here, the punch descends rapidly on the blank, which gets indirectly extruded onto the punch to give a tubular cross section. The length of the tube formed is controlled by the amount of metal in the slug and by the blank thickness. Collapsible tubes for pastes are commonly extruded by this method. Hydrostatic extrusion is a process in which the billet is completely surrounded by a pressurized liquid, except where the billet contacts the die. This process can be done hot, warm, or cold; however, the temperature is limited by the stability of the fluid used. Hydrostatic extrusion must be carried out in a sealed cylinder to carry the hydrostatic medium. The fluid can be pressurized in two manners: (1) by constant-rate extrusion where a ram is used to pressurize the

Table 24.3 Typical lubricants and their coefficient of friction values in hot and cold extrusion operations of various metals [6]

Material	Hot extrusion— lubricant	Hot extrusion— COF	Cold extrusion— lubricant	Cold extrusion— COF
Cu and Cu alloys	Graphite	0.2	Castor oil	0.03
Refractory metals	Glass coating plus graphite on die	0.05	N/A	N/A
Steel	Graphite, molten glass, glass powder	0.2	Graphite	N/A
Ti alloys	Graphite	0.2	N/A	N/A
Al and Mg alloys	None	Sticking friction	Lanolin	0.07

fluid inside the container or (2) by constant-pressure extrusion where a pump is used, possibly with a pressure intensifier, to pressurize the fluid, which is then pumped to the container. In the hydrostatic extrusion process, the friction between the container wall and the billet is eliminated; however, this process has got limited applications in industry due to specialized equipment, tooling cost, and a low production rate due to a long setup time.

Extrusion operations are similar to many other metal forming operations where friction is undesirable. Friction on the die during the extrusion operation can cause increases in extrusion pressure and destroy the homogeneity of the extruded material. Friction on the die also contributes to heat generation and hinders the performance of the extrusion process by minimizing the speed of the process and attainable cross-sectional configurations of the extruded material. To thwart friction, lubricants are used in some cases. Extrusion can be unlubricated or lubricated. Unlubricated extrusions are used in the process of extruding tubes, hot aluminum alloys, and copper alloys. Table 24.3 details some of the common lubricants for various metals undergoing hot or cold extrusion operations [6].

2.5 Drawing

Drawing is a cold metalworking process that uses tensile forces to stretch metal into long rods, wires, and tubes. In this process, a material is pulled through a die to reduce it to a desired shape and size. Figure 24.11 reveals a schematic of the drawing process for a rod or wire and a tube. In a typical wire drawing operation, one end of the wire is reduced and passed through the opening of the die, pulling with it the metal to reduce its diameter. By successive drawing operations through dies of reducing diameter, a rod can be reduced to a very small diameter. Undergoing annealing heat treatment between each successive drawing operation permits larger area reductions in the drawn material. Tungsten carbide dies are used for drawing hard wires, and diamond dies are the choice for fine wires. When a

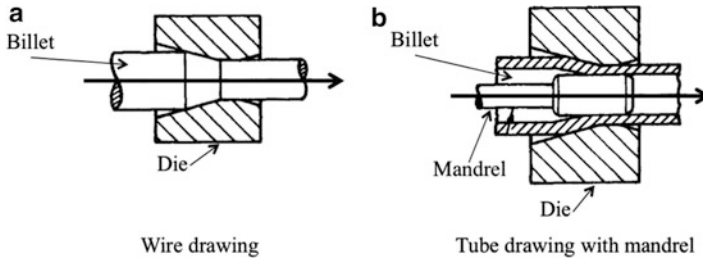
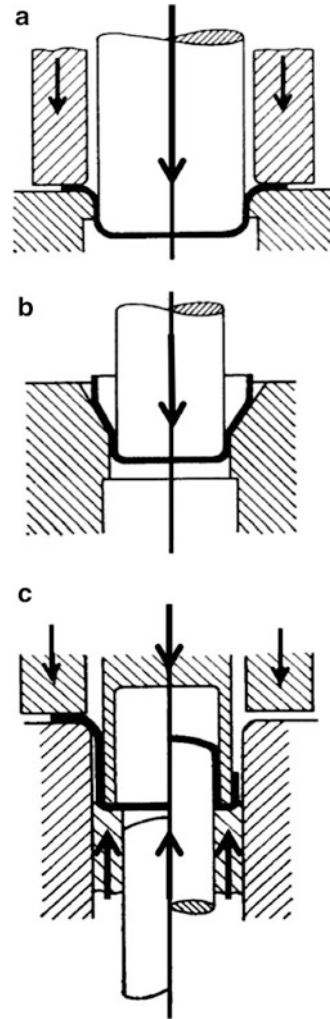


Fig. 24.11 Schematic of the drawing process of (a) rod or wire and (b) hollow tube

hollow tube is drawn through a die without any mandrel to support the inside of the tube, this process is known as tube sinking. When a mandrel or plug is used to support the inside diameter of the tube while being drawn through the die, this process is called tube drawing [4]. Tube drawing is similar to wire drawing, except that a mandrel is required to form the internal hole. As the blank is drawn into the die cavity, compressive stress is set up around the flange causing it to wrinkle or buckle the flange. Sheet metal drawing becomes deep drawing when the workpiece is drawing longer than its diameter. Figure 24.12 illustrates the deep drawing process where a sheet blank (hot or cold) is subjected to a peripheral hold-down pressure and is forced by a punch into and through the die to form a deep recessed part having a wall thickness the same as that of the blank [7]. This process is used to produce cylindrical or prismatic cups with or without a flange on the open end. Cylindrical-shaped parts such as cups, shells, or tubes from sheet metal can be redrawn to increase their length and to reduce their lateral dimensions. Along with deep drawing, it is common that the workpiece is also processed using other forming processes, such as piercing, ironing, necking, rolling, and beading.

Bar, wire, and tube drawing are often carried out at room temperature; however, because of the large compressive forces, which arise from the reduction of the metal with the die, significant deformations occur resulting in considerable temperature rises during the drawing operation [4]. These temperature rises along with increases in friction necessitate the use of lubricants during the drawing process. Drawing operations require lubricants to control the friction and to ensure adequate reductions in the size of the material. Lubricants are applied in drawing operations to reduce friction, wear, and heat generation. Drawing without lubricants results in material pickup, which can cause defects in the drawn material, large stresses in the deformation zones, fracture of the workpiece, or improper drawing processes. Minimal friction is required between the workpiece and the die in wire and tube drawing. Moderate friction is necessary in the process of drawing bars. Drawing operations can be performed with solid and liquid lubricants. Drawing under solid-lubricated conditions involves the use of soaps, whereas drawing under liquid-lubricated conditions involves the use of viscous oils or aqueous emulsions. Common applications of drawing utilize mixed-film regimes where lubricants are comprised of soaps with extreme additives. Table 24.4 presents the typically used lubricants for wire and tube drawing [6].

Fig. 24.12 Schematic of basic deep drawing processes with a rigid tool (a) first draw with a blankholder, (b) redraw without blankholder, and (c) reverse drawing



3 The Influence of Friction During Metal Forming

The knowledge of various parameters which control the friction forces is important in metalworking operations. Friction is an important process parameter that controls the tool load, product quality (geometry, tolerance, and surface finish), and tool wear. The coefficient of friction, if controlled properly, could generate the required stresses to deform the metal to the required shape. It could also lead to failure of the workpiece if not controlled properly, e.g., fracture of sheet in sheet metal forming.

In general, friction is controlled by many variables, such as surface texture, load, speed, temperature, lubricants, and material properties [8–16]. It is stated in the

Table 24.4 Typical lubricants and their coefficient of friction values in wire and tube drawing operations of various metals [6]

Material	Wire drawing—lubricant	Wire drawing—COF	Tube drawing—lubricant	Tube drawing—COF
Cu and Cu alloys	Mineral oil and fatty derivatives	0.03–0.15 (mixed film)	Soap film	0.05
Refractory metals	Copper and mineral oil	0.1	Copper and mineral oil	0.1
Steel	Mineral oil and fat and EP additives, phosphate and emulsion	0.07 0.1	Phosphate and soap	0.05
Ti alloys	Fluoride phosphate and soap	0.1	Metal and soap	0.07
Al and Mg alloys	Mineral oil and fatty derivatives	0.03–0.15 (mixed film)	Soap	0.07

literature that surface texture of the die is one of the key factors that control friction during metal forming. The influence of surface texture on friction is not well established although some efforts have been made to study the effect of surface texture on friction during metal forming processes using experiments. In one of the earliest experimental steps towards understanding the effect of surface texture on lubrication during metal forming, Schey [17] demonstrated the effect of different machined surfaces but did not examine in detail the effect of surface topography as such. Later, Geiger et al. [18] identified two types of lubricant pockets, closed and connected. In their investigation of cold forging, they were able to determine the proportion of surface area at the interface; they comprised it by analysis of the surface texture. They compared the difference between two types of surface texture but not in terms of surface roughness.

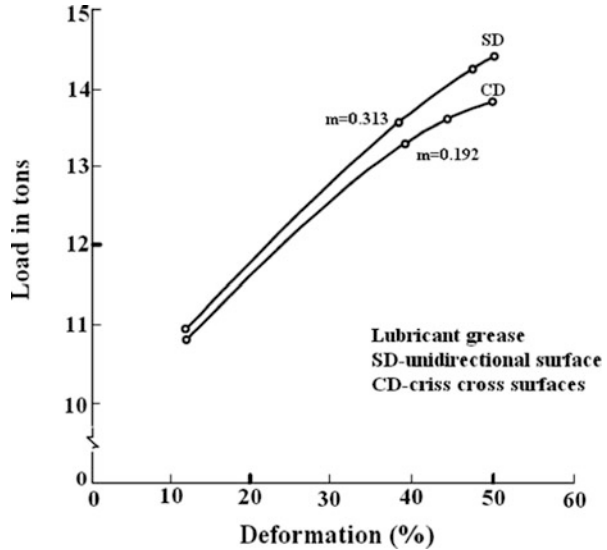
Many researchers have carried out experiments on friction to characterize the metal forming process and to study the effect of surface texture on friction during metal forming. With sheet metal forming as an industrial backdrop, Wagner [19] studied the influence of tool surfaces, coating on tool surfaces, sheet metal surfaces, coating on sheet metal surfaces, and with the influence of the lubrication on the frictional behavior. Wagner [19] summarized that the tribological conditions at the contact zones between the sheet surface and the tool surface play an important role in determining the limits of the forming process. It was concluded that the friction in various tribologically relevant contact zones affects the flow of the material at the tool and hence it was used deliberately to control the drawing process. Bello and Walton [20] studied the combined effect of surface roughness and lubrication on friction at the tool–metal interface in sliding contact in the presence of lubricant. In their experiment, strips of commercial pure aluminum were pulled through steel dies designed to give partial simulation of the conditions that exist in the flange and die radius profile regions of the deep drawing process. They found that the conventional surface roughness parameters do not provide a satisfactory functional

characterization of the surface in the context of the friction developed in sliding contact. They developed a new roughness parameter, which was found to be a better functional characteristic of the surface in regard to friction coefficient. Schedin [21] conducted experiments using U-bending test and strip drawing test to study the formation of transfer layer during forming processes. The experimental conditions resemble the contact conditions in sheet metal forming, where a hard and smooth tool surface will make repeated contacts with a soft and rough sheet surface. The research work inferred that it is impossible to completely avoid metal transfer in the sheet metal forming operation but that the growth of the transfer layer could be controlled by carefully designing the surface topography and using lubricants or coatings.

Rasp and Wichern [22] studied the effect of surface topography on frictional resistance using different kinds of surfaces. In their experiment, the five different specimen surfaces used were: as received, etched, coarse ground perpendicular to test direction, coarse ground parallel to test direction, and polished. It was found that the arithmetic roughness value (R_a) and lubrication regime have greater influence than the directionality of the surface lay. The influence of surface topography of the sheet material on the frictional characteristics of 3104 Al alloy sheet was investigated by Saha et al. [23] by stretching a strip around a cylindrical pin. They found that friction increased with the strain occurring during the contact, which supports the model relating friction to flattening of strip asperities and real area of contact. They also found that the coefficient of friction depends on the rolling direction of the strip. In all the above cases, the test material is deformable, so that the surface topography of deformable material cannot explain true friction values during metal forming process, and thus, it is important to have knowledge about the surface topography of tool material on the coefficient of friction.

A considerable amount of work has also been performed to study the effect of surface topography of harder materials on softer deformable materials during sliding in metal forming operations. Lakshmi pathy and Sagar [24], in their industrial relevant study, tried to understand the influence of die grinding marks' directionality on friction in open-die forging under lubricated conditions. Two sets of dies, one with unidirectional grinding marks and other with crisscross grinding marks, were used. It was found for the same percentage of deformation that the dies with the crisscross ground pattern required lesser forging loads when compared with the die having unidirectionally ground pattern (Fig. 24.13). Lower friction value was also observed for the forging process when the die with the crisscross surface pattern was used. They concluded that the lubrication breakdown tendency is more when pressing is done with unidirectionally ground die than crisscross ground die. Malayappan and Narayanasamy [25] analyzed the bulging effect of aluminum solid cylinders by varying the frictional conditions at the flat die surfaces. Different machining processes like grinding, milling, electro-spark machining, and lathe turning with emery finish were produced on the flat dies to vary the frictional conditions. It was concluded that the barreling depends on friction and ultimately the surface texture.

Fig. 24.13 Forging load versus deformation at different die surfaces [24]



Määttä et al. [26] studied the friction of stainless steel strips against different tool steels and reported that the surface texture of the steel, rather than its composition, had the greatest effect on the friction at the tool and workpiece interface. Staph et al. [27] studied the effect of surface texture and surface roughness on scuffing using a caterpillar disk tester. The authors used steel disks of varying roughness and texture and concluded that both surface texture and surface roughness affect frictional behavior. Koura [28] studied the effect of surface texture on friction mechanism using a universal testing machine. Steel specimens were prepared to various degrees of roughness by grinding, lapping, and polishing. The results showed that the behavior of surfaces and thus friction during sliding depends on the degree of roughness. Costa and Hutchings [29] investigated the influence of surface texture on friction during metal forming processes. Figure 24.14 shows the variation of friction coefficients for the tests with dies of different surface textures. It was found that the friction was strongly influenced by the relative orientation between the grooves generated on the die surfaces and the drawing direction. Hu and Dean [30] analyzed the relation between friction behavior and surface texture using a ring upsetting test. The tests were carried out using either a liquid lubricant or under clean dry conditions. Two types of workpiece surfaces, random and directional, were prepared by either shot blasting or EDM or turning to different levels of surface finish. It was found that for random surfaces, smoother surfaces could retain more lubricant and decrease the friction resistance.

Wakuda et al. [31] studied the frictional properties of silicon nitride ceramic surfaces in which dimple patterns were machined with different size, density, and geometry against hardened steel using abrasive jet machining (AJM) and laser beam machining (LBM) techniques. Figure 24.15 shows the friction coefficient of

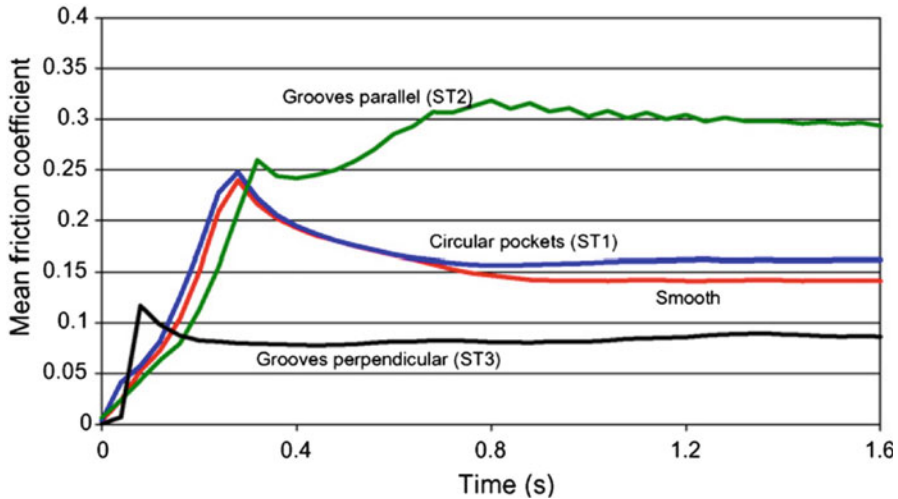
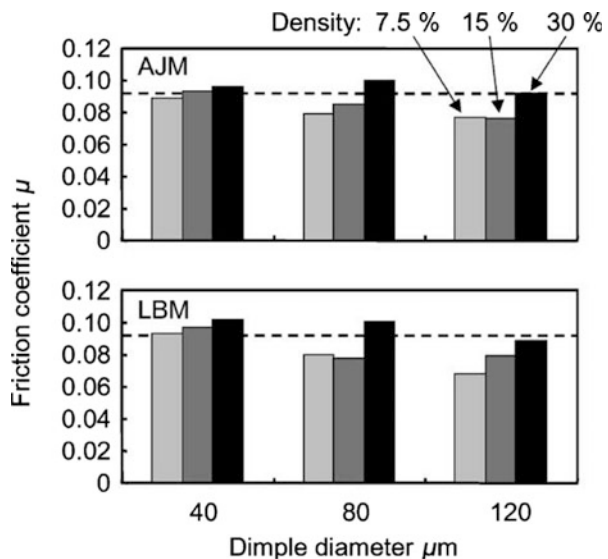


Fig. 24.14 Variation of friction coefficients for the tests with dies with different surface textures [29]

Fig. 24.15 Comparison of friction coefficient of the textured surfaces with different dimple diameter and density [31]



the textured surfaces with different dimple diameter and density. They found that surfaces with dimples show reductions in friction coefficient when compared to lapped smooth surfaces. It was concluded that the tribological characteristics depended greatly on the size and density of the micro-dimples rather than shape of the micro-dimples. Xie and Williams [32] proposed a model in order to predict the value of the overall coefficient of friction and wear rate, when the soft surface

slid against a rough harder surface. This model points to the fact that both friction and wear depend essentially on the roughness characteristics of the harder surface, the mechanical properties of both surfaces, nominal contact pressure or load, and the state of lubrication. The influence of directionality of surface grinding marks on the coefficient of friction was studied [9, 10, 33–37]. It was observed that the friction depends primarily on the directionality of the grinding marks but was less dependent on the surface roughness of the harder tool surfaces.

In metal forming processes such as sheet metal forming, the control of the friction level has a significant role since it influences the stress and strain distribution in the sheet. It should be neither too high nor too low to obtain a sheet with desirable quality. Thus, the stability of tribological conditions in metal forming operation will, to a large extent, influence the productivity and the quality of the formed product. Friction between the tool and workpiece has a significant effect on material deformation, forming load, component surface finish, and die wear. It is also an essential input parameter for the ever-increasing use of finite element (FE) simulation for metal forming. It was reported earlier that surface texture of the die indeed plays an important role on coefficient of friction during forming. Further, ring compression tests have been conducted for evaluating the frictional effects in bulk metal forming [38, 39]. The result [38] showed that under frictionless conditions, the hole size of the hollow cylinder increases proportionately to the outer diameter. However, with increasing frictional constraint, the rate of expansion of the hole decreases, and eventually the compressive hoop stress developed at the hole causes the hole to contract.

Significant efforts have been made to understand the influence of friction in forming using numerical analysis [40–43]. Liu et al. [40] analyzed a three-dimensional upsetting process and reported that under frictionless conditions bulging does not appear, whereas it occurs when friction is present. Wang and Zhu [41] performed the numerical simulation of deep drawing process and concluded that the larger the coefficient of friction, the smaller the drawing limit. Wang et al. [42] studied the numerical research of the cold upsetting–extruding of tube flanges and reported that the friction conditions at the interface of the tube free end with the male or the female dies have an important influence on the material flow. Analysis of the deformation characteristics of spike-forging through finite element simulations and experiments was done by Xu and Rao [43] who concluded that friction at the tool–workpiece interface plays a significant role in forcing the material and thus the spike height. Thus, it is clear from the above discussion that the friction influences material deformation and ultimately stresses and strain rates in the workpiece material.

Efforts have also been made to study the effect of deformation and strain rate on microstructural evaluation [44–50]. Strain rate is one of the important factors that control the microstructure evolution of the deforming material. Depending on the combination of strain rate and temperature, various kinds of microstructural mechanisms will operate, leading to different microstructural evolution. Eghbali [45] studied the effect of strain rate on the microstructural development in microalloyed steel. It was found that the deformation strain rate has a significant influence

on the flow behavior and deformed microstructure. Also, Li et al. [46] reported that the plastic deformation at higher strain rate in a Monel alloy induces dynamic recrystallization and ultimately affects the microstructure characteristics.

It is clear from the above discussion that by controlling the surface texture of the die, the interfacial friction can influence the net shape of the finished workpiece. The die surface and thus the friction can also affect the strain rate distribution in the workpiece, which is believed to ultimately determine the microstructure evolution of the deforming material. Thus, the die surface finish can be manipulated to obtain desired microstructure within the finished workpiece. The mechanical property and quality of the product depends on the microstructure of the workpiece material.

3.1 Effect of Surface Texture on Friction

Hence, efforts have been made to study the effect of surface texture of tool material on coefficient of friction using various soft materials during sliding under both dry and lubricated conditions [16, 51–60]. In these studies, various kinds of surface textures—namely, unidirectional grinding marks, 8-ground, and random—were prepared using simple metallographic techniques. Figure 24.16 shows the variation of coefficient of friction with surface textures when Al–Mg alloy pin slid on steel plate of different surface roughness [16]. It can be seen that the coefficient of friction depends on surface textures. It was found that the coefficient of friction was highest when sliding perpendicular to the unidirectional grinding marks (UPD) and lowest when tests were conducted on the random surfaces under both dry and lubricated conditions. For 8-ground and U-PL (sliding parallel to the unidirectional grinding marks) surface textures, the coefficient of friction lies in between these two extremes. The results obtained provide a basis for controlling the coefficient of friction across various locations along the interface between die and workpiece in metal forming process. These results may be employed to obtain a particular die surface finish in a particular area of the tool so as to obtain the desired coefficient of friction. By controlling the surface texture of the die, the friction at the interface and final shape can be controlled. This would affect the stresses and strain rates of the workpiece.

Thus, during the sliding tests, different friction values were obtained for the different surface textures. These friction values were subsequently used directly at the die–workpiece interfaces in finite element compression simulations to ascertain the state of stress, strain rate distribution, and the deformed shape in the workpiece. In the simulation work reported in literature for sheet metal and other forming operations [61–65], the coefficient of friction was assumed to be a constant at the interface or was set at different values at various locations. The criterion for choosing different values of coefficient of friction at different locations was made either arbitrarily or based on intuition.

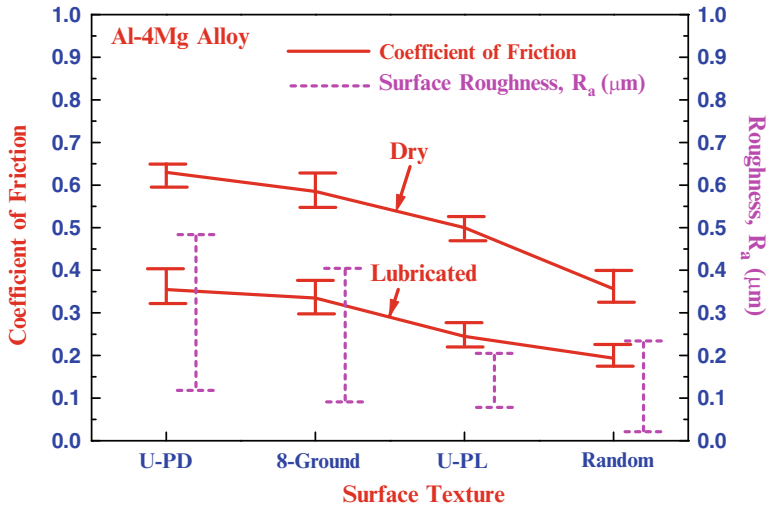


Fig. 24.16 Variation of average coefficient of friction and surface roughness (R_a) with surface texture for Al-4Mg alloy [8, 16]

3.2 Effect of Friction During Metal Forming

Attempts have been made to study the state of stress by implementing the obtained different coefficient of friction values at various locations between the die and workpiece during metal forming by using finite element (FE) analysis. In this simulation approach, the surface textures of various types [16] were not attained on the die surfaces. Instead, the coefficient of friction values, generated for these surface textures, were employed directly at the die–workpiece interfaces to study the state of stress in the workpiece and the deformed shape by conducting compression test using FE simulation.

In this study, the influence of friction between the tool and workpiece on the metal flow behavior was studied by simulating compression tests on cylindrical Al–Mg alloy using finite element method (FEM) technique. This has been done by changing the coefficient of friction values at different location on the die. Process simulation of compression tests was performed using commercially available nonlinear finite element code, DEFORM 3D, a general-purpose program performing both elastic–plastic and rigid–plastic analyses. The package is capable of simulating metal flow during forging, extrusion, rolling, drawing, and stamping operations.

In the simulation, the coefficient of friction values, generated for various surface textures, were employed directly at the die–workpiece interfaces. It was observed from Fig. 24.16 that the variation of friction with surface textures under both dry and lubricated conditions follows the same trend (i.e., the coefficient of friction values are high when sliding tests were performed perpendicular to the

Fig. 24.17 Schematic diagram of lower die (top view) [66]

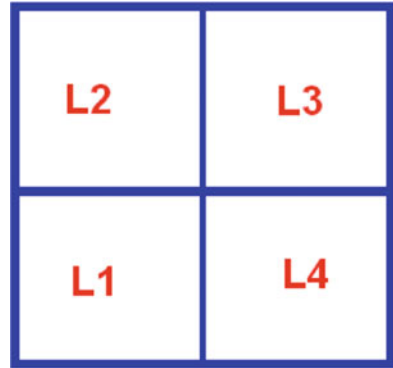


Table 24.5 Coefficient of friction values at four zones between the lower die and the workpiece interface [66]

Tests	Friction at different zones			
	L1	L2	L3	L4
First	0.65	0.65	0.65	0.65
Second	0.65	0.65	0.35	0.35
Third	0.65	0.35	0.65	0.35

unidirectional grinding marks and low for the tests conducted on the random surfaces) [8, 16]. Hence, in the simulation, the coefficient of friction values, obtained for the unidirectional and random surfaces under dry conditions, namely, 0.65 and 0.35, were considered.

Three kinds of compression tests were considered wherein a constant coefficient of friction (i.e., 0.65) was employed at upper die–workpiece interface. However, the coefficient of friction between the lower die–workpiece interfaces was varied in the tests. Thus, to vary the friction between lower die and workpiece interface, the lower die was divided into four zones, namely, L1, L2, L3, and L4. A schematic diagram of the lower die with four zones is shown in Fig. 24.17. Table 24.5 shows the different coefficient of friction values employed at different zones between lower die and workpiece interface for different tests. A schematic diagram of the compression tests is shown in Fig. 24.18 with similar friction values at the contacting interface as shown in the first test of Table 24.5.

The coefficient of friction values incorporated in this study were obtained for the case of Al–Mg alloy which is slid against steel counterface [16], and Al–Mg alloy material properties were assigned to the workpiece. The material parameters were obtained from the database library of DEFORM. All tests were performed by reducing the height of the workpiece by 70 %.

Figure 24.19 shows the variation of load with stroke for all the three tests. It can be seen from the figure that higher loads are required for the first test when compared to the second and third tests, since the coefficient of friction values are more in all the four zones (i.e., $L1 = L2 = L3 = L4 = 0.65$) of the lower die for this first test when compared to the second and third tests where half of the

Fig. 24.18 Schematic diagram of compression test [66]

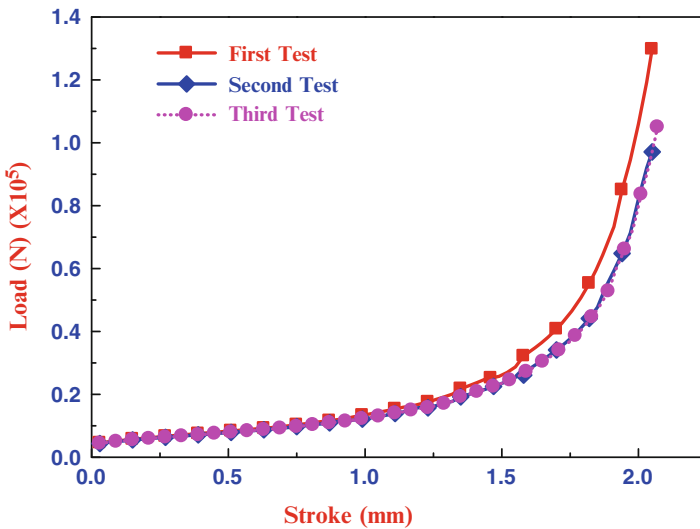
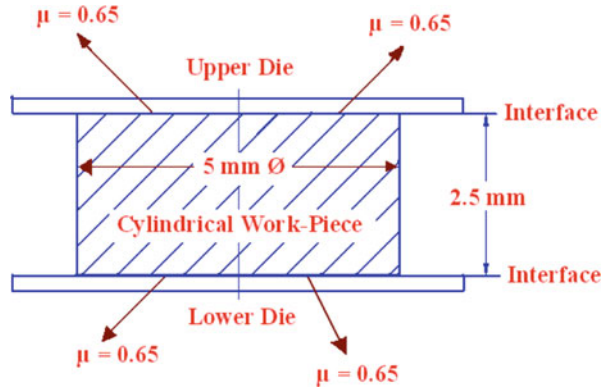


Fig. 24.19 Load–stroke curves for compression tests [66]

workpiece (two zones) experiences low coefficient of friction (i.e., $L1 = L2 = 0.65$; $L3 = L4 = 0.35$ for the second test and $L1 = L3 = 0.65$; $L2 = L4 = 0.35$ for the third test). For this reason, the second and third tests experience similar load–stroke curves and lower values of load when compared to the first test. Here, it is interesting to note that the variation in load is independent of the friction conditions at lower strokes and the difference in loads is greater at higher strokes. Another interesting fact is that there is almost no variation in load (Fig. 24.19) when the friction conditions are as per the second and third tests [66].

Figure 24.20a, b depicts the distribution of the stresses and strain rates for the simulation when the workpiece was compressed to 50 % [67, 68]. Here, the coefficient of friction values were the same (0.65) between all contacting surfaces.

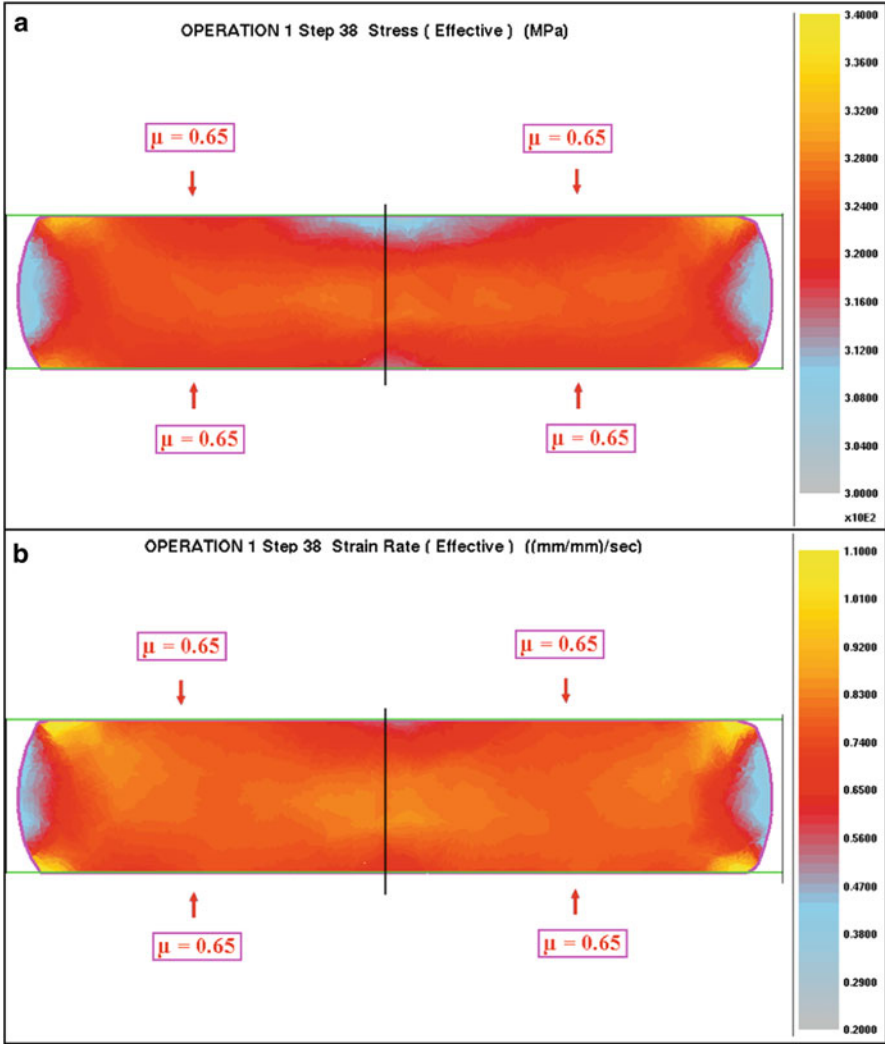


Fig. 24.20 Variation of (a) stresses and (b) strain rates when same friction values were assigned at the lower die–workpiece interface [67, 68]

It can be observed that the stress and strain rate distribution, as expected, is the same (i.e., the side view after sectioning perpendicular to the axes along the major diameter) for both the left-hand and right-hand sides near to the lower interface. In these regions, the friction values were assigned to be the same in both halves of the die–workpiece interface.

Another simulation was carried out by assigning different friction values at different locations on the lower die–workpiece interface. In these simulations, the friction values assigned for the left and right halves of the die–workpiece interface

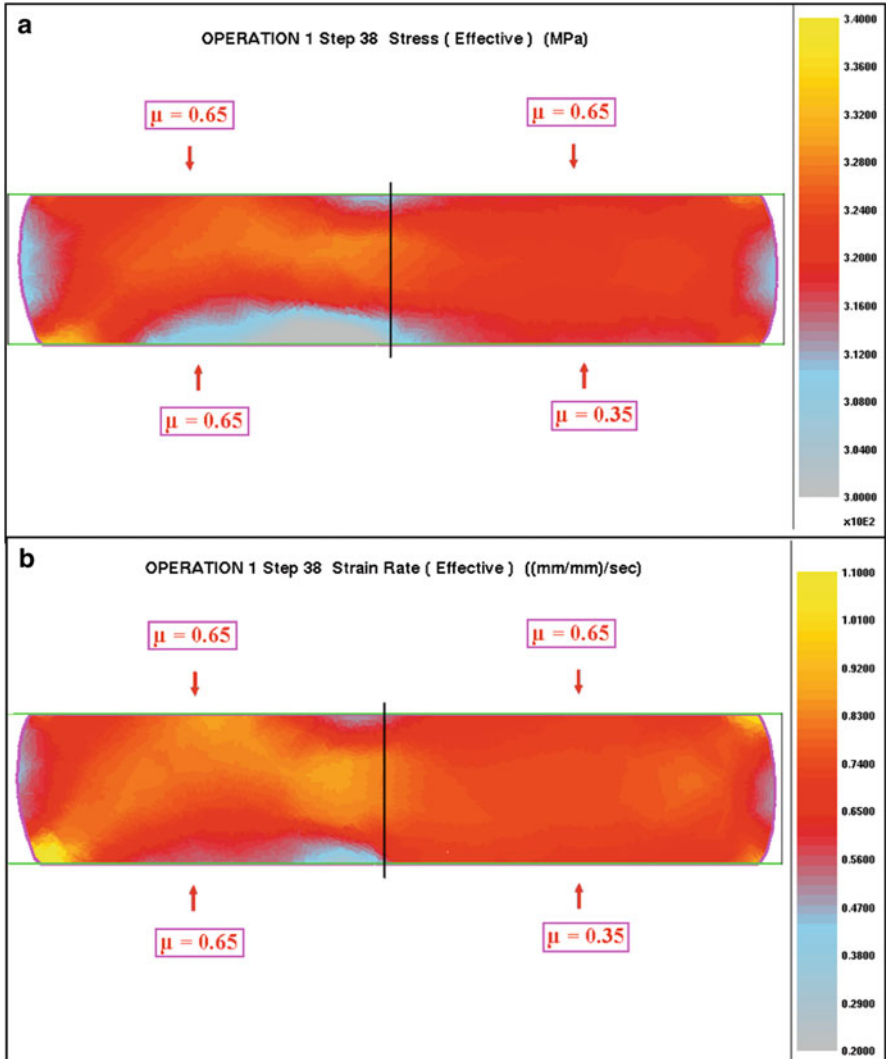


Fig. 24.21 Variation of (a) stresses and (b) strain rates when different friction values were assigned at the lower die–workpiece interface [67, 68]

were 0.65 and 0.35, respectively. The friction value was 0.65 between upper die and workpiece interface. Figure 24.21a, b shows that the distribution of stresses and strain rates was significantly different for the left-hand and right-hand sides near the lower interface where the friction is different. Low effective stress and strain rate is observed at the left half and near to lower die–workpiece interface when high friction value is assigned. However, high effective stress and strain rate is observed at the right side and near to the lower die–workpiece interface when low friction

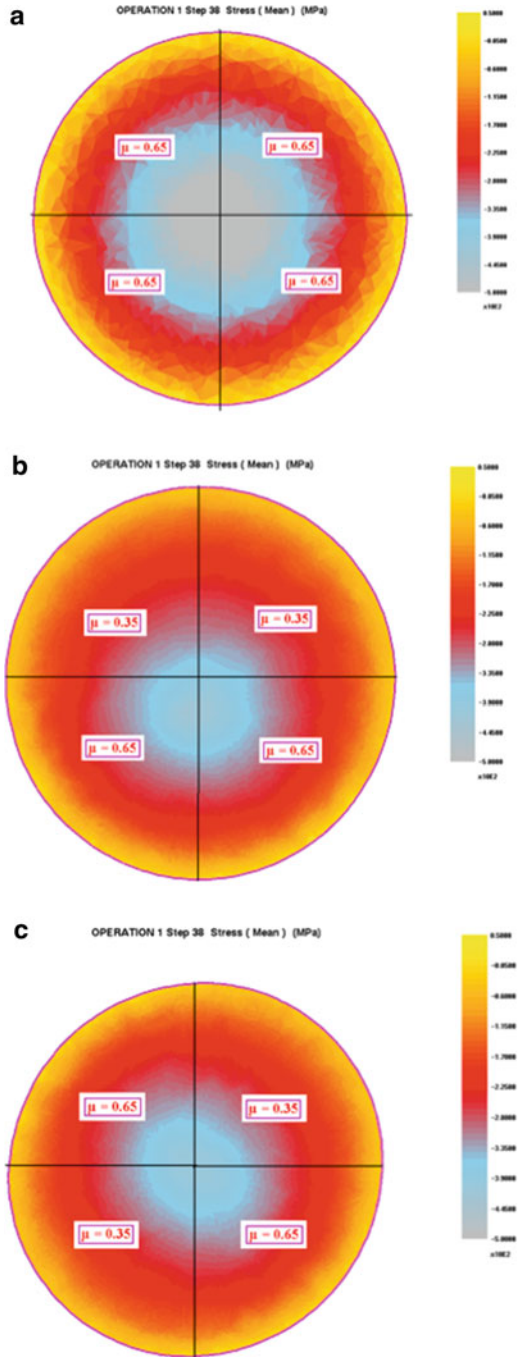
value is assigned. In addition, it can be seen that the high stress and strain rate region in the core of the workpiece in the first simulation (Fig. 24.20a, b) shifts towards the region of higher die–workpiece friction in the second simulation (Fig. 24.21a, b). Furthermore, the shape at the periphery of the workpiece is the same for the first simulation (Fig. 24.20a, b) and different for the second variable friction simulation (Fig. 24.21a, b) [67, 68].

Having seen the stress distributions for different coefficient of friction values at the cross section of the cylindrical workpiece, now results on the changes in shape of the cylindrical workpiece when compressed to 50 % in the compression test for different coefficient of friction values will be presented. Figure 24.22a shows the distribution of mean stresses for the first test. It can be seen from the figure that the shape of the workpiece remains circular when similar coefficient of friction values are assigned to all the four zones. In addition, the tension zone was observed at the periphery of the workpiece, while the compression zone was observed at the center of the workpiece. Figure 24.22b shows the distribution of mean stresses for the second test. It can be observed from this figure that the shape of the workpiece is different when different coefficient of friction values are assigned to each zone. The flow of the workpiece was much larger for the one half of the workpiece where lower coefficient of friction values were assigned at the interface when compared to the other half of the workpiece where higher coefficient of friction values were assigned. In addition, the compression zone changed its shape and the stress contours shift towards the half of the workpiece where high coefficient of friction values are assigned.

Figure 24.22c shows the distribution of mean stresses for the third test. In this case, as explained earlier, the compression test was conducted by assigning coefficient of friction values of 0.35 and 0.65 that are assigned alternatively to each quarter (zone) of the lower die–workpiece interface. It can be seen from Fig. 24.22c that the flow of the workpiece is much larger when low coefficient of friction values are assigned at the die–workpiece interface than when high coefficient of friction values are assigned. In addition, the compression zone becomes elliptical in shape with its semimajor axis aligned in direction of the quarters (of the workpieces) where high coefficient of friction values are assigned and its semiminor axis aligned in the direction of the quadrants where low coefficient of friction values are assigned. From this it can be inferred that the flow of metal and thus the changes in shape of the workpiece depend on coefficient of friction at the interface [37]. Similar observations were also reported in the literature using both experimental [25] and numerical analysis [40] methods for the upsetting process. In these efforts, it was reported that the shape of the workpiece depends on the coefficient of friction at the interface between the die and workpiece.

By controlling the surface texture and the friction at the die, the stress and strain rate can be controlled. Strain rate is one of the important factors that control the microstructure evolution of the deforming material [37, 44, 69–75]. Thus, desired microstructures can be derived by controlling the friction values at the die–workpiece interface. Depending on the combination of strain rate and temperature, various kinds of microstructural mechanisms will operate leading to different

Fig. 24.22 Distribution of mean stresses for the (a) first test, (b) second test, and (c) third test when the workpiece is compressed to 50 % [67, 68]



microstructural evolution. The different microstructural mechanisms that operate include dynamic recrystallization (DRX), dynamic recovery (DRY), adiabatic shear banding (ASB), wedge cracking (WC), void formation (VF), superplastic deformation (SPD), intercrystalline cracking (ICC), and prior particle boundary (PPB) cracking. In some of these mechanisms, including DRX, DRY, and SPD, the microstructural evolution leads to a more desirable microstructure. Other mechanisms, such as ASB, WC, SPD, VF, PPB and ICC, can lead to an undesirable microstructure. It is also important to have the desirable microstructures at preferred locations. In metal forming, the locations and area in the workpiece covered by a particular microstructure can be completely altered by just changing the die–workpiece friction.

3.3 *Effect of Surface Texture on Metal Forming*

Similar to finite element analysis, laboratory uniaxial compression tests were performed on cylindrical Al-4Mg alloy at constant true strain rates of 4 s^{-1} at room temperature. Instead of assigning different friction values from the experiments, in this study, different surface textures (unidirectional and random) were generated at each halves on the lower die surface so that the workpiece would experience variable friction at the interface. In the compression experiments, the random texture generated on the die surface was similar to the texture generated on the friction test sample [16]. However, the unidirectional texture on the die was prepared by creating circular grinding marks on the die surfaces by maintaining the same roughness level as that of friction test samples. This was done to maintain similar material flow (i.e., perpendicular to the die grinding marks' direction) of the cylindrical sample at the contacting interface. After the experiments, the deformed workpiece was sectioned along the compression axis. The sectioned half was then metallographically polished, etched to reveal the microstructure prior to optical microscopy examination.

Figure 24.23a shows the photograph of the cross section of compressed workpiece. The arrows indicate the type of texture generated on the low die surfaces. It can be observed that the material flow was found to be greater at the right-hand side of the workpiece that experiences low friction coefficient due to random surface texture. The optical micrographs taken near the interface are also presented in the figure (see Fig. 24.23b, c). It can be seen that microstructural features are different in both sides of the workpiece. More specifically, coarse-grained structure was observed at the left half and near the lower die–workpiece interface (Fig. 24.23b), while a fine-grained structure was observed at the right half and near the lower die–workpiece interface (Fig. 24.23c). Thus, it can be inferred that the grain size of the samples near the interface is largely influenced by the surface texture of the die.

From the above analysis, it is evident that low effective strain rate was observed when a high coefficient of friction value was assigned at the interface due to constraint to flow of the workpiece material. In contrast, high effective strain rate

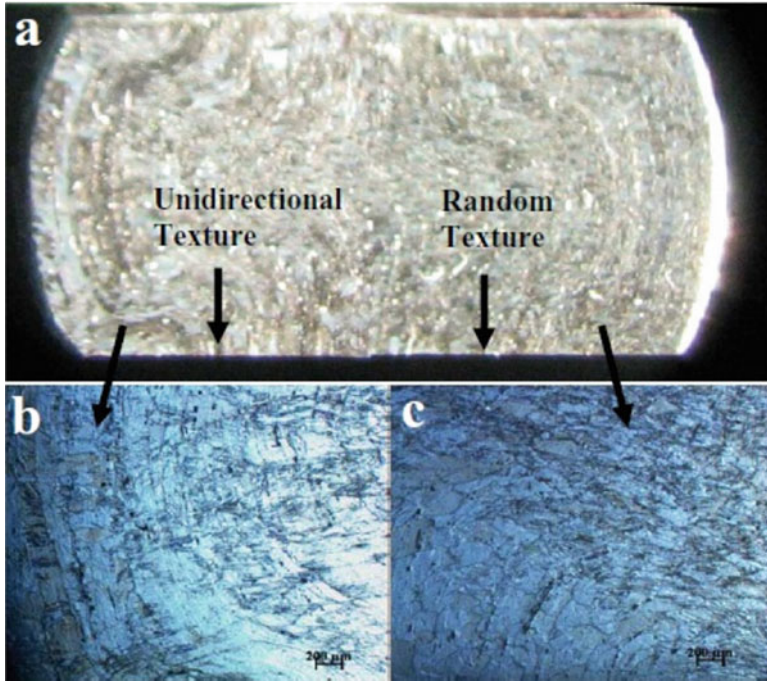


Fig. 24.23 (a) Photograph of the cross section of the workpiece, (b) the microstructure of the workpiece compressed against a unidirectional texture, (c) the microstructure of the workpiece compressed against a random texture [68]

was observed when a low coefficient of friction value was assigned at the interface due to less constraint to flow as shown in the simulation results. Hence, coarse-grained structure was observed at low strain rate region, and fine-grained structure was observed at high strain rate region as revealed in the microstructure of the compression test samples.

The surface texturing technology can be utilized in metal forming process to design a particular texture at different locations of the die so that the coefficient of friction could be varied according to the requirement. In locations where the coefficient of friction needs to be high, a unidirectionally ground surface with the flow perpendicular to the grinding marks can be machined, and in locations where the coefficient of friction needs to be low, a randomly ground surface can be machined. Designing textures on the die may also enable the reduction of conventional lubricants that are needed to achieve the required friction. The die–workpiece friction affects material flow, stresses, and strain rate distribution in the deformed material, which in turn influences the microstructural evolution in the material. The microstructure evolution will affect the mechanical properties of the formed product. The mechanical properties of the formed product at different locations depending on the requirements can also be tailored by designing proper surface texture.

4 Conclusions

Friction in metal forming processes is a very complex phenomenon as it depends on many parameters. Metal forming is a vital part to the way in which industries, applications, and consumers utilize and create metal components. Companies that manufacture metals often supply materials in the form of ingots, which are obtained by casting liquid metals into square cross sections known as slabs, billets, or blooms. These shapes are further processed through rolling, forging, extrusion, or drawing to produce metal materials that are in standard form for distribution in the form of plates, sheets, tubes, rods, and various structural sections. As with many applications, the ability to control the friction forces is important, especially in metalworking operations. Friction is an important process parameter, which controls the tool load, product, and tool wear. The coefficient of friction, if controlled properly, could generate the required stresses to deform the metal to the required shape. It could also lead to failure of the workpiece if not controlled properly. In general, friction is controlled by many variables, such as surface texture, load, speed, temperature, lubricants, and material properties. The influence of surface texture on friction was investigated in this chapter and revealed to be an important parameter that influences metal forming. Designing textures on workpieces enables the reduction of conventional lubricants that are needed to achieve the required friction within a metal forming process. The change in friction affects material flow, stresses, and strain rate distribution in deformed materials, which in turn influences the microstructural evolution in the materials. The microstructure evolution will affect the mechanical properties of the formed products. Thus, the mechanical properties of formed products can be tailored by designing proper surface texture.

References

1. Valberg HS (2010) Applied metal forming: including FEM analysis. Cambridge University Press, New York, NY
2. Kumar S (2008) Technology of metal forming processes. Prentice-Hall India Private Limited, New Delhi
3. Pater Z, Tomczak J, Bartnicki JÇ, Lovell MR, Menezes PL (2013) Experimental and numerical analysis of helical-wedge rolling process for producing steel balls. *Int J Mach Tool Manuf* 67:1–7
4. Dieter GE (1986) Mechanical metallurgy. McGraw-Hill Science, New York
5. Lange K (1985) Handbook of metal forming. McGraw-Hill, New York
6. Davim JP (2011) Tribology for engineers: a practical guide. Woodhead Publishing, Cambridge, UK
7. Kobayashi S, Oh S-I, Altan T (1989) Metal forming and the finite-element method. Oxford University Press, Oxford
8. Menezes PL, Kishore K, Kailas SV (2006) Studies on friction and transfer layer using inclined scratch. *Tribology International* 39(2):175–183

9. Menezes PL, Kishore, Kailas SV (2006) Effect of roughness parameter and grinding angle on coefficient of friction when sliding of Al-Mg alloy over EN8 steel. *Journal of Tribology* 128 (Compendex):697–704
10. Menezes PL, Kishore, Kailas SV (2009) Influence of inclination angle of plate on friction, stick-slip and transfer layer—a study of magnesium pin sliding against steel plate. *Wear* 267 (1–4):476–484
11. Reeves CJ, Jen T-C, Menezes PL, Lovell MR (2013) The size effect of boron nitride particles on the tribological performance of biolubricants for energy conservation and sustainability. *Tribol Lett* 51(3):437–452
12. Menezes PL, Kailas, Kishore SV, Lovell MR (2011) Response of materials during sliding on various surface textures. *J Mater Eng Perform* 20(8):1438–1446
13. Menezes PL, Kishore, Kailas SV, Lovell MR (2011) Role of surface texture, roughness, and hardness on friction during unidirectional sliding. *Tribology Lett* 41(Compendex):1–15
14. Menezes PL, Kishore, Kishore SV, Lovell MR (2011) Friction and transfer layer formation in polymer–steel tribo-system: role of surface texture and roughness parameters. *Wear* 271 (9–10):2213–2221
15. Menezes PL, Kishore, Kishore SV, Lovell MR (2009) Studies on friction and formation of transfer layer in HCP metals. *J Tribol Trans ASME* 131(3)
16. Menezes PL, Kishore, Kailas SV (2006) Chapter 14 Studies on friction and transfer layer using inclined scratch. In: Sujeet S (ed.) *Tribology and interface engineering series*. Elsevier. pp. 262–279
17. Schey JA, Mysliwy REM (1977) The effect of die surface finish on lubrication in ring upsetting. Second European Tribology Congress, Euro Trib'77
18. Geiger M, Engel U, Niederkorn S, Pfestorf M (1995) Experimental investigation of contact phenomena in cold forging. ICFG plenary meeting, Denmark
19. Wagner S (2001) Optimizing friction between die and sheet metal. Proc. in proceedings of global symposium on innovations in materials, processing and manufacturing. pp. 245–267
20. Bello DO, Walton S (1987) Surface topography and lubrication in sheet-metal forming. *Tribol Int* 20(2):59–65
21. Schedin E (1994) Galling mechanisms in sheet forming operations. *Wear* 179(1/2):123
22. Rasp W, Wichern CM (2002) Effects of surface-topography directionality and lubrication condition on frictional behaviour during plastic deformation. *J Mater Process Technol* 125(1):379
23. Saha PK, Wilsona WRD, Timsitb RS (1996) Influence of surface topography on the frictional characteristics of 3104 aluminum alloy sheet. *Wear* 197(1–2):123
24. Lakshmi pathy R, Sagar R (1992) Effect of die surface topography on die-work interfacial friction in open die forging. *Int J Mach Tool Manuf* 32(5):685–693
25. Malayappan S, Narayanasamy R (2004) An experimental analysis of upset forging of aluminium cylindrical billets considering the dissimilar frictional conditions at flat die surfaces. *Int J Adv Manuf Technol* 23(9–10):636–643
26. Määttä A, Vuoristo P, Mäntylä T (2001) Friction and adhesion of stainless steel strip against tool steels in unlubricated sliding with high contact load. *Tribol Int* 34(11):779–786
27. Staph H, Ku P, Carper H (1973) Effect of surface roughness and surface texture on scuffing. *Mech Mach Theory* 8(2):197–208
28. Koura MM (1980) The effect of surface texture on friction mechanisms. *Wear* 63(1):1–12
29. Costa HL, Hutchings IM (2009) Effects of die surface patterning on lubrication in strip drawing. *J Mater Process Technol* 209(3):1175–1180
30. Hu ZM, Dean TA (2000) A study of surface topography, friction and lubricants in metalforming. *Int J Mach Tool Manuf* 40(11):1637–1649
31. Wakuda M, Yamauchi Y, Kanzaki S, Yasuda Y (2003) Effect of surface texturing on friction reduction between ceramic and steel materials under lubricated sliding contact. *Wear* 254 (3–4):356–363

32. Xie Y, Williams JA (1996) The prediction of friction and wear when a soft surface slides against a harder rough surface. *Wear* 196(1/2):21–34
33. Menezes PL, Kishore, Kailas SV (2006) Effect of directionality of unidirectional grinding marks on friction and transfer layer formation of Mg on steel using inclined scratch test. *Mater Sci Eng A* 429(1–2):149–160
34. Menezes PL, Kishore, Kailas SV (2008) On the effect of surface texture on friction and transfer layer formation—a study using Al and steel pair. *Wear* 265(11–12):1655–1669
35. Menezes PL, Kishore, Kailas SV, Lovell MR (2010) Response of materials as a function of grinding angle on friction and transfer layer formation. *Int J Adv Manuf Technol* 49 (Compendex):485–495
36. Menezes PL, Kishore, Kailas SV, Lovell MR (2011) Influence of inclination angle and machining direction on friction and transfer layer formation. *J TribolTrans ASME* 133(1)
37. Menezes PL, Kishore, Kailas SV (2010) Influence of die surface textures during metal forming—a study using experiments and simulation. *Mater Manuf Process* 25(9):1030–1039
38. Hawkyard JB, Johnson W (1967) An analysis of the changes in geometry of a short hollow cylinder during axial compression. *Int J Mech Sci* 9(4):163–182
39. Robinson T, Ou H, Armstrong CG (2004) Study on ring compression test using physical modelling and FE simulation. *J Mater Process Technol* 153–154:54–59
40. Liu YH, Chen J, Yu S, Chen XW (2006) Analysis of three-dimensional upsetting process by the rigid-plastic reproducing kernel particle method. *Acta Metall Sin (Eng Lett)* 19(5):371–378
41. Wang XW, Zhu XH (1995) Numerical simulation of deep-drawing process. *J Mater Process Technol* 48(1–4):123–127
42. Wang Z, Lu J, Wang ZR (2001) Numerical and experimental research of the cold upsetting—extruding of tube flanges. *J Mater Process Technol* 110(1):28–35
43. Xu WL, Rao KP (1997) Analysis of the deformation characteristics of spike-forging process through FE simulations and experiments. *J Mater Process Technol* 70(1–3):122–128
44. Prasad YVRK, Sasidhara S (1997) Hot working guide : a compendium of processing maps. ASM International, Materials Park, OH
45. Eghbali B (2010) Effect of strain rate on the microstructural development through continuous dynamic recrystallization in a microalloyed steel. *Mater Sci Eng A* 527(15):3402–3406
46. Li Q, Xu YB, Lai ZH, Shen LT, Bai YL (2000) Dynamic recrystallization induced by plastic deformation at high strain rate in a Monel alloy. *Mater Sci Eng A* 276(1–2):250–256
47. Venugopal S, Mannan SL, Prasad YVRK (1996) Influence of strain rate and state-of-stress on the formation of ferrite in stainless steel type AISI 304 during hot working. *Mater Lett* 26 (3):161–165
48. Venugopal S, Mannan SL, Prasad YVRK (1994) Processing maps for hot working of commercial grade wrought stainless steel type AISI 304. *Mater Sci Eng A* 177(1–2):143–149
49. Urcola JSC (1987) Influence of changing strain rate on microstructure during hot deformation. *Acta Metall* 35(11):2649–2657
50. Klimanek PPA (2002) Microstructure evolution under compressive plastic deformation of magnesium at different temperatures and strain rates. *Mater Sci Eng A* 324(1–2):145–150
51. Menezes PL, Kishore, Kailas SV (2006) Influence of surface texture on coefficient of friction and transfer layer formation during sliding of pure magnesium pin on 080 M40 (EN8) steel plate. *Wear* 261(5–6):578–591
52. Menezes PL, Kishore, Kailas SV (2006) Studies on friction and transfer layer: role of surface texture. *Tribol Lett* 24(3):265–273
53. Menezes PL, Kishore, Kailas SV (2008) Effect of surface roughness parameters and surface texture on friction and transfer layer formation in tin–steel tribo-system. *J Mater Process Technol* 208(1–3):372–382
54. Menezes PL, Kishore, Kailas SV (2009) Study of friction and transfer layer formation in copper-steel tribo-system: role of surface texture and roughness parameters. *Tribol Trans* 52 (5):611–622

55. Menezes PL, Kishore, Kailas SV (2009) Influence of roughness parameters and surface texture on friction during sliding of pure lead over 080 M40 steel. *Int J Adv Manuf Technol* 43 (Compendex):731–743
56. Menezes PL, Kishore, Kailas SV (2008) Influence of roughness parameters of harder surface on coefficient of friction and transfer layer formation. *Int J Surf Sci Eng* 2(1–2):98–119
57. Menezes PL, Kishore, Kailas SV (2009) Influence of surface texture and roughness parameters on friction and transfer layer formation during sliding of aluminium pin on steel plate. *Wear* 267(9–10):1534–1549
58. Menezes PL, Kishore, Kailas SV (2008) Studies on friction in an iron-steel tribo-system under dry and lubricated conditions. *Mater Manuf Process* 23(7):698–707
59. Menezes PL, Kishore, Kailas SV (2008) Effect of surface topography on friction and transfer layer during sliding. *Tribol Online* 3(1):25–30
60. Kumar CP, Menezes PL, Kailas SV (2008) Role of surface texture on friction under boundary lubricated conditions. *Tribol Online* 3(1):12–18
61. Subhash G, Zhang W (2002) Investigation of the overall friction coefficient in single-pass scratch test. *Wear* 252(1–2):123–134
62. Wang F-X, Lacey P, Gates RS, Hsu SM (1991) A study of the relative surface conformity between two surfaces in sliding contact. *J Tribol* 113(4):755
63. Sahoo P, Roy Chowdhury SK (2002) A fractal analysis of adhesive wear at the contact between rough solids. *Wear* 253(9–10):924–934
64. Váradí K, Néder Z, Friedrich K (1996) Evaluation of the real contact areas, pressure distributions and contact temperatures during sliding contact between real metal surfaces. *Wear* 200(1–2):55–62
65. Yoshioka N (1997) A review of the micromechanical approach to the physics of contacting surfaces. *Tectonophysics* 277(1–3):29
66. Menezes PL, Kumar K, Kishore, Kailas SV (2009) Influence of friction during forming processes—a study using a numerical simulation technique. *Int J Adv Manuf Technol* 40 (11–12):1067–1076
67. Menezes PL (2007) Role of surface texture on friction and transfer layer formation—a study using pin-on-disk sliding tester. Ph.D. dissertation. Indian Institute of Science, Bangalore
68. Menezes PL, Kishore, Kishore SV, Lovell MR (2012) Analysis of strain rates and microstructural evaluation during metal forming: role of surface texture and friction. *Tribol Trans* 55(5):582–589
69. Leszczynska-Madej BRM (2010) The effect of strain rate on the evolution of microstructure in aluminium alloys. *J Microsc* 237(3):399–403
70. Kailas S (2003) A study of the strain rate microstructural response and wear of metals. *J Mater Eng Perform* 12(6):629–637
71. Menezes PL, Kishore, Kailas SV (2008) Subsurface deformation and the role of surface texture—a study with Cu pins and steel plates. *Sadhana Acad Proc Eng Sci* 33 (Compendex):191–201
72. Menezes PL, Kishore, Kailas SV (2009) Role of surface texture of harder surface on subsurface deformation. *Wear* 266(1–2):103–109
73. Menezes PL, Kishore, Kailas SV, Lovell MR (2013) The role of strain rate response on tribological behavior of metals. *J Tribol* 135(1):011601
74. Rao KP, Prasad YVRK, Sivaram K (1990) Deformation processing map for control of microstructure in Al4Mg alloy. *Mater Lett* 10(1–2):66–70
75. Menezes PL, Kailas SV (2007) Influence of surface textures during metal forming, STLE/ASME international joint tribology conference (IJTC 2007). ASME, California, USA, pp 713–715

Questions

1. What are the three manufacturing processes?
2. Explain direct-compression-type processes and indirect-compression-type processes.
3. Describe tension-type processes, bending processes, and shearing processes.
4. Describe the rolling process.
5. Describe the forging process. Explain two types of forging.
6. Describe the extrusion processes. List four types of extrusion techniques.
7. Describe the drawing process.
8. Explain how surface texture affects friction and the relevance this has on metal forming processes.
9. How does surface texturing influence metal forming and affect the microstructure of the die workpiece?
10. What are primary and secondary metal forming processes?
11. What are hot-working and cold-working processes?

Answers

1. The three manufacturing processes are casting, forming, and machining. Casting is the process where molten liquid is poured into a mold that holds the required shape, and allowing hardens the metal with or without external pressure. This process occurs in the liquid state. Forming is a process where the volume and mass of metal are preserved and the metal is displaced from one location to another location by applying pressure. This process occurs in the solid state. Machining is the process where material is removed in order to give it the required shape. This process also occurs in the solid state.
2. A direct-compression-type process is one in which the force is applied to the surface of the workpiece and the metal flows at right angles to the direction of the compression. An indirect-compression-type process is one in which the primary applied forces are frequently tensile, but indirect compressive forces are developed by the reaction of the workpiece with the die. Therefore, the metal flows under the action of a combined stress state, which includes high compressive forces in at least one of the principal directions.
3. A tension-type forming process is stretch forming, where a metal sheet is wrapped to the contour of a die under the application of tensile forces. A bending process involves the application of bending moments to the sheet. A shearing involves the application of shearing forces of sufficient magnitude to rupture the metal in the plane of shear.
4. Rolling is the process where a sheet or plate is drawn by means of friction in between two rollers. The compressive forces applied by the rollers reduce the thickness of the material while minimizing the cross-sectional area and causing the rolled material to elongate and spread.

5. Forging is the process of hammering or pressing material between two dies to achieve the desired shape and structure through plastic deformation. Two types of forging are open-die forging and closed-die forging. Open-die forging is the process where metal is compressed by hammering or pressing between flat or contoured dies either mechanically or manually and the shape of the material is deformed through plastic deformation. Open-die forging gets its name from the fact that the dies (the surfaces that are in contact with the workpiece) do not enclose the workpiece, allowing the metal to flow except where contacted by the dies. Closed-die forging is the process where the metal is compressed between a shaped die and a hammer that presses the metal deforming it within the die causing the metal to flow and fill the die cavities.
6. Extrusion is the process where a material is compressed in a chamber and the deformed material is forced to flow through a die. The die opening corresponds to the cross section of the required product. Extrusion is primarily a hot-working process; however, for softer materials, cold extrusion is also performed. There are a few types of extrusion processes that are used extensively in industry: direct extrusion, indirect extrusion, impact extrusion, and hydrostatic extrusion.
7. Drawing is a cold metalworking process that uses tensile forces to stretch metal into long rods, wires, and tubes. In this process, a material is pulled through a die to reduce it to a desired shape and size. In a typical wire drawing operation, one end of the wire is reduced and passed through the opening of the die, pulling with it the metal to reduce its diameter. By successive drawing operations through dies of reducing diameter, a rod can be reduced to a very small diameter.
8. The coefficient of friction depends on surface textures. Research shows that the coefficient of friction was highest when sliding perpendicular to the unidirectional grinding marks and lowest when tests were conducted on the random surfaces under both dry and lubricated conditions. In the test conducted for 8-ground and U-PL (sliding parallel to the unidirectional grinding marks) surface textures, the coefficient of friction values were in between these two extremes. The results obtained provide a basis for controlling the coefficient of friction across various locations along the interface between die and workpiece in metal forming process. These results may be employed to obtain a particular die surface finish in a particular area of the tool so as to obtain the desired coefficient of friction. By controlling the surface texture of the die, the friction at the interface and final shape can be controlled. This would affect the stresses and strain rates of the workpiece.
9. The surface texturing technology can be utilized in metal forming process to design a particular texture at different locations of the die so that the coefficient of friction could be varied according to the requirement. In locations where the coefficient of friction needs to be high, a unidirectionally ground surface with the flow perpendicular to the grinding marks can be machined, and in locations where the coefficient of friction needs to be low, a randomly ground surface can be machined. Designing textures on the die may also enable the reduction of

conventional lubricants that are needed to achieve the required friction. The die–workpiece friction affects material flow, stresses, and strain rate distribution in the deformed material, which in turn influences the microstructural evolution in the material. The microstructure evolution will affect the mechanical properties of the formed product. The mechanical properties of the formed product at different locations depending on the requirements can also be tailored by designing proper surface texture.

10. The plastic working processes, which are designed to reduce an ingot or billet to a standard mill product of simple shape, such as sheet, plate, and bar, are known as primary mechanical working processes. Forming methods, which produce a part of a final finished shape, are called secondary mechanical working processes. Most sheet metal forming operations, wire drawing, and tube drawing are secondary processes.
11. Hot-working is defined as the process of deformation of the workpiece under conditions of high temperature and strain rate such that the recovery process takes place along with the deformation of the workpiece. Cold-working is defined as the process of deformation under conditions where the recovery process is ineffective.

Part VII
Applications and Components

Chapter 25

Tribology in Machine Components

Satish C. Sharma

Abstract Proper tribological practices are extremely important from the view point of reliable and maintenance free operation of machine components. Friction, wear, and lubrication are three main domains of tribology. Proper interfacing among these domains is essential to have a better performance of machine components. Bearings are most critical machine elements which imparts constrained relative motion between two machine components. Bearings either have sliding contact or rolling contact. In the present chapter different types of bearings have been discussed. The main focus of this chapter is on hydrostatic/hybrid fluid-film journal bearings. The components of the hydrostatic/hybrid bearing system that have significant impact on bearing performance have been described. The analysis of fluid-film journal bearings and their performance characteristics parameters have been discussed. The chapter also discusses some current research trends in the design of hydrostatic/hybrid journal bearings. In concluding section the chapter discusses some of the results pertaining to the current issues of research, which needs to be considered for an accurate and realistic design of hydrostatic/hybrid journal bearing system, such as the number of recesses, type of restrictor, shape of recess, influence of turbulence and flexibility, etc.

S.C. Sharma (✉)

Department of Mechanical and Industrial Engineering, Indian Institute of Technology
Roorkee, Roorkee 247667, India
e-mail: sshmefme@iitr.ac.in

Nomenclature

Dimensional Parameters

a_b	Axial land width, mm
a_s	Extent of slot width, mm
d_o	Orifice diameter, mm
c	Radial clearance, mm
A_m	Effective area of membrane, mm ²
A_p	Area of the pocket, mm ²
A^e	Area of each element (mm ²)
C_{ij}	Fluid-film damping coefficients ($i, j = x, z$), N.s/m
C_1	Clearance due to circumscribed circle on the bearing (mm)
C_2	Clearance due to inscribed circle on the bearing (mm)
D	Journal diameter, mm
d_c	Diameter of capillary, mm
E	Modulus of elasticity of bearing material, MPa
e	Journal eccentricity, mm
F	Fluid-film reaction ($\partial h/\partial t \neq 0$), N
F_x, F_z	Fluid-film reaction components in X and Y direction ($\partial h/\partial t \neq 0$), N
F_o	Fluid-film reaction ($\partial h/\partial t = 0$), N
K_m	Membrane stiffness, N mm ⁻¹
g	Acceleration due to gravity, m.s ⁻²
h	Nominal fluid-film thickness, mm
h_T	Average fluid-film thickness, mm
h_m	Gap height for membrane restrictor, mm
h_{\min}	Minimum fluid-film thickness, mm
Δh_m	Membrane deflection, mm
h_{mo}	Gap height for zero external load in case of membrane restrictor, mm
h_0	Fluid-film thickness in rigid bearing, mm
l_c	Length of capillary, mm
L	Bearing length, mm
m	Consistency index, N.m ² .s ⁻ⁿ
M_c, M_j	Critical mass and Mass of journal, kg
n	Power law index
n_x, n_y	Direction cosines in α and β directions respectively
O_L	Lobe center
p	Pressure, N.mm ⁻²
p_c	Pressure at recess/pocket/hole, N.mm ⁻²
p_s	Supply pressure, N.mm ⁻²
Q	Lubricant flow, mm ³ .s ⁻¹
Q_R	Flow through restrictor, mm ³ s ⁻¹
r_c	Radius of capillary, mm
r_1, r_2	Membrane radii, mm

r_m	Mean radius of cone from apex, mm
R_j, R_b	Radius of journal and bearing, mm
S_{ij}	Fluid-film stiffness coefficients ($i, j = x, z$), $\text{N}\cdot\text{mm}^{-1}$
t	Time, sec
t_h	Thickness of bearing shell, mm
t_m	Thickness of membrane, mm
V_{rj}, V_{rb}	Variance ratio of journal and bearing respectively
W_o	External load, N
x	Circumferential coordinate
y	Axial coordinate
X_j, Z_j	Journal center coordinate
X, Y, Z	Cartesian coordinate system
z	Coordinate along film thickness

Greek Letters

γ, κ	Material coefficient, N s; spin viscosity, N s m^{-2}
μ	Lubricant Dynamic viscosity, N s m^{-2}
μ_r	Reference viscosity of lubricant, N s m^{-2}
σ	RMS value of combined roughness, $\sigma = \sqrt{\sigma_j^2 + \sigma_b^2}$, μm
σ_j	RMS value of journal surface roughness, μm
σ_b	RMS value of bearing surface roughness, μm
ω_l	$(g/c)^{1/2}$, $\text{rad}\cdot\text{sec}^{-1}$
ω_j	Journal rotational speed, $\text{rad}\cdot\text{s}^{-1}$
ω_{th}	Threshold speed, $\text{rad}\cdot\text{s}^{-1}$
ρ	Density, $\text{kg}\cdot\text{m}^{-3}$
ψ_d	Coefficient of discharge for orifice
τ	Shear stress, $\text{N}\cdot\text{m}^{-2}$
$\dot{\gamma}$	Shear strain rate, s^{-1}

Nondimensional Parameters

\bar{a}_b	a_b/L
\bar{C}_d	Deformation coefficient
\bar{C}_{ij}	$C_{ij} \left(\frac{c^3}{\mu_r R_j^4} \right)$
\bar{C}_{s2}	Restrictor design parameter
\bar{F}, \bar{F}_o	$(F, F_o/p_s R_j^2)$
\bar{F}_x, \bar{F}_z	$(F_x, F_z/p_s R_j^2)$
\bar{F}'_o	Cross film viscosity integrals, $F'_o(\mu_r/h_L)$
\bar{F}'_1	Cross film viscosity integrals, $F'_1(\mu_r/h_L^2)$
\bar{h}	h/c

$\bar{h}_{\min}, \bar{h}_T$	$(h_{\min}, h_T)/c$
\bar{K}	Nonlinearity factor
l_m	Nondimensional characteristic length, c/l
\bar{m}	$m \left(\frac{cp_s}{\mu_r R_j} \right)^n \left(\frac{R_j}{cp_s} \right)$
\bar{M}_j	$M_j \left(\frac{c^5 p_s}{\mu_r^2 R_j^6} \right)$
N	Coupling number, $\left(\frac{\kappa}{2\mu + \kappa} \right)^{1/2}$
N_i, N_j	Shape functions
\bar{p}, \bar{p}_c	$(p, p_c)/p_s$
\bar{p}_{\max}	p_{\max}/p_s
\bar{Q}	$Q (\mu_r/c^3 p_s)$
SWR	Slot width ratio, $a_s/(a_s)_{\max}$
\bar{S}_{ij}	$S_{ij} \left(\frac{c}{p_s R_j^2} \right)$
\bar{t}	$t (c^2 p_s / \mu_r R_j^2)$
\bar{W}_o	$\frac{W_o}{p_s R_j^2}$
$(\bar{V}_{rj}, \bar{V}_{rb})$	$((\sigma_j, \sigma_b)/\sigma)^2$
(\bar{X}_j, \bar{Z}_j)	$(X_j, Z_j)/c$
α, β	$(x, y)/R_j$
β^*	Concentric design pressure ratio, (p^*/p_s)
ε	e/c
γ	$\frac{\lambda_{0.5x}}{\lambda_{0.5y}}$, Surface pattern parameter
Λ	$1/\bar{\sigma}$, Surface roughness parameter
$\bar{\sigma}$	σ/c
φ_x, φ_y	Pressure flow factors
φ_s	Shear flow factor
λ	L/D , Aspect ratio
$\bar{\mu}$	μ/μ_r
ν	Poisson's ratio of bearing material
Ω	$\omega_j (\mu_r R_j^2 / c^2 p_s)$, Speed parameter
$\bar{\omega}_{th}$	ω_{th}/ω_l , Speed parameter
$\bar{\tau}$	$\tau(R_j/c p_s)$, shear stress parameter
$\bar{\dot{\gamma}}$	$\dot{\gamma} (\mu_r R_j / c p_s)$, shear strain parameter

Matrices and Vectors

$[\bar{F}]$	Fluidity matrix
$\{\bar{p}\}$	Nodal pressure vector
$\{\bar{Q}\}$	Nodal flow vector
$\{\bar{R}_{X_j}, \bar{R}_{Z_j}\}$	Nodal RHS vectors due to journal center velocities
$\{\bar{R}_H\}$	Column vector due to hydrodynamic terms

Subscripts and Superscripts

–	Nondimensional parameter
e	e^{th} element
j	Journal
max	Maximum value
min	Minimum value
o	Steady State Condition
R	Restrictor
r	Reference value
s	Supply Pressure
*	Concentric operation
.	First derivative w.r.t. time
..	Second derivative w.r.t. time

1 Introduction

Friction, wear and lubrication are three main elements of tribology, of which friction and wear play a significant role in design of machine components. Friction encountered between the machine components has significant influence on the longevity of the machine system as lesser the friction longer is the operating life and vice versa. Reduction in the value of friction is achieved by an adequate and efficient lubrication system. Various machine components such as bearings, gearbox, camshaft, crank shaft, etc. require excellent tribological properties and practices to ensure longer life.

Bearings are the machine elements that support an external load and simultaneously permit relative motion between two members. This transmits the load from a rotating member to a stationary member known as housing. The bearing permits relative motion between two members in one or two directions with minimum friction and restrains the unwanted motion due to the applied external load.

The bearings are broadly classified into two categories on the basis of contact that exists between the rotating and the stationary member

1. Rolling Element Bearing
2. Sliding Element Bearing

1.1 *Rolling Element Bearing*

The term rolling element bearings include all forms of bearings that utilize rolling action of balls or rollers to permit minimum friction and provide constrained motion of one body relative to another. Most of the rolling element bearings are used to permit rotation of a shaft relative to some fixed structure [1].

- Commercially the bearings are available as assemblage of two hardened steel rings (raceways) with hardened rolling elements. The rolling elements are either balls or rollers, capable of rolling freely without friction on the raceways. The rolling elements are geometrically constrained in an angularly spaced relationship by a separator or a retainer also known as cage in bearing terminology.
- Rolling bearings are generally manufactured from steel hardened to a high degree, at least on the surface. The AISI 52100 is in universal use by the ball bearing industry, steel moderately rich in chromium and easily hardened throughout (through-hardened) the mass of most bearing components to 61–65 Rockwell C scale hardness [1].
- Depending upon the type of rolling elements, bearings are classified as ball bearings, cylindrical roller bearings, taper roller bearings and needle bearings. On the basis of the direction of applied load, the bearings are classified as radial bearings and thrust bearings. There is, however, no clear distinction between these two groups. Certain types of radial bearing also support thrust load whereas some of the thrust bearings do support the radial loads.

1.1.1 Advantages of Rolling Element Bearing

The rolling contact bearings offers certain advantages as compared to other bearing types, as mentioned below [1]:

- They operate with a lesser frictional torque than hydrodynamic fluid-film bearings and therefore there is considerably less power loss and friction heat generation.
- The starting friction torque is slightly greater than the moving friction torque.
- The bearing deflection is less sensitive to load fluctuation than it is with hydrodynamic bearings.
- Requires small quantities of lubricant for satisfactory operation and have the potential for operation with a self-contained, lifelong supply of lubricant.
- They occupy shorter axial lengths than conventional hydrodynamic bearings.
- Combinations of radial and thrust loads can be supported simultaneously.
- Individual designs yield excellent performance over a wide load–speed range.

1.1.2 Disadvantages of Rolling Element Bearing

The rolling contact bearings do possess certain disadvantages as compared to other bearing types [1]. These are as mentioned below:

- Greater diametric space.
- More severe alignment requirements.
- Frictional torque increases rapidly at higher speeds
- Higher initial cost.
- Noisier operation.
- Finite life due to eventual failure by fatigue.
- Susceptible to damage by foreign matter.
- Poor capacity to damp out oscillations.

1.1.3 Applications of Rolling Element Bearings

The rolling element bearings find their use in variety of applications such as [1]:

- Automotive wheel bearings
- Cam follower bearings
- Aircraft gas turbine engine and power transmission bearings

1.2 Sliding Element Bearing

In sliding contact bearings, the relative motion between shaft and support is purely sliding. These bearings have surface contact and falls under the domain of lower kinematic pair.

1.2.1 Application of Sliding Element Bearing

Sliding contact bearings are generally used in the following applications [2–4]:

- Steam and gas turbines
- Crankshaft bearings in petrol and diesel engines
- Large size electric motors
- Centrifugal pumps
- Marine installation, rope conveyors
- Concrete mixers

1.2.2 Advantages of Sliding Element Bearing

These bearings have certain advantages over the rolling contact bearings such as

1. Simple design of the bearing and housing.
2. Occupy less radial space and are more compact.
3. Less costly.
4. Design of shaft is simple.
5. Silent operation.
6. Good shock load capacity.
7. Ideally suited for medium and high speed operations.

1.2.3 Disadvantages of Sliding Element Bearing

Sliding contact bearings has certain disadvantages such as:

1. The frictional power loss is more.
2. Requires good attention for lubrication.
3. They are normally designed to carry radial load or axial load only.

2 Purpose of Lubrication in Machine Components

Lubricants are used in rotating machinery to enhance the longevity of the contacting members. A lubricant is defined as a substance which is introduced between the two moving surfaces to reduce friction and wear between them. The primary function of a lubricant is to separate the moving parts, thereby reducing friction and wear in contacting parts. Debris removal and lowering the temperature are the other important benefits accrued by a fluid lubricant.

Lubricants are typically blended chemical compounds possessing 90 % of base stock and approximately 10 % of additive package. The base stock in common applications is petroleum-derived products; however, the vegetable oils (edible/nonedible) or liquids obtained through synthetic chemistry too are being used as base stocks in lubricant formulations.

Lubricants are blended with additives in order to enhance their lubricating capabilities. Solid lubricants are often used to reduce dry or boundary friction. Greases and waxes are widely used for light duty bearings. In addition, coatings of polymers such as PTFE (Teflon) and polyethylene can reduce friction and are used successfully in light duty applications. The liquid lubricants are used in larger quantities in industries and automotives because of their advantages over solid lubricants.

In the case of liquid lubrication, the molecules possessing affinity with the surfaces get adhered on the surface and forms thin fluid film that separate the surfaces in relative motion. The thin hydrodynamic fluid film so formed is capable to withstand the applied loads and temperatures and protects the surfaces from severe damage. Liquid lubricants also act as heat dispensing medium and offers cooling to the bearing by effective convection heat transfer. Due to their ease of application and replenishment, the liquid lubricants are widely used. Currently, the most common liquid lubricants are mineral oils, which are derived from petroleum. Mineral oils are blends of base oils and additive package. The additives are chemical compounds used to enhance the lubrication characteristics of base oil. Base oils are extracted from crude by vacuum distillation process. Crude oils contain a mixture of large number of organic compounds, mostly hydrocarbons (compounds of hydrogen and carbon). Certain hydrocarbons are suitable for lubrication and they are extracted from the crude oil as base oils.

The lubricant performs the following main functions:

1. Keep moving parts apart
2. Reduce friction
3. Allow heat transfer
4. Carry away contaminants & debris
5. Transmit power
6. Protect against wear
7. Prevent corrosion
8. Act as a seal for gases

2.1 Selection of Lubricant

The lubricant selection is usually done on the basis of following factors:

- (a) High component life
- (b) Less number of failures
- (c) Longest drain interval
- (d) Easy availability
- (e) Low cost depending upon the design, operating parameters, and environmental conditions.

3 Regimes of Lubrication

The interaction between the lubricant and the lubricating surfaces need to be understood in order to provide the machine elements with satisfactory life. A useful concept for the understanding of the role of different regimes of lubrication is the Stribeck curve. The Stribeck Curve is a log-log scale plot of the friction vs the nondimensional parameter relating viscosity, speed, and load. This consists of three lubrication regimes as indicated in literature elsewhere. Understanding the features that distinguish the three lubrication regimes from one another is discussed here.

3.1 Regime I: Boundary Lubrication

The first regime on Stribeck curve is identified as Boundary Lubrication. The characteristic of this regime is to support high load with low speeds or very less lubricant inside, such that it has no role to play within the contact. The lubrication regime characterized by these conditions is known as Boundary lubrication. It is one of the most common types of lubrication phenomena prevalent in day-to-day machinery contacts. The boundary lubrication finds its application where the hydrodynamic and elastohydrodynamic lubrication fails and the conditions are such that the surface speeds are relatively slow with high contact pressures and rough surfaces. With the severity of the operating conditions wear becomes inevitable, and in order to combat failures related to wear, surface preparation of contacting bodies is desired. The EP (extreme pressure) or boundary additives blended into the lubricant creates a lubricant film that strongly adheres over the surface. The boundary lubrication regime is characterized by very less lubricant separating the bodies in contact, thereby resulting into large area of contact and a high value of friction.

3.2 *Regime II: Mixed Fluid-Film Lubrication*

The second regime of Stribeck curve is the mixed fluid-film lubrication. The lubricant film in contact is so thin in comparison to the applied load that the complete separation of bearing surfaces is seldom achieved. This regime is known as the mixed lubrication regime. The shift of the mixed lubrication regime to slower speeds or higher loads can be influenced by various parameters such as:

1. Viscosity of fluid
2. Strength of boundary films
3. Long wavelength in surface roughness (low slopes for small pressure gradients)
4. Transverse roughness so that the fluid film does not easily flow through

With an increase of surface speed and lubricant viscosity or a reduction in applied load, the surfaces begin to separate, thereby favoring the formation of lubricant films in the contact. The developed film is relatively thin but is competent to support the applied load. This results into mixed lubrication, with a sharp visible drop in the value of friction coefficient.

3.3 *Regime III: Full Fluid-Film Lubrication*

The last portion of Stribeck curve is known as the full fluid film lubrication. The surfaces will continue to separate as the speed or viscosity increase until there is full fluid film and no surface contact. Full fluid-film lubrication can be hydrostatic/hydrodynamic, or elasto-hydrostatic/elasto-hydrodynamic. The lubricant film is sufficiently thick as a result of which the coefficient of friction reaches its minimum value and a transition to hydrodynamic lubrication is visible. As a consequence of this, there is lesser friction and negligible wear in hydrodynamic lubrication.

4 Fundamentals of Fluid-Film Journal Bearings

The opposing surfaces of hydrodynamic fluid-film bearings are completely separated by a lubricant film. The lubricant may be a liquid or a gas. The load-carrying capacity is derived from the fluid-film pressure within the lubricating film, generated by the motion of the machine elements (self-acting or hydrodynamic bearings) or by external pressurization (hydrostatic) or hydrodynamic squeeze motion, or by a combination of these actions [2, 5]. These types of bearings are especially suitable for operation at high loads and low speeds or when fluid film stiffness perpendicular to surface motion is important

4.1 Hydrodynamic Journal Bearings

In a hydrodynamic lubricated bearing, there exists a thick fluid film between the journal and the bearing as depicted in Fig. 25.1a. When the bearing is supplied with adequate lubricant, pressure builds up in the clearance space when journal is rotating about its axis that is eccentric with the bearing axis. So the external load can be supported by fluid-film pressure without any actual contact between the journal and bearing. Load carrying capacity of these bearings increases mainly due to the resistance of a viscous fluid being pushed around.

4.2 Hydrostatic Journal Bearings

In hydrostatic journal bearings thick lubricant films are allowed to form in between the bearing and journal surfaces by supplying lubricant at high pressure via restrictors or flow control devices. Flow control devices such as capillaries, orifices, constant flow valves, etc. as indicated in Fig. 25.1 are widely being used.

The oil is pumped to the restrictors through oil supply lines by a pump which is driven by a motor. The filter is also provided in the supply line in order to remove the dirt and suspended particles which may cause blockage in the supply lines. A pressure gauge is provided to monitor the pressure and a pressure control valve is also attached in order to relieve the pressure in case of excessive pressure buildup. Bearings operating under hybrid mode of operation utilize both hydrostatic and hydrodynamic action in an optimal manner.

The hydrostatically lubricated bearings offer certain excellent characteristics [3, 4, 6] such as:

- Extremely low friction
- Extremely high load-carrying capacity at low speeds
- High bearing stiffness
- High positional accuracy in high-speed, light-load applications
- Better dynamic characteristics

4.3 Hybrid Journal Bearings

A hybrid bearing combines the physical mechanisms of both hydrostatic and hydrodynamic lubrication system [2, 7]. Hybrid bearings are superior in performance over pure hydrodynamic bearings as with former, wear is avoided during start up and stop down operations. In comparison with the pure hydrostatic bearings the hybrid bearings are able to tolerate substantial loads over and above the normal designed loads. Also these bearings are capable of withstanding dynamic loads that vary widely in the direction of rotation.

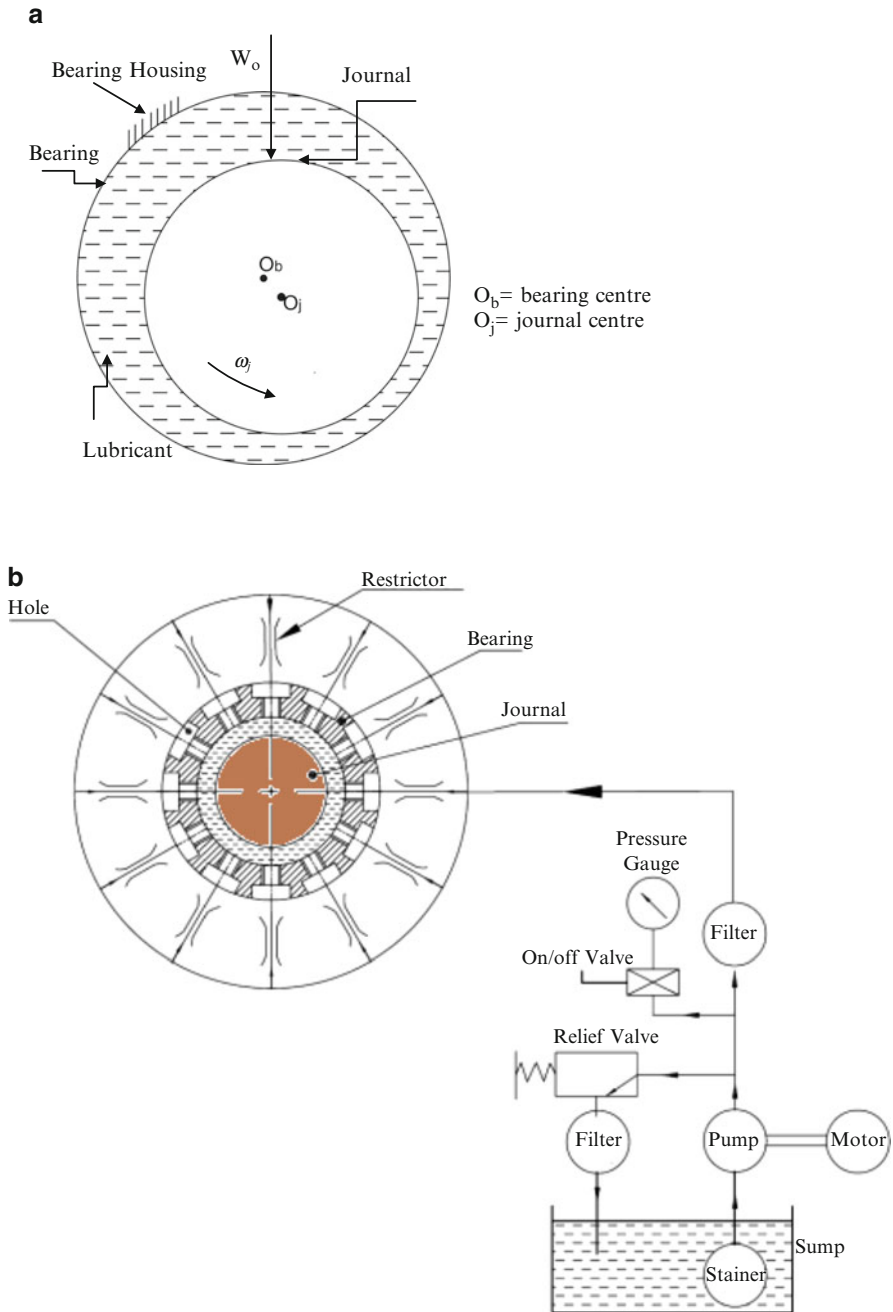


Fig. 25.1 (a) Hydrodynamic journal bearing system. (b) Non-recessed hydrostatic journal bearing system [2]

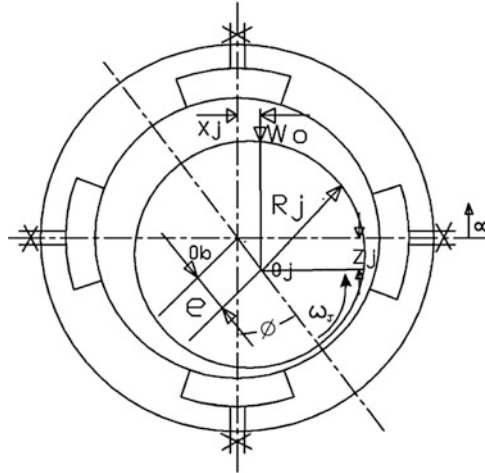


Fig. 25.2 Four-pocket hydrostatic/hybrid journal bearing system [5, 9, 19]

4.4 Classification of Hydrostatic/Hybrid Journal Bearings

In general, the hydrostatic/hybrid journal bearing configurations are broadly classified into two main groups, named as recessed (pockets) and non-recessed (plain) journal bearings [2, 3, 5]

4.4.1 Recessed Journal Bearings

The recessed bearings generally consist of multiple recesses or pockets disposed around the circumferential direction. These recesses occupy a significant portion of bearing area in comparison to the total bearing area as shown in Fig. 25.2. Thus, when this type of bearing operates in hybrid mode, load carrying capacity is mainly due to hydrostatic action.

4.4.2 Non-recessed Journal Bearings

Non-recessed hybrid journal bearing configurations are generally of two types. The first one is the hole-entry type [7] in which two rows of six or more holes are provided around the circumferential direction of the bearing in a symmetric or asymmetric manner as shown in Fig 25.3. The other type of non-recessed hybrid journal bearing configuration is known as slot-entry bearing as shown in Fig 25.4.

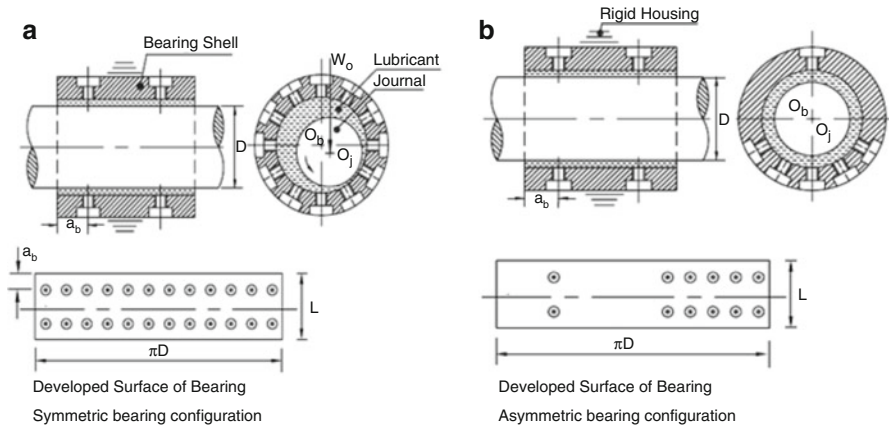


Fig 25.3 Non-recessed hole entry journal bearing (a) Symmetric bearing configuration (b) Asymmetric bearing configuration [5, 17, 33]

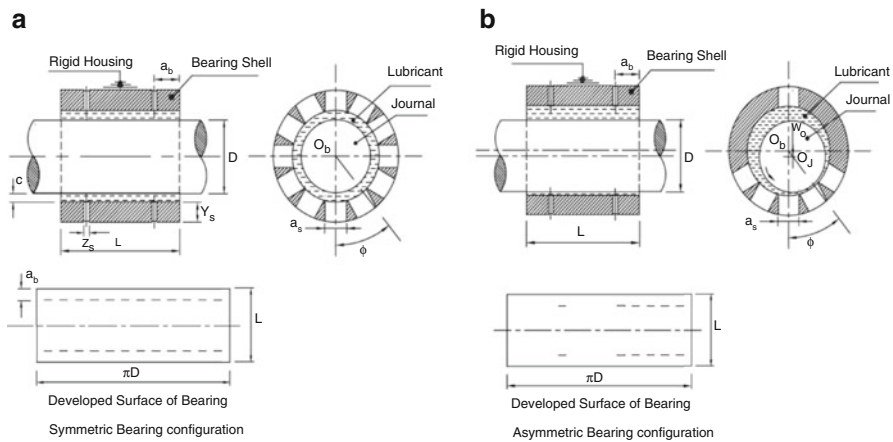


Fig 25.4 Non-recessed Slot entry journal bearing (a) Symmetric bearing configuration (b) Asymmetric bearing configuration [5, 43]

4.5 Elements of Hydrostatic Journal Bearing

For the successful operation of a hydrostatic journal bearing system, some of the elements such as hydraulic pumps, compensating element, etc. are required to be used in conjunction with hydrostatic bearings system. These elements are indispensable to the hydrostatic bearing system. These elements have been described in subsequent sections.

4.5.1 Hydraulic Pumps

A positive-displacement pump is widely used for lubrication in gear pumps. The use of gear pumps is well known in the lubrication system of automotive engines. Gear pumps, as well as piston pumps, are positive-displacement pumps that deliver, under ideal conditions, a fixed quantity of liquid per cycle, irrespective of the flow resistance (head losses in the system). However, it is possible to convert the discharge at a constant flow rate to discharge at a constant pressure by installing a pressure relief valve that maintains a constant pressure and returns the surplus flow.

The advantages of the gear pump over the other type of pumps are as follows:

1. It is a simple and compact pump, and does not need inlet and outlet valves, such as in the piston pump. However, gear pumps require close running clearances.
2. It involves continuous flow (unlike positive-displacement reciprocating pumps).
3. Ability to handle very-high-viscosity fluid.
4. Generates very-high heads (or outlet pressure) in comparison to centrifugal pumps.
5. Ability to act like a compressor and pumps out trapped air or vapor.
6. Provides good efficiency at very-high heads and over a wide speed range.
7. Easy to operate at relatively low suction heads.

4.5.2 Compensating Elements

Flow control devices form an integral part of hydrostatic fluid film bearing system and hence their use in application is inevitable. The pocket pressure is a function of applied load and pocket area. The high pressures developed inside the pockets provide the required resistive force to support the applied load. The pressure control devices or the restrictor between the lubricant supply and the pocket provide stiffness to the lubricant film.

If fluid-film stiffness or load variations are important criterions then selection and design of the flow control device becomes critical. Each of the bearing recess has to be supplied with a separate control device to achieve desired fluid film stiffness. The control device is designed in a manner to provide desired pressure ratio for the bearing at the given concentric position. The pressure ratio is defined as the ratio of the concentric recess pressure to the supply pressure. Proper selection of values of pressure ratio is of vital importance. Proper selection ensures high bearing stiffness and load capacity along with protection against loss of load capacity due to manufacturing tolerances. Various types of restrictors have been developed and are being successfully used in hydrostatic bearings [3, 6].

The main factors that influence the choice of restrictor in a hydrostatic bearing system are [3]:

- Fluid film stiffness
- Manufacturing simplicity

- External dimensions
- Effect on bearing stability
- Costs

4.6 Various Type of Flow Control Devices

In practice, the selection of type of restrictor is undertaken in parallel with the bearing configuration because both have significant influence on the bearing performance and are essential elements of a bearing system. In hydrostatic bearings generally capillary, orifice, constant flow valve, and membrane restrictor are used [4]. The first three aforementioned are categorized as fixed-flow restrictors while the fourth one is a variable flow restrictor. The flow in the membrane restrictors is automatically adjusted as soon as the pressure differential between the pads is sensed. For a stiffer bearing system, variable flow restrictors are the best suitable options; however, they are more expensive than the fixed-flow restrictors. The purpose of the compensating element is to bring a pressurized fluid from the supply manifold to the recess. The type of compensation used in a bearing system affects the quantity of the fluid in the recess. The compensating elements are extremely important in controlling the bearing fluid-film stiffness. The bearing fluid-film stiffness is the measure of the strength of compensation [4]. The control devices which include capillary tube, orifice, constant flow valve, and membrane restrictors have been briefly described in the following sections.

4.6.1 Capillary Compensation

The capillary compensated bearings possess advantages of (a) being insensitive to viscosity variations and (b) predictable performance behavior. Moreover, the flow control arrangement using capillaries is simple and easy to manufacture. The flow through the capillary is laminar, thus maintaining the Reynolds number less than 2000. However, their usage is constrained with end effects. The end effects have to be minimum and in order to achieve this capillary length has to be at least 100 times the tube diameter. The commercial Hypodermic tubings available in different sizes are used as capillaries.

Capillary compensation is most commonly used in hydrostatic bearing applications. The small diameter of the capillary tube provides restriction and resultant pressure drop in the bearing pad. In capillary compensation, a long tube of relatively small diameter ($l_c > 20d_c$) is used. The laminar flow of fluid through such a tube, when inlet and outlet effects and viscosity changes due to temperature and pressure are neglected can be expressed as [8]:

$$Q_R = \frac{k_c(p_s - p_c)}{\mu} \quad (25.1)$$

where, $k_c = \frac{\pi d_c^4}{128l_c}$

For a given capillary tube, k_c is a constant expressed in cubic meter. Thus, from (25.1) flow through a capillary tube is related linearly to the pressure drop across it. The Reynolds number is expressed as [8],

$$R_e = \frac{4\rho Q_R}{\pi d_c \mu} < 2000 \quad (25.2)$$

Where, ρ is the density of the lubricant in kg/m^3 . Hypodermic needle tubing serves quite well as capillary tubing for hydrostatic bearings. Very small diameter tubings are commercially available, but diameters less than 6×10^{-4} m should not be used because of their tendency to clog.

The flow through capillary restrictor may be expressed in nondimensional form as [5, 9]

$$\bar{Q}_R = \bar{C}_{s2}(1 - \bar{p}_c) \quad (25.3)$$

$$\text{where, } \bar{C}_{s2} = \frac{1}{12} \left(\frac{\pi r_c^4}{8 c^3 l_c} \right)$$

4.6.2 Orifice Compensation

Flow control by orifice compensation, leads to greater flow variations due to manufacturing inaccuracies. The performance of an orifice restrictor depends on fluid viscosity. It is due to this reason that every time a change in viscosity is encountered, the flow characteristics are also changed. Exact performance prediction with orifice compensation is difficult as the later is more prone to blockage due to stray particles if present in the lubricating system. It is extremely difficult to totally eliminate stray particles even when the lubricating system is rigorously flushed during assembly. However, the major advantage of this system is its compact nature which reduces the total size of the bearing system. The flow of an incompressible fluid through a sharp-edge orifice is expressed as [8],

$$Q_R = k_o(p_s - p_r)^{1/2} \quad (25.4)$$

$$\text{where, } k_o = \frac{\pi \psi_d (d_o)^2}{\sqrt{8\rho}}$$

For a given orifice size and lubricant, k_o is a constant expressed in $\text{m}^4/(\text{s-N}^{1/2})$. ψ_d is known as orifice discharge coefficient and is a function of Reynolds number. Thus, from (25.4), flow through an orifice is proportional to the square root of the pressure difference across the orifice. For an orifice the Reynolds number is given as,

$$R_e = \frac{d_o}{\mu} [2\rho(p_s - p_r)]^{1/2} \quad (25.5)$$

For orifice the value of ψ_d is approximately 0.55 for $R_e = 10^6$ [8]

The flow through an orifice restrictor in nondimensional form may be expressed as [5, 9]

$$\bar{Q}_R = \bar{C}_{s2}(1 - \bar{p}_c)^{1/2} \quad (25.6)$$

where,

$$\bar{C}_{s2} = \frac{1}{12} \left(\frac{3\pi d_o^2 \mu_r \psi_d}{c^3} \right) \left(\frac{2}{\rho p_s} \right)^{1/2} \quad (25.7)$$

4.6.3 Constant Flow Valve Compensation

Constant flow valve compensation is achieved by pumps and pressure compensating valves. The pressure compensating valves provide better stiffness and load bearing capacity. However, its performance is limited by, (1) maximum pump pressure at which constant flow can be maintained and (2) minimum pressure difference across the valve which should not be less than 0.2 MN/m² for satisfactory operation [8]. This type of restrictor maintains a constant flow irrespective of the pressure difference across the valve. Hence, the flow is independent of the recess pressure.

Basically, any type of compensating device can be used along with a hydrostatic bearing system if load on the bearing is static. However, if stiffness, load, or flow varies, judicious choice of proper compensating element is of paramount importance. In this context the variable type restrictor is better.

4.6.4 Variable Type Restrictor (Membrane)

It is a well-known fact that the fluid-film stiffness of externally pressurized journal bearings depend on the type of restrictor used. Membrane restrictors were first used by DeGast in 1966. Stiffness of these bearings can be increased by using variable-flow restrictors rather than fixed restrictors [10]. This combination of bearing system provides highest fluid-film stiffness as compared to any other flow control device. It is possible to achieve higher fluid-film stiffness over a limited load range by efficient design considerations or by employing stiff membranes. Membrane restrictor is a variable type restrictor. A schematic of membrane restricted two-lobe journal bearing configuration is shown in Fig. 25.5. Membrane compliance capable of offering desired bearing stiffness for a given combination of pressure ratio and eccentricity, may report poor stiffness characteristics for bearings operating at same pressure ratio but with different eccentricities.

In general the typical values of design parameters for membrane restrictors used are as follows [11]: $p_s = 3.04 \text{ N/mm}^2$, $K_m = 3.23 \text{ kN/mm}$, $A_m = 19 \text{ mm}^2$, $h_{mo} = 0.026 \text{ mm}$, $E = 2 \times 10^5 \text{ N/mm}^2$, $\nu = 0.3$.

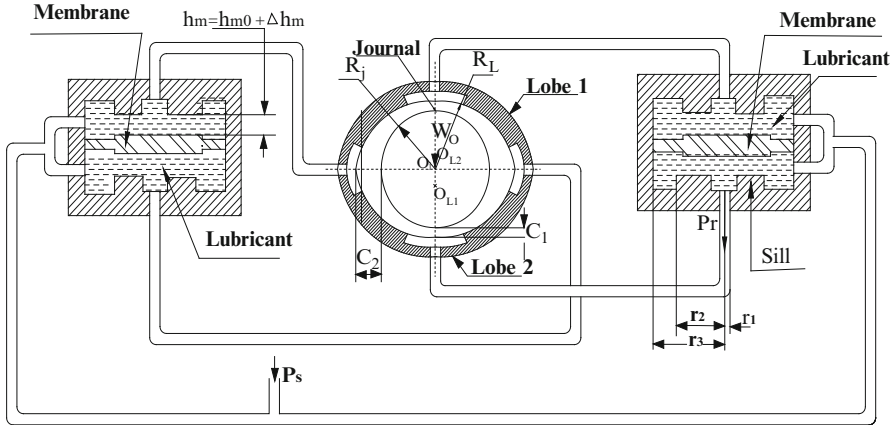


Fig. 25.5 Membrane Restricted 2-Lobe Journal Bearing [11]

For a membrane compensated multirecess (four-pocket) journal bearings, the lubricant flow rate through various pockets (1, 2, 3, 4) may be expressed in its nondimensional form as:

$$\begin{aligned}
 \bar{Q}_{R1} &= \bar{C}_{s2} [1 + \bar{C}_m (\bar{P}_{c1} - \bar{P}_{c3})]^3 (1 - \bar{P}_{c1}) \\
 \bar{Q}_{R2} &= \bar{C}_{s2} [1 + \bar{C}_m (\bar{P}_{c2} - \bar{P}_{c4})]^3 (1 - \bar{P}_{c2}) \\
 \bar{Q}_{R3} &= \bar{C}_{s2} [1 + \bar{C}_m (\bar{P}_{c1} - \bar{P}_{c3})]^3 (1 - \bar{P}_{c3}) \\
 \bar{Q}_{R4} &= \bar{C}_{s2} [1 + \bar{C}_m (\bar{P}_{c2} - \bar{P}_{c4})]^3 (1 - \bar{P}_{c4})
 \end{aligned} \tag{25.8}$$

where, the terms \bar{P}_{c1} , \bar{P}_{c2} , \bar{P}_{c3} and \bar{P}_{c4} indicate the values of fluid-film pressure in respective recesses/pockets.

$$\bar{C}_m = \frac{P_s A_m}{K_m h_{m0}} = \text{Membrane Compliance}$$

The nondimensional flow rate equations for a membrane restrictor becomes similar to a capillary restrictor when $\bar{C}_m = 0$. The stiffness of the membrane K_m is given as,

$$K_m = \frac{4\pi E t_m^3 (\gamma^2 - 1)}{3(1 - \nu^2) r_2^2 [(\gamma^2 - 1)^2 - 4\gamma^2 (\ln \gamma)^2]} \tag{25.9}$$

where $\gamma = r_3/r_2$

5 Noncircular Journal Bearing Configurations

Instabilities are common phenomena encountered during the operation of journal bearings. Oil film whirl and whip are common instabilities encountered in the journal bearings. Oil film whirl characterizes the phenomenon in which the oil film develops an average speed slightly less than 50 % of the journal surface speed, whereas oil film whip represents the conditions when the oil whirl frequency coincides with system's natural frequency. These bearing instabilities cause the journal/bearing to wobble in the clearance space of the bearing. With severe operating conditions the amplitude of wobbling becomes large enough resulting in metal to metal contact between the shaft and the bearing, i.e., failure induced instability [12].

To eliminate or control whipping, noncircular hydrostatic/hybrid bearings are used. The two-lobe multirecess hydrostatic/hybrid journal bearing is an externally pressurized bearing with design features to overcome the limitations of conventional (circular) multirecess hydrostatic bearings, when used under high or medium load conditions. This bearing is designed as an arc of the circle with the center points placed on the symmetry line of the single lobe, as shown in Fig. 25.6. The novel features of noncircular journal bearings gets incorporated into the hybrid journal bearings, thereby reducing the adverse effects of circular journal bearings such as poor stability and self excited vibration characteristics. The noncircular journal bearings have better stability as compared to circular journal bearings. They suppress the oil whirl [13].

Two-lobe journal bearings possess good damping at critical speed. As the number of lobes increases, it enhances the oil whirl suppression at large. This trend shows good whirl suppression up to maximum four lobes.

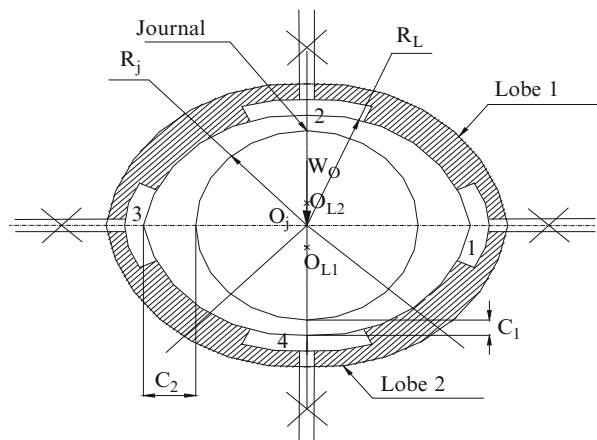


Fig. 25.6 Two-Lobe Four-Pocket Hybrid Journal Bearing [13]

6 Conical Hydrostatic Journal Bearing System

The conical Hydrostatic journal bearings are capable to support both the thrust and radial loads. This configuration eliminates the complexity of using separate thrust and journal bearings [8, 14, 15]. In recent times extensive research activities have been carried out and reported concerning analysis and design of multirecess conical journal bearing systems. The conical journal bearing reduces axial and radial vibrations and provides high accuracy for sensitive and precision equipments. A schematic of multirecess conical hydrostatic journal bearing is shown in Fig. 25.7. Nowadays conical journal bearing configurations are most commonly used because of their load carrying capacity in the radial and axial directions. For a moderate size bearing, low flow rate, excellent stiffness characteristics, reduced cost, and ease of manufacture with advanced numerical machining are the reasons

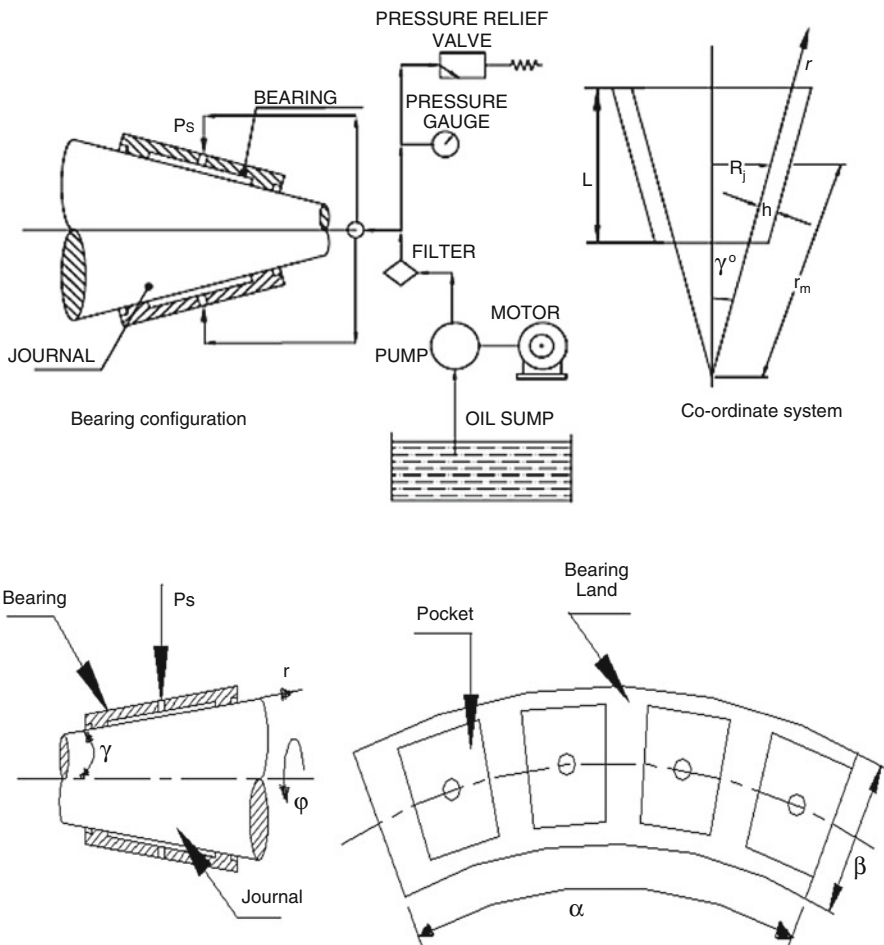


Fig. 25.7 A Schematic of Multirecess Conical Hydrostatic Journal Bearing [14]

for their popularity [16]. Conical hydrostatic journal bearings are most suitable candidates for precision machine tool applications that demand high load carrying capacity along with high fluid-film stiffness.

7 Analysis of Fluid-Film Journal Bearings

Osborne Reynolds in the year 1886 proposed the famous Reynolds equation which forms the basis of modern day lubrication science. The Reynolds equation in differential form is derived using Navier–Stokes equation in conjunction with the continuity equation and consists of terms associated with pressure, fluid-film thickness, and lubricant properties. The solution of this equation gives fluid-film pressures in thin lubricant films in the narrow, converging gap between two surfaces. In fluid-film bearings, external load is supported by generation of fluid-film pressure within the thin layer of lubricant. A necessary condition for the fluid-film pressure to develop in a thin film of fluid is that the gradient of the velocity profile must vary across the thickness of the film. Reynolds equation is capable of predicting hydrodynamic, squeeze, and hydrostatic film mechanisms within the given geometry. Osborne Reynolds proved through analytical solutions that a viscous liquid can physically separate two sliding surfaces by hydraulic pressure. This action in turn results into low friction and theoretically zero wear. The Reynolds equation thus forms the basis for the fluid-film pressure distribution within a given contact.

After utilizing the usual assumptions, the complete generalized Reynolds equation in three-dimensional form is derived as,

$$\begin{aligned} \frac{\partial}{\partial x} \left(-\frac{\rho h^3}{12\mu} \frac{\partial p}{\partial x} \right) + \frac{\partial}{\partial y} \left(-\frac{\rho h^3}{12\mu} \frac{\partial p}{\partial y} \right) + \frac{\partial}{\partial x} \left[\frac{\rho h(u_a + u_b)}{2} \right] \\ + \frac{\partial}{\partial y} \left[\frac{\rho h(v_a + v_b)}{2} \right] + \rho(w_a - w_b) - \rho u_a \frac{\partial h}{\partial x} - \rho v_a \frac{\partial h}{\partial y} + \rho \frac{\partial h}{\partial t} = 0 \end{aligned} \quad (25.10)$$

7.1 Generalized Reynolds Equation

The flow of lubricant in the clearance space of a smooth journal bearing system with usual assumptions can be simplified and expressed in the form of Reynolds equation [5]:

$$\frac{\partial}{\partial x} \left(\frac{h^3}{12\mu} \frac{\partial p}{\partial x} \right) + \frac{\partial}{\partial y} \left(\frac{h^3}{12\mu} \frac{\partial p}{\partial y} \right) = \frac{U}{2} \frac{\partial h}{\partial x} + \frac{\partial h}{\partial t} \quad (25.11)$$

After incorporating the following nondimensional parameters, the Reynolds equation applicable for a journal bearing system as indicated in Fig. 25.8a is reduced to a nondimensional form as defined in (25.12) [5, 9].

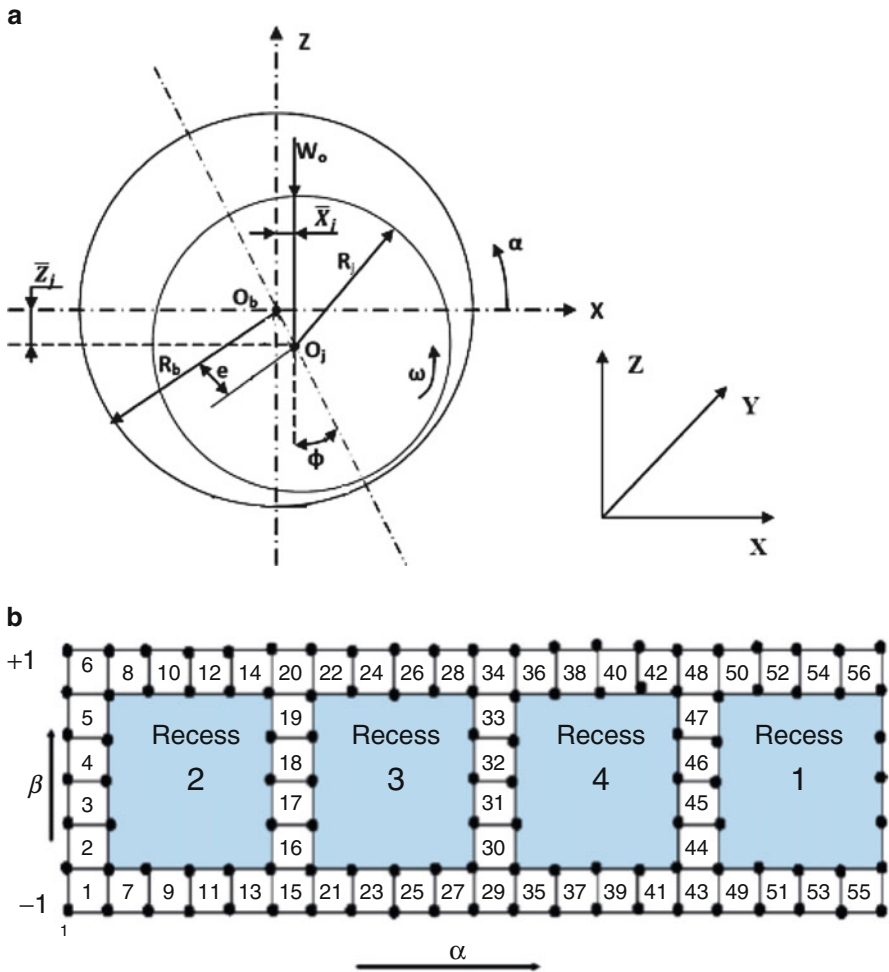


Fig. 25.8 (a) Schematic of journal bearing system [5, 20]. (b) Discretized fluid-film domain in case of Multirecess Hydrostatic Journal Bearing [11]

$$\alpha = \frac{x}{R_j}; \beta = \frac{y}{R_j}; \bar{z} = \frac{z}{h}; \bar{h} = \frac{h}{c}; \bar{p} = \frac{p}{p_s};$$

$$U = \omega_j R_j; \bar{\mu} = \frac{\mu}{\mu_r}; \Omega = \omega_j \left(\frac{\mu_r R_j^2}{c^2 p_s} \right); \tau = t \left(\frac{c^2 p_s}{\mu_r R_j^2} \right)$$

$$\frac{\partial}{\partial \alpha} \left(\frac{\bar{h}^3}{12} \frac{\partial \bar{p}}{\partial \alpha} \right) + \frac{\partial}{\partial \beta} \left(\frac{\bar{h}^3}{12} \frac{\partial \bar{p}}{\partial \beta} \right) = \frac{\Omega}{2} \frac{\partial \bar{h}}{\partial \alpha} + \frac{\partial \bar{h}}{\partial \tau} \tag{25.12}$$

The solution of Reynolds equation is usually obtained by employing the numerical techniques such as finite difference method, finite element method, finite

volume method, perturbation method etc. In recent times the fluid-film lubrication problems are generally handled by FEM in which the flow field is discretized into sub-domains or smaller elements. FEM has the capability to handle irregular geometry of bearing over the other mathematical techniques. A typical lubricant flow domain of multirecess hydrostatic journal bearing system is shown in Fig. 25.8b.

The finite element analysis of generalized Reynolds equation (25.12) in nondimensional form results into following algebraic equation [5, 9].

$$\begin{aligned}
 [\bar{F}^e]_{n*n} \{ \bar{p}^e \}_{n*1} &= \{ \bar{Q}^e \}_{n*1} + \Omega \{ \bar{R}_H^e \}_{n*1} + \bar{X}_j \{ \bar{R}_{X_j}^e \}_{n*1} \\
 &+ \bar{Z}_j \{ \bar{R}_{Z_j}^e \}_{n*1}
 \end{aligned}
 \tag{25.13}$$

where,

$$\bar{F}_{ij}^e = \iint_{A^e} \frac{\bar{h}^3}{12} \left[\frac{\partial N_i}{\partial \alpha} \frac{\partial N_j}{\partial \alpha} + \frac{\partial N_i}{\partial \beta} \frac{\partial N_j}{\partial \beta} \right] d\alpha d\beta = \text{Fluidity matrix}
 \tag{25.13a}$$

$$\begin{aligned}
 \bar{Q}_i^e &= \int_{\Gamma^e} \left\{ \left(\frac{\bar{h}^3}{12} \frac{\partial \bar{p}}{\partial \alpha} - \frac{\Omega}{2} \bar{h} \right) n_x + \left(\frac{\bar{h}^3}{12} \frac{\partial \bar{p}}{\partial \beta} \right) n_y \right\} N_i d\Gamma^e \\
 &= \text{Nodal flow vector}
 \end{aligned}
 \tag{25.13b}$$

$$\bar{R}_{H_i}^e = \iint_{A^e} \frac{\bar{h}}{2} \frac{\partial N_i}{\partial \alpha} d\alpha d\beta = \text{Column vector due to hydrodynamic term}
 \tag{25.13c}$$

$$\begin{aligned}
 \bar{R}_{X_{j_i}}^e &= \iint_{A^e} N_i \cos \alpha d\alpha d\beta \\
 &= \text{Nodal RHS vector due to journal velocity in X-direction}
 \end{aligned}
 \tag{25.13d}$$

$$\begin{aligned}
 \bar{R}_{Z_{j_i}}^e &= \iint_{A^e} N_i \sin \alpha d\alpha d\beta \\
 &= \text{Nodal RHS vector due to journal velocity in X-direction}
 \end{aligned}
 \tag{25.13e}$$

where, n_x and n_y are the direction cosines in α and β directions respectively.

The algebraic equations (25.13) have a single unknown parameter, i.e., fluid-film pressure. The algebraic equations are solved for the values of fluid-film pressures by applying the following boundary conditions,

7.2 Boundary Conditions

In general boundary conditions used for the analysis of lubricant flow field are described as [5, 11, 17]:

1. The nodes lying on external boundary of bearing have zero relative pressure with respect to atmospheric pressure, i.e., $\bar{p} \Big|_{\beta=\mp 1.0} = 0$
2. Nodes lying on holes have equal pressure.
3. Flow of lubricant through the restrictor is equal to the bearing input flow at hole.
4. At the trailing edge of positive region, the Reynolds boundary condition is applied, i.e., $\bar{p} = \frac{\partial \bar{p}}{\partial \alpha} = 0.0$

8 Performance Characteristics of a Journal Bearing System

The performance of a bearing is usually described in terms of its static as well as dynamic performance characteristics parameters. The static performance characteristic parameters include the load carrying capacity, minimum fluid-film thickness, lubricant flow, etc. The dynamic performance characteristic parameters mainly comprises of bearing rotor dynamic coefficients, i.e., fluid-film stiffness and damping coefficients and stability threshold speed margin [2, 5, 6].

8.1 Static Performance Characteristics

The static performance characteristic parameters are computed for the static condition (i.e., $\bar{X}_j = \bar{Z}_j = 0$) of loading. For the computation of performance characteristics, it is first of all essential to establish the journal center equilibrium position for a specified vertical external load (\bar{W}_0).

8.1.1 Journal Center Equilibrium Position

When the bearings support a specified vertical external load, the equilibrium position of journal center coordinates are needed to equilibrate the external load. This may be carried out for two cases, i.e., either for specified external load or for a specified eccentricity.

- (a) For specified external load (\bar{W}_0)

For a given geometric and operating parameters of bearing and for a specified external vertical load, journal center position (\bar{X}_j, \bar{Z}_j) is unique. For a given external load (\bar{W}_0), the tentative values of journal center coordinates are fed as an input. The corrections ($\Delta \bar{X}_j, \Delta \bar{Z}_j$) on the assumed journal center coordinates (\bar{X}_j, \bar{Z}_j) are computed using following algorithm. The fluid-film reaction components \bar{F}_x, \bar{F}_z are expressed by Taylor's series about i^{th} journal center position. Assuming that the alteration in the journal center position are quite

small and retaining the terms only up to first order in the Taylor’s series expansion, the corrections $(\Delta\bar{X}_j|_i, \Delta\bar{Z}_j|_i)$ on the coordinates are obtained as:

$$\Delta\bar{X}_j|_i = -\frac{1}{D_j} \left[\frac{\partial\bar{F}_z}{\partial\bar{Z}_j|_i} \quad -\frac{\partial\bar{F}_x}{\partial\bar{Z}_j|_i} \right] \left\{ \begin{matrix} \bar{F}_x|_i \\ \bar{F}_z|_i - \bar{W}_0 \end{matrix} \right\} \tag{25.14a}$$

$$\Delta\bar{Z}_j|_i = -\frac{1}{D_j} \left[-\frac{\partial\bar{F}_z}{\partial\bar{X}_j|_i} \quad \frac{\partial\bar{F}_x}{\partial\bar{X}_j|_i} \right] \left\{ \begin{matrix} \bar{F}_x|_i \\ \bar{F}_z|_i - \bar{W}_0 \end{matrix} \right\} \tag{25.14b}$$

where,

$$D_j = \left[\frac{\partial\bar{F}_x}{\partial\bar{X}_j|_i} \frac{\partial\bar{F}_z}{\partial\bar{Z}_j|_i} - \frac{\partial\bar{F}_x}{\partial\bar{Z}_j|_i} \frac{\partial\bar{F}_z}{\partial\bar{X}_j|_i} \right] \tag{25.14c}$$

The new journal center coordinates $[\bar{X}_j|_{i+1}, \bar{Z}_j|_{i+1}]$ are expressed as:

$$\bar{X}_j|_{i+1} = \bar{X}_j|_i + \Delta\bar{X}_j|_i \tag{25.14d}$$

$$\bar{Z}_j|_{i+1} = \bar{Z}_j|_i + \Delta\bar{Z}_j|_i \tag{25.14e}$$

(b) For a specified eccentricity ratio (ϵ)

Journal center coordinates, for a specified eccentricity ratio (ϵ) are computed using the equations given below [2, 5].

- Hydrostatic mode of operation ($\Omega = 0$)

$$\begin{aligned} \bar{X}_j &= 0.0 \\ \bar{Z}_j &= -\epsilon \end{aligned} \tag{25.14f}$$

- Hybrid mode of operation ($\Omega \neq 0$)

$$\begin{aligned} \bar{X}_j &= \epsilon \sin \varphi \\ \bar{Z}_j &= -\epsilon \cos \varphi \end{aligned} \tag{25.14g}$$

The final equilibrium position of journal is established using a suitable iterative scheme for an attitude angle (φ).

Using the computed values of journal center coordinates (\bar{X}_j, \bar{Z}_j) , the value of minimum fluid-film thickness is computed from the expression as defined below:

$$h_{\min} = \min \text{ of } \langle h \rangle_n, \quad n = 1, 2, 3, \dots, n_1 \tag{25.15}$$

where, n_1 is the number of nodes in the lubrication flow field solution domain for solving Reynolds equation.

$$\epsilon = \sqrt{(|\bar{X}_j|^2 + |\bar{Z}_j|^2)} \quad (\text{For given Load}) \tag{25.16}$$

8.1.2 Load Carrying Capacity

The fluid-film reaction components in the X and Z direction are expressed as [5]:

$$\bar{F}_x = - \int_{-\lambda}^{\lambda} \int_0^{2\pi} \bar{p} \cos \alpha \, d\alpha \, d\beta \quad (25.17a)$$

$$\bar{F}_z = - \int_{-\lambda}^{\lambda} \int_0^{2\pi} \bar{p} \sin \alpha \, d\alpha \, d\beta \quad (25.17b)$$

The resultant fluid-film reaction is expressed as

$$\bar{F} = [\bar{F}_x^2 + \bar{F}_z^2]^{1/2} \quad (25.17)$$

8.2 Dynamic Performance Characteristics

The dynamic performance characteristic parameters of bearings include bearing rotor dynamic coefficients, i.e., fluid-film stiffness and damping coefficients ($\bar{S}_{ij}, \bar{C}_{ij}; i, j = x, z$). For a two degree of freedom system, there exist four fluid-film stiffness coefficients and four damping fluid-film coefficients, which have a strong influence on the stability of the system. These coefficients are defined as:

8.2.1 Fluid-Film Stiffness Coefficients

The fluid-film stiffness coefficients are defined as:

$$\bar{S}_{ij} = - \frac{\partial \bar{F}_i}{\partial \bar{q}_j} (i = x, z) \quad (25.18)$$

where, “i” represents the direction of force and “ \bar{q}_j ” represents the direction of displacement of journal center coordinate (\bar{X}_j or \bar{Z}_j).

Stiffness coefficient matrix is defined as:

$$\begin{bmatrix} \bar{S}_{xx} & \bar{S}_{xz} \\ \bar{S}_{zx} & \bar{S}_{zz} \end{bmatrix} = - \begin{bmatrix} \frac{\partial \bar{F}_x}{\partial \bar{X}_j} & \frac{\partial \bar{F}_x}{\partial \bar{Z}_j} \\ \frac{\partial \bar{F}_z}{\partial \bar{X}_j} & \frac{\partial \bar{F}_z}{\partial \bar{Z}_j} \end{bmatrix} \quad (25.18a)$$

8.2.2 Fluid-Film Damping Coefficients

The fluid-film damping coefficients are defined as:

$$\bar{C}_{ij} = -\frac{\partial \bar{F}_i}{\partial \bar{q}_j} \quad (i = x, z) \quad (25.19)$$

Where, \bar{q}_j represent the velocity components of journal center (\bar{X}_j or \bar{Z}_j).

Damping coefficient matrix is expressed as:

$$\begin{bmatrix} \bar{C}_{xx} & \bar{C}_{xz} \\ \bar{C}_{zx} & \bar{C}_{zz} \end{bmatrix} = - \begin{bmatrix} \frac{\partial \bar{F}_x}{\partial \bar{X}_j} & \frac{\partial \bar{F}_x}{\partial \bar{Z}_j} \\ \frac{\partial \bar{F}_z}{\partial \bar{X}_j} & \frac{\partial \bar{F}_z}{\partial \bar{Z}_j} \end{bmatrix} \quad (25.19a)$$

8.2.3 Stability Parameters

For an infinitely small journal disturbance from its equilibrium position, the fluid-film forces in the bearing can be considered as a linear function of displacement and velocity vectors. The equation for disturbed motion of the journal can thus be rewritten by equating the inertia forces with the fluid-film stiffness and the damping forces. Thus, the linearized equation of journal motion in nondimensional form reads [2, 5, 16]:

$$[\bar{M}_j] \{\ddot{\bar{q}}_j\} + [\bar{C}] \{\dot{\bar{q}}_j\} + [\bar{S}] \{\bar{q}_j\} = 0 \quad \text{where } \bar{q}_j = \bar{X}_j, \bar{Z}_j \quad (25.20)$$

Or,

$$\begin{bmatrix} \bar{M}_j & 0 \\ 0 & \bar{M}_j \end{bmatrix} \begin{Bmatrix} \ddot{\bar{X}}_j \\ \ddot{\bar{Z}}_j \end{Bmatrix} + \begin{bmatrix} \bar{C}_{xx} & \bar{C}_{xz} \\ \bar{C}_{zx} & \bar{C}_{zz} \end{bmatrix} \begin{Bmatrix} \dot{\bar{X}}_j \\ \dot{\bar{Z}}_j \end{Bmatrix} + \begin{bmatrix} \bar{S}_{xx} & \bar{S}_{xz} \\ \bar{S}_{zx} & \bar{S}_{zz} \end{bmatrix} \begin{Bmatrix} \bar{X}_j \\ \bar{Z}_j \end{Bmatrix} = \begin{Bmatrix} 0 \\ 0 \end{Bmatrix} \quad (25.20a)$$

The characteristic polynomial equation for a two-degree of freedom system is the quartic (biquadratic) equation of the following form [2, 5, 18]:

$$a_1 s^4 + a_2 s^3 + a_3 s^2 + a_4 s + a_5 = 0 \quad s = \text{complex variable} \quad (25.21)$$

$$a_1 = 1$$

$$a_2 = \frac{1}{\bar{M}_j} (\bar{C}_{xx} + \bar{C}_{zz})$$

$$a_3 = \frac{1}{(\bar{M}_j)^2} \{ \bar{C}_{xx} \bar{C}_{zz} + \bar{M}_j (\bar{S}_{xx} + \bar{S}_{zz}) - \bar{C}_{xz} \bar{C}_{zx} \}$$

$$a_4 = \frac{1}{\bar{M}_j^2} (\bar{S}_{xx} \bar{C}_{zz} + \bar{S}_{zz} \bar{C}_{xx} - \bar{S}_{xz} \bar{C}_{zx} - \bar{S}_{zx} \bar{C}_{xz})$$

$$a_5 = \frac{1}{\bar{M}_j^2} (\bar{S}_{xx} \bar{S}_{zz} - \bar{S}_{xz} \bar{S}_{zx})$$

Applying Routh's Criterion for stability

$$(a_1, a_2, a_3, a_4, a_5) > 0 \quad (25.22a)$$

$$(a_2 a_3 - a_4) > 0 \quad (25.22b)$$

$$(a_2 a_3 a_4 - (a_4)^2 - (a_2)^2 a_5) > 0 \quad (25.22c)$$

Using the characteristic equation (25.21) and applying Routh's Stability criterion, the stability margin of the bearing system, in terms of critical mass \bar{M}_c is obtained. The system is said to be stable when $\bar{M}_j < \bar{M}_c$. The critical mass \bar{M}_c of the journal is thus expressed in nondimensional form as [5]:

$$\bar{M}_c = \frac{\bar{G}_1}{\bar{G}_2 - \bar{G}_3} \quad (25.23)$$

$$\bar{G}_1 = (\bar{C}_{xx} \bar{C}_{zz} - \bar{C}_{zx} \bar{C}_{xz}) \quad (25.23a)$$

$$\bar{G}_2 = \frac{(\bar{S}_{xx} \bar{S}_{zz} - \bar{S}_{zx} \bar{S}_{xz})(\bar{C}_{xx} + \bar{C}_{zz})}{(\bar{S}_{xx} \bar{C}_{zz} + \bar{S}_{zz} \bar{C}_{xx} - \bar{S}_{xz} \bar{C}_{zx} - \bar{S}_{zx} \bar{C}_{xz})} \quad (25.23b)$$

$$\bar{G}_3 = \frac{(\bar{S}_{xx} \bar{C}_{xx} + \bar{S}_{xz} \bar{C}_{xz} + \bar{S}_{zx} \bar{C}_{zx} + \bar{S}_{zz} \bar{C}_{zz})}{(\bar{C}_{xx} + \bar{C}_{zz})} \quad (25.23c)$$

Threshold speed, i.e., the speed of journal at the threshold of instability, can be obtained using the relation given below [5]:

$$\bar{\omega}_{th} = [\bar{M}_c / \bar{F}_0]^{1/2} \quad (25.24)$$

where, \bar{F}_0 is resultant fluid-film force or reaction at $\left(\frac{\partial \bar{h}}{\partial r} = 0\right)$

9 Design of Hydrostatic/Hybrid Journal Bearings System

The design of a Hydrostatic/Hybrid journal bearing system is a quite complex phenomenon that involves judicious selection of several factors. These factors may include bearing aspect ratio (λ), restrictor design parameter (\bar{C}_{S2}), type of

compensating element, external load (\bar{W}_0), total pocket area to total bearing area, number of pockets, speed parameter, and a safe value of operating fluid-film thickness, etc.

9.1 Geometric and Operating Parameters

The geometric and operating parameters of a hydrostatic bearing system are of great significance and therefore needs to be suitably chosen by the bearing designer in order to obtain optimal performance of the bearings. Many investigators working in the area of hydrostatic/hybrid bearings carried out and reported studies dealing with an optimum performance. The commonly used values for these parameters are as given in Table 25.1.

The reported studies indicate that for most of the applications, the value of land width ratio of 0.14 for recessed and 0.25 for non-recessed journal bearings be used [6, 15]. In the cases of thick land bearings, a_b/L greater than 0.25, support a lower hydrostatic load and cause more heat at higher speeds. The optimum value for the concentric pressure ratio β^* is 0.5 and the minimum value of 0.4 corresponds to minimum load condition. Apart from this, tolerances too need to be determined for the clearance between the shaft and the bearing. The tolerance range of $0.4 \leq \beta^* \leq 0.7$ may be ensured by proper selection criterion [4, 15].

Table 25.1 Bearing Operating and Geometric Parameters [3–6, 15, 20]

Bearing Aspect Ratio (λ)	1.0
Restrictor Design Parameter (\bar{C}_{s2})	0.1–1.0
Type of compensating element	Capillary, orifice, constant flow valve, membrane, and slot
Nondimensional External Load (\bar{W}_0)	0.25–2.0
Area of each pocket	0.95
Total pocket area to total bearing area	0.30
Speed parameter	0.0–1.0
Recess shapes	Square, Circular, Elliptical, Triangular
Slot width ratio (SWR)	0.25
Land width ratio (\bar{a}_b)	0.25
Characteristics length (l_m)	10–40
Coupling number parameter (N^2)	0.1–0.9
Concentric pressure ratio (β^*)	0.5
Reynolds number (Re)	0–15,000
Bearing flexibility parameter (\bar{C}_d)	0.0–1.0
Wear depth parameter ($\bar{\delta}_w$)	0.0–0.5
Nonlinearity factor (\bar{K})	0, 0.58, 1.0

10 Current Research Trends in the Design of Hydrostatic/Hybrid Journal Bearings

The hydrostatic/hybrid journal bearings are highly specialized and customized items. These bearings are custom made for a given application and operating conditions. Latest technological developments require these bearings to operate under very stringent, precise and exact conditions. Thus, the bearings need to be designed more accurately for realistic operating conditions. In order to generate realistic design data, the analysis of hydrostatic/hybrid bearing system be based on more realistic conditions by including some essential aspects individually/ combined as indicated below:

1. Influence of surface roughness
2. Influence of bearing flexibility
3. Influence of wear
4. Influence of turbulence
5. Influence of thermal effect
6. Influence of loading arrangement
7. Influence of type of recess shape
8. Influence of bearing configuration
9. Influence of journal misalignment
10. Influence of flow control device
11. Influence of number of pockets
12. Influence of nonlinear behavior of lubricant

10.1 *Influence of Surface Roughness*

In actual practice, the geometric profile of any engineering surface is controlled by the characteristics of the finishing process employed to produce them. Close analysis of these surfaces indicates that, even after the most careful polishing, they are still rough at microscopic scale. The roughness takes the form of successive hills and valleys which often result due to characteristics of machining process and its accompanying defects. The surface roughness may also occur due to wear, impulsive damage, foreign particles, rust, etc. [2]. It is well known fact that the smooth surfaces fail due to seizure as it is difficult to maintain the lubricating film between the sliding surfaces. Higher load bearing capabilities of the bearing surfaces are obtained when the surfaces have large number of crests and troughs. These features on rough surfaces reduce metal to metal contact and also act as reservoirs retaining the lubricant. At microscopic scale the aspect ratio and absolute height of the crests and troughs vary significantly as they are the functions of material properties and method of surface preparation. In most of the cases the mean height of asperities ranges from 0.05 μm or less for polished surfaces to 10 μm

on medium ground surfaces. The asperity height is of the same order as the mean separation in lubricated contacts. Moreover, the fluid-film thickness in journal bearing systems is of the order of few micro-meters, thus surface roughness have significant effect on the bearing performance. Therefore, in order to have a realistic prediction of the bearing performance characteristics, consideration of surface roughness effect is highly desired.

10.2 Influence of Bearing Flexibility

In case of heavily loaded bearings the pressure generated within the thin lubricating films is extremely large. The high fluid film pressure result into the local elastic deformation of the bearing surfaces. The deformations are generally of the order of the magnitude of bearing clearance. The elastic deformation modifies the shape of the lubricant film to such an extent that the separation of the contacting surfaces is achieved. Thus, the performance characteristics of hydrostatic journal bearings are significantly affected by the bearing shell deformation under heavy load conditions. A number of studies [5, 19, 20] have been carried out to investigate the influence of bearing flexibility on the performance of hydrostatic/hybrid journal bearing. These studies reveal that flexibility of the bearing shell significantly affects the bearing performance.

10.3 Influence of Wear

During the design process of a machine component an attempt is made to ensure that the failure does not occur before a specified designed life of the component. In almost all industrial situations, 60 % of failures are generally accounted for wear and a substantial amount of the gross national product is consumed to replace the worn out parts. Thus, the effect of wear on component is very important and has greater economical impact and needs to be considered in the analysis. Wear is defined as “Deterioration of the surface due to use which results in diminution of the parts”. Wear occur as a natural consequence when ever two loaded surfaces with relative motion interact with each other. No machine member is immune to wear. Wear rate can be reduced by correct lubrication, careful design and material selection [11, 16, 17].

10.4 Influence of Turbulence

In the modern high speed machinery, the fluid-film bearings operate in turbulent regime. The turbulent flow may occur in bearings due to two main reasons. The first is high-speed operation required in modern machinery. The second is the use of

unconventional lubricants such as water or liquid metals due to the need to simplify equipment design or to overcome the difficulty in shaft sealing. These materials are generally used as process fluids. A high velocity of journal with a low kinematic viscosity leads to higher Reynolds numbers and departure from laminar flow conditions. High speed hybrid bearings operating with low viscosity cryogenic fluid require external pressure to provide sufficient load carrying capacity. Various studies have been carried out to consider the influence of turbulence [7, 21] in the analysis of journal bearings. These studies report that the performance of bearing is affected quite significantly.

10.5 Influence of Thermal Effect

In the present day technological scenario, turbo machinery is required to operate at an ever increasing higher speed and loads. Higher operating speeds of bearings result in higher operating temperatures of lubricant and the surfaces. The heat generated due to viscous friction has an adverse effect on lubricant viscosity. The increase in lubricant temperature decreases the viscosity, thus changing the fluid-film profile. In order to predict the temperature distribution in the fluid-film bearings, a three-dimensional energy equation along with three-dimensional conduction equation is to be solved simultaneously.

10.6 Influence of Loading Arrangement

For the recessed hydrostatic journal bearing systems, external loads on the bearing are applied using specific loading arrangements. Two types of loading arrangements are commonly used in industrial applications; these include (1) arrangements in which the load line acts through the center of pockets and (2) arrangements in which the load line bisects the land between two pockets. Numerically simulated results for these loading arrangements are reported by [22–24]. The results clearly indicate that the loading arrangements have significant influence on the bearing performance and the latter of the two arrangements have higher values of direct fluid-film stiffness and damping coefficients in z-direction [25].

10.7 Influence of Recess Shape

In earlier days, the shapes of recesses used in hydrostatic bearings were restricted to rectangular due to the simplicity in manufacturing. However, recent advances in manufacturing technology have paved the paths to fabricate any geometric

shape of recess as specified by the designer. Thus, in recent times the designers have wide range of options to select desired shapes of the recess. However, still there persists a void of design data regarding performance of hydrostatic bearings for different shapes of recess. Studies reported in literature clearly indicate that the recess shapes have significant affect on the bearing performance [26, 27].

10.8 Influence of Bearing Configuration

Hydrostatic/hybrid Journal bearing configurations are broadly classified into two groups as recessed (pockets) and non-recessed, on the basis of mechanism of supply of lubricant to the bearings. In hydrostatic/hybrid journal bearings, the lubricant is supplied to each recess/hole through restrictors. The restrictors used can be of any form or type among the capillary, orifice, and constant flow valve or membrane restrictors. Recesses introduced into the bearings surfaces aid in reducing friction and increase the load support. Bearings with four recesses are quite common; however, any number of recesses can be employed for the bearings with aspect ratio (L/D) less than unity [28]. In case of multiple recess bearings, these recesses occupy large bearing area in comparison to the total bearing area. Moreover, when such type of bearing operates in a hybrid mode, sufficient hydrodynamic action is seldom generated. Hence, the non-recessed bearings came into existence. There are basically two types of non-recessed hybrid fluid-film journal bearing configurations, (1) hole-entry type and (2) slot-entry in which two rows of six or more holes/slots are provided around the circumference of the bearing symmetrically /asymmetrically as shown in Figs. 25.3 and 25.4. One of the major advantages of multirecess journal bearing configuration over non-recessed bearing is its ability to support higher load even at zero eccentricity due to reduction in the net downward force on the journal. The reported studies [2, 4, 7, 15, 20] state that the type of bearing configuration chosen for a given operating and geometric parameters has a strong influence on the bearing performance.

10.9 Influence of Journal Misalignment

Studies pertaining to the journal bearings by and far are undertaken with the basic assumption that the journal and bearing are properly aligned. However, in an actual practice there exists certain degree of misalignment due to improper assembly, shaft deflection (due to elastic and thermal distress), eccentric loading, etc. As a result of this, the fluid-film thickness profile in axial and circumferential directions gets modified resulting into changes in bearing performance characteristics. Therefore, it becomes mandatory to consider the effects due to journal misalignment for the accurate prediction of bearing performance [2]. The effect of journal misalignment is more pronounced when the bearing operates in hydrostatic mode of

operation when compared with the hybrid mode of operation. Thus, in order to attain realistic performance characteristics, consideration of journal misalignment in bearing analysis is highly desired [29].

10.10 Influence of Types of Flow Control Device

Basically, any type of flow control device can be used in a hydrostatic bearing system. The lubricant is supplied at a predetermined pressure through a restrictor that aid in providing desired fluid-film stiffness. Orifice, capillary and variable flow restrictors are commonly used in hydrostatic bearing arrangements. Of these the former two are fixed-flow type restrictors while the later one is a variable flow restrictor. The variable flow restrictor is capable of performing desired functions with the help of a valve that automatically adjusts the flow as it senses pressure differentials between the pads. Variable flow restrictors aid in enhancing bearing system, but the costs associated with them are high. The advantages and disadvantages of flow control devices have been briefly discussed in [4].

Studies indicate that for a specified value of external load, the bearing performance characteristics such as minimum fluid-film thickness, stiffness coefficients, damping coefficients, and threshold speed are generally higher for membrane restrictor than the other restrictors [20].

10.11 Influence of Number of Pockets

Performance of hydrostatic bearings is greatly influenced by the number of pockets/recesses used. The studies have reported that the bearing with more number of pockets (say 6) operates at a lower attitude angle when compared with those with lesser number of pockets (say 4) under similar operating conditions and like geometric parameters [6, 15, 19]. Journal bearings with six pockets have lower values of minimum film thickness when compared with that of the bearings with four pockets, for both the hybrid and hydrostatic mode of operations. Thus, on the basis of minimum film thickness it can be concluded that the bearings with four pockets seems to perform better than one having six pockets [19].

10.12 Influence of Nonlinear Behavior of Lubricant

Lubricant characteristics play a vital role in the operation of a journal bearing system. The mono- and multi-grade lubricants used in present-day industrial applications are blended with additives which are polymeric in nature. This blending results into deviation of lubricant rheology from Newtonian to non-Newtonian

(Nonlinear). The viscosity of such lubricants in heavily loaded concentrated non-conformal contacts is not constant and varies in some nonlinear relation between shear stress and shear strain rates. There are a number of models that describe the nonlinear behavior of lubricants such as cubic stress model, shear strain power law models, etc. Numerous studies address the rheological behavior of the lubricant [30–32]. These studies reveals that the performance of a journal bearing system is affected significantly using non-Newtonian lubricant as compared to the Newtonian lubricant.

11 Some Recent Studies

The design of bearing system has been evolved through rigorous computations, simulation and experimentations by the researchers in recent past. The technological and intellectual inputs in this domain have moved far ahead resulting into development of efficient bearing systems for the stringent and precise operating conditions of present-day industry. The approach of design has shifted from traditional to more realistic operating conditions. In recent times many studies have been carried out and reported in literature by considering the influence of various issues concerning these classes of bearings. This section describes some illustrative studies reported recently along with their salient observations:

1. Influence of Surface Roughness
2. Influence of Wear in Journal Bearing
3. Flexibility of the bearing shell
4. Influence of Turbulence
5. Influence of Nonlinear behavior of lubricants
6. Influence of Recess Shape

11.1 *Influence of Surface Roughness*

Surface roughness on a mechanical component is inherent to the process of manufacturing employed. Surface roughness identified in terms of asperity height, curvature and peak height distributions are random in nature and can be mathematically represented using a Gaussian probability distribution. This fact suggests that the surfaces can thus be modeled statistically by proper consideration of random functions. Rough surfaces, as random process, are characterized mainly by two statistical functions namely the height distribution and the spatial distribution of peaks and valleys across the surface. Most of the engineering surfaces exhibit roughness with directional pattern resulting from the type of manufacturing process used. These directional patterns (roughness orientations) of the rough surface may be isotropic or anisotropic depending upon the nature of the surface finishing

process. The anisotropic roughness orientation are generally classified as transverse and longitudinal roughness pattern depending upon the principle directions of the surface textures with the sliding direction of opposing surfaces. Many studies have been reported in literature to predict the influence of surface roughness on the performance of hydrostatic/hybrid journal bearing. Nagaraju et al. [33] carried out following analysis to investigate the influence of surface roughness on the performance of non-recessed hybrid Journal Bearing.

The average Reynolds equation applicable for roughened journal bearing system in nondimensional form is given as [33]:

$$\frac{\partial}{\partial \alpha} \left(\varphi_x \frac{\bar{h}^3}{12} \frac{\partial \bar{p}}{\partial \alpha} \right) + \frac{\partial}{\partial \beta} \left(\varphi_y \frac{\bar{h}^3}{12} \frac{\partial \bar{p}}{\partial \beta} \right) = \frac{\Omega}{2} \frac{\partial \bar{h}_T}{\partial \alpha} + \frac{\Omega}{2\Lambda} \frac{\partial \varphi_s}{\partial \alpha} + \frac{\partial \bar{h}_t}{\partial t} \tag{25.25}$$

where,

$$\bar{h}_T = \begin{cases} \frac{\bar{h}}{2} \left(1 + erf \left(\frac{\bar{h}}{\bar{\sigma} \sqrt{2}} \right) \right) + \frac{\bar{\sigma}}{\sqrt{2\pi}} \exp(-\bar{h}^2/2\bar{\sigma}^2) & \dots\dots\dots \text{for } \frac{\bar{h}}{\bar{\sigma}} < 3 \\ \bar{h} & \dots\dots\dots \text{for } \frac{\bar{h}}{\bar{\sigma}} \geq 3 \end{cases} \tag{25}$$

φ_x and φ_y are pressure flow factors given as [2]

$$\begin{aligned} \varphi_x &= 1 - Ce^{-r\Lambda\bar{h}} \quad \text{for } \gamma \leq 1 \\ \varphi_x &= 1 - C(\Lambda\bar{h})^{-r} \quad \text{for } \gamma > 1 \\ \varphi_y(\Lambda\bar{h}, \gamma) &= \varphi_x(\Lambda\bar{h}, 1/\gamma) \end{aligned}$$

where, C and r are the function of surface pattern parameter (γ)

The expression for the shear flow factor φ_s is expressed as, $\varphi_s = \bar{V}_{rj} \Phi_s(\Lambda\bar{h}, \gamma_j) - \bar{V}_{rb} \Phi_s(\Lambda\bar{h}, \gamma_b)$ where, \bar{V}_{rj} and \bar{V}_{rb} are the variance ratio of journal and bearing respectively.

In general, the term shear flow factor is used for both φ_s and Φ_s , keeping in mind that Φ_s is associated with single surface while φ_s is associated with the combination of two surfaces brought together. The shear flow factor Φ_s for individual surface is expressed as [2]

$$\begin{aligned} \Phi_s &= A_1(\Lambda\bar{h})^{\alpha_1} \exp^{-\alpha_2(\Lambda\bar{h}) + \alpha_3(\Lambda\bar{h})^2} \quad \text{for } \Lambda\bar{h} \leq 5.0 \\ \Phi_s &= A_2 \exp^{-0.25(\Lambda\bar{h})} \quad \text{for } \Lambda\bar{h} > 5.0 \end{aligned}$$

Where, $A_1, A_2, \alpha_1, \alpha_2$ and α_3 are constants for different surface pattern parameters (γ).

The transversely oriented roughness patterns during hydrostatic mode of bearing operation provide higher load bearing capacity for both the configurations (Fig. 25.9a). The circumferential flow of lubricant reduces the load carrying

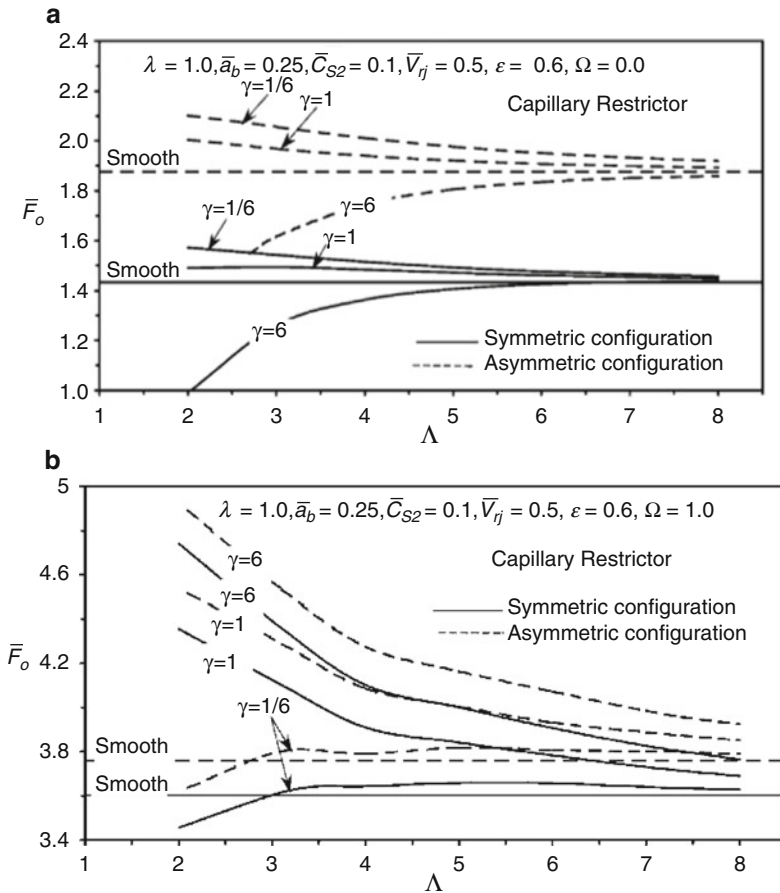


Fig. 25.9 Variation of \bar{F}_0 with Λ (a) Hydrostatic Mode, (b) Hybrid Mode [33]

capacity of hydrostatic journal bearing system. The circumferential flow is restricted by the transversely oriented roughness patterns providing higher load carrying capacity. On the contrary in hybrid mode of operation, the longitudinally oriented roughness pattern provides higher load carrying capacity in both configurations as depicted in Fig. 25.9b.

11.2 Influence of Wear in Journal Bearing

Bearings during its entire span of useful life traverse over millions of cycles and is subjected to several start and stop operations. Intermittent bearing operations (frequent start and stop) result into progressive wear of bearings due to rubbing action. Wear of bearing surfaces alter the bearing geometry, thereby affecting its

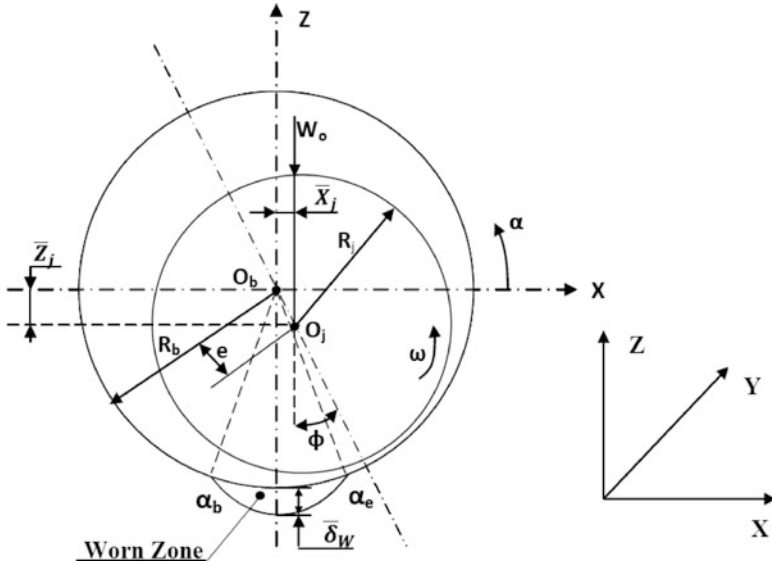


Fig. 25.10 Worn Journal bearing geometry along with the coordinate system [17]

performance characteristics. Thus, from the design perspective, it is highly desirable to consider the effects of bearing wear on the performance of the bearings, so that the designer can accommodate appropriate changes at the design stage. To analyze the influence of wear on the bearing performance characteristics, Dufrane et al. [34] proposed an abrasive wear model for the analysis of journal bearing system. Later on, many researchers used this model in their study to investigate the influence of wear on the bearing performance. Figure 25.10 shows the geometry of the worn out zone in bearing. Some of the recent studies [17, 27, 35] concerning influence of wear on performance of hydrostatic/hybrid journal bearings are discussed below.

The findings emerged from visual observations were as follows: (a) symmetrical shaft footprint at the bottom of the bearing and (b) uniform wear pattern along axial length of the bearing. The change in bush geometry is expressed as:

$$\partial \bar{h} = \bar{\delta}_w - 1 - \sin \alpha \quad \text{for } \alpha_b \leq \alpha \leq \alpha_e \quad (25.26a)$$

$$\partial \bar{h} = 0 \quad \text{for } \alpha < \alpha_b \text{ or } \alpha > \alpha_e \quad (25.26b)$$

where $\bar{\delta}_w$ is nondimensional wear depth parameter.

The angles α_b and α_e are computed by equating (25.26a) with (25.26b) as

$$\sin \alpha = \bar{\delta}_w - 1 \quad (25.26c)$$

The defect value $\partial \bar{h}$ is added to the nominal fluid-film thickness for rigid circular bearing as the wear in bearing geometry results in an increase in the clearance space in the worn zone [17].

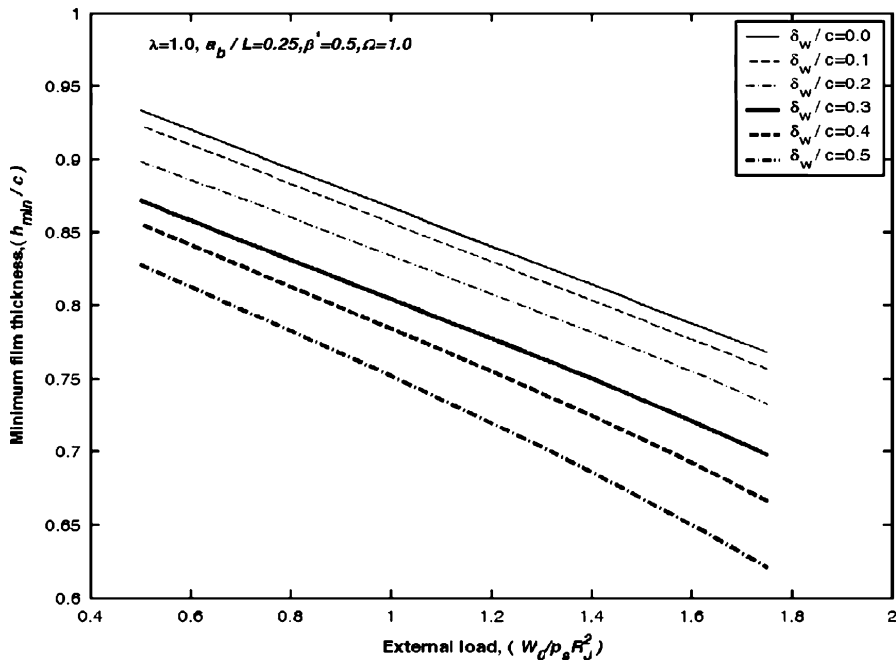


Fig. 25.11 Minimum fluid-film thickness (\bar{h}_{\min}) versus external load (\bar{W}_0) [17]

For a worn journal bearing system, the fluid-film thickness is defined as,

$$\bar{h} = \bar{h}_0 + \partial\bar{h} + \Delta\bar{h} \tag{25.26}$$

where, nominal fluid-film thickness is expressed as [9],

$$\bar{h}_0 = 1 - \bar{X}_j \cos \alpha - \bar{Z}_j \sin \alpha$$

The term in (25.26) $\Delta\bar{h}$ is the perturbation on the fluid-film thickness due to dynamic conditions.

Figure 25.11 shows the variation in minimum film thickness with applied load for different values of wear depth parameter ($\bar{\delta}_w$). It is observed that the minimum fluid-film thickness decreases with increase in magnitude of wear depth parameter for an applied load. The reason for such a behavior is that at higher loads, due to excessive wear the bearing cavity so formed is larger in size, as a consequence the journal operates at higher eccentricities. The decrease in values of minimum film thickness with increase in load is quite significant. From the given figure one can select a safe value of (\bar{h}_{\min}) for a worn bearing operating under a given applied load (\bar{W}_0).

Figure 25.12 shows the variation of threshold speed ($\bar{\omega}_{th}$) with external load (\bar{W}_0) for different values of wear depth. Each and every curve corresponds to a stable and an unstable region. The area under the curve represents a stable region

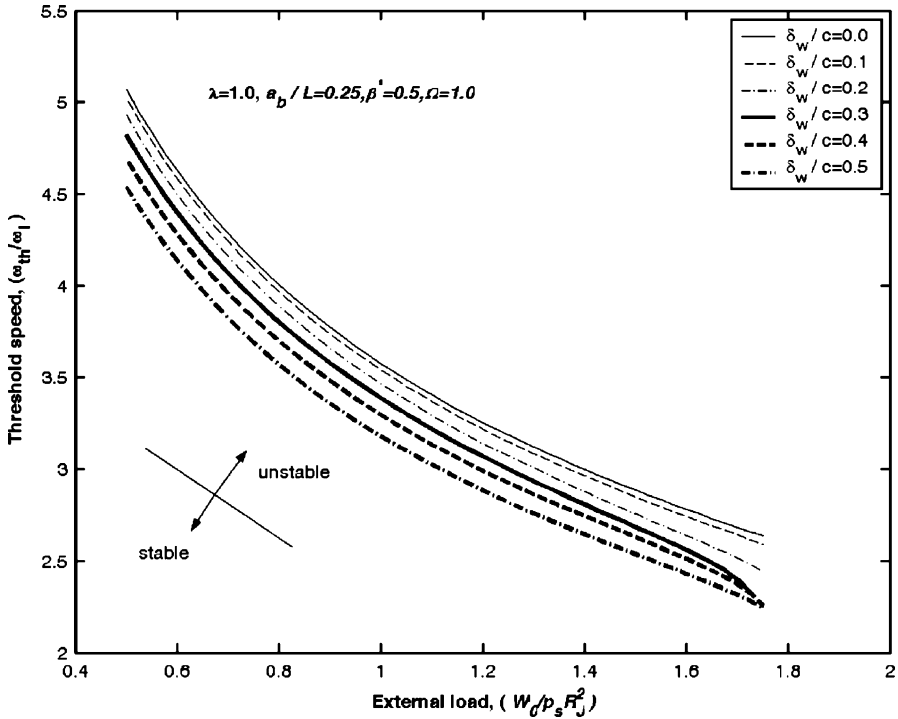


Fig. 25.12 Threshold speed ($\bar{\omega}_{th}$) versus external load (\bar{W}_0) [17]

while above the curve it represents an unstable region. A given bearing system is said to be stable when the journal speed ($\bar{\omega}_j$) is less than the stability threshold ($\bar{\omega}_{th}$), i.e., ($\bar{\omega}_j < \bar{\omega}_{th}$). It is further attributed that the direct fluid-film stiffness coefficients ($\bar{S}_{11}, \bar{S}_{22}$) are quantitative measures of susceptibility to instability. Reduction in the values of these coefficients leads to deterioration of stability. Since the value of the coefficients $\bar{S}_{11}, \bar{S}_{22}$ significantly reduces for a given configuration, the reduction in $\bar{\omega}_{th}$ is observed with an increase in the load and the wear depth parameter.

11.3 Influence of Flexibility of the Bearing Shell

For the bearings operating under heavy loads, deformation in bearing shell is quite significant. Various studies [5, 19, 20, 36] have been undertaken in recent past to study the influence of flexibility on the performance of the hydrostatic/hybrid bearing system. The interfacial displacement (i.e., the displacement of the interface between fluid film and bearing shell) is responsible for the changes in the fluid-film profile and consequently the pressure distribution in the film. The performance

characteristics of bearing system therefore get significantly affected with the bearing shell deformation. In order to account the flexibility of bearing shell, a nondimensional parameter known as deformation coefficient (\bar{C}_d) is incorporated into the analysis. The deformation coefficient (\bar{C}_d) is a function of the supply pressure, Young's modulus of bearing material, bearing shell thickness, and the radial clearance [5, 19, 20, 36]. The nondimensional parameter \bar{C}_d is defined as

$$\bar{C}_d = \left(\frac{p_s}{E}\right) \left(\frac{t_h}{c}\right) \text{ for hydrostatic/hybrid journal bearing system}$$

$$\bar{C}_d = \left(\frac{p_s}{E}\right) \left(\frac{t_h}{h_o}\right) \text{ for hydrostatic/hybrid thrust bearing system}$$

The study [20] pertaining to the influence of bearing flexibility on its performance indicates that the pocket pressures and the minimum fluid-film thickness both share direct proportionality with the value of restrictor design parameter. At a constant external load, the bearing operates at a higher eccentricity in the flexible bearing than that of a rigid bearing due to deformation in the bearing shell, the clearance space increases and so the minimum film thickness is reduced. With an increase of bearing flexibility, the bearing characteristics, such as pocket pressures, minimum fluid-film thickness, fluid-film stiffness and damping coefficients, decreases but bearing flow (end leakage) has been observed to increase.

The stability threshold speed margin of the bearing system is influenced by the bearing flexibility. Figure 25.13 shows the variation of stability threshold speed margin with bearing flexibility parameter for hybrid mode of operation. It is clearly visible that for a constant external load, the stability threshold speed is directly proportional to the bearing flexibility parameter for all the restrictors studied. Also the membrane restrictor compensated bearings offer a large stable zone as compared to those compensated with other restrictors.

11.4 Influence of Turbulence in Fluid-Film Bearings

Usually, the flow of lubricant in journal bearings is assumed to be laminar; however, high-speed operations and use of unconventional lubricants of low viscosity give rise to large Reynolds numbers. In general, four turbulence lubrication theories are available in literature for the analysis of bearing performance operating at large Reynolds number. Constantinescu et al. [21] applied mixing length theory for determining the velocity profiles and pressure distribution in turbulent films and also the same theory was used for determining the friction stresses. Ng and Pan [36] presented a linearized turbulent lubrication theory utilizing the Reichardt's formula for eddy viscosity. They also utilized the concept of eddy viscosity to represent the turbulent stresses in terms of mean velocity gradient. Hirs [37] conducted an experiment and developed bulk flow theory for turbulence phenomena. He also verified experimental results with other turbulent lubrication theories available in

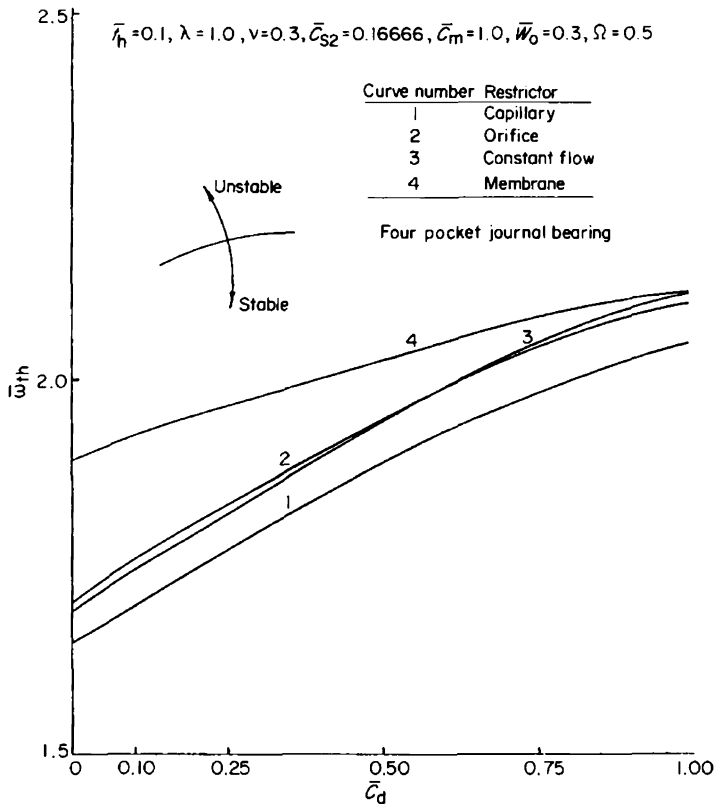


Fig. 25.13 Variation of threshold speed ($\bar{\omega}_{th}$) vs. bearing flexibility parameters [20]

the literature and showed that his theory is compatible with available results. Wada et al. [38] proposed another turbulent theory based on the friction law of fluid. Recently, many researchers focused their attention towards the influence of the turbulence on the performance of journal bearing. The modified Reynolds Equation considering the influence of turbulence on the performance of hybrid journal bearing [21] is presented as follows:

$$\frac{\partial}{\partial \alpha} \left\{ \frac{\bar{h}^3 \partial \bar{p}}{G_\alpha \bar{\mu} \partial \alpha} \right\} + \frac{\partial}{\partial \beta} \left\{ \frac{\bar{h}^3 \partial \bar{p}}{G_\beta \bar{\mu} \partial \beta} \right\} = \frac{\Omega \partial \bar{h}}{2 \partial \alpha} + \frac{\partial \bar{h}}{\partial \tau} \tag{25.27}$$

where, G_α and G_β are turbulent coefficients.

These coefficients are functions of Reynolds number R_e and are expressed by Constantinescu et al. [21] as.

$$G_\alpha = 12 + 0.026(R_e)^{0.8265} \tag{25.27a}$$

$$G_\beta = 12 + 0.0198(R_e)^{0.741} \tag{25.27b}$$

Fig. 25.14 Variation of \bar{h}_{\min} vs. \bar{W}_o [39]

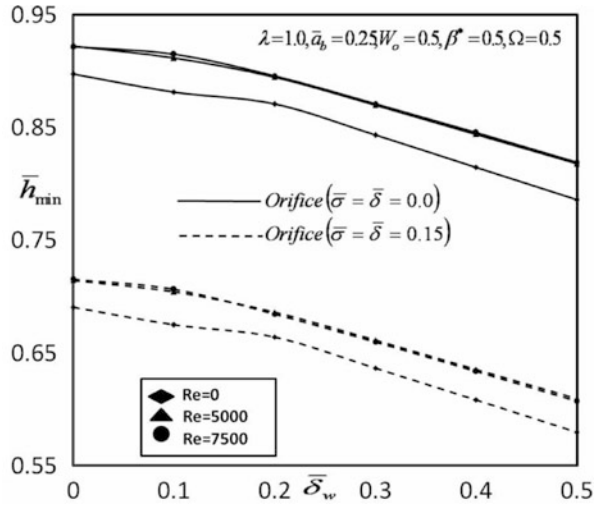
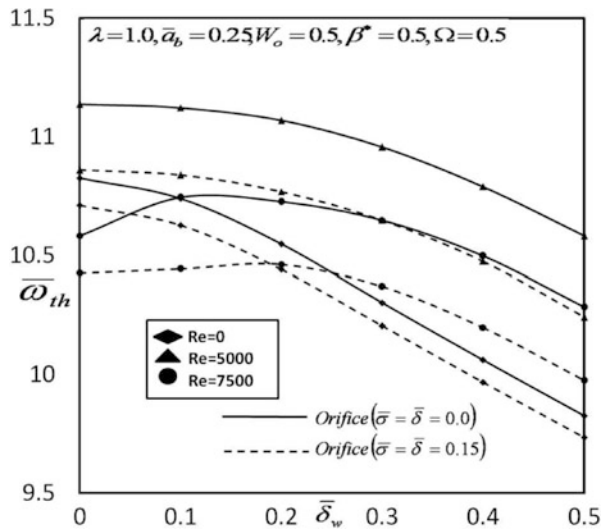


Fig. 25.15 Variation of $\bar{\omega}_{th}$ vs. \bar{W}_o [39]



Some of the typical illustrative results describing the influence of turbulence on the performance of hybrid journal bearings have been discussed as follows [39].

As indicated in Fig. 25.14 the value of \bar{h}_{\min} get enhanced as the value of Reynolds number increases for the constant value of external load.

For the turbulent lubricated hybrid journal bearings, the stability threshold speed margin ($\bar{\omega}_{th}$) of the bearing gets affected significantly. It may be observed that the stability threshold speed margin of a turbulent lubricated bearing gets improved as compared to bearing operating in laminar regime for higher values of wear depth parameter as shown in Fig. 25.15.

The study reported in [39] indicates that,

1. The influence of turbulence is quite significant on the bearing performance.
2. The value of \bar{h}_{\min} increases with an increase in the value of Reynolds number, when operating at constant external load.
3. The value of bearing rotor dynamic coefficients change due to the effect of turbulence.
4. The stability threshold speed margin of the bearing gets improved when the bearing operates in the turbulent regime.

11.5 Influence of Nonlinear Behavior of Lubricants

Generally the lubricant used in bearing lubrication is commercial blend of a petroleum-derived base oil and additive package. Additives are blended with base oils in order to obtain desired performance characteristics during operation. Most commonly used additives in bearing oils include the Viscosity Index modifier, belonging to the family of polymethacrylate or polyisobutylene that prevents uncontrollable viscosity variation with temperature change. Inclusion of such polymer based compounds into the lubricants changes the lubricant rheology from Newtonian to non-Newtonian [40] and for such lubricants there exists nonlinear relationship between shear stress (τ) and shear strain rate ($\dot{\gamma}$). However, with the present technological advances, improved and reliable performance from the machines is high on demand. This in turn has necessitated the bearing designers to incorporate more realistic conditions that include the nonlinear behavior of the lubricants into the design so that the accurate prediction of bearing performance can be attained.

The non-Newtonian lubricants do not possess a definite viscosity. However, viscosity of such fluids is represented by an apparent viscosity ($\bar{\mu}_a$) which is a function of shear strain ($\bar{\gamma}$)

$$\bar{\mu}_a = \frac{\bar{\tau}}{\bar{\gamma}} = f(\bar{\gamma}) \tag{25.28}$$

In nondimensional form, the shear strain rate ($\bar{\gamma}$) at a point in the fluid–film is expressed as:

$$\bar{\gamma} = \left[\left\{ \frac{\bar{h}}{\bar{\mu}} \left(\bar{z} - \frac{\bar{F}_1}{\bar{F}'_o} \right) \frac{\partial \bar{p}}{\partial \alpha} + \frac{\Omega}{\bar{\mu} \bar{h} \bar{F}'_o} \right\} + \left\{ \frac{\bar{h}}{\bar{\mu}} \left(\bar{z} - \frac{\bar{F}_1}{\bar{F}'_o} \right) \frac{\partial \bar{p}}{\partial \beta} \right\}^2 \right]^{1/2} \tag{25.28a}$$

The studies [30–32] concerning rheological behavior of the lubricant have shown that many non-Newtonian fluids follow cubic shear stress and shear strain power laws. The popular constituent equations for these fluids are described below:

11.5.1 Shear Strain Power Law Fluid Model

In this model shear stress varies as some power of the shear strain rate and is described as [32]

$$\bar{\tau} = \bar{m} (\bar{\dot{\gamma}})^n \quad (25.29)$$

where, n is known as flow behavior (power law) index and \bar{m} is known as consistency index. The deviations of indices “ n ” and \bar{m} from unity determine the change in Newtonian behavior of the lubricant.

For $n = 1$, the fluid becomes Newtonian.

For $n < 1$, it characterizes a pseudo-plastic behavior, i.e., the viscosity of the fluid decreases as shear strain increases.

For $n > 1$, the fluid becomes dilatant, i.e., the viscosity of the fluid increases as shear strain increases.

11.5.2 Cubic Shear Stress Law Fluid Model

The cubic shear stress law adequately represents the flow behavior of most non-Newtonian oils. Experimental study [41] reported that large number of polymer added mineral base lubricants follow this behavior. The constituent equation for this model is described as [31]:

$$\bar{\tau} + \bar{K} \bar{\tau}^3 = \bar{\dot{\gamma}} \quad (25.30)$$

The rheological behavior of most of the non-Newtonian lubricants can be represented by the cubic shear stress law. In recent times, journal bearings lubricated with non-Newtonian lubricants have gained considerable attention of researchers and bearing designers. The same is reflected from the quantum of studies reported in the literature. The non-Newtonian effect is introduced by the modification of viscosity terms using the cubic shear stress law $\bar{\tau} + \bar{K} \bar{\tau}^3 = \bar{\dot{\gamma}}$.

The non-Newtonian effect is represented by the nonlinearity factor (\bar{K}) in the constitutive equation (cubic shear stress law) of the lubricant. The nonlinearity factor (\bar{K}) significantly influences the bearing performance characteristics, especially the dynamic characteristics. Some typical results of recessed hybrid journal bearing system compensated with orifice restrictor [30] is presented here.

Figure 25.16a depicts that an increase in value of external load results in a significant rise in the value of direct stiffness coefficient (\bar{S}_{22}). For a constant value of external load, the combined effect of nonlinear behavior of the lubricant and bearing flexibility lowers the value of direct stiffness coefficient (\bar{S}_{22}) substantially. Therefore in order to have requisite values of stiffness coefficients, a careful selection of \bar{K} and \bar{C}_d is desired. Figure 25.16b shows that for a constant value of external load (\bar{W}_0), the effect of the nonlinearity factor (\bar{K}) is to reduce the stable

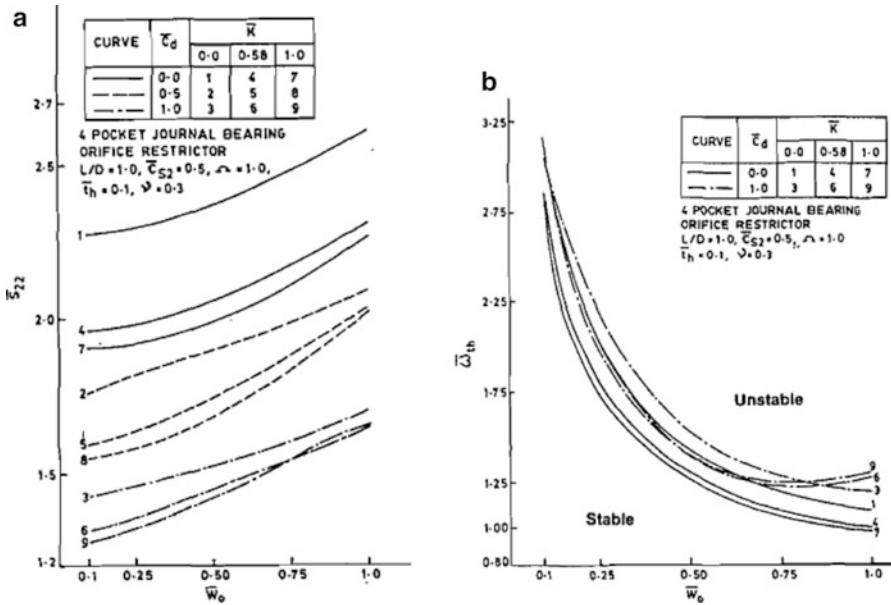


Fig. 25.16 (a) Variation of direct stiffness coefficient (\bar{S}_{22}) (b) Variation of minimum fluid-film thickness (\bar{h}_{min}) [30]

zone; however, the effect of \bar{C}_d is to increase $\bar{\omega}_{th}$. In general, the effects of \bar{C}_d and \bar{K} on the stability of an orifice compensated hybrid journal bearing system is opposite in behavior and the loss in $\bar{\omega}_{th}$ may be partially compensated by choosing proper values of these parameters.

11.5.3 Influence of Micropolar Lubrication

Micropolar lubricants in general terminology are the lubricants possessing microstructures. They are the fluids consisting of rigid, randomly oriented particles suspended in a medium, where the deformation of the fluid particles is ignored (e.g., polymeric suspensions, animal blood, liquid crystals). Behavior of these class of lubricants is governed by the geometry and intrinsic motion of individual material particles. Eringen [42] incorporated the angular velocity field of rotation of particles and the principles of conservation of angular momentum in the theory of micropolar fluids. The theory of micropolar fluids is conceptualized by ignoring the deformations encountered by the fluid microelements and considering two independent kinematic vector fields viz. (a) vector field for translation velocity of the fluid particles and (b) vector field for the angular (spin) velocity of the particle. The micropolar fluid theory in physical sciences provide satisfactory model that describes the flow behavior of real fluid suspensions and polymeric fluids. The concept of micropolar model has been successfully utilized in lubrication

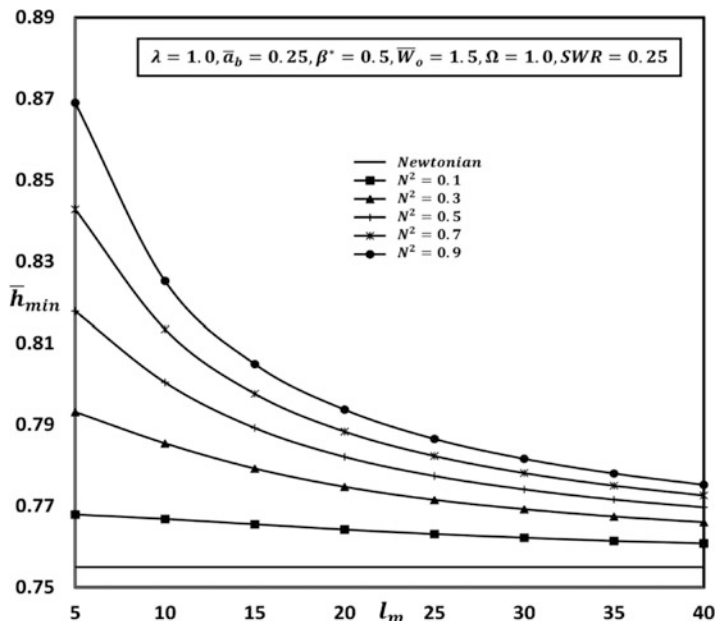


Fig. 25.17 Variation of \bar{h}_{min} vs. characteristic length (l_m) [43]

problems as the clearance in bearings are of the order of average grain size of non-Newtonian lubricants. The modified Reynolds equation for journal bearings operating with micropolar lubricant is given as follows [25, 26, 43–45]

$$\frac{\partial}{\partial \alpha} \left\{ \frac{\bar{h}^3 \Phi \partial \bar{p}}{12 \bar{\mu} \partial \alpha} \right\} + \frac{\partial}{\partial y} \left\{ \frac{\bar{h}^3 \Phi \partial \bar{p}}{12 \bar{\mu} \partial \beta} \right\} = \frac{\Omega \partial \bar{h}}{2 \partial \alpha} + \frac{\partial \bar{h}}{\partial \bar{t}} \tag{25.31}$$

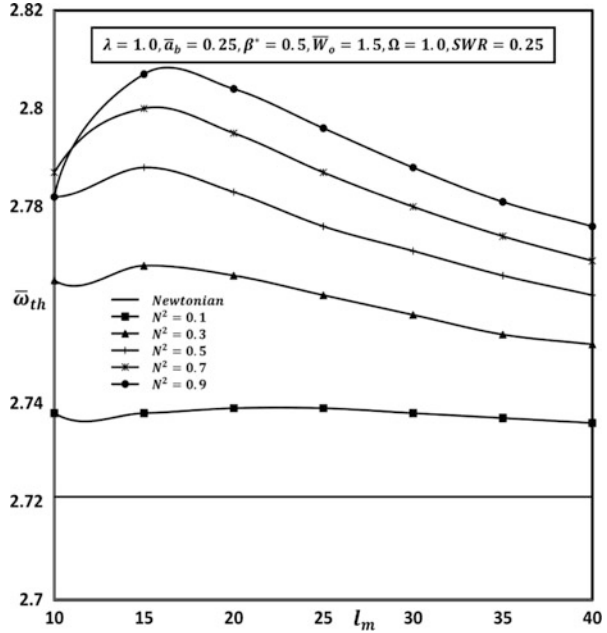
where, $\bar{\Phi} = 1 + \frac{12}{\bar{h}^2 l_m^2} - \frac{6N}{\bar{h} l_m} \coth\left(\frac{N \bar{h} l_m}{2}\right)$

$$N = \left(\frac{\kappa}{2\mu + \kappa} \right)^{1/2}, l = \left(\frac{\gamma}{4\mu} \right)^{1/2}, l_m = c/l$$

N and l_m are the parameters that characterize the micropolar lubricants and differentiate them from the Newtonians. The micropolar effect of lubricant share a direct proportionality with N^2 and an inverse relation with l_m . As a special case when l_m approaches infinity and N^2 to zero, the lubricant behaves as Newtonian lubricant. Very recently a study [43] on hybrid journal bearing with micropolar lubricants has been reported. Some of the salient points of the study are presented as follows:

The plot in Fig. 25.17 indicates that the value of minimum fluid-film thickness \bar{h}_{min} reduces with an increase in characteristic length of micropolar lubricant (l_m). However, the value of \bar{h}_{min} increases as the value of coupling number N^2 increases

Fig. 25.18 Variation of $\bar{\omega}_{th}$ vs. characteristic length (l_m).[43]



for a given external load $\bar{W}_0 = 1.5$. It has been observed that the percentage increase in the value of \bar{h}_{min} is nearly 10 % for a bearing operating with micropolar lubricant corresponding to a value of coupling number $N^2 = 0.9$ at $l_m = 10$ as compared to the bearings operating with Newtonian lubricant.

For the bearings operating with micropolar lubricants having large coupling numbers of ($N^2 = 0.9$), a drastic increase in the stability threshold speed margin ($\bar{\omega}_{th}$) followed by gradual decrease is observed with an increase in the value of characteristics length of micropolar lubricant (l_m) as shown in Fig. 25.18. An improved value of ($\bar{\omega}_{th}$) is obtained for the bearings operating with micropolar lubricants when compared with those operating with Newtonian fluids.

11.6 Influence of Recess Shape

The bearing designer has flexibility in selecting a particular type of recess shape for a given bearing configuration so as to obtain desired bearing performance. Recently, Rajshekhar et al. [26, 27] studied the influence of different recess shapes in hydrostatic/hybrid journal bearing under similar operating conditions. The recessed bearing configurations studied by Rajshekhar et al. [26, 27] are shown in Fig. 25.19. The variation in the values of minimum fluid-film thickness (\bar{h}_{min}) and

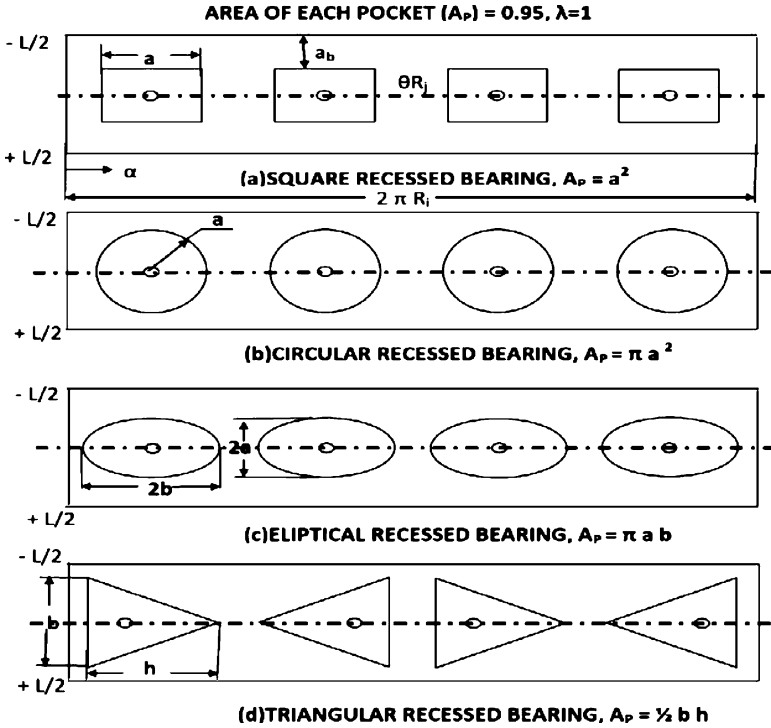


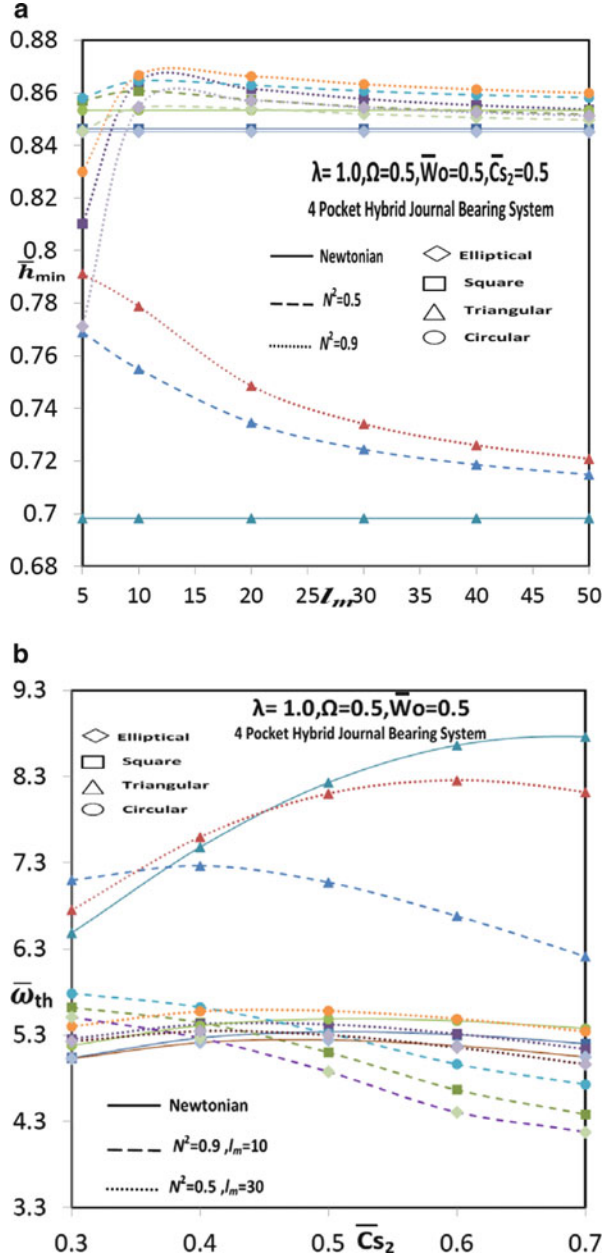
Fig. 25.19 Different recessed bearing configurations [27]

stability threshold speed margin ($\bar{\omega}_{th}$) with respect to characteristic length (l_m) have been shown through Fig. 25.20a, b respectively. The bearing characteristics parameters of a 4-pocket hydrostatic journal bearing system operating with micropolar and Newtonian lubricants with different geometric shape of recess are given in the tabular form in the Table 25.2.

The salient observations reported in the study of Rajshekhar et al. [26] regarding the influence of recess shape on bearing system operating with micropolar lubricant are as follows:

1. For a micropolar lubricated hydrostatic/hybrid journal bearing system, the following pattern vis-à-vis \bar{h}_{min} is observed: $\bar{h}_{min}|_{Circular} > \bar{h}_{min}|_{Square} > \bar{h}_{min}|_{Elliptical} > \bar{h}_{min}|_{Triangular}$
2. The influence of micropolar lubricant on the values of direct fluid-film stiffness coefficients ($\bar{S}_{11}, \bar{S}_{22}$) is found to be appreciably affected by the value of its restrictor design. Therefore, a proper selection of micropolar parameters based on the geometric shape of recess and restrictor design parameters is required, in order to obtain the enhanced values of fluid-film stiffness coefficients ($\bar{S}_{11}, \bar{S}_{22}$).

Fig. 25.20 (a) Variation of \bar{h}_{\min} with l_m (b) Variation of $\bar{\omega}_{th}$ with l_m for different recessed bearing configurations [26]



In general it has been observed that, a circular recessed journal bearing is found to be better from the point of view \bar{S}_{22} whereas a triangular recessed bearing provides higher value of \bar{S}_{11} when operating with either micropolar lubricant among the bearing configurations studied. For a micropolar lubricated

Table 25.2 Performance characteristics of four-pocket hydrostatic journal bearing for different Geometric Shape of Recess [26]

	Newtonian											
	$N^2 = 0.9, l_m = 10$				$N^2 = 0.5, l_m = 30$							
	$\bar{C}_{s,2} = 0.3$	$\bar{C}_{s,2} = 0.5$	$\bar{C}_{s,2} = 1.0$		$\bar{C}_{s,2} = 0.3$	$\bar{C}_{s,2} = 0.5$	$\bar{C}_{s,2} = 1.0$		$\bar{C}_{s,2} = 0.3$	$\bar{C}_{s,2} = 0.5$	$\bar{C}_{s,2} = 1.0$	
\bar{p}_{max}	Square	0.578	0.742	0.950	0.770	0.926	0.999	0.620	0.787	0.980		
	Triangle	0.537	0.696	0.920	0.724	0.891	0.996	0.577	0.742	0.955		
	Circle	0.584	0.745	0.953	0.773	0.928	0.999	0.625	0.790	0.983		
\bar{h}_{min}	Ellipse	0.606	0.771	0.970	0.798	0.948	0.993	0.649	0.815	0.972		
	Square	0.814	0.838	0.809	0.865	0.849	0.676	0.831	0.845	0.799		
	Triangle	0.475	0.590	0.593	0.644	0.670	0.384	0.537	0.621	0.586		
\bar{Q}	Circle	0.810	0.833	0.801	0.861	0.843	0.662	0.827	0.841	0.789		
	Ellipse	0.802	0.823	0.781	0.852	0.828	0.616	0.819	0.830	0.739		
	Square	0.892	1.237	1.596	0.713	0.865	1.113	0.856	1.158	1.397		
\bar{s}_{11}	Triangle	0.942	1.343	1.867	0.780	0.988	1.388	0.910	1.271	1.681		
	Circle	0.895	1.245	1.614	0.781	0.875	1.114	0.860	1.167	1.421		
	Ellipse	0.876	1.202	1.505	0.692	0.823	1.143	0.839	1.122	1.461		
\bar{s}_{22}	Square	2.348	2.674	2.519	3.153	2.793	1.578	2.610	2.947	2.204		
	Triangle	2.384	2.913	2.612	3.283	3.065	1.765	2.653	3.086	2.464		
	Circle	2.523	2.965	2.430	3.313	2.822	1.542	2.789	3.093	2.252		
	Ellipse	2.386	2.772	2.203	3.090	2.627	1.451	2.633	2.878	2.084		
	Square	2.618	2.703	1.946	3.060	2.393	1.225	2.806	2.850	1.672		
	Triangle	1.657	1.929	1.535	2.146	1.866	0.577	1.654	1.861	1.368		

\bar{C}_{11}	Circle	2.702	2.859	1.951	3.122	2.406	1.256	2.890	2.903	1.671
	Ellipse	2.591	2.683	1.695	2.914	2.136	1.184	2.759	2.700	1.584
	Square	4.668	3.951	2.392	6.880	4.782	2.205	5.178	4.230	2.352
	Triangle	5.777	4.650	3.544	8.130	6.638	10.427	6.172	5.061	3.886
	Circle	4.251	3.572	2.213	6.221	4.389	2.378	26.13	3.826	2.212
\bar{C}_{22}	Ellipse	4.032	3.347	1.942	5.806	3.911	1.788	4.453	3.560	1.967
	Square	5.091	3.976	1.999	6.833	4.197	1.328	5.554	4.167	1.749
	Triangle	8.528	6.317	5.179	11.07	9.46	21.407	8.779	6.867	5.906
	Circle	4.506	3.530	1.860	6.075	3.843	1.717	23.84	3.708	1.692
	Ellipse	4.340	3.314	1.502	5.662	3.255	1.158	4.680	3.439	1.515

$\lambda = 1.0, \Omega = 0.0, \bar{W}o = 0.5, A_p = 0.95, \frac{A_s}{A_b} = 0.30$

hydrostatic/hybrid journal bearing, the following pattern in the value of $\bar{S}_{11}/\bar{S}_{22}$ is observed:

$$\begin{aligned} \bar{S}_{11}|_{\text{Triangular}} &> \bar{S}_{11}|_{\text{Circular}} > \bar{S}_{11}|_{\text{Square}} > \bar{S}_{11}|_{\text{Elliptical}} \bar{S}_{22}|_{\text{Circular}} > \bar{S}_{22}|_{\text{Square}} \\ &> \bar{S}_{22}|_{\text{Elliptical}} > \bar{S}_{22}|_{\text{Triangular}} \end{aligned}$$

3. The triangular recessed bearing provides significantly larger values of direct fluid-film damping coefficients ($\bar{C}_{11}, \bar{C}_{22}$) among all the bearing configurations studied when the bearings are lubricated with either Newtonian or micropolar lubricants. Further, the influence of micropolar effect of lubricant on the values of direct fluid-film damping coefficients ($\bar{C}_{11}, \bar{C}_{22}$) is of the same order for all the bearing configurations studied. For a micropolar lubricated hydrostatic/hybrid journal bearing, the following pattern in the values of $\bar{C}_{11}/\bar{C}_{22}$ is observed.

$$\bar{C}_{11}/\bar{C}_{22}|_{\text{Triangular}} > \bar{C}_{11}/\bar{C}_{22}|_{\text{Square}} > \bar{C}_{11}/\bar{C}_{22}|_{\text{Circular}} > \bar{C}_{11}/\bar{C}_{22}|_{\text{Elliptical}}$$

4. A triangular recessed bearing is found to provide the largest value of the bearing stability threshold speed margin among all the bearing configurations studied when the bearing is lubricated with either micropolar or Newtonian lubricant. However, it has been observed that the influence of micropolar effect of lubricant is significantly lesser for a triangular recessed bearing as compared to other bearing configurations studied. For a micropolar lubricated hybrid journal bearing, the following pattern is observed:

$$\bar{\omega}_{th}|_{\text{Triangular}} > \bar{\omega}_{th}|_{\text{Square}} > \bar{\omega}_{th}|_{\text{Circular}} > \bar{\omega}_{th}|_{\text{Elliptical}}$$

Acknowledgement The author is extremely grateful to Elsevier Publication, Taylor and Francis Publication, Emerald Group Publication, Sage Publication, and ASME publications for granting permission to use their copyright material in the present chapter. The used materials have been cited in the references. Further, I would like to acknowledge and thank my PhD scholars Mr. Arvind Kumar Rajput, Mr. G.D. Thakre, Mr. Nathi Ram, and Mr. P.B. Kushare, who provided their valuable assistance during the course of writing of this chapter.

Exercise

1. Write a brief engineering note on the purpose of lubrication in machine component? How a liquid lubricant is better than a solid lubricant?
2. Classify different bearing configurations? List the application of rolling contact Bearing?
3. Enumerate the advantages of hydrostatic journal bearing over a hydrodynamic journal bearing?

4. Describe in brief need of a restrictor in a hydrostatic journal bearing system? Which type of restrictor will you prefer in high variable load?
5. Describe the phenomena of whirl and whip in journal bearing system? How these problems could be overcome?
6. What are the advantages of recessed journal bearing over non-recessed journal bearing?
7. Derive the generalized form of Reynolds equation in nondimensional form by using suitable nondimensional parameter.
8. Write a brief engineering note on bearing performance characteristics parameters.
9. Explain Elastohydrostatic/Elastohydrodynamic Lubrication phenomenon. How do these affect the performance of a journal bearing?
10. What do you mean by the term Nonlinearity of lubricant? How does the nonlinearity of lubricant affect the performance of a journal bearing?
11. Explain the phenomenon of turbulence in the fluid-film journal bearing system. Describe different theories for turbulence applicable to journal bearing.
12. A capillary compensated hydrostatic journal bearing system has the following parameters-

Discharge through capillary	$4 \times 10^{-5} \text{ m}^3/\text{s}$
Length of capillary	10 cm
viscosity of lubricant	$2.18 \times 10^{-3} \text{ N-s/m}^2$
Supply pressure	1.4 MPa
Recess pressure	0.5 MPa

Determine the radius of the capillary.

13. Determine the value of discharge of the lubricant through an orifice restrictor for an orifice restricted recessed hybrid journal bearing system with the following data.

Orifice diameter	10 mm
Coefficient of discharge	0.55
Density of lubricant	800 Kg/m ³
Supply pressure	0.15 MPa
Recess pressure	0.06 MPa

14. Determine the load carrying capacity and shear stress for a hydrodynamic journal bearing system for the following data.

Pressure	1 MPa
Aspect ratio	0.8
Length of the bearing	1 m
Clearance	10^{-3} m
Viscosity	$2.08 \times 10^{-5} \text{ N-s/m}^2$
Speed of journal	1,000 rpm

15. Determine the value of the coupling number and characteristics length for the lubricant with the following characteristics.

Linear viscosity	$2.5 \times 10^{-3} \text{ N-s/m}^2$
Spin viscosity	$1.2 \times 10^{-3} \text{ N-s/m}^2$
Characteristics coefficients	$0.8 \times 10^{-9} \text{ N-s}$

16. Compare the value of the turbulent coefficients for the value of Reynolds number $Re = 10,000$ using Constantinescu theory.
17. Derive the expression of critical mass of journal using the Routh's criterion of Stability.
18. Determine the wear zone for a hydrostatic journal bearing system for the values of nondimensional wear depth parameter of 0.25 and 0.5.

Solutions

12. Given that

$$Q_R = 4 \times 10^{-5} \text{ m}^3/\text{s}; \quad l_c = 0.1 \text{ m}; \quad \mu = 2.18 \times 10^{-3} \text{ N-s/m}^2; \quad p_s = 1.4 \text{ MPa}; \\ p_c = 0.5 \text{ MPa}$$

$$Q_R = K_c \frac{(p_s - p_c)}{\mu} = \frac{\pi d_c^4}{128 l_c} \frac{(p_s - p_c)}{\mu} \\ 4 \times 10^{-5} = \frac{\pi d_c^4}{128 \times 0.10} \frac{(1.4 - 0.5) \times 10^6}{2.18 \times 10^{-3}} \\ d_c = 7.926 \times 10^{-4} \text{ m}$$

13. Given that

$$d_0 = 10 \text{ mm}; \quad \rho = 800 \text{ kg/m}^3; \quad p_s = 0.15 \text{ MPa}; \quad p_c = 0.06 \text{ MPa}$$

$$Q_R = \frac{\pi \psi_a d_0^2}{\sqrt{8\rho}} (p_s - p_c)^{\frac{1}{2}} \\ Q_R = \frac{\pi \times 0.55 \times (10 \times 10^{-3})^2}{\sqrt{8 \times 800}} ((0.15 - 0.06) \times 10^6)^{\frac{1}{2}} \\ = 6.4795 \times 10^{-4} \text{ m}^3/\text{sec}$$

14. Given that

$$p = 1 \text{ MPa}; \quad L/D = 0.8; \quad L = 1 \text{ m}; \quad C = 10^{-3} \text{ m}; \quad N = 1,000 \text{ rpm};$$

$$\mu = 2.08 \times 10^{-5} \text{ N-s/m}^2$$

Load carrying capacity

$$F_o = p \cdot A = p \cdot \pi L D = 1 \times 10^6 \times \pi \times 1.25 = 3.92699 \times 10^6 \text{ N}$$

Shear stress

$$\tau = \mu \frac{du}{dy} = 2.08 \times 10^{-5} \times \frac{\pi \times 10000 \times 1.25}{60 \times 10^{-3}}$$

$$= 13.6135 N/m^2$$

15. Given that,

$$\mu = 2.5 \times 10^{-3} N - s/m^2$$

$$\text{Spin velocity, } \kappa = 1.2 \times 10^{-3} N - s/m^2$$

$$\gamma_1 = 0.8 \times 10^{-9} N - s$$

$$N = \left(\frac{\kappa}{2\mu + \kappa} \right)^{\frac{1}{2}} = 0.4399$$

$$l = \left(\frac{\gamma_1}{4\mu} \right)^{\frac{1}{2}} = 2.828 \times 10^{-4} m = 0.2828 \text{ mm.}$$

16. Given that,

$$R_e = 10000$$

$$G_\alpha = 12 + 0.026(R_e)^{0.8265} = 64.5985$$

$$G_\beta = 12 + 0.0198(R_e)^{0.741} = 30.2249.$$

18. Given that,

$Sin\alpha = \delta_w - 1$ by Dufrane's abrasive wear model

for, $\delta_w = 0.25$

$$Sin\alpha = 0.25 - 1$$

$$\alpha = 228.59^\circ, 311.40^\circ$$

for, $\delta_w = 0.50$

$$Sin\alpha = 0.50 - 1$$

$$\alpha = 210^\circ, 330^\circ$$

References

1. Kankar PK (2011) Fault diagnosis and prognosis of high speed rotor bearing systems. Ph.D. Dissertation, IIT Roorkee, Roorkee (India)
2. Nagaraju T (2003) Performance of non-recessed hybrid journal bearings with surface roughness effects. Ph.D. Dissertation, IIT Roorkee, Roorkee (India)
3. O'Donoghue JP, Rowe WB (1968) Hydrostatic journal bearing (exact procedure). Tribology 1(4):230–236
4. Cheng K, Rowe WB (1995) Selection of strategy for the design of externally pressurized journal bearing. J Tribol Int 28(1):465–474
5. Sharma Satish C (1990) Elastohydrostatic lubrication of thrust and journal bearing. Ph.D. Dissertation, University of Roorkee, Roorkee (India)
6. Stout KJ, Rowe WB (1974) Externally pressurized bearings- design for manufacturer part3- design of liquid externally pressurized bearing for manufacturer including tolerance procedures. J Tribol Int 7:195–212
7. Rowe WB, Xu SX, Chong FS, Weston W (1982) Hybrid journal bearing with particular reference to hole-entry configurations. J Tribol Int 15:339–348
8. Rowe WB (2012) Hydrostatic, aerostatic and hybrid bearing design. Butterworth & Co Ltd, Belfast
9. Sinhasan R, Sharma Satish C, Jain SC (1989) Performance characteristics of an externally pressurized capillary-compensated flexible journal bearing. J Tribol Int 22:283–293

10. Cusano C (1974) Characteristics of externally pressurized journal bearings with membrane-type variable-flow restrictors as compensating elements. *Proc Instn Mech Engrs* 188:52–74
11. Phalle VM, Sharma Satish C, Jain SC (2011) Influence of wear on the performance of a 2-lobe multirecess hybrid journal bearing system compensated with membrane restrictor. *J Tribol Int* 44:380–395
12. Singh A, Gupta BK (1984) Stability analysis of orthogonally displaced bearings. *Wear* 97:83–92
13. Jain SC, Sharma Satish C, Basavaraja JS, Kushare P (2010) Study of two-lobe four recessed hybrid journal bearing. *Ind Lubr Tribol* 62(6):332–340
14. Sharma Satish C, Phalle VM, Jain SC (2011) Influence of wear on the performance of a multirecess conical hybrid journal bearing compensated with orifice restrictor. *J Tribol Int* 44:1754–1764
15. Stout KJ, Rowe WB (1974) Externally pressurized bearings- design for manufacturer part1- journal bearing selection. *J Tribol Int* 98–106
16. Phalle VM (2011) Influence of wear on the performance of Multirecess Fluid Film Journal bearing. Ph.D. Dissertation, IIT Roorkee, Roorkee (India)
17. Awasthi RK, Jain SC, Sharma Satish C (2006) Finite element analysis of orifice compensated multiple hole-entry worn hybrid journal bearing. *Finite Elem Anal Des* 42(14–15):1291–1303
18. Lin JR (2001) Linear stability analysis of rotor- bearing system: couple stress fluid model. *Comput Struct* 79:801–809
19. Sharma Satish C, Jain SC, Sinhasan R, Shalia R (1995) Six pocket and four hydrostatic/hybrid flexible journal bearings. *Tribol Int* 28:531–539
20. Jain SC, Sinhasan R, Sharma Satish C (1992) Analytical study of a flexible hybrid journal bearing system using different flow control devices. *Tribol Int* 25:387–395
21. Constantinescu VN, Galetuse S (1965) On the determination of friction forces in turbulent lubrication. *ASLE Trans* 8:367–380
22. Davies PB (1970) A general analysis of multirecess hydrostatic Bearing. *Proc Inst Mech Eng* 184(1):43
23. Ghosh B (1973) Load and flow characteristics of a capillary compensated Hydrostatic journal bearings. *Wear* 23:377–386
24. Ghai RC, Singh DV, Sinhasan R (1976) Load capacity and flow characteristics of hydrostatically lubricated four pocket journal bearing by Finite Element Method. *Int J Mach Tool Des* 16:233–240
25. Nicodemus RE, Sharma Satish C (2010) Influence of wear on the performance of multi recess hydrostatic journal bearing operating with micropolar lubricant. *J Tribol* 132:021703-1-11
26. Nicodemus RE, Sharma Satish C (2011) Orifice compensated multirecess hydrostatic/hybrid journal bearing system of various geometric shapes of recess operating with micropolar lubricant. *J Tribol Int* 44:284–296
27. Nicodemus RE, Sharma Satish C (2010) A study of worn hybrid journal bearing system with different recess shapes under turbulent regimes. *ASME J Tribol* 132:41704–41712
28. Rowe WB, Koshal D, Stout KJ (1977) Investigation of recessed hydrostatic and slot-entry journal bearings for hybrid hydrodynamic and hydrostatic operation. *WEAR* 43(1):55–69
29. Bou-Said B, Nicolas D (1992) Effects of misalignment on static and dynamic characteristics of hybrid bearings. *STLE Tribol Trans* 35(2):325–331
30. Sharma Satish C, Jain SC, Sinhasan R, Sah PL (2001) Static and dynamic performance characteristics of orifice compensated hydrostatic flexible journal bearing with Nonnewtonian lubricants. *STLE Tribol* 44(2):242–248
31. Tayal SP (1982) Static and dynamic analysis of circular and non-circular bearings having non-Newtonian lubricant by a finite element method. Dissertation, University of Roorkee
32. Tayal SP, Sinhasan R, Singh DV (1981) Analysis of hydrodynamic journal bearing with non-Newtonian power law lubricants by the finite element method. *Wear* 71:15
33. Nagaraju T, Sharma Satish C, Jain SC (2002) Influence of surface roughness effects on the performance of Non-recessed hybrid journal bearings. *J Tribol Int* 35:467–487

34. Dufrane KF, Kannel JW, McCloskey TH (1983) Wear of steam turbine journal bearings at low operating speeds. *ASME J Lubr Technol* 105:313–317
35. Kumar A, Mishra SS (1996) Steady state analysis of Non-circular worn journal bearings in non-laminar lubrication regimes. *Tribol Int* 29(6):493–498
36. Ng CW, Pan CHT (1965) A linearized turbulent lubrication theory. *Jr Basic Engg* 87:675–688
37. Hirs GG (1974) A systematic study of turbulent film flow. *Jr Lubr Technol* 96:118–126
38. Wada S, Hashimoto H (1979) Turbulent lubrication theory using the frictional Law. *Bull JSME* 22:249–256
39. Ram N, Sharma Satish C (2013) A study of misaligned hole-entry worn journal bearing operating in turbulent regime. *Ind Lubr Tribol* 65(2):108–118
40. Daring DW, Dayton RD (1992) Non-Newtonian behavior of powder lubricants mixed with ethylene glycol. *STLE Tribol Trans* 35(1):114–120
41. Sheja D, Prabhu BS (1993) Thermal and Non-Newtonian effect on the steady state and dynamic characteristics of hydrodynamic journal bearings—theory and experiments. *STLE Tribol Trans* 35(3):441
42. Eringen AC (1966) Theory of micropolar fluids. *J Math Mech* 16:1–18
43. Sharma Satish C, Ram N (2011) Influence of micropolar lubricants on the performance of slot-entry hybrid journal bearing. *J Tribol Int* 44:1852–1863
44. Khonsari MM (1989) On the performance of finite journal bearings lubricated with micropolar fluids. *STLE Tribol Trans* 32(2):15
45. Wang XL, Zhu KQ (2006) Numerical Analysis of journal bearings lubricated with micropolar fluids including thermal and cavitating effects. *Tribol Int* 39:227–237

Chapter 26

Macroscale Applications in Tribology

Carlton J. Reeves, Pradeep L. Menezes, Michael R. Lovell,
and Tien-Chien Jen

Abstract This chapter addresses some of the basic mechanical and chemical issues affecting tribology in a broad range of macroscale applications such as space; automotive; rail transport; earthmoving, mining, and mineral processing; marine equipment; and gas and steam turbines. Many of the featured system's successes rely on understanding and solving tribological issues involving friction, lubrication, and wear of mating components. In many instances, solutions require a multidisciplinary approach to achieve the desired efficiency, reliability, compliance, and safety necessary to ensure economical and feasible operation. The presented topics were chosen to illustrate the broad range and importance that tribology plays beyond the traditional industrial and manufacturing applications, as well as to illustrate the numerous encounters of tribology in our lives.

1 Space Tribology

1.1 Introduction

This section on space tribology will primarily focus on the application of lubrication mechanisms used in extraterrestrial environments where reliable performance of satellites, spacecraft, and space stations is the principal concern. Space tribology involves a broad range of tribological regimes from boundary lubrication to

C.J. Reeves • T.-C. Jen (✉)
Department of Mechanical Engineering, University of Wisconsin-Milwaukee,
Milwaukee, WI 53211, USA
e-mail: jent@uwm.edu

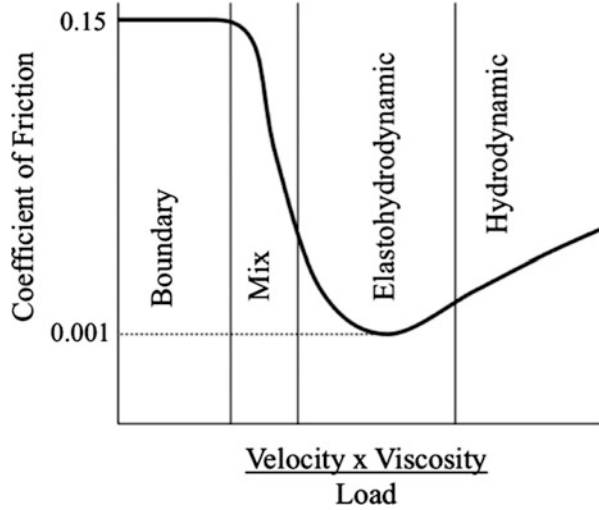
P.L. Menezes • M.R. Lovell
Department of Industrial Engineering, University of Wisconsin-Milwaukee,
Milwaukee, WI 53211, USA

mixed, elastohydrodynamic, and hydrodynamic lubrication. Traditionally, it has been the role of tribologists to utilize lubricants based on space heritage rather than the prestige of the technology or optimization of materials. This perspective often sufficed because mission lifetimes were short and mechanical duty cycles were low. As space exploration has developed, mission lifetimes began increasing, resulting in more component failure in nonlubricated systems such as electronics, batteries, and computers [1]. In recent times, a shift has occurred where these auxiliary components have improved to the point where the lubricating systems are now the limiting factor depleting spacecraft reliability and performance. Although tribological systems are relatively inexpensive in comparison to the rest of the spacecraft and its components, the importance of such systems plays a crucial role in the operational compliance of spacecraft, and their singular failure can potentially render a spacecraft or satellite inoperable [2]. An example of a narrow margin for an expensive tragedy is the Galileo spacecraft that was launched in 1989 from the Space Shuttle Atlantis. A vital component on Galileo was a high-gain umbrellalike antenna that was in the closed position during the launch into space. In 1991, after the Galileo spacecraft was released from the Atlantis shuttle, the high-gain antenna partially opened. It was later determined that four of eighteen ribs had seized up and were stuck in place on the antenna because of the loss of the bonded dry film lubricant [3]. As a result, the high-gain antenna was virtually unusable, and the mission was only salvaged by the use of a secondary low-gain antenna that was able to undergo upgrades in its data transmission capabilities.

1.2 Mechanism Components

Satellites, spacecraft, and space stations have many instruments and components that require lubrication, for example, solar array drives; momentum, reaction, and filter wheels; tracking antennas; scanning devices; and various sensors. Each of these devices has unique hardware designed for a specific application that requires lubrication to prevent serious damage caused by friction and wear. As a result, a variety of lubrication regimes are present in space tribology. In all of the aforementioned tribological applications, two or more surfaces are in relative motion with one another. To protect the surfaces from unwanted wear and potential damage, a lubricant with low shear resistance that can maintain surface separation is applied to the contacting surfaces. In many space applications, these lubricants can be adsorbed gas, reaction films, and liquid or solid lubricants. Lubrication regimes are classified by the film thickness of the lubricant using a Stribeck curve [4], as shown in Fig. 26.1, that plots the coefficient of friction against the nondimensional Stribeck number [5]. The Stribeck number is composed of viscosity, speed, and load and is used to determine which lubrication regime is present.

Fig. 26.1 Friction coefficient as a function of the Stribeck number



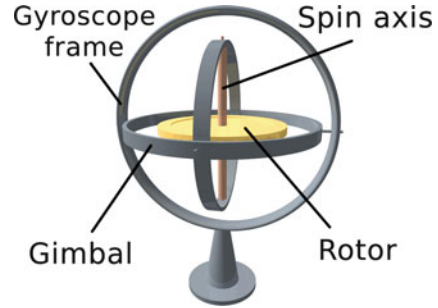
1.3 Lubrication Regimes

Boundary lubrication is a complex regime dealing with metallurgy, surface topography, corrosion, catalysis, reaction kinetics, and physicochemical adsorption [6, 7]. Boundary lubrication takes place when the Stribeck number is low and the asperities of the two opposing surfaces come into contact. In this regime, the asperity contacts support much of the applied load, and there is minimal thin-film lubrication. As for this reason, it is important in boundary lubrication that there is a formation of a protective surface film to minimize the wear and damage to the surfaces. As the Stribeck number increases, the mixed lubrication (ML) regime begins to occur, where both asperity contacts and fluid film effects take place. The elastohydrodynamic (EHL) regime follows where high loads can cause elastic deformation of the surfaces and the pressure-viscosity effects of the lubricant dominant over asperity contacts. As the Stribeck number enters the region of high viscosities, high speeds, and low loads, the surfaces become completely separated by a thick lubricant film; this is the hydrodynamic (HD) regime. In this regime, friction is determined by the rheology of the lubricants, and as shown in Fig. 26.1, the friction coefficient tends to increase in comparison to the mixed or elastohydrodynamic regimes.

1.4 Gyroscopes

The occurrences of the aforementioned lubrication regimes occurring in a spacecraft often take place in many of the gyroscope applications. Gyroscopes (Fig. 26.2) such as gimbal are designed for relatively low-speed applications,

Fig. 26.2 3D gyroscope schematic [75]

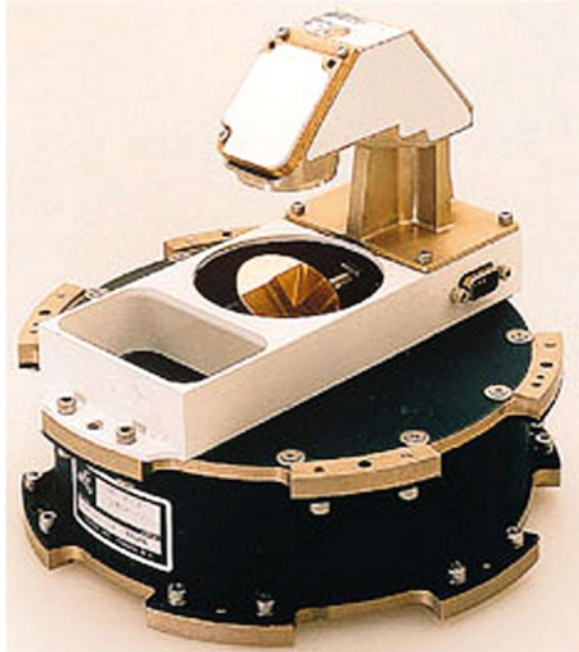


and the bearings involved operate in the boundary regime. Other gyroscopes that measure changes in orientation with high precision have been shown to operate in the hydrodynamic regime with speeds upwards from 8,000 to 20,000 RPM. Within a gyroscope, the bearing is the critical component and fluctuations in the bearing reaction cause torque, noise, and excess heat generation that can have an ill effect on the determination of the zero position of the gyroscope, rendering it inept [8].

1.5 Momentum and Reaction Wheels

Momentum and reaction wheels are flywheels (Fig. 26.3) used to provide attitude control authority and stability on spacecraft [9]. They operate by adding or removing energy from the flywheel by applying torque to a single axis of the spacecraft, causing it to react by rotating. Stability about a single axis arises by maintaining the flywheel rotation or momentum. Through coordination of multiple momentum or reaction wheels, full three-axis attitude control and stability can be achieved [10]. Momentum wheels operate at speeds from 3,000 to 10,000 RPM (i.e., hydrodynamic regime), whereas reaction wheels operate at lower speeds and remain in the mixed lubrication regime. The majority of the problems that lead to failures with these wheels are a result of inadequate lubrication, loss of lubrication, and lubricating degradation [8]. Due to the high speeds in the momentum wheels, the lubricants are subjected to higher operating temperatures. This makes the lubricant susceptible to increases in creep or accelerated degradation. Solutions for the momentum wheels have been to incorporate a lubricant circulation system, lubricant impregnation retainers, labyrinth seals, barrier coatings, or the use of synthetic lubricants. When utilizing reaction wheels, tribologists and lubrication engineers primarily focus on supplying them with lubricants having excellent boundary lubrication characteristics that create a sustainable protective surface film to minimize the wear and damage to the surfaces in the support bearings.

Fig. 26.3 A momentum/reaction wheel comprising a high-accuracy Conical Earth Sensor to maintain a satellite's precise attitude [9]



1.6 Control Momentum Gyroscope

A control momentum gyroscope (CMG) is an attitude control device that incorporates aspects of the gyroscope and the momentum wheel through a spinning rotor and multiple motorized gimbals that can shift a rotor's angular momentum. As a result of the rotor tilting, the angular momentum causes a gyroscopic torque that rotates the spacecraft allowing it to stabilize the spacecraft's attitude control system. Control momentum gyroscopes are currently used on the International Space Station for stabilization. In their use, similar design considerations to that of the gyroscope and momentum wheels must be included when selecting an appropriate lubricant that could possibly operate in the full spectrum of lubrication regimes [8]. Figure 26.4 shows Boeing technicians removing the cover from a CMG in the Space Station Processing Facility at the Kennedy Space Center [11, 12].

1.7 Attitude Control Sensors

Another instrument that aids in the attitude control system in spacecraft is scanning or rotating sensors. One example is the scanning horizon sensor that detects the Earth's horizon allowing for a spacecraft to orientate itself. These sensors require lubrication of the bearing components to ensure the accuracy, operational lifetime, and reliability of the sensor throughout the entire mission lifetime. Failure in the



Fig. 26.4 NASA personnel handle a single control moment gyroscope for the International Space Station [12]

lubricant by contamination or evaporation would lead to a lack of sensory information that would adversely affect the spacecraft's systems that rely on horizon-sensor-derived information such as the orientation of instruments and antennas. The bearings within these systems have moderate operational speeds from 400 to 1,600 RPM with minimal loading, therefore allowing a lubricant to operate in the boundary lubrication regime [2]. Some scanning sensors such as the Gemini horizon sensor use azimuth-scan edge tracking with a single field of view to track a planet's horizon. In this sensor, the scanning head oscillates over the azimuth-scan angle as shown in Fig. 26.5 [13]. This oscillatory motion, in conjunction with the rotation in the azimuth-scan angle, places higher demand on the lubricant. As a result of the small oscillatory angle, no new lubricant flows back into the contact zone of the scanning head. This places greater importance on the lubricant, which operates in the boundary lubrication regime, to establish a sufficient protective surface film to prevent wear and damage to the sensor [14].

1.8 Lubricants and Accelerated Life Testing

Lubricants in space applications are primarily liquid or solid, and in some instances, they can consist of adsorbed gas or reaction films. Often the choice is left up to the designer, but each type has its merits and deficiencies. Table 26.1 highlights a few of the differences between liquid and dry lubricants [15]. Liquid lubricants can consist of mineral oils, silicones, polyphenyl ethers, esters, synthetic hydrocarbons, perfluoropolyethers, and silahydrocarbons. Dry lubricants are lamellar solids such as

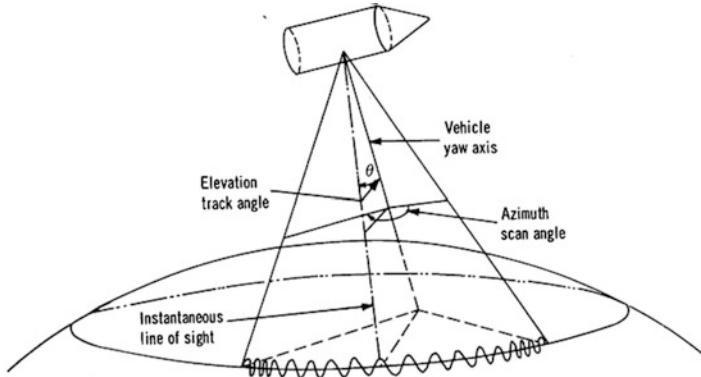


Fig. 26.5 Azimuth-scanning geometry [13]

Table 26.1 Comparison of liquid and dry lubricants [15]

Liquid lubricant	Dry lubricant
Finite vapor pressure	Negligible vapor pressure
Viscosity, creep, and vapor pressure, all temperature dependent	Wide operating temperature
Sealing required	Negligible surface migration
Invalid accelerated testing	Valid accelerated testing
Insensitive to air or vacuum	Short life in moist air
Low frictional noise	Debris causes frictional noise
Friction speed dependent	Friction speed independent
Life determined by lubricant degradation	Life determined by lubricant wear
High thermal conductance	Poor thermal characteristics
Electrically insulating	Electrically conductive

molybdenum disulfide and tungsten disulfide; soft metals including lead, gold, silver, or indium; and polymers consisting of polyimides and polytetrafluoroethylene [2].

Due to the importance of lubricants to sustain the desired performance of the spacecraft, they must undergo extensive ground-based testing to ensure that they will meet the cycle and operational condition requirements for current and possibly future space missions. Two approaches are used to qualify the performance of a lubricant; the first is system-level tests on actual flight hardware and the second is laboratory tests to simulate actual operational conditions that the lubricant would experience in an actual flight system [8]. The first method is economically infeasible and impractical to test for all lubricants used throughout a spacecraft; therefore, the second method is the common practice. One of the premier laboratory tests is accelerated life tests, where lubricants are easily tested and monitored providing fast and reliable qualitative results. Often these tests are indicative of lubricant characterization by subjecting a lubricant to similar operational conditions it would

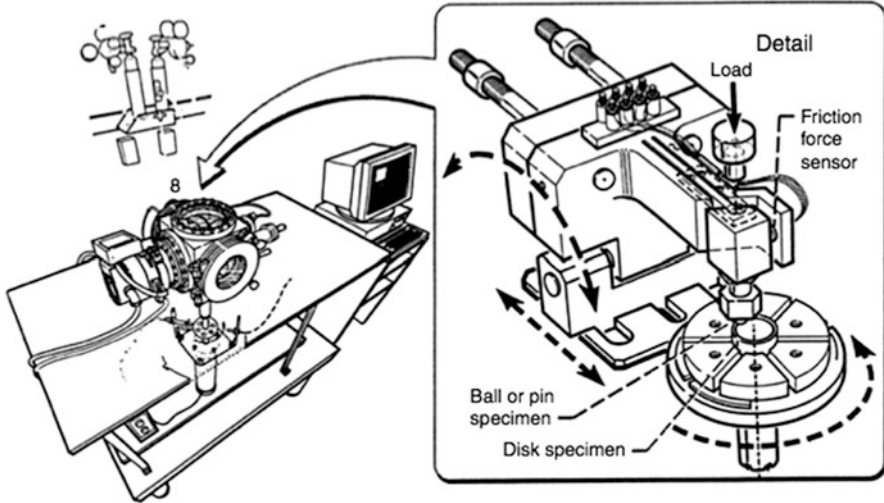


Fig. 26.6 Ultra-high-vacuum pin-on-disk tribometer [21]

experience in the field [16]. Additionally, data from these tests can be used to enhance the lubricant or additive design allowing for a baseline data set to be generated. In accelerating life tests, various test parameters such as speed, load, temperature, contaminants, quantity of lubricant available, and surface roughness are all varied to gauge the reliability of a lubricant [17]. Although these tests provide immediate results, they cannot accurately predict properties that evolve with time such as lubricant creep, lubricant loss through evaporation or centrifugal forces, and lubricant degradation [16]. Accelerated life tests are often conducted using tribometers that can come in a variety of designs. There are primarily four types of testing apparatuses used: (1) an eccentric bearing test apparatus [8], (2) a spiral orbital rolling contact tribometer (SOT) based on the design of a thrust bearing [18, 19], (3) a vacuum four-ball tribometer designed to test liquid lubricants under purely sliding conditions [20], and (4) a vacuum pin-on-disk tribometer for testing solid film coatings as shown in Fig. 26.6 [21].

1.9 Conclusion

Space tribology is an integral aspect in providing spacecraft, satellite, or space station performance. Although it can often be overlooked, examining the consequences of what can happen when a component or mechanism stops functioning as a result of an improperly used lubricant or the lack of using a lubricant can have serious effects on the reliability, safety, and performance of spacecraft. This section provides a brief review on the importance of lubricants in space applications, the types of lubricants used, and the testing that goes into each lubricant.

2 Automotive Tribology

2.1 Introduction

Automotive tribology is the aspect of tribology focused on automobile performance and reliability. The automobile is undisputedly the most widely used machine in the world today, with over 600 million passenger cars worldwide (approximately 1 for every 11 people) [22, 23]. In the United States, it is estimated that with only a few modifications to improve friction and minimize wear, this would result in significant reductions in fossil fuel usage with saving upwards of \$120 billion per year [24, 25]. The automobile has become vital in commerce and transportation for developed and developing nations throughout the world. Automobiles consist of thousands of components with many of them relying on their surface interactions to function properly such as bearings, pistons, transmissions, clutches, gears, tires, and electrical contacts [2]. Investigating the tribological phenomena in these applications is imperative to the reliability, durability, and performance of automobiles. Many advances in lubricants, bearings, and surface topography have risen as a result of the automobile industry. An example of a less subtle tribological application within the automobile industry is the advent of the windshield wipers. Although, at first, it seems more like a trivial application, optimization of the materials, loads, pressures, and environmental conditions plays a role to the solution to this problem and is of interest to tribologists to provide a clear windshield for a driver to operate a vehicle safely. This is but one example of the many impacts tribology has made within the automotive industry. In this section, three tribological systems are investigated that are paramount to the success and ubiquitous use of the automobile: the engine, tires, and brakes. Each operates under different lubrication regimes, operating conditions, and environments, thereby making their use of lubricants, surface technology, and materials drastically different.

2.2 The Internal Combustion Engine

The reciprocating internal combustion (IC) engine has risen to popularity due to its performance, reliability, and versatility. It has quickly become the most common machine in regard to locomotion and transportation by being utilized in a vast array of vehicles such as motorcycles, scooters, mopeds, cars, vans, trucks, buses, agricultural vehicles, construction vehicles, trains, boats, ships, and airplanes [26]. Despite the broad application of IC engines, they do have major flaws such as their relatively low thermal and mechanical efficiencies, with much of the energy potential produced by fuel dissipating as heat and friction losses [26]. The most detrimental effect from the use of IC engines is their contribution to atmospheric pollution through hydrocarbons, particulate, nitrogen oxides, and carbon dioxide

emissions [2]. As a result of the many hundreds of millions of IC engines in use, minimal improvements in engine efficiency, emission levels, and durability would lead to tremendous effects on the world economy directly affecting the petroleum industry. In addition, improvements to IC engines would lessen their environmental impacts by reducing their contributions to the greenhouse effect [27]. In order to reduce the friction and wear, effective lubrication of all the engine components with minimal impact on the environment must be achieved for all the various operating conditions of speed, load, temperature, and chemical reactivity. Improvements in engine performance would result in reduced fuel consumption; increased engine power output; reduced oil consumption; a reduction in harmful exhaust emissions; improved durability, reliability, and engine life; reduced maintenance requirements; and longer service intervals [2, 28].

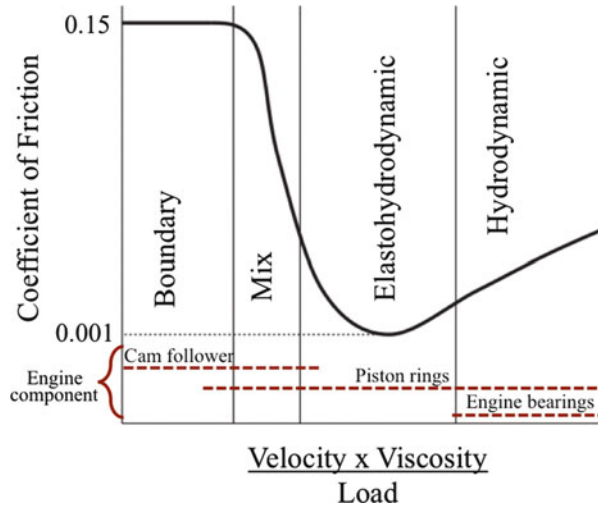
2.3 Lubrication Regimes

Within the engine, the three major components that contribute to an increase in friction and a decrease in efficiency are the engine bearings, piston assembly, and valvetrain. Each of these components is lubricated with a liquid lubricant that may operate in a different lubrication regime. In order to quantify the lubrication mechanism that is taking place within each of these multicomponent systems, a film thickness ratio parameter (as shown in 26.1) has been developed that is a function of the lubrication film thickness and the roughness of the two surfaces in relative motion. A film thickness ratio (λ) is used to quantify the regimes:

$$\lambda = \frac{h}{\left(\sigma_{\text{surface1}}^2 + \sigma_{\text{surface2}}^2\right)^{1/2}} \quad (26.1)$$

In (26.1), h is the lubricant film thickness calculated through traditional thin-film analysis by the Reynolds equation, and σ is the root-mean-square of the roughness of the two contacting surfaces. To quantify which lubrication regime is taking place, Fig. 26.7 illustrates how the film thickness ratio can be used. Similar to the lubrication regimes present in space tribology, the first regime is the boundary lubrication where the surfaces are in contact and emphasis is put on the lubricant to produce a thin protective film to subdue wear and prevent damage to the surfaces. The mixed and elastohydrodynamic regions are where a fluid film develops limiting the amount of contact between the asperities on the surfaces. The last regime is the hydrodynamic lubrication regime where a thick film prevents the surfaces from contacting one another. In many of the components in an automobile, they may experience multiple lubrication regimes within one cycle, thus stressing the importance of understanding the different lubrication modes to achieve the desired performance levels.

Fig. 26.7 Relationship between friction coefficient and oil film thickness ratio for engine components



2.4 Engine Components

Engine bearings generally consist of rotating journal bearings that operate in the hydrodynamic lubrication regime where the bearing surfaces are separated by a thick film. However, at low speeds, low viscosities, and high loads, this can cause increased metal-to-metal contact to occur. Journal bearings in an engine are typically used to support the camshaft, crankshaft, and connecting rods. Inspecting the tribodynamics of a journal bearing, there are many complicated issues that must be addressed with the lubricant such as the lubricant supply, thermal effects, dynamic loading, and elasticity of the bounding solids [2].

The piston assembly is the vital link in transforming the energy created by the combustion of the fuel-air mixture into mechanical energy that is used to drive the vehicle. The tribological importance of the piston is to provide an effective gas seal between the combustion chamber and the crankcase. This is done by a series of metallic rings carried by the piston that creates a labyrinth seal. Throughout a piston cycle, the rings can experience large, rapid, dynamic variations at various loads, speeds, temperatures, and lubricant availability. Examining the piston ring-cylinder wall interface, boundary, mixed, and hydrodynamic lubrication regimes can be experienced [29].

The valvetrain is a system of many components including valves, valve springs, valve spring retainers, valve keys, rocker arms, piston rods, lifter (tappets), and a camshaft. The valvetrain's primary function is to transform the rotary camshaft motion into a linear valve motion in order to control the fluid flow into and out of the combustion chamber. A secondary function is to control the auxiliary devices such as distributors, fuel pumps, water pumps, and power steering pumps. There are many mechanisms used to transmit the motion of the camshaft to the valvetrain. The most often used mechanism is the roller follower that utilizes a rolling motion to transmit the required motion allowing for lower friction. Other less frequent

mechanisms include the finger follower and direct acting bucket follower. These two mechanisms operate by means of a sliding motion resulting in higher friction than the roller follower. For tribologists, the most critical interface in the valvetrain is the cam and follower due to the problem of providing effective lubrication. Often, it was assumed that the cam and follower operated in the boundary lubrication regime; however, more recent investigations have shown that mixed and elastohydrodynamic lubrications are the dominant regime [30].

2.5 *The Tire*

Within automotive tribology, the tire has received extensive scrutiny over the years because of its importance for retaining traction while driving. A tire is a protected cover for the compressed air toroidal tube that is attached to the steel rim or wheel in an automobile. The tire has six functions as follows [31]:

- To allow relatively free and frictionless motion of the vehicle by means of rolling
- To avoid excessive stress in the wheel and road by distributing the vehicle weight over a substantial area of the ground surface
- To cushion the vehicle against road shocks such as bumps, potholes, and debris
- To efficiently transmit engine torque to the road surface with little power loss
- To provide adequate braking, driving, and steering loads through tire adhesion
- To ensure lateral and directional stability

The construction of a tire casing and rubber ply layout is important to the load-carrying capacity, lifecycle, steering characteristics, resistance to damage, ride quality, and noise. Radial plies are the more common ply among passenger cars and trucks [32]. The outer portion of the tire is made up of a patterned rubber tread that is vital to the tribological interaction between the road and the tire. The treads can be various styles as shown in Fig. 26.8 and are optimized for different driving circumstances. The purpose of the tread is to squeeze and channel water out of the contact zone to prohibit skidding or hydroplaning. In wet conditions, a fluid film can develop between the contact area of the tire and the road. This contact area can be divided into three zones as shown in Fig. 26.9. The first zone is a purely hydrodynamic area with complete separation between the tire and the road. Zone 2 is a mixed or elastohydrodynamic area where the fluid film thickness decreases to zero permitting partial contact between the tire and the road. The third zone is a boundary area where the fluid has been squeezed out through the plies and the tire is in full contact with the road. From a safety standpoint, zone 3 is the only zone that ensures sufficient frictional traction for driving, steering, and braking. When driving at high speeds and when zone 3 becomes absent, a dangerous scenario can occur. Here, the tire is no longer contacting the ground, but riding on a thin fluid film with inadequate frictional traction, which is known as hydroplaning. Hydroplaning is one of the major reasons for automobile crashes because the tire can no longer adhere to

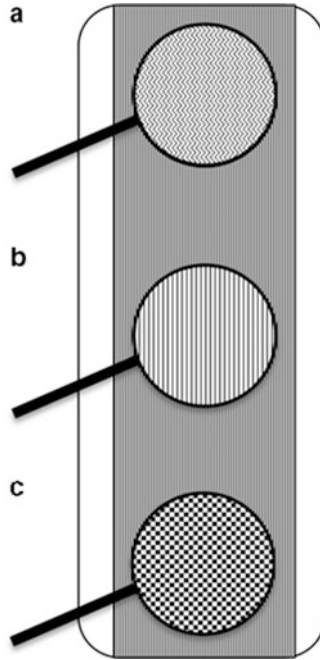


Fig. 26.8 Three basic tire tread pattern designs: (a) zigzag; (b) ribbed; (c) block pattern

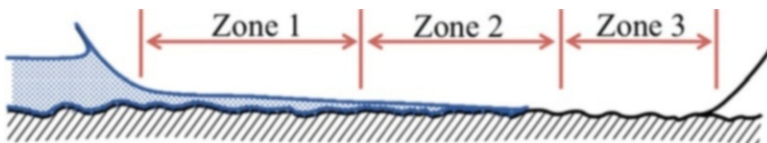


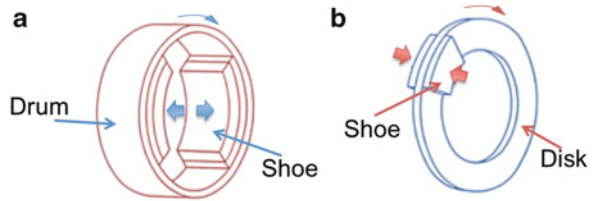
Fig. 26.9 Hydroplaning contact area zones

the pavement resulting in a disastrous driving, steering, and braking situation that can lead to serious injury or even death in the event of a collision. Investigation into the tire dynamics is often difficult because the influencing parameters such as tire design, pavement design, tire construction, tread composition, tire load, inflation pressure, vehicle speed, driving style, ambient temperature, and weather conditions can be variably different from each vehicle, person, or driving location [2].

2.6 The Brakes

Another tribological application that is vital to the performance of a vehicle is the brakes. Brakes can be either drum or disk as shown in Fig. 26.10, and they typically operate by dissipating mechanical energy by means of friction. In some energy-

Fig. 26.10 Vehicle brake types: (a) drum brakes; (b) disk brakes



conscious vehicles, regenerative braking systems are used that convert the mechanical energy in the vehicle into rotational kinetic energy for later use to accelerate the vehicle after breaking. Traditional braking methods utilize a drum brake that applies a normal force by means of a shoe to the drum circumferential area or in the case of a disk brake to the exterior circumferential area as depicted in Fig. 26.10. The main concern for tribologists is the utilization of materials that can provide high coefficients of friction with low wear rates as well as endure the frictional heating that can occur as a result of the dissipation of the mechanical energy. During the braking process, frictional heating can cause brakes to reach temperatures upwards to a few hundred degrees Celsius with asperity flash temperatures reaching beyond 1,000 °C [31, 33]. When considering the function of brakes, attention in the design process must take into account several factors such as thermal wear, abrasive wear, adhesion-tearing, fatigue, and macro-shear wear. These various tribological phenomena all contribute to brake degradation especially in the brake shoe which wears faster than the drum and therefore is often the component needing the most maintenance [31]. Additionally, tribologists must consider contamination in the form of water, oil, dust, and corrosion that can change the effectiveness of the braking system when choosing materials in the design process. It goes without saying that the importance of reliable brakes is vital to the continued success of automobile transportation and the safety of the public.

2.7 Conclusion

The tribological implications in IC engines and drivetrains are vast; it is estimated that in the United States, a few modifications to lower friction and wear would have tremendous reductions in fossil fuel usage and would result in the US economy saving over \$120 billion per year. The continued success of automobiles throughout the world is dependent on the solution of many tribological problems from those in the engine and drivetrain to the tires and brakes. Still, there are other less subtle tribological applications that are taken for granted, such as the windshield wipers. Many of the solutions to tribological problems within the automotive industry require optimization of materials, loads, pressures, and environmental conditions to operate a vehicle safely. The impact of tribology is critical in the automotive industry, and as technology improves, new tribological problems will arise.

3 Rail Transport Tribology

3.1 Introduction

In North America, there are 25,000 locomotives, totaling to 1.4 million freight vehicles riding on 13 million wheels that travel over 170,000 miles of rail, which equates to 35 million tons of steel track [2]. For these reasons, it can be understood that the railway industry has invested more money into rails than anything else except maybe land and bridges. Protecting this investment means extending the life of the rails and wheels. For the railway industry to operate effectively and economically, it is imperative that the tribological issues associated with the wheel-rail interaction be addressed and continually improved upon. Additional tribological issues involve the diesel engine, axle bearings, dampers, and traction motor bearings. This section will focus primarily on the aspects of the wheel-rail system. At the start of the nineteenth century, mechanically powered rail transport began to develop; by the end of the century, a German physicist by the name of Heinrich Rudolf Hertz published a paper on contact mechanics titled “On the contact of elastic solids” [34]. In this publication, Hertz attempted to describe the contact of glass lenses, which ultimately gave way to Hertzian contact stresses. This interfacial contact analysis can be used to describe the contacts between the rails and wheels [35] as shown in Fig. 26.11.



Fig. 26.11 A locomotive's steel wheel rolling on a steel track in a railway system, 1920s

3.2 *Wheel-Rail Interaction*

Passenger trains can weigh about 30 tons, and heavy freight trains can weigh upwards to 140 tons. Each cab has eight wheels that each have an area of contact with the rail of about 300 mm²; this corresponds to approximately the size of a penny [31]. The small surface contact area leads to extremely high stresses and fatigue in the rail. Fatigue results from the cyclic loading due to the multiplicity of four wheels per rail per cab applying the same load to the same contact area. In some severe cases, the stresses normal to the plane of contact can exceed the wheel and rail tensile strength, and at times, the shear stresses can exceed the shear yield stress. During the wheel-rail interaction, slippage can occur between the wheel and the rail causing high shear forces that result in drastic frictional heating with temperature rises reaching several hundred degrees Celsius in normal operation and peaking at over 1,000 °C in extreme operation. As a result of these conditions, the wheel-rail interaction is undisputedly one of the most vital tribological interfaces in the railway system beyond the diesel engine. Since the inception of steel, rather than iron, the wheel-rail system has remained virtually unchanged. The high loading, extreme pressures, and high wear rates taking place are often so immense that it is impressive that the wheel-rail system has been operational with much success and little downtime. To this day, no wheel or rail material has been discovered that offers superior wear or fatigue resistance and yet is economically viable. The complexity of the tribology involved in the wheel-rail system requires a deep understanding of the interactions between the materials of the wheel, rail, and any potential third-body lubricants or debris mixtures. In addition, the vehicle weight, wheel-rail interaction, wheel profile, wheel adhesion, and vehicle speed must be taken into consideration when studying the tribological influences in the wheel-rail system [2].

3.3 *Wheel-Rail Contact*

The rolling resistance of a locomotive is due to the material grade, acceleration resistance, aerodynamic and wind drag, bearing resistance, and wheel-rail contact resistance. From an engineering perspective, the wheel-rail contact is the only resistance that is directly affected by the choice of material and can be optimized through tribological analysis. Within the wheel-rail contact, there are several contributing factors: first, elastic deflection during rolling of the wheel on the rail surfaces; second, energy dissipation by plastic deformation; and third, surface adhesion phenomena can dissipate energy [36]. Additionally, there is plastic flow of the steel surfaces in both the wheel and the rail, which accounts for the smooth shiny appearance of wheels and rails in continuous operation. By comparison, wheels and rails that are intermittently used can become rusted in appearance from lack of use [31]. As the wear continues in the wheel and rail, the contact

profile widens becoming more elliptical. Tribologists investigating the pressure distribution have adopted the three-dimensional Hertzian contact model as a basis for curved bodies in elliptical form to calculate the pressure distribution, which can be described by (26.2)

$$p = p_o \left(1 - \frac{x^2}{a^2} - \frac{y^2}{b^2} \right)^{1/2} \quad (26.2)$$

where p_o is the maximum pressure at the center of the contact, a and b are the semi-axes of the contact area, and x and y are coordinates with their origin in the center of the contact area [2]. The maximum pressure at the center of the ellipse is given by (26.3), which is primarily a function of the weight of the wheels on the rail and the affects of the mechanical properties of the material:

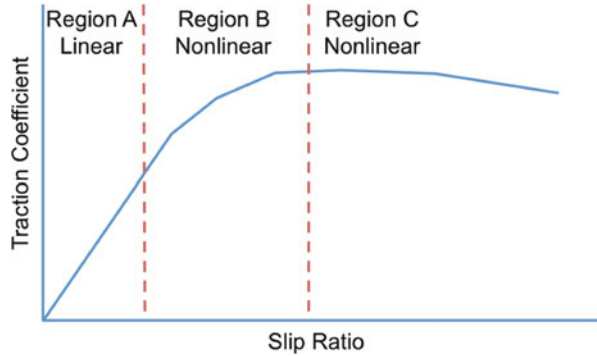
$$p_o = \left(\frac{6PE^{*2}}{\pi^3 R_e^2} \right)^{1/3} \left[f \left(\frac{R'}{R''} \right) \right]^{-2/3} \quad (26.3)$$

In (26.3), P is the normal load (weight) of the wheels on the rail, E^* is the composite modulus of elasticity of the wheel and rail, R_e is the equivalent relative curvature of the wheel-rail system, and $f \left(\frac{R'}{R''} \right)$ is a function of the wheel and rail radius of curvature [35, 37]. Initial approximations indicate that the contact resistance is proportional to the length of the contact area. Therefore, to retard the widening of the contact area, materials are chosen with a high elastic modulus. Steel is the widely chosen material because it offers superior mechanical properties such as high elastic modulus, strength, ductility, and wear resistance at an economical price.

3.4 Wheel-Rail Adhesion

In the wheel-rail contact, the forces acting in the direction of the locomotive's velocity are known as the traction or brake force. The traction coefficient is equal to the traction force divided by the vertical load, which is a function of the weight of the wheels on the track and the slip ratio. The maximum traction coefficient is known as the adhesion coefficient, which is an indicator of the brake performance of a locomotive. The relationship between the traction coefficient and the slip ratio is important when analyzing the frictional heat generation and the shearing that takes place on the surfaces of the wheel and rail [38]. This relationship represented by the traction-slip curve can be divided into three segments as shown in Fig. 26.12 [39]. The first segment represents a region of linear low slip caused by isothermal shearing of a linear viscous fluid or linear elastic solid [40]. The second segment is of a nonlinear, isothermal region with nonlinear viscous elements. The third

Fig. 26.12 Traction-slip curve



segment represents a region with low traction and a high degree of slippage. In this region, dissipative shearing and heat generation in the viscous film are significant. Understanding the relationship between traction and the slip ratio is an important step in understanding the tribological phenomena between the wheel and rail that aid in improving the performance of the railway system. Under high Hertzian pressure, the adhesion coefficient is independent of surface roughness, which is thought to be the result of surface asperities being heavily deformed. Another influencing effect occurs when the rails are coated with water and the locomotive is operating at high rolling speeds; the adhesion coefficient tends to decrease. This is a result of the thin fluid film building up between the wheel and the rail and thus loss of traction from lack of asperity contact. In summary, there is a delicate balance that must be maintained between the wheel-rail contacts. Suitable adhesion and traction must be present at all times in order to ensure a locomotive has adequate steering on straight and curved rails and sufficient braking performance to operate safely. However, to minimize wear of both the wheel and rail, a lubricant is incorporated into the interface, which lowers the adhesion coefficient to tolerable levels.

3.5 Wheel-Rail Repeated Contact

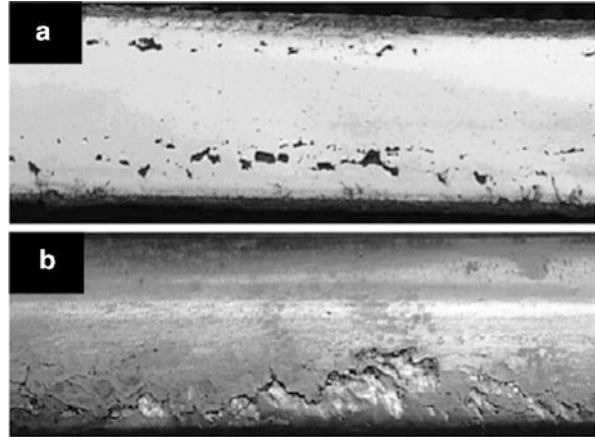
In addition to the wheel-rail adhesion, another concern for tribologists is the lifetime performance of the wheels and rails. During the course of a year, a passenger train can routinely travel 200,000 miles, about 100 million revolutions. This contributes to a significant amount of repeated sliding or rolling contacts [2]. Repeated contacts are of interest because they cyclically stress the material producing four net effects. The first is a perfectly elastic behavior whereby the contact pressure at the interface does not exceed the wheel or rail elastic limit during any load cycle. The second result takes place when plastic deformation occurs in early cycles causing a development of residual stresses and strain hardening, ultimately ending in a perfectly elastic steady-state behavior known as elastic shakedown. A third result takes the forms when no plastic deformation occurs and

only a steady-state elastic-plastic behavior exists; this is known as plastic shakedown. The last result is known as ratcheting and occurs when the steady-state behavior is an open elastic-plastic loop that undergoes material accumulation and a net unidirectional stress during each cycle. In order to minimize the effects of repeated contact, tribologists try to minimize the plastic deformation which can lead to accelerated rates of wear and surface degradation. Surface engineering has led to a minimization of the plastic deformation and the shakedown by utilizing techniques such as variable hardening and surface texturing by changing the surface roughness of the material used on the wheel and rail [41–47].

3.6 *Wheel-Rail Wear*

Recent efforts within in the railway industry have been focused on the prevention of wear on the wheels and rails. Wear of components is the fundamental cause for replacement of most components. All railroad systems throughout the world have different criteria for removing worn rails; however, the majority of them fall within the bounds that a rail should be replaced when 30–50 % of railhead area has been removed. Rails tend to wear on the inner edge of the outer rail in curved tracks where the wheel flange initiates the contact. In straight and large radius curved tracks, the rail wear is generally vertical due to wheel tread. For the wheels, they do not necessarily need to be replaced when the flange has worn down too thin or the tread wear has left the flange too high. Wheels are traditionally re-profiled by machining when they cause a reduction in steering ability and are replaced when enough material has been lost through wear and machining that the stresses within the wheel are unacceptably high making the material a high risk for failure. Presently, four wear mechanisms occur in the wheel-rail system adhesion, abrasion, fatigue, and fretting. Adhesion takes place in the absence of a third-body lubricant or contaminant between the wheel and rail causing the metal surfaces to bond strongly to each other's asperities in contact. Due to the relative motion between the wheel and the rail, the contact interface experiences shear resulting in wear debris and damage to the rail and wheel. Abrasion occurs when the wheel or rail material hardness is significantly different enough to cause the harder material or in some instances wear debris to plow through the softer material by plastic deformation or fracture [37]. The third wear mechanism is fatigue; this arises from the cyclic normal and shear stresses produced by the rolling and sliding motion of the wheel on the rail. Fatigue causes cracks to initiate and propagate through the surfaces of the wheel or rail and causes a delamination of the surfaces to occur as illustrated in Fig. 26.13. Contrary to the previous wear mechanisms that are directly responsible for the wear in the wheels and rails, fretting is a consequence of low-amplitude vibratory motion between two bodies, either the wheel and rail or the wheel or rail and any accumulated wear debris [48]. In addition, ratcheting is important because it can cause plastic deformation that can result in significant wear damage from highly sheared surface layers.

Fig. 26.13 (a) Low rail surface damage caused by rolling contact fatigue; (b) high rail surface damage caused by rolling contact fatigue



3.7 Conclusion

Railway tribology is a vital part to the sustainability of railway transport. It investigates the crucial problems that would inevitably cause deterioration in the railway network through rail deterioration, performance of bearings and current collection equipment, and the maintenance of these systems. The millions of miles of railway track around the world require important tribological issues to be addressed at the wheel-rail interface to minimize railway maintenance and to provide safe and economical railway operation. Major strides in developing materials and understanding the tribological phenomena in railway transport would lead to a better understanding of the mechanical and chemical interfaces. The focus on increasing the allowable axle and wheel loads while maintaining low wheel and rail wear and damage is necessary for the future of locomotive transportation both for industrial and commuter needs. In addition, advances in track monitoring and inspection must be at the forefront of research in order to better manage rail lifetime and extend the period between maintenance inspections.

4 Tribology of Earthmoving, Mining, and Mineral Processing

4.1 Introduction

The practices of earthmoving, mining, and mineral processing are tribologically intensive activities that involve digging, loading, hauling, crushing, handling, screening, and grinding mineral ore. These processes result in significant wear in the mechanical interaction between the metals and the abrasive mineral ore.

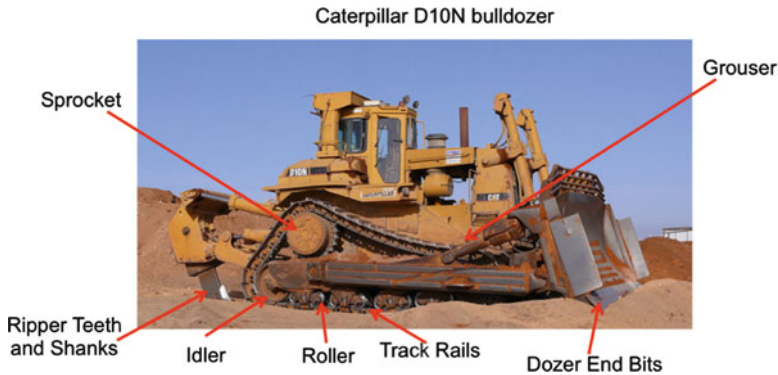


Fig. 26.14 View of a Caterpillar D10N bulldozer showing major components affected by abrasive wear [76]

The construction of a building, bridge, dam, road, or highway involves the use of earthmoving devices such as bulldozers (depicted in Fig. 26.14), scrapers, graders, excavators, front-end loaders, draglines, stripping shovels, and dump trucks. Mining and mineral processing involves the operation of digging, drilling, loading, and hauling materials using equipment such as crushers, grinders (mills), sand pumps, classifiers, flotation machines, and magnetic separators [49]. As a direct result of the operation of such machinery, there is an inherent tribological loss due to the amount of energy that is required to overcome the frictional forces. Despite the significant frictional forces, the wear loss due to the abrasion in these processes can be upwards to five times greater than the frictional losses [50] with many components on a single machine suffering from abrasive wear as shown in Fig. 26.14 with the bulldozer.

Earthmoving, mining, and mineral processing machinery makes significant use of easily replaceable, repairable, and inexpensive wear components that are very tolerable to the high wear rates. The wear mechanisms that transpire during these construction processes are complex and depend on the wear mechanism, the wear material, the nature of the abrasive material, the type of loading, and the environment [51–53]. From a tribological perspective, the interaction between the metal components and the earth demands materials that exhibit excellent ductility and work-hardening properties. For example, the transportation of ore through a chute, conveyor, and screen or the scraping of earth and gravel with a blade requires that the interacting components maintain a high surface hardness. Mining and mineral processing often operate in corrosive environments that require materials to be both wear and corrosion resistant. Through practice, tribologists and material engineers have been able to combat the wear losses, frictional resistance, and environmental demands by developing innovative materials. These materials offer superior wear, abrasion, and impact resistance that can be used in a broad range of in-service operational conditions as well as daily in excavation operations.

In the last few decades, the earthmoving, mining, and mineral processing industries have increasingly enlarged their equipment, which subsequently has

led to more disastrous tribological issues involving wear, abrasion, and impact levels [53]. The growth of the equipment in these industries has been propelled by the mining industry to seek out lower-grade ores, thereby requiring a larger output of raw material while simultaneously lowering operating costs, therefore making the entire process economically feasible. As a result of the larger equipment, the quantity of material handled per unit of operation has led to more severe conditions to which wear, abrasion, and impact resistance materials must be subjected to. Additionally, emphasis is put on the importance of prolonging component lifetimes and projecting failure rates to minimize the amount of unscheduled maintenance. This is because despite all of the capital and operating costs for purchasing the equipment and other auxiliary expenses within these industries, the cost of downtime and loss in production drastically outweigh the cost of replacing worn components [50, 54, 55]. Although replacement of worn components is routine and the cost is relatively minimal, the selection of material and design of components that promote longer component lifetimes, easier installation, and lower cost remains to be important. In addition, engineers must concern themselves with the selection of materials based on availability, potential risk for catastrophic failure, and environmental considerations such as noise abatement [54]. The use of higher-cost materials and components is often restricted to two constraints. The first constraint being the use of more expensive wear-resistant materials to boost performance may in fact be cost-effective in terms of component life; however, in the macroscale, these materials ultimately drive up the capital requirements. The second constraint being the original design for much of the equipment used in these industries may not be optimal for a given process, causing it to be retrofitted later. It is for this reason that the use of expensive wear-resistant materials may not necessarily be cost-effective in the long term.

4.2 Wear Mechanisms in Mining and Mineral Processing

The tribological problems affecting earthmoving, mining, and mineral processing operations are the wear mechanisms and friction losses that cause the equipment used in these industries to expend large quantities of energy to perform their function. The wear mechanisms in these applications are affected by the properties of the wear material, the properties of the abrasive material, and the nature and severity of the interacting materials. For example, the interaction between adjacent metal surfaces, the abrasive mining materials, and the worn metal debris all contribute to the various wear mechanisms occurring. These interactions are further influenced by the size, density, and hardness of the abrasive particles, for example, if the abrasive particle is sharp and remains sharp after fracture, then cutting or gouging action of the abrasive particle will continue to abrade material from the machine components. Figure 26.15 shows the abrasive wear classification, relating the particle size to the wear mechanism [54]. The design and function of

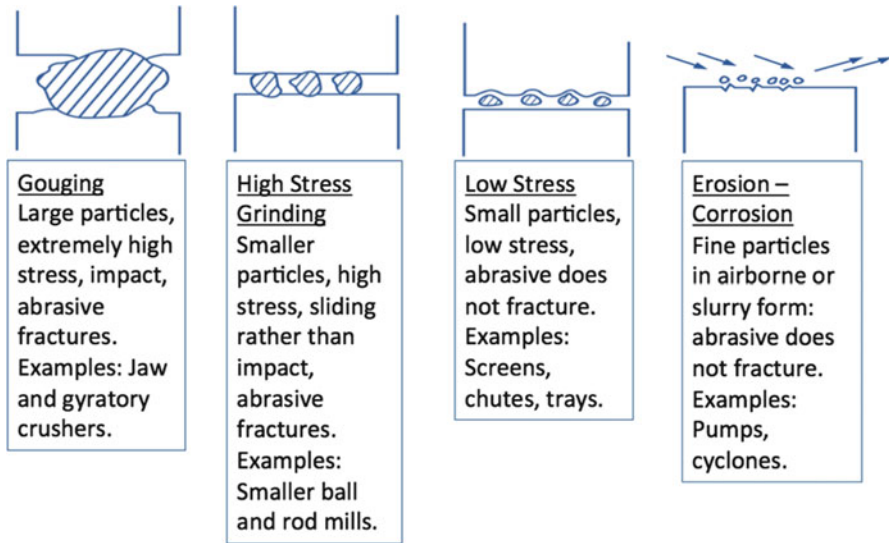


Fig. 26.15 Schematic representation of the abrasive wear classifications [54]

earthmoving, mining, and mineral processing equipment play a significant role in the quantity of wear that they experience. Earthmoving equipment experiences more abrasive wear from digging and removal of earth (such as the wear of digger teeth on a bucket excavator) than they do from scraping operations. The wear rates exhibited in crushing and grinding operations are higher than those which occur in chute linings, screens, and classifiers, because they are more energy demanding and require greater impacts and thus increase the abrasive wear.

The abrasive wear mechanism that occurs in earthmoving, mining, and mineral processing operations can be classified into five categories as shown in Fig. 26.15: gouging and abrasion which describes the removal of large amounts of material per cycle from the wear surface; high-stress grinding abrasion (or three-body abrasion) where the abrasive particle is crushed during the wear interaction; low-stress scratching abrasion where the abrasive particle remains intact as it moves freely across the wear surface; low-stress scratching in the form of erosion; and low-stress scratching abrasion in a corrosive environment described as erosion-corrosion. As mentioned previously, the occurrence of any one of these abrasive wear mechanisms arising depends on the equipment, environmental conditions, and ore material being excavated. Table 26.2, primary tribological loss mechanisms in mining, highlights the tribological losses that occur in earthmoving, mining, and mineral processing operations [50]. It can be seen from Table 26.2 that the three-body abrasion occurs in all mining and drilling operations and is responsible for the majority of the wear to the equipment. Ore processing operations involve many tribological loss mechanisms revealing how detrimental the ore material is to components in the mining industry. Earthmoving, mining, and mineral processing operations each experience their own unique wear mechanism depending on the

Table 26.2 Primary tribological loss mechanisms in mining [50]

Operational activity	Active tribological mechanism					Lubricated wear
	Three-body abrasion	High-stress gouging	Impact wear	High friction	Erosion	
<i>Surface mining</i>						
Exposing and digging	X	X	X	X	–	X
Loading	X	–	X	–	–	–
Transporting	X	–	–	X	–	–
<i>Shaft mining</i>						
Digging	X	–	X	–	–	X
Transporting	X	–	–	X	–	X
<i>Ore processing</i>						
<i>Drilling</i>	X	X	X	X	X	X
Mud pumps	X	–	–	–	X	–
Drill pipe	X	X	–	X	X	–
Drill bits	X	X	X	–	X	–

required force levels, abrasive particle type and size, and operating or environmental factor. For these reasons, it is important to monitor the performance of components and replace worn components in order to minimize the risk of catastrophic failure.

As described, the dominant wear mechanism is abrasion; however, the secondary wear mechanism arises from metal-to-metal contact. In earthmoving, mining, and mineral processing equipment, metal-to-metal contact occurs in engines, drivetrains, connectors, bearings, and gears. In most of the equipment, the engine and drivetrains are closed off to the operational environment and wear surfaces are lubricated. However, the metal-to-metal wear is often worsened by abrasive particles due to the environmental conditions in which the machinery operates, which have the ability to cause severe problems. Discussion of the engine, drive-train, bearings, and other components was discussed previously in this chapter and is beyond the scope of this section.

4.3 Conclusion

In earthmoving, mining, and mineral processing, much of the research has focused on the equipment design, unit operation processes, wear-resistant materials, and repair and replacement techniques that can all be used to combat the effects of abrasion, erosion, impaction, and wear-corrosion. As the quality of ore minerals decreases, there will be a driving force for larger-scale mining operations that will necessitate new and improved materials that are energy efficient. The effort put into understanding the relationships between wear mechanisms and processes in earthmoving, mining, and mineral processing operations will facilitate the development of

innovative wear, corrosion, and impact-resistant materials that will be less expensive, easy to install and repair in the field, and require less energy. Many of the tribological mechanisms involved in these industries will prove to be beneficial in other industries such as metal production, agriculture, and pulp and paper processing.

5 Tribology in Marine Equipment

5.1 Introduction

Investigations into the tribological challenges of marine equipment present a unique set of problems for tribologists in terms of fuels and lubricants used within the confines of an engine and propeller shafts. Many of the components of interest are cams, gears, chains, hydrodynamic thrust bearings, journal bearings, pistons, and rolling element bearings. The major differences in marine equipment when compared to their terrestrial counterpart is the environment and operating conditions, necessitating chemically modified fuels and lubricants to function properly under the demands of seafaring vessels. One of the issues that arise with boats, ships, tankers, and other seafaring vessels is their need to be self-sufficient throughout an entire voyage. The varying scales of equipment from large aircraft carriers and warships to small commuter boats and fishing vessels require many unique solutions to solve the wide range of applications.

On one side of the spectrum, there are very large ships such as aircraft carriers that operate with a nuclear reactor capable of powering a medium-sized city. Here, nuclear-powered vessels are used to power onboard steam turbines. The tribological issues in turbine engines focus primarily on the journal and thrust bearings that require the development of large hydrodynamic films and the gears used in the speed reduction systems that require lubricants with extreme pressure additives for wear and friction reduction. On the other side of the spectrum, there are relatively small ships that typically operate with a diesel engine of only a few horsepower and have been modified from their original use in automobile engines to work in maritime applications. This section will explore the tribological issues pertaining to maritime lubricants and discuss the challenges presented in maritime diesel engines of these smaller ships.

5.2 Maritime Lubricants

Over the last several decades, diesel engines have become the engine of choice in commercial ships. Maritime diesel engines are powered using fuels that have a higher viscosity index than the traditional automotive diesel engine. A benefit of these fuels is that they have lowered the fuel cost by reducing the necessary refinement. However, this is not without consequences; thicker fuels are more

difficult to pump or atomize in the combustion chamber at ambient conditions, and thus, they must be preheated to acceptable temperatures, resulting in higher operating temperatures [56]. In addition, marine fuels are more susceptible to contaminants and increased acidity due to the higher levels of sulfur used as an extreme pressure additive. The high sulfur concentration produces the acidic environment in the engine due to the byproduct of sulfur oxides in the combustion process. Another tribological concern is the suspension of carbon particles in the fuel, which can lead to fouling in the cylinders and cause rings and pistons to stick. Furthermore, abrasive particles matriculate into the engine due to the lack of refinement of the fuel causing an increase in engine component wear rates when compared to traditional fuels used in automotive or aviation diesel engines.

The goal of tribologists and lubrication engineers in marine equipment is to formulate lubricants with the appropriate additives to minimize the acidic effects and reduce the harmful emissions from the combustion process. The importance of minimizing the sulfur oxide and nitrous oxide emissions in maritime engines is a result of their significant environmental impact. Sulfur oxide emissions are generally released in the sea and, through the hydrological cycle, create acid rain [57]. A number of countries are enforcing stringent emission regulations in coastal waters to help combat environmental issues that could potentially harm sensitive ecological systems surrounding many coastal regions [58].

5.3 *Maritime Diesel Engines*

Maritime diesel engines can be categorized into three groups: high-speed engines operating above 1,000 RPM, medium-speed engines operating between 250 RPM and 1,000 RPM, and slow-speed engines (see Fig. 26.16) operating under 250 RPM [56]. Typically high-speed diesel engines are used in pleasure or sport boats and have engine characteristics similar to automobiles in terms of design, fuel, and lubricants used. Medium-speed maritime engines consist of a four-stroke engine with a high power-to-weight ratio. These engines are used mainly in ferries, container ships, and cruise ships. They use the same fuel as slow-speed engines and have many similar tribological issues. Slow-speed diesel engines are of the two-stroke arrangement and are the largest of the three categories of maritime diesel engines with bore sizes around 1 m and stroke lengths over 3 m. In these engines, the cylinder and crankcase are separated by a diaphragm and stuffing box and the motor directly drives the propeller shaft without the need of a reducing gear or clutch. Slow-speed engines are customarily used in large tankers and passenger liners because of the high fuel efficiency due to their long combustion times and low friction.

The tribological problems that arise in slow-speed engines present themselves when trying to lubricate the separate cylinder and crankcase. The benefit in such a system is that an optimized lubricant can be used for each component without adversely affecting the other. A drawback to having separate lubricant supplies is the requirement of independent preventative maintenance schedules. Solutions to

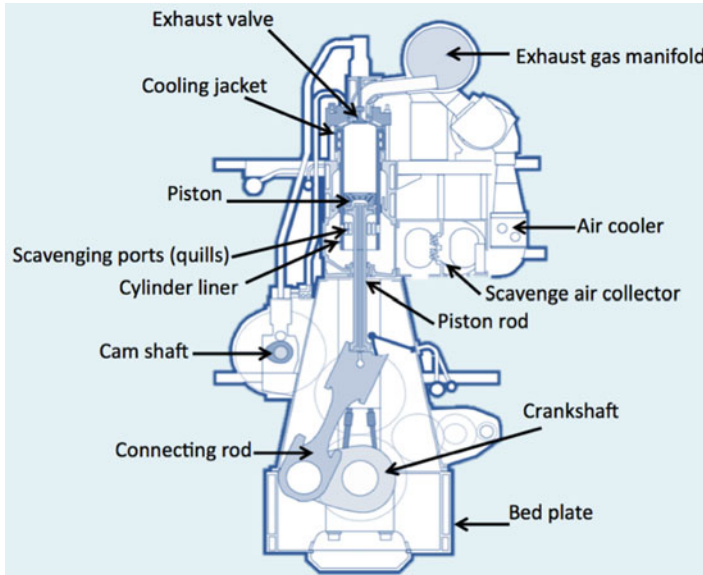


Fig. 26.16 Schematic illustration of a slow-speed (<math><250\text{ RPM}</math>) crosshead diesel engine

slow-speed engine problems often circumvent around lubricant chemistry and coating optimization to thwart corrosion and corrosion-assisted fatigue and wear in the engine due to the acidic nature of the fuels and combustion by-products. Further, problems can develop if lubricant flow rates are too high or low. If over-lubrication occurs, fouling of the cylinder or worse post-cylinder fires can become prevalent, resulting in significant repair costs. Under-lubrication causes the oil to insufficiently neutralize the sulfuric acid and become less effective. The result is periodic wear patterns where significant corrosion fatigue wear and corrosion-assisted abrasive wear have damaged the cylinder liner [59]. To prevent damage against cylinder liners and piston rings, chrome-electroplated and chrome-plated or plasma-sprayed coatings are applied, respectively. Oils in the crankcase lubricate the gears and bearings among other engine components. Within the crankcase, oil leeching through the piston rod diaphragm can become a major concern because it can introduce external contaminants such as cylinder liner wear debris, combustion by-products, and seawater leakage. These contaminants degrade the lubricant's performance and facilitate galvanic corrosion and rusting of tin-based alloys (which are used in journal bearings) producing a black oxide layer. This oxide layer can cause increased asperity contact and higher friction between the bearing and journal resulting in failure. Additionally, the oxide layer can flake off and become a third-body wear particle.

Due to the adverse effects of contaminants in the crankcase, engineers have developed a set of requirements for oils and additives to be used in lubricants, and they are as follows: sufficient viscosity, oxidation and thermal stability, demulsibility, rust and corrosion prevention, antifoaming, detergency, extreme

pressure performance, and biocides [60]. It is important that highly refined or high-viscosity-index oils or synthetic oils are used as bases to produce lubricants that have appropriate viscosities for operating at high temperatures. In addition, the oxidative and thermal stability of the oils and additive become a concern because the piston temperature generated during engine operation can be high enough to thermally degrade the lubricant resulting in a loss of viscosity. In the event of seawater contamination, additives are incorporated into the lubricant facilitating emulsification of the seawater in the oil for easy separation. As previously mentioned, rust and corrosion are contributors to wear debris and degradation of components, and thus, the importance of inhibiting additives will extend the lifetime of the engine. Antifoaming additives are used to ensure proper flooding of contacts and pump operation. Detergency additives are included in the lubrication formula because combustion by-products such as carbon- or ash-based soot can foul components and inhibit effective engine performance. During engine operation, many of the contacts occur under high pressure resulting in tremendous friction and wear; extreme pressure additives in the lubricant are used to minimize these affects. The last requirement for lubricants has become prevalent due to biological attacks from organisms that survive in the seawater. The microorganisms reduce the effectiveness of lubricants by clogging filters. Their effects can be minimized by reducing the amount of seawater that leak into the crankcase. Despite the best preventative maintenance, in some instances, this is unavoidable and thus biocide additives must be added to the lubricants to prevent microbial growth. The other solution is that the oil must be heated to a high enough temperature to sufficiently kill the microbes; however, this process can cause thermal fatigue of the oil.

5.4 Conclusions

Many of the tribological concerns with slow-speed engines are also present in medium-sized engines except that often the same lubricant is used to lubricate both the cylinder and crankcase in slow-speed engines. The primary concern of maritime equipment is designing the systems and lubricants to operate and function reliably while meeting the demands of seafaring vessels and maintaining a sense of self-sufficiency throughout an entire voyage. The environment and operating conditions in maritime applications present significant challenges that necessitate the development of chemically modified fuels and lubricants to ensure safe, reliable, and compliant operation. In recent developments, tribologists have begun investigating other maritime tribological issues. One such issue is the study of frictional drag reduction between the outer surface of a ship and the ocean water through the development of surface manipulation techniques such as surface texturing and hydrophobic coatings. As maritime equipment advances, new concerns will undoubtedly arise prompting more innovative solutions to the internal propulsion and lubrication systems or external surfaces of the hull. No matter where the advances occur, tribology will certainly play a role in the progression of marine equipment.

6 Tribology in Gas and Steam Turbines

6.1 Introduction

Gas and steam turbines are variants of the basic turbine engine type used to generate power output in the form of thrust or shaft horsepower. A gas turbine burns fuel to create thrust and is generally found in aircraft engines as turbfans or turbojets to propel an aircraft forward. Steam turbines are extensively used in the power generation industry and on large ships to convert high-pressure steam into shaft (mechanical) power through expansion, which can then be used to produce electricity or shipboard propulsion. Within these turbine systems, there are bearings, seals, and gearboxes that require lubrication to ensure proper operation. Often, the lubricant has three roles: to provide lubrication, to remove heat, and collect contaminants. In these systems, the starvation of the lubricant would cause increased friction and wear in the moving parts, thus generating larger amounts of heat that can have detrimental effects on the turbine performance and create dangerous safety hazards. The tribological considerations involved with gas and steam turbines are directly related to their environmental and operational conditions. Gas turbines used in aircraft must constantly circulate, cool, and filter the oil as it travels through the internals of the engine. Similarly, steam turbines must perform the same tasks as well as deal with corrosion issues due to the presence of water and particles in the lubricant and in the steam. The performance issues associated with gas and steam turbines are also present in wind turbines. Wind turbines similarly suffer from particulate and water contamination that affect critical machinery such as gearboxes, yaw drives, pitch drives, bearings, and filtration systems [61, 62]. Many of these issues are so severe in wind turbines due to their lack of maintenance that failure occurs before their designed lifetime [63]. In the following sections, gas and steam turbine systems will be discussed in detail to provide an overview of the tribological challenges plaguing each of their systems.

6.2 Gas Turbines

6.2.1 Overview

Gas turbines are typically used to power aircraft, helicopters, small ships, power stations, pumping stations, and sometimes in vehicles. Figure 26.17 reveals the various mechanical arrangements of aeroengine gas turbines [64]. Regardless of their application, the construction of a gas turbine is composed of three main systems—the compression, combustion, and turbine systems. Throughout each of these systems, there are ancillary components that are critical to the operation of the turbine. The compression system introduces air into the gas turbine while simultaneously compressing it before the air enters the combustion system where the

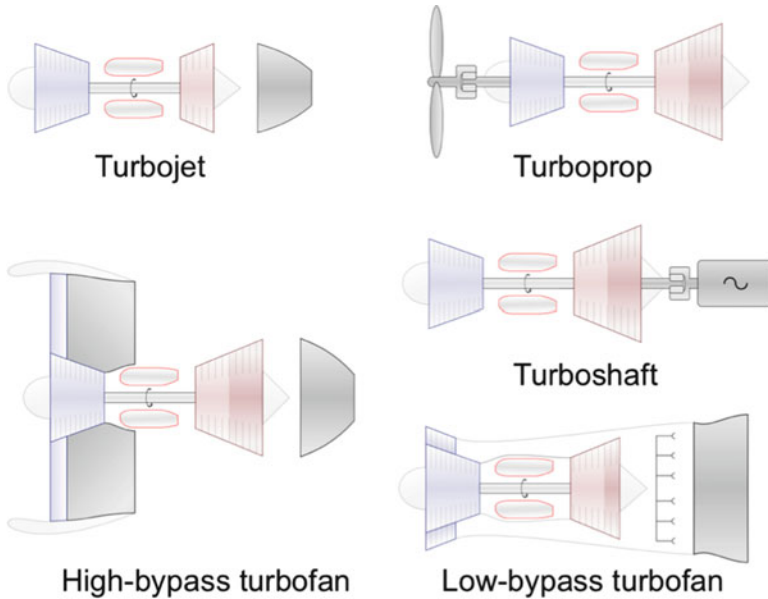


Fig. 26.17 Schematics of various aeroengine gas turbines [77]

fuel-air mixture is burned providing heat energy to the system where the turbine blades can rotate as low as 2,500 RPM and increasing beyond 40,000 RPM providing the necessary power output [64]. Due to the requirements of gas turbines to operate at the highest possible efficiency, the combustion system is designed to operate at the highest temperature possible. The largest restriction that prevents reaching the maximum operating temperature and thus having the highest thermal efficiency is the selection of material in both the combustion and turbine systems. Throughout the gas turbine engine, bearings, gearboxes, and seals are used to ensure that shafts rotate smoothly between fixed parts of the engine's internal structure and lubricants remain in their prospective domains. The bearings and gearboxes generate large amounts of excess heat through frictional heating from the contact between the rollers or balls in the bearing and the bearing inner and outer races or the meshing of the teeth between rotating gears. In an attempt to minimize the heat generation, frictional resistance, and other detrimental effects, oil is supplied as a lubricant into the bearings and gears.

6.2.2 Oil System

The gas turbine lubrication system is a full engine circulatory system that provides lubricating oil to all the necessary rotating assemblies such as gears, drives, and bearings. The purpose of the oil is to remove the excess heat, lubricate the components, and accumulate contaminants and wear debris within the system

throughout all operational and environmental conditions and power settings. The lubrication system is designed to provide the appropriate amount of lubricant to each of the rotating assemblies with regard to cleanliness, pressure, temperature, and quantity. This is performed by the oil feed, cooling system, oil return system, and the oil breather (vent) system. Within the lubrication system, heat management is important because one of the pivotal jobs of the oil is to remove excess heat by acting as a coolant. However, as the oil system is circulatory, there must be a subsystem that removes heat from the oil to ensure the oil remains within its thermal operating limits and does not undergo thermal degradation or stress. The subsystem generally utilizes one of two methods for cooling the oil, a fuel-cooled or air-cooled heat exchange system. The fuel-cooled heat exchange system allows the fuel being supplied to the combustion system to absorb the heat through a cross-flow heat exchanger. The air-cooled heat exchange system uses one of two techniques. The air diverted from a compressor is diverted into a heat exchanger, or the air passing over the engine's nacelle is diverted into a heat exchanger. Both of these techniques are similar to the air passing over a car's radiator to cool the oil. A beneficial feature to cooling the oil with the fuel-cooled heat exchange system is that it allows the oil to warm up the hygroscopic fuel and melt any potential ice crystals that may have developed as the fuel sat in the wing tanks while flying at high altitudes. The ice crystals pose a threat by blocking fuel filters or damaging parts of the fuel control system.

6.2.3 Component Lubrication

Due to the high temperatures reached in gas turbines and the extreme rotational speeds, the importance of providing lubricant to the moving components is vital for sustained operation. Ball bearings, roller bearings, and thrust bearings are used to support and allow correct axial rotation of the shafts. Gearboxes are used to provide drive to rotating accessories, power transfer to off-take shafts, and as reducers for drive propellers. Lubricating these components can be performed by three methods: jet feed where oil is directed to the annulus gap in a bearing between the inner and outer races or at the teeth meshing in a gearbox, under shaft feed where oil fed from holes within the shaft to lubricate the inner race surfaces by centrifugal forces, or through splash feed where oil is splashed onto the bearings and gears. An additional feature of the oil is its ability to act as a vibrational damper, where a squeeze film can develop between the outer race and the bearing housing, thereby dampening out any induced vibration. To ensure the lubricant only flows within its system, a series of carbon, brush, labyrinth, ring, and hydraulic seals are utilized to seal the rotating assemblies. As with many seals, degradation can occur in the form of wear and corrosion that can cause oil to leak into other portions of the engine and mix with air resulting in losses of oil. As a precautionary measure, many gas turbines incorporate oil system indicators relaying information about oil pressure, temperature, quantity, and filter blockages that will aid in preventative system maintenance and minimize gas turbine downtime.

6.3 *Steam Turbines*

6.3.1 Overview

Steam turbines operate by taking steam and feeding it through an inlet casing, throttle valves, and into a turbine. After entering the turbine, the steam expands and accelerates through a stationary nozzle flowing past a series of rotating blades on a turbine where the kinetic energy is converted into torque. The rotary motion of the turbine causes the steam to lose pressure and decrease in temperature, while the torque is used as mechanical energy to power drive machinery. In most cases, the driving machinery consists of generators but can also involve centrifugal pumps, compressors, blowers, and propellers. Steam turbines are typically designed to operate continuously for years at a time without shutting down. Due to the design of a steam turbine, it is vital for the lubricant to be separated from the steam path to prevent contamination of the exhaust steam. This allows for the exhaust steam to be recycled by undergoing condensation and reheating within the system. Moreover, the lack of internal lubrication to the steam path results in relatively low oil consumption [65]. The major components of a steam turbine are the rotor, the stationary parts, the governing and trip systems and valves, and the auxiliary systems such as the lubrication and monitoring systems. From a tribological perspective, the lubrication system and the steam path are important because this is where the majority of the tribological issues affecting friction, wear, lubrication, erosion, and corrosion occur. When these systems are not running at their desired performance levels, they can render a steam turbine inoperable in the worst case.

6.3.2 Tribological Issues of Lubricated Components

Steam turbine lubricating oil performs four functions: (1) lubricate bearings and gears; (2) cool lubricated components by removing excess heat; (3) act as a hydraulic fluid for governor, control valves, and safety devices; and (4) act as a sealant for gas seals. The components in a steam engine that require lubrication are similar to those found in a gas turbine, except in a steam turbine they reside outside the steam path. Proper isolation techniques must be in place to prevent contamination of the steam or contamination of the lubricant by environmental factors. Journal, thrust, hydrodynamic, and rolling element bearings are used to support the rotation of shafts, ensure proper axial positioning of shafts, and support thrust loads that may arise from the steam forces. Within these systems, components are lubricated in the clearance spaces. In a bearing, these clearance spaces occur between the inner race, outer race, and bearing housing. Improper lubrication can cause bearing distress, failure, overloading, insufficient oil flow, insufficient bearing clearance (or endplay), excessive overspeed (or vibration), and high inlet oil temperatures, all of which are detrimental to the bearing, detract from its

performance, and limit its operational lifetime. During maintenance inspections, bearings are examined for wear or distress, such as scoring, cracks, pivot fretting, electrostatic discharge, heat discoloration, corrosion, flaking, signs of overheating, contamination of oil in the form of varnish deposits, and loss of babbitt bonds [64]. Other tribological issues involve various lubrication techniques to reduce friction, decrease wear, and minimize thermal expansion, thus reducing the likelihood of binding which can cause distortion, misalignment, and vibration.

Due to the continuous use of steam turbines and the many functions the lubricant plays, it is often necessary that the oil is optimal in regard to chemical, physical, and performance criteria. Oil is modified through the addition of additives to ensure proper viscosity, oxidation stability, freedom from sludge, anticorrosion protection, water separability, air separability, and resistance to foaming [66]. Degradation of the oil can occur from contamination, additive depletion, thermal cycling, oxidation, and bacteriological deterioration. Contamination is an unavoidable occurrence in the lubrication system due to imperfect seals or sealant degradation. The hygroscopicity of the oil causes water to be present in oil at all times whether in free or emulsified forms. The water itself does not pose any problems to the lubricating properties of the oil or have any corrosive effects to components. However, when hot oil cools, water droplets can emerge from the oil [67]. It is these water droplets, which cause corrosion to some metallic surfaces by foaming, sludge formation, or changes in viscosity. Additionally, the water droplets can cause oxidation, additive removal, and bacteriological contamination and reduce the effectiveness of filtration systems. Soluble contaminants such as gases, solvents, flushing oils, preservatives, sealants, and other lubricants can also percolate into the oil; however, they can be removed by vacuum dehydration methods [64]. The normal operation of bearings, journals, gears, and other control mechanisms produce abrasive wear debris that can often contaminate the lubricating oil. If this occurs, flow filtration techniques are required to remove the unwanted contaminants in order to prevent possible failure of components. Additive depletion is a natural occurring phenomenon in lubricants because as additives undergo chemical, physical, or biological reactions, the additive becomes depleted and must be replenished. In some instances, contaminants in the oil react with the additives causing premature additive depletion. Thermal degradation in oil occurs when the oil becomes thermally stressed through the absorption of heat that is often beyond the operating conditions of the oil. Oxidation degradation arises when the oil reacts with the oxygen present in the ambient air. This can cause rust, corrosion, foaming, and poor demulsibility of the oil. Bacteriological deterioration occurs in the form of bacteria or fungal growth in lubricating oils and is the result of biological contamination, high water content, and habitable temperatures. Biological growth in the lubrication system can cause filter blockages and the formation of deposits. Prevention techniques involve the use of proficient cleaning methods, high-temperature sterilizing practices, frequent draining of moisture from the oil, the avoidance of dead legs or noncirculatory areas in pipes, as well as using biocide and antimicrobial additives [68]. Despite the many ways that lubricating oils can deteriorate, by

establishing effective preventative procedures, lubricant lifetimes can range from 10 to 20 years or longer with periodic additions of fresh oil [69].

6.3.3 Tribological Issues of Nonlubricated Components

Within the steam path of the steam turbine, there are tribological issues that can arise beyond the scope of lubricants. As mentioned previously, components such as casings, rotating blades, stationary nozzles, seals, valves, and valve guides are nonlubricated components to prevent contamination of the steam. Multiple erosion, corrosion, and wear mechanisms can occur to components in the steam path resulting in loss of power, efficiency, and operation of the turbine. The three prevalent deleterious mechanisms are moisture impingement erosion, erosion-corrosion, and solid particle erosion. Water droplets in the steam cause moisture impingement erosion to the turbine blades as well as compromise the integrity of seals. The result is a change from the optimal thrust loading and a decrease in system performance [70]. Erosion-corrosion problems caused by impurities in the steam develop deposits on the inner surfaces of the steam path such as the casing, nozzles, blades, seals, and sealing surfaces. The deposits may be corrosive if they contain, for instance, chlorine which can lead to pitting and stress corrosion cracking [71]. Other instances of corrosion can develop in geothermal steam turbines due to the presence of mineral constituents and the high acidic levels [72]. When particulates from boiler tubes and steam leads become entrained in the steam, they can lead to solid particle erosion [73]. To prevent steam path erosion and corrosion, it is important to properly condition the steam to ensure reliable operation. This can be done by utilizing separators, moisture removal devices, and strainers upstream and inside the turbine to remove water, contaminants, and particles from the steam. Other solutions to prevent steam path erosion and corrosion involve the use of hardened materials inside the steam path or by providing vulnerable components with corrosion-resistant protective coatings [73]. Other erosive wear mechanisms such as standby corrosion can occur when steam turbines are not in use and suddenly become filled with water vapor due to a valve leak. The stagnant steam can enter the steam path, condense, and cause pitting to various components [74].

6.4 Conclusion

Gas and steam turbines have many tribological issues that plague their performance, reliability, efficiency, and safety. Although a number of performance advancements have been made in gas and steam turbine technology through improved condition monitoring techniques such as magnetic chip detectors, advanced filtration techniques, and lubricant modifiers to aid in the immediate future, there is still a great deal of current and future tribological issues that need effective solutions. Many of the issues that plague gas and steam turbines are now

gaining attention in recent decades through the development of wind turbines. Gas and steam turbines as well as wind turbines suffer from particulate and water contamination that affect the performance of gearboxes, drives, bearings, filtration systems, and lubrication systems. In fact, when examining wind turbines, many of these issues are so severe that their components are failing quite rapidly within a few years in contrast to their proposed lifetime of 20 years. As mechanical and tribological research progresses, the various types of turbine technology should improve through the development of corrosion-erosion-resistant materials, improved lubricants, and by better understanding the physical phenomena that plague these systems.

7 Closure

Tribology is a vast field with applications in almost any industry from aerospace to rail transport, from automotive to mining. Understanding of tribological principles is essential for continued success and development of many systems. This chapter sought to shed light upon the interdisciplinary aspects of tribology by portraying the tribological challenges involved in a broad range of macroscale applications and to provide the reader with an accurate portrayal of the science of tribology.

References

1. Fleishauer PD, Hilton MR (1991) Assessment of the tribological requirements of advanced spacecraft mechanisms, Aerospace Corp., El Segundo, CA, Report No. TOF-0090 (5064)-1
2. Bhushan B (2001) Modern tribology handbook. CRC Press, Boca Raton, FL
3. Miyoshi K, Pepper SV, United States, National Aeronautics and Space Administration (1992) Properties data for opening the Galileo's partially unfurled main antenna, National Aeronautics and Space Administration ; For sale by the National Technical Information Service, Washington, DC/Springfield, VA
4. Stribeck R (1902) Characteristics of plain and roller bearings, *Zeit. V.D.O.*, 46
5. Hersey MD (1914) The laws of lubrication of horizontal journal bearings. *J Walsh Acad Sci* 4:542–552
6. Godfrey D (1980) Review of usefulness of new surface analysis instruments in understanding boundary lubrication. *Fundamentals of tribology*, MIT Press, Cambridge
7. Jones WR Jr (1982) Boundary lubrication-revisited. NASA TM 82858
8. Kalogeras C, Hilton M, Carré D, Didziulis S, Fleischauer P (1993) The use of screening tests in spacecraft lubricant evaluation, No. TR-93(3935)-6, Aerospace Corporation
9. NASA (2012) Attitude control, <http://spinoff.nasa.gov/spinoff1997/t2.html>
10. Sathyan K, Hsu HY, Lee SH, Gopinath K (2010) Long-term lubrication of momentum wheels used in spacecrafts—an overview. *Tribol Int* 43(1–2):259–267
11. National Aeronautics and Space Administration (1998) John F. Kennedy Space Center
12. NASA (2012) Control Moment Gyroscope <http://mediaarchive.ksc.nasa.gov/detail.cfm?mediaid=2442>

13. Thomas JR, Wolfe WL, Electronics Research C (1969) Spacecraft earth horizon sensors: NASA space vehicle design criteria (guidance and control), National Aeronautics and Space Administration ; for sale by the Clearinghouse for Federal Scientific and Technical Information], Washington/Springfield, VA
14. Postma RW (1999) Pointing mechanisms. In: Fusaro R (ed) NASA space mechanisms handbook, NASA TM-206988, chap. 9, pp 113–123
15. Roberts EW, Todd MJ (1990) Space and vacuum tribology. *Wear* 136(1):157–167
16. Conley P, Packard D, Purdy W (1998) Space vehicle mechanisms : elements of successful design. Wiley, New York
17. Murray SF, Heshmat H, United States, National Aeronautics and Space Administration (1995) Accelerated testing of space mechanisms, National Aeronautics and Space Administration; National Technical Information Service, distributor, Washington, DC/Springfield, VA
18. Pepper SV, Kingsbury EP (2003) Spiral orbit tribometry—part I: description of the tribometer. *Tribol Trans* 46(1):57–64
19. Pepper SV, Kingsbury EP (2003) Spiral orbit tribometry—part II: evaluation of three liquid lubricants in vacuum. *Tribol Trans* 46(1):65–69
20. Jones WR Jr (1995) Properties of perfluoropolyethers for space applications. *Tribol Trans* 38(3):557–564
21. Miyoshi K, Center NGR (1999) Friction and wear properties of selected solid lubricating films, National Aeronautics and Space Administration, Glenn Flight Research Center; NASA Center for Aerospace Information [distributor], Cleveland, OH/Hanover, MD
22. Worldometers (2011) “Cars,” <http://www.worldometers.info>
23. WorldMapper (2011) Passenger Cars, <http://www.sasi.group.shef.ac.uk/worldmapper/index.html>
24. Fessler R (1999) U.S. department of energy workshop on industrial research needs for reducing friction and wear, Argonne National Laboratory
25. Hsu S (1995) National Institute of Science and Technology (NIST) Engine Materials and Tribology, Workshop, Gaithersburg, MD, pp 3–5
26. Priest M (2002) Special issue on engine tribology. *Proc Inst Mech Eng Part J: J Eng Tribol* 216(J4):I–II
27. Taylor CM (1998) Automobile engine tribology—design considerations for efficiency and durability. *Wear* 221(1):1–8
28. Aluyor EO, Obahiagbon KO, Ori-jesu M (2009) Biodegradation of vegetable oils: a review. *Sci Res Essays* 4(6):543–548
29. Ruddy BL, Dowson D, Economou PN (1982) A review of studies of piston ring lubrication. In *Proceedings of 9th leeds-lyon symp. on tribology: tribology of reciprocating engines*, paper V (i):109–121
30. Taylor CM (1994) Fluid film lubrication in automobile valve trains. *J Eng Tribol Proc Inst Mech Eng* 208(J4):221–234
31. Moore DF (1975) Principles and applications of tribology. Pergamon Press, Oxford, NY
32. French T (1989) Tyre technology. A. Hilger, Bristol, NY
33. Anderson AE (1992) Friction and wear of automotive brakes. In: Blau PJ (ed) *ASM handbook*, volume 18: friction, lubrication, and wear technology, 10th edn. ASM International, Materials Park, OH, pp 569–577
34. Hertz H (1896) *Miscellaneous papers*. MacMillan and Co., London
35. Johnson KL (1985) *Contact mechanics*. Cambridge University Press, Cambridge
36. Baumeister T, Sadegh AM, Avallone EA (2007) *Marks’ standard handbook for mechanical engineers*. McGraw-Hill, New York
37. Bhushan B (2002) *Introduction to tribology*. Wiley, New York
38. Johnson KL, Tevaarwerk JL (1977) Shear behavior of elasto-hydrodynamic oil film. *Proc Roy Soc (London)* A356(1685):215
39. Tevaarwerk JL (1982) *Traction in lubricated contacts*. University of Waterloo Press, Waterloo, ON, Canada

40. Johnson KL, Cameron R (1967) Shear behavior of elastohydrodynamic oil films at high rolling contact pressures. *Proc Instn Mech Eng (London)* 182(14):307
41. Kapoor A, Johnson KL (1993) Steady state topography of surfaces in repeated boundary lubricated sliding. *Tribol Ser* 25:81
42. Menezes PL, Kishore, Kailas SV (2009) Influence of surface texture and roughness parameters on friction and transfer layer formation during sliding of aluminium pin on steel plate. *Wear* 267(9):1534
43. Menezes PL, Kishore, Kailas SV (2006) Influence of surface texture on coefficient of friction and transfer layer formation during sliding of pure magnesium pin on 080 M40 (EN8) steel plate. *Wear* 261(5):578
44. Menezes PL, Kishore, Kailas SV (2008) Effect of surface roughness parameters and surface texture on friction and transfer layer formation in tin-steel tribo-system. *J Mater Process Technol* 208(1):372
45. Menezes PL, Kishore, Kailas SV (2008) On the effect of surface texture on friction and transfer layer formation—a study using Al and steel pair. *Wear* 265(11):1655
46. Menezes PL, Kishore, Kailas SV (2008) Role of surface texture and roughness parameters in friction and transfer layer formation under dry and lubricated sliding conditions. *Int J Mater Res* 99(7):795
47. Menezes PL, Kishore, Kailas SV (2009) Role of surface texture of harder surface on subsurface deformation. *Wear* 266(1):103
48. Widiyarta IMF, Franklin FJ, Kapoor A (2008) Modelling thermal effects in ratcheting-led wear and rolling contact fatigue. *Wear* 265(9–10):1325–1331
49. Stoody C (1984) The rebuilding and hard-facing of earth-moving equipment. Stoody Company, Industry, CA
50. Imhoff CH, Brown DR, Hane GJ, Hutchinson RA, Erickson R, Merriman T, Gruber T, Barber S, Pacific Northwest Labs RWA (1985) Review of tribological sinks in six major industries, USA
51. Avery HS (1961) The measurement of wear resistance. American Brake Shoe Company, New York, NY
52. Avery HS (1974) Work hardening in relation to abrasion resistance. In: Barr RQ (ed) materials for the mining industry symposium, Climax Molybdenum Co., Greenwich, CT, USA, pp 43–77
53. Hawk JA, Wilson RD, Albany Research Center AOR (2001) Tribology of earthmoving, mining, and minerals processing, CRC Press LLC, Boca Raton, FL, USA
54. Mutton PJ, Macdonald AM, Sinclair WJ, Australian Mineral Industries Research A, and Broken Hill Proprietary Company Melbourne Research L (1988) Abrasion resistant materials for the Australian minerals industry, Australian Mineral Industries Research Association, Melbourne
55. Gill CB (1991) Materials beneficiation. Springer, New York
56. Pevzner LA (1998) Aspects of marine low speed cross-head diesel engine lubrication. *Lubr Eng-IL* 54(6):16–21
57. Lanz R (1995) Sulfur sours emissions level agreement. *Motor Ship* 5:22–23
58. Mang T, Dresel W (2006) Lubricants and lubrication. Wiley-VCH, Wiley (distributor), Weinheim, Chichester
59. Pevzner LA (1998) Cylinder lubrication and feed control in relation to low-speed, cross-head engine load and speed. *Lubr Eng-IL* 54(6):22–28
60. Wilkison JL (1983) Marine equipment. CRC Press, Boca Raton, FL
61. United States, Department of E, National Renewable Energy L, United States, Department of Energy. Office of S, Technical I (2007) Improving wind turbine gearbox reliability preprint. <http://www.osti.gov/servlets/purl/909663-2eS9A6/>
62. Bartz WJ (2007) Tribological aspects of wind power plants. *Tribologie und Schmierungs-technik* 54(6):42–48
63. American Gear Manufacturers A (2010) Standard for design and specification of gearboxes for wind turbines. American Gear Manufacturers Association, Alexandria, VA

64. Totten GE (2006) Handbook of lubrication and tribology. CRC Press, Boca Raton, FL
65. Church EF (1950) Steam turbines. McGraw-Hill, New York
66. Young WC, Robertson RS, Conference: Turbine oil monitoring O.F.L.D. (1989) Turbine oil monitoring. ASTM, Philadelphia, PA, USA
67. Booser ER, American Society of Lubrication E, Society of T, Lubrication E (1983) CRC handbook of lubrication : theory and practice of tribology. CRC Press, Boca Raton, FL
68. United States. Army Corps of E (1999) Engineering and design lubricants and hydraulic fluids
69. Swift ST, Butler KD, Dewald W (2001) Turbine oil quality and field application requirements. ASTM Special Tech Publ 1407:39–52
70. Hackel RA, Keyes HM (1980) Steam turbines in process industries, in Sawyer's turbomachinery maintenance handbook. 2, Steam turbines : power recovery turbines, Turbomachinery International Publications, Norwalk, CT
71. (1989) Steam turbines and auxiliaries. McGraw-Hill, New York, NY
72. Pilicy FX, Dundas RE (1980) Insurance for steam turbines. In: Sawyer JW, Hallberg K (eds) Sawyer's turbomachinery maintenance handbook. 2. Steam turbines : power recovery turbines. Turbomachinery International Publications, Norwalk, CT
73. Westhofen B (1986) Enhancing the availability of industrial turbines. Brown Boveri Rev 73 (31)
74. Welch HJ (1983) Transamerica Delaval engineering handbook. McGraw-Hill, New York
75. Commons W (2012) Gyroscope
76. Mathknight (2008) Caterpillar D10N bulldozer. GNU Free Documentation License. <http://commons.wikimedia.org/wiki/File:CAT-D10N-pic001.jpg>. Accessed 6 Oct 2013
77. Cleyen O (2013) Gas turbine applications. Creative Commons Attribution-Share Alike 3.0 Unported license, Mountain View

Exercises

1. Explain the importance of lubricants in space tribology using example of applications.

Solution: In space tribology, lubrication of moving parts is important to ensure the spacecraft operates at its peak performance and reliability for the duration of a voyage. Examples of space applications include solar array drives; momentum, reaction, and filter wheels; tracking antennas; scanning devices; and various sensors. The Galileo spacecraft is good example of a narrow margin for a potentially expensive tragedy illustrating how the need to develop adequate, sustaining lubricants is pivotal to the success of space tribology.

2. In automotive applications, friction plays a distinct role. Describe two situations where moderate to high friction is necessary for safe operation of a vehicle.

Solution: The first situation in which moderate friction is necessary is in the tire-road interface. If there is too much friction, the automobile will constantly have to overcome this resistive force to operate, and if there is too little friction, an automobile will have insufficient lateral and directional stability to steer and operate safely. Vehicle brakes are the second situation where high friction is necessary to ensure proper braking power facilitating safe operation. Brakes operate by dissipating mechanical energy by means of friction; thus, if there is

not enough friction, an automobile will require more stopping distance; for this reason alone, high friction is necessary.

3. Why is the preservation of the wheel-rail contact vital to the sustainability of the railway transport industry? Briefly explain three deleterious mechanisms that plague railway transport.

Solution: The wheel-rail contact is vital to the sustainability of the railway transport industry because the largest investment outside of real estate is steel rails. These rails are worn down through the continuous interaction of the steel wheel that rides along them, through four wear mechanisms: adhesion, abrasion, fatigue, and fretting. Adhesion is the bonding of the wheel to the rail in the absence of a lubricant that shears causing damage to both interfaces. Abrasion occurs when the harder material plows through the softer material. Fatigue arises from the cyclic normal and shear stresses produced by the relative motion of the wheel on the rail causes cracks to initiate and propagate through the surfaces resulting in delamination of the surfaces. Fretting is a consequence of low-amplitude vibratory motion between two bodies, either the wheel, rail, or any accumulated wear debris.

4. List three mechanisms that are detrimental to the performance of earthmoving equipment?

Solution: Earthmoving equipment suffers tremendously from (1) wear, (2) abrasion, and (3) high impact levels. Much of this is due to the growth of the equipment in the mining and mineral processing industries which are progressively developing methods to seek out lower-grade ores, thereby requiring a larger output of raw mineral while simultaneously lowering operating costs, thus making the entire processes economically feasible.

5. What are some of the requirements for oils and additives in marine equipment?

Solution: Engineers have developed a set of requirements for oils and additives to be used in lubricants in marine equipment, and they are as follows: sufficient viscosity, oxidation and thermal stability, demulsibility, rust and corrosion prevention, antifoaming, detergency, extreme pressure performance, and biocides. Many of the additives are used to minimize lubricant deterioration from seawater contamination, microbes, and other environmental and operational factors.

6. In gas and steam turbines, what are the three pivotal roles of a lubricant?

Solution: In gas and steam turbines, the three pivotal roles of a lubricant are to (1) provide lubrication to critical mating components, (2) remove heat from frictional interfaces, and (3) collect and remove contaminants from lubricating interfaces.

Chapter 27

Microscale Applications in Tribology

Carlton J. Reeves, Pradeep L. Menezes, Michael R. Lovell,
and Tien-Chien Jen

Abstract This chapter focuses on microscale applications involving basic mechanical and biological issues affecting tribology in magnetic storage devices, microelectromechanical devices, flexible media, and biomedical systems. Similar to the factors influencing macroscale applications—described in the earlier chapter—microscale applications of tribology rely on understanding and solving complex tribological issues involving friction, adhesion, lubrication, and wear of components in relative motion. Although many of the presented solutions are multidisciplinary in approach, they also depend on a thorough understanding of the smaller length-scales to achieve the desired efficiency, reliability, compliance, and safety necessary to ensure economical and practical operation. The presented topics are chosen to further illustrate the broad range and importance that tribology plays in lesser known applications which people encounter in their daily lives from computer hard drives to printers and from contact lenses to basketballs.

1 Tribology of Magnetic Storage Devices

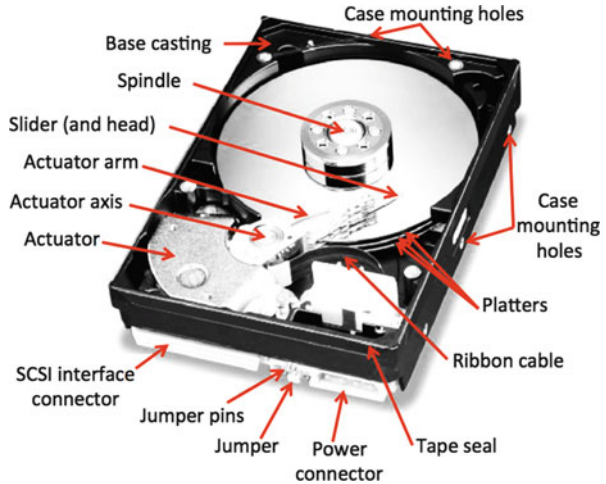
1.1 Introduction

Magnetic storage devices are devices such as tape, floppy (flexible) disk, and rigid disk drives used for audio, video, and data processing applications. The magnetic storage industry is a \$60 billion a year industry with nearly one third (\$20 billion) of

C.J. Reeves • T.-C. Jen (✉)
Department of Mechanical Engineering, University of Wisconsin-Milwaukee,
Milwaukee, WI 53211, USA
e-mail: jent@uwm.edu

P.L. Menezes • M.R. Lovell
Department of Industrial Engineering, University of Wisconsin-Milwaukee,
Milwaukee, WI 53211, USA

Fig. 27.1 The inside look of a hard drive with its components labeled



the value going towards audio and video recording for use in tape drives and media and the remaining two-thirds (\$40 billion) going towards data storage such as hard drives (see Fig. 27.1). The \$40 billion of data storage can be divided into \$25 billion for magnetic rigid disk drives and media, \$6 billion for tape drives and media, \$6 billion for optical disk drives and media, and \$3 billion for flexible disk drives and media [1]. During the magnetic recording process relative motion occurs between the magnetic medium (tape or disk) and the stationary or rotating read–write magnetic head [2]. Magnetic heads are designed with the purpose of developing a hydrodynamic air film that is capable of supporting the load of the head, while sustaining the air film under steady operational conditions to prevent head to medium contact. During non-steady operational conditions such as start-up or stopping physical contact occurs between the medium and the head, also known as contact start–stop (CSS) due to the boundary or elasto-hydrodynamic lubrication regime that is present [3–5]. Magnetic storage devices typically operate with a head to medium separation (or flying height) between 20 and 50 nm and surface roughness on the order of 1.5–10 nm RMS. In some of the more modern tape drives with flexible and rigid disks, the flying height is even broader between 0.3 μm and 20 nm with roughness on the order of 1–2 nm RMS. An analogy regarding a 25 nm flying height for the head and medium and with a relative speed of 20 m/s is that of an aircraft traveling 900 km/h at a distance of 0.2 μm from the ground as illustrated in Fig. 27.2. This represents the negligible separation between the read–write head and the magnetic medium in some consumer tape and floppy disk drives [3–5]. Furthermore, as magnetic storage devices evolve to necessitate the need for increased storage capacities, an increase in the recording density is required. To facilitate higher storage capacities, the head and medium surfaces need to be as smooth as possible and the head to medium separation needs to be at a minimal. Tribological concerns that impede the rapid growth and commercialization of such technology are friction, lubrication and wear at the macroscale, microscale, and nanoscale. The tribological objective in magnetic storage devices is to allow two surfaces to be in relative motion with effectively no physical separation.

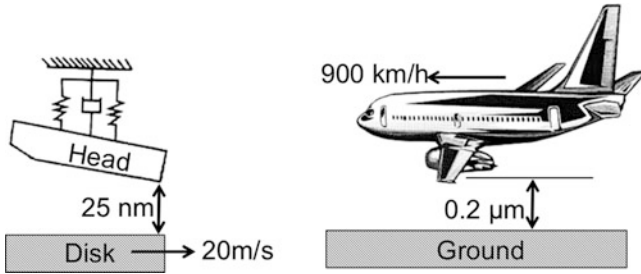


Fig. 27.2 Comparison of a magnetic head flying over a disk and an aircraft flying over the ground

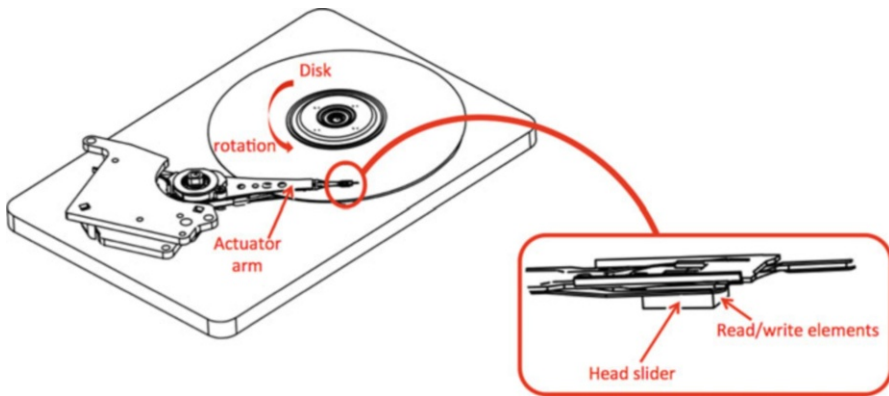


Fig. 27.3 Schematic diagram of a hard drive with the magnetic media as a rotating disk and a magnetic head on the tip of an actuator arm

1.2 Components

Magnetic storage drives consist of two major components that are of relative importance to tribologists—the magnetic medium, which can be a tape or disk and a magnetic head that can remain stationary or rotate as shown in Fig. 27.3. A tape drive operates by first loading it with a cartridge where the tape header is threaded into the drive past a read–write head and onto the take-up reel by a pentagon threading mechanism. A decoupler column placed near the cartridge entrance decouples any tape vibrations that may occur inside the cartridge. The tension is sensed and controlled by a tension transducer. In a rigid drive, a stack of disks is mounted on a sealed, grease-lubricated ball bearing spindle. A DC motor rotates the disks at speeds ranging from 1,000 or 2,000 RPM to a maximum of 15,000 RPM. Each disk surface is provided a head slider. A stepper motor or voice-coil motor for read–write operation is used to actuate the slider-suspension assembly [3, 6]. Within rigid drives, air-bearing spindles are being developed for high track density drives and operation at extremely high rotational speeds beyond 15,000 RPM.

Air bearings have the potential for less run-out, generate less noise, and can operate at higher operation speeds than traditional ball bearing spindles because of their lack of rolling elements. The major impediment of air bearings is that manufacturability is difficult and costly due to the tight tolerances caused by the radial and vertical stiffness being only a few microns.

The two types of magnetic media used in tape and disk drives are flexible and rigid media. One example of flexible media consists of a particulate media, where magnetic particles are dispersed in a polymeric matrix and coated onto a polymeric substrate. Another example of a flexible media consists of a thin-film media, where continuous films of magnetic materials are coated by vacuum deposition techniques onto a polymeric substrate. This thin-film media can also be deposited onto a rigid substrate such as aluminum, glass, or glass ceramic producing rigid disks [7]. Requirements of higher recording densities with low error rates have resulted in increased use of thin-film media, which are smoother and have considerably thinner magnetic coatings than particulate tapes. Thin-film rigid disks are exclusively used for rigid disk application such as high-density audio and video, and data-processing media.

Magnetic heads used in the process of reading and writing to magnetic media are of two styles (1) magnetoresistive (MR) or giant magnetoresistive (GMR) and (2) conventional or thin-film inductive. Magnetoresistive style heads are only used in the process of reading, where the core and coils for the magnetoresistive stripes are deposited by thin-film technology to be used in the magnetoresistive film head. Furthermore, thin-film technology allows for the production of high-track density heads with reasonably accurate track positioning and high reading sensitivity. Inductive head design consists of a body forming the air bearing and a magnetic ring core. The magnetic ring core carries the wound coil with a read–write gap. The body of a thin-film inductive head is fabricated from magnetic ferrites and the head construction includes coatings of soft magnetic alloys, insulating oxides, and bonding adhesives [8]. For both magnetic head types film-head manufacturing utilizes cost saving fabrication processes similar to those in semiconductors. Air bearing surfaces of tape heads are generally cylindrical in shape, with the tape slightly underwrapped over the head surface to facilitate the hydrodynamic lift during the read–write process. For dual-sided flexible disk heads, the two heads are either spherically contoured or slightly offset to reduce normal pressure or they are flat and loaded against each other. Rigid disk heads used in head sliders are generally supported by a nonmagnetic steel leaf spring (flexure) suspension to allow motion along the vertical, pitch, and roll axes.

1.3 Tribological Issues

The tribological issues involved with magnetic storage devices are a result of the increasing need to reach higher recording density with low error rates. This has propelled the use of thin-film media, which are significantly smoother than

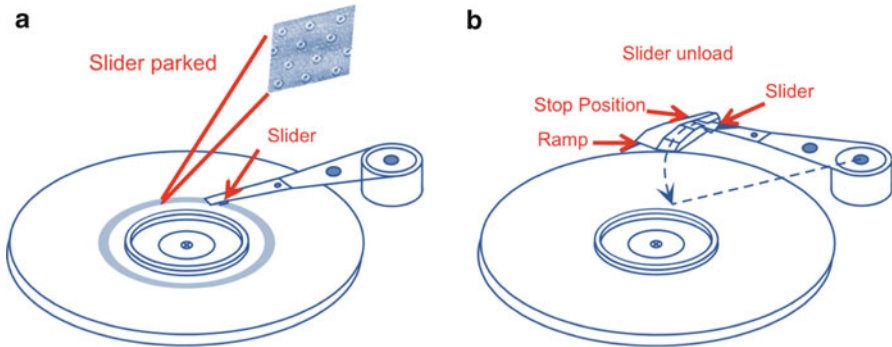


Fig. 27.4 Schematics of read–write head in off position (a) contact start–stop (CSS) system (b) Load/unload (L/UL) system [64]

particulate media and operate with considerably smaller head-to-medium separation. The stringent operational conditions have led to an increase in surface adhesion, friction, and interfacial temperatures. A result of the decreased flying height, there are more intermittent contacts between the asperities on the surfaces of the medium and head during steady-state operation and throughout contact start-stop (CSS) as illustrated in Fig. 27.4. The design of the tape heads to promote the elastohydrodynamic or hydrodynamic air film to mitigate the frequency of asperity contacts is an important issue. Interestingly, this has become more difficult because the air film must be thin enough as to not influence the magnetic read-back signal generated between the head and the medium, but also thick enough to prevent head-medium contact. In rigid disk drives, a technology is being implemented known as head load/unload (L/UL) to alleviate high static friction (stiction) and wear failure as a result of starting up and stopping [9]. A L/UL system (see Fig. 27.4) involves a lifting mechanism that actuates when the head has reached the outer radius of the disk therefore moving the head off the disk and placing it in a parking position. As a result, the starting and stopping of the disk can only take place with the head is in the unloaded state i.e. off the disk. The benefits of such a system are increased areal density due to smooth disk surfaces, thinner protective overcoats for the disk surfaces, and lower head flying heights. As with any system, there are disadvantages that include accumulation of wear debris during the L/UL, spatial requirements for the L/UL mechanism, and added cost.

Two tribological mechanisms that are detrimental to the performance of a magnetic storage device are stiction and wear. Stiction is the result of meniscus and viscous effects, microcapillary evacuation, or changes in surface chemistry. Within the computer industry, stiction generally refers to the presence of environmental moisture (i.e. humidity), liquid contaminants, or lubricant films at the medium–head interface and is often described as liquid-mediated adhesion. This form of adhesion is primarily due to the meniscus term that depends on the surface tension of the liquid and the viscous term, which does not depend on the

surface tension. Viscous effects can occur between two surfaces even when they are submerged in a liquid. Most importantly, the liquid-mediated adhesion affects the rate at which the medium and the head can be separated. For instance, if the medium and head are adsorbed with a liquid film they may be separated easily if they are removed from one another very slowly. However, when the rate of separation is rapid, liquid must flow into the space between the medium and head. This causes the viscosity of the liquid film to be the determining factor in the stiction. As a result, the impact of stiction is that during the contact start-stop, a relatively large force could be required to separate the magnetic head and medium surfaces. This force can be on the order of several milliNewtons up to 1 Newton in extreme instances. Furthermore, to exacerbate this problem increasingly smaller magnetic head and medium gaps heights in conjunction with the increasing disk speeds of 7,200 RPM or more has led to the development of more severe stiction which inevitably causes more medium-head contact that results in disk failure [10–12].

During contact of the tape and head in the CSS or through other instances of contact, tape debris is produced by adhesive wear. This wear debris is made up of loose magnetic particles, worn head material, or foreign contaminants that can act as a third body abrasive material that further deteriorates the tape and head [13]. Wear debris can also exist inside the drive where lubricating films on the tape and head act as bonding agents for the wear debris, enabling it to again act as a third body abrasive material. The effects of wear are damaging because they can disrupt the magnetic signal leading to magnetic read–write errors or to total component failure [3, 14]. An additional problem in the magnetic medium and head interface is that during the read–write process the mechanical sliding energy is converted into frictional energy, which is converted into heat. In low-speed drives, temperatures can reach upwards of 5 °C above the ambient conditions causing the tape’s mechanical properties to slightly transform resulting in high friction generation scenarios [15]. However, in high-speed drives where the magnetic particles are contacting the head surface for a duration of milliseconds, flash temperatures can reach upwards to an average of 600 °C or even to a maximum of 900 °C. The range for the average and maximum transient temperatures for typical thin-film read–write head interfaces is about 56–77 °C and 81–110 °C, respectfully. The effect of such thermal gradients and temperature spikes causes breakdown of the medium lubricant and degradation of the medium binder thus leading the way for excessive friction and eventual seizure of the tape and head.

1.4 Conclusion

Magnetic storage devices have become a vital component in information storage. The tribological issues that plague the relative motion between the magnetic medium and the read–write head were brought to attention in this section. As the need for increasing data storage capacity evolves, so will the importance of

understanding the tribological phenomena to prevent friction and wear of the low flying magnetic head over the magnetic tape. The importance of sustaining the hydrodynamic air film between the head and tape to prevent asperity contact was described. Furthermore, techniques to mitigate the damage caused by repetitive starting and stopping of the head over the disk; stiction from entrapped liquids at the head–medium interface; thermal degradation by flash temperatures; and abrasive wear by third body debris are all factors depleting the performance of magnetic storage devices. As magnetic storage devices continue to decrease in size with an inversely proportional recording density, the importance of micro and nanotribology will become inherent through micro/nanomechanical investigations.

2 Tribology in Microelectromechanical Systems

2.1 Introduction

Microelectromechanical systems (MEMS) are the technology of very small mechanical devices. MEMS developed in the 1960s from advances in silicon photolithographic processes for the fabrication of microscale components. Recently, lithographic processes have emerged for non-silicon materials in addition to nonlithographic micromachining processes. Advances in microelectromechanical technology have led to the emergence of nanoelectromechanical systems (NEMS) and nanotechnology. Applications of MEMS or NEMS technology include acceleration, pressure, and chemical sensors; linear and rotary actuators; electric motors; gear trains; gas turbines; nozzles; pumps; fluid valves; switches; grippers; tweezers; and optoelectric devices [16]. MEMS technology is still relatively new with much of the emphasis put on the fabrication and validation of these miniature devices. A commercial application of MEMS devices include the \$1 billion a year use of a silicon-based high gravitational force (High-G) acceleration sensors used in the deployment of airbags during an automobile collision [17, 18]. Another application is the digital micromirror devices (DMDs) used in digital light processing (DLP) technology for digital projection displays in portable and home theater projectors as well as table top and projection televisions [19, 20].

2.2 Manufacturing Techniques

MEMS devices are fabricated by one of three processing methods of photolithography; (1) bulk micromachining, (2) surface micromachining; and (3) LIGA. LIGA a German acronym for “Lithographie Galvanofornung Abformung” is a MEMS manufacturing technique that involves lithography, electroforming, and

Fig. 27.5 MEMS Ratchet device



plastic molding. Bulk micromachining is the oldest method of producing silicon based MEMS at high volume. This process involves a single-crystal silicon wafer between 250 and 500 μm thick that undergoes anisotropic etching, bonding with glass plates or other silicon wafers for adding details in three dimensions, and finally a hermetically sealing process. During the deposition of silicon layers, the structure can potentially collapse upon itself or adhere to the underlying substrate thus weakening the structural integrity of the MEMS device rendering it vulnerable to failure [21]. It is for this reason many tribologists are still studying the phenomena responsible for the occasional adhesion in order to improve upon the bulk micromachining process and understand what causes faulty MEMS devices [22]. Bulk micromachining is primarily used for accelerometers, pressure sensors, and magnetic head sliders. The surface micromachining process involves the low-pressure chemical vapor deposition of polysilicon films (or sacrificial layer) on the order of 2–20 μm in thickness on a surface of a substrate to produce a freestanding structure that is then etched to produce the necessary features. Often, surface micromachining is used to create motors, gears (see Fig. 27.5), grippers, integrated circuits, and acceleration sensors [23]. LIGA is primarily used to produce high-aspect ratio (HAR) MEMS devices, which are significantly larger by an order of 1,000, than the previously described fabrication methods. HAR MEMS devices can be as small as a few microns upwards to a couple millimeters with comparatively higher degrees of structural rigidity. The LIGA process can incorporate a combination of X-ray photolithography, electroforming, and molding.

2.3 Tribological Issues

The tribological issues associated with MEMS devices are a direct result of the downscaling. As the length (L) of a device decreases from 1 mm to 1 μm , the corresponding area has decreased by a factor of the length squared (L^2), a million, and the volume by a factor of the length cubed (L^3), a billion [24]. For these reasons, resistive forces that are proportional to the area such as friction, viscous drag, and surface tension have only decreased by a factor of a million, whereas the resistive forces proportional to the volume such as inertia and electromagnetic force have decreased by a factor of a billion. Moreover, due to the large surface area to volume ratio, gravity and inertial forces are no longer important, but atomic forces and surface effects dominate in MEMS technology [25]. This is of even more of a concern due to the relatively low power output of MEMS devices. Tribological issues such as friction, stiction, wear, and surface contamination have a larger effect on MEMS devices that can impede their performance. For example, in a MEMS side-drive micromotor with 12 stators and a four-pole rotor, the stator–rotor interface and the rotor–hub flange interface are locations where tribological issues occur. The concern is that if intermittent contact occurs between the interfaces, wear can degrade the surfaces and stiction can occur between the surfaces resulting in a decrease in performance that can lead to an inoperable device. In order to reduce the effects of stiction, friction, and wear, it has become apparent that there is a need for solid and liquid monolayer films as well as hard coatings to provide both superior friction and wear reduction capabilities [26, 27].

The tribological issues affecting MEMS devices also affect magnetic storage devices, which in some instances utilize MEMS components. In magnetic storage devices, the tribological issues that occur between the read–write head and the magnetic disk are wear debris caused by asperity contact and stiction from unwarranted liquids becoming entrained in the head–medium interface. In an attempt to protect against corrosion and wear, hard diamond-like carbon (DLC) coatings are applied at the interface. Additionally, within a MEMS magnetic disk drive, two electrostatically driven rotary and linear microactuators (see Fig. 27.6) produced by surface-micromachining of a polysilicon structure are used to activate motion of a movable plate in opposing directions [28]. This magnetic disk drive uses DLC coatings to protect the counterfaces that suffer from wear and stiction.

2.4 Conclusion

Tribologists have investigated the friction and stiction mechanisms involved in micromotors and microgear systems, along with the development of solid and liquid lubricants and hard coatings to minimize the friction and wear. Despite the ongoing research, optimum materials are still needed for solid and liquid lubricants and for coatings in MEMS devices. Other tribological issues arise in MEMS device

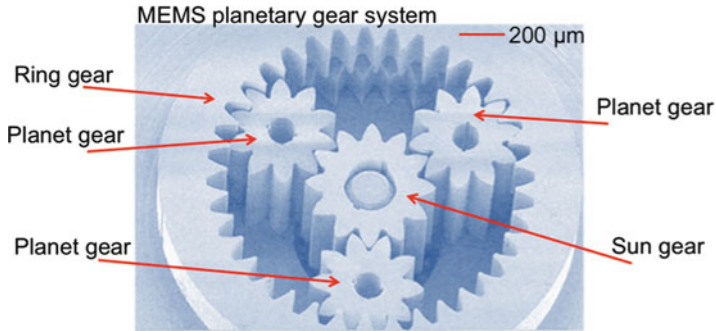


Fig. 27.6 MEMS planetary gear system used as a microactuator for driving microrobotic systems

fabrication such as in bulk micromachining, during the deposition of silicon layers on a substrate. In this process, the layered silicon structure can collapse upon itself or adhere to the underlying substrate reducing the structural integrity and damage the device. The mechanism responsible for the occasional adhesion still requires explanation. The effects of friction, stiction, and wear are the dominant issues affecting the lifetime, performance, and reliability of MEMS devices. The underlying reasons are attributed to the downscaling, which leads to the design of smaller tolerances thus causing a larger impact of environmental factors, surface contamination, and debris, which are all deleterious to micro-devices.

3 Tribology of Flexible Media

3.1 Introduction

The modern office is often supplied with printers, copiers, fax machines, scanners, tape drives, and other machines that are used in typical day-to-day routines as depicted in Fig. 27.7. To meet productivity demands, these devices must precisely handle flexible sheets or webs such as paper sheets or magnetic tapes through continuous paths, in a small amount of space without jams, tears, or damages to the flexible media. This presents both mechanical and tribological challenges that must be addressed. The use of traditional office paper has the advantage of being flexible, which comes in handy when it is forced around rollers such as in a typical office printer. A thin magnetic tape can use self-entrained air to lubricate its passage around posts in a tape drive; however, air entrapment during the roll winding process causes poor stacking of the coils. This section examines the design opportunities and challenges involved in handling flexible media in information processing systems by exploring foil bearings, air reversers, wound rolls, transport of sheets through rollers, and mechanisms of paper jams.



Fig. 27.7 Office printer (a); scanner and copier machine (b)

3.2 Foil Bearings

Foil bearings are a type of air bearing, where a shaft or drum is supported by a tensioned flexible axially moving foil (strip) that lines the stationary or rotating shaft. As the shaft or foil begins spinning, a thin lubricating film develops between the surfaces pushing the foil away from the shaft, minimizing the contact between the shaft and the foil. In most applications of foil bearings, the working fluid that provides the lubricating film is air. In the foil bearing, the shaft and foil remain separated because of the high air pressure that is generated by the rotational motion that pulls the air into the annulus by viscous effects. Unlike aero or hydrostatic bearings, the air entrained from the motion of the foil provides the lubrication in a foil bearing, thus no external pressurization system for the working fluid is necessary. Hydrodynamic foil bearing systems of this nature are referred to as self-starting or self-acting. In externally pressurized foil bearings or air reversers the shaft is porous and pressurized air is pumped through the holes in the shaft to enhance the air film. Figure 27.8 illustrates a schematic of a self-acting foil bearing and an air reverser depicting a sample hole-pattern in the porous shaft.

Self-acting foil bearings are used in applications when it is necessary to change the transport direction of a foil without contact, which is necessary in many common devices found within an office such as a printer, copier, or fax machine. The benefits of a foil bearing stem from their non-contacting components resulting in extremely low wear rates and friction; high efficiency, reliability, and speed capabilities; and low noise operation. In addition, foil bearings benefit from not requiring external pressurization systems. Despite their advantages, foil bearings cause problems and degrade system performance in contact recording and winding operations. Investigation into the mechanical and tribological issues caused by self-acting foil bearings is a result of the fluid–structure interaction. The contact between the air and shaft causes pressure and shear stress to occur in the air. This provides structural loading, which deforms the elastic body of the shaft, therefore

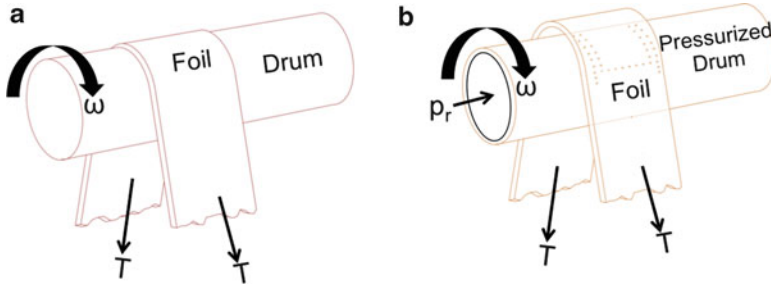


Fig. 27.8 Schematic of a foil bearing; (a) self-acting foil bearing (b) air reverser

changing the boundary of the fluid domain and altering the stress state of the air. Furthermore, in the foil bearing, the air is constrained on one side by a flexible foil, where the pressure and shear loading on the foil are dependent upon the direction of motion of the foil. The dependence of the fluid domain changing with the deformation of the shaft and the flexible foil results in a coupling of the equations of motion, complicating the analysis. A delicate balance that must be retained when developing a mathematical model is to accurately represent the physical phenomena in a simple and robust manner. Often, when solving foil bearing problems, engineers must resort to numerical methods to simultaneously solve the Reynolds equation and the foil equation to find the pressure gradient and the air film thickness [29–32]. To simplify the calculations, the following assumptions are generally made—the foil is perfectly flexible, the lubricant is incompressible, the bending stiffness in the foil is negligible, and the operating conditions are in steady state.

A similar component to foil bearings is an air reverser. An air reverser is essentially a foil bearing with a porous shaft that ejects a pressurized lubricant (air) through holes on the surface of the shaft into the gap between the shaft and the flexible foil. In air reversers, the effect of the forced air in the annulus is significantly greater than the intrinsic air entrainment caused by the motion of the foil around the shaft that occurs much like a self-acting foil bearing. Air reversers are used in applications such as tape drives or other magnetic media storage devices, where handling of flexible foils that are coated (magnetic medium) must have minimal contact. Air reversers are necessary in such applications to ensure that the material can change travel directions without contacting the flexible foil, because unwarranted contact could damage the thin coating. In many regards, air reversers are similar to externally pressurized foil bearings and are analyzed using the Reynolds equation with the addition of a source term [33]. The significant operating differences between pressurized foil bearings and air reversers are the gap distance and the material of the foil. In a pressurized foil bearing, the gap distance is measured on the order of micrometers, whereas the gap distance in an air reverser is measured on the order of millimeters. Inspection into the effects of the larger gap size has led to the departure of the Reynolds equation in the modeling process and is described as follows. The modified Reynolds numbers Re^* is the ratio of the inertial

forces to the viscous forces in the annulus between the shaft and the foil. Equation 27.1 characterizes the Reynolds number.

$$Re^* = \frac{\rho_f V h^2}{\mu L} \quad (27.1)$$

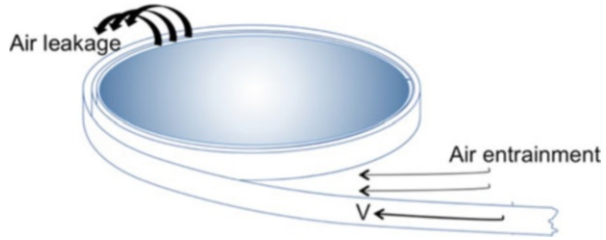
In Eq. 27.1, ρ_f is the density of the air, V is the velocity of the foil, h is the gap height, μ is the dynamic viscosity of the air, and L is the gap length. In self-acting foil bearings the use of the Reynolds equation assumes that the inertial forces in comparison to the viscous forces are small and can be neglected. Conversely, in the case of air reversers, this is not true and the inertial forces must be accounted for. The presence of the h^2 term in the definition of the modified Reynolds number means that the Reynolds number will be significantly larger in the air reverser than in the self-acting foil bearing by an order of the gap distance squared. The modified Reynolds number can be on the order of ten for most air reversers, thus inertial forces dominate over viscous forces and the Reynolds equation is not applicable. In order to facilitate the mathematical analysis, it is common to neglect viscous forces [34]. Through the study of one and two-dimensional models, it has been revealed that the most efficient use of the supply pressure in air reversers is to design them with densely packed holes uniformly distributed over the outer region of the air reverser.

3.3 *Wound Rolls*

The tape in cartridges for cassette players, VCRs, digital audio tape players, and computer backup devices, all involve the winding of films to be stored in a wound roll. Many of these applications require the tape to be simultaneously unwound and rewind repeatedly for thousands of cycles throughout the product's lifetime. In these processes, it is important to understand the mechanical and tribological issues involved in the winding process, especially how to remove the entrained air trapped between layers when the film is being wound. When winding a film into a wound roll it is important to have adjacent layers in direct contact with one another. This intimate contact prevents relative motion between the layers of the roll and proper release in the unwinding process.

During roll winding, air entrainment between film layers is undesirable. Similarly to a foil bearing, in the roll winding process, air becomes entrained by the transport of the film being wound. Despite this similarity, wound rolls differ from foil bearings in three distinct manners: (1) there is no exit region in a wound roll, (2) both surfaces of a wound roll are flexible, and (3) the "shaft" of a wound roll moves with the same velocity as the incoming foil. In a wound roll, the shaft is composed of the spool of previously wound layers of film. If significant air film develops between layers in the wound roll, relative motion can occur between

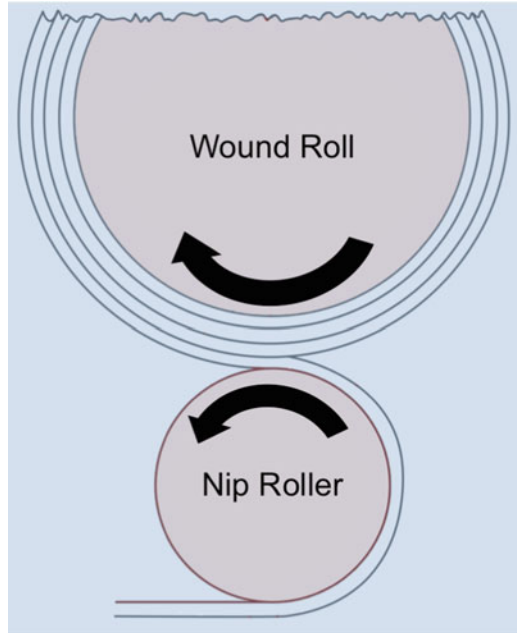
Fig. 27.9 Schematic of a wound roll showing air entrainment and leakage



layers in the winding or lateral directions causing wear and damage to the film. Furthermore, slippage in the winding direction causes a reduction in wound-in tension that would otherwise keep the roll compact. Roll collapse can also occur from slippage as a result of axial compression or buckling of layers. If the slip occurs in the lateral direction, this can damage the lateral edges and cause uneven wraps to telescope.

In the winding process the only place for air to escape is laterally across the edges of the tape as shown in Fig. 27.9. This occurs because the lateral deformation across adjacent layers is relatively equal and the deformation at the outer edge does not trap the air and thus permits side leakage. In some mechanisms, the wound roll has guide flanges that can obstruct the flow of the exiting air. Investigation into the principles of wound rolls has revealed that during the winding process, an equilibrium occurs between the rate of air entrainment into the spool and the rate of air leakage out of the spool. Further analysis indicates that this equilibrium of air entering and exiting the spool is not sustainable at higher winding speed. Thus, more air becomes entrained, resulting in a larger region of the spool where adjacent wound layers are separated by an air film preventing contact between adjacent layers. Naturally, the air will leak out of the wound roll. This can take several seconds, however, which may not be enough time if immediate unwinding is to take place. Air entrainment problems have become a formidable adversary for engineers when trying to improve the performance of tape recording devices. Typically, performance is improved by increasing the winding speed thereby reducing the seek time. Attempts to overcome this problem include solutions to squeeze out the entrained air during the winding process. Wind-on or nip rollers attached to spring-loaded dancer arms (as shown in Fig. 27.10) are used to press the incoming tape against the spool, thereby squeezing the entrained air out and ensuring intimate contact of adjacent layers. Similar applications involve the use of highly elastic drive belts to be stretched around the spool to compress the outer layers and force the entrained air out. In attempt to mitigate the air entrainment problem in magnetic tape applications, engineers have resorted to surface texturing of the backside of the tape with a striated pattern running laterally across the tape to further facilitate air leakage. Although these solutions have shown promise, further investigation is needed to ensure that no additional wear is taking place during the winding process.

Fig. 27.10 Schematic diagram of a winding process



3.4 Mechanisms of Flexible Media Transport Failure

In many printers, fax machines, scanners, copiers, and other office machines, it is often necessary to push a flexible medium, such as paper along a frictional surface. To ensure proper operation, it is important to understand whether the sheet sticks to or slides along the surface. In the process of making a copy, a sheet of paper is fed as a cantilevered beam against a photoreceptor, fuser rolls, and various guiding surfaces. The process can become even more complex if the paper sheet is being imaged in color or if two-sided copying is performed. In modern copiers there are generally two paper paths: one for the imaged sheet and the other for the automatic processing of the original copy. Examining how elastic flexible media combined with the frictional rubbing against guided surfaces is important to prevent paper jams, stalls, or rollover during processing. Figure 27.11 illustrates the geometry involved with a curved sheeting being fed against a frictional surface with an inclination angle ψ^* from the horizontal. On the first contact the sheet has progressed forward a distance of L , past the first roller and the leading edge of the sheet is contacting the frictional surface with a coefficient of friction between the sheet and the wall as μ . In understanding how the sheet will progress, it is important to know whether the sheet will slide up the surface, stick to the surface, or slide down the surface. This determination is performed by first assuming that the sheet will stick to the surface and then determining the resistive force ΔF and the angle ψ that develops when an additional length ΔL of the sheet is pushed past the feeding rollers. The stick or slip behavior of the sheet is determined through a set of

Fig. 27.11 Schematic diagram representing the geometry of a curled flexible sheet on first contact with a frictional surface

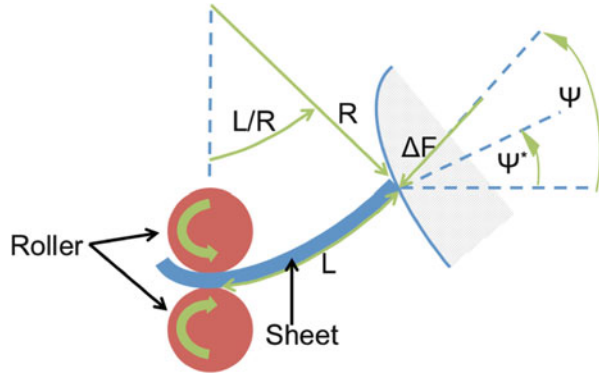
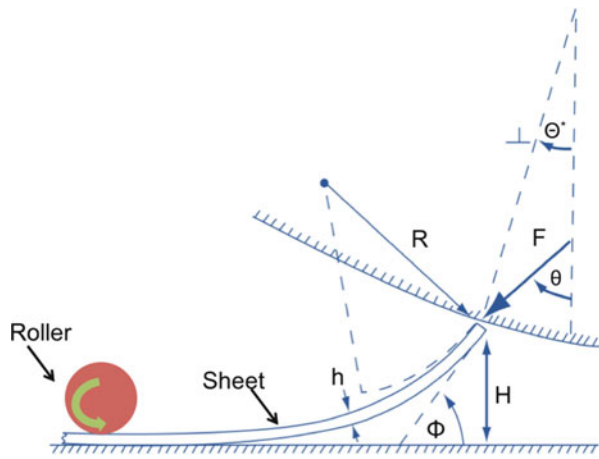


Fig. 27.12 Schematic diagram representing the geometry of a curled flexible sheet wedged in a frictional channel



frictional limits by use of the Theory of Elastica [35, 36]. Figure 27.12 depicts the geometry of a curled flexible sheet being fed through a roller into a frictional channel wedge. In this illustration of a common scenario in many office machines, the flexible sheet having a curved radius R is forced into a wedged channel with a flat lower surface and a curved upper surface. Throughout the channel the height H and the angle θ^* are known. In this scenario as the sheet is pushed forward, the leading edge will drag against the top surface with a resistive force F , an angle θ , and have a coefficient of friction μ , between the sheet and the wall [36, 37].

The tribological challenge present in a system that transports flexible media through channels occurs because of the reaction force between the sheet and the walls. It is important to understand their interaction when determining how a sheet will progress through a channel. The combination of the resistive force and the wedging that can occur within a channel can cause three types of failure in the sheet transport: jam, roll-over, and stall. A jam describes the phenomenon that occurs when the friction is sufficient to retard the forward progression of the sheet's

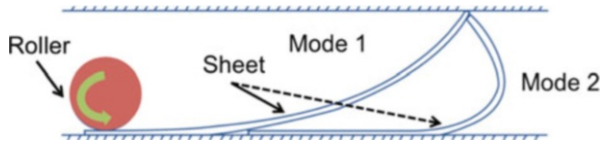


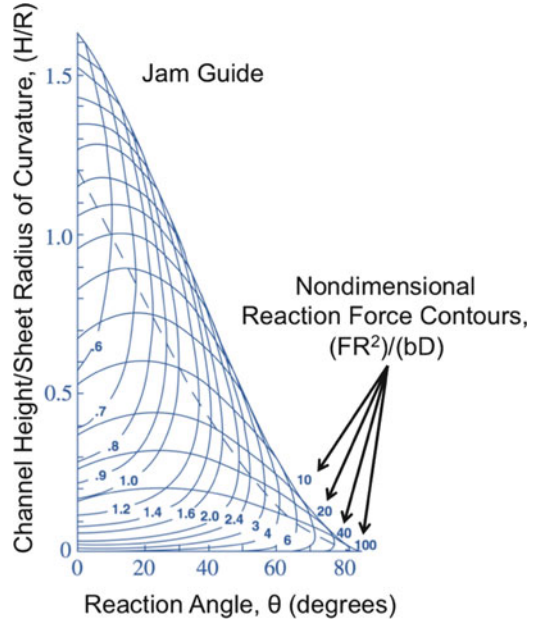
Fig. 27.13 Illustration of two admissible modes of sheet transport through a parallel frictional channel

leading edge. In a jam, if the drive-roller continues to push the sheet forward, more material will enter the channel, however, the leading edge of the sheet will not move. For this reason, pushing harder with the drive roller will only cause the sheet to jam faster. The geometry of a curved sheet being pushed forward by a roller in a parallel channel where the top and bottom surfaces are flat is depicted in Fig. 27.13. In this illustration, Mode 1 is the preferred movement of the sheet and Mode 2 is the problematic movement of the sheet. Mode 1 is superior to Mode 2, because the resistive forces are smaller and the sheet lies flatter with the leading edge being the most forward portion of the sheet. Mode 2 is ill-advised because the sheet is slightly wedged in the channel and the leading edge is not the most forward portion of the sheet. In Mode 2, the portion of the sheet that has progressed the furthest through the channel is known as a “knuckle.” This knuckle can lead to larger issues further downstream in the channel, for instance if there was a pair of counter-rotating fuser rolls as found in many copiers and printers, this would create a larger jam. The fuser rolls are designed to catch the leading edge as shown in Mode 1, however in Mode 2 the knuckle would be caught first, causing the sheet to be folded, mangled, or destroyed. This could cause a paper jam or temporarily make a machine inoperable until the stuck sheet is removed.

The phenomenon of a sheet progressing down a channel in the desired Mode 1 configuration and switching to the undesired Mode 2 configuration is known as roll-over. Roll-over occurs when the leading edge of the sheet becomes temporarily jammed upon a rough spot or extrusion in the channel and when further material is fed into the channel by the drive roller. In this instance, the leading edge of the sheet remains stationary against the surface of the guide wall and an increasing slope angle resulting in the protrusion of a knuckle. Upon the sheet’s leading edge becoming free, it may progress downstream in the Mode 2 configuration. If this occurs, the sheet may experience stalling. A stall arises when the drive roller cannot apply sufficient force to the sheet to overcome the unexpectedly high drag force. As a result the sheet will become stalled in the channel where it will remain stationary while the drive roller continues to turn. Unlike the case of a jam where the sheet is affected by contact geometry and independent of the drive force, in a stall if a larger drive force is applied then the sheet can be made to move again. However, as mentioned previously, issues can occur downstream due to the nature of the sheet traveling in a Mode 2 configuration.

Design guidelines can be extracted by analyzing the reaction angle θ and the ratio of the channel height to the sheet radius of curvature in a plot known as a jam

Fig. 27.14 Jam guide for calculating the magnitude of the lead-edge reaction force restraining the motion of the sheet through a frictional channel



guide shown in Fig. 27.14 [16]. To minimize the risk of jam, roll-over, and stall, the objective is to remain as far from the jam envelop or as close to the origin as possible. This can be achieved in four ways: (1) by reducing the steepness of the upper wall, (2) by reducing the friction with the upper wall, (3) by flattening the curvature of the sheet, and (4) by narrowing the channel height. Further, information regarding the dynamics of the stick and slip phenomenon occurring in a flexible sheet transport has been studied [38–40].

3.5 Conclusion

Many of the devices used in a modern office such as printers, copiers, fax machines, scanner and tape drives rely on a thorough understanding of the mechanisms governing the transport of flexible media. In many cases this media consists of sheets of paper and magnetic tapes. To ensure efficient, robust, and effective operation of these devices, tribologists has established unique processes to allow these flexible sheets or webs to travel through these continuous paths in a confined space without succumbing to jams, tears, or unwanted damage. The use of foil bearings and wound rolls have afforded success within many of these devices allowing them to gain prominence within the home or office without one needing to consider the many mechanical and tribological challenges that must be addressed to allow for the relatively simple operation for the user.

4 Biomedical Tribology

4.1 Introduction

Tribological applications often focus on metal-to-metal contact in a broad range of components that are important in our transportation and manufacturing industries. However, tribology also plays a vital role in biological systems. Biomedical tribology is the study of tribological and biological phenomena pertaining to the human body. It has a diverse array of applications from intimate studies of the human body involving cardiovascular systems, stents, and artificial joints to slightly less intrusive roles as contact lenses and cosmetics. In the medical and dental industries, scientists are concerned with tribological phenomena such as wear and lubrication involving surgical procedures, prostheses, root canals, grinding of teeth, and the movement of joints. Biomedical tribology can even extend to the friction involved in walking to prevent slips and falls or the interaction between an athlete's hand and ball. What encompasses all of these systems is the quantification of the mostly subjective tactile feedback and sensation to create safe and comfortable operational conditions for the human body. The human body is a complex system that depends on the tribological interaction from touching or rubbing between the body and a sensed object to the intimacy of tactile sensation. The human body uses the tactile information to physically evaluate an object based on shape, roughness, viscoelasticity, friction coefficient, among other attributes as well as to emotionally evaluate the object based on the sensation of comfort and how it makes the body feel [41, 42].

4.2 Skin and Cosmetics

The personal-care industry is one in which the tribological problems associated with the tactile sensation inspired by the contact between the human skin and the cosmetic are vital to a product's success. Hair-care products, nail-polish, makeups, foundations, skin creams, and lotions (shown in Fig. 27.15) all require an understanding of the fundamentals of tribology and a deep understanding of the skin-cosmetic interaction. Skin is made up of three primary layers: the epidermis, dermis, and hypodermis, each with different structural and functional features. Friction modeling of the skin is a daunting task due to the complexity of the skin itself. It becomes even more complicated with the addition of lubricative perspiration originating from glands within the body or foreign contaminants such as cosmetics. The skin and lubricant or skin and cosmetic compose a tribosystem, comprised of stacked interconnected layers that vary laterally in elasticity, shear strength, and continuity [43]. If there is lubrication on the outer layer of the skin then the epidermis may experience minimal relative motion to the opposing object resulting in the subsequent skin layers below not accommodating the imposed shear and

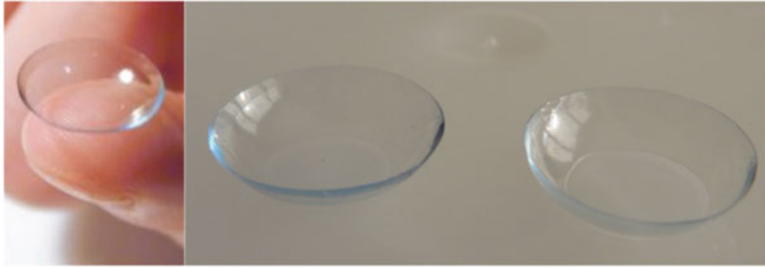
Fig. 27.15 Assortment of various cosmetics used in the personal-care industry



behaving like a viscous liquid. The uniqueness in this system is that each of the skin's layers has its own compliance and the transmission of the load causes different layers to reach their elastic limit independently. This causes deformation in the skin that can result in buckling of the skin in the contact zone and elastic exhaustion in the subsurface layers resulting in slippage at the contact area or tissue trauma. The tactile sensation within the skin varies due to the heterogeneity of the human body and differences from person to person. Furthermore, the issues of adhesion and wear become important when applying or removing cosmetics such as lotions or nail polish to or from the body.

4.3 Contact Lenses

Human eyes are one of the many organs that tactile sensation is critically important in establishing comfort, especially when it pertains to contact lenses. Contact lenses as those shown in Fig. 27.16 have been a commercial success dating back to the 1950s, providing people with visual and cosmetic enhancements [44]. The tribological issues with contact lenses are creating a suitable device that physically fits on the surface of the eye and that is comfortable without irritating the retina. Normally, eyes are lubricated by tears composed of three layers: (1) the highly viscous lipid outer layer, (2) the lower viscous tear layer, and (3) the inner most viscous mucous layer. The tears work to protect the eyes from wear, debris, and



Contact lenses with the concave side upwards

Fig. 27.16 Image of modern contact lenses

contamination and minimize the friction involved in the blinking process. Different studies have shown that during the blinking process hydrodynamic lubrication can prevail. However, in the presence of contacts the friction coefficient increases and boundary or even mixed-elastohydrodynamic lubrication can occur [43]. The latter taking place in the presence of saline solutions applied to the contacts.

4.4 Artificial Joints

One of the most researched areas in biotribology is joint replacement. Artificial joints are implanted in over one million people worldwide annually. In many of these implants the long-term failure is due to the tribological issue of wear and the creation of millions of wear particles within the body [45]. The particles can cause adverse biological reactions that can lead to osteolysis, bone resorption, loosening, and failure. These are the reasons joint replacements have become a focal point in tribological investigations of artificial joints [46–48]. In joint replacements, it has been shown through clinical and laboratory testing that smooth polished metal femoral heads have an average wear rate of about $40 \text{ mm}^3/\text{year}$. Moreover, damage to the femoral head, oxidative degradation, and larger diameter heads and cups can accelerate the wear rate to 100 or $200 \text{ mm}^3/\text{year}$ [49]. This illustrates the need to understand the tribological issues in joint replacement and the need to develop wear resistance materials that are biologically benign.

4.5 Cardiovascular System and Stents

The cardiovascular system is an organ circulatory system for pumping blood, nutrients, waste products, energy, gases, and hormones throughout the human body to keep it functioning and healthy. The system is composed of the heart,

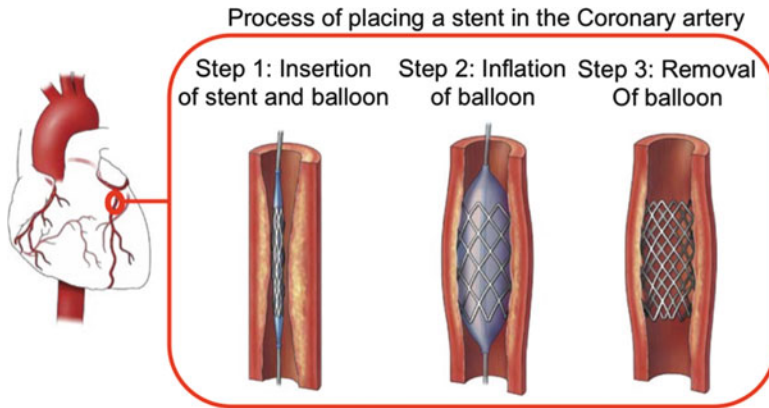


Fig. 27.17 Illustration of the insertion of a stent into the coronary artery

blood, blood vessels, arteries, and veins that work to help fight diseases, to stabilize body temperature and pH, and to maintain homeostasis. The flow of blood through major veins and small capillaries within the cardiovascular system are examples of low Reynolds number flow of non-Newtonian multicomponent fluids. As with most pumping systems many tribological challenges can be found, for example within the heart there are two independent pumping chambers, the left and right ventricles which consist of flexible valve leaflets which open and close approximately 40 million times per year. Over time, wear and abrasion to the leaflet valves can occur reducing the lubricating effect of blood causing complications. In severe situations when blood flow is constricted, medical appliances known as stents can be placed within a passageway to open the valve leaflet facilitating improved blood flow. A stent as shown in Fig. 27.17 is an expandable wire mesh tube that is generally inserted into the body when flow in a passageway is being restricted. In Fig. 27.17, the insertion of a stent into a coronary artery where an aneurysm has occurred can reduce the pressure placed on the artery by the aneurysm. A stent and deflated balloon are inserted via a catheter through the groin artery. The balloon is inflated, thus expanding the stent, and then the balloon is removed, leaving behind the expanded stent in the artery and reestablishing the flow of blood to the heart [50]. Along with facilitating the flow of blood, stents have also been used to permit the flow of bile, urine, and air [43]. During the insertion or removal process of a stent, attention to the friction forces must be considered to prevent tissue damage. Two techniques are often used to minimize the friction, the first is by coating the outside of the stent with a biolubricant usually a hydrophobic polymer and the second is to introduce a biolubricant into the guiding catheter to be ejected into the passageway [51, 52]. A multidisciplinary approach to understand the tribological and biological phenomena is important when one considers the procedure to intravenously place a stent into a patient's body with minimal health issues.

4.6 *Slips and Falls*

On a daily basis, billions of people around the world rely on friction and the resilience of the human body to prevent slips, falls, and injury when walking on wet or slippery floors caused by rain, snow, wax, or other contaminants. Slips and falls are a serious issue because they can lead to bone fractures, disability, medical expenditures, and fatalities [53–55]. When walking with a particular gait, there is a required amount of friction necessary to maintain proper balance and to ensure that a slip does not occur. In a similar manner to an automobile hydroplaning, instances can occur when a third body contaminant becomes entrained between the floor and the bottom of a shoe producing a thin lubricating film. This thin film can reduce the nominal contact of the asperities within the shoe–floor interface resulting in a lower available coefficient of friction. At this instance, if the available friction coefficient falls below the required coefficient of friction, this can result in loss of traction where a slip or fall is most likely to occur [56, 57]. Often, the interactions are not this simple because in the event that a person realizes that a floor is wet or slippery that person can change to a non-slip gait by walking carefully to reduce the required friction from 33 to 16 % [56]. Due to human correction, the available friction quantifies the slip-resistance at the floor–shoe interface. Tribological investigations into slips and falls have revealed that the underlying mechanism that causes a slip and fall is the dynamic coefficient of friction, which is the ratio of shear force to the normal ground reaction force. In the presence of even dry ground, a safe level of the dynamic coefficient of friction is between 0.20 and 0.40, and to ensure safe walking the required coefficient is about 0.17–0.23 [58–62]. During a typical stride, a peak normal force and shear force occur around 0.1 s after a heel strikes the ground [61]. Thus, during a stride a slip may not occur immediately, but shortly after the heel strike as the normal force reaches its peak value and lowers the dynamic coefficient of friction facilitating a slip.

4.7 *CASE Study: Tribology and the NBA*

An example of friction in everyday life arose in the National Basketball Association (NBA) during 2006 when the NBA transitioned from leather basketballs to synthetic basketballs and back to leather basketballs. The motivation for the change in basketball material was to ensure consistent feel and bounce in each ball used because the leather material was not the same for different leather balls due to the natural reasons that no two cowhides are the same, they differ biologically. During the adoption process of the new synthetic basketballs, players began to experience difficulty in controlling the new balls because they bounced differently than the leather ones under dry and wet conditions. An investigation was performed and the results concluded that frictional differences between the balls substantiated the players' complaints. The synthetic balls when dry have a coefficient of static friction of

about 3.20, which is about twice as large as the leather balls coefficient of static friction of 1.69, and for this reason the synthetic balls appeared stickier and thus easier to grip. The situation was quite the opposite when moisture was added to the surface of each ball. The synthetic balls exhibited a 30 % lower coefficient of friction than the leather balls when moist, because synthetic balls had a lower moisture absorption rate which was approximately 8.6 g of water per minute, when compared to the 70 g/min absorption rate for the leather balls. Moreover, the synthetic balls maintained a thin lubricating film on the surface that made them feel more slippery and thus harder to grip and control. In contrast, the leather balls having the higher moisture absorption rate were easier to handle in the presence of moisture. Tribological testing was performed using a lubricant such as Visine to mimic the properties of sweat and a silicon substrate was used to replicate human tissue. After applying the Visine lubricant to the silicone, the coefficient of friction gradually increased by at least 30 % for the leather ball, thereby making it stickier and thus easier to grip and control. A quasi-saturation test was performed on the leather ball indicating that by adding an excess amount of lubricant, a reduction of 20 % in the coefficient of friction was observed relative to a dry ball. For the synthetic ball, the coefficient of friction reduced immediately by 55 % with the first drop of lubricant and further reduction was seen with excessive application of the lubricant in the quasi-saturation testing. This is indicative of the poor absorption rate of the synthetic basketballs and the presence of a thin lubricating film. The results indicate that the coefficient of friction increased initially for the leather ball before decreasing when wet, whereas for the synthetic ball, the coefficient of friction decreased instantly when wet. In the end, the wet synthetic ball is significantly more slippery compared to a wet leather ball. This conclusion is important because basketball players perspire during the game and the synthetic ball would continually become more slippery throughout the game, whereas the leather basketball would maintain its ability to be grasped and controlled by the players. At the end of the investigation the NBA rejected the use of the synthetic balls and continues to use the traditional leather balls [63].

4.8 Conclusion

Biomedical tribology plays an important role in our daily lives from our sense of touch on our skin to blood flowing through our cardiovascular system. When investigating biomedical applications, it is important that the solutions incorporate biocompatibility to ensure health, performance, and safety for those involved. Future biomedical applications will necessitate the development of biologically benign materials that limit the number of adverse affects to the human body such as wear debris produced in artificial joint replacements. In addition, biolubricants and biocoatings for interfacing between natural and artificial tissues will aid in the utilization of biodevices and promote longevity in natural joints and organs. The largest challenges yet to be fully understood biologically will involve macro and microscopic studies in vivo and in vitro simulations and the formulation of multidisciplinary research. The tools and

framework that are currently available in biomedical engineering are extensive. Moving forward, the responsibility of engineers and tribologists will be to ensure that the patients' needs are met efficiently, economically, and effectively with the patient's health and safety being the most critical aspects.

5 Closure

The importance of tribology is event as it plays a vital role in our daily lives from computer hard drives to contact lenses and almost every machine, object, or piece of technology in the modern office. Understanding the fundamental principles of friction, adhesion, lubrication, and wear afford the continued success and development of many microscale applications such as magnetic media storage, MEMs devices, flexible media, and biomedical systems. The goal of this chapter is to illustrate the interdisciplinary aspects of microscale tribology and reveal the breadth of applications in which the science of tribology exists.

References

1. Bhushan B (2005) *Nanotribology and nanomechanics: an introduction*. Springer, Berlin
2. Mee CD, Daniel ED (1996) *Magnetic storage handbook*. McGraw-Hill, New York
3. Bhushan B (1996) *Tribology and mechanics of magnetic storage devices*. Springer, New York
4. Bhushan B (2000) *Mechanics and reliability of flexible magnetic media*. Springer, New York
5. Bhushan B (2000) Macro- and microtribology of magnetic storage devices. *Tribology series*, 38, pp 183–194
6. Bhushan B (1992) *Mechanics and reliability of flexible magnetic media*. Springer, New York
7. Miller RA, Bhushan B (1996) Substrates for magnetic hard disks for gigabit recording. *IEEE Trans Magn* 32(3):1805
8. Bhushan B (2002) *Introduction to tribology*. Wiley, New York
9. Albrecht TR, Sai F (1999) Load/unload technology for disk drives. *IEEE Trans Magn* 35(2):857–862
10. Zhao X, Bhushan B (2000) Lubrication studies of head–disk interfaces in a controlled environment Part 1: effects of disk texture, lubricant thermal treatment and lubricant additive on the durability of the head–disk interface. *J Eng Tribol* 214(J6):535–546
11. Zhao X, Bhushan B, Kajdas C (2000) Lubrication studies of head–disk interfaces in a controlled environment Part 2: degradation mechanisms of perfluoropolyether lubricants. *J Eng Tribol* 214(J6):547–559
12. Zhao Z, Bhushan B (2000) Effect of head slider DLC overcoats produced by various deposition techniques on the interface failure. *IEEE Trans Magn* 36:2663–2666
13. Bhushan B, Phelan RM (1986) Frictional properties as a function of physical and chemical changes in magnetic tapes during wear. *Tribol Trans* 29(3):402–413
14. Chandrasekar S, Bhushan B (1988) Control of surface finishing residual stresses in magnetic recording head materials. *J Tribol* 110(1)
15. Bhushan B, Society of, T., Lubrication, E., and Conference, A.-S. T (1987) *Tribology and mechanics of magnetic storage systems, vol IV*. Society of Tribologists and Lubrication Engineers, Park Ridge, IL

16. Bhushan B (2001) *Modern tribology handbook*. CRC, Boca Raton, FL
17. Bryzek J (1994) Signal conditioning for smart sensors and transducers. *Sensors* 11(7):43
18. Bryzek J, NovaSensor L (1994) Smart sensors and transducers-signal processing considerations. *Proc Int Instrum Symp* 40:33
19. Bhushan B (2004) *Springer handbook of nanotechnology*. Springer, Berlin; New York
20. Hornbeck LJ, Nelson WE (1988) Bistable deformable mirror devices. *OSA Technical Digest Series*, 8, pp 107–110
21. Guckel H, Burns D, Christenson T, Tilmans H (1989) Polysilicon X-ray masks. *Microelectron Eng* 9(1–4):159–161
22. Mastrangelo CH (1997) Proceedings of international conference on solid-state sensors and actuators, Chicago, IL, 16–19 Jun 1997. Transducers Research Foundation, Lausanne
23. Mcwhorter P (2012) About MEMS, <http://www.memx.com>. Accessed 5 Oct 2013
24. Adams TM, Layton RA (2010) Introductory MEMS fabrication and applications. <http://site.ebrary.com/id/10358568>. Accessed 7 Nov 2012
25. Bhushan B (1998) Tribology issues and opportunities in MEMS. Proceedings of NSF/AFOSR/ASME workshop on tribology issues and opportunities in MEMS Kluwer Academic
26. Bhushan B (1995) *Handbook of micro/nanotribology*. CRC, Boca Raton, FL
27. Tai Y-C, Muller RS (1990) Frictional study of IC-processed micromotors. *Sensors Actuator Phys* 21(1–3):180–183
28. Lehr H, Abel S, Doepper J, Ehrfeld W, Hagemann B, Karoper KP, Michel F, Schulz C, Thuerigen C (1996) Microactuators as driving units for microrobotic systems (Invited Paper) [2906–2921]. Proceedings-SPIE The International Society for Optical Engineering(2906), SPIE, p 202–210
29. Mizukawa M, Hosaka H, Hara S (1985) Study on spherical foil bearings. *Bull JSME* 28(243):2105–2111
30. Mizukawa M, Ono K (1985) Study on spherical foil bearings. *Bull JSME* 28(243):2097–2104
31. Heinrich JC, Connolly D (1992) Three-dimensional finite element analysis of self-acting foil bearings. *Comput Meth Appl Mech Eng* 100(1):31–43
32. Lacey CA, Talke FE (1990) A tightly coupled numerical foil bearing solution. *IEEE Trans Magn* 26(6):3039–3043
33. Gross WA (1980) *Fluid film lubrication*. Wiley, New York
34. Muettue S, Lewis TS, Cole KA, Benson RC (1998) A two-dimensional model of the fluid dynamics of an air reverser. *Trans-Am Soc Mech Eng J Appl Mech* 65(1):171–177
35. Benson RC (1982) Stick/slip conditions for a thin, incomplete, elastic ring impinging on a frictional barrier. *J Appl Mech* 49(1):231
36. Frish-Fay R (1962) *Flexible bars*. Butterworth, London
37. Benson RC (1981) The deformation of a thin, incomplete, elastic ring in a frictional channel. *J Appl Mech* 48(4):895
38. Stolte J, Benson RC (1992) Dynamic deflection of paper emerging from a channel. *J Vib Acoust* 114(2):187–193
39. Stolte J, Benson RC (1993) An extending dynamic elastica: impact with a surface. *J Vib Acoust* 115(3):308
40. Stolte JJ (1992) An extending dynamic elastica: analysis of deformation due to inertial loads and impact with a surface. Thesis (Ph. D.)—University of Rochester. College of Engineering and Applied Science. Dept. of Mechanical Engineering
41. Nakano K, Horiuchi K, Soneda T, Kashimoto A, Tsuchiya R, Yokoyama M (2010) A neural network approach to predict tactile comfort of applying cosmetic foundation. *Tribol Int* 43(11):1978–1990
42. Horiuchi K, Kashimoto A, Tsuchiya R, Yokoyama M, Nakano K (2009) Relationship between tactile sensation and friction signals in cosmetic foundation. *Tribol Lett* 36(2):113–123
43. Blau PJ (2009) *Friction science and technology: from concepts to applications*. CRC, Boca Raton, FL
44. Care VV (2011) Contacts can now take care of themselves!. 16-Nov 2011. Vision Service Plan. <http://vspblog.com/contacts-can-now-take-care-of-themselves/>. Accessed 5 Oct 2013

45. Schmalzried TP, Jasty M, Harris WH (1992) Periprosthetic bone loss in total hip arthroplasty. Polyethylene wear debris and the concept of the effective joint space. *J Bone Joint Surg* 74(6):849–863
46. Shanbhag AS, Jacobs JJ, Glant TT, Gilbert JL, Black J, Galante JO (1994) Composition and morphology of wear debris in failed uncemented total hip replacement. *J Bone Joint Surg* 76(1):60–67
47. Howie DW, Haynes DR, Rogers SD, McGee MA, Pearcy MJ (1993) The response to particulate debris. *Orthop Clin North Am* 24(4):571–581
48. Fisher J (1994) Wear of ultra high molecular weight polyethylene in total artificial joints. *Curr Orthop* 8(3):164–169
49. Livermore J, Ilstrup D, Morrey B (1990) Effect of femoral head size on wear of the polyethylene acetabular component. *J Bone Joint Surg* 72(4):518–528
50. Images, N. M. A. G. (2012) Coronary artery: insertion of a stent into a coronary artery. *Encyclopedia Britannica*
51. Kelley DW (2000) Lubricious medical devices, U.S. Patent 6,071,266
52. Dobies DR, Cohoon A (2006) Injecting lubricant into the guiding catheter enables stent deployment. *J Invasive Cardiol* 18(5):146–148
53. Courtney TK, Webster BS (1999) Disabling occupational morbidity in the United States. An alternative way of seeing the Bureau of Labor Statistics' data. *J Occup Environ Med* 41(1):60–69
54. Cumming RG, Klineberg RJ (1994) Fall frequency and characteristics and the risk of hip fractures. *J Am Geriatr Soc* 42(7):774–778
55. Runge JW (1993) The cost of injury. *Emerg Med Clin North Am* 11(1):241–253
56. Cham R, Redfern MS (2002) Changes in gait when anticipating slippery floors. *Gait Posture* 15(2):159–171
57. Redfern M, Cham R, Gielo-Perczak K, Gronqvist R, Hirvonen M, Lanshammar H, Marpet M, Yi-Chung Pai C, Powers C (2001) Biomechanics of slips. *Ergonomics* 44(13):1138–1166
58. Gronqvist R, Roine J, Jarvinen E, Korhonen E (1989) An apparatus and a method for determining the slip resistance of shoes and floors by simulation of human foot motions. *Ergonomics* 32(8):979–995
59. Gronqvist R, Hirvonen M, Rajamaki E, Matz S (2003) The validity and reliability of a portable slip meter for determining floor slipperiness during simulated heel strike. *Accid Anal Prev* 35(2):211–225
60. Redfern MS, Bidanda B (1994) Slip resistance of the shoe-floor interface under biomechanically-relevant conditions. *TERG Ergon* 37(3):511–524
61. Strandberg L (1983) On accident analysis and slip-resistance measurement. *Ergonomics* 26(1):11–32
62. Buczek FL Jr, Banks SA (1996) High-resolution force plate analysis of utilized slip resistance in human walking. *J Test Eval* 24(6):353
63. National Geographic Society (2012) <http://kids.nationalgeographic.com/kids/stories/spacescience/basketball/>. Accessed 5 Oct 2013
64. Totten GE, Bruce RW (2006) *Handbook of lubrication and tribology*. CRC Press, Boca Raton, FL

Exercises

1. Provide an analogy that illustrates the scalability of how difficult a task it is to lubricate the interface of a read–write head hovering over a spinning disk. Explain two mechanisms that are detrimental to the performance of a magnetic storage device.

2. What are some possible applications of MEM systems?
3. Provide examples of each, where foil bearings, flexible media, and wound roll transport play a role. In your home, office, or school, how many machines utilize flexible media?
4. Briefly describe four applications of biotribology.
5. Why did the NBA eventually reject synthetic basketballs reverting back to leather balls?

Answers

1. An analogy that illustrates a 25 nm flying height for the head and medium with a relative speed of 20 m/s is that of an aircraft traveling 900 km/h at a distance of 0.2 μm from the ground. Stiction and wear are two mechanisms that are detrimental to the performance of a magnetic storage device. Stiction is liquid-mediated adhesion from ambient moisture that becomes entrained between the lubricating interfaces. During the contact start-stops adhesive wear can occur resulting in tape debris which can behave as a third-body abrasive material further damaging the tape and disrupting the magnetic signal reading.
2. Possible applications of MEMS or NEMS technology include acceleration pressure, and chemical sensors; linear and rotary actuators; electric motors; gear trains; gas turbines; nozzles; pumps; fluid valves; switches; grippers; tweezers; and optoelectric devices.
3. Foil bearings and flexible media transport are used extensively in devices such as printers, scanners, copiers, and fax machines. Wound rolls are used in various size cassette tape drives from large movie films to VHS tapes to smaller audio cassettes used in portable media devices. In the authors' office there is a printer and scanner connected to the computer and copier for making duplicates.
4. Applications of biotribology include the (1) personal-care industry (hair-care products, nail-polish, makeups, foundations, skin creams, and lotions); (2) contact lenses; (3) artificial joints; and (4) stents used in the cardiovascular system. The personal-care industry investigates the tribological interaction between the body, particularly the skin and the cosmetic for tactile sensations. Contact lens tribology is important because minimal friction between the eye and the lenses is important for comfort and safety. Artificial joints are investigated for the effects of wear, which can cause wear debris contamination within the body. Stents must be well understood in terms of friction to prevent unwanted tissue damage and adequate blood flow with minimal resistance.
5. A synthetic basketball does not adsorb moisture as much as a leather basketball. Thus, when in use synthetic basketballs became more slippery than leather basketballs, and ultimately harder to control. For this reason, the NBA rejected the use of synthetic basketballs and went back to the use of leather basketballs, which they currently use.

Erratum

Tribology for Scientists and Engineers

From Basics to Advanced Concepts

**Pradeep L. Menezes • Sudeep P. Ingole • Michael Nosonovsky •
Satish V. Kailas • Michael R. Lovell**

Editors

P.L. Menezes et al. (eds.), *Tribology for Scientists and Engineers:
From Basics to Advanced Concepts*, DOI 10.1007/978-1-4614-1945-7,
© Springer Science+Business Media New York 2013

DOI 10.1007/978-1-4614-1945-7_28

The publisher regrets that the department name was mistakenly swapped between two coeditors. The correct address details are given below.

Sudeep P. Ingole
Department of Marine Engineering
Texas A&M University
Galveston, TX, USA

Michael Nosonovsky
Department of Mechanical Engineering
University of Wisconsin-Milwaukee
Milwaukee, WI, USA

The online version of the original book can be found at
<http://dx.doi.org/10.1007/978-1-4614-1945-7>
